Distribution Categories:
Magnetic Fusion Energy (UC-20)
Fusion Systems (UC-20d)

ANL/FPP-82-1

ARGONNE NATIONAL LABORATORY
9700 South Cass Avenue
Argonne, Illinois 60439

A DEMONSTRATION TOKAMAK POWER PLANT STUDY (DEMO)

Fusion Power Program

September 1982

M. Abdou (ANL)
C. Baker (ANL)
J. Brooks (ANL)
D. DeFreece (MDAC)
D. Ehst (ANL)
R. Mattas (ANL)
G. D. Morgan (MDAC)
D. Smith (ANL)
C. Trachsel (MDAC)

G. Arvey (RMP)
V. Bailey (PSI)
K. Barry (RMP)
M. Billone (NU)
C. Boley (ANL)
R. Burk (MDAC)
Y. Cha (ANL)
J. de la Mora (RMP)
K. Evans (ANL)
P. Finn (ANL)
M. Foss (ANL)
Y. Gohar (ANL)
A. Hassanein (ANL)
S. Huang (RMP)
J. Jung (ANL)
R. Kee (RMP)
H. Klumpe (RMP)
J. Leloudis (RMP)
R. Leonard (ANL)
Y. Liu (ANL)
S. Majumdar (ANL)
H. Mantz (MDAC)
R. McGrath (PSU)
A. Mense (MDAC)
B. Misra (ANL)
A. Moretti (ANL)
R. Nygren (ANL)
C. Petty (UM)
V. Stubblefield (MDAC)
W. Terry (PU)
L. Turner (ANL)
L. Waganer (MDAC)

ANL - Argonne National Laboratory
MDAC - McDonnell Douglas Astronautics Company
NU - Northwestern University
PSI - Pulse Sciences, Inc.
PSU - Pennsylvania State University
PU - Purdue University
RMP - The Ralph M. Parsons Company
UM - University of Missouri-Columbia

Acknowledgements

We would like to express our appreciation to W. Bird (University of Texas at Austin) for information on compulsator design, and to G. Rohwein and M. Buttram (Sandia National Laboratory) for information on REB pulsed power systems. We would also like to thank R. Stimac (ANL), and D. Riser and R. Williams (MDAC) for the preparation of graphics. We would like to acknowledge the substantial efforts of C. Hytry, L. Legerski and J. Ruettiger (ANL), and R. Seger, L. Merritt and S. Davidson (MDAC), for preparation of the manuscript. Special thanks are due to M. Pagnusat (ANL) for excellent overall coordination of the editing and preparation of the report.

Table of Contents

ABSTRACT

A study of a Demonstration Tokamak Power Plant (DEMO) has been completed. The study's objective was to develop a conceptual design of a prototype reactor which would precede commercial units. Emphasis has been placed on defining and analyzing key design issues and R&D needs in five areas: noninductive current drivers, impurity control systems, tritium breeding blankets, radiation shielding, and reactor configuration and maintenance features. The noninductive current drive analysis surveyed a wide range of candidates and selected relativistic electron beams for the reference reactor. The impurity control analysis considered both a single-null poloidal divertor and a pumped limiter. A pumped limiter located at the outer midplane was selected for the reference design because of greater engineering simplicity. The blanket design activity focused on two concepts: a Li_2O solid breeder with high pressure water cooling and a lead-rich Li-Pb eutectic liquid metal breeder (17Li-83Pb). The reference blanket concept is the Li_2O option with a PCA structural material. The first wall concept is a beryllium-clad corrugated panel design. The radiation shielding effort concentrated on reducing the cost of bulk and penetration shielding; the relatively low-cost outboard shield is composed of concrete, B_4C, lead, and FE 1422 structural material. Major configurational features include eight TF coils with a substantially reduced vertical dimensions, eight first wall/blanket limiter modules, and a common vacuum boundary for the TF coils and plasma chamber. This feature was chosen primarily to simplify TF coil replacement operations. The DEMO reactor delivers 330 MW(e) of net power from a total thermal power of 1138 MW. The reactor has a major radius of 5.2 m and an average neutron wall loading of 2.1 MW/m^2. An overall availability goal of 50% was selected. The total estimated PACE cost is $2350 M. Substantial comparisons are made with the STARFIRE Commercial Tokamak Power Plant design.

CHAPTER 1

INTRODUCTION

Chapter 1

Table of Contents

1.0 INTRODUCTION

This document is the final report of a Demonstration (DEMO) Tokamak Power Plant Study which was carried out from October 1980 to September 1982. An interim report[1] was issued in March, 1982 which documented the results of the first year of the study as well as summarizing the results of a workshop held at ANL in January, 1982, to review the status of DEMO Study. Thus, this final report and the interim report represent a full documentation of the results of the study.

This chapter will briefly restate the objectives and approach of the study as well as the anticipated role of the DEMO in the U.S. fusion program. Further discussion is presented in the interim report. The next chapter will present an overview of the study along with major study conclusions. Chapter 3 will discuss R&D needs for the five major areas emphasized in this study: plasma current drive, impurity control, tritium breeding blankets, radiation shielding, and remote maintenance and reactor configuration. The next five chapters (4 to 8) deal with these five areas in detail. Balance of plant design considerations are discussed in Chapter 9 and a cost estimate/economic analysis is presented in Chapter 10.

1.1 Study Objectives and Approach

The past several years have seen substantial progress in the U.S. and world fusion energy programs. In particular, successes in the tokamak research program have resulted in a high degree of confidence that the Tokamak Fusion Test Reactor (TFTR) will demonstrate energy breakeven and thus culminate the demonstration of the scientific feasibility of fusion. This has stimulated a substantial effort on defining the next step in the tokamak development program as well as defining a program to demonstrate the engineering feasibility of fusion energy. This activity has centered in the past around the concept of a Fusion Engineering Device (FED)[2] and has been supported by the INTOR project.[3] During this past year, a new program strategy has been developed by the U.S. Department of Energy which calls for the design, construction, and operation of an Engineering Test Reactor (ETR) which would probably be a more aggressive step than the FED, but would be initiated at a later time than originally planned for the FED. At the same

time, the STARFIRE study[4] and other tokamak reactor designs have examined the potential commercial applications of the tokamak approach. We have, then, a situation where one has a firm picture of the current research program (ongoing experiments and TFTR), initial consideration of an ETR, and a perspective on the long-range goal of a commercial tokamak reactor.

A major issue for the U.S. magnetic fusion energy program is to determine the step or steps between TFTR and a commercial tokamak reactor. While we are concerned here with the development path for tokamaks, it is recognized that there are other viable commercial fusion reactor concepts. By attempting to better understand the development steps for tokamaks, we anticipate that much useful information will be generated of relevance to the other magnetic fusion concepts. Also, a better definition of the post-ETR step will provide very useful feedback to the ETR project in terms of its mission and desirable design features. In fact, features viewed as desirable for commercial reactors (e.g., RF heating with current drive, and pumped limiters) are being considered for the ETR.

The basic goal of this study was to provide a technical perspective and conceptual design of the tokamak device that might follow the ETR. The role of such a device in the overall program is discussed further in the next section. The effort was focused on designing the key features of such a device with the objective of providing design information for guiding the research and development efforts. While a reference conceptual design for the DEMO has been developed, less emphasis was placed on a single point (as was done in the STARFIRE study) and more emphasis was placed on exploring major design features. Certain areas (e.g., plant design) received only a limited effort. However, a sufficiently detailed design was developed to provide a reasonable preliminary cost estimate for the DEMO.

1.2 Role of the DEMO

The objectives and requirements of the DEMO can only be viewed as a part of a comprehensive fusion research and development plan. Because the required research and development programs are substantial and because the time scale involved is long, the fusion development plan has to remain flexible. Consequently, the missions (and even the number) of the various devices to be constructed between now and fusion commercialization cannot be firmly

determined at this time. The focusing and sharpening of the objectives and features of the specific devices will occur as a part of an evolutionary process over a number of years. One purpose of this study was to define a set of objectives for the DEMO that can serve as input to this evolutionary process.

The DEMO does not need to produce economically competitive electric power. It needs only to demonstrate that it extrapolates to an economically competitive system. This will be done during the design and development effort for DEMO and during early operation. A key requirement for a commercial reactor to be economically competitive is that it achieve a plant availability factor of ~ 65-75%. Minimizing the risk in achieving such an availability factor in commercial reactor requires that: (a) extrapolation of technologies from the DEMO to a commercial reactor should be straightforward--practically all technologies to be used in the commercial reactor should be demonstrated in the DEMO; (b) extrapolation of performance parameters between the DEMO and the commercial reactor should be minimized; and (c) achievement by DEMO of a sufficiently high availability during initial operation so that the additional improvement in availability required for commercial reactors can be shown to be a reasonable extrapolation, after modifications that were identified during the operation construction of DEMO and the data obtained from tests in other development programs are incorporated.

The above considerations provide incentives for constructing as advanced a DEMO as possible. On the other hand, there are incentives for constructing a "less-advanced" DEMO in order to minimize the risk associated with the construction and operation of the DEMO itself. An examination of the results of near-term and commercial reactor studies carried out over the past several years indicate that the advances required in technology, component reliability, and availability between present devices and commercial reactors are very substantial. To minimize the risk associated with commercial reactors, the burden of demonstrating the required advances in physics and technology beyond ETR will have to be borne by the DEMO and complementary development programs. All commercial fusion technology and physics requirements which are not demonstrated in ETR will represent risks deferred from ETR that must be taken in the DEMO. Therefore, results derived from the DEMO study should provide feedback into defining the requirements on ETR.

In reviewing past demonstration devices, a range of two to ten is typical for the step size (scale factor) in reactors from DEMO (pilot) to commercial. When only power plants are considered, the step size range reduces to approximately three to five. The range of step sizes was exhibited by the LWR (60 to 180 to 500 MWe). The Phoenix (French breeder) DEMO has an output of 230 MWe, and the Creys Malville commercial plant will have an output of about 1200 MWe. The Clinch River Breeder Reactor is designed for 350 MWe, and design studies for the Prototype Large Breeder Reactor show outputs of approximately 1000 MWe. A further example of step size is obtained by comparing the Fort St. Vrain HTGR, with an output of 330 MWe, to the next units which were designed for 800 to 1200 MWe. Based on these prior examples, a fusion DEMO sized for 200 to 300 MWe would be appropriate.

For the purposes of this study, we have made some broad assumptions concerning ETR and the fusion development program:

- ETR construction and operation will demonstrate integrated technologies for confining, heating, fueling, and burn control of the plasma. These include superconducting magnets, RF or other plasma heating technology, pellet injection or an alternative, vacuum, and tritium processing (except tritium recovery from the blanket).

- A credible impurity control system will be developed through testing in ETR and complementary physics and engineering facilities.

- Although ETR may not be operated in steady-state, sufficient testing will be performed in ETR and other complementary facilities to demonstrate the feasibility of steady-state operation before the construction of the DEMO.

- Tritium-breeding blanket technology will be aggressively pursued by testing in fission reactors and other complementary facilities in order to select no more than three blanket concepts. Testing in ETR will provide sufficient information to confirm the selection of the blanket design for the DEMO.

- There will be insufficient time prior to construction of the DEMO to develop and qualify a structural material other than stainless steel. A combination of testing in ETR, fission reactors, and other complementary facilities will provide the required information for stainless steel. Other materials will have to be qualified for special applications such as limiters or divertor collector plates.

- An availability factor of about 20% or more will be achieved in ETR. Learning experience from complementary technology development efforts and early ETR operation will confirm the design extrapolation to the DEMO.

Based on the above assumptions, we can state the following broad objectives for the DEMO:

- Demonstrate a level of performance for all components in an integrated power plant system which is satisfactorily extrapolatable to a first commercial reactor.

- Demonstrate system availability at a level which will be satisfactorily extrapolatable to a first commercial reactor.

- Demonstrate that a tritium-breeding, power-producing blanket can operate at conditions required for commercial reactors; i.e., a net tritium breeding ratio greater than unity, an acceptably low tritium inventory in the blanket, a sufficiently high temperature operation to permit acceptable thermal conversion efficiency, and other requirements similar to other components (e.g., reliability, safety, lifetime, etc.).

- Demonstrate safe and environmentally acceptable operation.

- Demonstrate compatibility with utility grid operations including off-normal conditions.

REFERENCES FOR CHAPTER 1

1. M. A. Abdou, et al., "A Demonstration Tokamak Power Plant Study - Interim Report," Argonne National Laboratory, ANL/FPP/TM-154 (1982).

2. "The Fusion Engineering Device," U.S. Department of Energy, DOE/TIC-11600 (1981).

3. "International Tokamak Reactor - Phase One," International Atomic Energy Agency, Vienna (1982).

4. C. C. Baker, et al., "STARFIRE - A Commercial Tokamak Fusion Power Plant Study," Argonne National Laboratory, ANL/FPP-80-1 (1980).

CHAPTER 2

STUDY OVERVIEW

Chapter 2

Table of Contents

Chapter 2

List of Figures

Chapter 2
List of Tables

2. STUDY OVERVIEW

2.1 Introduction

The DEMO study focused on in-depth investigations of key issues for the DEMO elements that require extensive development in parallel to and beyond ETR. These elements are: (1) non-inductive current driver, (2) impurity control and exhaust, (3) first wall and breeder blanket, and (4) reactor configuration and maintainability. These elements will have a large impact on the capital cost and availability of the DEMO. Some of these components (e.g., breeder blanket and current driver) may not be used in ETR, while for others (e.g., impurity control and configuration) the ETR solution must be checked for suitability to commercial systems.

Over the past decade, design studies and research and development efforts have been devoted to the systems for impurity control and exhaust, breeder blankets, and, to a lesser extent, non-inductive current drive. However, the state-of-the-art for these systems is not advanced enough to select a single design option, nor is it possible at this time to assure that any of the presently proposed concepts will eventually prove viable. There is a lack of important data in many critical areas and limited experimental verification of theoretical predictions in other areas. In addition, there are some design problems for which more attractive solutions must be developed.

Given the state-of-the-art for the components discussed above and recognizing the role of the DEMO in fusion development, it was judged undesirable for the DEMO study effort to focus solely on developing the details of a single design point. Rather, it is more beneficial for the national fusion program to utilize the DEMO design study as a framework for identifying key research and development paths for critical subsystems. The approach for each component was to: (1) investigate design options, (2) identify key problems and develop design solutions whenever possible, (3) select the most promising two or three design concepts, and (4) characterize the critical problems and identify key experimental and analytical data required for resolving these problems.

This study has benefited considerably from the major design studies carried out over the past decade. In particular, the results of the STARFIRE,[1] FED,[2] and INTOR[3-4] have strongly influenced the DEMO study.

In addition, the DEMO and FED/INTOR[5] activities were carried out in parallel; thus providing a good opportunity for developing consistent design strategies for tokamak development.

An interim report[6] documenting the earlier results of the DEMO work was published in March 1982. Some of the detailed results published in the interim report are not repeated in this final report.

This chapter provides an overview of the results of the study. The R&D requirements are summarized in Chapter 3.

2.2 Selection of Key Design Features and Parameters

Satisfying the DEMO objectives defined in Chapter 1 requires that the DEMO design features and performance be as close as practicable to those of a commercial reactor. Two practical constraints must be clearly recognized: (1) the DEMO capital cost should be minimized, and (2) the DEMO performance requirements should be consistent with a realistic fusion research and development plan. The constraint of a realistic fusion R&D plan has its major influence on the selection of the availability goal for the DEMO. The availability goal depends on the reliability and lifetime of all reactor components. Therefore, achieving high availability is judged to be the most costly and time-consuming phase of fusion development.

For given technological (e.g., maximum magnetic field) and physics (e.g., maximum beta) constraints, the minimum size that can be considered for the DEMO is defined primarily by ignition requirements. The FED (10 T case) and INTOR designs shown in Table 2-1 provide the range for such a minimum. For a maximum magnetic field, $B_m \simeq 10$ T, and a plasma elongation $\kappa = 1.6$, the major and minor radii are in the range of $R \simeq 5.0$-5.2 m and $a \simeq 1.2$-1.3 m. For the DEMO, we selected $B_m = 10$ T in order to reduce the design risks and cost associated with higher fields. Furthermore, results from STARFIRE, INTOR, FED, and other studies[7] indicate that $\kappa = 1.6$ is a reasonable compromise between the benefits (higher beta) of increased elongation and the equilibrium field (EF) coils requirements, particularly when all these coils are placed outside the TF coils. The optimum blanket/shield thickness for a wide range of DEMO conditions was found previously[8] to be $\Delta_{BS}^{i} = 1.2$ m. FED and INTOR operate at an average toroidal β of ~ 0.052-0.056. With these values defined, the minimum size DEMO device produces a neutron wall load, $W_n \sim 1.0$-1.3 MW/m^2.

Table 2-1. Range of DEMO Parameters Compared to TFTR, FED, INTOR, and STARFIRE

	TFTR	FED	INTOR	DEMO	STARFIRE
Thermal Power, MWth	20 Fusion	180/450	620	800-1000	4000
Elec. Power, MWe (Net)	--	--	> 10	200-300	1240
Major Radius, R (m)	2.5	5.0	5.2	5.0-5.2	7.0
Minor Radius, r_p (m)	0.9	1.3	1.2	1.2-1.3	1.9
Plasma Elongation	1.0	1.6	1.6	1.6	1.6
B_{max} (T)	--	8/10	12	10	11
Wall Loading (MW/m^2)	0.2	0.4/1.0	1.3	1.5-2.0	3.6
Availability	--	0.1-0.2	0.35	0.50	0.75
β	0.012	0.052	0.056	0.06-0.08	0.067
Q (Plasma)	> 1	5/50	60	> 10	35
Plasma Heating	Neutral Beam	RF	Neutral Beam (RF Backup)	REB or RF	RF
Impurity Control	--	Pumped Limiter	Divertor or Limiter	Limiter or Divertor	Pumped Limiter
Operating Mode	Pulsed 1.5-s burn	Pulsed 100/50-s burn	Pulsed 100-s burn	Steady-state Driver	Steady-state RF Driver
Lifetime	4×10^3 Pulses	5×10^4 Pulses	10^6 Pulses	20 y	40 y
Tritium Breeding Ratio	--	Experiment	0.6	> 1.0	> 1.0
First Wall/Blanket Material	SS (304 LN)	SS (316)	SS (316)	SS	SS (PCA)
Coolant	H_2O	H_2O	H_2O	H_2O	H_2O

The size of FED and INTOR, slightly increased to assure a comfortable ignition margin, is adequate for the DEMO except for the somewhat low value of the neutron wall load. Based on the results of STARFIRE and other studies (see, for example, Ref. 7), commercial tokamaks will likely operate with $W_n \sim$ 3.0-4.0 MW/m^2. The importance of the neutron wall load is that it directly impacts the power density and, hence, the performance characteristics and failure rate of the first wall and blanket. Therefore, it is very desirable to demonstrate high wall load operation in the DEMO. A higher wall load can be achieved only by: (a) increasing the power density in the plasma (i.e., increasing B_m or β), and/or (b) increasing the physical size of the device ($W_n \sim \beta^2 B^4 a$). Both will increase the capital cost of the DEMO. In general, better economics is obtainable for fusion reactors by increasing the plasma power density rather than increasing the reactor physical size. In particular, tokamaks are most attractive at higher beta operation. We assume in this study that some improvement in beta beyond that employed for FED and INTOR will be achievable in the DEMO. Therefore, $\beta = 0.075$ has been selected as the goal for the DEMO.

With R = 5.2 m, a = 1.3 m, $\kappa = 1.6$, $\Delta_{BS}^{i} = 1.2$ m, $B_m = 10$ T, and $\beta =$ 0.075, the neutron wall load is in the range $W_n \sim$ 1.5-2.3 MW/m^2, depending on the operating conditions selected for the plasma. The fusion power and neutron wall load vary with the average plasma electron temperature, $\bar{T}_e$. The fusion power and neutron wall load peak at $\bar{T}_e = 8$ KeV. However, the electron density, $\bar{n}_e$, also decreases in going to higher $\bar{T}_e$, and the power required for a non-inductive current drive also decreases. Selection of a relatively high wall load (2.1 MW/m^2) for the DEMO is acceptable when a current driver, such as the REB, with low circulating power requirement is utilized. Higher wall loads are desirable in most respects and can be achieved by further increases in the size of the device but with a substantial increase in the capital cost. Preliminary analysis indicates that, for the conditions defined above, the capital cost of the DEMO is directly proportional to the neutron wall load. The inability to test for higher power density in the DEMO blanket without substantial increase in the capital cost of the DEMO implies the need for appropriate parallel engineering development and testing facilities not necessarily based on a plasma confinement device.

A major conclusion of the economic analysis for STARFIRE is that the

greatest uncertainties in the economics of future tokamak power plants concern the plant availability factor. For fusion reactors to be economically competitive, a plant availability of 65-75% must be achieved. Yet, there is practically no quantitative data base for making a reliable prediction of the achievable availability factor in power-producing tokamaks. The availability factor is crucially dependent on component lifetime and reliability (low frequency of component failure) and maintainability (short downtime to replace failed components). The data base for the lifetime and reliability of components must be obtained primarily from the technology development program. Definitive information on reactor maintainability will come primarily from experience with operation and maintenance of future fusion devices such as ETR.

In the DEMO study, the great importance of the availability factor has been recognized in two ways. First, a plant availability goal of 50% was adopted for the DEMO. This DEMO goal provides an ambitious target for technology development. Since commercial reactors will be required to achieve 65-75% availability, the selected DEMO goal of 50% is a necessary minimum in order to avoid "high risk" extrapolations. Second, every effort has been taken in the DEMO study to incorporate design features and select design and technology options that enhance the probability of achieving high availability. The single most important design feature selected to maximize component lifetime and reliability in the DEMO is steady-state plasma operation. By eliminating cyclic loads, steady-state operation significantly enhance the reliability of key components such as the first wall, blanket, limiters, divertors, and magnets. In addition, the frequency of plasma disruption is greatly reduced for two reasons: (a) most plasma disruptions occur during startup and shutdown and (b) a non-inductive current driver will permit current density profile control, thus providing effective measures for controlling plasma disruptions. Accommodating the thermal energy dump and the electromagnetic forces associated with plasma disruptions currently represents a key engineering design problem, particularly for the first wall and the limiter or divertor.

Component lifetime and reliability are also enhanced in the DEMO by locating key components, whenever feasible, away from the harsh radiation environment. All the EF coils (all superconducting) are located outside the

TF coils, except for some small control coils which are located inside the TF coils but outside the radiation shield. All vacuum pumps are located in the reactor building basement where the radiation field is low.

The STARFIRE strategy of simplifying the reactor design in order to enhance component reliability and maintainability continues to be adopted in the DEMO. This has been a key approach in developing the non-inductive current drive, blanket, and impurity control concepts. Other features adopted to enhance maintainability include modularity, locating the vacuum boundary at the shield with all mechanical seals at the exterior, and placing all service connections outside the vacuum boundary.

There is a tradeoff between maintainability and capital cost in selecting the reactor configuration. The configuration developed for the DEMO favors better maintainability. This is reflected particularly in the choice of the low number (8) of TF coils and the use of one blanket/shield sector per TF coil which result in the use of larger TF coils.

2.3 Reactor Configuration and Reference Parameters

2.3.1 Reference Design

The major reactor parameters are shown in Table 2-2. The parameters were derived based on tradeoff studies to define a commercially relevant demonstration reactor that could produce a significant amount of electrical power. Emphasis has been placed on simplifying the reactor configuration by combining components, simplifying maintenance operations and providing adequate access for maintenance.

The reactor design has a major radius of 5.2 m and operates steady state at a neutron wall loading of 2.1 MW/m^2. The reactor delivers 330 MWe in addition to providing 55 MWe for recirculating power. Figure 2-1 shows the DEMO power flow. The power deposited on the limiter is dumped to minimize the power system cost.

An isometric view of the reactor is shown in Fig. 2-2. The reactor configuration utilizes 8 TF coils, 8 shield sectors, 8 limiter modules, 8 EF coils, 4 CF coils and 2 REB launchers. Figure 2-3 shows the reactor cross section. The different shadings in this figure indicate the envelopes of the

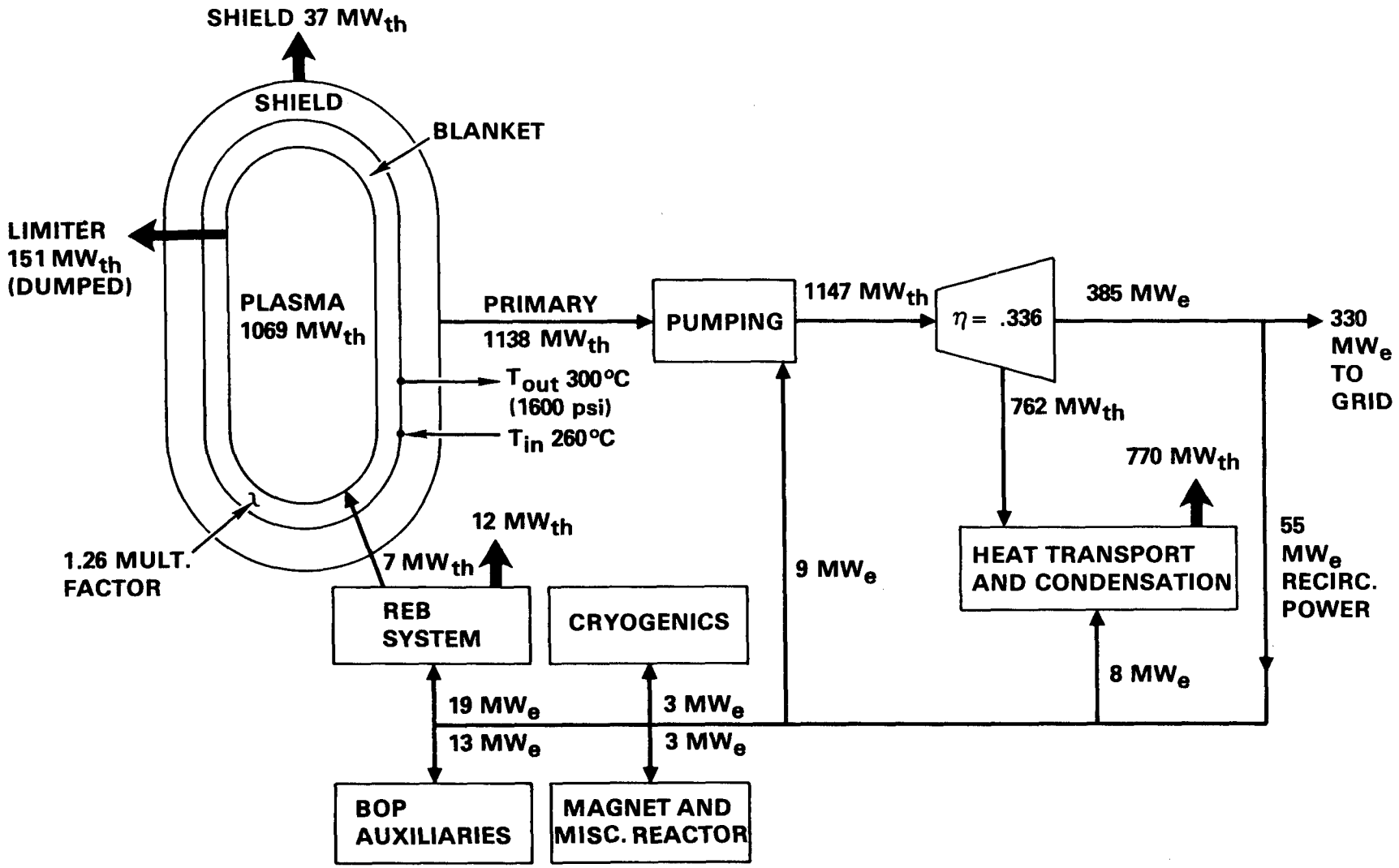

Figure 2-1. Power flow diagram for DEMO.

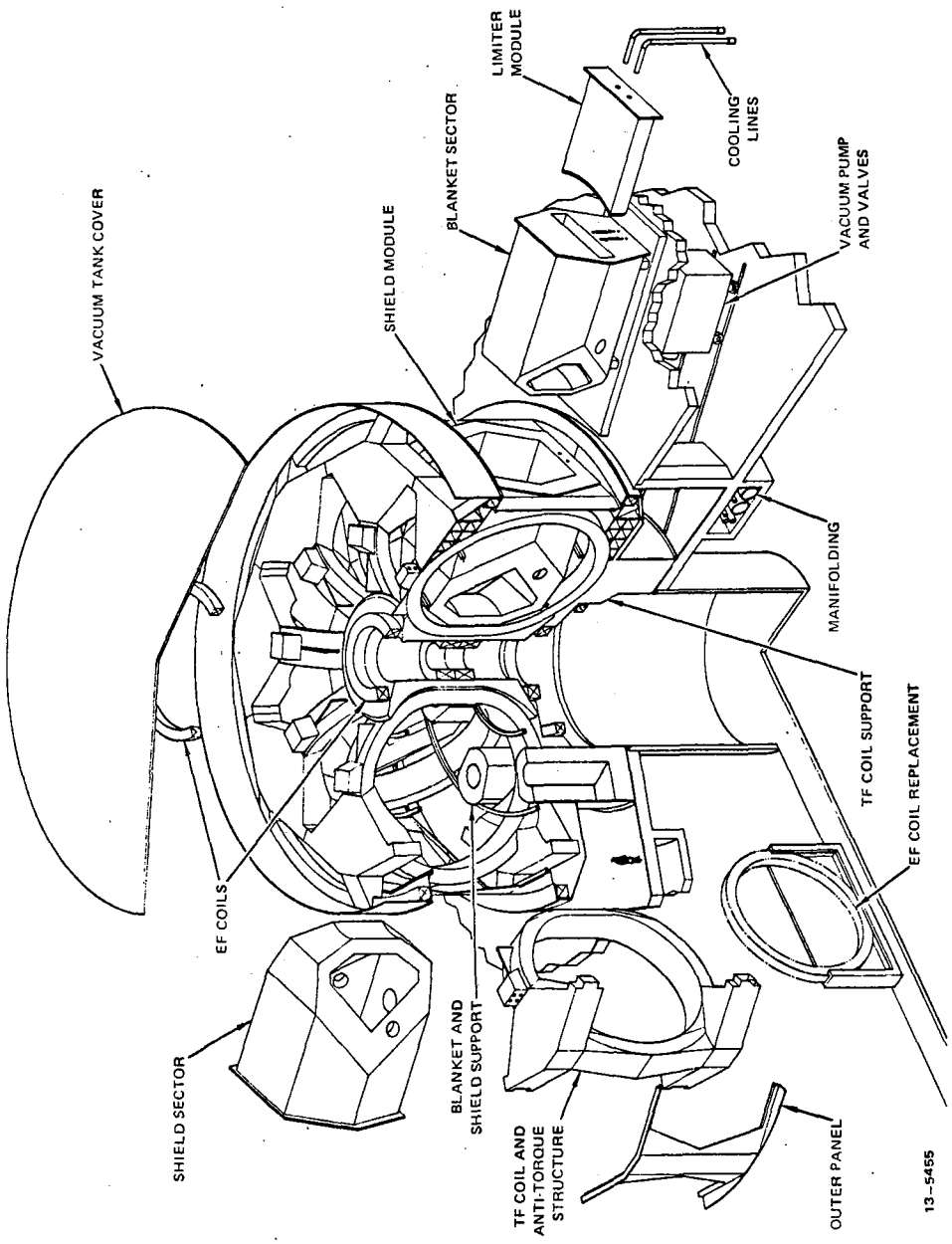

Figure 2-2. Isometric view of DEMO reference design.

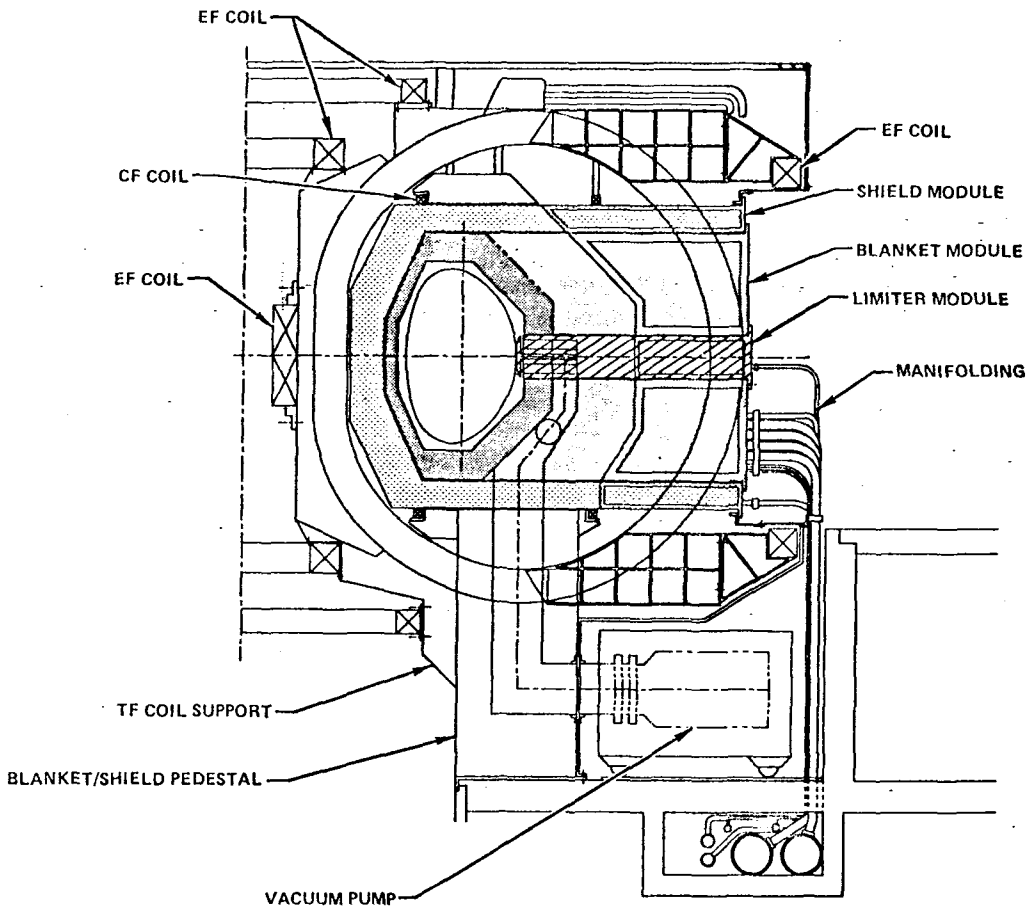

Figure 2-3. Vertical cross section of DEMO reference design.

shield, blanket, and limiter removable modules; isometric figures in Chapter 8 illustrate more clearly the solid and open (i.e., structural framework) portions of these modules.

The TF coils are designed for a 10 T peak field and utilize a NbTi bath cooled design. The design uses the center post to support the coil in-plane loads at the top and bottom of the coil inner leg. This permits the coil

Table 2-2. DEMO Major Parameters

Net Electric Power, MWe	330
Gross Electric Power, MWe	385
Fusion Power, MW	1069
Thermal Power, MW	1138
Gross Turbine Efficiency, %	33.6
Overall Availability, %	50
Average Neutron Wall Load, MW/m^2	2.1
Major Radius, m	5.2
Plasma Half-Width, m	1.3
Plasma Elongation (b/a)	1.6
Inboard Blanket/Shield Thickness, m	1.2
Plasma Scrapeoff Thickness - Inboard, m	0.2
Plasma Scrapeoff Thickness - Outboard, m	0.17
Plasma Current, MA	8.7
Average Toroidal Beta	0.075
Toroidal Field on Axis, T	4.8
Maximum Toroidal Field, T	10
Number of TF Coils	8
Peak-To-Peak Field Ripple (Plasma Edge), %	3.5
Major Radius of TF Mid-Outboard Leg, m	11.6
Plasma Burn Mode	Continuous
Plasma Heating Method	Relativistic Electron Beam
Current Drive Method	Relativistic Electron Beam
Impurity Control	Pumped Limiter
Tritium Breeder	Li_2O (or $Li_{17}Pb_{83}$)
Breeding Ratio, Net	1.05
Maximum Component Weight (TF Coil), Mg	440
EF Coil System Stored Energy, GJ	5.7
TF Coil System Stored Energy, GJ	20

height to be reduced by ~ 3 m, as compared to the conventional pure tension shape, which reduces the total EF coil stored energy by a factor of ~ 3. The coil half height is 5.46 m with an outer leg radius of 11.6 m. The

overturning forces are reacted through a 4 K beam structure which leaves a 6.2 m wide by 7.5 m high opening between TF coils for blanket/shield installation.

The EF coils also utilize a NbTi bath-cooled design. The EF coils are supported inside a common vacuum tank from the TF coils. All EF coils can be replaced without major reactor disassembly. The upper EF coils can be replaced by removing the upper dome of the vacuum tank. The lower outer EF coil requires removal of an additional ring for replacement. The lower inner EF coils can be replaced through a pit below the center of the reactor.

The TF coil and plasma chamber vacuum walls have been combined into a common boundary to simplify TF coil replacement and to minimize the inboard shield radial build. The vacuum boundary is formed by a tank over the top and sides of the reactor. The shield sector is inserted through the sides of this vacuum enclosure and join at a plane directly under each TF coil where dual seals are used to form a separate plasma vacuum chamber. Two of the eight shield sectors include dielectric breaks. The TF, CF, EF, and pocket shield sectors are designed to be long life components and should not require replacement; however, provisions are made for remotely replacing them.

The blanket, limiters, vacuum pumps and REB current drive launchers are remotely replaceable. The components are designed so they may be replaced independently of each other except for the blanket, which will require removal of limiter and REB diodes with the blanket sector.

The vacuum pumps are located in the reactor building basement and can be maintained independently of other reactor components. Each of the 8 pumps are manifolded into a common plenum inside the blanket sector shield door cavity so that four of the eight can be regenerated while the other four are operating. A regeneration time of two hours is anticipated, which results in four hours between pump regeneration. Dual gate valves are included on each pump for redundancy and to permit pump removal without breach of vacuum.

The anti-torque structure consists of a 4 K bending beam structure that forms a ring at the top and bottom of the coils in addition to the outer legs of the TF coil. This structural approach is based on the design development work done for FED/INTOR.[5] Additionally the shield rests on pedestals which are made up primarily of the shielding that surrounds the vacuum ducts. The

TF coil vertical supports are via the center post and G-10 fiberglass support pads under each TF coil. A common vacuum tank encloses all TF, EF, and CF coils and the center post. The TF coil is the heaviest component at

A total remote maintenance approach was selected for DEMO based on the desire to minimize radiation exposure to workers. It is believed that since remote maintenance is desired in a commercial reactor then DEMO should show its feasibility for all maintenance operations. Workers can be utilized in the radiation environment as a backup to the remote maintenance system.

2.3.2 Configuration Tradeoffs

The reactor configuration and maintenance approach are major factors in determining the economic viability of commercial fusion reactors. DEMO utilizes a reactor configuration and maintenance approach that typifies a commercial reactor so that shortcomings can be identified and modifications incorporated prior to construction of the first commercial demonstration reactor. In addition, cost of electricity (COE) is one of the most important aspects for commercial reactors so emphasis in DEMO was placed on reducing the elements that contribute to COE, namely:

(1) Simplified component replacement (outage time)
(2) Improved system reliability (time between outages)
(3) Reduced capital cost

These three goals were achieved during selection of the configuration by a series of innovative modifications to the reactor configuration and maintenance approaches for STARFIRE.[1]

First, simplified TF coil replacement was achieved by eliminating the need for a common vacuum tank around the inner legs of the TF coils and by adopting the 4 K anti-torque structure of INTOR.[3] It was found that, if the basic vacuum boundary was moved to the exterior of all TF and EF coils and that shield sectors were inserted through this boundary and sealed together under each TF coil, that separate vacuum boundaries could be provided for the plasma and TF coils using all planar seals. These seals are inherently simpler to replace than the common vacuum tank of previous designs where structural welds had to be cut and remade. Dual seals and a sandwich

structure wall with intermediate vacuum pumping limit tritium leakage. Additionally the 4 K anti-torque structure of INTOR was segmented with a key and slot equidistant between the coils to permit load carrying without structural welding. This permits radial coil removal after the blanket and shield sectors and the outer vacuum wall panel are removed. It is estimated that TF coil replacement can be achieved in less than six months using remote maintenance with this approach. This represents an improvement of a factor of at least two over previous designs. Additionally the inner EF coils below the reactor midplane can be replaced through a service pit below the reactor that is connected to an outside tunnel.

Simplified blanket/shield replacement was achieved by keeping the number of blanket/shield sectors equal to the number of TF coils. This permits direct access for replacement and reduces the number of coolant lines that must be disconnected for maintenance.

Design choices can affect the outage rates, but quantitative data on the reliability and lifetime of components is presently lacking. Data on the required design margins, redundancy levels, specific component designs, etc. will become available as reactors such as TFTR and ETR begin operations. Availability analysis of tokamaks has provided some guidance to DEMO to indicate that some components (e.g., magnets) will have to be significantly more reliable than other components (e.g., first wall) if a reasonable availability is to be achieved. The major factor in overall system reliability, once operating environments are established, is the total number of parts.

Improved system availability was achieved by reducing the number of parts that must be replaced (which reduces replacement time) and by reducing the number of seal joints and coolant connections that must be opened during maintenance (improves reliability). This was achieved primarily by reducing the number of TF coils since it can be shown that the minimum allowable number of blanket/shield sectors is equal to the number of TF coils. Additionally the number of connections and seals is proportional to the number of blanket/shield sectors so one sector per TF coil was chosen. The number of TF coils was reduced to eight, which was the point where access to permit single blanket and shield sector replacement (i.e., one per TF coil) and the ripple limit of 3.4% peak-to-peak at the outer plasma edge corresponded. These design changes plus the change to a common vacuum boundary reduced the number of major parts

by approximately a factor of two from STARFIRE, and reduced the number of major seals and connections by a factor three.

Capital cost of the reactor was decreased by the use of reduced height TF coils which reduces the EF coil stored energy and the overall reactor and building size. In addition a flat top vacuum tank was used to save building cost. The use of a common vacuum tank eliminated the need for an extra structural wall at the inner shield of the reactor and permits a decrease of ~ 10 cm in this area. These design modifications permit a capital cost savings in excess of $50M. The reduced height TF coil was made possible by using the centerpost to provide curvature support to the TF coils at the top and bottom which reduced overall coil height by ~ 3 m over the conventional Dee shaped coil with support at only the straight inner leg.

The reactor configuration features adopted for DEMO are reactor relevant and should be incorporated in the commercial tokamak. Major modifications to STARFIRE would include (1) combined TF coil and plasma vacuum boundaries, (2) a 4 K anti-torque structure, (3) a reduced height non-pure tension TF coil with larger outer leg radius, (4) fewer TF coils, and (5) a single blanket sector per TF coil. These modifications should make it possible to replace a TF coil in ~ 6 months and enhance replacement of all components. This should improve reactor availability without a significant change in the reactor capital costs. Incorporation of reactor relevant features into all near term devices or experiments will provide useful guidance in the development of commercial reactors.

2.4 Noninductive Current Drive

A large number of external momentum and energy sources have been proposed as candidates to sustain the toroidal current in a tokamak plasma in a purely steady-state mode of operation, without transformer windings. These drivers, which include both particle and wave sources, are cataloged in Table 2-3 and were surveyed for application to the DEMO, as reported in Ref. 6. On the basis of this survey, one driver, the relativistic electron beam (REB) was selected for more detailed study; engineering considerations and system options for the REB driver are discussed in Chapter 4.

Table 2-3. DEMO Current Driver Options

	Parallel Momentum Input	Indirect Means (Heating, Canonical Angular Momentum, etc.)
Particle injection driven currents	Neutral beam (NB) Partially ionized heavy atom beam Pulsed relativistic electron beam (REB) Pulsed intense (charge neutral) ion beam	Bootstrap Preferential alpha loss
Wave-driven currents	Compressional Alfven wave (CAW), $\omega \ll \Omega_i$ Shear Alfven wave, $\omega \ll \Omega_i$ Low-speed magnetosonic $(\omega \gg \Omega_i)$ wave $\left.\begin{matrix}\\ \\ \\ \end{matrix}\right\} \frac{\omega}{k_\parallel} < v_e$	Minority ICRH Alpha Landau and transit time damping
	Lower hybrid wave, Ion cyclotron wave, $\omega \approx \Omega_i$ High-speed magnetosonic (HSMS) wave $\left.\begin{matrix}\\ \\ \\ \end{matrix}\right\} \frac{\omega}{k_\parallel} > v_e$	ECRH Anisotropic reflection of synchrotron radiation

The dominant consideration in the driver survey[6] was the net electric power produced for each driver, since this is the primary goal of a demonstration electric power plant. Results for three drivers are presented in Fig. 2-4. For this comparison, plasma beta and current are held constant, and both the fusion power, P_f, and driver power, P_d, are computed for different temperature and density combinations. The net electric power, P_n, was estimated by the formula $P_n = 0.36 \times P_f - 22 - (P_d/\eta_d)$, where the units are megawatts. The driver electric power efficiency, η_d, is not known very accurately since these systems are all experimental, but we see that systems vary in their sensitivity to η_d. As an example, neutral beams, which have convincingly demonstrated current drive,[9] require $P_d \approx 100$ MW to maintain the toroidal current in DEMO. Since this is a substantial portion of the gross electric power ($0.36 \times P_f$), the net power is very sensitive to the driver efficiency, η_{NB}. It appears likely that an attractive steady-state DEMO is possible with a neutral D^0 driver, but advanced technology (negative ions, efficient accelerators, photo-neutralizers) would need development to achieve this promise.

At the other extreme, the REB has received relatively little experimental study, but it promises in theory to require power input of only a few times the conventional ohmic heating power, i.e., $P_d \lesssim 10$ MW. This power is almost negligible compared to the gross electric output, and, thus, the net power is insensitive to the efficiency η_{REB}, as shown in the figure. Another driver (not shown) is the compressional Alfven wave (CAW) at frequencies less than the ion cyclotron frequency, and this also promises very low circulating power.[10] Ironically, this driver has received virtually no experimental study. Prospects for efficient REB and CAW current drive are confounded by questions regarding the current density profiles which are likely to result in the steady state. If electrons behave neoclassically, there are reasons to suspect that hollow current densities would be obtained. While the stability of hollow current densities has only recently begun to receive theoretical study,[11] it seems likely that centrally peaked current densities will allow stable operation at higher betas.[12]

The lower hybrid (LH) wave has been the most successful experimental driver, but it may fail to simultaneously satisfy the DEMO requirements of substantial net power, centrally peaked current density, and purely steady-

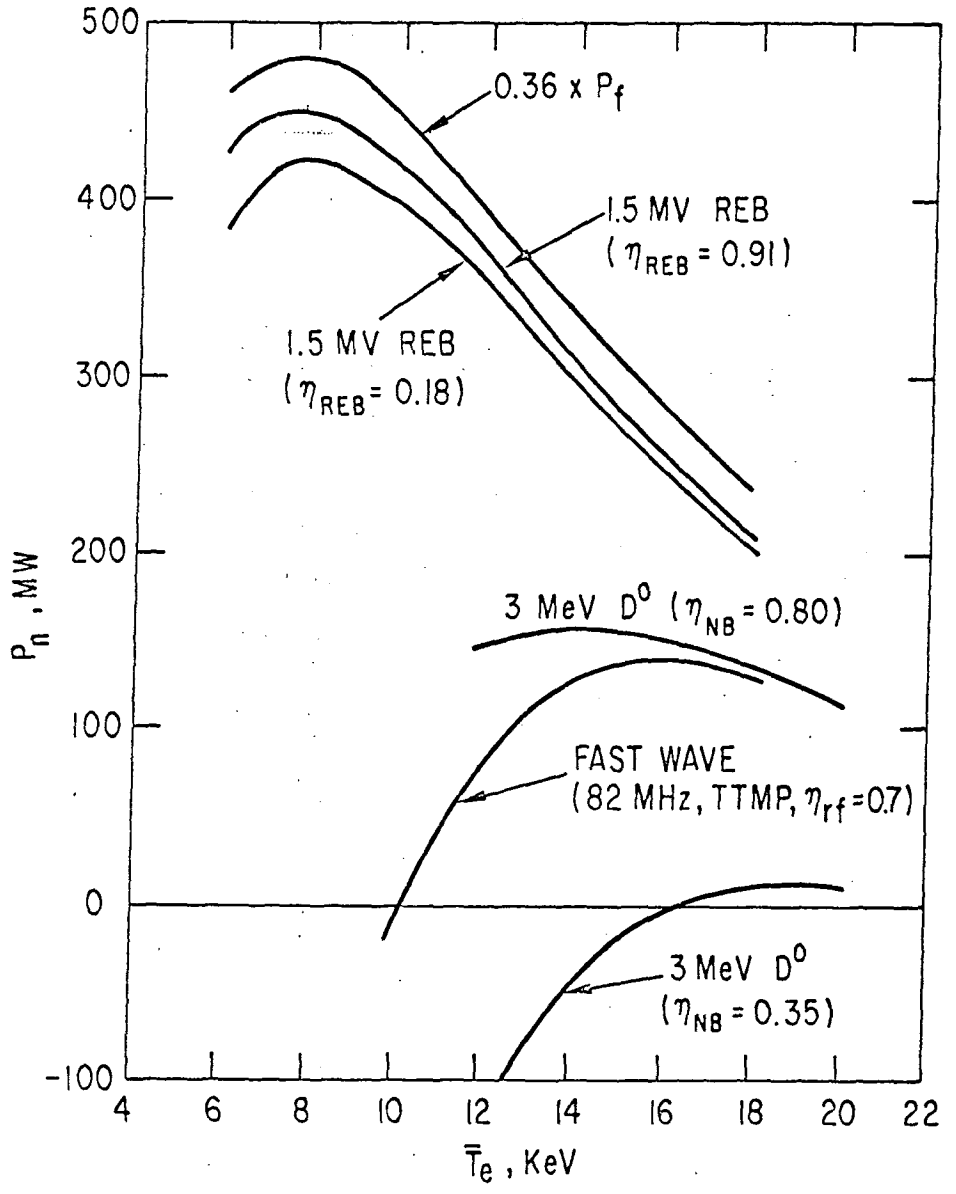

Figure 2-4. Net electric power for DEMO with three different current drivers.

state plasma operation. The reason for this is that the wave requires slow phase speeds (large $n_{\parallel}$) to be accessible to the high density central region. In consequence, in order to generate centrally peaked current density, the driver efficiency is quite small; values of $P_{LH} \gg 50$ MW are predicted for DEMO, based on a study of LH performance for FED-A.[13] One solution to this circulating power limitation would be to operate DEMO in a mode in which the plasma density (and resistivity) are periodically cycled.[14] The relative costs and benefits of this operating mode were not addressed in the present study but deserve future attention.

At frequencies above the ion cyclotron frequency, the fast wave can be a relatively efficient driver. This high-phase-speed magnetosonic wave (HSMS) has no accessibility limitation, so $n_{\parallel}$ is not limited by wave reflection. However, if $n_{\parallel}$ is close to unity, ion cyclotron damping competes with electron transit time magnetic pumping (TTMP), reducing current drive efficiency. Results for single-pass absorption in DEMO are shown in the figure. Theory suggests more favorable current drive results should occur if a tokamak reactor were designed with an aspect ratio $A \geq 5$,[15] since this would remove alpha particle resonances and permit multipass absorption at lower $n_{\parallel}$. Unfortunately, this driver has not yet received experimental tests in collisionless tokamaks.

Reactor availability and maintainability are crucial factors to a DEMO power plant. From this point of view, the neutral beam driver would be a particularly poor choice since it is physically quite large and requires a line of sight to the plasma. These features combine to hinder access to the reactor, which results in long down times for reactor maintenance, and increase the frequency of failures. In contrast, the REB and wave drivers have power transmission lines which are easily routed around corners. Additionally, these latter drivers permit the location of primary power sources in a room distant from the reactor hall, so hands-on maintenance of the sources is permissible, possibly even during reactor operation.

The capital cost of the current drive for the DEMO is important. Capital cost grows in significance if the DEMO design is extrapolated to a full scale reactor of the STARFIRE class. Preliminary estimates of the value of pure steady-state operation for STARFIRE[1] suggest this operating mode results in a 15-20% reduction in the cost of energy, compared to conventional pulsed

ohmic current generation, due to a variety of effects (less fatigue, longer component lifetime, cheaper materials, higher wall load, etc.). It would appear that the driver capital cost could be substantial (e.g., 20% of the total power plant) before it would significantly affect the economics of power generation. Roughly speaking, drivers exceeding several hundred million dollars in cost appear unattractive for DEMO, whereas costs less than $100 million appear acceptable. Those drivers requiring the smallest circulating power (e.g., the REB) allow the greatest margin for error in our cost estimates. (See Table 3-1 for a comparison of projected DEMO current driver capital costs.) It is significant to notice that most of the current drivers considered appear likely to provide enough plasma heating for ignition, with minor modifications. This feature is desirable in order to remove the need for a separate system to provide auxiliary heating.

As a result of the interim survey,[6] three systems were identified as being of the most interest as the DEMO current driver for purely steady-state plasma operation. Two of the three options, CAW and HSMS, have similar engineering requirements: 10-100 MHz frequencies, phased antennas, Faraday screens, coaxial transmission lines, ceramic windows, circulators, and high power tubes. This technology is currently being developed in support of ICRH experiments on tokamaks and, consequently, is receiving a modicum of attention for reactor applications. In contrast, the third option, the REB, has received the least attention, so in the design phase for the DEMO current driver, we concentrated on this particular option. Our conclusions, reported in Chapter 4, show the REB provides an attractive system in a reactor environment. The beneficial engineering features of the REB, and the promise of low circulating power, should stimulate future study of beam penetration and the resulting current profile from this driver.

The ratio of time averaged REB power, $\langle P_d \rangle$, to $I_o^2 R$ is displayed for the DEMO in Fig. 2-5. Our analytical theory, which assumes adequate beam penetration, is valid between the box and the circle on each curve. Our first observation is that the beam parameters can be arranged such that $\langle P_d \rangle$ is approximately twice the conventional ohmic heating value. Although the value of the toroidal tokamak resistance is controversial, we can estimate $I_o^2 R \lesssim 3$ MW, hence $\langle P_d \rangle \lesssim 6$-7 MW. A variety of beams can achieve this low a $\langle P_d \rangle$, e.g., a 1 MV-beam (relativistic mass ratio, $\gamma_d = 3$) delivering $W_d = 2.4$

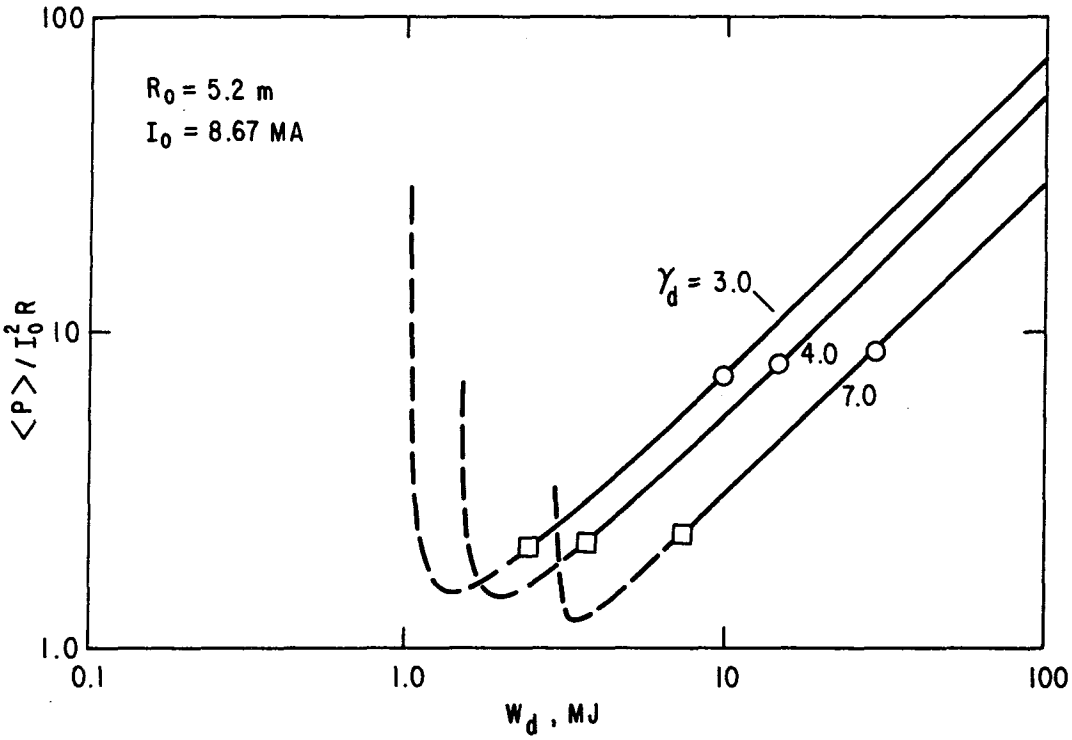

Figure 2-5. Time average power required for REB current drive in DEMO, normalized to I_o^2R.

MJ per pulse at a rep rate δt^{-1} = 2.5 Hz, or a higher energy beam, e.g., at 3.0 MV with W_d = 7.3 MJ and δt^{-1} = 1 Hz. Lower energy beams may be cheaper due to the smaller energy storage and lower voltages involved, but the higher rep rate increases the total number of shots required from the pulsed power system. For reference purposes, we have designed a 1.5 MV system with parameters as listed in Table 2-4. The large return current resistivity factor, $\alpha \gg 1$, is essential to the success of pulsed REB current drive.(6)

The plasma diode delivers 3.6 MJ at 1.533 MV with a nominal pulse width t_{t-o} = 400 μs and a cathode current I_c = 5.87 kA. Assuming a cathode current density j_c = 11.1 A/cm^2 is possible for this pulse width, a cathode area A_c = 530 cm^2 is required. Such long pulse widths are possible using compulsator energy storage (see Chapter 4), but diode operation for such pulse widths has not been achieved. With the addition of an intermediate energy storage capacitor to the power train, pulse compression to $t_{t-o} \lesssim 3$ μs is possible; plasma diode operation is more likely in this short pulse regime. The requisite technology for such high voltage pulsed power systems is currently under development at Sandia for inertial fusion applications.(16)

The plasma anode has proven effective on the toroidal experiments at the megavolt level and hundreds of kiloamperes, but for relatively short (100 ns) pulses. The longer (microsecond) pulse width will simplify the transmission line design through the blanket/shield since an impedance match will be unnecessary. Moreover, cathode currents as large as 100 kA should permit the use of magnetic insulation, which minimizes the transmission line cross-sectional area. The cathode may be located between the limiter and the first wall, and the return current flows to the anode enclosure behind the cathode, which is at ground potential. The diode is thus well protected from normal and disruptive thermal loading. The relativistic electrons are launched from the open (higher density plasma) side of the diode and follow the toroidal field lines, moving poloidally according to the rotational transform. If the REB is not completely current neutralized, it will move inwards in minor radius due to interactions with the plasma and the conducting first wall. Radial motion and partial beam trapping was observed on Macrotor,(17) but it is to be expected that some beam loss will occur due to reincidence on the top

Table 2-4. REB Characteristics (Steady State)

γ_d	= 4.0	Relativistic mass ratio
β_d	= 0.9682	$\sqrt{1 - \gamma_d^{-2}}$
β_s	= 0.4	
E_d	= 3.6 MJ	Kinetic energy per pulse
$\langle P \rangle / I_0^2 R$	= 2.15	
$\langle P \rangle$	= 6.7 MW	Time average current drive power
δt	= 0.535 s	$E_d / \langle P \rangle$
δt^{-1}	= 1.9 Hz	REB rep rate
I_{d_0}	= 23.7 MA	REB stacked current
ΔI	= 17.9 kA	Fluctuation in toroidal current
$\Delta I / I_0$	= 0.2%	
Q_d	= 2.35 C	Electric charge per pulse
n_D	= 5.4×10^{16} m^{-3}	Average beam particle density
n_d / n_e	= 2.3×10^{-4}	
$\alpha(\theta = 17°)$	= 3.1×10^3	Resistivity enhancement of return current
Δt	= 162 μs	EMF slowing-down time
t_{tr}	= 99.1 ns	Toroidal transit time
	Each Cathode (Nominal; 50% Beam Trapping Assumed)	
V_d	= 1.533 MV	Cathode (negative) voltage
t_{t-o}	= 400 μs (3 μs)	Generator pulse width
I_c	= 5.87 kA (783 kA)	
J_c	= 11.1 A/cm^2 (0.8 kA/cm^2)	340 eV, 2×10^{17} m^{-3}, DT
A_c	= 529 cm^2 (1000 cm^2)	Cathode area

of the limiter blade. It may thus be necessary to inject energy in excess of the 3.6 MJ, perhaps with an identical, synchronous diode operating at another toroidal location.

The vacuum transmission line is separated from a water line by a double ceramic window several meters beyond the first wall. The insulator is large in order to reduce the electric field strength and inhibit surface breakdown. The vacuum dimensions appear adequate to minimize neutron degradation of the insulator and allow a reasonable lifetime.

Beyond the reactor, the line extends to the nearby power supply building, where it is charged from six 0.25 MV air core pulse transformers,[16] connected in series. The 12.5 kV input to each transformer is supplied by an active rotary flux compressor (ARFC) or compulsator, which delivers the energy with a pulse width ~ 400 μs. Each ARFC is a compact, rotating energy storage device which is powered by a 2000-Hp dc or synchronous motor. The pulsed power supply has not been optimized, and a variety of electrical systems have been considered. The ARFC/transformer power train should be reliable with an acceptably long life and minimal servicing requirements. Each diode delivers $\langle P_d \rangle$ = 6.7 MW for an η_{REB} = 69%. Each diode power train costs ~ $4-5 million for steady-state current drive, assuming no special pulse shaping or compression is required. Two such systems are envisaged for the DEMO.

It is proposed that, with minor modifications, this same system can initiate, heat, and ramp up the DEMO discharge. By properly adjusting the decay index of the initial vacuum vertical magnetic field, the electrons from the first diode pulse will be launched onto contained orbits with elliptical projections in a vertical plane. Electron energy loss shrinks the orbit, so it will miss the diode on subsequent passes. A current increment, ΔI, of ~ 15 kA will result from each diode pulse, and the vertical field will be increased to maintain toroidal equilibrium. The toroidal current channel will be drawn towards the center of the vacuum chamber as the toroidal current builds up. Closed flux surfaces are expected after very few REB pulses. (SPAC VI achieved full toroidal current and a fully ionized, 800 eV plasma with a single REB pulse into its vacuum chamber, prefilled from a plasma gun.[18])

Plasma heating is possible by raising the kinetic energy per REB pulse relative to the steady-state current drive requirement. Reference to Fig. 2-5 shows that an increase of W_d from 3.6 MJ to 7.2 MJ decreases the current drive

efficiency and increases the heat input rate by about a factor of two. Since there is no need for an ohmic heating transformer, the current ramp can be fairly slow, and a long startup (~ 30 s) was selected, which minimizes the EF coil power requirement. The vertical field gives an ohmic assist to the REB current drive via the $\dot{B}_v$-induced emf. It appears possible to keep the loop voltage V_ℓ below a few volts. The ARFC/transformer system can operate at higher rep rates for several seconds without significant cost increments. If this REB heating option were selected, the ARFC rating would be increased from the current drive requirement to 7.2 MJ. An additional startup motor, rated for 2600 Hp, cw, would be attached through a clutch to each current drive motor and disconnected during the steady-state operating period. This REB system has a particular attraction in that capital costs do not increase in linear proportion to the power output since the motors and ARFC can be overpowered by large factors for the short period required for auxiliary heating.

2.5 Impurity Control System

A comprehensive effort has been devoted to the study of impurity control for DEMO. The work has focused on trade-off studies in the areas of systems selection, system location in the reactor, materials selection, and plasma edge considerations. Since the impurity control system operates in an extremely severe environment, a major goal of the trade-off studies was to maximize the component lifetime while maintaining adequate impurity removal. Following the trade-off studies, a reference design was selected, and the lifetime of the system was calculated.

In general, the lifetime of the impurity control system tends to be short because of rapid surface erosion and the relatively small thickness of the plasma side material that can be tolerated under high heat flux conditions. The key erosion mechanisms of physical and chemical sputtering along with vaporization and melting were analyzed in detail. Redeposition of sputtered material was examined, and net erosion rates were estimated. Maximum allowable thickness were determined using the results of thermal-hydraulic, stress/fatigue, and radiation effects analyses. The results of the trade-off analyses along with the reference design parameters are summarized below.

2.5.1 Concept Selection

The primary purposes of the impurity control system are to exhaust a small amount of helium ($\lesssim$ 5%) from the plasma, to remove heat, and to provide for an acceptably small level of sputtered impurities in the plasma. Most impurity control systems can be divided into two groups: divertors and limiters. A divertor system employs modifications to the magnetic field such that ionized particles escaping from the plasma are swept out of the plasma chamber and into the divertor where they are neutralized at the divertor collector plates. Most of the neutralized particles are then pumped into the vacuum system. The limiter projects directly from the first wall and intercepts ionized particles escaping from the plasma. These particles strike the limiter surface and are neutralized. The pumped limiter has holes or slots where a small fraction (5-10%) of the incident particles are captured and neutralized. Most of the captured particles are then pumped into the vacuum system.

The present study has considered both divertor and pumped limiter systems for impurity control. For the purposes of comparison, a single-null, poloidal divertor, similar to that used in INTOR, has been selected as the baseline divertor system, and a pumped limiter similar to that used in STARFIRE, has been selected as the baseline limiter system.

The selection of a reference system is based upon impurity removal efficiency, overall mechanical and magnetic configuration, and maintenance requirements. Both the divertor and limiter concepts can provide acceptable helium exhaust, and both concepts appear capable of handling the heat loads. The effect of sputtering and radiation damage is comparable for divertors and limiters leading to roughly equivalent lifetimes. However, the potential for preventing sputtered impurities from entering the plasma is certainly better for the divertor, which is further removed from the plasma. There is also some experimental evidence that poloidal divertors function to provide cleaner discharges. On the other hand, poloidal divertors require additional magnets and large power supplies. The poloidal divertor also occupies a larger volume in the reactor. Thus, there are additional costs and engineering complexities associated with the use of poloidal divertors. Overall, there are considerable uncertainties in the performance of both concepts, but because of the

potential for a reduced reactor size and greater engineering simplicity, the pumped limiter was selected as the reference impurity control system.

The limiter location has an impact on the overall reactor design and configuration. Three locations, the outer midplane, the upper and lower 45° blanket segments, and the bottom of the plasma chamber, were evaluated. The major considerations for limiter placement are: (1) sensitivity to variations in plasma shape and position, (2) impact on reactor and magnet size, (3) impact on tritium breeding, (4) response to disruptions, (5) impact on component fabricability, and (6) impact on reactor accessibility. Overall, the outer midplane location is favored. This location is the least sensitive to plasma variations, and it also results in the minimum size blanket/shield and TF coil configuration. The impact of tritium breeding, disruptions, and fabrication on limiter location selection is minor. The midplane location reduces the available access for other reactor penetrations. However, for DEMO, the reduced access is not expected to present any significant problems. Therefore, the outer midplane has been selected for the limiter location.

2.5.2 Reference Design

The reference impurity control system is a shaped, double-edged, pumped limiter located at the outer midplane of the reactor, as shown in Figs. 2-6 and 2-7. The limiter configuration utilizes removable limiter modules to facilitate maintenance of the relatively short-lived limiter blades. One module is used in each of the eight reactor sectors. The limiter consists of six replaceable limiter blade segments per module, mounted by the coolant manifolding to the main body of the module. The overall height of each segment is 100 cm, and the toroidal width is 85 cm. The limiter blade consists of a water-cooled heat sink covered by a protective surface material. The protective material on the front surface is beryllium, ~ 2.5 cm thick, and the protective material on the leading edges is tantalum, ~ 1 mm thick. The heat sink thickness varies from ~ 1.5 cm at the leading edges to ~ 10 cm at the center. The heat sink material has not been selected, but the leading candidates are copper and vanadium alloys.

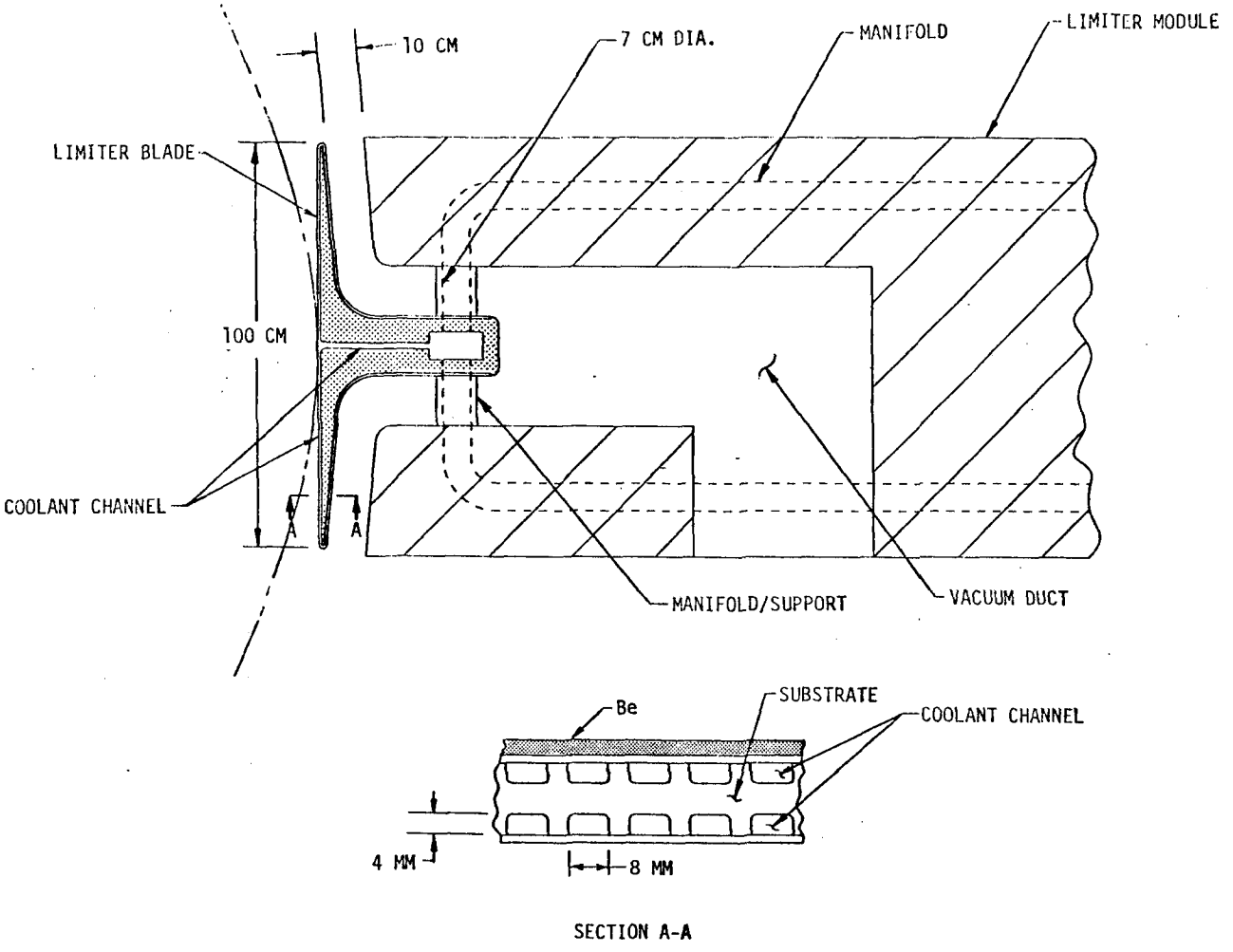

Figure 2-6. Cross Section of DEMO Limiter Design

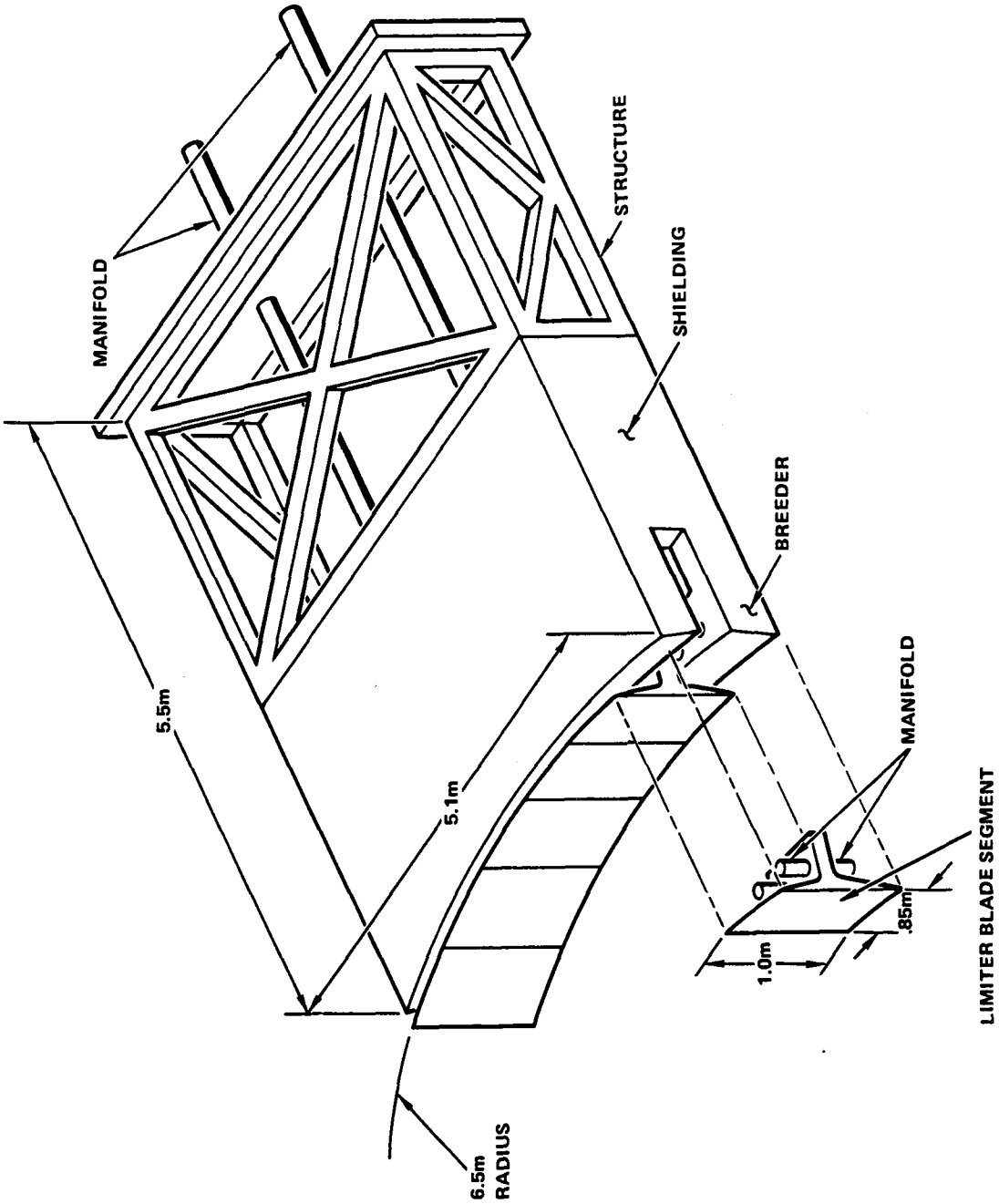

Figure 2-7. Limiter module.

The reference limiter operating parameters are shown in Tables 2-5 and 2-6. The total number of operating cycles is estimated to be only 500 because of steady-state operation. A disruption is assumed to occur once every ten cycles for a disruption frequency of 2.5/y. The total heat load to the limiter is 151 MW out of a total α-heating power of 213 MW. The remaining energy is radiated to the first wall. The peak surface heat flux is 2.4 MW/m^2 which decreases linearly to 1 MW/m^2 at the leading edge. The plasma-edge temperature is 150 eV, and the temperature and density e-folding distances are both 3.75 cm.

2.5.3 Trade-Off Studies

The development of the reference limiter system involved trade-off studies in the areas of plasma transport, erosion/redeposition, materials, plasma disruptions, thermal hydraulics, stress analysis, and tritium and vacuum systems.

The results of the plasma transport studies indicate that some control of the plasma edge conditions is possible by varying the limiter pumping efficiency (i.e., placement of the leading edges), and the fueling methods. For the high plasma reactivity operating point selected for DEMO, the plasma edge temperature is predicted to vary from ~ 100-250 eV for the different cases investigated. The reference edge temperature for the engineering trade-offs was set at 150 eV. A small amount of iodine ($< 5 \times 10^{-4}$) is added to the plasma for burn control. The addition of the iodine results in approximately one half of the alpha heating power being radiated to the plasma chamber and the other half being deposited on the limiter as transport power.

The engineering studies emphasized the maximization of the limiter lifetime while maintaining adequate impurity control. Shaping the limiter to reduce the peak heat loads to the front surface minimizes the temperatures and stresses through the structure. The use of a double edged rather than a single edged limiter also results in lower particle and heat fluxes for a given pumping efficiency. This limiter geometry results in reduced peak erosion rates and a larger allowable thickness for the plasma side materials. Materials selection is also a key part of limiter design optimization. The choice of material is largely dependent upon the plasma edge conditions. At low edge temperatures (< 50 eV), high-Z materials such as W or Ta are

Table 2-5. DEMO Limiter Parameters

PLASMA:	
Thermonuclear power (MW)	1069
α power (MW)	213
Neutron wall loading (MW/m^2)	2.1
DEMO OPERATING SCENARIO:	
Years of operation	20
Availability (%)	50
Cycle time (s)	$\sim 6 \times 10^5$
Burn time (s)	$\sim 6 \times 10^5$
Total burn time (s)	3.1×10^8
Total cycles	500
Total neutron fluence	1.1×10^{29}
Total wall loading ($MW\text{-}y/m^2$)	21
DISRUPTIONS:	
Major disruptions	
Frequency	10^{-1}
Disruptions/year	2.5
Total disruptions	50
Total energy (MJ)	290
Thermal phasing energy (MJ)	230
Field energy (MJ)	60
Disruption time	
Poloidal time (ms)	20
Plasma current (ms)	20
Thermal energy (ms)	
Reference case	20
Alternate case	5
DISRUPTION ENERGY DENSITY REFERENCE CASE:	
First wall (J/cm^2)	175
Limiter (J/cm^2)	270
DISRUPTION ENERGY - ALTERNATE CASE:	
First wall (J/cm^2)	35
Limiter (J/cm^2)	535
ENGINEERING:	
Plasma chamber surface area (m^2)	400
Limiter	Outer midplane
Configuration	8 separately removable modules each weighing ~ 60 Mg
Pumping system	Compound cryopumps located below nuclear island
Desired lifetime	> 2 y at 50% availability
Coolant	H_2O at < 100°C

Table 2-6. DEMO Limiter Heat and Particle Fluxes

Parameter	Value
Alpha heating (MW)	213
Radiation (MW)	100
Ions, to limiter (MW)	80
Neutrals to limiter (MW)	25
Neutrals to wall (MW)	8
Limiter ion current (s^{-1})	6.75×10^{23}
Limiter neutral current (s^{-1})	1.0×10^{23}
Wall neutral current (s^{-1})[a]	3.3×10^{22}
Ion energy (eV)	675
Neutral energy (eV)	1500
Edge electron temperature (eV)[b]	150
Edge density (cm^{-3})[b]	5×10^{13}
e-folding distances (cm)[c]	
Temperature	3.75
Particle Flux	2.5
Power	1.5
Density	3.75

[a]The neutral wall flux falls on two 0.5 m poloidal width strips at each of the limiter.
[b]At start of scrapeoff.
[c]At midplane.

preferred because the DT sputtering yields are low and the self sputtering coefficient is less than unity at the corresponding ion energies. The net erosion rate is predicted to be almost zero. These materials cannot be used at higher edge temperatures since the self sputtering coefficient exceeds unity resulting in a runaway sputtering condition. At higher edge temperatures, only low-Z materials have self sputtering coefficients which remain below unity. The trade-off studies considered several low-Z materials including C, Be, BeO, and SiC. The non-metals have a major problem with radiation-induced reductions in thermal conductivity. In addition, graphite

exhibits high chemical sputtering by DT ions. Although no low-Z material is free of problems, Be is preferred because it does not suffer from either chemical sputtering or radiation induced thermal conductivity loss.

The lifetime of the limiter is determined by the net erosion rates and the maximum allowable thickness for the plasma-side material. Erosion is caused by sputtering during normal operation and vaporization and melting during disruptions. Detailed calculations for sputtering and redeposition were made for the limiter using the REDEP code. For the beryllium coating, the net erosion rates on the front face of the limiter are acceptable ($\lesssim 1$ cm/y), but the net erosion rates at the leading edges are unacceptably high ($\sim$ 29 cm/y). This high erosion rate can be controlled by replacing beryllium with a high-Z material, like tantalum, at the leading edge. The ion temperature at the leading edge is $\lesssim$ 50 eV which is in the range where high-Z materials can be used, as discussed above. The effect of disruptions on the erosion rates in DEMO is predicted to be small because of the low disruption frequency associated with steady state operation. The allowable thickness for plasma-side materials is set by a variety of criteria including maximum permissible temperature, maximum allowable stress, crack growth and fatigue limitations, and radiation effects. Detailed calculations of the temperatures and stresses through the front face and leading edge of the limiter were performed, and the calculations were then used to determine thickness limitations. In the case of Be on the front face, the maximum allowable thickness is $\sim$ 2.5 cm which is set by temperature limitations. The predicted lifetime for the reference operating conditions is 2.7 y at 50% availability.

2.6 Tritium Breeding Blanket

The study focused on the definition of materials and design issues for first wall/blanket concepts using two different breeders: (2) solid lithium oxide (Li_2O) breeder; (2) a liquid metal breeder, the lead-rich Li-Pb eutectic (17 at % Li, 83 at % Pb). These two breeders were not chosen based on evaluation of all candidate tritium breeders, but were instead selected at the study's outset to provide the national fusion program with both an in-depth assessment of their potential and an R&D strategy for addressing the key issues regarding their viability for the DEMO blanket. Analyses related to materials selection, neutronics, tritium recovery, thermal-hydraulics and

stress were performed, and critical design and operating criteria were defined for both concepts. The following paragraphs describe the reference first wall/blanket concept and present summaries of the analyses and evaluations performed in developing both the Li_2O breeder and 17Li-83Pb breeder blanket concepts.

Reference Design Description

The DEMO reference first wall/blanket design is illustrated in Fig. 2-8. Major parameters are listed in Table 2-7 and key features of the design are shown in Table 2-8. The first wall and blanket are integrated mechanically and structurally into modules, assembled into eight blanket sectors identical except for local variations required for other reactor components (e.g., REB current drive launcher). The first wall is a beryllium-clad corrugated panel, with channels of circular segment cross section. The breeder and first wall are cooled by high pressure (11.0 MPa), high temperature (260°C inlet, 300°C outlet) water. The breeder coolant is contained in small-diameter tubes connected to inlet and outlet manifolds at the rear of the blanket. The tubes are joined to the surrounding breeder through a stainless steel metallic felt, which accommodates thermal expansion differences between the breeder and tube and conducts the heat from the breeder to the tube. The Li_2O breeder is fabricated at 70% of theoretical density with bi-modal porosity to enhance tritium release. Helium purge gas at approximately 1 atm flows through 2 mm diameter holes in the breeder to remove tritium. Dual parallel primary coolant loops are provided to effect safe removal of afterheat in the event of a coolant circuit failure. Maintenance of the first wall/blanket is performed by sector removal and replacement, to minimize downtime.

Table 2-7. DEMO Reference First Wall/Blanket Concept Description

SELECTED MATERIALS	
- Tritium Breeder	Li_2O (solid; 70% d.f.)
- Coolant	Pressurized H_2O (11.0 MPa) - Inlet temperature 260°C - Outlet temperature 300°C
- Tritium Processing Fluid	Low-velocity Helium (0.05 MPa)
- Structure	Titanium-modified Austenitic Stainless Steel
SELECTED DESIGN OPTIONS	
- First Wall	Be-clad Corrugated Panel
- Breeder Coolant Containment	Small-diameter Tubes
- Other:	
- First wall and blanket mechanically and structurally integrated	
- Coolant flow in toroidal direction	
- Dual parallel primary coolant loops	
- Maintenance by sector removal and replacement	

Table 2-8. Key Features of Selected Design Details for DEMO Reference First Wall/Blanket Concept

FIRST WALL: BE-CLAD CORRUGATED PANEL

- Minimum number of pressure boundary welds
- Separates structural and surface-related requiremens
- All plasma chamber components coated with same material (~ 2 mm Be)
- Low structure temperature (< 400°C)
- Mechanically and structurally integrated with blanket

BREEDING ZONE: SINTERED CERAMIC WITH COOLANT IN TUBES

- All tube pressure boundary welds located outside of breeder zone in low-fluence region
- High pressure coolant contained in small-diameter tubes
- Coolant tubes oriented toroidally
- Tube spacing graded to conform to energy deposition profile
- Reduced density ceramic (70% d.f. with bi-modal porosity) to facilitate tritium recovery
- Low pressure He purge stream for tritium recovery
- Coolant outlet temperature and pressure reduced (from STARFIRE) to increase reliability

MANIFOLD ZONE: TUBULAR MANIFOLDS

- Most coolant system welds located within vented secondary containment to accommodate minor leakages while reactor continues to operate
- Steel and water, together with shield, serve as neutron reflectors

DUAL INDEPENDENT PRIMARY COOLANT LOOPS

- Dual loops throughout each module and sector to provide adequate afterheat removal even if only one loop is operable

Li_2O Breeder Blanket Concept

Pressurized water (260-300°C) was selected for the first wall and blanket coolant. The range of operating temperatures required for acceptable Li_2O performance is very limited, and thus the low system ΔT characteristic of pressurized water systems appears necessary for a satisfactory design. The use of water coolant permits a smaller reactor size or a higher fusion power for a given size compared to helium coolant, provides for much lower pumping power losses, and results in lower cost of the heat transport system. An advanced austenitic stainless steel (designated PCA in the Alloy Development Program) similar to Type 316 was selected as the structural material. Mechanical properties and radiation damage resistance are considered acceptable for reasonable lifetimes (~ 7 MW-yr/m^2) at the relatively low projected operating temperatures, which are below the temperatures at which severe displacement damage embrittlement, and helium embrittlement occur. Swelling is not predicted to be excessive for these conditions.

Neutronics analyses were performed to evaluate (1) the impact of ^6Li enrichment on the tritium breeding performance, (2) the tritium-breeding enhancement provided by a neutron multiplier, and (3) the geometrical dependence of the nuclear heating and the decay heat for a reference first wall/blanket configuration. The 1-D neutronics calculations indicate that, in the absence of a neutron multiplier, the tritium breeding potential of a Li_2O blanket decreases significantly with ^6Li enrichment. With no breeding in the inner blanket, the maximum breeding ratio (100% blanket) is 1.23 for a Li_2O blanket with stainless steel first wall and armor 13.4 mm thick, compared to a breeding ratio of 1.41 for the same blanket design with a 10 mm thick beryllium cladding and 3.4 mm stainless steel first wall. Beryllium was found to be the only effective neutron multiplier for a Li_2O blanket. The beryllium multiplier is found more effective when placed behind several cm of Li_2O. For the reference design concept with no neutron multiplier and a neutron wall load of 1.8 MW/m^2, nuclear heating in the Li_2O varies by approximately two orders of magnitude from the front of the blanket (13.4 MW/m^3) to a depth of 60 cm (0.19 MW/m^3). A significant fraction of decay gammas from the stainless steel structure are absorbed in the Li_2O resulting in significant decay

heat. The total decay power in the first wall/blanket is ~ 14.5 MW (1.6% of the total thermal power) at shutdown, decreasing to about 3 MW within 7 h and then leveling off at about 2 MW for several weeks.

The physical properties, thermodynamic properties and the effects of radiation on the properties and behavior of Li_2O were evaluated in detail. Fabrication and handling problems associated with Li_2O were also assessed. Lithium oxide is very hygroscopic, reacting readily with moisture to form LiOH. Thus, high purity Li_2O is difficult to obtain and is difficult to maintain during handling. Recent investigations indicate that the solubility of LiOH in Li_2O is very low, and is expected to be less than 1 ppm in the reference blanket. Fabrication of Li_2O with small ($\leq$ 2 μm) grain size and interconnected (bimodal) porosity, although difficult, appears feasible. However, the stability of this microstructure under anticipated thermal and radiation environments of a reactor blanket is a major concern. Large weight losses have been observed at 1000°C when Li_2O is exposed to vacuum or helium with very low moisture concentration. This is generally attributed to mass transfer of LiOH. Also, chemical effects produced by burnup of lithium and displacement damage effects produced by energetic recoils of T and He are predicted to cause sintering and pore closure under certain conditions. Preliminary data indicate substantial restructuring of Li_2O after irradiation at temperatures > 750°C.

Tritium recovery is considered to be a key feasibility issue regarding the viability of Li_2O as a tritium breeder material. Tritium generated within the Li_2O grains must diffuse to the surface of the grains, desorb as T_2O, and migrate through interconnected porosity to a helium purge stream where it is transported to the tritium processing system. Similar to the case for STARFIRE, a Li_2O microstructure with small grain size ($\leq$ 1 μm) and a bimodal pore distribution is believed to offer the most potential for acceptable tritium recovery. The difficult design problems arise from the limited operating temperature range projected for Li_2O and the fact that the thermal conductivity, although higher than that of the ternary oxides such as $LiAlO_2$, is relatively low (about 4 W/m-K at 500°C for 70% dense unirradiated material). The thermal conductivity of irradiated Li_2O is estimated to be ~ 2 W/m.K. Effects that result in a projected allowable operating temperature range between 410 and 660°C for Li_2O are summarized in Table 2-9. The

Table 2-9. Basis for Allowable Operating Temperature Range of Li_2O

Maximum Allowable Temperature	
Radiation-induced sintering	700°C
Mass Transport of LiOH (1% of T_2O)	660°C
Minimum Allowable Temperature	
Solid state diffusion (1 μm grain)	410°C
LiOT precipitation (160 Pa)	410°C

critical concerns relate to the fact that some of the phenomena may cause irreversible propagating-type effects. For example, precipitation of LiOT could lead to enhanced sintering at low temperatures, which in turn would produce higher tritium partial pressures, and hence, more LiOT precipitation and subsequently more sintering. Mass transport of LiOT leads not only to a loss of lithium from the blanket but to possible corrosion problems caused by precipitation of liquid LiOT in the tritium processing circuit. Analyses indicate that, in the absence of radiation effects, the blanket tritium inventory can be maintained at relatively low levels (< 50 g in Li_2O). However, radiation effects are expected to substantially increase the tritium inventory, possibly to unacceptable levels.

Materials compatibility issues include breeder-structure, coolant-structure, and breeder-coolant compatibility. The first two issues involve normal operation whereas breeder-coolant compatibility is of interest only in the event of off-normal conditions such as a coolant leak into the breeder region. Limited data from short-term sealed capsule experiments indicate that the reactivity of Li_2O with stainless steel is probably not excessive. However, no data exist under the more severe conditions of appropriate oxygen and moisture pressures. The potential for stress corrosion cracking of cold-worked austenitic steel under attainable conditions in the presence of tritium or hydrogen needs to be assessed. Likewise, detailed analyses must be conducted to assess the severity of a breeder-coolant reaction that would result from a coolant tube leak.

Thermal-hydraulics analyses were conducted to evaluate the sensitivities of the blanket design, particularly with respect to tritium recovery, to variations in breeder physical properties, geometrical parameters, and power level. The results indicated that the tolerances required for adequate predictability of heat transfer through a helium gap at the breeder-to-coolant-tube interface were too small for use in a practical system. A different design concept has been considered for the interface, consisting of a commercial stainless steel metallic felt between the breeder and tube. The proper thermal conductance value for the interface is determined through selection of the proper thickness and density of the felt. The reference blanket is designed to accommodate anticipated changes (with fluence) and uncertainties in breeder thermal conductivity, breeder-to-tube interface parameters, and local wall loading. The blanket was also analyzed to determine the design changes necessary to accommodate deliberate large-scale changes in reactor power level. A power factor change PF = 2 (PF = maximum power/minimum power) could potentially be accommodated by making design detail changes, which would result in a reduction of ~ 0.08 in tritium breeding ratio (100% blanket coverage).

Thermal stress analyses of the Li_2O breeder were conducted using a cylindrical model to determine the breeder's propensity to fracture under operational thermal gradients (410°C to 660°C radially outward from the cylinder's central coolant tube, over a 2 to 6 cm cylinder thickness). Circumferential and axial stresses in the cyliner were higher by factors of 10 to 20 than the reported fracture strength level. Breeder cracking, if it occurs, will change the blanket configuration and hence increase the difficulty in predicting breeder performance during operation. The most undesirable effect of cracking appears to be difficulties created in controlling thermal conductance at the breeder-to-tube interface. Similar to nuclear fuels, Li_2O breeder may fracture into fragments and thus greatly complicate the thermal conductance control. The impact of breeder cracking on the flow characteristics of the helium purge stream is also an important consideration. Of the critical Li_2O properties that affect cracking, fracture strength and Young's modulus, in particular, warrant separate experimental investigation.

Li-Pb Alloy Breeder Blanket Concepts

Liquid Li-Pb alloys have several attractive properties for use as a tritium breeder in a fusion reactor. The neutron multiplication by the lead provides excellent tritium breeding performance and the neutron attenuation properties of the alloy are attractive for radiation shielding. The 17Li-83Pb eutectic alloy, which has a relatively low melting temperature of 235°C, was selected as the reference breeding material for the liquid breeder portion of the DEMO blanket study. Although the 10Li-50Bi-40Pb alloy has a melting temperature approximately 100°C lower than the Li-Pb binary alloy, the polonium generation from the bismuth and the poorer compatibility of bismuth (compared to lead) with structural materials make this ternary alloy less desirable.

The most important initial consideration for the blanket design is whether to use Li-Pb as both breeder and coolant (i.e., self-cooled), or to use a separate gas or liquid coolant. Economics-related issues (e.g., pumping power losses, energy conversion system component design, and efficiency), safety, and blanket and coolant system design complexity are of primary concern. The most important materials-related concerns pertinent to the design evaluations are: (1) the high density of Li-Pb, which increases blanket structural requirements (and pumping power requirements if used as a coolant); (2) the maximum allowable structural temperature, set at ~ 450°C for ferritic steel because of compatibility concerns; and (3) the low solubility of tritium in Li-Pb, which impact both tritium containment and tritium recovery. For separate coolant concepts, additional important design considerations are breeder-coolant compatibility, control of tritium permeation into the coolant, breeder containment approach, and coolant containment approach (e.g., fully pressurized module or small-diameter coolant tubes). Induced MHD effects are also important concerns for Li-Pb breeder self-cooled concepts and for separately-cooled concepts using liquid metal coolant (i.e., sodium).

Helium, pressurized water, and liquid sodium have been considered as potential coolants for the separate-coolant concepts. Sodium, on balance, is considered to be the best separate coolant, primarily because of its good thermal-hydraulic characteristics, its low reactivity with Li-Pb, and its

potential to serve as a tritium-recovery medium without requiring Li-Pb circulation. However, MHD effects and reactivity of sodium with water and air are major concerns.

Compatibility with structure is a key feasibility question for Li-Pb. The maximum blanket operating temperature was limited by corrosion/compatibility criteria. Critical issues include (1) corrosion/mass transfer effects, and (2) stress corrosion effects. Ferritic steel and vanadium alloys are considered to be the best candidates for the structural material. Because of the high solubility of nickel in both lithium and lead, structural alloys containing significant amounts of nickel are subject to extensive mass transfer at high temperatures. Corrosion of austenitic steels in a large heat transport system is believed to be excessive at acceptable operating temperatures (> 400°C). Those ferritic steels with no nickel should be more resistant to mass transfer effects; however, liquid metal embrittlement phenomena at low temperatures (~ 350°C) are of concern for structures under high stress. Vanadium alloys probably have better compatibility with Li-Pb because of lower solubilities in lithium and lead; however, no experimental data are available. Also, for separately-cooled concepts compatibility of structure with the separate coolants is a major consideration.

Neutronics analyses for the Li-Pb breeder blanket indicate that breeding ratios of ~ 1.5-1.6 (1-D basis) are attainable for blankets at 100% coverage and 70 cm depth, depending on first wall materials and thicknesses. However, the Li-Pb must be highly enriched to ~ 60-70% of ^{6}Li to achieve these breeding ratios. A Li-Pb blanket with natural lithium will provide a breeding ratio of only 1.2-1.3 for otherwise similar conditions.

Key properties of 17Li-83Pb that have major impact on the designs include melting temperature (235°C), relatively high density (9.4 g/cm^3), and its relatively low solubility for hydrogen (tritium). For a relatively high tritium pressure of 1 Pa, the amount of tritium dissolved in the alloy is only about 4.4 wppb at projected operating temperatures. This low solubility has important implications regarding tritium recovery, tritium inventory and tritium containment. At this pressure, tritium permeation rates are quite high for most structural materials. The heat of reaction of the 17Li-83Pb alloy with air and water is lower than that of liquid lithium by a factor of ten when compared on a unit volume basis.

Tritium recovery and containment problems were evaluated for both self-cooled and separately-cooled concepts. Because of the low solubility of tritium in 17Li-83Pb, fairly high tritium pressures (about 1 Pa) are required for acceptable flowrates if Li-Pb is used as the tritium recovery fluid. These high tritium pressures create tritium containment difficulties for self-cooled concepts in the ex-reactor system, e.g., the steam generator and piping. An intermediate heat exchanger or a double-walled steam generator would be required to reduce leakage of tritium to acceptable levels. Molten salt extraction, the use of solid getters, and gas sparging are considered feasible methods for direct recovery of tritium from Li-Pb. For sodium coolant in a separately-cooled concept, permeation rates into the sodium appear to be sufficient to use the sodium as the tritium recovery fluid. Cold-trapping is the most attractive method for recovery of tritium from the sodium.

Blanket design concepts were developed for both the separately-cooled and self-cooled approaches. Sodium coolant was selected for the separately-cooled approach. The module/sector approach used for the Li_2O breeder blanket was adopted for this Li-Pb breeder blanket concept. The first wall and blanket are integrated mechanically and structurally. The first wall consists of a beryllium-clad corrugated panel. The breeder zone and first wall are cooled by low pressure ($\lesssim$ 0.5 MPa), high temperature (275°C inlet, 400°C outlet) liquid sodium, contained in small-diameter toroidally-oriented tubes which are connected to inlet and outlet manifolds at the rear of the blanket. Tritium permeates from the Li-Pb (which does not circulate out of the modules) through the coolant tube walls into the sodium; a small percentage of the sodium flow rate is processed externally by cold trapping to remove the tritium.

For the Li-Pb self-cooled first wall/blanket concept, the beryllium-clad first wall of each module is formed by the two semi-ellipsoidal domes which comprise the module front face. The flat side walls of the module are connected to full internal frames (oriented normal to the toroidal direction) which self-react loads due to internal pressure (~ 1-2 MPa). The frames also react the gravity loads of the Li-Pb from the side walls and first wall (depending on module location in the sector) to the back wall and sector structure. The Li-Pb enters the rear of the blanket at about 300°C, flows to the front of the blanket through radial feedpipes, and is channeled directly

behind the first wall to cool it. The liquid metal then circulates at a lower velocity toward the back of the blanket, and exits at 400°C to the outlet manifold. A fraction of the Li-Pb flow is diverted to an ex-reactor tritium processing system for tritium recovery.

2.7 Radiation Shield

The development of a low cost shield option for the DEMO reactor has evolved from a strong incentive to reduce the capital cost of the shield system which represents typically 8 to 16% of the total direct cost[1,2] of a tokamak reactor. In addition, attention was given to improving reactor maintainability and performance. The main function of the shielding system during reactor operation is to reduce the neutron and photon leakage intensities from the shield to: a) protect the different reactor components from radiation damage and excessive nuclear heating, b) reduce the neutron reaction rates in the reactor components which produce undesirable radioactive isotopes, and c) protect the worker and the public from radiation exposure. Another requirement is to attenuate the decay gamma rays to permit personnel access to the reactor building with all shield components in place within one day after shutdown. Personnel access to the reactor building will help to reduce the reactor downtime and the capital cost of the remote equipment required for maintenance.[19] The materials selection for the shield system has developed from the tradeoff analyses and the results of previous designs.[20] The selection of the reference materials is based on cost, resource, and performance considerations.

The inboard section of the shield system was designed to protect the toroidal field (TF) coils from radiation damage and excessive nuclear heating so that the coils will last the operating lifetime of the reactor without change in the performance. The inboard blanket and shield thickness (the radial thickness from the edge of the scrape-off region to the position of maximum toroidal field) is 120 cm. This thickness includes 7 cm of vacuum gaps and a 27 cm thick inboard blanket. In the analysis of the inboard shield, the inboard blanket employs Li_2O with an 0.7 density factor which results in another 7 cm of vacuum in the inboard section of the reactor. This allows for 86 cm of actual materials to shield the TF coils.

Two shielding options were studied for the DEMO design, tungsten-water and Fe14Mn2Ni2Cr steel alloy-boron carbide-water. The impact of the inboard shield thickness, material arrangement, and boron carbide density factor on the radiation response parameters in the TF coils were analyzed. The tradeoff analysis shows that the use of the tungsten-water shield option reduces the required inboard blanket and shield thickness by about 18 cm and increases the cost of the shield system.

Table 2-10 lists the shield parameters for the reference design evolved from the tradeoff and optimization studies. Boron carbide with an 0.7 density factor is used to eliminate the cost associated with high density fabrication. The low concentration of nickel, and chromium, as well as good shielding characteristics, motivated the use of Fe14Mn2Ni2Cr steel alloy as a shield material for the inboard shield and structural material for the whole shield system. Low nickel concentration reduces the dose equivalent after shutdown and the production of long-lived isotopes. Low chromium concentration is a desirable feature to minimize the consumption of strategic materials.

Table 2-11 summarizes the radiation response parameters in the inboard section of the TF coils. The maximum neutron fluence in the superconductor material is 7×10^{17} n/cm^2 which does not produce significant changes in the critical current density or the critical temperature of NbTi material[21]. The maximum induced resistivity in the copper stabilizer is 5.3×10^{-8} Ω•cm assuming no magnet anneal and it drops very fast with respect to the depth in the TF coils. The maximum nuclear heating in the superconductor material is 8.7×10^{-5} W/cm^3 which corresponds to less than 1.7 KW total nuclear heating in the TF coils. The maximum dose in the electrical insulator is 1.05×10^9 rads which is acceptable from a radiation damage point of view. This analysis is based on the use of an inboard tritium breeding blanket. The use of a nonbreeding blanket in the vertical section of the inboard blanket reduces the radiation response parameters listed in Table 2-11 by a factor of 2 to 3.

The outboard and penetration shield design are driven by personnel access requirements to the reactor building and the desire to reduce the cost of the shielding system. Several design options were studied for the outboard shield with different combinations of shielding materials. Four options were con-

Table 2-10. Material Composition and Dimension of the Different Components of the Shield System

Component	Major Radius (cm) From	To	Thickness (cm)	Composition Percentage by Volume
a. Inboard Shield				
Shield Jacket	262	264	2	100% Fe14Mn2Ni2Cr
Boron Carbide Zone	264	274	10	75% B_4C*, 25% H_2O
Steel Zone	274	339	65	92% Fe14Mn2Ni2Cr, 8% H_2O
Shield Jacket	339	341	2	100% Fe14Mn2Ni2Cr
b. Outboard Shield				
Shield Jacket	722	724	2	100% Fe14Mn2Ni2Cr
Water Zone	724	749	25	100% H_2O
Boron Carbide Zone	749	761	12	42% Fe14Mn2Ni2Cr, 58% B_4C*
Lead Zone	761	771	10	100% Pb
Ordinary Concrete Zone	771	911	140	100% Ordinary Concrete
Boron Carbide Zone	911	917	6	42% Fe14Mn2Ni2Cr, 58% B_4C*
Lead Zone	917	922	5	100% Pb
c. Vacuum Lines Inside the TF Coils and First Section of REB Duct			2	100% Fe14Mn2Ni2Cr
			25	100% H_2O
			5	10% Fe14Mn2Ni2Cr, 90% B_4C*
			5	100% Pb
			48	100% Ordinary Concrete
			5	10% Fe14Mn2Ni2Cr, 90% B_4C*
			5	100% Pb
d. Vacuum Lines Outside the TF Coils and Second Section of the REB Duct			2	100% Fe14Mn2Ni2Cr
			20	100% H_2O
			5	10% Fe14Mn2Ni2Cr, 90% B_4C*
			5	100% Pb
			38	100% Ordinary Concrete
			5	10% Fe14Mn2Ni2Cr, 90% B_4C*
			5	100% Pb
e. Vacuum Pumps and the Third Section of the REB Duct			2	100% Fe14Mn2Ni2Cr
			53	100% Ordinary Concrete
			5	10% Fe14Mn2Ni2Cr, 90% B_4C*
			5	100% Pb

* 0.7 Density factor for B_4C.

Table 2-11. Maximum Radiation Effects Related to the Shield System

Maximum neutron fluence in the superconductor material, E > 0.1 MeV (n/cm^2)	7.05×10^{17}
Maximum induced resistivity in the copper stabilizer ($\Omega \cdot cm$)	5.30×10^{-8}
Maximum atomic displacement in the copper stabilizer (dpa)	3.59×10^{-4}
Maximum nuclear heating in the superconductor material (W/cm^3)	8.67×10^{-5}
Maximum nuclear heating in the magnet case (W/cm^3)	4.63×10^{-4}
Maximum nuclear heating per unit length of the TF coils including the magnet case (W/cm)	4.18
Maximum dose in the electrical insulator (rads)	1.05×10^{9}
Maximum dose in the thermal insulator (rads)	3.41×10^{9}
Maximum nuclear heating in the concrete shield (W/cm^3)	1.15×10^{-3}
Maximum dose equivalent in the reactor building during operation (mrem/hr)	3.00×10^{4}
Maximum dose equivalent outside the reactor building during operation (mrem/hr)	0.10
Maximum dose equivalent inside the reactor building one day after shutdown (mrem/hr)	0.41
Maximum neutron flux outside the outboard shield ($n/cm^2.s$)	1.37×10^{6}

sidered which consist of one basic shielding material (water, ordinary concrete or heavy concrete), neutron absorber (boron carbide or boric acid), and lead at the outermost surface of the shield to attenuate the decay gamma rays. The results show that the use of heavy concrete saves about one third of the required ordinary concrete shield thickness to satisfy the same dose equivalent criterion. However, the heavy concrete installed cost-per-cubic yard is about three times the cost of ordinary concrete which makes the ordinary concrete option more attractive. The water shield option requires more shielding thickness (about 28 cm more than ordinary concrete option) to reduce the dose equivalent to the same required level after shutdown. This penality for the water shield results from the poor attenuation characteristic of water for gamma rays and 14 MeV neutrons.

The use of a concrete shield behind the blanket generates unacceptable high heating rates in the concrete. A shield section was introduced between the blanket and the concrete shield to reduce the maximum nuclear heating in the concrete to 1 mW/cm^3. This heating limit[23] protects the concrete against loss of water, temperature effects, radiation absorption effects and stress conditions.

Table 2-11 gives the radiation response parameters related to the outboard shield. The maximum dose equivalent achieved in the reactor hall is 0.4 mrem/hr after one day from shutdown. During operation, the dose equivalent is 3×10^4 and 0.1 mrem/h in the reactor hall and outside the reactor building, respectively.

A three-dimensional streaming calculation was performed to assess the radiation damage in the ceramic material of the relativistic electron beam (REB) system. Monte Carlo method was used for the calculation with a continuous energy representation for the nuclear cross sections. The neutron energy spectrum from the DT plasma was employed in the calculations. The neutron fluence and radiation dose (neutrons and photons) were calculated for three ceramic materials (magnesium oxide, aluminum oxide and silicon oxide) as a function of the distance from the first wall. The calculations show that locating the ceramic material 270 cm from the first wall results in total dose of less than 10^{12} rads at 21.2 $MW \cdot y/m^2$ integrated neutron wall loading at the first wall.

Activation analysis for several shielding options with the same breeding blanket was performed to compare the biological hazard potential, afterheat, and radioactivity concentration. Table 2-12 gives the average activation parameters in each component for the reference design at 10 and 100 years after shutdown. At 10 years after shutdown, the radioactivity of the first wall and blanket are dominated by ^{55}Fe isotope (2.7 years half-life, electron capture decay) and ^{60}Co isotope (5.27 years half-life, β and α decay) generated from iron and nickel isotopes. During the time period from 10 to 100 years after shutdown, the long half-life isotopes start to dominate the radioactivity concentration. At 100 years after shutdown, ^{63}Ni isotope (100 years half-life, β decay), ^{93}Mo (3500 years half-life, electron capture decay), and ^{93}Nb isotope (13.6 years half-life, electron capture decay) generated from nickel and molybdenum isotopes are causing more than 99.6% of the total radioactivity. Nickel and molybdenum are essential for the PCA steel alloy.

The long-term activation in the shield components, 40 years after shutdown, is caused by the nickel content in the Fe14Mn2Ni2Cr steel alloy and the nickel impurity (0.3% by weight) in the ordinary concrete. Replacing or isotopically tailoring the 2% nickel in the steel alloy could reduce the radioactivity concentration by two orders of magnitude. For example, the maximum radioactivity concentration in the Fe14Mn2Ni2Cr steel alloy drops from 3.79×10^{-3} to 3.23×10^{-5} Ci/cm^3. The remaining radioactivity is due to ^{14}C generated from the 0.019% by weight nitrogen impurity. Also, eliminating nickel from ordinary concrete reduces the average radioactivity concentration from 1.22×10^{-6} to 1.9×10^{-9} Ci/cm^3. A low nickel content in the concrete can be achieved through the selection process of cement and aggregate materials.

Table 2-12. Average Activation Parameters in the Different Reactor Components

Reactor Component	Activity Ci/cm^3	Activity Ci/W_{th}	Afterheat W/cm^3	Afterheat $W/cm^3.W_{th}$	Biological Hazard Potential Km^3 air/Kw_{th}
a. 10 Years After Shutdown					
First Wall	8.04	6.07×10^{-2}	2.22×10^{-2}	9.84×10^{-8}	3.38×10^{1}
Breeding Blanket	5.08×10^{-2}	1.19×10^{-2}	1.42×10^{-4}	6.27×10^{-9}	6.79
Shield Jacket	7.80×10^{-2}	8.80×10^{-4}	3.89×10^{-5}	1.72×10^{-10}	8.98×10^{-2}
Water Zone	-	-	-	-	-
Boron Carbide Zone	5.15×10^{-4}	3.35×10^{-5}	4.08×10^{-7}	1.81×10^{-12}	3.93×10^{-3}
Lead Zone	4.92×10^{-8}	3.34×10^{-9}	9.98×10^{-11}	4.41×10^{-16}	5.11×10^{-6}
Ordinary Concrete Zone	2.42×10^{-6}	3.01×10^{-6}	4.63×10^{-10}	2.05×10^{-15}	1.54×10^{-3}
Boron Carbide Zone	7.37×10^{-10}	4.01×10^{-11}	3.64×10^{-13}	1.61×10^{-18}	4.51×10^{-9}
Lead Zone	1.53×10^{-13}	8.45×10^{-15}	3.24×10^{-16}	1.43×10^{-27}	1.02×10^{-11}
Magnet Case	9.15×10^{-11}	2.32×10^{-11}	1.52×10^{-13}	6.71×10^{-25}	1.09×10^{-8}
b. 100 Years After Shutdown					
First Wall	7.66×10^{-2}	5.78×10^{-4}	9.39×10^{-6}	4.15×10^{-11}	2.27×10^{-1}
Breeding Blanket	8.95×10^{-4}	2.10×10^{-4}	1.09×10^{-7}	4.81×10^{-13}	8.29×10^{-2}
Shield Jacket	3.79×10^{-3}	4.27×10^{-5}	4.67×10^{-7}	2.06×10^{-12}	2.12×10^{-2}
Water Zone	-	-	-	-	-
Boron Carbide Zone	5.26×10^{-7}	3.42×10^{-8}	7.48×10^{-11}	3.31×10^{-16}	2.06×10^{-5}
Lead Zone	2.34×10^{-9}	1.59×10^{-10}	2.41×10^{-17}	1.14×10^{-23}	1.59×10^{-6}
Ordinary Concrete Zone	1.22×10^{-6}	1.52×10^{-6}	1.48×10^{-16}	6.56×10^{-21}	7.57×10^{-4}
Boron Carbide Zone	4.37×10^{-11}	2.38×10^{-6}	5.39×10^{-15}	2.38×10^{-21}	1.18×10^{-9}
Lead Zone	1.67×10^{-15}	9.20×10^{-17}	3.24×10^{-16}	1.43×10^{-21}	9.19×10^{-13}
Magnet Case	3.67×10^{-11}	9.29×10^{-12}	4.17×10^{-15}	1.85×10^{-20}	2.23×10^{-9}

2.8 Cost Estimate

This cost estimate includes the capital cost for all reactor equipment, balance-of-plant equipment, structures and site facilities plus all associated indirect costs and escalation of costs during the six-year construction period. The DEMO device follows, and is based upon, an engineering test reactor which will contribute to the technology, engineering and manufacturing base necessary to accomplish the design, construction and operation of DEMO. Likewise, DEMO will form the basis for the subsequent commercial fusion plants. The direct capital cost of FED[2] was estimated to be roughly $1B, DEMO is estimated at $1.5B and STARFIRE,[1] when escalated to 1982 dollars, would be estimated at $2B. This comparison is not a rigorous cost comparison because of the differing design and costing groundrules, but the relative costs indicate the progression of costs are in concert with the size and the capabilities of the devices. When indirect costs are considered, the three device classes can no longer be compared. The engineering and management services should reduce the percentage of direct capital costs as the devices mature. Varying accounting groundrules apply as the devices proceed from government-financed projects toward private-sector financing. Handling of the interest (if considered) and escalation during varying construction periods yield significant cost variances. Thus, the best economic yardstick for comparison is the direct capital cost of the plant.

The DEMO Total Direct Cost for the complete reactor plant is 1.52 billion dollars. Adding in the indirect and escalation costs during construction brings the total to 2.35 billion dollars. The high-level cost accounts are summarized in Table 2-13. The largest single cost account is the Reactor Plant Equipment which represents fifty percent of the plant costs. The Structures and Site Facilities account for roughly one-quarter of the cost. These values seem reasonable for a large power producing facility based upon a high technology heat source.

The area of most interest is the Reactor Plant Equipment. Table 2-14 illustrates the DEMO costs of this area and compares these to the STARFIRE estimate (escalated to 1982 dollars). The STARFIRE costs reflect an estimate based on a tenth-of-a-kind reactor with an appropriate learning-curve factor applied, minimal design allowances and reasonable contingency allowances. The DEMO cost estimate has a mix of hardware ranging from mature production

Table 2-13. Summary of DEMO PACE Costs

Account Number	Account Title	Cost (M$)
20	Land and Land Rights	0.20
21	Structures and Site Facilities	396.90
22	Reactor Plant Equipment	763.32
23	Turbine Plant Equipment	198.08
24	Electrical Plant Equipment	117.38
25	Miscellaneous Plant Equipment	45.88
26	Special Materials	0.30
	Subtotal	1522.06
91	Construction Facilities, Equipment and Services (10%)	152.21
92	Engineering and Construction Management Services (20%)	304.41
	Subtotal	1978.68
95	Escalation During Construction	375.16
	Total PACE Cost	2353.84

equipment to first-of-a-kind hardware. Correspondingly, the design allowances range up to 50% and the contingency allowables are increased to 20%. The cost of the Blanket and First Wall is reduced due to a smaller surface area (approximately 400 m^2), absence of a neutron multiplier and neutron reflector, lower neutron wall loading and use of natural Li_2O breeder in place of 60% enriched $LiAlO_2$. Care was exercised in choosing shielding materials that were cost effective and this effort significantly reduced the shielding system costs ($47M versus $216M for STARFIRE). The use of large amounts of concrete reduced the need for the Fe1422 which functioned both as structure and shielding in STARFIRE. Also, tungsten was completely eliminated from the shielding design ($48M savings). A reduced number of magnets (8 versus 12), lower field and smaller overturning loads resulted in a lower magnet system cost. Elimination of the ohmic heating coils also helped reduce the costs.

Table 2-14. Comparison of STARFIRE and DEMO Reactor Plant Equipment Costs

Account	Account Title	STARFIRE Cost (M$)[a]	DEMO Cost (M$)[a]
22.01	Reactor Equipment	683.54	408.50
22.01.01	Blanket and First Wall	95.54	45.81
22.01.02	Shield	215.84	46.71
22.01.03	Magnets	199.02	160.73
22.01.04	Heating and Current Drive	38.85	11.13
22.01.05	Primary Structure and Support	61.18	95.29
22.01.06	Reactor Vacuum	5.64	2.84
22.01.07	Power Supply Switching and Energy Storage	61.36	28.90
22.01.08	Impurity Control	2.84	17.09
22.01.09	ECRH Plasma Breakdown	3.27	---
22.02	Main Heat Transfer and Transport	81.01	52.56
22.03	Cryogenic Cooling System	17.28	17.38
22.04	Radioactive Waste Treatment and Disposal	5.57	4.80
22.05	Fuel Handling and Storage	44.78	46.75
22.06	Other Reactor Plant Equipment	50.75	66.91
22.07	Instrumentation and Control	27.16	39.20
22.98	Spare Parts	77.00	---
22.99	Contingency	136.50(15%)	127.22(20%)
Total Reactor Plant Equipment Cost, C_{22}		1123.60	763.32

[a]STARFIRE cost is normalized to 1982$ by inflating the 1980 dollar estimate with a 1.16 multiplier.

Use of the simpler REB heating and current drive system resulted in reduced system costs.

The concept of Primary Structure and Support System is changed from that proposed in the STARFIRE approach. This resulted in a structure for the smaller reactor which is only slightly lighter than STARFIRE. Thus, the design allowance (20%) and the learning-curve effect (72%) caused the Primary Structure and Support System cost to be much higher. The Impurity Control (limiter) System is significantly heavier than STARFIRE, uses different materials and has a higher design allowance (40%). Thus, its cost, although still small, increased several-fold. The other cost accounts decreased due to reduced design requirements or slightly increased due to design allowances and learning-curve effects.

2.9 DEMO Parameter List

		UNIT	STARFIRE VALUE	DEMO VALUE
1.	**Machine Characteristics**			
1.1	Reactor Envelope			
1.1.1	Height	m	28.6	18
1.1.2	Width	m	33.0 dia.	24 dia.
1.1.3	Length	m	N.A.[a]	N.A.
1.2	First Wall			
1.2.1	Major Radius	m	7.0	5.2
1.2.2	Minor Radius (to First Wall)			
1.2.2.1	Inboard	m	2.14	1.500
1.2.2.2	Outboard	m	2.14	1.465
1.2.3	Volume, Plasma	m^3	781	272
1.2.4	Volume, Chamber	m^3	950	385
1.2.5	Plasma Surface Area (at scrape off edge)	m^2	755	347
1.2.6	First Wall Surface Area	m^2		
1.2.6.1	Used in Wall Load Calculations			400
1.2.6.2	Actual		780	404
1.3	Plant Life	years	40	20
1.4	Number of On/Off Cycles		(Unknown)	500
1.5	Availability		75%	50%
1.6	Number of Disruptions			50
1.7	Inboard Scrapeoff (Δ_v)	m	.2	0.2
1.8	Outboard Scrapeoff (Δ_v)	m	.15	0.165
1.9	Inboard Blanket/Shield ($\Delta^i_{B/S}$)	m	1.20	1.20
1.10	Outboard Blanket Thickness (Δ^o_B)	m	0.68	0.70
1.11	Outboard Shield Thickness (Δ^o_S)	m		2.00
1.12	Inboard Leg TFC (R_1)	m	3.17	2.10
1.13	Outboard Leg TFC (R_2)	m	13.00	11.6
1.14	TF Coil Half Height (H_{max})	m	7.06 (@R=6.73)	5.47(@R=6.59)
1.15	TF Coil Case Thickness (Δ_{TFC})	m	.98	0.80
1.16	Support Cylinder Thickness (Δ_{sup})	m	0.62	0.40
2.	**Plasma Parameters**			
2.1	Plasma Dimensions			
2.1.1	Major Radius, R	m	7.0	5.2
2.1.2	Minor Radius, a	m	1.94	1.3
2.1.3	Plasma Elongation		1.6	1.6
2.1.4	Plasma Triangularity (d)		.5	0.2
2.2	Peak Fuel Density (n_{DTO})	m^{-3}	1.7×10^{20}	2.40×10^{20}
2.3	Average Density ($\bar{n}_{DT}$)	m^{-3}	0.806×10^{20}	1.84×10^{20}
2.4	τ_E, Electron Energy Confinement Time	s	3.6	3.4
2.5	τ_I, Ion Energy Confinement Time	s	10	12
2.6	τ_p, Particle Confinement Time	s	1.8	1.0
2.7	$\bar{n}_{DT}\tau_E$	s/m^3	2.9×10^{20}	6.3×10^{20}
2.8	β_o, Peak Toroidal Beta		0.194	0.193
2.9	$\langle\beta\rangle$, Average Toroidal Beta		0.067	0.075
2.10	β_{po}, Peak Poloidal Beta			N.A.
2.11	$\langle\beta p\rangle$, Average Poloidal Beta		2.91	1.59
2.12	I_p, Plasma Current	MA	10.1	8.68

			UNIT	STARFIRE VALUE	DEMO VALUE
2.	Plasma Parameters (cont'd)				
	2.13	T_{io}, Peak Ion Temperature	keV	31.3	17.7
	2.14	$\overline{T}_i$, Average Ion Temperature	keV	24.1	8.38
	2.15	T_{eo}, Peak Electron Temperature	keV	22.5	16.9
	2.16	$\overline{T}_e$, Average Electron Temperature	keV	17.3	8.0
	2.17	Z_{eff}, Effective Plasma Ion Charge		3.4	1.48
	2.20	Reactor Cycle		Steady-state	Steady-state
	2.20.1	Burn Pulse Length	s	N.A.	N.A.
	2.20.2	Total Pulse Length	s	N.A.	N.A.
	2.21	Fuel Cycle (i.e., D-T, D-D, etc.)		D-T	D-T
	2.22	Plasma Heating Method		Lower Hybrid	REB
	2.23	Plasma Heating Power	MW	90.4	6.7
	2.24	Plasma Heating Energy or Frequency		1.677×10^9 Hz	1.5 MeV
	2.25	Plasma Energy Gain, Q_p (Plasma Fusion Power/Plasma Heating Power)		39	160
	2.26	$(\overline{n}_e)$	m^{-3}		2.33×10^{20}
	2.27	(n_α/n_{DT})			0.080
	2.28	(n_{Be}/n_{DT})			0.025
	2.29	(n_I/n_{DT})			5.10×10^{-5}
	2.30	Plasma Resistance (R)	ohm		4.14×10^{-8}
	2.31	Wall Load $(\overline{W}_{neutron})$	MW/m^2	3.6	2.12
	2.32	Neutron Current Density $(J_{neutron})$	$m^{-2}s^{-1}$		9.42×10^{17}
	2.33	$(I_{DT,lim})$	s^{-1}		1.5×10^{23}
	2.34	$(I_{CX,FW})$	s^{-1}		1.5×10^{22}
	2.35	$(\overline{J}_{cx})$	$m^{-2}s^{-1}$		3.75×10^{20}
	2.36	$(\overline{W}_{rad})$	MW/m^2		0.402
	2.37	(γ)			0.05
	2.38	(τ_{DT})	s		12
	2.39	$(\tau_{DT,p})$	s		1.0
	2.40	MHD Parameters			
	2.40.1	Safety Factor			
	2.40.1.1	Limiter			2.0
	2.40.1.2	Axis			1.0
	2.40.2	Pressure profile: $p(\psi) = p_o \hat{\psi}^{\alpha p}$			
	2.40.2.1	Peak pressure (p_o)	MPa		1.78
	2.40.2.2	Average pressure $(\overline{p})$	MPa		.690
	2.40.2.3	Pressure profile exponent (α_p)			1.4
	2.40.3	Diamagnetic function profile: $F^2 = F_o^2 (1-\delta\hat{\psi}^{\alpha F})$			
	2.40.3.1	Vacuum diamagnetic function (F_o) T-m			25.0
	2.40.3.2	Magnetic well depth (δ)			.0889
	2.40.3.3	Diamagnetic function profile exponent (α_F)			1.730
	2.40.4	(α_J)			0.569
	2.40.5	Shape factor (ℓ)			1.32
	2.40.6	Magnetic Axis (R_{mag})	m		5.46
	2.40.7	Self-inductance (L_p)	μH		10.7
	2.40.8	Inductive Volt-seconds	V-s		93.0
	2.40.9	Temperature profiles: $T_e = T_o \hat{\psi}^{\alpha T}$			

		UNIT	STARFIRE VALUE	DEMO VALUE
2.	Plasma Parameters (cont'd)			
2.40.9.1	Temperature profile exponent (α_T)			1.1
2.40.10	Density profiles: $n = n_o \psi^{\alpha_n}$			
2.40.10.1	Temperature profile exponent (α_n)			0.3
2.41	Edge Parameters			
2.41.1	($n_{e,edge}$)	m^{-3}		$5x10^{18}$
2.41.2	($T_{i,edge}$)	keV		700
2.41.3	($T_{e,edge}$)	keV		150
2.41.4	Density e-folding Length in Limiter Shadow (δ_p)	cm		2.5
2.41.5	Temperature e-folding Length in Limiter Shadow (δ_T)	cm		3.75
2.41.6	Heat Flux e-folding Length in Limiter Shadow (δ_E)	cm		1.5
3.	Power Output			
3.1	Plasma Fusion Power (Peak)	MWth	3510	1069
3.2	Plasma Fusion Power (Total Cycle Time Average)	MWth	3510	1069
3.2.1	Thermal Power	MWth	4000	1290
3.2.2	P_{cx} to first wall	MW		8
3.2.3	P_{REB} Heating and Current Drive	MW		6.7
3.3	Power to First Wall (Radiation)	MWth	661	98
3.4	Power to First Wall/Blanket (Fusion Neutron Power)	MWth	2810	849
3.4.1	Nuclear Heating in First-Wall/Blanket	MW	3205	1070
3.5	Blanket Power Amplification Factor		1.14	1.26
3.6	Power to Direct Convertor (Peak)	MWth	N.A.	N.A.
3.7	Power to Direct Convertor (Total Cycle Time Average)	MWth	N.A.	N.A.
3.8	Limiter Power (Average)			
3.8.1	Radiated	MWth	90	10
3.8.2	Charge Exchange (CX)	MWth	56	25
3.8.3	Transport	MWth		80
3.8.4	Nuclear Heating	MWth	54	36
3.9	Limiter Power (Total Cycle Time Average)	MWth	200	151
3.10	Plasma Chamber Power Density (Total Cycle Time Average)	MW/m^3	3.7	2.77
3.10.1	Plasma Power Density	MW/m^3	4.5	3.93
3.11	Engineering Power Density[g]	MW/m^3	0.30	0.173
3.12	Plant Gross Electrial Output	MWe	1440	388
3.13	Plant Net Electrical Output	MWe	1200	333
3.14	Thermal Cycle Efficiency	%	35.7	33.6
3.15	Direct Convertor Efficiency	%	N.A.	N.A.
3.16	Net Plant Efficiency	%	30	25.8

		UNIT	STARFIRE VALUE	DEMO VALUE
4.	Reactor Coolant System			
4.1	Blanket Coolant Type		H_2O	H_2O
4.2	Blanket Outlet Temperature (Hot Leg)	°C	320	300
4.3	Blanket Inlet Temperature (Cold Leg)	°C	280	260
4.4	Blanket Outlet Pressure	MPa	15.0	10.8
4.5	Blanket Inlet Pressure	MPa	15.2	11.0
4.6	Blanket Coolant Flow Rate	kg/s	10823	4453
4.7	Blanket Coolant Tube Material		PCA[c]	PCA[c]
4.8	First Wall Coolant Type		H_2O	H_2O
4.9	First Wall Outlet Temperature	°C	320	300
4.10	First Wall Inlet Temperature	°C	280	260
4.11	First Wall Outlet Pressure	MPa	15.0	10.8
4.12	First Wall Inlet Pressure	MPa	15.2	11.0
4.13	First Wall Coolant Flow Rate	kg/s	5811	1099
4.14	Total Number of First Wall/Blanket Coolant Loops		2	2
4.15	Type of Blanket Coolant Circulator		Vertical, 1-Stage	Vertical, 1-Stage
4.16	Power Input to Each Circulator	MWe	5.5	---
4.17	Energy Storage	J	N.A.	N.A.
5.	Intermediate Coolant System		N.A.	N.A.
6.	Steam Generation System			
6.1	Steam Outlet Temperature	°C(°F)	299 (570)	282 (540)
6.2	Steam Outlet Pressure	MPa(psia)	6.3 (910)	5.2 (754)
6.3	Steam Flow Rate	kg/s(lb/hr)	2060 (16.4×10^6)	600 (4.75×10^6)
6.4	Feedwater Temperature	°C(°F)	235 (455)	216 (420)
6.5	Number of Steam Generators per Loop		2	1
6.6	Number of Sectors per Steam Generator		6	4
6.7	Steam Generator Materials, Shell/Tube		Low Carbon Stl/Inconel 600	Low Carbon Stl/Inconel 600
7.	Shield Coolant System			
7.1	Total Energy Deposited in the Shield	MWth	65	37
7.2	Coolant Type		H_2O	H_2O
7.3	Coolant Outlet Temperature-Peak	°C	60	60
7.4	Coolant Inlet Temperature-Peak	°C	43	43
7.5	Coolant Outlet Pressure-Peak	MPa	0.48	0.48
7.6	Coolant Inlet Pressure-Peak	MPa	0.34	0.34
7.7	Coolant Flow Rate	kg/s	1300	736
8.	Reactor Auxiliary Systems			
8.1	Vacuum Pumping System			
8.1.1	Plasma Chamber Pressure (Base)	Pa	1×10^{-6}	1×10^{-6}
8.1.2	Plasma Chamber Volume	m^3	950	385

		UNIT	STARFIRE VALUE	DEMO VALUE
8.	Reactor Auxiliary Systems (cont'd)			
8.1.3	Number of Pumps		48 (24 on line, 24 regenerating)	8 (4 on line, line, 4 regenerating)
8.1.4	Capacity of Each Pump	$Pa\text{-}m^3$	2.7×10^5	2.7×10^5
8.1.5	Helium Pumping Speed of Each Pump	m^3/s	120	71
8.1.6	Conductance Ratio (μ)			7.4
8.2	Magnet Coolant System			
8.2.1	Cooling Load	W	23,300	(TBD)
8.3	Plasma Heating System			
8.3.1	Heat Removal From REB System	MW	90	12
8.4	Plasma Fueling System			
8.4.1	Type		Gas Puffing	Plasma Gun
8.4.2	Fuel Composition (i.e., %D, %T, etc.)		50%D, 50%T	50%D, 50%T
8.4.3	Fueling Rate	kg/s	1.5×10^{-5} (T) 1.0×10^{-5} (D)	(TBD) (TBD)
8.4.4	Pellet Size (if used)	m	N.A.	N.A.
8.4.5	Pellet Injection Frequency (if used)	s	N.A.	N.A.
8.5	Tritium Processing and Recovery System			
8.5.1	Total Tritium Inventory	kg	11.6[h]	4[h]
9.	Reactor Components			
9.1	First Wall			
9.1.1	First Wall Loading (Peak/Average)			
9.1.1.1	14.1 MeV neutrons	MW/m^2	4.0/3.6	---/2.12
9.1.1.2	Alpha Particle Flux	MW/m^2	(very small)	---
9.1.1.3	Electro-Magnetic Radiation Plus Charge Exchange neutrals[d] (Peak/Average)	MW/m^2	1.17/0.90	---/10.25
9.1.1.4	Heat load, two 0.5-m strips adjacent to limiter (peak/average)	MW/m^2	N.A.	---/0.45
9.1.1.5	Plasma Thermal Conduction (Particle Transport)	MW/m^2	<0.01	---
9.1.1.6	Wall Life	$MW\text{-}yr/m^2$	16	7
9.2	Blanket			
9.2.1	Structural Material		PCA[c]	PCA[c]
9.2.2	Breeding Material/Neutron Multiplier		α-$LiAlO_2$/Zr_5Pb_3	Li_2O/N.A.
9.2.3	Breeding Ratio		1.044	1.055
9.2.4	Number of Sectors		12 (Large) 12 (small)	8 identical
9.2.5	Weight of Sector	tonnes	65 (Large) 60 (small)	290
9.2.6	Weight of Largest Single Component	tonnes	65	290
9.2.7	Dimensions of Largest Component	m x m x m	3.9 x 12.4 x 13.8 high	8.6 x 5.8 x 5.9 high
9.2.7.1	Thickness of Blanket	m	0.68	0.70

		UNIT	STARFIRE VALUE	DEMO VALUE
9.	Reactor Components (cont'd)			
9.3	Shielding			
9.3.1	Material			
9.3.1.1	Inboard		W, Steel, B_4C, H_2O	Fe1422 Steel, B_4C, H_2O
9.3.1.2	Outboard		Ti-6-4, TiH_2, B_4C, Steel, H_2O	Concrete, B_4C, H_2O, Fe1422, Lead
9.3.1.3	Ducts		Steel, B_4C, H_2O, Ti-6-4, TiH_2	Concrete, B_4C, H_2O, Fe1422, Lead
9.3.2	Number of Sectors		12 large, 12 small	8 identical
9.3.3	Weight of Each Sector	tonnes	179 Large Sec. 226 Small Sec.	249
9.3.4	Weight of Largest Single Component	tonnes	411 (Large Sec. Plus 2 Ducts)	249
9.3.5	Dimensions of Largest Component	m x m x m	3.5 x 7.8 x 12.75 high	9.4 x 6.7 x 7.2 high
9.4	Magnets			
9.4.1	Toroidal Field Magnets			
9.4.1.1	Superconducting	yes/no	yes	yes
9.4.1.2	Conductor/Stabilizer Material		Nb_3Sn/Cu, NbTi/Cu	NbTi
9.4.1.3	Structural Material		316 LN stainless	316 LN stainless
9.4.1.4	Operating Temperature	K	4.2	4.2
9.4.1.5	Coolant		Liquid He, Bath Cooling	Liquid He, Bath Cooling
9.4.1.6	Stress in Coil	N/m^2	550×10^6 (max)	147×10^6 (avg)
9.4.1.7	Maximum Force Transmitted to Building	N/m^2	N.A.	N.A.
9.4.1.8	Maximum Field	T	11.1	10
9.4.1.9	Field on Plasma Axis	T	5.8	4.81
9.4.1.10	Number of Magnets		12	8
9.4.1.11	Field Ripple-Plasma Edge/Plasma Axis (Peak to Average)	%	$\pm 1.14/\pm 0.06$	$\pm 1.7/\pm 0.4$
9.4.1.12	Stored Energy	J	50×10^9	20×10^9
9.4.2	Equilibrium Field Magnets			
9.4.2.1	Superconducting	yes/no	yes	yes
9.4.2.2	Conductor/Stabilizer Material		NbTi/Cu	NbTi/Cu
9.4.2.3	Structural Material		316 LN stainless	316 LN stainless
9.4.2.4	Operating Temperature	K	4.2	4.2
9.4.2.5	Coolant		Liquid He, Bath Cooling	Liquid He, Bath Cooling
9.4.2.6	Maximum Stress in Coil	N/m^2	550×10^6	---

		UNIT	STARFIRE VALUE	DEMO VALUE
9.	Reactor Components (cont'd)			
9.4.2.7	Maximum Force Transmitted to Building	N/m^2	N.A.	N.A.
9.4.2.8	Maximum Field	T	4.5	---
9.4.2.9	Field on Axis	T	0.35	0.556
9.4.2.10	Number of Magnets		6	8
9.4.2.11	Field Ripple-Edge/Center	%	0/0	---
9.4.2.12	Stored Energy	J	$10x10^9$	$5.66x10^9$
9.4.3	Ohmic Heating Magnets		yes	N.A.
9.4.4	Correction Field Magnets			
9.4.4.1	Superconducting	yes/no	no	no
9.4.4.2	Conductor Material		Cu	Cu
9.4.4.3	Structural Material		Cu	Cu
9.4.4.4	Operating Temperature	K	353	353
9.4.4.5	Coolant		H_2O	H_2O
9.4.4.6	Maximum Stress in Coil	N/m^2	$14x10^6$	---
9.4.4.7	Maximum Force Transmitted to Building	N/m^2	N.A.	N.A.
9.4.4.8	Maximum Field	T	7.7	---
9.4.4.9	Field on Axis	T	0.26	---
9.4.4.10	Number of Magnets		4	4
9.4.4.11	Stored Energy	J	33×10^6	$3x10^6$
9.5	Energy Transfer and Storage			
9.5.1	Plasma Preparation			
9.5.1.1	Type		Electron Cyclotron Resonance Heating	Relativistic Electron Beam
9.5.1.2	Energy Per Unit	MJ	15	(Same as
9.5.1.3	Total Energy	MJ	15	Current Drive
9.5.1.4	Peak Power Transfer Rate	MW	5	System)
9.5.1.5	Transfer Time	s	3	
9.5.1.6	Depth of Discharge	%	N.A.	
9.5.1.7	Recharge Time	s	N.A.	
9.5.1.8	Pulse Frequency	s	CW	
9.5.1.9	Switching Requirements			
9.5.1.9.1	Current, Power Supply Output	A	11-15	
9.5.1.9.2	Volts, Power Supply Output	V	$25x10^3$	
9.5.1.9.3	Number of Power Supplies		432	
9.5.2	Primary Power Supply		N.A.	---
9.5.3	Current Drive Power Supply			
9.5.3.1	Type		Solid State Rectifier DC	13kV, 3-phase
9.5.3.2	Input Power	MWe	152.9	18.7
9.5.3.3	On Time	s	Continuous	Continuous
9.5.4	Poloidal Coil Supplies			
9.5.4.1	Main Equilibrium Coil Supply			
9.5.4.1.1	Type		Solid State Rectifier, Inverter	Solid State Rectifier Inverter
9.5.4.1.2	Peak Power Rating	MVA	290	156
9.5.4.1.3	On Time	s	1440	1440

		UNIT	STARFIRE VALUE	DEMO VALUE
9.	Reactor Components (cont'd)			
9.5.4.2	Correction Coil Supply			
9.5.4.2.1	Type		Solid State Rectifier/ Inverter	Solid State Rectifier/ Inverter
9.5.4.2.2	Peak Power Rating	MW	33	18
9.5.4.2.3	Average Power Rating	MW	2	1
9.5.4.4	Emergency Shutdown Equilibrium Coil Supply			
9.5.4.4.1	Type		Variable Dump Resistor	Variable Dump Resistor
9.5.4.4.2	Peak Power Rating	GW	10	5
9.5.4.4.3	On Time	s	3	3
9.5.5	Impurity Control			
9.5.5.1	Throughput (D-T)	molecules/ sec	5.0×10^{21}	3.8×10^{21}
	(He)	atoms/sec	1.25×10^{21}	3.8×10^{20}
9.5.5.2	Limiter Life	years	- - - - -	2
9.5.5.3	Limiter Materials		Be (leading edge and front surface); Ta-5W, FS-85, V-20Ti, or AMAX-MZC (heat sink)	Ta (leading edge), Be (front surface); Cu-2Be or V-15Cr-5 Ti (heat sink)
9.5.5.4	Peak Heat Flux	MW/m^2		
9.5.5.4.1	Front Surface		4.0	2.4
9.5.5.4.2	Leading Edge		2.3	1.0
9.5.5.5	Coolant		H_2O	H_2O
9.5.5.6	Coolant Inlet/Outlet Temp.	°C	115/145	< 100
9.5.5.7	Coolant Inlet/Outlet Pressure	MPa	---/4.2	< 0.1
9.5.5.8	Total surface area	m^2	---	61
10.	Electrical Power Requirements			
10.1	Cold Start Power from Grid	MWe/s	300/60	---
10.2	Auxiliary Power Requirements (Normal Operation)	MWe	240	55
10.2.1	Electrical Energy Storage (EF Coils)	MWe	None	None
10.2.2	Magnet Power Supply (other than energy storage)[e]	MWe	3.3	3
10.2.3	First-Wall/Blanket Circulators	MWe	30	9
10.2.4	Limiter Coolant Circulators	MWe	2.8	(Incl. in 10.2.3)
10.2.5	Shield Coolant Circulators	MWe	1.0	(Incl. in 10.2.3)
10.2.6	Refrigeration System	MWe	7.0	3
10.2.7	Vacuum System (Roughing)	MWe	0.15	(Incl. in 10.2.13)
10.2.8	Plasma Heating System	MWe	152.9	19

			UNIT	STARFIRE VALUE	DEMO VALUE
10.	Electrical Power Requirements (cont'd)				
	10.2.9	Miscellaneous Reactor Plant Auxiliaries	MWe	(Incl. in 10.2.13)	(Incl. in 10.2.2)
	10.2.10	Feed Pump System	MWe	N.A. (Turbine Driven)	N.A. (Turbine Driven)
	10.2.11	Condensing System	MWe	6	(Incl. in 10.2.12)
	10.2.12	Heat Rejection System	MWe	21.2	8
	10.2.13	Misc. BOP Auxiliaries	MWe	13.0	13
11.	Buildings				
	11.1	Reactor Building			
	11.1.1	Characteristic Dimensions	m x m x m	120x50x44 High	124x54x44 High
	11.1.2	Enclosed Volume	m^3	2.55×10^5	2.84×10^5
	11.1.3	Minimum Wall Thickness for Shielding	m	1.5	1.5
	11.1.4	Internal Pressure, Normal/Accident (gage)	MPa	-0.00001/+0.165	0.000001/ +0.165
	11.1.5	Containment Atmosphere		CO_2	CO_2
	11.2	Electrical Energy Storage Building		N.A.	N.A.
	11.3	Reactor Service Building			
	11.3.1	Characteristic Dimensions	m x m x m	($4160\ m^2$)x23 High	($5500\ m^2$)x 44 High
	11.3.2	Special Functions (i.e., hot cells, blanket processing equipment, etc.)		o Hot Cells o Waste Processing and Storage o New Component Receiving	o Hot Cells o Waste Processing and Storage o New Component Receiving
12.	Reactor Maintenance				
	12.1	Blanket/First Wall Replacement	% Surface Area/yr.	16.7	---
			Tonnes/yr.	139.6	---
	12.2	Radioactive Material Storage Requirement, Years/Volume	yr/m^3	(see Chap. 12 of final report)	---

[a] N.A. = Not Applicable; TBD = To Be Determined; TBR = To Be Revised.
[b] The "Nuclear Island" is defined as everything covered by Account No. 22 in PNL-2648, "Fusion Reactor Design Studies--Standard Accounts for Cost Estimates."
[c] PCA = Prime Candidate Alloy; a titanium-modified 316 austenitic stainless steel.
[d] Includes electro-magnetic radiation components from synchrotron, Bremsstrahlung, and impurity inputs.
[e] Transformer losses, conductor and rectifier.
[f] Values for 600 s after shutdown
[g] Defined as MWth rating divided by volume enclosed by and including field coils.
[h] Includes estimates of 10 kg for STARFIRE and 1 kg for DEMO as blanket tritium inventory. These estimates are subject to large uncertainties. (See Sec. 6.4.4.2 of this report.)

REFERENCES FOR CHAPTER 2

1. C. C. Baker, et al., "STARFIRE - A Commercial Tokamak Fusion Power Plant Study," Argonne National Laboratory, ANL/FPP-80-1 (1980).

2. "The Fusion Engineering Device," U. S. Department of Energy, DOE/TIC-11600 (1981).

3. W. M. Stacey, Jr., et al., "U. S. Contribution to the International Tokamak Reactor Phase-I Study," Georgia Institute of Technology, USA-INTOR/81-1 (1981).

4. "International Tokamak Reactor - Phase One," International Atomic Energy Agency, Vienna (1982).

5. W. M. Stacey, Jr., et al., FED/INTOR - Phase 2A (October, 1982).

6. M. A. Abdou, et al., "A Demonstration Tokamak Power Plant Study - Interim Report," Argonne National Laboratory, ANL/FPP/TM-154 (1982).

7. M. A. Abdou, et al., "Impact of Major Design Parameters on the Economics of Tokamak Power Plants," Proc. IAEA Workshop on Fusion Reactor Design Concepts, Madison, Wisconsin, 1977, IAEA-TC-145/44 (1978).

8. M. A. Abdou, "Radiation Considerations for Superconducting Fusion Magnets," J. Nucl. Mater., 72, 147 (1978).

9. K. B. Axon, et al., Plasma Physics and Controlled Nuclear Fusion Research 1980, IAEA, Vienna, Vol. 1, p. 413 (1981).

10. N. J. Fisch and C. F. F. Karney, Phys. Fl., 24, 27 (1981).

11. A. Sykes, J. A. Wesson, S. J. Cox, Phys. Rev. Lett., 39, 757 (1977); Ya. I. Kolesnichenko, et al., Proc. 9th International Conference on Plasma Physics and Controlled Nuclear Fusion Research, Paper W-8, Baltimore, Maryland (1982), to be published.

12. D. A. Ehst, et al., J. Fusion Energy, 2, 83 (1982).

13. H. Iida, Fusion Engineering Design Center, Private Communication (1982).

14. N. J. Fisch, Proc. 4th Topical Conference on RF Plasma Heating, Paper B-1, Austin, Texas (1981).

15. C. C. Baker, et al., Proc. 9th International Conference on Plasma Physics and Controlled Nuclear Fusion Research, Paper E-1-1, Baltimore, Maryland (1982), to be published.

16. "Particle Beam Fusion Progress Report," Sandia National Laboratory, SAND81-1459 (1982).

17. V. Bailey, et al., Physics International Company, PIFR-1466-1 (1982).

18. A. Mohri, et al., Plasma Physics and Controlled Nuclear Fusion Research 1980, IAEA, Vienna, Vol. 1, p. 511 (1981).

19. C. A. Flanagan, et al., "Fusion Engineering Device Design Description," Oak Ridge National Laboratory, ORNL/TM-7948 (1981).

20. W. M. Stacey, Jr., et al., "U. S. Contribution to the International Tokamak Reactor Workshop," (1979).

21. Y. Gohar and M. A. Abdou, "INTOR Radiation Shielding for Personnel Access," Proc. 9th Symposium on Engineering Problems of Fusion Research, Chicago, Illinois (1981).

22. B. S. Brown, "A Review of Radiation Effects in Superconducting Fusion Magnet Materials," J. Nucl. Mater., 97, 1-14 (1981).

23. A. E. Profio, "Radiation Shielding and Dosimetry," Wiley-Interscience Publication, New York (1979).

CHAPTER 3

R&D STRATEGIES

Chapter 3

Table of Contents

Chapter 3

List of Figures

Chapter 3

List of Tables

3.0 R&D STRATEGIES

The focus of this study was on critical assessments of key reactor components. An important part of the effort was the identification of key issues and the R&D requirements to resolve these issues.

The R&D needs to resolve the key issues are presented in this chapter for the following areas: 1) Current Drive and Plasma Engineering, 2) Impurity Control, 3) Tritium Breeding Blanket, 4) Data and Methods for Radiation Shield, and 5) Maintenance and Configuration. The R&D needs identified here are limited to those impacting key issues.

3.1 R&D Needs -- Current Drive and Plasma Engineering

Experimental and theoretical plasma research has identified a variety of means to maintain the toroidal tokamak current by noninductive means. In what follows we analyze a number of these options in light of our present understanding of their respective reactor requirements. Near term R&D needs are listed for the more promising drivers, and the need for a longer term program for steady state tokamak experiments is pointed out.

3.1.1 Reactor Prospects for Various Current Drivers

The DEMO interim report[1] included a broad survey of current driver options and compared circulating power and net electric plant power production (P_{net}), which represent one set of important tests for the different options. Additional considerations -- capital cost, reliability, ease of maintenance, and reactor compatibility -- are important in the of selection of approaches that deserve future R&D support and are emphasized in this section. The analysis here assumes that a reasonably constant plasma condition is to be maintained, i.e., the current, density, and temperature are to be held constant. Other scenarios, which require oscillating plasma parameters, will be considered in Sec. 3.1.2.

Table 3-1 summarizes information from this section and includes both net electric power and the driver capital costs for the purely steady-state operating mode. After the following briefly stated conclusions each current drive method is individually discussed. Indirect current drive, via wave heating (ECRH, ICRH), does not promise significant P_{net} to justify its use in

Table 3-1. Current Driver Performance Based on DEMO Interim Report Assuming Steady-State Plasma

Driver	P_{net} (MW)	$\bar{T}_e$ (keV)	$\langle P_d \rangle$ (MW)	$\langle P_d \rangle / \eta_d$ (MW)	Capital Cost, Driver plus Power Supply[a]	Shielding Area (m^2)	Reactor Maintenance	Driver Maintenance
NB	140	17	80	100	$\$(2.8\text{-}6.0)/W \times \langle P_d \rangle$ = \$220-480 M	692 (2 beam lines)	Difficult	Difficult
REB[b]	430	8	6.7	18.7	$\$(1.1\text{-}1.5)/W \times \langle P_d \rangle$ = \$7.4-10.1 M	43 (2 beam lines)	OK	OK
He^3ICRH	30	20	103	146	$\$2.6/W \times \langle P_d \rangle$ = \$270 M	Very small	OK	OK (?)
ECRH	20	18	80	235	$\$(5\text{-}6)/W \times \langle P_d \rangle$ = \$400-480 M	Very small	OK	OK
CAW[c]	400	9	46	65	$\$2.6/W \times \langle P_d \rangle$ = \$120 M	Very small	OK	OK (?)
FW	110	18	80	114	$\$2.6/W \times \langle P_d \rangle$ = \$208 M	Very small	OK	OK (?)

[a]This cost excludes shielding and containment building costs; approximately 1981 dollars.

[b]REB can be upgraded to provide $\langle P_d \rangle$ = 30 MW for auxiliarly heating (20-30 s) @ \$0.4/W, for a total of ~ \$12 M.

[c]Neoclassical effects ignored.

a demonstration reactor. The capital costs associated with neutral beams (NB) and the fast wave (FW) appear to be a good fraction of the total DEMO cost, i.e. $200-500 M. The maintenance concerns attached to neutral beams further mitigate against their selection. The most promising choices, the relativistic electron beam (REB) and compressional Alfven wave (CAW), need the smallest circulating power, and consequently their capital costs are the least, being no more than a few per cent of the total power plant cost. These latter two drivers unfortunately have theoretical complications which make our conclusions quite tentative. In particular, the current density profiles to be obtained with these drivers are somewhat speculative. Various neoclassical theoretical concerns suggest that hollow current densities might result, and the general question of stability for such tokamak equilibria has only recently begun to receive serious consideration.[2,3] It will be necessary to implement an experimental program to evaluate accurately the current drive potential for these various options.

Neutral beam-driven current results in substantial net power (~150 MW) only when the electric efficiency of the driver system, η_{NB}, exceeds about 0.80 and if the neutral energy exceeds ~ 0.5 MeV. For these conditions a negative ion (D^-) source, electrostatic quadrupole (ESQ) focused accelerator, and a laser neutralizer would be required. This technology will require extensive development. The ESQ accelerator is the least advanced component. For DEMO, two beam lines each rated at 2 MeV and 20 A would suffice. The systems would be shielded and located in the reactor hall[4] (see Fig. 3-1). It is expected that neutron damage to components (magnets, ion sources, laser optics) can be minimized and that the heat load on the vacuum system can be reduced to the point that a practical system can be built. TRW expects capital costs to range from $2.50/W to $6.00/W, exclusive of development, depending on the power rating of the beam system.[4] This cost includes power supplies but does not include radiation hardening and massive shielding around the neutral beams, and it does not reflect the extra costs of the enlarged reactor hall floor space. Remote maintenance of the tokamak will be severely hindered by the presence of these beam lines, and the beams themselves will require remote servicing.

A pulsed relativistic electron beam (REB) would require the least circulating power; the net power production is quite insensitive to the efficiency, η_{REB}, of the power train. Rep-rated technology development for the REB is

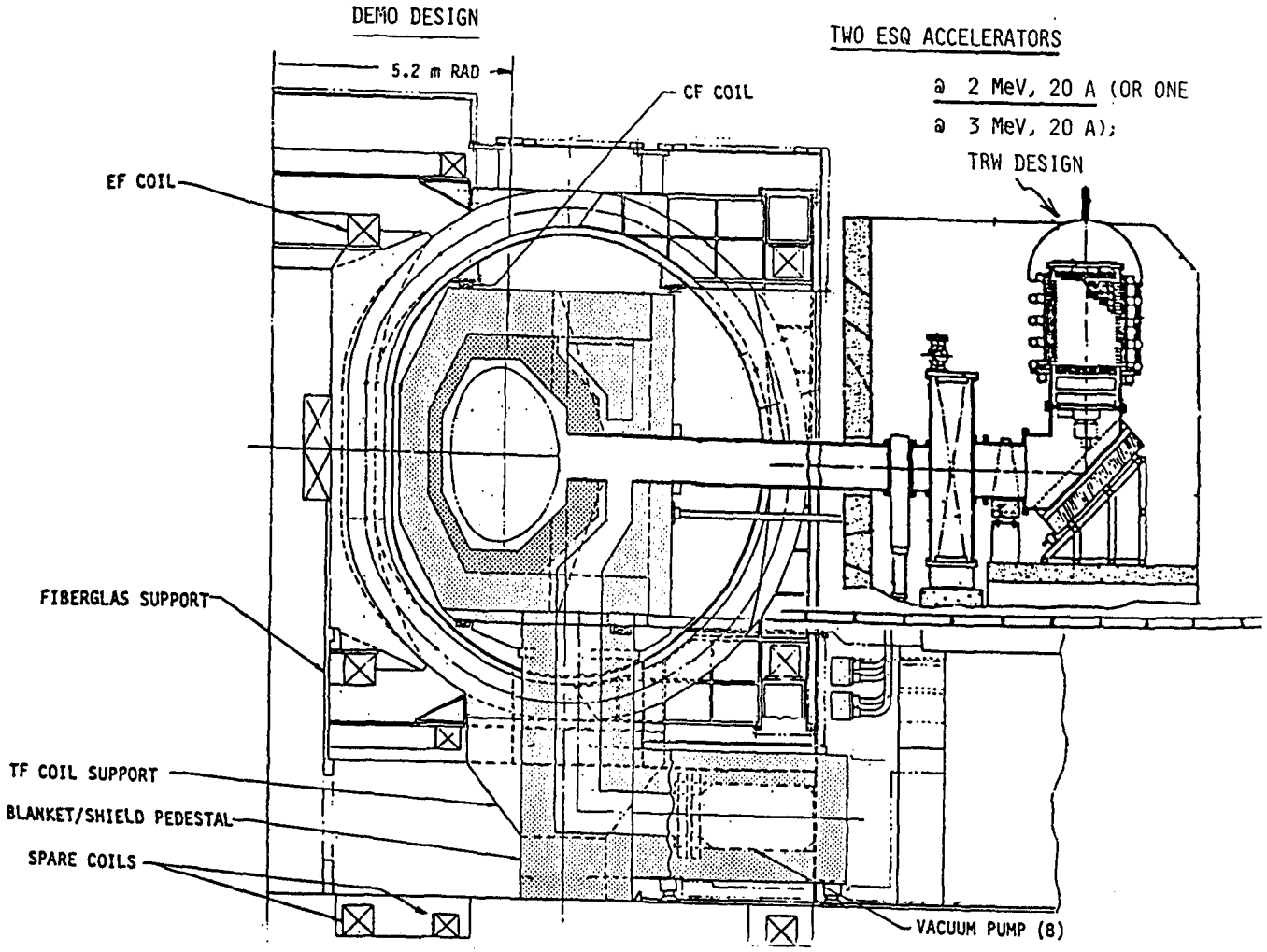

Figure 3-1. Neutral beam current drive option.

currently carried out at Sandia National Laboratory for inertial fusion applications, and requisite components for DEMO could be available in a few years. Two coaxial diodes (see Fig. 3-2) would be adequate. The lines could have several bends to minimize radiation streaming and a vacuum window to contain tritium. Magnetic insulation will permit vacuum gaps as small as a centimeter through the blanket and shield. The system is expected to provide months of continuous operation, and the life-limiting components may be readily serviced in a separate power supply building. It may be possible to recess the cathode (central conductor) by locating it behind the limiter blade for protection from disruptions and to minimize surface heating and sputtering during normal operation. Prices for pulsed power systems are generally controlled by energy storage costs and have historically been around \$10/J for Marx-generator technology.[5] Recent developments in inertial energy storage (rotating flux compressers) promise substantial cost reductions — \$3/J to \$5/J -- for rep-rated systems. Since the REB system can be overpowered by large factors for tens of seconds, the current drive system can be upgraded for auxiliary heating for very small cost increments. Of equal importance to the features above, the REB transmission line may be routed in a manner which permits almost unimpeded access to the tokamak during remote maintenance activity. The premier issue at present is whether the REB will penetrate sufficiently far into the plasma to create an acceptable equilibrium current density profile. In view of the nonclassical electron transport which characterizes tokamaks it appears that this question might only be adequately answered with a moderate scale experimental test.

Minority cyclotron heating has been demonstrated and seems to agree with wave damping theory. There is good reason to believe that anisotropic heating (e.g. ^{3}He in DT) will generate current. However, the theoretical plasma efficiency ($\hat{j}/\hat{p}$) for this driver is so poor that a maximum net power, P_{net}, of only 30 MW is likely, and even this would require $\eta_{ICRH} = 0.70$, which is an optimistic value.

Anisotropic ECRH has been shown to generate current; however, achieving one-sided damping near the cyclotron layer appears to be difficult in practice because the ray paths would require very accurate trajectories to assure damping on the tail of the electron distribution function. In addition, the projected system efficiencies are relatively poor for cw operation of high

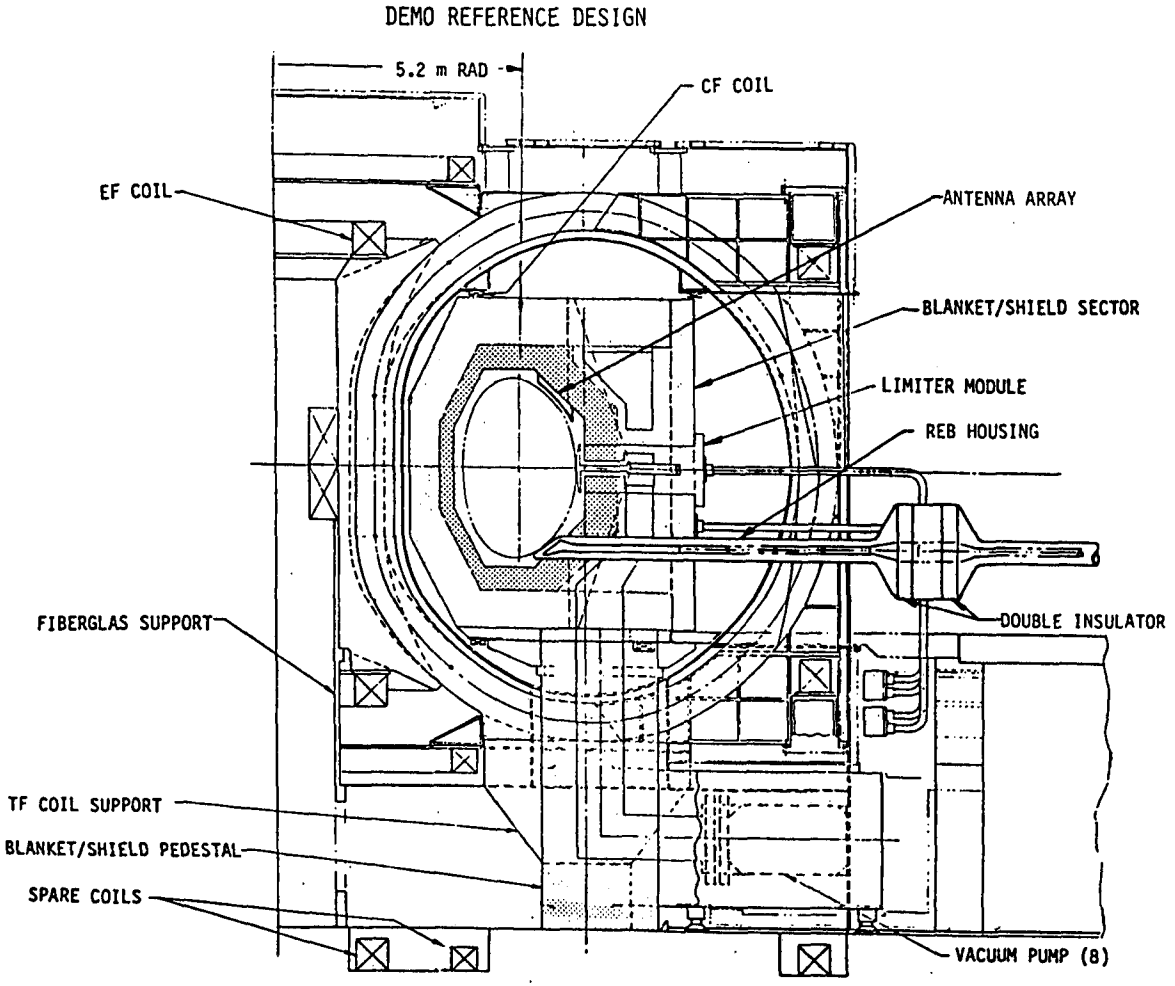

Figure 3-2. DEMO displaying REB and fast wave hardware options.

frequency, high power tubes such as gyrotrons and quasi-optical klystrogyrotrons. The R&D needs for these tubes are considerable, and TRW estimates of capital costs[4] would suggest that prices will exceed those for lower frequency rf systems. In many respects ECRH is quite compatible with a reactor environment; horn couplers are mounted flush to the first wall, waveguides are small and easily located to permit access to the tokamak, and high maintenance items (e.g., tubes) can be located outside the reactor hall. However, radiation damage to waveguide windows and optics has not been adequately assessed.

At very low frequencies (~ 5 MHz) the compressional Alfven wave (CAW) promises very high current drive efficiency, but its prospects are clouded by concerns that neoclassical effects may be important since momentum is added to electrons in the magnetically trapped region of phase space. If neoclassical effects are ignorable (infinite aspect ratio) this current driver requires the least circulating power of all waves, and net power (~ 400 MW) is close to the gross electric power output, assuming a power efficiency $\eta_{CAW} = 0.70$. Moreover, (assuming low order eigenmodes may be excited) it appears that centrally peaked current densities are likely. RF technology is fairly standard at these frequencies. Sources would be located in a remote building, and coaxial transmission lines would carry power to the tokamak. Remote maintenance of the reactor and rf components in the reactor hall seems possible. The principal reliability issue is the lifetime of the phased antenna array which must be situated within the reactor chamber. Presumably, some sort of recessed first wall configuration would be needed, but no design studies have been performed. The issue of electron neoclassical effects is crucial in determining the success of this promising driver option. While transit time magnetic pumping (TTMP) has been demonstrated on ions,[6] there has been little experimental effort on electron damping. Since the present experimental work in this frequency regime is very limited [e.g. TCA (Lausanne), Pretext] it would be worthwhile to expand the investigation of current drive with trapped electron effects.

Even at frequencies (~ 82 MHz) somewhat above the deuteron cyclotron frequency the fast wave is predicted to generate current via the TTMP mechanism. Since momentum is given in this case to suprathermal electrons neoclassical effects are irrelevant, and, with an η_{FW} of 0.70, net power of ~ 100 MW is possible with an rf input of ~ 80 MW. Technology is well developed at this

frequency, and costs are expected to be about \$2.60/W.[4] Remote sources and coaxial transmission lines provide the same advantages as for the lower frequency CAW, but it may be possible to use reentrant waveguides[7] which would considerably ease the engineering difficulties.

3.1.2 Critical Issues: Theory and Experimental Needs

Near-term needs for the four most promising current drive techniques (lower hybrid — LH, fast waves — FW, compressional Alfven waves — CAW, and relativistic electron beams - REB) are summarized in Table 3-2 and discussed in this section. Discussion of the LH wave was deferred from the last section because its practical application apparently will imply constraints on reactor operation (e.g., oscillating power).

According to linear theory, the LH wave accessibility constraint forces the selection of slow phase speeds (large $n_\parallel$) in order to permit wave penetration to the high density plasma at the magnetic axis. Consequently the circulating power will be large in order to drive a centrally peaked current density, since the current drive efficiency drops as the square of $n_\parallel$: $(j/p) \propto [n_e n_\parallel^2]^{-1}$. This accessibility limit and resulting large circulating power for high density current drive were recognized early,[2,8] and recently proposals have been made to utilize oscillating plasma density and temperature with pulsed LH current drive in order to reduce the time-averaged circulating power.[9] Since neutral beams and all waves are more efficient at lower n_e these oscillating plasma scenarios have been suggested as a general means of reducing the time-averaged circulating power[10,11] for steady-state current maintenance. In view of the experimental verification[12] of LH current drive at low density ($n_e \leq 4 \times 10^{19}$ m^{-3}) it appears worthwhile to study the oscillating plasma approach to current drive. The LH wave is receiving worldwide attention on experimental tokamaks and has a waveguide power transmission system which has attractive reactor features. However, if an oscillating plasma mode is proposed for reactors we must seriously assess its advantages (steady plasma current, low-average circulating power) and disadvantages (oscillating first wall flux, oscillating neutron heating of the blanket, disruption frequency, oscillating vertical fields, energy storage, driver capital cost). This type of reactor calculation can be performed readily with time-dependent plasma simulations coupled to thermal-

Table 3-2. Near-Term Current Drive Program in Support of DEMO for the Four Most Promising Driver Options

Driver	Theory/Calculation Needs	Experimental Tests[a]	Technology R & D
LH	Assess oscillating plasma scenario for reactors.	PLT/Alcator C: test linear theory, accessibility, resonance cones, frequency selection, $k_{\parallel}$ spectrum, density effects, etc.	High power cross-field amplifiers; radiation effects on waveguide windows; vacuum density control in waveguides.
FW	Ray tracing t $\omega/k_{\parallel} > 3\ v_e$ and $A \gtrsim 5$; antenna coupling theory - spectrum for loops vs. phased reentrant waveguides.	PLT: Test electron TTMP, current drive; test reentrant waveguide performance.	Radiation effects on waveguide windows; design possibilities for antenna loops, recessed cavities, reentrant or ridged waveguides.
CAW	Effects of non-neoclassical electron orbits; phased antenna loop coupling, spectral theory; spatial damping, current density profile.	PLT/TEXT: study selective coupling to CAW; test electron TTMP, current drive; determine $k_{\parallel}$ spectral width.	Radiation effects on coax windows; design possibilities for antenna loops.
REB	Relativistic electron orbits, beam capture and penetration, resulting current density profile.	TEXT: test beam penetration, long pulse current density evolution; diode voltage, pulse width, current density, location, configuration relationships.	High voltage spark gaps; high energy density liquid dielectric capacitors; compulsators, rotating flux compressors; high voltage pulse transformers; radiation effects on coax windows; diode protection from disruptions.

[a] Device identified represents either ongoing experimental program or an indication of the type of device required to perform the experiments.

hydraulic and magnetic computations with appropriate constraints such as fatigue and eddy-current limitations. In Table 3-2 the LH option is listed as part of a general program of calculations and experiments needed in support of DEMO.

The high phase speed fast wave (termed HSMS in Ref. 1) is an attractive current driver since it has no accessibility constraint inhibiting current drive at high density and since TTMP is a relatively efficient mechanism for momentum transfer. One means for reducing circulating power[11] from that in Table 3-1 is to design reactors at fairly large aspect ratio, $A \gtrsim 5$, since this permits the use of higher phase velocities without the concern of increased damping of alpha particles. This wave has received little attention for current drive, the only experimental test has been performed on a small, collisional toroidal plasma, Synchromak.[13] In fact, there has been no unambiguous test of electron TTMP in a hot plasma, although the theory is well understood. The promises of moderate circulating power, centrally peaked current density, steady-state plasma operation, and the possibility of a reactor-compatible power delivery system combine to make this a good target for further evaluation.

The CAW is the most efficient wave candidate if neoclassical effects are not present. In the U.S. there have been no experimental studies of this wave, although the related shear wave has been excited on Pretext. There are reports of current drive attempts in this frequency range $(\omega \ll \Omega_0)$ from abroad.[14] Again, the electron TTMP mechanism remains largely untested. At these low frequencies it is possible to excite desirable traveling wave eigenmodes if the tokamak dimensions are large, so it may be most appropriate to study CAW current drive in fairly large machines, e.g. PLT or DOUBLET III. The (loop) antenna structure clearly requires serious analysis concerning its viability in a reactor environment. However, at these low frequencies the antenna may be recessed a good distance from the plasma without sacrificing its performance. (The DEMO design team was not aware of any detailed analysis of a low frequency loop antenna for a fusion reactor.) CAW offers the possibility of low circulating power, steady-state plasma operation, and the relative ease of reactor and rf system maintenance and this option should receive greater emphasis for tokamak current drive.

The principal question regarding REB current drive revolves around the issue of relativistic electron orbits in the tokamak. For an ideal axisymmetric tokamak, neoclassical theory predicts radial penetrations of only a few centimeters as 1.5 MeV electrons lose energy and canonical angular momentum in the presence of the reverse emf. Therefore there is concern that in the long term the REB can support only hollow current density, j(r), equilibria with unacceptably low beta. These concerns may be addressed by a number of theoretical appraches, as follows:

- The permissible hollowness of j(r) needs to be understood. A number of studies,[6,7] motivated by the accessibility limitations to lower hybrid current drive, have found attractive stability properties for various hollow equilibria.

- Higher γ_d (relativistic mass ratio) permits larger radial penetration in neoclassical theory.[15,16] Since high voltage and energy REB sources are available, the option of high voltage (~ 50 MeV) may deserve further consideration.

- Electrons do not behave in tokamaks as predicted by neoclassical theory, as is well known. Numerous experimental studies[17-19] of relativistic electron transport have been made (LT-3, ORMAK, TFR, Pulsator, PLT), and the anomalously large transport has been variously attributed to ergodic magnetic field topology, internal disruptions, and magnetic islands. Most remarkable is a set of calculations[18] demonstrating that $\gamma_d \approx 10$ electrons can traverse large fractions of the minor radius in a few hundred toroidal transits in the presence of strong, nonaxisymmetric islands and yet remain completely contained within the plasma. If magnetic helicity does not occur naturally in tokamaks it might be transiently induced during diode operation by extending the diode's center conductor and winding it along a helical path part way around the torus, inside the vacuum vessel.

- An additional threat to the postulate of axisymmetry is that the self fields of the REB may be sufficiently strong to locally perturb the tokamak equilibrium field. (The cathode current density can exceed that of the plasma current density.) The Cornell device clearly demonstrated the REB's ability to divert the toroidal field during

diode operation.[20] In order for the REB to "dig a hole" into the plasma column it would have to propagate a distance without being current neutralized (by the return current).

- Even if the REB cannot provide a strong current source on axis it is conceivable that the nonlinear activity of nonaxisymmetric MHD modes may serve to fill in the central current density, perhaps in a manner analogous to the relaxation of skin currents during the startup of ohmic discharges. Intensive study of this possibility has already started for conventional tokamaks.[17,21]
- Ions, having larger mass, appear to behave approximately as predicted by neoclassical theory and have already demonstrated current drive (neutral injection on DITE). Recent studies[10] have demonstrated the desirability of using pulsed neutral injection on INTOR/DEMO to minimize the time-averaged power for current drive, but these proposals require periodic temperature reductions to increase the return current resistivity. Intense pulsed ion beams[22] may achieve the same effects without varying plasma temperatures or density, and may achieve better penetration than the REB. The technology is similar to that for the REB, and, if a plasma diode can be used, it would circumvent beam transport problems associated with neutral[10] and charged ion injection.[23]
- Hybrid scenarios with the REB and a transformer could prove valuable to DEMO. The obvious choice would be to use the REB's demonstrated ability to ionize the fill gas and generate toroidal current without a transformer and subsequently maintain a very long ohmic discharge with a low loop voltage.
- The REB may enhance tokamak reactor prospects if used in combination with another driver. For example, the fast wave might provide current density on axis while the REB could broaden j(r) or provide stabilizing force free currents[24] near the plasma boundary.

A one-dimensional theory of REB current drive is being developed (at ANL) which can quantitatively address ideas such as those above. Subroutines can be developed for transport code analysis of the temporal and spatial evolution of REB-driven currents. Plasma theory developments should be constantly cali-

brated against experiments. In addition, experiments should be supported by appropriate theory. Thus, it appears essential to carry out both theory and a new experimental effort to settle the REB feasibility question.

While intense pulsed ion current drive can be tested on a small machine, it appears necessary to test REB penetration on a larger device for which the neoclassical orbit width is a small fraction of the minor radius. The appropriate tokamak would thus require $I_0 \gtrsim 100$ kA, and multipulse injection would be required in order to sustain I_0 for a period long enough for the current density profile to reach equilibrium. Figure 3-3 shows the REB requirements for an experiment on TEXT (R_0 = 1.0 m) for 100 kA and 400 kA. In either case $\langle P_d \rangle \approx 2\ I_0^2 R$. Since $I_0 R$ on TEXT is always about 2 V, an average power of 400 kW to 1600 kW is needed. For example, a 1.5-MV beam $(\gamma_d = 4)$ must be injected with W_d = 8 kJ every 20 ms. Such high rep rates appear reasonable for short bursts (~ 1 s) from equipment presently under development at Sandia. Other combinations of rep rates and beam energy for I_0 = 100 kA are given in Fig. 3-4 along with the current amplitude fluctuation, ΔI. From stability considerations it would appear desirable to operate at the highest practical rep rates, such that $\Delta I/I_0$ is as small as possible.

The REB hardware, described in detail in Chapter 4, promises to provide a robust, inexpensive driver system which is compatible with a reactor environment and which requires very little circulating power, without the need for density and temperature oscillations. Considering its potential for creating a truly steady-state plasma, as well as other applications (e.g., initiating the toroidal current without a transformer), the REB merits continued study as a current drive option and has been included in Table 3-2.

3.1.3 Longer-Term Experimental Needs

Should experiments prove successful on devices such as PLT and TEXT, additional and more ambitious demonstrations around 1985 would be required to support DEMO. Three options merit consideration and will be discussed here: use of either (1) TFTR; or (2) the big D at General Atomic Company; or (3) a device specifically designed for noninductive current drive experiments. We will discuss these in turn.

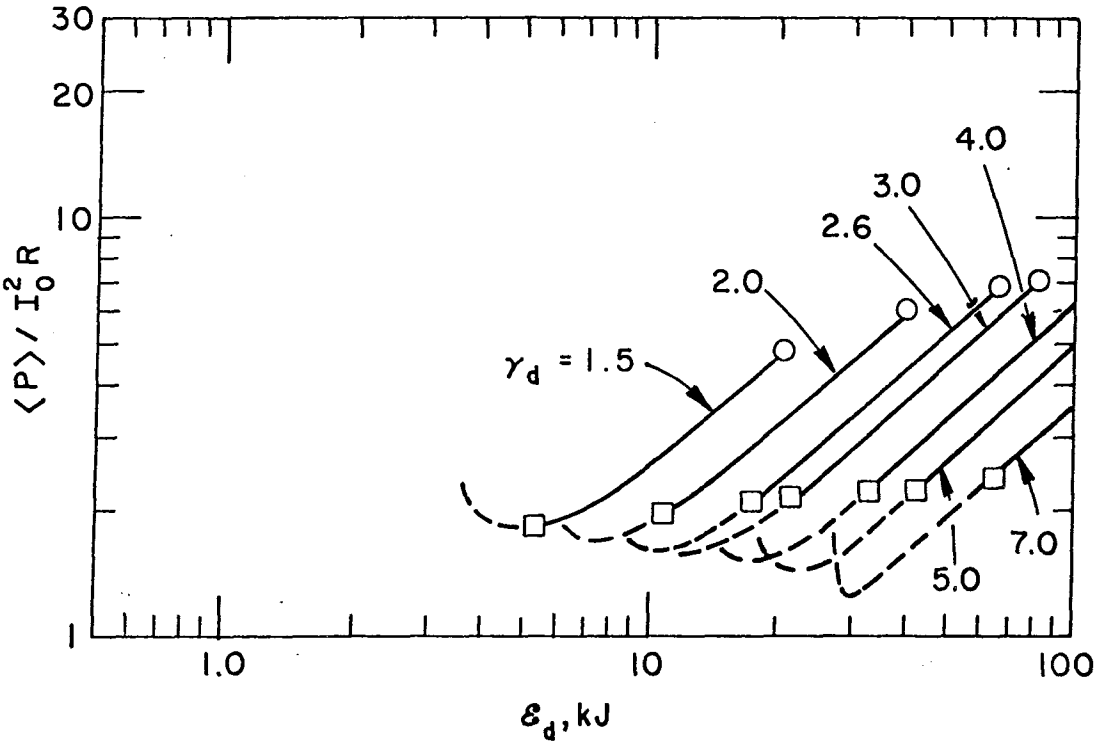

Fig. 3-3a. REB current drive requirement for I_0 = 400 kA and R_0 = 1.0 m (TEXT).

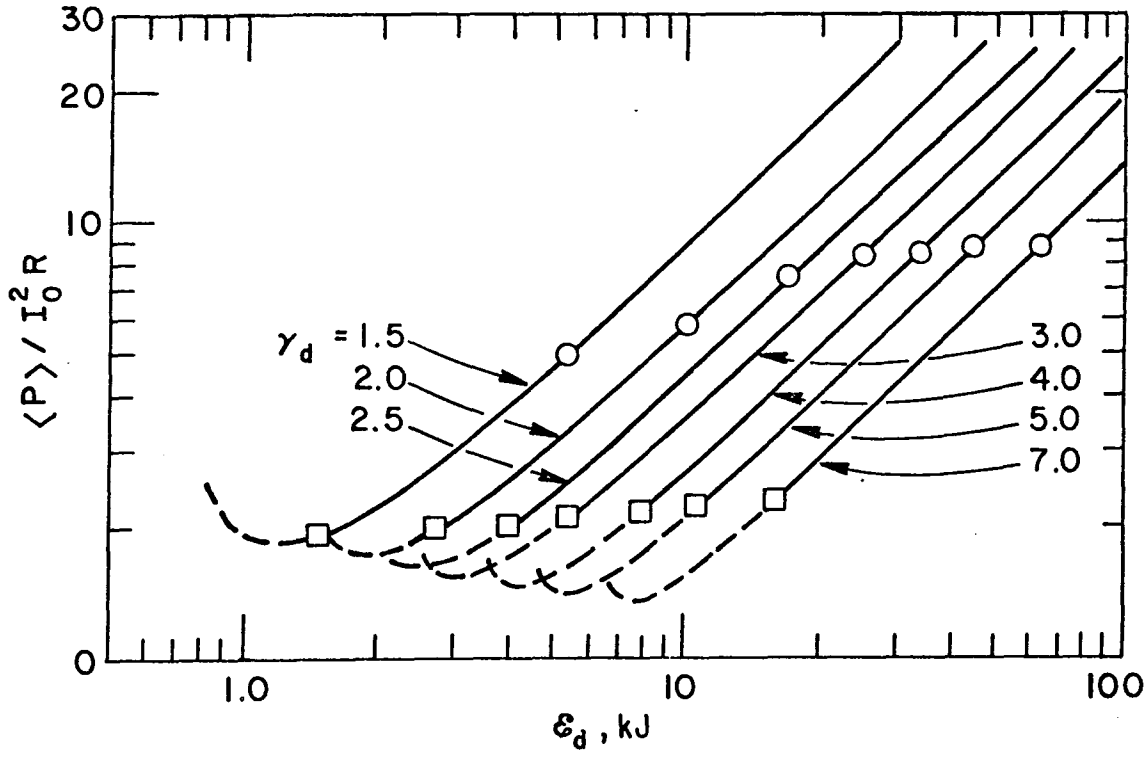

Fig. 3-3b. REB current drive requirement for I_0 = 100 kA and R_0 = 1.0 m (TEXT).

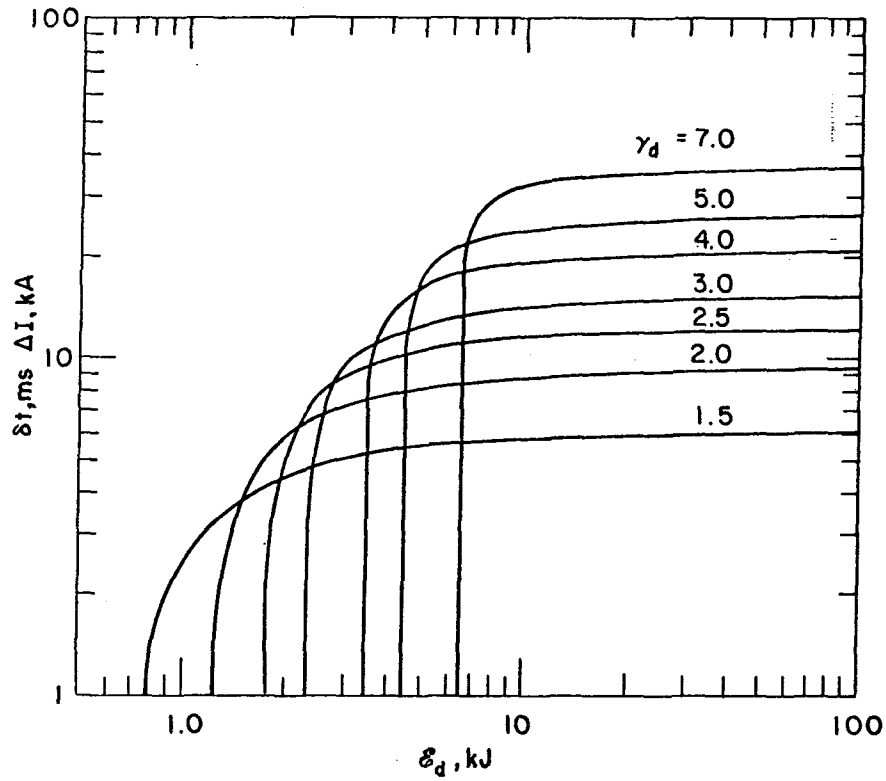

Figure 3-4. REB interpulse period and current increment on TEXT for I_0 = 100 kA, assuming I_0^2R = 200 kW; note, L/R = 100 ms.

TFTR should support 2.5 MA of toroidal current and would thus provide a test bed for short duration current drive experiments. However, even if the toroidal field is derated, the maximum discharge would be limited to about 20 s.[25] This is far too short if "steady-state" current drive is a goal. An important concern with many drivers is that the current density profile may be hollow or otherwise pathological. An adequate test of these issues will therefore require current drive periods exceeding the magnetic diffusion time scales ($\approx L/R$) in the test devices. With central temperatures of 12 keV we expect $L/R \approx 300$ s in TFTR, so definitive tests of the current density evolution could not be performed.

When DOUBLET III is reconfigured as a big D it might provide opportunities to test current drive. This tokamak should contain currents up to 5.0 MA, and the coils may provide a toroidal field for several seconds. Reactor densities ($> 10^{20}$ m^{-3}) and, with the advent of 16 MW of auxiliary heating, reactor temperatures are expected. This device is not encumbered with an igloo or other biological shielding and so may be more flexible than TFTR for physics experimentation. As with TFTR, though, the severe limitation is that the discharge is far too short to test current profile equilibration adequately.

It seems necessary, therefore, to test current drive in a long pulse tokamak capable of operation in excess of $\sim 10^3$ s. (Such a long pulse would doubtless also be useful for impurity generation monitoring and control attempts.) Such a tokamak would not need D-T fuel in order to address current drive questions, but auxiliary heating would be desirable in order to maintain reactor temperatures for long pulses. While resistive magnet designs may be capable of such long pulse operation, it would be worthwhile considering superconducting toroidal magnets. A superconducting tokamak would in principle permit true steady-state operation (many hours) and would require continuous power ($\approx$ 10 MW), for example from ICRH, to maintain reactor temperatures, as well as to maintain the toroidal current. Figure 3-5 gives REB current drive requirements for a hypothetical tokamak with $I_0 = 1.0$ MA and $R_0 = 2.1$ m. If a 1 MV beam were used with $W_d = 120$ kJ per pulse then $\langle P_d \rangle \approx 2.1\ I_0^2 R$. Provided auxiliary heating maintained a central temperature $T_{e_{\Omega 1}} = 10$ keV then $I_0^2 R \approx 120$ kW, so the REB system would be pulsed at a rate $\delta t^{-1}_{\Omega 1} = 2.1\ s^{-1}$. Assuming about 50% energy transfer efficiency, a constant

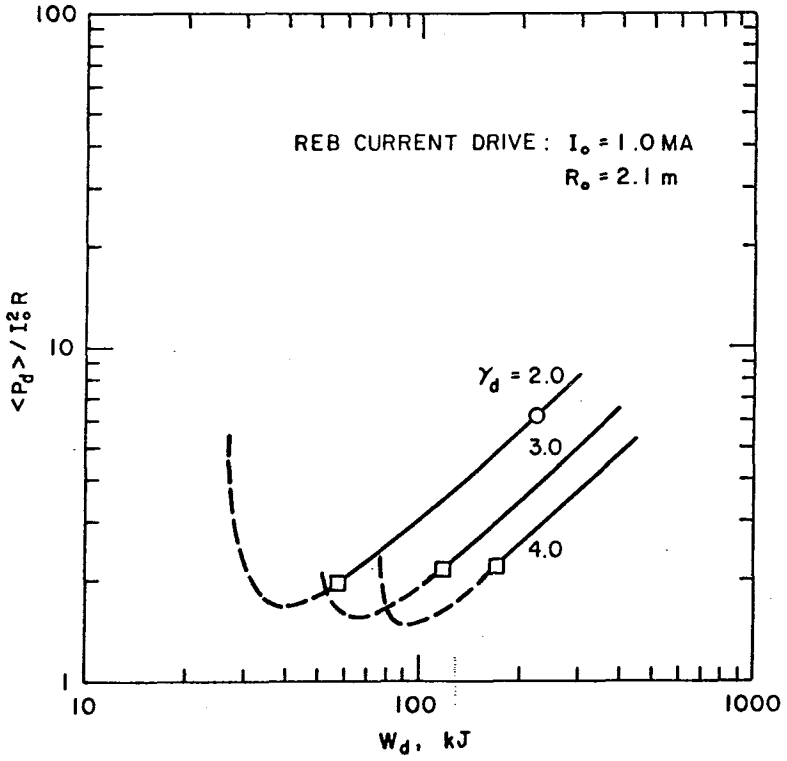

Figure 3-5. REB current drive requirements for advanced tokamak with I_0 = 1.0 MA and R_0 = 2.1 m.

electric power of ≈ 500 kW would be necessary. An REB power train based on the magnetically insulated transmission line (MITL), liquid capacitor, high voltage pulse transformer, and compulsator concept would cost ~ $1.5-4.5 M, depending on the pulse width desired and number of MITLs needed.

In order to confidently design DEMO for steady-state operation it appears very desirable to test current drive options on a dedicated tokamak capable of operation for periods in excess of 10^3 s. We would thus recommend a more detailed cost/benefit analysis for a large, possibly superconducting, tokamak devoted to current drive experiments, which would not be a D-T fueled device.

3.2 R&D Needs -- Impurity Control

Impurity control is intimately tied to several disciplines including plasma physics, surface science, materials science and engineering, and vacuum technology. As such, the R&D strategy encompasses a wide breadth, and there are a large number of questions which must be answered prior to design and construction of DEMO. The R&D issues have been categorized as feasibility issues, crucial design issues, lifetime issues, and safety issues.

Table 3-3 shows the relationship between R&D issues and recommended R&D tasks and disciplines that address these issues in three key areas: plasma engineering, plasma-materials interactions, and materials engineering. Work in these three areas can be carried out in parallel, but interaction between them is essential for a successful program. The feasibility issues and some of the crucial design issues involve questions concerning plasma engineering and plasma-surface interactions. The other issues are related primarily to materials behavior and materials development. The feasibility issues should have the highest priority, although work should be initiated on the other issues because the R&D required is likely to be long term. This section emphasizes the development of the pumped limiter which is the reference impurity control system for DEMO. The R&D required for development of divertors is, in many cases, the same as that required for limiters, so that much of the following discussion also applies to divertors.

To some degree the R&D needs stated here will be addressed by ongoing programs, particularly in the areas of first-wall-plasma interaction and materials and component engineering; however currently planned programs are by no means complete. National programs in these specific areas include the

Table 3-3. R&D Tasks and Issues

R&D Tasks / R&D Issues	Plasma Engineering			First Wall-Plasma Interaction			Materials & Comp. Engineering				
	Pumping Efficiency	Plasma Edge Char.	Enhanced Rad.	Erosion/ Redep.	Self Sputtering	Disrupt. Response	Coat/Clad Develop.	Recoating	Mat. Properties	Thermomech. Response	Electromagnetic Response
Feasibility Issues											
Pumping Characteristics	X	-	-	-	-	-	-	-	-	-	-
Impurity Behavior											
Sputtering/Redeposition	-	X	-	X	X	-	-	-	-	-	-
Buildup in Plasma	-	X	X	-	-	-	-	-	-	-	-
Plasma Dynamics	X	X	X	-	-	-	-	-	-	-	-
Crucial Design Issues											
Plasma Edge Operating Characteristics	X	X	X	-	-	-	-	-	-	-	-
Fabrication Development											
Procedures	-	-	-	-	-	-	X	-	-	-	-
As Fabricated Properties	-	-	-	-	-	-	X	-	X	-	-
Electromagnetic Effects During Disrup.	-	-	-	-	-	-	-	-	-	X	X
Lifetime Issues											
Disruption Characteristics	-	-	-	-	-	-	-	-	-	X	X
Vaporization/Melting Losses	-	-	-	-	-	X	-	-	-	X	-
Sputtering/Redeposition	-	X	X	X	X	-	-	-	-	-	-
In-Situ Recoating	-	-	-	-	-	-	-	X	-	-	-
Long Term Materials Considerations											
Radiation Damage	-	-	-	-	-	-	-	-	X	-	-
Corrosion	-	-	-	-	-	-	-	-	X	-	-
Bond Integrity	-	-	-	-	-	-	X	-	X	-	-
Life Testing	-	-	-	-	-	-	-	-	X	X	X
Safety Issues											
Tritium Retention and Permeation	-	-	-	-	-	-	-	-	X	-	-
Off Normal Response	-	-	-	-	-	X	-	-	X	X	X

Plasma-Materials Interaction and Special Purpose Materials Tasks in the U.S. Fusion Reactor Materials Program, Program Elements I (Thermomechanical and Thermal-hydraulic Testing of First Wall Components) and III (Electromagnetic Effects) of the First Wall/Blanket/Shield Engineering Technology Program and the High Heat Flux Component Development Program. The activities in these programs are described in the DOE Office of Fusion Energy's Program Plan.[26]

3.2.1 Plasma Engineering

An analysis of pumping characteristics of the pumped limiter system for DEMO indicates that high conductance for the pumping duct conductance (and therefore a large duct) will be necessary to remove the helium. Typically, 5-10% of the particles escaping the plasma must be pumped to remove the helium produced during operation. The large pumping ducts required for helium removal have a negative impact on the overall configuration in general, and the tritium breeding and neutron shielding, in particular. Due to the lack of a data base related to the pumping channel characteristics, there is an unacceptable uncertainty in pumping requirements (ranging from 10^5 to 10^6 liters/sec.)

Experiments should be planned to develop an understanding of the neutral behavior, including plasma-neutral interactions, in a limiter pumping channel for edge conditions appropriate to DEMO. These experiments should include studies of directed momentum effects in the plasma channel and pumping duct, and provide a test of codes that model pumping channels and include these effects. The parameters of interest include limiter channel length and position of the leading edge with respect to the edge of the plasma.

Edge Plasma Characteristics - An understanding of the conditions in the plasma scrapeoff region, and the factors which control these conditions, is common to essentially all the impurity control R&D and should be highlighted as a separate issue. Until we develop an understanding of the processes controling edge conditions, confident predictions of any important design related conditions required for a detailed limiter design will not be possible.

Experiments should be planned to test individual elements of edge plasma theory (e.g., particle and energy transport parallel and perpendicular to magnetic field, and transport across the limiter sheath). The experiments

should operate over a range of edge plasma regimes to determine the importance of the factors controlling the edge conditions. The most important parameters to be determined are the particle fluxes and energies in the scrape-off region, and the associated e-folding distances. Factors to be considered include particle pumping rates, fueling methods, and burn control methods. Results from these experiments should be used to improve the models.

Enhanced Radiation - The α-heating power is deposited on the surface of the plasma chamber in the form of particle transport power and atomic radiation. The tranpsort power is concentrated on either the limiter or divertor collector plates, whereas the radiation is spread uniformly over the entire plasma chamber. 1-D transport code studies predict that the relative amounts of transport and radiation power can be controlled by the injection of high-Z impurities, such as Xe, into the plasma. This technique can be used to control the heat and particle loads to the limiter/divertor and first wall and thus optimize the conditions for most efficient operation. For DEMO, the α-heating power of 213 MW is divided almost equally between radiation (line, recombination, and Bremsstralung) and particle transport. The Xe injection also serves as a method for burn control. The suitability of this technique has yet to be shown in practice.

An experimental program to examine the effects of high-Z impurities in the plasma should be undertaken. The program should examine the effects of the impurity type, concentration, and concentration profile on the transport and radiation characteristics of the plasma.

3.2.2 First Wall-Plasma Interaction

Erosion/Redeposition - The lifetime of the limiter and divertor plates is critically dependent on the net erosion of the plasma-side materials. Theoretical models predict that most of the sputtered material will be rapidly redeposited on the limiter or divertor plates. The models predict that the net erosion can range from $\sim$ 30 cm/y to $<$ 1 cm/y depending on the plasma edge conditions and position on the limiter. The delicate balance between sputtering erosion and redeposited materials can seriously affect the engineering performance of the plasma-side materials and current data are wholly insufficient to characterize the erosion and redeposition.

The definitive results on the characteristics of erosion/redeposition will have to be obtained from physics experiments and will require an upgrade of present experimental physics devices to obtain sufficient particle and heat fluxes and adequate pulse length. This will require an upgrade of present experimental physics devices. Smaller scale laboratory experiments, using for example ion bombardment techniques for simulating erosion and redeposition of materials, can provide key information. The physical characteristics of redeposited materials should be investigated as a function of substrate temperature during redeposition, internal gas (H, He) concentration, and particle fluxes for particle energies ranging from 20 to 2000 eV. Candidate materials for these experiments are Be, BeO, SiC, C, W, and Ta. The redeposited layer should be thick enough (several microns) so that the bulk properties can be determined.

Self Sputtering Yield - The lifetime of first wall, limiter and divertor plates is seriously shortened by erosion. A large portion of the erosion may be caused by self sputtering. The viability of medium-Z and high-Z materials is limited to particle energies below which the self sputtering yield is less than unity. Thus, both the selection of materials and the lifetime determination depend strongly on the magnitude of self sputtering. Presently, available information indicates that self sputtering of high-Z materials exceeds unity in the range of 400-800 eV, but the present data base for self sputtering yields for materials is inadequate for design purposes.

Self sputtering yields should be measured for a number of the most promising candidate plasma-side materials. Some development of techniques for generating data on self-sputtering of compounds will be required. Candidate materials include beryllium, silicon carbide, stainless steel and tungsten. Yields are needed for particle energies in the range 10 eV to 2 keV. The self sputtering yields of redeposited materials should also be investigated.

Response of Materials to Plasma Disruption - Intense surface heating of the first wall and limiter during plasma disruptions leads to surface vaporization. Concurrent with this vaporization, formation of a melt layer has been predicted for many of the candidate materials. The melt layer will be subjected to modest electromagnetic forces as the plasma current decays and there is concern that the melted material may move and thus significantly enhance the erosion of plasma-side components. At present, there is no

experiment verification of theoretical predictions. An R&D program can be carried out effectively in two phases.

Phase 1 -- Simulation without electromagnetic forces. Phase 1 would also include model development in such areas as the interaction of vaporized material with the disrupted plasma, and 2-D or 3-D models for disruption behavior.

Objectives: Measurements which determine (1) the existence of a melt layer, (2) the extent of surface vaporization, (3) surface temperatures, and (4) spatial and temporal characterization of vapor (flow).

Specimen: Stainless steel, beryllium, SiC, W

Magnitude of surface energy deposition: less than 10^3 J/cm^2

Pulse duration: 5-50 ms

Environment: High vacuum ($\sim 10^{-6}$); vacuum vessel dimensions must exceed several mean-free-path lengths for vaporized material at high vacuum.

Phase 2 -- Simulation with electromagnetic forces. Phase 2 will be necessary only for those materials that are shown in Phase 1 to develop a melt layer.

Objective: To examine the motion of molten material in the presence of the electromagnetic forces generated in the melt layer as the plasma current decays.

Test parameters: Same as in Phase 1, plus magnets (and power supplies) to simulate induced forces (also considered are existing tokamaks).

3.2.3 Materials and Component Engineering

The components of the impurity control system must withstand high heat and particle fluxes plus intense neutron radiation and body forces from magnetic loads. The heat fluxes can range from 1-5 MW/m^2 and neutron exposure levels can reach 2-5 MW-y/m^2. At present, there is a grossly inadequate data base for designing the limiter and assuring successful operation. Therefore, a number of interrelated programs are proposed to acquire the necessary information. The major areas of investigation are:

Materials Engineering		Component Engineering	
(A)	Coat/Clad Development	(D)	Thermomechanical Response
(B)	In-Situ Recoating Development	(E)	Electromagnetic Response
(C)	Materials Properties Data Base		

This program should be closely coordinated with the plasma physics programs in order to identify the designs and materials of greatest interest and to focus the research into the areas with the greatest payoffs.

Coat/Clad Development - The high heat flux components of the impurity control system are likely to consist of duplex structures where a plasma side material is attached to a heat sink composed of a structural material. The necessity for a duplex structure introduces a number of design and fabrication issues, and a fabrication development program is needed.

Work should be undertaken to examine the fabrication of plasma side materials, bonding techniques, and fabrication of heat sink materials. Plasma side materials include Be, BeO, C, SiC, W, and Ta and thicknesses for plasma side materials range from 1 to 30 mm. In addition to standard fabrication techniques for plasma side materials, deposition processes such as plasma spraying should be investigated. Bonding techniques include diffusion bonding, explosion bonding, and brazing. Heat sink materials include copper alloys, vanadium alloys, and austenitic stainless steels. The goal of the program would be to establish the most suitable fabrication methods in order to maximize the component lifetime. Fabricated specimens from this program would be utilized in other materials testing programs.

The use of duplex structures in the impurity control system requires that the surface material be bonded in some fashion to the heat sink. The bond itself, however, introduces additional complexities and uncertainties into the design. Two types of bonds have been identified as having potential for use in DEMO: (1) a high strength, high conductance bond, and (2) a low modulus, low thermal conductance bond. The first type of bond is typified by diffusion bonds and brazes while the latter is typified by a compliant layer consisting of low density, sintered metal fibers. A test program is recommended to identify acceptable fabrication procedures and to establish the physical and mechanical properties of the bonds.

The tests and information needed to evaluate bonds are similar for the two bond concepts. First, duplex structures must be fabricated, and the thermophysical properties of the bond should be measured. The mechanical properties such as the tensile strength and fatigue life should also be determined. A particular concern for the long term operation of the limiter is the effect of neutron radiation damage on the bond properties, and thus irradiation tests should be conducted. For the porous compliant layer, the outgassing characteristics of the material also should be determined.

Recoating Development - Another approach for improving plasma impurity control and increasing component lifetime is to maintain the surface of first wall and limiter components through intermittent recoating to patch local problem sites on the (plasma-side) surfaces. "In-situ" techniques for applying the coatings appears to be highly desirable and the development of successful in-situ coating techniques would offer the following benefits:

(a) Flexibility in Repair -- Reconditioning of first wall components, in particular local spots where thinned or failed cladding/coating has resulted from disruptions or erosion, could be done essentially as often as necessary.

(b) Low Impact on Availability -- The need to disassemble reactor components for surface repairs would be eliminated with the overall results of shorter reactor shutdown periods for first wall maintenance and lower cost for the reconditioning of the first wall components.

In-situ deposition techniques which permit the coating of large-size vessels should be explored and developed, and the thickness of the coating should be well controlled, particularly during recoating.

Materials Properties - Several materials have been identified as potential plasma side materials. The low-Z materials, for use at plasma edge temperatures $\geq$ 50 eV, are Be, BeO, C, and SiC, and the high-Z materials, for use at plasma edge temperature $\geq$ 50 eV, are W, Ta, and Mo. The data base for the bulk properties of these materials is small, and thus experiments are required to measure the relevant properties of these materials.

A number of areas should be investigated. The physical and mechanical properties should be determined over a range of temperatures. The effect of neutron irradiation on these properties should be determined. Since the properties of these materials can vary over a considerable range depending on the fabrication method, specimens representing different fabrication methods

should be tested. Because of the interaction of these materials with both the plasma and the rest of the component structure, this program should be closely coordinated with the plasma testing programs and other materials development programs.

The heat sink materials required for impurity control must have favorable thermophysical properties to withstand the high heat loads necessitating the use of non-standard structural materials. The materials being considered, copper alloys and vanadium alloys, have a limited data base, and additional information is required before the best material can be selected.

There are a number of areas where information is needed. Candidate alloys should be tested for water corrosion resistance, fatigue and crack growth properties, compatibility with plasma side materials, and radiation damage resistance. The candidate alloys should be tested over a range of potential operating temperatures. In addition, the fabrication and joining procedures should be developed.

Thermomechanical Response - The predictability of the thermomechanical response of limiters and divertor collector plates to the heat loads and forces in DEMO suffers from deficiencies in theoretical modeling techniques and uncertainties in several engineering properties. The properties of concern are the values for the thermal conductance of the bond at the surface material/heat sink interface particularly for the compliant layer, the mechanical properties of the bond, and the heat transfer characteristics for the water coolant traveling through channels of complicated geometry. The stress distribution and its evolution in time is also very difficult to model in three dimensions. A test program is recommended to examine the thermomechanical response of prototypic components in order to establish the relevant engineering properties and to determine the effectiveness of particular designs and fabrication procedures.

Prototypic impurity control components consisting of a plasma side material bonded to a heat sink would be fabricated and tested under simulated operating conditions. The test apparatus should be capable of simulating the heat fluxes and stresses anticipated for DEMO. The temperature distribution and the fatigue life would be determined. The engineering properties determined from the tests would be used in the actual design of in-reactor components. Response of components to off-normal conditions (e.g., disruptions and loss of coolant accidents) would also be investigated.

Electromagnetic Response - Body forces resulting from eddy currents produced in first wall components during plasma disruptions are the primary electromagnetic effect of interest for impurity control systems. The motion of melted material is one specific case (already described in Section 3.2.2). The capability to predict accurately the eddy currents that will occur in, for example, a limiter blade are beyond our current analytical capabilities.

A program to develop suitable electromagnetic codes will of necessity be based on experimental verification and such a program (already in progress) is endorsed here. The program's experimental facility (FELIX) has the capability to test components and such testing is recommended.

3.3 R&D Needs - Tritium Breeding Blanket

The timely development of the fusion reactor blanket is critical for the following reasons: (1) acceptable breeding and extraction of tritium in a high temperature blanket are key feasibility issues for fusion; (2) breeding tritium in the next generation reactors (after TFTR) may be an operational requirement; (3) extensive materials and engineering development will be required to develop any reliable blanket system; and (4) the blanket system will have major impacts on perceived environmental and safety features of fusion.

The research and development strategy for the development of a tritium breeding blanket for fusion power reactors involves (1) consideration of proposed blanket concepts, (2) identification of critical feasibility issues associated with the leading candidate concepts, and (3) assessments of the time-scale, cost, and difficulty of providing the required data base. Based on previous studies[27,28] and the present study, two development paths shown in Table 3-4 for breeding blanket R&D are proposed. Path 1 is for liquid metal breeding concepts, which focus on the use of liquid lithium or liquid 17Li-83Pb alloy breeder materials. Path 2 is for solid breeding concepts, which focus on Li_2O or ternary ceramics such as $LiAlO_2$ for the breeder material. Since the present study has considered only two of these options, viz., 17Li-83Pb and Li_2O, the proposed R&D strategy focuses on these two concepts. However, a similar approach would be appropriate for the other two concepts.

Table 3-4. Development Paths for Tritium-Breeding Blankets

Path 1:	Liquid Metal Breeder
	Liquid Lithium
	Liquid Li-Pb Alloy
Path 2:	Solid Breeder
	Li_2O Ceramic
	Ternary Ceramic (e.g., $LiAlO_2$)

In general, the approach is to provide the basis for selection of the best liquid metal blanket concept and the best solid breeder concept. Critical issues, both materials related and engineering have been identified in the present study for the Li_2O and Li-Pb concepts. These critical issues are summarized in Table 3-5. The issues listed impact the feasibility and desirability of the two blanket concepts, and therefore, must be resolved before the viability of these concepts can be established and before in-depth investigations in other areas should be conducted. Of course, those aspects such as radiation damage of the structure, which are important for both development paths must be pursued simultaneously. The important criteria in defining an effective R&D program is to establish an appropriate balance between the relative importance of a critical issue and the difficulty or cost of resolving the issue. For example, solely on the basis of blanket development considerations, one should identify compatible structural materials and allowable operating limits before extensive radiation damage studies are completed to ensure that appropriate parameters are being evaluated. Similarly, acceptable tritium recovery from solid breeder materials and the operating temperature limits must be established before complex, expensive experiments are conducted.

Establishment of an effective R&D program requires close coordination between materials and engineering R&D and the design studies. The design studies provide a basis for determining the appropriate ranges of important test parameters and for establishing the relative priorities and importance of the various issues.

Table 3-5. Critical Issues - Tritium Breeding Blanket

Liquid Metal Breeding (17Li-83Pb)

- Determine operating temperature limits for candidate structural materials on basis of corrosion/compatibility.
- Determine magneto-hydrodynamic (MHD) effects associated with the use of liquid metals in high magnetic fields.
- Evaluate safety/environmental impacts related to the use of reactive liquid metals (coolant and environment).
- Develop concepts that permit reliable hydraulic operation of a liquid metal system.

Solid Breeder (Li_2O)

- Develop satisfactory tritium recovery scenarios for Li_2O blanket.
- Develop engineering solutions that will provide adequate temperature control of breeder to obtain satisfactory tritium recovery.
- Evaluate consequences of Li_2O reactions with pressurized water coolant in event of a coolant leak.
- Determine mechanical integrity and thermodynamic stability of Li_2O under projected operating conditions.

General Issues

- Establish methodology and criteria for comparing blanket concepts.
- Develop definitive design studies of blanket systems that will incorporate experimental and analytical progress (on key individual issues).

3.3.1 Materials

Many materials issues are critical to the development of a viable fusion reactor blanket. An attempt here is made to identify the most critical generic-type issues that must be evaluated. In some cases, programs are in place to address these or related issues. In the areas discussed below where ongoing programs are in place, it is concluded that these programs should be given higher priority in the proposed R&D strategy.

Solid Breeder Data Base - The available materials data base for candidate solid breeder materials is inadequate to evaluate their potential performance characteristics. Although considerable effort is correctly being placed in this area, the following data are required for the primary candidate breeder materials:

- H(T) diffusivity/permeability
- Radiation effects on tritium trapping/release characteristics
- Mechanical properties (elastic modulus, fracture stress, etc.)
- Fabrication characteristics
- Compatibility with structural/bonding materials
- Kinetics of reaction with H_2O

Structural Materials - In general, the data base for the structural materials will be similar for most concepts. However, it is particularly important to determine the property data base under appropriate conditions, e.g., temperature, for the leading concepts, e.g., H_2O coolant. Compatibility with the breeder under appropriate operating conditions has not been well established.

Neutron Multiplier - For all of the ceramic breeder materials, with the possible exception of Li_2O, a neutron multiplier will be required. Beryllium and lead currently appear to be the only reasonable candidates. The data base for these materials is inadequate. Primary concerns are the radiation response of beryllium and the corrosion of liquid lead. (Lead would be molten at reasonable operating temperatures.)

Corrosion/Compatibility - Compatibility with the structure is, perhaps, the most critical issue associated with the use of the Li-Pb blanket concept. Most probably, the maximum operating tmeperature will be limited by compatibility with the structure. Mechanisms of concern involve effects of

the liquid metal on the mechanical properties of the structure, e.g., liquid metal embrittlement, and corrosion mass transfer.

Reactivity - Reactivity of Li-Pb with water, air and other reactor components. Reactivity with pressurized water is one of the key issues regarding the viability of the water-cooled concept.

Hydrogen (Tritium) Effects of Structure - The Li-Pb blankets will operate at relatively high tritium partial pressures in the liquid metal. The impact of this high hydrogen pressure on the mechanical properties of the structure is an important issue.

3.3.2 Engineering and Design

The main emphasis here is devoted to defining the design/analysis and engineering test efforts which lead to selection of the best solid breeder and best liquid breeder (first phase). The results of materials tests (Sec. 3.3.1) are crucial to the breeder selections, and therefore the principal materials tests will be mentioned briefly when appropriate, for completeness.

Table 3-6 lists the key issues that must be addressed by design/analysis or test efforts during the first phase. Section 3.3.3 and 3.3.4 present, for the solid and liquid breeder blanket concepts respectively, discussions of the rationale for addressing each issue and of the effort (including materials testing) necessary to adequately resolve the issue. Section 3.3.5 contains a brief general discussion of the design/analysis and test efforts required in the second and third phases.

3.3.3 Key Issues to be Resolved for Selection of Best Solid Breeder

At present, the most important area in solid breeder development is materials testing to obtain basic data for irradiated breeders on tritium release and thermophysical properties. These tests are mandatory for determining the viability of the candidate solid breeders. However, it is important that near-term effort be applied in the area of blanket design, so that each of the candidate breeders can be shown to its best advantage during the solid breeder selection process. The reason is that each breeder is likely to have unique characteristics - e.g., fabrication technique, or the requirement for a neutron multiplier - which may require a blanket concept having design details specifically tailored to that breeder.

Table 3-6. Key Issues to be Resolved Prior to Selection of Best Solid Breeder and Best Liquid Breeder

Key Issue	Effort Required: Design/ Analysis	Effort Required: Eng'g/Dev't Testing	Comment
SOLID BREEDERS			
Breeder-to-Structure Interface	X	X	Extremely important; generic to all solid breeders.
Blanket Configuration			
- General Arrangement	X		Studies in greater depth are
- Coolant-containing Structure	X	X	needed, to ensure (1) fair comparisons among solid
- Mechanical and Structural Configuration	X		breeders, and (2) best use of solid in later comparison
- Incorporation of Neutron Multiplier	X		to liquid breeder (second phase).
Breeder Configuration			Present work indicates po-
- Fabrication	X	X	tentially significant dif-
- Physical Integrity	X	X	ferences among solids in these areas.
LIQUID BREEDERS			
MHD Effects	X	X	Especially important for concepts with circulating Li-Pb/water reactions.
Safety in Accidents			Li-Pb spills.
Tritium Recovery	X	X	
Tritium Containment		X	Important for water-cooled Li-Pb blanket concept.
Blanket Configuration	X		In-depth studies needed for all concepts.
Primary coolant system design and costs	X		Double-walled and intermediate heat exchangers are particularly important.

Breeder-to-Structure Interface - The interface between the coolant-containing structure and the solid breeder was identified as the key design issue for the solid breeder blanket concept. As discussed in Section 6.3.7, the most important operating requirements for the interface are (1) a predictable thermal conductance value (with reasonable uncertainty), and (2) accommodation of thermal expansion mismatch between breeder and structure. The metallic felt concept proposed for the STARFIRE/DEMO reference design blanket is considered overall to be a better solution than either the helium gap approach[28] proposed for STARFIRE, or the ceramic insulator approach proposed in the STARFIRE/DEMO Interim Report.[1] However, these and other possible solutions require both design studies and engineering development tests, to determine their comparative advantages from the standpoints of fabricability, predictability in performance, radiation damage tolerance, and effects on tritium release.

Blanket Configuration - This category includes a number of sub-topics which should be explored in greater depth through design studies:

- Coolant-containing Structure - The small diameter blanket coolant tubes in U-bend shapes proposed for the STARFIRE and STARFIRE/DEMO reference blanket designs are optimum in terms of structural efficiency. However, other design considerations such as overall fabricability and thermal-hydraulics are also important. Other coolant-containing configurations, such as actively cooled panels or straight tubes connected to end-wall plenums, may be preferable overall to U-bend tubes. Concerns over breeder physical integrity (Section 6.3.8) in particular may dictate the use of alternate configurations.

- Incorporation of Neutron Multiplier - For power reactor blankets a neutron multiplier will be required with any of the candidate solid ceramic breeders, with the possible (though not certain) exception of Li_2O. Incorporation of a neutron multiplier into the blanket requires significant changes to the breeder-only blanket concept, including: (1) optimum location for maximum breeding; (2) provisions for cooling; (3) mechanical and structural integration into blanket; (4) accommodation of volume changes of the neutron multiplier (e.g., helium swelling of Be); and 5) selection of best neutron multiplier material. Design studies

addressing these topics are needed to ensure that solid breeders that require neutron multipliers are not handicapped by an inferior blanket design when compared to each other or to a solid breeder (i.e., Li_2O) that does not require a neutron multiplier.

- Breeder configuration - Work performed since the STARFIRE study in two areas related to solid breeders indicate that the STARFIRE breeder fabrication approach of sintered blocks may require modification. First, the results of efforts to make sintered pellets of solid breeders at high density (~ 70%) with bimodal porosity indicate that this will be difficult for mass-production scale and complex geometric shapes. Alternate breeders fabrication methods (e.g., cold pressing) may be required. Second, the results of analyses for STARFIRE/DEMO of breeder physical integrity under applied thermal gradients (Section 6.3.8) indicate that segmentation of the breeder into quite small individual pieces may be necessary to preclude large-scale cracking of the breeder. Both of these developments point out the need for an on-going breeder fabrication development program, together with further studies to show the feasibility of adapting the allowable breeder configurations into blanket designs.

3.3.4 Key Issues to be Resolved for Selection of Best Liquid Metal Breeder

The primary near-term emphasis for liquid metal breeder blankets should be placed on: (1) choice of separately-cooled or self-cooled concept for 17Li-83Pb breeder blankets; (2) design optimization for the selected Li-Pb blanket concept, and (3) design optimization for a liquid lithium breeder blanket. The majority of the key issues discussed below need to be addressed for Li blankets as well as Li-Pb blankets. The results of materials testing in both Li and Li-Pb liquid metal loops to determine operating temperature limits for flowing and non-flowing systems (Li-Pb only) will also be extremely important in determining viable blanket/coolant system designs and materials combinations.

MHD Effects - The effects of magnetic fields on the pumping requirements for Li and Li-Pb in self-cooled blanket concepts, and for other liquid metal coolants (e.g., sodium) in separately-cooled Li-Pb blanket concepts, need to be determined by in-depth analyses based on realistic blanket configurations, and confirmed through simple tests using liquid metal coolant loops. Cooling

of the inboard blanket and the first wall require particular emphasis. The results of these analyses and tests will be important in determining overall coolant system pumping requirements.

Safety in Accidents - One of the largest uncertainties associated with the use of pressurized water as a coolant in Li-Pb blankets is the degree of damage likely to result from contact during accidents between the water and the Li-Pb. Previous tests[29] have shown slight to moderate degrees of incompatibility between water and Li-Pb, but they have not incorporated both molten Li-Pb and high temperature, high pressure water in simulated blanket configurations. Such tests are needed to help determine the feasibility of water as coolant in Li-Pb blankets. In addition, tests are needed to determine how Li or Li-Pb spills can best be cleaned up, and the impact of such operations on reactor maintainability.

Tritium Recovery - At present, there is considerable uncertainty regarding the best method for ex-reactor tritium recovery from circulating Li-Pb, from the standpoints of system complexity and costs and of steady-state tritium inventory levels achievable in the Li-Pb. The Li-Pb tritium inventory level for sodium-cooled and water-cooled Li-Pb blankets (in which the Li-Pb remains in the reactor) also need to be determined. The results of these analyses will be important both to selection of the preferred Li-Pb blanket concept and to the comparison between the Li-Pb and Li liquid breeder blanket concept.

Tritium Permeation - The degree to which tritium will permeate from the Li-Pb into water coolant is the second major uncertainty regarding the use of pressurized water as a coolant for Li-Pb blankets. For self-cooled Li-Pb blankets, tritium permeation into a steam generator from the Li-Pb coolant via the secondary water is a serious concern. For both situations, double-walled tubes with an annular helium purge gas for tritium removal have been previously proposed as a solution; however, control of tritium permeation into the water and minimization of the temperature drop across the tube assembly remain as major concerns. To help resolve these questions, the results of previous and ongoing LMFBR double walled steam generator analyses and tests need to be obtained and applied in analyses of water-cooled Li-Pb blankets to determine for both situations the degree to which the concerns can be alleviated.

Blanket Configurations - An in-depth design study on liquid metal blankets for tokamaks is important. Both self-cooled (Li and Li-Pb) and separately-cooled (Li-Pb breeder only) concepts should be considered. The results of the studies and tests discussed above for MHD effects, safety, tritium recovery and tritium permeation will be key inputs in helping to determine the best blanket geometry and mechanical and structural configuration for each concept. The unique characteristics of the candidate structural materials (e.g., high DBTT values for irradiated ferritic steel) and maintainability considerations (e.g., drain and fill requirements, heaters for melting in-situ liquid metal) must also be addressed in such a study.

Primary Coolant System Design and Costs - A significant number of key items in the primary coolant system require in-depth investigation prior to selection of the best liquid metal breeder because they figure strongly in determining overall coolant system complexity and costs. Realistic operating temperature limits for all system components, determined through tests, must be used in the designs. Specific areas of concern, particularly for Li-Pb coolant, are: (1) design, efficiency, costs and tritium containment capabilities of Li-Pb/water heat exchangers (steam generators); (2) pump design, efficiencies, costs, operating limits (e.g., mass flowrates) and lifetime/maintenance considerations; (3) overall costs and efficiencies for Li coolant systems using Na/water intermediate heat exchangers; (4) total system pumping requirements for Li and Li-Pb coolants, including in-reactor MHD effects and friction losses for the total system.

3.3.5 Second and Third Phases: Selection of Best Breeder and Development of DEMO Breeder Blanket

Most of the analytical and design efforts necessary for selection of the best breeder will have been accomplished during the first phase of the breeder blanket development process. The primary focus for the second phase should be engineering development tests specifically constructed to obtain confirmation of analytical predictions and initial test results from the first phase. The tests would be focused on the key areas of tritium recovery (especially for the solid breeder), materials compatibility (including safety and long-term corrosion and mass transfer), and heat recovery. The tests would be performed out-of-reactor, with the exception of some solid breeder blanket tests performed in fission reactors.

Further speculation on second and third phase effort is not considered warranted at this time, not only because the specific breeders to be compared in the second phase are not known, but also because of the changing nature of the national magnetic fusion program.

3.4 R&D Needs -- Nuclear Data and Methods for Shielding System

Radiation shield system represents 8 to 16% of the total direct cost in a tokamak fusion power reactor.[1,28,29,30] The design of such a system requires an accurate prediction of the radiation field and on engineering data base on the behavior of different materials in the fusion environment. International recommendations and national standards define the radiation exposure limits for the shield system to achieve inside and outside the reactor building. The prediction of radiation field requires three basic steps: a) evaluation of the radiation sources, b) transport of radiation from the source to the points of interest, and c) evaluation of the radiation effect in physical quantities such as dose equivalent, heat generation, or radiation damage.

This section gives a brief discussion on the research and development required to design a radiation shield system which satisfies the exposure limits and protects the different reactor components from radiation damage. The evaluation of the radiation sources involves neutrons, neutron-induced photons, and decay gamma rays. Energy spectrum and spatial distribution of the DT neutrons can be described with adequate accuracy from the plasma parameters. Neutron induced photons and decay gamma rays sources depend on the neutron flux, gamma production cross-sections, and neutron activation data. Radiation transport methods and nuclear data libraries are employed to get the neutron and photon fluxes from these sources. Neutron cross sections, gamma production cross sections, and energy-angular distributions for secondary neutrons and photons are used as a function of the incident neutron energy. Nuclear cross sections are available from the evaluated nuclear data files (ENDF) maintained at the national nuclear data center. However, activation data are missing for many important isotopes, and a significant improvement for the existing ENDF data is needed for selected energy regions and above 10 MeV. Systematic sensitivity studies are required and are essential to provide guidelines for re-evaluation or request for the

measurement of nuclear data for the next fusion reactors. Also, an adjustment to the existing nuclear data files for key materials to conserve the reaction energy is important for the nuclear heating calculations. This adjustment will require modifications for the gamma production cross section, secondary neutron and photon spectra, and isotopic evaluations for elements with many isotopes (Mg, Ti, Cr, Fe, Ni, Cu, and Pb). Isotopic evaluations are essential for kinetic energy release in material atom (Kerma) and activation analysis.

The main transport methods applied to shielding problems are the discrete ordinate and Monte Carlo methods. At present, the discrete ordinate method is limited to one and two dimensions, although several three-dimensional codes are under development. Therefore, Monte Carlo method is the only method available for rigorous three-dimensional analysis. The discrete ordinate methods give complete differential results over the whole geometry without extra effort; whereas, the Monte Carlo method can only generate integrated results at a few selected points or regions. Both methods require development to overcome some of the difficulties. The discrete ordinate methods are suffering from negative fluxes caused by a large flux gradient or the truncation of the legendre expansion for the scattering cross sections. Also, ray effect causes a problem for the penetration shield analyses. Monte Carlo methods require a careful, efficient, and consistent use of the variance reduction techniques to avoid wrong answers and long computational time. All the existing variance reduction techniques require a good knowledge of the important distribution which can be obtained by adjoint calculations for a specific response at one point of the geometry or by an educated guess. Development of automated variance reduction techniques for the Monte Carlo codes will improve the prediction of the radiation field. Additional computational capabilities are needed to perform a decay gamma transport with the existing Monte Carlo codes for after shutdown analyses (dose equivalent, decay heat, etc.).

For some materials, the significance of potential damage from radiation is not yet well understood because we lack information either on the engineering effects of fundamental damage on properties or on the potential sources for component failure. Several applications for ceramic insulators and various diagnostic instrumentation inside and outside the reactor shielding fall into this category. For these design applications there are

also needs for neutronics information but progress will await development of more complete evaluations of design criteria for these components.

3.5 Maintenance and Configuration R&D Needs

The key maintenance issue in the development of the DEMO is to assure that an availability goal of ~ 50% can be demonstrated. This goal must be attained to assure that the first commercial reactor can attain an availability of $\geq$ 70% to permit economic electrical power generation. The ability to attain this goal is affected by the choice of reactor configuration, the outage rate (component failure rate) and the ability to perform rapid and repeatable maintenance processes.

3.5.1 Major Issues in Maintenance and Configuration

Selecting the "Optimum" configuration requires a thorough understanding of the plasma and engineering limitations and the development of analytic tools which permit accurate tradeoffs between design options. The plasma limitations of most concern are field ripple and plasma control which effect magnet location and first wall blanket segmentation. Plasma heating, current drive and impurity control choices affect the peripheral space requirements and may limit maintenance options. Engineering limitations are primarily related to component failure rates and the time required to perform the repair.

The system outage (failure) rate is dependent on the operating environment, design margins, and design approach selection. Data on outage rate can be partially attained prior to DEMO but data is required on several new subsystems where adequate operating experience does not exist. Examples of these subsystems are large superconducting coils, first wall and blanket, vacuum pumping in a radiation environment, tritium handling, plasma heating, fueling, and remote handling. Additionally, data collection is required on those subsystems where experience does exist such as with cooling loops, overhead cranes, etc., so that supportive analysis can be performed and proper emphasis can be placed on each subsystem.

For major reactor subsystems, the number of samples, environments, and test time required for developing statistical data prohibits obtaining a complete data base prior to operation of several commercial reactors.

However, an approach that includes use of DEMO-relevant systems in the next new machine, a complementary test program, and a system for cataloging and developing data can identify trends to guide DEMO development. The complementary test program is currently being implemented through programs such as LCP, LCTF, TSTA and the First Wall/Blanket/Shield Engineering Technology Program. Other programs will be required as fusion development proceeds.

Some general requirements for the maintenance equipment reactor design are listed in Table 3-7. Both the outage rate and replacement time goals represent very significant advances over current technology.

Table 3-7. Preliminary DEMO Maintenance Requirements

Component	Weight (tonnes)	Allowable Replacement Time	Acceptable Forced Outage Rate
Blanket sector	~ 200-300	~ 2 weeks	1 time in 5-10 years
Limiter blade	~ 1	~ 1 weeks	1 time in 2-5 years
Single toroidal coil	400-600	~ 1/2 year	1 time in 20-40 years

The DEMO study offers reactor configuration that conceptually has readily replaceable components and an acceptable overall reliability. However, there are significant risks in assuming that the reactor could be designed and built if a serious design and construction effort was undertaken. Key areas where significant effort is required to reduce risks are:

1) Component reliability
   - Magnets
   - First wall, blanket, shield
2) Rapid maintenance process development
   - Sealing
   - Fault isolation
   - First wall connectors
   - Rapid startup/shutdown time

3) Plasma related limitations
   - Toroidal field ripple
   - Plasma control needs
   - Cleanliness
4) Analytic tool development

3.5.2 Reliability of Components - Data on the reliability and lifetimes of components is presently lacking and substantial development work will be required to provide the necessary data to a high confidence level prior to construction of DEMO. Testing in the expected operating environment for a period of 3 to 5 times the desired mean-time-between-failure generally would provide adequate confidence but the cost of such full scale component testing is expected to be prohibitive. The higher risk approach recommended here involves simulation testing of critical element coupled with "development by doing".

With the recommended approach to reactor development any new reactors built would utilize a configuration, subsystem components and operating conditions as close as possible to the perceived commercial reactor. This requirement implies use of superconducting magnets, remote maintenance processes, plasma current drive and heating and impurity control systems that attempt to operate at performance and stress levels perceived for DEMO. This approach will permit the designs to evolve toward DEMO in a cost effective manner by providing information on failure modes, failure rates and time-to-repair that is essential to the successful development of a DEMO reactor. Collection of data from these reactors will lead to definition of required design margins, redundancy levels and specific component designs which operate more reliably and will improve the prospects for DEMO achieving its goals.

In addition to the building of prototype reactors for testing, some additional work will be required. The prototype reactors will not simulate all critical environments simultaneously so multiple samples of key elements of components will have to be tested in environments that approximate the expected operating environments. The following description illustrates how reliability development might proceed when past availability analyses had indicated that some components cannot utilize redundancy and would require a significantly higher reliability than other components. A key component is

the toroidal field coil which is required to operate ~ 500,000 hours[31] without failure (MTBF) based on a time for coil replacement of ~ 1 year. A MTBF of 50,000 hours would have a severe detrimental effect on reactor availability. Thereafter, it is appropriate for more extensive analysis of such subsystems to identify the anticipated failure modes and to attempt correlation of data on similar applications to predict an overall system reliability. Experience from the Large Coil Program and other large superconducting coils would be invaluable in this projection. This effort would lead to identification of those elements deemed critical. These elements would then be subjected to extensive testing in simulated environments to determine failure rates that could improve the reliability projection for the magnet.

The first wall/blanket and limiter reliability are also critical in determining reactor availability. Development of reliability data should be accomplished by testing materials and components in a reactor prior to DEMO at conditions that closely approximate the DEMO conditions.

3.5.3 Development of Rapid Maintenance Processes - While maintenance processes required in DEMO are achievable using state-of-the-art techniques, the key uncertainty is how long it will take to perform a given process or successfully complete each operation. Examples of critical areas include sealing, fault isolation, and first wall (electrical) connectors. Undoubtedly a good seal can be performed between components if the proper alignment, cleanliness and procedures are utilized. The key question is to define those seal processes (approaches) which are most tolerant of the variations that are expected in a reactor. Similarly a good electrical connection can be made between first wall sectors by internally bolting straps between sectors, however, the effect on outage time would be unacceptable when blanket replacement is required.

The approach to resolving these issues is to continue identifying the most critical issues through reactor studies and to develop key components that may have a significant impact on the maintainability of the reactor. Incorporation of these processes into the next large machine (preceding DEMO) so that it can be constructed with a reactor relevant configuration should

provide an adequate understanding of the ability to perform these processes and an understanding of their impact on the DEMO configuration.

3.5.4 Determine the Limitations of Plasma Related Issues - The overall reactor configuration must meet certain constraints imposed by the plasma. These constraints can significantly affect the overall concepts for reactor configuration and maintenance, however, as yet the constraints themselves are not all well defined. Two specific examples are (1) limits for toroidal field ripple limits which determine the number and size of the TF coils and (2) the plasma control needs which determine the necessary location of control field coils and the toroidal resistance (and segmentation) of the first wall/blanket/shield. At present only general guidelines are available and these may not include adequate design margins. A decrease of 1% peak-to-peak in the allowable field ripple can require the addition of two TF coils; with the greater number of coils a configuration with one sector per TF coil would either be unmaintainable or would require an increase in the reactor diameter by $\sim$ 3m.

Future reactor studies should continue to emphasize the importance of this information and the (physics) emphasis should be placed on defining these limits by experiment or analysis prior to construction of the next large tokamak so that a relevant configuration is used.

3.5.5 Analytic Tool Development

Systems codes are the necessary tool by which we can select among design options to develop prototypical reactor systems which will lead to minimum cost of electricity in a commercial reactor. The systems codes used for this purpose have not been updated in recent years and presently no consistent process for evaluating design options exists.

Capital cost and availability are the major drivers that determine the cost of electricity. Capital cost is an integral part of the systems code and estimates should be based on algorithms provided by subsystem designers. Assessments of availability depend on reliability of components, sophistication of the maintenance system, reactor configuration and the exact sequencing of maintenance operations. The interactive and complex nature of availability assessments requires that special emphasis be placed on this

effort. In the near future, a common basis for evaluating component reliability should be established and used until it can be updated with better data and a method for evaluating the time to perform maintenance operations. Simulation methods such as mockups or computer generated images can significantly assist this effort.

A centralized group should be established that has responsibility for developing these codes and evaluating concepts in a consistent manner from the standpoint of reactor relevance. Such assessments will clarify the benefits of various configurations and improve the accuracy of reactor design tradeoffs.

REFERENCES FOR CHAPTER 3

1. M. A. Abdou, et al., "A Demonstration Tokamak Power Plant Study, Interim Report," Argonne National Labortory, ANL/FPP/TM-154 (1982).

2. D. A. Ehst, et al., J. Fusion Energy 2, 83 (1982).

3 Ya. I. Kolesnichenko, et al., Proc. 9th Intern. Conf. on Plasma Physics and Controlled Nuclear Fusion Research, Baltimore, MD, October 1982, Paper W-8, to be published.

4. "Final Report: A Design Analysis of Supplemental Heating Systems," TRW Report under Contract DE-AC03-80ER 52058 (1981).

5. C. A. Ekdahl, Los Alamos National Laboratory, LA-8496-MS (1980).

6. E. Canobbio, Nucl. Fusion 12, 561 (1972).

7 F. W. Perkins, Proc. 4th Top. Conf. on RF Plasma Heating, Austin, TX (1981), Paper B13.

8. D. A. Ehst, Nucl. Fusion 19, 1369 (1979).

9. N. J. Fisch, Princeton Plasma Physics Laboratory, PPPL-1772 (1981); N. J. Fisch, in Proc. 4th Top. Conf. on Radiofrequency Plasma Heating, Austin, TX (1981), Paper B-1.

10. C. E. Singer and D. R. Mikkelsen, Princeton Plasma Physics Laboratory, PPPL-1936 (1982), to be issued.

11. C. Baker, et al., Proc. 9th Intern. Conf. on Plasma Physics and Controlled Nuclear Fusion Research, Baltimore, MD, October 1982, Paper E-1-1 (to be published).

12. M. Porkolab, et al., ibid., Paper C-4.

13. M. Fukuda and K. Matsuura, J. Phys. Soc. Japan 44, 1344 (1978).

14. R. A. Demirkhanov, et al., Proc. 9th Intern. Conf. on Plasma Physics and Controlled Nuclear Fusion Research, Baltimore, MD, October 1982, Paper J-1-2.

15. D. W. Swain, P. A. Miller, and M. N. Widner, Sandia National Laboratory Report, SAND75-0214 (1975).

16. D. A. Spong, Ph.D Dissertation, University of Michigan (1975); also, Oak Ridge National Laboratory, ORNL/TM-5147 (1976).

17. I. H. Hutchinson and A. H. Morton, Nucl. Fusion 16, 447 (1976).

18. G. Fussman, et al., Plasma Physics and Controlled Nuclear Fusion Research, Vol. I (IAEA, Vienna, 1979), p. 401.

19. C. W. Barnes and J. D. Strachan, Princeton Plasma Physics Laboratory, PPPL-1879 (1982).

20. G. A. Proulx and B. R. Kusse, Phys. Rev. Lett. 48, 749 (1982).

21. T. H. Stix, Phys. Rev. Lett. 36 521 (1976); S. V. Mirnov and I. B. Semenov, Fiz. Plazmi 4, 50 (1978); Yu. N. Dnestrovskii, D. P. Kostomarov, and A. M. Popov, Fiz. Plazmi 5, 519 (1979) [Sov. J. Plasma Phys. 5, 289 (1979)]; B. Carreras, H. R. Hicks, and B. V. Waddell, Nucl. Fusion 19, 583 (1979).

22. W. M. Manheimer and N. K. Winsor, Nucl. Fusion 21, 1559 (1981).

23. J. M. Dawson and K. R. MacKenzie, Center for Plasma Physics and Fusion Engineering, University of California-Los Angeles, PPG-470 (1980).

24. D. A. D'Ippolito, et al., Phys. Fluids 21, 1600 (1978).

25. Based on information presented at TFTR/TFET Information Meeting, Princeton University, June 1982.

26. "Department of Energy Comprehensive Program Plan for Magnetic Fusion" to be published by the U.S. Department of Energy, Office of Fusion Energy.

27. D. L. Smith, et al., "Fusion Reactor Blanket/Shield Design Study," Argonne National Laboratory, ANL/FPP/79-1 (1979).

28. C. C. Baker, et al., "STARFIRE - A Commercial Tokamak Fusion Power Plant Study," Argonne National Laboratory, ANL/FPP-80-1 (1980).

29. J. G. Crocker et al., Fusion Reactor Safety Research Program Annual Report, Fiscal Year 1981," Report EGG-2205, EG&G Idaho, Inc. (July 1982).

30. C. A. Flanagan, et al., "Fusion Engineering Device Design Description," Oak Ridge National Laboratory, ORNL/TM-7948 (1981).

31. W. M. Stacey, et al., "Engineering Testing," Chapter XII, U.S. FED-INTOR Activity and U.S. Contribution to the International Tokamak Reactor Phase-2A Workshop, Critical Issues, Volume 2, USA FED-INTOR/82-1 (1982).

CHAPTER 4

PLASMA ENGINEERING AND REB CURRENT DRIVE

Chapter 4

Table of Contents

Chapter 4

List of Figures

Chapter 4

List of Tables

4.0 PLASMA ENGINEERING AND REB CURRENT DRIVE

4.1 Relativistic Electron Beam Current Drive: Introduction

The use of a relativistic electron beam (REB) for current maintenance, an idea pursued by a number of researchers over the past decade,[1-9] benefits from two phenomena associated with REB injection into a plasma. In the first place, REB technology development has been focussed on pulsed power injection, rather than cw operation. Secondly, the bulk of theoretical and experimental evidence demonstrates that the plasma's electrical resistivity is increased by orders of magnitude during REB injection. In practice, then, REB current maintenance would be achieved by repetitive injection ("overdrive") of an REB current with a simultaneously oscillating resistivity. Several authors[10,11] have discussed how the injection of pulsed power can reduce the time-averaged power requirement for current drive when combined with density or resistivity oscillations. The REB's performance is distinguished from alternatives by two features. First, this driver capitalizes on the advantages of pulsed power current drive without significant changes in the macroscopic plasma parameters (density, temperature, current, Z_{eff}), since the resistivity is enhanced by phase space activity (e.g., by the two stream instability). Secondly, extremely large resistivity enhancements are possible under these conditions; in effect most of the injected energy is transferred to the poloidal magnetic fields associated with the (subthermal) drift velocity of the electron distribution so the principal energy dissipation is neoclassical joule heating, the average power consumption being close to ohmic, $\langle P_d \rangle \approx I_0^2 R$.

The REB was identified as a possible candidate for DEMO as a result of an earlier survey[12] which compared a large number of drivers. Figure 4-1 displays the normalized ratio of current density to dissipated power density, and shows the potential superiority of the REB when α is large. We define α as the resistivity enhancement factor. (A crucial assumption in the current theory of REB current drive is that centrally peaked current densities are obtainable; all of our present calculations are based on a zero-dimensional analysis. Deficiencies in this model and possible remedies are discussed at the end of this section.)

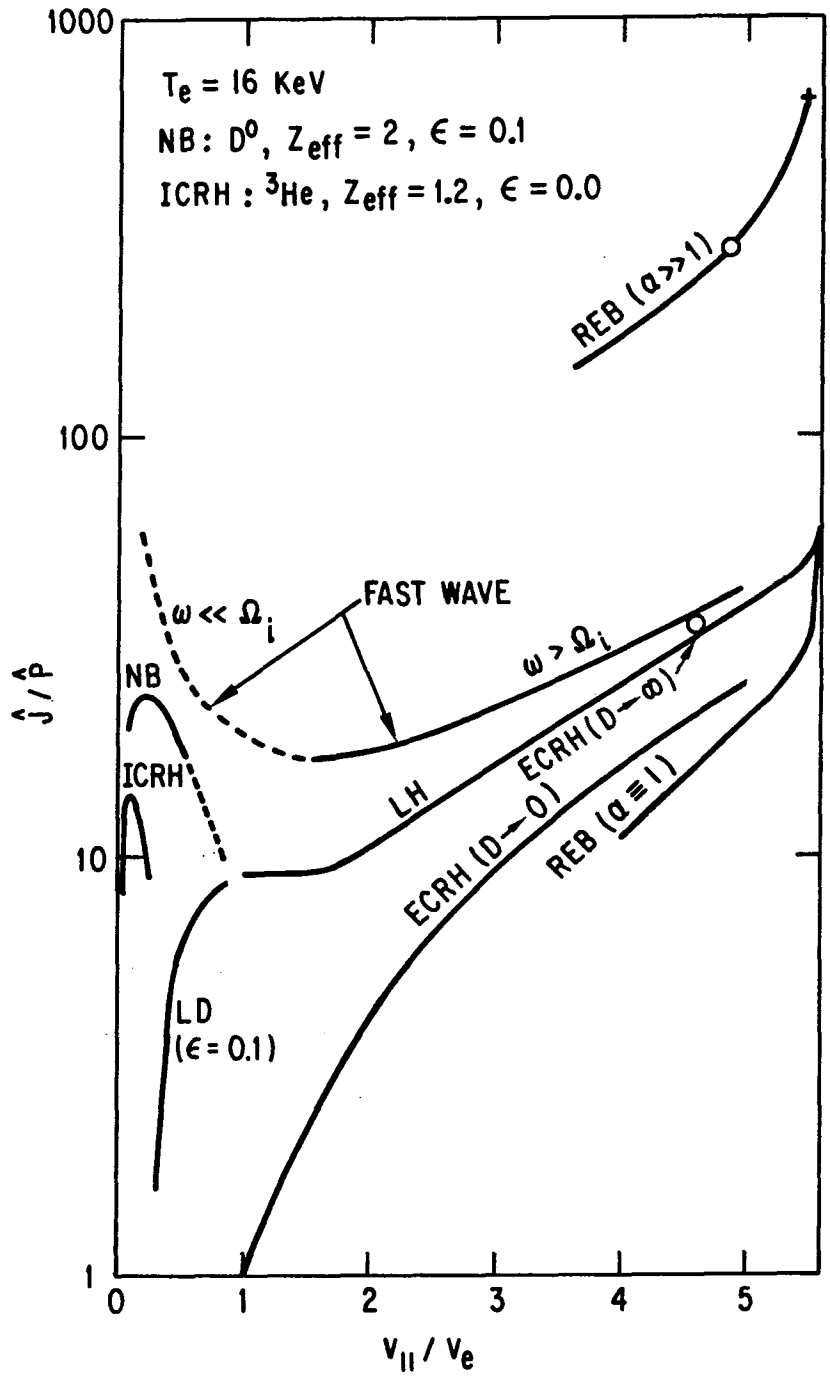

Figure 4-1. Normalized current density to power density ratio for various drivers of DEMO reactor at T_e = 16 keV and n_e = 1.0×10^{20} m^{-3}. REB has $\mathcal{E}_d$ = 4.0 MJ. Neutral deuterium injection (NB) calculation assumes Z_{eff} = 2 and A^{-1} = 0.0 and result deteriorates if neoclassical effects are included. ECRH results are shown in the linear ($D \to 0$) and high power, nonlinear ($D \to \infty$) limits. Lower hybrid (LH) wave is shown at high phase speeds, but neoclassical effects may reduce $\hat{j}/\hat{p}$ for Landau damping (LD) at slow speeds. The fast wave benefits from transit time magnetic pumping, but at slow phase speeds (dotted) neoclassical effects are a concern.

is little increase in the net electric power production, P_n, if the circulating power is reduced below a few per cent of the gross electric output. This is shown graphically in Fig. 4-2. Notice, for the REB since $\langle P_d \rangle << 0.36 \times P_f$ (the gross electric power) a factor of five reduction in circulating electric electric power has only a small influence on P_n. The corollary is that the REB system is relatively insensitive to the electric conversion efficiency of

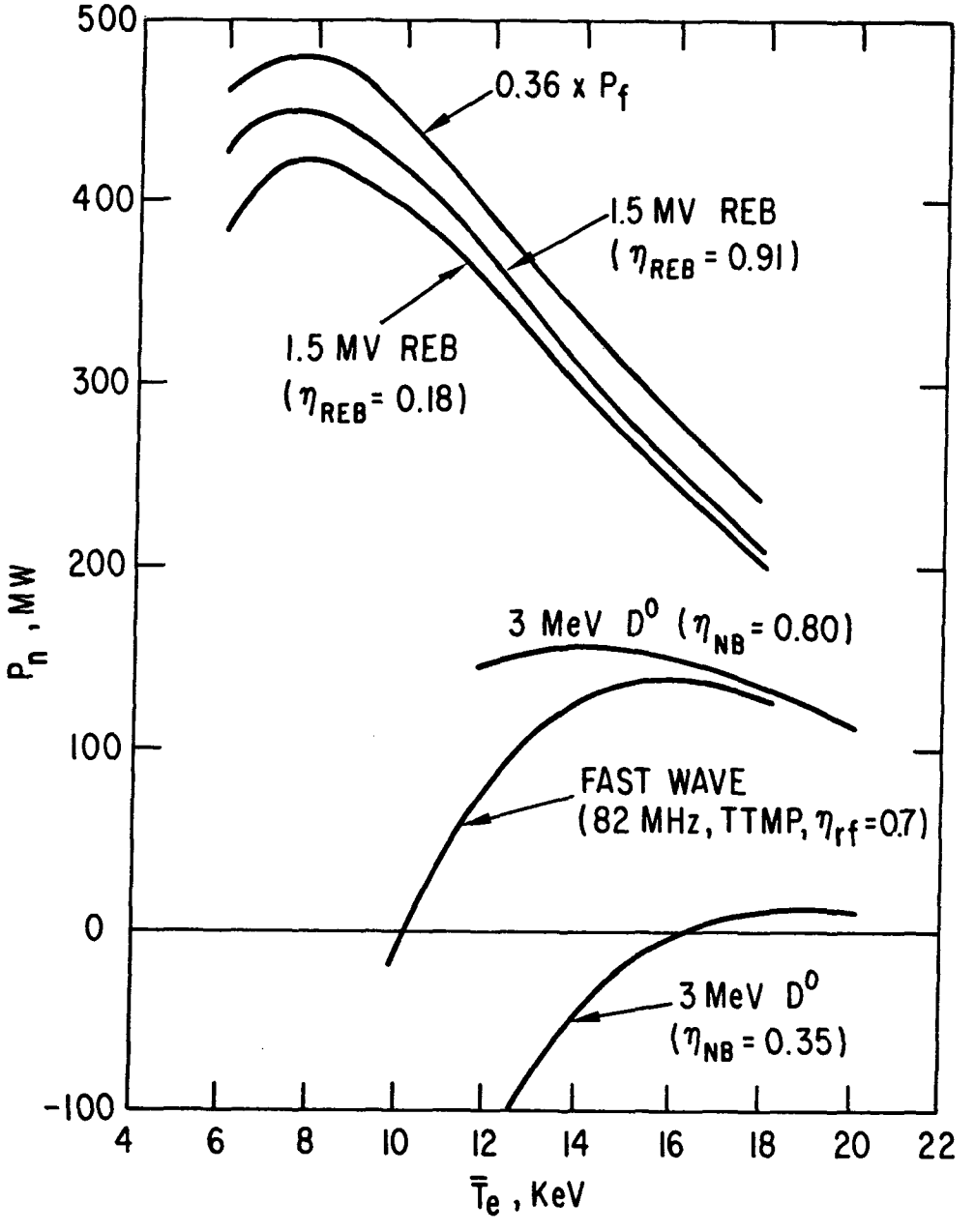

Figure 4-2. Gross power ($0.36 \times P_f$) for DEMO reactor and net electric power for three driver candidates operating at different average temperatues; R_0 = 5.2 m and I_0 = 90 MA. Results plotted for β = 0.08; $P_n = (0.36 \times P_f) - 22 - (P_d/\eta_d)$, in megawatts.

the driver hardware (18% vs. 91% in the illustration). In contrast, the fast wave and neutral beam drivers may require a circulating power for cw current maintenance which is a large fraction of the gross power. In this case the net power production is quite sensitive to the efficiency of the power delivery system, as shown for two values of neutral beam efficiency. A related consideration is the capital and maintenance costs of the driver, which are roughly proportional to the circulating power.

While the emphasis of our investigation centers on the issue of steady-state current drive we will point out other applications. In particular, the tokamak discharge may be initiated completely by the REB, without the aid of a transformer or rf (ECRH) assistance. This was demonstrated on SPAC VI,[13] in which the neutral gas fill was ionized and heated to several hundred eV and the full plasma current was created with a single shot (about one kilojoule) from the REB source. The return current heating mechanism[14] also appears adequate to consider using the REB for heating to ignition.

4.2 Reference Design Description

After the current driver survey was performed for the DEMO[12] a minor change in the reference design was made. This was a result of selecting the REB driver which, unlike most other drivrs, yields maximum net power at a relatively low plasma temperature, $\bar{T}_e \approx \bar{T}_i = 8$ keV. The original DEMO performance was predicated on a volume-averaged plasma beta, $\beta = 0.08$, and a field on axis of $B_0 = 4.81$ T. At 8 keV, however, the DEMO would produce a neutron wall load $W_n = 2.6$ MW/m^2 at such a high beta. This was deemed too ambitious a goal for a tokamak of the DEMO time frame, due to reactor structure and heat removal considerations, so we opted for a lower beta for the current reference design. A new MHD equilibrium with $\beta = 0.075$ and a lower current, $I_0 = 8.68$ MA, was found and used as the basis for computing plasma performance. The toroidal field was kept unchanged, and the resulting DEMO has an acceptable wall load, $W_n = 2.1$ m^2. The steady-state operating parameters for the reactor are given in Chapter 2.

The ideal MHD equilibrium contours are given in Figs. 4-3 to 4-5. Note that current density is fairly broad, with a single peak, and that the safety factor is monotonic but fairly small at the limiter. The external (EF) field required for this equilibrium is plotted in Fig. 4-6. This field is supplied

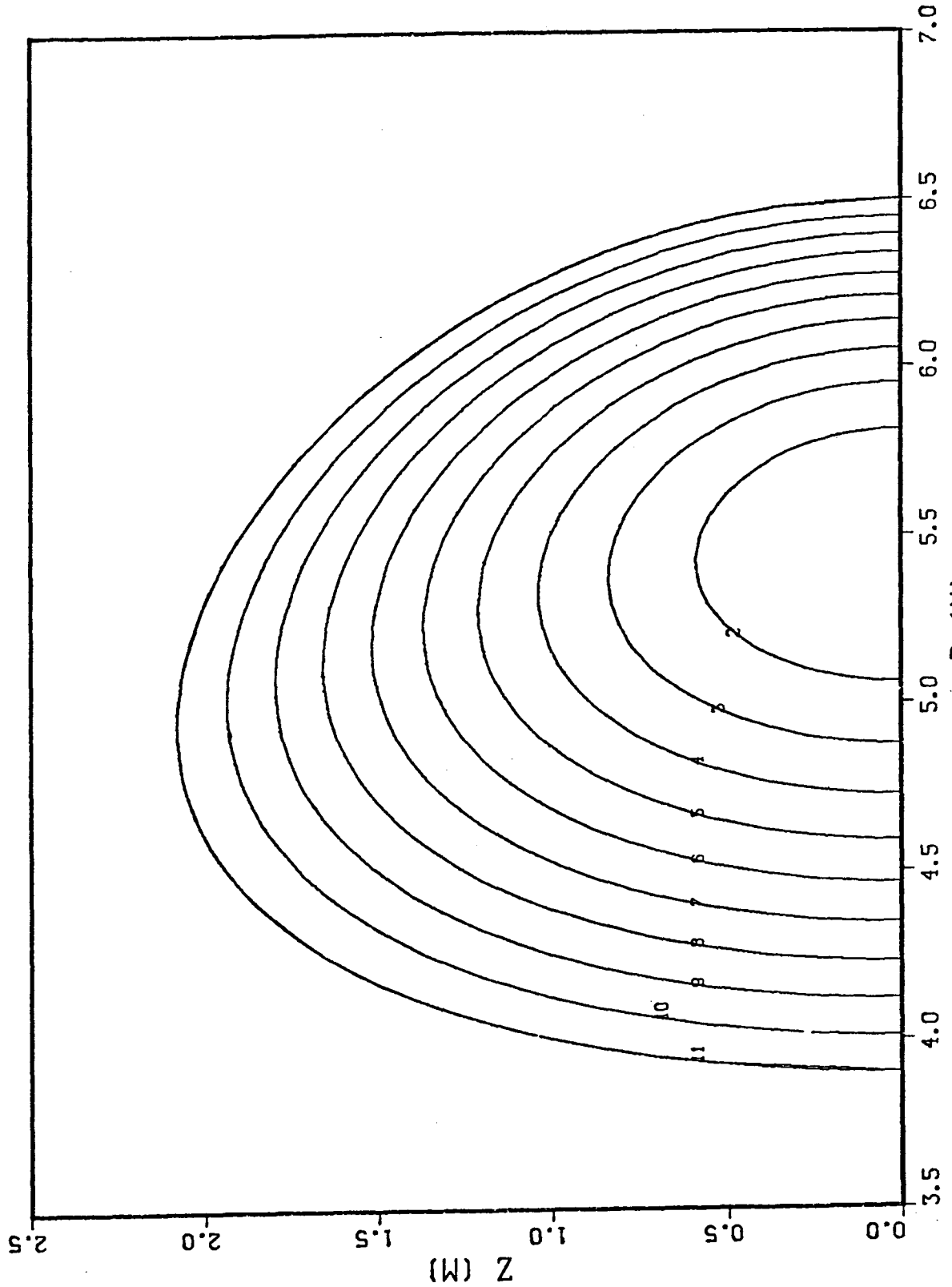

Figure 4-3. Poloidal flux contours.

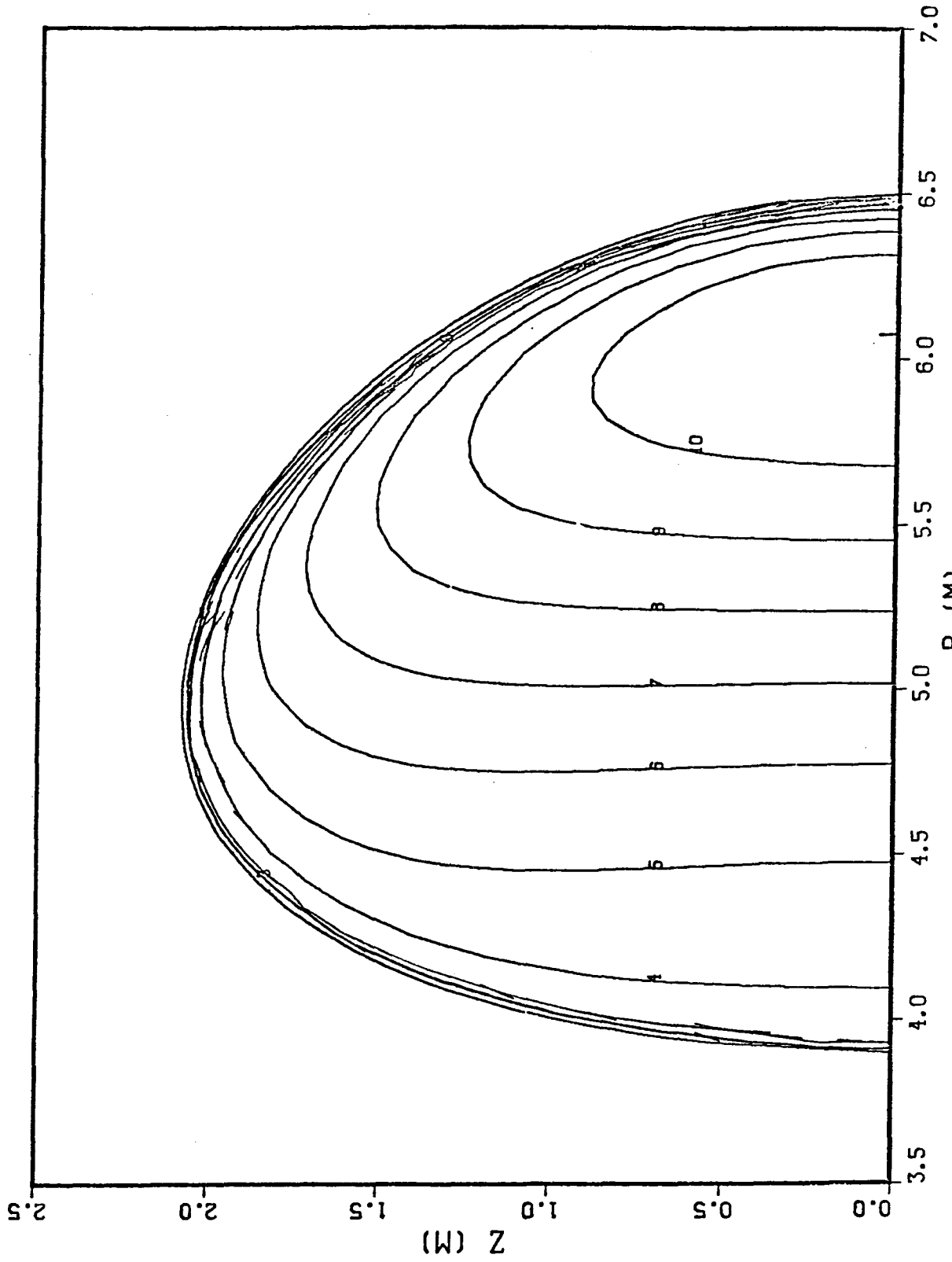

Figure 4-4. Toroidal current density contours.

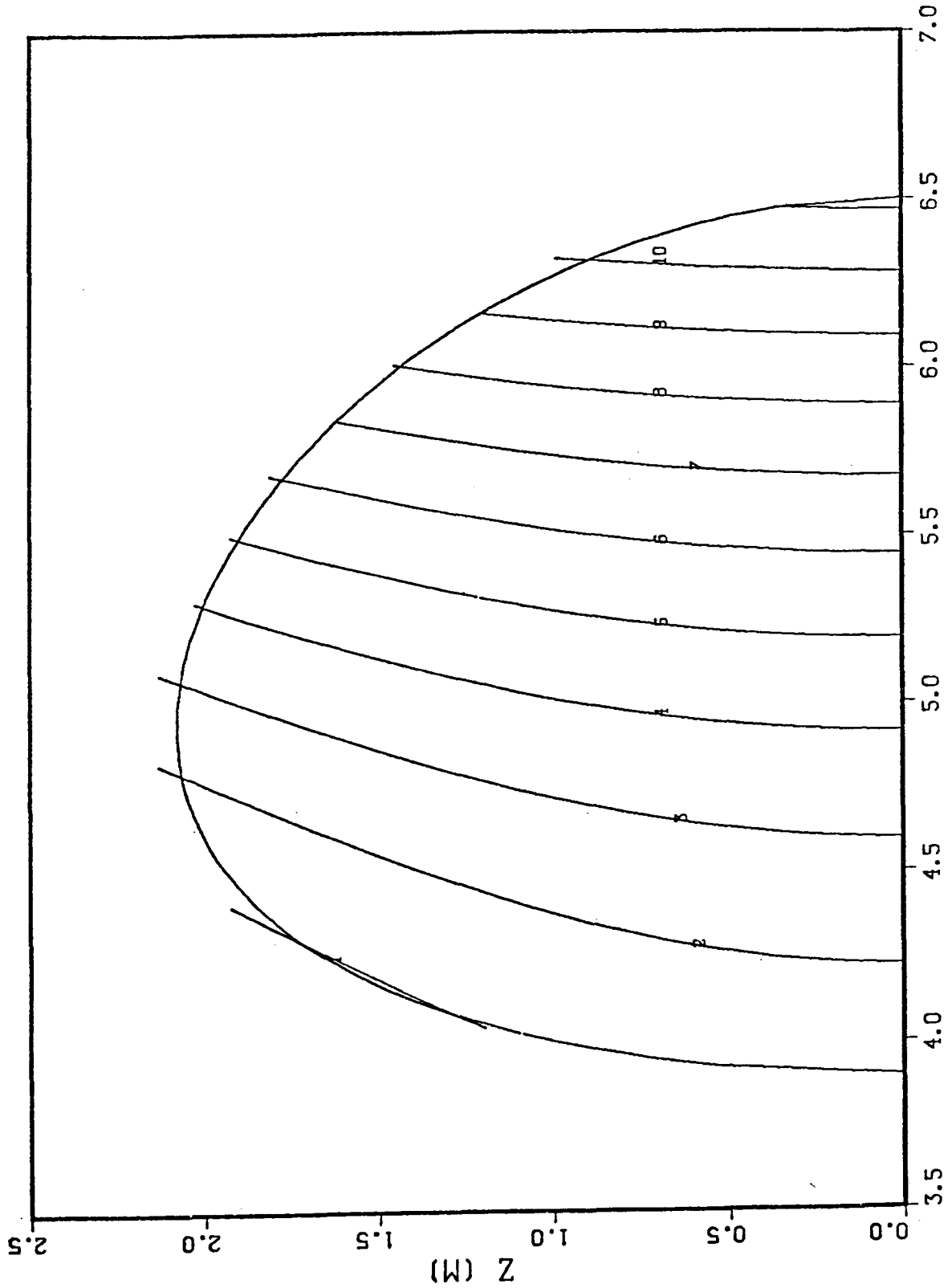

Figure 4-5. Required external flux for equilibrium.

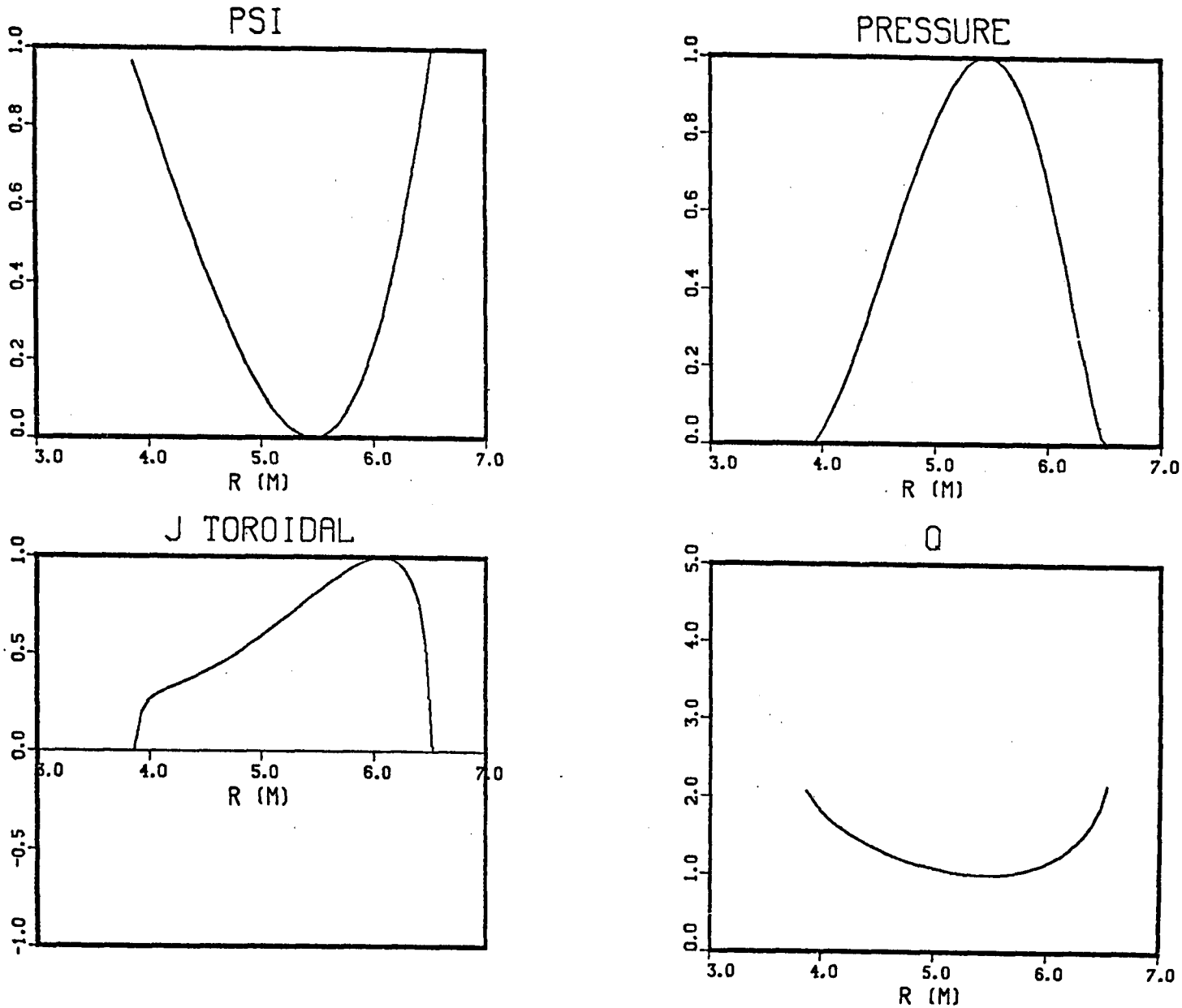

Figure 4-6. Equilibrium profiles in equatorial plane.

by four EF coil pairs, as illustrated schematically in Fig. 4-7. The resulting field, given in Fig. 4-8, closely matches the required field. This EF system supplies a flux of $\Delta\Phi_V$ = 41.6 V-s to the plasma, which aids the startup phase of toroidal current generation. There are no Ohmic heating coils devoted specifically to inductive current generation. Due to the unfavorable sign of the decay index the equilibrium is vertically unstable, so additional small (resistive) control field (CF) coils are provided close to the plasma for feedback stabilization.

The characteristics of the REB current driver are summarized in Table 4-1. The time-averaged current drive power for the repetitively pulsed REB, $\langle P \rangle$ = 6.7 MW, is based on a conservative calculation of plasma resistivity, which yields $I_0^2 R$ = 3.1 MW. Other formulas for R yield values considerably smaller (by as much as a factor of five or six), so it is possible that the REB system and its capital cost could be proportionally smaller than the reference system considered in this report. In any event, the circulating electric power to the REB will be almost negligible compared to the DEMO's gross electric power. The large enhancement of the return current's resistivity, α = 3100, is predicted on the basis of the nonlinear theory of the

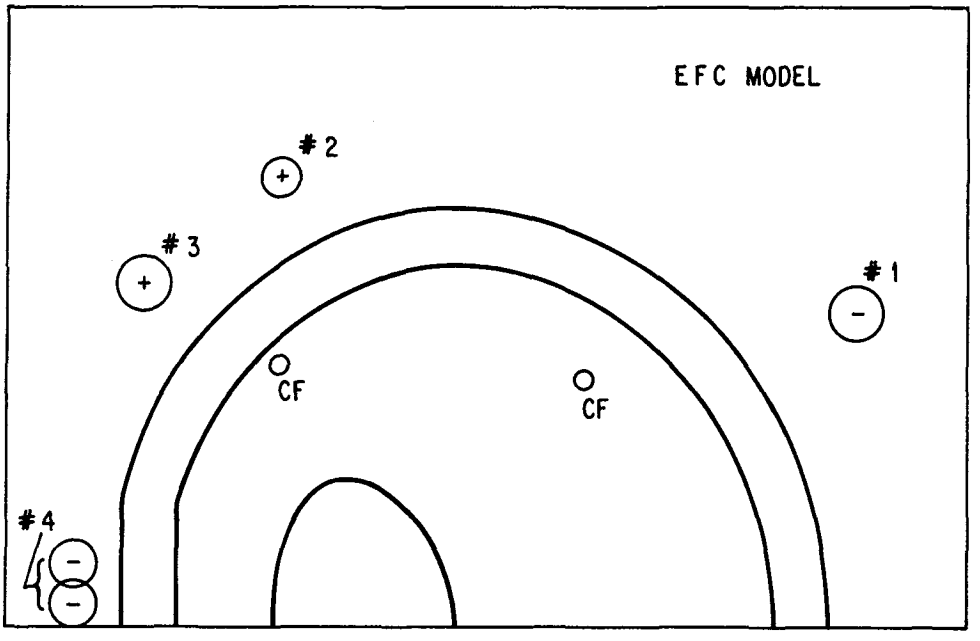

Figure 4-7. DEMO model for equilibrium field coil pairs, Nos. 1-4, showing sense of current relative to plasma current, which is positive; resistive control field coils (CF) feedback stabilize against the vertical mode.

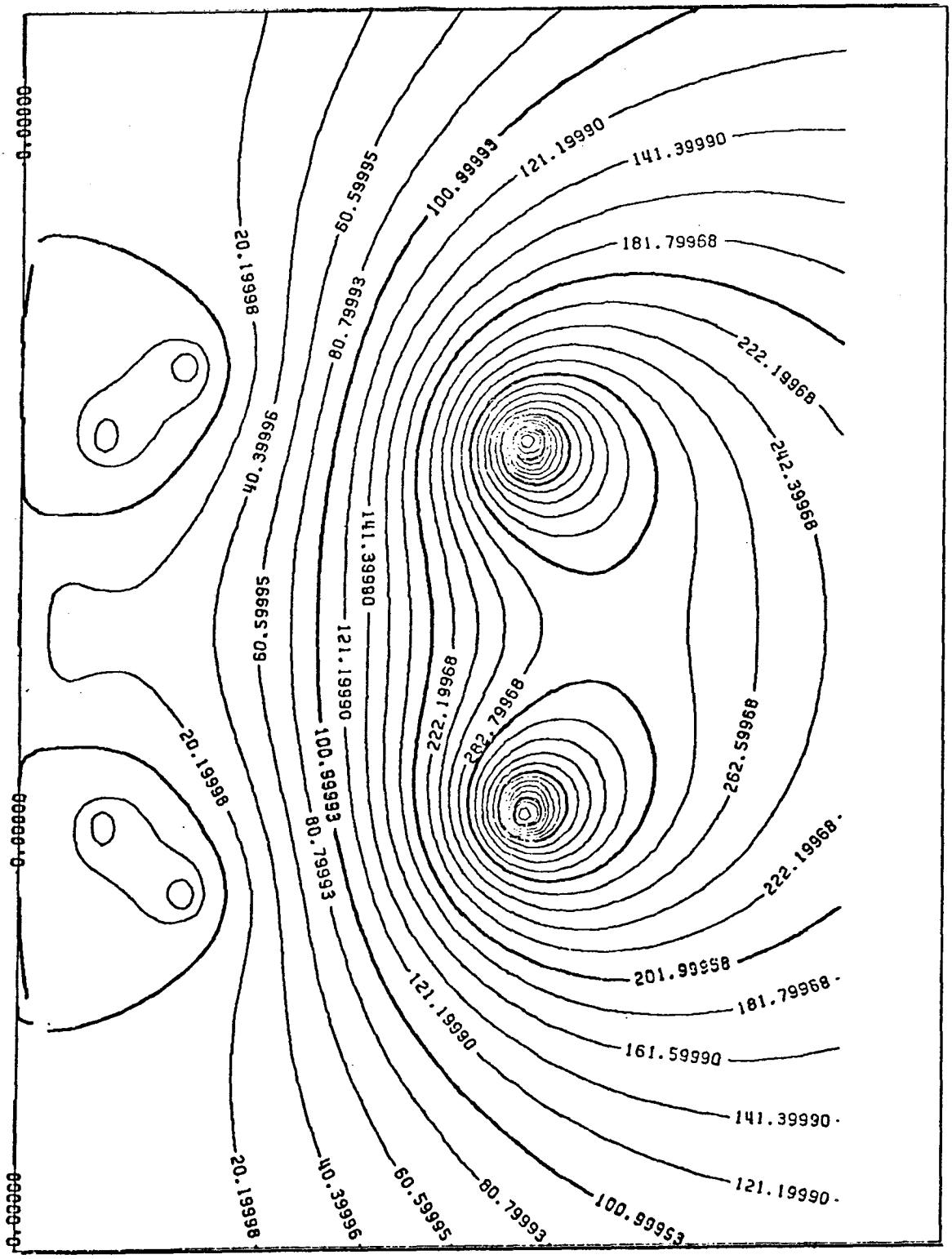

Figure 4-8. Actual flux pattern produced by EFC pairs in Fig. 4-7.

Table 4-1. REB Characteristics (Steady State)

γ_d	= 4.0	Relativistic mass ratio
β_d	= 0.9682	$\sqrt{1 - \gamma_d^{-2}}$
β_s	= 0.4	
E_d	= 3.6 MJ	Kinetic energy per pulse
$\langle P \rangle / I_0^2 R$	= 2.15	
$\langle P \rangle$	= 6.7 MW	Time average current drive power
δt	= 0.535 s	$E_d / \langle P \rangle$
δt^{-1}	= 1.9 Hz	REB rep rate
I_{d_0}	= 23.7 MA	REB stacked current
ΔI	= 17.9 kA	Fluctuation in toroidal current
$\Delta I / I_0$	= 0.2%	
Q_d	= 2.35 C	Electric charge per pulse
n_D	= 5.4×10^{16} m^{-3}	Average beam particle density
n_d / n_e	= 2.3×10^{-4}	
$\alpha(\theta = 17°)$	= 3.1×10^3	Resistivity enhancement of return current
Δt	= 162 μs	EMF slowing-down time
t_{tr}	= 99.1 ns	Toroidal transit time
	Each Cathode (Nominal; 50% Beam Trapping Assumed)	
V_d	= 1.533 MV	Cathode (negative) voltage
t_{t-o}	= 400 μs (3 μs)	Generator pulse width
I_c	= 5.87 kA (783 kA)	
J_c	= 11.1 A/cm^2 (0.8 kA/cm^2)	340 eV, 2×10^{17} m^{-3}, DT
A_c	= 529 cm^2 (1000 cm^2)	Cathode area

kinetic two-stream instability.[11,14] Note the total current oscillates by a very small amount, $\Delta I = 17.9$ kA $\ll I_0 = 8.68$ MA.

Two diodes penetrate the reactor structure to supply REB power to the plasma. This provides redundancy during normal operation and also permits considerably higher power injection during reactor startup when the REB provides auxiliary heating to ignition. Each diode employs the plasma as an anode, the solid central cathode being pulsed to negative 1.5 MV. The 3.6 MJ from each diode is supplied by a power train similar to that in Fig. 4-9.

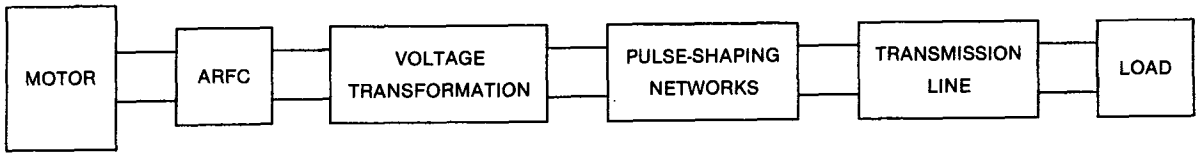

Fig. 4-9. REB power train.

Energy is stored in an active rotary flux compressor (ARFC)[15] and dumped every 535 ms into a high voltage transformer. In the reference system the power is fed directly to the transmission line and diode, which results in a 400-μs pulse half-width at the diode (determined by the ARFC operation). Our cost analysis of DEMO is based on this assumption, although shorter pulse widths are the present state of the art. An alternative power train would store the 3.6 MJ in an intermediate water capacitor which would be discharged by a spark gap in ~3 μs, resulting in much higher cathode current densities and permitting the use of smaller diameter, magnetically insulated transmission lines.

The REB system can be overpowered by factors of two to four for short periods without damaging components so for a modest cost increment the steady-state current drive system can be upgraded to provide plasma heating. This design feature was selected, so the DEMO requires no neutral beams or rf equipment for plasma heating.

4.3 Comparison of Theory and Experiment

All experimental REB work so far has involved only single pulse injection, so the increase in toroidal current, ΔI, is the relevant measurement we must consider. The increase is predicted to be[11,12]

$$\Delta I = \frac{2\pi R_0 mc}{eL} \left(\gamma_d \beta_d - \gamma_s \beta_s\right) \tag{4-1}$$

where R_0 is the major radius, L the toroidal current's self inductance, c is the speed of light, and e and m are the electron charge and rest mass. The relativistic mass ratio is γ, and $\beta \equiv \sqrt{1 - \gamma^{-2}}$. The subscript d refers to the initial value when the relativistic electrons leave the diode, while s refers to the value at the time when the REB has slowed down to the point that the reverse emf has gone to zero. Specifically, the theory provides

$$\beta_s = \frac{(I_0 + \Delta I)\beta_d}{I_{d_0}}$$

and

$$\gamma_s = \left[1 - \beta_s^2\right]^{-1/2} ,$$

where I_0 is the toroidal current before the REB pulse and I_{d_0} is the total stacked REB current immediately after the diode pulse. If the diode operates for a pulse width t_{t-o} and the toroidal transit time for a relativistic electron is $t_{tr} = 2\pi R_0/(\beta_d c)$, then the stacking factor is t_{t-o}/t_{tr}, and the stacked curent is related to the instantaneous cathode current, I_c, by $I_{d_0} = t_{t-o} I_c / t_{tr}$. The kinetic energy delivered in the pulse is

$$W_d = (\gamma_d - 1) \frac{mc^2}{e} I_c t_{t-o} .$$

The theory assumes a resistivity enhancement α during the beam's slowing-down period, and this should be observable as a rapid onset of ΔI after diode operation. The current increase should occur in a period short compared to the classical L/R time:

$$\Delta t \approx (L/R)/\alpha . \tag{4-2}$$

Additionally the analytic formulas above assume a diode pulse width even shorter than the beam slowing-down time:

$$t_{t-o} << \Delta t . \tag{4-3}$$

We shall compare these predictions with the results of four experiments.

SPAC V[9] was a toroidal vacuum chamber with $R_0 = 0.11$ m and a specific inductance estimated in the range $L/2\pi R_0 = 0.17 - 0.48$ μH/m. Since it had no transformer the initial toroidal current was identically zero, $I_0 = 0$. For typical experimental values, $\gamma_d = 2$ (~500 kV) and $W_d = 2.6$ kJ $(I_{d_0} = 2.2$ MA), the analytic formulas predict $\Delta I = 15$ kA if $L/2\pi R_0 = 0.2$ μH/m. Experimental values are larger, $\Delta I \approx 30$-40 kA. This discrepancy is not surprising since expression (4-3) was not satisfied. Fast $\dot{B}_p$ probes showed[16] that $t_{t-o} \approx \Delta t \approx 100$ ns, and we would thus expect larger ΔI values. However, for W_d this large, $\gamma_d \beta_d >> \gamma_s \beta_s$ so Eq. (4-1) would predict $\Delta I \propto \gamma_d$, and we find this linear relationship was in fact observed[16] on SPAC V.

A larger device, SPAC VI,[13] was also built at Nagoya with $R_0 = 0.24$ m. In this case $t_{t-o} \approx 80$ ns $<< \Delta t \approx 700$ ns so the analytic theory should hold. Since the torus is prefilled with a cold plasma (≈20-30 eV) from a gun the classical $L/R \gtrsim 1$ ms. Thus, the observed $\Delta t \lesssim 1$ μs is evidence for a large resistivity enhancement, $\alpha \gtrsim 10^3$. For the particular shot shown reproduced in Fig. 4-10, $\gamma_d = 3.5$ (1.3 MV) and $W_d = 8$ kJ ($I_{d_0} = 1.2$ MA); $I_0 = 0$ since there is no transformer. We would expect ΔI as low as 15 kA for a peaked current density ($L/2\pi R_0 = 0.4$ μH/m) or as high as 30 kA for a hollow current density ($L/2\pi R_0 = 0.2$ μH/m). As shown in the figure the observed $\Delta I = 28$ kA,

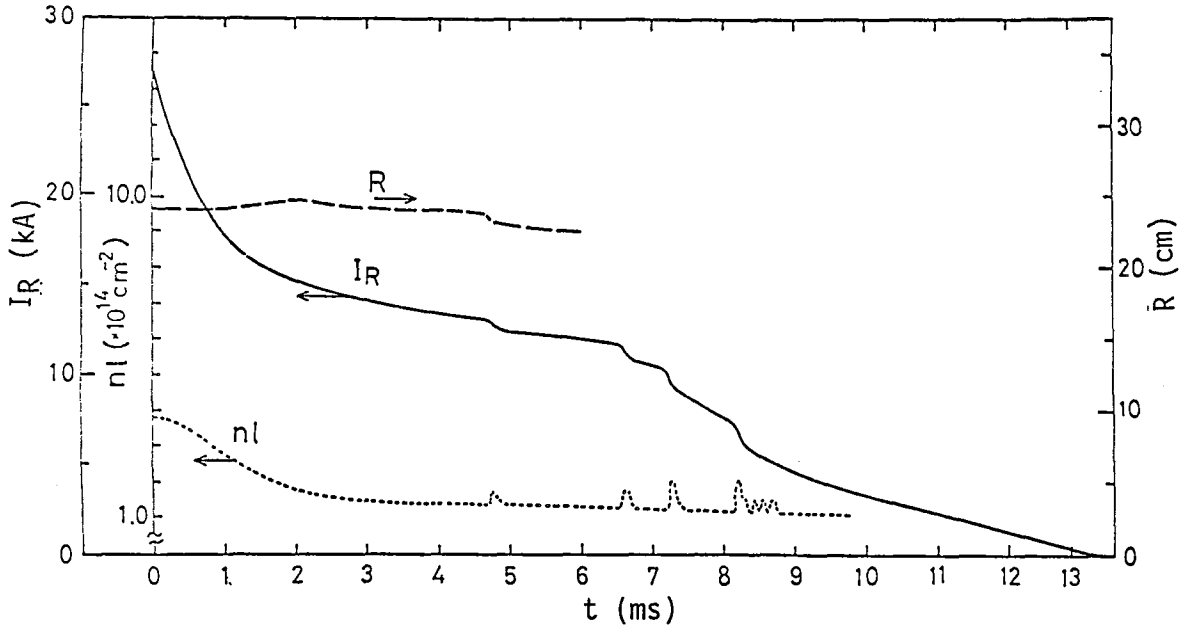

Figure 4-10. Time variations of the net ring current (I_R), the major radius (R), and the plasma line density ($\overline{nl}$) in SPAC VI.

which is within the bounds predicted. The experimentalists also cite a monotonic increase in ΔI with γ_d, as we would expect from the theory.

Experimental results on a racetrack torus at Cornell[17] also demonstrate large resistivity enhancements with $\Delta t \approx 1$ μs and $\alpha \gtrsim 10^2$. In a typical shot there is an initial current $I_0 \approx 300$ A and $\gamma_d = 1.3$ (150 kV). However, insufficient REB energy is supplied to reliably test Eq. (4-1). If the full beam energy (≈40 J) were trapped in the torus and if the relativistic electrons had $v_\perp \ll v_\parallel$ then the stacked current for $I_c = 4.5$ kA, $t_{t-o} = 60$ ns, and $t_{tr} = 45$ ns would be $I_{d_0} = 6.1$ kA, corresponding to ΔI in the range 1.4-3.9 kA, depending on the specific inductance. The problem is that the beam is launched at a large pitch angle $(v_\perp \approx v_\parallel)$ which reduces the toroidally circulating current. This is compounded by an increase in t_{tr} (≈80 ns) due to the slower $v_\parallel$ of the relativistic electrons, further reducing I_{d_0}. Moreover, some injected energy may be lost to the limiter. Thus I_{d_0} is uncertain within a factor of two or three (the experimental limits), and β_s may be considerably larger than in the ideal case assumed by the theory. Consequently, by reference to Eq. (4-1), it would not be surprising to find ΔI much less than 1 kA. The observed value, $\Delta I \approx 1.4$ kA, falls within the upper bounds predicted, but uncertainty in I_{d_0} prevents a definitive comparison with the theory.

The most ambitious effort so far was the PI/UCLA collaboration[18] on Macrotor. Current increments were successfully obtained in this $R_0 = 0.95$ m tokamak with initial currents as high as 50 kA. A typical example from the data is $\gamma_d = 1.78$ (a 400-kV beam) with $I_{d_0} = 87$ kA, corresponding to $W_d = 840$ J; this assumes about 50% beam loss to the back of the diode after injection. All the constraints are satisfied to validate the analytic theory: pulse width, $t_{t-o} \approx 60$ ns $\ll$ current rise time, $\Delta t \approx 1$ μs; resistivity enhancement was large, $\alpha = (L/R)/\Delta t \approx 10^3$, assuming $T_e \approx 40$ eV initially; and the REB was launched toroidally, with zero pitch angle. In this case Eq. (4-1) predicts $\Delta I = 4.2$-6.8 kA for $I_0 = 45$ kA and $L/2\pi R_0$ in the range 0.41-0.25 μH/m. This agrees well with the experimental values, which were in the range $\Delta I = 5$-8 kA. A sample tokamak waveform is shown in Fig. 4-11. The REB pulse occurs at 4 ms into the discharge in the figure.

Additional data in the report showed that ΔI is nearly independent of I_0 but is proportional to γ_d in the Macrotor experiment. As discussed above, this is a natural consequence of the theory when $\beta_s \ll \beta_d$, i.e., when the injected energy W_d is sufficiently large such that $(I_0 + \Delta I) \ll I_{d_0}$. A

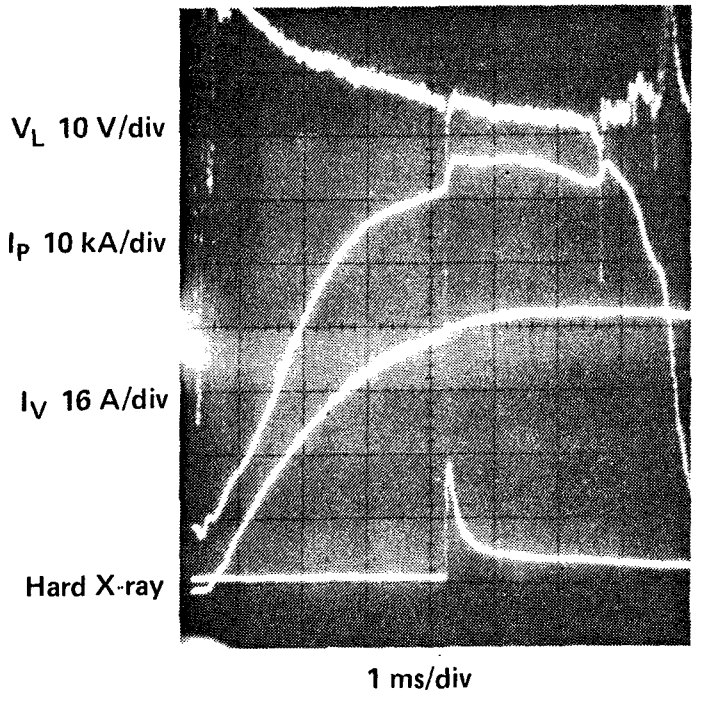

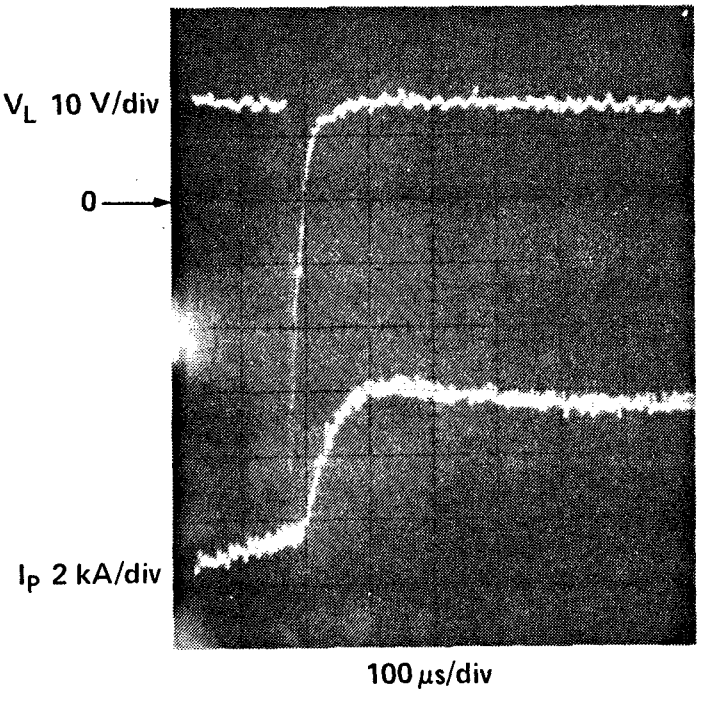

Figure 4-11. Tokamak waveforms for an H_2 plasma with co-injection of an REB into Macrotor. The second sharp increase in I_p is believed to be due to a disruption.

detailed, shot-by-shot comparison of theory and experiment has not been performed, partially due to the difficulty in estimating the injected ("trapped") energy and thus the value of I_{d_0}.

We conclude this subsection with a summary of single-shot REB experimental observations compiled from the four devices listed above:

- Preionization of fill gas was achieved;[9,13] a partially ionized fill was supplied by a plasma gun and the REB completely ionized the neutrals. For this purpose the REB may serve as well or better than ECRH.

- Current generation was achievable without any transformer-driven ohmic current.[9,13]

- REB-assisted startup allowed ohmic current initiation at reduced loop voltage (see Fig. 32 of Ref. 18). Thus, a hybrid ohmic heating/REB system could reduce initial voltages on the conducting first wall and also extend the burn length by conserving the OH volt-seconds, if such an operating mode were desirable.

- Significant plasma heating was observed, presumably due to the return current. On SPAC VI, spectroscopy indicated that T_i was raised from ~30 eV to 800 eV at $n_e \approx 10^{13}$ cm^{-3} with a single REB pulse.[13] The β and β_p values were claimed to be 0.05 and 2.0. It is not clear that the ions were truly a thermal distribution, however. Diamagnetic signals on Macrotor[18] likewise evinced plasma heating. Hence, the REB may serve well for auxiliary heating,[14] although the issue of penetration and heating near the magnetic axis is unsettled.

- At low densities $(n_e < 10^{13}$ cm$^{-3})$ runaway (or "slideaway") discharges can be created with single-pulse injection and maintained for long periods with almost zero loop voltage.[18] The results are strikingly similar to low density current maintenance with lower hybrid waves.

- Current drive at high density was achieved, as demonstrated by the increases, ΔI, observed in the four experiments. In Macrotor and on the Cornell racetrack n_e was as large as 2×10^{13} cm^{-3};[17,18] SPAC V was successful with $n_e \approx 1 \times 10^{14}$ cm^{-3}.[9] Unlike lower hybrid current drive, there are no theoretical or experimental density limitations to REB current drive.

4.4 DEMO Design Analysis

4.4.1 Steady-State Reference Specifications

According to the theoretical assumption, the plasma resistivity should return to its classical value immediately after ΔI has reached its peak, so the current will ohmically decay to its initial, preinjection value of I_0 in a time period $\delta t \approx (\Delta I/I_U)(L/R)$, where we assumed $\Delta I \ll I_0$. Using Eq. (4-1) and noting that $\Delta t \ll \delta t$ in a hot plasma, the time-averaged power required to keep the current oscillating near the I_U value is

$$\langle P_d \rangle = W_d/\delta t = \frac{(\gamma_d - 1)}{\beta_s} \frac{I_0^2 R}{|\gamma_d \beta_d - \gamma_s \beta_s|} . \qquad (4\text{-}4)$$

The normalized quantity $\langle P_d \rangle / I_0^2 R$ is a function of the two beam parameters γ_d and W_d as well as the tokamak parameters R_U and I_U. We have plotted this ratio for DEMO in Fig. 4-12. The dashed portions of the curves correspond to $\beta_s \geq 0.4$, and the solid portions above the open circles correspond to $\beta_s \leq 0.1$; our analytic REB theory is valid in the range $0.1 \lesssim \beta_s \lesssim 0.4$.

Our first observation is that the beam parameters can be arranged such that $\langle P_d \rangle$ is approximately twice the conventional ohmic heating value.

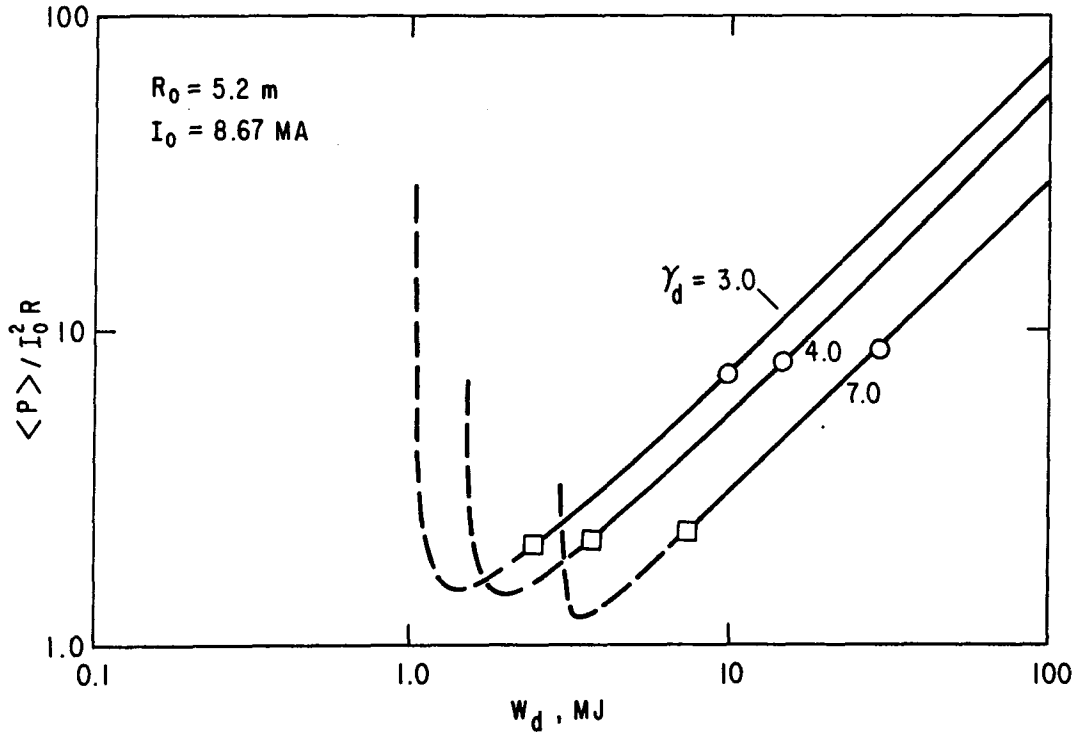

Figure 4-12. Time average power required for REB current drive in DEMO, normalized to $I_0^2 R$.

Athough the value of the toroidal tokamak resistance is controversial we will adopt a conservative value, I_0^2R = 3.12 MW, and $\langle P_d \rangle \approx$ 6-7 MW. A variety of beams can achieve this low $\langle P_d \rangle$, for example, a 500-kV beam with W_d = 1.0 MJ per pulse and a rep rate $(\delta t)^{-1}$ = 7 Hz, or a higher energy beam, e.g., at 3.0 MV with W_d = 7.0 MJ and $(\delta t)^{-1}$ = 1.0 Hz. Lower energy beams may be cheaper due to the smaller energy storage and lower voltages involved, but the higher rep rate increases the total number of shots required from the pulsed power system. Since high reliability is demanded from the DEMO we would opt for relatively high energy, lower rep rate beams. For reference purposes we have designed a 1.5-MV system with parameters as listed in Table 4-1.

4.4.2 Discharge Initiation

The REB can be used to create the initial toroidal current and to ramp the plasma up to its steady-state condition. In order to understand this procedure we will consider first the single relativistic electron orbits in a vacuum magnetic field consisting of a toroidal component and a poloidal field, B_v, supplied only by external coils.

For this phase only two pairs of EF coils need to be energized. We will assume EFC currents of I_1 and I_4 in the coils labelled #1 and #4, respectively, in Fig. 4-7. If the decay index, $n = -\partial \ell n\, B_v / \partial \ell n\, \rho$, is positive the electron orbit projection is closed within the torus, and the locus is centered[18] at a major radius

$$R_e = \frac{\gamma m v_\zeta}{e B_{v_0} (1 - n)} - \frac{n R_0}{(1 - n)} .$$

Here we define ρ to be the distance from the symmetry axis, v_ζ to be the toroidal velocity ($\approx c$), and subscript zero refers to the value at R_0 = 5.2 m. For example, if an approximately circular orbit (n = 0.5) centered on R_e = 6.0 m is desired for a γ = 4 electron, we would invert this formula to find B_{v_0} = 1.2×10^{-3} T would be required. The required EFC currents were found numerically by computing the field from the vector potential ($\underline{B} = \nabla \times A$) associated with the currents. In this calculation the poloidal flux, $\Psi = -2\pi\rho A_\zeta$, is used for the explicit orbit tracing. We find I_1 = -11.1 kA and I_4 = +58.9 kA yields the requisite decay index and B_{v0}. From the constancy of canonical angular momentum for relativistic particles[19] we can compute the orbit projection:

$$\gamma m \rho v_\zeta - e\Psi/2\pi = \text{constant}$$

$$\equiv \gamma m \rho_0 v_\zeta - e\Psi_0/2\pi \ .$$

The result, displayed in Fig. 4-13, assumes $\rho = \rho_0$ at $\rho = 6.5$ m ($\Psi = \Psi_0 = 9.3 \times 10^{-2}$ Wb), corresponding to an electron origin at the outboard edge of the equatorial plane. The actual locus will differ from that plotted for several reasons. First, the minor radius of the "circle" decreases because of particle energy losses (from the reverse emf and also collisions) which decrease γ. Secondly, the vertical field strength will be increased during startup, which will reduce the major radius of the orbit, R_e. Hence, the electrons will not return to their point of origin, and the beam can be expected to miss the back of the diode after injection.

The choice of diode location for a tokamak reactor will depend on such factors as the presence of magnetic divertors, limiter locations, as well as coax routing constraints, diode protection from normal and off-normal plasma

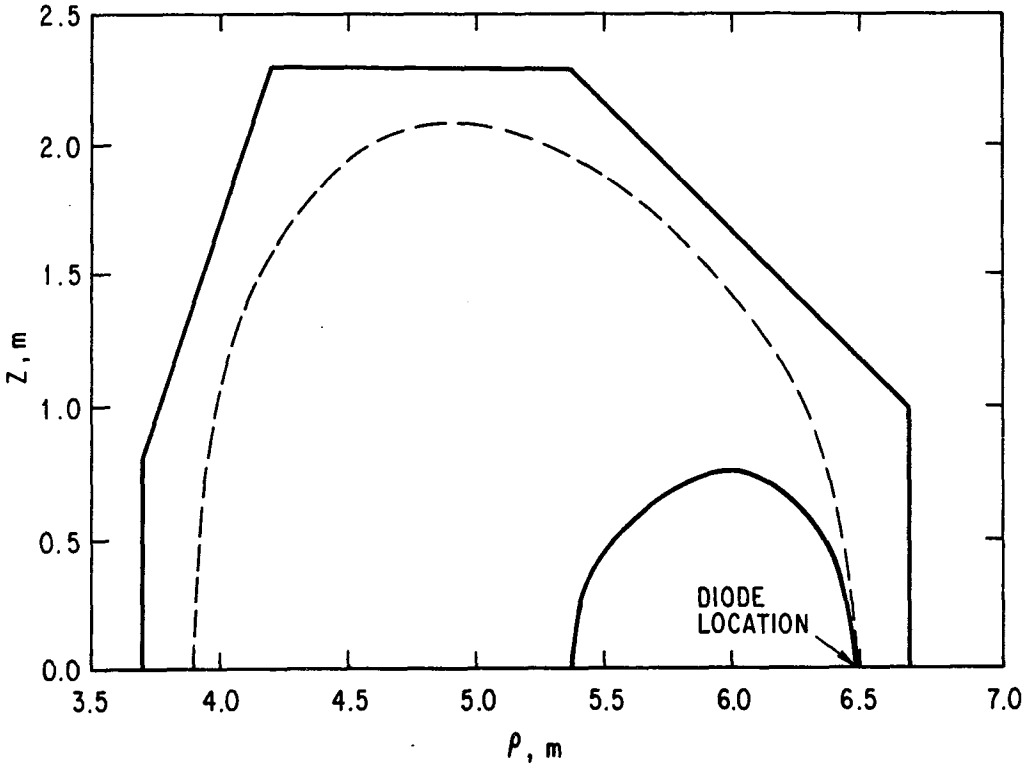

Figure 4-13. Projection of $\gamma = 4$ (1.5 MeV) electron orbit into evaluated torus with DEMO toroidal field and initial vertical field $B_v = 1.2 \times 10^{-3}$ T and decay index = 0.5, resulting from currents of -11 kA and +60 kA in EF coils Nos. 1 and 4, respectively.

conditions, and the temporal mode of plasma operation. By the appropriate selection of EFC currents a wide variety of diode locations may be accommodated. Figure 4-14, for example, shows the locus of particles injected above the equatorial plane. This elliptical orbit, centered at R_e = 5.8 m, has I_1 = -12.4 kA and I_4 = +24.8 kA, resulting in n = 0.17 and B_{v0} = 1.2×10^{-3} T.

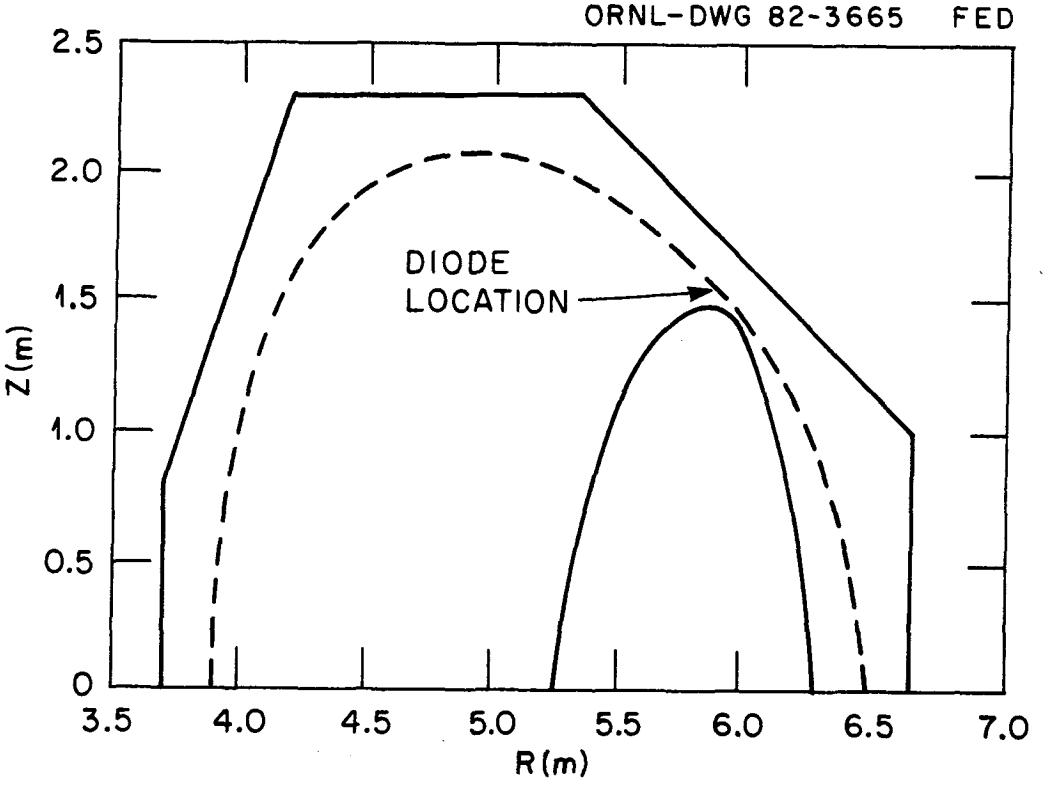

Figure 4-14. Electron orbit (γ = 4) with decay index = 0.17 (I_1 = 12 kA, I_4 = +25 kA).

For the sake of illustration, let us suppose W_d = 4.0 MJ is injected and captured on the very first REB pulse. According to Eq. (4-1) with γ_d = 4.0 and I_0 = 0, we expect ΔI = 20 kA, assuming L = 10.7 μH. The inductive energy of the toroidal current, $\frac{1}{2} L(\Delta I)^2$ = 2.1 kJ, is trivial compared to W_d, so most of the REB energy is deposited in the plasma as heating. After about five pulses the toroidal current reaches $I_0 \approx$ 100 kA, and by this time closed magnetic flux surfaces are likely, so the energy containment time should be adequate to permit efficient heating.

4.4.3 Auxiliary Heating and Current Ramp

We have developed two treatments of the reactor start-up phase. The first which we describe is zero-dimensional and serves to estimate time scales and required ratings for the REB power supply. The second treatment uses a one-dimensional transport code to study the evolution of plasma and current density profiles. This latter calculation will serve as a tool to assess questions of REB penetration and MHD equilibrium. Such profile considerations are emerging as crucial issues for non-inductive current drive, and our calcu-lational method should prove useful for any driver option if the effort is made available to develop the appropriate driver subroutines.

Our zero-dimensional simulation was performed with the following set of equations (all units are SI and keV). Equation (4-4) was recast to give the current maintained by a given time-averaged power input:

$$I_0 = \frac{\langle P_d \rangle 2\pi R_0 mc/e}{R\, W_d} \left[\beta_d \gamma_d - \beta_s \gamma_s\right] ,$$

where the toroidal resistance is modelled by

$$R = 5.85 \times 10^{-8}\, R_0/(a^2 \bar{T}_e^{3/2}) ,$$

where a is the minor radius and a parabolic temperature profile is assumed. The superbar indicates the volume average. This expression for I_0 shows that $\langle P_d \rangle$ can be increased, if W_d is proportionally increased, without increasing I_0. Thus, during the early stages of startup when high power heating is desired, it is possible to achieve this goal without overdriving the toroidal current (which would violate the Kruskal limit), provided W_d is increased. Figure 4-12 bears this out; for our reference REB ($\gamma_d = 4.0$) current drive efficiency is decreased and plasma heating increased by raising W_d above the steady-state requirement (3.6 MJ). In all cases the REB rep rate is, of course, $\delta t^{-1} = \langle P_d \rangle / W_d$. In addition, we use the relationship $\beta_s = (\gamma_{d-1}) mc2R_0 I_0/(eW_d)$. In order to solve these equations it is necessary to know the relationship between $\bar{T}_e$ and $\langle P_d \rangle$, which is predictable from a plasma power balance. At this stage of the REB current drive analysis we have not completely assembled a consistent dynamic calculation, but we will illustrate the solution to this problem by applying our method to an analogous tokamak

start-up situation, that of the neutral beam heated FED,[20] which has R_0 = 5.0 m, a = 1.2 m, κ = 1.6, and I_0 = 5.4 MA and which requires at least $\langle P_d \rangle$ = 30 MW to reach ignition (assuming favorable heating profiles).

We assume long start-up times will be desirable in order to reduce the EFC power requirement and to slowly raise the reactor's blanket and first wall temperatures. Thus, the steady-state power balance is of interest, and the POPCON plots[20] for FED are quite useful. We assume that $\langle P_d \rangle \approx 13$ MW will be adequate to raise the plasma to $\bar{T}_e$ = 1.5 keV at $\bar{n}_e = 0.6 \times 10^{20}$ m^{-3}; if W_d = 1.47 MJ, with both diodes operating out of phase (δt = 0.108 s), the current at this point is I_0 = 1.59 MA. From this point a constant density path is followed with $\bar{T}_e$ increasing monotonically with $\langle P_d \rangle$ until $\langle P_d \rangle$ = 30.8 MW. The $\langle P_d \rangle$ and $\bar{T}_e$ relationship is shown in Fig. 4-15 for this neutral beam analogue. The REB performance during this period is shown in Fig. 4-16, where we see W_d is increased (and δt^{-1} decreased, with the diodes firing in phase) in order to not overdrive the current as the plasma heats up and resistance decreases. Once $\bar{T}_e$ reaches 8 keV, fusion power, P_f, becomes substantial and $\langle P_d \rangle$ must decrease to sustain a power balance. Consequently, W_d must decrease to its steady-state value to maintain I_0 efficiently.

The vertical field gives a ohmic assist to the start-up phase, although this effect was not included in the zero-dimensional simulation. Specifically, a toroidal equilibrium requires $B_v = (I_0/R_0)[\ell n(8A) - 1.25 + \beta_0]\mu_0/4\pi$, where A is the aspect ratio and the poloidal beta, β_p, is given by the POPCON analysis. The loop voltage is given in terms of the total EFC flux, $\Delta\Phi_v$, roughly by $V_\ell = \Delta\Phi_v (dB_v/dt)(B_v^\infty)^{-1}$, where B_v^∞ is the value for steady-state operation. Four considerations place lower limits on the startup time: (1) V_ℓ should be small enough to avoid current generation or arcing in the conducting shells or circuits surrounding the plasma; (2) the EFC power should be reduced to the point that the power supply capital cost becomes negligible; (3) auxiliary heating costs should be minimized; and (4) P_f should increase slowly enough to minimize the effects of thermal stresses in the reactor structure. If we denote the total energy stored in the EFC system as U_{EF}^∞ then the power requirement for the EFC system can be modelled as

$$P_{EF} = U_{EF}^\infty (d/dt)\left[(B_v/B_v^\infty)^2\right] .$$

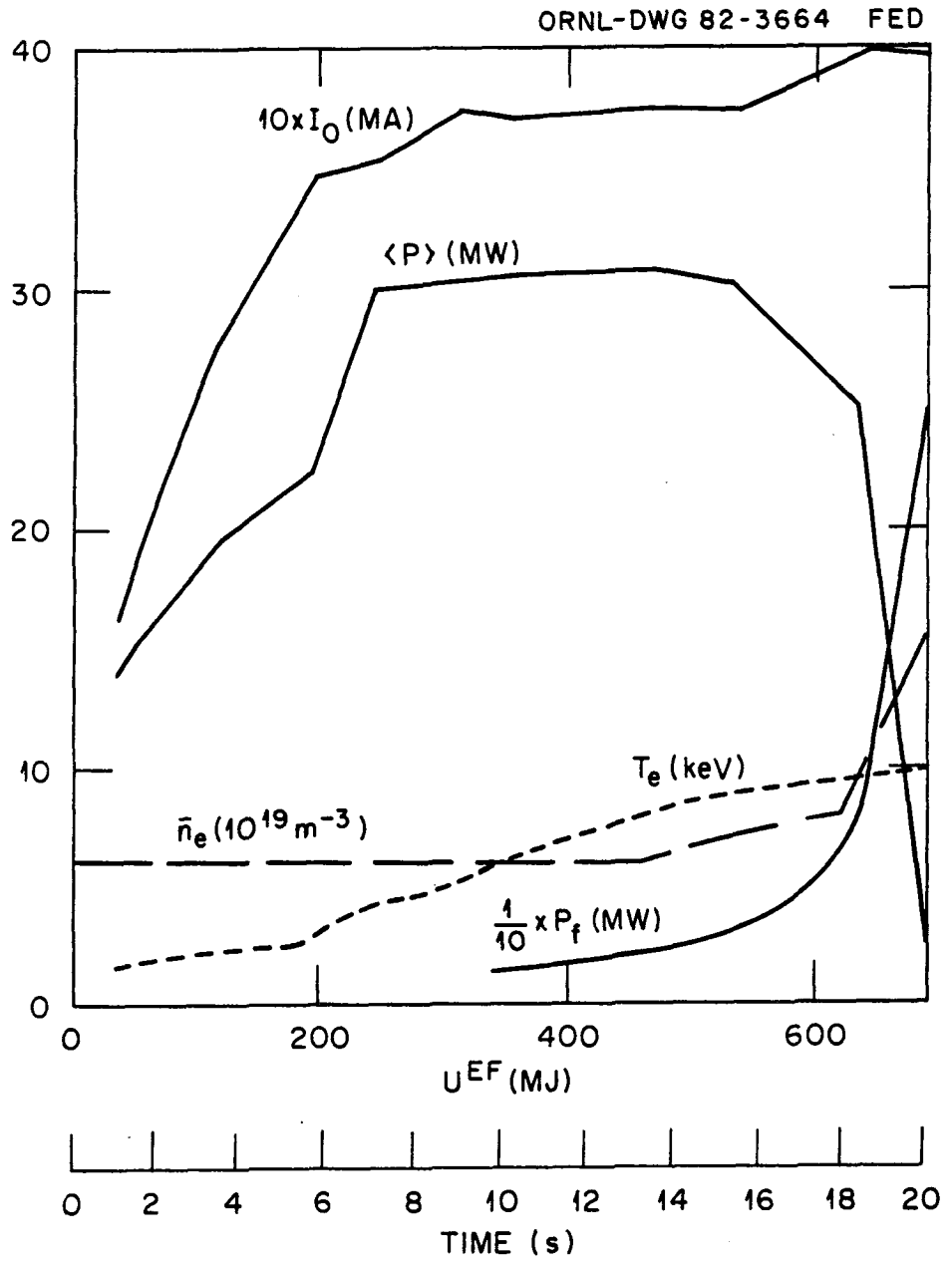

Figure 4-15. REB heating and current ramp at constant power to EFC system.

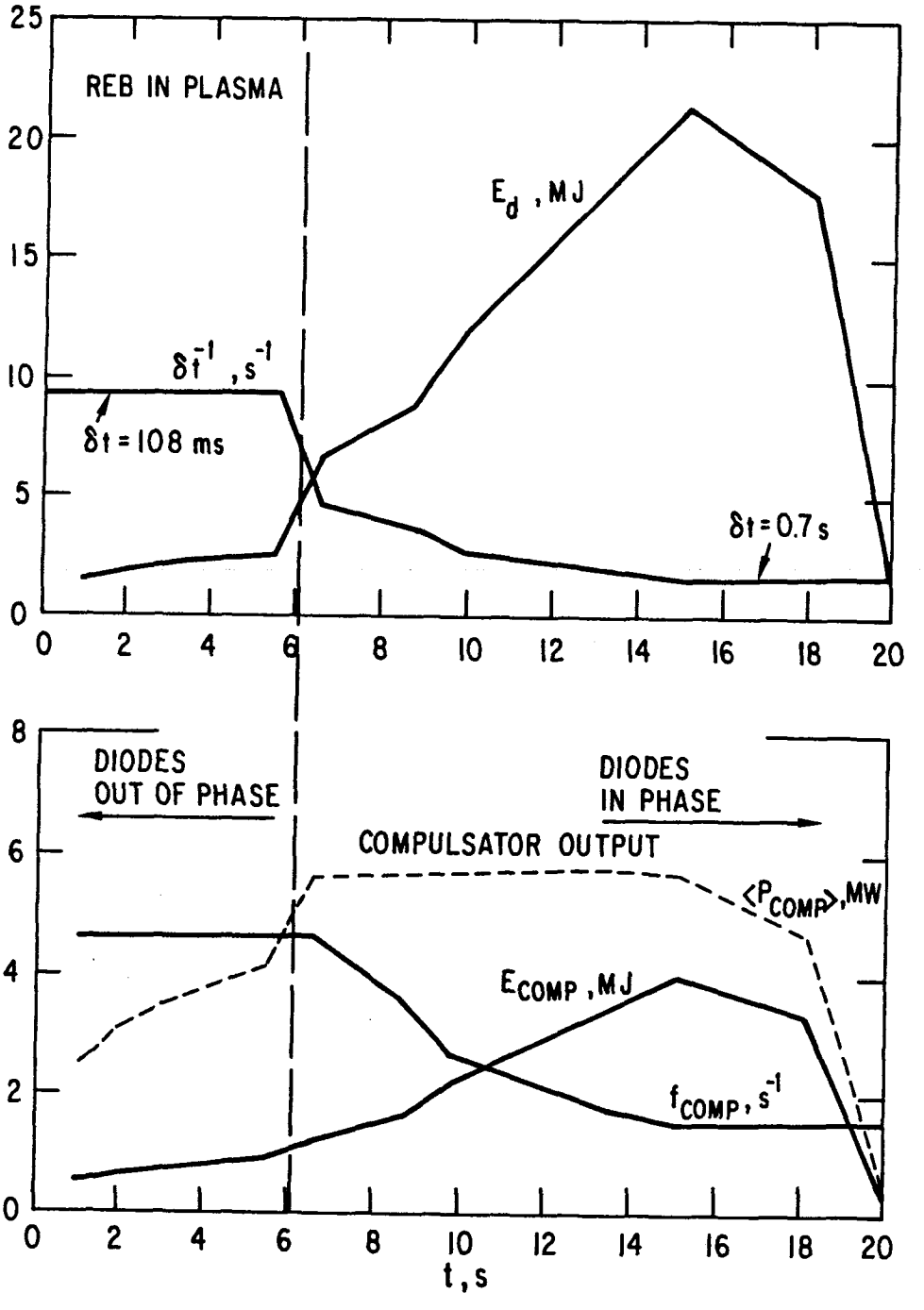

Figure 4-16. Compulsator and REB performance during reactor startup.

A separate study was done to gauge the impact of start-up time on the cost of the EFC power supplies. The results, using approximate cost algorithms, indicate substantial savings in power supply costs if start-up periods are as long as 20-30 s for FED. A 20-s startup at constant EFC power was the basis for Figs. 4-15 and 4-16, where V_ℓ was found to be always less than a few volts.

It is desirable and plausible to have even longer ramp times for the DEMO. Based on the neutral beam simulations in Ref. 20 we estimate 30-60 MW must be absorbed in the plasma to ignite the DEMO reactor.

In the transport code analysis (WHIST) of REB heating and current ramp, the quantities β_s, B_v, and V_ℓ are computed as given above, and R is determined by the transport calculation. The toroidal current variation is, however, calculated more accurately. At every δt the REB is turned on, and an increment ΔI is instantaneously added to the toroidal current. If the self-inductance is assumed to not vary, then ΔI is given by Eq. (4-1) and the new current density is distributed with the same radial profile as the old current density. Likewise, an instantaneous increase in the electron kinetic energy (due to return current heating) is assigned as

$$\int dV \, \frac{3}{2} n_e T_e = W_d - \Delta \frac{1}{2} LI^2 ,$$

and this heat increment is distributed with a radial profile proportional to $\eta(r)j(r)^2$, the classical ohmic heating profile. Between REB pulses the current evolves according to the usual Ohm's Law: $IR = V_\ell - L\, dI/dt$.

In order to explicitly calculate current density profile evolution (variable self-inductance), a one-dimensional treatment of the relativistic electron fluid is being pursued. The treatment described here considers an axisymmetric tokamak with neoclassical relativistic electron orbits.

The basic equations for a system of relativistic electrons having negligible perpendicular velocity are:

$$\frac{\partial n}{\partial t} + \vec{\nabla} \cdot (n\vec{U}) = S \qquad (4\text{-}5)$$

$$\frac{\partial}{\partial t} (\gamma n v_\parallel) + \vec{\nabla} \cdot (\gamma n v_\parallel \vec{U}) = \frac{en}{m} E_\parallel + S' , \qquad (4\text{-}6)$$

where $n(\vec{r},t)$ is the density, $v_\parallel(\vec{r},t)$ the parallel velocity, $\gamma = \left[1 - (v_\parallel/c)^2\right]^{-1/2}$, S and S′ are source terms describing the rate and momentum of injected electrons, and $\vec{U}$ is the local drift velocity:[21]

$$\vec{U} = \hat{b} v_\parallel + \frac{1}{B} \hat{b} \times \left[-\vec{E} + \frac{m}{e} \gamma v_\parallel^2 (\hat{b} \cdot \vec{\nabla}) \hat{b} \right] , \qquad (4\text{-}7)$$

with $\hat{b}$ a unit vector in the direction of $\vec{B}$. The terms in square brackets correspond to the $\vec{E} \times \vec{B}$ drift and the curvature drift, respectively. The gradient drift is absent since perpendicular velocity is ignored. Taking magnetic and electric fields appropriate to a large aspect ratio tokamak,

$$\vec{B} = \hat{\phi} \frac{B_{\phi 0}(r)}{h} + \hat{\theta} \frac{B_{\theta 0}(r,t)}{h} \tag{4-8}$$

$$\vec{E} = \hat{\phi} \frac{E_{\phi 0}(r,t)}{h}, \qquad \left(h \equiv 1 + \frac{r}{R_0} \cos\theta\right), \tag{4-9}$$

and expanding the drift velocity, one has[22]

$$\vec{U} \simeq \frac{B_{\theta 0}}{B_{\phi 0}} \left(-\hat{r} \frac{E_{\phi 0}}{B_{\phi 0}} + \hat{\theta} v_{\parallel} \right), \tag{4-10}$$

plus a toroidal component which is not needed. Note that the curvature shift does not contribute in this approximation, and $|U_\theta| >> |U_r|$. Inserting Eq. (4-10) into Eqs. (4-5) and (4-6), one sees that the effect of U_θ is to force the dependence

$$n \simeq n(|r|,t), \qquad v_{\parallel} \simeq v_{\parallel}(|r|,t).$$

One then is left with the one-dimensional equations

$$\frac{\partial n}{\partial t} - \frac{1}{r} \frac{\partial}{\partial r} \left(rn \frac{B_{\theta 0} E_{\phi 0}}{B_{\phi 0}^2} \right) = S, \tag{4-11}$$

$$\frac{\partial}{\partial t} (\gamma n v_{\parallel}) - \frac{1}{r} \frac{\partial}{\partial r} \left(r \gamma n v_{\parallel} \frac{B_{\theta 0} E_{\phi 0}}{B_{\phi 0}^2} \right) = \frac{ne}{m} E_{\phi 0} + S', \tag{4-12}$$

where, in the right-hand side of Eq. (4-12), the approximation $E_{\parallel} \simeq E_{\phi 0}$ has been used.

Equations (4-11) and (4-12) must be supplemented with equations for the poloidal field and the toroidal electric field. The equation for $B_{\theta 0}$ follows from Faraday's law:

$$\frac{\partial B_{\theta 0}}{\partial t} = \frac{\partial E_{\phi 0}}{\partial r} . \qquad (4\text{-}13)$$

The equation for the toroidal electric field follows from Ampere's law, along with the decomposition of the current density into Ohmic and nonthermal (source terms), $\vec{J} = \eta^{-1}\vec{E} + ne\,\vec{v}$. Neglecting the difference between parallel and toroidal composition of $\vec{v}$, one finds

$$E_{\phi 0} = \frac{\eta}{\mu_0 r}\frac{\partial}{\partial r}\left(rB_{\theta 0}\right) - \eta ne v_{\parallel} . \qquad (4\text{-}14)$$

The complete one-dimensional description of the relativistic electron fluid then consists of Eqs. (4-11), (4-12), and (4-13), with the electric field given by Eq. (4-14). This is a coupled nonlinear system for the evolution of three basic unknowns: n, $v_{\parallel}$, and $B_{\theta 0}$. The equations are first order with respect to spatial derivatives of n and $v_{\parallel}$, and they are second order with respect to spatial derivatives of $B_{\theta 0}$. The resistivity is given by the conventional Spitzer expression, multiplied by a factor to take into account the momentary anomalous enhancement. The source terms are localized at the edge of the tokamak (r = a), and have a time-dependance fixed by the pulse shape of the diode.

This system of one-dimensional time-dependent equations is currently being coded, for inclusion in the main plasma transport code now in operation at ANL. Since the time scale appropriate to the slowing down of relativistic electrons (approximately tens of microseconds) is short compared to the time scale of the transport code (approximately tens of milliseconds), the effect of the relativistic-electron subroutine will be an instantaneous readjustment of the outer current profile, followed by a slow Ohmic diffusion process.

Although the radial transport calculation for pulsed REB current drive has not yet been fully implemented, we feel that this will be a useful tool to investigate issues of beam penetration and radial profile evolution of the tokamak equilibrium. The relativistic electron transport may be revised to include nonclassical behavior such as is described in Sec. 3.1.2 of this report.

4.4.4 Beam Injection Code

In order to investigate the processes which occur during the injection and trapping of a relativistic electron beam within a tokamak, a numerical

code which calculates the motion of the beam in the scrape-off region has been constructed. The code solves the relativistic equations of motion for a test particle within the beam and includes the following: (1) beam self-magnetic fields; (2) induced electric fields caused by the increase in beam current and the relative motion of the beam with respect to the tokamak plasma; (3) the induced currents in both the plasma and the wall; (4) the spatial and temporal evolution of the induced currents; (5) the motion of the beam and the evolution of induced currents followed in two dimensions (r, z); (6) an arbitrary resistance of the vacuum vessel; and (7) an external magnetic field configuration, specified by the user. The code includes the following approximations:

(1) The beam is modeled as a single loop of current (i.e., there is no beam-beam interaction).

(2) Toroidal symmetry is tacitly assumed.

(3) The code assumes that only toroidal currents are flowing within the plasma.

(4) The beam is assumed to be electrostatically neutral.

(5) The number density of the beam is a specified function of time. However, the effect of dissipative plasma currents on the beam is included in the code.

The code is a zero-order code in which the beam and plasma are modeled as a system of current loops. The evolution of the induced current distribution in the plasma is calculated by flux linking the plasma current loops with the beam. This model for n plasma current loops reduces to a system of n first-order differential equations for the toroidal current in the plasma loops which can be written as $[L]\{\dot{I}_p\} = \{C\}$. The [L] matrix is the inductance matrix where the diagonal terms are the self-inductance of each loop and the off-diagonal terms are the mutual inductance between the loops. The $\{C\}$ vector contains the resistive decay term and driving terms due to the beam. The beam term includes both the effect of an increase in beam current $(\dot{I}_B L_{iB})$ and the change in relative position of the beam with respect to the plasma $(\dot{L}_{iB} I_B)$.

The matrix equation for the rate of change of the plasma current distribution is solved simultaneously with the relativistic equations of motion for a test particle within the beam by a fast differential equation solver.

The spatial dependence of the initial toroidal current and conductivity can be specified by the user. The code was originally designed to calculate the motion of the beam when the beam is external to the plasma and has not been checked or debugged for the case where the beam is internal to the plasma.

4.4.4.1 Beam Injection Code Details

We first start with Maxwell's equations and neglect displacement currents:

$$\nabla \times \underset{\sim}{H} = \underset{\sim}{J}$$

$$\nabla \times \underset{\sim}{E} = -\frac{\partial B}{\partial t} .$$

Define the vector potential

$$\underset{\sim}{B} = \nabla \times \underset{\sim}{A}$$

$$\nabla \times \underset{\sim}{E} = -\frac{\partial}{\partial t} \nabla \times \underset{\sim}{A}$$

or

$$\nabla \times \left(\underset{\sim}{E} + \frac{\partial A}{\partial t} \right) = 0 .$$

Thus, in general

$$\underset{\sim}{E} + \frac{\partial A}{\partial t} = -\nabla \phi$$

$$\underset{\sim}{E} = -\nabla \phi - \frac{\partial A}{\partial t} .$$

We now assume that the plasma and the beam are space-charge neutralized (i.e. $\nabla \phi = 0$). Thus

$$\underset{\sim}{E} = -\frac{\partial A}{\partial t}$$

$$\nabla \times \underset{\sim}{B} = \mu_0 \underset{\sim}{J} .$$

We now make the approximation that currents only flow in the toroidal direction

$$\underset{\sim}{A} = A_\phi \hat{i}_\phi$$

where i_ϕ is the unit vector in the toroidal direction. Thus

$$E_\phi = -\frac{\partial A_\phi}{\partial t} \tag{4-15}$$

and

$$\frac{\partial^2 A_\phi}{\partial z^2} + \frac{\partial}{\partial r}\frac{1}{r}\frac{\partial}{\partial r} rA_\phi = \mu_0 J_\phi \, . \tag{4-16}$$

The electric field is obtained from the momentum equation for the plasma electrons

$$E_\phi = \frac{J_\phi^P}{\sigma}$$

where

$$\sigma = \frac{e^2 n_e^P}{\nu_{ei} m_0}$$

and J_ϕ^P is the plasma current density.

This means that (1) the collisional drag of the beam electrons on the plasma electrons is small; and (2) the inertial term is small. In the code constructed for the beam current drive in DEMO both of these terms were included. The inertial term was represented by ε. For most devices, including a reactor, the fractional contribution of this term was $\lesssim 10^{-4}$ and thus our approximation is correct. The collisional drag term in the momentum equation for the plasma electrons was also relatively small (i.e. to first order $E_\phi \approx J_\phi^P/\sigma$). Thus

$$\frac{J_\phi^P}{\sigma} = -\frac{\partial A_\phi}{\partial t} \, .$$

The plasma and the beam are modelled as a configuration of circular current loops (circular in the toroidal direction) such as shown in Fig. 4-17. The plasma can take on any geometrical shape by the proper definition of the current loops. The current within the loops can change but the position of each loop is fixed.

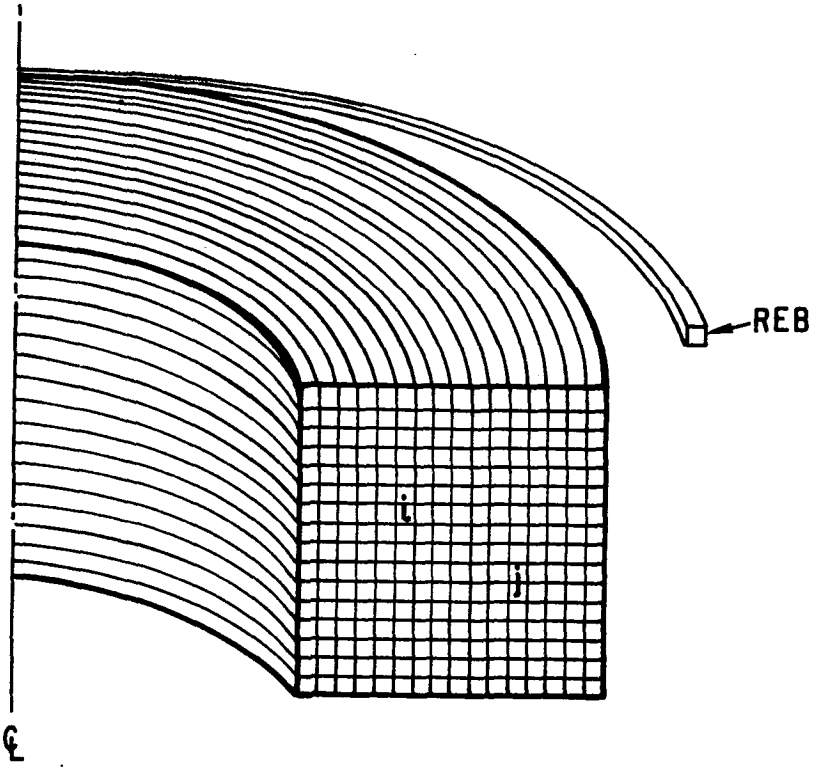

Figure 4-17. Model for REB interaction with toroidal current-carrying plasma.

The beam is also modelled as a single current loop. However, the position of the beam can change. With this model the equation

$$\frac{J_\phi^P}{\sigma} = -\frac{\partial A_\phi}{\partial t}$$

reduces to a system of n equations

$$\frac{J_\phi^i}{\sigma_i} = -\frac{\partial}{\partial t}\sum_{i=1}^{n+B} A_\phi^{ij} ,$$

where J_ϕ^i is the plasma current density at the center of the i-th loop. Thus J_ϕ^i is a function of r_i and z_i. We note that the conductivity σ_i can also be a function of r_i, z_i, and t if we so desire. Also A_ϕ^{ij} is the vector potential at r_i, z_i due to the j-th current loop. The sum on the right-hand side includes the beam (n plasma plus B for beam) or equivalently the equation could be written as

$$\frac{J_\phi^i}{\sigma_i} = -\frac{\partial}{\partial t}\sum_{i=1}^{n} A_\phi^{ij} - \frac{\partial}{\partial t} A_\phi^{iB} \tag{4-17}$$

where A_ϕ^{iB} is the vector potential at r_i, z_i due to the beam current.

The equivalent equation for the beam is

$$E_\phi(r_B, z_B) = -\frac{\partial}{\partial t}\sum_{j=1}^{n} A_\phi^{Bj} - \frac{\partial}{\partial t} A_\phi^{BB} . \tag{4-18}$$

Multiplying Eq. (4-17) by $2\pi r_i$

$$\frac{2\pi r_i J_P^i}{\sigma_i} = -\frac{\partial}{\partial t} 2\pi r_i \sum_{i=1}^{n} A_\phi^{ij} - \frac{\partial}{\partial t} 2\pi r_i A_\phi^{iB} .$$

We now assume that the current density in each loop is spatially uniform or can be represented by an average. Thus

$$\frac{2\pi r_i}{A_i \sigma_i} I_p^i = -\frac{\partial}{\partial t} 2\pi r_i \sum_{i=1}^{n} A_\phi^{ij} - \frac{\partial}{\partial t} 2\pi r_i A_\phi^{iB} \tag{4-19}$$

and for the beam

$$2\pi r_B E_\phi^B = -\frac{\partial 2\pi r_B A_\phi^{BB}}{\partial t} - \frac{\partial}{\partial t}\sum_{j} 2\pi r_B A_\phi^{Bj} . \tag{4-20}$$

To determine the physical significance of the terms, let us calculate the mutual inductance of loops i and j as shown in Fig. 4-17. If there is a need

to calculate the voltage induced in loop i due to a change in current in loop j, we use

$$\int_i \underset{\sim}{E}\, d\underset{\sim}{\ell} = -\frac{\partial}{\partial t}\int_i \underset{\sim}{B}\cdot d\underset{\sim}{s}\ ,$$

where $d\underset{\sim}{s}$ is the surface area. Since the line integral is in the toroidal direction and we have assumed toroidal symmetry the loop voltage is

$$V_\phi^i = E_\phi^i 2\pi r_i = -\frac{\partial}{\partial t}\int 2\pi r B_z^{rj}\, dr\ .$$

By definition

$$B_z = \frac{1}{r}\frac{\partial}{\partial r}\left(rA_\phi^{rj}\right)\ .$$

Substituting into the loop voltage

$$V_\phi^i = -\frac{\partial}{\partial t}\int_0^{r_i} 2\pi \cancel{r}\,\frac{1}{\cancel{r}}\frac{\partial}{\partial r}\left(r\ A_\phi^{rj}\right) dr$$

$$= -\frac{\partial}{\partial t}\,2\pi r A_\phi^{rj}\Big|_0^{r_i}\ ,$$

$$V_\phi^i = -\frac{\partial}{\partial t}\,2\pi r_i A_\phi^{ij}\ .$$

From our assumptions A_ϕ^{ij} is linearly proportional to the current in the j-th loop. Thus $2\pi r_i A_\phi^{ij}$ is just $M_{ij}I_j$ where M_{ij} is the mutual inductance of loop i and j. By the same reasoning then

$$2\pi r_i A_\phi^{ii} = L_{ii}I_p^i\ ,$$

where L_{ii} is the self-inductance of the loop.

Using this fact in Eq. (4-19)

$$L_{ii}\dot{I}_p^i + R_i I_p^i = -\frac{\partial}{\partial t} 2r_i\pi \sum_{\substack{i=j \\ i\neq j}}^{n} A_\phi^{ij} - \frac{\partial}{\partial t} 2\pi r_i A_\phi^{iB} , \tag{4-21}$$

where we note that L_{ii} is independent of time and just a function of r_i. The corresponding equation for the beam is from Eq. (4-20)

$$2\pi r_B E_\phi^B = -\frac{\partial L_B I_B}{\partial t} - \frac{\partial}{\partial t} \sum_j 2\pi r_B A_\phi^{Bj} . \tag{4-22}$$

Since we know that A_ϕ^{ij} is linearly proportional to I_p^j we now define L_{ij} from the following equality

$$L_{ij} I_p^j = 2\pi r_i A_\phi^{ij}$$

and substitute into Eq. (4-21)

$$L_{ii}\dot{I}_p^i + \sum_{\substack{i=1 \\ i\neq j}}^{n} L_{ij}\dot{I}_p^i = -R_i I_p^i - \frac{\partial}{\partial t} 2\pi r_i A_\phi^{iB} .$$

The corresponding beam equation then is

$$2\pi r_B E_\phi^B = -\frac{\partial L_B I_B}{\partial t} - \frac{\partial}{\partial t} \sum_j 2\pi r_B A_\phi^{Bj} .$$

In order to include the motion of the beam we must also solve

$$\frac{d\gamma\, m\underset{\sim}{v}}{dt} = -e\left[\underset{\sim}{E} + \underset{\sim}{v} \times \underset{\sim}{B}\right] + F_{Hoop}$$

$$\frac{d\gamma}{dt} = -\frac{e\underset{\sim}{v}^B \cdot \underset{\sim}{E}}{mc^2} = -\frac{ev_\phi^B E_\phi^B}{mc^2} .$$

We can now define an [L] matrix, a plasma current vector $\{I_p\}$, and a $\{C\}$ vector and write the equation to be solved as

$$[L]\ \{\dot{I}_p\} = \{C\} \qquad \text{n unknowns}$$

$$\frac{d\gamma\, m\underset{\sim}{v}}{dt} = -e\left[\underset{\sim}{E} + \underset{\sim}{v} \times \underset{\sim}{B}\right] \qquad \text{4 unknowns}$$

$$\frac{d\gamma}{dt} = -\frac{ev_\phi^B E_\phi^B}{mc^2} ,$$

where

$$2\pi r_B E_\phi^B = -\frac{\partial L_B I_B}{\partial t} - \frac{\partial}{\partial t}\sum_j 2\pi r_B A_\phi^{Bj}$$

and

$$C_i = -R_i I_p^i - \frac{\partial}{\partial t} 2\pi r_i A_\phi^{iB} .$$

If we assume that $n_b(t)$ is known then the system of equations is closed provided we add a hoop force to account for the motion of the beam electrons on their own self-field. Equation (4-16) is used to calculate A_ϕ. It is done loop by loop and is made up of a spatially dependent portion and a time-dependent portion, since we assume non-uniform current density.

This formulation includes the two-dimensional diffusion of toroidal current in the r-z plane and thus is superior to a cylindrical shell model.

The equations are formulated in such a manner that the inductance matrix [L] need be inverted only once, at the beginning of the calculation. As one would expect

$$r_i \frac{A_\phi^{ij}}{I_j} = r_j \frac{A_\phi^{ij}}{I_i} ,$$

and the [L] matrix is symmetric. The inverse matrix is stored and used in a fast differential equation solver. Thus the L matrix can be determined numerically by using a code such as EFFI which does it very accurately. However, A_ϕ^{iB} must be determined at each timestep since the position of the beam is a function of time.

The code at present uses the analytical vector potential of a circular loop for A_ϕ^{ij} and B. There is some question as to the accuracy of the method for the loop where the beam is inside the loop.

The equation of motion for the beam also includes a hoop force; this additional term has been verified experimentally.[23] It also can be shown that if the $\dot{L}_B I_B$ is included then the hoop force term must be included.

4.4.4.2 Present Version of Code

In the present version of the code we use the vector potential:

$$A_\phi^{ij} = \frac{\mu_0 I^j}{\pi k}\left(\frac{r_j}{r_i}\right)^{1/2}\left[\left(1 - \frac{k^2}{2}\right)K - E\right]$$

where K and E are the complete elliptic integrals of the first and second kind with modulus

$$k^2 = \frac{4r_i r_j}{\left[(r_j + r_i)^2 + (z_j - z_i)^2\right]}.$$

The magnetic field at r,z due to current loop at r_j, z_j is

$$B_r = \frac{\mu_0 I_p^i}{2\pi}\frac{1}{r}\frac{(z - z_j)}{\left[(r + r_j)^2 + (z - z_j)^2\right]^{1/2}}\left[-K + \frac{r_j^2 + r^2 + (z - z_j)^2}{(r - r_j)^2 + (z - z_j)^2}E\right]$$

$$B_z = \frac{\mu_0 I_p^i}{2\pi}\frac{1}{\left[(r + r_j)^2 + (z - z_j)^2\right]^{1/2}}\left[K + \frac{r_j^2 - r^2 - (z - z_j)^2}{(r - r_j)^2 + (z - z_j)^2}E\right]$$

where

$$k^2 = \frac{4rr_j}{(r + r_j)^2 + (z - z_j)^2}.$$

To determine the total field at any given point the fields are summed over the n toroidal loops plus the beam. If the position at which the field is to be determined is inside a current loop j then the current is reduced by

ρ^2/ρ_i^2 where ρ is the distance from the centroid of the minor cross section of the j-th loop and ρ_j is the minor radius of the j-th loop. This method is not as accurate as desirable (it is assumed that the magnetic axis is the same as the minor axis for the loop) and probably should be improved.

The equations for the loop then reduce to

$$[L]\{\dot{I}_p\} = \{C\}$$

where

$$L_{ii} = \mu_0 r_i \ln \frac{8r_i}{\rho_i} - 1.75 \qquad i = j$$

$$L_{ij} = 2r_i D^{ij} \qquad i \neq j ,$$

where

$$D^{ij} = \frac{\mu_0}{k}\left(\frac{r_j}{r_i}\right)^{1/2}\left[\left(1 - \frac{k^2}{2}\right)K - E\right]$$

$$k^2 = \frac{4r_j r_i}{(r_j + r_i)^2 + (z_j - z_i)^2} ,$$

and

$$C_i = -R_i I_i - 2\pi r_i \dot{I}_B D_\phi^{iB} - 2\pi I_B r_B\left[\dot{r}_B \hat{B}_z - \dot{z}_B \hat{B}_r^i\right] ,$$

where $\dot{r}_B, \dot{z}_B$ are the velocities of the center of the beam and $\hat{B}_z^i$ and $\hat{B}_r^i$ are the magnetic field at r_B, z_B due to unit current at r_i, z_i, the position of the loop.

To this set of equations is added the equations of motion for the beam test electron:

$$\frac{d\gamma\, m\underset{\sim}{v}}{dt} = -e\left[\underset{\sim}{E} + \underset{\sim}{v} \times \underset{\sim}{B}\right] + F_{Hoop}$$

and the energy for the beam test electron

$$\frac{d\gamma}{dt} = -\frac{ev_\phi^B E_\phi^B}{mc^2},$$

where there is an electric field only in the toroidal direction

$$E_\phi(r_B, z_B) = -\frac{\partial}{\partial t}\sum_j A_\phi^{Bj} - \frac{\partial A_\phi^{BB}}{\partial t}.$$

The number of unknowns is then

$I_p^i \rightarrow i = 1,n$	n	unknowns	plasma currents
$r_b, \theta_B, z_B, \dot{r}_B, \dot{\theta}_B, \dot{z}_B, \gamma$	7	unknowns	beam parameters.
	n + 7		

The number of first-order differential equations is:

$[L]\{I_p\} = \{C\}$	n	equations	
$\frac{d\gamma\, m\underset{\sim}{v}}{dt} = e\left[\underset{\sim}{E} + \underset{\sim}{v} \times \underset{\sim}{B}\right] + F_{Hoop}$	6	first-order equations	
$\frac{d\gamma}{dt} = -\frac{ev_\phi^B E_\phi^B}{mc^2}$	1	equation.	
	n + 7		

The system of equations is closed. It is easier to assume that γ is an unknown and use the $d\gamma/dt$ equation than it is to write γ in terms of the velocities, differentiate, and substitute into the momentum equation.

The code uses a fast differential equation solver to solve the n + 7 equations. The inductance matrix is inverted only once at the beginning of the run.

The beam injection code has been developed to the point that it is now available for studies of beam transport from the diode to the plasma surface. This will be an important part of future REB design work, since it will be desirable to avoid REB incidence on the limiter and back of the diode.

4.4.5 REB Diode and Transmission Line Design

Each of the two diodes will be designed to deliver the full energy, W_d = 3.6 MJ, required for steady-state current maintenance, in order that tokamak operation can continue should one of the REB systems fail. The current density, j_c, drawn from the cathode depends on the pulse width, t_{t-0}, among other parameters. At a potential of 1.5 MV we expect $j_c \approx 1$ kA/cm^2 for t_{t-o} = 1 μs and $j_c \approx$ 10A/cm^2 for t_{t-o} = 100 μs. For the shorter pulse width the cathode current must be much larger than that for the longer pulse width, in order to have the same stacked current, I_{d_0}, as illustrated in Table 4-1. As a consequence of this scaling the cathode area is nearly independent of pulse width, being about 500 to 1000 cm^2. Although a very long pulse width, t_{t-o} = 400 μs, is assumed for our reference power system, present-day experience is far greater with submicrosecond pulses. As an example, Rayo, presently under construction at Sandia National Laboratory,[24] will operate for 0.2 μs at 1 MV and 330 kA. (A microsecond version of Rayo has likewise been designed.) These parameters are similar to the DEMO requirements if a short pulse width were selected. We point out that plasma anode experiments have only been performed at the megavolt level and hundreds of kiloamperes for $t_{t-o} \lesssim 100$ ns.[9,25] Longer pulse widths ($\gtrsim$1 μs) will simplify transmission line design through the blanket/shield since an impedance match will be unnecessary. The large cathode currents associated with a short pulse width will permit the use of magnetic insulation to minimize the transmission line cross-sectional area, whereas the longer width ($t_{t-o} \approx$ 400 μs) of our reference REB system cannot take advantage of this feature.

The cathode may be fabricated exclusively from steel or from almost any other conductor (tungsten, graphite, beryllium); the choice of materials is not expected to affect its electrical behavior. Moreover, the cathode surface area is so small that surface erosion should not seriously contaminate the plasma. Surface whiskers or grooves may be desirable to enhance field emission. Active cooling of the structure will be necessary in light of severe nuclear and surface heating, and it may be possible to locate the diode physically behind the limiter for protection from disruptions. Figure 4-18 typifies the approximate diode configuration for use with a single blade pumped

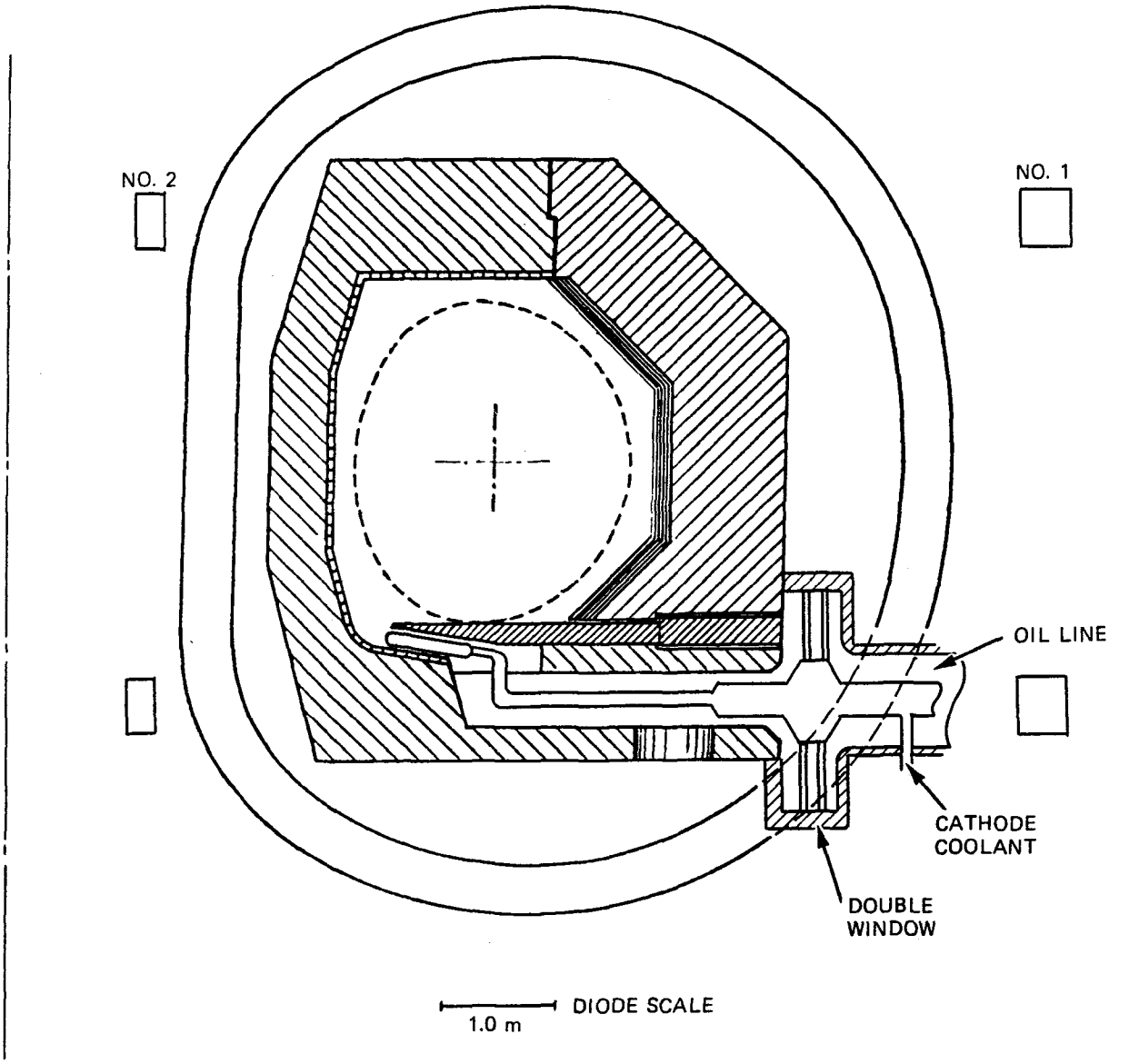

Figure 4-18. Diode location with bottom limiter option.

limiter. The cathode, shown in detail in Fig. 4-19, is located between the limiter and the first wall, and the return current flows to the anode enclosure, which is at ground potential, behind the cathode. The relativistic electrons are launched from the open (higher density plasma) side of the diode and follow the toroidal field lines, moving poloidally according to the rotational transform. If the REB is not completely current neutralized it will move inwards in minor radius due to interactions with the plasma and the conducting first wall. Radial motion and partial beam trapping was observed on Macrotor.[18]

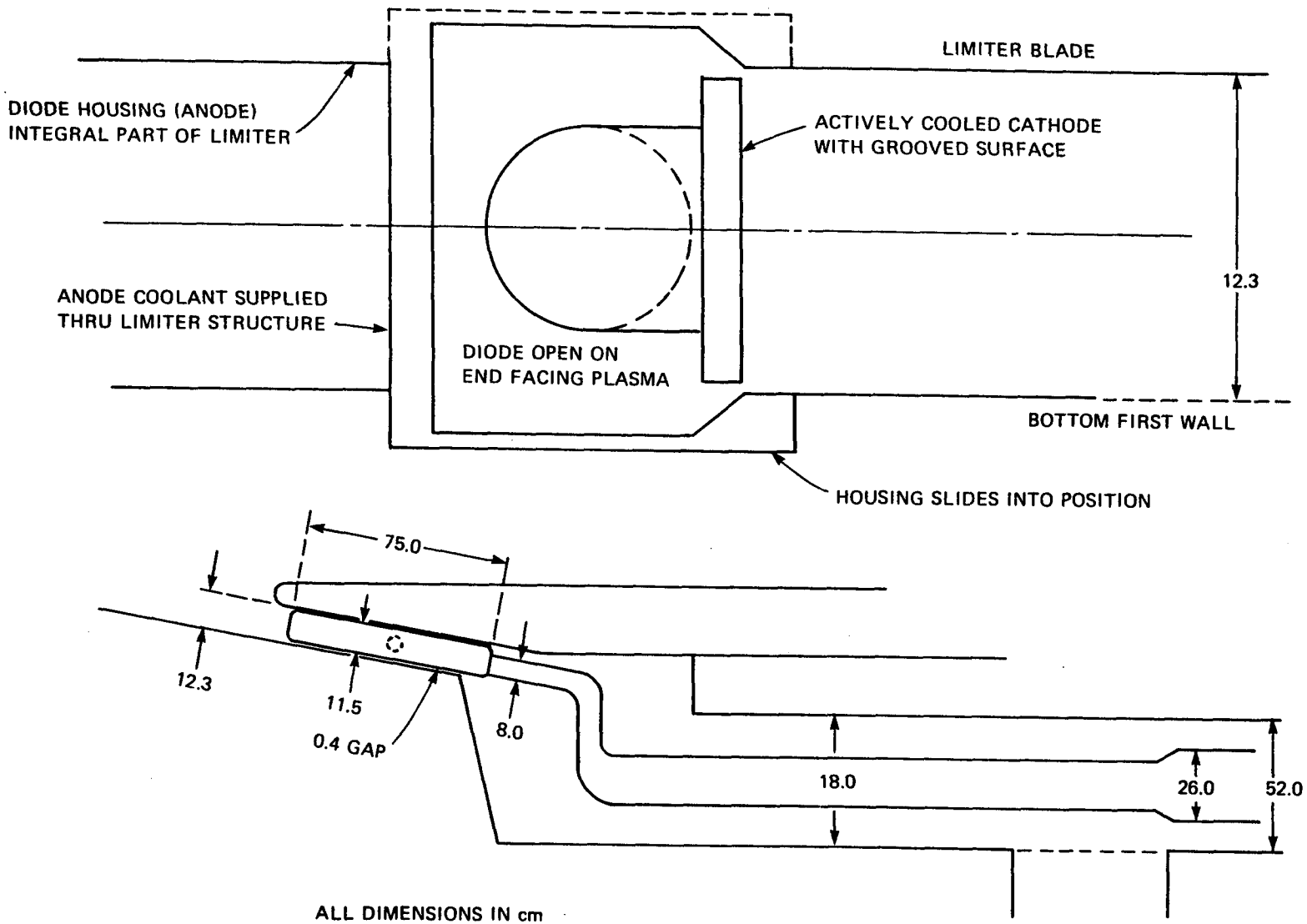

Figure 4-19a. Detail of typical diode.

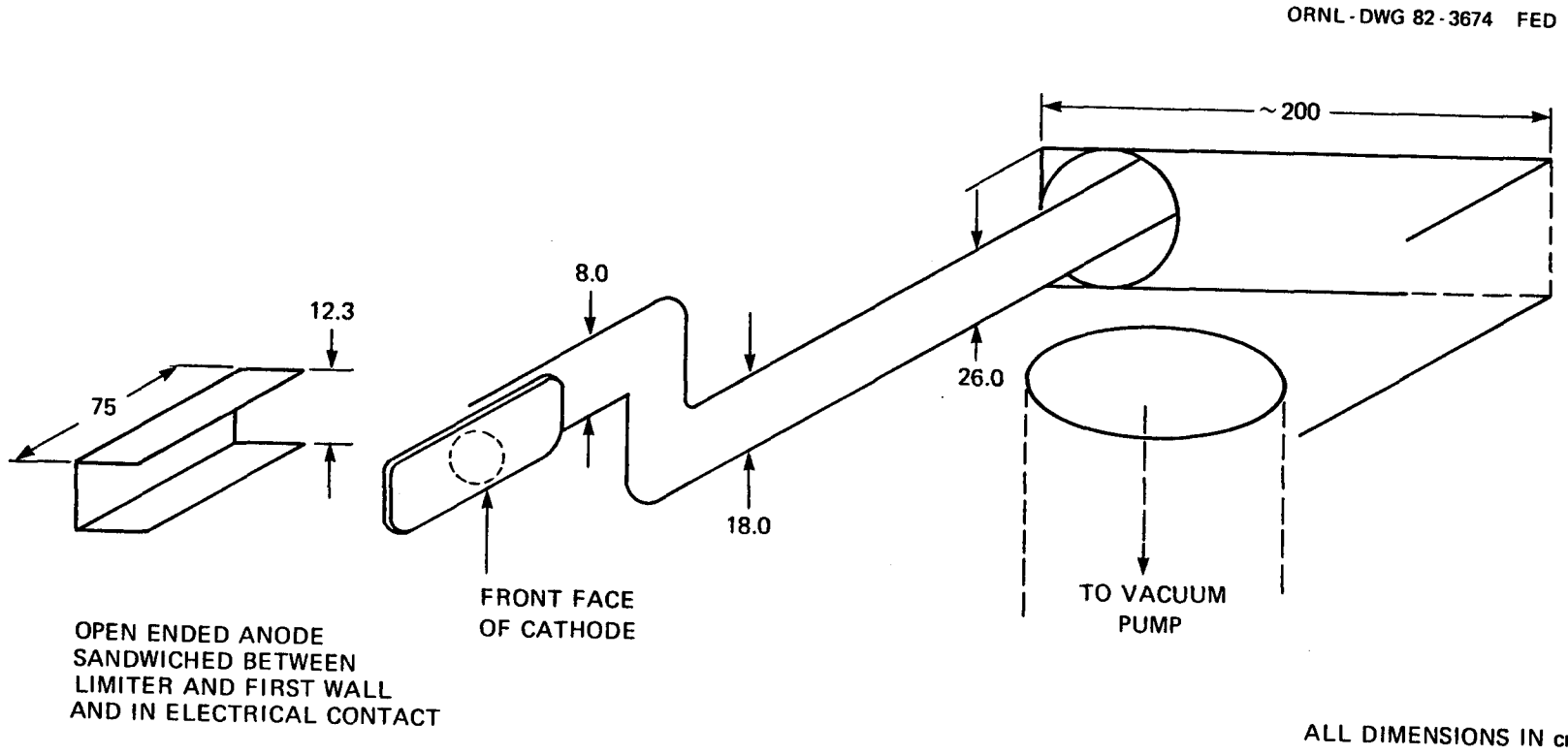

Figure 4-19b. Isometric view.

The vacuum transmission line is separated from a water line by a double ceramic window several meters beyond the first wall. The insulator is large, in order to reduce the electric field strength and inhibit surface breakdown. The vacuum dimensions appear adequate to minimize neutron degradation of the insulator and allow a reasonable lifetime. Beyond the vacuum window the water line extends to the power supply area.

4.4.6 Repetitive Pulsed REB Power Supply

4.4.6.1 Power Supply Options

A large variety of power supply configurations have been considered and these differ in several respects: beam pulse width, t_{t-o}; component lifetimes; capital cost; and size of the power supply building. For all options studied in detail we assumed power is drawn steady state to drive compulsators or active rotary flux compressors[15] (ARFC), which serve as the primary energy storage devices in the power train. These flywheel devices are superior to capacitor storage since they have higher energy density, are long-lived, and cheaper (at megajoule levels). The ARFC is also a superior match to the short pulse requirements of the REB when compared with homopolar devices. The ARFC stores energy for about 0.5 s for the DEMO and discharges it at low voltage (10-20 kV) in a short pulse (~0.5 ms). For REB generation it is thus necessary to employ a voltage step-up transformer in the pwoer train.[26] If long pulse ($t_{t-o} > 100$ μs) diodes can perform well for this current drive application it would be straightforward to connect the transformer directly to the diode's water line, as done for the reference DEMO power supply system. The power train would employ only low voltage switches (ignitrons) and would probably operate flawlessly for over 10^8 shots (several years). On the other hand, if short pulse ($t_{t-o} \lesssim 1$ μs) diodes are necessary or desirable, pulse compression with intermediate energy storage will be essential.

Figure 4-20 displays a few power trains which have been suggested for the REB. The compulsators and transformers will be described in Sec. 4.4.6.2 along with the long pulse power supply option (Fig. 4-20a). Pulse compression with magnetic switches or a high voltage capacitor/spark gap combination will be discussed in the following two sections. In this design analysis we keep in mind the possibiity that the REB may provide the requisite auxiliary heating

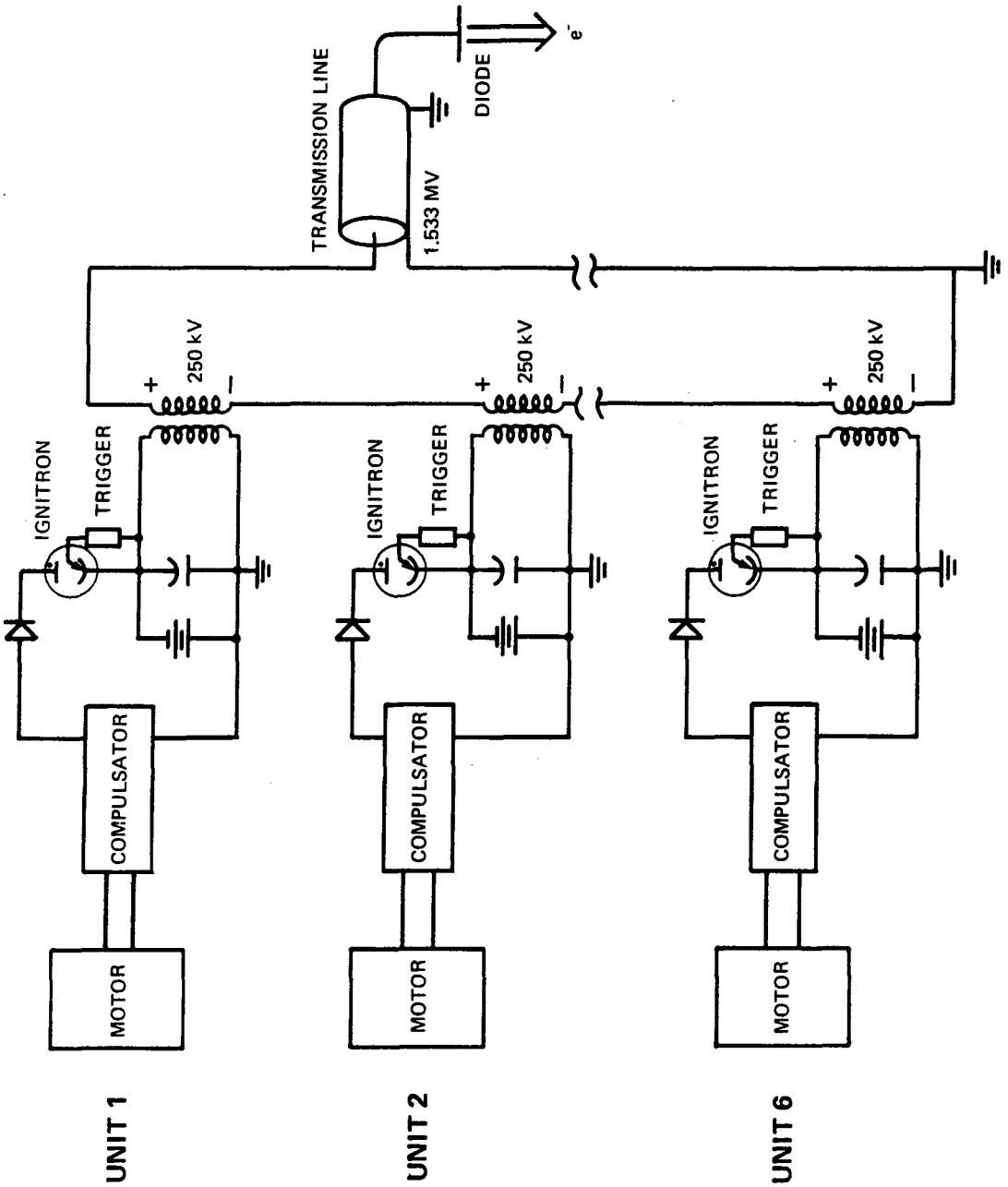

Figure 20-a. Parallel-compulsator series output approach. Switching is provided for each compulsator by the ignitron.

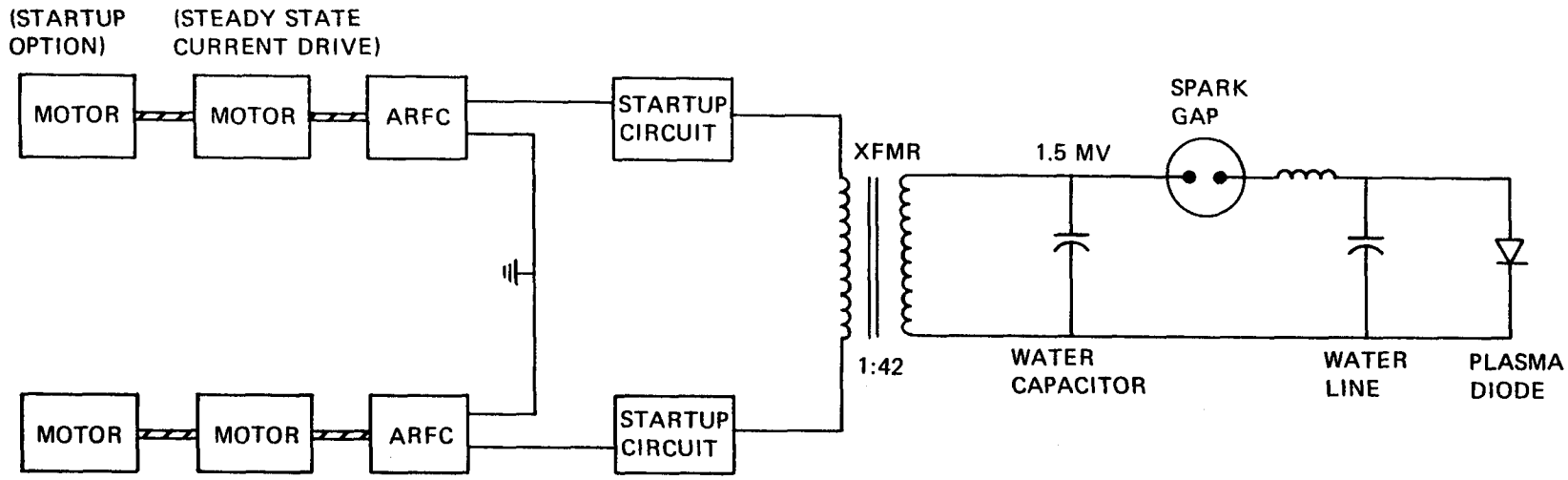

Figure 20b. Microsecond pulse configuration with two center-tapped compulsators and liquid (water) capacitor.

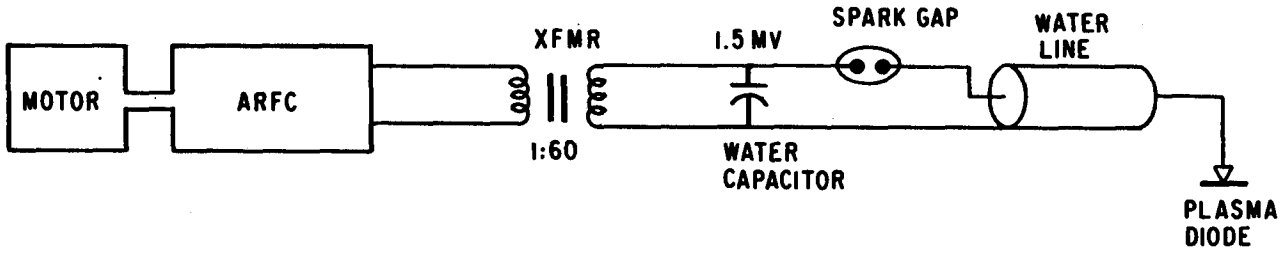

Figure 4-20c. Microsecond pulse configuration with single compulsator and liquid capacitor.

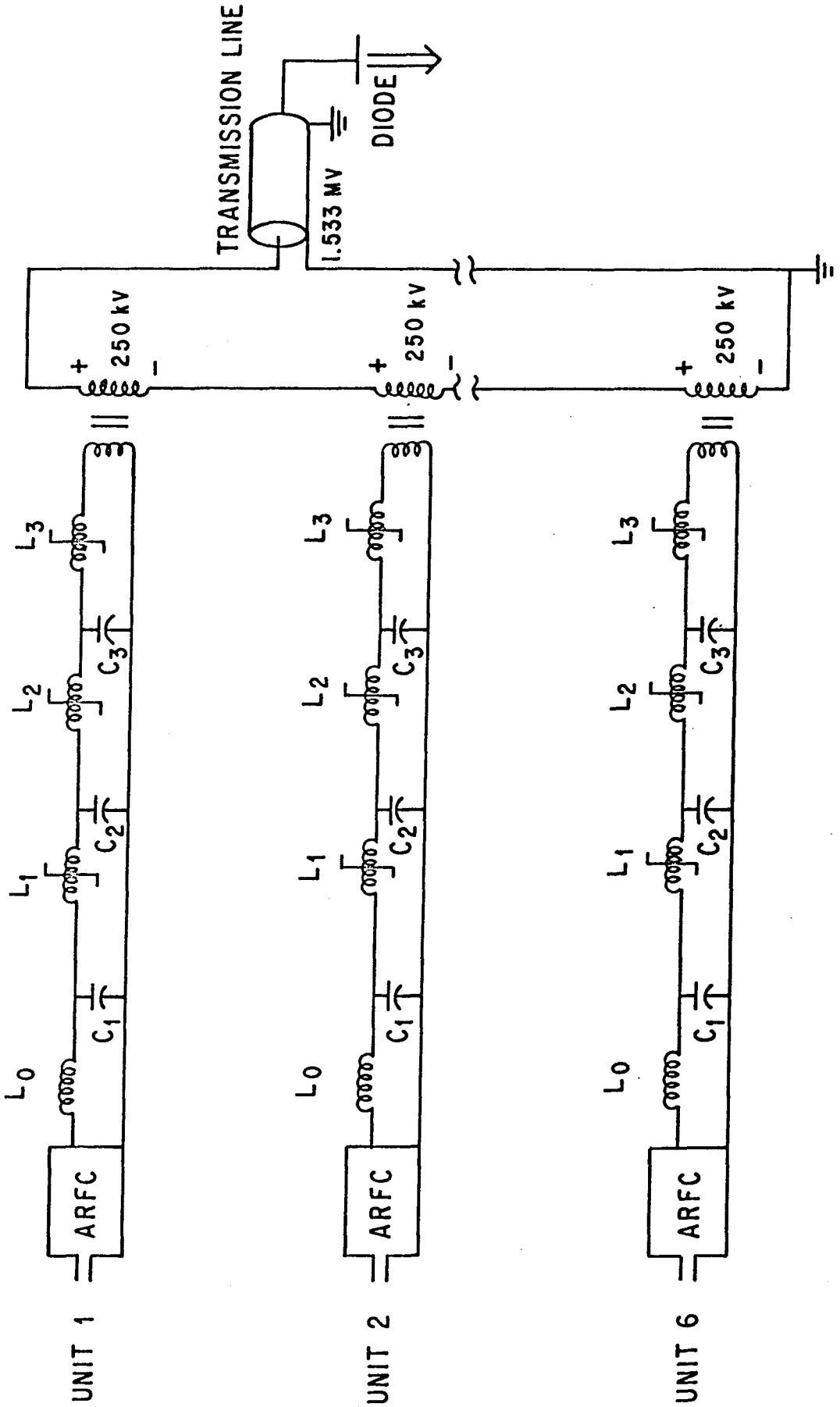

Figure 4-20d. Microsecond pulse configuration using magnetic switches.

needed to ignite the DEMO. For this reason the power trains are provided with additional motors designed to provide ≈30 MW to the plasma; these start-up motors would be disconnected for the steady-state phase of reactor operation.

4.4.6.2 Compulsator Drive Systems for Long Pulse REBs

A compulsator[15] (compensated pulsed alternator) is basically a single phase ac generator with a special compensating stator winding nearly identical to the armature winding. The armature winding and compensating winding are connected in series through slip rings and brushes. This type of connection leads to a cyclical variation of the armature inductance. The variable armature circuit inductance leads to flux compression which, coupled with the alternator action, delivers high current, high voltage pulses to the load.

The Center for Electromechanics, University of Texas at Austin (CEM-UT) has studied and is developing a number of compulsator concepts. Of these, the active rotary flux compressor (ARFC), Fig. 4-21, offers the capability of being repetitively discharged into a load with a pulse duration of a few hundred μs.

An active rotary flux compressor is essentially a compulsator without a field winding. Since the field winding is removed, the stator can be fabricated in a simpler cylindrical rather than salient pole fashion. The compulsator is driven by a motor at several thousand rpm. A capacitor bank is used to provide the start-up current. The start-up current is initiated when the rotor is in the maximum inductance position (rotor and stator winding aiding). As the rotor position changes the inductance decreases, driving the current to a value more than a factor 10 larger than the startup current. This can be understood from the principle of conservation of flux; i.e., LI = constant.

Figure 4-22 shows the circuit diagram arrangement. The capacitor bank C is charged negative by a voltage nearly equal to the desired voltage for a resistive load and a little less than desired voltage for a capacitor load. (The compulsator is ideally suited for driving resistive or capacitive loads. It is less effective in driving inductive loads.) The ARFC is driven at several thousand rpm by a prime mover such as a dc motor or synchronous motor. At the proper time (inductance maximum) a timing circuit triggers the ignitron IG and discharges the capacitor bank into the circuit. At voltage reversal

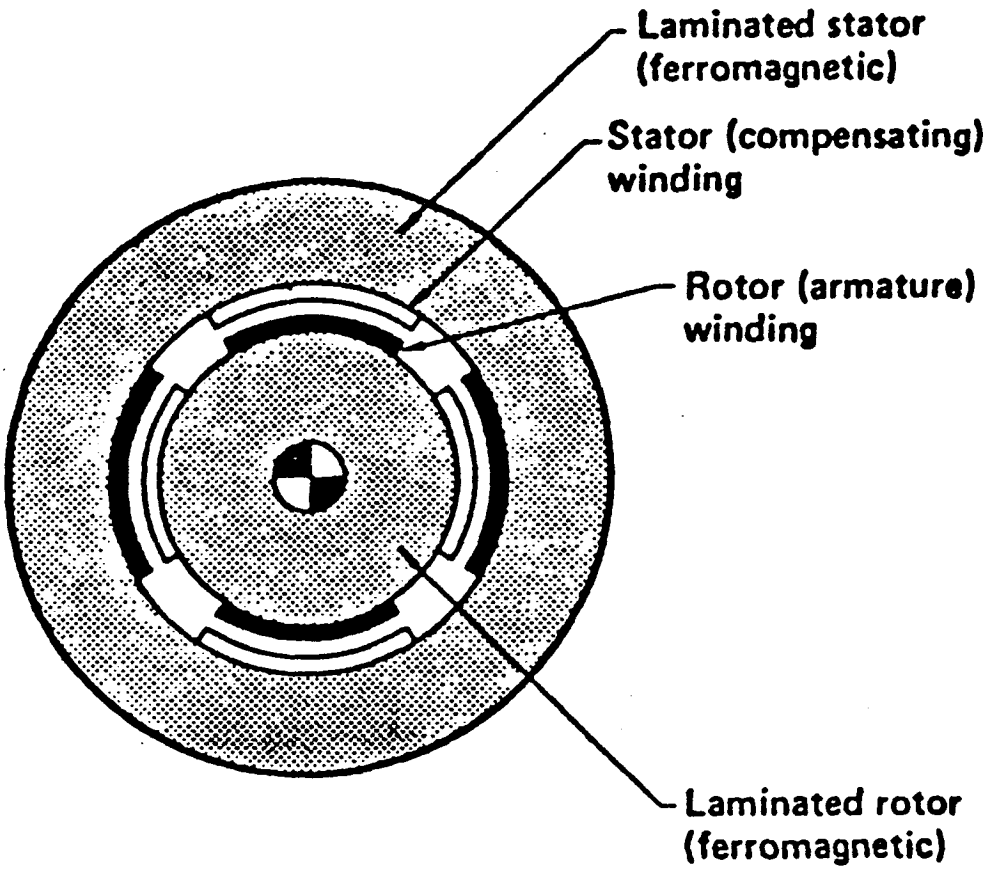

Fig. 4-21. Active rotary flux compressor (ARFC).

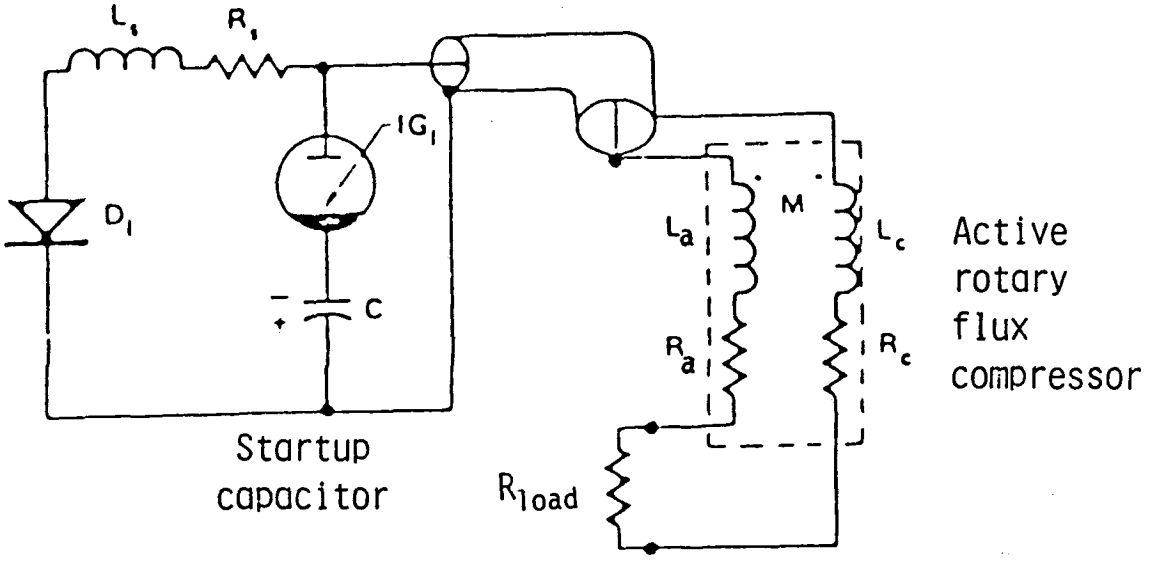

Figure 4-22. Simplified ARFC circuit diagram.

the diode array D_1 becomes forward biased and crowbars the capacitor bank and ignitron. The current and voltage then rise as the armature flux is compressed. The circuit is ready for another pulse as soon as the capacitor bank

is recharged to the desired value. For a multi-compulsator array being discharged into a load requiring synchronous pulses, the individual drive motors would also have to be synchronized before commencing another pulse.

Physics International (PI) has proposed the use of six compulsators to drive six 20-to-1 pulse transformers, the secondaries of which are connected together in series-aiding to provide the required 1.5-MV REB diode voltage. Figure 4-23 is a block diagram of the PI proposal. The compulsators would be designed to produce 12.5 kV pulses and driven independently by individual motors. Two of these systems would be used to satisfy the DEMO current drive requirements.

The problems associated with the multiple transformer/compulsator approach are mainly: (1) that the motor drives for the compulsators have to be tightly synchronized to about one-half of a mechanical degree; and (2) fault modes could produce damaging transient voltages or currents.

The solution to synchronizing the motor drives of the compulsators can be provided by precision servo controlled dc motors or variable frequency driven synchronous motors with servo controls. The choice would primarily depend on size and speed requirements of the drive. The synchronous motor has an advantage of lower cost at rating above 1000 hpand 3000 rpm.

The problem of possible damaging transients during a fault in a multi-transformer coupled compulsator system is a critical issue and requires a fault analysis. The transformer ratings would have to be increased and over-voltage and over-current protection added to the compulsator circuit to protect the compulsator system from damage. For example, simultaneous faults in a compulsator (either shut or open) with a faulted REB diode, say, as open, would cause the other five compulsators to drive the faulted compulsator as load. This would produce currents as high as five times the nominal short circuit current or five times the open circuit voltage. One protective device would be a steel-resistor at liquid nitrogren temperature, installed at each compulsator output. The temperature variation of steel's resistivity assures that the resistor would absorb the energy from an off-normal situation.

Figure 4-24 shows the circuit diagram of an alternative approach, a single-pulse transformer and single compulsator-driven REB diode. The compulsator would be designed to deliver the required energy per pulse to the REB

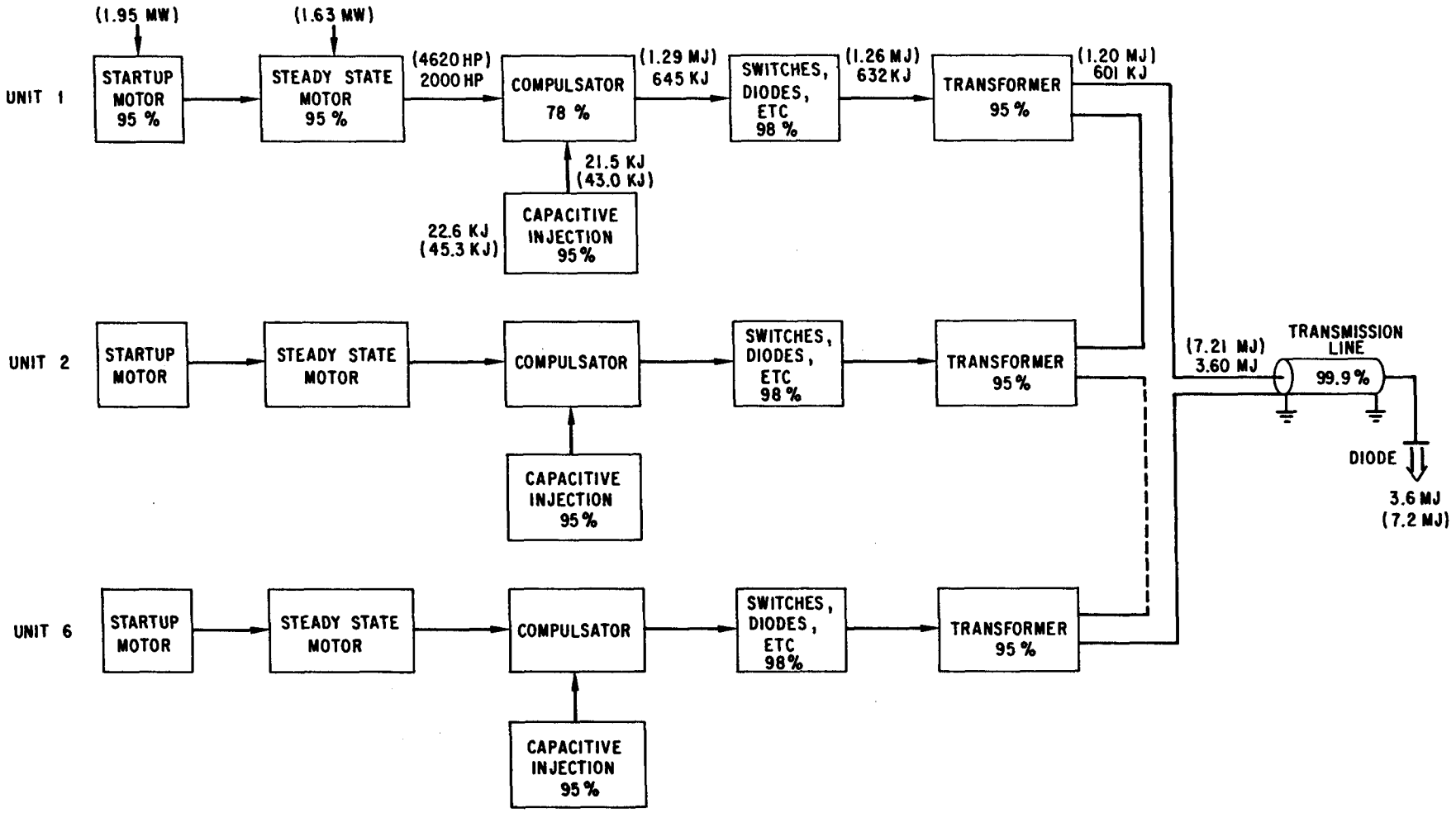

Figure 4-23. Block diagram of multiple compulsator approach showing energy and power ratings and efficiencies for current drive; values in parentheses are for auxiliary heating.

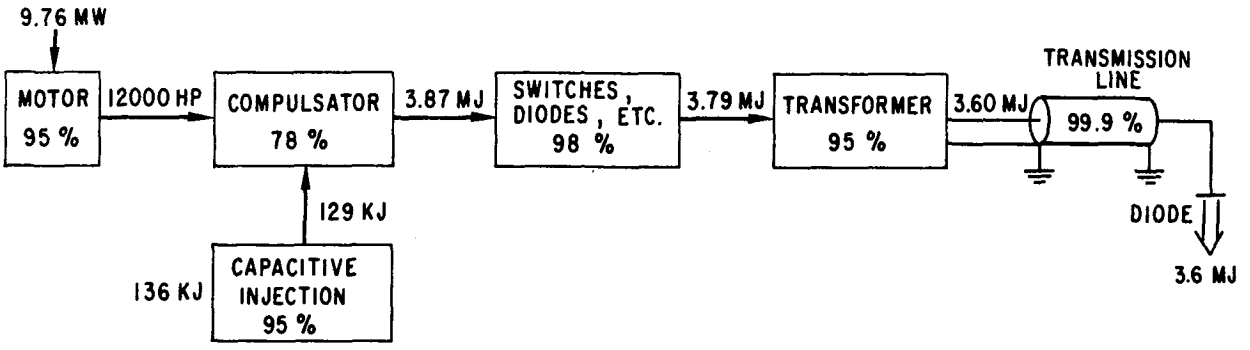

Figure 4-24. Block diagram of single compulsator approach for current drive.

diode at 12.5 kV. A 120-to-1 pulse step-up transformer would increase the voltage to 1.5 MV. The compulsator would be driven by a single motor. Two of the above would be required for current drive.

The problems associated with the single transformer/compulsator approach are similar to the multiple approach. The motor driver would have to be synchronized to about three mechanical degrees to reduce the separation times between the two diodes to a few tens of microseconds. Fault modes could produce damaging transient voltages or currents. However, a nominal safety factor of two should be adequate for this case.

The power required for startup and auxiliary heating is a factor of 4 to 20 times larger than the power required for steady-state current drive and is needed for periods of up to 30 s. This is larger than the short time overload factor of most electrical motors. Therefore, extra motor drive would need to be coupled to the compulsator during the startup and heating period. Thus, the figures show extra drive motors added to satisfy the startup requirements of each compulsator. Extra motor drives would be added to each compulsator in a system and would be disengaged after startup with a clutch disconnect.

Four systems have been studied in detail, multiple vs. single compulsators and steady state vs. auxiliary heating function.

- Multiple Compulsator System for Current Drive Only

Figure 4-23 shows the block diagram for a typical current drive unit. The system is designed to use two units, each of which delivers 3.6 MJ to the diode at 1.5 MV. The expected efficiency and rating of each unit are also specified in the diagram. The rep-rate of the system is ~2 Hz. The unit has

an overall efficiency of 68% from ac motor input power to output power at the diode. The cost of a multiple compulsator/transformer system to deliver 3.6 MJ to the diode is shown in Table 4-2. Note that the total circulating electric input power to the system when both diodes are operating is 19 MW.

Table 4-2. Cost of Multiple Compulsator System to Deliver 3.6 MJ to Each Diodes Every 0.535 s

	$
Motors - variable frequency drive + controls to 1/2 deg - with factor 2, 30-s overload rating	125/hp
Compulsator - with a factor 4, 30-s overload rating	0.19/J
Capacitor bank and controls	0.11/J
Switches, diodes, ignitrons	0.06/J
Transformer	0.08/J
Transmission line and diode (PI estimate)	1.14 M
Steady-State Current Drive Case - Multiple Compulsators	$/K
Motors (2000 hp × 125) × 6	1500
Compulsators (645 kJ × 0.19) × 6	735
Capacitor bank (22 kJ × 0.11) × 6	15
Switch, diodes, etc. (645 kJ × 0.06) × 6	232
Transformer (630 kJ × 0.08) × 6	300
Transmission line and diode	1140
Control room, computers, and interface	100
Total equipment/unit	4022
Installation cost	1000
Total/unit	5022
Total system (2 units), 13.5 MJ/s	10044

- Single Compulsator System for Current Drive Only

Figure 4-24 shows the block diagram for the typical current drive unit to deliver 3.6 MJ/pulse to the diode load. The expected efficiency and ratings of each unit are also listed in this figure. The rep-rate of the system is ~2 Hz and has an overall efficiency of 68%.

The cost of single compulsator/transformer system to deliver 3.6 MJ/pulse to diodes is shown in Table 4-3.

Table 4-3. Cost of Single Compulsator System to Deliver 3.6 MJ to Each Diode Every 0.535 s

	$
Motors - variable frequency drive + controls to 3 deg	115/hp
Compulsators - with small overload factor	0.19/J
Rest of cost - same as Table 4-2	
Steady-State Current Drive - Single Compulsator	$/K
Motor (12,000 hp × 115)	1380
Compulsator (3.87 MJ × 0.19)	735
Capacitor bank (136 kJ × 0.11)	15
Switches, etc. (3.87 MJ × 0.06)	232
Transformer (3.79 MW × 0.08)	303
Transmission line and diode	1140
Control room, computor, interfaces	60
Total equipment	3865
Installation cost	966
Total/unit	4831
Total system (2 units), 13.5 MJ/s	9663

- Multiple Compulsator for Current Drive and Auxiliary Heating

Figure 4-23 also shows the block diagram for the typical compulsator to deliver 1.3 MJ/pulse at 12.4 kV to the transformer. Six compulsators and transformer with secondaries in series are required to deliver 7.2 MJ/pulse to the diode. The expected efficiency and rating of each component are listed. The rep-rate of the system is 2.1 Hz and has an overall efficiency of 68%. Two of the above are required to deliver 30 MJ/s to the REB diodes for 30 s. The overload rating of the motors is 2 and that of the compulsator is 4 for 30 s, so this system could operate at 60 MJ/s for the start-up period, if necessary, without increases in the capital cost.

The cost of a multiple compulsator/transformer system for startup to deliver 30 MJ/s is shown in Table 4-4. The component costs are the same as for the steady-state current drive. Six additional motors, six clutch boxes, and more controls have to be added. The capacitor bank has to be increased. The switches, diodes, ignitrons, etc. only have a safety factor of two. The transformer has a built-in short-term, 30-s, safety factor of two.

Table 4-4. Cost of Multiple Compulsator System to Deliver 7.2 MJ to Each Diode Every 0.480 s

	$/K
Motors (4619 hp × 125) × 6	3464
Compulsators (1.29 MJ × 0.19) × 6	1471
Capacitor bank (45 kJ × 0.11) × 6	30
Switches, etc. (1.29 MJ × 0.06) × 6	464
Transformer (1.26 MJ × 0.08) × 6	605
Transmission line and diode	1140
Controls, etc.	130
Clutch box (2,619 hp × 5) × 6	79
Total equipment/unit	7383
Installation cost	1846
Total/unit	9229
Total system (2 units), 30-60 MW for 30 s	18458

- Single Compulsator System for Current Drive and Auxiliary Heating

The compulsator used for this case would exceed the maximum size limit for 500-μs pulse length. Such a machine would be bigger in rotor diameter and in order to limit rotor speed to 150 m/s it would require a lower rotational frequency and longer pulse length. The only way to increase the power output with pulse lengths less than 500 μs to increase of to number of units and REB diodes.

Figure 4-25 displays the ARFC output current waveform calculated for a specific ARFC design. The assumption here was a 41-inch rotor diameter. The fully laminated rotor is 1.6 m long and has eight poles. The rotor and its shaft rotate at 2685 rpm and have a mass of 15.6×10^3 kg, storing 83.6 MJ of rotational kinetic energy. The machine inductance can be designed to vary from 7.7 μH to 1.4 mH; consequently, 935 kJ can be delivered in the discharge pulse, which has a half width of 430 μs. The startup capacitor is 150μF at 18 kV and delivers 24.3 kJ to the ARFC so the energy gain is 38.5. The output voltage peaks at 18 kV. The total ARFC weight is 60,950 pounds, and it is estimated to transfer energy from the motor to the transformer with a 77.25% efficiency. This design is not optimized.

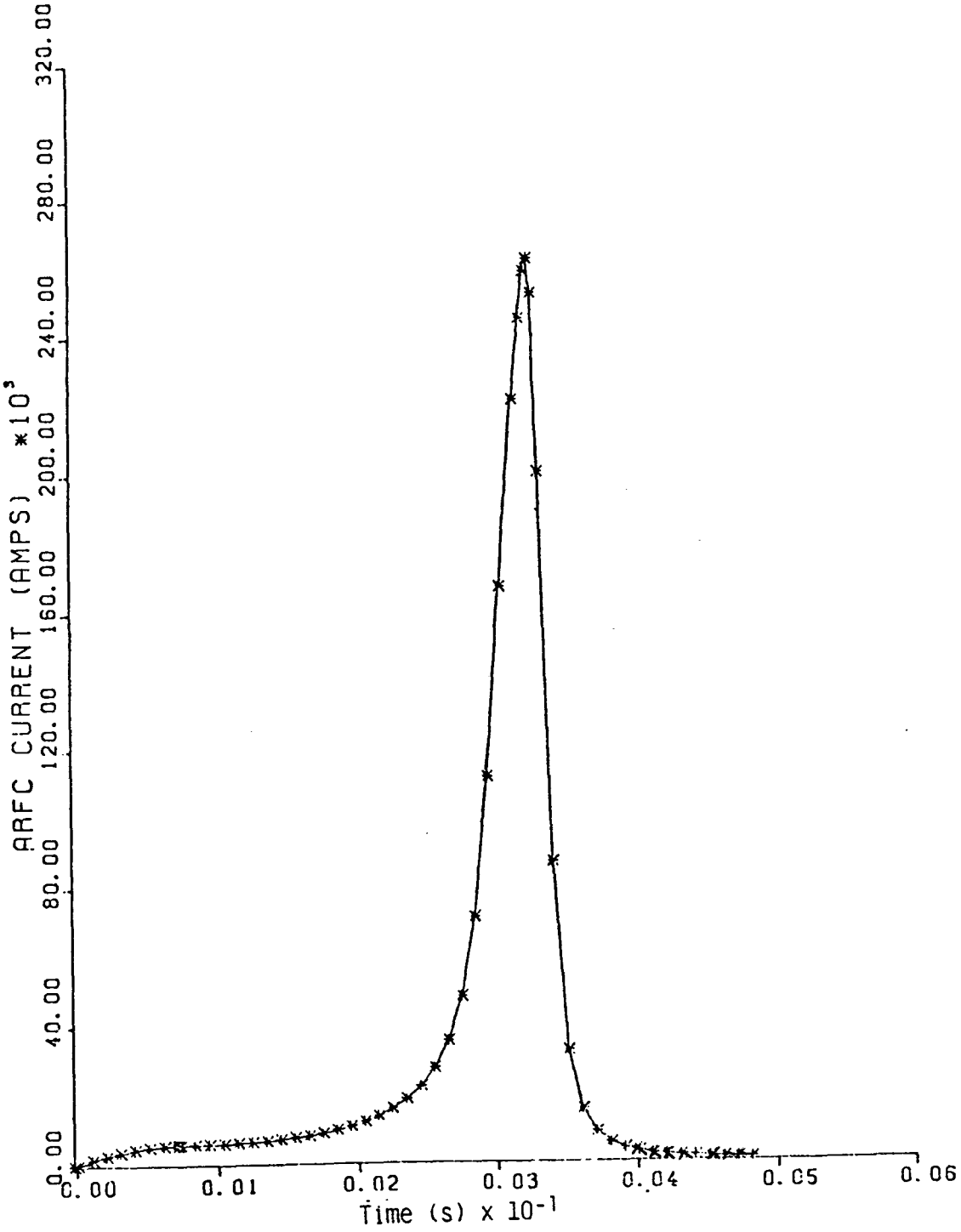

Figure 4-25. Current output pulse from ARFC into a 66 mΩ load; 935 kJ is discharged.

4.4.6.3 Pulse Compression Using Magnetic Switching

A pulse compression line using magnetic switching has been designed for the proposed DEMO relativistic electron beam current driver. Two electron beam generators are each powered by six compulsators, with each compulsator producing a 12-kV, 600-kJ pulse of 400-μs pulse width. This pulse is then compressed 64 times by the pulse compression line. The resultant 6.25-μs pulse is then stepped up in voltage by a 20:1 transformer, with the transformer outputs of the six compulsators hooked in series. The net result is a 1.533-MV, 3.6-MJ pulse of 6.25-μs pulse width.

The electron beam generator requires 10^8 pulses over the lifetime of the reactor. Compulsators have the high reliability needed to produce 10^8 pulses, but they also produce a pulse with a long pulse width (about 400 μs). The electron beam generator may require a pulse width of less than 10 μs. Therefore, an intermediate pulse compression line is of interest.

A multistage magnetic switch is shown in Fig. 4-20d, the design of which is based on Ref. 27. Several of the design equations in this reference are incorrect, however. The corrected equations are given here.

The capacitor values can be calculated from the energy equation

$$E = \frac{1}{2} C V^2 . \tag{4-23}$$

Since all capacitors store (very closely) the same energy at the same voltage, all capacitor values should be the same. In order for the magnetic switch to work properly, the saturation of inductor L_n must occur at π/ω on the charging voltage for C_n. The saturated inductance is calculated from

$$L_{n-1}^{sat} = \frac{2}{c}\left(\frac{\tau_{charge}^{C_n}}{\pi}\right)^2 , \tag{4-24}$$

where

$$\tau_{charge}^{C_n} = \frac{\text{initial pulse length}}{(\text{compression factor per stage}) \cdot (\text{stage number})} . \tag{4-25}$$

The compression factor (or gain) is therefore given by

$$\text{gain} = \left(\frac{C_n}{\tau_{\text{charge}}} \Big/ \frac{C_{n+1}}{\tau_{\text{charge}}} \right). \tag{4-26}$$

The unsaturated inductance is calculated from

$$L_n^{\text{unsat}} = \frac{\mu_n^{\text{unsat}}}{\mu^{\text{sat}}} \cdot L_n^{\text{sat}} . \tag{4-27}$$

The value of μ^{sat} will be close to μ_0. The value of μ^{unsat} is a function of pulse length. Above a critical frequency f_{cr} μ^{unsat} will vary as $\sqrt{\text{pulse length}}$. The critical frequency is found from[28]

$$f_{cr} = \frac{4\rho}{\pi \mu_i D^2} , \tag{4-28}$$

where ρ is the specific electrical resistance, μ_i the initial permeability, and D the thickness. Some conditions placed on the inductor values are

(1) $L_n^{\text{unsat}} \geq 20 \cdot L_{n-1}^{\text{sat}}$

(2) $L_n^{\text{unsat}} \geq 20 \cdot L_{n+1}^{\text{unsat}}$

(3) The saturated impedance of the final inductor must be much less than the load impedance.

The maximum practical compression factor per stage is

$$\frac{\tau_{n-1}}{\tau_n} \leq \left(\frac{\mu^{\text{unsat}}}{\mu^{\text{sat}} \cdot 20} \right)^{1/2} . \tag{4-29}$$

The volume of each inductor core (assuming toroidal geometry) is

$$\text{Volume} = (\text{gain})^2 \cdot \text{energy} \cdot \left(\frac{\mu^{\text{sat}} \cdot \pi^2}{4 \cdot (\Delta B_s)^2} \right), \tag{4-30}$$

where $\Delta B_s = B_{sat} + B_{remanent}$. For maximum energy efficiency all core volumes should be equal. The turns-area for each inductor core is calculated from

$$N_n A_n = \left(\frac{L_n^{sat} \cdot \text{volume}}{\mu^{sat}} \right)^{1/2} . \tag{4-31}$$

The inductor core losses were calculated from core loss graphs.

Results

While higher values are theoretically possible, the maximum compression per stage for this high energy line was taken to be four. Therefore, three stages are needed to compress a 400 μs pulse to less than 10 μs. The actual output pulse width is 6.25 μs. A three-stage line requires three capacitors and four inductors (the first inductor does not saturate while the next three do). Since the DEMO reactor will require 12 compression lines (for two sets of six compulsators), 36 capacitors and 48 inductors will be needed in all.

The required capacitance is:

$$C = \frac{2E}{V^2} = \frac{2(600 \text{ kJ})}{(12 \text{ kV})^2} = 8.33 \text{ mF} .$$

The capacitors will cost approximately 20¢ per joule to build, or $120,000 per capacitor. The total cost of 36 capacitors will be 4.32 million dollars. The volume of each capacitor can be calculated from the energy density

$$\frac{dW_e}{dV} = \frac{1}{2} \varepsilon E^2 . \tag{4-32}$$

For a water capacitor, $\varepsilon = 80\ \varepsilon_0$. E is calculated by $t^{1/3}$ scaling assuming that E = 20 MV/m at τ = 1 μs:

$$E = \frac{20 \times 10^6}{(\tau/10^{-6})^{1/3}} \frac{V}{m} \tag{4-33}$$

where τ is the pulse length. Table 4-5 lists the volume of each capacitor along with the required floor space (assuming a 4-m high ceiling). The total required capacitor volume is 4290 m^3 and the total required floor space is 1070 m^2.

Table 4-5. Capacitor Volumes and Floor Space

	C_1	C_2	C_3
Pulse length (μs)	400	100	25
E (MV/m)	2.71	4.31	6.84
dWe/dV (kJ/m^3)	2.61	6.58	16.6
Volume (m^3)	230	91.2	36.1
Floor space (m^2)	57.5	22.8	9.03

The compulsator output is not a square wave, and so the compression line output will also not be a square wave. By replacing C_3 with a pulse forming line of 8.33 mF capacitance, however, a pulse with a fast rise time may be achieved. Reference 27 explains this consideration in more detail.

Metglas 2605SC and Permalloy F were both studied as inductor core materials. The sheet thickness for each was assumed to be 1 mm. The core losses, core volumes, and total cost of Metglas and Permalloy F are given in Table 4-6. The core losses were calculated from core loss graphs given in Ref. 30 for Permalloy F and Ref. 29 for Metglas 2605SC. In calculating the core losses for Metaglas it was assumed that all the core losses took place at the point of saturation. The μ^{sat} for Metglas and Permalloy F is practically the same and very close to μ_0.[30] This magnetic switch design assumed $\mu^{sat} = 1.5\ \mu_0$. The cost of Metglas is based on a price of $4.50/kg by 1986.[29] The price of Permalloy F is assumed to be the same (to be competitive).

The inductance, permeability, and energy losses for each inductor is given in Table 4-7 for Metglas 2605SC and Table 4-8 for Permalloy F. Even though inductor L_0 does not saturate, it is still a metal core inductor because the losses in an air-core inductor at that pulse length (400 μs) would be large.

The variance of μ^{unsat} with frequency was found from a plot of the impedance permeability versus frequency[29] by the assumption $\mu_z \approx \mu^{unsat}$. For Permalloy F μ^{unsat} was found by assuming

$$\mu^{unsat} = (\text{constant}) \sqrt{\text{pulse length}} \qquad (4\text{-}34)$$

Table 4-6. Comparison of Metglas 2605SC and Permalloy F

	Metglas 2605SC	Permalloy F
Losses per line (J)	11,300	2830
% losses	1.9	0.5
ΔB_s (T)	3.03[a]	2.4[b]
Volume per inductor (m^3)	4.86	7.75
Total volume (m^3)	233	372
Density (g/cm^3)	7.32[a]	8.4[c]
Total mass (10^6 kg)	1.71	3.12
Total cost (1982 M$)	7.68	14.1

[a]From Ref. 29.

[b]From Ref. 30.

[c]From Ref. 28.

Table 4-7. Inductor Related Numbers for Metglas 2605SC

	L_0	L_1	L_2	L_3
Pulse length (μs)	400	100	25	6.25
Saturation time (μs)	200	50	12.5	3.13
L^{sat} (μH)	----	243×10^{-3}	15.2×10^{-3}	950×10^{-6}
μ^{unsat} (μ_0)	4000	3000	2000	1000
L^{unsat} (μH)	10.4×10^3	487	20.3	634×10^{-3}
Energy loss (J)	611	1340	2940	6440
Turns-area (m^2)	3.17	0.792	0.198	0.0495

Table 4-8. Inductor Related Numbers for Permalloy F

	L_0	L_1	L_2	L^3
Pulse length (μs)	400	100	25	6.25
Saturation time (μs)	200	50	12.5	3.13
L^{sat} (μH)	----	243×10^{-3}	15.2×10^{-3}	950×10^{-6}
μ^{unsat} (μ_0)	4400	2200	1100	550
L^{unsat} (μH)	11.4×10^3	356	11.1	348×10^{-3}
Energy loss (J)	504	543	620	1160
Turns-area (m^2)	4.00	1.00	0.250	0.0625

above some critical frequency. The critical frequency is[28]

$$f_{cr} = \frac{4(35 \times 10^{-8})}{\pi(3000)\mu_0(10^{-3})^2} = 118 \text{ Hz}$$

at which $\mu^{unsat} = 20{,}000\ \mu$.[30] This makes the evaluation of the constant in Eq. (4-34) possible:

$$\mu^{unsat} = 220{,}000 \sqrt{\text{pulse length}} . \qquad (4\text{-}35)$$

We can summarize our concusions for magnetic switches as follows. The technology needed for magnetic switching has been around for 30 years and so is well known and practicable. The designs for both Metglas 2605SC and Permalloy F meet the conditions for multistage operation. The design parameters are conservative, and therefore a magnetic switch should certainly work.

The total cost of a Metglas compression line is 12 million dollars, while the total cost of a Permalloy F compression line is 18.4 million dollars. Therefore, Metglas is recommended over Permalloy F for its reduced costs since the two metals compare almost equally in other regards.

Other power supply schemes for the DEMO reactor, however, promise a lower cost and a lower required volume. Therefore, this compulsator-compression line approach may not be the best possible approach.

4.4.6.4 Pulse Compression Using a Storage Capacitor

A pulse compressor using a storage capacitor and a high voltage switch has been designed for the DEMO relativistic electron beam current driver. The DEMO reactor has two such electron beam generators and so would require two power systems. A compulsator delivers a 300-μs, 3.6-MJ pulse at 12 kV. The pulse voltage is stepped up in a transformer and stored in a water capacitor. The capacitor voltage is then discharged through a spark gap. A coaxial transmission line brings the pulse to the plasma diode of the electron beam generator. The design goal is to deliver 90% of the 3.6 MJ to the plasma diode in 3 μs. See Fig. 4-20c.

The electron beam generator requires 10^8 pulses over the liftime of the reactor. The use of a pulse compression line (by magnetic switching) is questionable because of the large volume required and high costs. A high voltage switch can survive 10^6 pulses and is inexpensive and easy to replace. Therefore, the design of Fig. 4-20c is being studied as an alternative to magnetic switching.

The value of the charging capacitor C can be found from the energy equation

$$W_e = \frac{1}{2} C V_0^2 , \tag{4-36}$$

where W_e and V_0 are the energy and voltage required by the electron beam generator. The volume of the capacitor can be calculated from the energy density equation:

$$\frac{dW_e}{dv} = \frac{1}{2} \varepsilon E^2 , \tag{4-37}$$

where E, the electric field, can be calculated by extrapolating from $\tau^{1/3}$ scaling knowing that E = 20 MV/m at τ = 1 μs:

$$E = \frac{20}{(\tau/1\ \mu s)^{1/3}} \frac{MV}{m} . \tag{4-38}$$

The spark gap impedance can be modeled as an inductance of value:

$$L_{sp} = 2\ell_{sp}\, \ell n(b/a)\ nH , \tag{4-39}$$

where ℓ_{sp} is measured in cm, a is the discharge diameter size, and b is the electrode diameter.

The transmission line needs to be ≈30 m in length. The time that a pulse takes to travel this distance is ≈100 ns. Since the pulse length will be 3 μs, the transmission line can be treated as a lumped impedance. The resistance of the transmission line is

$$R_T = \ell_T/\sigma S \tag{4-40}$$

and is expected to be small. The inductance of a coaxial transmission line is

$$L_T = \ell_T \frac{\mu_0}{2\pi} \ell n \frac{r_0}{r_i}, \tag{4-41}$$

where ℓ_T is the length. The capacitance is

$$C_T = \frac{2\pi\varepsilon}{\ell n(r_0/r_i)}. \tag{4-42}$$

If C_T is small compared to C (the storage capacitance), then C_T can be neglected as an approximation.

The plasma diode will simply be modeled as a resistance R. The discharge part of the power system can then be represented by a simple RLC circuit as shown in Fig. 4-26. The inductor L is the sum of the spark gap and transmission line inductance. For now the transmission line is assumed to be lossless.

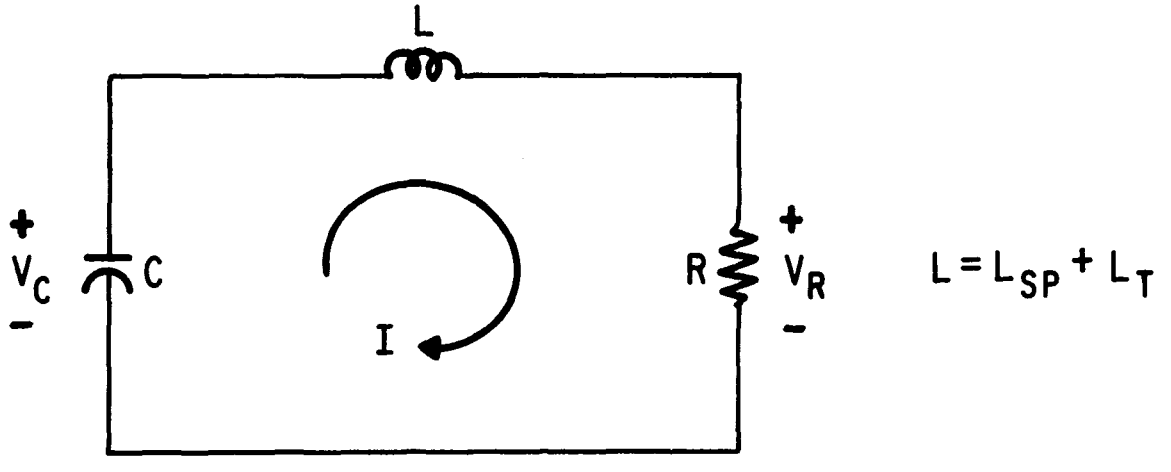

Figure 4-26. Power system approximation.

The solutions for this RLC circuit are:

Under damped case: $(R/L^2) - (4/LC) < 0$

$$I = \frac{V_0}{L}\left[\frac{e^{-(R/2L)t}\sin\sqrt{(1/LC) - (R/2L)^2}\,t}{\sqrt{(1/LC) - (R/2L)^2}}\right] \tag{4-43}$$

$$V_R = \frac{V_0 R}{L}\left[\frac{e^{-(R/2L)t}\sin\sqrt{(1/LC) - (R/2L)^2}\,t}{\sqrt{(1/LC) - (R/2L)^2}}\right] \tag{4-44}$$

$$V_C = \frac{V_0}{\sqrt{1 - (R^2C/4L)}}\, e^{-(R/2L)t}\sin\left[\sqrt{\frac{1}{LC} - \left(\frac{R}{2C}\right)^2}\,t + \mathrm{Tan}^{-1}\sqrt{\frac{4L}{R^2C} - 1}\right] \tag{4-45}$$

Critically damped case: $(R/L)^2 - (4/LC) = 0$

$$I = \frac{V_0}{L}\, t\, e^{-(R/2L)t} \tag{4-46}$$

$$V_R = \frac{V_0 R}{L}\, t\, e^{-(R/2L)t} \tag{4-47}$$

$$V_C = V_0\left(1 + \frac{R}{2L}\, t\right)e^{-(R/2L)t}\ . \tag{4-48}$$

Over damped case: $(R/L)^2 - (4/LC) > 0$

$$I = \frac{V_0}{2L\sqrt{(R/2L)^2 - (1/LC)}}\left\{e^{\left[-(R/2L)+\sqrt{(R/2L)^2-(1/LC)}\right]t} - e^{\left[-(R/2L)-\sqrt{(R/2L)^2-(1/LC)}\right]t}\right\} \tag{4-49}$$

$$V_R = \frac{V_0 R}{2L\sqrt{(R/2L)^2 - (1/LC)}} \left\{ e^{\left[-(R/2L)+\sqrt{(R/2L)^2-(1/LC)}\right]t} - e^{\left[-(R/2L)\sqrt{(R/2L)^2-(1/LC)}\right]t} \right\} \quad (4\text{-}50)$$

$$V_C = \left\{ V_0 \frac{(R/2L) + \sqrt{(R/2L)^2 - (1/LC)}}{2\sqrt{(R/2L)^2 - (1/LC)}} e^{\left[-(R/2L)+\sqrt{(R/2L)^2-(1/LC)}\right]t} - \frac{(R/2L) - \sqrt{(R/2L)^2 - (1/LC)}}{2\sqrt{(R/2L)^2 - (1/LC)}} e^{\left[-(R/2L)-\sqrt{(R/2L)^2-(1/LC)}\right]t} \right\}. \quad (4\text{-}51)$$

The energy received by the plasma diode is:

Under damped case:

$$\Delta E = \frac{V_0^2 R}{\left[(4/2L) - (R^2/LC)\right]} \left\{ - \left[\frac{R}{L} \sin\sqrt{\frac{R}{2L}^2 - \frac{1}{LC}}\, t + 2\sqrt{\left(\frac{R}{2L}\right)^2 - \frac{1}{LC}} \cos\sqrt{\left(\frac{R}{2L}\right)^2 - \frac{1}{LC}}\, t \right] e^{-(R/L)t} \sin\sqrt{\left(\frac{R}{2L}\right)^2 - \frac{1}{LC}}\, t + \left(\frac{R}{2L} - \frac{2}{RC}\right) \left[e^{-(R/L)t} - 1 \right] \right. \quad . \quad (4\text{-}52)$$

Critically damped case:

$$\Delta E = V_0^2 \left[\frac{C}{2} - \left(\frac{t^2}{L} + \frac{2}{R} t + \frac{C}{2} \right) e^{-(R/L)t} \right] . \quad (4\text{-}53)$$

The gap needed between the inner and outer conductors of the transmission line is

$$r_0 - r_i = \frac{V_0}{E_b}, \tag{4-54}$$

where E_b is the break-down voltage. The final 5 m of the transmission line is vacuum, and so the gap need only be large enough to insure magnetic insulation. Therefore,

$$r_0 - r_i > \frac{1}{2}\rho_L = \frac{\pi V_\perp \gamma m r_i}{e\,\mu_0 I} \tag{4-55}$$

where $\gamma = 4$ and $V_\perp = 3 \times 10^8$ m/s.

The energy loss in the transmission line, derived in the DEMO Interim Report,[12] is

$$E_{DIS} = \left(\frac{I^2 \ell_T}{\pi^{1.5}}\sqrt{\frac{\mu\tau}{\sigma}}\right)\cdot\left(\frac{1}{r_i} + \frac{1}{r_0}\right), \tag{4-56}$$

where τ is the pulse length.

Results

The plasma diode is to receive a 1.533-MV, 3.6-MJ pulse. The needed storage capacitance is therefore

$$C \geq \frac{2(3.6\ \text{MJ})}{(1.533\ \text{MV})^2} = 3.1\ \mu\text{F}\ .$$

Since the compulsator pulse length is 300 μs, the capacitor needs to hold the charge for that length of time. The breakdown field is therefore

$$E = \frac{20\ \text{MV}}{(300)^{1/3}} = 2.99\ \text{MV/m}\ .$$

The energy density is ($\varepsilon = 80\ \varepsilon_0$ for water)

$$\frac{dW_e}{dV} = \frac{80\ \varepsilon_0}{2} (2.99\ \text{MV/m})^2 = 3.16\ \text{kJ/m}^3 .$$

The capacitor volume is then

$$\text{Volume} = \frac{3.6\ \text{MJ}}{316\ \text{kJ/m}^3} = 1140\ \text{m}^3 .$$

Since there will be two power systems in all, the total capacitor volume is 2280 m^3. The floor space for each (assuming a 4-m ceiling) is 285 m^2, or 570 m^2 in all. The cost of each capacitor (at 20¢/joule) is \$720,000, or 1.44 M\$ for both.

In order to achieve a 3 μs pulse, values for R, L, and C in the simple model of Fig. 2-2 needed to be calculated. Using the critically damped case as a baseline, the time constant

$$\tau = \frac{2L}{R} \qquad (4\text{-}57)$$

was changed to

$$\tau = \frac{RC}{2} \qquad (4\text{-}58)$$

by using $R^2 = 4L/C$. To get a small time constant the values of R and C need to be made small. Fixing C at its smallest possible value (3.1 μF), the diode energy equation (4-53) becomes a function only of R (using $L = R^2C/4$). Then in order to have 90% of the 3.6 MJ in storage delivered to the diode in 3 μs, R must be 0.727 Ω. The value of L is then 410 nH. In order to increase L to its maximum value and yet meet the 90% criteria, the under-damped solution was used. L reaches a maximum of 538 nH at R = 0.5 Ω. The circuit solutions are then (with t in seconds)

$$I = 4.60 \times 10^6\ e^{-4.65\times10^3 t} \left(\sin 619 \times 10^3\ t\right) \quad \text{A}$$

$$V_R = 2.30\times 10^6\ e^{-465\times10^3 t} \left(\sin 619 \times 10^3\ t\right) \quad \text{V}$$

$$V_C = 1.92 \times 10^6 \, e^{-465\times10^3 t} \sin(619 \times 10^3 \, t + 0.927) \quad \text{V}$$

$$\Delta E = 4.41\{[-929 \times 10^3 \sin(619 \times 10^3 \, t) - 1.24 \times 10^6 \cos 619 \times 10^3 \, t]e^{-929\times10^3 t} \sin(619 \times 10^3 \, t) - 826 \times 10^3 \, (e^{-929\times10^3 t} - t)\} \quad \text{J}$$

Figures 4-27 through 4-30 plot I, V_R, V_C, and ΔE as functions of time. The current I is zero at

$$t = \frac{\pi}{\sqrt{(1/LC) - (R/2L)^2}} = 5.07 \ \mu s \qquad (4\text{-}59)$$

by which time 99.1% of the storage capacitor's initial energy has been delivered to the plasma diode. The average current over this time is 1.03 MA. (The diode voltage would be about twice as large if a Blumlein configuration were used.)

The spark gap inductance can be calculated by taking a nominal value of 8 for ℓn b/a, and having ℓ_{sp} = 0.5 cm for 1.533 MV. Therefore, L_{sp} = 8 nH.

The transmission line inductance is then 538 nH - 8 nH or 530 nH. For a water transmission line, the break-down voltage is 20 MV/m. The gap between the inner and outer conductors is therefore at least

$$r_0 - r_i = \frac{1.533 \text{ MV}}{20 \text{ MV/m}} = 7.5 \text{ cm} .$$

If r_i = 0.7 m, then r_0 = 0.775 m. For the 5-m long vacuum transmission line, the gap distance is

$$r_0 - r_i > \frac{\pi(3 \times 10^8)(4)(9.1 \times 10^{-31})(0.7)}{(1.6 \times 10^{-19})(4\pi \times 10^{-7})(1.03 \times 10^6)} = 1.16 \text{ cm}$$

assuming that r_i is constant the entire length of the transmission line. If r_0 is 0.715 m for the vacuum part of the line, then the inductance of the vacuum transmission line is

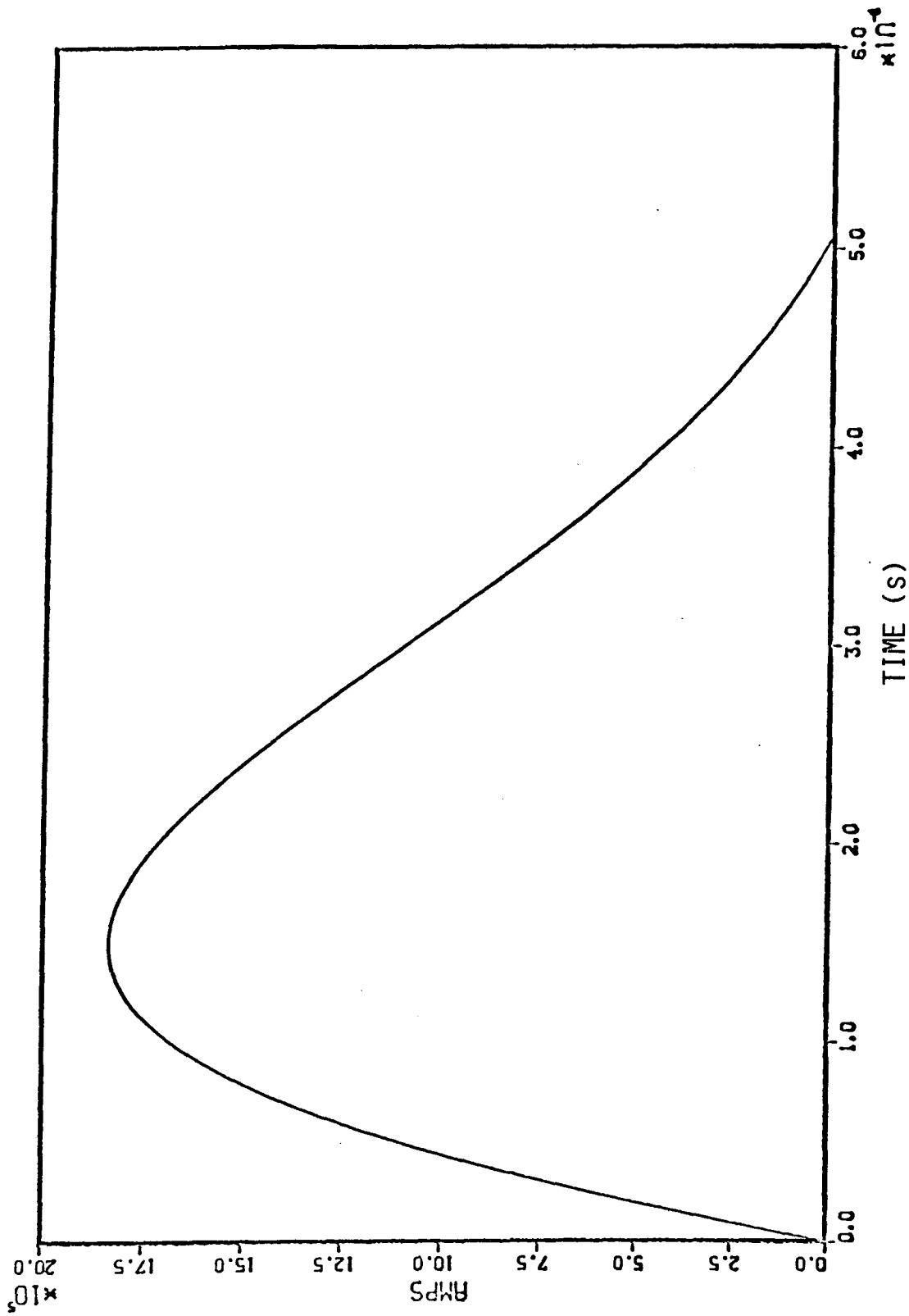

Figure 4-27. Diode current.

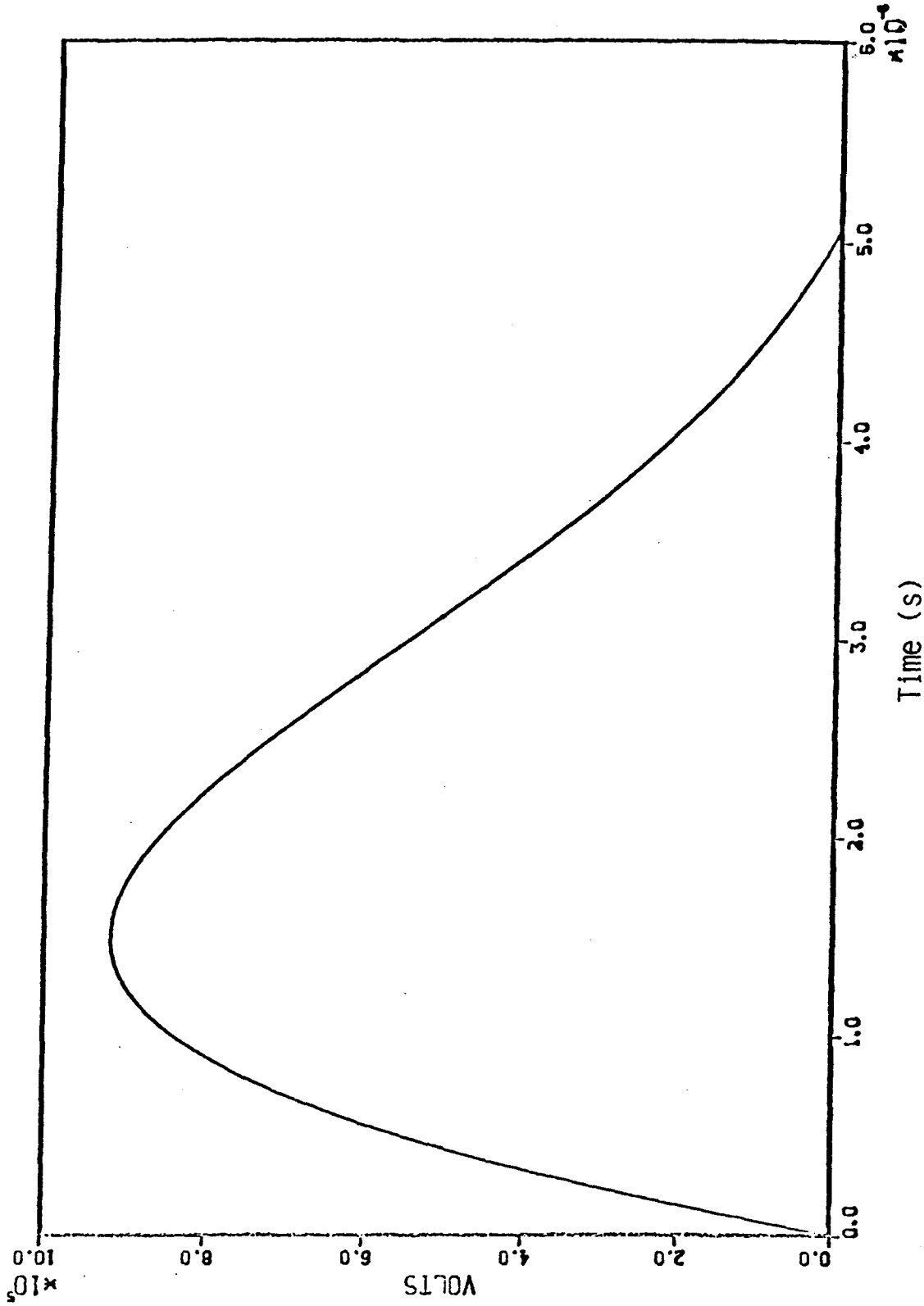

Figure 4-28. Diode voltage.

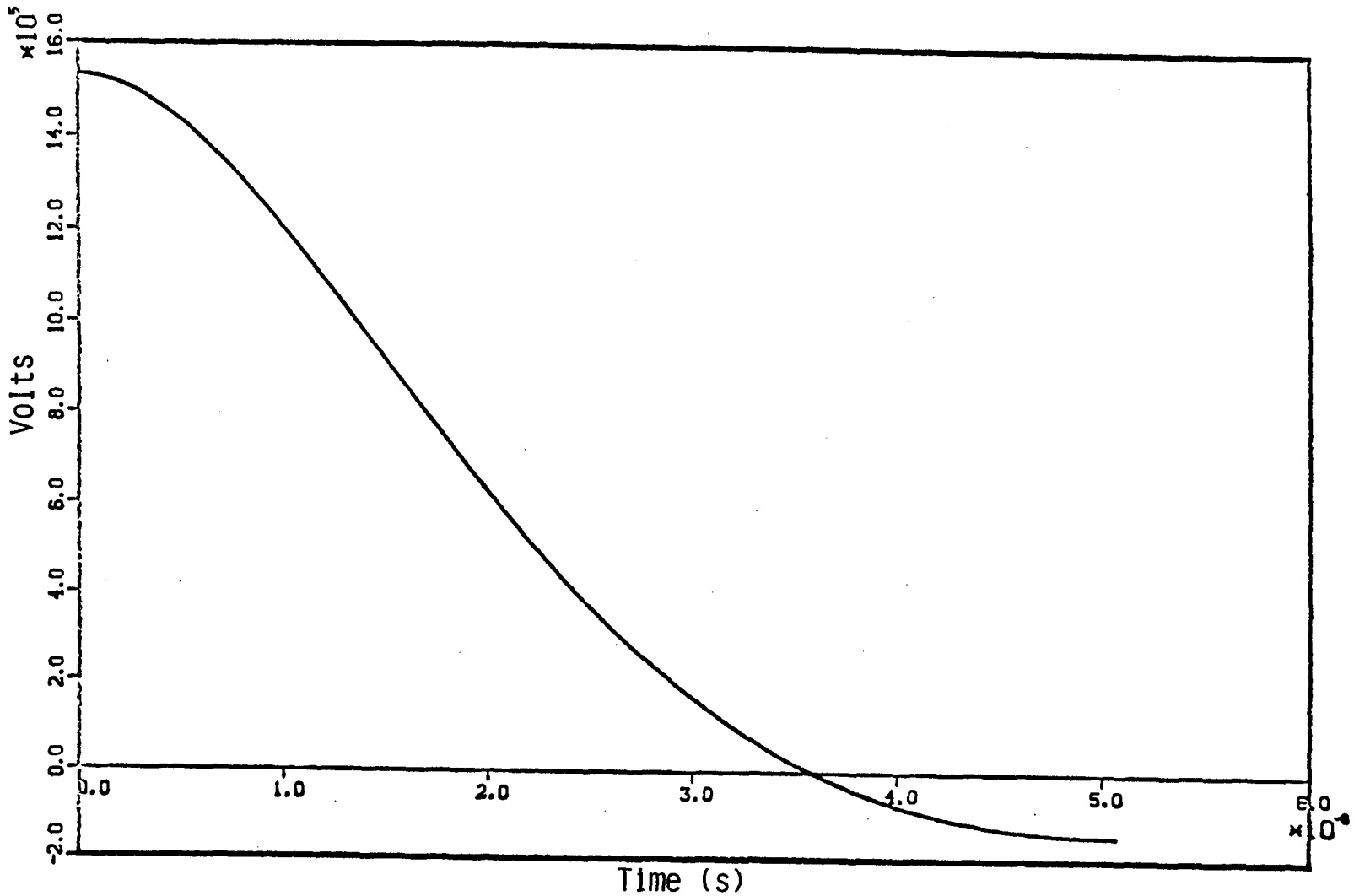

Figure 4-29. Capacitor voltage.

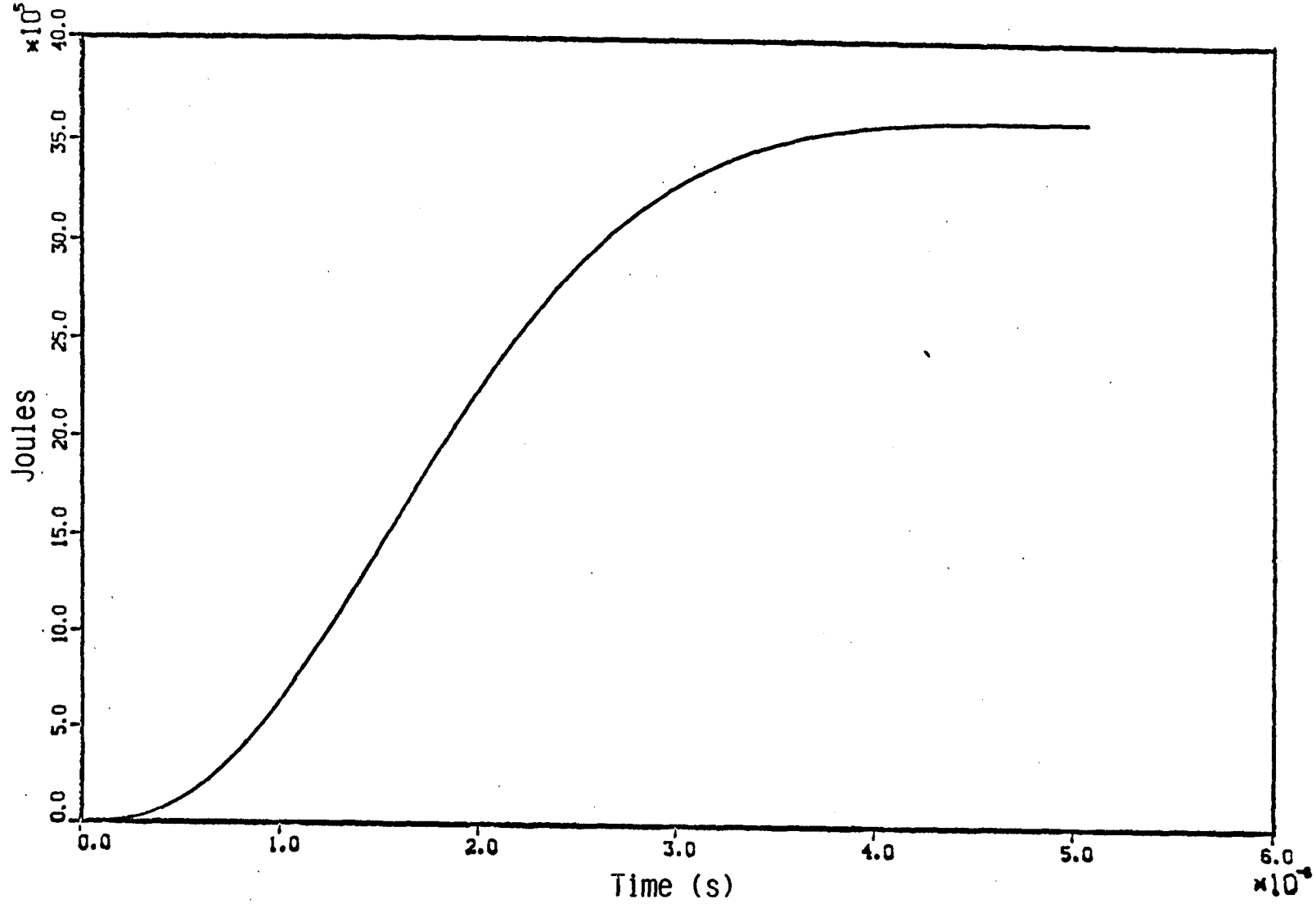

Figure 4-30. Diode energy.

$$L_{TV} = (5)\frac{\mu_0}{2\pi} \ell n \frac{0.715}{0.7} = 21.2 \text{ nH}$$

and the capacitance is

$$C_{TV} = \frac{2\pi\varepsilon_0}{\ell n(0.715/0.7)} = 2.62 \text{ nF} .$$

The inductance of the water transmission line is therefore 530 nH - 21.2 nH = 509 nH. The length of the water transmission line must then be

$$\ell_{TW} = \frac{509 \text{ nH}}{\{2\pi/[u_0 \ell n(0.775/0.7)]\}} = 25 \text{ m}$$

The capacitance is

$$C_{TW} = (25) \frac{2\pi(80 \varepsilon_0)}{\ell n(0.775/0.7)} 1.09 \mu\text{F} .$$

The resistance of the inner conductor of the transmission line is

$$R_T = \frac{30}{(1.4 \times 10^6)(\pi)(0.7)^2} = 13.9 \mu\Omega$$

for stainless steel. This is small compared to the plasma diode impedance and can be neglected.

Figure 4-31 shows a model of the power system which includes the transmission line capacitance. The plasma diode current is

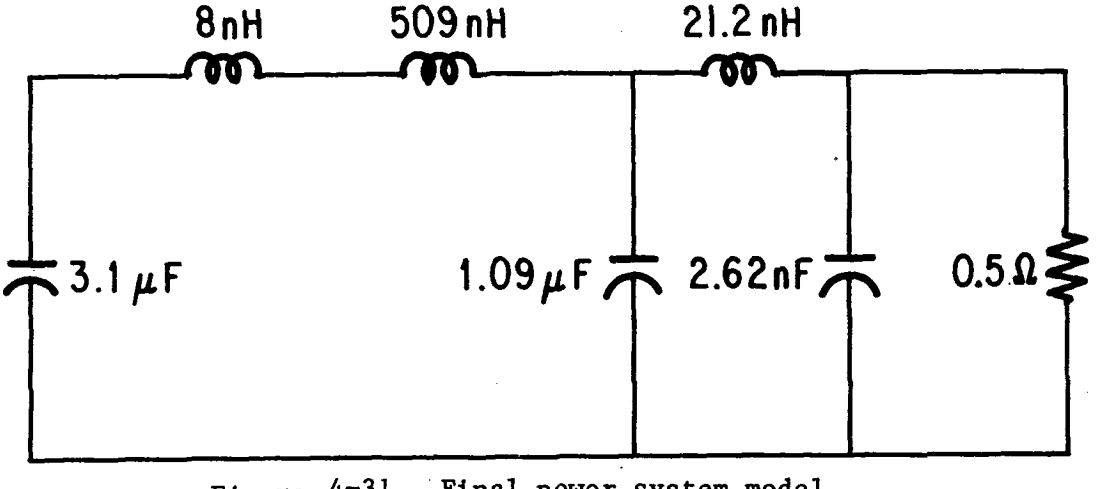

Figure 4-31. Final power system model.

$$I_p = -13.5 \times 10^3 \, e^{-22.3\times10^6 t} + 4.9 \times 10^6 \, e^{-774\times10^3 t}$$
$$+ 4.91 \times 10^6 \, e^{-613\times10^3 t} \sin(1.11 \times 10^6 \, t - 1.47) \text{ amps} .$$

Figure 4-32 shows a plot of the plasma diode current. In 3 μs, the energy delivered to the diode is 3.4 MJ, or 93.2%, of the initial stored energy. The diode current is zero after 4.6 μs, by which time all of the initial storage energy has been delivered to the diode. The average diode current over this period is 1.06 MA.

The energy dissipated in the transmission line (both water and vacuum) is 67 kJ. This amounts to 1.8% of the transferred energy.

Conclusions Regarding Water Capacitor Energy Storage

If spark gap failure is not a problem, then this system should reliably deliver a 3-μs pulse to the electron beam generator. The storage capacitor should not have large losses and does not take up a great amount of space. It can be constructed around the transmission line terminal in a circle of 10-m radius. The transmission line should prove long enough and reasonably lossless. The effect of the actual plasma diode impedance upon this design remains to be determined.

This design appears superior to the pulse compression line (using magnetic switching). Using one storage capacitor per line instead of three reduces the costs by a factor of 3. Also, expensive inductor core materials are not needed by this high voltage switch design. In all, the required floor space and cost of a high voltage switch power supply should be less than a comparable magnetic switch power supply.

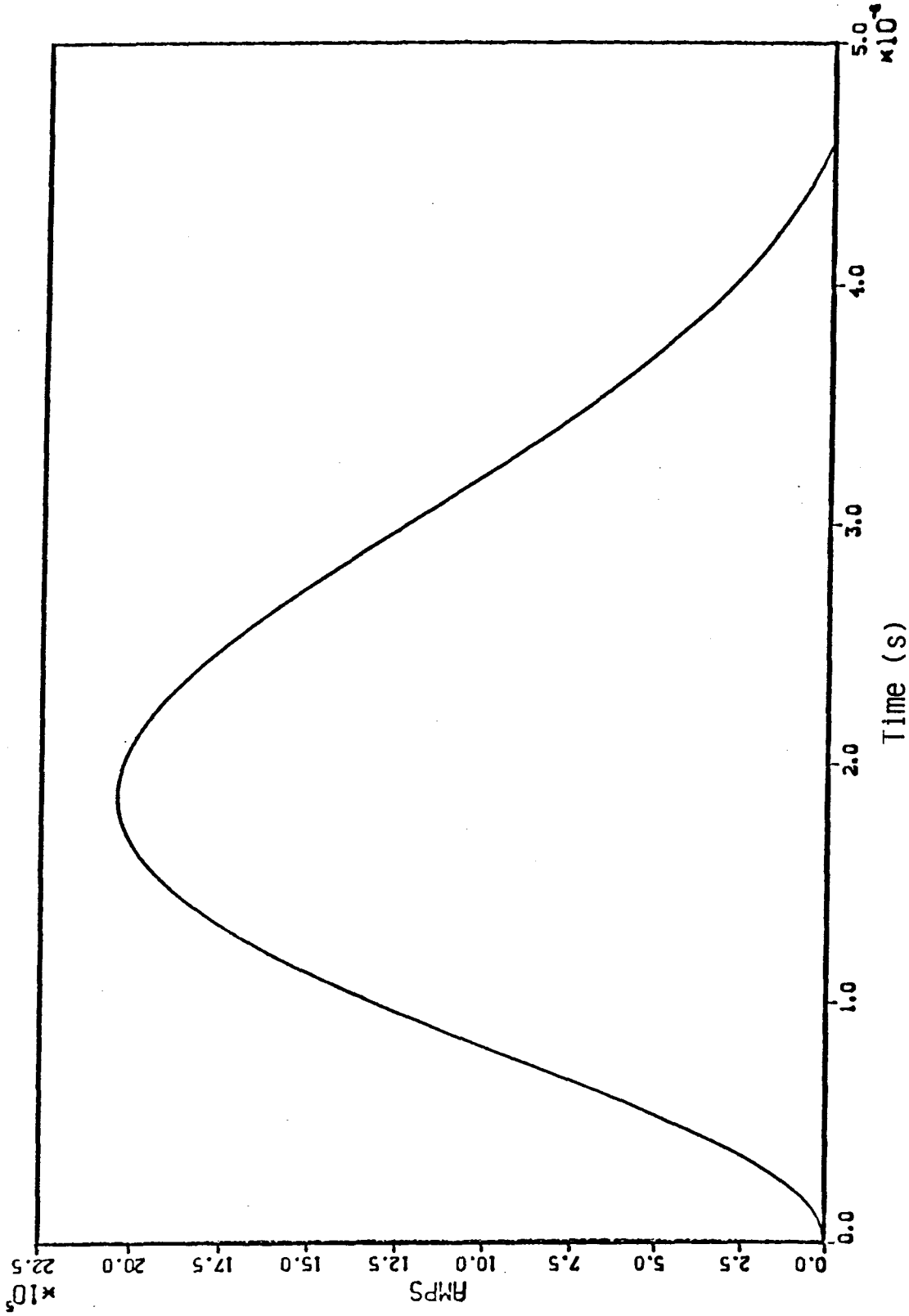

Figure 4-32. Diode current.

REFERENCES FOR CHAPTER 4

1. S. Yoshikawa, Phys. Rev. Lett. 26, 295 (1971).

2. K. Ikuta, Japan J. Appl. Phys. 11, 1684 (1972).

3. J. Benford, B. Ecker, and V. Bailey, Phys. Rev. Lett. 33, 574 (1974).

4. P. Gilad, B. R. Kusse, and T. R. Lockner, Phys. Rev. Lett. 33, 1275 (1974).

5. D. W. Swain, P. A. Miller, and M. M. Widner, Sandia Laboratory Rep. SAND-75-0214 (1975).

6. A. Mohri, et al., Phys. Rev. Lett. 34, 574 (1975).

7. M. Masuzaki, et al., Japan J. Appl. Phys. 14, 1413 (1975).

8. A. Mohri, et al., in Plasma Physics and Controlled Nuclear Fusion Research, Vol. III, p. 395 (IAEA, Vienna, 1977).

9. A. Mohri, et al., in Plasma Physics and Controlled Nuclear Fusion Research, Vol. III, p. 311 (IAEA, Vienna, 1979).

10. N. J. Fisch, Princeton Plasma Physics Laboratory Rep. PPPL-1772 (1981); N. J. Fisch, in Proc. 4th Top. Conf. on Radiofrequency Plasma Heating, Austin, TX (1981), Paper B-1.

11. D. A. Ehst and V. Bailey, "Theory of Steady State Toroidal Current Maintenance with a Pulsed Relativistic Electron Beam," submitted for publication.

12. "STARFIRE/DEMO, A Demonstration Tokamak Power Plant Study, Interim Report," Argonne National Laboratory Rep. ANL/FPP/TM-154 (1982).

13. A. Mohri, et al., in Plasma Physics and Controlled Nuclear Fusion Research, Vol. I, p. 511 (IAEA, Vienna, 1981).

14. D. A. Hammer and K. Papadopoulos, Nucl. Fusion 15, 977 (1975).

15. W. L. Bird, et al., Proc. 3rd IEEE Intern. Pulsed Power Conf., Albuquerque (1981).

16. K. Narihara, et al., Proc. 3rd Intern. Top. Conf. on High Power Electron and Ion Beam Research and Technology, Novosibirsk (1979), Vol. I, p. 70.

17. G. A. Proulx and B. R. Kusse, Phys. Rev. Lett. 48, 749 (1982).

18. V. Bailey, et al., Physics International Co. Rep. PIFR-1466-1 (1982).

19. J. D. Jackson, Classical Electrodynamics (Wiley & Sons, New York, 1962), p. 408.

20. C. A. Flanagan, et al., Oak Ridge National Laboratory Rep. ORNL/TM-7948/V1 (1981).

21. T. G. Northrop, The Adiabatic Motion of Charged Particles (Interscience Publishers, 1963).

22. D. A. Spong, Ph.D Dissertation, University of Michigan (1975); also, Oak Ridge National Laboratory Rep. ORNL/TM-5147 (1976).

23. J. Benford, B. Ecker, and V. Bailey, Phys. Rev. Lett. 33, 574 (1974).

24. J. J. Ramirez, Sandia Laboratory Rep. SAND-81-1459 (1982), p. 124 ff.

25. V. Bailey, et al., Proc. 4th Intern. Top. Conf. on High Power Electron and Ion Beam Research and Technology, Palaiseau (1981).

26. G. Rohwein, Sandia Laboratory Rep. SAND-81-1459 (1982), p. 118ff.

27. D. L. Birx, E. J. Laver, L. L. Reginato, D. Rogers, Jr., M. W. Smith, and T. Zimmerman, "Experiments in Magnetic Switching," Proc. 3rd IEEE Intern. Pulsed Power Conf., (1981), p. 162-268.

28. I. C. Heck, Magnetic Materials and Their Applications (Crane, Russak & Company, Inc., New York, 1974).

29. Allied Chemical Company information on Metglas.

30. D. L. Birx, "Basic Principles Governing the Design of Magnetic Switches," UCID 18831 (Nov. 18, 1980).

CHAPTER 5

FIRST WALL, IMPURITY CONTROL, AND EXHAUST

Chapter 5

Table of Contents

Chapter 5

List of Figures

Chapter 5

List of Tables

5.0 FIRST WALL, IMPURITY CONTROL, AND EXHAUST

5.1 Introduction and Summary

A comprehensive effort has been devoted to the study of impurity control for DEMO. The work has focused on trade-off studies in the areas of systems selection, system location in the reactor, materials selection, and plasma edge considerations. Following the trade-off studies, a reference design was selected, and the lifetime of the impurity control components was calculated. The lifetime tends to be short because of rapid erosion and the relatively small thickness of the plasma side structure that can be allowed under high heat flux conditions. The key erosion mechanisms of physical and chemical sputtering along with vaporization and melting during disruptions were analyzed in detail. Redeposition of sputtered material was examined and net erosion rates were estimated. Maximum allowable thicknesses were determined using the results of thermal-hydraulic, stress/fatigue, and radiation effects analyses. The study was performed in conjunction with the impurity control studies for FED/INTOR,[1] and because of the similarity in reactor conditions, many of the results are applicable to both studies.* A summary of the work along with the major conclusions of the study are reported below. The rest of the chapter reports the details of work which has been performed since the DEMO Interim Report.

5.1.1 System Selection

The primary purposes of the impurity control system are to exhaust a small amount of helium ($\lesssim$ 5%) from the plasma scrape off region, to remove heat, and to provide for an acceptably small level of sputtered impurities in the plasma. Most impurity control systems can be divided into two groups -

---

* The work of several individuals involved in the FED/INTOR study is summarized in this chapter, and their contributions are gratefully acknowledged. They are: M. Baskes (SNL), B. Cramer (FEDC), J. Davis (MDAC), B. DeWald (GIT), J. Draley (ANL), R. Domagala (ANL), R. Gold (W), D. Gruen (ANL), J. Haines (FEDC), J. Jones (EG&G), J. Klinger (ANL), B. Loomis (ANL), D. Mattox (SNL), B. Merrill (EG&G), G. Miley (U of IL), A. Mullendore (SANL), J. Roberto (ORNL), F. W. Wiffen (ORNL), K. Wilson (SNL), and W. Wolfer (U of W).

divertors and limiters. A divertor system employs modifications to the magnetic field such that ionized particles escaping from the plasma are swept out of the plasma chamber and into the divertor where they are neutralized at the divertor collector plates. A fraction of the neutralized particles are then pumped into the vacuum system. The limiter projects directly from the first wall and intercepts ionized particles escaping from the plasma. These particles strike the limiter surface and are neutralized. The pumped limiter has holes or slots where a small fraction (5-10%) of the incident particles are captured and neutralized. Most of the captured particles are then pumped into the vacuum system.

The present study has considered both systems for impurity control. For the purposes of comparison, a single-null, poloidal divertor, similar to that used in INTOR,[2] has been selected as the baseline divertor system, and a pumped limiter similar to that used in STARFIRE,[3] has been selected as the baseline limiter system. The two designs are shown in Figs. 5-1 and 5-2.

The selection of a reference system is based upon impurity removal efficiency, overall mechanical and magnetic configuration, and required maintenance. Both the divertor and limiter concepts can provide acceptable helium exhaust, and both concepts appear capable of handling the heat loads. The effect of sputtering and radiation damage is comparable for divertors and limiters leading to roughly equivalent lifetimes. However, the potential for preventing sputtered impurities from entering the plasma is certainly better for the divertor, which is further removed from the plasma. There is also some experimental evidence that poloidal divertors function to provide cleaner discharges. On the other hand, poloidal divertors require additional magnets and their large power supplies to provide the necessary modifications to the magnetic field. The poloidal divertor also occupies a larger volume in the reactor. Thus, there are additional costs and engineering complexities associated with the use of poloidal divertors. Overall, there are considerable uncertainties in the performance of both concepts, but because of the potential for a reduced reactor size and greater engineering simplicity, the pumped limiter was selected as the reference impurity control system.

The limiter location has an impact on the overall reactor design and configuration. Three locations, the outer midplane, the upper and lower 45° blanket segments, and the bottom of the plasma chamber, were evaluated. The

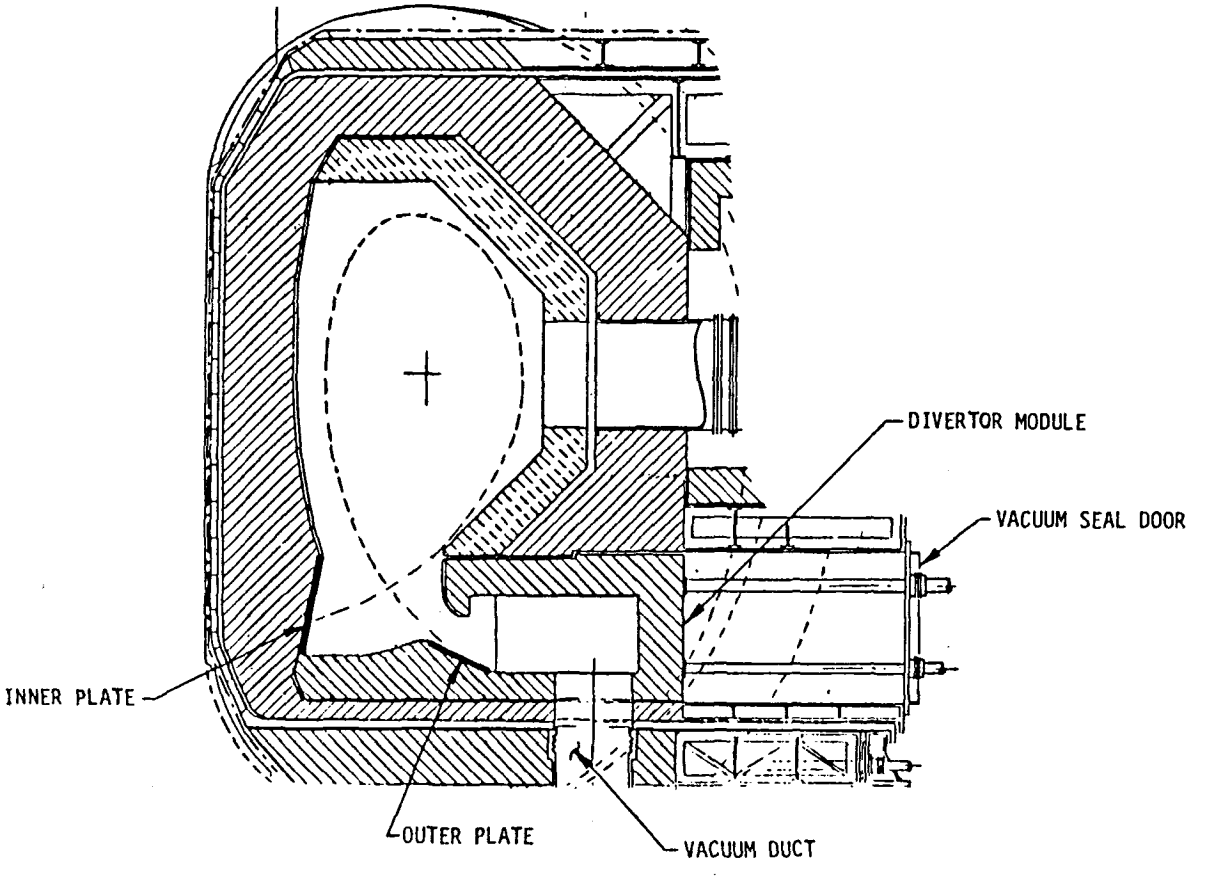

Figure 5-1. Cross sectional view of divertor system.

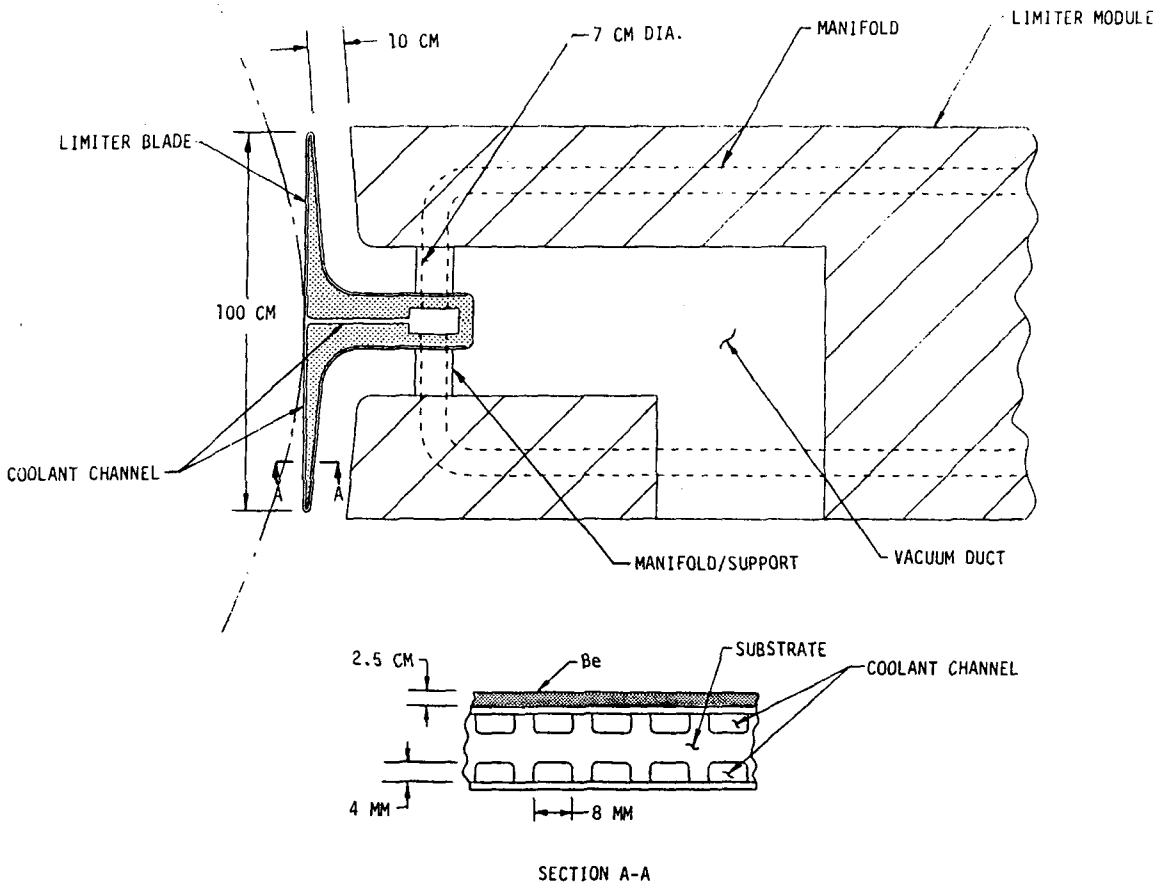

Figure 5-2. Cross section of DEMO limiter design.

major considerations for limiter placement are: (1) sensitivity to variations in plasma shape and position, (2) impact on reactor and magnet size, (3) impact on tritium breeding, (4) response to disruptions, (5) impact on component fabricability, and (6) impact on reactor accessibility. Overall, the outer midplane location is favored. This location is the least sensitive to plasma variations, and it also results in the minimum size blanket/shield and TF coil configuration. The impact of tritium breeding, disruptions, and fabrication on limiter location is minor. The midplane location reduces the available access for other reactor penetrations. However, for DEMO, the reduced access is not expected to present any significant problems. Therefore, the outer midplane has been selected for the limiter location.

The information presented in the rest of the chapter is aimed specifically at the issues associated with a limiter at the outer midplane, but it should be noted that several issues are generic to tokamak impurity control systems. In particular, the materials analyses, including plasma-surface interactions, radiation damage, corrosion, and fabrication, are applicable to other concepts. Since the heat and particle fluxes are comparable for divertor and limiters, the thermal hydraulics, stress analysis, and lifetime analysis generally apply to both limiter and divertor systems.

5.1.2 Summary

The impurity control analyses are in the areas of plasma transport studies, erosion/redeposition, materials, plasma disruptions, thermal hydraulics and stress analysis, and tritium and vacuum considerations. This section summarizes the results of those analyses.

5.1.2.1 Plasma Transport Studies

The plasma transport studies involve investigations of steady state plasma profiles, particularly in the vicinity of the plasma edge, and possible ways of controlling edge conditions. The analysis utilized a plasma transport code adopted from the WHIST code. Starting from an initial set of plasma profiles and appropriate boundary conditions, the code advances the profiles in time, in accordance with specified diffusion laws and with various source terms describing heating and fueling. The code is one and one-half dimensional, in the sense that the diffusion takes place in one dimension,

normal to the magnetic flux surfaces, while the evolving geometry of the flux surfaces is calculated in two dimensions. Major parameters are the removal efficiency of the limiter, the method of refueling (i.e., gas puffing or pellet injection), and the high-Z impurity content and profiles in the plasma.

The results of the calculations indicate that the plasma edge conditions can be controlled by selecting the appropriate conditions of pumping efficiency and plasma fueling methods. The calculated edge temperatures ranged from 235 to 805 eV.[4] It was also determined that plasma stability, edge conditions, and power output are sensitive to the concentration and profiles of high-Z impurities. For DEMO, a small amount of iodine is used for burn control and for increasing the amount of power which is uniformly radiated to the plasma chamber. The concentration of iodine never exceeds 5×10^{-4}. Most of the work since the interim report has concentrated on impurity effects on plasma performance. Compared with the plasma operating point in the interim report, the selected operating point has considerably higher reactivity because the plasma temperature is lower. The additional α-power tends to come out as line radiation rather than transport power to the limiter due to the presence of iodine. If insufficient iodine is present, a thermal runaway is predicted. It was found that plasma performance was particularly sensitive to the impurity profile. If the profiles are peaked near the edge, then the edge temperature tended to collapse, with the cold region expanding rapidly into the discharge. Profiles which are peaked in the center or nearly flat lead to stable plasma configurations.

Two impurity profiles, designated cases A and B, were investigated in detail. In case A, the profile was taken as smoothly peaked at the center, dropping by a factor of about ten at r = 100 cm, and thereafter declining quite rapidly. In case B, the profile was taken to be flat out to r = 100 cm, and thereafter falling at about the same rate as the fuel profile. The amount of ripple for case B was increased from 1.05% to 2.4% to provide additional transport. The final values of the average temperatures and powers are listed in Table 5-1. The plasma edge temperatures vary from ~ 100-250 eV for all cases considered. The density profiles are hollow by ~ 15% owing to the fact that the pellet fuel penetrates only to a radius of ~ 95 cm. The temperature profiles, in contrast, are rather sharply peaked at the center.

Table 5-1. Average Temperatures and Alpha Power P_α for Two Basic Cases. Both have $\beta = 0.075$

Note: $\bar{T}_e = \langle T_e \rangle$, $\tilde{T}_e = \langle n_e T_e \rangle \langle n_e \rangle^{-1}$, and similarly for $\bar{T}_i$ and $\tilde{T}_i$.

Case	$\bar{T}_e$	$\tilde{T}_e$	$\bar{T}_i$	$\tilde{T}_i$	P_α
A	8.5	10.8	9.7	11.9	215
B	9.6	11.6	9.5	11.3	196

5.1.2.2 Erosion/Redeposition

Detailed calculations of the rates of erosion and redeposition were made for the limiter using the REDEP code. The code follows the trajectories of neutral sputtered surface atoms through the scrape-off zone and the plasma. Eventually, most of these particles undergo ionizing collisions and follow magnetic field lines in the vicinity of the ionizing event back to the limiter surface. Upon impacting the limiter surface, additional neutral particles are formed due to self sputtering. An iterative calculation is carried out to determine the solution for the net erosion redeposition profile for the entire limiter surface. The analysis has centered on a beryllium coated limiter for plasma edge temperatures ranging from 20 to 1200 eV.

The erosion/redeposition results can be briefly summarized as follows. For beryllium coatings, net erosion rates on the front face of the limiter are acceptable at all edge temperatures, subject to model uncertainties. Leading edge erosion is a problem, however, at most temperatures, but simple conceptual solutions have been identified. Solutions proposed include (1) the use of a dual material limiter (tungsten or tantalum for the leading edge, beryllium for the front face) at low edge temperatures and (2) in-situ recoating at moderate temperatures. The use of tungsten is restricted to plasma edge temperatures of ~ 50 eV or lower due to self-sputtering considerations. If very low edge temperature operation can be realized, virtually zero net erosion is predicted by the present model over the entire surface for tungsten coatings.

An effort was also devoted to examining the erosion/redeposition behavior of the reference limiter design and operating conditions. The plasma side material on the face is beryllium and the surface material on the leading edges is tantalum or tungsten. High-Z materials are attractive for use at the leading edges when the energies impacting particles is $\lesssim$ 700 eV where the self sputtering coefficient is less than unity. The reference edge temperature is 150 eV. This temperature was chosen because it is representative of the most probable edge temperatures calculated from plasma transport studies. The predicted erosion and redeposition rates for an all beryllium limiter at 150 eV are shown in Fig. 5-3. Points 1-7 represent the leading edge and the remaining points represent the limiter face. The peak net loss rate is ~ 29 cm/y at the leading edge, but the loss rate is $\lesssim$ 1 cm/y over the face of the limiter. Hence, the use of a high-Z material at the leading edge is required to extend the lifetime of the limiter.

The REDEP code was modified so that the time dependent behavior of the erosion profile across the Be-Ta limiter could be studied. The results indicate that relatively high net erosion rates occur at the point adjacent to the tantalum leading edge. Within ~ 12 days of continuous operation, this area has eroded to the degree where it is shadowed by the leading edge and no longer receives a charged particle flux. Areas further down on the limiter face are subjected to an increased, particle flux since the effective area of the limiter is reduced. The time evolution of the limiter shape is therefore an important consideration in determining its lifetime. Unfortunately, the REDEP code is presently not capable of analyzing shadowed areas. Modification to the code are now being incorporated to examine the long term changes in the shape of the limiter surface.

5.1.2.3 Materials Considerations

A materials data base assessment has been conducted. The purpose of the assessment is to evaluate and develop a data base for candidate materials for the first wall and limiter. Recommended values for critical materials properties have been provided for use in design. Uncertainties in the data base have been determined so that the impact on critical design parameters can be evaluated. The assessment has focused on surface plasma side materials that will be directly exposed to the plasma, candidate heat sink materials,

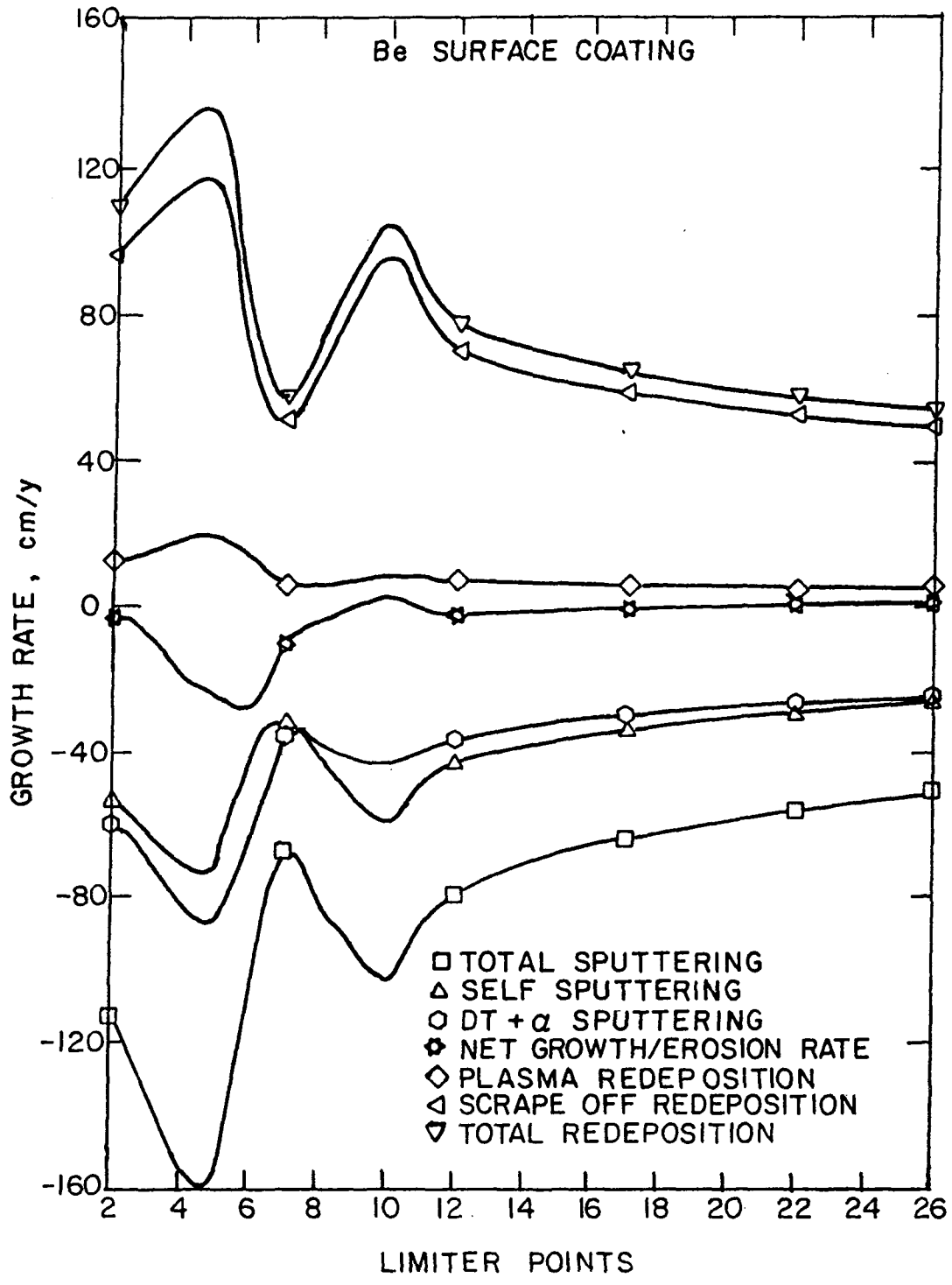

Figure 5-3. Contributors to the net growth/erosion rate for T_e = 150 eV.

and fabrication and characterization of duplex walls (coating/cladding and a structural substrate).

Candidate plasma side materials along with the primary advantages, disadvantages, and limitations are listed in Table 5-2. Major issues are associated with all materials limiting their potential use in fusion devices. The high-Z materials with atomic numbers $\geq$ 20 are limited to operating at plasma edge temperatures $\leq$ 50 eV because of self sputtering considerations. There are relatively few materials available whose self sputtering coefficients never exceed unity. The candidate low-Z materials are graphite, Be, B, BeO, and B_4C. SiC appears to be a borderline case, and additional analysis is required to determine whether its self sputtering coefficient ever exceeds unity. The emphasis to this point has been placed on graphite, Be, BeO, and SiC, since B and B_4C have inferior thermophysical properties. A major issue for the non-metals, graphite, BeO, and SiC, is the radiation-induced reduction in the thermal conductivity. The reduction in conductivity occurs rapidly, and the irradiated conductivity can be only a small fraction of the unirradiated values. For example, the conductivity of SiC can be reduced by a factor of approximately five by radiation. In addition, graphite has a serious problem of chemical sputtering. The operating temperatures are limited to $<$ 500°C in order to remain below the peak temperature for methane formation. Only the low-Z metal Be is not expected to be affected by either of these problems. The major issue for Be is the large melt layer thicknesses which are predicted during disruptions. This problem, however, can be alleviated through design considerations and additional understanding of disruptions and melt layer stability. The steady state operation in DEMO reduces the frequency of disruptions and therefore reduces material loss.

Copper and vanadium alloys have been examined as potential heat sink materials. The requirements of these materials are the ability to withstand high heat fluxes, to withstand a modest level of radiation damage (10 to 20 dpa), and to be environmentally compatible with the surface material and coolant. The desirable properties of the heat sink material are a high thermal conductivity, a low coefficient of thermal expansion, resistance to fatigue failure, resistance to radiation damage and coolant corrosion, and good availability and fabricability.

Table 5-2. Surface Materials Comparison

Material	Advantages	Disadvantages	Limitations
Be[a]	Fabricability	Melt Layer Formation During Disruptions	Operating Temperature < 700°C
	Thermal Properties	Safety	
C	Availability	Chemical Sputtering	Operating Temperature < 500°C
	Low Induced Stresses	Radiation Induced Reduction in Thermal Conductivity	
	Resistant to Disruptions		
BeO[a]	High Temperature Capability	Radiation Effects on Thermal Conductivity	Minimum Operating Temperature 600°C
	More Resistant to Disruptions than Be	Safety	
SiC (TiC)	Availability	Radiation Effects on Thermal Conductivity	Edge Temperature < 50 eV Required
	Resistant to Disruptions	Self Sputtering	
W	Low DT Sputtering	Self Sputtering	Edge Temperature < 50 eV Required
	Resistant to Disruptions	Poor Fabricability	
Ta[a]	Low DT Sputtering	Self Sputtering	Edge Temperature < 50 eV Required
	Resistant to Disruptions		

[a] First choices.

Several groups of copper alloys have been examined. They are pure copper; oxide-dispersion-strengthened copper alloys; low-concentration, age-hardened alloys; and Cu-Be alloys. All these alloys have adequate thermal conductivity and low temperature strength. Pure copper, however, loses its strength at relatively low temperatures. The oxide-dispersion and age-hardened alloys present fabrication difficulties due to the importance of cold-work in achieving their mechanical strength. The bonding processes proposed (i.e., welding and brazing) require temperatures where the cold-work will be annealed out of the structure, and the strength will be significantly reduced. Only the Cu-Be alloys can achieve high strength without cold working. The Cu-Be alloys are available in a wide variety of forms, and they are easily fabricated. Therefore, they appear promising as a heat sink material.

The swelling of pure copper is expected to be very low if the material remains below 235°C. The major concern of radiation damage at low temperatures is embrittlement. The corrosion of copper and copper-beryllium alloys by water should not be excessive at temperatures below 200°C if the water chemistry is controlled to reasonable impurity levels. The fatigue properties of copper and Cu-Be are generally poor.

The analysis of vanadium alloys has concentrated on a single material, V-15Cr-5Ti, because of its superior properties in several areas. It has high tensile and creep strength at elevated temperatures, has excellent radiation damage resistance, and fabrication procedures have been developed. Recent scoping studies of water corrosion indicate acceptable corrosion rates at 250°C in deoxygenated water. The fatigue properties of V-15Cr-5Ti are generally quite good, giving this material an advantage over Cu alloys. At the low operating temperatures of DEMO, radiation swelling is not expected to be a problem. However, this material is expected to embrittle with radiation at temperatures less than ~ 400°C. Because of the superior fatigue properties, V-15Cr-5Ti has been used as the reference heat sink material. There are still uncertainties, particularly in the effects of radiation at low temperatures, which must be resolved before a final selection of the heat sink material can be made.

5.1.2.4 Plasma Disruptions

Erosion of limiter, divertor and first wall surfaces due to the thermal energy dump during plasma disruptions can be significant. Disruptions result in vaporization and, for some materials, a thin melt layer may develop. The stability of the melt layer is a major concern.

The characteristics of disruptions for DEMO are presented in Sec. 5.2. During a disruption, the peak energy density at the limiter is 270 J/cm^2. The plasma energy deposited on the limiter surface during disruptions is assumed to have a spatial energy distribution similar to that of the heat load during normal operation. The peak energy density on the first wall is ~ 175 J/cm^2 and occurs on the inboard region. An extremely severe case for major disruptions in which all the plasma energy goes to the limiter has also been considered. This case results in a peak energy density of 535 J/cm^2. The reference time constant for plasma current decay and thermal quench is 20 ms. An alternate case of 5 ms for the thermal quench was considered.

The very high-Z materials such as tungsten are more resistant to plasma disruptions. However, these materials experience serious melting at very high peak energy density (> 535 J/cm^2) and short time constants (< 5 ms). SiC decomposes rather melts. Beryllium and stainless steel are the least-resistant to plasma disruptions. They melt at energy densities as low as 170 J/cm^2. The amount of material which is vaporized and melted is predicted to increase as the initial surface temperature increases. For example, the melt layer thickness of Be is calculated to increase from 70 μm to ~ 220 μm as the initial surface temperature is increased from 300 to 900°C for the reference disruption conditions.

Melt layer stability during disruptions has been analyzed for a variety of conditions. Magnetic forces caused by the interaction of induced currents during the plasma current quench with the magnetic field are considered to be the primary forces which could create an instability. The time dependent magnetic forces have been calculated for the bottom limiter and the first wall. This information is then coupled with the time dependent behavior of the melt layer to predict stability or instability.

The time-dependent analysis considers the Rayleigh-Taylor instability criteria for fluid layers subjected to perpendicular body forces. The

stability of a beryllium coated limiter was evaluated for disruption energy densities of 535, 270, and 175 J/cm^2 and for thermal quench times of 20 and 5 ms. The results indicate that for the reference disruption conditions (270 J/cm^2, 20 ms) the melt layer is stable at both the center and the leading edge of the limiter. However, at 535 J/cm^2 for both 20 ms and 5 ms disruption times, the melt layer is predicted to be unstable or marginally stable.

There still remain considerable uncertainties in the melt layer analysis. First, additional forces, such as structural vibrations need to be considered. Second, there is no indication of how much of the melt layer is lost even if instability is predicted. A kinetic model is needed to analyze the actual amount of melt layer loss. Finally, the magnetic forces are strongly dependent on the first wall and limiter designs. These forces can be reduced considerably if small tiles are used on the surface of the limiter. The larger number of tiles would effectively increase the resistance of the surface and thereby reduce the magnetic forces.

5.1.2.5 Thermal Hydraulic and Stress Analysis

Thermal hydraulic and stress analysis has been performed for the limiter using a number of candidate materials and for surface material thicknesses ranging from 1 to 50 mm. The configuration used in the analysis is that of an actively cooled heat sink of either a copper or vanadium alloy upon which is attached a surface material, possibly in the form of tiles. The front face analysis utilizes plate geometry whereas the leading edge analysis utilizes a cylindrical geometry. The water coolant temperature is maintained below 100°C, and perfect thermal contact is assumed between the surface material and the heat sink. Peak heat fluxes to the front face and leading edges are 2.4 and 1.0 MW/m^2 respectively.

Figure 5-4 shows the maximum temperature at the limiter plate tiles as a function of the tile thickness at the top surface. Beryllium and tungsten result in much lower temperature than irradiated graphite, TiC and conventional SiC. The rapid reduction in the thermal conductivity of BeO with temperature causes BeO tiles to have much higher temperature than beryllium for tile thicknesses > 1 cm. The maximum temperature of the copper heat sink is generally ~ 150°C with a modest decrease for those cases where the tile temperature is high enough for significant radiative heat transfer to occur at

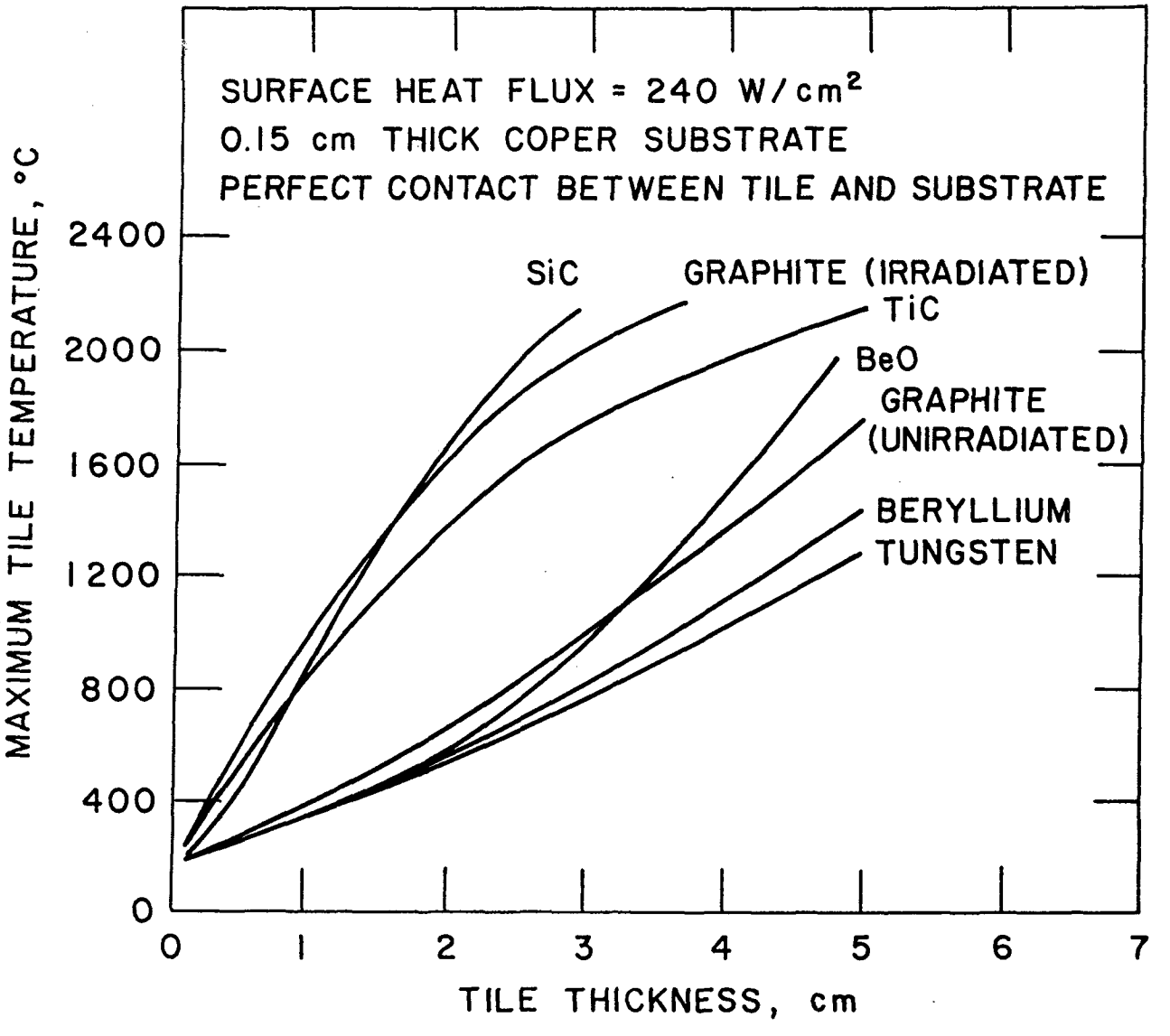

Figure 5-4. Maximum tile temperature vs. thickness for various tile materials at the top surface of limiter/divertor.

the plasma side. The maximum temperature in a vanadium heat sink is ~ 250°C. Therefore, the maximum tile temperatures with a vanadium heat sink are ~ 100°C higher than those in Fig. 5-4. The tile temperatures at the leading edge with a peak heat flux of 1 MW/m^2 are always lower than those at the top surface (peak heat flux of 2.4 MW/m^2). In contrast, the maximum temperature of the heat sink is generally higher at the leading edge than at the top surface. The maximum heat sink temperature increases significantly with tile thickness but it remains < 200°C for Cu and < 350°C for vanadium for a tile thickness < 3 cm.

Stress and fatigue analyses were carried out for a number of heat sink and tile materials. The stresses within the heat sink depend upon the constraint imposed by the coating or tiles. Three constraint conditions have been considered, i.e., no tile constraint, constraint of a tile whose width is large compared to its thickness, and constraint of a tile whose width is 2 cm. The results of the stress calculations are summarized in Table 5-3. If one assumes that the constraint of the tile is minimal, then the stresses are more severe at the leading edge than at the top surface because of the additional geometric constraints at the leading edge. On the other hand, if the tile constraints are included, then the stresses at the top surface are more severe than at the leading edge. For the case of tiles whose width to thickness ratio is large, the $3S_m$ stress criteria is exceeded at tile thicknesses between 1 and 2 cm. If the tile width is only 2 cm, then the effective tile thickness acting to constrain the substrate is reduced, and the $3S_m$ stress criteria is not exceeded.

5.1.2.6 Lifetime Analysis

The lifetime of the limiter is dependant on the maximum allowable thickness of the surface material as determined by thermal-hydraulics and stress analysis and on the net erosion rates as determined by the sputtering and disruption analysis. The maximum allowable temperatures for surface materials are set by the onset of melting, excessive vaporization, excessive chemical sputtering, radiation induced swelling (cracking, and microstructural changes (e.g., sintering and phase changes). The allowable thickness due to stress limitations is determined by applying ASME stress and fatigue criteria to the heat sink structural material. For beryllium the maximum allowable

Table 5-3. Maximum Stresses in the Limiter Structural Material (Vanadium Alloy)[a] With and Without Constraint of Coating

Coating Material	Coating Thickness (mm)	(Without Constraint) Maximum Stress Range (MPa)		(With Constraint) Maximum Stress Range (MPa)		(With Constraint and Tile Width of 2 cm) Maximum Stress Range (MPa)	
		Top Surface	Leading Edge	Top Surface	Leading Edge	Top Surface	Leading Edge
Be	1	212	180	242	153	241	152
	10	219	377	499	228	471	253
	20	226	435	810	225	501	292
	30	231	589	1210	263	528	305
W	1	214	185	215	110	215	109
	10	232	446	234	179	234	257
SiC	1	214	186	214	108	214	107
	10	218	400	367	221	357	238
	20	226	456	748	204	373	274
	30	232	610	974	219	322	326
BeO	10	---	371	247	218	245	229
	20	---	431	667	215	346	264
	30	229	561	1240	278	375	339

[a] $3S_m$ = 560 MPa.

temperature is estimated to be 973 K which is set by the onset of rapid helium driven swelling, and for tantalum, the maximum temperature is estimated to be 773 K which is set by the onset of void swelling. The combined temperature and stress limits restrict the beryllium thickness to ~ 2.5 cm and the tantalum thickness to ~ 1 cm. These thicknesses result in lifetimes of 2.7 y for beryllium and greater than the reactor lifetime for tantalum. Sputtering erosion represents the single most important material loss mechanism.

5.1.2.7 Tritium and Vacuum

The limiter vacuum system consists of eight ducts beyond the limiter blades that are coupled to eight cryopumps located below the nuclear island. Four of the pumps are on line while the other four are being regenerated. The use of a minimum number of vacuum duct/cryopump configuration results in a relatively high pressure in the limiter slot (0.4 Pa) and a relatively high inventory per pump (~ 40 g). It was determined that this configuration is capable of meeting the pumping requirements for DEMO, but that the loss of a single pump could result in inadequate pumping and higher pump inventories. Additional analysis is required to determine the impact of cryopump failure.

The limiter is expected to be the major source of tritium permeation to the coolant due to the very high particle flux to the limiter surface. The amount of tritium that penetrates to the coolant and the amount of tritium that builds up in the limiter has been calculated using the DIFFUSE code. The major uncertainty in these calculations is the effect of tritium trapping in the limiter as a result of neutron damage. If no trapping is assumed, then tritium permeation breakthrough to the coolant is predicted to occur after one-half year of continuous operation. The equilibrium permeation rate is 0.16 g/day. If the effect of neutron trapping is included, then breakthrough does not occur for 10 y. Without neutron trapping, the tritium inventory reaches 0.4 kg, and with neutron trapping the tritium inventory is estimated to reach 1.2 kg.

5.2 Reference Design

The reference impurity control system is a shaped, double-edged, pumped limiter located at the outer midplane of the reactor, as shown in Fig. 5-2. The advantages of the outer midplane location are a reduced TF coil size, potential reductions in disruption damage, and reduced sensitivity to plasma variations. The limiter configuration utilizes removable limiter modules to facilitate maintenance on the relatively short-lived limiter blades. One module is used in each of the eight reactor sectors. The limiter consists of six replaceable limiter blade segments per module, mounted by the coolant manifolding to the main body of the module. The overall height of each segment is 100 cm, and the toroidal width is 85 cm. The limiter blade consists of a water-cooled heat sink covered by a protective surface material. The protective material on the front surface is beryllium, ~ 2.5 cm thick, and the protective material on the leading edges is tantalum, ~ 1 mm thick. The heat sink thickness varies from ~ 1.5 cm at the leading edges to ~ 10 cm at the center. The heat sink material has not been selected, but the leading candidates are copper and vanadium alloys.

The reference limiter operating parameters are shown in Tables 5-4 through 5-6. The total number of operating cycles is estimated to be only 500 because of steady-state operation. A disruption is assumed to occur once every ten cycles for a disruption frequency of 2.5/y. The disruption conditions are assumed to be the same as those for FED/INTOR[1] since both the reactor sizes and internal plasma energies are nearly identical. The total heat load to the limiter is 115 MW out of a total α-heating power of 213 MW. The remaining energy is radiated uniformly to the first wall. The peak surface heat flux is 2.4 MW/m^2 which decreases linearly to 1 MW/m^2 at the leading edge. The plasma-edge temperature is 150 eV, and the temperature and density e-folding distances are both 3.75 cm.

Table 5-4. DEMO Limiter Parameters

Plasma:	
Thermonuclear power (MW)	1069
α power (MW)	213
Neutron wall loading (MW/m^2)	2.1
Operating scenario:	
Years of operation	20
Availability (%)	50
Cycle time (s)	$\sim 6 \times 10^5$
Burn time (s)	$\sim 6 \times 10^5$
Total burn time (s)	3.1×10^8
Total cycles	500
Total neutron fluence	1.1×10^{29}
Total wall loading ($MW\text{-}y/m^2$)	21
Disruptions (Stage I, Stage II):	
Major disruptions	
Frequency	10^{-1}
Disruptions/year	2.5
Total disruptions	50
Total energy (MJ)	290
Thermal phasing energy (MJ)	230
Field energy (MJ)	60
Disruption time	
Poloidal field (ms)	20
Plasma current (ms)	20
Thermal energy (ms)	
Reference	20
Alternate	5
Disruption Energy Density, Reference Case (J/cm^2):	
First wall	175
Limiter	270
Disruption Energy Density, High Load to Limiter (J/cm^2):	
First wall	35
Limiter	535
Engineering:	
Plasma chamber surface area (m^2)	400
Limiter	Outer midplane
Configuration	8 separately removable modules each weighing ~ 60 Mg.
Pumping system	Compound cryopumps located below nuclear island.
Desired lifetime	> 2 y @ 50% availablity
Coolant	$\tilde{H}_2 0$ @ < 100°C

Table 5-5. DEMO Limiter Heat and Particle Fluxes

Parameter	
Alpha heating (MW)	213
Radiation (MW)	100
Ions to limiter (MW)	80
Neutrals to limiter (MW)	25
Neutrals to wall (MW)	8
Limiter ion flux (s^{-1})	6.75×10^{23}
Limiter neutral flux (s^{-1})	1.0×10^{23}
Wall neutral flux (s^{-1})[a]	3.3×10^{22}
Ion energy (eV)	675
Neutral energy (eV)	1500
Edge electron temperature (eV)[b]	150
Edge density (cm^{-3})[b]	5×10^{13}
e-Folding distances (cm)[c]	
Temperature	3.75
Particle flux	2.5
Power	1.5
Density	3.75

[a] The neutral wall flux falls on two 0.5-m poloidal width strips at each end of the limiter.

[b] At the "separatrix".

[c] At midplane.

Table 5-6. Limiter Operating Parameters

Heat loads (MW/m^2):	
Peak, front surface	2.4
Peak, leading edge	1.0
Average, 0.5-m strips adjacent to limiter	0.45
First wall	0.25
Particle fluxes ($s^{-1}m^{-2}$):	
CX, limiter	1.67×10^{21}
CX, 0.5-m strips adjacent to limiter	8.3×10^{20}
CX, first wall	$\sim 1 \times 10^{20}$
Ions, middle of limiter	1.25×10^{22}
Ions, leading edge	3.1×10^{22}
Engineering:	
Limiter configuration	Curved, double-edged, and shaped to have approximately uniform heat flux distribution.
Limiter segment dimensions	1.0 m, leading edge to leading edge ~ 0.85-m width with 6 segments/sector
Total surface area (m^2)	61
Plasma side cladding	
Material	Beryllium (BeO)
Thickness (mm)	~ 20
Sputtering/redeposition rate (50% availability mm/y)	9
Bond type	High thermal conductance ($\gtrsim 4 \times 10^4$ W/m^2 K)
Leading edge cladding	
Material	Ta (W,V)
Thickness (mm)	~ 1
Sputtering/redeposition rate (50% availability mm/y)	0
Heat sink	
Configuration	1.5-mm sheet bonded to a thick (1.5 cm to 10 cm) core structure, water cooled.
Material	V15Cr5Ti (Cu-2Be)
0.5 strips adjacent to limiter - configuration	Beryllium on stainless steel
First wall configuration	2 mm beryllium on 4 mm stainless steel

5.3 Edge Conditions and Plasma Transport Studies

A portion of the work in impurity control has involved an investigation of the steady-state plasma profiles, particularly in the vicinity of the edge, and of possible ways of controlling the edge conditions. This analysis has utilized a plasma transport code adapted from the code WHIST, which has been developed over the past several years at Oak Ridge National Laboratory. Starting from an initial set of plasma profiles and suitable boundary conditions, the code advances the profiles in time, in accordance with specified diffusion laws and with appropriate source terms describing heating and fueling. The code is one and one-half dimensional, in the sense that the diffusion takes place in one dimension, normal to the magnetic flux surfaces, while the evolving geometry of the flux surfaces is calculated in two dimensions. The latter calculations are done by a new, rapid set of routines based on a variational moment expansion of the MHD pressure balance equation.[5] The version of WHIST used in the DEMO interim report[4] did not compute MHD equilibria.

Since the issues addressed here concern the steady-state phase of the burn, an ignited plasma with full current was taken to be present initially. The plasma behavior was then followed with the code until a time-independent configuration developed.

The D, T, and α species, the electron temperature, the ion temperature, and the poloidal field were allowed to diffuse according to the following transport laws:

(a) empirical expressions for the electron heat conductivity and particle diffusion coefficients,

$$\chi_e = (5 \times 10^{19}\ m^{-1}s^{-1})(\alpha/n_e) ,$$

$$D = \chi_e/5 ,$$

where α is a parameter which normally equals unity (FED/INTOR recommendation) but which was sometimes set to 1.5 or 2. in order to test the sensitivity of the results to the assumed transport;

(b) neoclassical expressions, including the Ware pinch, multiplied by a factor of three; and

(c) the ripple trapping and ripple plateau contributions to the ion thermal conductivity.

The commonly accepted selection of transport coefficients has $\alpha = 1$. In the scrape-off region the transport was neoclassical with an additional constant of 1 m^2/s added to the electron and ion thermal conductivities and the diagonal particle diffusion coefficients. The particle and energy loss rates to the toroidal limiter were taken from a frequently used model.[6]

Because the MHD equilibrium is now allowed to evolve in time, the poloidal magnetic field diffuses in such a way that the safety factor q at the magnetic axis slowly declines. When q(0) falls below unity, sawtooth disruptions are expected to redistribute the current and plasma thermal energy for some distance outward, so that q(0) rises above unity again and the central temperature and density profiles are flattened. Thus sawtooth activity imposes an intermittent effective radial transport within the disrupted portion of the plasma. Unfortunately, models appropriate to the time scales of transport codes are still in the developmental stage. In the runs discussed here, sawtooth disruptions were accounted for in a rough manner by flattening out the central q profile to unity whenever q(0) fell below a trigger value, taken to be 0.98. The plasma profiles were smoothed within the affected region out to a maximum radius of 40 cm.

The recycling of plasma particles from the limiter and wall strongly influences the edge conditions and plasma performance. The model employed here was discussed in the interim report.[4] In brief, complete recycling occurs at the wall, and a fraction $1 - \varepsilon$ is recycled from the limiter. The removal efficiency was normally the design value, $\varepsilon = 0.05$, although variations were also considered. The pumped and burnt fuel was replenished by pellet injection, with deuterium and tritium pellets treated separately. The pellet speed was 2 km/s, and the pellet radius was 1.5 mm in some runs (Case A below) and 1.8 mm in other runs (Case B).

A high-Z impurity, iodine, was added to the plasma in order to maintain thermal stability during the burn and also to convert part of the alpha heating to radiation. Since the transport properties and source term for high-Z impurities are still speculative, the iodine profile was held fixed. The concentration was varied, through a feedback loop, to maintain a specified average electron temperature. Once a steady state had been achieved, the concen-

tration fluctuated by only a few parts in a thousand over a period of several seconds. The concentration itself never exceeded 5×10^{-4}, relative to the fuel density.

The quantities which are subject to direct control, then, are the average fuel densities (governed by the pellet injection rate) and the average electron temperature. In the MHD equilibrium calculations, the elongation and triangularity of the flux surface bounding the plasma proper can also be fixed; these were taken as $\kappa = 1.6$ and $d = 0.2$, respectively, in agreement with the design. The total toroidal current was maintained at its design value of 8.68 MA by the imposition of a boundary condition. Transport models of current drive via injection of relativistic electrons have not yet been fully developed.

To obtain a steady state with the desired characteristics, one chooses values of $\bar{T}_e$, $\bar{n}_D$, and $\bar{n}_T$, and follows the plasma evolution until the profiles become steady. Depending on the particular regime, this may take as little as a fraction of a minute of tokamak time, or the profiles may explode or collapse in bizarre ways. The steady state having the maximum fusion power for a given $\beta = 0.075$ is then selected.

Compared with the plasma operating point discussed in the interim report, the operating point chosen here has considerably higher reactivity because the temperature is lower. In the present runs the extra power tends to come out as line radiation rather than as transport power to the limiter. This obviously is a favorable result from the standpoint of minimizing the heat load on the limiter. If insufficient iodine is present, a thermal runaway occurs. Consequently, the postulated iodine profile has a stronger effect on plasma performance than was found previously. In particular, it was found that, for profiles peaked near the edge, the edge temperature tended to collapse, with the cold region expanding rapidly into the discharge. Possibly this instability could be averted if the local impurity concentration decreased as the temperature dropped (e.g. if the impurity were sputtered from the limiter), but the relevant physics is not yet in the code. The tendency of an edge-peaked profile to cause this instability holds when the empirical transport coefficients have their normal value ($\alpha = 1$). If, however, the expressions for empirical transport are doubled ($\alpha = 2$), then the fraction of the alpha power removed by radiation decreases markedly, and there is accordingly less sensi-

tivity to the distribution of the impurities. The sensitivity of the power split and of edge conditions to variations in α is discussed below.

In very rough terms one might picture three types of impurity profiles: peaked near the edge, peaked at the center, or nearly flat. As noted above, the first possibility did not lead to a steady-state plasma. The remaining two possibilities did, however, lead to satisfactory steady states, which will be categorized as Cases A and B, respectively. In Case A the profile was taken to be smoothly peaked at the center, dropping by a factor of about 10 at $r = 100$ cm, and thereafter declining quite rapidly. As will be explained in more detail, a more strongly peaked profile would also lead to a steady state, but a less strongly peaked profile, in the absence of additional transport, would tend to produce the cold-edge instability. In Case B the profile was taken to be flat out to about 100 cm, thereafter falling off in about the same manner as the fuel profile. The iodine concentration in this case could not be brought up to the level of that in the previous case, owing to the cold-edge instability. To provide additional transport, the magnetic ripple was increased from its design peak-to-average value of 1.05% (used in the first case) to 2.4%.

In each case the initial plasma profiles were taken to be those displayed in the interim report, which had an average ion temperature near 20 keV and an alpha power of about 150 MW. Since, in this regime, most of the alpha power was removed by the limiter, the plasma performance was relatively insensitive to the assumed iodine profile. For definiteness, the iodine profile of Case B was initially employed. The ripple was initially the design value. To increase the alpha power the average temperature was gradually lowered and the density was increased to maintain β. This was done sufficiently slowly so that the plasma passed through a sequence of quasi-static configurations. After a drop of a few keV, a steady-state could no longer be maintained because of the collapsing edge temperature. To allow descent to lower temperatures, the strategies appropriate to the two particular cases were then employed. In Case A, the impurities were shifted more toward the center; in Case B, the impurity profile was left unchanged but the ripple was gradually increased. After a continuing decrease of the temperature, the alpha power was eventually maximized in each case.

The final values of the average temperatures and the alpha power are listed in Table 5-7. Note that the second case produced about 9% less alpha power than the first, because the higher value of the ripple depressed the ion temperature. The pellet radius was 1.5 mm in the first case and 1.8 mm in the second case. Larger pellets were employed in the latter case in order to boost the alpha power, the difference in pellet radius accounting for about 10 MW.

Table 5-7. Average Temperatures and Alpha Power P_α for Two Basic Cases. Both have $\beta = 0.075$.

Note: $\bar{T}_e = \langle T_e \rangle$, $\tilde{T}_e = \langle n_e T_e \rangle \langle n_e \rangle^{-1}$, and similarly for $\bar{T}_i$ and $\tilde{T}_i$.

Case	$\bar{T}_e$	$\tilde{T}_e$	$\bar{T}_i$	$\tilde{T}_i$	P_α
A	8.5	10.8	9.7	11.9	215
B	9.6	11.6	9.5	11.3	196

The steady-state profiles for Case A, including the iodine profile, are shown in Fig. 5-5, and the power balances and other pertinent data are summarized in Table 5-8. The coordinate r in Fig. 5-5, an effective minor radius in the horizontal midplane, is a flux surface label. The geometry of the flux surfaces is shown in Fig. 5-6. As shown in Fig. 5-5, the deuterium profile is hollow by about 15%, owing to the fact that pellets do not penetrate within a radius of about 95 cm. Also shown in this figure are the profiles which result when the empirical transport coefficients are doubled. Aside from a general flattening, the changes in the fuel and temperature profiles do not seem dramatic. Such subtle changes do, however, have a significant effect on the power balance, as can be seen in Table 5-8. In the first column are the results for the case $\alpha = 1$. Here line radiation from the iodine accounts for fully two-thirds of the alpha power, and the load on the limiter is only 32 MW. If, however, the empirical transport coefficients are increased by 50% (Column 2), the load on the limiter doubles, with a corresponding decrease of the line radiation. Finally, a doubling of empirical transport (Column 3) leads to a tripling of the limiter load.

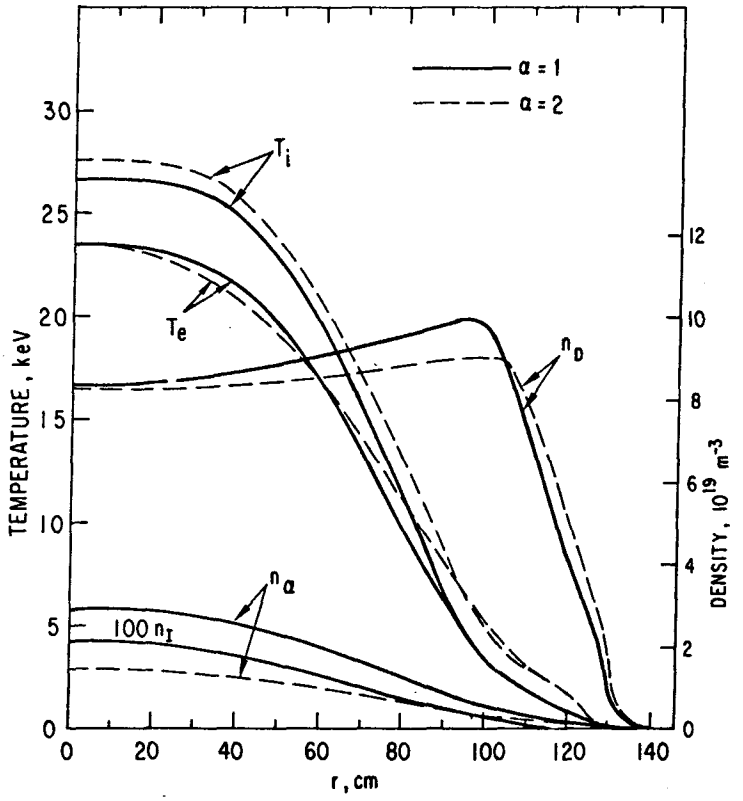

Figure 5-5. Steady-state plasma profiles for Case A, shown for two choices of empirical transports.

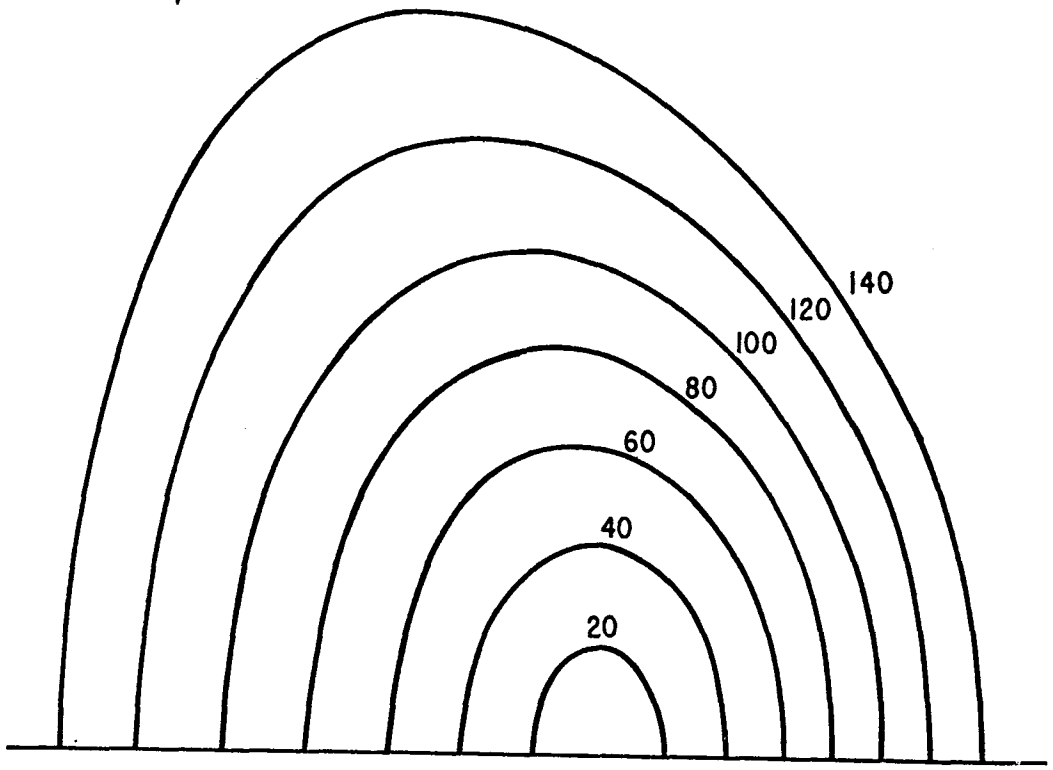

Figure 5-6. Some flux surfaces for Case A, $\alpha = 1$. Up-down symmetry is assumed, and only the top half of each flux surface is drawn. The label on a flux surface is one-half its width (cm) in the horizontal midplane, and thus serves as an effective minor radius.

Table 5-8. Power Balances and Other Data for Steady States Corresponding to Case A

Multiplier of empirical transport, α	1	1.5	2	1
Removal efficiency, ε	0.05	0.05	0.05	0.15
Fusion heating, MW	215	221	219	228
Ohmic heating, MW	2	1	1	2
Limiter, MW:				
Electrons	24	49	75	17
Ions	8	13	20	4
Line radiation, MW	141	119	89	164
Bremsstrahlung and cyclotron radiation, MW	42	37	31	43
Charge-exchange and ionization, MW	2	4	5	2
τ_E, s	5.54	2.48	1.56	8.02
τ_I, s	16.7	10.7	7.40	30.0
τ_{DT}, s	0.123	0.096	0.071	0.250
τ_α, s	0.442	0.293	0.222	1.13
DT ions to limiter, 10^{23} s^{-1}	3.34	4.31	5.87	1.64
Alpha ions to limiter, 10^{21} s^{-1}	6.69	7.20	7.08	2.57
n_{DT} at limiter tip, 10^{19} m^{-3}	1.62	1.86	2.42	0.784
T_e at limiter tip, eV	97	159	181	135
T_i at limiter tip, eV	84	107	119	91
Charge-exchange neutrals to wall, 10^{22} s^{-1}	6.84	9.76	12.1	4.41
Alpha concentration, n_α/n_{DT}	0.0718	0.0512	0.0381	0.0710
Iodine concentration, n_I/n_{DT}	$4.40\ 10^{-4}$	4.21×10^{-4}	3.53×10^{-4}	4.38×10^{-4}

The increased heat to the limiter is consistent with the edge conditions noted in Table 5-8. (To check this, recall that the heat carried by electrons varies as $n_e T_e T_i^{1/2}$, while that carried by ions varies as $n_i T_i^{3/2}$, but with a different constant of proportionality.) The decrease in line radiation can be qualitatively inferred from the profiles in Fig. 5-5, since the effect of increased transport is to raise the electron temperature in the outer region of the discharge. As Table 5-8 indicates, the edge temperatures for $\alpha = 1$ are slightly less than 100 eV, thus qualifying as cool but still not sufficiently cold to avoid sputtering runaway for medium or high-Z materials. It is interesting that the edge temperatures do not increase drastically with α. When $\alpha = 2$, the electron temperature remains below 200 eV, and the ion temperature is still in the neighborhood of 100 eV.

An interesting effect which can be noted in Fig. 5-5 and in Table 5-8 is that, when empirical transport doubles, the alpha concentration drops by nearly a factor of two. The effectiveness of the additional transport in removing the alpha ash may have important and favorable implications. One still notes, however, that the alpha confinement time is more than three times longer than the DT confinement time, and so the alpha concentration is much higher than for the case when $\tau_\alpha = \tau_{DT}$. As with the earlier operating point,[4] helium tends to remain in the center of the plasma.

Also listed in Table 5-8 are the energy and particle confinement times, the particle currents to the limiter, and the charge-exchange current and power, all of which show the expected trends with respect to increasing transport. Note that the electron energy confinement times decrease faster than what would be predicted by the relation $\tau_E \alpha \simeq$ constant. The main reason is that, as transport increases, the radiation losses decrease, thus allowing τ_E to drop below the nominal scaling value. (The electron heating due to temperature equilibration also decreases, but not as fast as the radiation.) The last column of Table 5-8, which refers to an increase in particle removal efficiency, will be taken up after a discussion of Case B.

The steady-state profiles for Case B are shown in Fig. 5-7, and the power balances and edge data are listed in Table 5-9. The geometry of the flux surfaces is very similar to that of Case A in Fig. 5-6. The principal difference with respect to Case A is that, owing to the greater ripple, the ion temperature profile now takes a considerably flatter shape -- cooler at the center

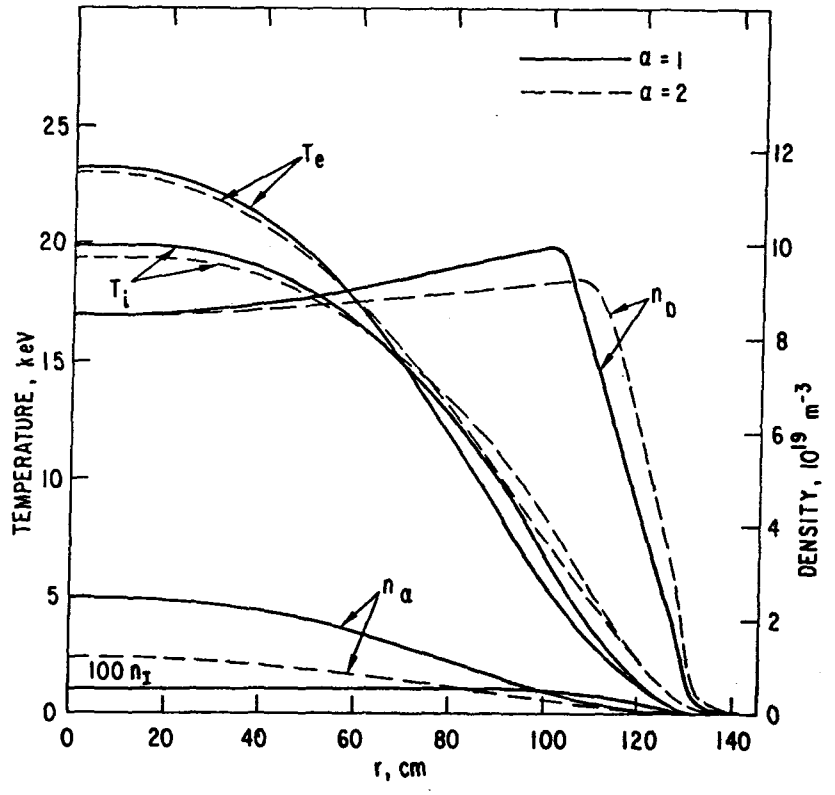

Figure 5-7. Steady-state plasma profile for Case B, shown for two choices of empirical transport.

and hotter at the edge. Because of electron-ion temperature equilibration, which is more effective at the edge, the electron temperature is higher at the edge than it was in the previous case. The edge density, though, is about the same as before. Consequently, the load on the limiter increases by about 40%, and the line radiation decreases accordingly. Still, when $\alpha = 1$, about 60% of the alpha power is removed via line radiation. The behavior with respect to increasing empirical transport shows the same dramatic trends as were noticed for Case A. In particular, the load on the limiter again triples when empirical transport is doubled. The other results in Table 5-9 show about the same dependence on α as those for Case A. In particular, note that the alpha concentration again drops by a factor of two when $\alpha = 2$.

Thus far the principal control mechanism which has been considered is the magnetic ripple, although the impurity profile may also be controllable to some extent by different injection techniques. Another possible mechanism is the particle removal efficiency ε defined by the pumping system. Variations with respect to ε were considered in some detail in the interim report, and

Table 5-9. Power Balances and Other Data for Steady States Corresponding to Case B

Multiplier of empirical transport, α	1	1.5	2	1
Removal efficiency, ϵ	0.05	0.05	0.05	0.15
Fusion heating, MW	196	194	195	206
Ohmic heating, MW	1	1	1	1
Limiter, MW				
Electrons	34	76	117	26
Ions	11	19	30	6
Line radiation, MW	117	66	19	138
Bremsstrahlung and cyclotron radiation, MW	31	25	20	33
Charge-exchange and ionization, MW	4	9	10	4
τ_E, s	4.02	1.70	1.11	5.32
τ_I, s	12.2	7.36	4.72	19.3
τ_{DT}, s	0.120	0.093	0.064	0.240
τ_α, s	0.416	0.277	0.215	1.09
DT ions to limiter, 10^{23} s^{-1}	3.53	4.52	6.89	1.75
Alpha ions to limiter, 10^{21} s^{-1}	6.34	6.55	6.34	2.36
n_{DT} at limiter tip, 10^{19} m^{-3}	1.54	1.70	2.48	0.72
T_e at limiter tip, eV	134	237	244	200
T_i at limiter tip, eV	108	144	155	127
Charge-exchange neutrals to wall, 10^{22} s^{-1}	8.84	13.8	17.3	6.08
Alpha concentration, n_α/n_{DT}	0.0625	0.0429	0.0312	0.0612
Iodine concentration, n_I/n_{DT}	2.84×10^{-4}	1.87×10^{-4}	5.52×10^{-5}	2.96×10^{-4}

the same trends can be seen here. In the runs discussed above, the removal efficiency was $\varepsilon = 0.05$. The results when ε is tripled are listed in the fourth columns of Tables 5-8 and 5-9. The edge density drops by about a factor of two, while T_e increases by about 50% and T_i increases only slightly. These changes are such that both the particle flux to the limiter (proportional to $nT_i^{1/2}$) and the heat flux to the limiter drop. The behavior for intermediate values of ε interpolates quite smoothly. The variation in the deuterium density profile within the edge region, as a function of ε, is shown in Fig. 5-8 (Case A, $\alpha = 1$).

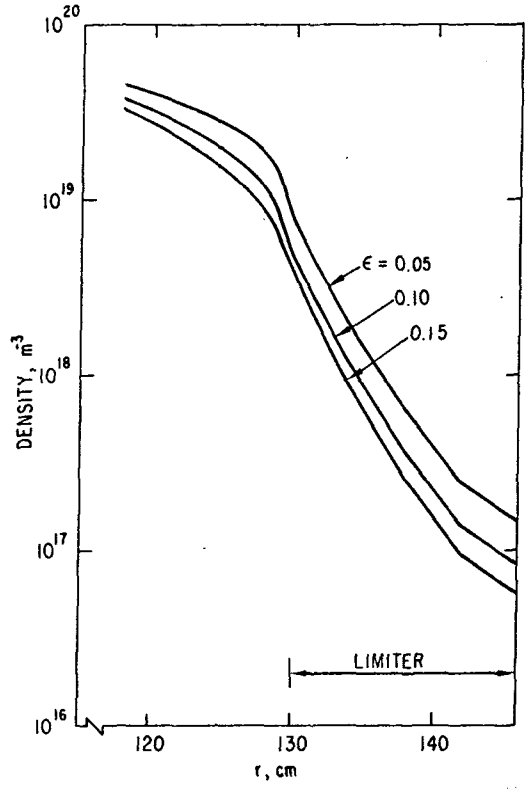

Figure 5-8. Deuterium density profile in the edge region (Case A, $\alpha = 1$) for various values of the particle removal efficiency.

In summary, this analysis with the one-and-one-half-dimensional plasma transport code leads to the following general conclusions:

(1) In the presence of "standard" empirical transport ($\alpha = 1$), the alpha power tends to be removed primarily via line radiation. If insufficient impurities are present, a thermal runaway is predicted. If the impurities are concentrated at the edge, there is danger of a cold-

edge collapse (in the absence of a mechanism to decrease the local impurity level when the temperature drops).

(2) The power split between transport and radiation changes markedly in favor of transport when the coefficient multiplying empirical transport is increased. Except perhaps for Case B with $\alpha = 2$, the limiter transport load is tolerable in all cases. In some cases (e.g. $\alpha = 1$), the load so so low that some of the limiter design problems would be substantially eased. (We have used a more conservative value for the limiter design, in view of the uncertainties in the physics.)

(3) Some flexibility in the shape of the impurity profile is afforded by a variation of the magnetic ripple.

(4) Under all circumstances considered here and in the interim report, the fuel profiles are very broad and slightly hollow; the temperature profiles, in contrast, are rather sharp.

(5) The particle flux to the limiter and, to a lesser extent, the heat flux to the limiter can be controlled by variation of the particle removal coefficient ε.

(6) The helium concentration is fairly high (3% to 7%) in all cases examined, owing to the fact that the helium is born near the plasma center and hence tends to be removed more slowly than the fuel. The helium concentration, however, is tolerable.

5.4 Erosion/Redeposition

5.4.1 Introduction and Summary

Erosion/redeposition calculations for the DEMO limiter have been carried out using the REDEP computer code. The code follows the trajectories of neutral sputtered surface coating atoms through the scrape off zone and plasma. Eventually, most of these particles undergo ionizing collisions and follow the magnetic field lines in the vicinity of the ionizing event back to the limiter surface. Upon impacting the limiter surface, additional neutral atom ejection takes place due to self sputtering. An iterative calculation is carried out to determine the solution for the net erosion/redeposition profile along the entire limiter surface. The algorithm for this model has been described in detail elsewhere.[7,8]

The top half of the symmetric midplane limiter for DEMO is shown in Fig. 5-9. It is designed to yield a constant heat flux across the front face. Since it appears that carbon may be unacceptable due to chemical sputtering problems, beryllium was used as a reference low-Z material. However, the trends found for beryllium will be similar for physical sputtering of all low-Z materials.

Analysis of the limiter performance was carried out for a variety of plasma edge temperatures ranging from 20 eV to 1200 eV. The erosion/redeposition results can be briefly summarized as follows. For beryllium coatings, net erosion rates on the front face of the limiter are acceptable at all edge temperatures, subject to model uncertainties. Leading edge erosion is a problem, however, at most temperatures, but simple conceptual solutions have been identified. Solutions proposed include (1) the use of a dual material limiter (tungsten or tantalum for the leading edge, beryllium for the front face) at low edge temperatures and (2) in-situ recoating at moderate temperatures. The use of tungsten is restricted to plasma edge temperatures of $\sim$ 50 eV or lower due to self-sputtering considerations. If very low edge temperature operation can be realized, virtually zero net erosion is predicted by the present model over the entire surface for tungsten coatings.

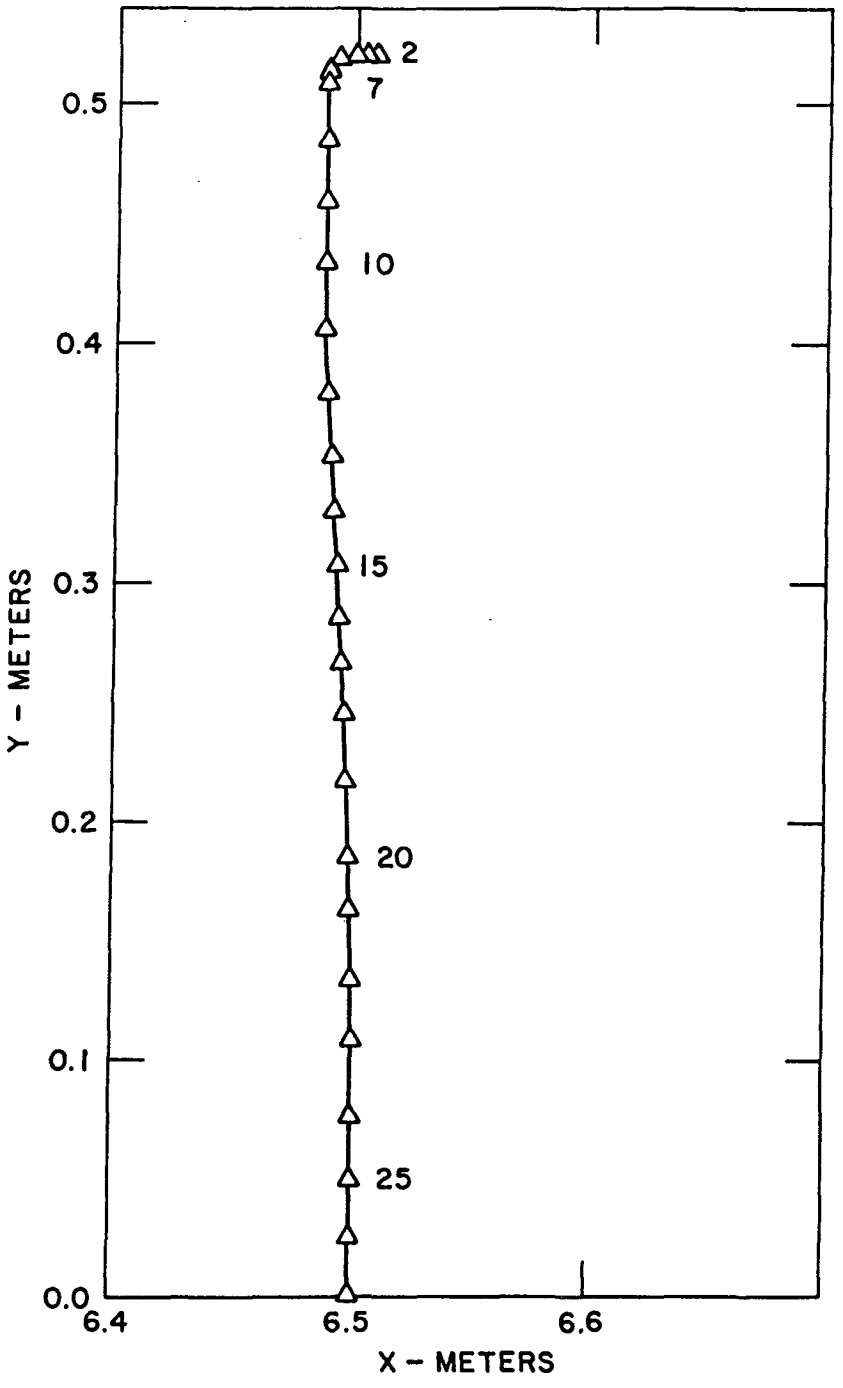

Figure 5-9. Top half of the DEMO limiter profile.

5.4.2 Limiter Analysis - Beryllium Coating

Plasma parameters used for the limiter analysis are listed in Table 5-10. Edge temperatures ranging from 20 eV to 1200 eV were investigated. Reference values of 150 eV and 700 eV were selected for high and low edge operation, respectively. An edge temperature of 20 eV was included to model a radiative edge condition.

Using the parameters in Table 5-10, a midplane limiter surface profile was constructed which yielded a constant heat flux over most of the limiter face. In this analysis, each half of the limiter surface profile was divided into 25 segments numbered as shown in Fig. 5-9. The heat flux and the spatial variation of the plasma temperature and charged particle flux, Γ_{DT}, along the limiter face are shown in Fig. 5-10. In general, the values of the heat and particle flux depend upon the e-folding distances and the limiter geometry. As shown in the figure, the heat flux is constant across the front face of the limiter and begins to drop off near the leading edge. The leading edge geometry used here, however, is such that the heat and particle fluxes to these segments are high, yielding peak values of sputtering at the leading edge. A modified leading edge design could probably lower the heat flux at the leading edge, and this needs further investigation.

The various terms contributing to the net erosion of the coating are shown in Fig. 5-11 for the 150 eV reference edge temperature. Points 2 through 26, representing half of the symmetric limiter face, are shown. The total sputtering rate is the sum of the DT + alpha sputtering and the Be on Be self-sputtering rates. The bulk of the sputtered material undergoes electron impact ionization in the scrape off zone and returns directly to the limiter surface (Curve 6 in Fig. 5-11). A small contribution to redeposited flux comes from sputtered material entering the bulk plasma and subsequently diffusing back out into the scrape off zone (Curve 5 in Fig. 5-11). Impurity atoms diffusing from the bulk plasma are assumed to be fully ionized, Z = +4, for beryllium. Those atoms ionized in the scrape off zone and returning directly to the limiter surface are modeled with Z = +3, consistent with analysis of impurity particle dynamics in the scrape off zone. The net erosion rate is nearly constant over the front face at < 1 cm/yr. The peak value of net erosion at the leading edge climbs to a value of 35 cm/yr for continuous operation (100% duty factor at 100% availability; for 50% availability, erosion rates would be half these values).

Table 5-10. Plasma Parameters for Limiter Erosion Calculations

Plasma edge temperature (at start of scrape off):

Variable, T_e = 20 - 1200 eV

Transport power to limiter:

P_{TR} = 80 MW, T_e > 20 eV

6 MW, T_e = 20 eV (radiative edge)

Charge exchange power to limiter:

P_{cx} = 26 MW

Plasma edge density (at start of scrape off):

$N_e = 2.5 \times 10^{19} m^{-3}$, T_e = 20 eV

$.5 \times 10^{19} \left(\frac{700 \text{ eV}}{T_e}\right)^{1.5} m^{-3}$, T_e > 20 eV

e-folding distances (at midplane):

(a)	density	δ_N = 3.75 cm
(b)	temperature	δ_T = 3.75 cm
(c)	particle flux	δ_P = 2.5 cm
(d)	energy flux	δ_E = 1.5 cm

Charged DT current to limiter:

$$I_{DT} = \frac{P_{TR}}{2KT_e(1 + \gamma)} \frac{\delta_P}{\delta_E}$$

where sheath factor γ = 3.1

Helium current to limiter:

$$I_\alpha = .05\ I_{DT}$$

Charge exchange sputtering:

Scaled with I_{DT} from PPPL DEGAS code results

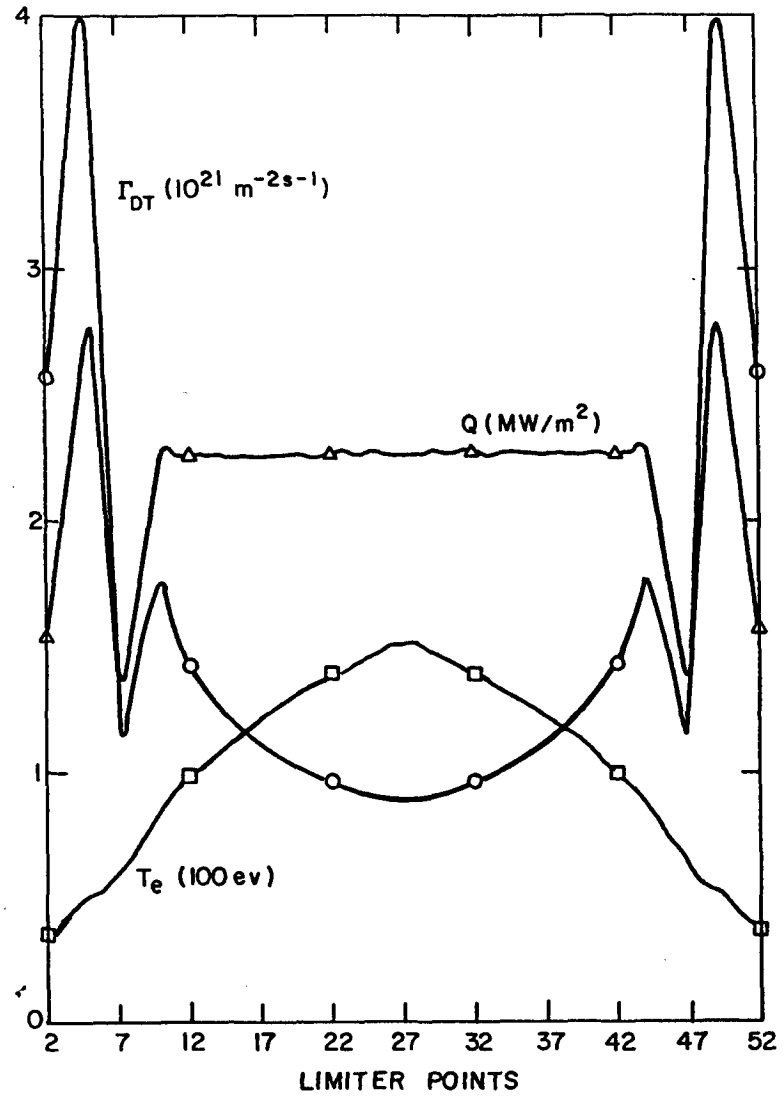

Figure 5-10. Temperature, particle flux, and heat flux across the limiter surface.

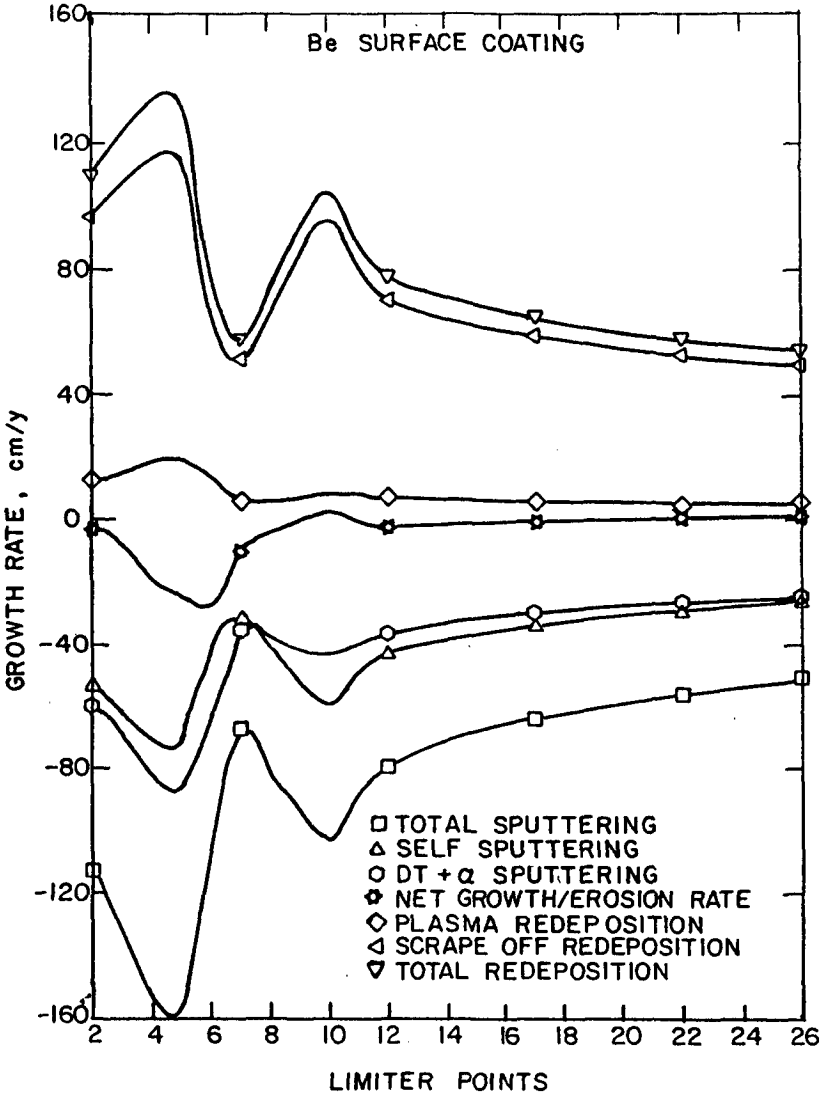

Figure 5-11. Contributors to the net growth/erosion rate for T_e = 150 eV.

Figure 5-12 shows the same contributors for the high edge temperature operation, T_e = 700 eV. Both DT and self sputtering are reduced from those levels observed in the 150 eV case. This occurs for two reasons: (1) the DT particle flux is reduced by a factor of 7/1.5 in the high edge temperature case and (2) sputtering coefficients are reduced in the 700 eV case since the incident particle energy spectrum is shifted to higher energies, away from those associated with maximum sputtering yields. The fraction of sputtered material that is redeposited is greater in the 150 eV case than at 700 eV. This results because the increased electron density at low temperatures decreases the mean free path of the sputtered neutral beryllium atoms in the scrape off zone. For example, the electron density just above limiter segment 8 is 2.3 x $10^{20} m^{-3}$ in the T_e = 150 eV case yielding a neutral Be mean free path for an atom emitted at one-half of the binding energy (the peak in the emitted distribution) of only 0.27 cm. The electron density above this segment in the T_e = 700 eV case is an order of magnitude lower producing a corresponding neutral atom mean free path of 2.7 cm.

For the midplane limiter analysis, leading edge erosion is enhanced by somewhat unfavorable field line geometry compared to a bottom limiter. For the midplane limiter, the poloidal field lines are almost vertical. A neutral beryllium atom sputtered from the leading edge need only traverse a short distance from the surface before becoming associated upon ionization with a field line that carries it several centimeters from its point of origin. The steep angles that the poloidal field lines make with the limiter surface produce then a net migration of coating material from the leading edge toward the front face of the limiter. This migration produces the net erosion for points 2 through 8 and the net build-up in the vicinity of point 10 shown in Figs. 5-11 and 5-12.

The net erosion rates expected from a beryllium surface at various temperatures are shown in Fig. 5-13. Note that erosion of the leading edge increases dramatically with decreasing edge temperature reflecting the increased particle flux and the energy dependence of the sputtering yields. As shown in the figure, very high peak erosion rates in excess of 25 cm/yr are predicted for 150 eV edge temperature operation. This value is clearly too large for acceptable DEMO operation. For low edge temperature operation, maximum erosion rates could be reduced by modifying leading edge geometry subject to limitations imposed by pumping requirements. However, another

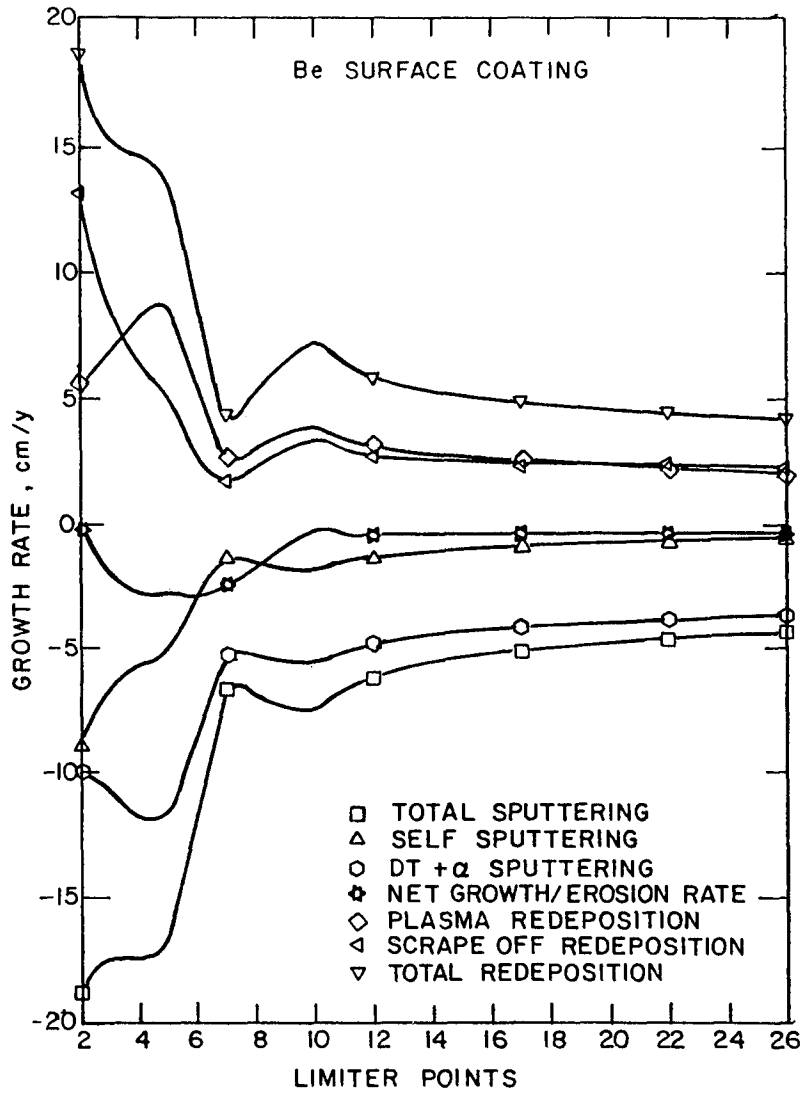

Figure 5-12. Contributors to the net growth/erosion rate at T_e = 700 eV.

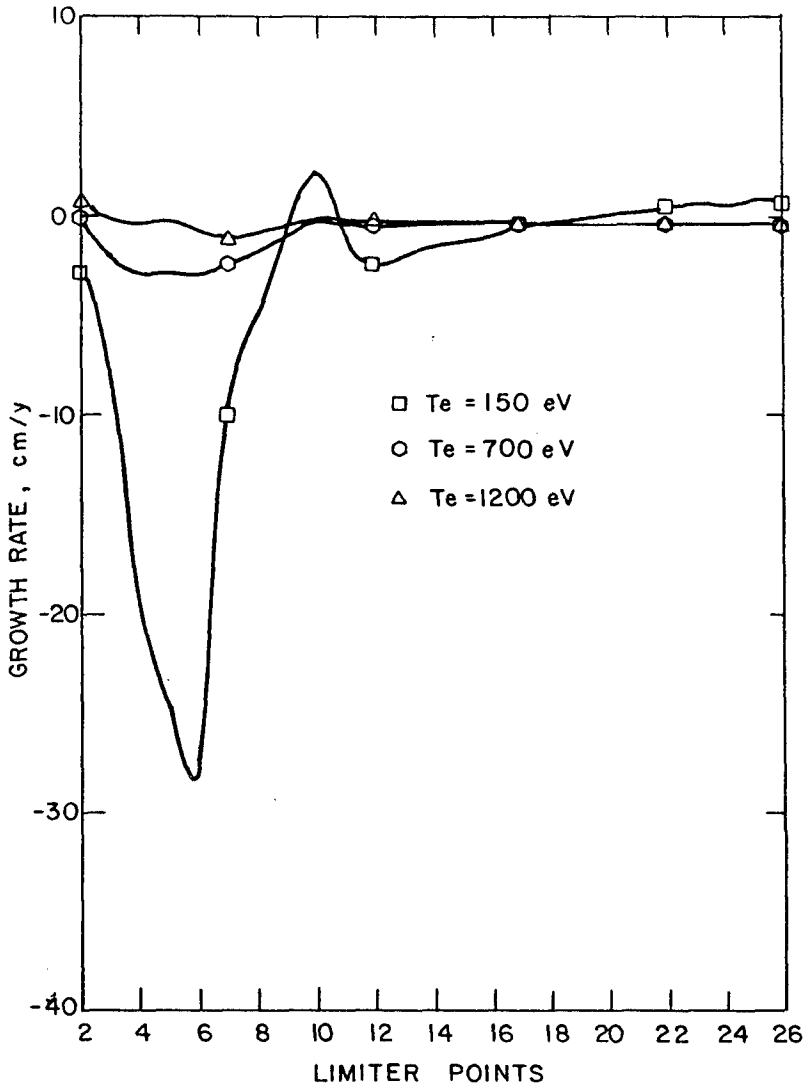

Figure 5-13. Net erosion/growth rates for a Be-coated limiter surface at various temperatures.

solution to the leading edge problem at low temperature has been investigated, but variation of leading edge geometry was not analyzed in detail.

During the course of this investigation, the REDEP code was modified so that the time-dependent behavior of the erosion profile across the face of the limiter could be studied. The code uses the net erosion profile computed in the previous iteration to calculate the new location of each surface segment after a specified period of time. The time increment used is chosen such that the maximum change in the location of any segment of the limiter is less than 1 mm. The original and redefined limiter profiles after sputtering for 150 eV and 700 eV edge temperatures are shown in Figs. 5-14 and 5-15, respectively. For the 150 eV case, a time increment of 48 hours was used, while for the 700 eV case where the peak erosion rate is considerably less, a time increment of 15 days was used. In each case, significant erosion of the leading edge eventually results, with a minor material buildup over most of the front face.

Time evolution analysis presently cannot be carried out beyond the point where shadowing begins to occur. Shadowing occurs when the plasma edge is no longer defined by the limiter tip (point 27 in this analysis) but instead is defined by some other point on the limiter surface. The REDEP code is not currently written to treat this case. Steps to modify the program logic have been initiated. Consequently, the redefined limiter face is shown after 75 days of continuous operation for the 700 eV case and after 12 days of continuous operation for the 150 eV case.

The analysis shows that spatial points experiencing net material buildup are subsequently subjected to higher particle fluxes yielding net erosion at these locations at later times. We find then that at high or low edge temperature operation the front face of the DEMO constant high flux limiter retains a spatial profile closely resembling its original shape. In either temperature regime, significant leading edge erosion eventually occurs if no corrective action is taken.

5.4.3 Leading Edge Options

Two conceptual solutions to the leading edge problem have been examined. For high edge temperature operation, in-situ recoating as described in Refs. 9-10 is proposed. In this method, an additional Be atom flux is supplied to the limiter by one of two injection methods. The first is "plasma

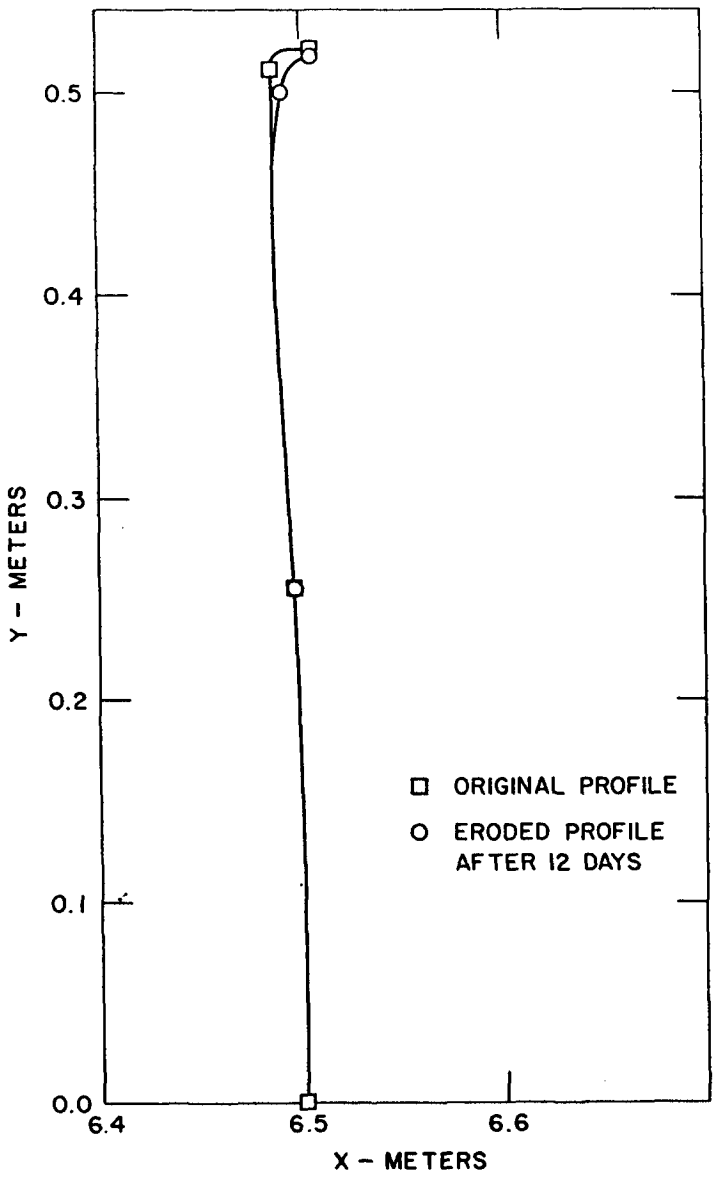

Figure 5-14. Original DEMO limiter profile and the eroded profile expected after 12 days continuous operation at T_e = 150 eV.

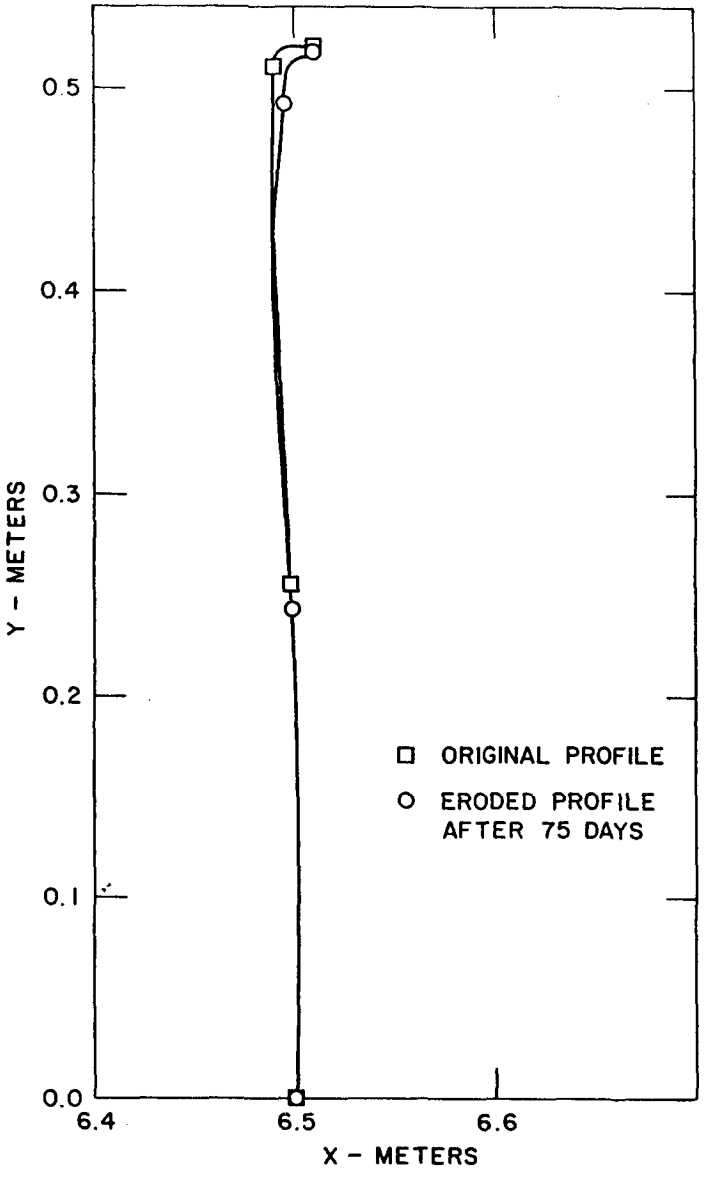

Figure 5-15. Original DEMO limiter profile and the eroded profile expected after 75 days continuous operation at T_e = 700 eV.

injection",[9] whereby beryllium is supplied to the bulk plasma by gas puffing or pellet injection. The second method, "edge injection",[10] involves injection of beryllium gas into the scrape off zone near the limiter leading edge. Both methods have been simulated with the REDEP code, and the results are reported in Ref. 11. At an edge temperature of 700 eV, injection schemes producing bulk plasmas containing 1% to 2% Be result in the reduction of peak erosion rates by 55% and 75%, respectively. For the more effective edge injection schemes, net growth of the leading edge coating can be achieved. By a combination of techniques and proper tailoring of the edge injection profile, it is possible that the net growth/erosion rate could be held to very low values. Obviously, this would require experimental verification.

A second proposed solution to the leading edge problem[1] involves the use of dual material coatings on the limiter surface. On the front face, where self sputtering must be limited, a low-Z material is used, while on the leading edge, where low DT sputtering and high redeposition is desired, a high-Z material is used. A beryllium-tungsten combination was assessed for 150 eV edge temperature operation. Analysis of tungsten ion kinetics in the scrape off zone indicates that, on the average, redeposited tungsten ions return to the limiter surfce in the $Z \simeq +4$ charge state. Due to the presence of the accelerating sheath potential, modeled as $3kT_e(x)$ where $T_e(x)$ is the local electron temperature, the use of tungsten is limited to regions where $T_e(x)$ is below 50 eV. Remaining within the bounds imposed by this constraint, limiter points 2 through 7 and 47 through 52 were modeled as being tungsten coated in the REDEP calculation. A typical tungsten atom mean free path was found to be between 0.4 and 0.8 mm for these segments so that 96% or more of the sputtered tungsten atoms return immediately to the same spatial increment from which they were sputtered. Consequently, very little tungsten migration or loss is observed and this portion of the limiter surface remains intact almost indefinitely for normal operating conditions.

Beryllium sputtering from the remaining limiter front face segments, points 8 through 46, was also investigated. Sputtering yields from the leading edge were modified to reflect the dual material mode of operation. In the iterative procedure used to obtain the erosion profile, sputtering yields in each iterative step were restricted so that the sputtered beryllium atom source term could not exceed the redeposited beryllium flux at any point on the leading edge. As one would expect, all beryllium deposited on the leading

edge is quickly sputtered away yielding a net erosion/growth rate of zero on the leading edge. A comparison of the net erosion rates found for the all-beryllium-coated limiter and the dual-material limiter is shown in Fig. 5-16. As mentioned above, no net limiter erosion or growth is predicted for the leading edge segments (points 2 through 7). The first beryllium segment (point 8) now experiences the peak erosion rate of about 12 cm/yr. Erosion on this portion of the limiter increases over that predicted in the all-beryllium case since the leading edge no longer supplies a large redeposited flux of beryllium. Obviously, more desirable limiter lifetimes result since the maximum erosion rate drops from 28 cm/yr to 12 cm/yr.

After 12 days of continuous operation, the time-dependent REDEP analysis predicts the limiter profile shown in Fig. 5-17. The results indicate that a depression occurs near the first few beryllium segments. As this depression develops, the particle flux to limiter segments in this vicinity is altered largely due to the changing angle of orientation of these segments. What results is the flatting of the erosion profile with time shown in Fig. 5-18. We see that after 12 days of continuous operation, the peak erosion rate drops from 12 cm/yr to 9 cm/yr. Eventually, one finds that the first beryllium segment (segment 8) is eroded to the point where it is completely shadowed by the tungsten portion of the limiter. In this situation, segment 8 receives no charged particle flux. Segments further down on the limiter face are subjected to an increased particle flux since the effective limiter surface area has been reduced. As mentioned, modification to the REDEP code are required before this phenomenon can be investigated in detail. However, the results indicate that for a dual-material limiter erosion of the low-Z coating may be naturally spread over a large portion of the front face rather than being concentrated on one limiter segment. This would result in extended limiter lifetimes.

5.4.4 Limiter Face Shaping

The limiter design proposed for DEMO requires detailed shaping of the front face to achieve the constant heat flux profile shown in Fig. 5-10. In order to assess the benefits resulting from this shaping, a second limiter design constructed with a simple flat vertical face was also analyzed. This flat face construction shown in Fig. 5-19 would certainly simplify the fabrication process. The spatial variation of temperature, particle flux, and

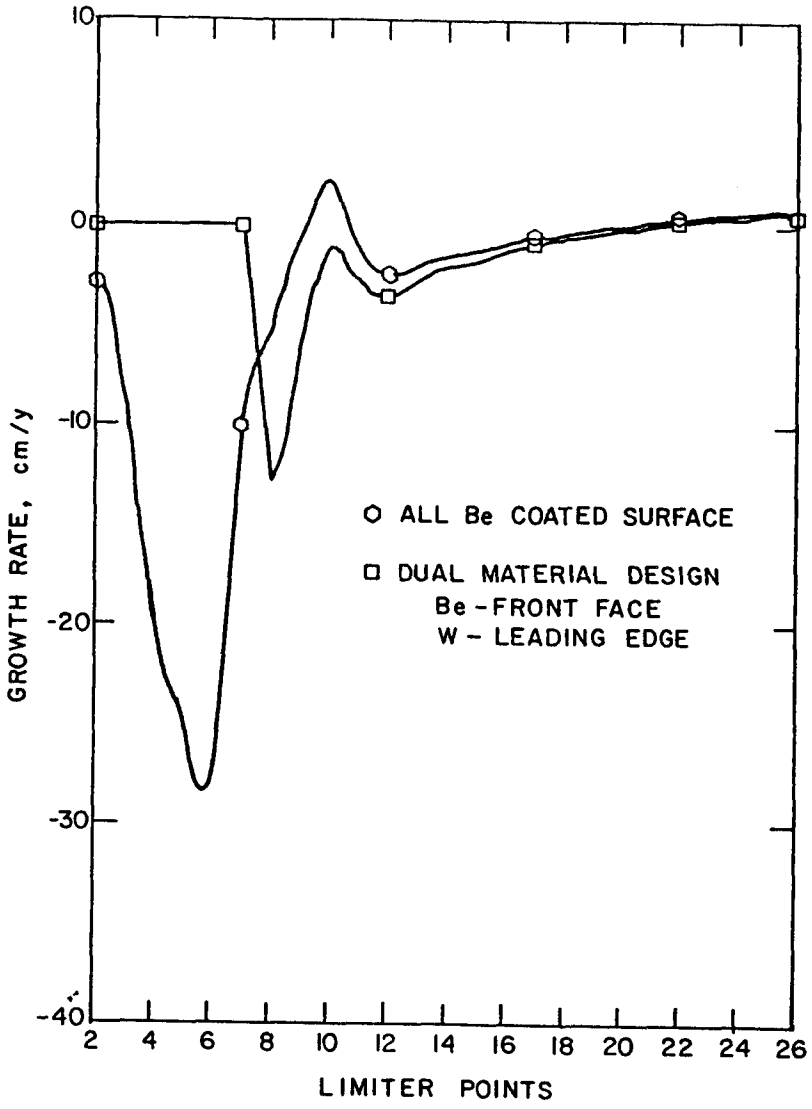

Figure 5-16. Net growth/erosion rates for a Be-coated limiter and for a dual-coating material design.

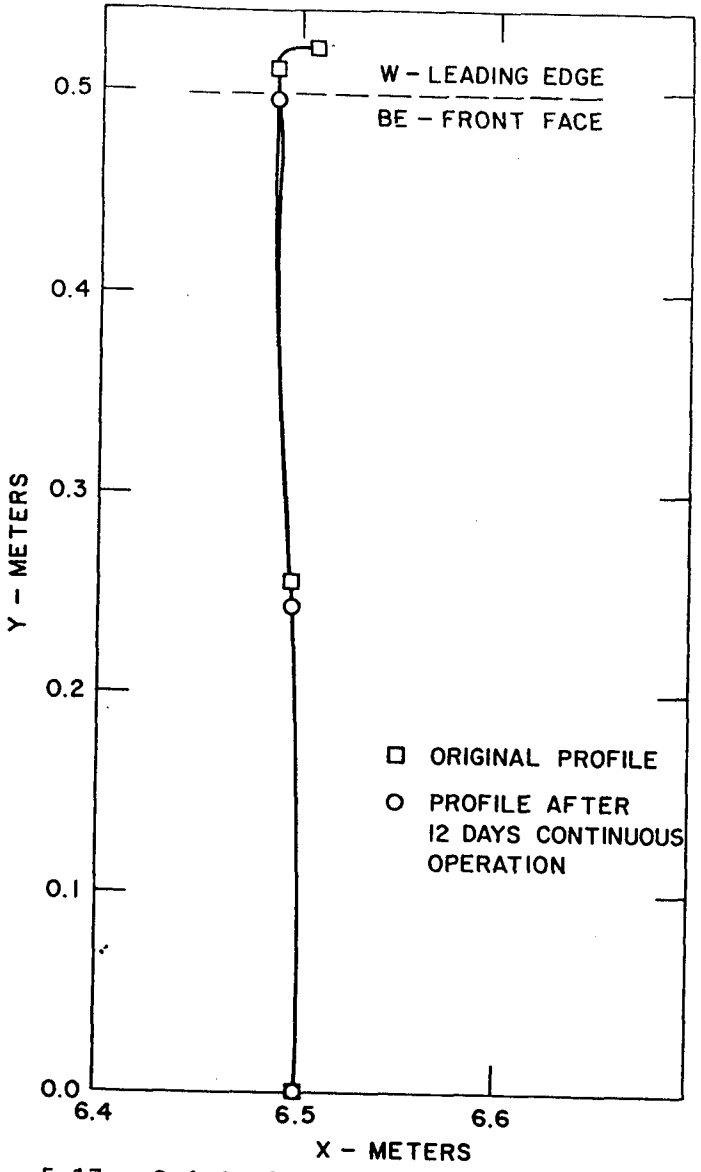

Figure 5-17. Original DEMO limiter profile and the eroded profile after 12 days continuous operation at T_e = 150 eV for the dual-coating material design.

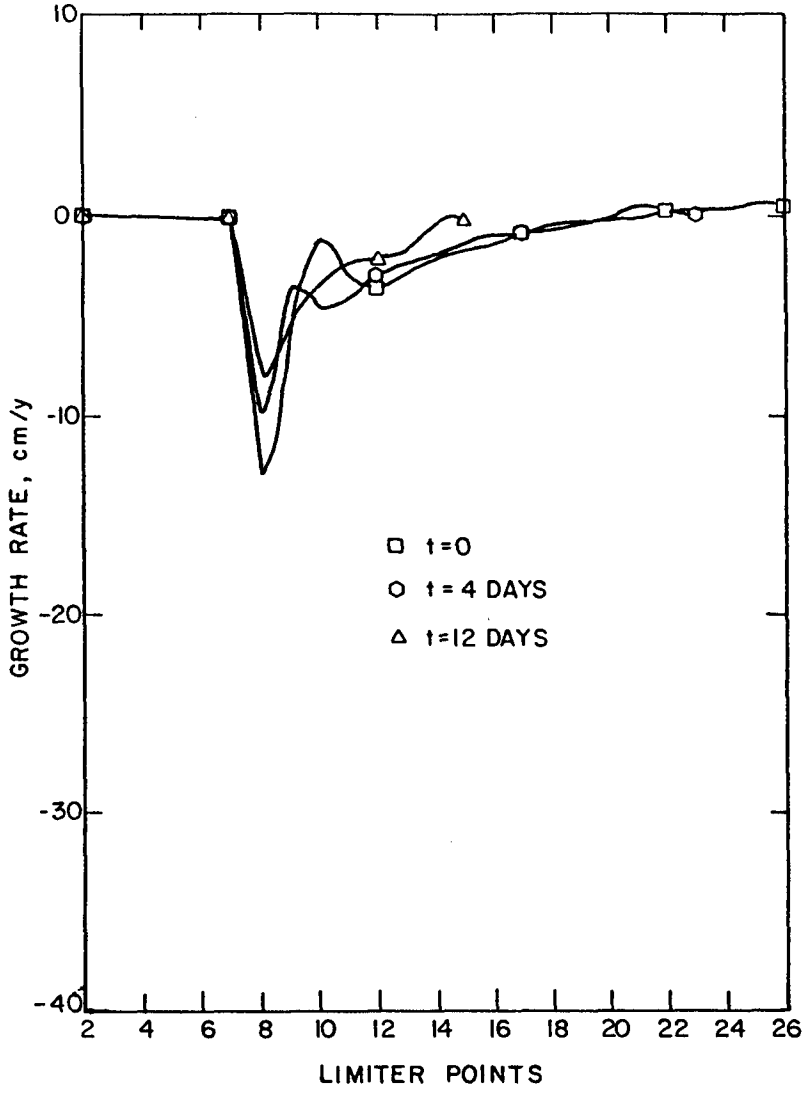

Figure 5-18. Net growth/erosion rates for the Be front face, W leading edge limiter surface after 0, 4 and 12 days continuous operation at T_e = 150 eV.

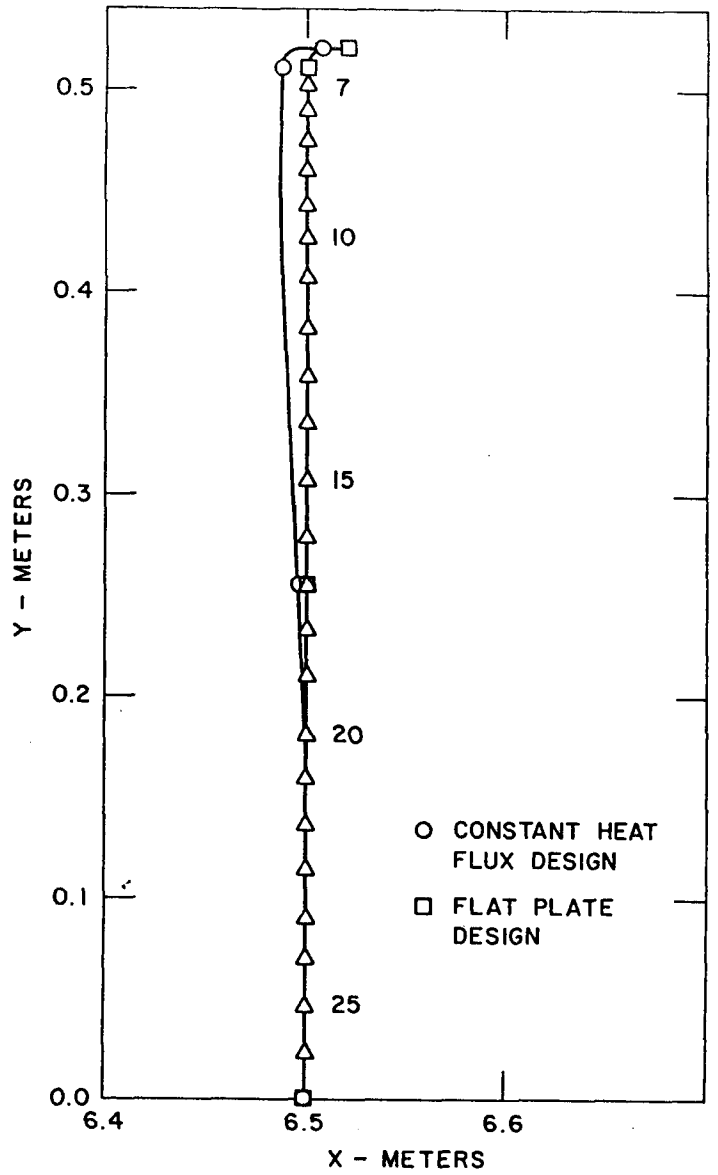

Figure 5-19. Reference DEMO limiter profile and the flat plate limiter profile.

heat flux along the limiter surface at T_e = 150 eV is shown in Fig. 5-20. Because this limiter face is not curved to conform to the plasma shape, field line bunching occurs near segments 17 and 37. This produces a fairly large particle flux in these regions and smaller particle loads near the limiter tip.

The net erosion profiles obtained for an all-beryllium-coated flat limiter face and for a dual material, beryllium/tungsten, flat face design are shown in Fig. 5-21. Because of the energy dependence of the sputtering yields, maximum erosion rates still occur on or near the leading edge. A net material migration is again found to take place with beryllium being carried down the face toward the limiter tip. The field line bunching in the vicinity of segment 17 results in a material buildup in this region of about 5 cm/yr for the all-beryllium and the dual-material design. For both designs, the limiter tip gradually erodes away, losing its coating material to the bulk plasma. Near the tip, a large fraction of the limiter face, segments 20 through 26 on the top half and the corresponding segments on the bottom half, are shadowed by the growing bulge in the face near segment 17. This reduces the effective limiter surface area by a significant amount. While one would expect this bulge to wear away in time, the drastic changes in limiter shape associated with the migration of large amounts of coating material and the accompanying changes in the spatial heat flux profile and coating thicknesses would yield difficult heat removal problems for this limiter.

We conclude then that some limiter surface shaping is highly desirable for a midplane limiter. The constant heat flux design proposed as the reference DEMO limiter tends to maintain its original profile for some time (see Figs. 5-15 and 5-17), while the simple flat plate design immediately deviates from its original profile. The length of time over which the DEMO reference limiter can be expected to retain its constant heat flux profile depends upon the plasma edge conditions. As mentioned earlier, modification to the REDEP code must be completed before more detailed time-dependent calculations can be carried out.

5.4.5 Discussion and Conclusions

The symmetric, midplane, constant heat flux limiter shown in Fig. 5-9 is taken as the reference design for DEMO. Operation at a variety of plasma edge temperatures, 20 eV to 1200 eV, has been analyzed, and satisfactory limiter

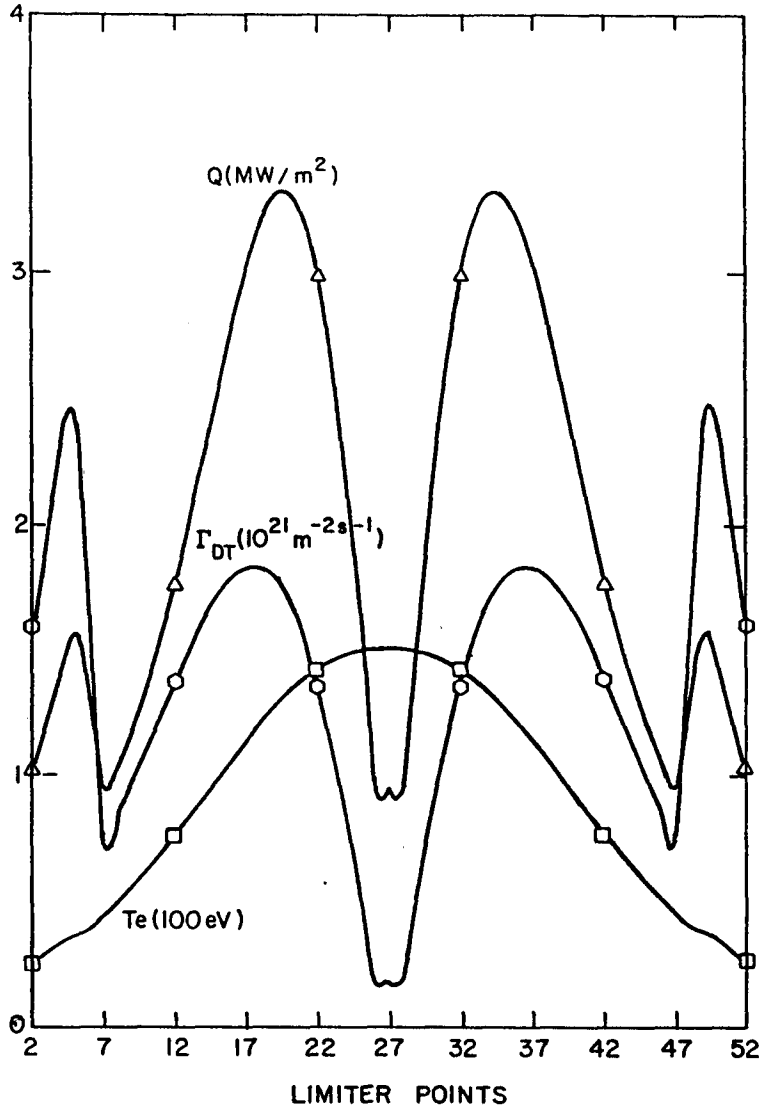

Figure 5-20. Temperature, particle, and power flux across the flat plate limiter surface at T_e = 150 eV.

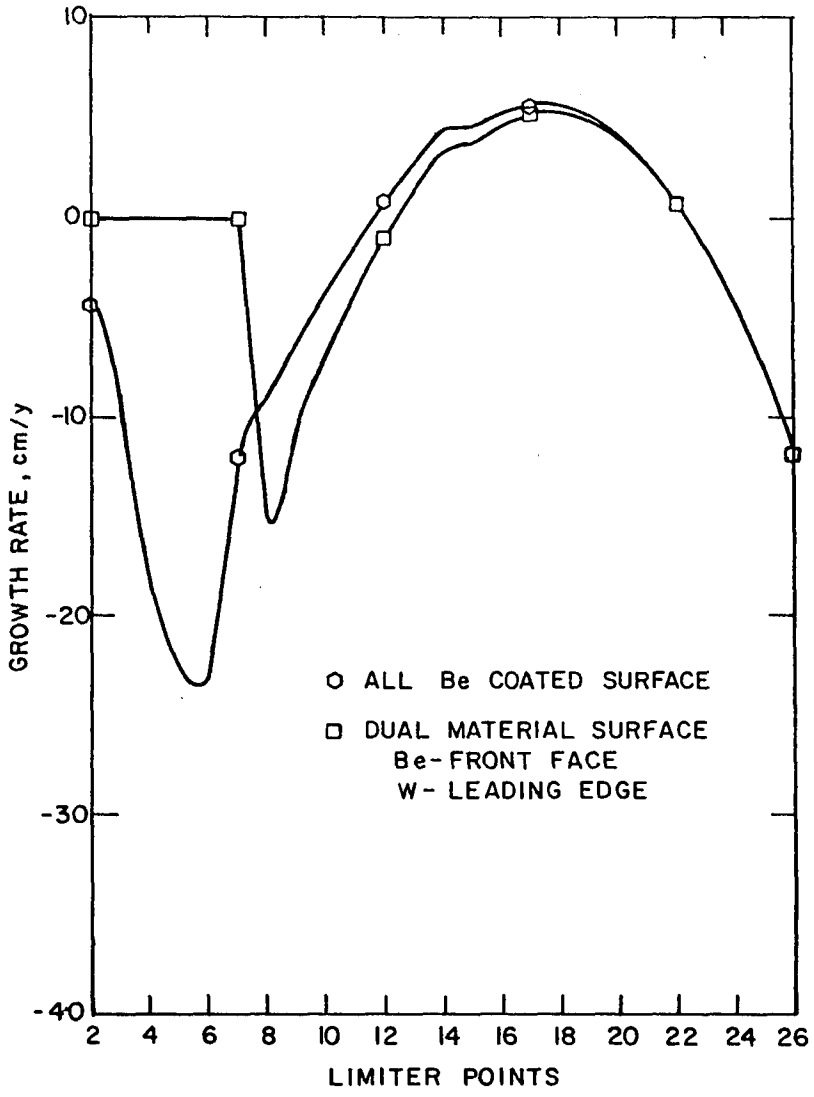

Figure 5-21. Net growth and erosion rates on a flat plate limiter at T_e = 150 eV for an all Be-coated surface and for a dual-material surface.

performance appears to be achievable in each temperature regime. For high edge temperature operation at T_e = 700 eV, peak erosion rates of 2.9 cm/yr at continuous operation are predicted on the leading edge when beryllium is used as a surface coating material. For this edge temperature, gas puffing or injection could be carried out in order to reduce the limiter leading edge erosion. At T_e = 1200 eV, erosion rates near zero are predicted throughout the limiter surface including the leading edge for beryllium coatings.

At lower edge temperatures, enhanced erosion prohibits the use of beryllium or other low-Z coatings on the leading edge. A dual coating material design is proposed for operation in this regime. Analysis of a beryllium/tungsten limiter at T_e = 150 eV shows that a 57% reduction in the initial maximum erosion rate, from 28 cm/yr to 12 cm/yr (Fig. 5-16), can be expected for the dual coating material design. Note, though, that time-dependent analysis predicts further reduction in the maximum erosion rate down to less than 9 cm/yr after only 12 days of continuous operation. This reduction in the rate of erosion, shown in Fig. 5-18, is due to the change in the surface orientation that results as erosion takes place. The time integrated maximum erosion is found to be ~ 4 mm after 12 days of continuous operation. For later times, the erosion will continue to drop so that continuous operation in excess of several months may be possible if no further steps are taken to limit erosion.

Injection schemes could be used to reestablish the beryllium coating for low edge temperatures. In the dual-coating design, note that all of the injected beryllium deposited on the leading edge would eventually migrate to the front face where it is needed. Injection of beryllium may not be necessary for the dual material limiter design, since erosion of the first beryllium sector may be self limiting. As the depression shown in Fig. 5-17 develops, the eroded surface will be shadowed by the tungsten portion of the leading edge. Since the tungsten segments are essentially stationary, the particle and heat flux at points further down on the limiter face, below the depression, will increase. This enchances erosion on segments further down on the limiter, but the net effect is to spread the damage out over a larger portion of the limiter face. This would produce extended operational lifetimes. The modifications being made to the REDEP code must be completed before this type of process can be analyzed in detail and before any estimate of the resulting increase in operational lifetime can be made.

The results reported here for a midplane limiter differ somewhat from those obtained for a bottom limiter configuration such as that proposed for INTOR.[1,11] For the midplane limiter, the poloidal field lines intercept the limiter surface at very shallow angles all along the front face. Consequently, a neutral particle need only travel a short distance before finding itself in the vicinity of a field line which will carry the ionized particle several cenimeters away from its point of origin. For example, at T_e = 150 eV, we find that less than 70% of the material sputtered from segment 8 of the midplane limiter surface is redeposited on that same segment. The remaining sputtered material is spread over the rest of the limiter face or finds its way into the bulk plasma or on to the vessel walls. In contrast, the angles at which poloidal field lines intercept segments of the bottom limiter face are less shallow. We find then that at edge temperatures on the order of 150 eV, ~ 95% of the material sputtered from any segment of the front face, returns to that same segment.

One should note that neither limiter design has been optimized with respect to these material migration considerations and that satisfactory operation appears to be possible with either the midplane of the bottom limiter at a variety of edge temperatures.

A number of physical processes modeled in this analysis have yet to be verified experimentally. Most notably, material properties of the redeposited surface must be determined. Presently, the redeposited surface is modeled using energy-dependent sputtering yields anticipated for the original surface coating. For the dual material limiter design, material interface properties associated with the migration of the high- and low-Z material over one another must be investigated. These and other high priority items for near-term experimentation are discussed in Chapter 3.

5.5 Configuration

5.5.1 Limiter Location

The location of the limiter has an impact on the overall reactor design and configuration. Three locations for a toroidal belt limiter were evaluated. These are: the outer midplane (Fig. 5-22a), the upper or lower 45° blanket segment (Fig. 5-22b), and the bottom of the plasma chamber (Fig. 5-22c). All three limiter configurations appear to be capable of adequate impurity control during normal operation. The major considerations for limiter placement are: (1) sensitivity to variations in plasma shape and position, (2) impact on reactor and magnet size, (3) impact on tritium breeding, (4) response to disruptions, (5) impact on component fabricability, and (6) impact on reactor accessibility.

The midplane limiter appears to be the least sensitive to plasma variations. First, the curvature of the magnetic field lines is lowest at the midplane, and the lines are symmetric about the midplane. This means that small vertical changes in the plasma position should not cause major changes in heat and particle flux distributions to the limiter. Second, the field lines in this location are relatively insensitive to the elongation and triangularity of the plasma and, therefore, the overall plasma shape should have little effect on the limiter operation. On the other hand, the bottom and 45° locations are expected to be more sensitive to both the plasma shape and position.

The midplane location results in the minimum size blanket/shield and TF coil configuration. This configuration is more relevant to commercial applications because of the reduced cost associated with the reduced reactor size. The incorporation of the vacuum duct at the bottom location necessitates increasing the blanket thickness by $\sim$ 90 cm. The additional size required for the TF coils is also predicted to be $\sim$ 90 cm in the vertical direction. The savings is estimated to be $\sim$ 3% of the total TF coil cost.

The other considerations have a minor impact on the selection of the limiter location. The tritium breeding ratio is relatively unaffected by the limiter location. Disruptions may be less prone to strike the outer midplane, but there is considerable uncertainty in this area. At any rate, the low number of disruptions during the reactor lifetime (50) will not significantly

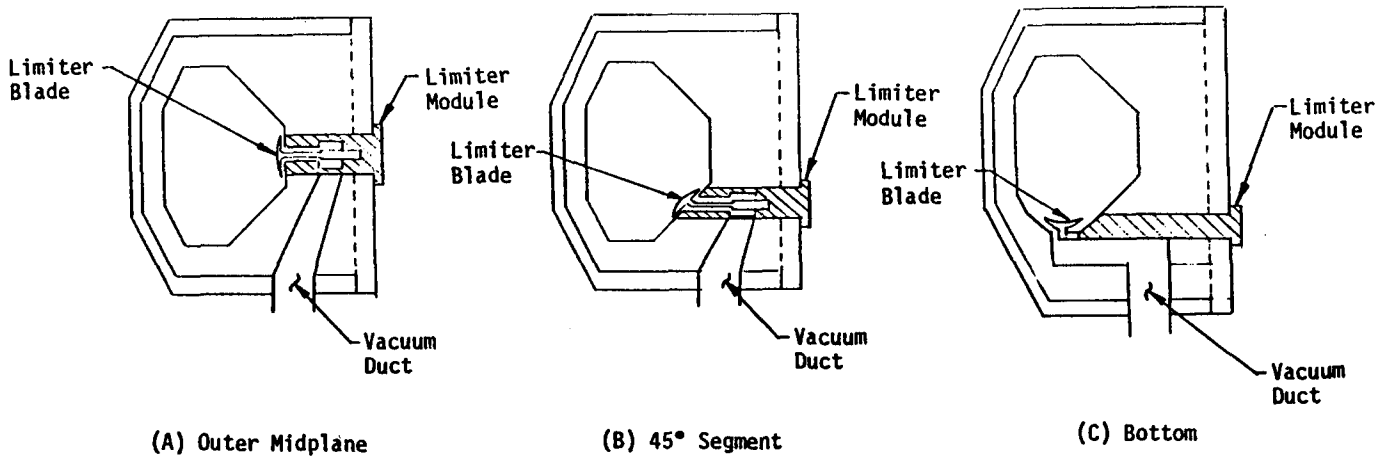

Figure 5-22. Limiter location options.

impact the limiter operation, since the limiter has been designed to survive the anticipated disruption damage. The midplane location offers a symmetrical design for both the limiter and blanket about the midplane, which should result in somewhat easier fabrication. One disadvantage of the midplane location is that it reduces the available access for other reactor penetrations, such as auxiliary heating and diagnostics. However, the principal goal of DEMO is to demonstrate high availability and reliability. This requirement is in contrast to an experimental device such as FED/INTOR, where space for diagnostics and test modules is of primary importance. Therefore, the loss of this space to the limiter modules is not considered significant.

Because of the advantages of the midplane location, it has been selected as the reference configuration for DEMO.

5.5.2 Limiter Configuration

The limiter configuration is shown in Figs. 5-23 and 5-24. The concept utilizes a removable limiter module. One module is used in each of the eight reactor sectors. Each module consists of six replaceable limiter blade segments mounted by coolant manifolding to the main body of the module.

The front surface of the limiter blade is contoured in the poloidal direction to obtain a constant heat flux over the surface. The result is a surface that is nearly flat due to the curvature of the flux lines in this area. The overall height of the blade in the poloidal direction is 100 cm. Each blade is flat in the toroidal direction and 85 cm in length. The blade consists of a water-cooled substrate covered by a protective surface. Water channels run in a poloidal direction over the entire limiter including the back and neutralizer area. Coolant channels follow the back of the limiter to the leading edges, to the front center and then through passages leading to the return manifold. The protective material on the face of the limiter is beryllium, 2.5 cm thick. The back surface of the limiter is contoured such that flux lines do not impinge on the blade until they contact the neutralizer portion near the center.

The pumping channel behind the blade is set at 10 cm and extends for ~ 50 cm behind each edge. The blade thickness varies from ~ 1.5 cm at the leading edges to 10 cm near the neutralizer plate. This thickness can be increased or decreased somewhat to accommodate the electromagnetic loads;

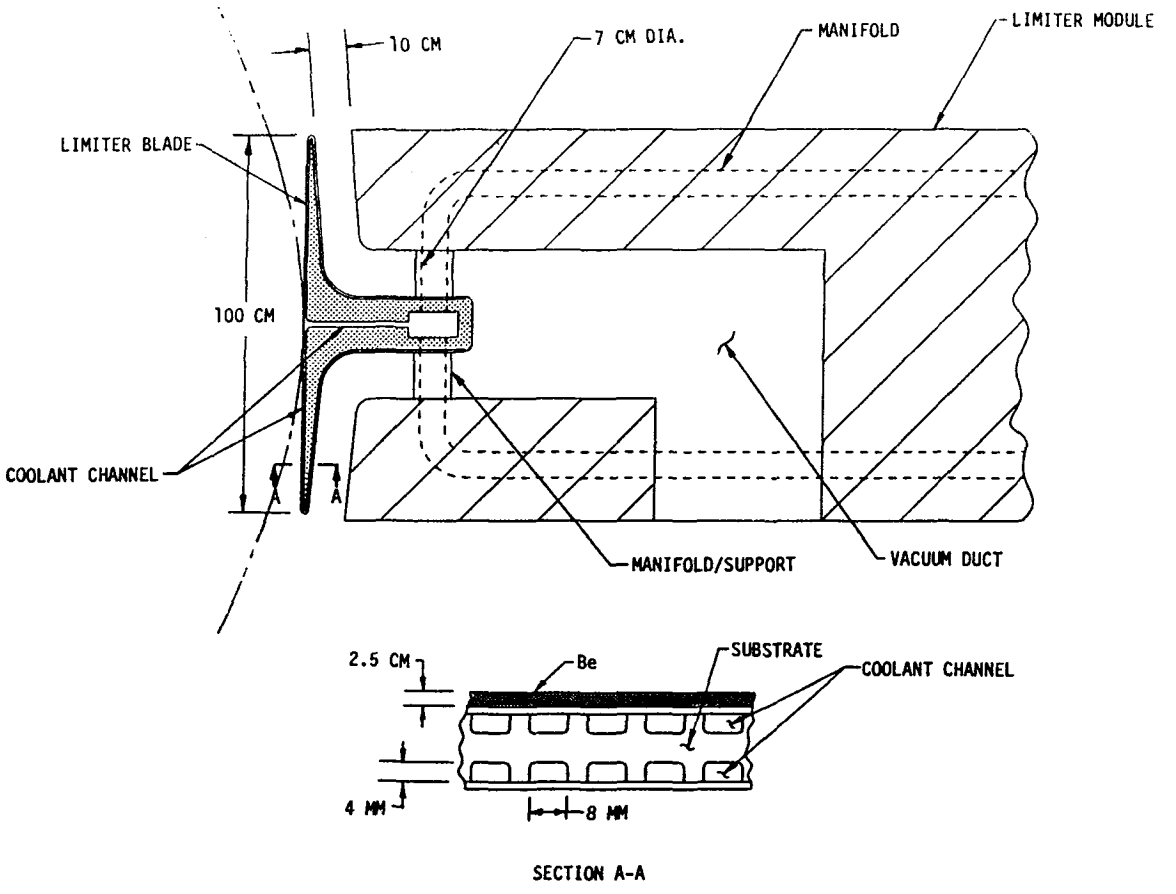

Figure 5-23. Cross section of DEMO limiter design.

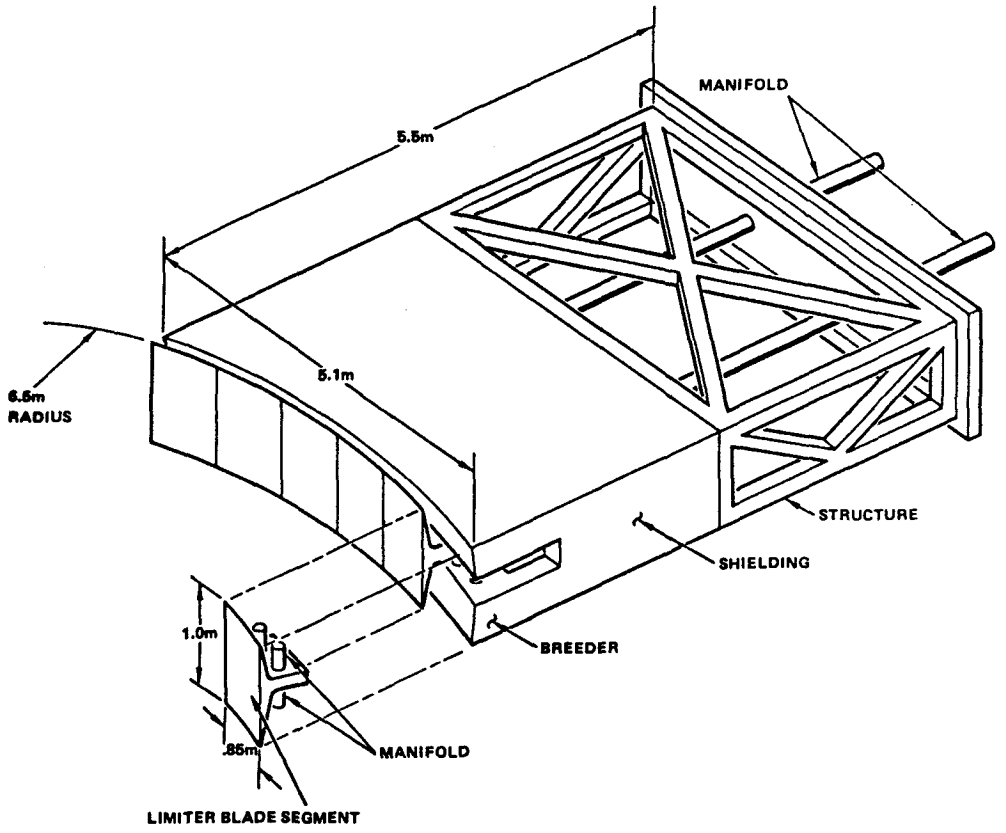

Figure 5-24. Limiter module.

however, the thickness of the leading edge should be as small as possible to maximize the pumping capacity. The thickness of the center section (neutralizer area) can be altered somewhat; however, adequate room must be allowed for supply and return water manifolds.

Three possible designs of the leading edge are shown in Fig. 5-25. At this area, the surface material must make the transition from a relatively thick layer (2.5 cm) of beryllium to a thin layer of tantalum. Additional work is required to investigate the erosion/redeposition at this transition. Concept (a) of Fig. 5-25 shows a design where the cooled substrate is maintained at a constant thickness, and the beryllium is tapered to the leading edge. As the beryllium thickness decreases with time, more of the substrate near the leading edge will possibly be exposed; therefore, tantalum is extended beneath the beryllium. In concept (b), the thickness of the substrate at the leading edge is increased. As the beryllium thickness decreases, the leading edge remains the same, resulting in a discontinuity at the front surface interface. This design may also be difficult to fabricate, and it creates a rather complex coolant flow path. In concept (c), the

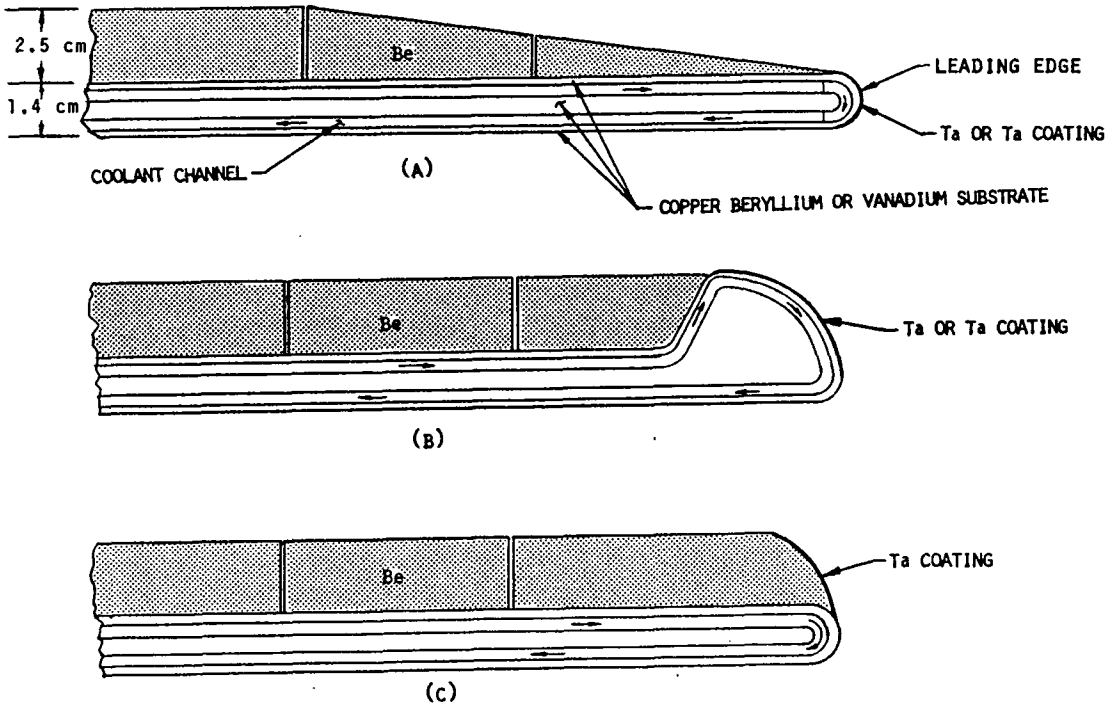

Figure 5-25. Limiter leading edge design concepts.

substrate and beryllium are maintained at a constant thickness, and a thin tantalum coating is extended over the beryllium front edge. As the beryllium thickness decreases, a discontinuity will form at the transition, unless the edge of the taltalum erodes or is removed in some manner, in which case a flat profile will be maintained. Concepts (a) and (c) would likely reach an equilibrium shape and permit use of a smaller leading edge. Further investigation is required to determine which design is best.

5.5.3 Limiter Module

The limiter module consists of the limiter blade, a breeding blanket, shielding, manifolding, and a vacuum plenum. The limiter module is shown in Fig. 5-24. The six limiter blades on each module are supported by cooling manifold piping that is 7 cm I.D. This piping can be cut and rewelded for limiter blade replacement in the hot cell. The breeding blanket is located in the 70 cm nearest the limiter blade. Its construction is similar to the other

portion of the blanket. It utilizes two coolant lines and two purge lines on each one-half of the module. A vacuum plenum slot behind the limiter connects the limiter pumping to the vacuum system through a low conductance interface. Shielding is located outboard of the plenum area. The shielding thickness is 202 cm which a composition of concrete, beryllium carbide, water, steel, and lead.

These compounds attach to a structural frame that is attached to a vacuum door cover. Manifolding is joined together in the area between the vacuum door cover and shield to minimize the number of lines that penetrate the vacuum door and that must be disconnected during maintenance.

The outer vacuum door will be sealed to the blanket module by an elastomer seal.

5.5.4 First Wall

The mechanical design of the first wall is discussed in Section 6.2. It consists of a panel coil cross section that is an integral portion of the blanket. The plasma side layer consists of 4 mm of stainless steel which is coated with 2 mm of Be. It can absorb 50 plasma disruptions with a loss of $\sim$ 2 mm of material over the plant life. Areas next to the limiter have not been evaluated; however, it is expected that the erosion due to charge exchange neutrals will require a thick coating of beryllium locally.

5.6 Materials Selection

A materials data base assessment has been conducted as part of the impurity control and first-wall engineering. The purpose of this assessment is to evaluate and develop a data base for candidate materials for the first-wall and limiter. Recommended values for critical materials properties are provided for use in the design activity. Uncertainties in the materials data base have been determined so that the impact on critical design parameters can be evaluated. The limiting features and favorable characteristics of the primary candidate materials are summarized and key materials research and development needs have been identified. Since it is predicted that material eroded from the first wall and limiter by physical sputtering, plasma disruptions, etc. will redeposit on the limiter or first wall or other in-vessel components, this assessment considered both material in the as-fabricated form and material characteristic of that redeposited during reactor operation.

This assessment has focused primarily on (1) materials that will be exposed directly to the plasma, (2) candidate heat-sink materials and (3) fabrication and characterization of duplex walls (coating/cladding on structural substrate) for use in the pumped limiter and divertor applications. Candidate plasma-side materials include low-Z (atomic number), medium-Z and high-Z materials listed in Table 5-11. A greater emphasis was placed on the underlined materials in the table. Properties considered include physical sputtering by energetic plasma particles and wall eroded materials (self-sputtering), chemical sputtering, H/He retention/release, and critical bulk materials properties including radiation effects.

The assessment of the heat-sink materials has focused primarily on copper-alloys with a high thermal conductivity and vanadium alloys, which are representative of the group-V refractory metals (Nb and Ta). Properties evaluated include physical and mechanical properties, corrosion/compatibility, radiation effects and fabrication characteristics.

The duplex wall, which consists of a coating or cladding of the plasma side materials on the heat-sink structure, is believed to offer the best design solution for the limiter. Methods of application of the coating/cladding to the substrate have been evaluated and the performance characteristics of the duplex structure have been assessed. Bonding methods

Table 5-11. Candidate Limiter/Divertor Materials

Plasma-Side Materials	
Low-Z:	C, Be, B, TiC, SiC, B_4C, BeO
Medium-Z:	Stainless Steel, V
High-Z:	W, Ta, Nb
Heat-Sink Materials	
Copper Alloy	
Vanadium Alloy	
Niobium Alloy	

considered include deposition processes such as plasma spray, direct diffusion bonding and brazing. Emphasis has been placed on the bonding of beryllium, graphite, silicon carbide, beryllium oxide, tungsten and tantalum to the candidate heat sink materials.

5.6.1 Plasma Side Materials

5.6.1.1 Physical Sputtering

Previous INTOR studies have indicated that physical sputtering by energetic plasma particles (D, T, He) which strike the wall is a major contributor to wall erosion.[2] Data for light ion sputtering indicate that physical sputtering yields are highly energy dependent typically peaking at energies of a few hundred electron volts for low-Z wall materials and a few thousand electron volts for medium and high-Z wall materials.[12,13] One possible solution for minimizing the erosion caused by light ions is to use a low-Z wall and maintain a relatively high edge temperature so that the incident ions are well above the peak yield. A second approach is to use a high-Z wall and maintain the plasma edge temperature below the threshold for light ion sputtering. Recent calculations (see Sec. 5.4) indicate that much of the wall material eroded from the limiter or divertor will be ionized within a short distance from the surface. These ions will then be accelerated back to the limiter surface by a sheath potential and produce self-sputtering. If the self sputtering yield exceeds unity, a propagating wall erosion problem will occur. One possible solution is to use a low-Z wall

material that will have a self sputtering yield less than unity at all incident energies. A second possible solution is to maintain a very low plasma edge temperature so that the self sputtering yield of the wall material remains below unity. For this case, the high-Z wall materials, such as W and Ta, have the highest energy (up to ~ 700 eV) at which the self sputtering yields exceed unity.

The present assessment has focused primarily on defining the energy-dependent sputtering yields for the light plasma particles (D, T, He) and the self-sputtering yields for the primary candidate wall materials, including selected compounds. Considerable experimental data on light-ion (D, He) sputtering for normal incidence have been generated in recent years. Much of these data are available in two compilations.[12,13] Variations in reported sputtering yields for similar systems have generally been attributed to differences in experimental methods (measurement of erosion yield), possible contamination effects (particularly for oxygen active materials such as Be and Al), and differences in surface condition or microstructure of the wall material. Although significant differences exist in the data base for certain materials, trends in the data base can generally be obtained within an uncertainty of a factor of two. Several analytical models[14-19] have been developed to provide estimates of the sputtering yields for materials and conditions for which data do not exist. These models are particularly useful for predicting tritium sputtering yields and self sputtering yields, both of which are dominant contributors to the wall erosion. For light ions, two empirical models[18,19] provide the best correlations with existing data for energy-dependent sputtering yields, and therefore, are recommended as a basis for the present INTOR study. The IPP model[18] which is a correlation of the Garching data, gives the sputtering yield in terms of a reduced energy parameter $E' = E/E_{th}$, where E_{th} is the threshold energy for sputtering. The total sputtering yield at normal incidence is given by

$$Y = Q(M_1, M_2, E_B)\, Y_N\,(E')$$

where Q is an empirical fitting parameter and Y_N is the normalized sputtering yield given by

$$Y_N = \left(8.5 \times 10^{-3}\ E'\right)^{1/4} \left[\left(1 - \frac{1}{E'}\right)\right]^{7/2}$$

Simple approximations are available[17] for Q and E_{th}, which allow estimates of normal incidence sputtering yield within a factor of two for most materials up to E' = 20. For higher energies, Y_N can be modified[17] by incorporating an additional function, viz., the ratio $S_n(E')/S_n(20)$. Excellent correlations with the Garching data result if experimentally determined values of Q and E_{th} are used in the model.

The computer code DSPUT[19] represents another empirical approach for predicting physical sputtering yields. In this model recent physical sputtering data have been incorporated into an analytical expression for the sputtering yield. The sputtering yield for normally incident particles is given by:

$$S(E) = \frac{CC'}{U_o} Z_1^A (Z_2 - 1.8)^2 \left(\frac{M_1 - 1}{M_2}\right)^{1.5} \frac{(E - E_{th})}{(E - E_{th} + 50\, Z_1^B\, Z_2)^2}$$

where

$C = 1$ for scoping studies

$C' = 500$ for $M_1 > 1$

$$B = \frac{40}{Z_1 + 40}$$

$$A = B - 0.2$$

$$E_{th} = \frac{(3M_1 + M_2)^2}{4\, M_1\, M_2} U_o$$

U_o = binding energy (eV)

The DSPUT code can be used to calculate normal incidence sputtering yields for both light and heavy ions on all targets at energies up to ~ 100 keV.

Figures 5-26 and 5-27 show a comparison of the energy dependent sputtering yields predicted by the IPP and DSPUT codes with some of the experimental data for Be and tungsten. The reported light-ion sputtering data for beryllium are very similar to that for BeO. It is generally believed that the beryllium was contaminated with oxygen and that the reported Be data are indicative of an oxide film on Be. Therefore, the sputtering yield predicted by the DSPUT code for beryllium is believed to be a better estimate of the

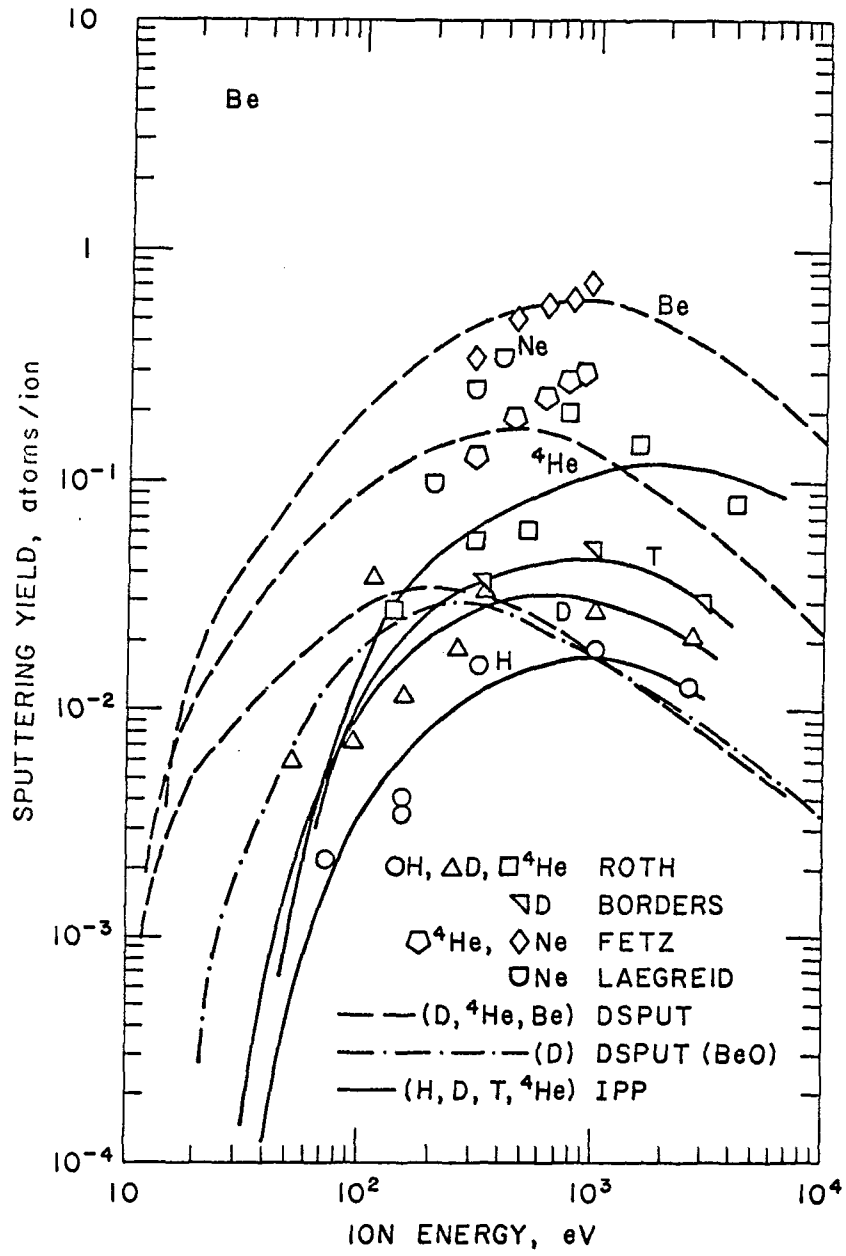

Figure 5-26. Energy dependent physical sputtering yields for Be.

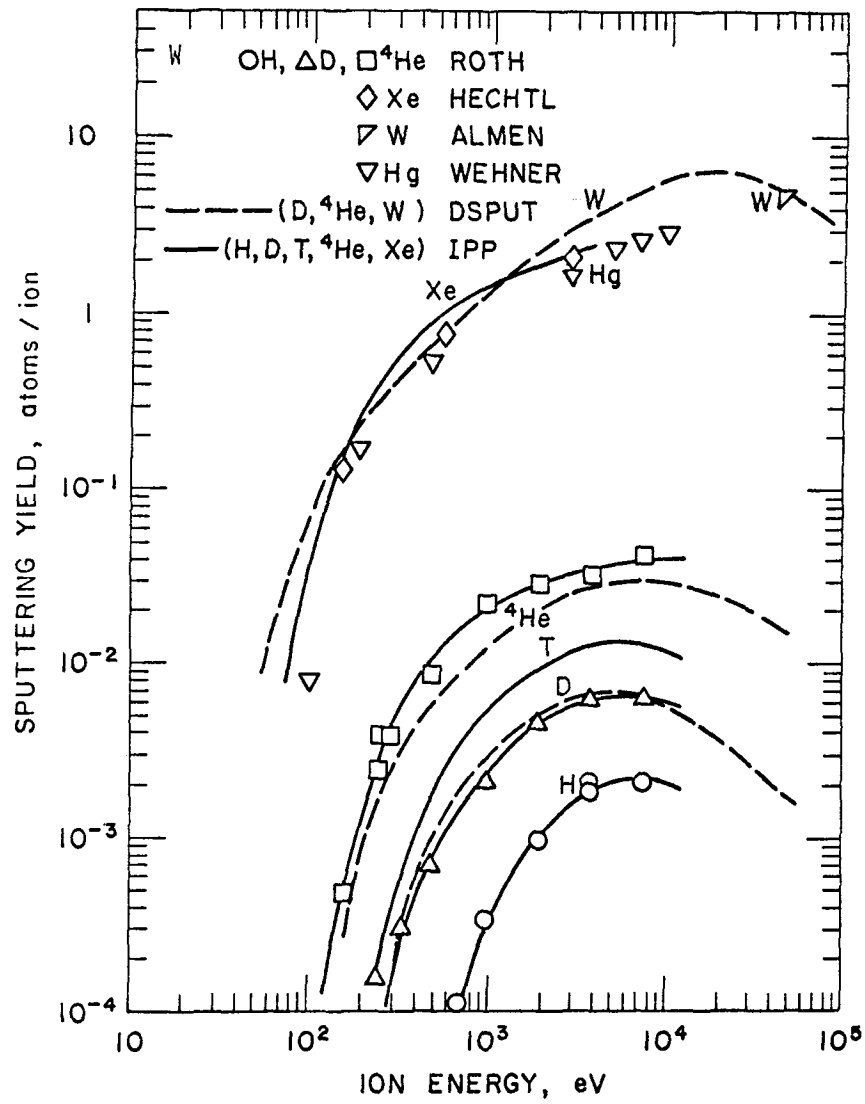

Figure 5-27. Energy-dependent physical sputtering yields for tungsten.

yield for beryllium than the experimental data. The models generally give good agreement with the experimental light-ion sputtering data for the other primary candidate materials. Very little data exist for self sputtering. Therefore, the models are based primarily on sputtering data for inert gas ions of similar mass. The results indicate that the self-sputtering yields (normal incidence) do not exceed unity for low-Z materials such as Be and C. The predicted self-sputtering yields for most high-Z materials such as vanadium, iron (stainless steel), molybdenum and tungsten exceed unity at incident particle energies of 400 - 800 eV. Therefore, incident particle energies must be maintained below these levels to avoid a propagating erosion effect if the sputtered wall material is ionized and accelerated back to the wall by a sheath potential as predicted (see Sec. 5.4). For incident particles with intermediate mass numbers (20-40), the uncertainty in the sputtering yield data is too large to reliably determine whether self-sputtering yields will exceed unity. The maximum self-sputtering yields for BeO are believed to be less than unity.

Since both models[18,19] are believed to adequately predict the sputtering yields for most materials of interest in the present study, the DSPUT code as been used as a basis for the limiter erosion yield calculations in Section 5.4 primarily because of its greater simplicity and flexibility. Appropriate refinements can easily be made by slight variations to the factor C, to improve the accuracy of specific calculations.

5.6.1.2 Chemical Sputtering

Possible chemical interactions that lead to wall erosion by chemical sputtering have been evaluated. The primary effort is on hydrogen (DT) effects on graphite. Hydrogen (DT) effects on candidate carbides (B_4C, SiC, and TiC) have also been assessed. Oxygen impurity may also cause chemical sputtering of reactive materials. This aspect has been evaluated primarily in terms of tungsten; however, extrapolation to other metals can be made.

Most investigations of chemical sputtering of graphite by light ion bombardment have focused on the formation of methane. Methane is formed in the temperature range between 200° and 800°C and it increases the graphite sputtering yield well above that observed for physical sputtering only. The maximum methane formation rate has been shown to occur at a temperature of

about 550°-600° and about 1 keV incident hydrogen ion energy. Until recently, not much attention was paid to studies of graphite erosion by hydrogen bombardment at temperatures above 700°C. Figure 5-28 (see Ref. 20) shows the sputtering yield of carbon for 1 keV H^+ and D^+ incident ions and for 3 keV He^+ ions at temperatures to 1600°C. While an erosion peak is observed at 525°C for carbon bombardment by H^+ and D^+, no peak is detected during helium bombardment at that temperature. However, a rapid rise in sputtering is seen at temperatures above 700°C for all three incident ions H^+, D^+ and He^+. These high erosion rates indicate that a mechanism other than classical physical or chemical sputtering must be present as no hydrocarbon formation was observed at these high temperatures.[20] Several possible mechanisms are being considered at present.

The effects of the chemical sputtering of carbides, e.g., B_4C, SiC and TiC, are much smaller than those observed in the case of graphite. Based upon limited data, a chemical erosion yield a factor of two higher than the physical sputtering yield for energetic hydrogen has been observed at temperatures of 500-650°C for SiC. The peak chemical sputtering yield for B_4C, which is similar to that of SiC, occurs at a temperature of $\sim$ 200°C. The TiC appears to be less sensitive to chemical sputtering by hydrogen than are SiC or B_4C.

Chemical sputtering on surfaces of tungsten centers on the effects of oxygen on tungsten erosion rates. It has been shown that there are several stages of oxygen adsorption on the tungsten surface. Below monolayer coverage, oxygen is adsorbed on the tungsten surface in the absence of tungsten oxide formation. As the amount of oxygen is increased above monolayer coverage, tungsten oxides begin to form. These oxides have a much higher volatility and can therefore be expected drastically to enhance the erosion of tungsten surfaces during light ion bombardment. When tungsten surfaces are covered with just a monolayer of oxygen, erosion of tungsten is suppressed. Computer calculations have shown that the sputtering yield for tungsten decreases two to four times, depending on the incident ions and their energy, when the surface is covered with a monolayer of oxygen. An important phenomenon that has to be taken into account is the self-sputtering of tungsten on both a clean and oxygen covered surface. If the self-sputtering could be brought under control at all incident ion energies, then tungsten could turn out to be a more useful candidate material.

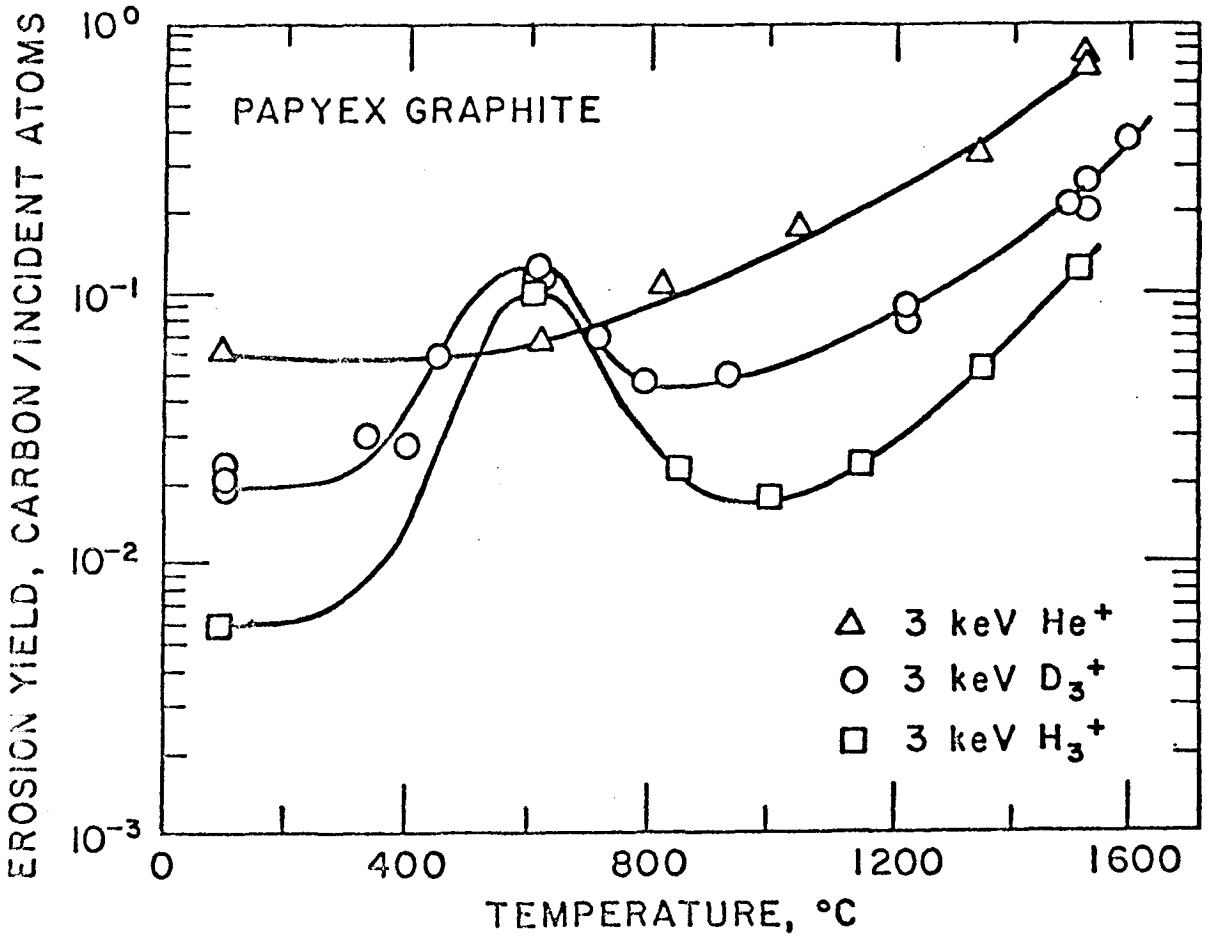

Figure 5-28. Temperature dependence of the chemical sputtering yield of papyex graphite.

5.6.1.3 H/He Retention/Release

The hydrogen and helium retention and release characteristics of the plasma side materials are important considerations in the selection of limiter materials. Hydrogen (DT) retention/release characteristics impact the tritium inventory in the wall and the tritium permeation into the coolant, and may affect the mechanical integrity of the wall materials. The focus of the present study is on the impact of energetic hydrogen (DT) and helium injected into the surface of the first-wall, limiter and divertor materials. In addition to the tritium issues, the effect of hydrogen and helium on the physical properties and mechanical integrity of the wall materials are also of concern.

Hydrogen retention and release for a material is generally assumed to be governed by diffusion, defect trapping, and the molecular recombination rate at the surface. The latter two factors are greatly influenced by the hydrogen solubility. Metals with an endothermic hydrogen heat of solution and reasonably high solubility (e.g., stainless steel) exhibit relatively weak trapping, while endothermic metals with low hydrogen solubility (e.g., Cu) typically have trap binding energies $\gtrsim$ 1 eV, causing high hydrogen retention as a result of the precipitation of hydrogen bubbles. The rate of release of hydrogen from an endothermic metal is often dominated by diffusion and detrapping at low temperatures. However, molecular recombination can become the rate limiting step for hydrogen release at higher temperatures. The temperature for the transition from diffusion and detrapping-limited kinetics to recombination-limited kinetics is materials dependent. In the case of stainless steels, recombination limited kinetics appear to control the hydrogen release rate by 150 C. Metals with an exothermic hydrogen heat of solution (e.g., V, Ta) often show hydride precipitation at low temperatures and high hydrogen retention in solid solution at higher temperatures controlled by recombination limited kinetics. Finally, trapping and release of hydrogen in non-metals such as carbon and carbides is characterized by high concentrations of strong traps. In general diffusivities and solubilities are not well known for non-metals. Temperatures above ~ 600°C are required for release of H from graphite and the carbides.

Helium release in metals is uniformly characterized by low migration energies ($\lesssim$ 0.4 eV), high trapping energies ($\gtrsim$ 2 eV), and high saturation

concentrations in bubbles (up to ~ 0.4 He/metal ratio). Once the available traps are saturated, additional implanted helium is rapidly released. Helium trapping in non-metals such as TiC appears at least qualitatively similar to the trapping observed in metals. Little is known about hydrogen-helium synergistic effects, although for metals with low hydrogen solubilities (e.g., beryllium) the hydrogen and helium appear to compete for the limited number of available trapping (i.e., bubble) sites.

Microstructural tailoring of the wall material is proposed to minimize the effects caused by hydrogen and helium injected into the wall. A tailored microstructure with relatively small grain size and significant interconnected porosity (10-25%), similar to that suggested to enhance tritium release from solid breeders, should tend to reduce both the concentration of the deuterium and tritium and the permeation of tritium into the coolant. Relatively high equivalent hydrogen pressures calculated at the injection depth should be relieved by the relatively short diffusion path to the grain boundary and the interconnected grain boundary porosity to the plasma-side surface. Temperature limits for acceptable release must be established for the candidate materials. The analyses indicate that the temperature gradient established in the wall by the surface heat flux tends to reduce tritium permeation compared to the case with a uniform wall temperature, because of the lowered temperature at the coolant side, and in the case of stainless steel because of thermal diffusion to the hot side of the wall (Soret effect). Tritium barriers on the coolant side of the wall will theoretically reduce the tritium permeation through the wall. Oxide films characteristic of those on many metals, e.g., stainless steel, exposed to elevated temperature water will tend to reduce the tritium permeation. The effectiveness of these barriers must be experimentally determined.

5.6.1.4 Bulk Properties and Radiation Effects

5.6.1.4.1 Low-Z Materials

The focus of the data-base assessment for the low-Z materials is on beryllium, graphite, silicon carbide and beryllium oxide. The critical materials properties for these materials are summarized in Table 5-12. Beryllium has a very low atomic number, good thermal conductivity and heat

Table 5-12. Property Values at 800K for Low-Z Materials

Property (Units)	Property Value			
	Be	BeO	C	SiC
Melting Temperature (K)	1557	2823	-	-
Sublimation Temperature @ 10^{-2} Pa(K)	-	-	2300	1800
Density[a] (Mg/m^3)	1.85	3.01	1.8[b]	3.20
Thermal Expansion, 300-800K (10^{-6} K^{-1})	15.9	8.2	4.2	4.9
Thermal Conductivity (W/mK)				
Unirradiated	103	66	103	37
Irradiated[c]	103	36	25	9
Specific Heat (J/kgK)	2250	1840	1620	1150
Young Modulus (GPa)				
Unirradiated	190	36	8	400
Irradiated	-	-	18	400
Yield Strength (MPa)				
Unirradiated	90	76	14[d]	360
Irradiated[c]	110	-	21[d]	360
Elongation, Irradiated[c] (%)	5	<1	<1	<1

[a] Density at 300K.
[b] Density of Graphite Ranges up to 2.25 Mg/m^3 Depending on Product Form.
[c] High Fluence Irradiation Properties.
[d] Tensile Strength for Graph-N3M is About 470 MPa (Unirradiated), Estimated 230 MPa After High Fluence Irradiation.

capacity and relatively high heats of vaporization and fusion. Graphite has many attractive properties including a much higher melting temperature; it normally tends to vaporize before melting. The vaporization rate becomes excessive at temperatures above ~ 2000 K. Although graphite has a relatively high thermal conductivity at low temperatures, the conductivity is rapidly reduced at relatively low radiation levels (< 1 DPA). Silicon carbide also tends to decompose and vaporize before melting, and therefore, avoids the melt layer problem. However, the maximum operating temperature (~ 1700 K) and the

thermal shock resistance of SiC are generally lower than those for graphite. As in the case of graphite, the low-temperature thermal conductivity of SiC decreases rapidly with radiation fluence. The BeO has a high melting temperature, high thermal conductivity at low temperatures, and is not believed to be susceptible to chemical sputtering. Although data for the liquid phase are sparse, calculations (see Sec. 5.7) indicate that a thin melt layer will form on BeO during a disruption. This compound is also susceptible to rapid deterioration of the low temperature thermal conductivity at low fluences.

The non-metals C, SiC and BeO all have relatively high thermal conductivities at low temperature. However, relatively low radiation doses tend to severely reduce the conductivity of these types of materials. Although considerable effort has been expended to develop high conductivity SiC, it is not clear that the high conductivity can be maintained in the radiation environment. The thermal conductivities of these types of materials generally decrease significantly as the temperature is increased above room temperature. For example, the thermal conductivity of the CVD β SiC is about a factor of 2 higher (67 W/m•K) at 25°C than at 525°C. Under irradiation the conductivity tends to become insensitive to temperature at values slightly below the high temperature values. Other compounds such as B_4C and Al_2O_3 show similar behavior. Limited data also indicate that the low temperature thermal conductivity of BeO decreases rapidly with radiation fluence.

5.6.1.4.2 High-Z Materials

Tungsten and tantalum are of interest for the plasma side materials because of their low light-ion sputtering yields, their relatively high threshold energy for DT sputtering, and their relatively high energy (~ 700 eV) at which self-sputtering exceeds unity. Values for the physical properties of tantalum and tungsten at temperatures in the range of interest are summarized in Table 5-13. Only limited data exist on the effects of radiation on the properties of tungsten and tantalum. The ductile-brittle transition temperature (DBTT) of tungsten is increased from 65 to 230°C after fast reactor irradiation at 385°C to fluences of 4-9 x 10^{25} n/m^2. At higher fluences (1.5 - 4.4 x 10^{26} n/m^2) and similar temperatures the uniform elongation of tantalum was reduced to ~ 0.1% with a total elongation of

Table 5-13. Properties of High-Z Materials at 500K

Property	Tungsten	Tantalum
Atomic Weight	183.85	180.95
Density, g/cm^3	19.25	16.6
Melting Point, °K	3683	3269
Thermal Expansion, $x10^{-6}K^{-1}$	4.2	6.58
Thermal Conductivity, W/m•K	145	61.8
Heat Capacity, J/kg•K	138	148
Modulus of Elasticity, GPa	398	176

8-10%. No relevant fatigue data for tungsten were found in the literature. Limited data indicate excellent low-cycle fatigue resistance of tantalum at temperatures below 732°C.

5.6.1.4.3 Comparative Analysis

Each of the materials considered for the plasma side of the limiter/divertor exhibit several favorable properties that make them primary candidate materials for this application. However, each of these materials also appear to have properties that could severely impact their performance under projected operating conditions. The favorable characteristics that distinguish each candidate material from the other primary candidates are summarized in Table 5-14. Important limiting features or considerations are also listed in the table. Those factors which are currently considered to produce the greatest impact are marked with a check.

Based on a comparison of the various options, it is concluded that a beryllium coating offers the best design solution for the front face of the limiter. Table 5-15 summarizes the key features of a beryllium coating. Some interconnected porosity should be beneficial in reducing some of the tritium related problems. The most critical issue regarding the use of beryllium relates to the formation and stability of the melt layer predicted to form during a plasma disruption.

Table 5-14. Summary of Favorable Characteristics and Limiting Features for the Primary Candidate Plasma-Side Materials

Material	Favorable Characteristics	Limiting Features
Be	*Self-sputtering less than unity at all energies. No chemical (H) sputtering. *Redeposited material is believed to be similar to base metal. *High thermal conductivity not affected by radiation. Relatively extensive fabrication experience for duplex wall.	*A melt layer is predicted to form on surface during a plasma disruption. Thickness of melt layer depends on disruption scenario. Stability of melt layer during disruption is uncertain. Maximum operating temperature is ~ 700°C. Well known chemical toxicity presents handling problems.
C	Low cost, readily available. Relatively extensive data base. *No melt layer formed during a disruption. Good thermal shock resistance (unirradiated). *Self-sputtering less than unity at all energies.	*Chemical sputtering (H) appears to be excessive. *Thermal conductivity at low temperatures greatly reduced by low-fluence irradiations. Characteristics of redeposited material may be substantially different (amorphous carbon) than base metal.

Table 5-14. (Continued)

SiC	Low cost, readily available. *No melt layer predicted during plasma disruption. Relatively extensive data base.	*Thermal conductivity at low temperatures greatly reduced by low-fluence irradiation. Chemical sputtering approximately two times physical sputtering at 500-600°C (much less than graphite). *Self-sputtering yields are highly uncertain. Yield may be greater than unity. Energy that yield exceeds unity (if it does) is not well established. *Surface during operation may not be stoichiometric SiC. Si/C ratio at surface <0.3 during thermal annealing. Redeposition process may cause additional effect.
BeO	Potential for high-temperature operation. Thinner melt layer formed during disruption compared to Be. Good thermophysical properties (unirradiated). *Self-sputtering believed to be less than unity. No chemical (H) sputtering.	*Thermal conductivity at low temperatures greatly reduced by low-fluence irradiation. *Relatively poor radiation damage resistance. *Uncertain stoichiometry of compound at surface because of redeposition may affect sputtering. Toxicity creates handling problem worse than Be. Limited technology base.

Table 5-14. (Continued)

W	*Low D-T sputtering at low energy.	Difficult fabrication compared to tantalum.
	*Good resistance to disruptions.	High DBTT after irradiation.
	No chemical sputtering.	*Self-sputtering > 1 for E > 700 eV.
	Good thermophysical properties.	*High-Z plasma impurity.
	*Redeposited material is believed to be similar to base metal.	
Ta	*Low D-T sputtering at low energy.	*Self-sputtering > 1 for E $\gtrsim$ 700 eV.
	*Good resistance to disruptions.	*High-Z plasma impurity.
	No chemical sputtering.	Greater potential for hydrogen embrittlment than W.
	Good thermophysical properties.	Higher cost than W.
	*Redeposited material is believed to be similar to base metal.	
	Easier fabrication than W.	
	Better ductility than W.	
	Note: Nb is similar to Ta except for slightly higher sputtering yields.	

* = Critical Issue

Table 5-15. Summary of the Characteristics of Beryllium Coating

- Fabrication
  - Plasma Spray
  - ~ 85% Theoretical Density
  - Experience, Flexible
- Low-Z, Self-Sputtering < 1
- Redeposited Material Properties Similar to Fabricated Material
  - No Composition Effects
  - Eroded Material Should Vapor Deposit as Adherent Film on Walls (e.g., Vacuum Duct)
- No Chemical Sputtering
- Porosity Should Enhance Gas Release and Minimize Tritium Retention and Permeation.
- Good Thermal Conductivity and Mechanical Properties Perpendicular to Wall (Not Greatly Affected by Irradiation)
- Porosity Should Accommodate Radiation Swelling and Facilitate Gas Release
- Low Activation/Afterheat

5.6.2 Heat Sink Materials

Copper and vanadium alloys have been examined as potential heat sink materials. The requirements of these materials are the ability to withstand high heat fluxes, to withstand a modest level of radiation damage (10-20 dpa) and to be environmentally compatible with the surface materials and the coolant. The desirable properties of heat sink materials are a high thermal conductivity, a low coefficient of thermal expansion, resistance to fatigue failure, resistance to radiation damage and coolant corrosion, and good availability and fabricability. The data base for these materials is summarized below.

5.6.2.1 Bulk Properties

Several groups of copper alloys have been examined. They are pure copper, oxide dispersion strengthened copper alloys, low concentration age-

hardened alloys, and Cu-Be alloys. All these alloys have adequate thermal conductivity and low temperature strength. Pure copper, however, loses its strength at relatively low temperatures. The oxide dispersion and age-hardened alloys present fabrication difficulties due to the importance of cold-work in achieving their mechanical strength. The bonding processes proposed (i.e., welding and brazing) require temperatures where the cold-work will be annealed out of the structure, and the strength will be significantly reduced. Only the Cu-Be alloys can achieve high strength without cold working. The Cu-Be alloys are available in a wide variety of forms, and they are easily fabricated. Therefore, they appear promising as a heat sink material. The analysis of vanadium alloys has concentrated on a single material, V-15Cr-5Ti, because of its superior properties in several areas. It has high tensile and creep strength at elevated temperatures, has excellent radiation resistance, and fabrication procedures have been developed.

A comparison of the room temperature properties of a Cu-Be alloy. M25 (1.8% Be, 0.2% Ni + Cr + Fe) and V-15Cr-5Ti is shown in Table 5-16. The Cu-Be alloy has a much higher value of thermal conductivity and is stronger than the V-15Cr-5Ti at room temperature. However, V-15Cr-5Ti has a lower thermal

Table 5-16. Property Values at Room Temperature for Cu Alloy M25 and V-15Cr-5Ti

Property	Value	
	Cu Alloy M25	V-15Cr-5Ti
Thermal Expansion ($x10^{-6}$/K)	16.5	9.3
Thermal Conductivity (W/mK)	105	21.3
Specific Heat (J/kg K)	420	451
Elastic Modulus (GPa)	125	127
Electrical Resistivity ($\mu\Omega$-cm)	5.7	26
0.2% Yield Strength (MPa)	1085	490
Ultimate Tensile Strength (MPa)	1125	690
Elongation (%)	7	28
Fatigue Limit $\Delta\varepsilon_T$ (%) (@ 10^8 cycles)	0.3	0.7

expansion coefficient, a greater ductility and superior fatigue properties. For DEMO conditions, the limiter or divertor will be required to withstand a modest number of thermal cycles ($\sim 10^3$), and thus the fatigue properties are not likely to be an important factor in the lifetime evaluation.

5.6.2.2 Radiation Effects

The effects of neutron and charged-particle radiations on the dimensional stability (swelling) and mechanical properties of copper alloys and a V-15 w/o Cr-5 w/o Ti alloy have been determined from analyses of existing experimental data.

5.6.2.2.1 Copper

The swelling of pure copper on neutron irradiation to fluence levels of 10^{26} neutrons/m^2 (30 dpa) (E > 0.1 MeV) is expected to be < 0.01% if the material temperature is maintained below 235°C.[1] However, the swelling of this material will increase to 9% if the material temperature is increased to 335°C. The swelling of copper can be reduced by use of fully cold-worked material, but partial annealing of the cold-worked material can result in increased swelling relative to the fully annealed material. The level of expected gaseous, i.e., oxygen and nitrogen, contamination of copper in the environment of a fusion energy device is not expected to increase the swelling. Moreover, the simultaneous implantation of helium and production of irradiation damage in copper from the deuterium-tritium fuel reaction is not expected to exacerbate the swelling that is obtained on neutron irradiation.

The alloying of copper with either 1-3% aluminum, germanium, silicon, nickel, or beryllium can result in significant increase in the resistance to void swelling. However, alloying copper with 1 a/o silver or cadmium increases the void swelling.

The yield stress of copper at room temperature is increased substantially with increasing neutron fluence up to $\sim 10^{23}$ neutrons/m^2. The yield stress attains a nearly constant value (350 MPa) for fluence levels above 10^{23} neutrons/m^2. The total elongation of copper is reduced from ~ 28% to ~ 7% following exposure to a fluence of 10^{24} neutrons/m^2. The reduction in areas at fracture also tends to decrease with neutron irradiation but only by a small amount, i.e., 5% at 10^{24} neutrons/m^2. The exposure of neutron

irradiated (10^{24} neutrons/m^2) copper to a cyclic fatigue stress giving 0.3% total strain range causes failure at ~ 10^8 cycles. The steady-state creep coefficient for copper during neutron irradiation at 150°C will be greater than 1 x 10^{-12} s^{-1} MPa^{-1}.

5.6.2.2.2 Vanadium

The swelling of the V-15Cr-5Ti alloy on neutron irradiation is expected to be very low (< 0.01%) for material temperatures less than ~ 800°C and for fluence levels less than ~ 10^{27}neutrons/m^2 (~ 60 dpa). The simultaneous implantation of helium and production of irradiation damage from the deuterium-tritium fuel reaction is not expected to exacerbate the swelling that is obtained on neutron irradiation.

The dimensional stability (swelling) of the V-15Cr-5Ti alloy can be maintained during neutron irradiation by reducing the chromium and titanium content in the alloy and simultaneously maintaining the approximate chromium to titanium ratio. The swelling of the alloys can also be reduced by use of cold-worked (~ 20%) material.

The yield strength of the V-15Cr-5Ti alloy is increased substantially (500 MPa to ~ 950 MPa) on neutron irradiation to 10^{25} neutrons/m^2 at 100°C. It is likely that this irradiation-induced increase of yield stress is a maximum value for still higher neutron fluence. The tensile elongation of the V-15Cr-5Ti alloy is reduced to ~ 1.5% following neutron irradiation to 10^{25} neutrons/m^2 at 100°C. This low value of elongation is characteristic of this alloy for a wide range of neutron fluence (10^{23} to 10^{27} neutrons/m^2) because of its deformation behavior. However, the elongation of the irradiated material during tensile deformation is expected to increase with increasing irradiation temperature above 400°C.

The ductile-brittle transition temperature for the V-15Cr-5Ti alloy is expected to remain below room temperature for the expected environmental conditions in DEMO. The endurance limit for the V-15Cr-5Ti alloy under cyclic fatigue conditions in the fusion energy device is ~ 10^7 cycles for approximately 0.7% total strain at 600°C.

A comparison of the radiation-damage effects on the dimensional stability and mechanical properties of copper and the V-15Cr-5Ti alloy shows that the

V-15Cr-5Ti alloy would be the preferable structural material in the environment of a fusion energy device if the limitation of the low tensile deformation (1.5%) below ~ 400°C can be tolerated. This limitation for the V-15Cr-5Ti alloy is increasingly minimized with increasing temperature above ~ 400°C.

5.6.2.3 Corrosion/Compatibility

Data on corrosion of the candidate heat sink materials is very limited under conditions projected for the limiter/divertor application. It is concluded, however, that corrosion of copper and copper-beryllium alloys should not be excessive at temperatures below 200°C if the water chemistry is controlled at reasonable impurity, e.g., oxygen, levels. Recent scoping studies conducted on corrosion of selected vanadium alloys (V-15Cr-5Ti and V-15Cr) by water were very encouraging in that good corrosion resistance was observed at 250°C in deoxygenated water.[21] Although vanadium alloys have generally not been recommended for use with water coolant, these data indicate acceptable corrosion resistance. Additional data should be obtained to confirm this conclusion.

5.6.2.4 Fabrication

Much of the existing fabrication technology for vanadium alloys was developed during the 1960's as part of the breeder reactor program. Both V-Ti and V-Cr-Ti alloys have been successfully fabricated in the form of rods, tubes and sheet.[22-24] Preliminary weld development[22,25] has indicated that the V-Cr-Ti alloys exhibit good weldability with a well controlled fusion zone and a fine microstructure. Both gas tungsten arc and electron-beam welding techniques have been used successfully. The Cu-Be alloy is commercially available and generally exhibits good fabricability.

5.6.3 Duplex Wall Characteristics and Fabrication

The limiter wall must withstand the most severe environment of any component in the reactor. The wall will be exposed to high heat loads, energetic particle fluxes, the hydrogen plasma environment, neutron radiation and the coolant during normal operation, and transient thermal heat loads and electromagnetic forces during a plasma disruption. In addition the wall must

not be a source of excessive plasma contamination or a source of atoms/ions that could subsequently cause a propagating wall erosion problem because of a self sputtering yield greater than unity. A duplex wall system is believed to offer the best solution for meeting these requirements. The major advantage of this concept relates to the greater flexibility of materials choices since the material facing the plasma can be selected primarily on the basis of its surface properties while the heat sink material can be selected primarily on the basis of its structural and coolant compatibility characteristics. This section summarizes the coating/cladding concept. The coating/cladding concept considers both low-Z materials and high-Z materials for the plasma-side surface with vanadium and copper alloys for the water-cooled substrate. Three methods of fabrication were considered: deposition processes such as plasma spray, direct bonding such as diffusion bonding, and brazing. The most appropriate fabrication process is specified for each combination of materials. The four low-Z materials considered in detail include beryllium, graphite, silicon carbide and beryllium oxide. Tungsten and tantalum were the high-Z materials considered. Based on anticipated erosion rates under service conditions, coating/cladding thicknesses of 10-20 mm are required.

5.6.3.1 Beryllium

Bonding of beryllium to the substrate appears feasible by all three methods considered: plasma spray, diffusion bonding and brazing. Considerable experience in bonding beryllium to substrates has been provided by the space programs. The plasma spray process, which has several advantages, is the preferred method of fabricating duplex limiter walls with beryllium. Centimeter-thick coatings of beryllium can be sprayed onto parts of relatively complex shape. Diffusion welding or brazing of beryllium onto complex shapes is much more difficult. Where necessary, an intermediate zone of graded thermal expansion could be made by spraying graded blends of beryllium and substrate metal powders or by spraying layers of intermediate expansion materials. Similarly, a diffusion barrier could easily be sprayed between beryllium and certain substrates to avoid formation of brittle intermetallic compounds. This may be necessary for the copper heat sink. Other advantages include easy adaptability for coating large areas and the possibility of in-vessel coating repairs. The properties of plasma sprayed beryllium are quite different than those of wrought material and they can be varied considerably

by adjusting the parameters. As-sprayed beryllium typically contains 10-20% porosity and is quite anisotropic. Both tensile strength and thermal conductivity perpendicular to the wall are much greater than the corresponding properties parallel to the wall. Typical properties of commercial grades of plasma sprayed beryllium are: yield strength = 240-290 MPa, elongation = 3-5.5%, and grain size = 6-14 μm.

Both brazing and diffusion bonding of beryllium are considered feasible; however, special care is required when designing joints with beryllium because of its high chemical activity and unique physical properties. Several commercial filler metals and numerous experimental alloys have been used to vacuum braze beryllium. For high-temperature service (550-650°C), the best filler metals appear to be silver brazes, e.g., BV Ag-0 and BAg-19. Shear strengths of 200-300 MPa are reported for BAg-19 joints. For service below 300°C a silver-copper alloy (BAg-18) is recommended. Brazing temperatures of ~ 800°C and ~ 900°C are required for BAg-18 and BAg-19, respectively.

Although direct diffusion welding of beryllium can be accomplished, coating both surfaces with silver and then diffusion welding the silver is recommended for high-integrity bonds. Joint strengths of 275-440 MPa have been obtained with silver bonding temperatures as low as 200°C.

5.6.3.2 Graphite

Considerable research, primarily for aerospace and nuclear applications, has been conducted to evaluate various methods for joining graphite to itself and to metals. Problems associated with the joining of graphite are generally similar to those for ceramic materials. Differences in coefficients of expansion between graphite and most metals are substantial. Also, graphite is not wet by conventional brazing alloys. Joining techniques that may prove useful for the present application involve the use of graphite cements, diffusion bonding, and brazing. Graphite cement is the most widely used method for joining graphite and is recommended for use here. The cements are heavily loaded suspensions of fine graphite powder in a resin binder. This bonding process is relatively simple and inexpensive. The surfaces are roughened, coated with cement and cured for up to 20 h at temperatures of 100-130°C. The strength and thermal conductivity of cemented joints, which are inferior to the properties of bulk graphite, are typically 10 MPa and

5 W/mK, respectively. Suggested service temperatures are 200-800°C. These joints typically have low ductility and the radiation response has not been determined.

Only limited research has been conducted on diffusion bonding of graphite. Most of the work is on bonding of graphite to graphite. Considerable development is required before diffusion bonding of graphite to metals could be recommended.

Metals that form stable carbides have produced the best brazed joints to carbon. Commercial brazing fillers such as 68.8 Ag - 26.7 Cu - 4.5 Ti and 70 Ti-15Cu-15Ni have been used to join pyrolytic graphite to copper. Braze temperatures of 900-1000°C are typical.

Materials such as carbon, which goes directly from solid to vapor cannot be sprayed as pure material. However, such materials can often be co-sprayed with a secondary binder material to form a composite coating.

5.6.3.3 Silicon Carbide

Acceptable methods for joining ceramics such as silicon carbide to substrates are more limited. Plasma spray is not considered feasible because SiC dissocates at elevated temperatures before melting. Metallization currently appears to be the preferred method of bonding SiC to a metal substrate. In the most widely used metallization technique, i.e., moly-manganese process, a mixture of metal and metal oxide powders suspended in nitrocellulose lacquer is painted onto the ceramic surface and fired in a wet H_2-N_2 atmosphere typically at 1400°C. Because of this high metallization temperature, a thick fiber metallization with Ti-Mo process is suggested for bonding the SiC and then hydrogen brazing the metallized surface to the substrate with a Ni-Cu-Ag braze. The metallization bond is typically quite strong (~ 35-70 MPa) but quite brittle.

Diffusion bonding has been used to bond SiC to SiC, W, Mo and an Fe-Co-Ni-Ti alloy. In general, very little has been published regarding possible bonding mechanisms or bond properties for non-oxide ceramics. The greatest potential problem with ceramic-to-metal bonds for the present application is to accommodate the large differences in thermal expansion between cladding and substrate.

Direct brazing of SiC to the substrate appears feasible but difficult. Silicon, which requires a brazing temperature of 1430°C, has frequently been used to braze SiC. Lower melting brazing materials such as germanium (937°C) or alloys may be acceptable. Since SiC is typically difficult to wet, only a few active elements appear acceptable for the braze.

5.6.3.4 Beryllium Oxide

Although there is limited experience with bonding of beryllium oxide, much of the experience with bonding other oxides is probably applicable. In general, the methods considered for SiC are probably applicable for BeO. The dual metallization/brazing process appears to offer the best solution. Most of the experience with metallization is for bonding oxides such as Al_2O_3. Silver, copper, and Ag-Cu brazes are most frequently used to braze metallized ceramics to metals. Further development is recommended for the bonding of BeO to the candidate substrates.

Direct ceramic-to-metal brazed joints can sometimes be made without premetallization by using filler metals that contain reactive elements such as titanium and zirconium. Beryllium oxide has been directly brazed to W, Zr and Nb-alloys with commercially available titanium-based fillers. Brazing temperatures were above 1000°C.

Although there is considerable experience with plasma spraying of thin ceramic coatings, e.g., turbine engine blades, very limited development has been conducted on thicker ceramic coatings. An attractive feature of the spray process is that blends of various materials can be sprayed to create composite coatings with specific properties. For example, graded coatings can be developed to vary the thermal expansion between substrate and coating or to improve bonding characteristics.

5.6.3.5 Tungsten

Plasma arc spraying, chemical vapor deposition, and brazing appear to represent reasonable manufacturing approaches for the duplex attachments of interest. Brazing is recommended over plasma arc spraying or CVD on the basis that it should be possible to produce W-substrate brazed composites using wrought-stress relieved tungsten, whereas both of the deposition processes yield tungsten coatings which are known to be quite brittle. The brazing

should be done in either vacuum or inert atmosphere furnaces. If complex geometries are required, it may be necessary to consider plasma spraying or CVD since those techniques offer the ability to achieve uniformly thick deposits over an irregular surface. This would not be a trivial requirement for brazing operations due to the close fitups which are required. Plasma sprayed coatings produced in an inert gas environment have as-deposited densities of about 90% of theoretical, tensile strengths of about 420 MPa, and DBTT of 350-400°C.

Tungsten-vanadium alloy brazing would require some development effort but should certainly be achievable. Brazes already exist which permit the brazing of tungsten to stainless steels or copper.

Direct bonding techniques such as diffusion bonding and explosive bonding are generally not recommended for joining tungsten because tungsten lacks the required deformability.

5.6.3.6 Tantalum

For tantalum coatings on the heat sink materials of interest here, the direct bonding processes - either diffusion bonding or explosive bonding - appear to be the most attractive. Although Ta-V alloy composites have not been produced or evaluated, there appears to be little reason to expect that these combinations would not be compatible. Since the metallurgy of these two refractory metals is generally very similar, this combination probably represents a better matching of physical, mechanical and chemical properties than the Ta-Cu.

Tantalum has been diffusion bonded with considerable success to both Cu and stainless steels. Ta-clad copper was used for heat sink applications for missile nose cones in the early 1960's. Bond joints of very high integrity were required to ensure maximum heat transfer. The bi-metal clad produced was a 1.5 mm layer of Ta on a 6.3 mm Cu base. Diffusion-controlled bonding was performed in vacuum to minimize contamination. A similar technique has been used to produce Ta-400 series stainless steel clads. This technique should work extremely well with V-base alloy substrates in view of the high mutual solubility of Ta and V.

Tantalum has been explosively bonded to a variety of materials including stainless steels and copper. Parts as large as 1 x 3 m are routinely produced. Ta-clad components of types 304, 316, and 321 stainless steel have been used for applications ranging from a mercury containment vessel for use in the SNAP-8 boiler to large processing tanks for the chemical industry. These claddings are generally only a few mm thick but direct contact with vendors indicates unalloyed Ta could be explosively bonded in thicknesses up to 2 or 3 cm without difficulty. Tantalum can also be explosively bonded to copper. In the early 1970's Ta-Cu cladding was produced for use as tanks for the chemical processing industry.

5.7 Disruption Considerations

5.7.1 Plasma Disruptions

An important consideration in the design of the limiter, divertor, and the first wall relates to the effects of plasma disruptions. The present study has focused on the response of various candidate first wall materials to the high energy deposited on the first wall during a plasma disruption. There is a high degree of uncertainty as to the time of the disruption, the region or fraction of the first wall over which most of the energy is deposited (peaking factor), and the time dependence of the deposition rate. For the DEMO the plasma energy is ~ 230 MJ and the total first wall area is 400 m^2. If the plasma energy were distributed uniformly over the entire first wall the energy density would be 75 J/cm^2. It is generally believed that most of the energy will be deposited on the inboard region of the first wall. The analyses presented are based on a uniform (time independent) deposition for times of 5 and 20 ms. Values of 270 and 175 J/cm^2 during a 20 ms disruption are believed to be representative of the probable disruption scenario for the DEMO's limiter and first wall, respectively. These values are considered reference design values. However, in the parametric analysis considered in this study the energy density was allowed to vary up to 1200 J/cm^2.

As a result of this study the loss of material by vaporization and melting is calculated. First, the thermal response of the materials is calculated for a range of disruption conditions. Second, the stability of the melt layer under various forces inside the reactor chamber is analyzed. The disruption conditions are similar to those assumed for the FED/INTOR[1] study, keeping in mind that disruption frequency per year in DEMO is much lower than that for the FED/INTOR.

5.7.2 Thermal Response

The vaporization and melting characteristics of candidate surface materials have been evaluated for a range of disruption conditions. The materials examined are the refractory compounds (SiC, TiC, and BeO), the metals (beryllium and molybdenum), and stainless steel along with graphite. The refractory compounds were analyzed using a model by Hassanein,[26] and the metals were analyzed using a model by Merrill.[27] It has been shown previously that the predictions of the two models are in reasonably good agreement.[27]

5.7.2.1 Refractory Compounds

The compounds SiC, TiC, and BeO have been analyzed for a variety of disruption conditions. Disruption times of 5 and 20 ms and energy densities ranging from 170 to 1070 J/cm^2 were used in the calculations. The physical properties of the three materials are given in Ref. 2. The calculations were made assuming no vapor shielding, and the assumed initial temperature of the materials is 573 K.

The predicted vaporization losses and melt layer thicknesses for the three materials are summarized in Tables 5-17 and 5-18, respectively. Table 5-18 shows the melting of TiC and BeO only, since SiC decomposes rather than melts. BeO exhibits the greatest vaporization losses and TiC the least. However, when vaporization and melting are combined, SiC, as might be expected, exhibits the lowest total losses. In general, all these materials exhibit lower vaporization and melting than the low- and medium-Z metals previously examined.(27)

5.7.2.2 Metals Plus Graphite

The effect of plasma disruptions on the reactor limiter and first wall is investigated for the metals beryllium, tungsten, molybdenum, and for graphite. The analysis was done using a model by Merrill.(27) The model was modified to incorporate the effect of plasma attenuation in the vapor shield produced by surface ablation developed by Hassanein.(26) Both the attenuated and unattenuated models were evaluated for the disruptive cases. The results illustrate the effect of vapor shielding and, hopefully, provides an optimistic and pessimistic bound on the melt layer and vaporization depths. These results are presented in Table 5-19 where the graphite predictions were obtained from Ref. 28. Results for a stainless steel first wall vaporization and melting are given in Ref. 2 for various energy densities. As shown in Table 5-19, a limiter made of tungsten or molybdenum subject to energy density of 270 J/cm^2 (reference condition) will not melt for either of the two disruption times considered here. The general conclusion of the disruption analysis is that materials with high melting points have thinner melt layers than those with low melting points. Also, longer disruption times generally result in larger melt layer formation. There is no melt layer for graphite since it sublimates rather than melts.

Table 5-17. Effect of High Heat Flux on Vaporization of SiC, TiC, and BeO (Vaporization in Microns per Pulse[a])

Material:	SiC		TiC		BeO	
Time (ms): / Energy Flux (J/cm^2)	5	20	5	20	5	20
1070	82.6	40.4	73.8	33.1	87.2	68.0
535	18.6	0.4	15.0	0.4	32.6	11.2
340	1.7	0.	1.1	0.	11.8	0.3
270	0.1	0.	0.1	0.	5.1	0.
170	0.	0.	0.	0.	0.	0.

[a]If thickness is less than 0.1 microns, it is given a value of 0.

Table 5-18. Effect of High Heat Flux on Melting of TiC and BeO (Melting in Microns per Pulse)

Material:	TiC		BeO	
Time (ms): / Energy Flux (J/cm^2)	5	20	5	20
1070	90	160	22	56
535	90	24	32	65
340	54	0	36	29
270	19	0	35	3
170	0	0	15	0

Table 5-19. Vaporization and Melting of Beryllium, Tungsten, Molybdenum, and Graphite

Material	Disruption Period (ms)	Disruption Model[a]	Melt Layer Thickness (microns)[b] 270	535	1070	Vaporized Depth (microns) 270	535	1070
Beryllium	5	A	85.0	121.0	125.0	1.00	14.00	55.00
			110.0	121.0	120.0	10.50	52.00	141.00
	20	A	70.0	155.0	220.0	0.08	2.10	30.50
		U	75.0	200.0	225.0	0.11	24.00	110.0
Tungsten	5	A	NM	88.0	175.0	$<10^{-2}$	0.03	1.80
		U		120.0	225.0	$<10^{-2}$	0.22	31.00
	20	A	NM	NM	120.0	$<10^{-2}$	$<10^{-2}$	0.04
		U			242.0	$<10^{-2}$	$<10^{-2}$	0.80
Molybdenum	5	A	NM	108.0	210.0	10^{-2}	0.06	6.30
		U		176.0	250.0	10^{-2}	2.70	54.00
	20	A	NM	NM	175.0	10^{-2}	10^{-2}	0.09
		U			350.0	10^{-2}	10^{-2}	7.70
Graphite	5	A	--	--	--	<1.00	7.00	23.00
		U	--	--	--	7.00	28.00	70.00
	20	A	--	--	--	<1.00	1.00	15.00
		U	--	--	--	<1.00	13.00	60.00

[a] A = flux attenuation by vapor shield.
U = no vapor shield attenuation.

[b] NM = no melting occurs.

Tungsten shows the lowest vaporization thickness compared to all the materials considered in this analysis for the same disruption conditions. On the other hand, beryllium shows the highest vaporization thickness. For a reference energy of 270 J/cm^2 only beryllium exhibits melt layer formation. This is an important issue when considering the problem of melt layer stability under different forces that may exist inside the reactor chamber. This stability issue will be addressed in the next sections.

To compare the response of the various materials during a disruption, the results from this analysis and Ref. 28 have been combined to determine the energy densities required for specific melt thickness and vaporization depths. Table 5-20 presents these results for 5 and 20 ms disruption periods with and without plasma attenuation.

Table 5-20. Required Energy Densities for Melting and Vaporizations

Material	Disruption		Energy Density Required to:			
	Period (ms)	Model[a]	Produce Onset of Melt (J/cm^2)[b]	Melt 20 μm (J/cm^2)	Vaporize 1 μm/20 μm (J/cm^2)	
Stainless steel	5	A	80	110	300	720
		U		100	150	340
	20	A	165	190	490	950
		U		185	290	500
Beryllium	5	A	100	125	270	600
		U		115	175	340
	20	A	200	220	460	970
		U		215	320	500
Molybdenum	5	A	280	340	790	1420
		U		310	460	710
	20	A	560	-	-	-
		U		600	860	1220
Tungsten	5	A	360	400	1120	1870
		U		380	560	930
	20	A	700	-	-	-
		U		740	1080	1480
Graphite	5	A	--	--	300	960
		U	--	--	200	420
	20	A	--	--	540	1300
		U	--	--	340	610

[a] A = flux attenuation by vapor shield.
U = no vapor shield attenuation.

[b] - = not predicted.

-- = not applicable.

5.7.2.3 Thermal Response with Different Starting Temperatures

The effects of different starting temperatures on the amount of material vaporized and melted during plasma disruption were determined for both beryllium oxide and beryllium using the model by Hassanein. Disruption times of 5 and 20 ms and energy densities ranging from 170 to 1070 J/cm^2 were used in the calculations. No vapor shielding calculations were considered in this analy-

sis. The starting temperature for beryllium oxide was varied from 300°C up to 2000°C, while for the beryllium case, the initial temperature was varied from 300°C up to 900°C.

As expected, the amount of material which is vaporized and melted increases as the initial temperature increases. The effects of disruption parameters and initial temperature on the vaporization and melt layer thickness are presented in Figs. 5-29 and 5-30 for beryllium. It can be seen that for a 20 ms disruption at energy densities >350 J/cm^2, the melt layer thickness of beryllium could exceed 300 μm for a starting temperature of 900°C. In the case of a 5 ms disruption the melt layer thickness is reduced because much more energy is predicted to be used for additional vaporization, as shown in Fig. 5-30.

5.7.3 Electromagnetic Analysis

As the plasma current decays during a plasma disruption, currents and voltages are induced in the first wall and impurity control systems. These currents can interact with the poloidal and toroidal fields to produce large forces and torques. The voltages can lead to arcing between segments of the limiter. It is important to determine how the forces, torques, and voltages depend on such system parameters as the first wall electromagnetic time constant, the limiter material (particularly its electrical resistivity), and the degree of toroidal segmentation. The study must include the limiter plus an electrically continuous first wall, poloidal field coils with fixed locations and currents, and a plasma current decaying to zero. A computer code has been developed to model the induced currents in the limiter and first wall as functions of time.

5.7.3.1 Model for Limiter and First Wall

Both the limiter and the first wall are modeled as a number of a coaxial wire conductors. The resistances of the limiter wires are determined from the electrical resistivity and the skin thickness. The resistance of the first wall wires are determined by the desired first wall time constant. The poloidal field coil locations and currents are specified; the currents are assumed constant during and following the disruption. The plasma is represented by a single current loop and the plasma current is assumed to decay linearly to zero in 20 ms.

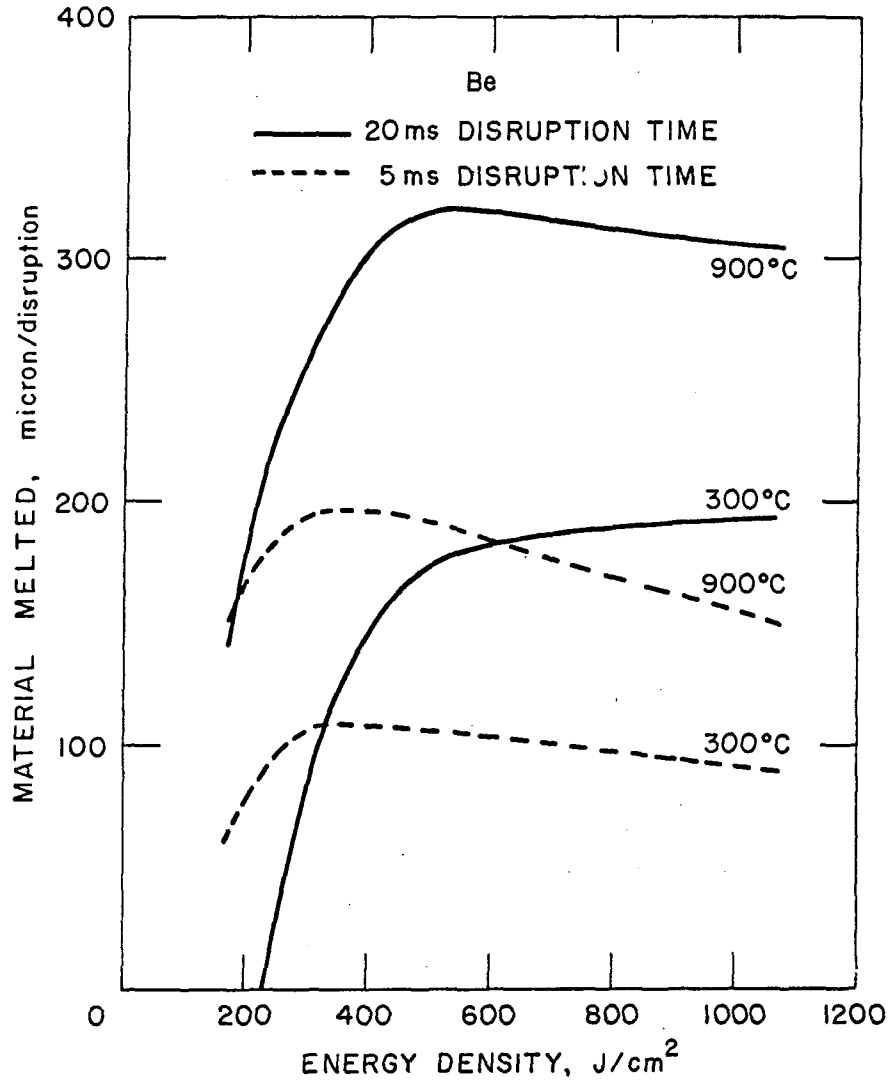

Figure 5-29. Effect of energy density on the amount of beryllium melted during a disruption.

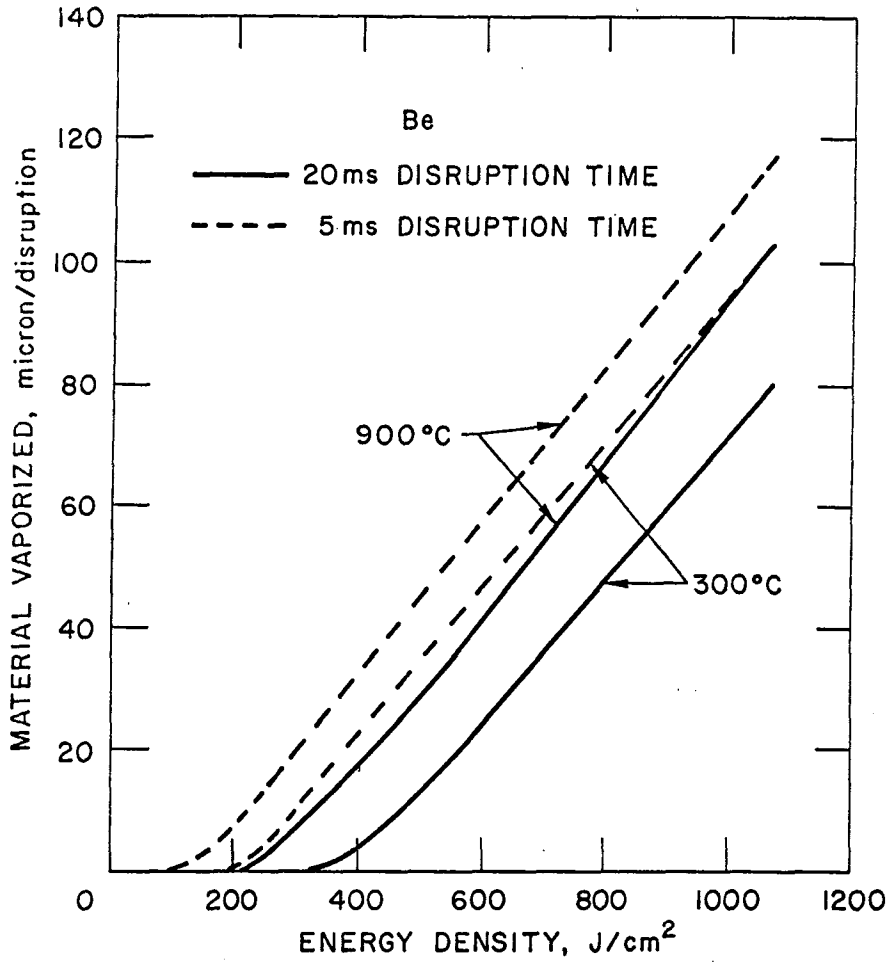

Figure 5-30. Effect of energy density on the amount of beryllium vaporized during a disruption.

The voltage generated in wire i by the plasma decay, V_{p_i}, is:

$$V_{p_i} = M_{ip} dI_p/dt ,$$

where M_{ip} is the mutual inductance between wire i and the plasma, and I_p is the plasma current. There is an additional voltage V_{IRi} due to the IR drop in each wire.

$$V_{IR_i} = -I_i R_i$$

where I_i is the wire current and R_i is the wire resistance. An additional voltage V_{mi} is generated by current changes in all the wires acting through their mutual and self-inductance.

$$V_{mi} = \sum_j M_{ij} dI_j/dt ,$$

where M_{ij} is the symmetrical mutual inductance between the j-th wire and the i-th wire. The diagonal elements are the self-inductances. The currents in the poloidal field coils are constant, and therefore are neglected.

The equations can be written in vector notation as

$$\vec{V} = \vec{V}_p + \vec{V}_{IR} + \vec{V}_M = 0 ,$$

and can be solved for the current change in a time interval dt.

$$\vec{I}(t + dt) - \vec{I}(t) = |M|^{-1} (\vec{V}_p + \vec{V}_{IR}) \, dt ,$$

where $|M|^{-1}$ is the inverse of $|M|$. Note that $\vec{V}_{IR}$ changes in the time interval. Mathematical stability of the solution to the equations is improved by adding one-fourth of the change in $\vec{V}_{IR}$ observed in the time interval to the initial value.

This model, in which the first wall and limiter are represented by coaxial circular current loops, does not lend itself to a treatment of segmentation effects. The first step toward segmentation, a single cut in the limiter, can be modelled by imposing an additional voltage term on the limiter wires only. The voltage is made large enough to make the sum of the limiter

currents vanish. Resistive voltages near the cut due to radial current flow are neglected.

Those radial currents interact with the toroidal field to produce large radial forces, of opposite direction on the two sides of the cut. Those forces can be calculated by multiplying the current in each limiter wire by the vertical displacement of the wire from the central radius of the limiter, summing, and multiplying the sum by the average toroidal field.

5.7.3.2 Results

Calculations of the forces on the bottom limiter in FED/INTOR were performed.[1] The results are summarized here because of their general applicability to the DEMO limiter. Studies were made of how the forces, torques, and voltages in the limiter vary with toroidal segmentation, first wall time constant, and resistivity of limiter material. In each case three forces and one torque are considered. F_R is the radial force per unit length of limiter due to interaction of the induced toroidal current with the vertical component of poloidal field. F_Z is the vertical force per unit length of limiter due to interaction of the induced toroidal current with the radial component of poloidal field. The poloidal field is the sum of the fields from the PF coils, the plasma current, and the induced currents themselves. N is the torque per unit length of limiter, about an axis in the toroidal direction, resulting from F_R and F_Z. F_{cut} is the radial force of interaction between the toroidal field and the vertical currents which flow wherever the limiter has a poloidal cut.

Computations were made of the effect of introducing a single cut in the limiter and of the effect on the forces of a first wall of 100 ms time constant. By reducing overall currents the single cut was found to reduce radial and vertical forces per unit length and torque above a toroidal axis by factors of between 2.5 and 10. However, the cut also led to vertical currents at the cut, which produce large radial forces of interaction with the toroidal field. The first wall with 100-ms time constant also decreases the forces and torques: by factors of between 1.5 and 2 for the uncut limiter and by even more (between 2.5 and 7) for the limiter with a cut. The basic influence of the first wall is to eliminate the sharp transients in forces associated with the plasma current quench. The peak forces are then observed at longer times

(~ 200 ms) which are associated with the longer current decay times of the first wall. The most significant result is that the presence of the first wall and a single cut in the limiter provides substantial protection from mechanical forces. The force of interaction between the toroidal magnetic field and the radial currents at the cut also is reduced by the conducting first wall.

As described above, segmentation effects cannot be calculated with the coaxial ring model. It is possible, however, to give a physical argument to estimate the forces on a segmented limiter on the basis of the forces on a limiter with a single cut and the increased resistance of current paths in a segmented limiter. The resistance of the radial current path at the cut is neglected in the calculations with a single cut, surely a good approximation because the radial width of the limiter is small relative to its circumferential length. If the number of segments is increased until the radial width and length are equal (about 24 segments), the resistance of the radial and azimuthal paths are equal and the current is roughly halved. If the number of segments is further increased, the resistance of the radial current paths become dominant, and the current varies inversely with the number of segments.

To study variation of force with first wall time constant, a series of computations were performed for a copper (ρ = 0.0117 $\mu\Omega$m) limiter with a single poloidal cut. Time constants of τ = 0, 10, 30, 100, and 1000 ms were used. The resulting peak values of F_R, F_Z, N, and F_{cut} are shown in Fig. 5-31. The dashed straight line in Fig. 5-31 shows the slope for a hypothetical force which varies inversely with the square root of τ. The three quantities, F_r, N, and F_{cut} have roughly the same behavior. For $\tau \ll$ 20 ms, the plasma current decay time, the force is largely independent of τ. The decrease of force with increasing τ is strongest for $\tau \sim$ 20 ms. Finally, for $\tau \gg$ 20 ms, the force decreases more weakly with increasing τ. The values of F_{cut} were divided by ten to fit them onto the same graph.

Computations were performed for a limiter with a single cut and a first wall time constant of 100 ms. The three computations differed only in limiter resistivity: values of ρ = 0.017 (copper), 0.07, and 0.32 $\mu\Omega$m were used. The resulting peak values of F_R, F_Z, N, and F_{cut} were found to vary inversely as the square root of the resistivity.

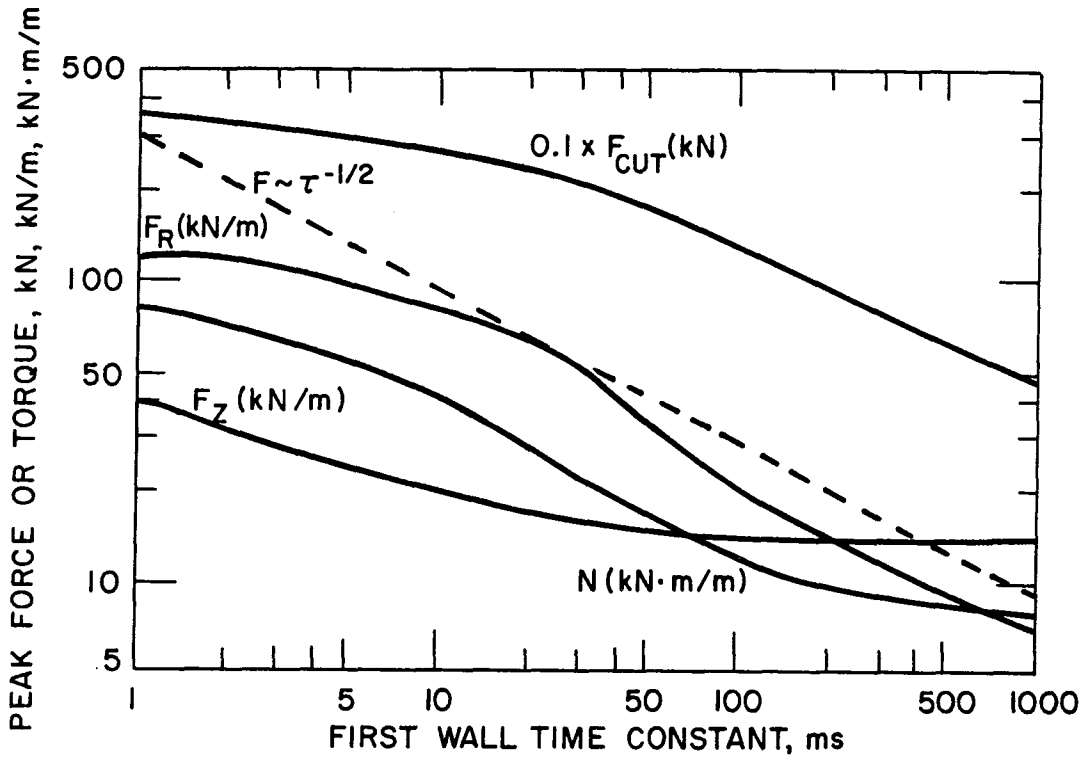

Figure 5-31. Variation of forces and torque on the limiter with time constant of the first wall.

Induced voltages between limiter segments is a concern with a segmented limiter in that the voltage induced by plasma disruptions may lead to arcing between segments. There is considerable uncertainty about how large the voltage between segments can be and still avoid damage from arcing, with values between 20 V and 200 V suggested. It is prudent to use the 20 V value if possible.

In the computations for a limiter with a single cut, the zero net current condition is imposed by finding the electrical potential which reduces the circulating current to zero. For a limiter with a single cut, this potential represents the voltage across the cut. For a limiter with n segments and n cuts, the voltage across each cut is given approximately by dividing the potential by n. This approximation is quite good, as discussed below.

The variation of the voltage with first wall time constant and with limiter resistivity was computed for a single cut and was estimated for multiple cuts. The variation with time constant was found to be similar to the varia-

tion of force with time constant: virtual independence for $\tau \ll 20$ ms, rapid decrease with increasing τ for $\tau \sim 20$ ms, and slow (inverse square root) decrease for $\tau \gg 20$ ms. For $\tau = 100$ ms and 72 segments, the voltage is below 10 V. The voltage was also found to be virtually independent of limiter resistivity; implying that the voltage is scarcely influenced by the current flowing in the limiter. It is to be expected that the voltages in the segmented limiter is similarly insensitive to the current in the segments and that the only effect on the voltage of increasing the number of segments is to divide the voltage by the total number of segments.

5.7.3.3 Conclusions

Several conclusions can be drawn from these studies:

(1) The electrical response of the limiter is sensitive to the electrical behavior of the first wall and cannot be studied independently from it.

(2) For a first wall time constant of 100 ms, and a limiter segmented into many pieces, the forces, torques, and voltages are manageable.

(3) For a shorter first wall time constant or fewer segments, electromagnetic considerations may cause problems in the design of the limiter.

(4) There is a characteristic variation of limiter forces and voltage with first wall time constant τ, with virtual independence of τ when τ is small compared with the plasma current decay time constant $\tau_0 = 20$ ms, rapid decrease with increasing τ when $\tau \sim \tau_0$ and inverse square root decrease with τ when $\tau \gg \tau_0$.

(5) Induced forces and torques vary inversely with the square root of limiter resistivity; voltages are virtually independent of limiter resistivity.

(6) In light of the importance of segmentation effects, an analysis which treats segmentation more directly is required.

5.7.4 Melt Layer Stability

The information concerning melt layer formation can be combined with the magnetic force calculations to determine the stability of the melt layer.

Stability calculations have been performed with and without time dependence of the melt layer thickness and magnetic forces.

The time-independent analysis considers the formation of a droplet due to magnetic forces perpendicular to the melt layer. The basic assumptions on the model are:

(a) Although the magnetic force is perpendicular to the overall plane of the surface, there are small local irregularities in the surface. The melt layer starts flowing along the surface at these irregularities, accelerated by the component of magnetic force along the surface and decelerated by the viscous force.

(b) By that motion the material from some regions of the melt layer is gathered together into a hemispherical drop.

(c) The drop is pulled into the plasma region by the magnetic force, a body force which is proportional to the cube of the drop radius, but held back by the surface tension force, which varies linearly with radius. Hence there is a critical radius above which the drop will break away from the surface.

The time-dependent model describes melt layer stability in terms of the Rayleigh-Taylor instability for semi-infinite and finite fluid layers. This model considers the time-dependent formation of the melt layer and time variations of the magnetic forces perpendicular to the melt layer. Details of the model are presented elsewhere.[29]

The magnetic forces used in the calculations, shown in Fig. 5-32, are those determined for the INTOR limiter system. These forces are believed to be representative of the forces expected during disruption in DEMO, since the disruption conditions and overall reactor configurtion are similar. The results of the calculations are presented in Table 5-21 for both models. The time-independent model appears to be more conservative than the time-dependent model. For the reference case of 270 J/cm^2 and 20 ms, the time-independent model predicts marginal stability, whereas the time-dependentmodel predicts stability. In either case, for disruptions more severe than the reference conditions, both models indicate that instability in the melt layer is likely. Therefore, melt layer loss remains a concern.

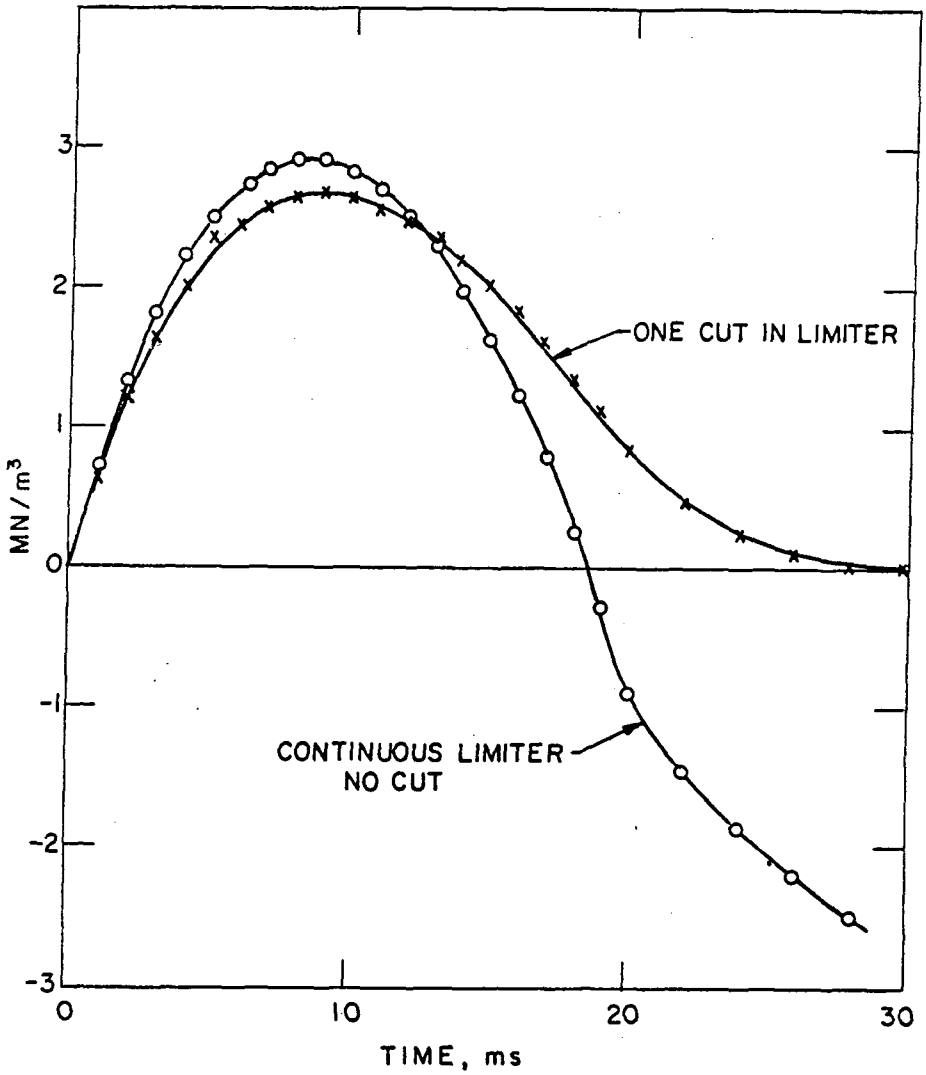

Figure 5-32. Force density on limiter melt layer including a first wall with 0.1 s time constant.

Table 5-21. Instability Index for Melt Layers on a Beryllium Limiter

Energy Deposition (J/cm^2)	Disruption Time (ms)	Instability Index			
		Time-Independent[a]		Time-Dependent[b]	
		Value	Conclusion	Value	Conclusion
535	20	--	--	0.992	Marginal
	5	6.6×10^{-3}	Unstable	0.436	Marginal
270	20	0.110	Marginal	7.7×10^{-6}	Stable
	5	0.049	Unstable	0.658	Marginal
175	20	--	--	No melting	Stable
	5	--	--	0.175	Stable

[a]Values much less than unity indicate instability.
[b]Values much less than unity indicate stability.

The analyses shown above represent initial attempts to examine the melt layer stability, and there is a considerable amount of effort required to understand this problem. First, there are other sources for the melt layer forces, such as structural vibrations and internal gas pressure, which could affect melt layer loss. Second, the estimates of the melt layer magnetic force contain uncertainties. There are also ways in which the magnetic forces can be reduced. For example, small limiter segments and small surface tiles will reduce the currents and forces at the top surface. Third, there are uncertainties in the disruption frequency, energy density, and time. Finally, the existence of an instability does not indicate that the entire melt layer will be lost. A separate kinetic model is necessary to determine the actual amount of loss.

5.8 Thermal Hydraulics and Stress Analysis

5.8.1 Introduction

The successful operation of the limiter depends to a large degree on the thermal and stress behavior. This section explores the thermal and stress aspects of the limiter operation in considerable detail. The thermal analysis considers the temperature distribution at the front surface and leading edges of the shaped limiter system. The temperatures were determined for a number of candidate materials and for a range of thicknesses from 1 to 50 mm. The results are used as input to the stress calculations presented in Sec. 5.8.3, and they are also used to determine the maximum allowable thicknesses of the plasma side materials in Sec. 5.9.

The stress analysis considers the effect of material selection and thickness on the stresses within the heat sink. The ASME Code Case N47 for Class I components has been used as a guide for the allowable stresses. The effects of the leading edge geometry and tile width have been included in the analysis. The major result of the analysis is that the various surface materials can reach 10 to 30 mm and still meet the stress requirements of the heat sink. The stress calculations still contain considerable uncertainties, however, and, ultimately, detailed 3-D calculations will be required.

5.8.2 Thermal Hydraulics

Work conducted in thermal hydraulics is mainly directed towards obtaining temperature distributions in the coating and structural materials of the limiter and the first wall. Parametric analyses using an extensive set of parameters, including material selection, thickness, surface heat flux, thermal conductivity, and effect of irradiation have been carried out. The results are expected to serve as a guide for design analysis and to assist in the selection of reference materials for the limiter and first wall. The results of temperature calculations are used as input for the stress and fatigue analysis in Sec. 5.8.3 and for the allowable thickness calculations in Sec. 5.9.3.

The areas investigated are shown in Table 5-22. For these calculations, the reference limiter heat load is a peak of 2.4 MW/m^2 at the center of the top surface. The heat flux is assumed to decrease linearly to the leading

Table 5-22. Areas Investigated for Thermal Hydraulic Analysis

Area	Heat Flux	Thickness		Materials		Comments
		Surface	Heat Sink	Surface	Heat Sink	
Limiter Front Surface	2.4 MW/m^2	1-50 mm	1.5 mm	Be, C, BeO, SiC, TiC, W	Cu V-15Cr-5Ti	Plate Geometry High Thermal Conductance
Limiter Leading Edge	1.0 MW/m^2, peak	1-30 mm	1.5 mm	Be, C, BeO, SiC, W	Cu V-15Cr-5Ti	Cylindrical Geometry High Thermal Conductance
First Wall	0.45 MW/m^2 0.25 MW/m^2	1-10 mm	4 mm	Be, 316 SS	316 SS	Plate Geometry High Thermal Conductance

edge value of 1.0 MW/m^2. The heat load then drops off to zero at the back surface of the leading edge. The heat load for the first wall immediately adjacent (0.5 m strips) to the limiter is 0.45 MW/m^2 and that for the rest of the first wall is 0.25 MW/m^2. The heat sink material thickness is constant at 1.5 mm, and the contact conductance between the heat sink and structural material is assumed to be infinite as would be the case for a braze joint. The top surface material thickness was varied from 1 mm to 50 mm for the various candidate materials. Two different geometries were used for the calculations. The top surface calculations employed a slab geometry. The leading edge calculations employed a cylindrical geometry shown in Fig. 5-33. A constant heat flux of 2.4 MW/m^2 was used for the limiter top surface calculations, and a variable heat flux with a peak of 1 MW/m^2 was used for the leading edge calculations. The assumed operating conditions for the temperature analysis are shown in Table 5-23 and a list of the candidate materials along with their thermal conductivities and nuclear heating rates are shown in Table 5-24. The heat transfer coefficient is much higher for the limiter than for the first wall in order to minimize the temperature difference between the coolant and the structure in the high heat flux areas. Nuclear heating is included in the analysis, but its influence is minor for the case of the limiter.

5.8.2.1 Limiter Top Surface

Figure 5-34 shows the maximum coating temperature vs. coating thickness for different coating materials on a copper substrate. With the exception of beryllium oxide, the maximum coating temperatures would increase by ~ 100 to 200°C for the case of a vanadium substrate. Beryllium oxide has very high conductivity at low temperatures, but the conductivity decreases rapidly with increasing temperature. Hence, BeO at large thicknesses exhibits high temperatures. This reduction in thermal conductivity with temperature resulted in large temperature differences (~ 600^0C) for thick BeO coating between a copper and a vanadium substrate. SiC and irradiated graphite exhibit the most rapid increase in temperature with coating thickness due to the relatively low thermal conductivities. It is important to note that radiation damage is known to rapidly decrease the conductivity on non-metallic compounds. The reduced conductivity will significantly reduce the allowable thickness for these materials. As the temperatures of the materials

Table 5-23. Operating Conditions for Temperature Calculations

Coolant Temperature:	
Inlet	60°C
Outlet	100°C
Coolant Velocity	9.2 m/s
Heat Transfer Coefficient:	
Limiter	4×10^4, 5×10^4, $W/m^2 \cdot K$
First Wall	1×10^4, $W/m^2 \cdot K$
Interface Conductance	Infinite
Neutron Wall Loading	1 MW/m^2
Effective Thermal Emittance	0.44

Table 5-24. Material Parameters Used in Thermal Analysis

Material	Thermal Conductance (W/m·K) 273 K	773 K	Nuclear Heating (W/cm^3)[a]
Be	192.0	117.0	7.8
BeO	229.0	70.0	~ 7.8
C (Unirradiated)	150.1	97.5	6.9
C (Irradiated)	30.0	30.0	6.9
SiC	91.5	33.1	~ 7.8
TiC	30.6	35.4	6.2
W	170.8	150.3	23.0
Cu	325.0	288.0	14.7
316 SS	13.5	22.0	10.8
V-15Cr-5Ti	21.3	28.1	7.4

[a] @ 1 MW/m^2

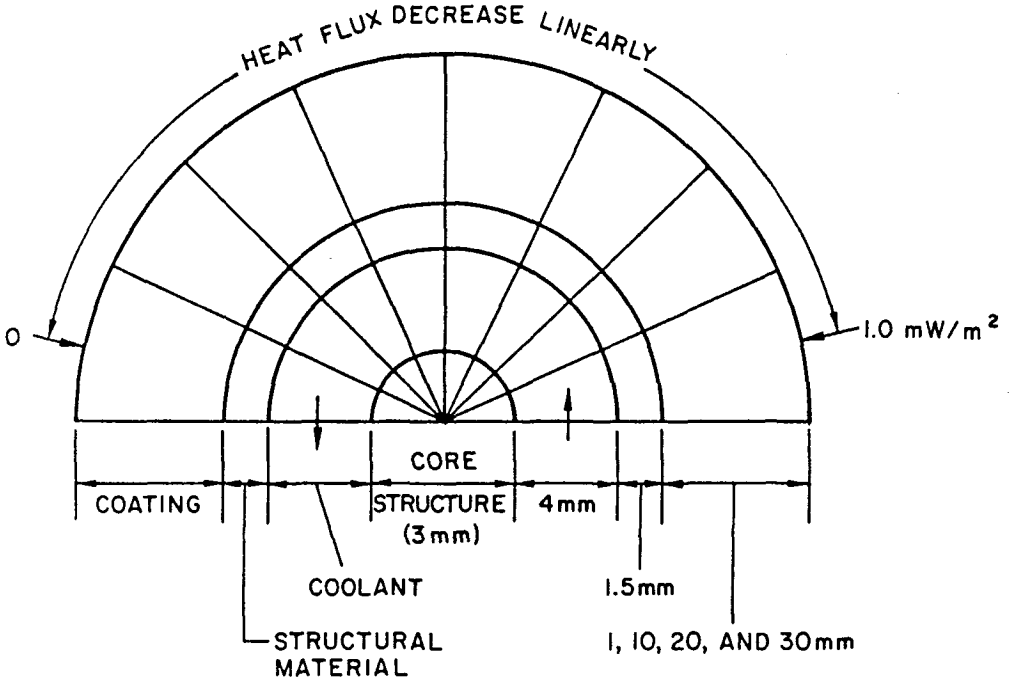

Figure 5-33. Geometry of the leading edge used for temperature calculations.

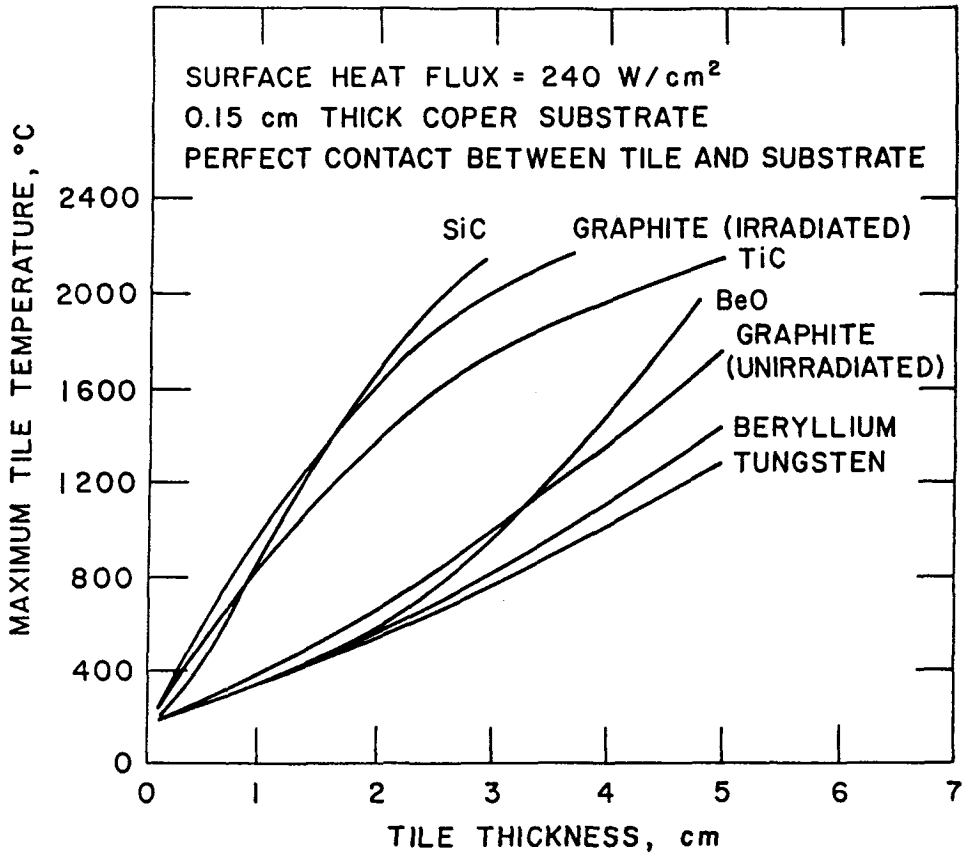

Figure 5-34. Maximum tile temperature -vs- thickness for limiter (perfect contact).

approach ~ 2000°C, the rate of temperature increase begins to slow due to enhanced radiation heat transfer.

Figure 5-35 shows the temperature distributions in the coating material with a function of depth into the coating for different coating thicknesses of BeO-V and Be-V. For Be-V, the temperature distribution in Be is almost linear (except near the surface) for all thicknesses. This is the result of fairly low beryllium temperatures. For BeO-V, with 10 mm thick coating, the temperature distribution in BeO is also close to linear. For BeO-V with 20 or 30 mm thick coating, the temperature distribution in BeO is non-linear and the gradient increases towards the surface. This is again the result of a sharp reduction in thermal conductivity with temperature for BeO.

Figure 5-36 shows the maximum structure (heat sink) temperature vs. coating thickness for different combinations of coating/structure materials. For relatively thin coatings (1 and 10 mm), the structure temperature increases slowly with the coating thickness and the maximum structure temperature is independent of the coating material on the top surface. Vanadium is always at higher temperatures than that of copper as a result of relatively poor thermal conductivity of vanadium. When the coating thickness is increased beyond 10 mm, the structure material temperature becomes dependent upon not only the coating thickness, but also the coating material, as shown in Fig. 5-37. This interesting behavior is the result of significant radiative heat transfer from the surface of the limiter to the first wall. The structural material temperature depends mainly on the surface heat flux, the thermal conductivity, and the thickness of the structural material. An increase in radiative heat transfer at high surface temperatures is equivalent to a net reduction in surface heat flux which in turn reduces the temperature of the structural material. This is why the temperatures of both vanadium and copper decreases with coating thickness for the cases of BeO and SiC when the coating is relatively thick. For the case of beryllium, radiative heat transfer is not significant even with a very thick coating, therefore, the temperature of the structural material beneath beryllium does not decrease with coating thickness.

Figure 5-38 shows the typical temperature distributions in the structural material. It can be seen that the temperature distributuion is always linear. This is expected since the structural material is always at fairly

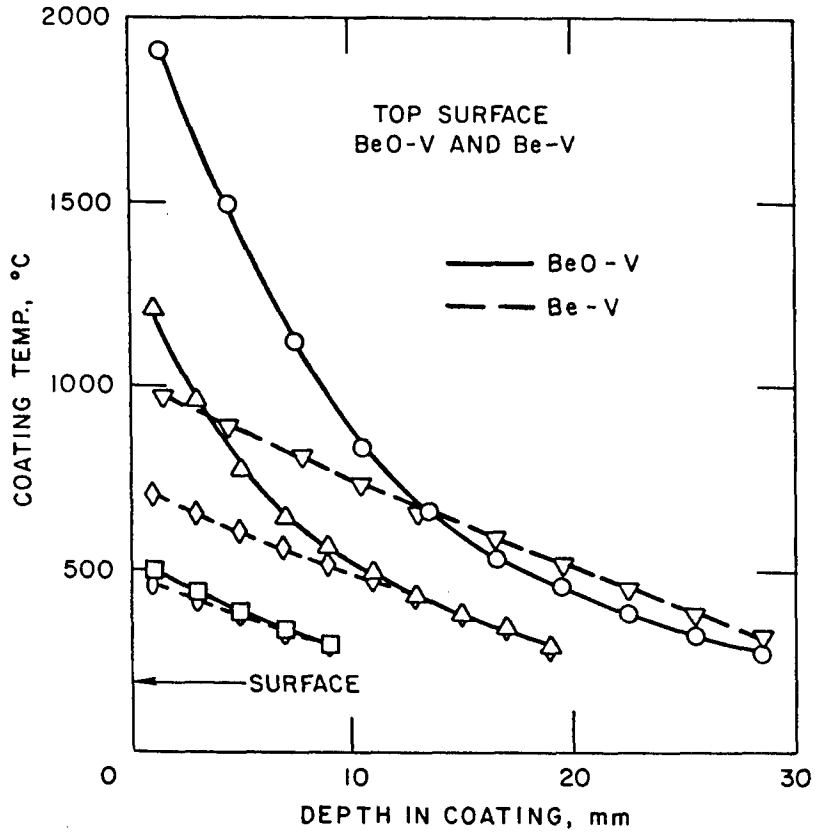

Figure 5-35. Temperature distributions through the coating materials Be and BeO on a vanadium heat sink.

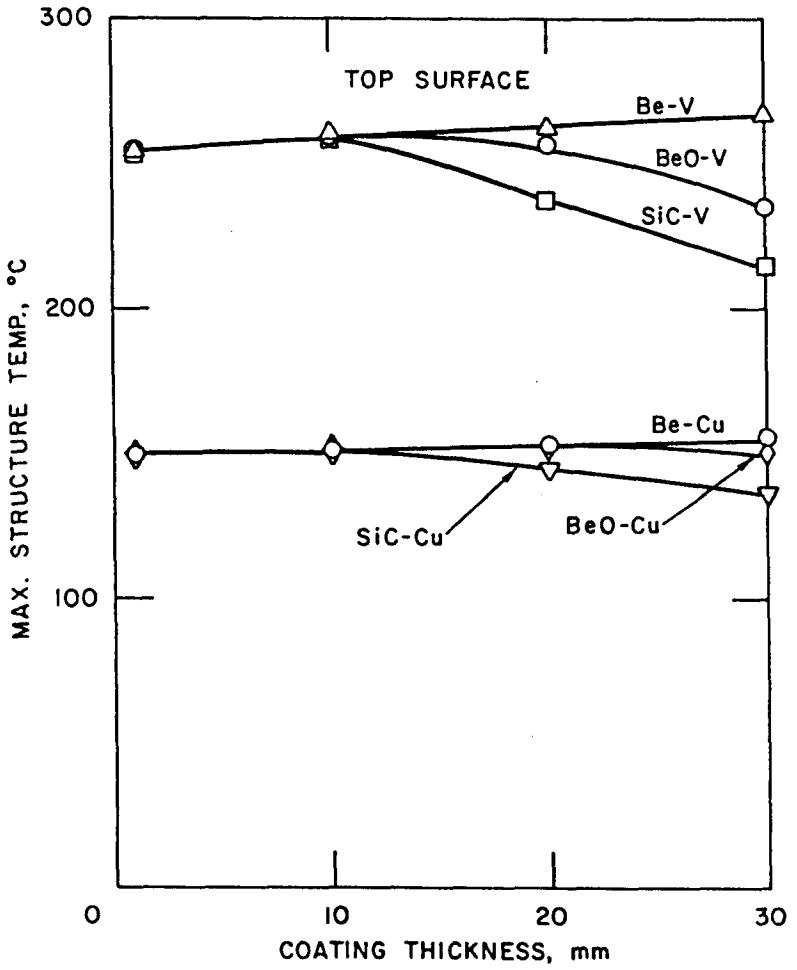

Figure 5-36. Maximum heat sink temperatures as a function of surface coating thickness.

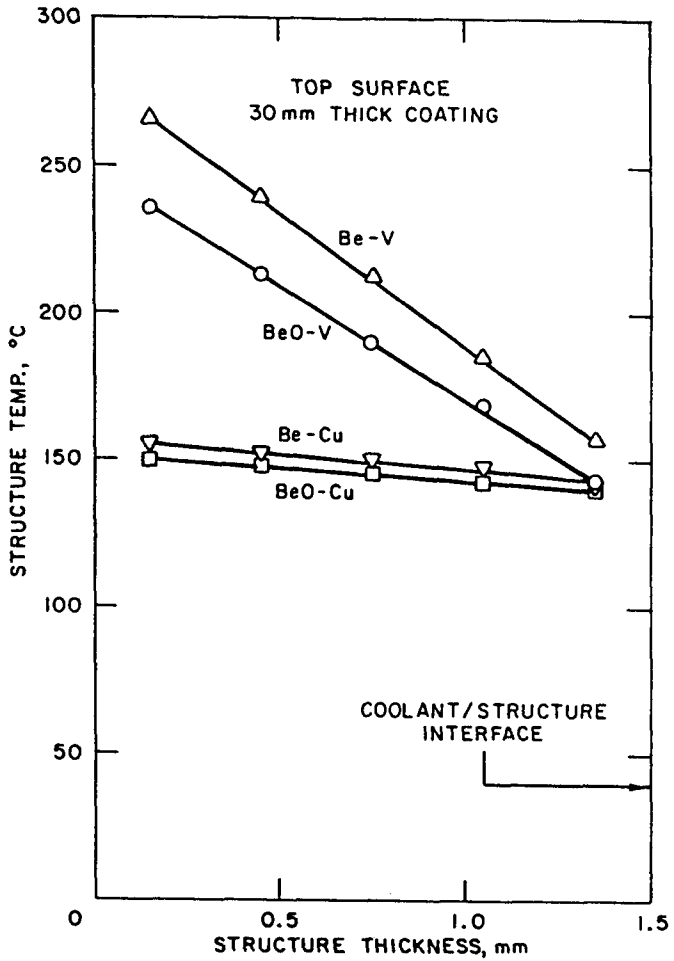

Figure 5-37. Temperature profile through the heat sink material with a 30 mm thick coating of either Be or BeO.

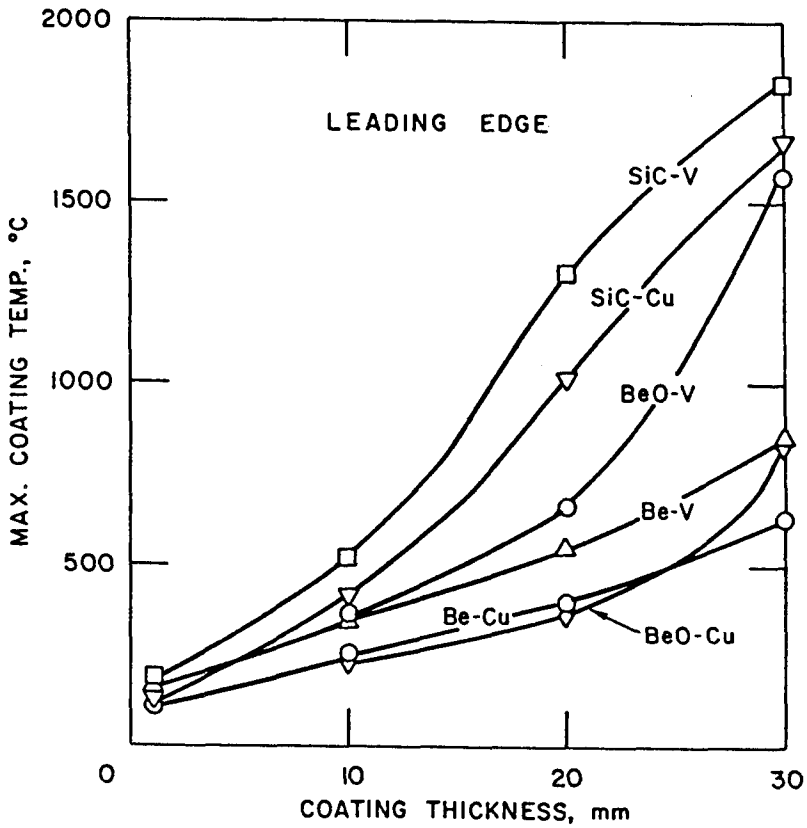

Figure 5-38. Maximum coating temperature at the leading edge as a function of thickness for several materials.

low temperature and the thickness is small (1.5 mm). It is also obvious that vanadium has a much larger temperature gradient than that of copper.

5.8.2.2 Limiter Leading Edge

Figure 5-38 shows the maximum coating temperature vs. coating thickness for different combinations of materials at the leading edge of a limiter. The trend for the coating temperature in the leading edge is similar to that of the top surface. However, the coating temperature in the leading edge is usually lower than that of the top surface for the same coating-structure material combination. This is the result of lower surface heat flux at the leading edge compared to that on the top surface. Again, radiative heat transfer becomes significant at higher temperatures for SiC-V and BeO-V.

Figure 5-39 shows the maximum structure temperature vs. coating thickness for various combinations of coating/structure materials at the leading edge. The temperature behavior at the leading edge is quite different from the temperature behavior at the top surface. First, for relatively thin coatings (< 10 mm), there is a sharp increase in structural material temperature with increasing coating thickness. This is the result of reduction in heat transfer area radially from the coating inward towards the coolant at the leading edge. This geometry effect does not exist at the top surface of the limiter where the structural temperature remains nearly constant with coating thickness. As the coating thickness is increased further, the previously described effect of radiative heat transfer becomes important for BeO-V, SiC-V, and SiC-Cu as shown in Fig. 5-38. At the leading edge, there are two factors competing with each other when the coating is thick (temperature is high). The radial reduction in heat transfer area tends to increase the temperature, while radiative heat transfer losses at high surface temperatures tends to decrease the structural temperatures. Figure 5-39 indicates that the effect of reduction in heat transfer area is controlling at high temperatures (thick coatings) and the structure temperature continues to increase with coating thickness at the leading edge.

Figures 5-40 and 5-41 show the radial temperature distributions in the coating and structural materials at the leading edge. Again the temperature gradient is nearly constant in the structural material and in the coating material when the temperature is relatively low. The temperature profile in

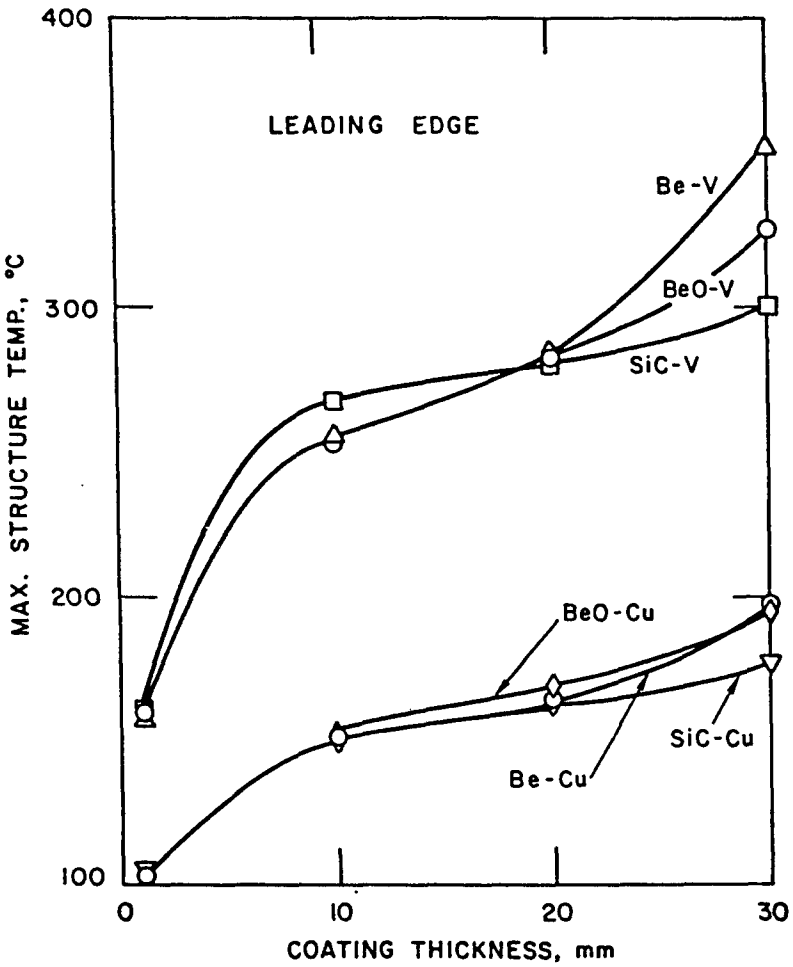

Figure 5-39. Maximum structural temperatures at the leading edge as a function of surface material thickness for several surface materials.

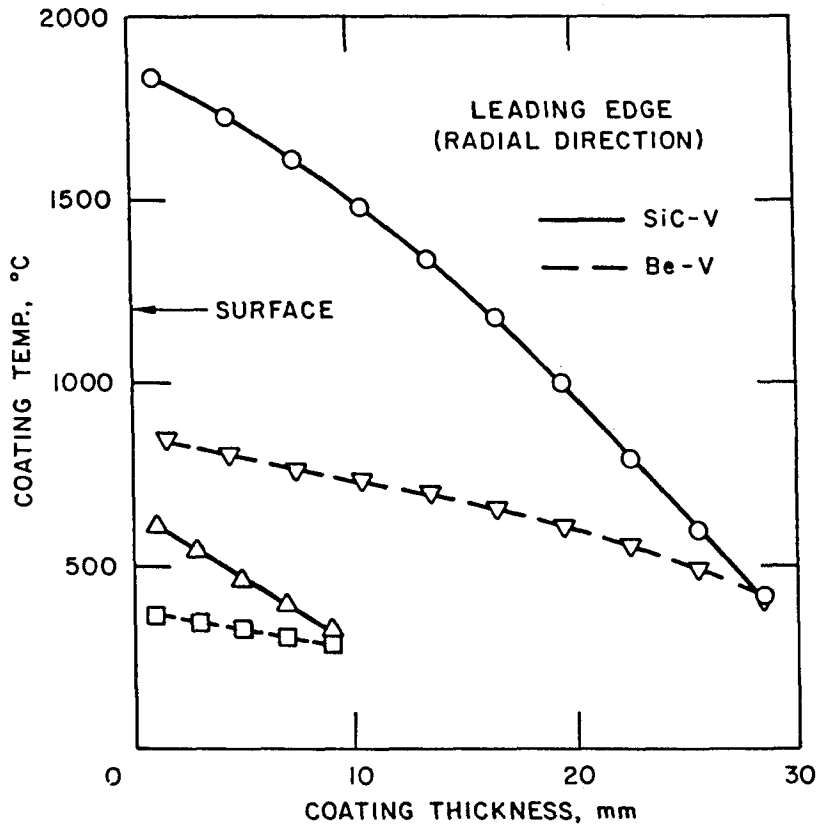

Figure 5-40. Radial temperature profiles in the coating material at the leading edge.

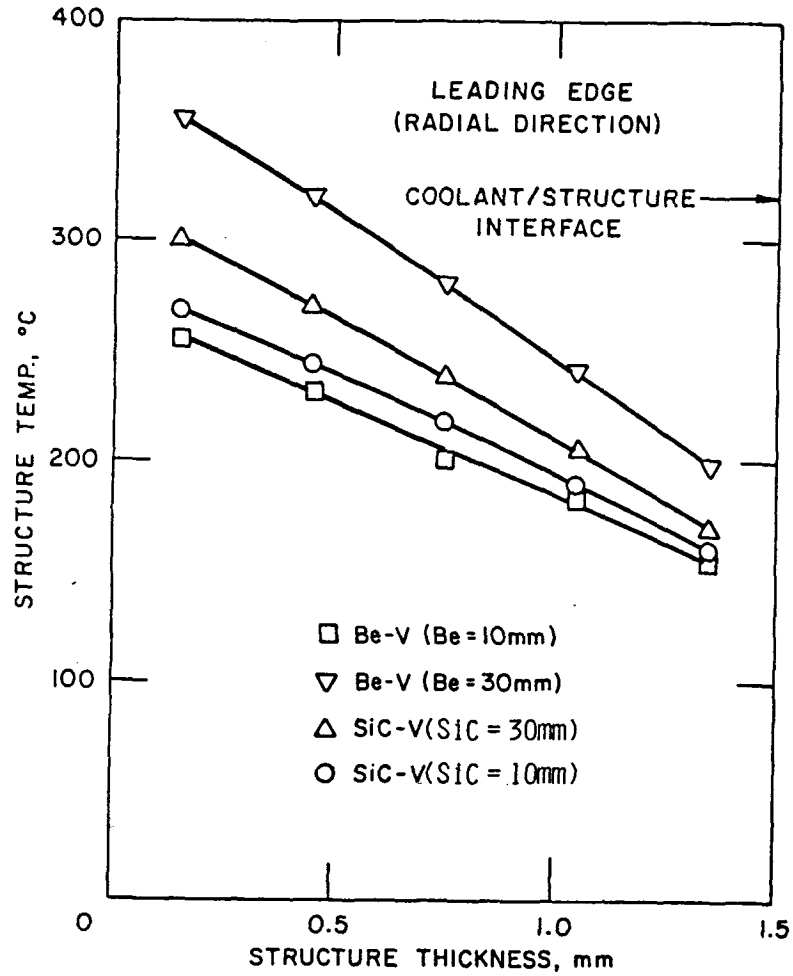

Figure 5-41. Radial temperature profile in the vanadium heat sink at the limiter leading edge.

the coating material becomes non-linear when the temperature is increased. The circumferential temperature gradient is usually much smaller than the radial gradient.

5.8.2.3 First Wall

The maximum surface temperature for a number of materials are shown in Figs. 5-42 and 5-43 for surface heat fluxes of 0.25 MW/m^2 and 0.45 MW/m^2. The 0.25 MW/m^2 case applies to the bulk of the first wall removed from the limiter, and the 0.45 MW/m^2 case applies to the areas adjacent to the limiter leading edges which receive a high charge-exchange neutral flux. In all cases, the substrate is Type 316 stainless steel which is 4 mm thick, and the surface materials are assumed to be perfectly bonded to the substrate. The

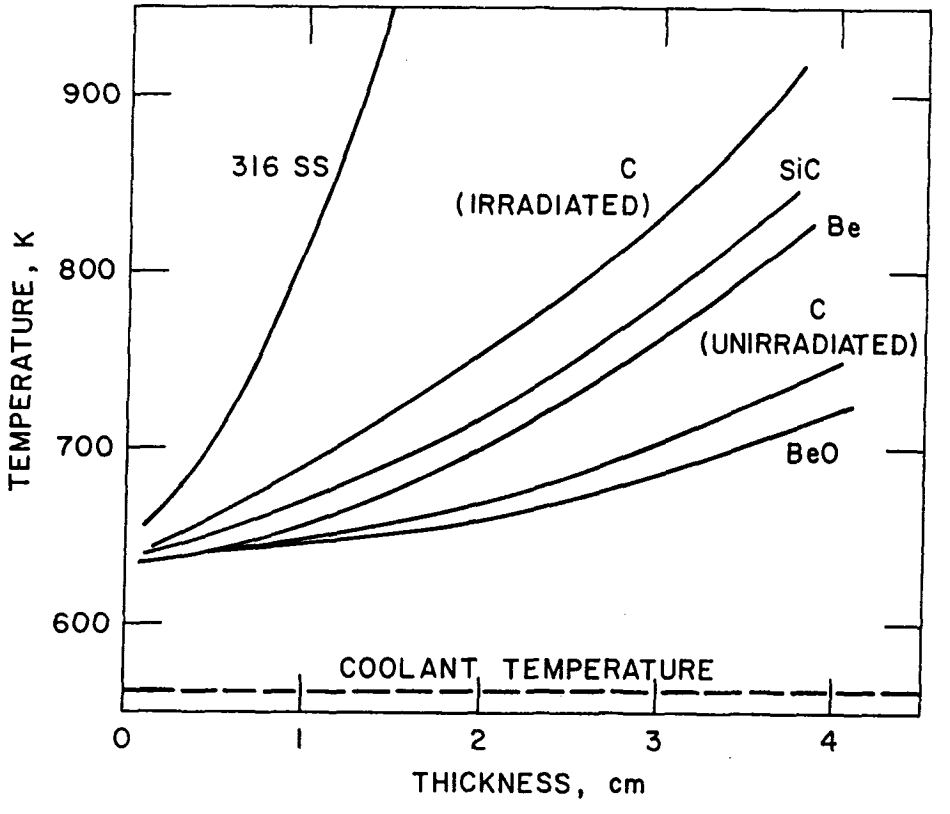

Figure 5-42. First wall surface temperature as a function of plasma side cladding thickness (0.25 MW/m^2).

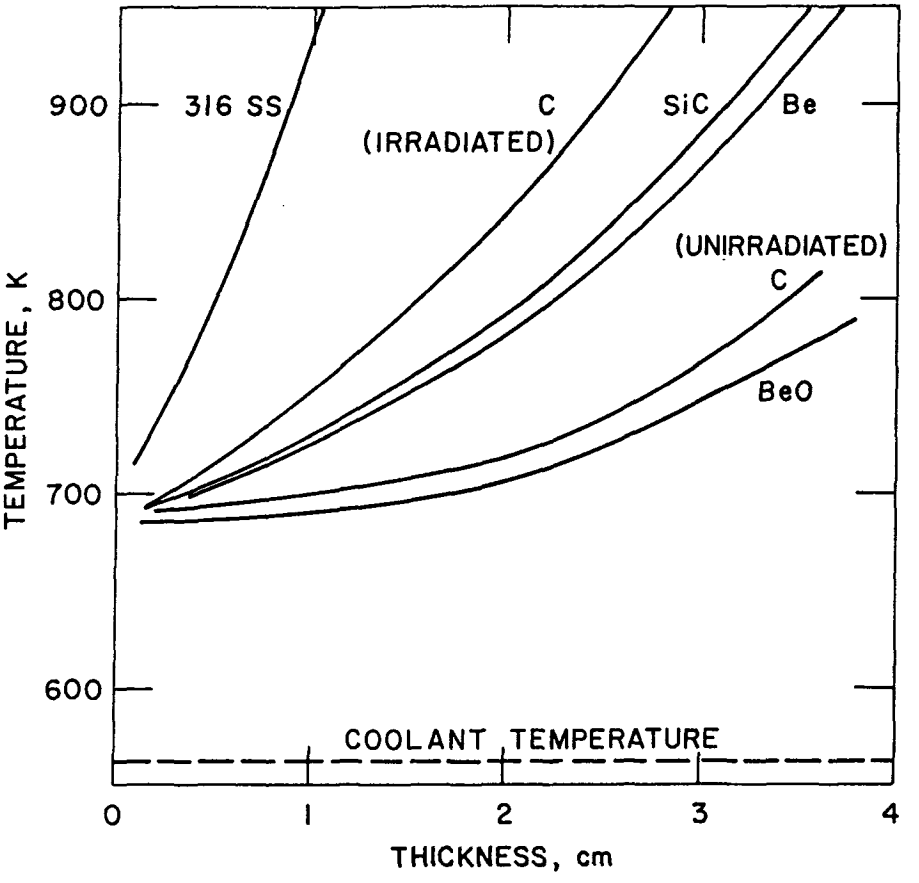

Figure 5-43. First wall surface temperatures for high charge exchange neutral flux areas (0.45 MW/m^2) as a function of plasma side cladding thickness.

coolant temperature is assumed to be 290°C. Bare stainless steel exhibits the highest temperatures at any given thickness, and BeO exhibits the lowest temperatures. Graphite loses much of its original thermal conductivity with irradiation damage, and therefore the surface temperatures for both unirradiated and irradiated graphite are shown. The refractory compounds, SiC and BeO, are also predicted to lose much of their original thermal conductivity with irradiation. With the exception of stainless steel, all candidate plasma side materials exhibit modest temperatures up to a thickness of 3-4 cm. The surface temperatures for the 0.45 MW/m^2 condition are 75-100°C greater than the temperatures for the 0.25 MW/m^2 condition.

5.8.2.4 Summary

The results of this Section are summarized below:

1. Both structural materials, V and Cu, exhibited fairly low temperatures (Cu < 200°C, and V < 360°C) and are acceptable under the assumed operating conditions shown in Table 5-22.

2. SiC and BeO have poor thermal conductivities at medium and high temperatures which resulted in much higher coating temperatures compared to Be with the same thickness. However, this does not imply that Be is preferred over SiC and BeO since both SiC and BeO have much higher melting points than Be. Tungsten is a very good coating material from a purely thermal point of view.

3. At high coating temperatures (which correspond to thick coating materials), radiative heat transfer becomes important which resulted in the reduction of structure material temperature with increasing coating thickness in the top surface. At the leading edge, the effect of reduction in heat transfer area radially is controlling, which resulted in a sharp increase in structural temperature with coating thickness when it is relatively thin (< 10 mm) and a gradual increase with coating thickness at thicknesses where radiative heat transfer becomes significant.

4. For the assumed surface heat flux distributions, the coating temperature in the top surface is always greater than that at the leading edge. This statement is also valid regarding the temperature of the structural material when the coating is thin (< 10 mm). However, when the

coating thickness further increases, the temperature of the structural material at the leading edge becomes greater than that of the structural material at top surface and condition at the leading edge becomes controlling.

5. The temperature gradients in the coating materials remain fairly constant in both the top surface and the leading edge in the radial direction when the coating temperature is fairly low. These temperature profiles become non-linear when the coating temperature is high (very thick coating). The temperature profiles in the structural materials are always linear as a result of the relatively low temperature and small thickness (1.5 mm) of the structural material. At the leading edge, the radial temperature gradient is always larger than the circumferential temperature gradient.

6. The first wall temperatures remain relatively low for all materials considered due to the relatively low surface heat flux. At these low fluxes, neutronic heating significantly adds to the heat load.

5.8.3 Stress Analysis

5.8.3.1 Introduction

The limiter is a critical component of the reactor and, consequently, a high degree of reliability is required. This is achieved in the present section by limiting the maximum stresses in the limiter to the design allowables. Since the DEMO is a "steady state" machine ideally its life should not be limited by fatigue.

Under steady-state conditions the assumed maximum heat fluxes at the top surface and the leading edge of the limiter are 2.4 MW/m^2 and 1 MW/m^2 respectively. This results in a higher temperature and temperature gradient at the top surface of the limiter than at the leading edge. If one assumes that the constraint of the coating on the substrate is minimal, then the stresses are more severe at the leading edge than at the top surface because of larger geometrical constraints present at the leading edge. On the other hand, if the constraint of the coating is taken into account, then the stresses are more severe at the top surface than at the leading edge.

Two structural materials - vanadium and copper, and several coating materials - beryllium, beryllium oxide, silicon carbide, and tungsten have been considered in the stress analysis.

The analysis shows that annealed tough pitch copper, because of its inferior strength properties, cannot meet the code requirement for any reasonable thickness of coating. Vanadium, on the other hand, can meet the code requirement with a coating thickness of up to 3 cm. It should be noted that a copper alloy such as Cu-2% Be has significantly higher strength properties than pure annealed copper and meets the allowable stress criteria.

A close examination of the results of the stress analysis shows that the majority of the stress in the limiter is caused by the constraint exerted by the cool core region away from the plasma on the hot front wall facing the plasma. Future efforts should focus on changing the design configuration in order to minimize this temperature difference. In fact, it can be shown that if the stresses in the heat sink hot wall were caused solely by the temperature gradient across the first wall and not by the constraint of the cool core region, then for a given wall thickness, copper, because of its superior thermal conductivity, should have a larger allowable surface heat flux.

5.8.3.2 Substrate Stresses

5.8.3.2.1 Assumptions

1) The basic configuration of the leading edge for stress analysis is the same cylindrical model as reported in Reference 4 and reproduced in Fig. 5-44. Details of the stress analysis are given in Reference 4.

2) Both the cooling and the heat sink structures are assumed to be linearly elastic. Because of rapid radiation hardening this assumption may not be unrealistic.

3) The coating is assumed to be segmented (Fig. 5-45). For small coating thicknesses ($\sim$ 1 mm), the width of the coating is large compared to its thickness (Case I), and the full thickness of the coating is effective in exerting constraint on the substrate structure. However, when the coating thickness is large ($\geq$ 1 cm) so that its thickness is of the same order as its width (Case II), either the constraint of the coating on the substrate is ignored or the effective thickness (h_{eff}) of the coating is obtained by using a shear lag type analysis (see Fig. 5-45). To be conservative, the lag angle ϕ is assumed to be 45°.

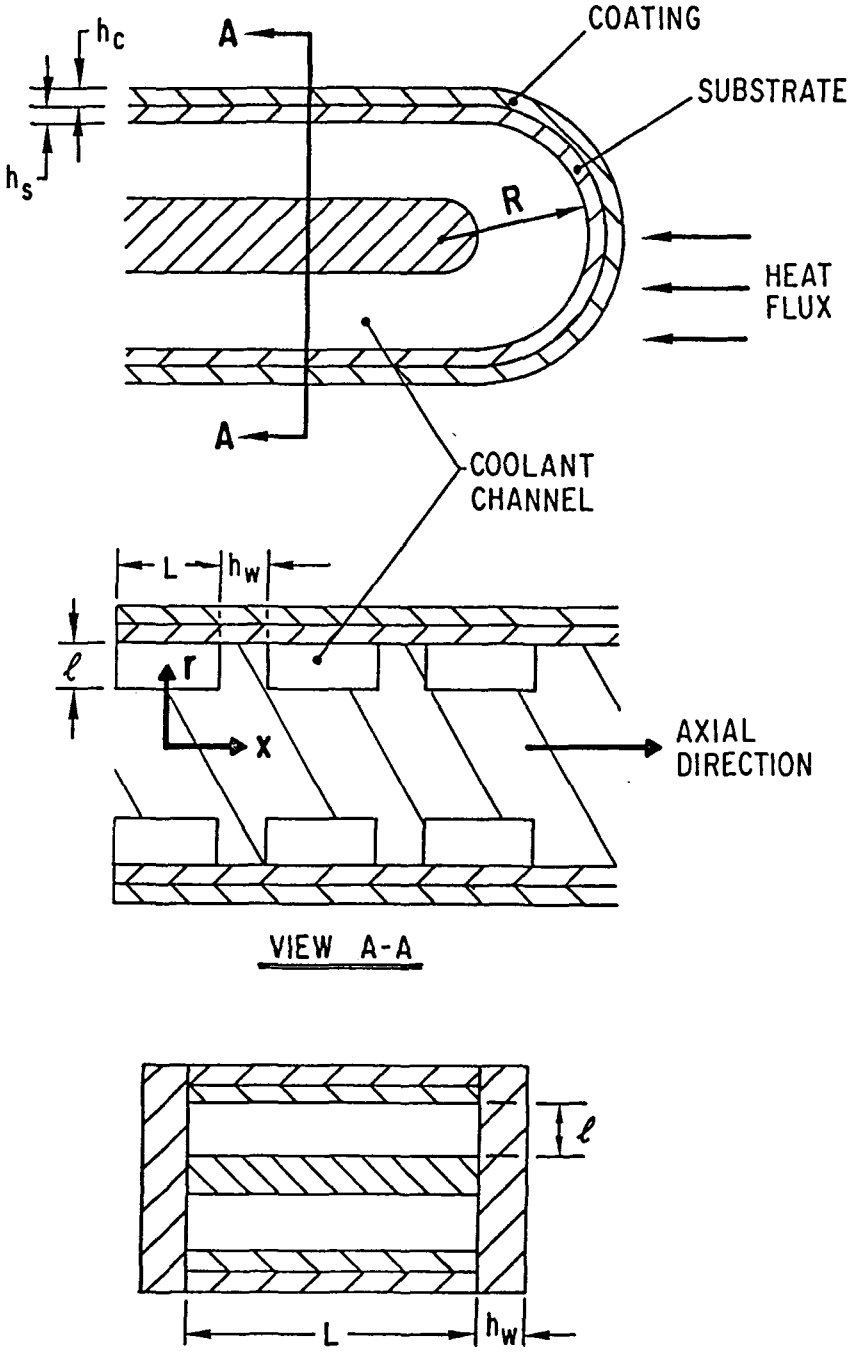

Figure 5-44. Leading edge geometry used for stress calculations.

CASE I $h \leq \frac{W}{2} \tan \phi$

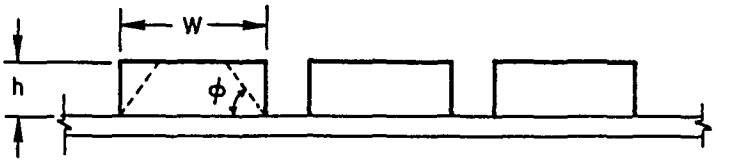

$$h_{eff} = h \left[1 - \frac{h}{W} \cot \phi \right]$$

CASE II $h > \frac{W}{2} \tan \phi$

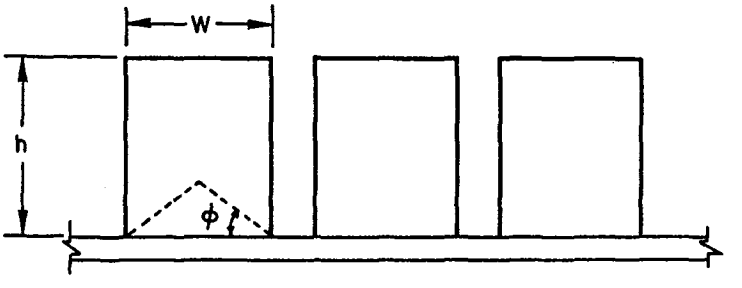

$$h_{eff} = \frac{W}{4} \tan \phi$$

Figure 5-45. Effective thickness for the coating.

4) Although the limiter is cantilevered in the poloidal direction, since the limiter core structure is much cooler than the plasma side structure, it is assumed conservatively that the plasma side structure is free to expand but constrained from bending in the poloidal direction. It is also assumed to be constrained from bending in the toroidal direction. However, because the plasma side structure is constrained from deforming in the toroidal and the radial direction by the relatively cooler radial walls between coolant channels, large toroidal stresses and shell-type membrane and bending stresses will be called into play. These stresses are computed to be much larger than the stresses due to the temperature gradient through the front wall of the heat sink.

5) The effects of the poloidal variation of temperatures on the stresses in the limiter are assumed to be small. The leading edge is analyzed assuming a radial temperature profile corresponding to the highest temperature gradient through the wall and the circumferential variation of the profile is neglected. Since the poloidal temperature gradient is small compared to the temperature gradient in the thickness direction, this is a reasonable assumption and is likely to produce conservative results at the leading edge.

6) The ASME code criterion of $3S_{mt}$ limit is applied on the effective stress range between uniform room temperature and the operating steady state temperature of the limiter. For the temperatures of interest $3S_{mt}$ represents the ultimate strength of the heat sink material.

5.8.3.2.2 Results

Table 5-25 shows a comparison of the maximum stresses with the allowable stress for various coating material and coating thicknesses for cases where copper is used as the structural material. Note that even though the constraining effects of the coating on the substrate are ignored, a typical annealed tough pitch copper does not have sufficient strength to meet the ASME code criterion for any thickness of coating considered. However, beryllium copper which is a much stronger alloy of copper can meet the $3S_m$ requirement in all cases.

Table 5-25. Maximum Stresses in the Limiter Structural Material (Copper) Assuming No Constraint of the Coating

Coating Material	Coating Thickness (mm)	Maximum Stress Range in Copper (MPa)		$3S_m$ (MPa) Value For	
		Top Surface	Leading Edge	Tough Pitch Copper	Beryllium Copper
Be	1	154	93	120	1225
	10	158	218	120	1225
	20	161	246	120	1225
	30	165	330	120	1225
W	1	154	96	120	1225
	10	165	250	120	1225
SiC	1	154	96	120	1225
	10	158	226	120	1225
	20	161	247	120	1225
	30	165	323	120	1225
BeO	10	-	213	120	1225
	20	-	240	120	1225
	30	-	310	120	1225

Table 5-26 shows a similar comparison when vanadium (V-15Cr-5Ti) is used as the structural material. Vanadium can meet the $3S_m$ requirement for up to ~ 3 cm thick coating.

The poor performance of pure copper in spite of its superior thermal conductivity as compared to vanadium is unexpected. The ability of a flat plate of thickness h which is constrained from bending to sustain thermal stress due to a surface heat flux q_w is governed by the stress index defined as:

$$\text{Stress index} = \frac{k}{q_w h} \frac{S_{mt}}{E\alpha}$$

where k = thermal conductivity

E = Youngs Modulus

α = coefficient of thermal expansion

S_{mt} = ASME code limit for primary stresses.

Table 5-27. Comparison of Fatigue Life Indices for Copper and Vanadium Limiter for a Wall Thickness of 1.5 mm and Surface Heat Flux of $1 MW/m^2$

Material	k W/m-K	α 1/K	E MPa	S_{mt} MPa	Stress* Index
Copper	310	18×10^{-6}	10^5	40	4.6
Vanadium	25	10×10^{-6}	1.2×10^5	187	2.6

*Stress Index $= \frac{k}{q_w h} \frac{S_{mt}}{E\alpha}$, $q_w = 1\ MW/m^2$, $h = 1.5$ mm

5.8.3.2.3 Tile Size Effects

The stress analysis provided above are based on the assumption that the coating provides no constraint on the substrate. This is a valid assumption provided the coating is extensively cracked due to stresses during operation, If, on the other hand, the coating is not extensively cracked, then it will exert some constraint on the substrate dependent on its thickness and segment width. It is assumed in the present analysis that the coating (or tile) consists of square segments that are perfectly bonded to the underlying substrate. For large width to thickness ratios of the coating segments, the full thickness of the coating is effective in constraining the substrate. However, for cases where the coating thickness is either large or comparable to its width, the effective thickness can be significantly less than its full thickness. As an example, Table 5-28 shows the maximum stresses in a vanadium substrate as a function of the coating thickness for a segment width of 2 cm. A comparison between Table 5-26 with Table 5-28 shows that the effect of the constraint of the coating is to raise the stresses at the top surface and reduce the stresses at the leading edge. As a result, all the coating materials can meet the $3S_{mt}$ criterion for a thickness of up to 3 cm.

Table 5-26. Maximum Stresses in the Limiter Structural Material (Vanadium Alloy) Assuming No Constraint of the Coating

Coating Material	Coating Thickness (mm)	Maximum Stress Range in Vanadium (MPa)		$3S_m$ (MPa)
		Top Surface	Leading Edge	
Be	1	212	180	560
	10	219	377	560
	20	226	435	560
	30	231	589	560
W	1	214	185	560
	10	232	446	560
SiC	1	214	186	560
	10	218	400	560
	20	226	456	560
	30	232	610	560
BeO	10	-	371	560
	20	-	431	560
	30	229	561	560

The higher the stress index the higher the capability of the material to sustain surface heat fluxes without violating the ASME Code criterion. Table 5-27 shows the stress indices for limiters made of tough pitch copper and vanadium. Note that inspite of its poor strength properties, copper has a higher value of stress index than vanadium because of its vastly superior thermal conductivity. Thus if a plate of given thickness were subjected to thermal stresses due only to a temperature gradient through its thickness because of an imposed surface heat flux, than the maximum allowable surface heat fluxes of such a plate would be about twice as high when copper is used as the plate material compared to when vanadium is used as the plate material. A close examination of the limiter stress analysis shows that although the stress due to the temperature gradient through the thickness is significantly higher in the case of vanadium than in the case of copper heat sink, the major components of the total stress which is caused by the toroidal constraint of the cooler central region of the limiter on the hot-front wall are almost identical for the two materials. Consequently, the superior performance of the vanadium limiter is a reflection of the superior strength properties and not a reflection of a superior stress index.

Table 5-28. Maximum Stresses in the Limiter Structural Material (Vanadium) Alloy Including Constraint of Coating (Tile)

Coating Material	Coating Thickness (mm)	Maximum Stress Range in Vanadium (MPa) *		$3S_m$ (MPa)
		Top Surface	Leading Edge	
Be	1	241	152	560
	10	471	253	560
	20	501	292	560
	30	528	305	560
W	1	215	109	560
	10	234	257	560
SiC	1	214	107	560
	10	357	238	560
	20	373	274	560
	30	322	326	560
BeO	10	245	229	560
	20	346	264	560
	30	375	339	560

* Stresses are computed on the basis of a coating (tile) width of 2 cms.

5.9 Lifetime Considerations

5.9.1 Design Criteria

The selection of the design criteria represents the first step in determining the lifetime of the limiter. The ASME Code Case N47 for Class I components has been used as a guide for the design of the limiter structural material in this report. The coating need not be restricted by the code since it is not a load bearing material. However, additional stresses in the structural material due to constraint of the coating must be considered in the analysis.

Section III and Code Case N47 are intended to cover a wide variety of design configurations and service conditions, and the design criteria are, therefore, quite conservative. The various possible modes of failure which confront the designers are:

(1) Excessive elastic deformation and elastic instability.
(2) Excessive plastic deformation.
(3) Brittle fracture.
(4) Stress rupture/creep deformation.
(5) Plastic instability - incremental collapse.
(6) High strain - low cycle fatigue and creep fatigue.
(7) Stress corrosion.
(8) Corrosion fatigue.

The code imposes various limits on stresses and strain in order to avoid the above modes of failure. The designer must consider, in addition to setting limits for allowable stress, some adequate and proper failure theory in order to define how the various stresses in a component react and contribute to the strength of that part.

Since different types of stress have different degrees of significance, the code allows a different allowable stress for each stress classification. The classes of stresses considered by the code are broadly categorized as: (1) primary stress, (2) secondary stress, and (3) peak stress.

Primary stress is a stress developed by the imposed loading which is necessary to satisfy the laws of equilibrium between the external and internal forces and moments. The basic characteristic of primary stress is that it is

not self limiting.

Secondary stress is a stress developed by the self constraint of a structure. It must satisfy an imposed strain pattern rather than be in equilibrium with an applied load. The basic characteristic of a secondary stress is that it is self limiting.

Peak stress is the highest stress in the region under consideration. The basic characteristic of a peak stress are that it causes no significant distortion and is objectionable mostly as a source of fatigue failure.

Each stress category is further divided into membrane and bending components. Thermal stress is seldom categorized as primary stress but can be either secondary or peak. Thermal stresses which can produce distortion of the structure are placed in the secondary category and thermal stresses which result from almost complete suppression of differential expansion, and thus cause no significant distortion, are classed as peak stresses. An additional common example of a peak stress is that due to a notch or a stress raiser.

The potential failure modes and various stress categories are related to the code provisions as follows:

(1) The primary stress limits are intended to prevent plastic and/or creep deformation and to provide a nominal factor of safety on the ductile burst pressure and creep rupture.

(2) The primary plus secondary stress limits are intended to prevent excessive plastic deformation leading to incremental collapse or ratchetting and to validate the application of elastic analysis by ensuring shakedown when performing the fatigue evaluation.

(3) The peak stress limit is intended to prevent fatigue failure as a result of cyclic loading.

(4) For elevated temperature designs, the code requires special considerations to prevent failure by creep-fatigue interaction.

(5) Special stress limits are provided for elastic and inelastic instability.

(6) Protection against brittle fracture is provided by material selection, rather than by analysis.

(7) Protection against environmental conditions such as corrosion and radiation effects are the responsibility of the designer, but procedures for protecting against these effects are not provided in the code.

(8) In addition to stress limits, the code also requires the maximum accumulated inelastic strain not to exceed prescribed values.

(9) The code allows the same stress limits for welds as for the base metal. However, the accumulated inelastic strain limit for welds is prescribed to be half of that of the base metal.

The allowable stresses in the code are given in terms of the stress intensity, S_{mt}, which is calculated from the tensile and creep properties as shown in Table 5-29. At lower temperatures, S_{mt} is a fraction of either the yield or the ultimate strength.

Table 5-29. Design Allowable Stresses

Time-Independent Allowable Stress, S_m (other than bolting)	Lowest value of	1/3 S_{ult} at Room Temperature 1/3 S_{ult} at Temperature 2/3 S_y at Room Temperature 2/3 S_y at Temperature
Time-Dependent Allowable Stress, S_t	Lowest value of	2/3 of Minimum Stress to Cause Creep Rupture in Time, t 80% of Minimum Stress to Cause Tertiary Creep in Time, t Minimum Stress to Produce 1% Strain in Time, t
General Primary-Membrane Allowable Stress, S_{mt}		Lesser of S_m and S_t at Temperature and Time

S_{ult} = Ultimate Strength
S_y = Yield Strength

The primary membrane stress is limited to a value of S_{mt}, whereas the sum of primary and secondary stresses at low temperatures, including thermal stress, is limited to a value of $3S_m$. The value of $3S_m$ is assumed to assure shakedown after the first cycle. When peak stresses are included, the allowable stress is then related to the fatigue property of the material. The design curve for fatigue has a factor of safety of two on strain range or twenty on life, whichever is more conservative. The safety factor accounts for various uncertainties in material properties as well as calculated stresses.

The ASME Code does not consider corrosion or radiation effects in order to establish the stress or strain limit. Although the safety margin in many cases may be adequate, the adequacy of these safety margins for fusion application has to be determined. Also, the code does not consider crack growth, using fracture mechanics-type analysis. Although such an approach is highly desirable, the applicability of linear elastic fracture mechanics to analyze crack growth in the thickness direction of a thin creeping solid is questionable. The elastic-plastic fracture mechanics approaches for crack growth are still undergoing development and are not considered to be at a stage to be used in design.

One aspect of the limiter design that requires attention is the bond shear stress between the coating and the structure. Procedures have to be developed in order to calculate and set an upper limit on the shear stress. For a very thick coating, where it is almost certain that the coating will crack, it has to be determined by a combined analytical/experimental approach whether such cracks will penetrate the structural material. Cracks might also initiate and propagate from the coolant side where corrosion may be a contributing factor.

5.9.2 Maximum Allowable Thickness

5.9.2.1 Introduction

The evaluation of the allowable thickness of surface materials is an important aspect of the lifetime determination. In general, the allowable thickness is set by a variety of criteria including maximum permissible temperatures, maximum allowable stresses, crack growth and fatigue

limitations, and radiation effects. The thicknesses are expected to be dependent on the heat flux conditions, materials, and design geometry. This section will present the results of the allowable thickness calculations for the limiter top surface and leading edge.

The surface heat flux to the top surface is held constant at 2.4 MW/m^2, and the heat flux to the leading edge is a maximum of 1 MW/m^2. The top surface has been analyzed using a cylindrical geometry. The primary inputs to the calculations are the temperature distributions and the stress and fatigue calculations discussed in Section 5.8.

5.9.2.2 Maximum Allowable Temperatures

The maximum allowable temperatures for the various materials are determined by: (1) melting, (2) vaporization losses, (3) excessive chemical sputtering, (4) radiation-induced swelling/cracking, and (5) microstructural changes (e.g., sintering, phase changes). For the present analysis, all the criteria but microstructural changes have been considered. The results of the analysis are presented in Table 5-30.

The vaporization limits have been determined by assuming that all vaporized atoms are lost from the surface. The flux of surface atoms leaving the surface, ϕ_s, can be related to the vapor pressure, P_v, by

$$\phi_s = \frac{P_v}{(2\pi\ mkT)^{1/2}}$$

where m is the mass of the surface atom, k is Boltzman's constant, and T is the absolute temperature.[30] The vapor pressure data are taken from Refs. 31-33. Table 5-30 shows two vaporization limits depending on whether 1 mm/yr or 10 mm/yr is vaporized. These temperatures range from ~ 0.6 to ~ 0.75 of the absolute melting temperature.

In most cases, the allowable temperatures are limited by radiation damage considerations. For Be, high helium bubble swelling is observed at temperatures $\geq$ 973 K, and for SiC, significant swelling rates are observed at temperatures $\geq$ 1473 K.[34,35] In the case of W and Ta, radiation swelling peaks are observed at relatively low temperatures.[36,37] BeO is a special case because it is an insulator with a non-cubic crystal structure. At low temperatures, radiation swelling is rapid and anisotropic which results in

Table 5-30. Maximum Allowable Temperatures (K) of Surface Materials

Material	MP	Vaporization 1 mm/y	Vaporization 10 mm/y	Swelling	Chemical Sputtering	Final
Be	1551	1130	1205	973	-	973
BeO	2823	1930	2055	>873	-	> 873 <2000
C	3925	2170	2280	1173	773	773
SiC	2970	1620	1715	1473	-	1473
W	3683	2770	2950	< 873 >1173	-	873
Ta	3269	2600	2770	< 773 >1073	-	773

microcracking of polycrystaline material.[38] Models and limited data suggest that the degree of swelling decreases at elevated temperatures, and it should remain at acceptable levels above ~ 873 K. Therefore, BeO also has a minimum operating temperature besides a maximum operating temperature. It should be noted that for radiation limited temperatures, there are often only limited data from which to determine temperature limits. The temperatures shown in Table 5-30 may be modified in the future as additional data become available.

The only material whose operating temperature is limited by chemical sputtering is graphite. The chemical sputtering peak for hydrogen bombarded graphite is ~ 873 K, and recently temperature dependent sputtering has been observed at temperatures above ~ 1273 K. In order to remain below the peak sputtering temperature, the graphite temperature limit has been set at ~ 773 K. Other materials, particularly the carbides, may exhibit chemical sputtering, but the effect is expected to be minor compared to graphite. Chemical sputtering is discussed in more detail in Section 5.6.

5.9.2.3 Allowable Thickness

The information presented in the previous section can be combined with the results of Section 5.8 to determine the allowable thicknesses. Table 5-31

shows the temperature limited thicknesses for the top surface materials in both the unirradiated and irradiated conditions. For the top surface, fatigue does not limit the thickness because it is assumed that the surface material offers little constraint to the heat sink. The difference in the materials in the irradiated and unirradiated conditions is the reduced thermal conductivity in non-metals which is observed following irradiation. It has been assumed for purpose of comparison that the effect of radiation is to reduce the thermal conductivity to 30 W/mK as has been observed for graphite.[2] This assumption was made because of the very limited data available for other non-metals. The actual thermal conductivity following irradiation could be greater are less than this value. The reduction in conductivity with irradiation is rapid with saturation levels reached after a damage level of only ~ 1 dpa.

In the irradiated condition, the metals offer the largest allowable thicknesses. In the case of graphite, the combination of a low allowable temperature and low conductivity after irradiation limits the thickness to only 4 mm. The thicknesses shown in Table 5-31 could be further reduced if more severe tile restraints significantly reduce the fatigue life of the

Table 5-31. Allowable Thicknesses (Temp.) Surface Materials

Material	Allowable Thickness Unirradiated (cm)	Irradiated (cm)
Be	2.5	2.5
BeO	4.5	2.4
C	1.5	0.4
SiC	1.4	1.0
W	3.6	3.6
Ta	3.2	3.2

heat sink. The width of the surface tile and the geometry of the heat sink will influence this restraint. For example, in the case of Be on a vanadium alloy heat sink, if the tile width is 25 cm, the $3S_m$ stress criteria is exceeded for a tile thickness of only 12 mm as shown in Fig. 5-46. If the tile width is restricted to 20 mm, then the $3S_m$ criteria is not exceeded at any thickness because the effective tile thickness is only ~ 10 mm. Since DEMO operates in a steady-state mode, fatigue is not life limiting. For small tile widths, the allowable thickness will, therefore, be governed by the maximum allowable temperature, but for larger tile widths, the stress considerations could limit the thickness.

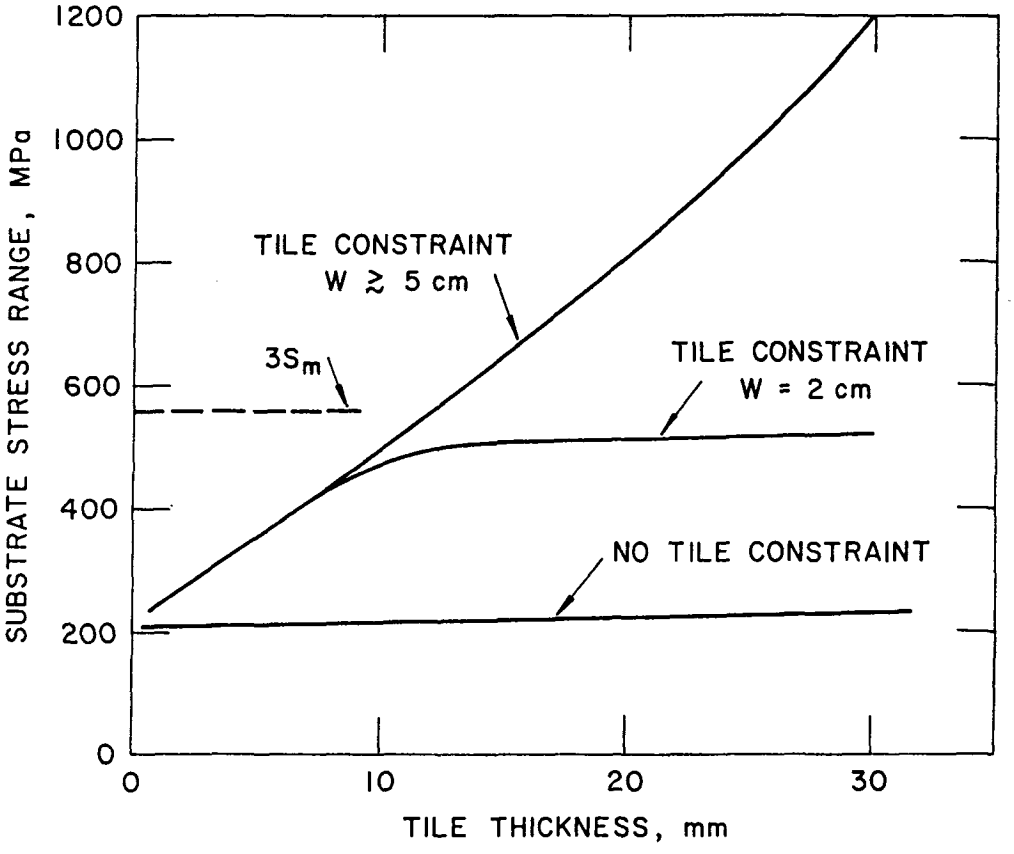

Figure 5-46. Vanadium heat sink stresses as a function of beryllium surface tile thickness.

The leading edge allowable thicknesses are different from the top surface thicknesses due to the different geometry. The cylindrical geometry results in a different temperature distribution and in different stress constraints than the plate geometry. The result for equivalent calculations of allowable thicknesses are shown in Table 5-32. For the leading edge, maximum allowable temperature usually limits the material thicknesses. Table 5-32 compares the temperature and stress limits for both copper and V-15Cr-5Ti heat sinks. The temperature limited thicknesses are less for the vanadium because the vanadium heat sink operates ~ 100°C hotter than the copper heat sink. Note, that the effects of radiation on the thermal conductivity has not been included in the thickness calculations at the leading edge.

Table 5-32. Allowable Thickness Leading Edge

Material	Temperature		Stress-Fatigue (No Tile Constraint)	
	Cu (cm)	V (cm)	Cu (cm)	V (cm)
Be	3.2	2.6	~ 0.3	2.9
BeO	>4	3.2	~ 3.0	3.0
C (Unirr.)	2.4	1.7	-	-
SiC	2.1	1.7	~ 3.0	2.7
W	2.8	2.2	2.5	1.1

5.9.3 Lifetime Estimates

5.9.3.1 Introduction

Lifetime calculations for the limiter and first wall have been performed. The analysis considers the influence of disruptions, sputtering/redeposition, temperature, and stress. Figure 5-47 shows the logic sequence used to determine lifetimes. First the operating parameters, such as particle and heat flux distributions and disruption scenarios, are used to calculate the effects of disruptions and sputtering on the net erosion rates

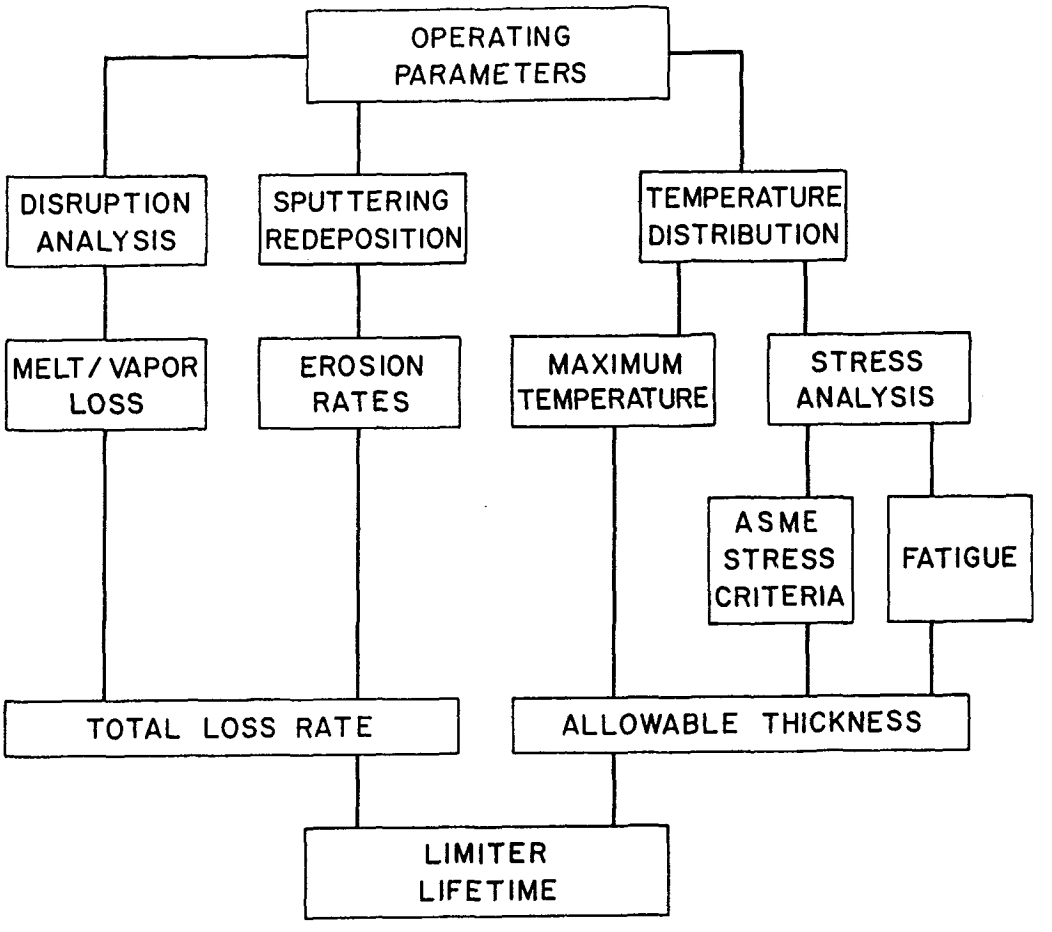

Figure 5-47. Flow chart of lifetime analysis.

of the surface materials. These analyses are discussed in Sections 5.4 and 5.1. The temperature distributions and stresses through the materials are used to determine the maximum allowable thicknesses, as discussed in the previous section. Comparison of the total loss rate to the maximum allowable thickness leads to the estimate of the component lifetime.

The diagram shown in Fig. 5-47 represents a simplification of the actual conditions. Another major consideration, not shown, is the effects of radiation on the various material properties. The influence of radiation has been included in the estimate of allowable temperatures, but the changes in the mechanical properties with time have not been considered. In addition, the major lifetime categories, shown in Fig. 5-47, are not necessarily independent of each other. For example, the erosion of material will alter the temperature and stress distribution. These changes will tend to increase the fatigue lifetime as the plates and leading edges get thinner. A more

complete analysis would examine the time evolution of the limiter to provide a more realistic estimate of the lifetime.

Several assumptions have been made in the lifetime analysis. First, stress and fatigue limits have been applied only to the heat sink and not to the surface materials. Since the surface material is not expected to carry a primary stress load, it is believed that it does not need to conform to the ASME code requirements. In fact, cracking of the surface material is not considered to be a failure as long as it remains attached to the heat sink and the crack does not continue to propagate into the heat sink. The influence of the surface material on the temperatures and stresses in the heat sink has been considered, however. Second, all vaporized/melted material is considered to be lost during a disruption. This is a conservative assumption, and there are some indications that the melt layer may be stable during a disruption (See Section 5.7 for details). Third, linear elastic behavior is assumed for the mechanical behavior of the surface material and the heat sink. A more complete analysis should include the effects of plastic deformation. Again, this is a conservative assumption, since plastic deformation will limit the stresses within the material. Fourth, a fatigue safety factor, in accordance with ASME specifications, has been used in the analysis. The fatigue data curves have been reduced by a factor of two in strain or by a factor of twenty in cycles to failure, whichever is lower, to estimate the lifetimes. The safety factor should be adequate to account for statistical fluctuations in the data and to account for the possible reductions in fatigue life due to the harsh reactor environment. Finally, the possible failure of the bond between the surface material and the heat sink has not been accounted for in the analysis. The possible loss of the bond is an important consideration, but it is difficult to make a reasonable estimate of bonding effects because of the lack of information on bond properties or on the influence of radiation. Work in this area is continuing.

5.9.3.2 Net Erosion Rates

Material can be lost from the limiter/divertor and first wall by sputtering and by disruptions. For the present conditions, where the charge exchange neutral flux is concentrated around the limiter, the net sputtering rate on the first wall is close to zero. Therefore, only disruption effects

need to be considered on the first wall. The sputtering loss rates at 50% availability for the top surface of the limiter are based on the results in Section 5.4, and only physical sputtering is considered. At 20 eV, both Ta and W are predicted to have no net erosion, whereas at $T_e \gtrsim 100$ eV, where the self sputtering coefficient exceeds unity, a runaway sputtering condition is predicted. The low-Z materials, including SiC, show comparable erosion rates at low temperatures. However, SiC may be unacceptable at $T_e \gtrsim 100$ eV because of high self sputtering.

The loss of material during disruptions depends on the energy density, the disruption time, the disruption frequency, and the material. Two disruption scenarios have been considered, as shown in Table 5-33. The disruption time is assumed to be 20 ms, and the effect of vapor shielding has been included in the calculations. The worst case scenario places all the plasma energy on the limiter during a disruption. The disruption time is 5 ms and vapor shielding is not included. The calculated material loss for these cases is shown in Table 5-34. Beryllium has the highest loss rate due to its relatively low melting point. For the reference conditions, neither W or Ta melt, but for the worst case conditions, melting is significant. Graphite and SiC are resistant to disruptions because of their high sublimation temperatures. For beryllium under the reference disruption conditions, when the surface temperature is raised to ~ 700°C, the melt layer thickness is calculated to increase from 70μm to ~ 170μm.

Table 5-33. Disruption Conditions Used for Lifetime Analysis

	Reference		Worst Case	
	Limiter	First Wall	Limiter	First Wall
Major Disruptions				
Energy (J/cm^2)	270	175	535	175
Time (ms)	20	20	5	5
Vapor Shield	Yes	Yes	No	No
Disruptions - 50 During Reactor Lifetime				

Table 5-34. Disruption Melt Layer Thicknesses and Vaporization Thickness (μm) Energy

Material	535 J/cm^2 5 ms	270 J/cm^2 20 μms
Be	173 (300 C) 190 (700 C)	71 (300 C) 170 (700 C)
BeO	64 (300 C) 108 (2000 C)	3 (300 C) 115 (2000 C)
C	28	1
SiC	19	0
W	120	0
Ta	~130	0

5.9.3.3 Results

The lifetime of different surface materials has been determined. For all lifetime calculations, a V-15Cr-5Ti heat sink has been assumed. The major emphasis of this work has been placed on Be because it has been selected as the reference surface material.

The lifetime of a Be coated limiter is shown in Table 5-35 for edge temperatures of 150, 700, and 1200 eV. The values shown are based upon average sputtering/redeposition rates for the entire limiter plus disruption losses for a disruption frequency of 2.5 per year. The entire melt layer is assumed to be lost during the disruption. The erosion lifetime for the reference edge temperature of 150 eV is 2.8 y. As expected, the average erosion rates decrease as the edge temperature increases. Other low-Z materials are predicted to have similar lifetimes, with the exception of graphite. The accelerated chemical sputtering rates and the reduction in thermal conductivity with irradiation, discussed in Section 5.4, will reduce its lifetime compared to other materials. The effect of disruptions on lifetime is negligible because of the low frequency which accompanies steady-state operation. This disruption effect is in contrast with other proposed reactors, such as INTOR, that would operate in a cyclic mode. The increased

number of disruptions with this mode of operation results in significantly reduced lifetimes.

Table 5-35. Predicted Lifetimes of Be Coated Limiter (50% Availability, Top Surface)

Erosion Mechanism	Edge Temperature (eV)	Lifetime (y)
Sputtering/Redeposition	150	2.8
	700	7.1
	1200	12.5
Sputtering/Redeposition + Disruptions (Reference)	150	2.7
	700	6.8
	1200	11.6
Sputtering/Redeposition + Disruptions (Worst Case)	150	2.7
	700	6.6
	1200	11.1

Erosion of the first wall is expected to be low. The sputtering losses are almost zero due to the low charge-exchange neutral flux to the bulk of the first wall. The losses due to disruptions are also low because of their low frequency. For the worst case disruption conditions, the loss rate is estimated to be only 240 μm per year. Therefore, the lifetime of the first wall should not be limited by erosion. The goal lifetime of the first wall of ~ 10 MW-y/m^2 appears to be reasonable.

5.9.3.4 Discussion and Conclusions

There are significant uncertainties in the lifetime analysis. The areas where the uncertainties exist are the plasma edge and scrape-off physics, physical and chemical sputtering of the surface materials, the sputtering/redeposition analysis, the disruption scenarios, fatigue and crack propagation analysis, the effect of irradiation on the material properties, and the tile/heat sink bond properties. The plasma edge uncertainties will influence the design curvature of the limiter blade, the placement of the leading edges, and the particle and heat fluxes to the limiter or divertor. For physical sputtering, data do not exist for tritium sputtering, and there

are uncertainties in the effect of the surface condition on the sputtering rates. In addition, there is considerable uncertainty in the energy at which the self-sputtering coefficients of medium and high-Z materials exceed unity. Chemical (or temperature dependent) sputtering data are limited and are primarily for hydrogen interactions with graphite. The predictions of the net erosion rates of surface materials include uncertainties in the ionization cross sections of sputtered atoms and the properties of redeposited materials. The disruption conditions may be different from the reference conditions. Changes in the disruption frequency, energy density, and time will have large effects on the vaporization and melt layer thickness. There is also considerable uncertainty in the melt layer stability after formation. Radiation is expected to reduce the thermal conductivity of non-metals and to alter the mechanical properties. Finally, the bond integrity has not yet been addressed.

The net result is that, at this time, the lifetime estimates are not likely to be accurate, and they should be used for comparison purposes only. In most cases, conservative assumptions were made to account for some uncertainties, but it should be noted that the lifetimes could be either greater or less than the results shown above. Considerably more work, both experimental and analytical, is required to provide more accurate lifetime estimates.

Given these uncertainties, the lifetimes of both the limiter and first wall appear to be acceptable. The limiter is predicted to last $\gtrsim$ 2.8 y, and the first wall is predicted to last $\gtrsim$ 10 y based upon erosion limitations.

5.10 Tritium and Vacuum

5.10.1 Introduction

The goal in the design of the tritium handling systems for the DEMO fusion plant is to have a completely integrated tritium fuel cycle, independent of off-site tritium sources once the plant is operational. The complete tritium fuel cycle scenario is shown in Fig. 5-48. The tritium handling systems perform the following functions: reprocess tritium for fueling, process tritium produced in the blanket, control the amount and location of tritium in the plant, and process tritiated wastes.

To minimize the effects of tritium upon the environment for the DEMO design, an attempt is made to contain all tritium releases, normal leakage or accidental releases within the confines of the plant. The outer walls of potential tritium containing areas are lined with a tritium barrier (stainless steel or aluminum). The materials and equipment used in a tritium area are selected to minimize surface adsorption. Tritium areas are operated at reduced atmospheric pressure to minimize tritium out-leakage. The atmospheric tritium level (HTO) in all areas is maintained at $\leq$ 5 $\mu Ci/m^3$ where possible. Tritium systems utilize triple containment where reasonable and practical; double containment is used throughout. The number and length of lines used to transport tritium between different buildings are minimized.

The major areas presented in detail are the vacuum system, the Be/Cu limiter-tritium permeation and inventory, and the tritium processing systems.

5.10.2 Vacuum System

The main function of the vacuum system is to remove the helium ash. Other design objectives are to achieve good reliability and maintainability and to minimize tritium inventory, neutron streaming, and the number of vacuum ducts within the vacuum system. In the limiter/vacuum system, the tritium fraction burned is high (0.1 for DEMO). Thus, there is a lowered gas load which relaxes the vacuum pumping capacity requirements.

The advantages and disadvantages of the different high vacuum pumping systems are shown in Table 5-36. The advantages of the liquid helium cryopumps make them the preferred high vacuum pumps for the DEMO design. Table

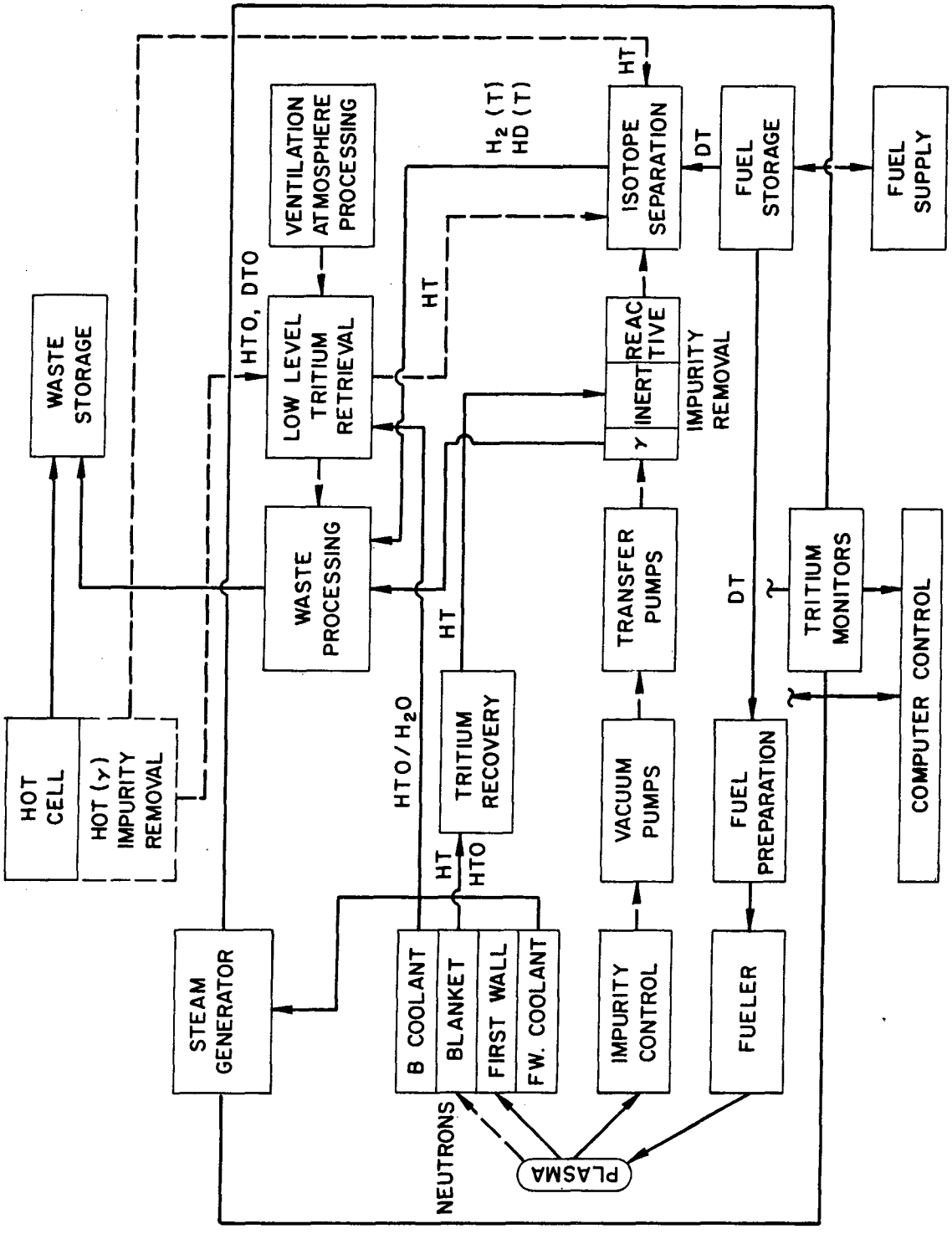

Figure 5-48. Tritium fuel cycle.

Table 5-36. Comparison of High Vacuum Pumping Systems

System	Advantages	Disadvantages
Turbomolecular pumps	- Good tolerance to thermal heating.	- Low hydrogen and helium capture probability - Components susceptible to radiation damage - Organic liquid required - Size limitations
Liquid helium cryopumps	- Highest helium capture probability (~ 0.2) - High reliability - Clean system (no organics) - Available in large sizes	- Regeneration required - Low tolerance to thermal heating - Liquid helium system required
Getters	- High radiation and thermal tolerance - Clean system - Available in large sizes	- Will not pump helium - Evaporable getters require frequent filament replacements - Nonevaporable getters require four pumps for regeneration
Diffusion pumps	- Acceptable hydrogen and helium capture probablity - Good tolerance to thermal heating	- Working fluids can produce system contamination - Organic components susceptible to radiation damage
Differential ion pumps	- Good tolerance to irradiation and thermal heating - Clean systems	- Low helium capture probability - Not regenerable - Potentially high tritium inventory - Magnetic compatibility

Table 5-37. Parameters for the DEMO Vacuum System

Vacuum system conductance, m^3/s	
Limiter duct	650
Plenum	2900
Vertical duct	80
Horizontal duct	130
Cryopump - helium	70
Cryopump - D-T	100
Total system - helium	110
Total system - D-T	130
Limiter operation	
Slot conductance, m^3/s	820
Entering particle fraction	0.1
Conductance ratio (γ) - helium	7.5
Inversion probabilty (κ) - helium	1.0
Transmission probability (ε) - helium	1.0
Reflection coefficient (R) - helium	0.85
Conductance ratio (γ) - D-T	6.3
Inversion probabilty (κ) - D-T	1.0
Transmission probabilty (ε) - D-T	1.0
Reflection coefficient (R) - D-T	0.85
Fractional burn	0.1
Gas load - helium, $Pa-m^3/s$	4
Pressure - helium, Pa	0.03
Gas load - D-T, $Pa-m^3/s$	40
Pressure - D-T, Pa	0.4

5-37 lists the parameters for the DEMO impurity removal system. The details of the analysis for the vacuum system are given in Section 8.4. The parameters for the pumped limiter operation are derived from the equations presented in the STARFIRE report.(3)

Each of the eight cryopumps (four on-line at a given time while the other four are regenerated) has a helium pumping speed of 70 m^3/s. A cryopump/vacuum duct combination has a conductance of 29 m^3/s; for four units, the effective conductance is 116 m^3/s. The addition of the plenum and the limiter ducts to the vacuum system results in a conductance of 110 m^3/s which is a minor reduction. As shown in Table 5-37 the use of the minimum number of cryopump/vacuum duct combinations results in a relatively high pressure in the limiter slot (0.4 Pa). This may be acceptable in terms of the operation of the impurity removal system. However, since there are so few pumps, the tritium inventory per pump is substantial (~ 40 g). (A two-hour regeneration

cycle is assumed which is set by valve seal life.) Failure within the system of one pump would result in a D-T pressure of 300 Pa in the plenum. Loss of one of the vacuum pump/duct combinations reduces the system conductance to 80 m^3/s which necessarily increases D-T pressure in the limiter slot pressure to 0.5 Pa. The effect of the loss of a pump on the operation of the limiter has not been assessed.

Besides interfacing with the limiter to pump helium during the burn, the vacuum system must produce a clean, high vacuum (10^{-6} Pa) for plasma startup, must provide for regeneration of the cryopumps, and must interface with the tritium recovery system. Primary considerations for the pump and valves used in the vacuum system are that they are tritium compatible (non-permeable, minimize tritium wastes, minimize tritium inventory) and that they reliably perform the roughing, regeneration, and high vacuum pumping functions. The rough pumping is accomplished with oil-less Normetex "scroll" pumps, currently being evaluated at TSTA, coupled with metal bellows pumps stages in series. Tritium containment is enhanced by providing double containment on components in which the tritium pressure exceeds 1 Pa. Any particulate debris (possibly gamma-emitting) generated in the plasma chamber is captured on filters located between the cryopumps and the roughing pumps. It is assumed that chemical separation bewteen D-T and helium is achieved in the compound cryopumps. However, during regeneration the chemical separation may not be maintained. Therefore, the fuel processing system incorporates a helium/D-T separation unit.

5.10.3 Tritium Permeation and Inventory in the Beryllium/Copper Limiter

Tritium permeation through first walls, limiters, or divertors subjected to energetic tritium charge-exchange neutrals bombardment is a potentially serious problem area for advanced D-T reactors operating at elevated temperatures. High concentrations of tritium in the near surface region can be reached by implantation of the charge-exchange neutral flux combined with a relatively slow recombination of these atoms into molecules at the plasma/first wall interface. Because of the large concentration of mobile tritium near the inner (plasma) wall surface, a concentration gradient is established, causing tritium to diffuse into the bulk and eventually to the outer wall surface where it can enter the coolant. The unknown surface conditions present

in a reactor result in a large uncertainty for the magnitude of the recombination processes which determine the driving force for permeation. In addition, the lack of neutron damage trapping characteristics severely limit any predictions on the tritium inventory and time to permeation breakthrough. Hence the numerical results presented[1] must be considered only as estimates of the expected behavior.

The calculations are made with the DIFFUSE CODE.[39] In essence, the diffusion equation with an implant source and point defect trapping is solved numerically. The surface boundary condition on the inner (plasma) surface is assumed to be characterized by a recombination constant for an endothermic metal as given by:[40]

$$k_r = \frac{5.25 \times 10^{25} \left(k^{1/2}\text{-atm}^{-1}\text{-cm}^{-2}\text{-s}^{-1}\right)}{C_o^{*2}\sqrt{T}} \alpha \exp\left[\frac{(E_s - E_D)}{kT}\right] ,$$

where E_D is the activation energy for migration, E_s is the heat of solution and C_o^* is the Sievert's Law constant. The factor α is the molecular sticking coefficient, and is taken to be a measure of surface cleanliness. Since α depends on surface composition, the presence of oxides, carbon contamination, etc., it cannot be uniquely defined, but instead must be measured for each particular experimental environment.

In the bulk of the sample simple diffusion is assumed to occur, with the diffusivity given by:

$$D = D_o \exp\left(-E_D/kT\right) .$$

In addition, hydrogen is allowed to diffuse because of a thermal gradient (the Soret effect). The tritium flux in the bulk is therefore given by:

$$J = -D \frac{\partial C}{\partial x} + \frac{CQ^*}{KT^2} \frac{\partial T}{\partial x} ,$$

where Q* is the heat of transport. The diffusion of hydrogen in a thermal gradient has not been studied in detail for many metals. While bcc iron and nickel show a negative Q*[41] (i.e., hydrogen diffusion to the hot side), a positive Q* has been reported for zirconium.[42] No data are available for beryllium. Deviations from Fickian diffusion due to the hypothesized inter-

action of hydrogen with mobile point defects[43,44] are not considered. Tritium trapping in neutron damage produced traps of total detrapping energy, E_T from zero time to a uniform concentration, C_T, is included.[45]

The potentially more complex surface conditions on the coolant wall interface are approximated by recombination limited kinetics or a C = 0 (diffusion limited) boundary condition. The existence of oxide layers, as well as the presence of water instead of vacuum, may complicate the situation, but little experimental data exist. Hydrogen produced by the radiolytic decomposition of the coolant water may also affect the boundary condition.

The DEMO design uses a pumped limiter to intercept all of the ion flux and the majority of the tritium charge-exchange neutral flux. Charge-exchange to the wall is expected to occur only at a narrow poloidal strip on each side of the limiter or divertor duct. Since both the limiter and the poloidal charge-exchange strips are planned to be fabricated from beryllium attached to water-cooled substrates, no significant tritium permeation or inventory is expected for the remaining stainless steel first wall. Hence tritium permeation and inventory need only to be calculated for the beryllium/copper composite. Unfortunately far less is known about the characteristics of hydrogen in beryllium than in stainless steels. Table 5-38 lists the parameters used in the limiter calculations. The diffusivity and solubility are from the work of Jones.[46] Since no data are available for the recombination rate constant, , for beryllium, it is assumed to equal 0.5. The neutron damage trap energy is based on recent ion damage measurements of Wampler.[47] The trap concentration of 1 at-% is arbitrary. In fact, ion implantation produces a saturation concentration of as much as 0.4 deuterium/beryllium over the ion penetration range,[47] and may represent a second phase hydride-like precipitate. Hence, the trapping in beryllium could be much higher than in the present calculations. The beryllium is assumed to be 100% dense and crack-free. The interface between the beryllium and copper is assumed to be continuous. The lifetime before component changeout is estimated to be < 3 y.

Figure 5-49 shows the calculated permeation rate. Without neutron damage, breakthrough occurs within one-half year of continuous operation and reaches a value of 0.16 g/day by end of the expected life. However, when the effect of possible neutron traps are included, breakthrough does not occur for 10 y.

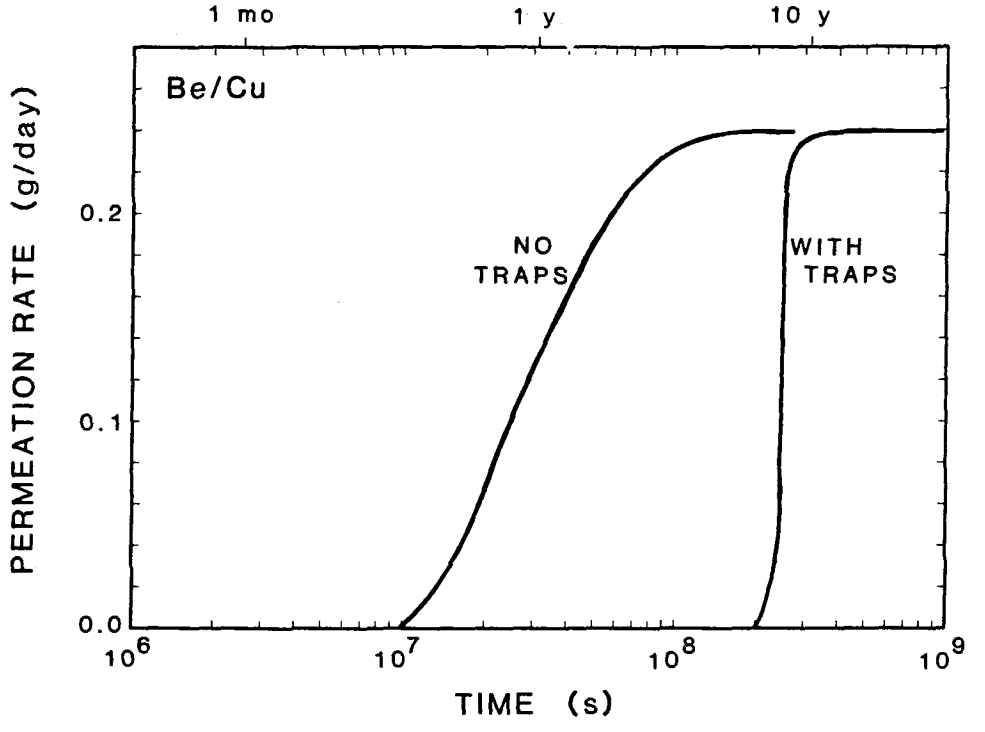

Figure 5-49. Permeation rate as a function of time for the beryllium/copper limiter with and without the assumed neutron damage traps.

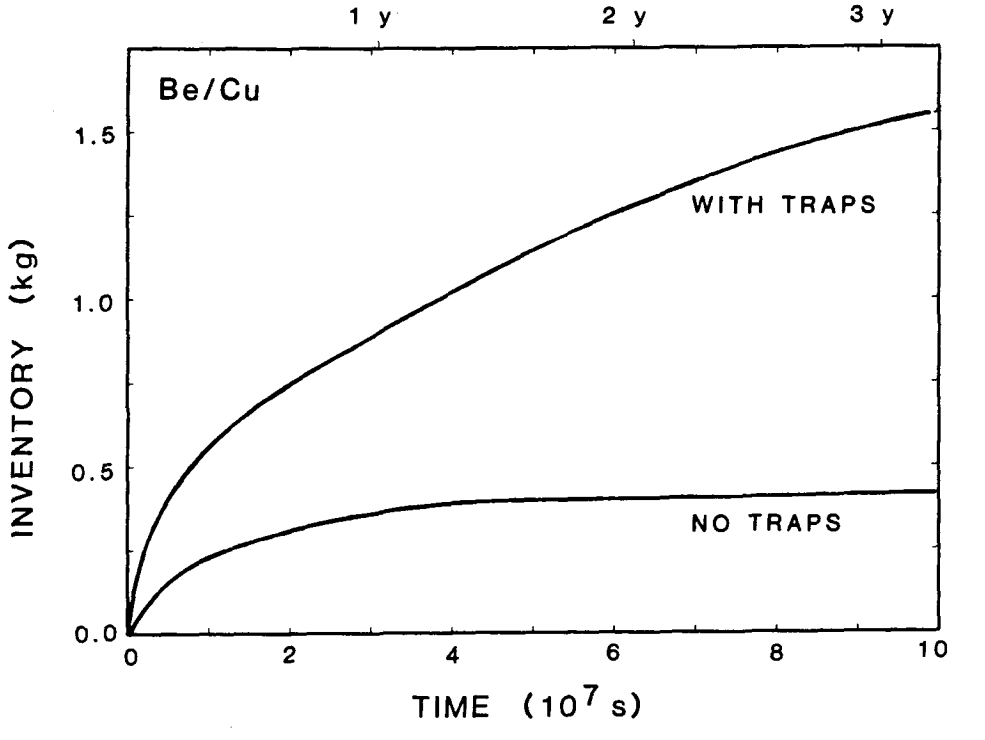

Figure 5-50. Inventory as a function of time for the beryllium/copper limiter plate with and without the assumed neutron damage traps.

Table 5-38. Material Parameters for the Beryllium/Copper Limiter

	Beryllium	Copper
Diffusivity		
D_o, cm^2/s	3×10^{-7}	1.1×10^{-2}
E_d, eV	0.19	0.4
Q^*	0	0
Solubility		
C_o, $atm^{-1/2}$	6.2×10^{-6}	1.6×10^{-3}
E_s, eV	0.0	0.37
Trapping		
E_T, eV	1.5	1.0
C_T, at. fr.	0.01	0.01
Surface condition		
c_{inner}	0.5	---
c_{outer}	---	0
Thickness, cm	1.0	0.15
Area, m^2	60	60
Operating conditions assumed		
Temperature, °C		
Plasma side	467	
Interface	200	
Coolant side	187	
Particle flux, cm^{-2}, s^{-1}	3×10^{18}	
Particle energy, eV	675	
Particle incidence	Normal	
Duty cycle	Continuous	

The tritium inventory calculations are presented in Fig. 5-50. With neutron trapping the inventory reaches 1.2 kg within 3 y of calendar operation (50% availability). Without traps, the inventory equals 0.4 kg due solely from the mobile tritium atoms in the bulk. The mobile concentration is as much as $\approx 6 \times 10^{-6}$ atom fraction/$\sqrt{atm}$;[46] this implantation-induced concentration is equivalent to a pressure of over 200 atm. Conceivably, this latter set of conditions could lead to precipitation of a brittle hydride phase, or to massive exfoliation from overpressurized voids or non-interconnected

porosity. On the other hand, microcracking (crazing) or deliberate connected microporosity (e.g., from plasma spraying) would provide short circuit pathways for release of implanted tritium. Permeation might therefore be virtually eliminated and lowered inventories could also be realized. Hence, based on the extremely limited database for hydrogen in beryllium and the lack of a detailed microstructural description, it is difficult to calculate any meaningful values for tritium permeation and inventory with a beryllium/copper composite limiter.

5.10.4 Fuel Processing Parameters

Mass flow rates for the primary fuel cycle of the DEMO design are shown in Table 5-39. The main fuel path as shown in Fig. 5-48 starts at the plasma chamber, proceeds to the compound cryopumps, and thence to the impurity removal unit. The purified fuel is passed to the isotopic separation system after which the D_2 and T_2 fuel streams are either stored until needed or are passed directly to the fuel blenders. There the needed fuel mixtures are prepared for use in the reactor fueling devices.

Removal of condensible impurities, molecules containing I, N, O, C, etc. from the mixture of unburned fuel (D-T) and helium is the first operation performed at the impurity removal unit. The helium is removed by means of a cryogenic stripping column. To minimize tritiated waste, the condensible impurities are processed. The technology for this step is still under development. TSTA incorporates both uranium getter beds and cooled molecular sieve beds into their design.

The basis of the isotopic separation system is cryogenic distillation. To fulfill DEMO requirements ($\geq$ 90% D_2, $\geq$ 90% T_2; $<$ 1% H_2 in either stream), the system consists of five distillation columns and two equilibrators. The three product streams consists of a 97% pure T_2 stream (3% D_2), 91% pure D_2 stream (9% T_2), and a waste protium-deuterium stream (57% H_2) containing a residual amount of tritium (0.2%).

Within the main fuel feedstream, the transfer of fuel between different components as well as the maintenance of uniform flow is handled by transfer pump units which are composed of surge tanks, metal bellows pumps, and appropriate valving systems. The transfer units are presently designed as separate units but could be incorporated into the larger systems. The advantage of

Table 5-39. Mass Flow Rates for DEMO Tritium Parameters

Plasma parameters	
Plant availability	0.50
Thermal power, MW	1290
Ion density, ions/m^3	1.84×10^{20}
Plasma volume, m^3	272
Particle confinement time, s	1.0
Reflection coefficient	0.83
Fractional burnup	0.1
Tritium mass flow rates, g/d	
Tritium burnup	197
Tritium fueled	2000
Tritium exhausted	1800
Tritium bred	207
Deuterium mass flow rates, g/d	
Deuterium burned	132
Deuterium fueled	1363
Impurity mass flow rates, g/d	
Helium exhaust	262
Protium exhaust	~ 8
Carbon exhaust	~ 50
Nitrogren exhaust	~ 4
Oxygen exhaust	~ 3

having separate transfer pump units is that they are easily accessible and easily removable for maintenance and repair. Easy maintenance is important since failures are expected to occur in these units.

Tritium is removed from the Li_2O blanket as T_2O by means of a helium purge stream and recovered by collection on molecular sieves. The T_2O is passed through ion exchange columns to remove radioactive species other than tritium and then electrolyzed. The T_2/H_2 is passed through a palladium diffuser before joining the main tritium processing stream at the fuel cleanup unit. Additional details are in Section 6.3.6. The different methods for tritium removal from 17Li-83Pb blanket are presented in Section 6.4.7.

To ensure that tritium levels in the primary coolant are maintained at < 1 Ci/L, a tritiated water recovery unit based on combined electrolysis/catalytic exchange (CECE) has been included in the tritium system design. Approximately 1% of the primary coolant, from which activated materials have been removed by means of ion-exchange units, is directed to the CECE unit.

There the HTO is converted to HT. The gas stream is then routed to the main fuel stream via the impurity removal unit. The impact of a tritium release from the coolant system is minimized by: maintaining the tritium inventory in the water coolant at < 1 Ci/L; minimizing leaks in the primary coolant system; and recovering all tritiated water and recycling it into the main fuel stream.

The atmospheric tritium processing systems are designed to scrub the atmosphere of a tritium handling area in the event of a tritium release. Timely decontamination of potential tritium spills within containment is provided by: dedicating an appropriately sized atmospheric tritium recovery unit to each tritium containing area; and interfacing the HVAC systems with the ATR systems to prevent a tritium release to the outside environment. The tritium waste generated (HTO) is reprocessed by the CECE unit. Other details are the same as presented previously.(3)

Additional tritium waste generated is minimized by processing tritiated water, minimizing use of organics, minimizing the contamination of organics where they are functionally necessary, using all metal seals in valves, pumps, etc., and reprocessing tritiated waste. Any waste generated within the plant is packaged in as small a volume as possible after being detritiated.

The location of tritium in the plant is handled by a storage and disposition system. This system is used to monitor all tritium process flows.

In Tables 5-40 and 5-41 the tritium inventory in the two blanket systems studied, Li_2O and 17Li-83Pb, are presented. The calculations required are found in Sections 6.3.6 and 6.4.7, respectively. These data are included in Table 5-42 where the total estimated tritium inventory in DEMO is listed.

Table 5-40. Tritium Inventory in Li_2O Blanket System[a]

System Component/Effect	g
Purge line	2
Tritium removal system	100
Li_2O	
No radiation effects	25
Radiation effects	700→50000
Best estimate	1000

[a]See Section 6.3.6.

Table 5-41. Tritium Inventory in 17Li-83Pb Blanket System[a]

System Option	g
17Li-83Pb/molten salt extraction	40
17Li-83Pb/helium sparging	40
17Li-83Pb/sodium	240/460[b]
Ferritic structure	0.2
Vanadium alloy	200→900

[a] See Section 6.4.1.

[b] A vanadium alloy is associated with the 240 g value. Inclusion of the tritium in the vanadium alloy increases the total blanket system inventory to > 440 g. When the ferritic alloy is used, the blanket inventory is 460 g; the total blanket system inventory is ~ 460 g (0.2 g for the structure).

Table 5-42. DEMO Tritium Inventory (g)

Tritium System	"Vulnerable"	"Nonvulnerable"
Vacuum pumps (2 h regeneration)	153	---
Fuelers (1 h of fueling)	90	---
Storage (10 d of burn)	---	1970
Fuel processing	---	200
Blanket		
Li_2O (estimate)[a]	---	~ 1000
Purge line (Li_2O)	2	---
Tritium recovery (Li_2O)	---	100
17Li-83Pb/molten salt/helium sparging	40	---
17Li-83Pb/sodium/cold trap	240	---
Vanadium alloy	---	200
Ferritic alloy	---	0.2
Limiter (beryllium/copper)[b]	---	400
First wall (beryllium/stainless steel)[c]	---	---
Total (with a Li_2O blanket)[a]	245	3670
Total (with 17Li-83Pb blanket)[d]	283	2570

[a] If radiation trapping is excessive, this value increases substantially.
[b] Steady-state operation value; lifetime 3 calendar years, no traps.
[c] Steady-state operation value; lifetime 10 calendar years.
[d] Minimum inventory assumed, no sodium, ferritic alloy.

The designation "vulnerable" or "nonvulnerable" refers to the degree of control which can be enforced on the associated system. To maintain levels of ~ 1 kg of tritium in the Li_2O blanket means that the tritium is in radiation traps from which it is not easily released. The tritium in storage, ~ 2 kg, in the form of small units of UT_x (each containing ~ 12 g of tritium), is located in a barricaded vault with an inert cover gas for fire protection, thus making it relatively "nonvulnerable" to accident. The fuel processing systems in the tritium facility contain ~ 200 g of tritium in the unoxidized form (T_2, D-T, H-T) distributed as follows: 120 g in an ISS unit, 40 g in the impurity removal unit, and ~ 40 g in surge tanks and piping used to ensure uniform flow throughout the plant. Each tritium processing unit is doubly contained and under monitor control to ensure maximum accident protection. Vacuum or an inert gas is present to reduce the fire hazard. The tritium in the fuel handling systems (vacuum pumps and fueling units) in the reactor building is considered to be "vulnerable" since the reactor area is subjected to severe thermal, magnetic, and radiation loads which may interfere with a unit's function or may accelerate its aging.

At initial plant startup, ~ 5 kg of tritium is supplied from offsite. This tritium is later recovered from the breeder blanket.

5.10.5 Conclusions

The four vacuum ducts used for the DEMO impurity/removal systems is the minimum number with which extraction of the helium ash can be achieved. Since the number of vacuum penetrations into the torus are miminimized, the tritium inventory in each of the high vacuum pump is maximized ~ 40 g each. Failure of one of the pumps would result in a further increase in the tritium inventory in the remaining pumps.

The tritium permeation rate through a beryllium/copper limiter is uncertain. The best estimate of this rate, assuming that neutron traps are prsent and that the reactor has 50% availability, is negligible for a 3-y lifetime. If there are no neutron traps, the rate is negligible for the first year, but increases thereafter until it reaches ~ 0.16 g/d after three calendar years. The steady-state tritium inventory at the end of three calendar years is 0.4 kg if no neutron traps are present and 1.2 kg if traps are present. If microcracking occurs or microporosity exists, permeation could be eliminated and the inventory would be reduced.

The total plant tritium inventory is dependent on the type of blanket chosen. The minimum inventory wtih a solid oxide blanket is ~ 245 g "vulnerable" and ~ 3670 g "nonvulnerable". The minimum with a liquid metal blanket is ~ 283 g "vulnerable" and ~ 2570 g "nonvulnerable". If radiation effects are negligible for the solid oxide the "nonvulnerable" inventory could be reduced to that of the liquid metal.

REFERENCES FOR CHAPTER 5

1. W. M. Stacey, Jr., et al., FED/INTOR Final Report, to be published.

2. W. M. Stacey, Jr., et al., "U.S. INTOR - The U.S. Contribution to the International Tokamak Reactor, Phase-1 Workshop," INTOR/81-1 (1981).

3. C. C. Baker, et al., "STARFIRE - A Commercial Tokamak Fusion Power Plant Study," Argonne National Laboratory, ANL/FPP-80-1 (1980).

4. M. A. Abdou, et al., "A Demonstration Tokamak Power Plant Study - Interim Report," Argonne National Laboratory, ANL/FPP/TM-154 (1982).

5. L. L. Lao, S. P. Hirshman, and R. M. Wieland, Phys. Fluids 24, 1431 (1981); L. L. Lao, R. M. Wieland, W. A. Houlberg, and S. P. Hirshman, Oak Ridge National Laboratory, ORNL/TM-7871 (1982).

6. A. T. Mense and G. A. Emmert, Nucl. Fusion 19, 361 (1979); G. A. Emmert, University of Wisconsin, UWFDM-343.

7. J. N. Brooks and R. T. McGrath, Proc. 9th Symp. on Engr. Problems in Fusion Research, Chicago, IL (October 26, 1981).

8. J. N. Brooks, Proc. 5th Intern. Conf. on Plasma Surface Interactions in Controlled Fusion Devices (to be published in J. Nucl. Mater., also).

9. J. N. Brooks, et al., Proc. 8th Symp. on Engr. Problems in Fusion Research, IEEE Publ. No. 79CH1441-5NPS, p. 1634 (1979).

10. J. Norem and B. Cramer, J. Nucl. Mater., 103-104, 235 (1981).

11. "FED/INTOR Impurity Control and First Wall Engineering," FED/INTOR/ICFW/82-13 (July 1982).

12. J. Roth, J. Bohdansky, and W. Ottanherger, MPI fur Plasmaphysik report IPP 9/26, Garching (May 1979).

13. H. H. Anderson and H. L. Bay, in Sputtering by Particle Bombardment I, edited by R. Behrisch, Springer-Verlay; (1981); J. Nucl. Mater. 93-94, 625 (1980).

14. P. Sigmund, Phys. Rev. 184, 383 (1969), 187, 768 (1969).

15. T. J. Hoffman, H. Dodds, M. T. Robinson, and D. K. Holmes, Nucl. Sci. Eng. 68, 204 (1978).

16. M. T. Robinson, and I. M. Torrens, Phys. Rev. B9, 5008 (1974).

17. J. P. Biersack and L. G. Haggmark, Nucl. Instr. and Meth. 174, 257 (1980).

18. J. J. Bohdansky, Nucl. Mater. 93-94, 44 (1980).

19. D. L. Smith, J. N. Brooks, D. E. Post, and D. Heifetz, "DSPUT: A Physical Sputtering Code for Fusion Applications," Argonne National Laboratory, ANL/FPP/TM-157 (1982); also Proc. 9th Symp. on Fusion Technology, IEEE Pub. No. 81CH195-2 NPS, 719 (1981).

20. J. Roth, J. Bohdansky, and K. L. Wilson, "Chemical Erosion of Carbon Due to Bombardment with Energetic Hydrogen Ions up to 1600°C," Proc. 5th Intl. Conf. Plasma-Surface Interactions, Gatlinburg, TN (May 1982).

21. W. E. Ruther, "Environmental Effects on Properties of Structural Alloys," ADIP Progress Report for October 1981, in press (March 1982).

22. W. C. Kramer, W. R. Burt, Jr., F. J. Karasek, J. E. Flinn, and R. M. Mayfield, "Vanadium Alloy Screening Studies and Fabrication of V-15 w/o Ti-7.5 w/o Cr Tubing for Nuclear Fuel Cladding," Argonne National Laboratory, ANL-7206 (1966).

23. W. R. Burt, Jr., W. C. Kramer, F. J. Karasek, J. E. Flinn, and R. M. Mayfield, "Improvements in Consolidation and Fabrication of Vanadium-20 w/o Titanium (TV-20)," Argonne National Laboratory, ANL-7127 (1966).

24. Monthly Progress Reports, Foundry and Fabrication Group, Argonne National Laboratory (1967).

25. D. L. Smith, R. H. Lee, and R. M. Yonco, Proc. of the 2nd Int. Conf. on Liquid Metal Technology in Energy Production, CONF-800401-P1/UC-79A, 2-72 (1980).

26. A. M. Hassanein, et al., "Dynamics of Melting, Evaporation and Resolidification of Materials Exposed to Plasma Disruptions," University of Wisconsin, UWFDM-468 (1982).

27. W. M. Stacey, Jr., et al., "Impurity Control and First Wall Engineering," USA Input to INTOR Workshop, Session III, Phase 2A, FED/INTOR/ICFW/81-02 (December 1981).

28. A. M. Hassanein, G. L. Kulcinski, and W. G. Wolfer, "Vaporization of Materials in Fusion Devices," University of Wisconsin, UWFDM-422 (1981).

29. W. G. Wolfer and A. M. Hassanein, "On Melt Layer Stability Following a Plasma Disruption," UWFDM-470, Presented at the 5th International Conference on Plasma Surface Interaction in Controlled Fusion Devices, Gatlinburg, TN (May 1982).

30. F. Reif, Fundamentals of Statistical and Thermal Physics, McGraw-Hill Book Company, New York (1965).

31. Y. S. Touloukian, ed., Thermophysical Properties of High Temperature Solid Materials, the MacMillan Co., New York (1967).

32. Y. S. Touloukian, R. W. Powell, C. Y. Ho, and P. G. Klemens, eds., Thermophysical Properties of Matter, IFI/Plenum, New York (1970-1979).

33. G. Hopkins, et al., "Fusion Reactor Studies: Potential of Low-Z Materials for the First Wall," Electric Power Research Institute, EPRI-115-2 (1975).

34. A. Ya Zavgorodii, et al., "Kinetics of Gas Swelling in Irradiated Beryllium," Solid State Radiation Physics and Reactor Materials Research - USSR, Department of Commerce, JPRS 53800, 268 (1971).

35. R. B. Matthews, J. Nucl. Mater., 51, 203 (1974).

36. J. Matolich, et al., "Swelling in Neutron Irradiated Tungsten and Tungsten - 25 Percent Rhenium," Scripta Met., 8, 837 (1974).

37. F. W. Wiffen, "The Microstructure and Swelling of Neutron Irradiated Tantalum," J. Nucl. Mater., 67, 119 (1977).

38. R. S. Wilkes, "Neutron-Induced Damage in BeO, Al_2O_3 and MgO - A Review," J. Nucl. Mater., 26, 137 (1968).

39. M. I. Baskes, SAND-80-8201, Sandia National Laboratories-Sandia, SAND-80-8201 (1980).

40. M. I. Baskes, J. Nucl. Mater. 92, 318 (1980).

41. O. D. Gonzales and R. A. Oriani, Trans. Met. Soc. 233, 1882 (1965).

42. A. Sawatzky, J. Nucl. Mater. 2, 321 (1960).

43. A. E. Gorodetsky, A. P. Zakharov, V. W. Sharapov, and V. Kh. Alimov, J. Nucl. Mater. 93 & 94, 588 (1980).

44. T. Tanabe, N. Saito, Y. Etoh, and S. Imoto, J. Nucl. Mater. 103 & 104, 483 (1981).

45. K. L. Wilson and M. I. Baskes, J. Nucl. Mater. 76 & 77, 291 (1978).

46. P. M. S. Jones and W. R. Gibson, J. Nucl. Mater. 21, 353 (1967).

47. W. Wampler, private communication (1982).

CHAPTER 6

BREEDING BLANKET

Chapter 6

Table of Contents

Chapter 6

List of Figures

Chapter 6

List of Tables

6.0 BREEDING BLANKET

6.1 Introduction and Strategy

The primary functions of the first-wall/blanket system of a tokamak demonstration reactor are to provide the first physical barrier to the plasma, to convert the fusion energy into sensible heat and provide for adequate heat removal, to breed tritium and provide for tritium recovery, and to provide some of the shielding for the magnet system. The first wall of a tokamak power reactor is generally perceived to be an integral part of the blanket. The first wall must withstand energetic particle fluxes and heat fluxes from the plasma, high thermal and mechanical stresses, elevated temperature operation, and high heat fluxes and magnetic forces during plasma disruptions. Also, the first wall must not be a source of excessive plasma contamination. The blanket must withstand high neutron fluences, elevated temperature operation, and thermal and mechanical stresses. The blanket and first wall materials must be compatible with each other and with the plasma.

Development of a viable blanket system is essential before the feasibility of fusion as a commercial energy source can be established. The importance of near-term blanket development is due partially to the recognition that breeding of tritium in the next-generation reactors may be necessary to supply tritium needed for projected operating scenarios. Near-term blanket development is also vital because of the impact on materials research and development requirements, and the need for testing in near-term devices such as FED and INTOR, which will require detailed definition of concepts.

The two solid breeder concepts and two liquid metal breeder concepts listed in Table 6-1 are generally considered to offer the most potential for power reactor blankets. Within the scope of this study it was not possible to analyze blanket concepts for all four breeders in depth. Therefore, the strategy for this study was to focus on only two concepts: the solid Li_2O breeder concept and the liquid Li-Pb breeder concept.

The recent STARFIRE design study[1] provides an in-depth analysis of the ternary ceramic ($LiAlO_2$) design. Most of the conclusions regarding the critical materials and design issues associated with the STARFIRE blanket concept are still considered valid. Therefore, for this study it was decided

Table 6-1. Leading Candidate Tritium Breeders for Power Reactor Blankets

SOLID BREEDERS:	Li_2O Breeder
	Ternary Ceramic ($LiAlO_2$) Breeder
LIQUID METAL BREEDERS:	Li-Pb Alloy Breeder
	Li Breeder/Coolant

to define the critical design and operating criteria for a Li_2O blanket. This will enable a later comparison of the performance characteristics, design implications, and operating limits for the two types of solid breeder concepts. No recent in-depth design study of a liquid lithium blanket concept has been made, but earlier studies[2-6] provide a general basis for comparison. Therefore, the present study focused on critical issues for blanket concepts using the lead-rich Li-Pb eutectic (17 at % Li - 83 at % Pb, subsequently referred to as 17Li-83Pb) as the tritium breeder. The definition by future studies of performance characteristics, design options, and operating limits for this blanket concept will permit comparison with a liquid lithium blanket concept.

The reference design blanket for the DEMO reactor is described in Section 6.2. The blanket features Li_2O breeder, high temperature, high pressure water coolant, and an advanced austenitic stainless steel structure. An assessment of the tritium breeding potential for both the Li_2O and 17Li-83Pb blanket concepts is presented in Sec. 6.3. Section 6.4 presents results of the Li_2O breeder blanket study, and Sec. 6.5 contains results of the Li-Pb breeder blanket study. The two blanket concept sections (6.4 and 6.5) present discussions of related to materials selection, stress analyses, neutronics analyses, properties of the breeder, tritium recovery, thermal-hydraulic analyses, and materials compatibility considerations. Critical design issues are summarized and proposed blanket design configurations are presented for the two breeder concepts.

6.2 First-Wall/Blanket Reference Design Configuration

This section provides a description of the Li_2O solid breeder blanket (Sec. 6.2.1) selected as the reference design concept for the DEMO reactor, and the related energy conversion system (Sec. 6.2.2). Rationale for blanket materials and design detail choices is given in Sec. 6.2.3, and operational and safety considerations are discussed in Sec. 6.2.4.

6.2.1 Design Description

The DEMO reference first wall/blanket design breeder concept is illustrated schematically in Fig. 6-1. Materials and design option selections and major operating parameters are listed in Table 6-2.

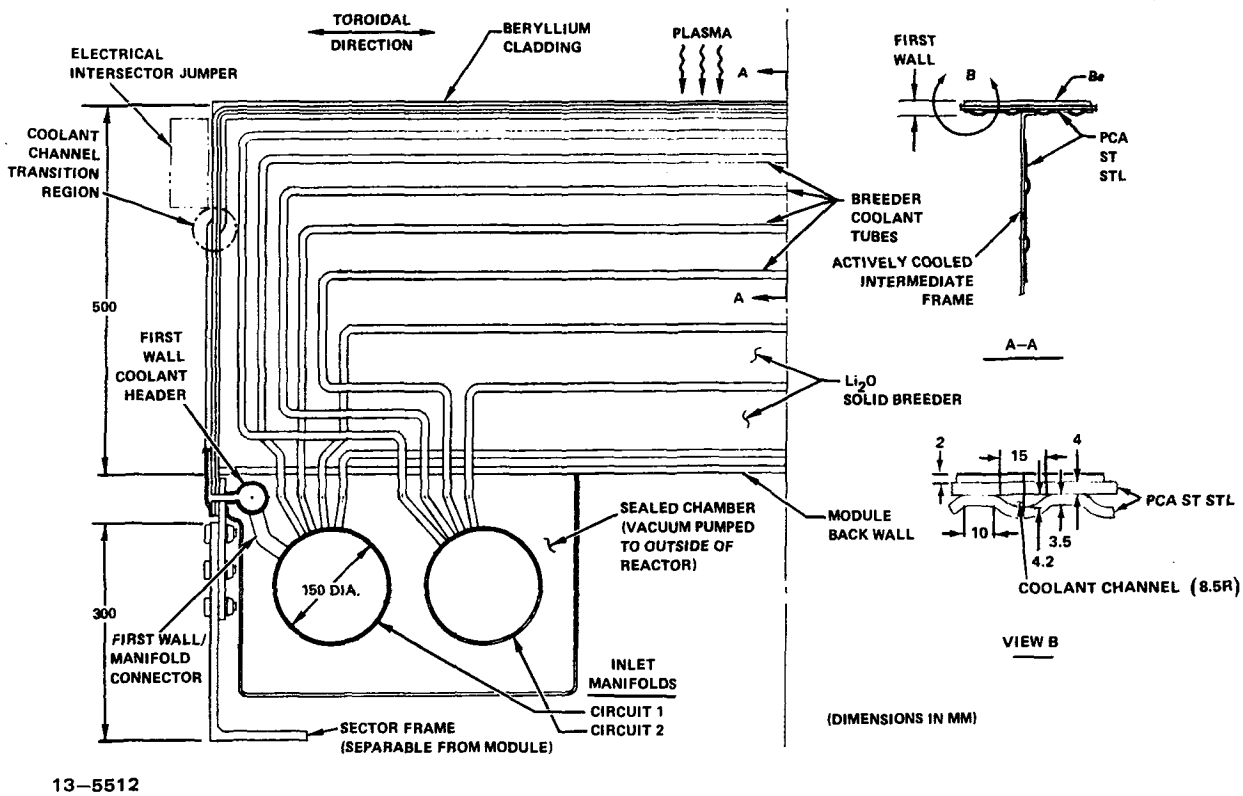

Figure 6-1. Li_2O breeder reference blanket design.

The reference blanket design uses the concept of individual first wall/blanket modules configured as parallelepipeds. These modules are assembled into sectors. Eight of these sectors, identical except for local modifications (e.g., to accommodate REB diode leads), comprise the reactor first

Table 6-2. DEMO Reference First Wall/Blanket Concept Description

Selected Materials	
- Tritium Breeder	Li_2O (solid; 70% d.f.)
- Coolant	Pressurized H_2O (11.0 MPa)
	- Inlet temperature 260°C
	- Outlet temperature 300°C
- Tritium Processing Fluid	Low-velocity Helium (0.05 MPa)
- Structure	Titanium-modified Austenitic Stainless Steel
Selected Design Options	
- First Wall	Be-clad Corrugated Panel
- Breeder Coolant Containment	Small-diameter Tubes
- Other	
	- First wall and blanket mechanically and structurally integrated
	- Coolant flow in toroidal direction
	- Dual parallel primary coolant loops
	- Maintenance by sector removal and replacement

wall/blanket system. Principal advantages of this sector/module approach, which was adapted from the STARFIRE reactor design, apply to DEMO as well and thus the related discussions will not be repeated here.

The first wall (shown in Fig. 6-1) is an actively cooled panel made of PCA (Prime Candidate Alloy), a titanium-modified advanced austenitic stainless steel. The plasma-facing portion of the first wall consists of a 4-mm thick flat plate of PCA with a corrugated 3.5-mm sheet of PCA which is resistance-seam-welded to the flat plate's rear face to contain the water coolant. A protective armor of only 2 mm of beryllium is required for the first wall (except for the regions near the mid-plane belt limiter), because the particle flux from the plasma is very low. The cooled structural panel is continuous

down both sides of the modules to the rear of the breeding zone. The inlet and outlet ends of the panel terminate in headers in the manifold zone. The first wall is mechanically and structurally integrated with the blanket. Actively cooled support frames within the breeding zone are welded to the back side of the first wall and to the rear wall of the breeding zone to provide structural rigidity to the module.

The Li_2O breeder is contained within the boundary formed by the six sides of the module. The toroidally-oriented coolant tubes in the breeder zone are arrayed in banks; each tube makes a single pass through the breeder. Each tube is fabricated from seamless PCA tubing in the cold worked (CW) condition; inside diameter is 10 mm for each tube, and wall thickness is 0.625 mm. Tube spacing radially and poloidally through the breeding zone is graded in proportion to the local nuclear heating rate, to ensure that the breeder is maintained within the design basis minimum and maximum temperature limits of 410°C and 660°C respectively at all points. For each tube, coolant temperature is increased from 260°C at the inlet to 300°C at the outlet by orificing at the tube entrance to produce the proper flow rate/flow velocity combination. The breeder coolant tubes are U-shaped and terminate in the inlet and outlet manifolds located immediately behind the back wall of the breeder zone. These manifolds connect all first wall/blanket modules within a sector. There are two inlet and two outlet manifolds, one of each for each of the two separate cooling circuits. The first wall and all even-numbered coolant tube banks are connected to the first circuit; the first coolant tube bank and all other odd-numbered banks are connected to the second circuit. Manifold segments are joined by welding to seals of omega-shaped cross section which accommodate misalignment and differential thermal expansion between segments.

Helium purge gas is used to remove tritium from the breeder. The low pressure (~ 1 atm), low flowrate gas is introduced into the pressure-tight breeding zone at one end of the module through the rear wall. The gas flows in the toroidal direction through narrow channels (~ 2 mm dia.) pre-formed in the breeder, and exits through the rear wall at the other end of the module. The Li_2O breeder is fabricated in the form of sintered or hot pressed blocks having 30% porosity, which are fitted around the U-bend tubes during assembly of the blanket. The configuration and the method of retention of the blocks

necessary to accommodate thermal strains (Sec. 6.4.6.1) must be determined through future studies and development efforts.

An alternate design approach to the Li_2O solid breeder, described in the DEMO Interim Report[7], adds a neutron multiplier and a second actively cooled panel (second wall) to the reference design. The neutron multiplier is solid beryllium, 5.7-cm thick at a 70 percent density factor. The second wall removes part of the nuclear heat from the beryllium and from the first few centimeters of Li_2O breeder. This alternate approach was not developed further, primarily because neutronics analyses (Sec. 6.3) indicate that adequate breeding can be obtained for DEMO using Li_2O without a neutron multiplier and without the use of inner breeding blankets.

6.2.2 Energy Conversion System

Based on the choice of H_2O as the first wall and blanket coolant for the Li_2O blanket concept (Sec. 6.2.3.1), the basic energy conversion system selected for STARFIRE was adopted for DEMO. Therefore, only a brief description of the system will be given here. The rationale for selection of this system is similar to that for STARFIRE.

Separate heat removal systems operating at different pressure and temperature levels are used for the first wall/blanket and for the limiter. Since it is not necessary to maximize thermal conversion efficiency for DEMO in order to fulfill the goals set for the reactor, the limiter's coolant thermal energy is dumped so that the limiter can be cooled with low temperature, low pressure water. This reduces limiter stresses and energy conversion system complexity. Thermal energy from other reactor components (e.g., shield, REB) is also dumped because the coolant is at such low temperature that it cannot feasibly be used in the power conversion system.

A simplified schematic of the primary coolant system is shown in Fig. 6-2, and major parameters of the primary coolant system are listed in Table 6-3. A residual heat removal loop similar to that for STARFIRE is included. Supporting systems are not shown since they have little impact on other reactor systems. Two independent circuits provide water coolant to each blanket sector through dual inlet and outlet headers (ring manifolds). From the outlet header the hot coolant passes through a steam generator and then to the

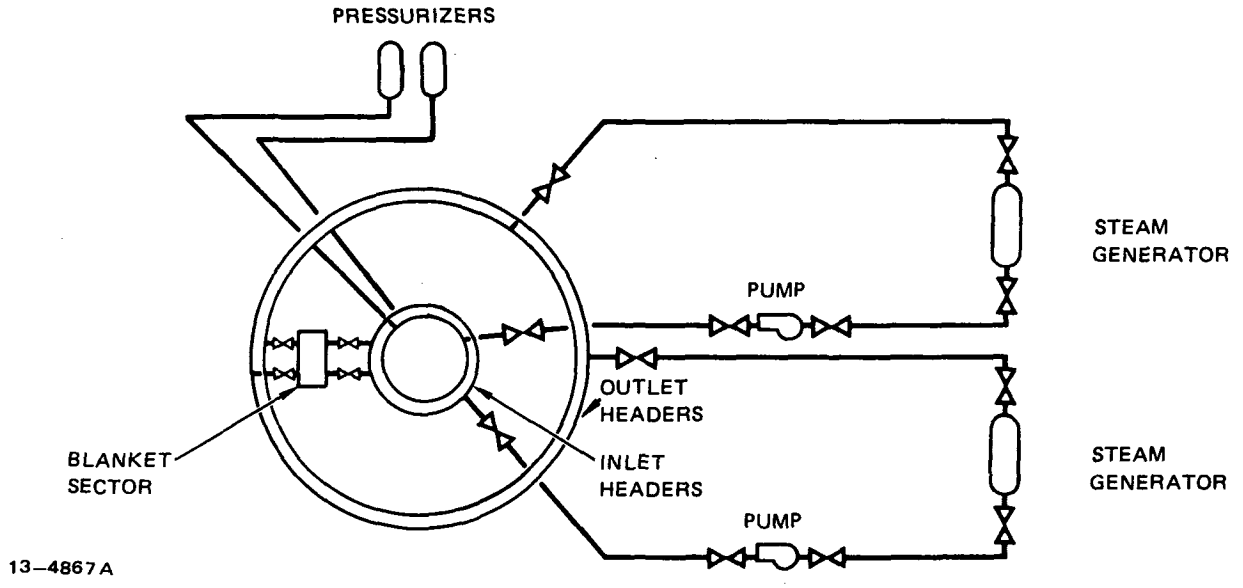

Figure 6-2. Schematic of energy conversion system for Li_2O breeder blanket.

Table 6-3. Major Parameters For Primary Loop (Li_2O Breeder Blanket)

Coolant	Water
Heat Load	1070 MW
Blanket Outlet Temperature	300°C
Blanket Inlet Temperature	260°C
Operating Pressure	11.0 MPa (1600 psig)
Number of Independent Loops	2
Maximum Pipe Size	~ 1.0 m I.D.
Maximum Coolant Velocity	~ 20 m/s
Pumping Power	9 MWe
Coolant Volume	~210 m^3 (excluding pressurizers)
Number of Steam Generators	1 per loop
Number of Pumps	1 per loop
Pump Capacity	100% of total required capacity per loop

pumps from which it is returned to the inlet ring manifold. Pressurizers (one per loop) are connected directly to the inlet manifolds. The residual heat removal loop connects directly across the two ring manifolds. Because DEMO operates in a steady-state mode, a thermal storage system is not required. An intermediate heat exchanger is not required for this system to protect against tritium permeation into the steam side.

6.2.3 Rationale for Selection of Materials and Design Details

The key features of the Li_2O breeder reference first wall/blanket design are listed in Table 6-4 together with the primary reasons for their selection. These features in general are similar to those for the STARFIRE

Table 6-4. Key Features of Selected Design Details for Li_2O Solid Breeder Reference First Wall/Blanket Concept

---

First Wall: Stainless Steel Panel

- 2-mm thick Be coating for protection during plasma disruptions
- Minimum number of pressure boundary welds
- Low structure temperature (<400°C)
- Mechanically and structurally integrated with blanket

Breeding Zone: Sintered Ceramic with Coolant in Tubes

- All tube welds located outside of breeder zone in low-fluence region
- High pressure coolant contained in small-diameter tubes
- Tube spacing graded to conform to energy deposition profile
- Reduced density ceramic (70% d.f. with bimodal porosity) to facilitate tritium recovery
- Low pressure He purge stream for tritium recovery
- Coolant outlet temperature and pressure reduced (from STARFIRE) to increase reliability

Manifold Zone: Tubular Manifolds

- Most coolant system welds located within vented secondary containment to accommodate minor leakages while reactor continues to operate
- Steel and water, together with shield, serve as neutron reflectors

Dual Independent Primary Coolant Loops

- Dual loops throughout each module and sector to provide adequate after-heat removal even if only one loop is operable

---

reference design blanket, and the rationale for their selection is likewise similar. The reasons for the changes made from the STARFIRE blanket, primarily in the first wall and manifold zones, are discussed below. The added neutron-multiplier/second-wall zone for the Li_2O alternate design concept is also discussed.

6.2.3.1 Materials Selection

Coolant

The choice of coolant has a major impact on the selection of other blanket materials, reactor operating parameters, the energy conversion system, shielding, maintenance and repair, tritium systems, and reactor building design. Although lithium, helium, water and molten salts have all been proposed as potential reactor coolants[5], water and helium are considered to be the preferred candidates for solid breeder blanket concepts[1]. Pressurized water was selected for the STARFIRE design and was also chosen for the DEMO reference blanket concept. There are a number of important advantages associated with the choice of water coolant:

- Operating temperature is compatible with Li_2O breeder temperature requirements and with structural material requirements.
- First-wall heat fluxes can be accommodated.
- Radiation attenuation is sufficient (no loss of shield space).
- Manifold sizes are tolerable.
- Recirculating power is minimal.

Since the range of operating temperatures required for acceptable Li_2O performance is quite limited (Sec. 6.4.3), the low system ΔT characteristic of pressurized water systems is very desirable for a satisfactory design. The range of water coolant temperatures that result in relatively good thermal conversion efficiency is comfortably below the minimum allowable operating temperature for Li_2O. This permits full utilization of the allowable temperature range for Li_2O, and maximizes the breeding ratio obtainable for the concept. The low operating temperature is also advantageous with respect to radiation damage effects of the structural materials.

The primary feasibility issue for water coolant relates to control of tritium permeation into the coolant. However, this is not a serious concern

for DEMO: particle flux to the first wall is very low, and tritium permeation into the blanket coolant is negligible. A critical design problem involves accommodating the high pressure coolant. The major penalty associated with pressurized water is the limited energy conversion efficiency attainable. The primary safety concern relates to pressure transients and formation of corrosive LiOH in the event of a coolant leak into the breeder zone.

Key factors in the non-selection of helium coolant include:

- Difficulty or inability to design systems with reasonable thermal conversion efficiencies within the temperature limits for Li_2O.
- Neutronic (shielding/breeding) penalty associated with helium, particularly losses in inboard shielding efficiency.
- The lack of a satisfactory structural material for use with high temperature helium.
- Potential helium leakage into plasma chamber, and difficulties in leak detection.
- Limited capability for first wall heat flux removal.
- High pumping power requirement for the first wall.
- High pressure/large manifold size requirement.

The first factor, which relates to the limited operating temperature range for Li_2O, is probably the most severe disadvantage. Overall, the prospects for design of a functional helium-cooled Li_2O first-wall/blanket system within the proposed constraints are considered questionable.

Structural Material

The selection of candidate structural material for the first-wall blanket of solid breeder concepts has been extensively evaluated in several designs[1,3,8]. Conclusions from these studies in addition to results generated in the fusion materials Alloy Development Program indicate that austenitic stainless steel is the primary candidate structural material. Ferritic steels are considered as the backup structural material. Vanadium-base alloys are considered to be attractive structural materials for liquid metal blankets, but may not be acceptable for water-cooled systems because of compatibility limitations with Li_2O and potentially excessive tritium permeation rates. Table 6-5 lists other structural materials that have been considered or proposed in various designs and the primary reasons these alloys have been

Table 6-5. Alloy Systems That Have Been Eliminated as Prime Candidate First-Wall/Blanket Structural Materials.

ALLOY	PRIMARY LIMITATIONS
Aluminum	Poor mechanical properties at elevated temperature. Loss of ductility caused by high transmutation rates under irradiation (He, H). Compatibility with liquid metal breeder.
Molybdenum	Difficult fabrication/welding. Effect of radiation on DBTT.
Nickel	Loss of ductility under irradiation. Compatibility with liquid metal breeder.
Titianium	Hydrogen interactions. Phase stability under irradiation. Low thermal conductivity.
Niobium	Generally less desirable than vanadium. Loss of ductility under irradiation. Long-term activation. Resource limitations.

eliminated as candidate structural materials for the DEMO design. Table 6-6 summarizes the important favorable and unfavorable characteristics of austenitic stainless steel (primary candidate alloy PCA) and the commercial ferritic steel (HT-9).

The radiation damage resistance of PCA seems adequate for water-cooled solid breeder blanket concepts. Structure temperatures in a water cooled system are below the temperatures where severe displacement damage, embrittlement, helium embrittlement and maximum swelling occur, and where mechanical properties are not substantially reduced. Steady-state reactor operation is important for acceptable wall lifetimes because of the relatively high thermal stress factor associated with stainless steel. The fact that solid breeder materials also have a limited lifetime because of Li burnup reduces the incentive for a very long lifetime structure.

Table 6-6. Favorable and Unfavorable Characteristics of Prime Candidate First-Wall Structural Alloys.

ALLOY SYSTEM	FAVORABLE CHARACTERISTICS	UNFAVORABLE CHARACTERISTICS
Austenitic Stainless Steels (316, PCA)	Good fabrication/welding	Physical Properties (k, α)
	Extensive property data-base	Limited operating temperature (radiation effect and mechanical properties)
	Availability/experience factor	Requires thermomechanical treatment (cold-work)
	Compatible with H_2O, air, H	
Ferritic steels	Low radiation swelling	Radiation effect on DBTT
	Better physical properties than austenitic steel	Welding difficulties (PWHT)
	Compatible with H_2O, air, H	Sensitivity to TMT
		Ferromagnetic property
		Limited radiation data base

6.2.3.2 Design Details Selection

First Wall/Blanket Configuration

A modular approach to blanket design was adopted for the STARFIRE/DEMO Li_2O solid breeder blanket. Selection of this approach was based on the results of the evaluations of various approaches conducted during the STARFIRE study. The basic idea is to build up blanket sectors from large, easily replaced blanket modules. The primary objective is to maximize reactor availability by minimizing the amount of in-reactor maintenance operations necessary for replacement of a failed blanket part. This is accomplished by removing the blanket sector which contains a failed module and replacing it immediately with a spare sector. The removed sector is then taken to a hot cell, where more sophisticated tools are available, for removal and replacement of the failed module while reactor operation is resumed.

First Wall

The first wall's panel-type construction provides integral cooling of the blanket wall and avoids the necessity for a large number of pressure boundary welds in the high radiation zone. The resistance seam weld method used to join the corrugated sheet to the front plate is considered to be the most resistant to weld zone radiation damage of any applicable welding method. Because of the low first wall particle flux in DEMO, except for the ~ 1-m-wide belt region to either side of the limiter only ~ 2-mm of Be is required as protective armor. The panel provides cooling to the blanket sides and to the first few centimeters of the Li_2O breeder as well. The flat surface resulting along the blanket sides near the first wall simplifies the inclusion of electrical connectors required between adjacent first wall/blanket sectors.

Mechanical and structural integration of the first wall and blanket helps to increase the breeding ratio and simplifies the structure and coolant systems. A separate actively cooled front wall for the breeding module is not needed; this improves breeding ratio since the additional amounts of steel and water are not included. Maintainability and availability are not affected, since downtime for changeout of an integrated module would be equal to or less than downtime for changeout of a separate first wall or a separate breeding blanket.

Neutron Multiplier/Second Wall Zone (Alternate Concept Only)

The primary motive for the use of Li_2O as the tritium breeding material in a power reactor blanket is the anticipated achievement of a net breeding ratio > 1 without using a separate neutron multiplier. However, the use of a neutron multiplier with Li_2O can significantly improve breeding performance (see Sec. 6.3). This can potentially lower the reactor's capital costs by reducing the reactor geometric envelope in one of two ways. First, if the use of Li_2O alone results in net breeding without the need for an inner breeding blanket (as in the DEMO reference design), the addition of a neutron multiplier will permit much thinner outer blankets. Second, if for Li_2O alone an inner breeding blanket is required, the addition of a neutron multiplier will probably result in net breeding with only a relatively thin non-breeding inner blanket.

The choice of beryllium as the neutron multiplier was discussed in Ref. 7.

Tritium Breeding Zone

The breeding zone configuration is similar to that of the STARFIRE blanket. The primary difference is the absence of the neutron multiplier and second wall. Elimination of the neutron multiplier automatically removes the need for a second wall because the first wall serves as the actively cooled front wall of the breeding zone. This simplifies the blanket design and the connections into the inlet and outlet manifolds.

The toroidal coolant flow direction was selected over the radial flow direction, because toroidal flow results in a number of important relative advantages for concepts using solid breeders and pressurized water coolant. An example of a radial flow blanket design is described in Reference 9. This blanket, designed for a field-reversed mirror device (FRM), uses helium coolant to cool Inconel-clad Li_2O plates. The choice of water coolant over helium was previously discussed. The perceived disadvantages of the radial flow blanket approach described in Ref. 9 may be briefly summarized as follows:

- Small-diameter tubes are more desirable than pressurized modules with flat walls to contain high pressure coolant. (Such modules would be needed for tokamaks; a more space-efficient large cylindrical module was used for the RFM.)
- The Li_2O plates (2.1 cm average width) have average centerline temperatures of ~ 800-1000°C or higher, which are considered to be excessively high (Sec. 6.4.3). The analysis assumes perfect contact between clad and Li_2O (i.e., no temperature increase at interface) an unconservative and undemonstrated assumption.
- The radial flow concept relies on closely controlled 1-mm constant width gaps between adjacent plates. The much lower Li_2O temperature range allowed for DEMO would require a design with gap widths which vary significantly with depth into the blanket, which would compound tolerance control difficulties.
- A helium purge gas piping system is required within the blanket. Separate inlet and outlet tubing connections must be made to each individual Inconel-clad Li_2O bar.
- An auxiliary cooling system for the blankets was identified as necessary to remove afterheat following a LOCA, but the design and method of operation of such a system were not described.

For these reasons, the toroidal flow concept was judged to be preferable overall to radial flow for the DEMO Li_2O blanket.

The breeder-to-tube interface concept proposed for the Li_2O blanket consists of a stainless steel metallic felt metallurgically bonded to the breeder and to the tube. This approach avoids the large uncertainties in thermal conductance value over the blanket lifetime inherent in the helium gaps and insulator/breeder contact pressure approaches previously proposed[1,8] for similar solid breeder blanket concepts. The interface medium is a commercially available product, for which thermal inductance can be closely controlled through proper selection of density (% of theoretical) and thickness. By applying a graded selection of the felts to the breeder-to-tube interfaces during fabrication, the rise in coolant temperature axially along the tube can be compensated by changing the thermal conductance, so that the allowable 250°C range of breeder temperatures can be fully utilized at all points along each tube. The close control of felt density and thickness, together with the very small ΔT values across the thin metallurgical bonds, is expected to result in actual breeder temperatures quite close to predicted values based on nominal thermal conductance values. (This process, also described in Sec. 6.4.5, was developed by McDonnell Douglas using corporate funds and is presently considered to be Company proprietary. It is included in this report for completeness.)

The selected coolant outlet temperature of 300°C for DEMO is 20°C lower than for STARFIRE, although the coolant inlet-to-outlet temperature difference of 40°C is the same. The lower outlet temperature will result in a lower thermal energy conversion efficiency (33.6% vs. 35.6% for STARFIRE), but permits a reduction in nominal coolant pressure from 2200 psi to 1600 psi. The reduction in coolant temperature and pressure is expected to lead to higher reliability for the blanket and coolant system, and therefore the reduction in efficiency is considered acceptable for DEMO.

Manifold Zone

The U-shaped breeder coolant tubes connect to the large-diameter inlet and outlet manifold tubes to permit dual parallel coolant circuits which ensures safe cooldown of all the first wall/blanket modules in the event of the loss of one coolant circuit. The manifold segments are joined between modules by welding to intermediate seal rings of omega-shaped cross section.

These rings accommodate initial misalignment during blanket sector assembly or module replacement, and accommodate differential thermal expansion during operation. The seals simplify removal of the modules during operations in the hot cell, since far fewer module replacement connections need to be cut and rewelded compared to the small-diameter headers placed between the U-bend tubes and manifolds in the STARFIRE blanket. Connecting the tubes to manifolds at the rear of the blanket is considered preferable to using end plenums (as in INTOR[8]) primarily because it avoids difficulties in integrating the high-pressure coolant plenums of the first wall with those of the blanket.

6.2.4 Operation/Safety Considerations

The most important considerations in the operation of a Li_2O solid breeder blanket are (1) maintaining breeder temperature within the allowable range, (2) safe removal of blanket (and first wall) afterheat during normal and accident situations, and (3) the consequences of breeder/coolant contact in an accident situation. These considerations are summarized in Table 6-7.

The importance of maintaining the breeder between 410°C and 660°C is discussed in Sec. 6.4.3. The concerns regarding (1) excessive vapor transport of LiOH from the blanket via the purge stream at breeder temperatures above ~ 660°C, and (2) the precipitation of LiOH as a second phase at temperatures below ~ 410°C, are both considered to be potentially serious problems for the tritium recovery from Li_2O which require further investigation.

The safe removal of afterheat from the Li_2O breeder and stainless steel blanket structure is ensured by the use of dual parallel coolant circuits, either of which is adequate to safely remove the heat even at very low coolant flowrates. Total blanket decay heat is ~ 14.5 MWth at shut-down, decreasing to ~ 2-3 MWth several hours after shutdown. This coolant system arrangement provides the maximum capital investment protection for the plant by keeping all blanket sectors and modules reusable except for an initially failed module.

The pressure pulse created when the high pressure, high temperature water coolant leaks from a coolant tube and contacts the hot solid breeder is assumed to be safely vented from the blanket by a system of blow-out plugs in the module walls at the end of channels which are in line with the axes of the

Table 6-7. Principal Operation/Safety Considerations For Li_2O Breeder Reference Blanket

Concern	Importance	Remarks
• Maintaining breeder temperature within limits	• Temperatures exceeding T_{max} = 665°C lead to excessive transport of LiOH vapor in purge stream • Temperatures below T_{min} = 410°C lead to precipitation of LiOH, and possible low-temperature sintering which tends to inhibit tritium release	• Further work required: - Combined effects on breeder temperature of local variations in breeder properties and wall loading - Conditions which can produce low-temperature sintering - Methods of controlling breeder/tube thermal conductance
• Safe removal of blanket afterheat following a coolant loop accident	• Temperature increases in blanket can lead progressively to annealing of structure and breeder thermal sintering, which preclude reuse	• Dual parallel coolant loops nearly eliminate possibility of unacceptable temperature increases
• Breeder/coolant contact as result of smaller large coolant leak	• Pressure pulse created can rupture module wall • Corrosive LiOH resulting from breeder/coolant reaction can damage other blanket areas, coolant system, or other components	• Further work required to determine consequences to system from LiOH corrosion • Blow-out plugs in module walls vent over-pressure without rupturing module

longest portions of the coolant tubes. This concept requires further analytical investigation. Of perhaps greater importance, in terms of protecting plant capital investment, is the LiOH formed in large quantities upon the occurrence of breeder/coolant contact. The LiOH could enter both the coolant system and purge system, with unknown consequences of increased corrosion. Further work is required to define the severity of such LiOH releases.

6.3 Tritium Breeding Assessment

A self-sustaining DT fusion reactor must breed tritium. In all fusion reactor concepts, this is accomplished in a lithium-containing blanket that circumscribes the plasma. The feasibility of producing tritium with an adequate breeding ratio (BR) was a serious issue in the 1950's and early 1960's. The release of reasonable data for the $^{7}Li(n,n'\alpha)t$ reaction led to estimates of BR > 1 in the 1960s. The early generation[2,10] of conceptual designs predicted BR of ~1.3 to 1.5 for natural-lithium blankets with full coverage. Early sensitivity studies[11] showed that the BR in the natural lithium system was not overly sensitive to variations in cross sections. Consequently, concerns about attaining adequate BR were alleviated and tritium breeding studies were not given high priority for most of the 1970s.

The safety problems of liquid lithium received a great deal of attention in the past several years. The STARFIRE, DEMO, and INTOR studies investigated breeder blanket concepts based on solid lithium compounds such as Li_2O, $LiAlO_2$, and Li_2SiO_3. Solid breeders appear now to be the leading candidates worldwide[12] for fusion blankets. However, the feasibility of solid breeders has not yet been established. Achieving adequate tritium breeding and acceptable tritium recovery from the blanket are the two most critical issues for solid breeders. Thus, the past three years have witnessed a serious interest in the tritium breeding issues.

The following subsections summarize the breeding assessment performed for the DEMO study. In Section 6.3.1 the determination of tritium breeding requirements for power reactor conceptual designs is discussed. Section 6.3.2 describes the geometrical models and computational methods used for the analyses. Finally, the results of neutronics analyses for breeder blanket concepts based on four candidate breeders, Li_2O, $LiAlO_2$, 17Li-83Pb, and lithium metal are discussed in Sections 6.3.3 through 6.3.6.

6.3.1 Tritium Breeding Requirements

The tritium breeding ratio is defined as $T = N^{+}/N^{-}$, where N^{+} is the rate of tritium production in the system (normally the blanket) and N^{-} is the rate of burning tritium in the plasma. T must exceed unity by a margin (G) to cover: (1) losses and radioactive decay during the period between production and use; and (2) supplying inventory for startup of other fusion reactors.

Detailed expressions were derived[13,14] to correlate tritium doubling time (t_d), and inventory. The expression has the general form

$$T = 1 + \frac{ID}{\bar{N} t_d} \qquad (6\text{-}1)$$

where I is the total tritium inventory and D is a complex function that accounts for radioactive decay and other losses. The magnitude of the total tritium inventory is determined by the tritium inventories in the breeding blanket (I_B), fueling and exhaust systems (I_F), storage (I_S), and startup (I_0). At present, there are large uncertainties concerning the magnitude of the tritium inventory achievable in fusion reactor systems. The tritium inventory in the blanket will likely be <1 kg for liquid lithium systems, but may be between 1 and 10 kg or greater in solid breeders because their tritium release characteristics cannot precisely be quantified at present. The magnitude of I_F depends strongly on many plasma-performance and exhaust-system operating parameters such as the fractional tritium burnup in the plasma. I_S is determined by the amount of fuel required in reserve to guard against a temporary malfunction of the tritium recovery system. I_0 is the tritium inventory that needs to be accumulated in order to start up a new reactor, and it is also a function of I_B, I_F and I_S.

Figure 6-3 shows the required tritium BR[14] as a function of the fractional tritium burnup in the plasma and the doubling time, assuming a blanket tritium inventory of 10 kg. The required tritium BR increases very rapidly as the fractional burnup decreases to ~1% and as t_d becomes very short. This is one of the reasons why achieving a fractional burnup of >5% has been identified as one of the key goals for the impurity control and exhaust system development. The doubling time goal is obviously related to the desired growth rate for fusion power. The historical growth of the power industry has been a doubling time of ~10 y. For the first generation of fusion power reactors, a short doubling time (<5 y) is highly desirable.

The required tritium breeding ratio (T_0) in an actual operating reactor should thus be

$$T_0 = 1 + G \,, \qquad (6\text{-}2)$$

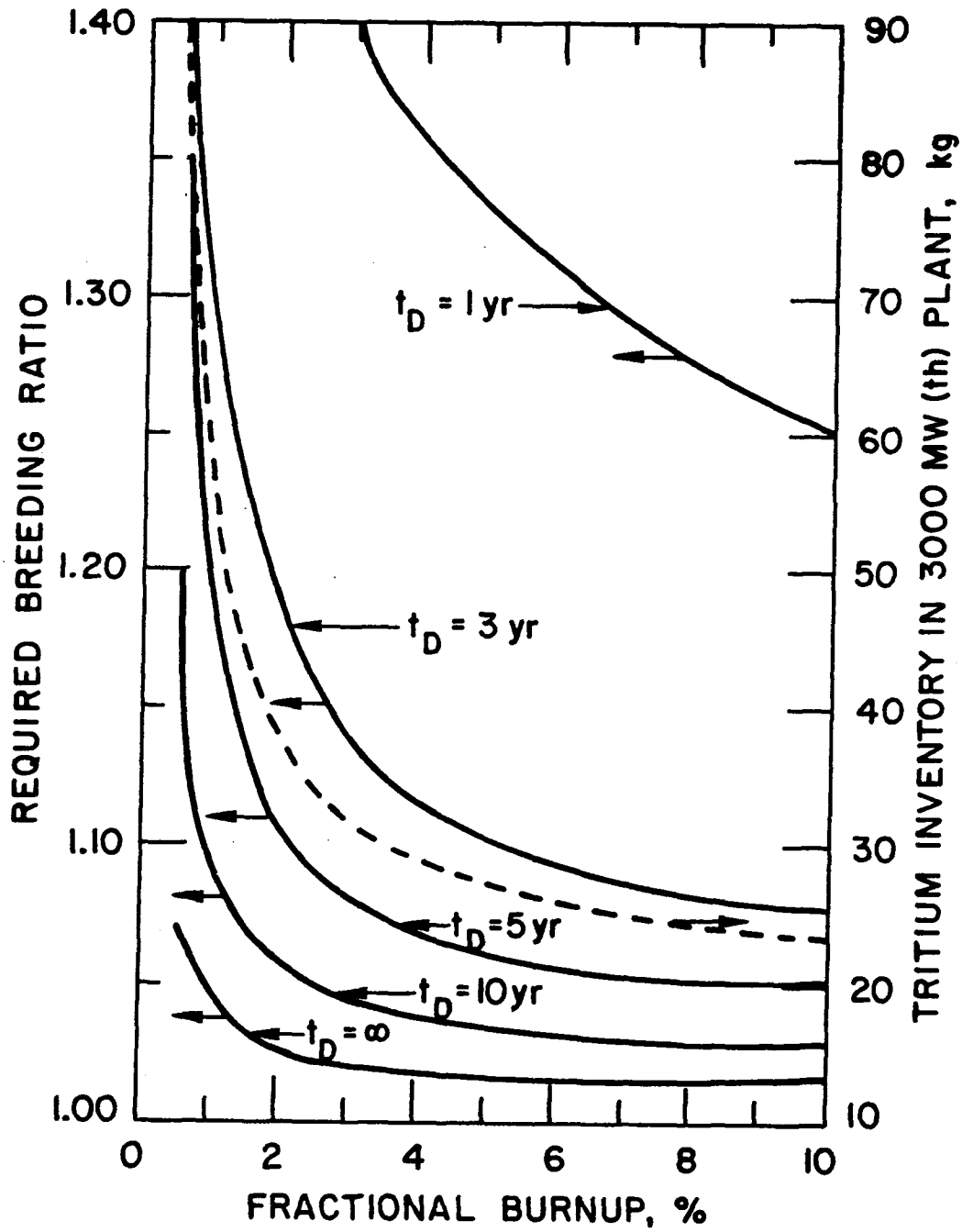

Figure 6-3. Effect of fractional burnup and doubling time upon required breeding ratio.

where G is the margin discussed above. For a fractional burnup of ~5% and doubling time of ~5 y, the required T_0 is ~1.05. It should be clearly realized that if a fractional burnup of only ~1% is achievable, then the required T_0 is ~1.2, a very difficult breeding requirement to achieve as will become evident in later sections.

T_0 as defined in Eq. (6-2) is the actual net tritium breeding ratio that must be obtained in an operating fusion power reactor. However, for a conceptual design, the goal for the BR (T_D) that must be achieved exceeds T_0 by an allowance (Δ) for the uncertainties in estimating T_0, i.e.,

$$T_D = 1 + G + \Delta \, . \tag{6-3}$$

The sources of uncertainties in estimating Δ are numerous, but can be broadly classified into three areas: (1) reactor design definition; (2) neutronics calculations; and (3) nuclear data. A few comments on these are in order.

The BR is sensitive to many of the design features of the fusion reactor. Some of the important features are: (1) the materials, geometry and size of the in-vessel components (e.g., limiter or divertor for impurity control) that intercept the fusion neutrons before they enter the blanket; (2) materials, volume fraction and distributions of structural materials and coolants in the first wall and blanket; (3) size and locations of the many void regions that penetrate the blanket, such as plasma heating, plasma-current drive, vacuum pumping and fueling; (4) the presence of nonbreeding regions in the blanket, which are reserved for requirements not yet well defined such as passive coils for plasma stabilization; and (5) overall plasma characteristics and reactor configuration, including fusion neutron source distribution, shape of first wall, modularity of components, etc. Fusion is still in a somewhat early stage of research and development with active conceptualization of reactor designs. Technology choices and design concept selections have not been made for many of the reactor systems. These selections will not be made for a number of years to come because a number of issues are yet to be resolved experimentally and analytically. The achievable tritium breeding ratio is certainly one of the key considerations in the selection among concepts.

The dependence of the tritium breeding ratio on technology and design concept choices can be quite large, 50% in some instances. Obviously, one cannot design a breeding blanket with a breeding potential that accommodates these large variations. Since the breeding potential for candidate breeding materials will be (and is already being) performed for various technology and design concept choices, we will require that T_D includes only 2% allowance for

design definition. This is merely enough to account for those additional design details that cannot be developed at present for a given conceptual reactor design.

Neutronics calculations of the breeding ratio in a given system are subject to two principal uncertainties. First, geometrical modeling of the fusion reactor configuration entails some approximations that are necessary to make the problem practical from viewpoints of computer storage and computing time. Second, there are errors that are inherent in all calculational methods and codes for a variety of reasons such as those related to numerical techniques, averaging, and/or discrete treatment of continuous variables. Reducing the errors due to calculations to <2% appears to be a very difficult goal.[15]

The third source of uncertainty in estimating the breeding ratio comes from errors in nuclear data (e.g., cross sections and energy and angular distribution of secondary neutrons). These include errors arising from the accuracy of measurements, representation of parameters in data files, and processing of the data into a form suitable for use in radiation transport codes. Over the past decade numerous studies[11,16-26] have been conducted on the cross-section sensitivities to the fusion blanket performance. Judging from experience in the fusion program and the estimated sensitivity of T to variations in nuclear data, it is not unreasonable to require accuracies in nuclear data that result in an error in T of no more than 1 to 2%.

From the above discussions, the allowance Δ in Eq. (6-3) required to compensate for a possible shortfall in tritium breeding due to the combined effects of uncertainties in design definition, calculations, and nuclear data is ~5 to 6%. Hence, the tritium breeding ratio required in a fusion reactor design must be ~1.1 (i.e., 1.05 plus ~5 to 6%) in order for the design concept to have a high potential of achieving self-sustaining DT fusion power economy. However, it appears somewhat premature to exclude blanket design concepts yielding T_D's of 1.05 to 1.1 from the consideration. The viability of these blanket designs needs to be further investigated as more accurate evaluations on BR become possible.

The possibility of operating fusion reactors with a tritium breeding ratio, $T < 1$, by using a tritium concentration in the plasma of <50%, has been suggested. However, it has been found[27] that the required magnetic field

and reactor size have to be increased rather quickly as T decreases for the same reactor power. Thus, small decrements in T appear very costly in terms of the required plasma performance and the increase in the cost of electricity.

6.3.2 Geometrical Model and Computational Method

Figure 6-4 illustrates a schematic view of the poloidal cross section of the DEMO reactor. This toroidal reactor system has been simulated by a three-dimensional Monte-Carlo transport code, MORSE-CG.[28] The number of DT-source neutron histories generated for each computation is 20,000. The spatial distribution of the source neutrons is assumed to be

$$f(r) \propto \left[1 - (r/r_m)^{c_1}\right]^{c_2}, \qquad (6\text{-}4)$$

taking into account the plasma shift due to the high-beta MHD equilibrium. The r and r_m stand, respectively, for the source point distance and the plasma boundary distance both measured from the shifted plasma center, $R_m + S_m$. Here R_m is the magnetic axis major radius (5.2 m) and S_m is the source shifting distance (0.26 m). The plasma contour is determined based on the following parametric equations:

$$z_b = a\kappa \sin t \qquad (6\text{-}5)$$

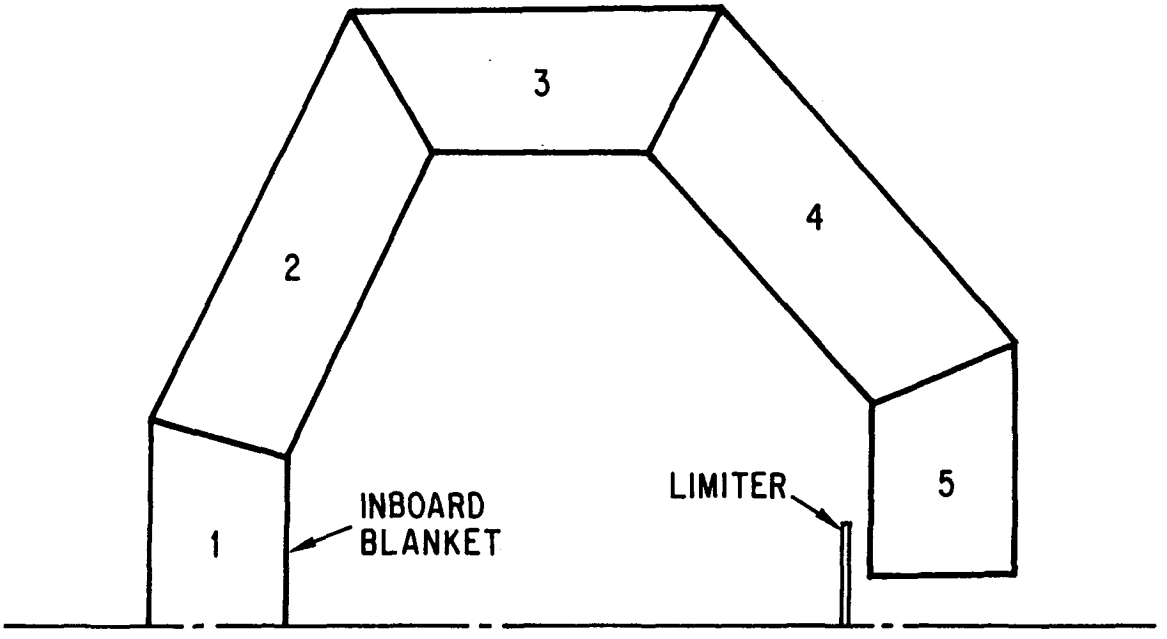

Figure 6-4. Schematic view of DEMO blanket cross section.

and

$$\rho_b = R_m + a \cos(t + d \sin t) , \qquad (6\text{-}6)$$

where

z_b = boundary contour height in the direction perpendicular to the reactor midplane;

ρ_b = boundary contour major radius;

a = plasma minor radius (1.3 m);

κ = plasma elongation factor (1.6); and

d = plasma triangularity (0.2).

The coefficients C_1 and C_2 appearing in the distribution function, are the source shaping factors used for the neutronic modeling of the 14-MeV source neutron distribution. In the present analysis, both coefficients are assumed to be 2.0. The effect of variation of these parameters on the neutronics performance remains to be studied.

In order to supplement the expensive three-dimensional Monte Carlo calculations, several one-dimensional analyses have been performed by using a discrete ordinate transport code, ANISN[29] with the S_8-P_3 approximation. The geometrical model used for these one-dimensional analyses is an infinite cylinder where reactor subsystems (e.g., first wall, blanket, shield, etc.) are represented by concentric cylindrical shells with axis along the plasma minor radius. The plasma minor radius and the scrape-off size are assumed to be 2.08 m and 0.165 m respectively, and the source neutron is uniformly distributed in the plasma region in this case.

Table 6-8 shows the system dimensions and material compositions used for most of the neutronics analyses. Some one-dimensional scoping studies conducted earlier in the DEMO study and reported here have used an armor/first-wall design slightly different from that defined in Table 6-8. For example, one solid-breeder design employed a 13.4-mm thick armor structure, based on a recent INTOR[30,31] design. This armor was followed by a 3.0-mm first-wall coolant region and then by a 3.0-mm first-wall structure. This design is considered neutronically equivalent to a design in which the armor thickness is redefined as 10 mm and a total first-wall thickness of 9.4 mm is composed of 68% structure and 32% coolant. It is expectd that such a minor difference (in comparison with the system defined in Table 6-8) yields only a minute

Table 6-8. System Dimensions and Material Composition Used for Neutronics Analyses

Component	Thickness (mm)	Composition
1. Armor	10	100% structure
2. First wall	10	65% structure + 35% coolant
3. Blanket	680	(a)
4. Shield	300	90% Fe1422[b] + 10% H_2O

[a] (1) Solid breeder systems
90% breeder(3) + 5% structure + 5% coolant.

(2) Liquid breeder systems
85% breeder + 10% structure + 5% coolant

(3) 70% of theoretical density.

[b] Fe14Mn2Ni2Cr.

effect on the overall neutronics performance. Unless otherwise stated, it is assumed that the system shown in Table 6-8 has been used in the neutronics analyses.

The VITAMIN-C[32] and MACKLIB-IV[33] cross-section libraries were used for the particle transport and reaction rate calculations, respectively. Both libraries were generated from the ENDF/B-IV[34] data, and possess a 46-neutron and 21-gamma group structure.

Recent experiments[35-42] have shown that $^7Li(n,n'\alpha)t$ cross-section data in ENDF/B-IV is substantially higher than that experimentally measured. The maximum difference amounts to ~15%. In order to be consistent with these experimental results, the $^7Li(n,n'\alpha)t$ reaction rate needs to be reduced for the purpose of calculating the breeding ratio. The necessary reduction is expected to be inherently large in "hard" neutron spectrum systems where the ^7Li reaction makes a significant contribution to tritium production. Unless otherwise mentioned, the total tritium production rate reported here is assumed to include a correction by -15% for the $^7Li(n,n'\alpha)t$ reaction rate. A more precise evaluation of the ^7Li reaction rate remains to be further investigated.

6.3.3 Li_2O Breeder Blanket Designs

The solid lithium oxide (Li_2O), which has been one of the most extensively studied breeder materials for fusion reactor applications, possesses several important advantages in comparison with other candidate tritium breeding materials: (1) a high potential for tritium production;[43] (2) the possible elimination of neutron multiplier because of the high breeding capability; and (3) low neutron-induced activation. However, whether or not blanket designs based on the use of Li_2O could eliminate the need of any additional neutron amplification for sufficient tritium production depends strongly upon the overall reactor design concept. The design considerations that must be taken into account in this regard include: (1) whether the inboard blanket is used for tritium breeding; (2) how much of the outboard blanket volume must be set aside for the impurity control system (e.g., divertor or limiter) and the plasma heating system; and (3) first-wall/blanket design details such as the thickness of the first wall and amount of structure and coolant in the blanket. The neutronics effort in this section is, therefore, devoted to scoping the tritium breeding capability of Li_2O blanket designs so that one can identify the impact or constraints on these pertinent design considerations.

6.3.3.1 Li_2O Blanket Designs Without Neutron Multiplier

The effects of armor erosion[12] with DEMO plant operation and of ^6Li enrichment were studied making use of the one-dimensional model and the result is shown in Fig. 6-5. Note that the result of Fig. 6-5 does not include the T_7 correction mentioned earlier. The breeding blanket is neutronically represented by a homogeneous mixture (90 vol % Li_2O + 5 vol % 316 SS + 5 vol % H_2O). Li_2O is assumed to be 70% of the theoretical density including the design porosity for tritium extraction. Displayed in Fig. 6-5 is the tritium BR as a function of ^6Li enrichment for two armor designs: (1) 10-mm thick Type 316 stainless steel armor; and (2) 10-mm thick beryllium armor. These armors are followed by: (1) 3.4 mm Type 316 stainless steel front-panel region; (2) 3.0 mm H_2O coolant region; and (3) 3.0 mm Type 316 stainless steel back-panel region — in this order. It is found that for both armor designs in the absence of a neutron multiplier, the natural lithium systems result in the highest BR's. The substantial decrease in the $^7Li(n,n'\alpha)t$ reaction with

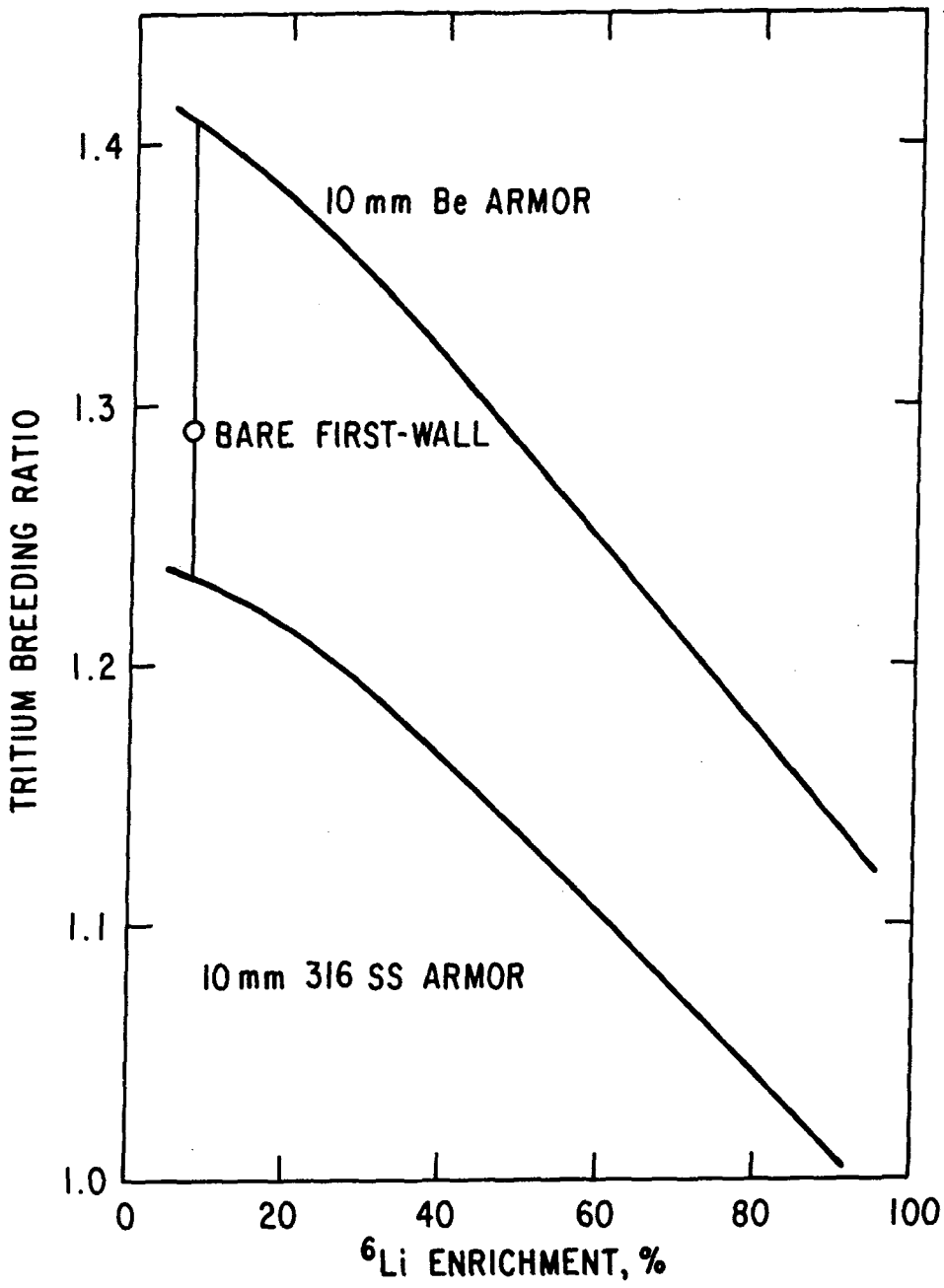

Figure 6-5. Effect of ^{6}Li enrichment upon tritium breeding for Li_2O breeder blanket designs. The T_7 correction is not included.

fewer ^{7}Li atoms is the reason for lower BR at the higher ^{6}Li enrichment. The result shown in Fig. 6-5 is consistent with the analysis of Ref. 38. At the reactor startup the Type 316 stainless steel armor system can yield a BR of about 1.23 which would increase to about 1.29 after the first 10-mm thick Type 316 stainless steel has eroded. In the case of the beryllium armor design the initial BR is significantly higher than the Type 316 stainless steel armor

case (1.41 vs. 1.23), but the BR will eventually drop significantly as the beryllium is eroded. The breeding gain in the beryllium armor system results from (1) an increase in the $^{7}Li(n,n'\alpha)t$ reaction rate due to the thinner stainless steel structure; and (2) an increase in the $^{6}Li(n,\alpha)t$ reaction due to the neutron amplification by the Be(n,2n) reaction. For example, the Be(n,2n) reaction rate for the case with natural lithium shown in Fig. 6-5 amounts to about 0.18 per fusion neutron.

In order to identify the multi-dimensional breeding effect in the DEMO configuration, a series of three-dimensional Monte Carlo calculations have been performed. Table 6-9 summarizes the results. In addition, Case A in the table shows the BR of full breeding coverage calculation by ANISN. This case is compared to the three-dimensional MORSE calculation given in Case B. The discrepancy between the two calculations is less than ~1% in the total BR evaluation. It is found that the breakdown of BR in each blanket sector is more or less proportional to its fractional area at the armor surface. For example, the fractional BR's in Sectors 1 through 5 vary as 8.5%, 18.0%, 18.0%, 31.8%, and 23.8% while the corresponding fractions of armor surface areas vary as 9.2%, 20.3%, 19.7%, 31.2%, and 21.4%. The discrepancy is attributable to the slight breeding enhancement in the outboard regions (Sectors 4 and 5) due to the source neutron shifting and the toroidal curvature of the system configuration.[44]

It is important to note that the Li_2O blanket design shown in Case B can accommodate a nonbreeding region which can possibly amount up to ~20% of the total breeding surface. This will be the case even after the BR is reduced by the amount required for the $^{7}Li(n,n'\alpha)t$ cross-section correction. The nonbreeding zones considered include several major penetrations such as a limiter opening (or divertor slot) for impurity control and an REB duct for plasma heating. The result of Table 6-9 implies, however, that if a neutron multiplier is not used, it is quite difficult to implement too large an outboard space allowance, e.g., an allowance for a divertor system which could take up ~20-25% of the outboard region.[45] Accommodation of a limiter opening as well as an REB duct appears quite feasible in an Li_2O blanket design without use of a neutron multiplier. Case C of Table 6-9 shows the BR in a blanket design where a 0.4-m high limiter opening penetrates through the outer blanket sector near the reactor midplane (Sector 5) all the way in the toroidal

Table 6-9. Tritium Breeding Performance in Li_2O Blanket Designs

Case:	A	B	C	D	E
Method:	1-D ANISN	3-D MORSE	3-D MORSE	3-D MORSE	3-D MCNP[b]
System: / TBR	Full Breeding	Full Breeding	With Limiter	With Limiter No Inboard Breeding	With Limiter No Inboard Breeding (FED/INTOR)
Sector 1		0.105 (2%)[c]	0.110 (2%)	-----	
2		0.223 (1%)	0.217 (1%)	0.214 (1%)	
3		0.223 (1%)	0.215 (1%)	0.226 (2%)	
4		0.394 (1%)	0.396 (1%)	0.399 (1%)	
5		0.295 (2%)	0.255 (2%)	0.259 (1%)	
Total T_6	0.916	0.904 (0.1%)	0.879 (0.2%)	0.810 (0.2%)	0.699 (0.7%)
Total T_7	0.315	0.335 (0.7%)	0.314 (0.7%)	0.288 (0.7%)	0.235 (0.5%)
Total (T_6+ T_7)	1.231	1.240 (0.2%)	1.193 (0.2%)	1.098 (0.7%)	0.934
Total (T_6 + T_7) with -15% T_7 correction	1.184	1.189	1.146	1.055	0.899

[a]Armor: 10 mm Type 316 stainless steel (SS).
First wall: 10 mm (65 vol % SS + 35 vol % H_2O).
Blanket: 680 mm (90 vol % Li_2O + 5 vol % SS + 5 vol % H_2O).
(Note: Li_2O is 70% of the theoretical density; natural lithium.)
Shield: 300 mm (90 vol % Fe14Mn2Ni2Cr + 10% vol % H_2O).

[b]Ref. 42.

[c]Standard deviation: read as ±2%.

direction. The limiter panel in front of the armor is modeled by a cylindrical annular ring and assumed to have a dimension of 1 m (height) × 20 mm (width). The limiter panel is located at ~80 mm away from the armor surface, and the material composition is assumed to be a homogeneous mixture of 65% SS + 35% H_2O. As shown in Table 6-9 the presence of the limiter system decreases the BR from 1.240 (or 1.189 after the T_7 correction) to 1.193 (1.146). The decrease is slightly less than 4% which is more or less proportional to the fraction of the limiter opening at the armor surface.

The breeding potential in excess of unity, as in Case C of Table 6-9, has several important design implications. For example, it can be utilized to eliminate tritium production in the inboard blanket and/or reduce the overall breeding blanket thickness. See Fig. 6-8 which will be shown later for the tritium accumulation analysis. One finds that a blanket thickness less than 0.3 m would be sufficient to yield a net BR > 1.0 provided that the blanket is fully covered (including the inboard section) by the breeding material. Such a thin blanket design is attractive for reducing not only the required breeder inventory but also the associated tritium inventory. On the other hand, the elimination of tritium breeding in the inboard blanket (the Sector 1 region) results in a net BR of 1.098 (or 1.055 after the T_7 correction) as shown in Case D of Table 6-9.

As discussed in Section 6.3.1 one cannot completely exclude, at present, a possibility that this Case D would result in $T_0 < 1.05$ [in Eq. (6-2)] due to the possible uncertainties involved in the present computational method including the nuclear data used. However, it should be noted that the nonbreeding inboard blanket design has a quite significant impact on the required thickness for the inboard radiation shielding. A particular emphasis should be placed on solid breeder systems for which a large porosity must be accommodated for breeder materials in order to alleviate the tritium extraction. Such an accommodation of breeder porosity will result in a thicker shield, leading to a costly degradation of the reactor power performance. In this regard Case D appears to deserve further elaboration for more precise breeding evaluation. The effort is vital to the final decision on whether the inboard blanket should be utilized for tritium production or not.

Case E of Table 6-9 shows the BR analysis by the MCNP[46] code for a recent INTOR breeding blanket design[47] in which the nonbreeding inboard

section extends vertically from the bottom to the top. One notices a significant design penalty of such a geometrical configuration, compared to the DEMO configuration (see Fig. 6-4) in terms of tritium production. Evidently in the INTOR blanket configuration one cannot completely eliminate the inboard breeding in order to achieve a self-sufficient tritium production.

So far the blanket has been assumed to have a material composition of 90 vol % Li_2O + 5 vol % 316 SS + 5 vol % H_2O. However, it is quite conceivable that the blanket composition would need to be revised as more detailed mechanical and thermal-hydraulic analyses are performed. It is, therefore, important to identify the possible change of BR with such a compositional variation. Figure 6-6 plots the BR (with the T_7 correction) as a function of stainless steel volume in the blanket. The analysis is based on the one-dimensional model. Two coolant volumes, 5% and 10%, assumed for the analysis are expected to cover most of the range of practical interest. As seen in the figure the BR is not excessively sensitive to the content of H_2O coolant. The sensitivity is much more appreciable for the variation of structure content. For a wide range of steel content a relationship of ~7% variation in BR for every 10% variation

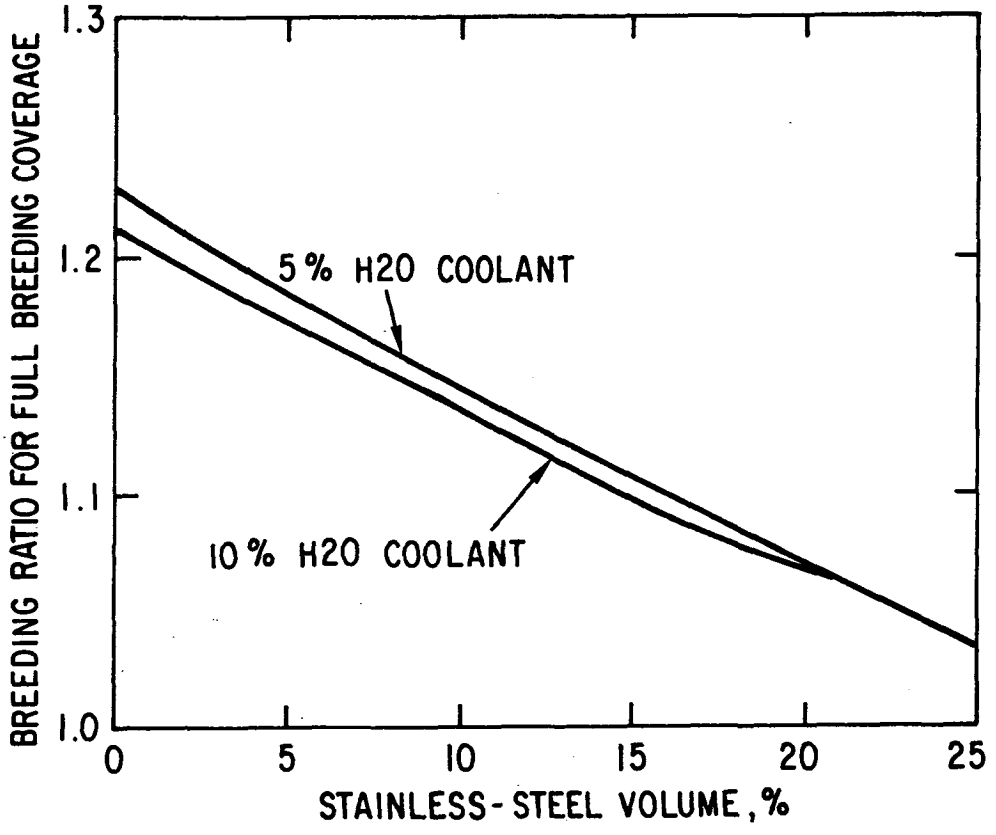

Figure 6-6. Effect of structural material content upon tritium breeding in Li_2O blanket designs.

in steel content can be considered approximately accurate. By extrapolating the result shown in Fig. 6-6 to a three-dimensional configuration, one finds that the volume fraction set aside for no tritium production region must be in a range from ~5% to ~15% for most of the coolant and structure contents of interest. If more than 15 vol % of the blanket is not used for breeding then the overall steel content is not allowed to exceed ~5% in order to yield a net BR > 1.0. As examined earlier (Case D in Table 6-9), the BR is lowered by ~11% due to the presence of the limiter opening and the nonbreeding Sector 1 blanket. The minimum one-dimensional BR allowed for a net BR [T_0 in Eq. (6-2)] > 1.05 for such a design is ~1.18. This BR leads to a maximum allowable steel content of ~5% as shown in Fig. 6-6. In the case of a full breeding blanket which includes the limiter opening, the maximum steel content can be as high as ~15%.

6.3.3.2 Li_2O Blanket Designs With Neutron Multiplier

The tritium breeding can be enhanced by use of neutron multipliers. The breeding enhancement has two obvious impacts on the design: (1) the potential for a complete elimination or substantial curtailment of the inboard breeding; and (2) a substantial reduction of breeder material inventory as well as the associated tritium inventory. Table 6-10 shows the effect of a beryllium multiplier on tritium breeding for two different blanket material layouts. System B is regarded as a more or less conventional design in which the multiplier is placed in front of the Li_2O breeder zone. In System A the beryllium multiplier zone is sandwiched by two Li_2O regions as studied in the UWMAK-II design.[3,48] Both systems employ an 80-mm thick beryllium zone (100% of the theoretical density) without internal coolant, and a Li_2O breeder with 30% enriched ^6Li. System B yields a BR of about 1.36, which is about 0.13 greater than the case without a multiplier, whereas System A enhances the tritium production by more than 0.32. The substantial breeding enhancement in System A stems largely from the blockage of neutron reflection into the armor/first-wall region, thereby drastically decreasing the parasitic neutron loss in this pre-blanket region. In fact, the BR in the first bank alone (40 mm thick) in System A amounts to about 0.71, which is slightly below one-half of the total BR. In the case of System B a majority of the secondary neutrons generated by the Be(n,2n) reaction, which are more than in System A, tend to be lost in the pre-blanket region

Table 6-10. Effect of Blanket Material Selection Near the First Wall Upon Tritium Breeding[a]

	System A	System B
1. Material layout		
Bank 1 (4 cm)	Li_2O[b]	Be[c]
Bank 2 (4 cm)	Be[c]	Be[c]
Bank 3 (4 cm)	Be[c]	Li_2O[b]
Bank 4 (54.5 cm)	Li_2O[b]	Li_2O[b]
2. Tritium breeding		
T_6	1.410 (0.646[d])	1.249
T_7	0.146 (0.068)	0.109
Total BR	1.556 (0.714)	1.358
3. Neutron balance/DT		
Net current into blanket	0.997	0.652
Reflection at interface[e]	0.549	0.812
Net loss in preblanket	0.003	0.348
Neutron multiplication in Be	0.520	0.727
Leakage to shield	0.057	0.057

[a]Based on one-dimensional model; T_7 is not corrected.

Armor: 10 mm 316 SS

First wall: 3.4 mm 316 SS
3.0 mm H_2O
3.0 mm 316 SS

[b]Li_2O: 5% SS + 5% H_2O + 90(63)% Li_2O (30% ^6Li enrichment).

[c]Be: 100% Be.

[d]Bank 1: BR only.

[e]J^-/J^+ at the interface between the first wall and blanket.

due to the strong neutron backflow. As shown in Fig. 6-7 the blanket designs based on the concept of System A can yield a continuously increasing BR with thicker multiplier while the conventional designs based on the System B configuration show a maximum BR at a beryllium thickness of ~50 mm.

The breeding performance of the blanket designs based on the System A concept (Li_2O/Be/Li_2O) is not significantly influenced by the material choice in the region following the second Li_2O breeder zone. Table 6-11 compares the tritium BR for five material choices (primary constituents of (1) Li_2O breeder

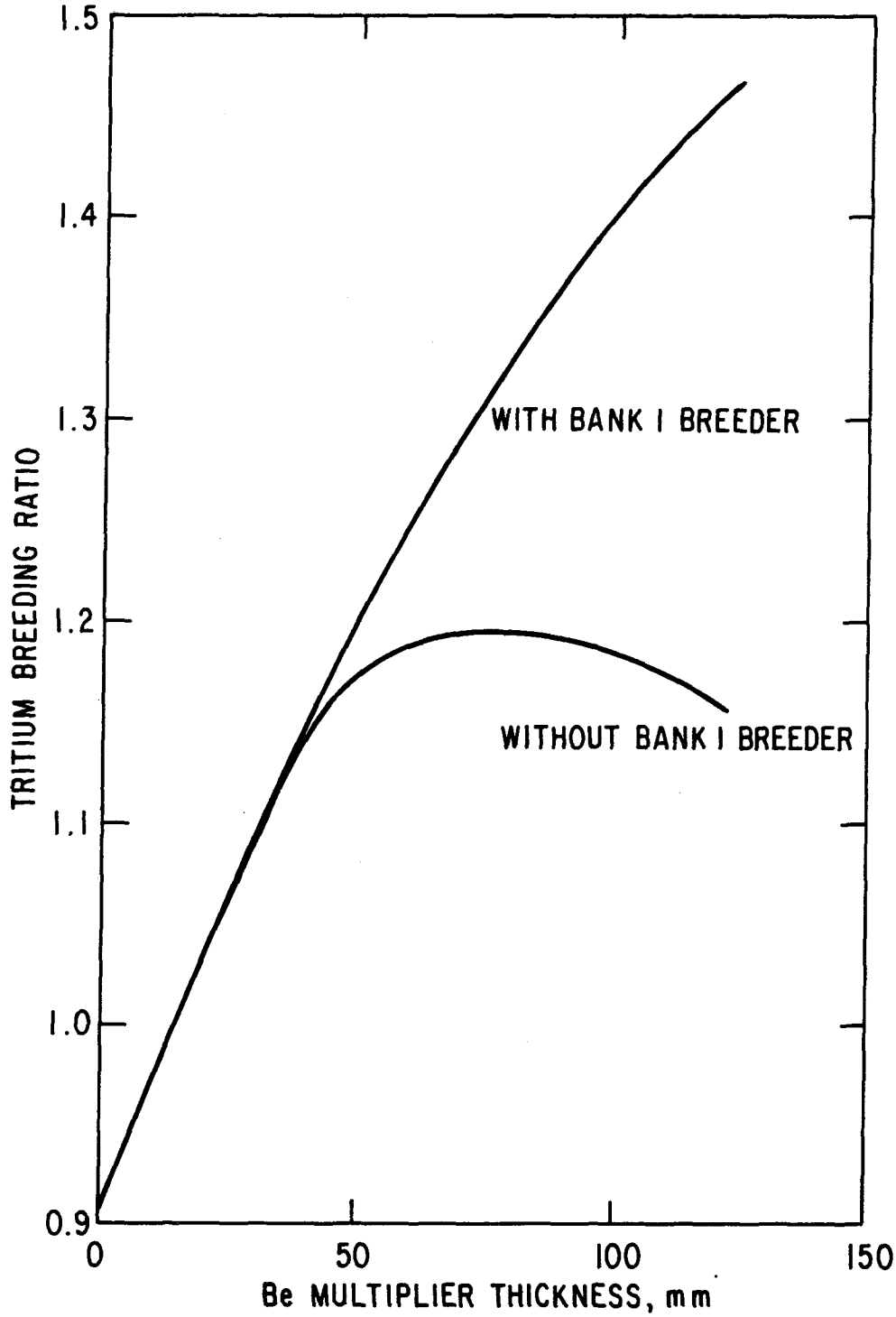

Figure 6-7. Effect of first-bank material selection upon tritium breeding for beryllium multiplier/Li_2O breeder blanket designs.

Table 6-11. Effect of Material Selection in Deep Blanket Region Upon Tritium Breeding[a]

Bank 1 (4 cm)	Li_2O[b]
Bank 2 (8 cm)	Be
Bank 3 (8 cm)	Li_2O[b]
Bank 4 (46.5 cm)	X

Case:	1	2	3	4	5
Material in Bank 4:	Li_2O[b]	C[c]	SiO_2[d]	Shield[e]	C/Shield[f]
Tritium Breeding					
T_b BR	1.410	1.250	1.242	1.209	1.243
T_f BR	0.146	0.108	0.107	1.106	0.107
Total BR	1.556	1.358	1.349	1.315	1.350

[a]Based on one-dimensional model; T_f is not corrected.

[b]90% Li_2O + 5% SS + 5% H_2O.

[c]90% C + 5% SS + 5% H_2O.

[d]90% SiO_2 + 5% SS + 5% H_2O.

[e]90% SS + 10% H_2O.

[f]12 cm C[c] + 34.5 cm shield.[e]

(2) graphite, (3) silicon dioxide, (4) stainless steel, and (5) a combination of graphite and stainless steel) in this deep blanket region. The result of Table 6-11 along with the result of Fig. 6-8 which displays the accumulation of bred tritium, indicates that the required breeding blanket thickness can be substantially reduced by making use of any of these material compositions. For example, the system of Case 5, which has a graphite reflector followed directly by a Type 316 stainless steel base shield, can yield a BR of about 1.35 with a breeder zone thickness of only 120 mm. Assuming a full breeding blanket coverage and a first-wall surface of ~400 m^2, this system has a breeder (Li_2O) inventory of ~60 MT and a pure lithium (30% ^6Li-enriched) inventory of ~18 MT. These figures are compared to the α-$LiAlO_2$ inventory of ~605 MT and the lithium (60% ^6Li-enriched) inventory of ~64 MT in the STARFIRE design which yields a net BR of 1.04 (one-dimensional BR of 1.21). The surface area of the first wall in STARFIRE is about a factor of two larger than that in the DEMO; therefore, the difference in the blanket concept alone results in more than 40% reduction in the lithium inventory.

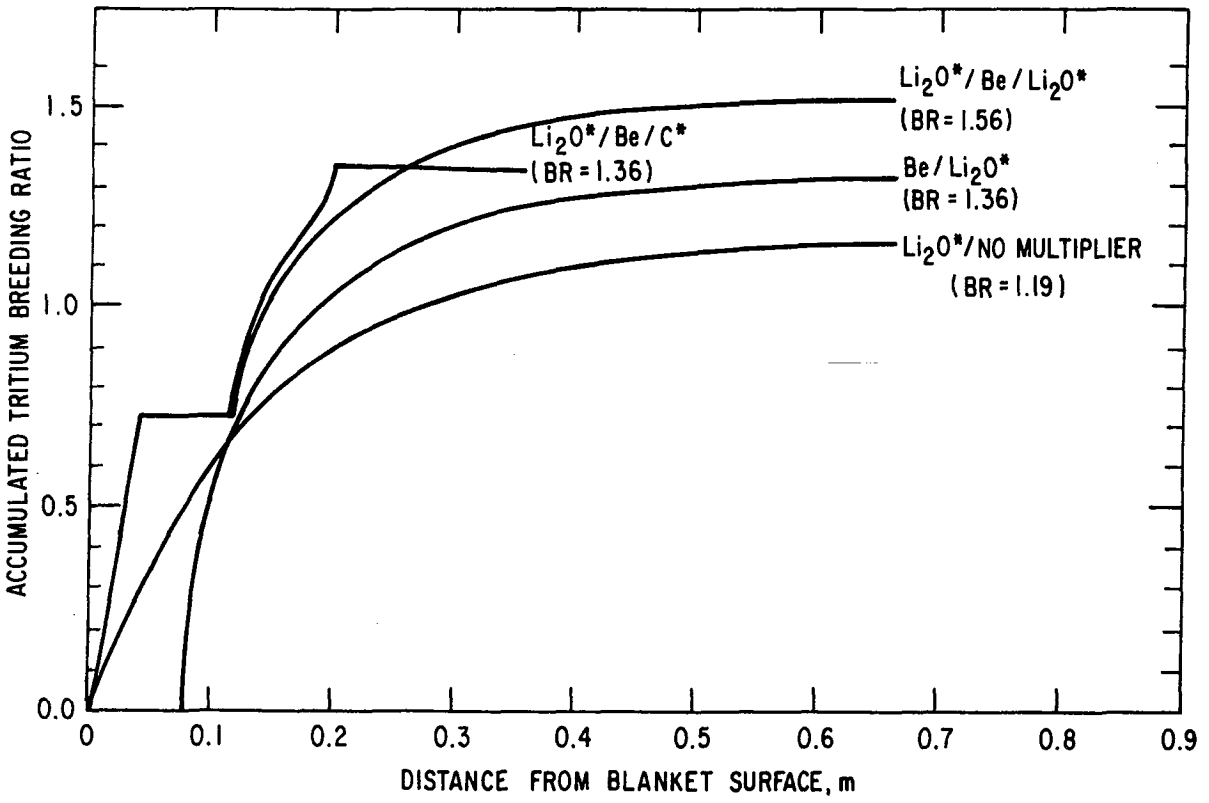

Figure 6-8. Accumulation of tritium breeding ratio in Li_2O blanket designs:

Li_2O*: 90% Li_2O + 5% SS + 5% H_2O
C*: 90% C + 5% SS + 5% H_2O
Li_2O: 70% of theoretical density; 30% ^6Li enrichment
Be: 100% of theoretical density.

One of the concerns associated with the use of a beryllium multiplier is the possibility of tritium production in beryllium because the threshold energy for the Be(n,t) reaction is 11.6 MeV and the cross section amounts to about 20 mb around the source neutron energy. The relatively long half-life (~12.3 y) of tritium leads to a continual increase of tritium inventory in the multiplier region without saturation, over the entire lifetime of the DEMO plant. For example, at an integral wall load of 10 MW-y/m^2 after reactor startup, the tritium inventories become ~1.6 kg, ~2.5 kg, and ~3.1 kg for total beryllium thicknesses of 40 mm, 80 mm, and 120 mm, respectively, in a System A blanket design described in Table 6-10. The estimate is based on a total fusion power of 900 MWt. These inventories are on the same order of magnitude as the anticipated steady-state tritium inventory in the Li_2O blanket. Provisions for removal of the tritium from the beryllium region are, therefore, warranted in such a design. Another concern with the use of

beryllium, and neutron multipliers in general, is the substantial increase in the heating rates and lithium burnup in the Li_2O regions adjacent to the multiplier.

Use of lead as a neutron multiplier was also considered during the course of the present study. However, the low melting point (327°C) of lead is of particular concern with its use in the high nuclear radiation environment. Based on a recent INTOR study[45] the maximum temperature rise in a 50-mm thick lead multiplier, for instance, is estimated to be about 190°C relative to the inlet coolant temperature for a given steel/lead gap conductance. Note that the neutron wall load and the inlet coolant temperature of the INTOR design are 1.3 MW/m^2 and 100°C, respectively, compared to ~2.1 MW/m^2 and 260°C of the DEMO design. As a result the allowable lead thickness for DEMO is expected to be appreciably smaller than 50 mm unless a molten multiplier is assumed. From the neutronics standpoint, use of such a thin multiplier provides little incentive for enhancement of tritium breeding because the possible increase in BR by a lead multiplier is estimated to be only ~0.04 for every 10 mm of lead.

6.3.4 $LiAlO_2$ Breeder Blanket Design

Two blanket design concepts based on use of solid breeders are believed to be most promising for the application to fusion reactors. One of them is a binary ceramic, Li_2O. The other group of solid breeders is a ternary ceramic represented by $LiAlO_2$, Li_2SiO_3, Li_2TiO_3, etc. In-depth breeding analyses have been performed for the $LiAlO_2$ ceramic in the UWMAK-II and STARFIRE design studies. The comprehensive work perfomed for the meta- and ortho-silicate breeders in a recent INTOR study also covers the general aspect of the breeding characteristics of ternary breeder materials.

This section presents the analysis of an alpha-phase $LiAlO_2$ blanket in the context of the DEMO blanket design. The primary objective is to identify the breeding characteristics of $LiAlO_2$ and thereby provide a comparison with the reference Li_2O blanket design.

Table 6-12 summarizes the BR's for several $LiAlO_2$ blankets. The analysis is based on the three-dimensional model previously used for the Li_2O systems. The MORSE code has been used for the computations with 20,000 neutron histories for each case. The BR's shown include the T_7 correction although the

Table 6-12. Effect of Multiplier Selection Upon Tritium Production in $LiAlO_2$ Blanket Design[a]

Case	Tritium Breeding Ratio[b]
A. No multiplier[c] Full breeding	0.883 (±0.1%)[d]
B. With Zr_5Pb_3[e] Full breeding	1.084 (±0.3%)
C. With Zr_5Pb_3[e] No Sector 1 breeding	0.978 (±0.4%)
D. With beryllium[e] No Sector 1 breeding	1.062 (±0.7%)
E. With Pb[e] No Sector 1 breeding	1.055 (±0.4%)

[a]Armor: 10 mm Type 316 stainless steel (SS)

First wall: 10 mm (65 vol % SS + 35 vol % H_2O).

Blanket: 680 mm (90 vol % $LiAlO_2$ + 5 vol % H_2O). (Note: $LiAlO_2$ is 70% of the theoretical density.)

Shield: 300 mm (90 vol-% Fe14Mn2Ni2Cr + 10 vol-% H_2O)

[b]Includes the T_7 correction; 60% ^6Li enrichment in $LiAlO_2$.

[c]Does not include limiter opening.

[d]Standard deviation.

[e]Includes limiter opening; multiplier thickness is 8 cm.

total BR's are contributed mostly by the $^6Li(n,n'\alpha)t$ reaction. Case A is a full breeding blanket design which does not have limiter nor multiplier. The net BR of 0.883 indicates that the $LiAlO_2$ breeder (and potentially ternary ceramic breeders in general) is not a viable candidate for the fusion reactor application unless the breeding is assisted by use of a neutron multiplier. The full breeding potential of BR = 0.883 in $LiAlO_2$ is approximately three-quarters of the BR = 1.189 in the reference Li_2O blanket without multiplier.

Case B of Table 6-12 replaces the first 8-cm zone of the Case A blanket by a 100% dense Zr_5Pb_3 multiplier as in the STARFIRE design. The resultant net BR is 1.084. The breeding margin is, however, not large enough to compensate for

possible breeding losses due to the limiter and nonbreeding sector implementation. Case C of Table 6-12, which corresponds to such a Zr_5Pb_3 multiplier blanket design indicates a net BR of only 0.998. The breeding performance can be substantially improved when the Zr_5Pb_3 multiplier is replaced by either beryllium (Case D) or lead (Case E) of the same thickness. The relative breeding enhancement by use of such a multiplier can amount to ~0.08 in the net BR. However, as discussed with the reference Li_2O blanket design, the breeding margin shown in Cases D and E might not be sufficient for assuring $T_0 \gtrsim 1.05$.

The two breeder/multiplier designs, System A and System B, that were studied earlier for the Li_2O breeder (see Table 6-10) were analyzed again, for α-$LiAlO_2$ this time, using the one-dimensional model. Figure 6-9 shows the impact of these material layouts on the tritium production using a beryllium neutron multiplier. As before, one notices quite different breeding characteristics between the two system configurations. The breeding amplification by the sandwich-type configuration (System A) is substantiated particularly for multiplier thicknesses greater than ~50 mm. In consequence, the multiplier may require to be internally cooled in order for blanket designs based on this system configuration to yield a much better tritium production rate than those based on the System B configuration.

Figure 6-10 examines the breeding enhancement for internally cooled multiplier designs based on the System A configuration. Three multipliers, beryllium, lead, and Zr_5Pb_3, are examined using the same one-dimensional model. In all cases, the multiplier region is represented by a homogeneous mixture (90% multiplier + 5% 316 SS structure + 5% H_2O coolant) and the T_7 correction is included. Figure 6-10 indicates several important results. The internally cooled multiplier designs significantly degrade the breeding peformance in comparison with the externally cooled designs. Evidently this reflects the reduced neutron amplification in the multipliers due to the presence of the water coolant and Type 316 stainless steel structure and the increased parasitic neutron absorption in the Type 316 stainless steel stucture. The breeding degradation is most significant in the beryllium system with a thick multiplier. For instance the breeding loss due to the internal coolant in the beryllium multiplier amounts to ~0.08 for a multiplier zone thickness of 8 cm; the loss is further increased to ~0.19 for 12 cm. Fortunately, however, the STARFIRE study indicates a possibility that a quite thick beryllium multiplier

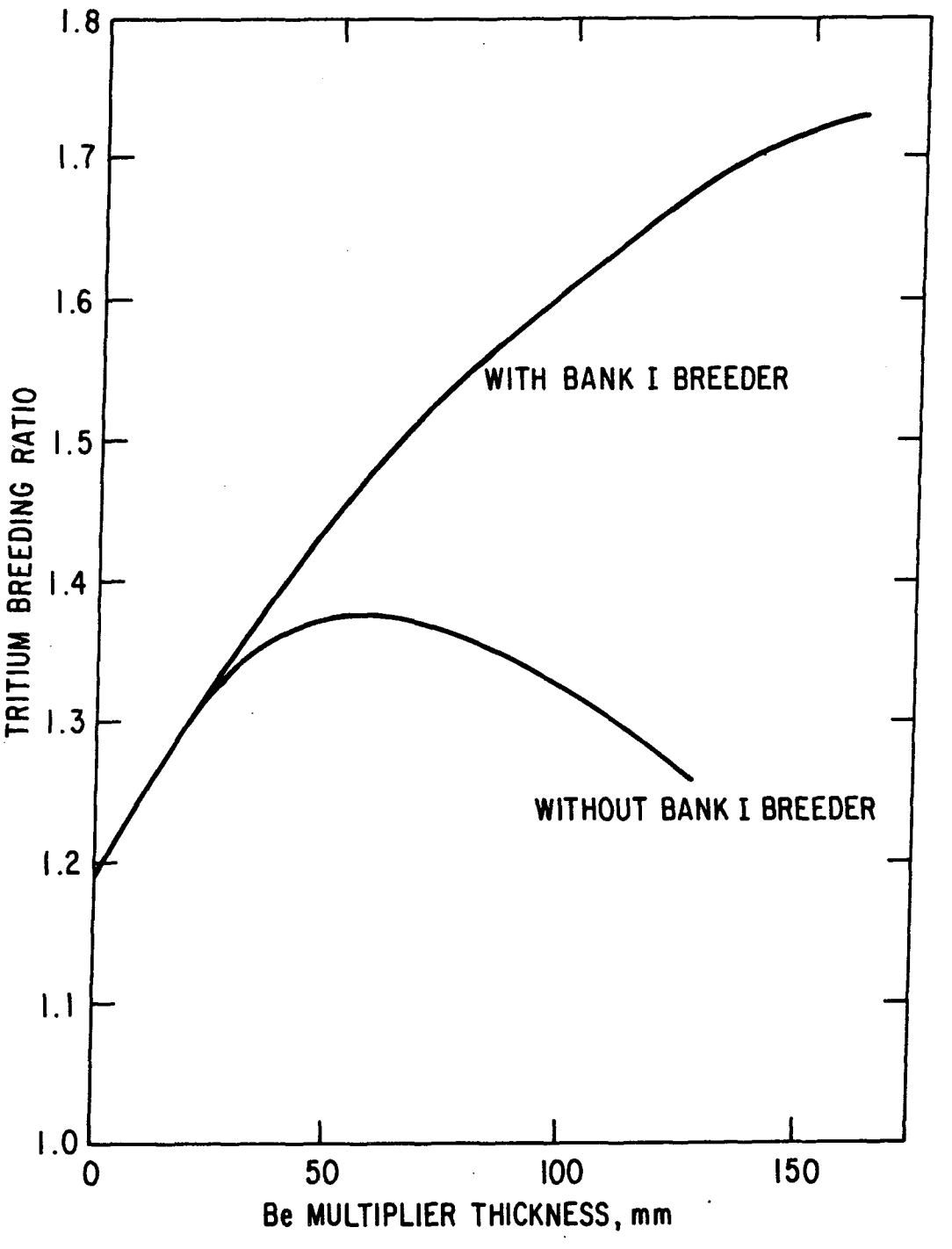

Figure 6-9. Effect of first-bank material selection upon tritium breeding for beryllium multiplier/α-$LiAlO_2$ breeder blanket designs.

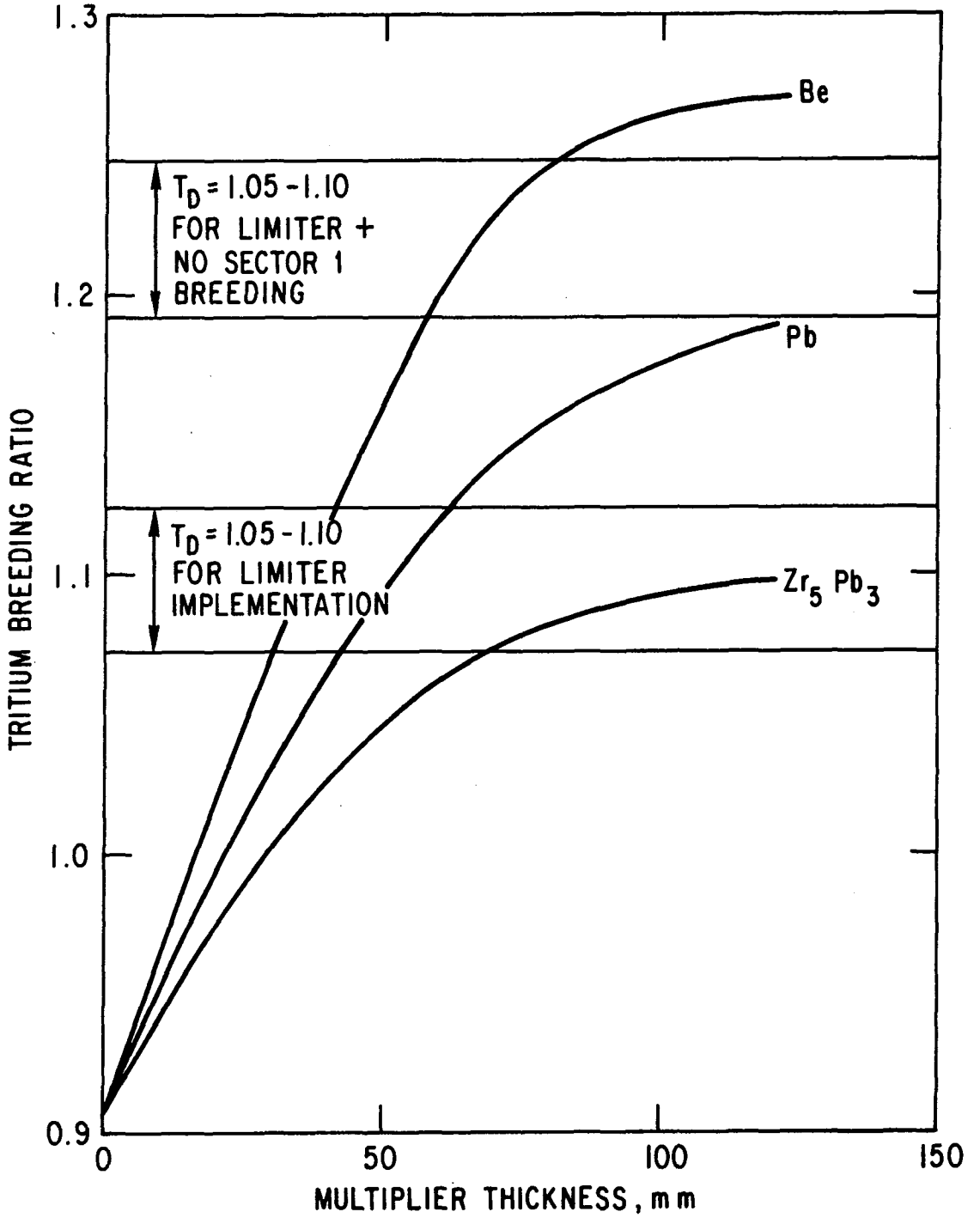

Figure 6-10. Comparison of neutron multipliers on tritium breeding for beryllium α-$LiAlO_2$ breeder blanket designs.

can be designed without use of an internal coolant in virtue of the high heat capacity and thermal conductance of beryllium. This possibility remains to be examined in the context of the DEMO design.

The beryllium system has the highest breeding potential among those examined. For example, at a multiplier zone thickness of 8 cm the relative difference in BR results in ~0.09 between beryllium and lead, and ~0.17 between beryllium and Zr_5Pb_3. These differences lead to substantially different design constraints as to the implementation of nonbreeding blanket regions. Based on the three-dimensional results shown in Table 6-12 along with the full breeding ratio (without the limiter) of 1.110 (based on an ANISN calculation) with an 8-cm thick Zr_5Pb_3 multiplier, the breeding losses due to (1) the limiter implementation; and (2) the implementation of limiter and nonbreeding Sector 1 blanket are estimated to be ~2.2% and ~11.9%, respectively. When the net BR requirement ranges from T_D = 1.05 to T_D = 1.10 as discussed in Section 6.3.1, one needs to have full BR's of 1.07-1.2 and 1.19-1.25 for the respective cases described above. These breeding requirement bands are shown in Fig. 6-10. It is found that the $LiAlO_2$ blanket has the least viability for its fusion reactor application if the Zr_5Pb_3 multiplier is used. In particular, considering a variety of small penetrations such as those for plasma diagnostics, clearances between blanket modules, etc., which were not incorporated in the present analysis, the $LiAlO_2/Zr_5Pb_3$ blanket design appears incapable of satisfying the breeding requirement. The $LiAlO_2$/Pb system does not seem to pose any serious breeding difficulty upon the limiter implementation. It is expected, however, that this system can be considered viable only when the entire, or at least a part of the inboard blanket (Sector 1 blanket) is utilized for the tritium production. The $LiAlO_2$/Be blanket design has the least impact on the design constraints in terms of the self-sufficient fuel production. Approximately 8 cm of the multiplier thickness will suffice the breeding criterion to incorporate the limiter as well as the nonbreeding Sector 1 blanket. If the Sector 1 blanket is fully utilized for breeding this system requires a multiplier zone thickness of only ~4 cm for T_D = 1.10 and ~3 cm for T_D = 1.05.

The observations made above strongly suggest that if $LiAlO_2$ (or ternary ceramics, in general) is a favorable choice as the fusion breeder material, the co-use of a beryllium multiplier will certainly be the most promising and viable design option to be selected.

6.3.5 17Li-83Pb Breeder Blanket Designs

Liquid 17Li-83Pb is one of the most attractive tritium breeding materials in that a substantial neutron multipliation can take place in the breeder itself through the Pb(n,2n) and Pb(n,3n) reactions. The resultant neutron spectrum is generally quite soft, implying great potential for tritium production by the $^{6}Li(n,\alpha)t$ reaction. The atomic number density of lithium in 17Li-83Pb is, however, only $\sim 5.6 \times 10^{21}$ atoms/cc (at density of 9.4 g/cc) compared to 8.1×10^{22} atoms/cc in Li_2O for instance. As a result the content of ^{6}Li or the enrichment of ^{6}Li in 17Li-83Pb plays the most important role in the tritium-breeding performance in 17Li-83Pb blanket designs. Figure 6-11 shows the variation of tritium BR with ^{6}Li enrichment in the 17Li-83Pb breeder for two possible armor designs: (1) 10 mm Fe9Cr1Mo ferritic steel (FS) armor; and (2) 10-mm thick beryllium armor. Also shown in the figure is the case with bare first wall at 90% ^{6}Li enrichment, to indicate the effect of armor erosion during reactor operation. The one-dimensional neutronics model was used for this analysis. The armor region is cooled by the 17Li-83Pb breeder itself from the first wall side. The blanket region immediately following the armor/first-wall region is neutronically represented by a homogeneous mixture, 85% 17Li-83Pb + 5% coolant + 10% Fe9Cr1Mo considering a bottle-type liquid breeder blanket design.[5] Although the result shown here does not include the T_7 correction mentioned earlier, the T_7 contribution is negligible due to the very soft neutron spectrum.

Based on the result of Fig. 6-11, one finds a very strong incentive for ^{6}Li enrichment in 17Li-83Pb. The increase in BR from the natural lithium to 90% ^{6}Li enrichment amounts to more than 0.5, compared to the Li_2O case shown in Fig. 6-5 where the BR monotonically decreases with ^{6}Li enrichment. As the neutron spectrum in 17Li-83Pb is intrinsically soft, the increase in BR with ^{6}Li enrichment comes solely from the increase in the $^{6}Li(n,\alpha)t$ reaction. In fact, the isotopic BR's for the Fe9Cr1Mo armor system with 90% ^{6}Li enrichment, for example, are 1.450 [$^{6}Li(n,\alpha)t$] and 0.002 [$^{7}Li(n,n'\alpha)t$] indicating that more than 99% of the total tritium production is made by the soft neutron reaction of $^{6}Li(n,\alpha)t$. Such an extremely unbalanced tritium production by ^{6}Li may yield a high lithium burnup rate in 17Li-83Pb. However, it has turned out that in the case of 90% ^{6}Li enrichment in the ferritic steel armor design, the

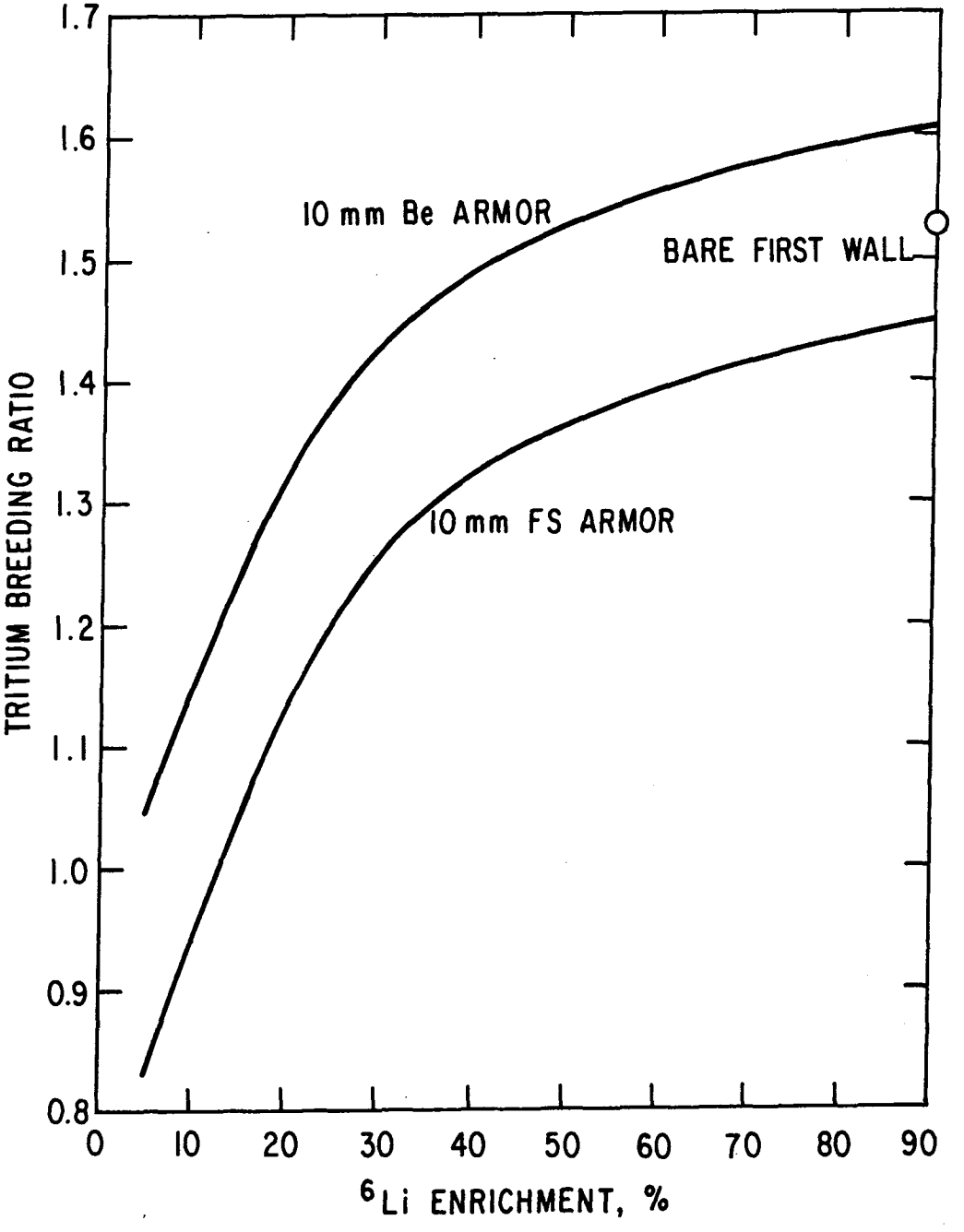

Figure 6-11. Effect of ^{6}Li enrichment upon tritium breeding for 17Li-83Pb breeder blanket designs.

average ^{6}Li burnup in the 17Li-83Pb blanket is ~1.32 × 10^{-5} (atom/cc)/DT-burn, which results in only ~10% of ^{6}Li burnup over an integral wall load of 18 MW-y/m^2, for instance.

Vanadium-base alloys are very attractive structural materials for application to liquid breeder blanket designs because of its corrosion resistance

to the breeder. In addition, as shown in an in-depth study carried out for a blanket/shield design[46] in which a vanadium-base alloy is employed along with a liquid lithium, blanket designs based on vanadium alloy structure have substantial potential for minimization of long-term activation induced in fusion reactors. The major concerns regarding the use of vanadium alloys are the lack of information on fabricability, particularly welding, and the effects of atmospheric environment during fabrication and operation.[5] A second-generation research alloy, V15Cr5Ti, is expected to alleviate the swelling and fabrication problems.

Table 6-13 shows the tritium breeding performance of a V15Cr5Ti/17Li-83Pb blanket design along with a comparison with the case in which the V15Cr5Ti structural material is replaced by ferritic steel. Again, the two cases of armor design, structural material itself and beryllium, are considered. The analysis is based on the one-dimensional model. It is found that the V15Cr5Ti structure systems can yield consistently higher BR's than the corresponding ferritic steel structure systems. This results from the less parasitic

Table 6-13. Effect of Structural Material Selection Upon Tritium Breeding for 17Li-83Pb Breeder Blanket Designs[a]

Structural Material:	Total Tritium Breeding Ratio[b]			
	Fe9Cr1Mo		V15Cr5Ti	
Armor: / Lithium Enrichment of 17Li-83Pb	Fe9Cr1Mo	Be	V15Cr5Ti	Be
A. Natural lithium	0.881	1.093	1.064	1.227
B. 50% ^{6}Li enrichment	1.364	1.529	1.473	1.604
C. 90% ^{6}Li enrichment	1.452	1.611	1.551	1.671

[a]Armor: 10 mm thick, 100% of theoretical density.

First wall: 3.4 mm structure
3.0 mm 17Li-83Pb
4.5 mm structure

Blanket: 664 mm (90% 17Li-83Pb + 10% structure)
15.0 mm structure

[b]Based on one-dimensional model; no correction for T_7.

absorption and the greater probability for the (n,2n) reaction with the V15Cr5Ti alloy. The difference becomes greater with lower ^{6}Li enrichment.

So far the coolant has been assumed to be the 17Li-83Pb breeder itself. There are several other candidate coolant materials that are considered for use with the liquid breeder material. They include sodium, light water, and helium. Table 6-14 lists the tritium BR's for the 17Li-83Pb breeder blanket designs using these coolants for three different ^{6}Li enrichment cases, 7.5% (natural lithium), 50%, and 90%. In all the cases examined the increase in

Table 6-14. Effect of Coolant Selection and ^{6}Li Enrichment Upon Tritium Breeding for 17Li-83Pb Breeder Blanket Designs[a]

	Tritium Breeding Ratio[b]			
	Coolant			
	Helium	H_2O	Sodium	17Li-83Pb
A. Natural Lithium				
T_6	0.822	1.231	0.834	0.862
T_7	0.018	0.017	0.018	0.019
Total BR	0.840	1.248	0.852	0.881
B. 50% ^{6}Li Enrichment				
T_6	1.322	1.410	1.316	1.354
T_7	0.010	0.009	0.010	0.010
Total BR	1.332	1.419	1.326	1.364
C. 90% ^{6}Li Enrichment				
T_6	1.425	1.448	1.417	1.450
T_7	0.002	0.002	0.002	0.002
Total BR	1.427	1.450	1.419	1.452

[a]Armor: 10.0 mm FS (Fe9Cr1Mo ferritic steel)

First wall: 3.4 mm FS
3.0 mm coolant
4.5 mm ferritic steel

Blanket: 664 mm (85% 17Li-83Pb + 10% FS + 5% coolant)
15.0 mm ferritic steel.

[b]Based on one-dimensional model.
No correction for T_7.

^{6}Li enrichment always results in a substantial improvement of the breeding performance. It is noticed that the presence of a small amount of light water (only 5% in the present case) affects the breeding to a very appreciable degree. Obviously, the breeding improvement is offered by the neutron energy moderation due to neutron collisions with the water coolant leading to a significant enhancement in the ^{6}Li(n,α) reaction. This is, in fact, the reason that the breeding enhancement is notable, particularly with the natural lithium case, as the atomic number density of ^{6}Li in 17Li-83Pb is quite low. As ^{6}Li is highly enriched, the choice of coolant becomes less important in terms of tritium production. For instance, the difference in BR among the four candidate coolants studied reduces to only ~2% in the case of 90% ^{6}Li enrichment. The selection of coolant, therefore, can be made for such a high enrichment system, based on design considerations other than the neutronics performance. In consequence, a great degree of design flexibility can be afforded to the relevant technical areas such as thermal-hydraulics and mechanical designs.

It should also be noted that the BR's for high ^{6}Li enrichment shown in Table 6-14 are much greater than those for Li_2O blanket designs without neutron multipliers. As the volumetric lithium content in 17Li-83Pb is more than a factor of 10 lower than that in Li_2O, there is a possibility of a drastic reduction in the required lithium inventory in 17Li-83Pb blanket designs. Even compared to the Li_2O blanket design with the beryllium multiplier presented in Section. 6.3.3.2, 17Li-83Pb blanket designs are expected to result in a much smaller lithium inventory. Based on a breeding accumulation analysis performed for the 17Li-83Pb breeder/coolant design, a BR of 1.35 for the 100% breeding coverage requires a blanket thickness of ~0.5 m. This blanket contains ~1600 MT of 17Li-83Pb and ~9 MT of pure lithium (at 90% ^{6}Li enrichment). These figures are compared to the respective inventories of ~60 MT and ~18 MT for the Li_2O blanket design with the 80-mm thick beryllium multiplier, indicating a factor of two reduction in the lithium inventory in the 17Li-83Pb blanket. As will be shown later (Fig. 6-13), use of 17Li-83Pb breeder/H_2O coolant further reduces the lithium inventory.

In order to identify the global impact of nonbreeding inboard blanket designs prior to more detailed three-dimensional analyses, three different inboard systems were studied with an approximate one-dimensional model. The resultant BR's are summarized in Table 6-15. The one-dimensional model used

Table 6-15. Effect of Inboard Tritium Breeding for 17Li-83Pb Breeder Blanket Designs[a] by a One-Dimensional Model

	Case A	Case B	Case C
1. Inboard First Wall			
Coolant	17Li-83Pb	17Li-83Pb	H_2O
2. Inboard Blanket			
Coolant	17Li-83Pb (5%)	17Li-83Pb (5%)	H_2O (5%)
Breeder	17Li-83Pb (85%)	----	----
Structure	FS (10%)	FS (95%)	FS (95%)
3. Tritium Breeding			
T_6	1.431	1.116	0.879
T_7	0.002	0.001	0.001
Total BR	1.433 (1.452)[b]	1.117	0.880
Inboard BR	0.467	0.094	----
Outboard BR	0.967	1.023	0.880

[a]Based on one-dimensional model; no T_7 correction.

Armor: 10 mm FS (Fe9Cr1Mo ferritic steel)

First wall: 3.4 mm ferritic steel
3.0 mm coolant
4.5 mm ferritic steel

Outer blanket: 664 mm (90% 17Li-83Pb + 10% ferritic steel)
15.0 mm ferritic steel

17Li-83Pb: 90% ^6Li enrichment

[b]One-dimensional infinite-cylinder calculation without toroidal system curvature.

is an infinite cylinder in which the toroidal axis of the reactor is taken as the cylinder axis, and the inboard and outboard subregions as well as the central plasma region are represented by concentric annuli about the axis. The plasma major and minor radii are assumed to be 5.2 m and 1.3 m, respectively, and the plasma scrape-off region size is taken to be 0.165 m on both sides of the plasma region. The three systems studied are: (A) full inboard plus outboard tritium breeding; (B) outboard breeding along with 17Li-83Pb coolant flow in the nonbreeding inboard blanket; and (C) outboard breeding only along with H_2O coolant flow in the nonbreeding inboard blanket. The coolant for the outboard breeding blanket is always assumed to be 17Li-83Pb. The results

in Table 6-15 indicate that: (1) it is impossible to obtain a BR greater than unity with the complete elimination (all the way from the bottom to the top) of the inboard breeding (Case C); (2) the use of 17Li-83Pb as an inboard coolant substantially increases the outboard breeding (Case B); and (3) the case of full breeding coverage yields a net BR of 1.4 (Case A). An INTOR neutronics analysis[50] which was done by the three-dimensional Monte Carlo method for a similar 17Li-83Pb blanket design shows BR's of 1.396 and 0.925 for the full-breeding blanket coverage and the outboard breeding only, respectively. This result leads to the same conclusion as (1) above as to the impact of the complete elimination of inboard tritium breeding. The system of Case B in Table 6-15, which is in fact a semi-nonbreeding inboard blanket design, can yield a net BR greater than unity. However, there seem to be several questions posed in this type of blanket design. One question is whether the BR in excess of unity is sufficient for implementation of outboard penetrations such as limiter (or divertor) and REB ducts. Another question is whether the pumping power requirement for the 17Li-83Pb coolant flow inside the inboard blanket, where the magnetic field is high, is tolerable from the practical design standpoint.

It is noticed in Table 6-15 that the difference in the inboard blanket design strongly affects the outboard breeding performance. For example, the outboard breeding in Case A, which amounts to ~67% of the total breeding reduces to ~61% when the inboard blanket is replaced by the nonbreeding blanket as in Case C. Table 6-16 compares the neutron balance of Cases A and C. It is observed that the significant decrease in the outboard BR of Case C is driven by two factors. First, the neutron current into the inboard region is increased in Case C compared to Case A because of the larger gradient in the neutron distribution caused by the one-sided neutron amplification through the Pb(n,2n) reaction in the outboard blanket. Secondly, neutrons reflected from the inboard region to the outboard region are substantially degraded in energy after they have experienced collisions, particularly with the water coolant in the inboard region. As a result, these reflected neutrons have higher probabilities of parasitic capture by the outboard structure, preferably by the outboard armor.

A more rigorous multidimensional analysis of 17Li-83Pb breeder blanket designs has been performed in the context of the DEMO configuration

Table 6-16. Neutron Balance 17Li-83Pb Breeder Blanket Designs[a] Using a One-Dimensional Model[b]

	With Inboard Breeding (Case A)	Without Inboard Breeding (Case B)
A. Inboard		
Net current to armor/DT	0.3550	0.3990
Neutron gain/DT	0.1808	0.0403
Neutron loss/DT	0.0692	0.4393
Tritium breeding ratio	0.4666	0.0000
B. Outboard		
Net curent to armor/DT	0.6450	0.6010
Neutron gain/DT	0.4676	0.4671
Neutron loss/DT	0.0963	0.1439
Tritium breeding ratio	0.9666	0.8805
Leakage to blanket jacket/DT	0.0497	0.0439

[a]Based on one-dimensional model; no correction for T_7.

Armor: 10 mm ferritic steel

First wall: 3.4 mm ferritic steel
3.0 mm 17Li-83Pb
4.5 mm ferritic steel

Blanket: 664 mm (90% 17Li-83Pb + 10% ferritic steel)

Blanket jacket: 15 mm ferritic steel.

[b]In the case without the inboard breeding, the inboard first-wall coolant is H_2O and the inboard blanket is represented as follows:

Blanket: 664 mm (95% FS + 5% H_2O).

[b]The rest of the system is the same as the case with the inboard breeding. In all cases 17Li-83Pb contains 90% enriched ^6Li.

illustrated in Fig. 6-4. The purpose of the analysis is to identify the breeding sensitivity to the local perturbation such as implementation of the limiter and/or nonbreeding blanket sector(s). Table 6-17 lists the BR's for several 17Li-83Pb blanket designs studied. The three-dimensional model used for the analysis is the same as that previously used for the $Li_2O/LiAlO_2$ systems. The MORSE Monte Carlo runs were carried out with 20,000 neutron histories for each case. The blanket composition is neutronically assumed to be a homogenous mixture of 85 vol % 17Li-83Pb + 10 vol % Fe9Cr1Mo + 5 vol % H_2O, implying a separate coolant concept. The 17Li-83Pb breeder is enriched to 90% of ^6Li.

Table 6-17. Tritium Breeding Performance in 17Li-83Pb Blanket Designs[a]

Case:	A	B	C	D	E
Method:	1-D ANISN	3-D MORSE	3-D MORSE	3-D MORSE	3-D MORSE
System: / TBR	Full Breeding	Full Breeding	With Limiter	With Limiter No Inboard (Sector 1) Breeding	With Limiter No Inboard (Sectors 1 & 2) Breeding
Sector 1		0.127 (2%)[b]	0.125 (2%)	-----	----
2		0.260 (2%)	0.255 (2%)	0.253 (2%)	----
3		0.267 (1%)	0.260 (1%)	0.253 (2%)	0.248 (2%)
4		0.475 (1%)	0.456 (1%)	0.453 (1%)	0.453 (1%)
5		0.354 (2%)	0.308 (1%)	0.301 (2%)	0.300 (2%)
Total T_6	1.460	1.481 (0.3%)	1.403 (0.3%)	1.258 (0.5%)	1.001 (0.6%)
Total T_7	0.002	0.002 (1.0%)	0.002 (1.0%)	0.002 (1.0%)	0.001 (1.0%)
Total (T_6 + T_7)	1.462	1.483 (0.3%)	1.405 (0.3%)	1.259 (0.5%)	1.002 (0.6%)
Total (T_6 + T_7) with -15% T_7 correction	1.462	1.483	1.405	1.259	1.002

[a]Armor: 10 mm Fe9Cr1Mo ferritic steel (FS).
First wall: 10 mm (65 vol % FS + 35 vol % H_2O).
Blanket: 680 mm (85 vol % 17Li-83Pb + 10 vol % FS + 5 vol % H_2O).
(Note: 17Li-83Pb contains 90% enriched ^6Li.
Shield: 300 mm (90 vol % Fe14Mn2Cr2Ni + 10 vol % H_2O).

[b]Standard deviation; read as ±2%.

As shown in Case B of Table 6-17, the full breeding blanket can yield a BR of 1.483, compared to 1.462 obtained by the one-dimensional ANISN calculation (Case A). Case C of Table 6-17 represents a 17Li-83Pb blanket design in which the outermost blanket (Sector 5) is penetrated through by the limiter system. By comparing Case C to Case B, one finds that the presence of the limiter opening results in a breeding loss of ~5.5% in BR. This breeding loss is slightly higher than what is expected from the corresponding Li_2O case shown earlier, or from the fraction of the limiter opening area at the armor surface. A conceivable reason is that due to the limiter penetration, not only a part of tritium production, but also a portion of neutron multiplication by lead in 17Li-83Pb are lost. This tendency is further enhanced as a larger fraction of blanket surface is removed from tritium production as presented by Case D and Case E of Table 6-17. The Case D blanket which incorporates the limiter as well as the nonbreeding inboard (Sector 1 only) blanket can still yield an excellent net BR of 1.259.

Such a great degree of breeding margin has important design implications. The breeding ratio in excess of $T_D = 1.05 \sim 1.10$ can possibly be utilized in two ways: (1) expanding the nonbreeding inboard region; or (2) reducing the overall breeding blanket thickness. Case E of Table 6-17, however, shows that the complete elimination of tritium production from Sector 1 and Sector 2 blankets results in a BR of only 1.002. The result is more or less consistent with the earlier observation based on the one-dimensional analysis (Table 6-15) as to the effect of nonbreeding inboard blanket design. It appears more attractive, therefore, to utilize the breeding margin in Case D for reducing the thickness of blanket Sectors 2 through 5. Figure 6-12 illustrates the tritium accumulation as a function of full-breeding blanket depth, based on the one-dimensional analysis. When this curve is extrapolated to the three-dimensional configuration under consideration, the Case D blanket of Table 6-17 requires minimum blanket thicknesses of only 30 cm and 34 cm in order to realize net BR's of 1.05 and 1.10, respectively.

The effect of structural material content on tritium BR has been examined using the one-dimensional model. The result is presented in Fig. 6-13 for two coolant systems, viz., self-cooled blanket and H_2O-cooled blanket. In both cases the coolant volume is fixed at 5% of the blanket volume. There appears to be an appreciable difference in BR between the two coolant systems, in

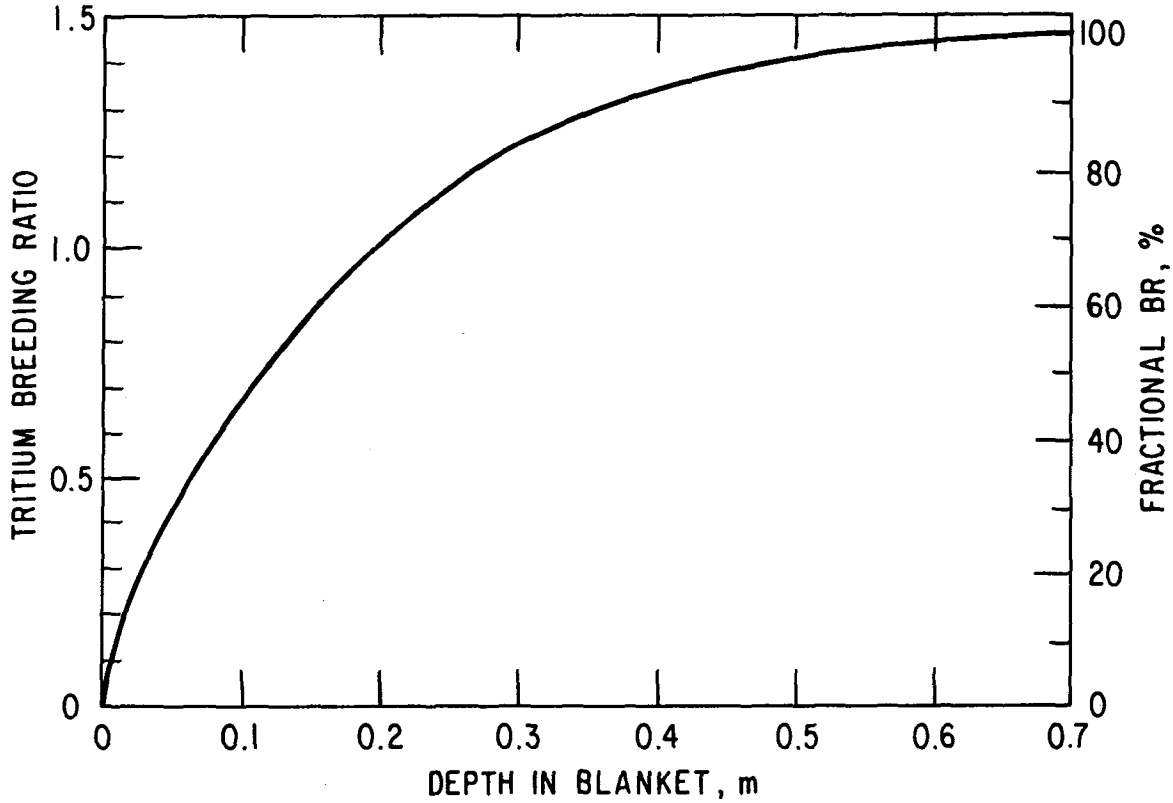

Figure 6-12. Accumulation of tritium breeding ratio in a 17Li-83Pb breeder blanket.

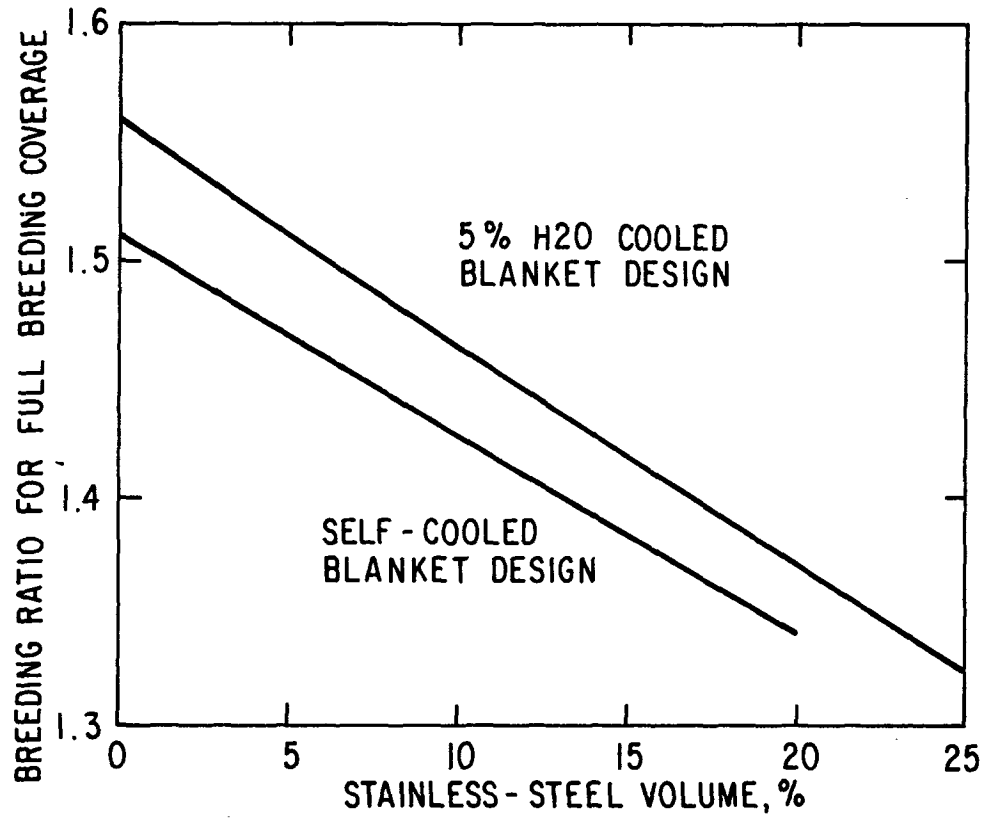

Figure 6-13. Effect of volumetric contents of ferritic stainless steel in 17Li-83Pb tritium breeding blanket designs.

particular for small structure contents. This reflects the strong neutron energy moderation by the water coolant, leading to a substantial increase in the $^{6}Li(n,\alpha)t$ reaction rates. In comparison with Fig. 6-8 for Li_2O, one notices that the 17Li-83Pb systems can incorporate a much larger space allowance for nonbreeding blanket and/or penetration openings. For example, to use up all extra tritium production (in excess of BR = 1.10 for instance) for the H_2O-cooled systems, one can have nonbreeding blanket fractions of ~27% and ~22% for ferritic steel contents of 5% and 15%, respectively. In the case of self-cooled systems, the corresponding nonbreeding blanket fractions come to ~25% and ~20%. These fractions seems to be large enough to implement even a divertor system for the plasma impurity control, which may take up ~20-25% of the blanket volume, as seen in a recent INTOR[45] design. The implication is that if a divertor system is preferred over a limiter system the liquid breeder designs such as the one studied in this section are certainly desirable design concepts.

6.3.6 Liquid Lithium Breeder Blanket Designs

Liquid lithium is one of the breeding materials that have been most extensively studied[2,4,5,51-53] for fusion reactor applications, particularly during earlier stages of fusion research. In general, lithium and the other alkali metals are excellent heat-transfer fluids.[5] They typically possess high heat capacities and thermal conductivities and produce high heat transfer coefficients. Considerable experience and technology related to liquid metals as heat transfer fluids have been developed in the Liquid Metal Fast Breeder Reactor Program. The primary incentive for use of lithium as a coolant in commercial fusion reactors is the fact that it is also a viable candidate for the tritium breeding medium.

Recently, however, somewhat less attention has been called to liquid lithium systems because of the perceived problems associated with the use of liquid lithium in the fusion environments. Major problems concerning the use of lithium breeder/coolant include: (1) reactivity of lithium with air and water, leading to possible lithium fire; (2) compatibility with structural material; and (3) MHD effects created by the strong magnetic field. Yet, liquid lithium appears one of the best breeding materials to use in fusion reactors from the neutronics standpoint. In addition, lower blanket tritium

inventories are expected to result from continuous processing of liquid lithium breeder/coolant as compared to solid breeder blankets.

This section presents a three-dimensional analysis of liquid lithium blanket designs. The primary objective is to neutronically compare these systems with blanket designs based on the primary candidate liquid breeder, 17Li-83Pb. The analysis was performed by the MORSE code for the geometrical configuration shown in Fig. 6-4, and the results are summarized in Table 6-18. Two blanket systems were studied: Case A, full breeding blanket without the limiter penetration; and Case B, no inboard breeding blanket (breeding in Sectors 2 through 5 only) with the limiter penetration. It is found that the liquid lithium can produce self-sufficient tritium for both blanket designs investigated. The breeding potential is, however, not as much as that of the 17Li-83Pb systems. The difference amounts to ~0.17 in Case A and 0.24 in Case B. The primary difference stems from the lack of the neutron multiplication, such as the (n,2n) and (n,3n) reactions in the lithium systems, as

Table 6-18. A Comparison of Tritium Breeding Performance[a] of Liquid Lithium and 17Li-83Pb Blanket Designs

		Lithium[b]	17Li-83Pb[c]
Case A.	Full Breeding		
	T_6	0.889 (±0.2%)[d]	1.481 (0.03%)
	T_7	0.358 (±0.7%)	0.002 (±1.0%)
	Total	1.247 (±0.3%)	1.483 (±0.3%)
Case B.	With Limiter + No Sector 1 Inboard Breeding		
	T_6	0.781 (±0.4%)	1.258 (±0.5%)
	T_7	0.307 (±0.8%)	0.002 (±1.0%)
	Total	1.088 (±0.3%)	1.259 (±0.5%)

[a] Li: Natural lithium
17Li-83Pb: 90% ^{6}Li enrichment
T_7 correction included.

[b] Armor: 10 mm Fe9Cr1Mo ferritic steel (FS).
First wall: 10 mm (65 vol % FS + 35 vol % Li).
Blanket: 680 mm (90 vol % Li + 10 vol % FS).
Shield: 300 mm (90 vol % Fe14Mn1Cr2Ni + 10% vol % H_2O).

[c] See Table 6-21.

[d] Standard deviation.

opposed to the 17Li-83Pb systems. In addition, the two breeder systems have quite different breeding characteristics. Normally liquid lithium systems are characterized by the much harder neutron spectrum than 17Li-83Pb systems. In fact, the result of Table 6.3-11 shows that the contribution of T_7 to the total BR amounts to almost 30% in the lithium blankets (even after the T_7 reduction) compared to the T_7 less than ~1% in the 17Li-83Pb systems. Every tritium production reaction by ^7Li releases one secondary neutron, substantially moderated in energy, that can be utilized for inducing the $^6Li(n,\alpha)t$ reaction. In consequence, the ^6Li enrichment (or ^7Li reduction) in liquid lithium systems generally does not increase, but instead decreases the BR because the loss in T_7 is larger than the gain in T_6. In fact, the tritium production in liquid lithium systems has been shown to be optimized at the natural lithium composition.[43]

It should be noted that the breeding evaluation presented here for liquid lithium systems remains to be further refined as more accurate lithium reaction cross-section data become available. The correction method used for the T_7 evaluation might result in an unduly underestimated BR for such a hard (or fast) neutron spectrum system.

6.4 Li_2O Breeder Blanket

6.4.1 Introduction and Summary

Lithium oxide is a candidate breeding material for fusion power reactors. The purpose of this portion of the DEMO reactor study was to develop a tritium breeding blanket concept that best utilizes the properties and characteristics of Li_2O as a breeding material. This effort involves numerous tradeoffs in the selection of materials and design features, and in the specification of the most appropriate or required operating conditions. The study included (1) a materials data base assessment (Sec. 6.4.3), (2) neutronics analyses to evaluate the breeding potential and determine nuclear heating profiles (Sec. 6.3), (3) development of a tritium recovery scenario (Sec. 6.4.4), and (4) thermal-hydraulics and stress analyses (Sections 6.4.5 and 6.4.6). Based on these analyses a reference blanket design (Sec. 6.2) was developed for a demonstration tokamak reactor. Reference reactor parameters used in this study were summarized in Table 2-2.

Pressurized water (260-300°C) was selected for the first-wall and blanket coolant. Since the range of operating temperatures required for acceptable Li_2O performance is very limited, the low system T characteristic of pressurized water systems appears necessary for a satisfactory design. The relatively low operating temperature is also advantageous for the stainless steel structural material, particularly with respect to the effects of radiation on the properties. Analyses indicate that pressurized water provides significant economic advantages over helium for tokamak reactor applications. The use of water coolant permits a smaller reactor size or a higher fusion power for a given size compared to helium coolant, provides for much lower pumping power losses, and results in lower cost of the heat transport system. An advanced austenitic stainless steel (designated PCA in the alloy development program) similar to Type 316 was selected as the structural material for the DEMO. Both the mechanical properties and radiation damage resistance are considered acceptable for reasonable lifetimes at the projected operating temperatures. Structure temperatures in a water-cooled system can be maintained below the temperatures at which severe displacement damage embrittlement and helium embrittlement occur. The resistance to radiation induced swelling is also greater than at higher

operating temperatures. Although data are limited for the projected operating conditions, chemical compatibility with the Li_2O is probably acceptable at the low operating temperatures. Steady-state reactor operation is important for acceptable wall lifetimes because of the relatively high thermal stress factor associated with stainless steel. The fact that solid breeder materials also have a limited lifetime because of Li burnup reduces the incentive for a very long lifetime structure. As discussed in Sec. 5.0, one of the most promising design options utilizes a beryllium cladding bonded to the structural wall to prevent excessive limiter erosion and plasma contamination.

Neutronics analyses were performed to evaluate (1) the impact of ^6Li enrichment on the tritium breeding performance, (2) the potential for a nonbreeding inboard blanket design, (3) the tritium-breeding enhancement provided by a neutron multiplier, and (4) the geometrical dependence of the nuclear heating and the decay heat for a reference first-wall/blanket configuration. The 1-D neutronics calculations indicate that, in the absence of a neutron multiplier, the tritium breeding potential of a Li_2O blanket decreases significantly with ^6Li enrichment above that for natural lithium. The maximum one-dimensional breeding ratio (100% blanket) for a Li_2O blanket with stainless steel first wall (13.4 mm thick) is 1.23 compared to a breeding ratio of ~ 1.3 for the reference design with a 2 mm thick beryllium cladding. Some breeding in the inboard blanket appears essential unless an effective neutron multiplier is used. Both breeding in the inboard blanket and a neutron multiplier may be required if a significant fraction of the outboard blanket is nonbreeding as in the case of a poloidal divertor. Beryllium is found to be the only effective neutron multiplier for a Li_2O blanket. In contrast to the STARFIRE design with $LiAlO_2$ as the breeder material, the beryllium multiplier is more effective when placed behind several centimeters of the Li_2O breeder material. The nuclear heating in the Li_2O varies by approximately two orders of magnitude from the front of the blanket to a depth of 60 cm. For the reference design the nuclear heating is 13.4 MW/m^3 at a distance 5 mm behind the first wall. Although the radioactive products (except tritium) generated within Li_2O completely decay within a minute, a significant fraction of the decay gamma's generated in the stainless steel structure are absorbed in the Li_2O resulting in significant decay heat for longer periods. The total decay power in the first-wall/blanket, which amounts to about 14.5 MW (1.6% of the total thermal power) at shutdown,

decreased to about 3 MW within 7 h and tends to level off at about 2 MW for several weeks.

The physical and mechanical properties, thermodynamic properties, and the effects of radiation on the properties and behavior of Li_2O have been evaluated in detail. Fabrication and handling problems associated with Li_2O have also been assessed. The melting temperature of Li_2O is 1438°C. The thermal conductivity is dependent on porosity and is believed to be significantly affected by radiation. The thermal conductivity of 70% TD Li_2O after modest irradiation is projected to be ~ 1.8 W/m-K. Uncertainties and variations in the data associated with grain size, purity, and radiation effects have not been studied in detail. Lithium oxide is known to be very hygroscopic, reacting readily with moisture to form LiOH. As a result, high purity Li_2O is not only difficult to obtain but contamination during handling is difficult to avoid. Commercially available material typically contains at least 2% of LiOH and 2% of Li_2CO_3; however, higher purity material can be obtained. Recent investigations[54] indicate that the solubility of LiOH in Li_2O is very low. Fabrication of Li_2O with small grain size (2-5 μm) and interconnected porosity, although difficult, appears feasible. However, the stability of this microstructure under anticipated thermal and radiation environments of a reactor blanket is a major concern. Large weight losses have been observed at 1000°C when Li_2O is exposed to vacuum or helium with very low moisture concentrations. This is generally attributed to mass transfer of LiOH. Also, chemical effects produced by burnup of lithium and displacement damage effects produced by energetic recoils (T and He) are predicted to cause sintering and pore closure under certain conditions. Preliminary data indicate substantial restructuring of Li_2O occurs after irradiation at temperatures of 750°C and above.

The materials compatibility issues include breeder structure, coolant-structure, and breeder-coolant compatibility. The first two issues involve normal operation whereas the breeder-coolant compatibility is of interest only in the event of off-normal conditions such as coolant leak into the breeder region. Limited data from short-term (< 2000 h) sealed capsule experiments indicate that the reactivity of Li_2O with stainless steel is probably not excessive. However, no data exist under the more severe conditions of appropriate oxygen and moisture pressures. Potential approaches for reducing

breeder structure reactions include coating of the steel surfaces with nickel or an oxide such as Al_2O_3. The potential for stress corrosion cracking of cold-worked austenitic steel in water under attainable conditions should be assessed in more detail. The impact of tritium or hydrogen containment has not been evaluated in detail. In the event of a water leak into the breeder region, pressurization of the breeder region and formation of corrosive LiOH will occur. The combination of high pressure, significant heat of reaction, and potentially high velocity as a result of turbulence from a leak could lead to rapid corrosion of adjacent structural material with a potential for a propagating-type failure. More detailed analyses must be conducted to assess the severity of a coolant breeder reaction that would result from a coolant tube leak.

Tritium recovery is considered to be the key feasibility issue regarding the viability of Li_2O as a tritium breeder material. Tritium generated within the Li_2O grains must diffuse to the surface of the grains, desorb as T_2O, and migrate through interconnected porosity to a helium purge stream where it is transported to the tritium processing system. Similar to the case for STARFIRE, a Li_2O microstructure with small grain size (< 1 μm) and a bimodal pore distribution is believed to offer the most potential for acceptable tritium recovery. The difficult design problems arise from the limited operating temperature range projected for Li_2O and the fact that the thermal conductivity for irradiated material is believed to be relatively low (about 1.8 W/m-K). Effects that result in a projected allowable operating temperature range between 410 and 660°C for Li_2O are summarized in Table 6-19. The critical concerns relate to the fact that some of the phenomena may cause irreversible propagating-type effects. For example, precipitation of LiOT could lead to enhanced sintering at low temperatures. This in turn would produce higher tritium partial pressures, and hence, more LiOT precipitation and subsequently more sintering. The mass transport of LiOT leads not only to a loss of lithium from the blanket but to possible corrosion or sintering problems caused by precipitation of liquid LiOT in the tritium processing circuit or a lower temperature region of Li_2O, respectively. Analyses indicate that, in the absence of radiation effects, the blanket tritium inventory can be maintained at relatively low levels (< 50 g in Li_2O). However, radiation effects are expected to substantially increase the tritium inventory, possibly to unacceptable levels. Additional experiments are required to more accurately predict the effects of irradiation.

Table 6-19. Basis for Allowable Operating Temperature Range of Li_2O

Maximum Allowable Temperature	
Radiation-Induced Sintering	700°C
Mass Transport of LiOT (1% of T_2O)	660°C
Minimum Allowable Temperature	
Solid State Diffusion (1 μm grain)	410°C
LiOT Precipitation (160 Pa)	410°C

Thermal-hydraulic analyses have been conducted to evaluate the sensitivities of the blanket design, particularly with respect to tritium recovery, variations in breeder physical properties, geometrical parameters and power level. Calculations based on specified materials properties data and idealized operation conditions were used to determine coolant tube spacing, coolant flow rates, and other design specifications required to maintain the Li_2O breeder within the projected allowable temperature range. The sensitivity studies then provided an indication of the impact on design tolerances and operation of performance uncertainties, such as (1) variations in thermal conductivity of the breeder caused by density variations or radiation effects, (2) variations of coolant tube-breeder gap conductances caused by thermal expansion effects, creep or fabrication tolerances, and (3) power level fluctuations. It was concluded that the tolerances required for a designed helium gap heat conductance (tube/breeder) were too small for use in a practical system. Also, significant variations in coolant tube spacing (and hence coolant, structure, and breeder volume fractions) are required to accommodate relatively small uncertainties. Normal effects such as thermal cycling during startup and shutdown, and lithium burnup have not been analyzed in detail but are a major concern. Preliminary analyses have also been conducted to evaluate the flow characteristics of the helium purge stream. Further analyses are required to evaluate effects caused by flow reductions in both the coolant and the helium purge gas.

Stress analyses were performed for both the Li_2O breeder region and the first wall. Thermally induced stresses in Li_2O near a coolant tube were calculated to be much greater than the projected yield strength of the

sintered ceramic. These results indicate that a cylindrical shell of Li_2O around a coolant tube would fracture and probably fragment as a result of excessive thermal stresses. Fracture or segmentation of the Li_2O around the coolant tube will considerably increase the difficult task of maintaining required temperatures in the breeder.

Structural analyses of various coolant channel geometries and sizes for actively-cooled first-wall panels were conducted to evaluate tradeoffs between thermal, pressure, and bending stresses. Results indicate that the corrugated panels with relatively small channels (< 20 mm wide) offer a good compromise solution. The semicircular cross sections provide the best combination of higher allowable coolant pressures and higher thermal or bending stresses. However, the sinusoidal segment cross sections may provide a better choice when fabrication aspects are considered.

The most important considerations related to the first wall/blanket mechanical and structural design (Sec. 6.2.3.2) were (1) choice of breeder coolant containment method, (2) Li_2O breeder temperature, and (3) the degree of first-wall/blanket mechanical and structural integration. Small-diameter toroidally-oriented coolant tubes were chosen to contain the high pressure water coolant within the breeder zone. This approach is considered to have relative advantages over a radial flow (pressurized module) approach in structural efficiency, neutronics (because of lower volume fraction of structure and coolant), compatibility with first wall designs, and certain fabricability aspects (e.g., no separate helium purge piping system is required within the blanket). The method presently assumed for keeping breeder temperature at all points within minimum and maximum temperature limits is to use a sintered metallic felt of controlled density and thickness to bond the breeder to the outside of the coolant tubes. This is preferable to the use of only a helium-filled gap of controlled width to control heat transfer at the breeder-to-tube interface, because of anticipated difficulties in achieving the very tight tolerances necessary for the gap both during fabrication and during blanket operation. The first wall and blanket coolant systems and structure were combined. This approach eliminates the need for an additional actively cooled front wall for the breeding zone, and enhances the tritium breeding by reducing the total amount of structure and coolant. First wall/blanket maintainability and availability are considered equal to or

better than those for a first wall and blanket which are mechanically and structurally separate.

The reference Li_2O breeder first wall/blanket design is illustrated in Fig. 6-14; major parameters are listed in Table 6-20. The first wall and blanket are integrated mechanically and structurally into modules, which are assembled into eight blanket sectors identical except for local variations required for other reactor components (e.g., REB current drive launcher). The first wall is a beryllium-clad corrugated panel, with channels of circular segment cross section. The breeder and first wall are cooled by high pressure (11.0 MPa), high temperature (260°C inlet, 300°C outlet) water. The breeder coolant is contained in small-diameter tubes connected to inlet and outlet manifolds at the rear of the blanket. The Li_2O breeder is fabricated at 70%

Table 6-20. DEMO Li_2O Breeder Reference First Wall/Blanket Concept Description

Selected Materials	
- Tritium Breeder	Li_2O (solid; 70% d.f.)
- Coolant	Pressurized H_2O
	- Ti_{in} = 260
	- T_{out} = 300
- Tritium Processing Fluid	Low-Velocity Helium (0.05 MPa)
- Structure	Titanium-Modified Austenitic Stainless Steel
Selected Design Options	
- First Wall	Be-Clad Corrugated Panel
- Breeder Coolant Containment	Small-Diameter Tubes
- Other	
- First Wall and Blanket Mechanically and Structurally Integrated	
- Coolant Flow in Toroidal Direction	
- Dual Parallel Primary Coolant Loops	
- Maintenance by Sector Removal and Replacement	

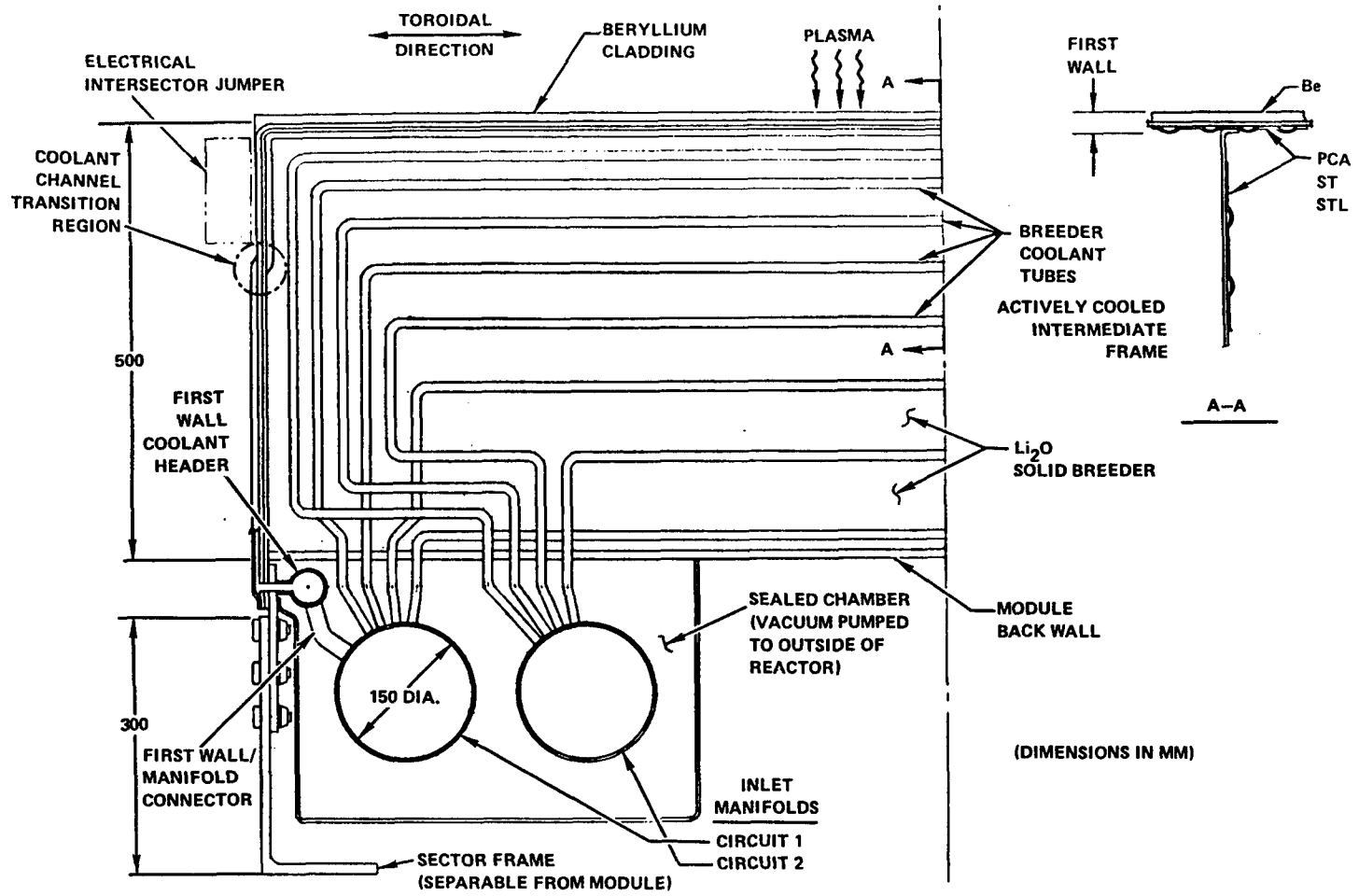

Figure 6-14. Li_2O solid breeder reference blanket design.

of theoretical density with bimodal porosity to enhance tritium release. Helium purge gas at approximately 1 atm flows through 2 mm diameter holes in the breeder to remove tritium.

Dual parallel primary coolant loops are provided to effect safe removal of afterheat in the event of a coolant circuit failure. Maintenance of the first wall/blanket is performed by sector removal and replacement, to minimize downtime.

6.4.2 Design Considerations

Table 6-21 lists most of the principal considerations, issues, or concerns, and candidate design detail options involved in the mechanical and structural designs of the Li_2O breeder first wall/blanket. Many of these issues were previously addressed in the STARFIRE study for the $LiAlO_2$ breeder blanket. They have been reviewed and reconsidered for $LiAlO_2$ breeder within the context of DEMO objectives and parameters. The information in the table assumes the prior selection (Section 6.2.3.1) of first wall/blanket materials: PCA structure, pressurized water coolant, helium purge gas, and Li_2O breeder. Issues and options pertaining specifically to other candidate materials are not shown. The reasons for the importance of the listed issues, and the advantages and disadvantages of the design detail options, were discussed in Sections 6.2.3 and 6.2.4 together with the rationale supporting the options selection for the reference first wall/blanket design configuration.

Table 6-21. Design Considerations for Li_2O Breeder Blanket

Consideration	Primary Issues or Concerns	Options
First wall design	• Plasma disruption loads • Reliability against leaks • Thermal-hydraulics	• Coolant containment method: - Tubes - Panels - Front wall of large pressurized blanket module
First wall/blanket coupling	• Effects on breeding ratio • Maintainability/availability	• Integrated with or separable from blanket - Structurally - Mechanically
Breeder temperature control	• Thermal conductance at breeder/coolant tube in interface	• Helium gap • Controlled-thickness ceramic insulation on coolant tubes • Metal felt bonded to breeder and structure
Breeder coolant containment	• Reliability against leaks • Structural coolant volume minimization • Structure temperature limit • Coolant pressure, T, T_{max}	• Coolant containment in breeder zone: - Small-diameter tubes - Panels - Large pressurized modules • Plenum location: - Module sides - Rear of blanket • Coolant flow direction
Energy conversion system	• Thermal energy recovery efficiency • Component capital costs • Pumping power losses	• Heat exchanger options: - Intermediate heat exchanger - Steam generator: - Single wall tubes - Double wall tubes
Safety	• Effects of breeder/coolant contact in accident • Blanket afterheat removal	• Blanket protection methods: - Double walled coolant tubes - Relief (blow-out) plugs - Module walls designed for full coolant pressure • Afterheat removal: - Dual parallel coolant circuits - Emergency coolant circuit - Via radiation and conduction only

6.4.3 Materials Assessment

The properties of Li_2O and the materials compatibility issues are summarized in Sections 6.4.3.1 and 6.4.3.2, respectively.

6.4.3.1 Properties of Li_2O

Lithium oxide and certain ternary lithium oxides are considered potentially viable tritium breeding materials. These materials have been the subject of a number of recent reviews.[1,55-58] The materials property data base for Li_2O, although far from being sufficient for the needs of fusion, is rather extensive compared to that of other solid breeders. An excellent summary of the data base for Li_2O, with 31 references was compiled by Nasu[59] in late 1979. Recently, experimental programs at ANL[54,60-62] and General Atomic Company[63] have generated a number of results which have significant implications regarding the use of Li_2O in fusion reactor blankets. Summarized below is an assessment of the current data base for Li_2O, with emphasis on certain key feasibility issues: (1) physical and mechanical properties, (2) fabrication, (3) thermochemical properties, and (4) radiation effects.

Physical and Mechanical Properties

As noted above, the data base for Li_2O has been summarized previously.[59] Selected properties of lithium oxide are listed in Table 6-22 Lithium oxide has a high lithium atom density and, therefore, has good tritium breeding capability. The melting temperature is 1430°C. A key property with

Table 6-22. Selected Properties of Li_2O

Density, g/cm^3	2.01
Lithium atom density, g/cm^3	0.93
Melting point, °C	1430
Thermal conductivity (irradiated, 70% TD), W/m-K	~1.8 @ 500°C
Heat capacity, J/g-K	2.6 @ 500°C
Enthalpy of hydrolysis, KJ/g	-3.9 @ 500°C
Thermal expansion coefficient, K^{-1}	29×10^{-6}
Elastic modulus (70% TD), MPa	1.6×10^5
Poisson's ratio	0.3

regard to blanket design is the thermal conductivity. Thermal conductivity for Li_2O of 70-93% theoretical density is shown in Fig. 6-15.[64] Although the effect of radiation on the thermal conductivity of Li_2O has not been reported, significant decreases are expected, particularly at lower temperatures. Based on the effects of radiation in the thermal conductivity of other ceramics, e.g., BeO, Al_2O_3, SiC, and B_4C, projected curves for the thermal conductivity of irradiated Li_2O are presented in Figs. 6-16 and 6-17.[65] The reduction in conductivity is predicted to occur at relatively low fluences, $<3 \times 10^{25}$ n/cm^2-s (~0.2 MW-y/m^2 integrated neutron wall loading), and then remain relatively constant with further irradiation.

The thermal expansion coefficient for Li_2O is presented in Fig. 6-18.[66] These data indicate that the thermal expansion for Li_2O is greater than that for some of the ternary ceramics and also greater than for stainless steel. A least-square fit to the data for Li_2O with 85% density and a grain size of ~2 μm yields

$$\frac{\Delta L}{L_0} = -1.296 \times 10^{-3} + 2.88 \times 10^{-5}\ T\ (°C)\ ,$$

where $\Delta L/L_0$ is the fractional length change. With the linear temperature dependence the thermal expansion coefficient α is given by $28.8 \times 10^{-6}\ K^{-1}$.

No experimental data for the elastic modulus E and Poisson's ratio ν have been found in the literature for Li_2O. Based on data for other ceramic oxides, viz., Al_2O_3, BeO, and MgO, the elastic modulus for 100% TD Li_2O is estimated to be 3.1×10^5 MPa. A porosity factor is obtained from the following theoretical relationship[67]

$$E = E_0(1 - 1.9\ P + 0.9\ P^2)\ ,$$

where E_0 is the elastic modulus for 100% TD material and P is the porosity fraction. This relationship has been compared with experimental data for Al_2O_3 having a uniform porosity.[68] The experimental and theoretical values of E/E_0 at P = 0.3 are 0.44 and 0.51, respectively. The predicted value of E for 70% dense Li_2O is 1.6×10^5 MPa.

In general, Poisson's ratio for different materials does not vary significantly from 0.3. Therefore, this value is suggested for use in calculations in the absence of experimental data for Li_2O.

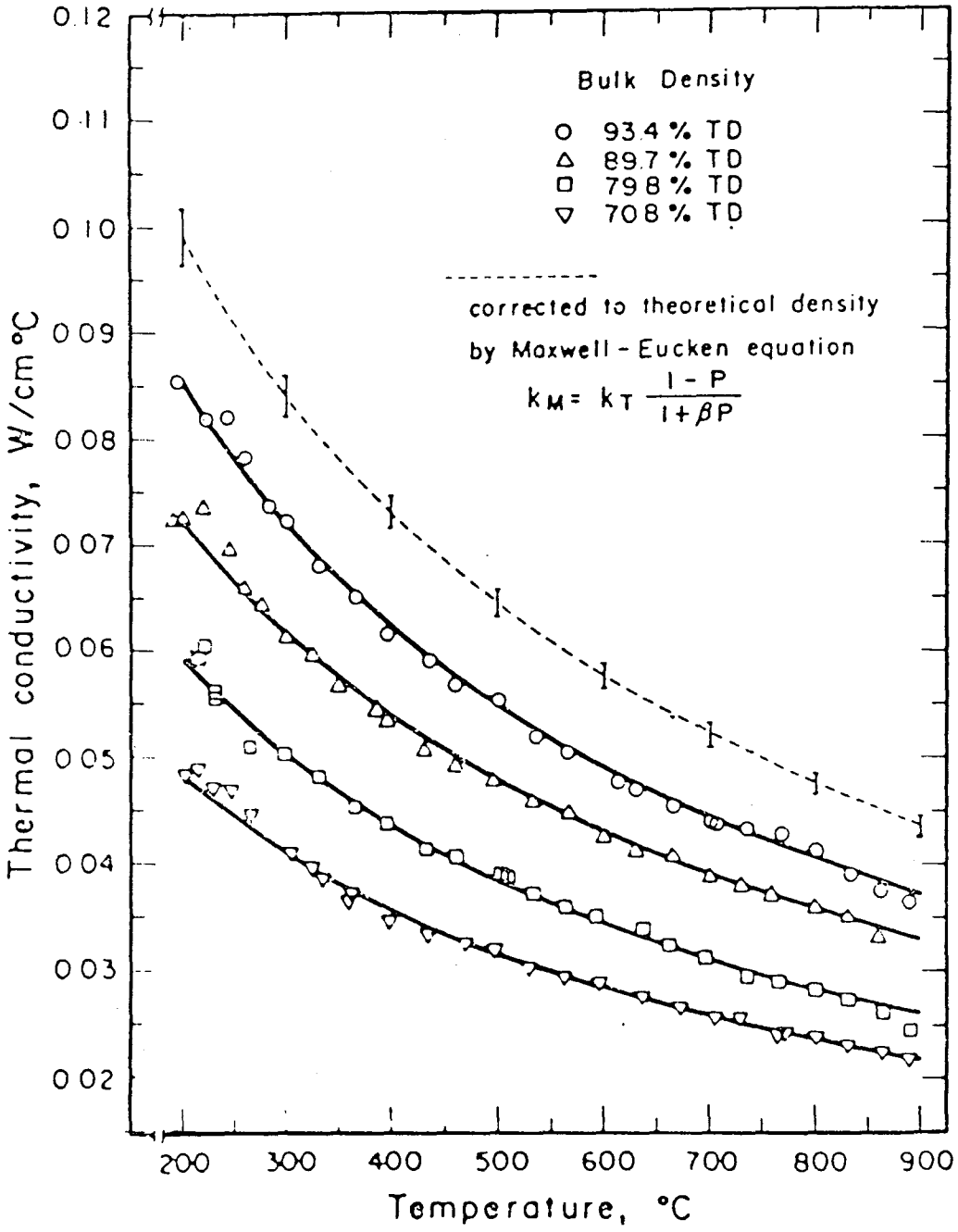

Figure 6-15. Thermal conductivity of Li_2O (Ref. 56).

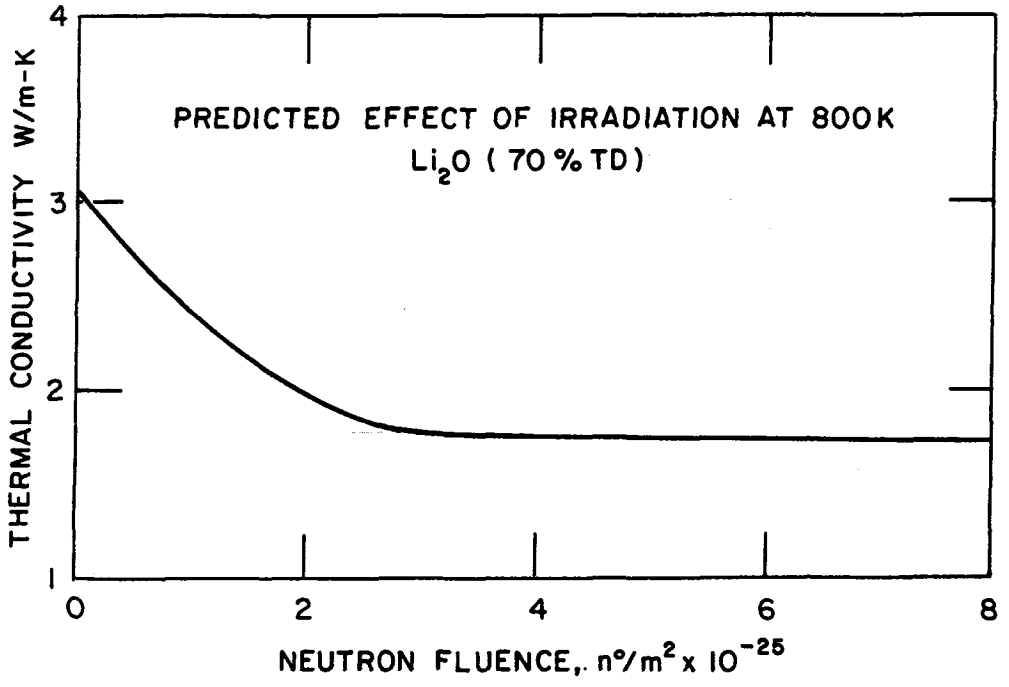

Figure 6-16. Effect of neutron irradiation on thermal conductivity of Li_2O.

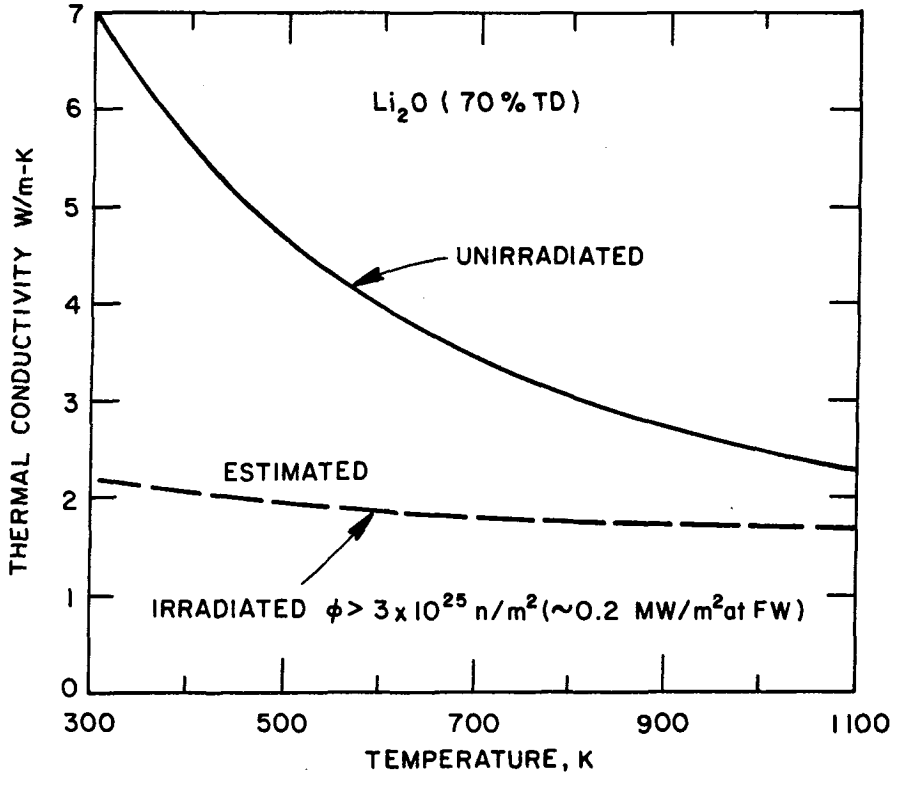

Figure 6-17. Thermal conductivity of irradiated and unirradiated Li_2O.

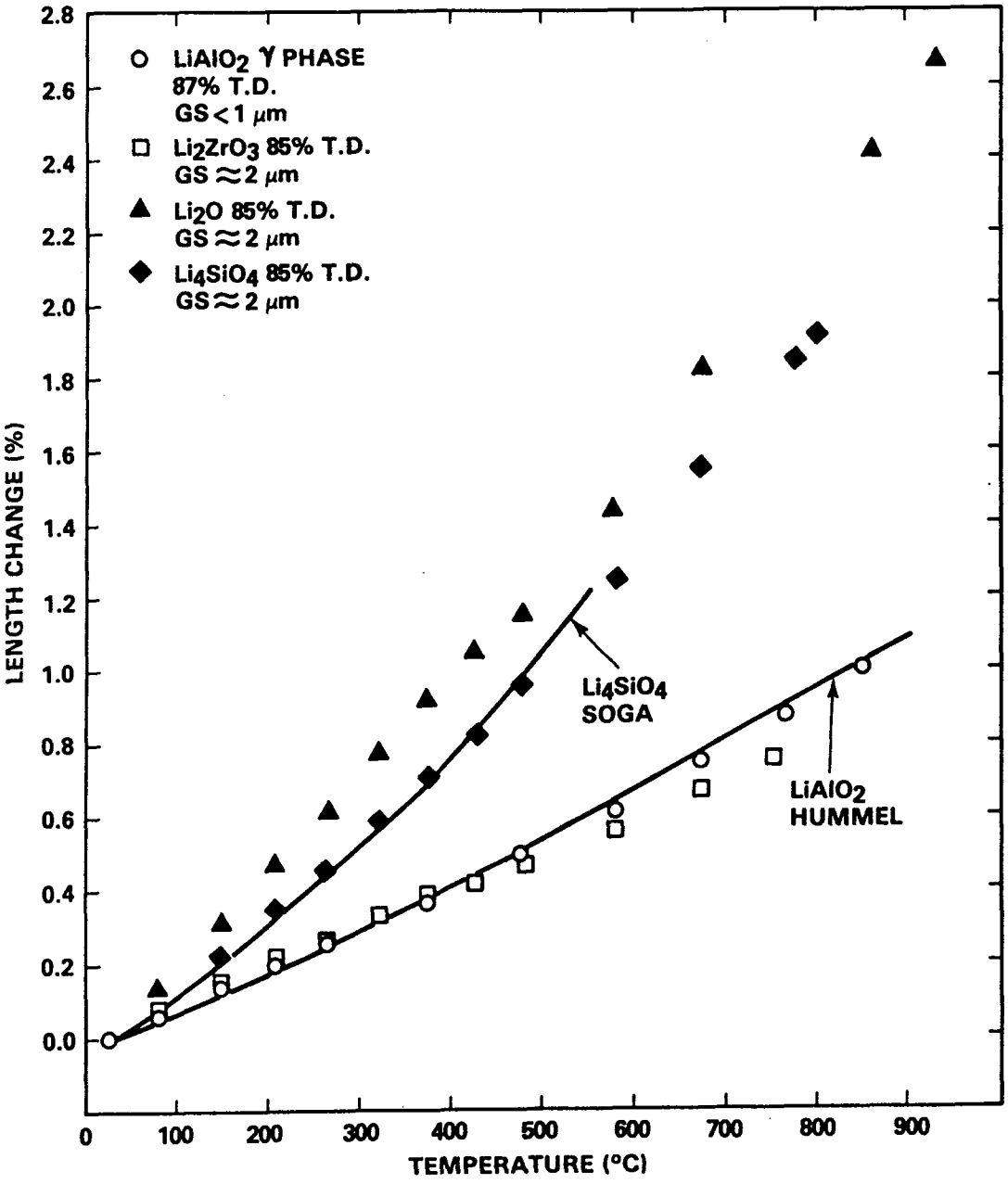

Figure 6-18. Thermal expansion of solid breeder materials.

Preparation/Fabrication

Preparation and fabrication of high purity Li_2O on a large scale for fusion reactor blanket applications is an important feasibility issue. One must not only be able to prepare high purity material but one must avoid contamination during handling, storage, and blanket assembly since the properties of Li_2O are very sensitive to material purity. This appears to be feasible on a laboratory scale but may be quite difficult on a large scale because of the high hygroscopicity of Li_2O and the fact that very small grain size with substantial porosity is essential for tritium recovery.

Lithium oxide is very hygroscopic, reacting readily with moisture to form LiOH. Li_2O also reacts with CO_2 in air to form Li_2CO_3. In addition, Li_2O reacts with a large number of metal oxides to form ternary oxides, e.g., $LiCrO_2$. Thus, samples of Li_2O obtained from commercial vendors or samples prepared in laboratories without the utmost care are likely to contain significant quantities of LiOH, Li_2CO_3, and cationic impurities. Reported chemical analysis of a number of Li_2O samples are given in Table 6-23. Commercially available material appears to have at least 2% by weight of each of LiOH and Li_2CO_3. Careful laboratory preparation has achieved rather pure material with 0.25% by weight of Li_2CO_3 and <0.1% by weight of LIOH.[54] Exposure of pure Li_2O to air will increase both the carbonate and hydroxide levels to about 2% by weight. Because of the corrosive nature of LiOH and Li_2CO_3 at elevated temperatures, preparation can introduce significant levels of metallic impurities, e.g., Prep A in Table 6-23.[54] It appears that it is possible to obtain samples with cation impurities of less than 10 ppm.[54,69]

Either sintering or hot pressing are probably acceptable fabrication methods. Arons, et al.,[54] have demonstrated that sintered pellets of high purity Li_2O can be fabricated. However, the purity and microstructure of the pellets are quite sensitive to minor variations in procedures. Sintering in vacuum at ~1000°C for 4 h resulted in large weight loss of the pellet whereas heating in vacuum at 950°C prior to sintering in oxygen 4-6 h at 1050°C gave a density of ~80%. A reverse procedure, i.e., sintering in O_2 at 1050°C prior to heating in vacuum at 950°C, gave >95% dense material. Moisture pickup during handling or storge at room temperature is significant unless extreme precautions are taken. Because of these sensitvities, microstructure control in Li_2O may be difficult to achieve in practice, particularly on a large scale.

Table 6-23. Impurity Content of Li_2O Samples

	wt-%			
	Li_2CO_3	LiOH	Wppm Cations	Ref.
Vendor A[a]	12.6	6.9	---	57
Vendor B	2.1	---	---	57
Vendor C	4.8	---	---	57
Vendor D	---	1.8	---	46
Prep A[b]	---	---	1000 (Pt)	46
Prep B[c]	---	2.4	---	46
Prep C[d]	---	0.5	~10	46
Prep D[e]	0.25	---	~10	58
Prep E[f]	---	<0.1	---	59

[a]Exposed to air.

[b]Decomposed Li_2CO_3 in Pt at 880°C - dark grey.

[c]Decomposed Li_2CO_3, some exposure to air.

[d]Decomposed Li_2CO_3, minimal exposure to air.

[e]Decomposed Li_2CO_3, 21 days at 700°C plus 14 days at 750°C.

[f]Heat treated impure Li_2O in dry (<5 ppm H_2O) flowing helium stream, 600°C, ~2 h.

Also, sintering temperatures may be quite low (possibly as low as 450°C) if significant amounts of LiOH are present. As a result, in-reactor sintering and grain growth may be a serious problem for Li_2O. Experience to date[54] indicates that a grain size <2 μm is very difficult to obtain. Fabrication of Li_2O with a bimodal pore distribution has not been demonstrated.

Chemical Properties of Li_2O

A key question regarding Li_2O is the tritium "solubility". As discussed in 1980,[1,55-58] it was presumed that there is an equilibrium of the bred tritium between the solid and gas phases:

$$2\ LiOT(s) \rightleftharpoons T_2O(g) + Li_2O(s) \qquad (6\text{-}7)$$

and

$$K_p = \frac{P(T_2O)}{a^2_{LiOT}}, \qquad (6\text{-}8)$$

where a_{LiOT} = the activity of LiOT. Previously it was assumed that a_{LiOT} was equal to the concentration of tritium in the solid phase (Raoult's Law). However, recent experiments[60,70] have shown that LiOH (also LiOT) is nearly insoluble in Li_2O and, thus, a_{LiOT} in Eq. (6-8) is close to unity. Thus, the tritium "solubility" previously calculated to result in very high tritium inventories for Li_2O blankets is in fact low, so that tritium inventories due to "solubility" do not appear to be prohibitive. Some experimental results of Tetenbaum[60] are given in Table 6-24. Two trends (Table 6-24) were observed: (1) solubility of H_2O decreases with decreasing temperature; and (2) solubility appears to be proportional to the concentration (pressure) of H_2O in the gas phase. In a separate experiment by Nasu[59] an irradiated Li_2O sample in equilibrium with 48.5 Pa T_2O at 650°C had a tritium content of ~0.4 wppm.[70] For hydrogen this would correspond to 0.1 wppm in the solid with 480 ppm H_2O in the gas phase. This appears to be consistent with the first trend noted above. This result also supports the assumption by Tetenbaum that upon cooling a lithium oxide sample to 650°C, the observed moisture evolved is equal to the amount in solution at 850-995°C (Table 6-25). It is evident that tritium "solubility" in an Li_2O blanket will be small (<1 ppm).

An important consequence of these results follows. Since LiOH (also LiOT) is nearly insoluble in Li_2O, the phase field can be represented in a manner previously described.[5] The curved line in Fig. 6-19 separating Li_2O from LiOH is the dissociation pressure of LiOH. During operation the Li_2O breeder must be maintained at temperature and pressure conditions to the left of and below the LiOH dissociation pressure curve in Fig. 6-19. This criterion implies significant temperature and pressure constraints upon blanket operation. For example, if the T_2O pressure in the blanket is 160 Pa (1.2 torr), a separate LiOT phase will form at temperatures below 410°C. In addition, it is evident that whenever the blanket is cooled to room temperature, the tritium in solid solution will precipitate out as a separate phase of LiOT.

Another important consideration relates to the vaporization of LiOH (LiOT), which has been studied by Tetenbaum. The results of that study (Table 6-25) show the effects of moisture on Li_2O vapor phase transport. The blanket purge stream has a T_2O partial pressure of about 1 Pa or 10 ppm. It is evident that at the high temperature in Table 6-25 (1100 K and

Table 6-24. Tentative Values for the Solubility of LiOH in Li_2O[a]

T (°C)	ppm H_2O in Helium Carrier Gas	wt-% LiOH		wppm H in Li_2O		C/P[b]
		Cooling	Reheating	Cooling	Reheating	Henry's Law Constant
650	500	c	c	c	c	c
800	150	0.0055	0.0034	2.3	1.4	0.012
800	150	0.0043	0.0026	1.8	1.1	0.010
850	65	0.0029	0.0024	1.2	1.0	0.017
850	100	--	0.0050	--	2.1	0.021
850	110	0.0038	0.0050	1.6	2.1	0.017
857	100	0.0060	--	2.5	--	0.025
900	140	0.0084	0.0098	3.5	4.1	0.027
950	110	0.0057	0.0053	2.4	2.2	0.021
958	120	0.0091	--	3.8	--	0.035
980	500	0.029	0.031	12.3	13.1	0.025
980	285	0.020	0.012	8.4	4.9	0.024
980	105	0.0059	0.0066	2.5	2.7	0.025
995	40	0.0021	0.0038	0.9	1.6	0.033
1000	135	0.014	0.012	5.8	4.9	0.040

[a]See Ref. 52.

[b]C = wppm H in Li_2O; P = partial pressure H_2O (ppm) in the He carier gas.

[c]Moisture peaks not observed.

Table 6-25. Vaporization Behavior of Lithium Oxide[a]

T (°K)	Carrier Gas Flow Rate (ml/min)	ppm H_2O	-log p[b]			-log k	
			ANL Work	Calculation via JANAF	Kudo, et al.	ANL Work	Calculation via JANAF
1073	158	105	5.62	5.35	9.81	7.25	6.71
1123	220	4	5.94	5.70	9.06	6.48	6.00
1123	175	65	5.19	5.13	9.06	6.19	6.08
1128	150	105	5.08	4.99	8.99	6.19	6.02
1173	142	420	4.43	4.40	8.35	5.49	5.42
1223	225	110	4.36	4.37	7.71	6.76	4.80
1258	225	110	4.33	4.18	7.29	4.70	4.41
1263	157	440	4.00	3.35	7.22	4.64	4.34
1268	143	115	4.18	4.10	7.16	4.42	4.28
1268	158	45	4.45	4.31	7.16	4.57	4.28

[a]See Ref. 59.

[b]p in atmospheres: 1 atm = 101.325 kPa.

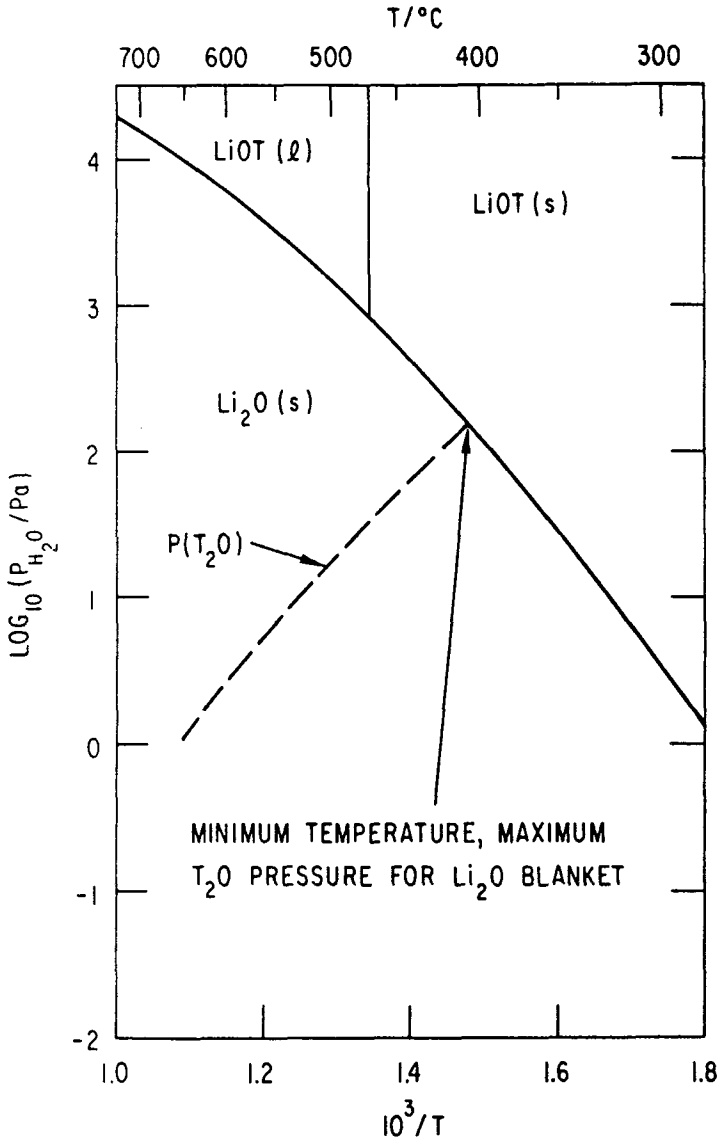

Figure 6-19. $LiOH-Li_2O$ phase diagram showing operating temperature limits for blanket.

higher), the LiOT pressures are >1 Pa. Vapor phase transport of lithium under these conditions would be excessive, >750 g/day, or >0.36% of the blanket per year. The data are in very good agreement with JANAF,[71] which are based on the work of Berkowitz, et al.[72] Using the JANAF data for the equilibrium

$$H_2O(g) + Li_2O(s) \rightleftharpoons LiOH(g) \qquad (6\text{-}9)$$

and setting $P(H_2O)$ = 1 Pa, the pressure of T_2O in the purge stream, the pressure of LiOH (LiOT) was calculated, as shown in Fig. 6-20. It is suggested as a design criterion that the LiOT pressure should not exceed 1% of the T_2O pressure. Thus, for $P(T_2O)$ = 1 Pa, P(LiOT) must not exceed 10^{-2} Pa. This corresponds to a maximum allowable Li_2O temperature of 660°C.

Radiation Effects

Fabrication of Li_2O with small grain size (1-5 μm) and uniform interconnected porosity, although difficult, appears feasible. However, the stability of this microstructure under the anticipated thermal and radiation environments of a reactor blanket is a major concern. Large weight losses have been observed at 1000°C when exposed to vacuum conditions or helium with very low moisture concentrations.[54,73] This is generally attributed to mass transfer of LiOH. Although experimental data are quite limited, chemical effects produced by burnup of lithium and displacement damage effects produced by the high energy recoils (several MeV tritium and helium) could cause enhanced sintering which would lead to pore closure and a buildup of tritium or LiOT. A buildup of LiOT would also enhance sintering as discussed in Sec. 6.4.3.2. A maximum temperature of 0.6 T_m, which corresponds to ~750°C for Li_2O, was suggested in the STARFIRE study.[1,56]

Scoping studies by Yang, et al.[63] tend to support the predicted results. Small capsules containing ~70% dense Li_2O were irradiated in ORR to fluences of ~2 × 10^{21} n/cm^2 at temepratures of 750, 850, and 1000°C. The samples were depleted to 0.05% ^{6}Li to more nearly approximate tritium generation rates projected for fusion reactor blankets. Therefore, the maximum lithium burnup was only 0.05%. This compares to an estimated burnup of ~0.04%/y near the first wall of the DEMO (or equivalent to about one month's operation). Post-irradiation examination revealed that the pores became com-

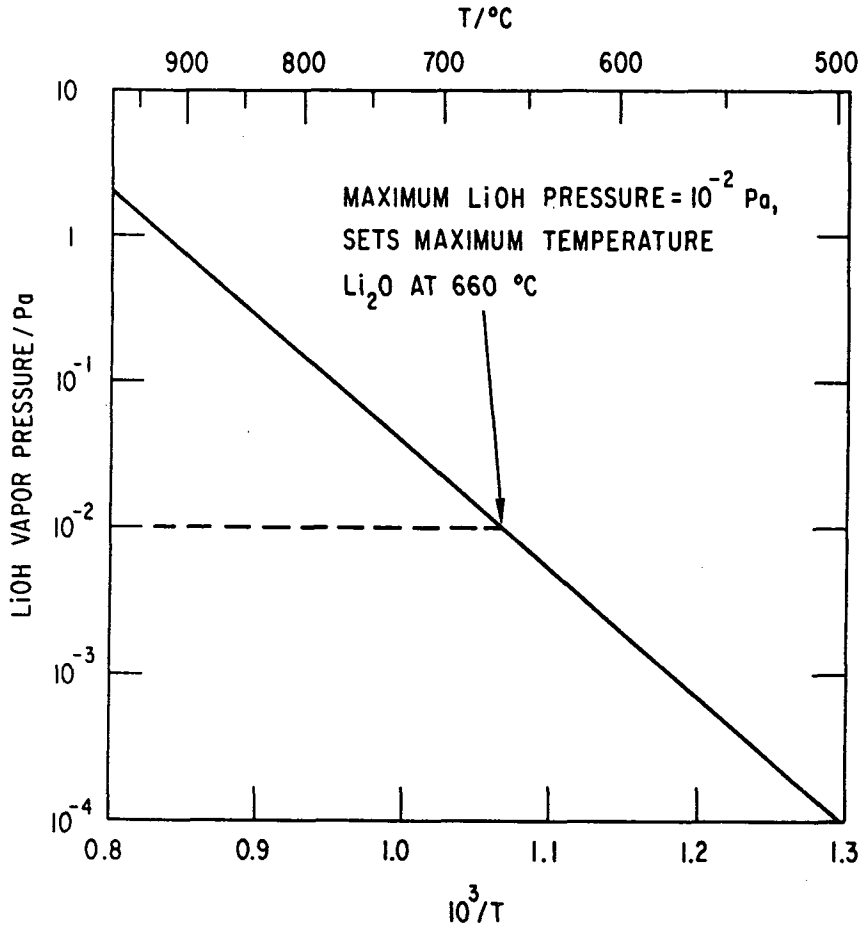

Figure 6-20. Vapor pressure of LiOT above Li_2O with $P(T_2O)$ equal to 1 Pa. The maximum temperature limit is ∿ 660°C.

pletely closed in samples irradiated at 850 and 1000°C. Although some interconnected porosity remained after the 750°C irradiation, significant changes were observed in the microstructure after irradiation. The grain size of the test samples was <47 μm. One would predict more extensive sintering in the small grain size (<1 μm) proposed for reactor applications and for the much higher burnup required for a practical system. These results indicate that Li_2O must be operated at temperatures considerably below 750°C if the desired open microstructure is to be stable. Obviously additional experimental investigations are required to more accurately determine the temperature limits. A maximum temperature of 650-700°C is proposed for the current study.

6.4.3.2 Materials Compatiblity

Materials compatiblity is an important consideration in the development of a viable blanket design. Primary areas of concern for the Li_2O breeder concept include: breeder/structure, coolant/structure, breeder/purge stream, and breeder/coolant compatibility. The first three issues involve normal operation whereas the breeder/coolant compatibility is of interest only in the event of off-normal conditions such as coolant leak into the breeder region.

Breeder-Structure Compatibility

The compatibility of solid breeder materials with candidate structural materials is an important consideration in the development of a solid breeder blanket. Chemical interactions between the structure and the breeder could impact the mechanical integrity of the structural material and the tritium release characteristics of the breeder. Limited experimental data are available on the compatibility of candidate structural materials with Li_2O. Also, most of the data are from short-term tests (<1000 h) and relatively high temperatures ($\geq$600°C). Temperatures of interest in the present design are approximately 400°C. In general, tests have been conducted in a closed system, i.e., sealed capsules. Results will probably be significantly different under more realistic conditions where the oxygen and moisture partial pressures are controlled by the tritium recovery system.

Much of the experimental work on the compatibility of Li_2O with structural alloys has been reported by Chopra,[62] Finn,[61] and Kurasawa.[74,75] Observations from these studies on Type 316 stainless steel, HT-9 alloy, and Inconel 625 exposed to Li_2O and several ternary ceramics, such as $LiAlO_2$ and Li_2SiO_3, are summarized as follows:

- Li_2O is much more reactive than the ternary ceramics under similar conditions.
- Nickel and high nickel alloys are more compatible with all ceramics than Type 316 stainless steel and HT-9.
- Although the reaction zones of Type 316 stainless steel and HT-9 exposed to Li_2O are significantly different, the reaction zone thicknesses do not differ greatly.
- The reaction products Li_5FeO_4 and $LiCrO_2$ are observed after exposure of both Type 316 stainless steel and HT-9 to Li_2O.
- Li_5FeO_4 is predominant in the outer scale next to the Li_2O whereas $LiCrO_2$ is present near the alloy.
- Significant amounts of iron and chromium are detected in the Li_2O scale after exposure to Type 316 stainless steel and HT-9.
- Sealed capsule tests tend to indicate a significant decrese in reaction rate with time.
- The reaction products Li_5FeO_4 and $LiCrO_2$ are quite volatile at the higher test temperatures (700°C).

The data base on the compatibility of Li_2O with Type 316 stainless steel and HT-9 alloy is insufficient to evaluate the importance of this problem area for the conditions of interest, viz., temperature and oxygen and moisture pressure. Potential approaches for reducing the reaction rates include coating the steel surfaces with nickel or an oxide such as Al_2O_3 or $LiAlO_2$. The impact of these solutions will require further neutronic and thermal-hydraulic analyses.

Coolant-Structure Compatibility

Austenitic stainless steels, in general, have good corrosion resistance to degassed high-temperature water. The corrosion resistance is attributed primarily to the formation of an adherent protective spinel film of the type M_3O_4. The corrosion rate under well controlled conditions is about 5 mg/dm^2-mo or about 0.75 μm/y.

The major concerns regarding compatibility of stainless steel and water relate to effects of water purity, stress, and steel microstructure. Sensitization, i.e., precipitation of chromium carbides at grain boundaries that occurs after certain heat treatments, appears to have little effect on the corrosion rate of stainless steels in pressurized water with a pH of 7 to 11. However, intergranular attack has been observed in both Types 304 and 316 stainless steel exposed to water with a pH of 3.5.[76] Stress corrosion cracking can occur in stainless steel structural components particularly under heat transfer conditions where steam blanketing can occur or at liquid-vapor interfaces which provide alternate wetting and drying. The principal problems in this area relate to boiling water reactor or steam generator applications where chlorides or free caustic in water become sufficiently concentrated to produce cracking. If there is a concentrating mechanism present, chloride and caustic concentrations of the order of ppm in the bulk water can cause cracking. It is generally agreed that some oxygen is required to cause chloride cracking whereas none is required for caustic cracking.

Hydrogen additions to water reduce the tendency for corrosion cracking. The most susceptible areas are welds and the heat affected zones where microstructural changes have occurred and a residual stress is often present. The microstructural effects in the heat-affected zones can be minimized by either reducing the carbon content or adding stabilizers such as titanium, niobium, or tantalum to the stainless steel. The cold worked materials are generally regarded as more susceptible to stress-corrosion effects than solution-annealed material.

Since the DEMO application is quite severe in that it includes (1) high thermal stresses, (2) radiation that can cause hydrolysis of the water and microstructural changes in the steel, and (3) cold-worked materials, attention

must be given to these compatibility problems. Further analyses should be conducted to evaluate the impact of tritium control requirements on the water chemistry and subsequently on the compatibility effects.

Breeder-Purge Stream Compatibility

The stability of Li_2O in the helium purge stream proposed for tritium recovery is a major concern. Two key issues include (1) the potential for mass transfer of lithium in the form of LiOT in the purge stream, and (2) the potential liquid phase (molten LiOT) sintering of the Li_2O if the tritium (or T_2O) pressure is high enough to precipitate LiOT. The assessment of these effects is given in Sec. 6.3.4.1. A secondary effect which must be evaluated relates to the potential problems that could arise as a result of LiOT precipitation on the down-stream structural wall.

Breeder-Coolant Compatibility

During normal operation the coolant will not come in contact with the Li_2O breeder material. However, the potential problems resulting from leakage of high pressure (12 MPa) water coolant into the breeder region are of concern since the blanket will contain on the order of 50,000 tubes with at least twice as many weld joints. Two key issues relate to (1) high pressure release into the breeder region, and (2) formation of highly corrosive LiOH upon contact of the water with Li_2O.

Thermodynamic analyses presented in Sec. 4.3.5.3 indicate that LiOH will form if water leaks into the Li_2O region. The kinetics of the reaction have not been analyzed; however, the reaction is known to be exothermic (ΔH = 8.4 KJ/g lithium). The corrosion rates of austenitic steels in LiOH have not been measured for conditions of interest; however, the alkali metal hydroxides are known to be highly corrosive. The combination of high pressure, significant heat of reaction, and potentially high velocity as a result of turbulence from a leak could lead to rapid corrosion of adjacent structural material with a potential for propagating effects. More detailed analyses must be conducted to assess the severity of a coolant-breeder reaction that would result from a coolant tube leak.

6.4.4 Tritium

The proposed method of tritium recovery from the Li_2O blanket is basically the same as that proposed for the STARFIRE study.[1,56] The Li_2O is in the form of a low-density (70% theoretical density) hot-pressed or sintered product with a tailored bimodal pore distribution, i.e., a small grain size (<1 μm) and a fine porosity within larger particles (~1 mm diameter) with a more coarse porosity between particles. The Li_2O is perforated with ~2 mm diameter holes through which low-pressure (0.1 MPa) helium passes to recover the tritium from the breeder. Tritium generated within the grains must diffuse to the surface of the grains, desorb as T_2O, and migrate (percolate) through the interconnected porosity to the helium purge stream where it is transported to the tritium processing system. Further analysis of the migration (percolation) of T_2O through the interconnected porosity have been conducted in an attempt to define the optimum particle-to-grain size ratio and the amount of porosity required. An assessment of the tritium inventory in the Li_2O blanket is presented for two cases. The first, an idealized case for which a more accurate estimate can be made because of a better data base, neglects any effects of radiation on the release characteristics. Although the effects of radiation on the tritium inventory are highly uncertain, estimates of possible impacts of various radiation effects are presented as a second case.

6.4.4.1 Percolation of T_2O through Interconnected Porosity

The tritium inventory in the grain matrix of a fusion blanket material (e.g., $LiAlO_2$ or Li_2O) depends on the partial pressure of tritium (T_2O) in the interconnected porosity between the grain surfaces and the helium purge stream. In addition the formation of LiOT, which can be detrimental to blanket operation, is a sensitive function of T_2O partial pressure. Calculations were performed to determine the T_2O partial pressure as a function of porosity distribution (monolithic or bimodal), grain radius ($0.25 \leq r_g \leq 2.5$ μm), particle radius ($0.25 \leq R_p \leq 2.5$ mm), and purge-stream pitch (spacing). The operating variables and fabrication variables for both the $LiAlO_2$ STARFIRE blanket and the Li_2O DEMO blanket are summarized in Table 6-26.

Table 6-26. Parameters for $LiAlO_2$ STARFIRE Blanket and Li_2O DEMO Blanket in the Region of the First Row of Coolant Tubes

Parameter	STARFIRE	DEMO
Nuclear heating rate,[a] W/cm^3	39.9	18.5
T_2O generation rate,[a], $g/s\text{-}cm^3$	4.34×10^{-10}	1.1×10^{-9}
Temperature, °C		
Maximum	850	660
Average	810	600
Minimum	500	410
Helium purge stream		
Diameter, mm	2	2
Pressure, MPa	0.0505	0.101
Pitch, mm	24	24
T_2O pressure limits, Pa	---	160 (at 410°C)
	---	1 (at 660°C)
Grain diameter, μm	0.5	0.5-5.0
Particle diameter, mm	1.0	0.5-5.0
Porosity fraction		
Monolithic	0.1-0.4	0.1-0.4
Fine bimodal	0.1-0.225	0.1-0.225
Large bimodal	0.1-0.225	0.1-0.225

[a]Per cc of solid (100% dense) volume.

For the purposes of modeling the T_2O pressure buildup in the interconnected porosity, it is necessary to first express the generation rate per unit of interconnected pore volume and to model the average pore radius as a function of grain (or particle) radius and porosity (ε). Based on Solomon's data for UO_2,[77] the interconnected porosity fraction for the monolithic structure is estimated to be $\varepsilon_i = \varepsilon - 0.03$ for $\varepsilon \geq 0.1$ and $\varepsilon_i = 0$ for $\varepsilon < 0.1$. Thus, the generation rate per unit volume of interconnected porosity is:

$$q_A = \frac{1 - \varepsilon}{\varepsilon_i} \dot{S} , \qquad (6\text{-}10)$$

where $\dot{S}$ = the generation rate per unit of solid (100% dense) volume.

The average monolithic pore radius is normalized to 20% of the grain radius at a reference interconnected porosity fraction of $\varepsilon_i = 0.222$ based on Graham's data for UO_2 and nickel[78] and to vary with interconnected porosity according to:

$$r_p = 0.406\left(\frac{1}{\varepsilon_i} - 1\right)^{-1/2} r_g \ . \qquad (6\text{-}11)$$

The above model assumes that the open porosity is cylindrical in geometry. (The fact that the pore channels are not straight is accounted for in the diffusion model by the introduction of a tortuosity factor, τ.)

For the bimodal structure the fine porosity, ε_f, within the particles is modeled in the same manner as the fine monolithic porosity. The model for the large porosity (between particles), ε_ℓ, assumes that all of ε_ℓ is interconnected and that the average large pore radius is related to the particle radius R_p. For the designs under consideration, $\varepsilon_\ell = \varepsilon_f$, leading to the following results:

$$\varepsilon_\ell = \varepsilon_f = 1 - (1 - \varepsilon)^{1/2}$$

$$\varepsilon_{\ell i} = \varepsilon_\ell$$

$$\varepsilon_{fi} = \varepsilon_f - 0.03 \ , \quad \text{for } \varepsilon_f \geq 0.1 \text{ and } \varepsilon_{fi} = 0 \text{ for } \varepsilon_f \leq 0.1$$

$$q_{Af} = \frac{1 - \varepsilon_f}{\varepsilon_{fi}} \dot{S}$$

$$q_{A\ell} = \frac{1 - \varepsilon_\ell}{\varepsilon_\ell} \dot{S}$$

$$r_f = 0.406\left(\frac{1}{\varepsilon_{fi}} - 1\right)^{-1/2} r_g$$

$$r_\ell = 0.372\left(\frac{1}{\varepsilon_\ell} - 1\right)^{-1/2} R_p \ .$$

In choosing a diffusion model it is important to estimate the ratio of the average pore radius to the mean free path of T_2O-He collisions. Under DEMO conditions the mean free path for intermolecular collisions is estimated to be $\lambda = 0.152$ μm (0.385 μm for STARFIRE). The range of radii for fine pores is 0.03 μm to 0.8 μm while for large pores the range is 60 μm to 1000 μm, depending on grain size, particle size, and porosity fraction. Thus, the large pore radii can be modeled by an ordinary diffusion law because λ/r_ℓ

$<< 1$. The diffusion through the fine pores lies in the transition region between ordinary diffusion and Knudsen diffusion ($0.1 < \lambda/r_p < 10$).[79] For low concentrations of gas A in gas B, the effective diffusion coefficient for gas A in a porous medium is:[79,74]

$$D_e = [\tau(1/D_{KA} + 1/D_{AB})]^{-1} , \qquad (6\text{-}12)$$

where

$$D_{KA} = \left(\frac{2r_p}{3}\right)\left(\frac{8}{\pi}\frac{RT}{W_A}\right)^{1/2} = 6.12\ r_p , \quad \text{cm}^2/\text{s under average DEMO conditions}$$

r_p = average pore radius in μm,

$D_{AB} = (3.5 \times 10^{-6}/p)T^{2.334} = 25.6\ \text{cm}^2/\text{s}$,

W_A = molecular weight of gas A

R = the universal gas constant,

T = temperature in K

p = pressure in atm, and

τ = tortuosity which accounts for the "tortuous" pathway of interconnected porosity; nominal value of $1/\varepsilon_i$ based on a random pore model; conservative value of $2/\varepsilon_i$; and $3 \leq \tau \leq 7$ based on experimental data for $\varepsilon_i \geq 0.2$.

For the above representation of D_e it can be shown that D_e increases by a factor of ~500 in making the transition from Knudsen diffusion to ordinary diffusion for the pore radii and porosity fractions considered in this study. As the T_2O partial pressure varies inversely with D_e, we can expect significant differences in results for different assumed microstructures.

The POROUS code,[80] which includes models for ordinary diffusion and pressure diffusion of a binary gas mixture in cylindrical coordinates, was used to investigate the influence of pressure diffusion and temperature gradients. Based on the POROUS results, it was concluded that the fractional rise in total pressure $\Delta P/P_i$ (where P_i is the purge stream pressure) is much less than 1 for the range of variables in this study and that the effect of temperature

gradient on the T_2O partial pressure results is relatively insignificant (<20%) compared to the other uncertainties in this study (e.g., τ and r_p). Thus, the following relationship was derived for the maximum increase in large pore T_2O partial pressure across a unit cylindrical cell of inner radius r_i (purge stream radius) and outer radius r_o (based on the purge stream pitch):

$$\left(P^{\ell}_{T_2O}\right)_{max} = \left(P_{T_2O}\right)_i + \frac{(1/\varepsilon_\ell - 1)R\bar{T}\,\dot{S}(r_o^2 - r_i^2)}{4W_{T_2O}\bar{D}_{e\ell}} f(r_o/r_i) , \quad (6\text{-}13)$$

where

$$f(r_o/r_i) = \left[(1 - r_i^2/r_o^2)^{-1} \ell n(r_o^2/r_i^2)\right] ,$$

$\bar{T}$ = the area-averaged cell temperature in K,

$\bar{D}_{e\ell}$ = the effective diffusion coefficient for large pores at the area-averaged temperature,

W_{T_2O} = molecular weight of T_2O, and

$\left(P_{T_2O}\right)_i$ = the T_2O partial pressure in the purge stream in Pa.

The diffusion of T_2O through the fine porosity and the large porosity of the bimodal structure is characterized by a series model. For diffusion through the fine porosity (transition region) the assumption of isothermal particles and negligible pressure diffusion is even more accurate (<1% error) than for the large pore case. The results presented below are for the particles near r_o at a temperature T_o where the maximum fine pore T_2O partial pressure is expected:

$$\left(P_{T_2O}\right)_{max} = \left(P^{\ell}_{T_2O}\right)_{max} + \frac{(1 - \varepsilon_f)RT_o\dot{S}\,R_p^2}{\varepsilon_{fi} f_{sc} W_{T_2O} D_{efo}} , \quad (6\text{-}14)$$

where

f_{sc} = 6 for a best estimate model of diffusion to the surface of a spherical particle,

= 1/2 for an upper bound estimate based on the diffusion through a cylindrical ring of thickness $2R_p$, and

D_{efo} = the effective diffusion coefficient for fine pores at temperature T_o.

Finally, for the case of fine monolithic pores, the maximum T_2O partial pressure is simply

$$\left(P_{T_2O}\right)_{max} = \left(P_{T_2O}\right)_i + \frac{(1 - \varepsilon)\bar{R}\bar{T}\dot{S}\left(r_o^2 - r_i^2\right)}{4\varepsilon_i \bar{D}_e} f\left(r_o/r_i\right) \qquad (6\text{-}15)$$

where

$\bar{D}_e$ = the effective diffusivity for monolithic pores at the area-averaged temperature.

Two studies were performed based on the equations derived above. In the first study, the DEMO values in Table 6-26 were assumed along with the nominal values of r_o = 13.6 mm, R_p = 0.5 mm, and r_g = 0.25 μm to find a simple relationship between maximum T_2O partial pressure and total porosity. The results for this base case are plotted in Fig. 6-21. Using the upper-bound estimates for conservatism ($\tau_f = 2/\varepsilon_{fi}$, $\tau_\ell = 2/\varepsilon_\ell$, and $f_{sc} = 1/2$), it is clear that both designs satisfy the T_2O partial pressure constraint of 160 Pa for fractional porosities greater than 0.19 (i.e., densities less than 81% TD). However, the bimodal structure certainly has the greater design margin for porosities between 0.19 and 0.4. For total porosity fractions less than 0.19, the fine pores within the bimodal particles are assumed to be isolated.

The second study was concerned with finding the maximum purge stream pitch ($S = \sqrt{\pi}\, r_o$) and particle diameter ($2R_p$) allowed by the 160-Pa limit for the range of porosities and grain sizes under investigation. Because the monolithic $\left(\Delta P_{T_2O}\right)_{max}$ varies as r_o^2 while the bimodal $\left(\Delta P_{T_2O}\right)_{max}$ varies as R_p^2, the two structures could be made to yield comparable values of $\left(\Delta P_{T_2O}\right)_{max}$ by increasing R_p over the nominal value of 0.5 mm and decreasing r_o from the nominal value of 13.6 mm. The issue of which structure is more desirable would then rest upon the issue of which structure is easier to fabricate and more stable under irradiation conditions. Figure 6-22 shows the results of the maximum blanket area $\left(S^2 - \pi r_i^2\right)$ allowed per purge stream for the DEMO Row 1 position as a function of the monolithic structure parameters of grain diameter and porosity fraction. In the most severe monolithic case considered (ε = 0.1, r_g = 0.25 μm), the center-to-center spacing of the purge streams would have to be ~10 mm.

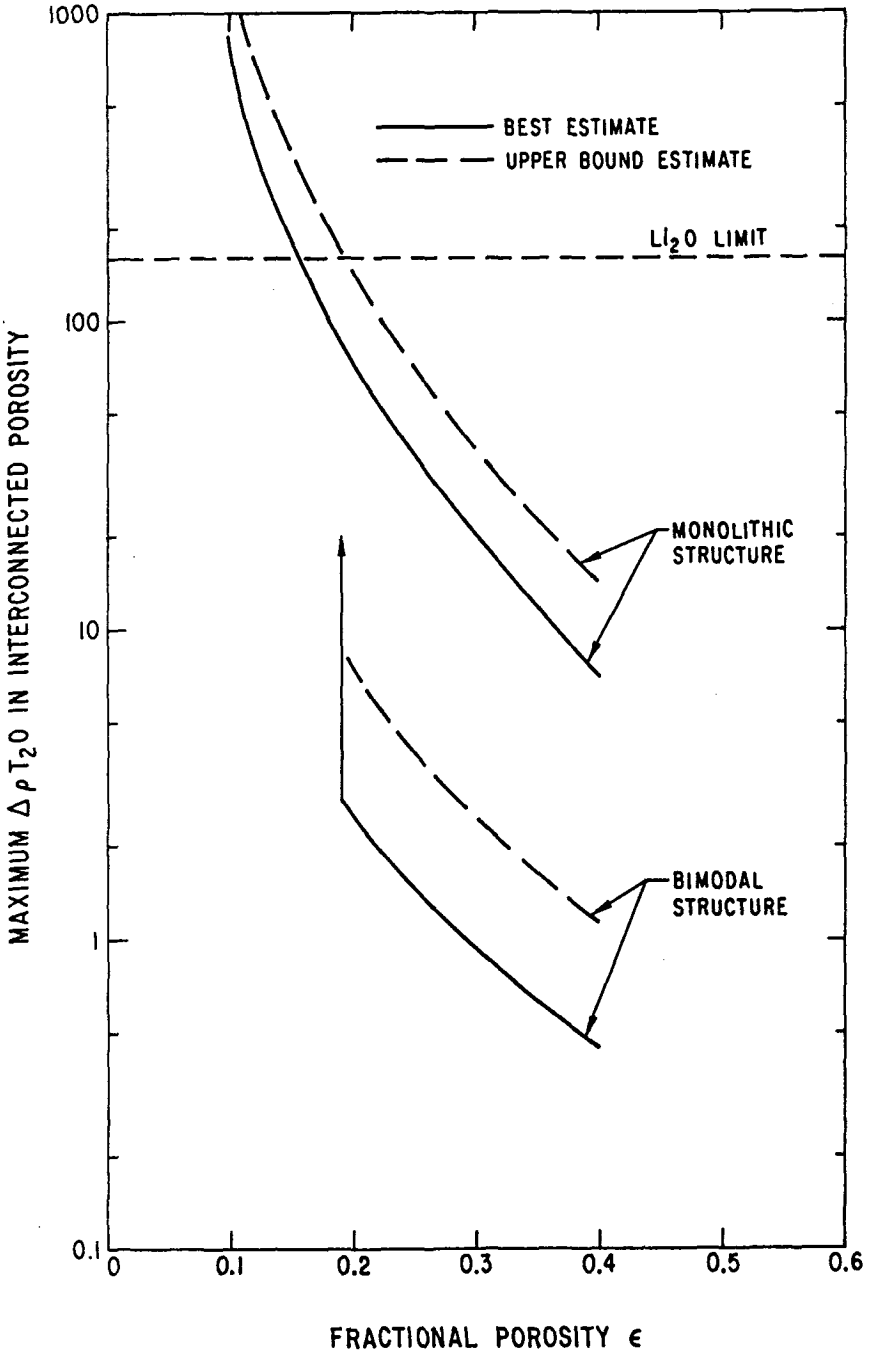

Figure 6-21. Maximum T_2O partial pressure in the DEMO Li_2O blanket near the Row 1 coolant tube position. The base case for the monolithic structure is: grain diameter of 0.5 μm and purge stream center-to-center spacing (pitch) of 24 mm. For the bimodal structure, 0.5 μm grains, 1 mm particles, and 24 mm pitch are assumed.

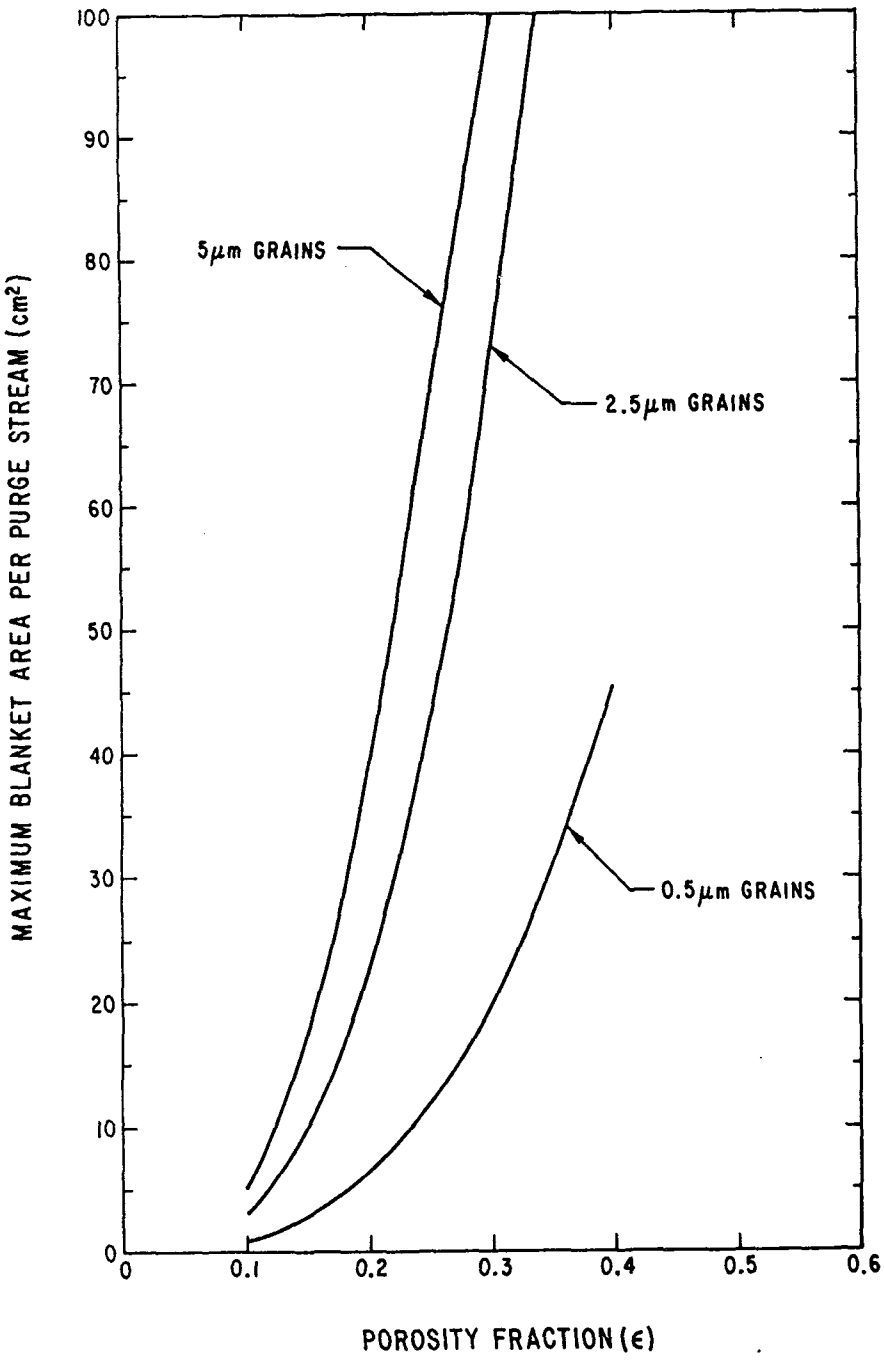

Figure 6-22. Maximum blanket area per purge stream allowed for the monolithic structure to maintain the T_2O partial pressure at a level of $\leq$ 160 Pa. The upper-bound-estimate model with $\tau = 2/\varepsilon_i$ was used for these calculations.

A similar study was done for the bimodal structure by varying R_p from the base case and keeping r_o fixed at 13.6 mm. The results indicated that for particle diameters of less than 6 mm, the T_2O partial pressure would be <160 Pa for all grain diameters (0.5 μm to 5 μm) and porosity fractions (0.19 to 0.4) considered in this study, even with the upper-bound estimates on the tortuousity and geometrical factor f_{sc}.

In summary, the bimodal structure with 1-mm diameter particle sizes has an excellent design margin (maximum T_2O partial pressure of ~10 Pa vs. the 160-Pa Li_2O limit) for all the grain diameters (0.5 μm to 5 μm) and fractional porosities (0.19 to 0.4) considered under the condition that there is one purge stream per coolant tube. The monolithic structure has, in general, a much smaller design margin for a comparable grain diameter and purge stream pitch (see Fig. 6-21). However, by decreasing the purge stream pitch to ~10 mm, the monolithic structure can be fabricated to satisfy the 160-Pa limit for porosity fractions as low as 0.1. Future efforts will concentrate on estimating the stability of these two structures under irradiation conditions and on improving the sophistication of the models to describe the shape and distribution of pores.

While the previous analysis demonstrates that the maximum T_2O partial pressure in the "cold region" interconnected porosity can be maintained at <10 Pa with the bimodal structure, a question still remains as to the maximum concentration of tritium within the grains. An excessive tritium concentration could still precipitate LiOT within the grains of the Li_2O. Assuming spherical grains and solid-state diffusion of tritium within the grains, we can compare the maximum tritium "partial pressure" within the grains to the saturation pressure for LiOT formation (see Fig. 4-29 in Ref. 7). Let $(P_{T_2O})_S$ be the T_2O partial pressure at the surface of the grain. Then the criterion which must be met to avoid precipitation of LiOT within the grains is:

$$\frac{(P_{T_2O})_S + (\Delta P_{T_2O})_G}{(P_{T_2O})_S} < \frac{(P_{T_2O})_{sat}}{(P_{T_2O})_S}, \qquad (6\text{-}16)$$

where

$$(\Delta P_{T_2O})_G = \left(\frac{\dot{S}RT}{W_{T_2O}}\right)\frac{r_g^2}{6D}$$

D = solid-state diffusion coefficient,

and

$(P_{T_2O})_{sat}$ = limiting T_2O partial pressure.

Solving the above equation for r_g gives:

$$r_g < \sqrt{\frac{(P_{T_2O})_{sat} - (P_{T_2O})_S}{RT} \left(\frac{6DW_{T_2O}}{\dot{S}}\right)} \quad . \tag{6-17}$$

Based on the data of Wiswall and Wirsing (see Ref. 56), the solid-state diffusion coefficient for tritium in Li_2O is estimated to be:

$$D = 1.07 \times 10^{-3} \exp(-29{,}340/RT) \ , \quad cm^2/s \ .$$

For example, at the Li_2O minimum allowable design basis temperature of 410°C, $r_g < 1.20$ μm for $(P_{T_2O})_S = 1$ Pa, $r_g < 1.17$ μm for $(P_{T_2O})_S = 10$ Pa, and $r_g < 0.74$ μm for $(P_{T_2O})_S = 100$ Pa. Allowing for uncertainties in the analysis, it is recommended that the grain diameter be ≤ 2 μm to avoid precipitation of LiOT within the grains.

6.4.4.2 Tritium Inventory

The methodology used to estimate tritium inventory in the blanket follows the procedures used for STARFIRE.[1,4,6,56] Selected blanket parameters are summarized in Table 6-27. In the absence of radiation effects, the tritium inventory is assumed to be the sum of the "diffusive" inventory and the "solubility" inventory. Estimates of the tritium inventory and the effects of irradiation are summarized below.

The diffusive inventory was estimated by the methods discussed previously.[1,4,6,56] The approximate temperature distribution was estimated from a thermal calculation using pure conduction with cylindrical geometry.[1] The breeder region is divided into 22 regions of equal volume, represented by nodes numbered 3 to 24 (Table 6-28). The total diffusive inventory is estimated to be about 20 g, over 80% of which is in the coldest 10% of the breeder volume i.e., at temperatures below 470°C.

Table 6-27. Selected Li_2O Blanket Parameters

Blanket Li_2O inventory, metric tonnes	54
T_{min}, °C	410
T_{max}, °C	660
Grain diameter, μm	2
Particle size (bimodal), mm	0.1-1.0
Tritium generation rate, g/s	1.74×10^{-3}
Purge stream T_2O pressure, Pa	1.0
Purge stream LiOT pressure, Pa	1.0×10^{-2}
T_2O generation rate, Pa-liter/s at 650°C	2.2×10^{3}
Tritium breeding rate, g/day	150
Purge stream helium pressure, atm	1 (1.013×10^5 Pa)
Purge stream volume, liters	1000[a]
Purge stream velocity, m/s	12

[a] 2% of blanket volume.

The solubility inventory can be estimated from preliminary experimental data. Assuming that the solubility is proportional to pressure, the results of Tetenbaum[81] extrapolate to 7×10^{-3} wppm tritium at 410°C and 0.12 wppm tritium at 650°C for a T_2O pressure of 1.0 Pa. For comparison, the results of Nasu[70] translate to a tritium solubility of 0.008 wppm at 650°C, for $P(T_2O)$ = 1.0 Pa. In the blanket, the T_2O pressure will increase at regions away from the purge channel, but this effect is compensated for by decreasing solubility at lower temperature. Thus, a reasonable estimate of the solubility is on the order of 0.1 wppm. This translates to a solubility inventory of about 5 g. Thus, in the absence of radiation effects, the total tritium inventory in the blanket is estimated to be about 25 g. This does not account for additional effects caused by engineering uncertainties or power variations that could result in breeder temperatures outside the specified operating temperature limits.

As discussed in STARFIRE,[1] radiation effects (sintering, restructuring, and trapping) can significantly increase tritium inventories in solid breeders. Radiation-induced sintering could result in some pore closure, thereby increasing the T_2O pressure and solubility. For example, a two-order-of-

Table 6-28. Diffusive Tritium Inventory

Node	T (°C)	Tritium Inventory (g)	% of Inventory	Cumulative Inventory (g)	Cumulative (%)
3	430.1	11.3	59.2	11.3	59.2
4	465.4	4.1	21.5	15.4	80.7
5	494.8	1.5	7.9	16.9	88.6
6	519.6	0.70	3.7	17.6	92.2
7	540.9	0.40	2.1	18.0	94.3
8	559.2	0.24	1.3	18.24	95.6
9	575.1	0.16	0.8	18.40	96.4
10	589.0	0.12	0.6	18.52	97.0
11	601.1	0.09	0.5	18.61	97.5
12	611.5	0.07	0.4	18.68	97.9
13	620.6	0.06	0.3	18.74	98.2
14	628.4	0.05	0.26	18.79	98.5
15	635.2	0.04	0.21	18.83	98.7
16	640.9	0.04	0.21	18.87	98.9
17	645.7	0.03	0.16	18.90	99.1
18	649.7	0.03	0.16	18.93	99.2
19	653.1	0.03	0.16	18.96	99.4
20	655.7	0.03	0.16	18.99	99.5
21	657.7	0.03	0.16	19.02	98.6
22	659.1	0.02	0.10	19.04	99.8
23	660.1	0.02	0.10	19.06	99.9
24	660.5	0.02	0.10	19.08	100.0

Cylindrical model: $q''' = 12.94\ W/cm^3$.

$h_g = 0.244\ W/m^2 \cdot K$ (430 $Btu/ft^2\text{-}hr\text{-}°R$) .

Tritium generation rate = 1.74×10^{-3} g/s.

Total tritium inventory = 19.1 g.

magnitude increase in the T_2O pressure would give a tritium concentration of 500 g. An important concern related to this increase in T_2O pressure caused by pore closure is the possibility of exceeding saturation and precipitating LiOT. This could further increase the tritium inventory and possibly lead to liquid phase sintering. Restructuring leading to increased grain size could also increase the diffusive inventory. Since the diffusive inventory will vary as the square of the grain size, a factor of three increase in the grain size as a result of restructuring would produce nearly an order of magnitude increase in the inventory. Although the degree of radiation-induced tritium trapping is highly uncertain, estimates[1,56] based on results from ion

bombardment studies indicate that tritium concentrations of the order of 1 to 20 at-% may occur. Concentrations of this order of magnitude, for example, would lead to unacceptably high tritium inventories of >50 kg. The results of estimates of tritium inventory with and without predicted radiation effects are given in Table 6-29.

Table 6-29. Estimated Tritium Inventory in DEMO Li_2O Blanket

	Without Radiation Effects (g)	Predicted Radiation Effects (kg)
Diffusion	20	0.2 - (>50)
Solubility	5	0.5
TOTAL	25	0.7 - (>50)

Several factors, such as surface desorption of LiOT, that could influence tritium inventory have not been accounted for. Also, chemical effects such as LiOH/LiOT formation and gas phase transport could promote restructuring and sintering, thereby increasing tritium holdup in the blanket.

6.4.5 Thermal-Hydraulics Analyses

The thermal-hydraulics analyses conducted for the DEMO reference Li_2O solid breeder blanket were focused on a number of specific areas: (1) sensitivity of breeder temperatures to key operating and breeder physical parameters (Sec. 6.4.5.1); (2) effects of designing the blanket to accommodate uncertainties and fluence-dependent variations in those parameters (Sec. 6.4.5.2); (3) effects on the blanket design of accommodating large-scale reactor power changes (Sec. 6.4.5.3); (4) helium purge gas flow distribution (Sec. 6.4.5.4).

These analyses in large part used or modified the analytical techniques developed during the STARFIRE blanket thermal-hydraulics analyses[1]. The STARFIRE effort was concentrated on blanket design details (e.g., tube spacings, tube flow parameters), neutron multiplier cooling, responses to off-nominal conditions (e.g., LOCF's), and response to plasma disruptions. Because the DEMO reference blanket concept is similar to that for STARFIRE, it was considered of lesser importance that DEMO reference blanket design details be developed to the depth accomplished for STARFIRE. Therefore, the DEMO analyses were concentrated on several areas of concern identified by the work on STARFIRE as meriting further effort. The results provide added confidence in the feasibility of solid breeder blankets for tokamak power reactors.

6.4.5.1 Sensitivity Studies

Parametric studies were carried out to determine the changes in breeder temperatures with variations in such key blanket parameters as breeder thermal conductivity (k_B), breeder-to-coolant-tube interface heat conductance (h_I), and reactor power level. In addition, differences in calculated breeder temperatures for cylinder cell and rectangular cell analytical models were investigated. The results of these studies and their implications for the reference blanket design are discussed in this section.

The cylindrical blanket-cell model shown schematically in Fig. 6-23(a), was used for most of the scoping studies. Although the temperature distribution in the breeding blanket is three-dimensional, the cylindrical blanket cells permit mathematical simplifications. The assumptions of uniform internal heat generation and invariant material and fluid properties permit the

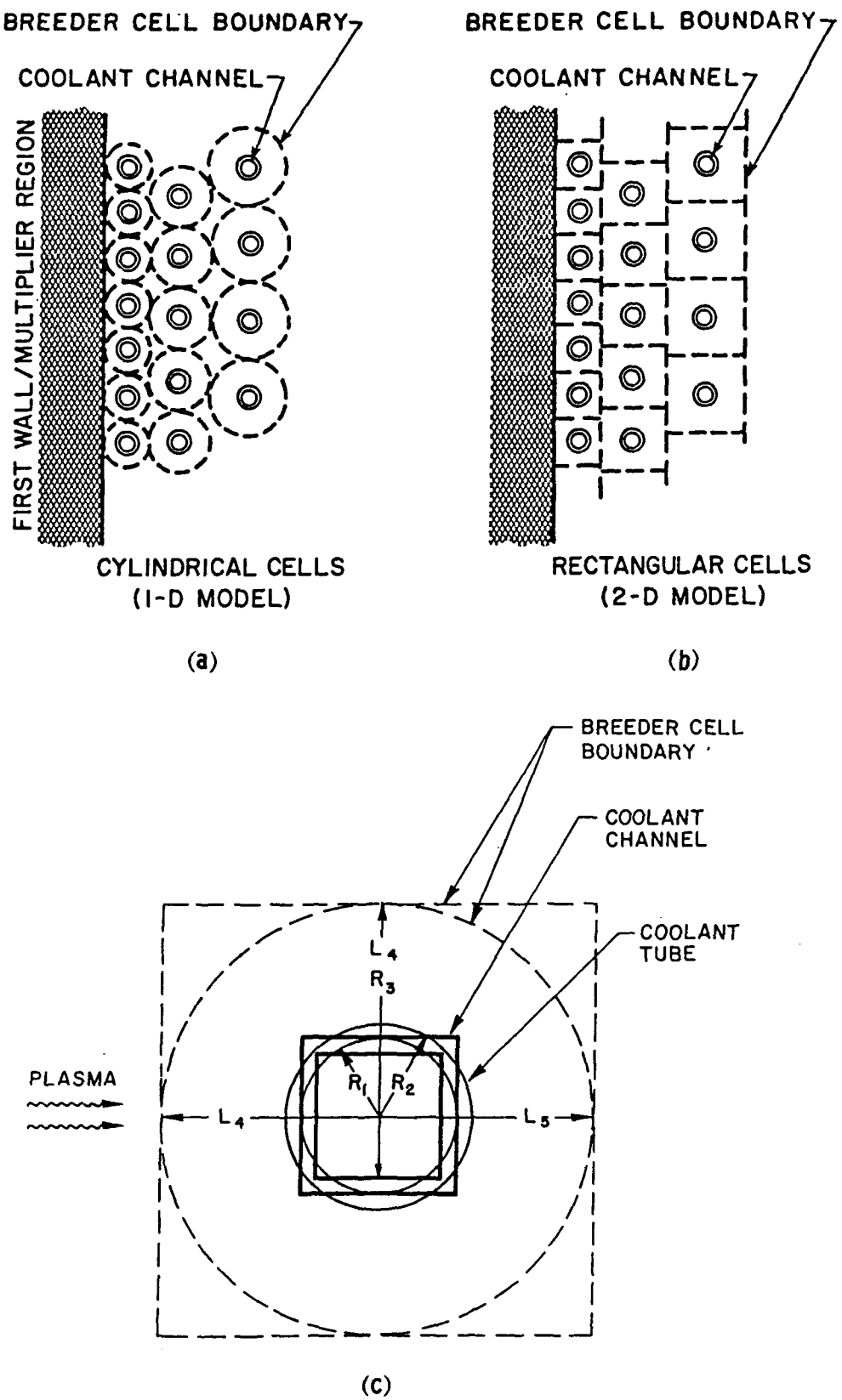

Figure 6-23. Schematics of cylindrical and rectangular cell models.

governing equations to be solved in closed form. Thus, a large number of parametric investigations can be conducted with a limited amount of effort.

Table 6-30 lists the important geometrical and operating parameters adopted for these studies. As indicated, three separate blanket regions with

Table 6-30. Summary of Blanket Parameters Used in Thermal-Hydraulics Calculations

Maximum allowable operating temperature for Li_2O	660°C
Minimum allowable operating temperature for Li_2O	410°C
Coolant inlet temperature	260°C
Coolant outlet temperature	300°C
Coolant pressure	11.0 Mpa
Integrated neutron wall load (average)	1.8 MW/m^2
Neutron heating rate in Li_2O (% of peak power level)	
Region 1, near first wall	12.94 W/cc (100%)
Region 2, central breeding zone	3.33 (25%)
Region 3, near back wall	0.47 (4%)

largely differing nuclear heating rates were investigated. For each region, constant zone-averaged nuclear heating rate values were assumed. Although not all parameter values are identical with those of the final reference design (e.g., coolant pressure, integrated neutron wall loading) the results of the studies are applicable.

Sensitivity to Breeder Thermal Conductivity

In the first part of this study (described in more detail in Ref. 7), a series of parametric analyses were carried out to determine the sensitivity of breeder temperature to minor variations in breeder thermal conductivity, k_B. The reference case assumed the temperature dependent k_B values given in Sec. 6.4.3 for Li_2O (at 70% of theoretical density) over the temperature range of 410-660°C. Variations of ±10% in these thermal conductivity values resulted in breeder maximum and minimum temperature variations of 25-35°C, a significant fraction of the allowable range. This indicates the importance to the

blanket design of achieving a high degree of predictability and repeatability in thermal conductivity values of fabricated breeder.

In the second part of the study, a parametric investigation was carried out covering a much wider range of k_B values, from 3 W/m-K for the higher conductivity solid breeders such as Li_2O to 1 W/m-K for the lower conductivity solid breeders such as Li_2ZrO_3. The breeder region radius and the required breeder/tube interface conductance values for various power factors (100% to 5% of maximum power) were calculated for these values. The results are summarized in Figs. 6-24 and 6-25. In the first figure, coolant tube structural material and coolant volume fractions are plotted against k_B for various power fraction values. There is a maximum decrease of 11% in breeder volume at the first wall (i.e., 100% power region) as k_B varies from 3 to 1 W/m-K; this decrease is only ~ 2% near the back of the blanket. Thus, when the thermal conductivity of the breeder is decreased from 3 to 1 W/m-K, the overall breeder volume is expected to decrease on the average of about 7%. For the k_B values examined, the breeder tube interface conductance values required in the blanket vary by approximately a factor of four (see Fig. 6-25) from the region near the first wall to the region near the reflector/shield. However, the absolute values of required gap conductance at a given power level decrease sharply with conductivity, which reflects the reduced heat flux across the breeder/tube interface resulting from the smaller breeder cell sizes (diameters) permitted for the lower conductivities.

Sensitivity to Breeder-to-Tube Heat Conductance

One of the greatest challenges today in the design of solid breeder blankets is to maintain breeder operating temperatures within the design basis upper and lower temperature bounds. Since the breeder minimum allowable temperature is significantly higher than the coolant inlet and outlet temperatures, an artificial thermal barrier between the coolant-carrying structure (tubes) and the solid breeder is necessary to modify the temperature distribution within the solid breeder. It is important to be able to predict the performance (heat conductance value) of this thermal barrier within acceptable limits, principally because of the combination of low breeder k_B values and narrow allowable temperature ranges for candidate solid breeders. A further difficulty is that interface conductance values (h_I) needed to keep the

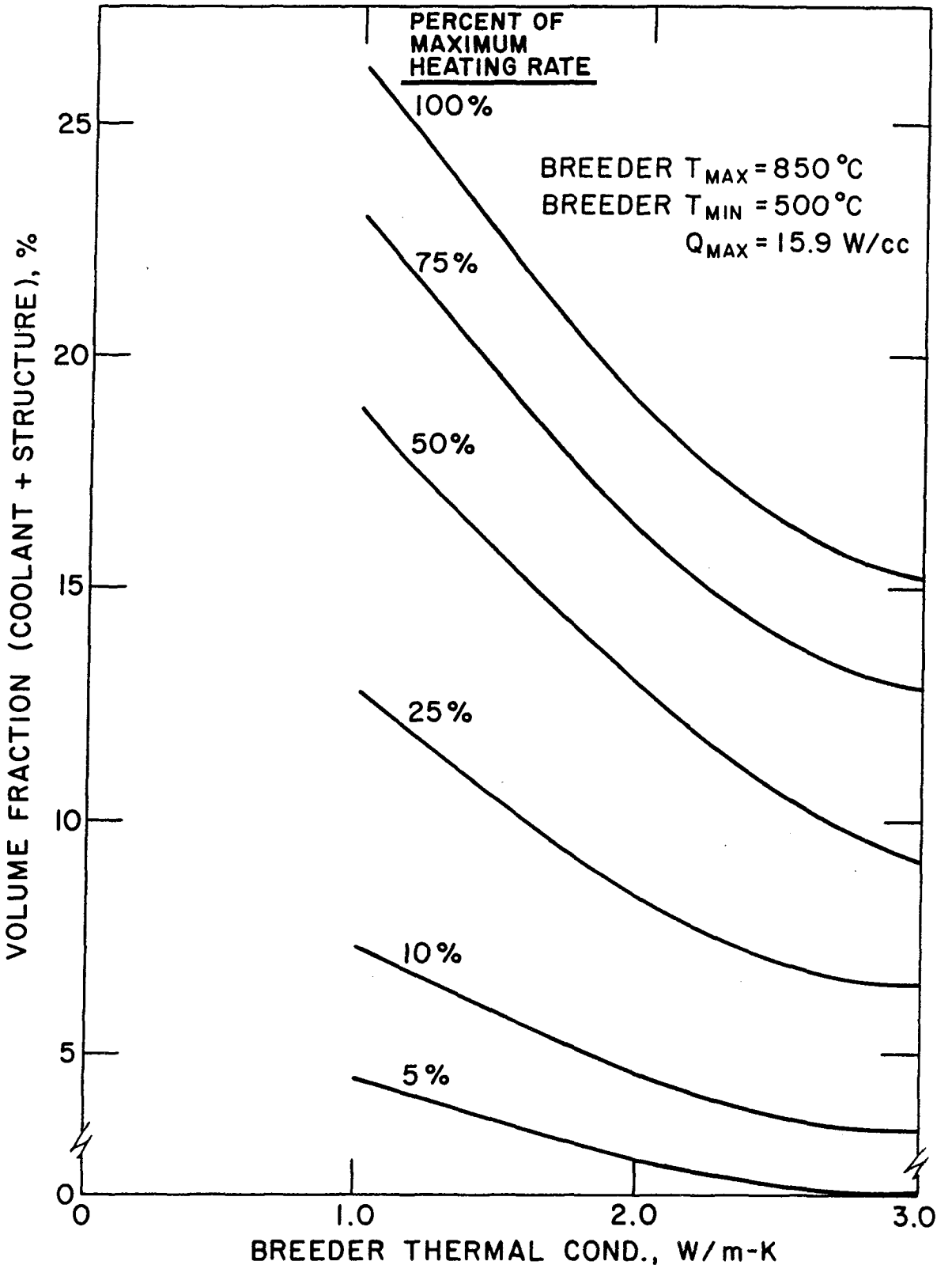

Figure 6-24. Coolant and structure volume fraction as a function of breeder thermal conductivity.

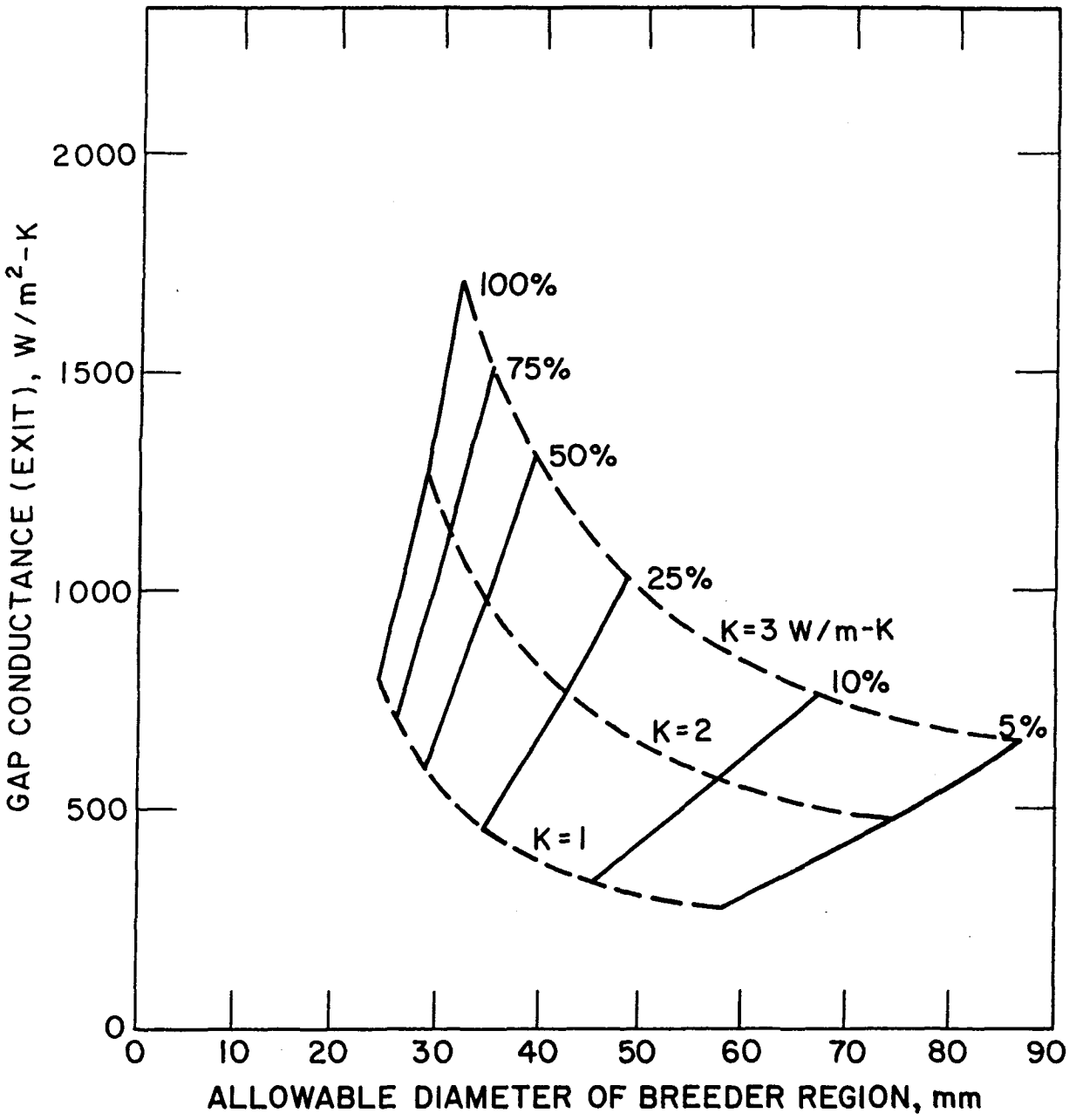

Figure 6-25. Breeder-to-tube interface heat conductance as a function of breeder region diameter, breeder thermal conductivity, and power factor.

breeder temperatures within the allowable range vary widely from the front to the rear of the blanket. Analyses using the cylindrical cell model show that these required h_I values vary from ~ 2500 to ~ 600 W/m-K through the blanket depth (Fig. 6-25). Also, the required conductance value must increase by 50% along the length of any given blanket coolant tube, to accommodate the coolant temperature increase of 40°C.

The sensitivity of breeder temperature distribution to uncertainties or variations in the interface heat conductance is indicated in Fig. 6-26. This

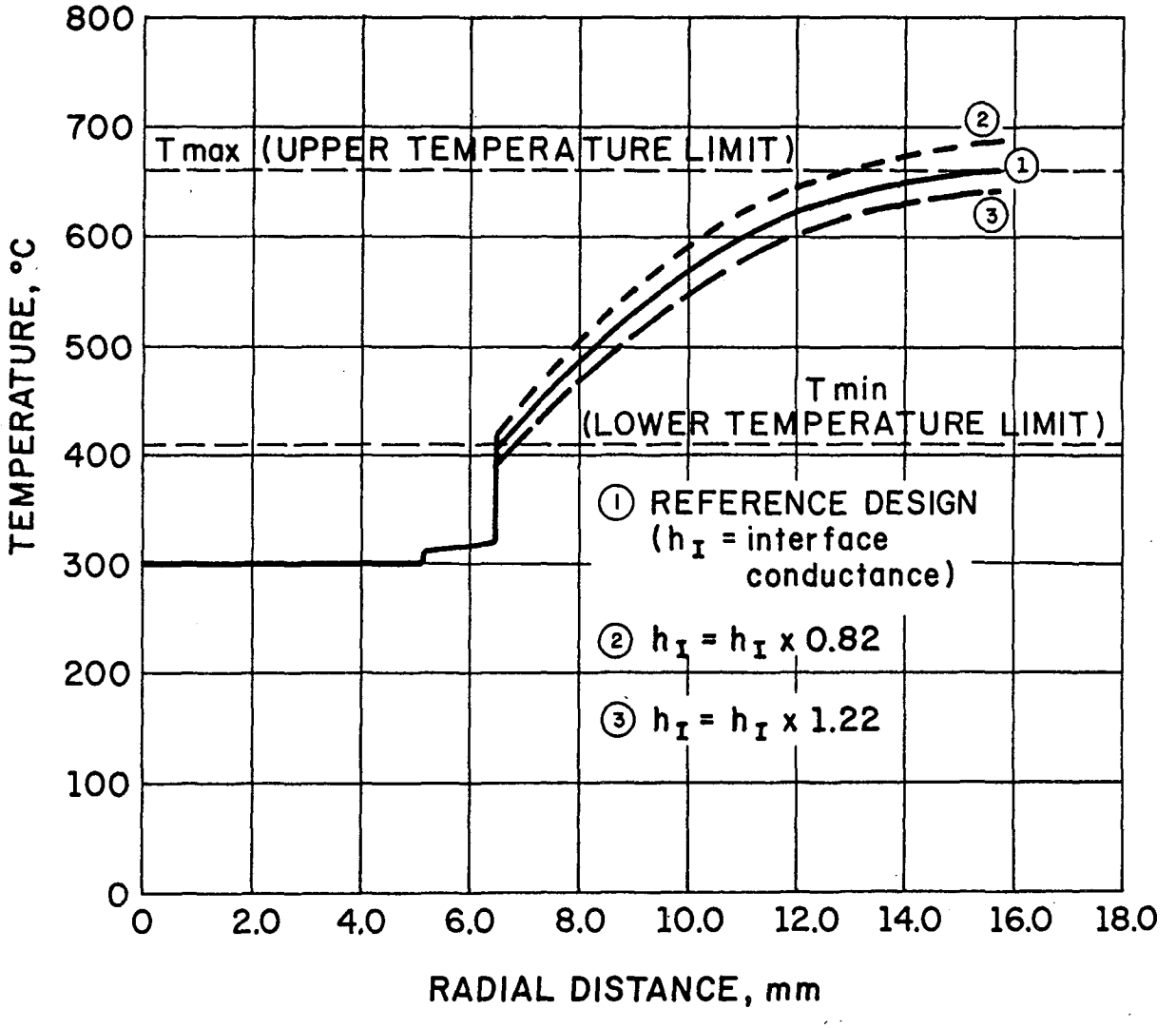

Figure 6-26. Temperature distribution in breeder as a function of interface heat conductance (cylindrical cell model).

figure shows the results of studies performed for DEMO[7] which assumed a ceramic insulator at the interface. Variation of the reference case h_I value by -18% and +22% were assumed; the figure shows the resulting breeder temperature distributions, as well as the reference case. The difference in maximum temperature between these two cases and the reference design is ~ +30°C and -26°C, respectively. For the -18% case, only a very small volume fraction of the cell is below the minimum temperature limit. However, for the +22% case a

significant fraction of the breeder region is above the maximum temperature limit. This indicates that even uncertainties in h_I as low as ~ ±20% can have adverse effects on the blanket design.

Sensitivity to Power Level Fluctuations

For this analysis, the case of modest power level fluctuations of ~ ±10% from the reference power levels was analyzed under steady-state operating conditions. The results indicated[7] that even a modest fluctuation in power level can lead to rather large variations in the maximum operating temperature. Varying the power level by -10% and +10% from the reference case value resulted in changes in breeder maximum temperature of -48°C and +49°C, respectively, and changes in breeder minimum temperature of +11°C and -17°C, respectively. The high temperature excursions in breeder temperature are of particular concern, since irreversible damage to part of the breeder could result from extended operation at such temperatures ($\gtrsim$ 700°C).

Rectangular Cell Analytical Model

Although the 1-D cylindrical cell model permits simplified and rapid parametric studies, it has several drawbacks for use in determining realistic temperature distributions in the blanket. Primarily, the model does not account for (1) non-uniform nuclear heat generation, (2) heat transfer among cells, or (3) the breeder regions which are surrounded by cells but are not included within any cell boundary.

A rectangular cell model is being developed to overcome these disadvantages. The cylindrical cell and rectangular cell models are shown schematically in Fig. 6-23. Unlike the cylindrical cells, there are no breeder regions outside the rectangular cell boundary; hence, there are no uncooled regions and all of the breeder volume can be accounted for by the individual blanket cells. The helium purge gas channels can be located appropriately to accommodate tritium extraction. For analytical simplicity, the coolant channels are assumed to be square. At the present stage of development, the outer boundary of each blanket cell is assumed to represent an insulated boundary (i.e., no heat transfer among cells). A three-dimensional heat conduction code capable of using temperature-dependent material properties, non-uniform heat flux, convective heat transfer in the coolant channels, and contact resistance

between dissimilar materials is used for thermal hydraulic analysis. Figure 6-23(c) shows a typical mathematical model of a rectangular blanket cell.

The differences in cell size resulting from calculations using cylindrical and rectangular cell models with the associated codes are shown in Table 6-31. The dimensions of the rectangular cell were calculated by an iteration process for each of the three regions, such that breeder minimum and maximum temperatures nearly matched the 410°C and 660°C design basis limits. For the rectangular cell model, the variation of the nuclear heating rate with depth across each cell was considered. The effect of the non-uniform heating rate is to slightly offset the coolant channel towards the side of the cell nearest the plasma. This is due to the slightly higher heating rates in the breeder nearer the plasma in each cell as compared to the rates in the breeder further away from the plasma. The rectangular cell area is smaller than the cylindrical cell area for each region, which indicates the reduction in tube spacing for the blanket that is necessary in order to preclude breeder regions with temperatures above 660°C. This is also reflected by cell width and height dimensions $2L_5$ and $2L_6$, which for each region are smaller than the cylindrical cell diameter ($2 \times R_3$).

Further development of the rectangular cell model is planned which will incorporate multiple cells, both poloidally and depthwise, and which will account for heat flow between adjacent cells. The use of this model in blanket thermal hydraulics studies will provide more realistic guidance for determining blanket parameters, in particular, coolant tube spacing and breeder temperature distribution.

6.4.5.2 Accommodation of Variations and Uncertainties in Design Parameters

Tritium breeding blankets for power reactors should be designed to maintain blanket performance characteristics within design guidelines for all anticipated values of operating and design parameters. For the DEMO blanket, this requires primarily that breeder temperatures be maintained within minimum and maximum temperature limits (as established by materials behavior considerations) upon reaching steady-state reactor conditions.

The parameters which most strongly influence the breeder temperatures in DEMO for the reference blanket concept are power density (as measured by nuclear heating rate, $\dot{q}$, in W/cc), breeder thermal conductivity (k_B, in

Table 6-31. Comparison of Results of Calculations Using Cylindrical and Rectangular Cell Models

Geometrical and Physical Parameters	Cylindrical Cell[a]			Rectangular Cell[b]		
	Regions			Regions		
	1	2	3	1	2	3
R_1, $2L_1$, mm	5.1	5.1	5.1	9.08	9.08	9.08
R_2, $2L_2$, mm	6.35	6.35	6.35	11.54	11.54	11.54
R_3, mm	15.7	23.7	47.0	-	-	-
$2L_5$ x $2L_4$, mm	-	-	-	25.65 x 26.96	39.54 x 41.57	78.26 x 78.26
Cell Area, $(mm)^2$	774	1764	6939	675	1603	6124
Vol. % Coolant	10.6	4.6	1.2	11.8	5.0	1.3
Vol. % Clad	5.8	2.5	0.7	7.4	3.1	0.9
H_I @ Inlet, W/m^2-K	1704	994	596	1278	795	443
H_I @ Outlet, W/m^2-K	2442	1420	852	1846	1136	625
T_{max}, °C	661	660	661	660	662	661
T_{min}, °C	415	416	415	407	404	401

[a]Heating rates assumed constant for each region.

[b]Heating rates assumed to vary with depth throughout each region.

NOTE: The length parameters are the appropriate radii for the cylindrical model and the sides of the rectangle for the slab model. (See Fig. 6-23)

W/m-K), and breeder-to-tube interface heat conductance (h_I, in W/m^2-K). For each of these parameters, estimates were made of (1) the variation of the nominal value with fluence from 0 to 10 MW-yr/m^2, and (2) the anticipated uncertainty in the nominal value at any fluence.

The analysis described in this section was performed in deriving the DEMO reference blanket design which would meet operating performance requirements over the DEMO blanket design lifetime. The equations governing breeder temperatures--the key operating parameter--were used in determining temperature distributions for various combinations of estimated (1) nominal design parameters and (2) their associated uncertainties. Those estimates and the results of the analyses are discussed below.

Method of Analysis

The simplified thermal-hydraulics cylindrical cell theoretical model described in Sec. 6.4.5.1 was used. The equations which describe the temperature gradient across the entire model for any axial location are summarized as follows:

$$T_3 - T_0 = (\Delta T)_B + (\Delta T)_I + (\Delta T)_{FT} \tag{6-18}$$

$$(\Delta T)_B = T_3 - T_2 = [\ddot{q}/K_B]\,[f_B\,(R_3, R_2)] \tag{6-19}$$

$$(\Delta_T)_I = T_2 - T_1 = [\ddot{q}/h_I]\,[f_I\,(R_3, R_2)] \tag{6-20}$$

$$(\Delta T)_{FT} = T_1 - T_0 = \ddot{q}\,[f_{FT}\,(R_3, R_2, R_1, R_0, K_S, h_F)] \tag{6-21}$$

where

T_i = temperature at points in model cross section, °C (see Fig. 6-23(a)).

$\ddot{q}$ = local nuclear heating rate in breeder, W/cc

$K_{B,S}$ = thermal conductivities of breeder (B) and steel tube (S)

$h_{I,F}$ = thermal conductances across breeder-to-tube interface (I) and across laminar coolant film (F)

$(\Delta T)_{B,I,FT}$ = temperature differences across breeder, °C

$f_{B,I,FT}$ = various functions of modeling geometry, etc.

Two further approximations were made to simplify the analysis: (1) $\ddot{q}_B$ was assumed the only source of heating (i.e., no nuclear heating of steel or

water); (2) h_F was empirically determined from previous work as a function of flow velocity for a fixed tube inside diameter of 10.0 mm.

Parameter Variations and Uncertainties

The most influential non-geometric parameters in the preceding equations are $\ddot{q}$, K_B and h_I. Of these, only k_B was estimated to vary significantly with fluence. The nominal nuclear heating rate, $\ddot{q}$, was taken as a fixed value over the DEMO blanket life for this analysis; the effect of large-scale reactor power changes is discussed in Sec. 6.4.5.3. Interface conductance, h_I, was also estimated not to vary significantly with fluence, for the method and materials proposed for the interface in DEMO (see below).

For $\ddot{q}$, the variation between predicted and actual power density (wall load) at a given point, attainable for the DEMO timeframe, was estimated to be ±5%. This does not include allowance for deliberate reactor power level variations, but is however intended to apply to the nominal predicted wall load value at any time.

The estimated variation in k_B for fluence up to the equivalent of 10 MW^2-yr/m^2 is shown in Figs. 6-16 and 6-17. The reduction in k_B with fluence is estimated (Sec. 6.4.3) to saturate to a steady-state level at ~ 3×10^{25} n/m^2, roughly equivalent to 0.2 MW-yr/m^2 at the first wall, and to maintain that level as fluence accumulates to 10 MW-yr/m^2. The uncertainty in the nominal value of k_B at any given fluence was judged to be ± 10%. The effects of other possible bulk material property changes such as densification were not considered.

The breeder-to-tube interface proposed for DEMO uses a metallic felt as the interface medium, metallurgically bonded to the breeder and tube. This approach avoids the much larger uncertainties inherent in the thermal conductance value over the blanket lifetime of a breeder-to-tube interface maintained only through mechanically-applied contact pressure in a helium environment or through a helium-filled gap of finite width. The interface medium is a state-of-the-art product, for which thermal conductance values are estimated to vary locally (i.e., the average for any one square centimeter) by ±15% or less from the nominal value desired. (The uncertainty is proportionately less as the area increases over which the average value is measured.) Uncertainties and

variations in h_I due to any changes in the metallurgical bond with fluence over the blanket life were estimated to not be significant.

Results

An iterative technique was employed to determine the combination of R_3 and h_I which satisfied all of the following three criteria for any combination of design parameter variations and uncertainties:

$$(\Delta T)_B + (\Delta T)_I + (\Delta T)_{FT} < 360^0C \quad (6\text{-}22)$$

$$(\Delta T)_I + (\Delta T)_{FT} > 110^0C \quad (6\text{-}23)$$

$$(\Delta T)_B < 250^0C \quad (6\text{-}24)$$

All three criteria relate to the 300°C coolant outlet temperature for DEMO, and to the 410°C and 660°C T_{min} and T_{max} limits established for Li_2O. The first criteria ensures that breeder maximum temperature is always $\leq$ 660°C. The second criteria ensures that breeder minimum temperature is always $\leq$ 410°C. The third criteria ensures that the 250°C breeder maximum allowable temperature range is not violated; the criteria is automatically satisfied when the first two have been met. The largest value of R_3 (i.e., the largest volume of breeder) that satisfies all criteria is determined by substituting the worst-case parameters producing maximum ΔT values (listed in Table 6-32) into the first criteria, and substituting the parameters producing minimum ΔT values into the second criteria. The value of R_3 may then be iterated until both criteria are satisfied exactly.

Table 6-33 lists the results obtained from the analysis for three blanket regions having different nuclear heating rates (Case 2). For comparison, the results are also shown for Region 1 (highest $\ddot{q}$) of a blanket designed only for nominal zero-fluence design parameter values, with no variations or uncertainties (Case 1). Comparison of the two cases for Region 1 shows the effects of reducing the breeder cylinder outside radius and changing the nominal h_I value, to keep breeder temperatures within limits for all combinations of variations and uncertainties. The volume percentages of water and steel increase by several percent, relative to the breeder. The breeding ratio (1-D

Table 6-32. Worst-Case Combinations Of Variations and Uncertainties in Blanket Design Parameters.[a]

Temperature difference	Maximum value results from:	Minimum value results from:
$(\Delta T)_B$	$+\Delta\ddot{q}$	$-\Delta\ddot{q}$
	$-\Delta K_B$	$+\Delta K_B$
$(\Delta T)_I$	$+\Delta\ddot{q}$	$-\Delta\ddot{q}$
	$-\Delta h_I$	$+\Delta h_I$
$(\Delta T)_{FT}$	$+\Delta\ddot{q}$	$-\Delta\ddot{q}$

[a]See text for explanation of symbols and equations for ΔT.

ANISN calculations, 100% coverage) is reduced approximately from 1.23 to 1.18, assuming a blanket 68 cm thick behind a water and steel first wall ~ 2 cm thick. It should be noted that the ΔT values for Case 1 exactly satisfy all three criteria, a truly optimum design in terms of maximizing breeder volume. In the more realistic Case 2, however, the first and second criteria can be satisfied exactly only for the worst-case maximum and worst-case minimum ΔT values, respectively. The Case 2 blanket geometry was adopted for the DEMO blanket.

6.4.5.3 Methods to Accommodate Power Large-Scale Variations in Blankets

The analyses described in this section were performed to determine for information only how the DEMO reference blanket design could be changed to permit large-scale variations in reactor power level during operation while keeping blanket performance characteristics within design guidelines.

Tritium breeding blankets in fusion power reactors will probably be required to accommodate minor and large-scale variations in power density (as measured at the plasma chamber surface, in MW/m^2) that may arise during operation. Minor differences will arise between analytically predicted nominal power levels and those actually experienced (measured) in the reactor during

Table 6-33. Effects of Accommodating Variations and Uncertainties in Key Blanket Design Parameters[a]

	CASE NO.	1[b]	2[c]		
	BLANKET REGION	1	1	2	3
	q, NUCLEAR HEATING RATE (W/cc)	12.94	12.94	3.33	0.47
	R_0 (mm)	5.0	→		5.0
	R_1 (mm)	6.25	→		6.25
	R_2 (mm)	7.25	→		7.25
	R_3 (mm)	16.6	13.6	18.95	33.0
	a (Lateral Spacing = 2 x R_3) (mm)	33.2	27.2	37.9	70.00
	b (Vertical Spacing = .9 x a) (mm)	29.88	24.48	34.1	63.0
CLNT	A_C (πR_0^2) (mm^2)	78.54	→		78.54
CLNT	$(t_{EQ})_C = A_C/a$ (mm)	2.37	2.87	2.1	1.1
TUBE	A_T ($\pi[R_1^2 - R_0^2]$) (mm^2)	44.17	→		44.17
TUBE	$(t_{EQ})_{STL} = A_t/a$ (mm)	1.33	1.62	1.1	0.6
INTERFACE	A_I ($\pi[R_2^2 - R_1^2]$) (mm^2)	42.41	→		42.41
INTERFACE	$(t_{EQ})_{He} = (A_I/a) \times .3$ (mm)	.38	0.47	0.3	0.2
INTERFACE	$(t_{EQ})_{STL} = (A_I/a) \times .7$ (mm)	.89	1.09	0.8	0.4
BREEDER	A_B ($\pi[R_3^2 - R_2^2]$) (mm^2)	700.57	415.9	963.0	3683.
BREEDER	$(t_{EQ})_B = A_B/a$ (at 70% T.D.) (mm)	21.1	15.3	25.4	52.6
t_{EQ}	$(t_{EQ})_{STL}$ (mm)	1.71	2.09	1.4	0.8
t_{EQ}	$(t_{EQ})_C$ (mm)	2.37	2.87	2.1	1.1
t_{EQ}	$(t_{EQ})_{He}$ (mm)	11.03	8.81	12.8	24.3
t_{EQ}	$(t_{EQ})_B$ (at 100% T.D.) (mm)	14.77	10.71	17.8	36.8
%V	%V STL ($[t_{EQ}/b] \times 100$)	5.7	8.5	4.1	1.3
%V	%V CLNT	7.9	11.7	6.2	1.7
%V	%V He	15.8	17.3	15.2	13.5
%V	%V Li_2O (at 70% T.D.)	70.6	62.5	74.5	83.5
	WORST-CASE MAXIMUM TEMPS (°C)				
	$(\Delta T)_B$	250	210	207	205
	$(\Delta T)_I$	49	109	119	128
	$(\Delta T)_{FT}$	61	40	33	27
	TOTAL ΔT	360	359	359	360
	WORST-CASE MINIMUM TEMPS (°C)				
	$(\Delta T)_B$	250	93	92	91
	$(\Delta T)_I$	49	73	80	86
	$(\Delta T)_{FT}$	61	38	31	26
	TOTAL ΔT	360	204	203	203
	1-D BREEDING RATIO	1.23	← 1.18 →		

[a] F= (maximum power)/(minimum power) = 1.0 (all cases). Maximum power density = 2.0 MW/m^2 (all cases).

[b] No variations or uncertainties in blanket design parameters; nominal zero-fluence values only.

[c] Current DEMO reference blanket design (see text).

operation. Two principal reasons would be (1) the inability to predict beforehand exactly how power density will vary poloidally around the chamber, and (2) slight changes in plasma power level and the plasma position, due both to control sensitivities and to the desire of the operators to make changes. Major long-term changes in blanket power density are assumed to occur only as the result of deliberate choices by the operators. A possible reason to accommodate changing load requirements in the grid (utility network) or to continue operating at reduced power in an off-normal situation (e.g., following failure or reduction in capability of a key component) until a more convenient time for reactor shutdown and maintenance is reached.

The remainder of this section describes the evaluation of various methods for accommodating power density changes in power reactor and blankets. For the DEMO reference blanket, the key design requirement is that the breeder temperatures be maintained at all times within the 410°C minimum and 660°C maximum limits, a range of 250°C. Therefore, all options are discussed below in terms of how and to what extent they can be used to accommodate power density changes without violating those temperature limits. The options are categorized as active or passive, in terms of the operator's ability to make changes in order to accommodate power density variations while the reactor continues to operate.

Active Methods

Previous studies of solid breeder blankets have identified two possible active methods for breeder temperature control: (1) changing gas pressure in a helium-filled gap control thermal conductance of the breeder-to-tube interface; (2) changing coolant temperatures.

The use of a helium gap at the breeder/tube interface has been considered previously. Changes in h_I of several orders of magnitude can be effected for a small-width helium-filled gap by varying the pressure of the helium within approximately the range 10^{-1} - 10^{1} Pa (roughly 10^{-3} - 10^{-1} torr). Outside this range, even several orders-of-magnitude pressure changes have little effect on thermal conductance across the gap. However, the pressures in the range required for h_I control are much lower than the nominal pressure (~ 10^{5} MPa, 1 atm) of the helium purge gas flowing through the DEMO solid breeder.

If the helium in the gap is the tritium purge helium, then reducing its pressure to the 10^{-1} - 10^{1} Pa range could result in helium mass flowrates in the blanket inadequate to remove the tritium at steady-state rates with acceptably low blanket tritium inventories. Operating the blanket in this manner for extended periods would therefore require that tritium for fueling be obtained from some source other than the blanket.

A second design approach to a helium gap involves the use of a double wall tube (DWT) with helium filling the narrow gap between the inner and outer tubes. The coolant can be contained by the inner tube with the breeder surrounding the outer tube, or vice versa. The breeder-to-coolant temperature difference would be controlled primarily as a function of the helium gap conductance. Thus, by changing the (static) helium pressure in the annulus within the 10^{-1} - 10^{1} Pa range, the breeder temperatures can be kept within their limits and the total temperature drop ($T_3 - T_0$) can be maintained relatively constant as power density changes over a relatively wide range. However, this approach has a fundamental disadvantage for power reactors such as DEMO: There are significant additional temperature increases introduced across the second tube wall, and across the annulus even at helium pressures of 0.1 MPa. For DEMO power densities near the front of the blanket, the temperature increase across the annulus is ~ 60^{0}C for each 0.1 mm (.004 in.) of gap width, at 1 atm pressure of He. For minimum gap widths considered reasonable for fabrication, and assuming DEMO coolant temperatures (300°C outlet), combining these additional temperature increases to the $(\Delta T)_{FT}$ which already exists across the coolant film and the first tube results in a minimum breeder temperature well above 410°C. This new temperature in effect becomes the design lower limit for breeder temperatures, reducing the design allowable breeder temperature range to a value much lower than the 250°C allowable range based on materials/tritium recovery considerations alone.

Coolant temperatures can in theory be varied during reactor operation to accommodate power density changes. Examination of Eqs. (6-19), (6-20), and (6-21) in Sec. 6.4.5.2 for $(\Delta T)_B$, $(\Delta T)_I$, and $(\Delta T)_{FT}$ shows that all three are linear with nuclear heating rate, $\dddot{q}$. If the blanket is designed to operate at the highest $\dddot{q}$ value (e.g., 1.33 x $\dddot{q}_{nom}$) with the coolant at its lowest temperature, then for the lowest $\dddot{q}$ value (e.g., 0.67 x $\dddot{q}_{nom}$) coolant temperatures can be increased as needed to keep breeder temperatures within the T_{min} and

T_{max} limits. The blanket in this example would permit a maximum power density change of F = 2, where F = maximum power/minimum power. (Coolant flowrate may also require adjustment.)

However, this method cannot be used to accommodate significant reactor power changes for power reactor blankets using water coolant, because the outlet coolant temperature would already be approximately in the 280°C-320°C range to obtain good thermal conversion efficiency for normal (i.e., peak power) operating conditions. Only small increases in coolant temperature would therefore be permissible to accommodate power density reductions, and those increases would be coupled with large increases in coolant system pressure. Changing the coolant temperature was therefore not considered for the DEMO Li_2O blanket.

Passive Methods

As defined here, passive methods for accommodation of power density changes are those which require only changes in the blanket design and for which no operator actions to change blanket conditions are required.

Because both maximum and minimum temperature limits are imposed on the Li_2O breeder, the only design change presently considered viable is to further increase the design breeder design minimum temperature value and/or to further decrease the breeder design maximum temperature value. This reduction in the breeder design temperature range has the effect of further reducing the allowable breeder cylinder outside radius (R_3 for the model in Fig. 6-23). In the actual blanket, this means the coolant tube spacing would be reduced which further reduces the blanket tritium breeding ratio, since the percent volume of steel and water in the blanket is increased relative to that of the breeder.

A parametric evaluation was performed to determine the effects of incorporating the capabilitity to accommodate various levels of power factor changes into the reference DEMO Li_2O blanket concept. The cylindrical model and equations previously described were used. The reference blanket for this analysis, as described in Sec. 6.4.5.2, is designed to accommodate all estimated variations in the nominal value of k_B with fluence over the blanket life, as well as uncertainties in k_B (± 10%), h_I (± 15%), and local power density (± 5%); no variation in reactor power level is assumed. The resulting

blanket thus has nominal design values for lowest and highest breeder temperatures which are higher and lower respectively than the 410°C T_{min} and 660°C T_{max} design basis limits set by materials considerations.

Table 6-34 lists the analysis results, some of which are shown graphically in Fig. 6-27. For each case, R_3 and h_I were adjusted to accommodate the associated power factor change without violating the breeder temperature limits (T_{min} = 410°C and T_{max} = 600°C) for any combination of uncertainties and variations in blanket key design parameters. Differences between Case 1 and Case 2 show the changes required to accommodate the design parameter variations and uncertainties. Case 1 assumes that no variations and no uncertainties occur over the life of the reactor; Case 2 is the more realistic DEMO reference blanket design. Cases 3 through 7 are the same as the Case 2 reference blanket except that reactor power is varied by factors (F) of 1.2 to 2.0. For all cases, the highest reactor power corresponds to a wall loading of 2.0 MW/m^2. Thus, for example, in Case 7 (F = 2) the highest reactor power is twice the value of the lowest reactor power (P_{nw} = 1.0 MW/m^2). The ± 5% uncertainty in local power density was applied to both extremes.

Tritium breeding ratios shown for Cases 1 and 2 are based on 1-D ANISN calculations assuming 100% coverage in the reactor. Breeding ratios shown for Cases 3 through 7 are rough extrapolated estimates, are not based on neutronics analyses, and are for illustrative purposes only. The reduction in breeding ratio (1-D basis) associated with changing the DEMO reference blanket (Case 2) to accommodate a factor of 2 capability for reactor power changes (Case 7) is estimated to be approximately 0.08. The actual reduction in net breeding ratio (3-D basis) is very dependent on the actual blanket design, and would also vary significantly with changes in reactor design assumptions (e.g., use of inner breeding blanket, impurity control method, first-wall and armor requirements, presence of test modules). However, the breeding ratio estimates in Table 6-34 provide some confidence at this time that a reasonable factor for reactor power variation can be accommodated through modification of the reference blanket geometry while maintaining a net tritium breeding ratio for DEMO.

Table 6-34. Effects of Accommodating Changes in Reactor Power Level

	CASE NO.	1[b]	2[c]	3	4	5	6	7
	F, POWER CHANGE FACTOR[a]	1.0	1.0	1.2	1.4	1.6	1.8	2.0
	R_0 (mm)	5.0	→	→	→	→	→	5.0
	R_1 (mm)	6.25	→	→	→	→	→	6.25
	R_2 (mm)	7.25	→	→	→	→	→	7.25
	R_3 (mm)	16.6	13.6	13.1	12.57	12.0	11.2	10.36
	a (Lateral Spacing = 2 x R_3) (mm)	33.2	27.2	26.2	25.14	24.0	22.4	20.72
	b (Vertical Spacing = .9 x a) (mm)	29.88	24.48	23.58	22.63	21.6	20.16	18.65
CLNT	A_C (πR_0^2) (mm^2)	78.54	→	→	→	→	→	78.54
CLNT	$(t_{EQ})_C = A_C/a$ (mm)	2.37	2.87	3.00	3.12	3.27	3.51	3.79
TUBE	A_T ($\pi [R_1^2 - R_0^2]$) (mm^2)	44.17	→	→	→	→	→	44.17
TUBE	$(t_{EQ})_{STL} = A_t/a$ (mm)	1.33	1.62	1.68	1.76	1.84	1.97	2.13
INTERFACE	A_I ($\pi[R_2^2 - R_1^2]$) (mm^2)	42.41	→	→	→	→	→	42.41
INTERFACE	$(t_{EQ})_{He} = (A_I/a) \times .3$ (mm)	.38	.47	.49	.51	.54	.57	.61
INTERFACE	$(t_{EQ})_{He} = (A_I/a) \times .7$ (mm)	.89	1.09	1.13	1.18	1.24	1.33	1.43
BREEDER	A_B ($\pi [R_3^2 - R_2^2]$) (mm^2)	700.57	415.9	374.0	331.2	287.3	229.0	172.1
BREEDER	$(t_{EQ})_B = A_B/a$ (at 70%. T.D.) (mm)	21.1	15.3	14.3	13.2	12.0	10.2	8.3
t_{EQ}	$(t_{EQ})_{STL}$ (mm)	1.71	2.09	2.17	2.27	2.38	2.54	2.74
t_{EQ}	$(t_{EQ})_C$ (mm)	2.37	2.87	3.00	3.12	3.27	3.51	3.79
t_{EQ}	$(t_{EQ})_{He}$ (mm)	11.03	8.81	8.40	8.00	7.55	6.97	6.31
t_{EQ}	$(t_{EQ})_B$ (at 100% T.D.) (mm)	14.77	10.71	10.01	9.24	8.40	7.14	5.81
%V	%V STL ($[t_{EQ}/b] \times 100$)	5.7	8.5	9.2	10.0	11.0	12.6	14.7
%V	%V CLNT	7.9	11.7	12.7	13.8	15.1	17.4	20.3
%V	%V He	15.8	17.3	17.5	17.9	18.3	19.4	20.5
%V	%V Li_2O (at 70% T.D.)	70.6	62.5	60.6	58.3	55.6	50.6	44.5
	WORST-CASE MAXIMUM TEMPS (°C)							
	$(\Delta T)_B$	250	210	176	144	113	76	46
	$(\Delta T)_I$	49	109	142	173	207	245	278
	$(\Delta T)_{FT}$	61	40	38	36	34	32	29
	TOTAL ΔT	360	359	356	353	354	353	353
	WORST-CASE MINIMUM TEMPS (°C)							
	$(\Delta T)_B$	250	93	65	45	31	19	10
	$(\Delta T)_I$	49	73	82	82	87	91	93
	$(\Delta T)_{FT}$	61	38	34	31	28	26	23
	TOTAL ΔT	360	204	181	158	146	136	126
	1-D BREEDING RATIO	1.23	1.18	1.17	1.16	1.15	1.13	1.10

[a] F = (maximum power)/(minimum power). Maximum power density = 2.0 MW/m^2 (all cases).

[b] No variations or uncertainties in blanket design parameters; nominal zero-fluence values only.

[c] DEMO reference blanket design (see text).

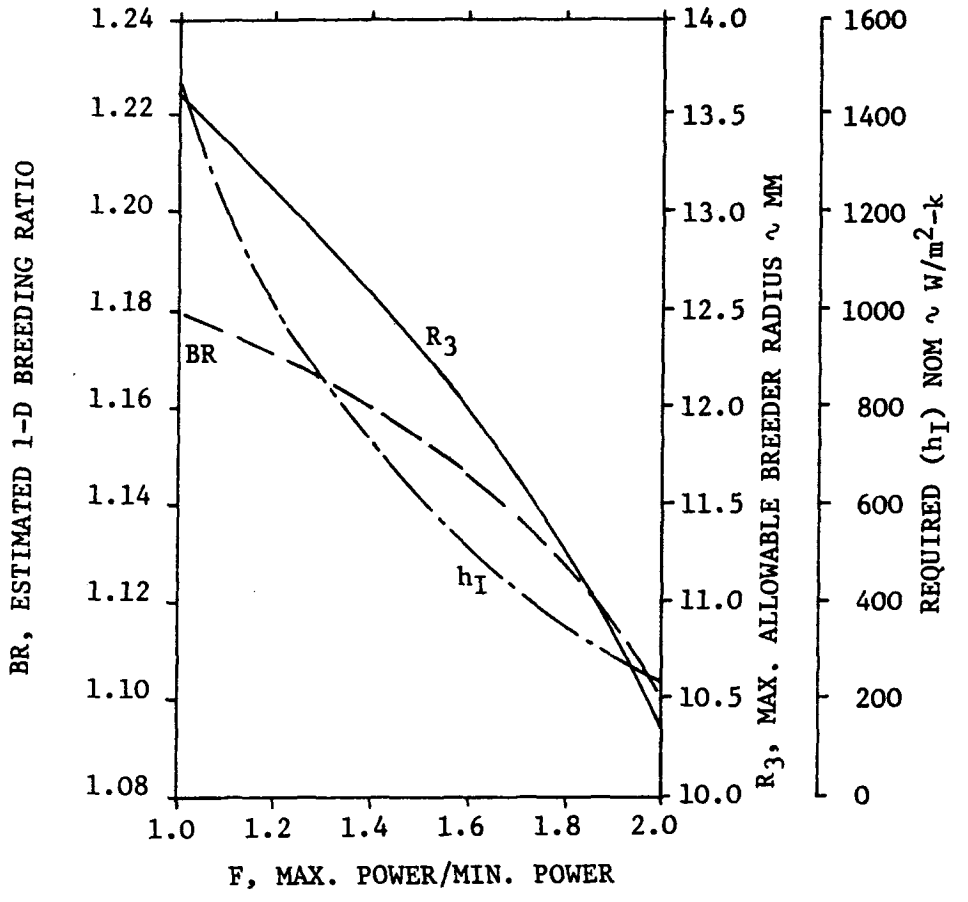

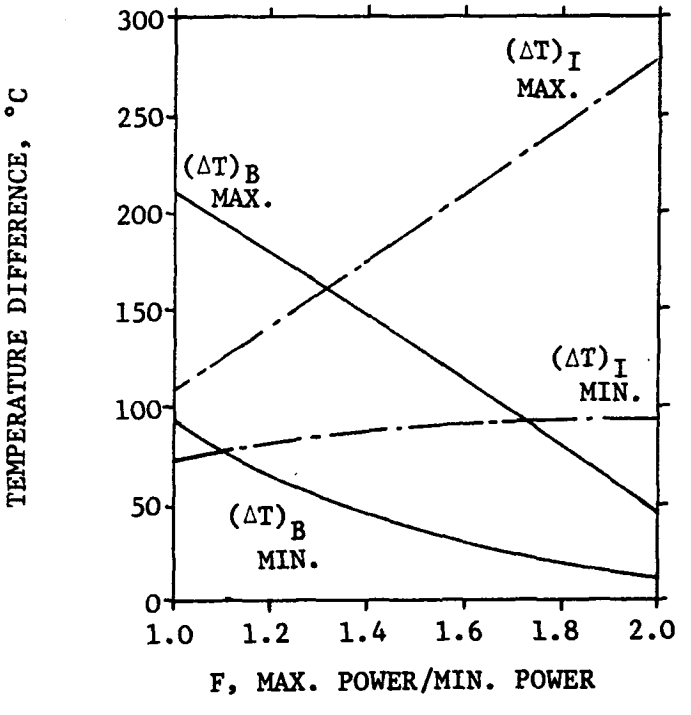

Figure 6-27. Changes in DEMO reference design necessary to accommodate large changes in reactor power level during operation.

6.4.5.4 Purge Stream Thermal Hydraulic Analysis

Some of the design considerations for the helium purge gas system are the total number of purge gas channels, flow rate through each channel, and the resultant pressure losses across each channel. Since the purge does not provide any cooling function for the breeder, the amount of purge gas and the total number of purge channels are based on considerations of adequate removal of the bred tritium and the processing needs for the purge gas stream. Based on 150 g/day tritium production, two cases were analyzed. The desired partial pressure of tritium (as T_2O) for the two cases was assumed to be 10^{-2} torr and 10^{-1} torr. The problem was approached indirectly for the conditions presented in Table 6-35. Tritium partial pressures were calculated to be 0.0091 torr

Table 6-35. Parameters Used for Purge Gas Flow Analysis

Purge gas channel diameter, mm	2.0
Number of purge gas channels	30,000
Purge gas flow velocity, m/s	10.0, 1.0
Purge gas inlet pressure, atm	1.0
Purge gas inlet temperature, °C	200
Purge gas channel length, m	2.5
Desired tritium partial pressure, torr	10^{-2}, 10^{-1}

and 0.091 torr, respectively, for the two cases. These values are very close to the design goals. The pressure losses across the purge gas channels were found to be 14 kPa and 1.4 kPa (2.0 psi and 0.2 psi), and are considered acceptable.

6.4.6 Structural Analysis

6.4.6.1 Solid Breeder Physical Integrity

Maintaining Li_2O breeder temperatures during blanket operation within the limits established by materials consideration is considered to be the key to successful tritium recovery. In the Li_2O blanket design concept, removal of heat from the breeder is achieved by toroidally-oriented coolant tubes which

contain high pressure, flowing water within the breeder zone. Previous design calculations showed that the minimum and maximum Li_2O temperature requirements can be satisfied by proper selection of coolant conditions, tube dimensions, and tube spacing. Previous studies[1,12,82] also illustrated the important role of breeder-to-tube interface thermal conductance and of breeder thermal conductivity on breeder temperatures. All previous calculations were made assuming that Li_2O remains intact (i.e., a sintered solid) and retains its as-fabricated configuration during operation. An assessment was made of Li_2O integrity under DEMO blanket steady-state operation conditions. The assessment, which focused specifically on the thermoelastic response of Li_2O under thermal gradients, is presented in the following paragraphs.

Analytical Method

For simplicity, the Li_2O solid breeder was represented either by a thick, hollow cylinder or by a thin disc with a central hole. Except for the region involving the coolant tube, the models are identical to the cylindrical cell model previously used in the blanket thermal hydraulic study.[7] Simplifying assumptions of axisymmetry and temperature-independent material properties were made and standard formulae[83] were used for the principal thermoelastic stress components under conditions of either generalized plane strain (for the thick, hollow cylinder) or plane stress (for the thin disc). Assuming uniform heat generation, radial heat flow in the cylindrical cells and a temperature-independent Li_2O thermal conductivity k, one can write the steady-state temperature distribution T(r) as

$$T(r) = T_a + \frac{Q}{4k}\left[2b^2 \ln(r/a) - (r^2 - a^2)\right]$$

where

a, b = inner and outer radii of the cylinder or disc

Q = volumetric heat source

T_a = surface temperature at r = a.

The evaluation of the temperature integrals using the above temperature distribution in the constituent stress equations (not shown here) is straightforward. For ease of future parametric studies, a computer program was written to facilitate the calculations. Breeder geometry (i.e., a and b), blanket operating conditions (i.e., T_a and Q), and breeder material properties

(Young's modulus E, Poisson's ratio υ, thermal expansion coefficient α and thermal conductivity k) from Section 6.4.3.1 are input to the computer program, from which the outputs of thermoelastic stresses and displacements are calculated.

Results

Three separate Li_2O blanket regions were selected for thermoelastic response evaluation. Region 1 has the highest nuclear heating rate and is taken near the first wall/multiplier region. Region 2 is taken within the breeder where nuclear heating is ~ 25% of that in Region 1. Region 3 is taken near the reflector/shield region where the nuclear heating rate is ~ 4% of the maximum value. Table 6-36 lists the geometrical and operating variables for these three regions, which are applicable to both the thick cylinder and the thin disc models.

Figure 6-28 shows the calculated temperatures and stresses in Region 1 of the thick cylinder; results are similar for Regions 2 and 3. Of the three principal stresses in each blanket region, σ_θ and σ_z are both tensile near the breeder-to-tube interface and compressive near the cell outer boundary. Maximum tensile stresses occur at r = a where $\sigma_\theta = \sigma_z$. If the maximum tensile principal stress is used as a fracture criterion for Li_2O, one can expect equal likelihood for the σ_θ-induced (radial) and σ_z-induced (axial) cracks to form first from the breeder-to-tube interface. In view of the relatively low flexural strength reported[84] for Li_2O (i.e., 48.3 MPa), the cracking tendency appears very high since the maximum tensile stresses, 1076.9, 1131.3, and 1203.1 MPa for Regions 1, 2, 3, respectively, have all greatly exceeded the flexural strength.

The radial displacements at r = a and the axial strains for the three blanket regions are listed in Table 6-37. The contribution to the gap-size change at the breeder-to-tube interface from Li_2O thermal expansion is an increase of ~ 0.12 mm. The axial thermal expansion strains are ~ 1.8%. If the breeder length is taken to be the same as the blanket coolant channel length of 3 m, the axial thermal expansion of the breeder will be ~ 54 mm. These thermal expansion values give a crude indication of the breeder dimensional change.

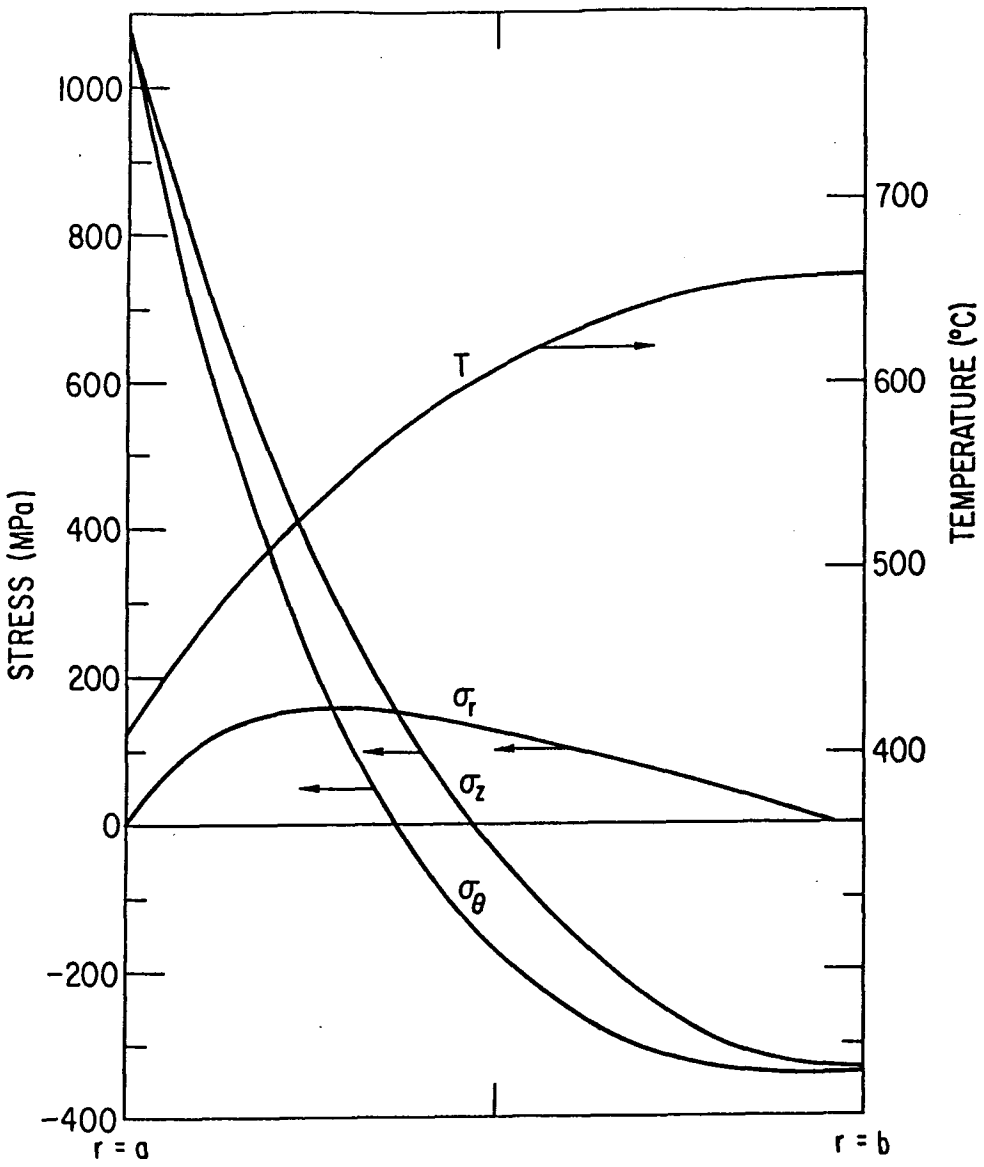

Figure 6-28. Calculated radial temperature and thermoelastic stress distributions in Region 1 of the blanket (thick, hollow-cylinder model).

Table 6-36. Geometrical and Operating Variables for Three Blanket Regions

	Region		
	1	2	3
Average nuclear heating rate, W/cm^3	12.94	3.33	0.47
[a]Breeder cell inner diameter, mm	12.7	12.7	12.7
Breeder cell outer diameter, mm	31.4	47.4	94.0
Breeder surface temperature, T_i(°C)	410	410	410

[a]Breeder cell inner diameter = coolant tube outside diameter.

Table 6-37. Calculated Radial Displacement at r = a and Axial Strains for the Three Blanket Regions

	Region		
	1	2	3
Radial displacements at r = a, mm	0.1133	0.1150	0.1174
Axial strain, %	1.784	1.812	1.848

For the thin-disc model, the maximum tensile stresses can be readily obtained from the thick-cylinder solution. One needs only to multiply σ_r and σ_θ in Fig. 6-28 by a factor of $(1 - \upsilon)$ to obtain the plane-stress results. With $\upsilon = 0.3$, the maximum tensile circumferential stresses (σ_θ) in the thin disc are, therefore, 753.8, 791.9, and 842.2 MPa for Regions 1, 2, and 3, respectively. Since all these stresses are still much higher than the flexural strength of Li_2O, the tendency for the formation of σ_θ-induced radial cracks in thin-disc Li_2O remains high, even though axial crack formation is prevented because $\sigma_z \sim 0$.

Discussion

Breeder cracking, if it occurs, will change the blanket configuration and increase the difficulty in predicting breeder performance during operation. For example, the effects of gap size change due to Li_2O thermal expansion at the breeder/tube interface must be accounted for in thermal conductance calculations. The cracks themselves, if unfavorably oriented, can increase the impedance to heat flow and thereby violate the breeder maximum temperature requirement. Fortunately, in the Li_2O blanket concept, the primary heat flow is in the radial direction, and the formation of circumferential (σ_r-induced) cracks to impede radial heat flow is least likely. Radial and axial cracks, on the other hand, do not represent barriers for radial heat conduction, even though the local temperatures will be influenced by the heat-transfer medium (helium purge gas) existing between the crack faces. The creation of new surfaces should also aid tritium release by reducing the diffusion path.

It is for these reasons, as well as fabrication difficulties in adequately controlling as-built helium gap width tolerances, that the DEMO breeder-to-tube interface concept will utilize metallurgical bonds and a closely-controlled conducting medium instead of a helium gap. The method also incorporates segmentation of the breeder cylinder both axially and circumferentially to relieve thermally-induced stresses to levels well below the fracture stress of Li_2O.

Further analytical and experimental work is warranted because the physical integrity of Li_2O in irradiation and thermal environments is still unknown. Specific recommendations are as follows:

- Experimental study to investigate dependence of Li_2O fracture strength and Young's modulus on porosity, temperature, and fluence.
- Refinement of the present analysis to include temperature and irradiation dependent material properties.

6.4.6.2 First Wall Stress Analysis

The coolant channel configuration is an important aspect of the first wall design. Four coolant panel design options were analyzed for stress in this study (see Fig. 6-29): (1) grooved channel in the back of the first wall, covered with a flat plate; (2) solid first wall with a corrugated panel in a sine wave shape; (3) solid first wall with a corrugated panel in a circular arc shape; and (4) solid first wall with a corrugated panel in a semicircular shape. The four configurations were compared for the same width (W). The sinusoidal and circular arc panels were compared for the same width to height (W/h) ratio. Primary and secondary stresses from mechanical and thermal loading were determined using the analytical methods and equations described in Section 4.3.3.2 of Ref. 7.

The maximum primary stress intensity (P_m) is plotted in Fig. 6-29(a) as a function of the panel wall thickness for unit pressure, at a W/h value of 4. The maximum stress intensity at any point is defined by twice the maximum shear stress at that point. The lowest primary membrane stress occurs for the semicircular case. For widths greater than 10 mm and thicknesses less than 4 mm, the primary membrane stress in the circular arc is less than that in either the flat plate or the sinusoidal panel. For lesser widths ($W \approx 5$ mm) the differences among the four geometries are small. Since the DEMO maximum coolant pressure p = 11 MPa, the primary membrane stresses are small compared to allowable values, particularly for channel widths $\leq$ 10 mm, and the primary stress intensities are less than the allowable S_m values for either annealed or cold-worked (CW) Type 316 SS.

Figure 6-29(b) is a plot of the maximum primary local membrane plus bending stresses. For small channel widths (~ 5 mm) both the flat plate and the sinusoidal panel have the lowest stress; however, the differences among the four geometries are not large. For larger channel widths and smaller thicknesses, bending effects are dominant, and the semicircular panel exhibits

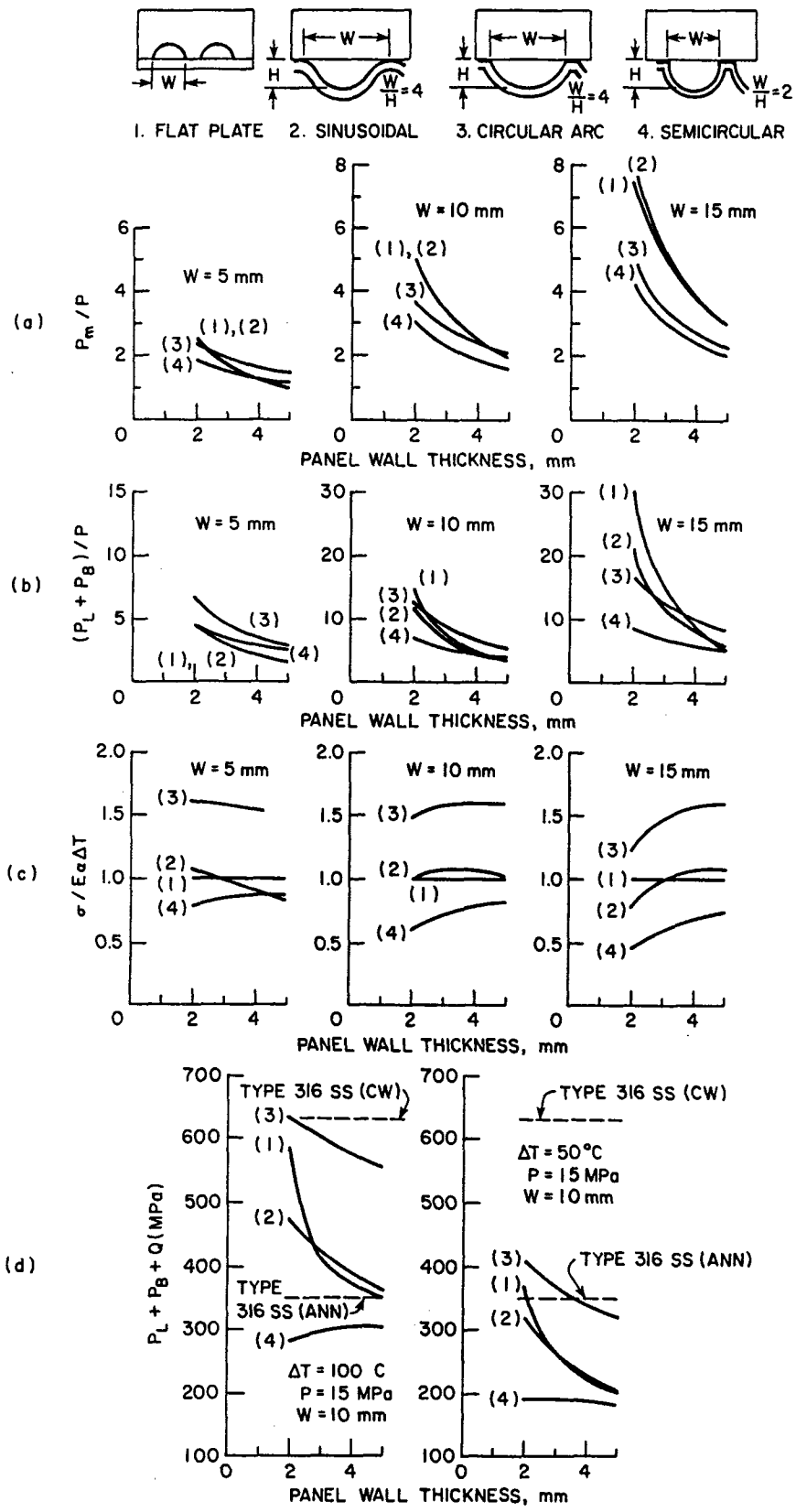

Figure 6-29. (a) Maximum primary membrane stress intensities.
(b) Maximum primary membrane local plus bending stress intensities.
(c) Thermal stresses.
(d) Maximum primary local membrane plus bending plus secondary stress and $3S_m$ allowable stresses.

the lowest stress intensity and the flat plate the highest stress intensity. For the 5 mm channel width, all four geometries satisfy the 1.5 S_M requirement for either annealed or CW Type 316 SS for all thicknesses considered. The same is true for 10 mm channel widths, provided the front plate thickness is greater than 2.5 mm.

Figure 6-29(c) shows the variation of maximum thermal stress for a differences (ΔT) between the average temperatures of the first wall and the rear panel. The semicircular panel provides the lowest stress. The circular arc panel experiences the largest thermal stress, which occurs at the attachments to the first wall due to bending. Figure 6-29(d) shows the total primary plus secondary stress for panels of 10 mm channel width, for ΔT = 50°C and 100°C. The figure also shows the allowable 3 S_m limits (dashed line) for both annealed and CW Type 316 SS. The CW material is acceptable for all geometries at both ΔT values. The annealed material is acceptable only for the semicircular panel at ΔT = 100°C, but for ΔT = 50°C the flat plate and sinusoidal panels also satisfy the 3 S_m limit.

From the viewpoint of stress, the semicircular panel configuration is the most desirable. However, considerations of cooling efficiency and of fabrication cost might indicate the circular arc or sinusoidal configuration to be a better choice. Further analysis should also be performed to determine the stress effects of using relatively thin front plates, which are permitted by the very low particle flux to most of the first wall for the DEMO reactor.

6.5 Li-Pb Alloy Breeder Blanket

A summary of the work performed in the assessment of the Li-Pb alloy breeder first wall/blanket concepts is presented in Section 6.5.1. The remaining subsections deal with specific related topics:

Section	Subject
6.5.2	Blanket Concepts and Design Considerations
6.5.3	Materials Properties and Compatibility Considerations
6.5.4	Tritium Recovery and Containment
6.5.5	Thermal-Hydraulics Analyses and MHD Effects
6.5.6	Stress Analyses

6.5.1 Introduction and Summary

Liquid Li-Pb alloys have several attractive properties for use as a tritium breeder in a fusion reactor, particularly neutronics properties. The neutron multiplication by the lead provides excellent tritium breeding performance and the neutron attenuation properties of the alloy are attractive for radiation shielding. The Li-Pb eutectic alloy, 17Li-83Pb, which has a relatively low melting temperature of 235°C, was selected at the beginning of the DEMO project as the breeding material for the liquid breeder portion of the blanket study. Although the 10Li-50Bi-40Pb alloy has a melting temperature approximately 100°C lower than the Li-Pb binary alloy, the polonium generation from transmutation of the bismuth and the poorer compatibility of bismuth (compared to lead) with structural materials make this ternary alloy less desirable than 17Li-83Pb.

Neutronics analyses for the Li-Pb breeder blanket indicate that breeding ratios of about 1.5 to 1.6 (1-D basis) are attainable for blankets with full coverage and 70-cm depth, depending on first wall materials and thicknesses. However, the Li-Pb must be highly enriched (~ 60-70% of ^{6}Li) to achieve these breeding ratios. A Li-Pb blanket with natural lithium will provide a breeding ratio of only 1.2-1.3 for otherwise similar condition.

The most important initial consideration for the blanket design is whether to use Li-Pb as both breeder and coolant (i.e., self-cooled), or to use a separate gas or liquid coolant. Economics-related issues (e.g., pumping power losses, energy conversion system component design, and efficiency), safety, and blanket and coolant system design complexity are of primary concern. The most important materials-related concerns pertinent to the design evaluations are: (1) the high density of Li-Pb, which increases blanket structural requirements (and pumping power requirements if used as a coolant); (2) the maximum allowable structural temperature, set at ~ 450°C for ferritic steel because of compatibility concerns; and (3) the low solubility of tritium in Li-Pb, which impacts both tritium containment and tritium recovery. For separate coolant concepts, additional important design considerations are breeder-coolant compatibility, control of tritium permeation into the coolant, breeder containment approach, and coolant containment approach (e.g., fully pressurized module or small-diameter coolant tubes). Induced MHD effects are

also important for Li-Pb breeder self-cooled concepts and for separately-cooled concepts using liquid metal coolant (i.e., sodium).

Helium, pressurized water, and liquid sodium have been considered as potential coolants for the separate-coolant concepts. Primary disadvantages of helium relate to: (1) shielding problems, particularly in the inboard blanket; (2) design constraints imposed by the use of a high pressure coolant in a liquid metal system; (3) lack of a structural material compatible with both helium and Li-Pb at acceptable operating temperatures; and (4) economic penalties associated with high pumping power requirements and a more expensive heat transport and energy conversion system. Pressurized water is considered to have two serious disadvantages: (1) perceived safety problems, in terms of a large-scale expulsion of Li-Pb breeder from the blanket as the result of Li-Pb/water contact; (2) high tritium permeation rates through coolant containment structure into the water. On balance, sodium is considered at present to be the best separate coolant, primarily because of its good thermal-hydraulic characteristics, its low reactivity with Li-Pb, and its potential to serve as a tritium-recovery medium without requiring Li-Pb circulation. However, MHD effects and reactivity of sodium with water and air are major concerns with sodium coolant.

Compatibility with structure is a key feasibility question for Li-Pb. The maximum blanket operating temperature was limited by corrosion/compatibility criteria. Critical issues include (1) corrosion/mass transfer effects, and (2) stress corrosion effects. Ferritic steel and vanadium alloys are considered to be the best candidates for the structural material. Because of the high solubility of nickel in both lithium and lead, structural alloys containing significant amounts of nickel are subject to extensive mass transfer at high temperatures. Corrosion of austenitic steels in a large heat transport system is believed to be excessive at acceptable operating temperatures ($\geq$ 400°C). Those ferritic steels with no nickel should be more resistant to mass transfer effects; however, liquid metal embrittlement phenomena at low temperatures (~ 350°C) are of concern for structures under high stress. Vanadium alloys probably have better compatibility with Li-Pb because of lower solubilities in lithium and lead; however, no experimental data are available. For separately-cooled concepts, compatibility of structure with the separate coolants is also a major consideration.

Key properties of 17Li-83Pb that have major impact on the design include melting temperature (235°C), relatively high density (9.4 g/cm^3), and its relatively low solubility for hydrogen (tritium). For a relatively high tritium pressure of 1 Pa, the amount of tritium dissolved in the alloy is only about 4.4 wppb at projected operating temperatures. This low solubility has important implications regarding tritium recovery, tritium inventory and tritium containment. Tritium permeation rates at this pressure are quite high for most structural materials. The heat of reaction of the 17Li-83Pb alloy with air and water is lower than that of liquid lithium by a factor of ten when compared on a unit volume basis.

Tritium recovery and containment problems associated with the Li-Pb breeder were evaluated for both blanket concepts. Molten salt extraction, the use of solid getters, and gas sparging are considered to be feasible methods for direct recovery of tritium from Li-Pb. Because of the low solubility of tritium in 17Li-83Pb, fairly high tritium pressures (about 1 Pa) are required for acceptable flow rates if Li-Pb is used as the tritium recovery fluid. These high tritium pressures create tritium containment difficulties in the ex-reactor system, e.g., the steam generator and piping. An intermediate heat exchanger or a double-walled steam generator is required in order to reduce leakage of tritium to acceptable levels. Tritium permeation in a water-cooled blanket concept is also excessive unless a double-walled coolant containment is employed in the blanket. For the case of sodium coolant, permeation rates into the sodium appear to be sufficient to use the sodium as the tritium recovery fluid. Recovery of tritium from the sodium by cold-trapping appears to be an attractive method.

The separately-cooled Li-Pb first wall/blanket concept that appears on balance to be the most attractive (Section 6.5.2.1) is sodium cooled, and is similar in overall configuration to the DEMO reference design blanket with Li_2O breeder. The module/sector approach used for the Li_2O breeder blanket was also adopted for this Li-Pb breeder blanket concept. The first wall and blanket are integrated mechanically and structurally. The first wall consists of an actively-cooled corrugated panel. The breeder zone and first wall are cooled by low pressure ($\lesssim$ 0.5 MPa), high temperature (275°C inlet, 400°C outlet) liquid sodium, contained in small-diameter toroidally-oriented tubes connected to inlet and outlet manifolds at the rear of the blanket. Tritium

permeates from the Li-Pb (which remains in the modules at all times) through the coolant tube walls into the sodium; a small percentage of the sodium flow rate is processed externally by cold trapping to remove the tritium. Ferritic steel and vanadium alloy (V-15Cr-5Ti) are the candidate structural materials.

For the Li-Pb self-cooled first-wall/blanket concept (Section 6.5.2.2), the first wall of each module is formed by the two semi-ellipsoidal domes which comprise the module front face. The flat side walls of the module are connected to full internal frames (oriented normal to the toroidal direction) which self-react loads due to internal pressure (~ 1-2 MPa). The frames also react the gravity loads of the Li-Pb from the side walls and first wall (depending on module location in the sector) to the back wall and sector structure. The Li-Pb enters the rear of the blanket at about 300°C, flows radially to the front of the blanket between two structural frames which form a channel, and is directed behind the first wall to cool it. The liquid metal then circulates at a lower velocity in a generally radial direction toward the back of the blanket, and exits at 400°C to the outlet manifold. A fraction of the Li-Pb flow is diverted outside the reactor to a tritium recovery system. As with the separately-cooled blanket concept, ferritic steel and V-15Cr-5Ti alloy are the candidate structure materials.

6.5.2 Blanket Concepts

The Li-Pb blanket study effort for the DEMO project focused on the assessment of both separately-cooled and self-cooled blanket concepts to help determine the relative advantages and disadvantages of each for tokamak power reactor blankets. Design considerations important to both approaches are discussed in Section 6.5.2.1. The two approaches are discussed in Sections 6.5.2.2 and 6.5.2.3, respectively; Section 6.5.2.4 presents a comparison of the two approaches.

6.5.2.1 Design Considerations

Table 6-38 lists the principal considerations, issues or concerns, and candidate design detail options involved in the mechanical and structural design of the Li-Pb alloy breeder first wall/blanket. Where appropriate, a

Table 6-38. Design Considerations for Li-Pb Alloy Breeder Blanket Approaches

Consideration	Primary Issues or Concerns	Options
Breeder temperature control	• Structure temperature limit • Breeder movement due to E-M forces and thermal gradients	(Separate coolant) • Actively-cooled structure
Breeder containment	• High gravity loads and hydrostatic pressures due to high density	• Containment method: - Compartmentalized Modules (separate coolant only) - Large modules - Large-diameter tubes
Coolant containment	• Reliability against leaks • Coolant pressure and temperature • Structure temperature limit • MHD effects (liquid metal coolants) from flow crossing field lines	(Separate coolant) • Containment method: - Bottle (cylinder) - Small-diameter tubes - Coolant panels • Plenum location: - Module sides (toroidally) - Rear of blanket (Li-Pb breeder/coolant) • Containment method: - Bottle (cylinder) - Pressurized module - Large-diameter tubes
Tritium removal	(Separate coolant) • Permeation into coolant	(Separate coolant) • Removal methods: - Permeation into coolant - Li-Pb circulation for out-of-reactor processing - Double wall coolant tubes with purge helium in annulus
Energy conversion system	• Thermal energy recovery efficiency - Coolant ΔT, T_{max} • Component capital costs • Pumping power losses: - MHD effects (liquid metal coolant) - Friction losses (Li-Pb breeder/coolant)	• Heat exchanger options: - Intermediate heat exchanger (IHX) - Steam generator: - Single wall tubes - Double wall tubes
Safety	• Effects of breeder/separate coolant contact in accident • Blanket afterheat removal • Tritium inventory in breeder and coolant	• Blanket protection methods: - Double wall coolant tubes (separate coolant) - Module walls designed to full coolant pressure • Afterheat removal - Dual parallel coolant circuits (separate coolant) - Emergency coolant circuit (separate coolant) - Via radiation and conduction

distinction has been made between areas applicable to only the separate coolant approach or to the Li-Pb breeder/coolant approach.

The issues listed below are considered to be the most important to blanket designs using Li-Pb breeder:

- Effects of breeder/separate coolant contact in an accident
- Structure temperature limit
- Control of tritium permeation into separate coolant
- Pumping power requirements
  - MHD effects (sodium or Li-Pb as coolant)
  - Friction losses associated with high coolant mass flow rate (Li-Pb coolant)
- Breeder containment approach

Most of the design issues listed in Table 6-38, as well as those listed above, are related to specific characteristics of the Li-Pb alloy:

- Relatively high corrosivity to structural materials
- High density
- Low tritium solubility

The reasons for the importance of the issues, and the advantages and disadvantages of the various design detail options, are discussed in Sections 6.5.2.2 through 6.5.2.4.

6.5.2.2 Separate Coolant Concepts

This section describes the definition and evaluation of design concepts in which the Li-Pb liquid breeder is cooled by another fluid. The rationale for selection of sodium as the best separate coolant for a DEMO Li-Pb blanket is discussed.

The three separate coolants considered were helium, pressurized water, and sodium. Blanket configurations and major operating parameters (Fig. 6-30) were selected to show each coolant to best advantage. The results of the comparative evaluation of the three candidate separate coolants for Li-Pb breeder blankets are shown in Table 6-39, and are discussed in the remainder of this section. The criteria of primary importance for selection of the best Li-Pb breeder/separate coolant concept were (1) extrapolability to commercial

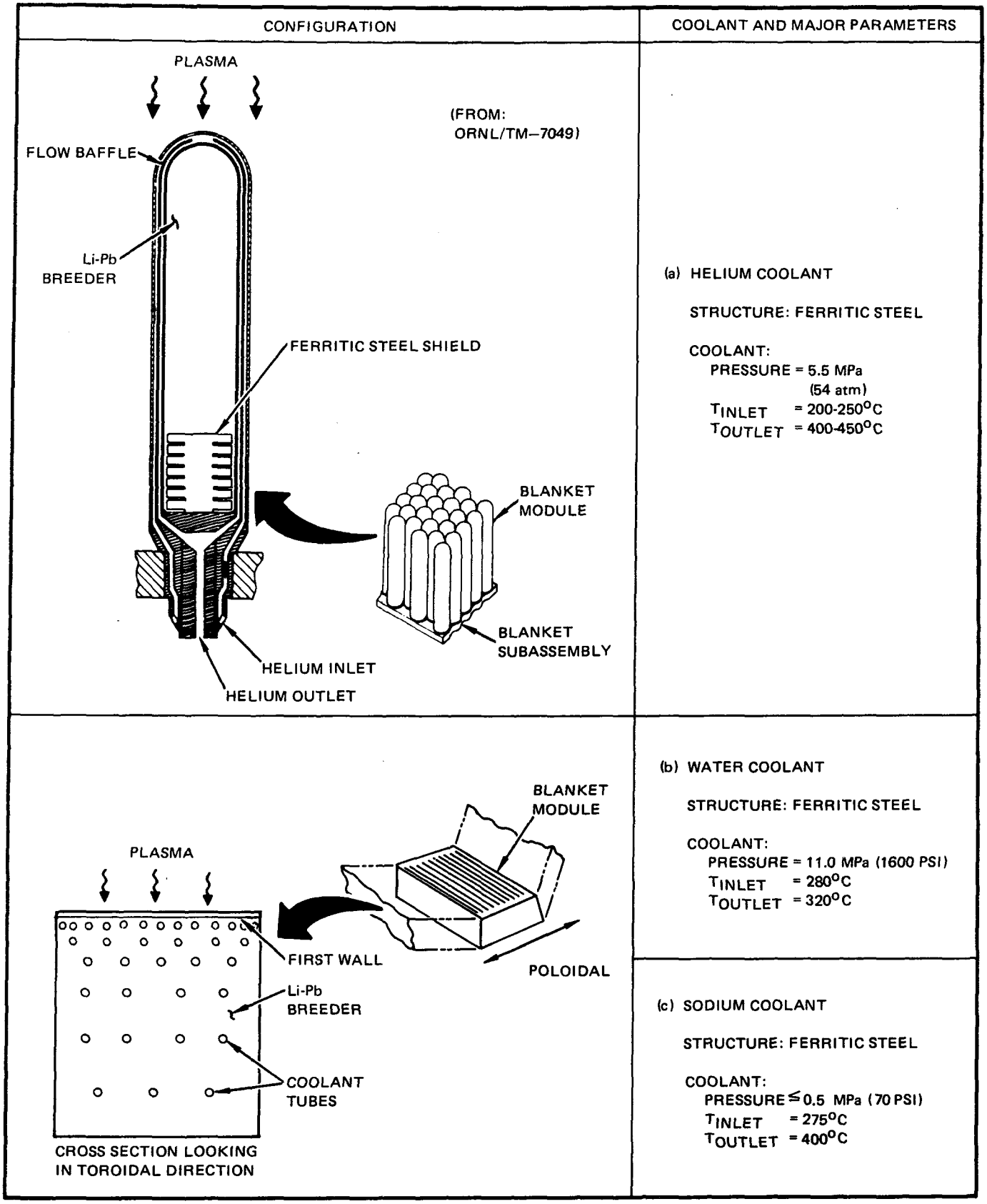

13-4861A

Figure 6-30. Blanket configurations selected for comparison of candidate separate coolants.

Table 6-39. Comparison of Separate Coolant Approaches for Li-Pb Breeder Blanket

Consideration	Helium	Water	Sodium
Blanket design	• Bottle	• Slab	• Slab
Tritium breeding	• 15-20% voids	• More than adequate	• More than adequate
Tritium Removal	• Permeation into helium coolant; no circulation of Li-Pb	• Processing of low-flowrate Li-Pb stream	• Cold trapping of sodium coolant; no circulation of Li-Pb
Safety • Afterheat removal following coolant system accident	• Dual circuits not possible; emergency circuit(s) needed	• Dual parallel circuits	• Dual parallel circuits
• Tritium permeation	• High permeation rate into coolant; used for tritium recovery	• High permeation rate into coolant requires costly processing or double wall containment	High permeation rate into coolant; used for tritium recovery
• Consequences of Li-Pb/coolant contact	• Possible pressurization of breeder region	• Possible expulsion of a Li-Pb • H_2 formed by chemical reaction	• No severe consequences; minimal chemical reaction
• Consequences of coolant contact with air, water, or concrete	• None	• None	• Highly reactive
Economics • Inboard blanket thickness	• Moderate	• Minimum	• Minimum
• Thermal conversion efficiency	• Low due to reduced coolant T_{max}	• Reduced if double walled tubes required in blanket or if IHX is required	• Acceptable
• Intermediate heat exchanger or double wall steam generator	• Not required	• Not acceptable (economic penalty)	• Required

reactor conditions in terms of economic competitiveness, (2) safety during accidents, and (3) protection of capital investment during an accident.

On balance, cooling with molten sodium appears to be the best approach, primarily because of its combination of perceived economics and safety advantages relative to helium and water. The use of sodium as coolant retains the desirable qualities of water as a separate coolant, while either eliminating or making use of water's disadvantages. Table 6-40 summarizes the relative

Table 6-40. Advantages and Disadvantages of Sodium-Cooled Li-Pb Breeder Blanket Relative to Other Coolants.

Advantages
- Circulation of Li-Pb is not required
- Low pressure coolant (< 0.5 MPa), nonreactive with Li-Pb
- Good thermal conversion efficiency
- Proven tritium recovery method (cold-trapping)
- LMFBR primary coolant system component technology is directly applicable
- Dual parallel coolant circuits for safe afterheat removal
Disadvantages
- Small volume (<5 vol. %) of chemically reactive liquid metal introduced into blanket
- Relatively corrosive coolant
- MHD effects result in pumping power losses
- May require IHX or double-walled steam generator for tritium containment

advantages and disadvantages of sodium relative to the other separate coolants. The risk of large-scale module rupture is negated since contact between Li-Pb and the low-pressure sodium in an accident will not cause a vapor explosion or high-pressure pulse. Tritium permeates readily from the Li-Pb through the ferritic steel blanket coolant tubes into the sodium, from which it is recovered using cold trapping. Tritium inventories are thereby maintained at acceptably low levels in the Li-Pb and in the sodium. The energy conversion system can utilize either an intermediate heat exchanger (IHX), or a liquid metal steam generator with double-wall tubes similar to those being developed for the LMFBR steam generator. The major concerns regarding the use of sodium

coolant relate to its reactivity with air, water, and concrete, and potential design constraints imposed by MHD effects.

Helium Coolant

The blanket configuration selected for the helium coolant is an adaptation of the ORNL/Westinghouse helium-cooled lithium cylinder[6]. This concept virtually eliminates the possibility of large-scale rupture of the Li-Pb container due to a pressure pulse, since the Li-Pb cylinder is designed to withstand the full coolant pressure level. The radial coolant flow approach also takes maximum advantage of the relatively low allowable helium outlet temperature, by (1) cooling the first wall before cooling the breeder, and (2) enabling coolant outlet temperature to be as close as possible to the maximum allowable structural temperature. Tritium would be recovered by processing the helium coolant stream to remove tritium which permeates through the cylinder wall. Thus the Li-Pb cylinders can be individually sealed and circulation of Li-Pb is not required, a distinct advantage.

The primary drawbacks of helium coolant for tokamak power reactor blankets, as discussed in Section 5.4.2 of Ref. 1, relate to its lower gross thermal efficiency and relatively high pumping power requirements for higher neutron wall loading (e.g., 3.5-4.0 MW/m^2). The allowable helium coolant outlet temperature is relatively low. The ferritic steel assumed for construction of the cylinder has a maximum temperature limit of 450°C, which is 29°C lower than the structural T_{max} reported[6] for austenitic stainless steel in the ORNL/Westinghouse design (10-cm cylinder o.d. at 4 MW/m^2 wall load). Reducing that T_{max} to the 450°C limit assumed in this study would also reduce the helium outlet temperature by approximately the same amount, i.e., from 421°C to 392°C. (The comparison of helium and water coolants in the STARFIRE report assumed a helium outlet temperature of 475°C, and PCA austenitic stainless steel as structure.) Since gross thermal efficiency was only 30%[6] for the 421°C helium outlet temperature (~ 6% less than STARFIRE's gross thermal efficiency), this further reduction in temperature would place a helium/Li-Pb blanket in a poor economic competitive position at commercial reactor conditions.

Pressurized Water Coolant

The slab module blanket configuration selected for water coolant (Fig. 6-30) has several relative advantages for water coolant over the bottle approach. First, the bottle approach's high percentage of lost breeding volume is reduced to a low value. Second, the first wall and breeder zones can each be cooled by separate branches of the flow circuit, each of which uses the full coolant ΔT. Third, the coolant would be contained within small-diameter channels or tubes, which are structurally more efficient than large-diameter cylinders. In addition, dual coolant circuits can be incorporated into the design for safe removal of afterheat in the event of a coolant circuit accident. However, the use of water coolant with 17Li-83Pb appears to have two serious disadvantages. The first is the possibility of reactor damage resulting from Li-Pb/water contact. If water coolant contacts the Li-Pb in a large-scale leak situation, pressurization of the module will occur. This pressure pulse will propagate to the module walls at the sonic velocity for Li-Pb. The result could be large-scale rupture of a module wall followed by ejection of a large fraction of the module's Li-Pb into the vacuum chamber. This type of accident could perhaps be precluded by use of the bottle configuration rather than the slab, although an economic penalty would be incurred because of the high non-breeding wall area. The probability of Li-Pb/water contact in the slab is minimized by using a double wall tube construction similar to that employed in LMFBR steam generators[85], with the annulus between tubes filled by helium purge gas for tritium removal and for detection of a water leak. Additional analyses and engineering tests simulating realistic blanket designs and conditions are necessary to properly quantify the results of a water/Li-Pb contact.

The second serious disadvantage of the water coolant is the high level of tritium permeation through single wall tubes into the water (see Section 6.5.4). Processing of substantial amounts of tritium from the water coolant is considered to be economically prohibitive. Excessive accumulation of tritium in the water coolant would have important safety implications in the event of a leak. Possible solutions to this problem -- double walled blanket coolant tubes with helium purge gas in the annulus, an IHX, or a steam generator with double walled tubes -- are likely to lower the overall thermal energy

conversion efficiency to levels that are economically unacceptable for commercial reactors.

Sodium Coolant

The Li-Pb alloy blanket configuration selected for liquid sodium coolant is similar to the water-cooled Li_2O solid breeder reference blanket design described in Section 6.2, and the rationale described therein for selection of design details is generally applicable. The principal differences are ant tube arrangement and thermal-hydraulic parameters, (2) module structural arrangement, (3) tritium removal method, and (4) the addition of resistance heaters for use during reactor startup.

The blanket configuration is shown in Fig. 6-31; selected materials and major design parameters and options are listed in Table 6-41. The module first wall configuration is the same as for the Li_2O blanket, except that the thickness and channel size in the corrugated sheet are reduced since sodium coolant pressures are low. Coolant tube spacing, both poloidally and radially (depthwise), is altered from that of the Li_2O blanket to account for (1) the different nuclear heating rate with depth into the blanket and (2) the higher thermal conductance at the outer surface of the coolant tubes. The module structure is modified somewhat to react the gravity loads resulting from the large mass of lead contained within each module. The poloidally-oriented internal frames are spaced ~ 20 cm apart toroidally, and are welded to the first wall, side wall and back wall of the module. Most of the breeder gravity load (for the vertical or slanted modules) is reacted through these frames to the back wall. Cutouts in the frames are provided to clear each coolant tube.

Resistance heaters arranged in dual parallel circuits are attached to the two toroidal sides of the module and to the back wall. During startup these heaters raise the blanket temperature above the 98°C melting point of sodium. Subsequently the two coolant circuits are filled with sodium (preheated outside the reactor) which is then circulated through the blankets to raise their temperature above the 240°C Li-Pb melting point to the blanket temperature selected for beginning the plasma burn.

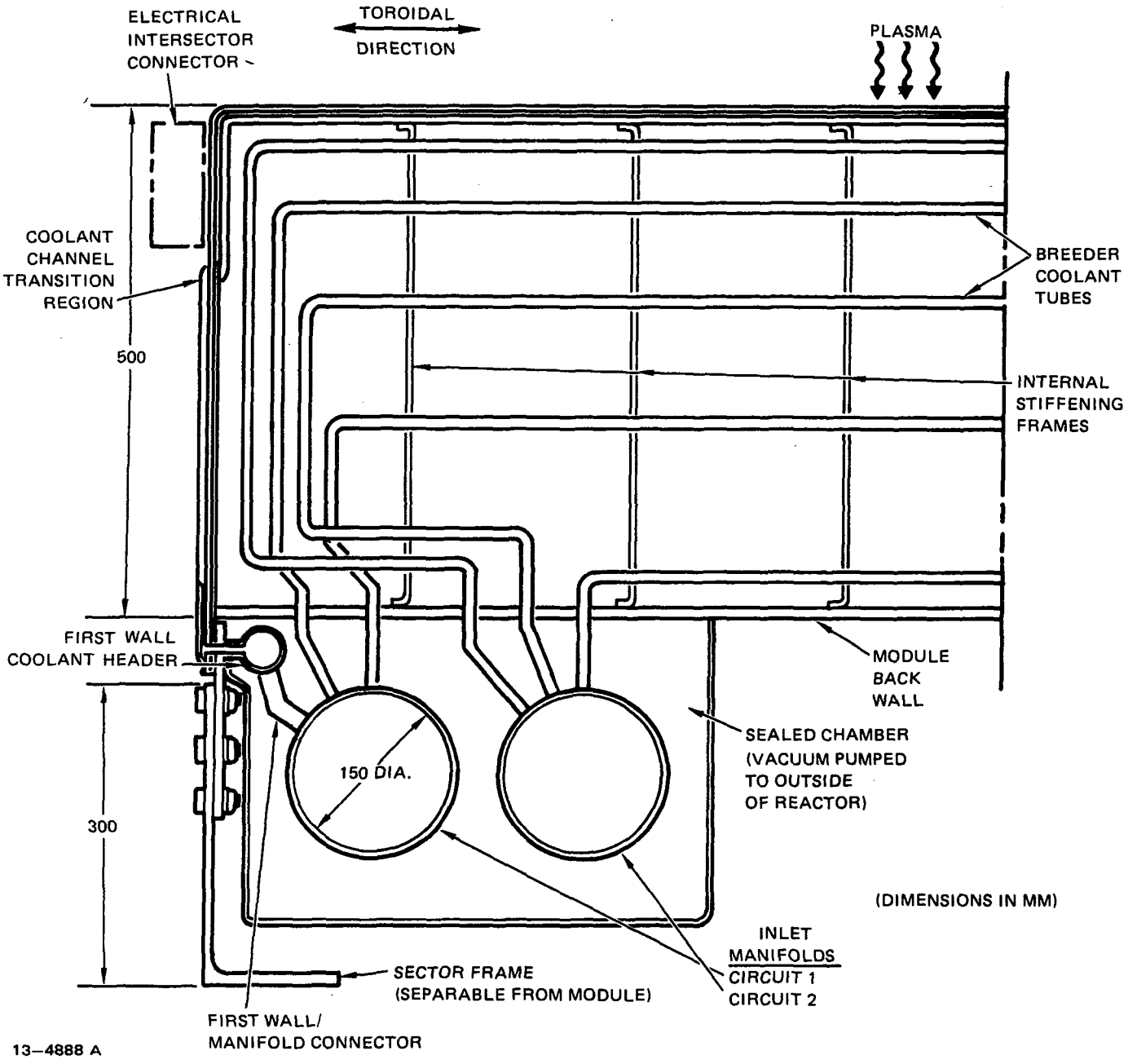

Figure 6-31. Sodium cooled Li-Pb breeder blanket concept.

The tritium removal scheme (Section 6.5.4) is to permit tritium permeation from the Li-Pb through the coolant tube walls into the sodium. A small fraction of the sodium coolant flow is diverted outside the reactor to the tritium processing equipment which uses cold trapping to extract the tritium from the sodium. The Li-Pb thus can remain in each blanket module.

Table 6-41. Sodium-Cooled Li-Pb Breeder Blanket Concept Description

Selected Materials	
- Tritium Breeder	Liquid 17Li-83Pb Alloy
- Coolant	Liquid Sodium ($\lesssim$ 0.5 MPa) - Inlet temperature $\simeq$ 325°C - Outlet temperature $\simeq$ 450°C
- Structure	Ferritic Steel or Vanadium Alloy (V-15Cr - 5Ti)
Selected Design Options	
- First Wall	Actively-Cooled Corrugated Panel
- Breeder Coolant Containment	Small-Diameter Tubes
- Other	- Toroidal direction for coolant flow - Dual parallel primary coolant loops - Maintenance by sector removal and replacement - Resistance heaters for use during reactor startup

Interconnection of the modules and circulation of the Li-Pb outside the reactor for tritium removal are therefore not required. This significantly reduces system complexity, and also lowers the internal pressure for each module which becomes a function of only the static head for each module.

It should be noted that impurity levels might build up in the stagnant Li-Pb to unacceptable levels; this would require that the modules be interconnected (increasing the pressure head) and the Li-Pb pumped outside the reactor for processing. Future studies and experiments should determine the necessity for impurity removal.

The basic elements and arrangements of the energy conversion system for the sodium-cooled Li-Pb breeder concept are similar to those for the Li_2O reference blanket, with the primary differences being (1) deletion of the pressurizers, (2) addition of dump tanks and transfer pumps, and (3) the use of double wall tubes in the steam generators. The future detail design of the steam generators for this concept is expected to borrow heavily from the LMFBR steam generator development program, which builds on earlier efforts[85] to develop steam generators for the Clinch River Breeder Reactor Plant. One of

the three steam generator types being developed is a double-wall straight tube configuration. The selected alloy is 2 1/4 Cr-1 Mo ferritic steel, based on its good performance in actual service and in current development activities. Materials and process development and qualification efforts are underway in critical areas such as double-wall tube fabrication and welding and inspection techniques. The development program for sodium-heated LMFBR steam generators, together with similar programs for other components such as pumps, is expected to result within the next 10 years in a proven technology base adequate for design and construction of sodium-heated fusion reactor blanket energy conversion system components.

The most important safety considerations for the sodium-cooled Li-Pb breeder blanket concept are (1) the consequences of a coolant tube rupture in the steam generator, and (2) removal of blanket afterheat in a reactor accident situation. These considerations and the reasons for their importance are listed in Table 6-42. A sodium coolant tube rupture within a module for the Li-Pb reference blanket is not expected to have serious consequences. The sodium/Li-Pb interaction will not produce high pressures inside the module, and the module walls are designed to withstand the sodium coolant pressure. Thus the damage should be confined to the single faulted module, so that consequential accidents (e.g., Li-Pb spill) will not occur. The designs proposed for LMFBR steam generators use primary coolant tubes manufactured, inspected and installed to very high standards. Regardless, a coolant tube rupture within the steam generator is still a possibility. However, the pressure pulse created will be contained by the thick shell of the steam generator and any damage will be confined to the internals. Thus the DEMO reactor will not be affected and reactor operation can continue after repair of the steam generator.

The safe removal of blanket afterheat following an accident involving a primary coolant loop is important to the protection of plant capital investment. If inadaquately cooled, the activated blanket structure could overheat past the temperature limit for safe reuse. In a worst case, the blanket structure could weaken sufficiently to permit rupture and thus release Li-Pb and sodium into the plasma chamber. Because of these possibilities, either dual parallel primary coolant circuits or an independent emergency coolant loop for all modules are considered virtual necessities for power reactor

Table 6-42. Principal Operation/Safety Considerations for Sodium-Cooled Li-Pb Breeder Blanket Concept

Concern	Importance	Remarks
• Breeder/sodium contact as result of small or large coolant leak	• Module internally pressurized to coolant pressure	• No breeder/coolant chemical reaction • Module designed to withstand coolant pressure
• Sodium/water contact in steam generator as result of small or large coolant leak	• Sodium/water reaction can damage steam generator internals	• Steam generator shell sized to withstand full steam/water pressure • Damage limited to a single steam generator • LMFBR technology development minimizes risk
• Safe removal of blanket afterheat following a coolant loop accident	• Temperature increases in blanket can lead progressively to annealing of structure, which precludes reuse	• Dual parallel coolant loops nearly eliminate possibility of unacceptable temperature increases • Further work needed to determine whether safe afterheat removal via conduction and radiation only is feasible

blankets. The relative design simplicity of providing dual circuits for the sodium-cooled Li-Pb blanket is a significant advantage for this approach.

6.5.2.3 Li-Pb Alloy Breeder/Coolant Concepts

The process of developing and evaluating candidate blanket configurations for the Li-Pb breeder/coolant (i.e., self-cooled) concept relied heavily on the results of similar efforts for liquid lithium blankets in the joint Argonne/MDAC study reported in Ref. 5. Based on those results, two concepts were given serious consideration in the present study: (1) the bottle-type cell concept; and (2) the elongated radial-flow cell concept. These are

described in Fig. 6-32. Ferritic steel and vanadium alloy V-15Cr-5Ti are the candidate structural materials for both.

A variation of the tube bank approach illustrated in Fig. 6-32(a) was adapted for the WITAMIR-I[86] tandem mirror reactor (TMR) Li-Pb breeding blanket, and is being further developed within the MARS study. The tube bank is a logical blanket concept for a TMR, but is not considered at present to be a feasible concept for a tokamak because its use results in two severe disadvantages which do not apply to a TMR: (1) a separate, additional first wall is required which can take surface heat loads equivalent to 25% of the neutron wall load; and (2) it is very difficult to incorporate either a pumped limiter or a poloidal divertor for impurity control.

The bottle-type, or cylindrical, cell has a first wall which is formed by the cell's dome and cooled from the back side by flowing Li-Pb. This is a relatively simple design mechanically and structurally, and adapts readily to non-uniform plasma changer regions such as the limiter zone. However, the void space enclosed by contiguous bottles would average 15% to 20% of available breeding volume. In addition, these spaces would have to be filled by some material such as graphite to avoid neutron streaming problems. This presents an added design complexity since these regions must be cooled in some way and protected from the plasma. The concept would also require a large number of individual bottles — probably 10,000 to 20,000 — for a STARFIRE-sized commercial tokamak. (Bottle diameter and quantity would likely be a function of cylinder stresses arising from induced electromagnetic forces during a disruption.)

The elongated radial-flow cell concept (Fig. 6-33) is similar to the STARFIRE backup lithium blanket concept[1] and to the lithium-cooled module

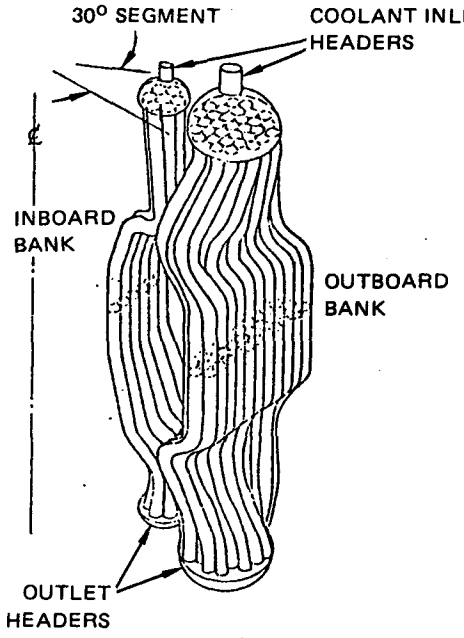

(a) TUBE BANK

ADVANTAGES
- SIMPLEST, MOST RELIABLE STRUCTURE TO CONTAIN Li-Pb

DISADVANTAGES
- SEPARATE FIRST WALL REQUIRED
- INCORPORATION OF LIMITER OR DIVERTOR IS VERY DIFFICULT

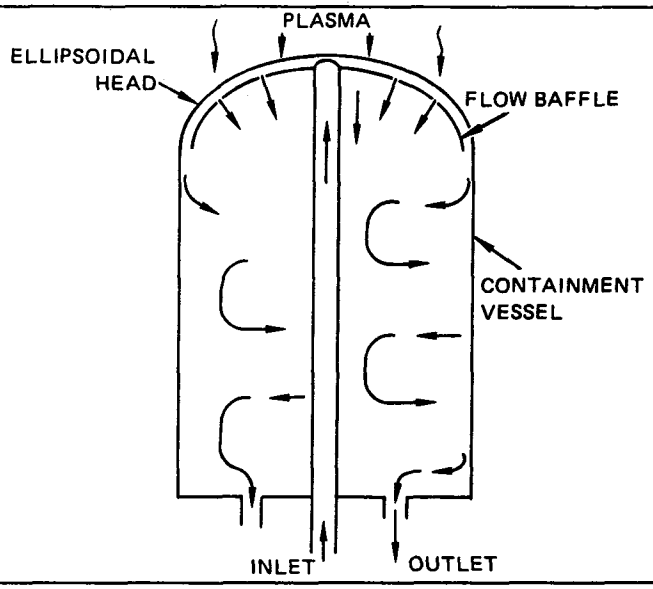

(b) CYLINDRICAL BOTTLE
FW FORMED BY ELLIPSOIDAL DOME; COOLED BY LIQUID ALLOY BREEDER/COOLANT

ADVANTAGES
- SIMPLEST DESIGN MECHANICALLY
- READILY ADAPTS TO LIMITER REGIONS AND INBOARD WALL

DISADVANTAGES
- VOIDS – 15-20% OF CHAMBER WALL AREA
- LENGTH & DIAMETER LIMITED BY E-M FORCES DURING DISRUPTION
- PRESSURIZED WELDS NEAR PLASMA
- VOIDS RESULT IN NEUTRON STREAMING PROBLEMS

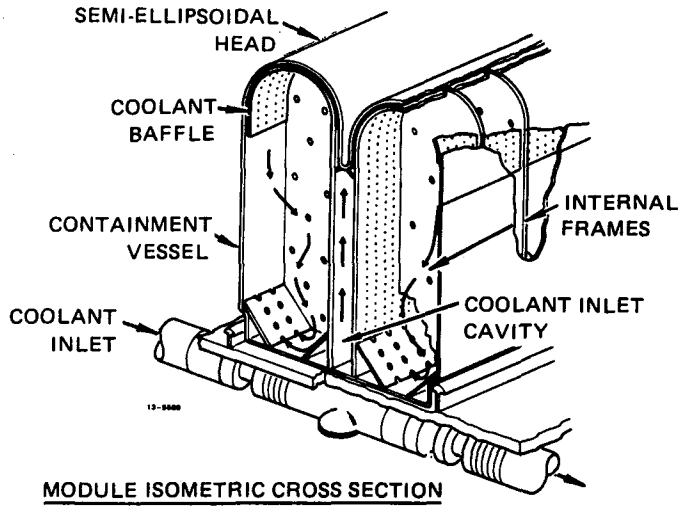

MODULE ISOMETRIC CROSS SECTION

(c) ELONGATED RADIAL-FLOW CELL

- ADAPTED FROM STARFIRE BACKUP DESIGN
- FW FORMED BY HEADS; COOLED BY BREEDER/COOLANT

ADVANTAGES
- MINIMUM VOIDS IN FW COVERAGE
- ADAPTABLE TO LIMITER OR DIVERTOR REGIONS
- LEAST RISK IN ATTAINING NET TBR >1

DISADVANTAGES
- PRESSURIZED FLAT MODULE WALLS
- PRESSURE BOUNDARY WELDS NEAR PLASMA

13–4860 A

Figure 6-32. Candidate blanket configurations for Li-Pb breeder/coolant concept.

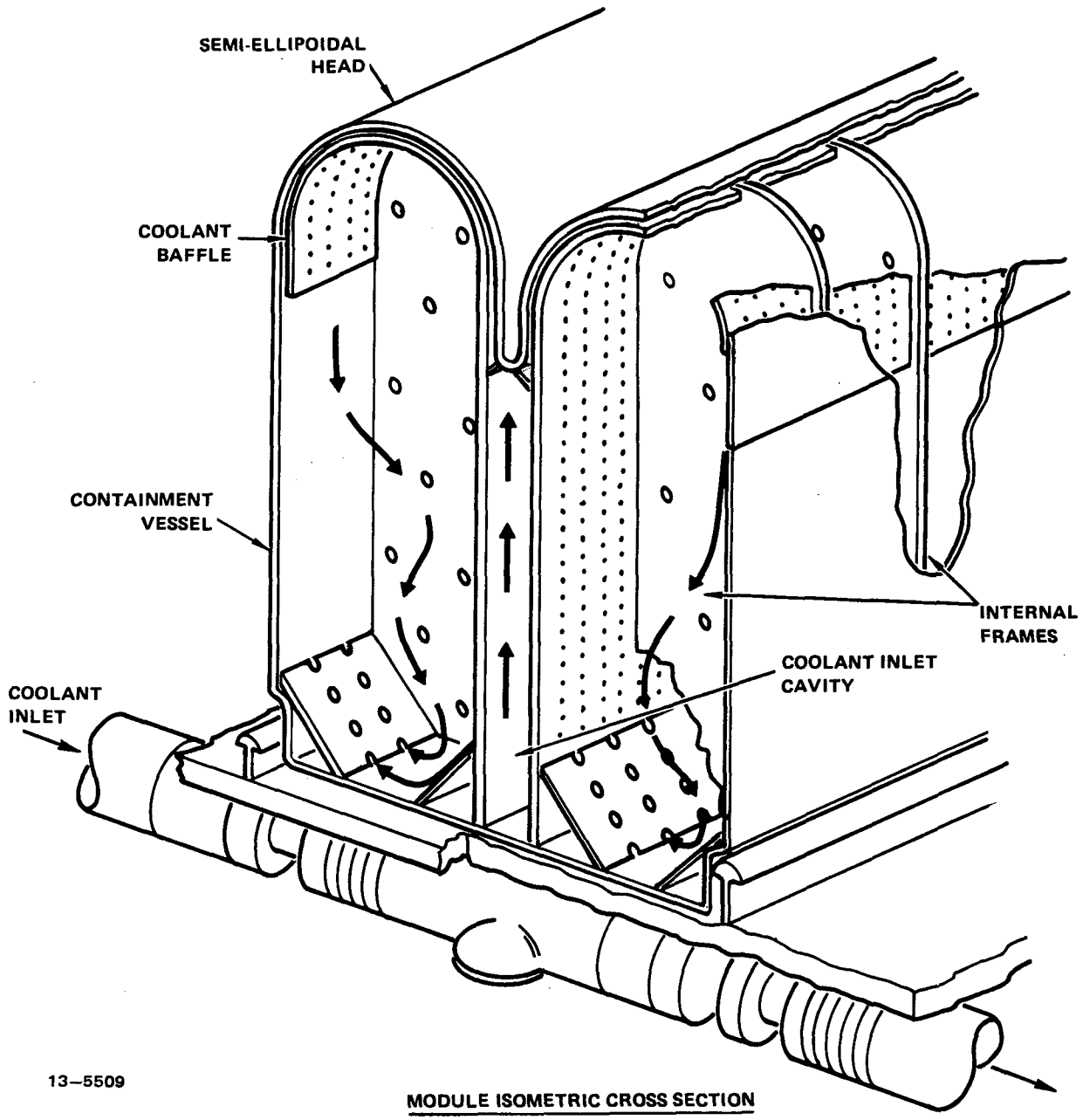

Figure 6-33. Selected blanket design configuration for Li-Pb breeder/coolant approach.

concept in Ref. 5. The semi-ellipsoidal heads form the first wall, which is cooled from the back side by flowing Li-Pb. The Li-Pb enters the blanket through a slot (which divides the entering flow from the rest of the blanket), flows through the gap between the thermal shield and the first wall, then reenters the blanket from which it is withdrawn through baffle plates at the

cell's rear wall. This configuration minimizes non-breeding void regions in the reactor and also minimizes associated neutron streaming problems. It is thus a lower risk in assuring that the DEMO blanket would produce a net breeding ratio > 1 in actual practice. The module walls are internally pressurized to ~ 1-2 MPa because of (1) the Li-Pb static head resulting from interconnection of the blanket modules in the sector, and (2) the pressure head required to overcome the blanket MHD forces and system frictional losses (Sec. 6.5.5.1) and to pump the Li-Pb through the primary coolant system. This requires poloidally-oriented internal frames spaced relatively close together to effectively divide up the large flat wall areas into smaller panels (Sec. 6.5.6).

The elongated radial-flow cell configuration was considered to be superior overall to the bottle cell, and was selected for use in the comparison of separately-cooled and self-cooled Li-Pb breeder blanket concepts, discussed in the following section.

6.5.2.4 Comparison of Separately-Cooled and Self-Cooled Blanket Concepts

The comparison of the sodium-cooled and self-cooled Li-Pb breeder blanket concepts for DEMO identified important differences in a number of areas. The results of the comparison are summarized in Table 6-43. The issue considered most important to the feasibility of either Li-Pb blanket concept is compatibility with structure. As discussed in Section 6.5.3, on the basis of available data, austenitic stainless steel is considered not acceptable for use with Li-Pb in power reactor blankets because of high corrosion rates at reasonable operating temperatures. It is also questionable whether Li-Pb is adequately compatible with ferritic steel for continuous use. Embrittlement of the steel at temperatures $\lesssim$ 350°C, and corrosion rates for flowing or non-flowing Li-Pb systems at temperatures $\gtrsim$ 450°C, are significant concerns. Test results from Li-Pb experimental coolant loops, currently under construction, are required for resolution of these concerns. The vanadium alloys such as V-15Cr-5Ti may ultimately be shown to be the only acceptable structure materials. The discussion in Sec. 6.5.3 also indicates that compatibility problems are likely to be significantly greater for systems in which Li-Pb is pumped through the blanket than for systems with stagnant Li-Pb (i.e., where Li-Pb is not pumped, and is not moved by other than thermal gradients or induced electromagnetic forces). The maximum temperature limits estimated in

Table 6-43. Comparison of Sodium-Cooled and Self-Cooled Li-Pb Alloy Breeder Blanket Concepts.

Category	Advantage: Sodium Cooled	Advantage: Li-Pb Cooled	Remarks
Li-Pb/Structure Compatibility	✓		Structure T_{max} limit for corrosion expected to be lower for system with flowing Li-Pb
Chemical Reactivity		✓	~ 5 vol % of reactive liquid metal added to blanket
Afterheat Removal Following Coolant Loop Accident	✓		Dual parallel coolant circuits for sodium-cooled blanket
Primary Coolant Loop Component Development	✓		LMFBR technology expected to be available for sodium-containing components
Blanket Module Internal Pressure	✓		Low Li-Pb static pressure within module, and low pumping losses for sodium-cooled concept system

Section 6.5.3 for vanadium alloy (600°C static system, 550°C recirculating system) are each 150°C higher than the respective limits for ferritic steel. These higher limits would permit significantly higher coolant outlet temperatures for either concept, with resulting higher thermal energy conversion efficiency values.

Blanket safety is an important concern for both concepts. The sodium-cooled concept introduces a small amount (< 5% of the blanket volume) of a more reactive liquid metal into the reactor. However, the blanket and shield construction results in at least three separate structural barriers between the sodium and any source of water (e.g., shield coolant), except that two structural barriers are interposed between the sodium and the non-breeding water-cooled inner first-wall/blanket. The double-wall construction of the steam generator minimizes the risk of sodium/water contact in that component.

The sodium-cooled blanket has dual parallel coolant circuits (similar to the arrangement for the Li_2O solid breeder blanket) which ensure safe removal of blanket afterheat in the event of failure of one coolant circuit. Such an arrangement is not possible with the self-cooled Li-Pb blanket. For that concept, a failure in the primary coolant circuit or a significant leak from a blanket module would require that the coolant circuit be shut down. Consequently, blanket afterheat would be removed only by radiation and conduction to regions away from the blankets. Whether this is possible without exceeding the safe reuse temperatures for ferritic steel or vanadium alloy, with or without draining of the Li-Pb from the modules, should be determined by further studies.

The availability and applicability of LMFBR steam generator and coolant pump technology from the LMFBR program appears to be a relative advantage for the sodium-cooled blanket. Because of the much higher mass flow rate required for Li-Pb in the self-cooled blanket concept (> 8X higher than for sodium coolant at the same ΔT), and the greater corrosivity problems anticipated for Li-Pb, the development of high-rate pumps and steam generators for Li-Pb coolant is considered to be more difficult than for sodium coolant. This development would have to be accomplished prior to DEMO final design. Li-Pb energy conversion system component costs are likely to be higher, also. For example, the twelve Li-Pb pumps for WITAMIR-I have total projected costs of \$112 M. Using the same cost equation, the costs for sodium pumps required for the same reactor thermal power level and coolant ΔT would be ~ \$22 M, a reduction of \$90 M.

Blanket module internal pressure levels should be much lower for the sodium-cooled concept, $\lesssim$ 0.5 MPa as compared to ~ 1-2 MPa for the self-cooled concept. This low pressure level is the result of (1) not requiring the interconnecting of the Li-Pb zones of blanket modules within a sector, and (2) the absence of any pumping pressure head applied to the Li-Pb. The low internal pressure levels are perceived as a distinct advantage in reduced stress levels and reduced risk of leaks for the module walls.

6.5.3 Materials Assessment

6.5.3.1 Properties of 17Li-83Pb

The materials property data base for liquid 17Li-83Pb and its use as a tritium breeding medium for fusion reactors have been recently reviewed.[87,88] Therefore, the information previously reported will not be reiterated here. Selected properties of the alloy are summarized in Table 6-44. Rather, emphasis is placed on key information relating to use of 17Li-83Pb and more recent data, with the focus on two key areas: safety and tritium recovery.

Table 6-44. Selected Properties of 17Li-83Pb

		Reference(s)
Composition, atom fraction, lithium	0.17	43,50
Melting temperature, °C	235	43,50
Density at 500°C, g/cm^3	9.4	50
Volumetric coefficient of thermal expansion	7×10^{-4}	43,50
Lithium atom density, g/cm^3	0.056	
Electrical conductivity, $\Omega^{-1}cm^{-1}$	8000	43,50
Heat capacity, J/g x K	0.17[a]	
Lithium vapor pressure at 500°C, Pa	0.5	43

[a]Averaged from lithium and lead data.

One of the reasons that 17Li-83Pb is of interest is that it is believed to be less reactive than lithium with oxidizing media such as air and water. In an experiment in which the alloy was heated to 500°C and then dropped into water at 90°C, only a modest chemical reaction was observed.[89] Also, measurements of activity coefficients by Saboungi, et al.,[90] showed that the lithium activity in the 17Li-83Pb eutectic was about 1×10^{-3}, which is three orders of magnitude lower than that of pure lithium. However, it is reported that a lithium-lead alloy (approximately 17Li-83Pb) burns in air with very high flame temperature (1200°C) when heated to about 300°C.[87] Experimental results to date have not fully resolved the issue of chemical reactivity.

Additional experiments more nearly simulating potential reactor situations are needed.

It is useful to quantify the potential exothermicity of reactions of air and water with 17Li-83Pb and compare the results with those of other breeder materials. Using available thermochemical data,[71,90] the heats of reaction (ΔH_R, enthalpy change) with water and air were calculated for various breeder materials (Table 6-45). It can be seen that per gram of lithium, the enthalpy of reaction of the alloy with water and with air is not significantly different than that of lithium. In fact, per mole of alkali metal, the exothermicity of the alloy is about the same as sodium. However, on a unit volume basis, since it has a low lithium density, the alloy is significantly less reactive than lithium. Overall, the alloy is expected to be less reactive than lithium, although exothermic reactions with oxidizing media, such as water and air, are possible. In addition, since the alloy is to be used as a liquid, reactions with pressurized water coolant could have severe consequences.

Table 6-45. Heat of Reaction (ΔH_R) of Breeders with Water and Air

Breeder	ρ_{Li} (g/cm^3)	Reaction with Water		Reaction with Air (O_2)	
		kJ/g Li	kJ/cm^3	kJ/g Li	kJ/cm^3
Li	0.48	-34.3	-16.5	-25.9	-12.4
17Li-83Pb	0.064	-28.4	-2.4	-20.0	-1.8
Li_2O	0.93	-8.4	-7.8	0.0	0.0
$LiAlO_2$	0.24	-0.9	-0.2	+10.5	+1.8
Li_2SiO_3	0.36	+2.1	+0.8	+10.5	+3.8

Another area of key interest for this material is the Sieverts' constant, which defines the partitioning of tritium between the gas phase (square root of pressure) and the liquid metal. Preliminary measurements of K have been reported.[92] Also, the Sieverts' constants were estimated from a model.[93] More recently the Sieverts' constants for hydrogen in 17Li-83Pb have been

measured by Veleckis.[94] It was found that $K_s = 7.1 \pm 1.5 \times 10^3$ $atm^{1/2}$ per atom fraction of hydrogen, in the range 400-600°C. As predicted by the model,[93] the constant was found to be independent of temperature. Assuming that, as is the case for Sieverts' constants in lithium,[95] the isotopic effect is approximately proportional to the square root of mass, K_s for tritium is higher by a factor of $\sqrt{3}$. Thus, for tritium in 17Li-83Pb, $K_s = 12.3 \pm 2.6 \times 10^3$ $atm^{1/2}$ per atom fraction of tritium. This expression can be converted into units more convenient for blanket design: $K_s = 4.4 \pm 0.9$ wppb/Pa. Thus, for a relatively high tritium pressure of 1 Pa, the amount of tritium dissolved in the alloy is only 4.4 ppb. It is clear that any tritium extraction method will result in a very low tritium inventory in 17Li-83Pb. However, tritium pressure will be quite high and permeation rates could be excessive. Design solutions to keep tritium permeation low represent additional cost and complexity.

6.5.3.2 Materials Compatibility

Compatibility with the structural material is a key feasibility question for the lithium-lead breeder concept. The maximum blanket operating temperature may be limited by corrosion/compatibility criteria. Since the data base for this system is very limited, much of the compatibility assessment must be extrapolated from available results from similar types of systems. Critical compatibility issues are of two types: (1) those problems related to corrosion/mass transfer effects; and (2) those problems related to effects on the mechanical integrity of the structure. Reference 96 is a recent summary on the corrosion and compatibility considerations of liquid metals for fusion reactor applications.

Corrosion/Mass Transfer

Relatively little experimental data exist for the corrosion of structural alloys in the 17Li-83Pb alloy system. Therefore, the importance of these effects must be deduced from fundamental solubility data and results from similar types of systems. General aspects of the compatibility problem can be summarized as follows:

- Nickel is highly soluble in both lead and lithium, therefore, alloys with significant concentrations of nickel will generally exhibit high corrosion rates.

- Preliminary static capsule tests with Type 316 stainless steel and HT-9 alloy indicate much higher (about 100X) corrosion rates at 500°C in 17Li-83Pb than in lithium under similar conditions.[97] Much lower corrosion rates have been reported in static tests at 350 and 400°C.[98]
- Preliminary results indicate that corrosion of ferrous alloys in 17Li-83Pb is more similar to testing in pure lead than in pure lithium.
- Ferritic steels with low or no nickel are more resistant to attack than austenitic steels.
- Results from Fe-2-1/4Cr-1Mo tests indicate that the extent of penetration by Li-3.5Pb is quite sensitive to the alloy microstructure. Results for 17Li-83Pb were less sensitive to alloy microstructure.
- The importance of impurities in the liquid metal has not been investigated. Nonmetallic impurity effects are generally important in liquid metal systems of interest for practical applictions.
- Pure iron is probably more resistant to corrosion than most ferrous alloys. Minimal alloying is probably desirable from a compatibility viewpoint.
- The refractory metals, e.g., vanadium and niobium alloys, are expected to be much more corrosion resistant than stainless steels or ferritic steels.

Effects on Mechanical Properties

Possibly a greater concern than the corrosion/mass transfer effects are potential stress-corrosion or liquid-metal embrittlement effects on the structural alloys exposed to the lithium-lead alloy. The heavy liquid metals, e.g., lead, bismuth, and tin, generally produce much more severe embrittling effects than the alkali metals. An important aspect of this problem is that it occurs at relatively low temperatures.

Armco iron and low-alloy steels wetted with lead, bismuth, or lead-bismuth eutectic showed severe ductility loss between 200°C and 400°C.[99-101] The largest drop of ductility loss was observed at approximately 350°C. Specimens

exposed to embrittling metals failed as a result of the growth of a brittle crack, whereas in an inert environment they failed by ductile fracture. The temperature range for embrittlement extends considerably below the melting point of the melt and is related to the temperature interval of reduced plasticity of "blue brittleness" of specimens tested in vacuum. Stress relaxation in this temperature range is inhibited, which promotes strain hardening that is more pronounced in specimens deformed in liquid metals.[99,102]

The influence of lead-bismuth eutectic environment on the fatigue strength of ferritic and austenitic steels has been investigated at temperatures between 300 and 600°C.[102,103] The fatigue strength of various grades of steels when wetted by molten lead-bismuth eutectic was substantially reduced by penetration of the liquid metals along the grain boundaries. The deleterious effects of liquid lead-bismuth eutectic can be prevented for the formation of an oxide film on the steel surface, which if maintained, inhibits the wetting of the steel by the liquid metal. Surface oxides are not expected to be stable in the lithium-lead system. The weakening effect of lead-bismuth eutectic can also be eliminated by controlling the cyclic frequency. The fatigue life of low-alloy steel tested in liquid lead-bismuth at a strain rate of 8.0×10^{-6}/s was about the same as that in air, but a drastic reduction in fatigue strength was observed at a strain rate of 5.3×10^{-3}/s.[104,105] The reverse strain-rate effect in liquid metals is explained by accelerated grain boundary diffusion of liquid metal under high cyclic stresses. The absence of the harmful effects at slow strain rates is associated with the relaxation of local stresses such that conditions conducive to grain-boundary diffusion by the liquid metal cannot be produced. Tests of austenitic steel under stress in 17Li-83Pb at 350°C show microcracks after 500 h.[98]

Design Limitations

The data base on compatibility of candidate structural alloys is insufficient to provide definite conclusions. However, based on the available information, the following conclusions are provided as a basis for the present design study:

- Corrosion rates of austenitic steels with significant nickel concentrations are believed to be excessive. Hence, these alloys have not been selected as the candidate structural materials for the lithium-lead breeder concepts.

- Although corrosion rates of ferritic steels are predicted to be quite high and the potential for liquid-metal embrittlement exists, these alloys are proposed as a candidate structural material.
- Although data for refractory metals are practically nonexistent, corrosion rates are predicted to be much lower than those for the ferrous alloys. Therefore, vanadium-base alloys are proposed as a candidate structural material.

Table 6-46 shows suggested temperature limits for lithium-lead blanket based on corrosion/compatibility criteria.

Table 6-46. Maximum Temperature Limits (°C) for Structural Alloys in 17Li-83Pb

Structural Alloy	Static System	Recirculating System
Austenitic steel (Type 316)	400	NA[a]
Ferritic steel (HT-9)	450	400
Vanadium alloy (V-Cr-Ti)	600	550

[a]NA = not acceptable.

6.5.4 Tritium Control and Recovery with Liquid-Metal Blanket Systems

6.5.4.1 Introduction

For the DEMO design, the liquid-metal blanket material was 17Li-83Pb. The coolant designs considered were self-cooled 17Li-83Pb or the use of either water, sodium, or helium as the coolant. The structural materials considered were vanadium alloy and ferritic steel. The methods assessed for tritium extraction from the blanket were molten salt extraction, helium sparging, cold trapping, and the use of yttrium getters. Some special design features to achieve tritium control in the primary coolant system were assessed: (1) double-wall blanket coolant tubes with helium/oxygen in the gap; and (2) a matrix steam generator with a gap containing helium/oxygen between the tubes.

To assist in identifying feasible designs from the standpoint of tritium recovery and tritium control, the numerous system options were analyzed and an attempt was made to define workable combinations.

6.5.4.2 Design and Materials Considerations

The nature of the alloy, 17Li-83Pb, used as the breeding material introduced several constraints on the design of the blanket system. The Sievert constant for tritium in 17Li-83Pb extrapolated from hydrogen[94] is $K_s = 4.4 \pm 0.9$ wppb/$Pa^{1/2}$ in the range 400 to 600°C. With a tritium partial pressure of 1 Pa, the amount of tritium dissolved in $\sim 10^7$ kg of 17Li-83Pb would be ~ 40 g. Thus, with any workable tritium extraction method, the tritium inventory in the 17Li-83Pb alloy should be low; however, the tritium partial pressure achievable with reasonable processing rates might be relatively high (i.e., ~ 1 Pa). At this pressure, relatively high tritium permeation rates and tritium inventories would result in some structural alloys, particularly the vanadium alloy. Therefore, an important consideration in design was the control of the tritium permeation.

It is also desirable to remove impurities other than tritium from the 17Li-83Pb, ideally by the same process. Helium sparging is not effective in removing non-gaseous impurities from a liquid metal. However, a companion process could be used with the helium sparging to remove the impurities. Therefore, helium sparging was considered as an option for tritium recovery. Since tritium solubility in 17Li-83Pb is not temperature dependent, direct

cold trapping was not used for tritium recovery even though other impurities would be removed. Yttrium getters in direct contact with 17Li-83Pb could form a separate phase of YPb_3.[106] Other impurities (O, N, C) could react irreversibly with the yttrium. Therefore, yttrium getters were not considered as a method of tritium recovery. Molten salt extraction should be able to handle the removal of impurities as well as tritium, and should not be affected by the lead species present.

A third consideration was the ability to replace the lithium burned while reactor operation continues, rather than by removal and replacement of blanket sectors. For a static 17Li-83Pb blanket, a subsystem may be needed both to add lithium and to remove impurities.

The temperature limit required with a particular material both from the standpoints of corrosion and tritium control requirements had to be considered. For vanadium alloy, the upper limit was 600°C in a static system and 550°C in a circulating system to minimize corrosion. For ferritic steels, the upper limit was 450°C in a static system and 400°C in a circulating system (see Section 6.5.3.2).

In the analysis of the different blanket systems, the following assumptions were made. For each tritium recovery or tritium control system, steady-state operation was assumed; i.e., the extraction system processed tritium at the rate at which it was bred, ~ 180 g/d. The tritium partial pressure was maintained at $\leq$ 1 Pa in all systems associated with the blanket. The design of the tritium control system minimized the amount of tritiated water formed and minimized the tritium lost from the system.

6.5.4.3 Tritium Control

Since the tritium solubility in 17Li-83Pb is extremely low, which results in a high tritium partial pressure, tritium control throughout the blanket system was the key design constraint for all blanket systems considered. To insure that tritium control could be achieved, especially with the use of a vanadium alloy, it was necessary to use a double-wall tube design for blanket coolant tubes or for a matrix steam generator, depending on the coolant considered. The interior annulus of the tube was assumed to be filled with a slowly flowing mixture of helium and oxygen. (Since the upper temperature limit for the vanadium alloy may be less than 450°C in the presence of oxygen,

this design needs further evaluation for use with this alloy.) One wall of the double-wall tube was constructed of the structural alloy of interest, either vanadium alloy or ferritic steel, and was ~ 1.5 mm thick. This tube was assumed to be at approximately the same temperature as the 17Li-83Pb (the conservative case). The other wall was constructed of stainless steel to reduce permeation and was ~ 0.9 mm thick. The temperature of the stainless steel wall was varied from 350°C to that of the structural alloy of interest. The thickness of the annulus was assumed to be ~ 0.1 mm.

Two general cases were required. For coolants other than 17Li-83Pb, the stainless steel wall was nearest the coolant. For flowing 17Li-83Pb (coolant or processing line), vanadium alloy or ferritic steel was adjacent to the 17Li-83Pb. The oxygen present in the annulus (~ 1.4 Pa) reduced tritium permeation in several ways. First, an oxide coating was assumed to be formed on the surfaces of both tubes, which reduced the tritium permeation through the vanadium alloy by a factor of 1000, through the ferritic steel by a factor of 100, and through the stainless steel by a factor of 10. Second, the oxygen present was assumed to react with the T_2 to form T_2O. Provided that the T_2O was removed at the rate at which it was formed, the T_2 partial pressure would be $< 10^{-10}$ Pa in the temperature range of interest--450 to 550°C. (The equilibrium constant for the reaction has been estimated to be ~ 5×10^{19} $Pa^{1/2}$ at ~ 525°C).[107]

To insure that minimum tritium was transported into the secondary system of the steam generator, a gap ~ 1 mm thick containing ~ 1 atm He with a partial pressure of 1.4 Pa oxygen was incorporated into the design. A thinner maintainable gap would be usable. However, no attempt was made here to minimize the gap size. The wall thickness of the steam tube (316 stainless steel) was ~ 12.7 mm, and the wall thickness of the coolant tube was ~ 10 mm. A steam generator of this design was used with a self-cooled 17Li-83Pb design and with a sodium coolant.

The effect of the design features cited above on tritium control are described here. Structural dimensions for the different coolant options are listed in Table 6-47. Tritium permeation and solubility constants for various materials have been summarized previously.[108] For a vanadium alloy, the tritium control achievable with different coolant tube designs is presented in Table 6-48. The permeation rate at 550°C with a tritium partial pressure of 10^{-4} Pa was 140 g/d to the coolant or to the reactor hall if a single-wall,

Table 6-47. Structural Dimensions Assumed for the Coolant Options Considered for a 17Li-83Pb Blanket

Dimensions	Self-Cooled 17Li-83Pb	Sodium/H_2O	Helium
Coolant Weight, kg	6×10^6	8×10^5	2×10^5
Coolant Volume, m^3	680	810	1299
Blanket Structure:			
Surface Area,[a] m^2	403	2052	3970
Volume,[a] m^3	2	10	20
Piping Structure:			
Surface Area,[b] m^2	1221	1082	3288
Volume,[b] m^3	6	5	17
Steam Generator Structure:			
Surface Area,[c] m^2	3693	3693	5899
Volume,[c] m^3	19	19	30

[a]Refers to surface area and volume of coolant structural material within the blanket.
[b]Refers to structural surface area and volume of coolant piping outside the blanket and steam generator.
[c]Refers to surface area and volume of structural material dedicated to the primary coolant in the steam generator.

unoxidized coolant tube 1.5 mm thick was used in the blanket. Use of a thicker tube (5 mm) and the achievement of a tritium partial pressure in the 17Li-83Pb of 10^{-6} Pa (a very optimistic projection) still resulted in a permeation rate of 4 g/d. If a thicker tube (5 mm), an oxide barrier, and a pressure of 1 Pa was assumed, the permeation rate was also ~ 4 g/d. The use of a double-wall, unoxidized tube with the vanadium alloy at 450°C and the stainless steel section at 350°C reduced the permeation to the coolant to ~ 1 g/d. However, most of the tritium was now in the small annular space. To extract all the bred T_2 from the narrow (~ 0.1 mm) annular space while maintaining the tritium partial pressure at $\leq$ 1 Pa would be difficult. If the vanadium alloy cannot be subjected at 450°C to an oxygen environment, then the 1 g/d loss to the coolant would have to be accepted. However, if oxygen was added to the helium in the annulus, the permeation rate to the annulus was reduced to ~ 3 g/d. In addition, the tritium in the annulus was now mainly T_2O, which would not permeate through the stainless steel wall to the coolant. The partial pressure of T_2 in equilibrium with the T_2O was

Table 6-48. Tritium Control Demonstrated for a 17Li-83Pb Blanket with a Vanadium Alloy Structure[a]

Material	Temperature (°C)	Permeation Constant[b]	Pressure (Pa)	Wall Thickness (mm)	Oxide Barrier	Tritium in Annulus (g/d)	Permeation Rate[c] (g/d)
V[d]	550	100	10^{-4}	1.5	--	--	140
V	550	100	10^{-4}	5.0	--	--	40
V	550	100	10^{-6}	5.0	--	--	4
V	450	20	10^{-2}	1.5	--	--	30
V	450	20	10^{-1}	1.5	--	~ 180	~ 180
SS[e]	350	0.005	10^{-1}	0.9	--	--	1
V	450	20	1	1.5	10^3X	~ 3	3
SS	350	0.005	10^{-10}	0.9	10X	--	~ 10^{-5}
V	550	100	1	1.5	10^3X	~ 14	14
SS	350	0.005	10^{-10}	0.9	10X	--	~ 10^{-5}
V	550	100	1	1.5	10^3X	~ 14	14
SS	550	0.1	10^{-10}	0.9	10X	--	~ 10^{-4}

[a] Surface area used was 2052 m^2.
[b] Units are $Ci/d \cdot m \cdot Pa^{1/2}$.
[c] The rate is expressed as $R = K_1$ area $(\text{pressure})^{1/2}/\text{thickness}$.
[d] V = vanadium alloy; the permeation constant for vanadium was considered to be representative.
[e] SS = 316 stainless steel.

$< 10^{-10}$ Pa, which corresponded to a permeation rate through the stainless steel wall held at 350°C of $\sim 10^{-5}$ g/d. The T_2O in the annulus was processed by passing the helium through cooled molecular sieves thereby trapping the T_2O. Removal of the temperature gradient in the double-wall, oxidized tube increased the permeation rate to the annulus to 14 g/d. If the T_2 partial pressure in the annulus was maintained at $< 10^{-10}$ Pa without a temperature gradient, then the permeation rate through the stainless steel wall was increased from 10^{-5} g/d to $\sim 10^{-4}$ g/d. Higher T_2 partial pressures in the annulus would result in higher permeation rates through the stainless steel wall.

The tritium control achieved with ferritic steel blanket coolant tubes employing a double-wall design is summarized in Table 6-49. The tritium permeation rate through the stainless steel wall of an oxidized tube was $< 10^{-5}$ g/d. The amount of tritium which had to be processed in the annular space was ~ 0.3 g/d.

In the matrix steam generator approach, the tritium partial pressure in the gap containing a mixture of helium/oxygen was $< 10^{-10}$ Pa. The temperature of the steam tube wall was $\sim$ 350°C. Thus, the expected tritium permeation rate to the steam was $\leq 10^{-6}$ g/d. The tenfold decrease as compared to that achieved using double-wall tubes was due to the thicker wall in the tube in the steam generator. In addition, the oxygen pressure in the helium gap in the steam generator resulted in a reduction in the protium (H_2) permeation rate from the steam to the coolant. At 50 atm, the protium partial pressure in the steam was $\sim 10^{-2}$ Pa. This corresponded to a protium permeation rate to the gap of $\sim 10^{-3}$ g/d with the use of a thicker wall, oxidized tube. Conversion of the protium to H_2O in the gap resulted in a protium partial pressure $\leq 10^{-12}$ Pa in the gap of the steam generator.

At 1 Pa, the tritium dissolved in the structural materials was < 0.2 g for ferritic steel, < 2 g for stainless steel, and ranged from 0.2 to 1 kg for the vanadium alloy (see Table 6-50). The use of a vanadium alloy resulted in a large tritium inventory in the structure.

The structural designs selected for the different coolant options were the following. For both a self-cooled and a semi-stagnant 17Li-83Pb system, concentric tubes of HT-9 and stainless steel were used for all 17Li-83Pb piping outside the reactor vacuum boundary. The annulus between the tubes

Table 6-49. Tritium Control Demonstrated for a 17Li-83Pb Blanket with a Ferritic Steel Structure[a]

Material	Temperature (°C)	Permeation Constant[b]	Pressure (Pa)	Wall Thickness (mm)	Oxide Barrier	Tritium in Annulus (g/d)	Permeation Rate[c] (g/d)
Fe[d]	400	0.2	1	1.5	--	--	29
Fe	400	0.2	1	5.0	--	--	9
Fe	400	0.2	10^{-6}	5.0	--	--	$\sim 10^{-2}$
Fe	400	0.2	1	1.5	--	--	29
Fe	400	0.2	1	1.5	--	29	29
SS[e]	350	0.005	1	0.9	--	--	1.2
Fe	400	0.2	1	1.5	10^2X	$\sim$ 0.3	0.3
SS	350	0.005	10^{-10}	0.9	10X	--	$< 10^{-5}$
Fe	400	0.2	1	1.5	10^2X	$\sim$ 0.3	0.3
SS	400	0.01	10^{-10}	0.9	10X	--	$\sim 10^{-5}$

[a]Surface area used was 2052 m^2.
[b]Units are $Ci/d \cdot m \cdot Pa^{1/2}$.
[c]The rate is expressed as $R = K_1$ area $(\text{pressure})^{1/2}$/thickness.
[d]Fe = ferritic steel.
[e]SS = 316 stainless steel.

Table 6-50. The Amount of Tritium Dissolved in the Structural Material at 1 Pa Tritium Partial Pressure[a]

Material	Temperature (°C)	Solubility Constant[b] ($ppm/Pa^{1/2}$)	Wall Thickness (mm)	Tritium Solubility (g)
V[c]	550	200	1.5	~ 225
V	450	400	1.5	~ 450
V	400	800	1.5	~ 900
V	550	200	5.0	~ 740
Fe[d]	350-450	~ 0.1	1.5	< 0.2[e]
SS[f]	350-450	~ 1.0	1.5	< 2.0

[a]Surface area used was 2052 m^2.
[b]The solubility is expressed as $S = K_2(Pressure)^{1/2}$.
[c]V = Vanadium alloy.
[d]Fe = Ferritic steel.
[e]At 100 Pa, the amount of tritium dissolved would be < 2 g.
[f]SS = 316 stainless steel.

contained a helium/oxygen mixture. Within the reactor, single-wall tubes were adequate for a self-cooled 17Li-83Pb system. The use of vanadium alloy in place of the ferritic steel would be possible if the alloy were not affected by the presence of oxygen. For the self-cooled system, a matrix steam generator was required.

With both water and helium coolants, the piping within the blanket consisted of concentric tubes of HT-9 and stainless steel. The annulus contained helium/oxygen. Tritium recovery was achieved via a side process stream from the 17Li-83Pb blanket (see above description). Single-wall coolant tubes were adequate outside the reactor. A matrix steam generator was not required since the tritium permeation into either water or helium was $< 10^{-5}$ g/d (0.1 Ci/d).

With sodium coolant, single-wall tubes were used in the blanket and double-wall tubes of stainless steel were used outside the blanket. The annulus contained helium/oxygen. A matrix steam generator was required.

6.5.4.4 Tritium Recovery

For 17Li-83Pb, the processing methods considered were molten salt extraction, vacuum pumping and/or inert gas sparging, regenerable solid hydride getters, and permeation "windows." All four methods had the potential of being used whether the blanket fluid was the primary coolant or the blanket was semi-stagnant with a slow rate of circulation necessary for processing. However, the use of yttrium getters was not considered because of potential impurity problems, i.e., the formation of YPb_3[106] or other O, N, C compounds if the 17Li-83Pb was in contact with the getter material. The permeation "window" method was considered for use with a sodium coolant. Therefore, the main focus of this analysis was to determine for molten salt extraction, helium sparging, and sodium cold trapping workable extraction systems in which the tritium partial pressure was maintained at ~ 1 Pa. The achievement of lower partial pressures was desirable but might not be possible in a large-scale operating system.

For all the coolants considered, the liquid-metal tritium recovery stream was pumped with electromagnetic pumps through double-wall tubes (previously described). The pump speeds required were such that the low efficiency of the electromagnetic pumps was not considered a penalty.[109] The limit on performance was considered to be the frequency with which the entire blanket was processed. With a breeding rate of 180 g/d and an extraction efficiency of 99%, the entire blanket had to be processed approximately five times per day to achieve the desired tritium partial pressure of ~ 1 Pa.

Molten Salt Extraction

A summary of the analysis done for the molten salt extraction method is shown in Table 6-51. The design of the overall system was based on data derived for lithium systems.[96,110] The main components of the system were contactors, electrolysis units, and uranium getter beds. The latter were used to store the recovered tritium. The analysis did not consider the effect of the electrolysis units nor the getter beds on process requirements. The contactor was expected to have a slightly different design than that used in the lithium system since 17Li-83Pb is more dense than the molten salt, whereas lithium is less dense. With a ferritic alloy, the maximum temperature in the contactor was 400°C; with a vanadium alloy, it was in the range of 450 to

Table 6-51. Analysis of Molten Salt Tritium Extraction for a 17Li-83Pb Blanket (6×10^6 kg)

Number of Times Total Mass 17Li-83Pb Processed/d	4.8	4.8	7.2	9.6	24
Flow Rate (kg/s)	332	332	500	664	1660
Residence Time (min)	5	5	3.3	2.5	1
Efficiency (%)	99	90	99	99	99
Tritium Concentration in 17Li-83Pb (10^{-9} kg/kg)	6.36	7.00	4.16	3.17	1.27
Tritium Partial Pressure (Pa)	2	2.5	0.9	0.5	0.08
Tritium Inventory (g)					
17Li-83Pb	38	42	25	21	8
Salt	< 0.1	< 0.1	< 0.1	< 0.1	< 0.1
Number of Contactors[a]	11	11	17	22	55
Total Power/Contactors (kw)	40	40	63	82	200

[a]Sizes were equivalent to those in Ref. 5.

550°C. It was expected that a molten salt compatible with 17Li-83Pb would be used, that no impurities which could activate entered the 17Li-83Pb, that the lithium remained in the alloy phase, and that the impurities were extracted into the molten salt. Verification of all these points has yet to be established in experimental studies. As seen in Table 6-51, 17Li-83Pb process flow rates of ~ 332 kg/s resulted in a tritium partial pressure of ~ 2 Pa.

Sodium Cold Trap

To use a sodium cold trap,[111,112] a permeation "window" was required. Therefore, with this option, double-wall tubes were not used in the blanket. A problem with this method was that the assumption had to be made that the single-wall tubes were not contaminated with oxide, which would impede tritium permeation. Since an impurity removal process for the 17Li-83Pb was not possible with a completely static blanket, a side stream was processed to remove impurities. It was assumed that the cold trap system was regenerated once per day, which resulted in ~ 180 g of tritium inventory in the cold traps. The reason for this choice was the following. The sodium flow rate required, ~ 1 kg/s, was about three times the rate for which the sodium cold trap at the Clinch River Breeder Reactor was designed. Since the latter unit was designed to be efficient, large-scale improvements were not anticipated.

The system planned for 17Li-83Pb would, to achieve redundancy, incorporate cold traps in multiples of four with each six hours out-of-phase with the other. Each trap held at 115°C during operation would require ~ 1 d to warm up to 450°C, after which the tritium would be removed by pumping. A summary of the analysis is shown in Table 6-52. The tritium partial pressure within the sodium was maintained below 10^{-3} Pa with flow rates of ~ 40 kg/s.

Table 6-52. Analysis of Cold Trapping (115°C) of the Sodium Coolant as a Means of Extracting Tritium from 17Li-83Pb (6×10^6 kg)

Number of Times Mass of Na Processed/d	4	0.4	0.08	0.04	0.02
Flow Rate (kg/s)	40	4	0.8	0.4	0.2
Residence Time (min)	5.5	55	278	555	1111
Efficiency (%)	99	99	99	99	99
Tritium Concentration in Na (10^{-8} kg/kg)	4.3	6.2	13	17	20
Tritium Partial Pressure (Pa)	1.2×10^{-3}	3×10^{-3}	1.4×10^{-2}	2×10^{-2}	3×10^{-2}
Tritium Inventory (g)					
Na	34	50	104	136	160
Cold Trap	180	180	180	180	180
17Li-83Pb[a]	25,250	25,250	25,250	25,250	25,250

[a]With vanadium alloy, it was 25 g; with ferritic steel, it was 250 g. The difference was due to the higher tritium partial pressure required with the ferritic steel.

Helium Sparging

The use of vacuum pumping/helium sparging was first advocated in the WITAMIR design.[86] Helium sparging was the system considered for DEMO to enhance mass transfer of the tritium. For this analysis, the equation derived by Geller[113] was used with the appropriate K value for 17Li-83Pb. To obtain good mass transfer, it was assumed that part of the 17Li-83Pb was circulated outside of the blanket to a unit where helium was brought in contact with the 17Li-83Pb. Thus, a liquid circulating system, a vacuum system composed of Roots blowers, and a system composed of mixing units were required. To remove non-gaseous impurities, additional processing (not specified) would be required. The results of the analysis are shown in Table 6-53. To achieve a

Table 6-53. Analysis of Helium Sparging as a Means of Extracting Tritium from 17Li-83Pb (6×10^6 kg)[a,b]

Number of Times Mass of 17Li-83Pb Processed/d	4.8	4.8	24	24	48	48
Residence Time (min)	5	5	1	1	5	5
Efficiency (%)	40	90	40	90	40	90
Tritium Concentration (10^{-9} kg/kg)	15	6.7	13	~ 4	6.7	~ 4
External Pressure Maintained (Pa)	1	1	1	1	1	1
Pump Speed (m^3/s)	0.4	3	2	15	4	30
Tritium Partial Pressure (Pa)	11.5	2	9	~ 1	2	~ 1
Tritium Inventory (g)	90	40	80	~ 25	40	~ 25
Flow Rate Required (kg/s)	332	332	1660	1660	332	332
Mass in Extractor (kg)	10^5	10^5	10^5	10^5	10^6	10^6

[a]A companion process would be necessary to remove non-gaseous impurities.
[b]Conductance losses were not considered.

tritium partial pressure of ~ 1 Pa, an extraction efficiency of 90% must be assumed with a 17Li-83Pb flow rate equivalent to that necessary in the molten salt extraction system. In addition, a vacuum pumping system capable of achieving speeds of 3 m^3/s must also be provided. The pumping speeds required would increase in an actual system where there could be substantial conductance losses. If the extraction efficiency were < 90%, both the 17Li-83Pb flow rate and the vacuum pumping speed would have to be increased.

In Table 6-54, the three methods analyzed were compared. With a sodium coolant, all three methods could be used. For the other coolants, either molten salt extraction or helium sparging could be used, resulting in comparable tritium partial pressures and inventories. To differentiate between the latter two methods, experimental studies are required in order to verify the overall extraction efficiency, pinpoint any compatibility problems, and demonstrate effective removal of undesired impurities. At this time, it is premature to advocate one over the other.

Table 6-54. Comparison of Molten Salt Extraction, Sodium Cold Trapping and Helium Sparging for Tritium Extraction from 17Li-83Pb

Process Variables	Molten Salt	Sodium Cold Trapping	Helium Sparging
Number of Times Mass of 17Li-83Pb or Na Processed/d	4.8	4	4.8
Efficiency (%)	90	99	90
Tritium Pressure (Pa)			
17Li-83Pb	2.5	1[a], 100[b]	2
He/Na	--	10^{-3}	1
Pump Speed[d] (m^3/s)	--	--	3
Tritium Inventory (g)			
17Li-83Pb	42	25[a], 250[b]	40
Na	--	34	--
Molten Salt	< 0.1	--	--
Cold Trap	--	180[c]	--
Flow Rate (kg/s)	332	40	332

[a]With vanadium alloy.
[b]With ferritic steel.
[c]Assumption made was that trap was charged once a day.
[d]No conductance losses were included.

6.5.4.5 Summary and Conclusions

The most important consideration with a 17Li-83Pb blanket was the control of tritium permeation. To achieve this, double-wall tubes constructed of two different materials (usually ferritic steel and stainless steel) with a mixture of helium/oxygen in the annulus were required. The location of tubes of this type was inside the reactor for water and helium coolants; they were outside the reactor for 17Li-83Pb and sodium coolants. In addition, a matrix heat exchanger with a gap containing helium/oxygen between the two sets of tubes was required for self-cooled 17Li-83Pb and sodium. For most coolants, a side stream of the 17Li-83Pb was diverted to effect tritium extraction, impurity removal, and lithium addition. Either molten salt extraction or helium sparging would be used to extract tritium from the side stream for coolants other than sodium. The choice between these two methods would depend on the results of experimental studies on their overall tritium process efficiencies, impurity removal requirements, and compatibility problems. With a sodium coolant, the combination of cold traps and the permeation "window"

method could be used. This extraction method was most applicable with a vanadium alloy but could be used with a ferritic alloy. The total tritium inventory in the blanket system was appreciably increased by the use of a vanadium alloy. Its use added 0.4 to 1 kg to the inventory. The tritium inventory associated with the different extraction processes, not including that in the structural alloy, ranged from 40 g for both the molten salt and the helium sparging methods to 240 to 460 g for the sodium cold trapping method. Tritium permeation rates to the systems connected to the blanket were expected to be $\leq 10^{-4}$ g/d (1 Ci/d) to the reactor hall and $\leq 10^{-6}$ g/d (10^{-2} Ci/d) to the secondary coolant.

6.5.5 Thermal-Hydraulics Analyses

Of the 17Li-83Pb breeder blanket approaches considered within the DEMO study, the most significant thermal-hydraulics issues involve the self-cooled concepts. The two most important concerns for these concepts relate to (1) the requirements for cooling the first wall and the resultant structural temperatures, and (2) the MHD effects on the flowing liquid metal and the frictional and MHD-related pumping power losses for the coolant system. These areas are addressed in Sections 6.5.5.1 and 6.5.5.2 respectively, for the self-cooled configuration discussed in Section 6.5.2.3.

6.5.5.1 Pumping Considerations and MHD Effects

This section considers the pumping power requirements and MHD effects associated with the use of 17Li-83Pb as a fusion reactor coolant. Comparisons are made with sodium, lithium, and water as coolants. Lithium is included since it can be used either as a coolant, like sodium, or as both the breeder and coolant, like 17Li-83Pb. Helium is not included here for the reasons given in Section 6.2.3.1.

Pumping Power

In evaluating the pumping power, the physical properties of the various coolants are used as shown in Table 6-55. For direct comparison between coolants, the coolant pumping power is calculated based on the same coolant system configuration including the same blanket geometry. The blanket geometry used is the elongated radial-flow cell proposed for the 17Li-83Pb

Table 6-55. Physical Properties of Various Coolants and Coolant Components

Coolant or Coolant Component	Reference	Melting Point, °C	(T) Temp., °C	(ρ) Density, kg/m^3	(c_p) Heat Capacity, J/(kg·K)	(μ) Dynamic Viscosity, Pa·s	(σ) Electrical Conductivity, S/m or $\Omega^{-1}\,m^{-1}$
H_2O	(114)	0.0	280	750	5.3×10^3	0.95×10^{-4}	$(4 \times 10^{-6})^a$
			320	664	6.6×10^3	0.80×10^{-4}	
Na	(115)	97.8	350	866	1.29×10^3	3.11×10^{-4}	5.0×10^6
			400	856	1.28×10^3	2.84×10^{-4}	4.5×10^6
Li	(116)	179	350	494	4.2×10^3	3.7×10^{-4}	$(1.67 \times 10^6)^b$
			400	490	4.2×10^3	3.0×10^{-4}	$(1.49 \times 10^6)^b$
Pb	(116)	327.4	350	1.057×10^4	0.160×10^3	24.6×10^{-4}	$(1.06 \times 10^6)^b$
			400	1.051×10^4	0.158×10^3	22.7×10^{-4}	$(1.02 \times 10^6)^b$
17Li-83Pb	(117)	235	350	$(1.050 \times 10^4)^c$	$(0.187 \times 10^3)^c$	$(24.5 \times 10^{-4})^c$	$(0.93 \times 10^6)^d$
			400	$(1.044 \times 10^4)^c$	$(0.185 \times 10^3)^c$	$(22.6 \times 10^{-4})^c$	$(0.90 \times 10^6)^d$

[a] Data for pure water at 18°C.(118)

[b] Data for electrical resistivity in μohms is assumed to be in μohm-cm .(116)

[c] This value is a mass average of the values for pure Li (mass fraction = 0.0068) and pure Pb (mass fraction = 0.9932).

[d] These values for electrical conductivity are interpolated from data for solid and liquid 17Li-83Pb(119) and for solid and liquid Pb.(116)

coolant and shown in Fig. 6-32. The cross-sectional area of this cell as it faces the plasma is assumed to be square with each side being 0.5 m. The cell is assumed to extend back from the first wall a distance of 0.7 m. The feed line to the first wall is considered as either (1) a tube with a radius (r) of 89 mm or (2) a channel slot with a half thickness (a) of 25 mm and a width (W) of 500 mm. In both cases, the incoming coolant uses 10% of the cell cross-sectional area.

Once the temperature rise (ΔT) of the coolant through the reactor blanket and the total thermal power (Q') released from the plasma are specified, the volumetric flow rate (q) of the coolant can be calculated using

$$q = \frac{Q'}{\rho c_p \Delta T} \cdot \tag{6-26}$$

The results are listed in Table 6-56. Note that, for the same ΔT, the 17Li-83Pb is actually a more effective coolant than the sodium and is comparable to the lithium on the basis of required volumetric flow.

All the coolant systems are assumed to be closed loop systems. Because of this, the total pressure does not determine the pumping power. The total pressure must be kept high with water as a coolant ($\geq$ 8 MPa) to keep steam from forming at 300°C. The total pressure will also be high for 17Li-83Pb because its static pressure can reach 1.0 MPa or higher (see Table 6-56). Instead of the total pressure, the pressure drop (Δp) due to frictional flow losses and the combined efficiency (E_{pm}) of the pump and motor are used to get the frictional pumping power (P) as

$$P = q\Delta p/E_{pm} \tag{6-27}$$

where q is the volumetric flow rate.

To calculate the frictional pressure drop, the various mechanical energy losses (F) due to fluid friction[120] are summed as

$$\Delta p = \rho \Sigma F \tag{6-28}$$

where ρ is the fluid density. For the 17Li-83Pb coolant system, ΣF is estimated to be about 20 m^2/s^2 for the reactor blanket so that Δp is 0.21

Table 6-56. Frictional Pumping Power

Total Thermal Power (O') = 1050 MW
Total Electrical Power (P_e) = 300 MW
Coolant Head (h) = 10 m
Combined Efficiency of Pump and Motor (E_{pm}) = 0.75

Coolant	(T) Outlet Temp., °C	ΔT, K	(q) Volumetric Flow Rate, m^3/s	(ρgh) Static Pressure, MPa	(Δp) Pressure Drop due to Frictional Flow Losses, MPa	(P) Frictional Pumping Power (No MHD Effects), MW	Total Frictional Pumping Power[a] Relative to Total P_e, %
H_2O	300	40	6.60	0.069	0.029	0.26	0.13
Na	400	125	7.52	0.084	0.052	0.52	0.26
Li	400	125	4.05	0.048	0.011	0.06	0.03
17Li-83Pb	400[b]	125	4.28	1.02	0.210	1.20	0.60

[a] Includes a 50% increase in the frictional pumping power (no MHD effects) so that frictional flow losses in the steam generator are included.

[b] Temperature at outlet is based on corrosion/compatibility data estimate for recirculating 17Li-83Pb blanket for HT-9 ferritic steel (see Sec. 6.5.3).

MPa. Note that frictional flow losses in the steam generator might increase this estimate as much as 50%. Because the total thermal power is 1050 MW, the total volumetric flow rate to remove this heat from the blanket must be 4.28 m^3/s. Thus, the power required to pump the Li-Pb alloy with a combined motor and pump efficiency of 0.75 will be 1.20 MW. This is 0.4% of the total electrical power generated. When frictional losses in the steam generator are included, the total electrical power required for pumping 17Li-83Pb will be 0.6% of the total electrical power generated.

If the flow channel geometry is held constant, the frictional pumping power required for various coolants and operating conditions is proportional to

$$P \quad \frac{\mu^{0.2}(\dot{Q}')^{2.8}}{\rho^2 c_p^{2.8}(\Delta T)^{2.8}} \quad . \tag{6-29}$$

Thus, from the frictional pumping power required for the 17Li-83Pb coolant, the power for the other coolants can be calculated. The results of these calculations, which are listed in Table 6-56 show that the pumping power for 17Li-83Pb will be more than twice that for sodium. The pumping power for lithium and water will be lower than that for either sodium or the Li-Pb alloy.

MHD Effects

The magnetohydrodynamic (MHD) effect was evaluated for the coolant flow to the first wall and through the first wall of the radial-flow cell. The flows in these two regions will be crossing the strong toroidal magnetic field (B) with a high velocity so that MHD effects will be most important here.

For the coolant feed line to the first wall, both a circular tube and a rectangular channel (slot) were considered. If the first wall is oriented to minimize the effects of the toroidal field (because the first wall is curved poloidally, it is impossible for the flow to always be completely parallel to B), the header that distributes the coolant from the circular feed line to the first wall will be oriented so that the flow will be perpendicular to B, and thus the MHD effects will be important. This will give more flow through the center of the first wall cooling channel than near the edges and will result in hot spots near the edges of the first wall. The use of a rectangular

channel for the coolant feed line to the first wall will give a better coolant distribution in the first wall cooling channel. For this reason, only the rectangular feed line to the first wall is evaluated in detail.

As a basis for calculation, the rectangular feed line is taken to have a thickness (2a) of 0.05 m, a width (W) of 0.5 m, and a length (L) of 0.6 m. The two rectangular coolant channels in the first wall each have a thickness or gap (2a) of 0.01 m, a width (W) of 0.5 m, and a length (L) of 0.4 m. This length is along the circumference of a semi-circle with a diameter of 0.25 m. The thickness of the channel walls (t_w) is taken to be 0.005 m for both the feed line and the first wall. The electrical conductivity of the walls (σ_w), if they are made of ferritic steel, will be about 1.4×10^6 siemens (or mho) per meter (S/m).[121] The toroidal field strength (B) on the outboard blanket will be about 3.5 tesla (T).[122] With a total first wall area of 400 m^2, the number (N_c) of identical blanket channels will be 1600 for the feed line and 3200 for the first wall. The coolant flow in a channel will be q/N_c.

The MHD pressure drop (Δp_m) for flow in a closed channel is given by[124] as:

$$\Delta p_m = \frac{\rho V^2 L M}{d_h Re} \left(\frac{M\phi + 1}{1 + \phi}\right) \tag{6-30}$$

which becomes

$$\Delta p_m = \frac{\rho V^2 L}{d_h} \left(\frac{M^2}{Re}\right) \left(\frac{\phi}{1 + \phi}\right) \tag{6-31}$$

when $M\phi \gg 1$. In this expression, the conductivity ratio (ϕ) is given by Ref. 123 as:

$$\phi = \frac{2t_w \sigma_w}{d_h \sigma} \Big/ \left(1 + \frac{4t_w \sigma_w R_c}{d_h^2}\right) \tag{6-32}$$

where R_c is the contact resistance between the liquid metal and the wall and d_h is the hydraulic diameter for the rectangular slot given by:

$$d_h = \frac{4aW}{(W + 2a)} \tag{6-33}$$

This reduces to

$$d_h \simeq 4a \tag{6-34}$$

for $W >> 2a$. When the contact resistance becomes small,

$$\phi \simeq \frac{2t_w\sigma_w}{d_h\sigma} \tag{6-35}$$

The other quantities in the expression for Δp_m are the Hartmann number (M) given by:

$$M = Bd_h \sqrt{\sigma/\mu} \ , \tag{6-36}$$

the Reynolds number (Re) given by:

$$Re = \rho V d_h/\mu \ , \tag{6-37}$$

and the velocity in the channel given by:

$$V = \frac{q}{2aWN_c} \ . \tag{6-38}$$

In addition, to use the expression for Δp_m, the flow must be laminar which means that Re/M must be less than 250. Experimentally measured MHD pressure drops (Δp_m) start to become less than predicted when the magnetic interaction parameter (N) defined by:

$$N = \frac{M^2}{Re} \tag{6-39}$$

becomes greater than 100.[124] Results for calculated Δp_m are listed in Table 6-57 for the flow in the feed line and the first wall.

The MHD pumping power (P_m) for the 17Li-83Pb coolant is also listed in this table. As stated above, P_m is given by $q\Delta p_m/E_{pm}$ which can be written as:

$$P_m = \frac{B^2L(Q')^2t_w\sigma_w}{4a^2c_p^2E_{pm}N_c(\Delta T)^2W\rho^2 \left(1 + \frac{t_w\sigma_w}{2a\sigma}\right)} \tag{6-40}$$

Table 6-57. MHD Pumping Power for 17Li-83Pb Coolant

$q = 4.28\ m^3/s$

$E_{pm} = 0.75$

B = 3.5 T (perpendicular to direction of flow)

	Feeder Line Channel	First Wall Channel
Ferritic Walls		
Re	4.59×10^4	2.29×10^4
M	6.82×10^3	1.364×10^3
Re/M	6.72	16.81
N	1014	81.1
ϕ	0.1505	0.753
V, m/s	0.1070	0.2675
Δp_m, MPa	0.0957	0.327
P_m, MW	0.546	1.867
Electrically Insulated Walls		
ϕ	0.0	0.0
$\Delta p_{m,\ \phi=o}$, MPa	0.0001	0.0006
$P_{m,\ \phi=o}$, MW	0.0006	0.0032

when $M\ \phi >> 1$, $W >> 2a$, and R_c is small. Thus, if only the coolant is changed, P_m will depend mainly on ρc_p. Since ρc_p is about the same for Li and 17Li-83Pb and higher for Na, P_m for the feed line to the first wall will be higher for Na than it is for Li or 17Li-83Pb. This is shown in Table 6-58.

To estimate the MHD pumping power in the first wall channel, the MHD power loss, given in Table 6-57 for the toroidal field perpendicular to the direction of the flow, has to be reduced as the first wall is turned to minimize this effect. If the first wall has a semi-circular shape, the effective length across the toroidal field is 60% of the full MHD pumping power loss. If the first wall is flat, there will be no toroidal field

effect. Depending on which of these conditions is chosen, the MHD pumping power loss in the first wall channel ranges from 0 to 60% of that given by the expression for P_m. This range is shown in Table 6-58 for the three liquid metal coolants, along with the resulting range in the total pressure drop across the reactor blanket and in the total pumping power.

A review of Table 6-58 shows that MHD effects result in a large increase in required pumping power when liquid metals are used for the blanket coolant. Several factors can work to reduce these MHD losses. The biggest effect would come from an electrically insulating layer on the wall of the flow channel. This would make σ_w, and hence ϕ, equal to zero. ϕ is also zero if R_c is very large. As shown at the bottom of Table 6-57, when $\phi = 0$, the MHD effects are reduced by three orders of magnitude. A second way to reduce the MHD effect is to increase the coolant ΔT through the blanket since P_m is inversely proportional to $(\Delta T)^2$. Since Na is still well above its melting point, its ΔT could be increased by 200 - 225 K. This would reduce the required pumping power for Na and bring it very close to that for Li. If a vanadium alloy is used, the exit temperature from the reactor could possibly be increased to 550°C (see Sec. 6.5.3) for a recirculating 17Li-83Pb coolant. This would also allow a significant decrease in pumping power. If the coolant channel gap next to the first wall can be increased while maintaining good heat transfer from the first wall, this will reduce the MHD losses in a curved first wall coolant channel.

There are also several factors that can work to increase MHD losses. The coolant lines to and from the blanket must also cross the toroidal field, and thus, could give significant additional MHD losses. The field strength will be lower but the coolant lines will be longer. The larger the diameter of the circular coolant line, the smaller the MHD losses. A second factor is the wall thickness, which might need to be greater than 5 mm, especially in the first wall. This will increase the MHD losses proportionately. A third factor increasing MHD losses is the toroidal field. The losses increase as B^2. B increases to 5 T for the top and bottom blanket modules and to 7 T for any inboard blanket modules. If a vanadium alloy is used, its σ_w will be higher, about 2×10^6 S/m,[121] which will increase the MHD losses proportionately as compared to HT-9 ferritic steel.

In conclusion, MHD losses are important and must be considered carefully in any detailed analysis of a liquid metal as a coolant for the reactor blanket.

Table 6-58. Coolant Pumping Power When MHD and All Frictional Losses Are Combined

$Q' = 1050$ MW $\quad E_{pm} = 0.75$
$P_e = 300$ MW $\quad B = 3.5$ T

Coolant	q, m^3/s	Pumping Power Losses in the Reactor Blanket, MW			Total Blanket Pressure Drop, MPa	Steam Generator Power Loss, MW	Total Pumping Power[b]	
		Frictional[a]	MHD				MW	$\%P_e$
			Feed Line to First Wall	First Wall				
H_2O	6.60	0.26	0.0	0.0	0.03	0.13	0.4	0.1
Na	7.52	0.52	1.89	0.0-5.32	0.24-0.77	0.26	2.7-8.0	0.9-2.7
Li	4.05	0.06	0.52	0.0-1.24	0.11-0.34	0.03	0.6-1.9	0.2-0.6
17Li-83Pb	4.28	1.20	0.55	0.0-1.12	0.31-0.50	0.60	2.4-3.5	0.8-1.2

[a] From Table 6-56.

[b] Includes frictional losses in the reactor and the steam generator, MHD losses as indicated, and pump/motor efficiency.

Flow-Induced Vibrations

Flow-induced vibrations can occur in liquid metal cooled systems.[125] These vibrations are serious as they can lead to failure of the metal walls. The detailed design of any liquid metal cooling system must be reviewed to see that flow-induced vibrations will not be a problem. Because of the greater density of the 17Li-83Pb coolant, flow-induced vibrations are expected to be more of a problem for the Li-Pb coolant; that is, greater structural stiffness of the walls and supports will be required for this coolant than for the other coolants considered.

Pumps

Centrifugal pumps have been built which can pump liquid metal at 0.915 m^3/s (1.45×10^4 gal/min).[126] These pumps were tested with sodium in preparation for their use in the Fast Flux Test Facility. Corrosion and erosion problems will be most severe at the pump impeller. For the 17Li-83Pb coolant, liquid-metal embrittlement of the materials of construction could also be a problem.

6.5.5.2 Thermal Hydraulic Analysis

A preliminary thermal hydraulics parametric analysis was performed for the Li-Pb self-cooled blanket concept described in Section 6.5.2.3, in order to determine the temperature distributions in the blanket's first wall/coolant channel region. For the analysis, the parameters of coolant channel width, first wall thickness, coolant temperature increase (inlet to outlet for the blanket), and module semi-ellipsoidal head diameter were varied in order to help determine a range of allowable values. The resulting temperature distributions were later used as input data for the thermo-structural analysis described in Section 6.5.6.

The model for the thermal hydraulic calculations is shown in Fig. 6-34. In this model, it is assumed that the first wall has a beryllium coating for plasma impurity control. The calculations are based on the following data and operating conditions for the reference module.

Surface heat flux, MW/m^2	0.5
Neutron heating rate, W/cc:	
Structural material (HT-9 or V-alloy)	11.5
Breeder coolant (17Li-83Pb)	22.2
Be coating (70% of theoretical density)	11.27
Breeder coolant (17Li-83Pb) temperature, °C:	
Inlet	300
Outlet	450
Diameter of cylindrical modules, cm	30
Assumed nominal thicknesses, mm:	
Be coating	3
First wall	3
Coolant channel	3
Baffle plate	3

The surface heat flux on the first wall is assumed to have a cos ϕ distribution (ϕ = angle away from the point closest to the plasma). Assuming uniform flux distribution in the lengthwise (toroidal) direction of the blanket modules, the thermal analysis can be carried out based on two-dimensional heat conduction. The module was divided into ten regions in the θ-direction, two regions in the Be coating, three regions in the structural material, one region in the coolant, and two regions in the baffle

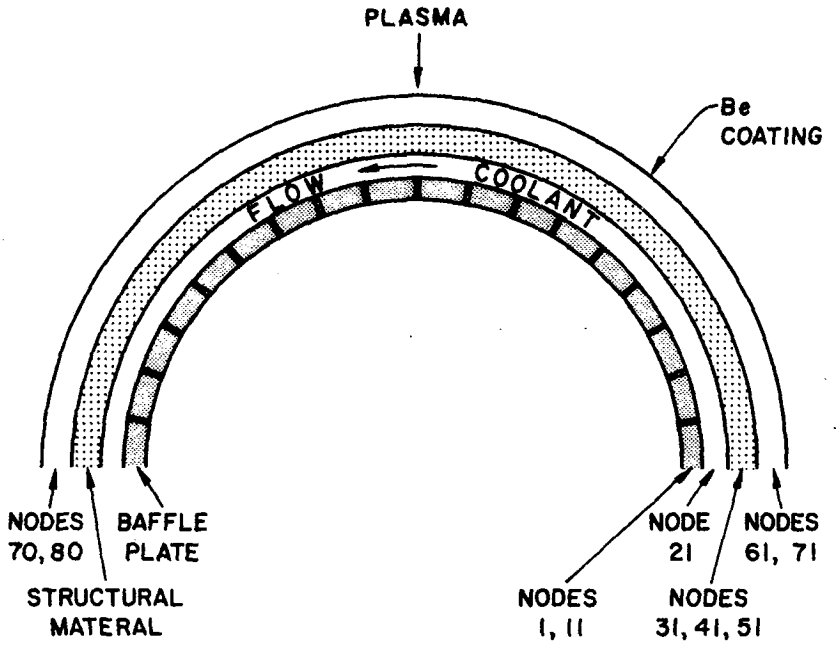

COOLANT NODES	21 - 30 (10)
BAFFLE PLATE NODES	1 - 19 (20)
STRUCTURAL NODES	31 - 51 (30)
COATING NODES	61 - 80 (20)

Figure 6-34. Thermal hydraulic model showing distribution of node points.

plate (all in the radial direction). The baffle plate between the first wall and the blanket region is assumed to be perforated to prevent stagnant thermal regions behind the baffle. To simplify the calculations, thermal interactions between the first wall region and other regions is assumed to be negligible.

Results

Typical temperatures for a selected set of nodes from the 80-node geometrical model are plotted in Figs. 6-35 and 6-36. (Note: R is the radius of the cylindrical head as shown in Fig. 6-34.) The temperature distribution in Fig. 6-35 corresponds to three angular positions: $\theta = 0$ (coolant inlet), $\theta = \pi/2$ (peak heat flux region), and $\theta = \pi$ (coolant exit from the first wall region). The results show that ~ 33% of the total temperature rise of the coolant (20% due to surface heat flux and 13% due to bulk heating) occurs across the first wall. The maximum surface temperature of the

structural material (HT-9) reaches ~ 425°C (obtained by interpolation between nodes 47 and 57). The surface temperature of the beryllium coating approaches 500°C (see Fig. 6-35). In this case, the maximum temperature of the structural material occurs just past the head centerline, at $\theta \simeq 120°$. At the first wall coolant exit, the structural material temperature will approach the coolant temperature.

The gravity load and internal pressure for a particular first wall/blanket module will depend on its location in the poloidal plane. Hence, the required material thickness may depend on the location of the modules. Calculations were carried out by varying the thickness of the first wall to estimate how the material thickness affects the temperature distribution. When this thickness is increased from 3 mm to 4.5 mm, and then to 6 mm, respectively, the structural material temperature is increased by 33°C and 75°C, respectively. The temperature distribution for the 6 mm thick first wall is plotted in Figs. 6-37 and 6-38, respectively. An examination of the circumferential temperature distribution shown in these figures illustrates the effect of the cos ϕ flux distribution. Also, it can be seen that the radial temperature gradients are much larger than the circumferential temperature gradients. Based on consideration of the upper temperature limit alone for the ferritic steel, a 6 mm thick first wall may constitute an unacceptable design for the nominal parameter values.

Steady state calculations for V-alloy were carried out corresponding to the above three cases for HT-9. The results indicate that the temperature distributions for the two materials are not significantly different. This is due to the fact that at the operating temperature, there is only a small difference in the thermal conductivity of the two materials.

For an electrically conducting fluid flowing perpendicular to the magnetic field, the pressure losses due to induced MHD forces are proportional to the linear velocity of the coolant. Hence, there is incentive to reduce coolant velocity as long as the reduced velocity causes no serious adverse effect on the heat transfer characteristics of the coolant. For the reference case, the coolant velocity is found to be slightly less than 1 m/s (3.4 ft/s). A set of calculations was carried out by increasing the coolant channel width from 3.0 mm to 4.5 mm, 6.0 mm, and 10.0 mm, thereby reducing the coolant velocity by 33%, 50%, and 70%, respectively (the corresponding coolant

velocities are 2.27, 1.70, and 1.02 ft/s). The calculations show that when the coolant channel width is increased as indicated above, the structural material temperature increased by 15°C, 26°C, and 54°C, respectively (the maximum structural material temperatures obtained by extrapolation are 425°C, 436°C, and 464°C). Hence, it is possible to reduce the coolant velocity in order to minimize the MHD pressure losses (coolant channel width of 10 mm may be an unacceptable design for HT-9). The results are shown in Figs. 6-39 and 6-40.

There are not sufficient data to fix the upper temperature limit for HT-9 and V-alloy. The experimental data base from other liquid-metal systems indicates that, due to mass transfer effects, the temperature limit for a refractory alloy will be higher than that for a ferritic steel. Hence, a series of calculations was carried out wherein the total blanket coolant temperature increase was varied from 150°C (reference case) to 100°C and 200°C. As expected, the resulting temperature distributions indicate that structural material temperature varies depending upon the coolant temperature rise (ΔT_c). For the case of ΔT_c = 100°C, the maximum temperature of the first wall was found to be ~ 400°C. When the coolant temperature rise was 200°C, the maximum first wall temperature increased to 426°C. However, it should be noted that for this case, the maximum temperature of the structural material in the module will occur at the module coolant exit point and will essentially be equal to the coolant outlet temperature (i.e., 500°C). If the required thickness of the first wall is of the order of 6 mm for HT-9, then the coolant temperature rise may have to be limited to ~ 100°C.

The interfacial contact resistance between the structural material and the beryllium coating is of interest due to unequal thermal expansion between the coating and the structural material. This resistance is expected to depend on how the coating is applied to the structural material. However, it is reasonable to expect that vapor-deposited or plasma-sprayed coatings will have less thermal resistance compared with mechanical contacts between two dissimilar materials. The interfacial contact resistance between lapped surfaces in a helium atmosphere has been reported to vary between 1 to 5 W/cm^2-K. Hence, the interfacial contact coefficient between the beryllium coating and the structural material is expected to be higher. The steady-state temperature distribution was calculated by varying the contact

coefficient between 1 and 10 W/cm^2-K. The results show that when the contact coefficient is increased by a factor of 10, the coating temperature deceases by ~ 45°C. The temperature distributions presented in this section are based on a coating thickness of 3 mm. For thicker coatings, the temperature of the Be-coating shown in the above tables may be increased by ~ 5°C per mm of coating (0.5 MW/m^2 and one-dimensional conduction was assumed here).

The size of the blanket modules has important impact on stress distribution, and will affect first wall/blanket subsystem costs at the first wall. The most cost-effective module is expected to be the largest module consistent with acceptable material property limitations. Hence, modules both smaller and larger than the reference modules were analyzed. The results indicated that there are only minor changes in the structural material temperatures among the four diameters examined (Diameter: 25 cm, 30 cm, 35 cm and 40 cm). These changes are due primarily to changes in the first wall coolant temperature since the coolant channel thickness and the coolant velocity are held constant for these calculations. A preliminary stress analysis for the blanket modules was carried out to determine an optimum size for the modules. The results of the stress analyses are presented in Section 6.5.6. The temperature distribution for a few selected nodes are also shown in Figs. 6-41 (radial variation) and 6-42 (circumferential variation).

Conclusions

For most of the cases included in this analysis, the coolant outlet temperature appears to set the upper temperature limit for the structural material.

If 450°C is assumed to be the upper temperature limit for HT-9, then the coolant temperature rise would be limited to 150°C. For the vanadium alloy, the allowable coolant temperature rise may be as high as 200°C. This provides additional flexibility in the blanket design. The thickness of the Be coating was assumed to be 3 mm, which resulted in a maximum temperature of 485°C for the reference case. On the basis of temperature alone, thicker coatings can be used if necessary for plasma impurity control; however, stress analyses should be carried out to determine maximum allowable coating thicknesses.

By using wider coolant channels, which reduces the required coolant velocities, the MHD pressure losses can be minimized. For all cases

considered, the coolant flow is in the turbulent regime; hence, adequate flow distribution along the coolant channels and behind the baffle plates can be achieved.

From the results of the thermal hydraulic analyses, it can be concluded that the elongated cylindrical blanket modules made from HT-9 or V-alloy appear to offer a viable first wall/blanket design concept. Analyses of the intermediate heat exchangers, fluid transport and power conversion systems, and tritium containment and extraction systems are necessary to evaluate the economic benefits of self-cooled Li-Pb systems.

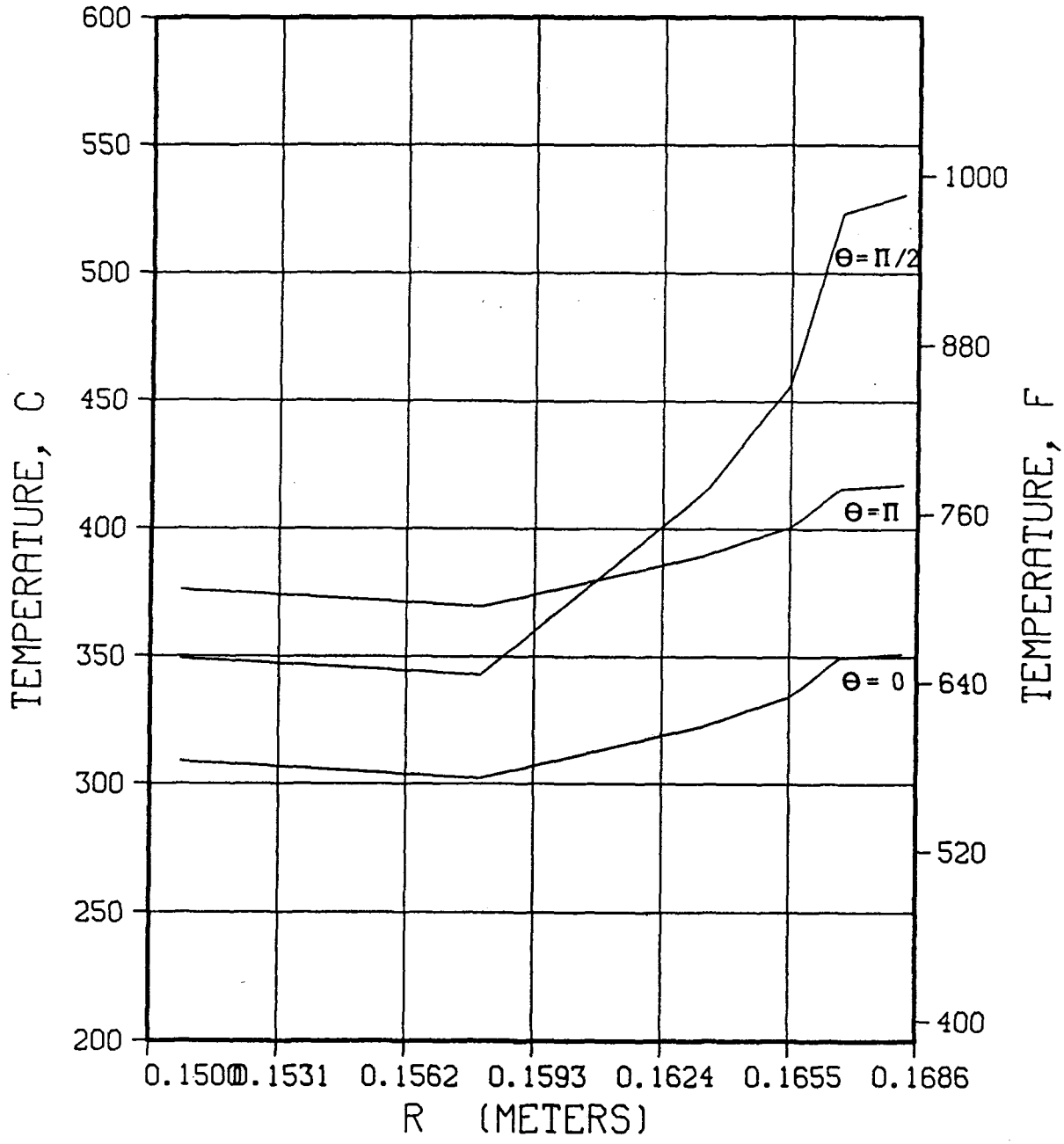

Figure 6-35. Circumferential temperature distribution for 3 mm thick HT9 first wall.

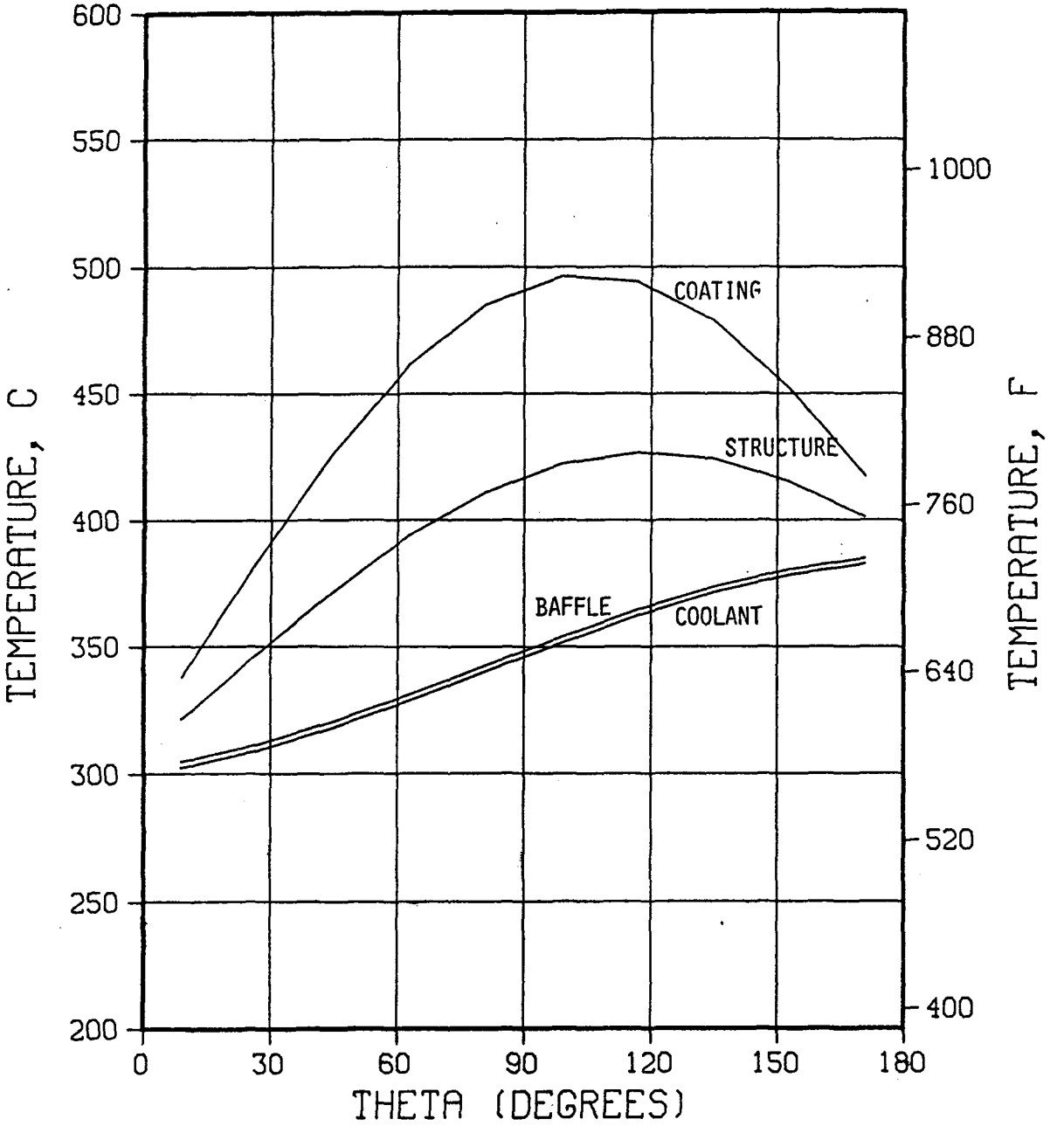

Figure 6-36. Radial temperature distribution for 3 mm thick HT9 first wall.

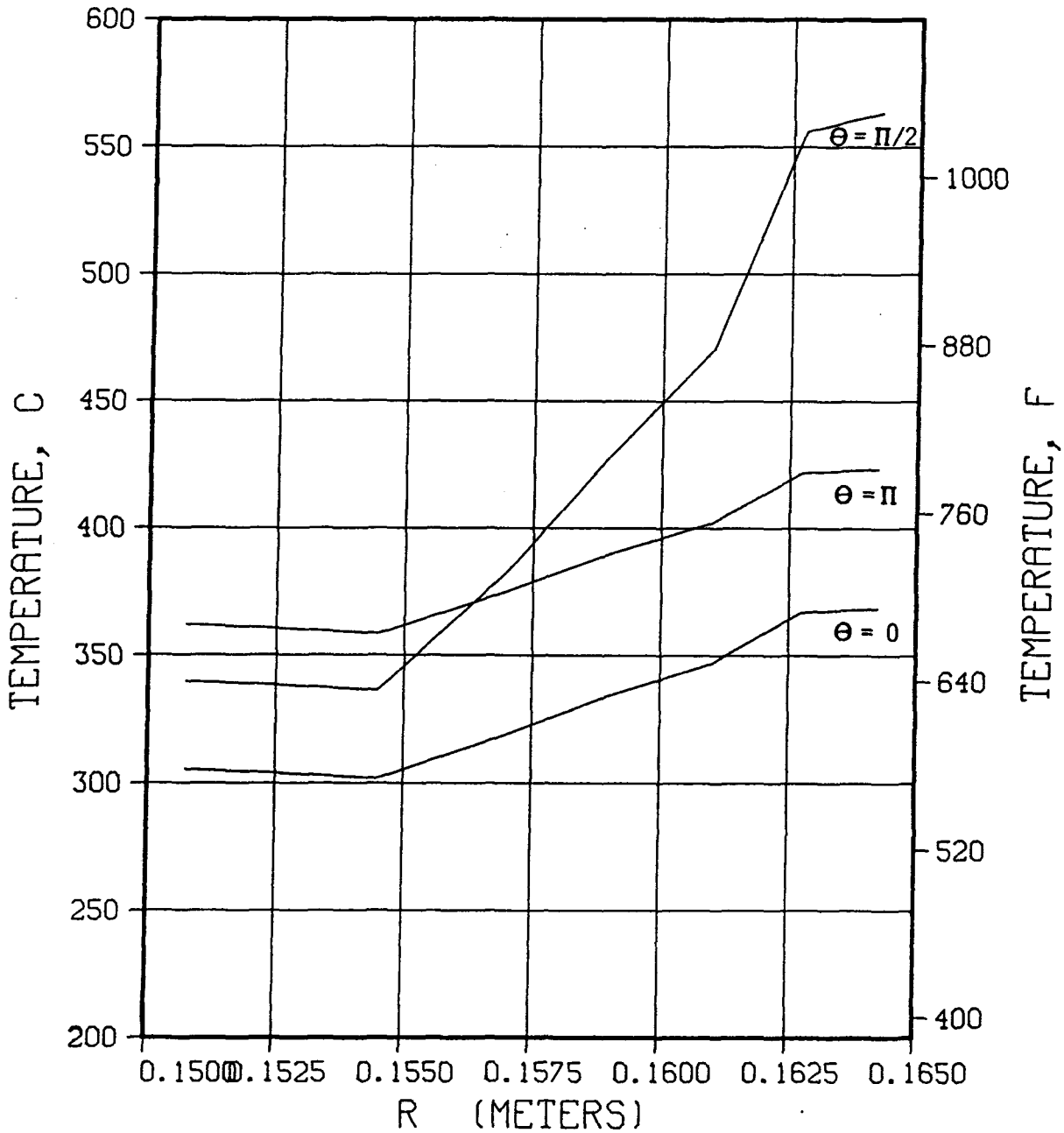

Figure 6-37. Circumferential temperature distribution for 6 mm thick HT9 first wall.

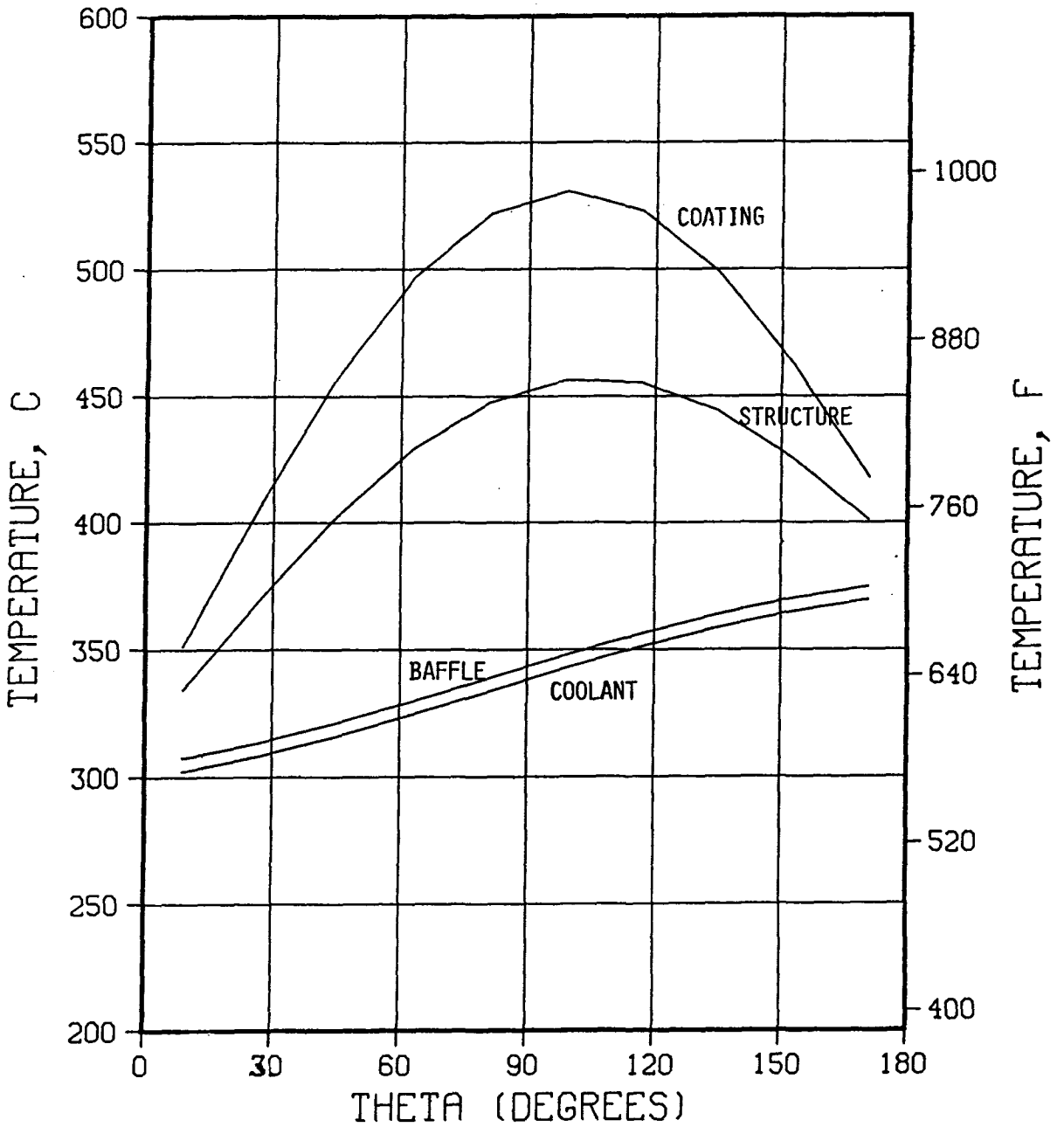

Figure 6-38. Radial temperature distribution for 6 mm thick HT9 first wall.

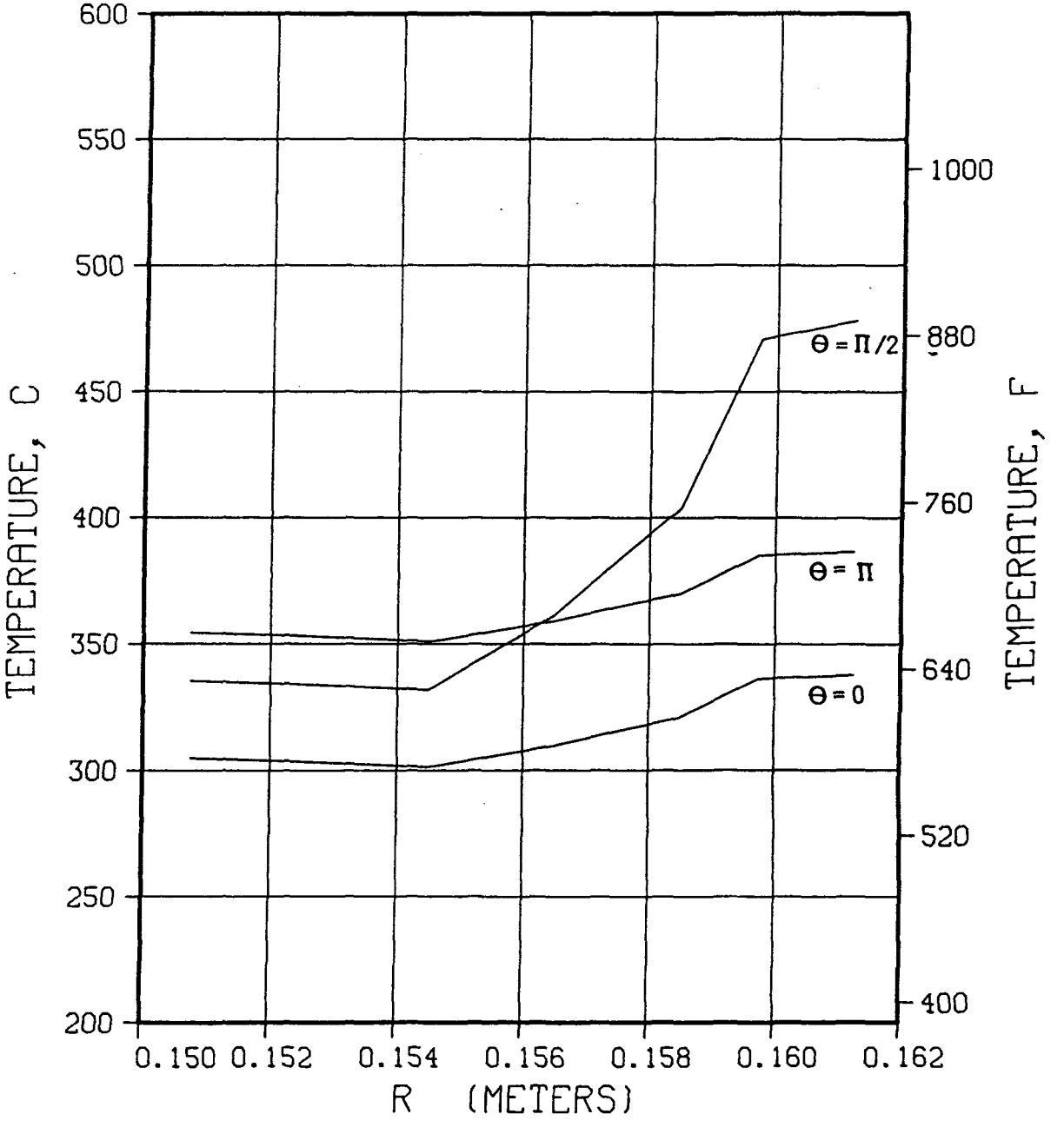

Figure 6-39. Circumferential temperature distribution for 10 mm thick coolant channel and 3 mm thick HT9 first wall.

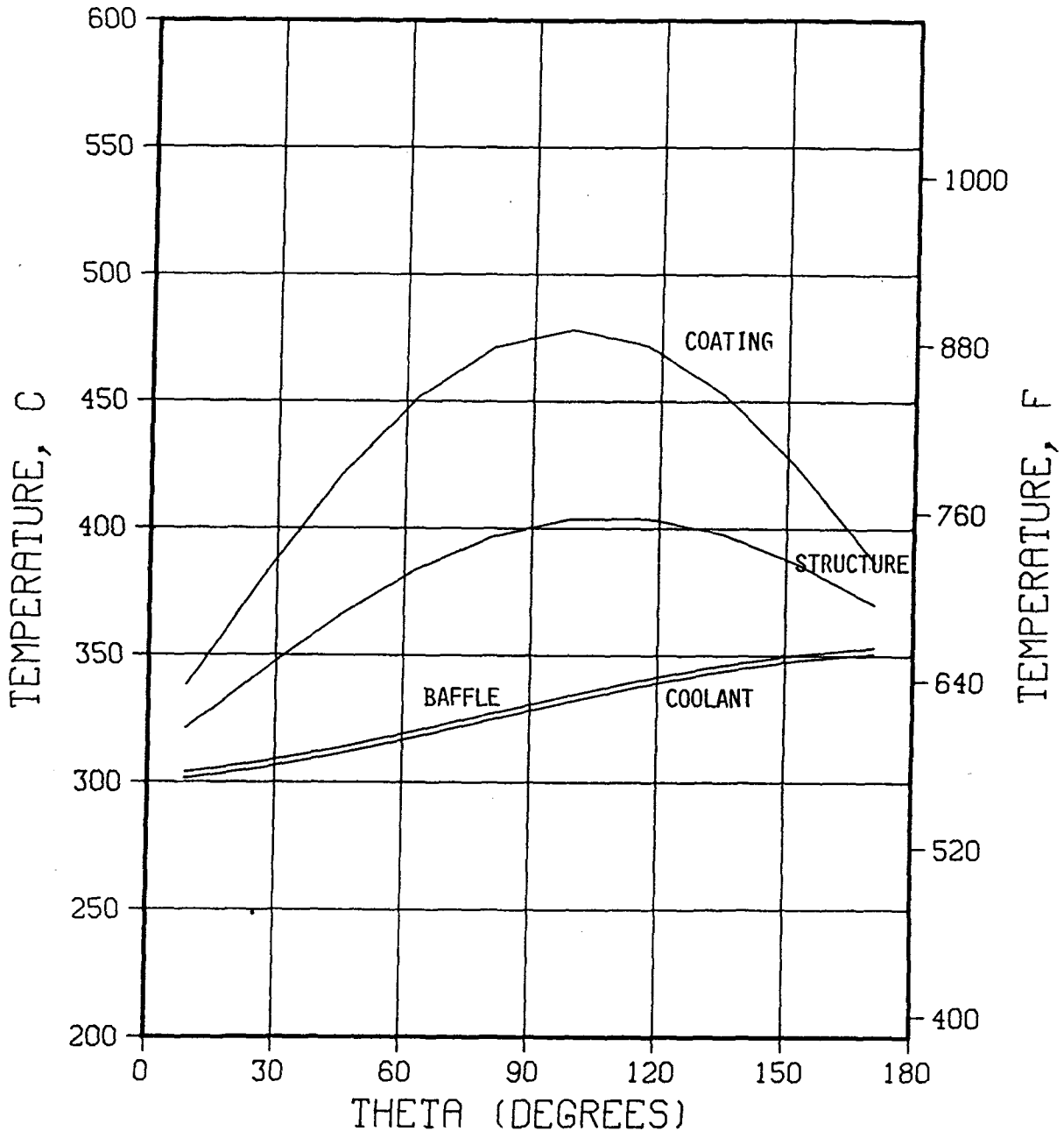

Figure 6-40. Radial temperature distribution for 10 mm thick coolant channel and 3 mm thick HT9 first wall.

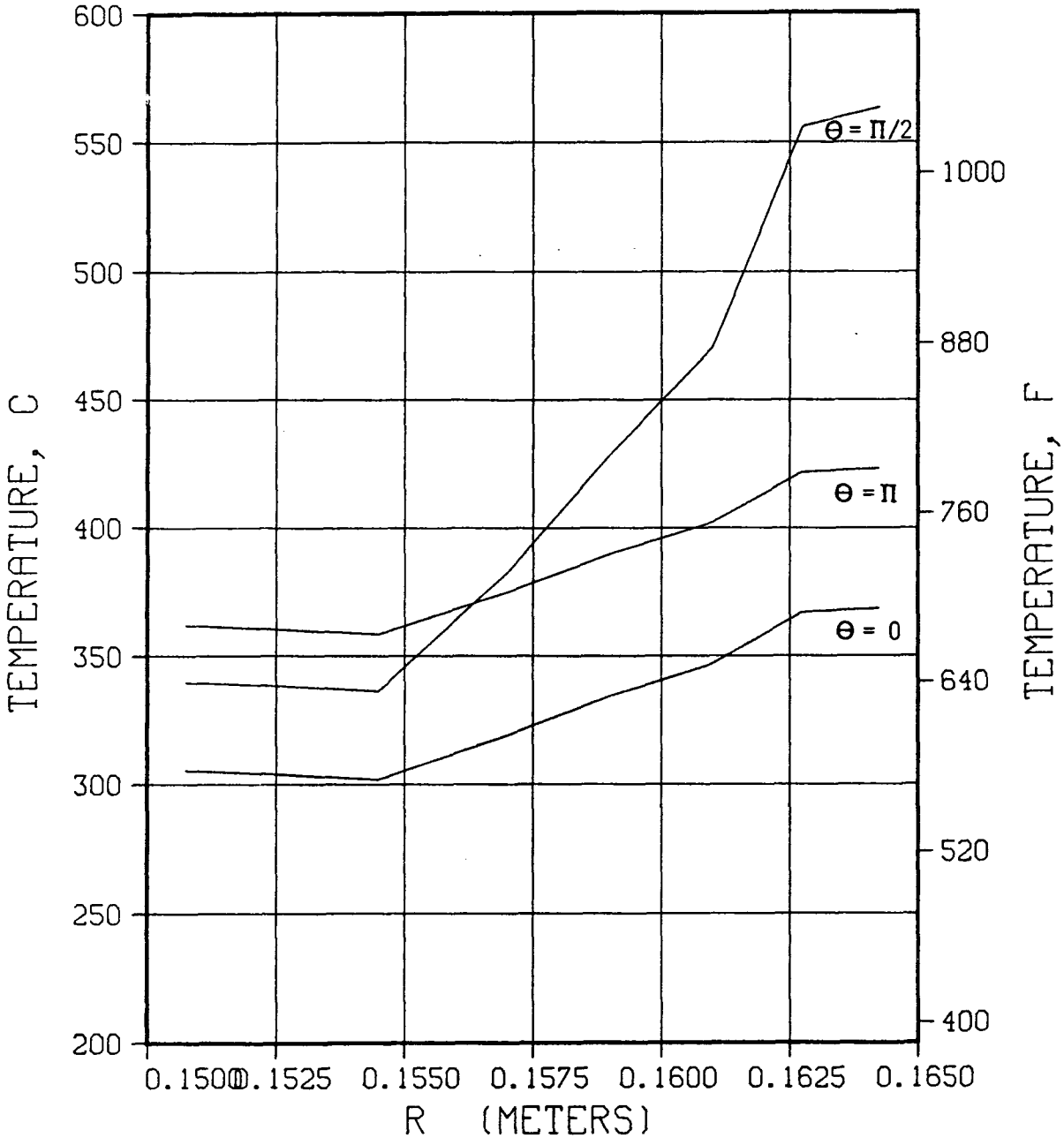

Figure 6-41. Circumferential temperature distribution for 50 cm first wall/ blanket module.

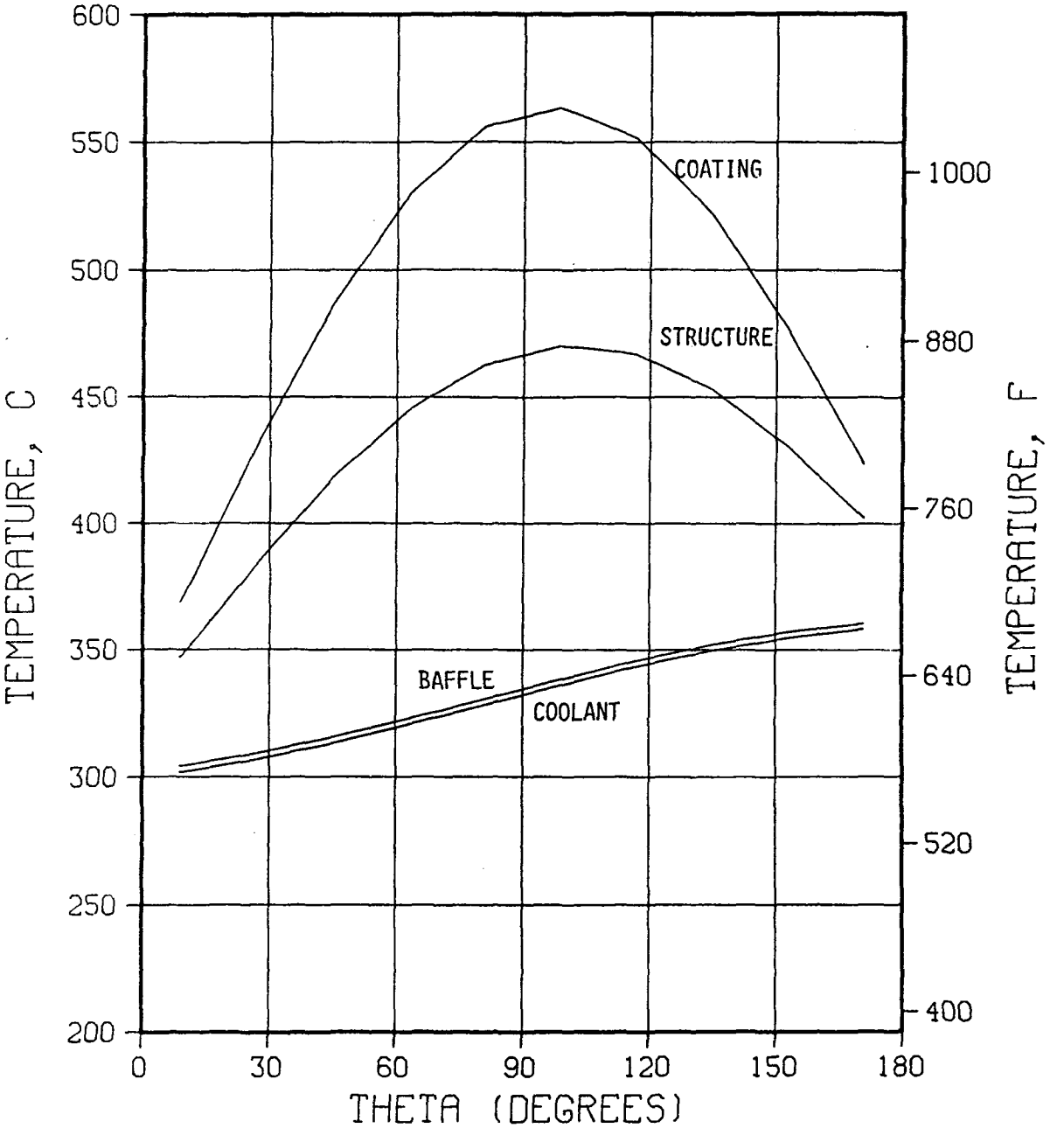

Figure 6-42. Radial temperature distribution for 50 cm first wall/blanket module.

6.5.6 Stress Analysis of Li-Pb Self-Cooled Blanket Module

The high density of 17Li-83Pb leads to two stress-related concerns for large non-cylindrical modules filled with Li-Pb: (1) relatively high internal pressures (static head), resulting primarily from interconnection of modules within a blanket sector; (2) reaction of gravity loads from the breeder mass, for all modules except those at the bottom of the sector.

To determine the structural requirements for the double-head module concept described in Sec. 6.5.2.3, a preliminary stress analysis was performed for a typical blanket module to determine the required structural arrangement and thicknesses and to determine the allowable relationships among various design parameters. Coolant pressure was assumed to be 200 psi (including pumping head pressure). Temperature distributions from the thermal-hydraulics analysis of Sec. 6.5.5.2 were used to determine thermal stresses. Allowable stresses for both HT-9 ferritic steel and V-15Cr-5Ti vanadium alloy were based on ASME Boiler Code Section III, Division I, Class 2. This defines (1) an allowable stress for primary loads (pressure in this instance) of 1.5 X S_m = 1.5 X ($F_{tu}/3$) = $F_{tu}/2$, and (2) an allowable stress for primary plus secondary loads (thermal stresses in this instance) as 3.0 X S_m = 3.0 X ($F_{tu}/3$) = F_{tu}. As a conservative simplification for this analysis, the latter limit was taken as 1.5 x S_m for primary stresses and 1.5 x S_m for secondary stresses. For the HT-9 material at 450°C, this is an allowable stress of 260 ksi.

Only elastic analysis was performed. Since the limit (F_{tu}) for primary and secondary stresses is above the yield stress, significant plasticity can occur during operational cycling of pressures and temperatures. The elastic analysis described here is thus only a first approximation of the structural requirements; future effort should include plastic analysis, particularly for life estimation.

Module Structural Configuration and Analysis

The module structural configuration is shown in Fig. 6-43. Dimensions shown are for HT-9 ferritic steel. The side walls in the toroidal plane are 3 mm thick and are supported by stiffened internal frames (tension webs) spaced 5.7 cm apart. The 1.4 MPa (200 psi) internal pressure acts on the side walls which beams this load to the internal frames. Loads on the side walls for vertically-oriented modules are equal and are self-reacted through the

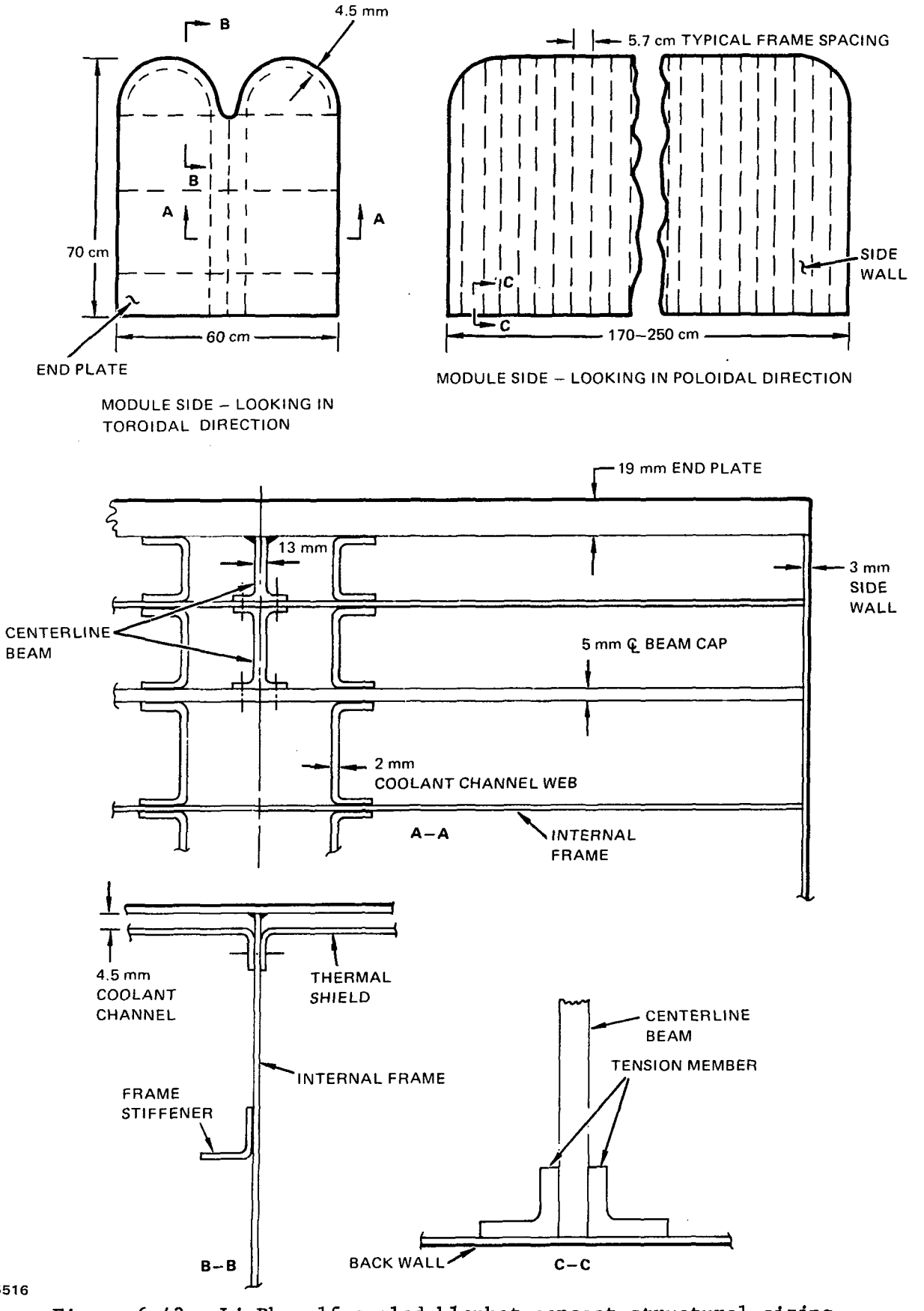

Figure 6-43. Li-Pb self-cooled blanket concept structural sizing.

frames. Differences in side wall loads for other modules due to the internal static head difference and breeder gravity loads are reacted by the side wall to the frames which in turn react these loads in shear to the back wall. Even though the side walls are cylindrical in the first wall section, the principal load path in the skin for internal pressure is still in the toroidal direction as the skin beams the pressure to the tension webs. In the present module design, the hoop tension path in the poloidal direction does not have a rigid support at the cusp between heads on the module center line, and hence is only partially effective. Accordingly, this analysis conservatively excludes the hoop tension load path.

It is desirable to minimize the structural volume of the blanket module in order to provide as large a breeder/coolant volume fraction as possible. Considering only the side walls (sized by pressure), and minimum gage internal frames (1-mm thick plus 25% for stiffeners), a minimum structural volume condition for HT-9 was found at a spacing of 8 cm as shown in Fig. 6-44.

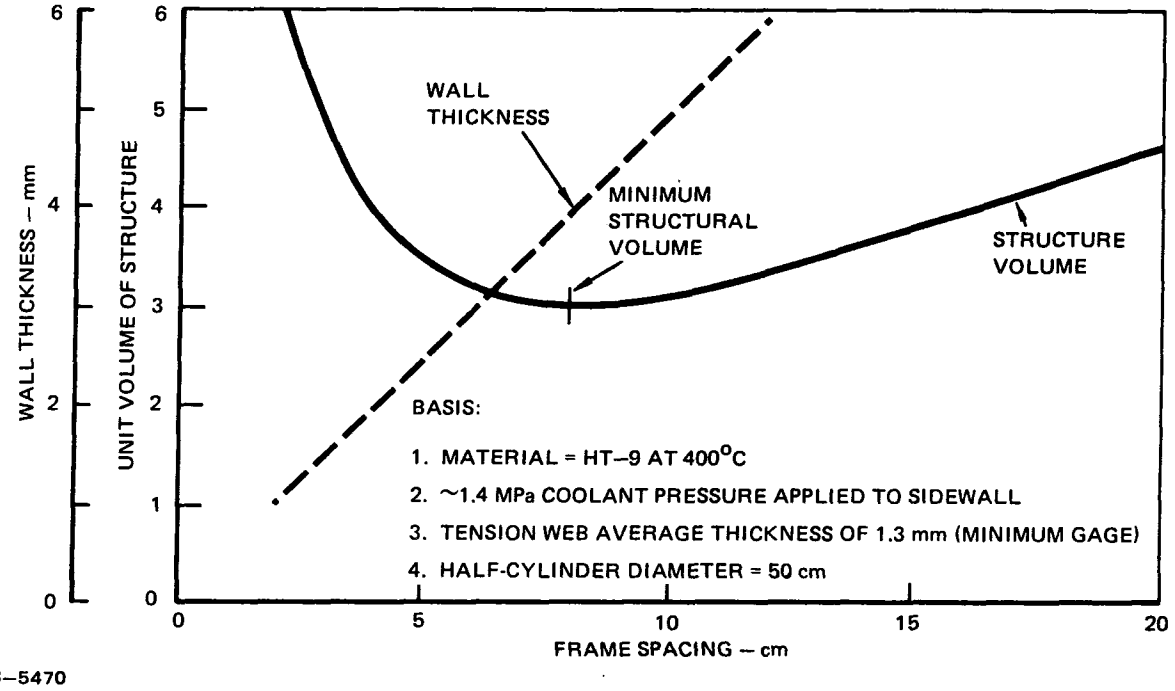

Figure 6-44. Frame spacing in Li-Pb self-cooled blanket for minimum structural volume.

Although this provides a rationale for selecting a frame spacing and wall thickness, other criteria (e.g., maximizing coolant temperature rise) will modify this solution for future analyses.

The ends of the blanket module are closed by 19-mm thick flat bulkheads. These bulkheads are supported by the side walls and by a center line beam which extends through the first two bays at each end of the module. This beam was added to the original module concept of Reference 5 , in order to efficiently react end wall pressure loads to the back wall and thus avoid extremely high end wall thicknesses. Two tension members react the end loads of this beam.

A preliminary elastic fatigue analysis was performed using the method in the ASME Boiler Code. In this method, elastic stresses are compared to an allowable curve constructed using typical life vs. strain (or stress) range data. The allowable curve is the smaller of 1/20 of the life, or 1/2 of the stress of the average test data. Using a strain range of zero to F_{tu}/E = 0.32% (equivalent to the 3 S_m limit), the allowable life is approximately 70,000 cycles (Fig. 6-45). This compares with an estimated 2000 full load/

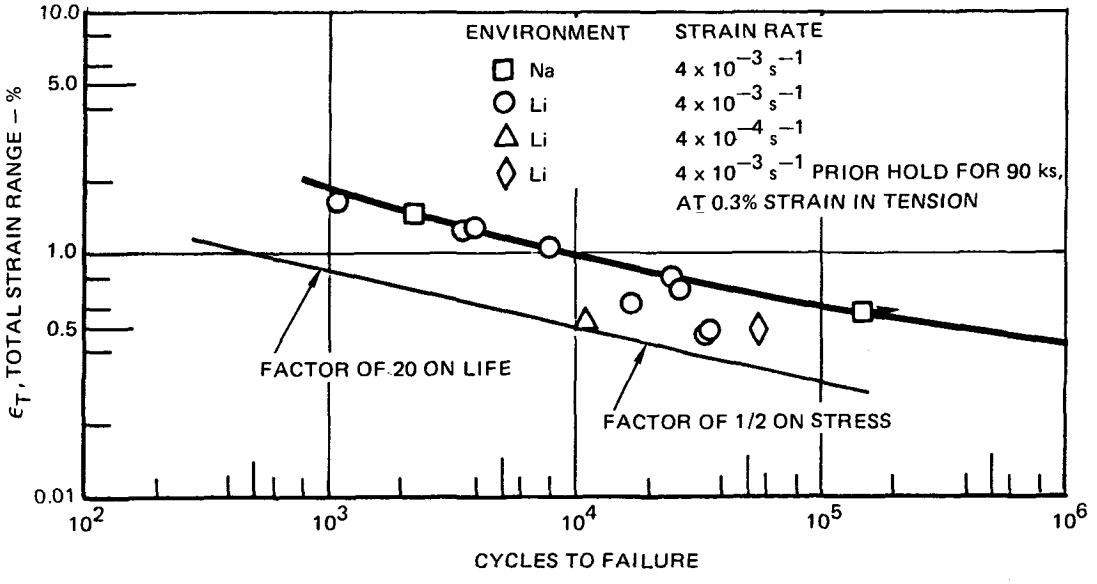

13-5511

Figure 6-45. Total strain range vs. cycles to failure for HT-9 alloy tested in lithium and sodium at 755 K. Concentration of nitrogen in lithium: < 500 wppm. (Reference 127).

temperature cycles in operation. Hence, the blanket should have adequate fatigue life. However, this analysis has not addressed local stresses, plastic stresses, and thermal stresses in the poloidal direction (which require a finite element model for accurate calculation). These areas should be examined in future fatigue life analyses.

Thermal stresses were calculated for the temperatures discussed in Sec. 6.5.5.2. They consist of two parts: (1) a local thermal stress (σ_{tl}) due to temperature variation through the wall thickness; and (2) overall thermal stress (σ_{to}) due to temperature variation on the blanket cross section (stress in toroidal direction). Temperature variation through the thickness is almost linear, and hence can be determined from a simple plate relationship. The baseline configuration analyzed has a ΔT through the thickness of 62.8°C which results in a local thermal stress for HT-9 of 94.6 MPa. This is about a third of the assumed allowable secondary stress (1.5 S_m). In a blanket sector, adjoining modules may act near-adiabatically so that through-thickness ΔT values in the side walls (and thus the related thermal stresses) will be negligible. However, this stress value has been included in the present analyses for conservatism.

The overall thermal stresses were elastically calculated using the blanket module cross section shown in Fig. 6-46. The analysis assumes the blanket

ELE.	TEMP. (°C)	THERMAL STRESS
1	300	151 MPa
2	315	107
3	332	60
4	349	15
5	363	−23
6	374	−52
7	381	−67
8	384	−68
9	381	−56
10	374	−33
11	364	− 1
12	370	− 1
13	378	− 1
14	385	− 1
15	392	− 1
16	399	− 1
17	406	− 1
18	414	− 1
19	421	− 1
20	428	− 2
21	435	− 2
22	444	− 2
23	450	− 4
24	450	− 4
25	450	− 4
26	450	− 4
27	450	− 4

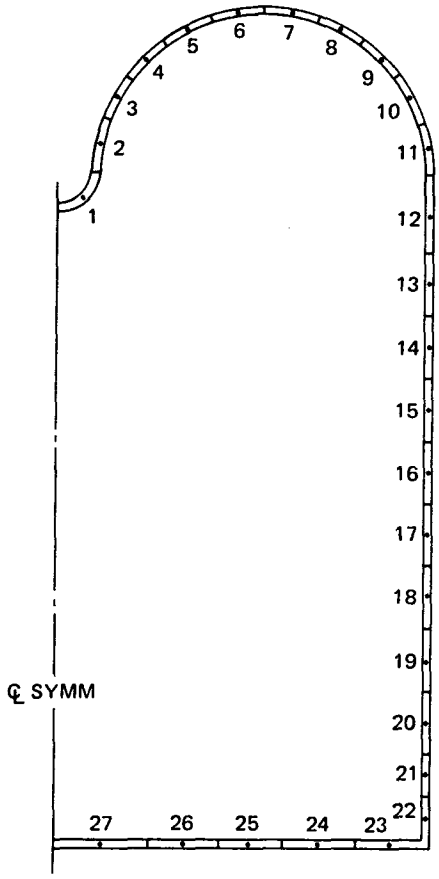

13-5517

Figure 6-46. Blanket module overall thermal stresses.

module is unconstrained either in axial extension or in bending (e.g., a "free" beam). Temperatures (from Sec. 6.5.5.2) and resulting thermal stresses are tabulated. A maximum overall thermal stress of 151 MPa occurs in the cusp area on the inboard wall. This represents about 2/3 of the assumed allowable secondary stress (1.5 S_m).

Parametric Evaluation

Temperatures for the first wall region of the module were calculated as discussed in Sec. 6.5.5.2 for different values of side wall thickness (t_w), coolant channel thickness (t_c), cylinder diameter (D), and coolant temperature rise (T_c). Temperatures for the flat portions of the side walls were calculated by linearly interpolating between the temperature of the last element in the first wall and the assumed coolant outlet temperature. The effects of using both the vanadium alloy (V-15Cr-5Ti) and HT-9 ferritic steel were evaluated. The effects of these variations (taken one at a time) on thermal stresses and allowables were calculated using linear approximations. By adding these sensitivities together and curve fitting through the baseline thermal stress, a linear equation for thermal stress was obtained as a function of the parameters t_w, t_c, T_c, and D. A similar equation was generated for the average temperature of the highest temperature element in the front wall region as a function of the same parameters. Since the allowable stress for a material is a function of temperature, the allowable stress was then known as a function of the other parameters. By equating allowable stress to the applied thermal stress, a relationship was obtained among the parameters that would not over-stress the side wall. This relationship is shown in Fig. 6-47 for both HT-9 and V-15Cr-5Ti. To maximize the allowable coolant temperature rise, it is desirable to minimize the wall thickness and half-cylinder diameter, and to a lesser extent to minimize the thickness of the first wall coolant channel. The vanadium alloy can be used at higher temperatures than HT-9 because it has a higher allowable stress and lower thermal stress. Thus the vanadium alloy can be used with a significantly higher coolant temperature rise (and hence a higher energy conversion efficiency) for a given wall thickness, as is evident from inspection of Fig. 6-47.

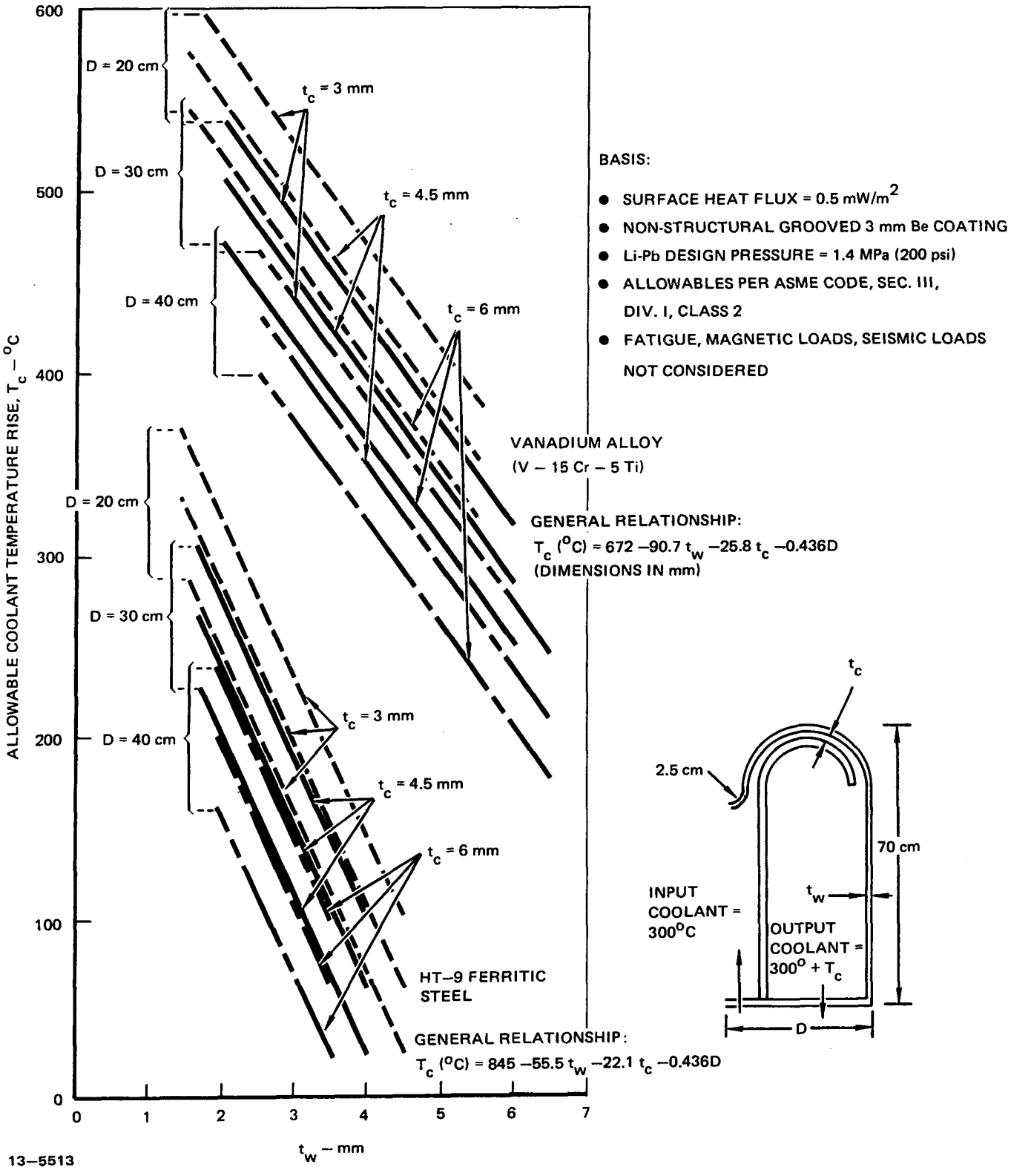

Figure 6-47. Allowable relationships of blanket parameters.

Summary and Conclusions

The module configuration using either HT-9 ferritic steel or V-15Cr-5Ti alloy appears adequate to provide sufficient life for the assumed pressures and coolant temperatures. However, the structure is complicated by the internal frames which are necessary to react pressure loads on the flat side walls. This may make the structure more difficult or more expensive to fabricate. Use of the V-15Cr-5Ti alloy allows increased cooling efficiency or a reduction in the number of internal frames due to its better mechanical and thermal properties.

The analysis described here is only a first approximation of the actual situation. Future work should use temperature distributions calculated for the full module cross section, and should include at least the following refinements:

- Plastic fatigue cycles
- Thermal stresses in poloidal direction
- Magnetic and seismic loads
- Local (non-typical) stresses.

REFERENCES FOR CHAPTER 6

1. C. C. Baker, et al., "STARFIRE - A Commercial Tokamak Fusion Power Plant Study," Argonne National Laboratory, ANL/FPP-80-1 (1980).

2. B. Badger, et al., "A Wisconsin Toroidal Fusion Reactor Design: UWMAK-I," University of Wisconsin, UWFDM-68 (1974).

3. B. Badger, et al., "UWMAK-II, A Conceptual Tokamak Power Reactor Design," University of Wisconsin, UWFDM-112 (1975).

4. B. Badger, et al., "UWMAK-III, A Noncircular Tokamak Power Reactor Design," University of Wisconsin, UWFDM-150 (1976).

5. D. L. Smith, et al., "Fusion Reactor Blanket/Shield Design Study," Argonne National Laboratory, ANL/FPP-79-1 (1979).

6. J. S. Karbowski, et al., "Tokamak Blanket Design Study," Oak Ridge National Laboratory, ORNL/TM-7049 (1979).

7. M. A. Abdou, et al., "A Demonstration Tokamak Power Plant Study - Interim Report," Argonne National Laboratory, ANL/FPP/TM-154 (1982).

8. W. M. Stacey, Jr., et al., "U.S. Contribution to the International Tokamak Reactor Phase-I Study," Georgia Institute of Technology, USA INTOR/81-1 (1981).

9. "Blanket/Shield and Power Conversion System for Small Field-Reversed Mirror Fusion Reactor," General Atomic Company, GA-A1553 (1979).

10. D. Steiner, "Analysis of a Benchmark Calculation of Tritium Breeding in a Fusion Reactor Blanket - The U.S. Contribution," Oak Ridge National Laboratory, ORNL-TM-4177 (1973).

11. D. Steiner and M. Tobias, "Cross-Section Sensitivity of Tritium Breeding in a Fusion Reactor Blanket: Effects of Uncertainties in Cross Sections of ^{6}Li, ^{7}Li, and ^{93}Nb," Nucl. Fusion, 14, 2, 153 (1974).

12. "International Tokamak Reactor - Phase One," International Atomic Energy Agency, Vienna (1982).

13. W. F. Vogelsang, "Breeding Ratio, Inventory, and Doubling Time in a D-T Fusion Reactor," Nucl. Tech., 15, 470 (1972).

14. R. Clemmer, "TCODE - A Computer Code for Analysis of Tritium and Vacuum Systems for Tokamak Fusion Reactors," Argonne National Laboratory, ANL/FPP/TM-110 (1978).

15. M. A. Abdou, "Problems of Fusion Reactor Shielding," Georgia Institute of Technology, GTFR-10 (1979).

16. D. E. Bertine, E. M. Oblow and F. R. Mynatt, "Radiation-Transport Cross-Section Sensitivity Analysis - A General Approach Illustrated for a Thermonuclear Source in Air," Nucl. Sci. Eng., 55, 147 (1974).

17. S. A. W. Gerstl, D. J. Dudziak and D. W. Muir, "Cross-Section Sensitivity and Uncertainty Analysis with Application to a Fusion Reactor," Nucl. Sci. Eng., 62, 137 (1977).

18. R. W. Conn and W. M. Stacey, Jr., "Variational Method for Controlled Thermonuclear Reactor Blanket Studies," Nucl. Fusion, 13, 185 (1973).

19. D. E. Bartine, et al., "Cross-Section Sensitivity of Breeding Ratio in a Fusion Reactor Blanket," Nucl. Sci. Eng., 53, 304 (1974).

20. S. A. W. Gerstl, "Blanket Design and Cross-Section Sensitivity Calculations Based on Perturbation Methods," Proc. 1st Topical Meeting on the Technology of Controlled Nuclear Fusion, CONF-740-402-P2, 136 (1974).

21. R. G. Alsmiller, et al., "Comparison of the Cross-Section Sensitivity of the Tritium Breeding Ratio in Various Fusion Reactor Blankets," Nucl. Sci. Eng., 57, 122 (1975).

22. R. G. Alsmiller, J. Barish and C. R. Weisbein, "Uncertainties in Calculating Heating and Radiation Damage in the Toroidal Field Coil of a Tokamak Experimental Power Reactor Due to Neutron Cross-Section Errors," Nucl. Tech., 34, 376 (1977).

23. J. Jung, "An Interpolation Method for the Transport Theory and Its Application in Fusion Neutronics Analysis," Argonne National Laboratory, ANL/FPP/TM-147 (1981).

24. B. Arcipiani, G. Palmiotti and M. Salvatores, "Neutron Heating Sensitivity to Cross-Section Variations in a Controlled Thermonuclear Reactor Blanket," Nucl. Sci. Eng., 65, 540 (1978).

25. T. Wu and C. W. Maynard, "The Application of Uncertainty Analysis in Conceptual Fusion Reactor Design," Proc. Seminar-Workshop on Theory and Applications of Sensitivity and Uncertainty Analysis," Oak Ridge National Laboratory, ORNL/RSIC-42 (1979).

26. S. Pelloni, "Cross-Section Sensitivity and Uncertainty Analysis for European INTOR and U.S. FED Designs," General Atomic Company, GA-A16685 (1982).

27. K. Evans, J. Gilligan and J. Jung, "Alternate Fuel Studies," Argonne National Laboratory, ANL/FPP/TM-162 (to be published).

28. M. B. Emmett, "The MORSE Monte Carlo Radiation Transport Code System," Oak Ridge National Laboratory, ORNL-4972 (1975).

29. "ANISN-ORNL: Multigroup One-Dimensional Discrete Ordinates Transport Code with Ansiotropic Scattering," Oak Ridge National Laboratory, RSIC/CCC-254 (1973).

30. D. L. Smith, et al., "Conceptual Design of the INTOR First Wall System," Proc. 9th Symposium on Engineering Problems of Fusion Research, IEEE Pub. No. 81CH1715-2 NPS, Vol. I, 723 (1981).

31. G. D. Morgan, et al., "Conceptual Design of Tritium Breeding Blanket for INTOR," ibid., 732.

32. R. W. Roussin, et al., "VITAMIN-C: The CTR Processed Multigroup Cross-Section Library for Neutronics Studies, Oak Ridge National Laboratory, ORNL/RSIC-37, ENDF-296 (1980).

33. Y. Gohar and M. A. Abdou, "MACKLIB-IV: A Library of Nuclear Response Functions Generated with the MACK-IV Computer Program from ENDF/B-IV," Argonne National Laboratory, ANL/FPP/TM-106 (1978).

34. D. Garken, Compiler, "ENDF/B Summary Documentation," Brookhaven National Laboratory, BNL-17541 (1975).

35. D. W. Muir and M. E. Wyman, "Neutronic Analysis of a Tritium-Production Integral Experiment," Proc. Symposium on Technology of Controlled Thermonuclear Fusion Experiments and the Engineering Aspects of Fusion Reactors, CONF-72111, 910 (1974).

36. H. Bachmann, et al., "Neutron Spectra and Tritium Production Measurements in a Lithium Sphere to Check Fusion Reactor Blanket Calculations," Nucl. Sci. Eng., 67, 74 (1978).

37. W. A. Ruepke, "The Consistency of Differential and Integral Thermonuclear Neutronics Data," Los Alamos National Laboratory, LA-7067-T (1978).

38. A. Hemmendinger, C. E. Ragan and J. M. Wallace, "Tritium Production in a Sphere of ^{6}LiD Irradiated by 14-MeV Neutrons," Nucl. Sci. Eng., 70, 274 (1979).

39. D. L. SMith, M. M. Bretscher and J. W. Meadows, "Measurement of the Cross Section for the ^{7}Li(n,n't)^{4}He Reaction in the Energy Range 7-9 MeV," Nucl. Sci. Eng., 78, 359 (1981).

40. M. T. Swinhoe and C. A. Uttley, "Tritium Breeding in Fusion," Proc. Conference on Nuclear Cross Sections for Technology, NBS Special Pub. 594 (1980).

41. P. F. Young, "Evaluation of n + ^{7}Li Reactions Using Variance-Covariance Techniques," Trans. Am. Nucl. Soc., 39, 272 (1981).

42. H. Liskiel, et al., "Determination of ^{7}Li(n,n')^{4}He Cross Sections," International Conference on Nuclear Data for Science and Technology, Antwerp, Belgium (September, 1982).

43. J. Jung, "A Comparative Study of Tritium Breeding Performance of Lithium, Li_2O, and Li_7Pb_2 Blankets in a Tokamak Power Reactor," J. Nucl. Tech., 50, 60 (1980).

44. J. Jung, "A Computational Method for Neutron Transport Problems in Toroidal Geometry," Nucl. Sci. Eng., 65, 130 (1978).

45. J. Jung, "Neutronics Analysis of Graphite-Moderated Solid Breeder Blanket Designs for INTOR," Proc. 9th Symposium on Engineering Problems of Fusion Research, IEEE Pub. No. 81CH1715-2 NPS, Vol. I, 736 (1981).

46. "MCNP - A General Monte Carlo Code for Neutron and Photon Transport," Los Alamos National Laboratory, LA-7396-M (1979 Rev.).

47. W. M. Stacey, Jr., et al., "FED/INTOR Tritium Issues," FED-INTOR/TRIT/82-1 (1982).

48. M. A. Abdou, L. J. Wittenberg and C. W. Maynard, "A Fusion Design Study of Nonmobile Blankets with Low Lithium and Tritium Inventories," Nucl. Tech., 26, 400 (1976).

49. J. Jung and M. A. Abdou, "Radioactive Inventories and Material Recyclability in a Tokamak Reactor," Trans. Am. Nucl. Soc., 34, 645 (1980).

50. W. M. Stacey, Jr., et al., "INTOR - U.S. Contribution to the International Tokamak Reactor Workshop, Phase I," USA INTOR/80-1 (1980).

51. A. Fraas, "Analysis of Recirculating Lithium Blanket Designed to Give a Low Magnetohydrodynamic Pumping Power Requirement," Oak Ridge National Laboratory, ORNL-TM-3756 (1972).

52. W. M. Wells, "ORNL Fusion Power Demonstration Study: Lithium as a Blanket Coolant," Oak Ridge National Laboratory, ORNL-TM-6214 (1978).

53. J. T. D. Mitchell and M. W. George, "A Design Concept for a Fusion Reactor Blanket and Magnet Shield Structure," Culham Laboratory, CLM-R 121 (1972).

54. R. M. Arons, et al., "Preparation Characterization and Chemistry of Solid Ceramic Breeding Materials," Proc. 2nd Topical Meeting on Fusion Reactor Materials, Seattle, Washington (1981).

55. R. G. Clemmer, "The Development of Tritium Breeding Blankets for DT-Burning Fusion Reactors," Proc. 4th Topical Meeting on the Technology of Controlled Nuclear Fusion, CONF-801011, 526 and references therein (1980).

56. D. L. Smith, et al., "Analysis of In-Situ Tritium Recovery from Solid Fusion Reactor Blankets," Proc. 4th Topical Meeting on the Technology of Controlled Nuclear Fusion, CONF-802022, 560 (1980) and references therein.

57. D. Okula and D. K. Sze, "Tritium Recovery from Solid Breeders: Implications of the Existing Data," University of Wisconsin, UWFDM-351 (1980) and references therein.

58. J. W. Davis, et al, Proc. Workshop on Tritium Breeding Solids Research and Development, DOE/ET-52039/1 (1981) and references therein.

59. S. Nasu, "Data Base for Breeder Choice," Japan Atomic Energy Research Institute, JAERI-M-8510 (1979).

60. M. Tetenbaum, Argonne National Laboratory, Personal Communication.

61. P. A. Finn, et al., "Solid Oxide Compounds - Properties Necessary for Fusion Applications," Proc. 9th Symposium on Engineering Problems of Fusion Research, IEEE Pub. No. 81CH1715-2, Vol. II, 1200 (1981).

62. O. K. Chopra and D. L. Smith, "Interactions of Solid Ceramic Breeding Materials with Structural Alloys," Proc. 2nd Topical Meeting on Fusion Reactor Materials, Seattle, Washington (1981).

63. L. Yang, et al., "Irradiation Study of Lithium Compound Samples for Tritium Breeding Application," General Atomic Company, GA-A16407 (1981).

64. T. Takahashi and T. Kikuchi, J. Nucl. Mater., 91, 93 (1980).

65. D. L. Smith, Argonne National Laboratory, Unpublished Work (1982).

66. G. W. Hollenberg, Hanford Engineering Development Laboratory (1982).

67. J. K. MacKenzie, "Electric Constants of a Solid Containing Spherical Holes," Proc. Phys. Soc. (London), 6313, 2-11 (1950).

68. R. L. Coble and W. D. Kingery, "Effect of Porosity on Physical Properties of Sintered Alumina," J. Am. Ceram. Soc., 39, 377 (1956).

69. G. K. Johnson, R. T. Grow and W. N. Hubbard, J. Chem. Thermodynamics, 7, 781 (1975).

70. S. Nasu, "A Preliminary In-Pile Test of Tritium Release from Li_2O Pellets," Japan Atomic Energy Research Institute, JAERI-Memo 9276 (1980).

71. JANF Thermochemical Tables, Dow Chemical Company, Midland, Michigan (1974).

72. J. Berkowitz, D. J. Meschi and W. A. Chopka, J. Chem. Phys., 33, 553 (1960).

73. A. B. Johnson, et al., "Tritium Production from Ceramic Targets," Battelle Northwest Laboratory, BNWL-2097 (1976).

74. T. Kurasawa, et al., J. Nucl. Mater., 80, 48 (1979).

75. T. Kurasawa, et al., J. Nucl. Mater., 92, 67 (1980).

76. J. E. Draley, et al., "Corrosion of Some Reactor Materials in Dilute Phosphoric Acid," Argonne National Laboratory, ANL-6206 (1961).

77. A. A. Solomon, K. M. Cochra and J. A. Habermeyer, "Modeling Hot Pressing 4R-4 of UO_2," NUREG/CR-2023 (1981).

78. R. A. Graham, University of Florida, Masters Thesis.

79. G. R. Youngquist, Ind. Eng. Chem., 62, 8, 52 (1970).

80. J. R. Hoffman, Nucl. Sci. Eng., 68, 73 (1978).

81. M. Tetenbaum, Argonne National Laboratory, Private Communication (1981).

82. "Home Task Report for INTOR Workshop Session 6, Phase 1, Nuclear Group Report-I," Japan Atomic Energy Research Institute (March, 1981).

83. B. A. Boley and J. H. Weiner, Theory of Thermal Stresses, John Wiley & Sons, 290 (1960).

84. J. H. Koenig, Rutgers University, Ceram. Res. Sta. Prog. Rpt. 2 (1953).

85. C. C. Stone, et al., Nucl. Tech., 55 (1981).

86. B. Badger, et al., "WITAMIR-I, A Wisconsin Tandem Mirror Reactor Design," University of Wisconsin, UWFDM-400 (1980).

87. D. K. Sze, R. G. Clemmer and E. T. Cheng, "Li-Pb, A Novel Material for Fusion Applications," Proc. 4th Topical Meeting on the Technology of Controlled Nuclear Fusion, CONF-801011, 1786 (1981); also, University of Wisconsin, UWFDM-378 (1981).

88. N. J. Hoffman, A. Darnell and J. A. Blink, "Properties of Lead-Lithium Solutions," ibid., 1745; also, Lawrence Livermore National Laboratory, UCRL-84273 (1981).

89. P. A. Finn, et al., Trans. Am. Nucl. Soc., 34, 55 (1980).

90. M. L. Saboungi, J. Marr and M. Blander, J. Chem. Phys., 68(4), 1375 (1978).

91. H. Kottowski, Joint Research Centre - Ispra Establishment, Personal Communication to R. Clemmer, Argonne National Laboratory (1981).

92. H. R. Ihle and C. H. Wu, "The Activity of Lithium and the Solubility of Deuterium in Lithium-Lead Alloys," Proc. 10th Symposium on Fusion Technology, Padova, Italy, 639-644 (1979).

93. E. M. Larsen, M. S. Ortman and K. E. Plute, "Comments on the Hydrogen Solubility Data for Liquid Lead, Lithium, and Lithium-Lead Alloys and Review of the Tritium Solubility Model for Lithium-Lead Alloys," University of Wisconsin, UWFDM-415 (1981).

94. E. Veleckis, Argonne National Laboratory, Personal Communication to N. Hoffman, ETEC (1981).

95. E. Veleckis, R. M. Yonco and V. A. Maroni, "The Current Status of Fusion Reactor Blanket Thermodynamics," Argonne National Laboratory, ANL-78-109 (1979).

96. W. Calaway, Nucl. Tech., 39, 63 (1978).

97. P. F. Tortorelli, Oak Ridge National Laboratory, Personal Communication.

98. Joint Research Centre, Ispra Establishment, "International Tokamak Reactor - European Contributions to the 6th Meeting of the INTOR Workshop," EURFUBRU/XII 2/81/EDV20, IAEA-Vienna (1981).

99. V. V. Popovich and I. G. Dmukhovskaya, Sov. Mater. Sci., 14, 365, English Translation (1979).

100. I. G. Dmukhovskaya and V. V. Popovich, Sov. Mater. Sci., 15, 366, English Translation (1979).

101. N. N. Breyeer and K. L. Johnson, J. Test. Eval., 2, 471 (1974).

102. A. L. Bichuya, Sov. Mater. Sci., 5, 352, English Translation (1969).

103. A. L. Bichuya, et al., Sov. Mater. Sci., 4, 12, English Translation (1968).

104. E. S. Nikolin and G. V. Karpenko, Sov. Mater. Sci., 4, 15, English Translation (1968).

105. M. I. Chaevskii and A. L. Bichuya, Sov. Mater. Sci., 5, 82, English Translation (1969).

106. Yu. B. Kuzma, R. V. Skolozdra and V. Ya. Markiv, Dopovidi Akad. Nauk. Ukr. RSR, 8, 1070 (1964).

107. V. A. Maroni, "An Analysis of Tritium Distribution and Leakage Characteristics for Two Fusion Reactor Reference Designs," Argonne National Laboratory, CEN/CTR/TM-9 (1974).

108. V. A. Maroni and E. H. VanDeventer, "Materials Considerations in Tritium Handling Systems," Proc. 1st Topical Meeting on Fusion Reactor Materials, Miami, Florida (1979).

109. D. Baker, ETEC, Private Communication to P. A. Finn, Argonne National Laboratory (1982).

110. V. A. Maroni, R. D. Wolson and G. E. Staahl, Nucl. Tech., 25, 83 (1975).

111. K. Natesan and D. Smith, Nucl. Tech., 22, 138 (1974).

112. S. B. Skadzien, D. J. Raue and C. C. McPheeters, "Method for Regenerating Sodium Cold Traps," Argonne National Laboratory, ANL-81-52 (1981).

113. W. Geller, "The Theory of Degassing Molten Metals with Watergas," Z. Metallk, 35, 213 (1943).

114. Steam Tables, Electrical Research Association, St. Martin's Press, New York (1967).

115. O. J. Foust, Ed., Sodium-NaK Engineering Handbook, Vol. 1, Gordon and Breach, New York (1972).

116. R. N. Lyon, et al., Ed., Liquid Metals Handbook, 2nd Ed. (Rev.), Atomic Energy Commission/Department of Navy (1954).

117. R. Hultgren, et al., "Selected Values of the Thermodynamic Properties of Binary Alloys," Am. Soc. Metals (1973).

118. N. A. Lange, Ed., Handbook of Chemistry, 10th Ed., McGraw-Hill, New York (1952).

119. D. K. Sze, et al., Proc. 4th Topical Meeting on the Technology of Controlled Nuclear Fusion, CONF-801011, Vol. 3, 1786-1793 (1981).

120. M. S. Peters and K. D. Timmerhaus, Plant Design and Economics for Chemical Engineers, 2nd Ed., McGraw-Hill, New York (1968).

121. R. F. Mattas, Argonne National Laboratory, Private Communication (1982).

122. L. R. Turner, Argonne National Laboratory, Private Communication (1982).

123. P. F. Dunn, Argonne National Laboratory, Private Communication (1982).

124. P. F. Dunn, Int. J. Heat Mass Transfer, 23, 373-385 (1980).

125. O. J. Foust, Ed., Sodium-NaK Engineering Handbook, Vol. 2, Gordon and Breach, New York (1972).

126. Ibid., Vol. 4 (1978).

127. "Alloy Development for Irradiation Performance Quarterly Progress Report for Period Ending December 31, 1980," Oak Ridge National Laboratory, DOE/ER-0045/5 (1981).

CHAPTER 7

RADIATION SHIELDING AND RADIOACTIVITY

Chapter 7

Table of Contents

Chapter 7

List of Figures

Chapter 7

List of Tables

7.0 RADIATION SHIELDING AND RADIOACTIVITY

7.1 Introduction

The DEMO shield design has evolved from a strong incentive to reduce the capital cost of the shielding system which represents 8 to 16% of the total direct cost in a tokamak fusion power reactor,[1,2] and from a desire to improve the reactor maintainability and performance. The shielding system was designed with low cost materials to perform several functions and satisfy the design constraints. The main function of the shield during reactor operation is to reduce the neutron and photon leakage intensities from the shield. This reduction ensures that a) the different reactor components are protected from radiation damage and excessive nuclear heating, b) the neutron reaction rates in the reactor components which produce undesirable radioactive isotopes are reduced, and c) the worker and the public are protected from radiation exposure. Another shield requirement is to attenuate the decay gamma rays so that personnel are permitted access to the reactor building, with all shields in place within one day after shutdown. The personnel access to the reactor building significantly reduces the reactor downtime and the capital cost of the remote equipment required for maintenance.[3]

The materials for the shielding system were selected based upon tradeoff studies and the results from the previous designs;[1,2] in the selection process, cost, resource availability, and performance were considered. The reference shielding materials are 68% ordinary concrete, 9% lead, 6% boron carbide, 7% Fe14Mn2Ni2Cr steel alloy (Fe1422), and 10% water by volume. Ordinary concrete and water are the main materials for the outboard and penetration shield. Water and Fe1422 are the coolant and structural materials for the whole shielding system. Also, Fe1422 is employed for the inboard shield where a material with high shielding performance is required. The low concentration of nickel and chromium motivated the use of Fe1422.[1,4] Low nickel concentration reduces the dose equivalent after shutdown and the production of long-lived isotopes, and low chromium concentration minimizes the consumption of strategic materials. A small amount of boron carbide is employed as a neutron absorber to reduce the activation in the reactor components and structural materials. A density factor of 0.7 is assumed for the boron carbide to avoid the fabrication cost required for a high density

material. Lead is used as a gamma ray attenuator at the outermost surfaces of the outboard and penetration shield so that the dose equivalent in the reactor building is reduced after shutdown. The contribution to the dose equivalent comes essentially from the 5 to 15 cm of materials, excluding water, located at the outermost region of the components located in the reactor building.

A description of the reference shielding system, including design criteria and constraints adopted for the DEMO design, as well as analyses and tradeoff studies for each shielding component are presented in this chapter. Induced activity, biological hazard potential, and decay afterheat are analyzed for several shielding options. The radiation exposure dose in the reactor building after shutdown as a function of the shield thickness are presented for the promising shielding options. Also the dose equivalent outside the reactor building during operation is shown for the reference design.

7.2 Reference Design Description

The DEMO shielding system consists of four main components: a) inboard bulk shield, b) outboard bulk shield, c) penetration and component shield, and d) biological shield. The distinction between the shield components during the design process is essential to satisfy the different design constraints and achieve various objectives.

7.2.1 Inboard Shield

The main goal of the inboard shield is to protect the toroidal field (TF) coils from radiation damage and excessive nuclear heating. The TF coils are assumed to last the operating lifetime of the reactor, with a 21.2 $MW \cdot y/m^2$ integrated neutron wall loading at the first wall, without change in the performance. The inboard radial thickness for the blanket and shield, i.e., the thickness from the first wall to the location of the maximum magnetic field, is 120 cm according to the parametric study discussed in Section 4.2. The thickness and composition of each zone at the midplane are listed in Table 7-1. This radial thickness includes 2-cm vacuum gap between the inboard blanket and shield, 5-cm vacuum gap between the inboard shield and the TF coils, 7-cm thick magnet case, and 27-cm inboard blanket, which leaves 79-cm for the inboard shield. The composition and dimension of the inboard blanket

Table 7-1. Blanket and Shield Parameters for the Reference Design at the Midplane

Zone Description	Radius (cm) From	Radius (cm) To	Thickness (cm)	Zone Composition Percentage by Volume
Magnet Case	163	170	7	100% type 304 steel
Magnet	170	250	80	5% NbTi, 23% Cu, 45% type 304 steel, 8% epoxy
Magnet Case	250	257	7	100% type 304 steel
Gap	257	262	5	Vacuum
Shield	262	341	79	Inboard shield[a]
Gap	341	343	2	Vacuum
Blanket	343	370	27	Inboard blanket[a]
Plasma	370	670	300	Vacuum
Blanket	670	720	50	Outboard blanket[a]
Gap	720	722	2	Vacuum
Shield	722	922	200	Outboard shield[a]
Gap	922	1120	198	Vacuum
Magnet Case	1120	1127	7	100% type 304 steel
Magnet	1127	1207	80	5% NbTi, 23% Cu, 45% type 304 steel, 8% epoxy
Magnet Case	1207	1214	7	100% type 304 steel

[a] Compositions are given in separate tables.

Table 7-2. Inboard and Outboard Blanket Parameters Used in the Shielding Analysis

Zone Description	Zone Thickness (cm)	Zone Composition Percentage by Volume
Armor	1.0	100% PCA steel
First Wall		
	0.4	100% PCA steel
	0.2	100% H_2O coolant
	0.4	100% PCA steel
Tritium Breeder	46.0 (outboard) 23.0 (inboard)[a]	5% PCA steel 5% H_2O coolant 90% Li_2O tritium breeder (0.7 DF)
Blanket Jacket	2.0	100% PCA steel

[a] Nonbreeding inboard blanket has a composition consisting of 90% PCA steel, 10% H_2O coolant.

are listed in Table 7-2. The inboard shielding analysis assumes that the inboard tritium breeding blanket consists of lithium oxide breeder (Li_2O) with an 0.7 density factor. However, the reference design calls for a nonbreeding blanket for the vertical section of the inboard blanket which extends from Z = -80 to 80 cm. The use of a nonbreeding inboard blanket increases the protection for the TF coils behind this section. In fact, the use of steel instead of Li_2O tritium breeder improves the inboard blanket shielding characteristic, and the elimination of the Li_2O porosity required for tritium recovery increases the shield thickness by 6.9 cm.

The inboard shield employs Fe1422 steel alloy, water, and boron carbide. The assumed 0.7 density factor for boron carbide eliminate the cost associated with the high density fabrication. Table 7-3 describes the inboard shield for the reference design, which was evolved from the tradeoff and optimization studies discussed in Section 7.4.1.

Table 7-4 gives the key radiation response parameters in the inboard section of the TF coils. The maximum neutron fluence with energy above 0.1 MeV in the superconductor material is 7×10^{17} n/cm^2, which does not produce significant change in the critical current density or the critical temperature

Table 7-3. Inboard Shield Parameters for the Reference Design at the Midplane

Zone Description	Radius (cm) From	Radius (cm) To	Thickness (cm)	Zone Composition Percentage by Volume
Shield Jacket	262	264	2	100% Fe1422
Boron Carbide Zone	264	274	10[a]	75% B_4C 25% H_2O
Steel Zone	274	339	65	92% Fe1422 8% H_2O
Shield Jacket	339	341	2	100% Fe1422

[a] Boron carbide zone has an 0.7 density factor.

Table 7-4. Radiation Response Parameters in the Inboard Portion of the Toroidal Field Coils (Based on 2.12 MW/m^2 Neutron Wall Loading and 21.2 $MW \cdot y/m^2$ Integrated Neutron Wall Loading at the First Wall)

Maximum fluence in the superconductor material, (E > 0.1 MeV)	7.05×10^{17} n/cm^2
Maximum induced resistivity in the copper stabilizer	5.30×10^{-8} $\Omega \cdot cm$
Maximum atomic displacement in the copper stabilizer	3.59×10^{-4} dPa
Maximum nuclear heating in the superconductor material	
neutron	5.20×10^{-6} W/cm^3
gamma	8.15×10^{-5} W/cm^3
total	8.67×10^{-5} W/cm^3
Maximum nuclear heating in the magnet case	
neutron	6.77×10^{-6} W/cm^3
gamma	4.56×10^{-4} W/cm^3
total	4.63×10^{-4} W/cm^3
Maximum nuclear heating in TF coils including the magnet case	
neutron	1.38×10^{-1} W/cm
gamma	4.04 W/cm
total	4.18 W/cm
Maximum dose in the electrical insulator	
neutron	7.20×10^{8} rad
gamma	3.30×10^{8} rad
total	1.05×10^{9} rad
Maximum dose in the thermal insulator	
neutron	1.57×10^{9} rad
gamma	1.84×10^{9} rad
total	3.41×10^{9} rad
Total nuclear heating in the inboard shield	17.1 MW

of NbTi alloy.[5,6] The induced resistivity in the copper stabilizer which has a maximum of 5.3×10^{-8} $\Omega \cdot cm$, drops very fast with respect to the depth in the TF coils. This result assumes no magnet annealing during the operating life of the reactor, with a 21.2 $MW \cdot y/m^2$ integrated neutron wall loading at the first wall. The TF coil design accommodate this change in the resistivity without difficulty. However, magnet annealing can be used to lower the maximum induced resistivity.[1] The maximum nuclear heating in the superconductor material is 8.7×10^{-5} W/cm^3, which does not cause any design difficulty for the TF coils. The total nuclear heating in the inboard section of the TF coils is < 1.7 kW based on the maximum heating per unit length of the TF coils at the midplane. The maximum dose in the electrical insulator is 1.05×10^9 rads, which is well below the acceptable limit.[7,8]

As mentioned above, the analysis given in this section is based on the use of an inboard tritium breeding blanket. The use of a nonbreeding blanket for the inboard vertical section of the reactor reduces the radiation response parameters listed in Table 7-4 by a factor of 2-3.

7.2.2 Outboard Shield

In addition to radiation protection of reactor components from radiation damage and excessive nuclear heating, the design of the outboard shield is an essential element in lowering the dose equivalent limits so that personnel are permitted access to the reactor building. The reference design for the outboard shield is given in Table 7-5. The total radial thickness of the reference design is 200 cm, including a 3-cm void for the boron carbide material. Ordinary concrete and water are the main shielding materials, with small amounts of B_4C and Pb (5.2% B_4C and 7.5% Pb by volume). The outboard shield is divided into two main sections. The first section consists of 2-cm Fe1422 shield jacket, 25-cm thick water zone, 12-cm thick B_4C-Fe1422 zone, and 10-cm thick lead zone. The second section represents most of the outboard shield and consists of 140-cm thick ordinary concrete zone, 6-cm thick B_4C-Fe1422 zone, and 5 cm thick lead zone. The first section of the outboard shield a) provides several functions: protection for the ordinary concrete against radiation damage, b) acts as a neutron reflector for the blanket to enhance the tritium breeding ratio and energy multiplication factor, and c) reduces the average neutron energy entering the concrete shield to minimize

Table 7-5. Outboard Shield Parameters for the Reference Design at the Midplane

Zone Number	Radius (cm) From	To	Thickness (cm)	Zone Composition Percentage by Volume
1	722	724	2	100% Fe1422
2	724	749	25	100% H_2O
3	749	761	12	42% Fe1422, 58% B_4C[a]
4	761	771	10	100% Pb
5	771	911	140	100% Ordinary Concrete
6	911	917	6	42% Fe1422, 58% B_4C[a]
7	917	922	5	100% Pb
Total	722	922	200	

[a] B_4C is used with an 0.7 density factor.

the production rate of long-lived isotopes, which are generated mainly by high energy neutron.

Table 7-6 gives the radiation response parameters related to the outboard shield. Nuclear heating rates in the outboard shield are shown in Fig. 7-1. The maximum nuclear heating in the ordinary concrete is ~ 1 mW/cm^3, which satisfies the design criterion[9] for protection of the ordinary concrete against loss of water, temperature effects, radiation absorption effects, and thermal stress conditions. The radiation response parameters in the outer portion of the TF coils are four orders of magnitude lower than the inboard section reflecting the difference in the total attenuation of the outboard blanket and shield compared to the inboard. In fact, the radiation level outside the outboard bulk shield is dictated by the personnel access requirement during shutdown. The maximum dose equivalent achieved in the reactor building is 0.4 mrem/h one day after shutdown which satisfies the 0.5 mrem/h design goal for DEMO. The neutron and photon fluxes at the end of the outboard shield are shown in Fig. 7-2. The dose equivalent outside the reactor building during operation is given in Fig. 7-3 as a function of the building wall thickness.

Table 7-6. Radiation Response Parameters Related to the Outboard Shield (Based on 2.12 MW/m^2 Neutron Wall Loading and 21.2 $MW \cdot y/m^2$ Integrated Neutron Wall Loading at the First Wall)

Total power in the outboard shield	
First section	1.96×10^{1} MW
Second section	1.37×10^{-1} MW
Total	1.97×10^{1} MW
Nuclear heating in the shield jacket	
Neutron	0.60×10^{-1} W/cm^3
Gamma	8.76×10^{-1} W/cm^3
Total	9.36×10^{-1} W/cm^3
Maximum heating in the ordinary concrete	
Neutron	0.76×10^{-3} W/cm^3
Gamma	0.39×10^{-3} W/cm^3
Total	1.15×10^{-3} W/cm^3
Maximum dose equivalent in the reactor hall	
During operation	3.00×10^{4} mrem/h
1 day after shutdown	4.11×10^{-1} mrem/h
1 week after shutdown	3.58×10^{-1} mrem/h
Maximum dose equivalent outside the reactor building during operation	1.05×10^{-1} mrem/h
Neutron at the outboard shield boundary	
$E > 0.1$ MeV	9.04×10^{5} $n/cm^2 \cdot s$
$E > 0.0$ MeV	1.37×10^{6} $n/cm^2 \cdot s$
Maximum nuclear heating in the outer leg of the TF coils	
Neutron	8.51×10^{-10} W/cm^3
Gamma	5.35×10^{-8} W/cm^3
Total	5.43×10^{-8} W/cm^3

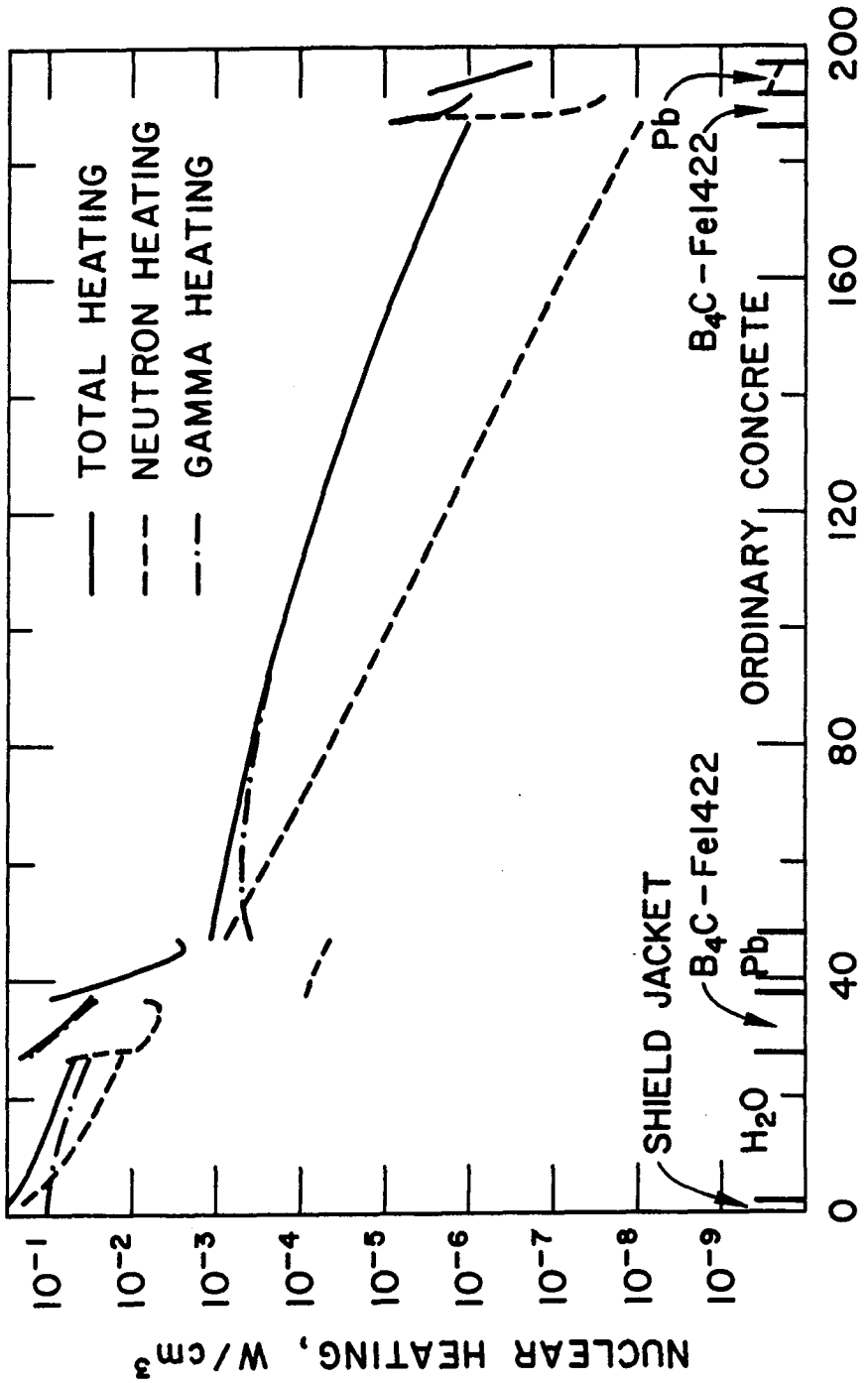

Figure 7-1. Nuclear heating in the outboard shield.

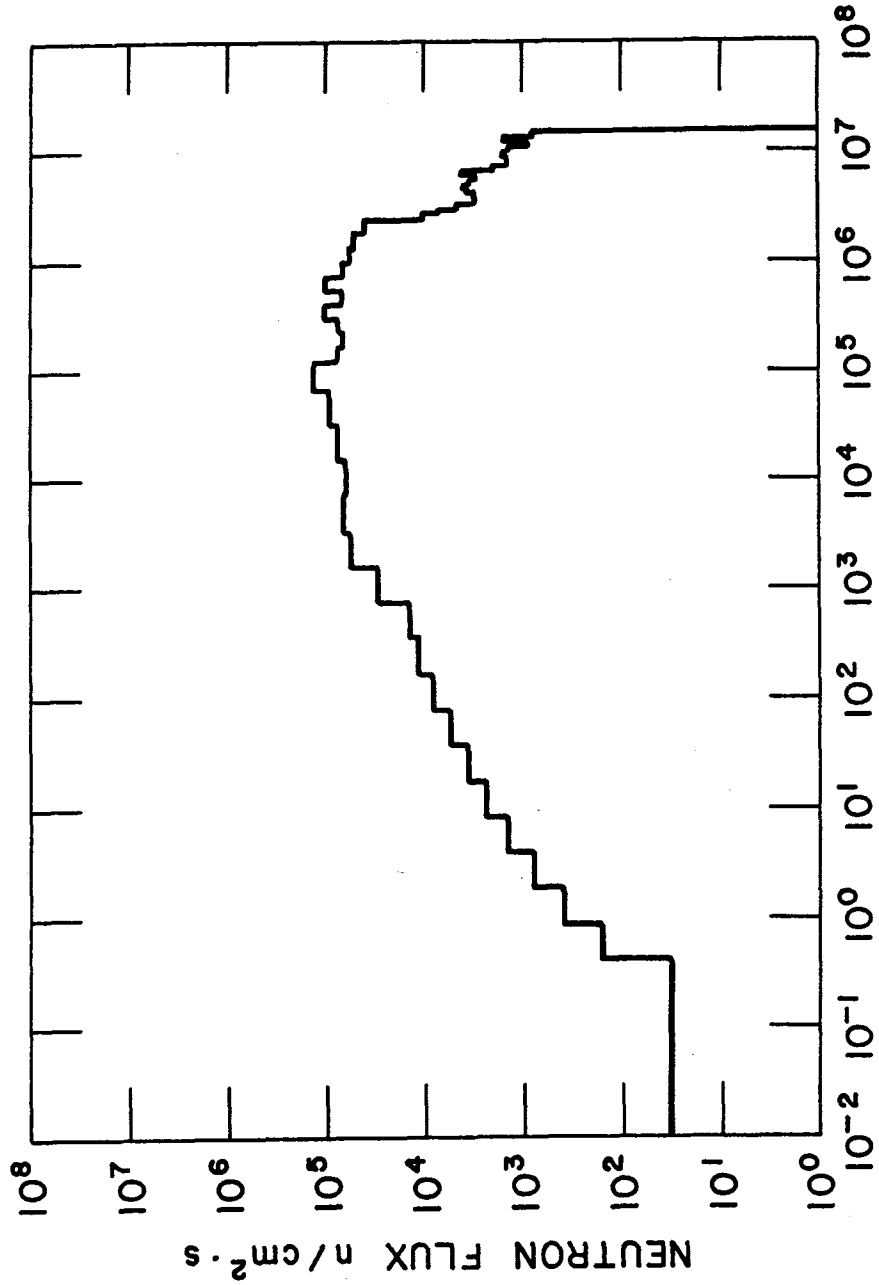

Figure 7-2a. Neutron spectrum at the outer surface of the outboard shield.

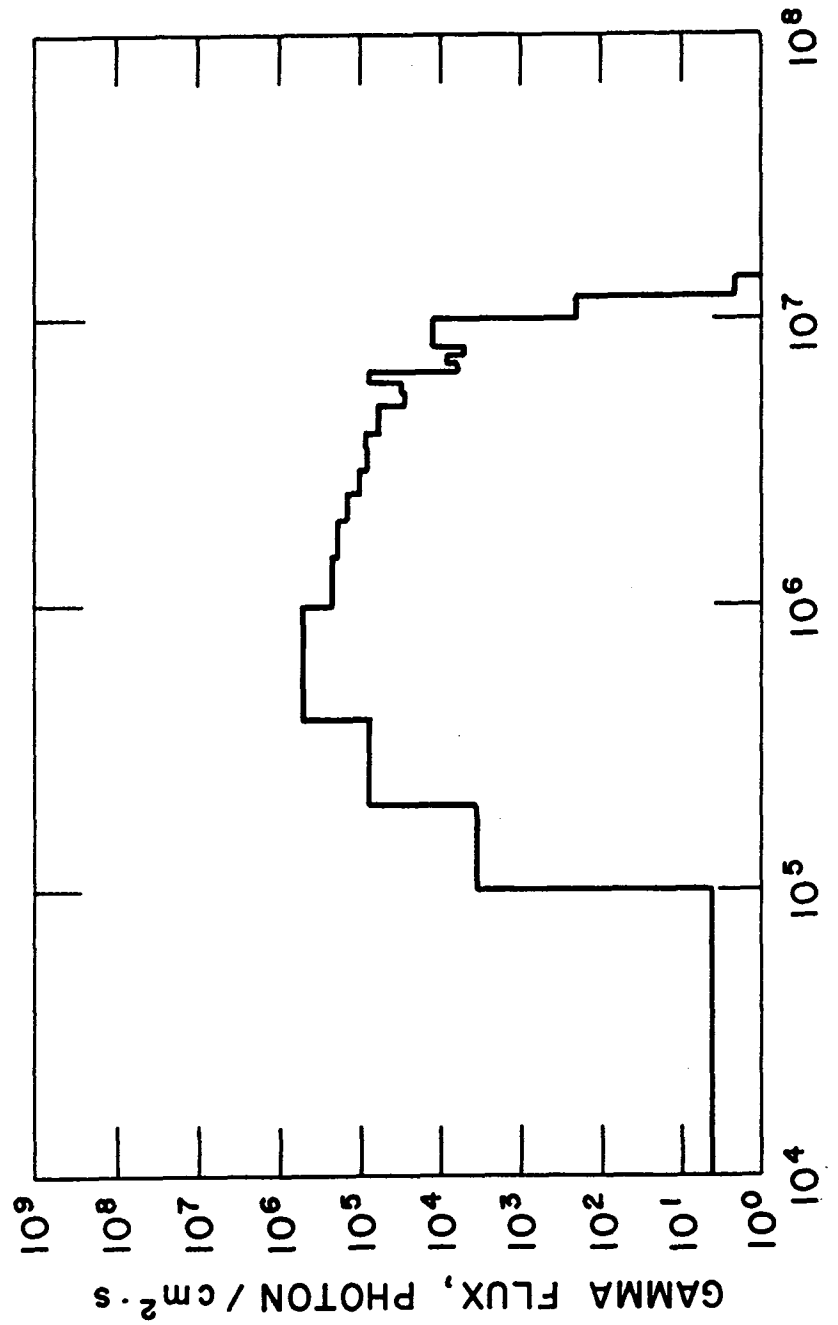

Figure 7-2b. Gamma rays spectrum at the outer surface of the outboard shield.

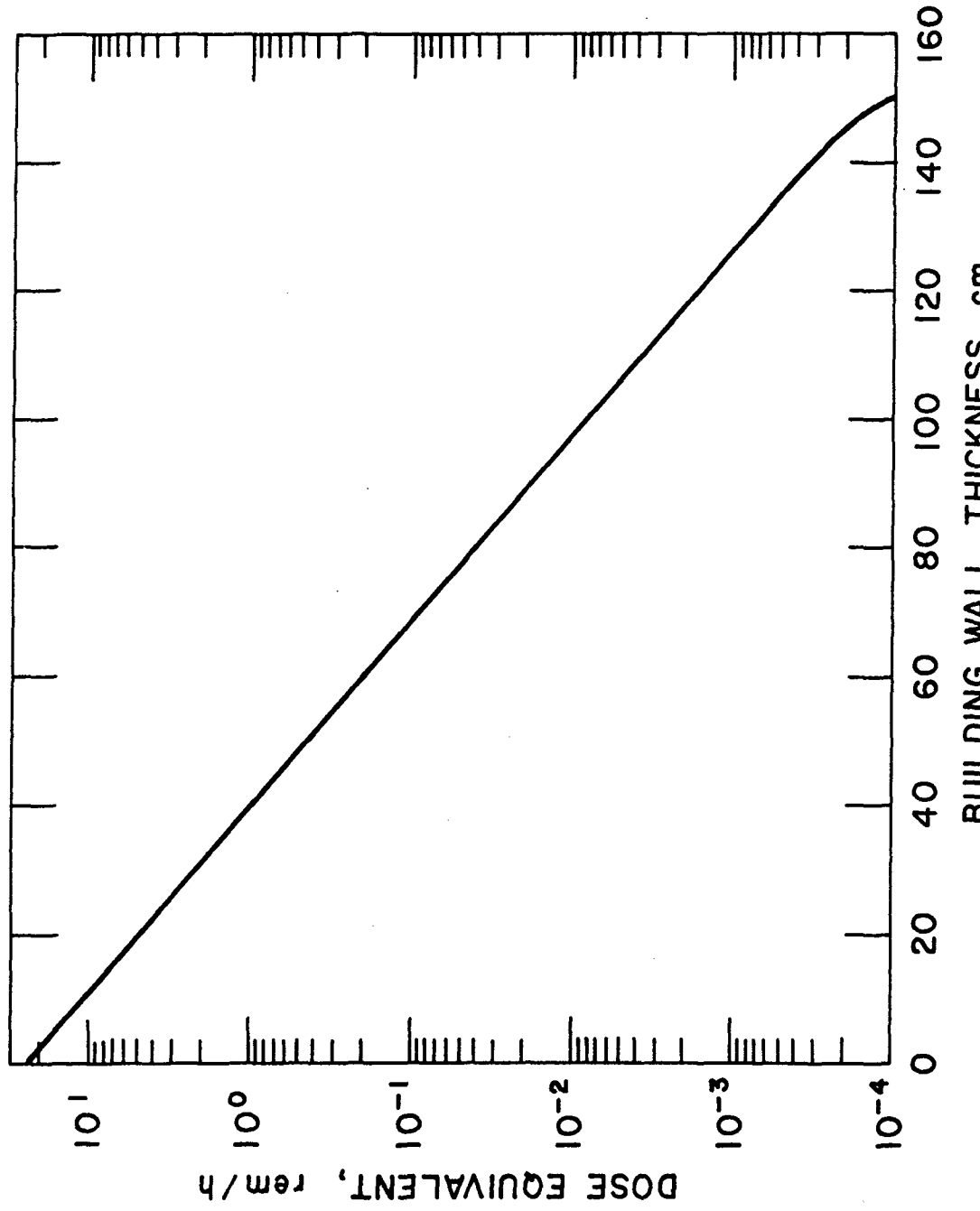

Figure 7-3. Dose equivalent during operation outside the reactor building as a function of building wall thickness.

The reference design uses a 150-cm thick wall for building structural purposes which reduces the dose equivalent to 0.1 mrem/h outside the building during operation. This dose represents an upper estimate since the dose calculations ignore the attenuation effect of the different components existing in the reactor building. However, the 0.1 mrem/h satisfies the design criterion discussed in Section 7.3.

The average activation parameters in the outboard shield as a function of the time after shutdown are given in Table 7-7. The results show that most of the outboard shield material (95% by volume) can be classified as a low level waste based on the radioactivity concentration.[10]

7.2.3 Penetration Shield

Since the penetration shield significantly affects reactor cost, personnel access, and reactor availability, special attention has been given to the main penetrations: (a) the relativistic electron beam (REB) system and (b) the vacuum duct system. The penetration shield was designed to perform the outboard shield functions given above. In addition, the REB annular duct was analyzed to assess the radiation damage in the ceramic material employed.

In order to determine the radiation damage in the ceramic material of the REB system, a three dimensional Monte-Carlo transport calculation was performed for the whole reactor, including the REB annular duct. The general-purpose Monte-Carlo code MCNP[11] was used for the calculation, with a continuous energy representation for the nuclear cross sections. The energy spectrum of 14 MeV neutrons from the DT plasma was considered in the calculations. The REB annular duct has 13-cm inner radius and 26-cm outer radius. The neutron fluence and radiation dose (neutrons and photons) were calculated for three ceramic materials: magnesium oxide, aluminum oxide, and silicon oxide. The calculations show that locating the ceramic material 270 cm from the first wall results in total dose $< 10^{12}$ rads at the end of the operating life, (21.2 MW•y/m^2 integrated neutron wall loading at the first wall). This dose corresponds to a neutron fluence of $\sim 10^{20}$ n/cm^2 (E > 0.1 MeV). At such a level of dose MgO or Al_2O_3 show insignificant change in the structural properties.[7,12] However, the DEMO design has a 90° bend for the REB duct outside the bulk shield. The bend reduces the dose in the insulator by an order of magnitude. The DEMO reference design locates the ceramic

Table 7-7. Average Activation Parameters

Time After Shutdown	Activity Ci/cm^3	Activity Ci/W_{th}	Afterheat (% of Thermal Power)	Biological Hazard Potential (km^3 air/kW_{th})
		A. All the Outboard Shield		
1 min	6.12×10^{-2}	1.02×10^{-1}	1.32×10^{-1}	7.49
1 d	9.64×10^{-3}	1.61×10^{-2}	2.22×10^{-3}	3.17
1 wk	9.39×10^{-3}	1.57×10^{-2}	1.97×10^{-3}	3.09
1 mo	8.86×10^{-3}	1.48×10^{-2}	1.82×10^{-3}	2.91
1 y	6.12×10^{-3}	1.02×10^{-2}	9.25×10^{-4}	1.46
10 y	5.49×10^{-4}	9.17×10^{-4}	4.66×10^{-5}	9.52×10^{-2}
100 y	2.65×10^{-5}	4.43×10^{-5}	5.44×10^{-7}	2.19×10^{-2}
1000 y	2.70×10^{-7}	4.51×10^{-7}	2.35×10^{-8}	4.27×10^{-5}
		B. Ordinary Concrete Shield		
1 min	4.00×10^{-5}	4.95×10^{-5}	7.92×10^{-5}	4.33×10^{-3}
1 d	3.37×10^{-6}	4.18×10^{-6}	1.05×10^{-6}	2.18×10^{-3}
1 wk	3.17×10^{-6}	3.93×10^{-6}	4.28×10^{-7}	2.09×10^{-3}
1 mo	3.09×10^{-6}	3.82×10^{-6}	3.65×10^{-7}	2.03×10^{-3}
1 y	2.72×10^{-6}	3.37×10^{-6}	1.24×10^{-7}	1.78×10^{-3}
10 y	2.43×10^{-6}	3.01×10^{-6}	5.75×10^{-8}	1.54×10^{-3}
100 y	1.23×10^{-6}	1.52×10^{-6}	1.84×10^{-8}	7.57×10^{-4}
1000 y	3.35×10^{-9}	4.15×10^{-9}	4.86×10^{-10}	9.79×10^{-7}

materials after the bend, where the dose is ~ 10^{11} rads at the end of the operating life.

The penetration shield thickness for the REB duct and the vacuum lines were determined based on a similar analysis to that for the INTOR shield system.[13,14,2] The shield thicknesses were designed to get a total neutron flux at the outermost surface of 2 x 10^6 n/cm^2.s during operation. These flux values are achieved at the outermost surface of the reference outboard shield for a biological dose of 0.4 mrem/h after one day from shutdown. Table 7-8 gives the thickness and composition for each penetration shield section.

7.3 Shield Design Criteria

In the design of a shielding system, a careful definition of the design criteria is an essential step.[15,16] The TF coils are designed to last the lifetime of the reactor without change in their performance. Therefore, the shielding system must protect the different components of the TF coils from radiation damage. In general, neutron irradiation of the superconductor materials tends to lower the critical current density (J_c) and the critical temperature (T_c). For NbTi superconductor, it has been shown that J_c is decreased by ~ 10% at 4 x 10^{18} n/cm^2 (E > 0.1 MeV) dose while T_c is unchanged.[4] The copper resistivity is more sensitive to the neutron fluence, and a neutron fluence of 10^{18} n/cm^2 generates an induced resistivity of 7 x 10^{-8} Ω•cm. This increase in the resistivity can be accommodated by using more copper stabilizer, which increases the thickness of the TF coils, or can be annealed out by warming the TF coils. The TF coil design allows 5 x 10^{-8} Ω•cm induced resistivity by radiation before an anneal process is required. The most sensitive component in the TF coil is the insulator materials because the radiation damage in them is irreversible and limits the operating life of the TF coils. It was demonstrated[8] that epoxy insulator (Kapton) can withstand a radiation dose of 10^{10} rads at cryogenic temperature and retains high resistivity and mechanical strength. The nuclear energy deposition in the magnet impacts the refrigeration power required since about 300 to 500 W of electrical power are consumed to remove one watt from the TF coils at 4 K. This removal efficiency calls for minimizing the nuclear energy deposition in the TF coils. Also, limiting the maximum nuclear heating to less than 10 mW/cm^3 is required to avoid any additional cooling requirements

Table 7-8. Penetration Shield Parameters for the Reference Design

Penetration Shield Section	Thickness (cm)	Composition Percentage by Volume
Vacuum lines inside the TF coils and first section of the REB duct	2	100% Fe1422
	25	100% H_2O
	5	90% B_4C + 10% Fe1422
	5	100% Pb
	48	100% ordinary concrete
	5	90% B_4C + 10% Fe1422
	5	100% Pb
Vacuum lines outside the TF coils and second section of the REB duct	2	100% Fe1422
	20	100% H_2O
	5	90% B_4C + 10% Fe1422
	5	100% Pb
	38	100% ordinary concrete
	5	90% B_4C + 10% Fe1422
	5	100% Pb
Vacuum pumps and the third section of the REB duct	2	100% Fe1422
	53	100% ordinary concrete
	5	90% B_4C + 10% Fe1422
	5	100% Pb

for the superconductor; this heat load is a small fraction of the eddy current losses in the superconductor.

The personnel access to the reactor building within one day after shutdown requires the satisfaction of regulations pertaining to occupational exposure. The federal regulations[17] limit the occupational dose to 5 rem/y, with a maximum of 3 rem/quarter. Occupational exposure based on working 8 h per day and 40 h per week is 2.5 mrem/h. However, the current practice limits worker exposure to 0.5 mrem/h. In fact, about 90% of U.S. radiation workers are exposed to less than 0.2 rem/y (0.1 mrem/h).[10] The DEMO design goal is 0.5 mrem/h in the reactor building within one day from shutdown.

Each shielding material has certain physical constraints that must be taken into consideration in the design process. For example, water shielding material requires careful design for the shield system (pipelines, pumps, bulk shield, etc.) so that the formation of gas pockets from radiolysis is not possible. In addition, special attention must be given to the pH-value and corrosion products. Concrete requires protective measures to avoid change in the performance over the lifetime of the reactor. The following design recommendations[9] adequately protect concrete against loss of water, temperature effects, radiation absorption effects, and stress conditions: a) maximum internal heat generation, 1 mW/cm^3, b) maximum temperature gradient, 1 °C/cm, c) maximum internal temperatures, 80°C; and d) maximum ambient temperature, 71°C. The temperature limitations may be achieved by lining the concrete with a jacket of steel and adequately ventilating the shield or cooling the steel jacket to avoid dependence on the surroundings for removing the heat load.

7.4 Analysis and Tradeoff Studies

Several analyses and tradeoff studies were performed to define the reference shield system for DEMO. The impact of the inboard shield thickness and material arrangement on the radiation response in the TF coils was analyzed for two shield materials options, tungsten and steel-boron carbide. The effect of the boron carbide density factor on the shield response was studied. Several shielding options were analyzed for the outboard shield. The dose equivalent results as a function of the radiation shield thickness are presented. The method and geometrical model used for the relativistic electron beam (REB) duct are given. The radiation responses in different ceramic materials for the REB duct window are shown as a function of the distance from the first wall.

One-dimensional calculations were performed using discrete ordinate code ANISN[18] with S_8 symmetric angular quadrature set and P_3 legendre expansion for the scattering cross sections. A 67-multigroup cross section set (46 neutrons and 21 photons) collapsed from the CTR Library[19] was used for ANISN calculations. The MACKLIB-IV[20] was employed to calculate the nuclear response functions (nuclear heating, radiation damage, gas production, etc.). RACC and DKR radioactivity codes[21] were used for activation

analysis. A general Monte Carlo code for neutron and photon transport, MCNP[11] with special update,[22] was used for three-dimensional analysis of the REB duct. A continuous energy representation for the nuclear cross sections from ENDF/B-IV was employed for MCNP calculations. The energy spectrum of the DT source neutrons was sampled for the REB duct analysis. The dose equivalent analysis is based on the neutron and gamma fluxes using the flux-to-dose conversion factor of the American National Standard ANSI/ANS-6.1.1-1977. Table 7-9 gives the density and composition of each material used in the shield system.

7.4.1 Inboard Shield

The inboard shield was designed to protect the TF coils from radiation damage and excessive nuclear heating so that they last the operating life of the reactor without change in performance. The inboard blanket and shield thickness (the radial thickness from the edge of the scrape-off region to the position of maximum toroidal field) is 120 cm. This thickness includes 2-cm vacuum gap between the blanket and shield, 5-cm vacuum gap between the shield and the TF coils, and 27 cm for the inboard blanket. In the inboard shield analysis, the inboard blanket employs Li_2O with 0.7 density factor for tritium breeding which results in another 7 cm vacuum in the inboard section of the reactor. This allows for 86 cm of actual materials to shield the TF coils. Two shielding options were studied for DEMO design, the tungsten option (90% tungsten, 10% water) and the steel option (80% Fe1422, 10% B_4C, and 10% water). The compositions of both options were obtained from previous optimization studies given in References 1 and 2. The thickness of the inboard shield, the section between the inboard blanket and the magnet case, was varied from 64 to 94 cm for both shield options, and a homogeneous composition was assumed. Figures 7-4 through -10 are plots of the different nuclear responses calculated for the steel and tungsten shield options. All the results are normalized to 2.12 MW/m^2 neutron wall loading or 21.2 $MW \cdot y/m^2$ integrated neutron wall loading for the operating life of the DEMO reactor (both loadings at the first wall).

Figure 7-4 gives the maximum dose in the electrical insulator at the end of the operating life. The tungsten shield option reduces the electrical insulator dose by a factor of ~ 25 compared to the steel option at 79 cm of

Table 7-9. Density and Composition of Each Material or Alloy Used in the Analysis

Material	Density (g/cm^3)	Atomic Density ($atom/cm^3 \times 10^{-24}$)	
PCA stainless steel	7.86	B	2.188-5[a]
		C	1.971-4
		N	3.380-5
		Al	5.264-5
		Si	8.427-4
		P	1.528-5
		S	7.382-6
		Ti	2.965-4
		V	9.292-5
		Cr	1.274-2
		Mn	1.723-3
		Fe	5.499-2
		Co	2.410-5
		Ni	1.290-2
		Cu	1.490-5
		As	1.264-5
		Nb	1.529-5
		Mo	9.868-4
		Ta	5.453-10
Li_2O	2.01	O	4.058
		Li	8.115
H_2O	1.00	H	6.700-2
		O	3.350-2
Fe1422	7.94	C	2.309-2
		N	6.487-5
		Si	3.916-4
		P	2.316-5
		S	2.983-6
		Cr	1.848-3
		Mn	1.219-2
		Fe	6.953-2
		Ni	1.580-3
Borated water (H_3BO_3)	1.05	H	6.846-2
		O	3.496-2
		B	4.850-4
B_4C	2.52	B	1.098-1
		C	2.745-1
Pb	11.34	Pb	3.348-2

Table 7-9. (Continued)

Ordinary Concrete	2.33	H	2.892-3
		O	4.325-2
		C	6.518-3
		Mg	1.204-4
		Al	2.656-4
		Si	9.392-3
		S	3.606-5
		Cu	8.730-3
		Ni	7.447-5
Ferrophosphorus concrete	4.68	H	1.398-2
		O	1.491-2
		C	1.153-4
		Mg	1.164-4
		Al	4.174-4
		Si	2.811-3
		P	1.880-2
		Cu	2.960-3
		Cr	2.664-5
		Mn	1.283-3
		Fe	3.043-2
Cu	8.96	Cu	8.493-2
Epoxy ($C_{10}H_{13}O_2$)	1.147	H	4.745-2
		C	3.650-2
		O	7.300-3
NbTi	6.54	Nb	2.777-2
		Ti	2.835-2

[a] 2.188-5 = 2.188×10^{-5}

shield thickness (the reference shield thickness for DEMO). The thermal insulator dose is ~ 2.2 times the electrical for both options. Figure 7-5 gives the maximum neutron fluence (E > 0.1 MeV) at the end of operating life in the NbTi superconductor for both options. The results of Fig. 7-5 are similar to the dose results. The maximum radiation damage in the copper stabilizer at the end of the operating life in terms of atomic displacement and induced resistivity is shown in Figs. 7-6 and -7, respectively. The induced resistivity for the steel option at the DEMO reference shield thickness is 5×10^{-8} Ω•cm at the end of the operating life. This means that an anneal process for the TF coils is not required during the lifetime of the reactor. Figures 7-8 through -10 give the heating rates in the TF coils. The

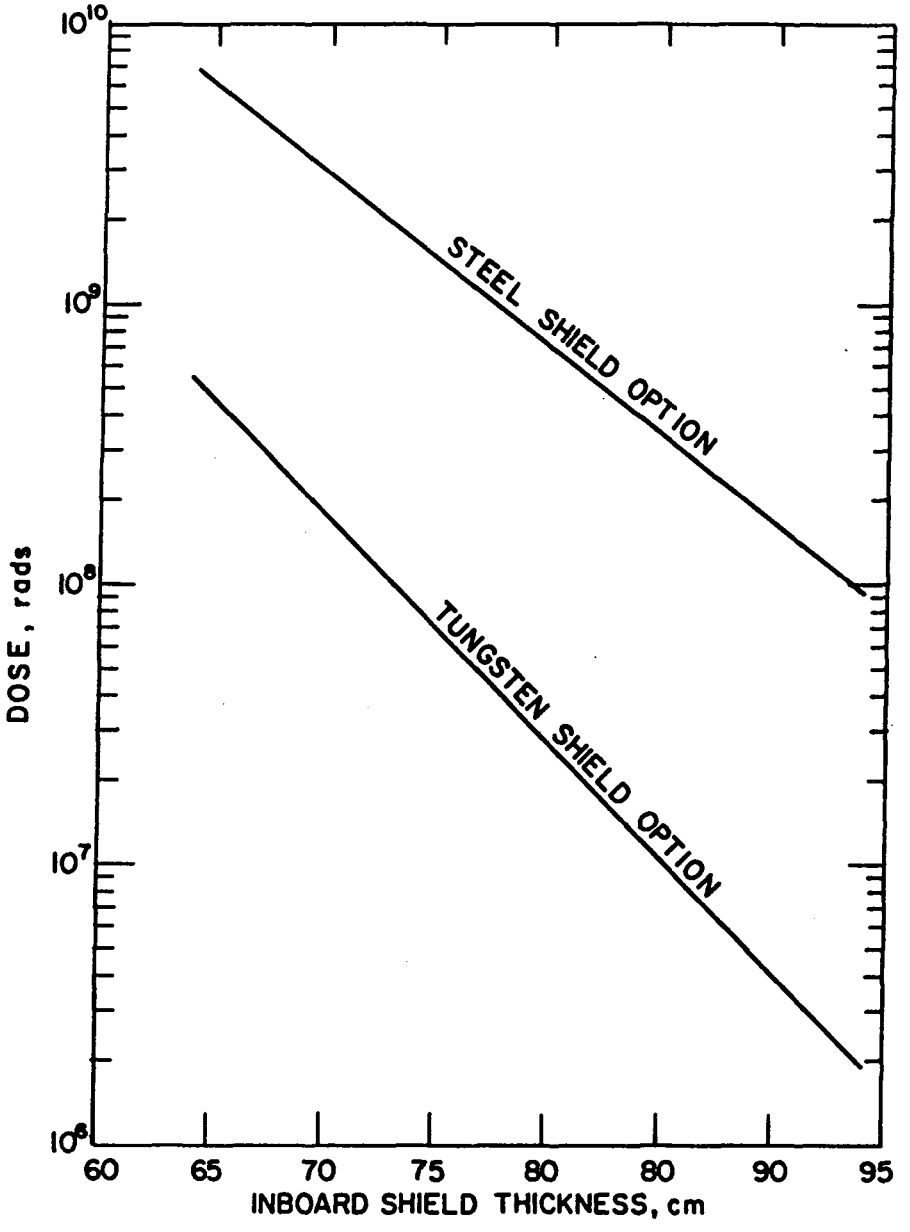

Figure 7-4. Maximum dose in the electrical insulator normalized to 21.2 $MW \cdot y/m^2$ integrated neutron wall loading at the first wall as a function of the inboard shield thickness for tungsten and steel shield option.

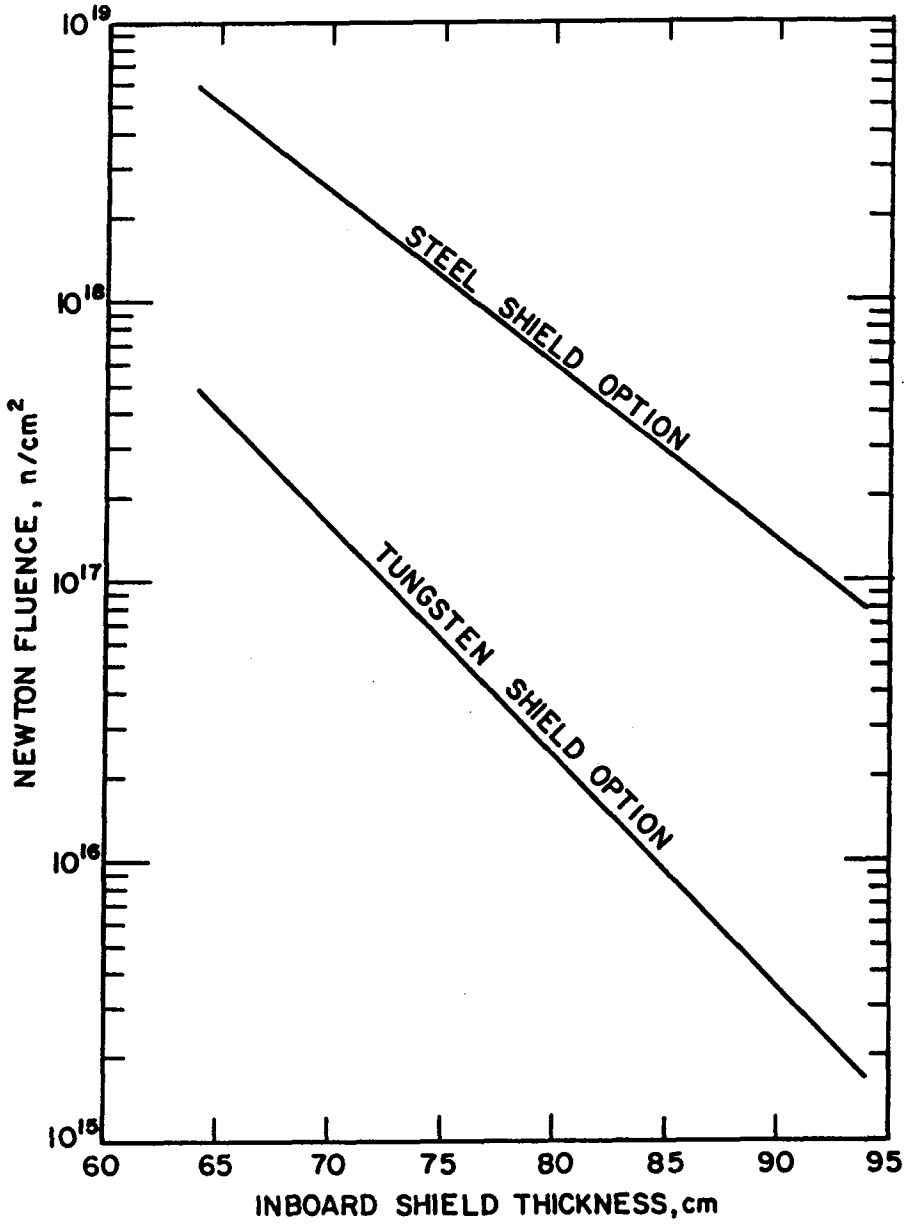

Figure 7-5. Maximum neutron fluence (E > 0.1 MeV) in the superconductor material normalized to 21.2 MW·y/m^2 integrated neutron wall loading at the first wall as a function of the inboard shield thickness for tungsten and steel shield option.

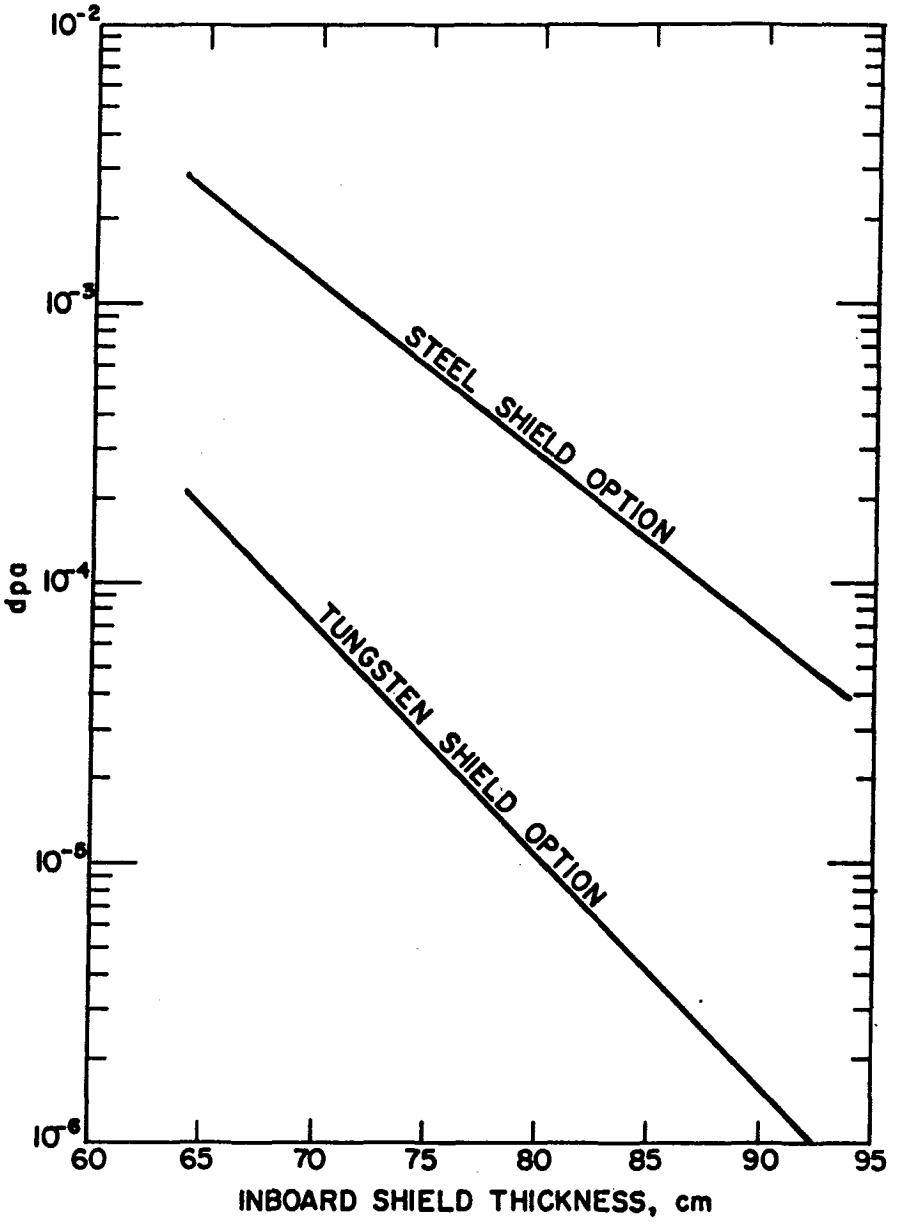

Figure 7-6. Maximum atomic displacement per atom in the copper stabilizer from 21.2 MW·y/m^2 integrated neutron wall loading at the first wall as a function of the inboard shield thickness for tungsten and steel shield option.

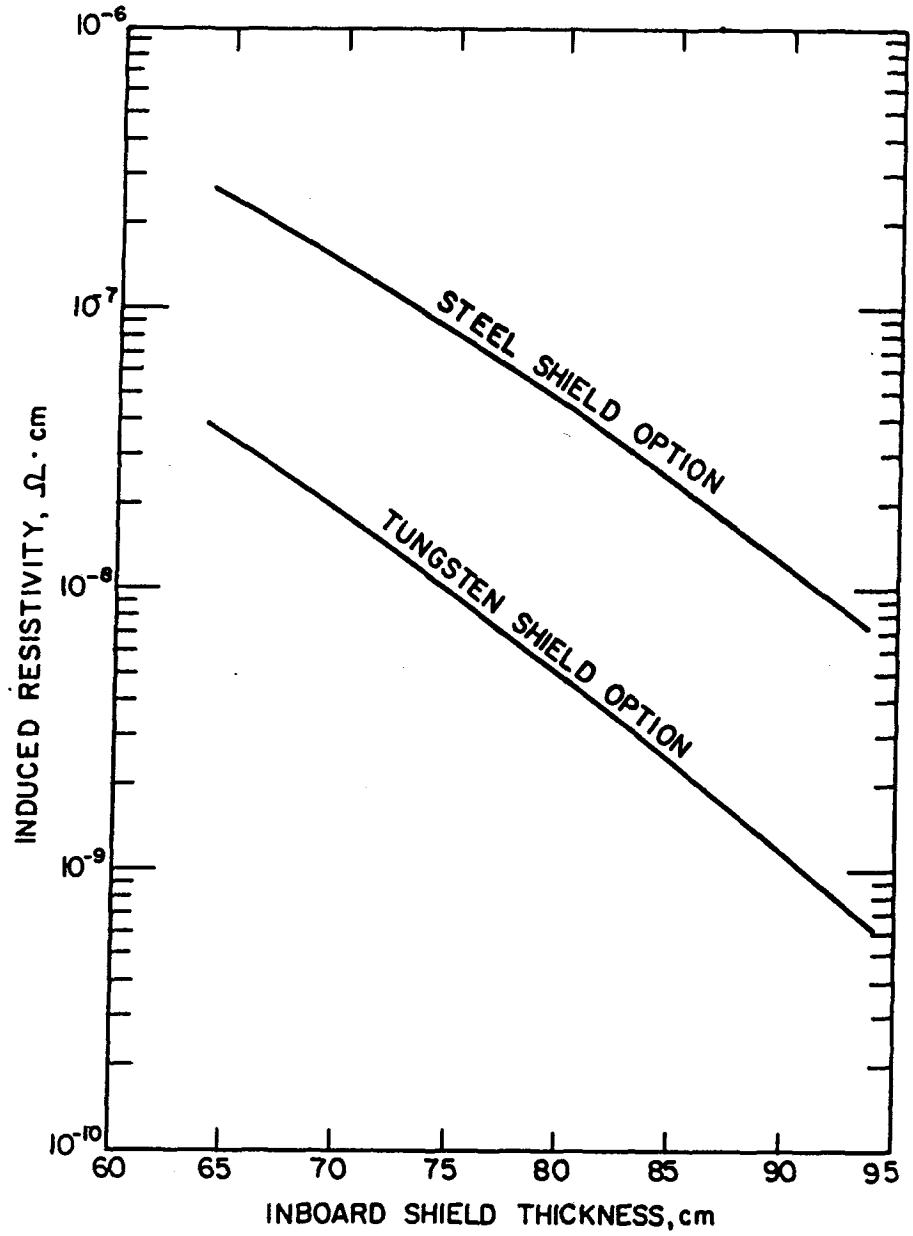

Figure 7-7. Maximum copper induced resistivity normalized to 21.2 MW·y/m^2 integrated neutron wall loading at the first wall as a function of the inboard shield thickness for tungsten and steel shield option.

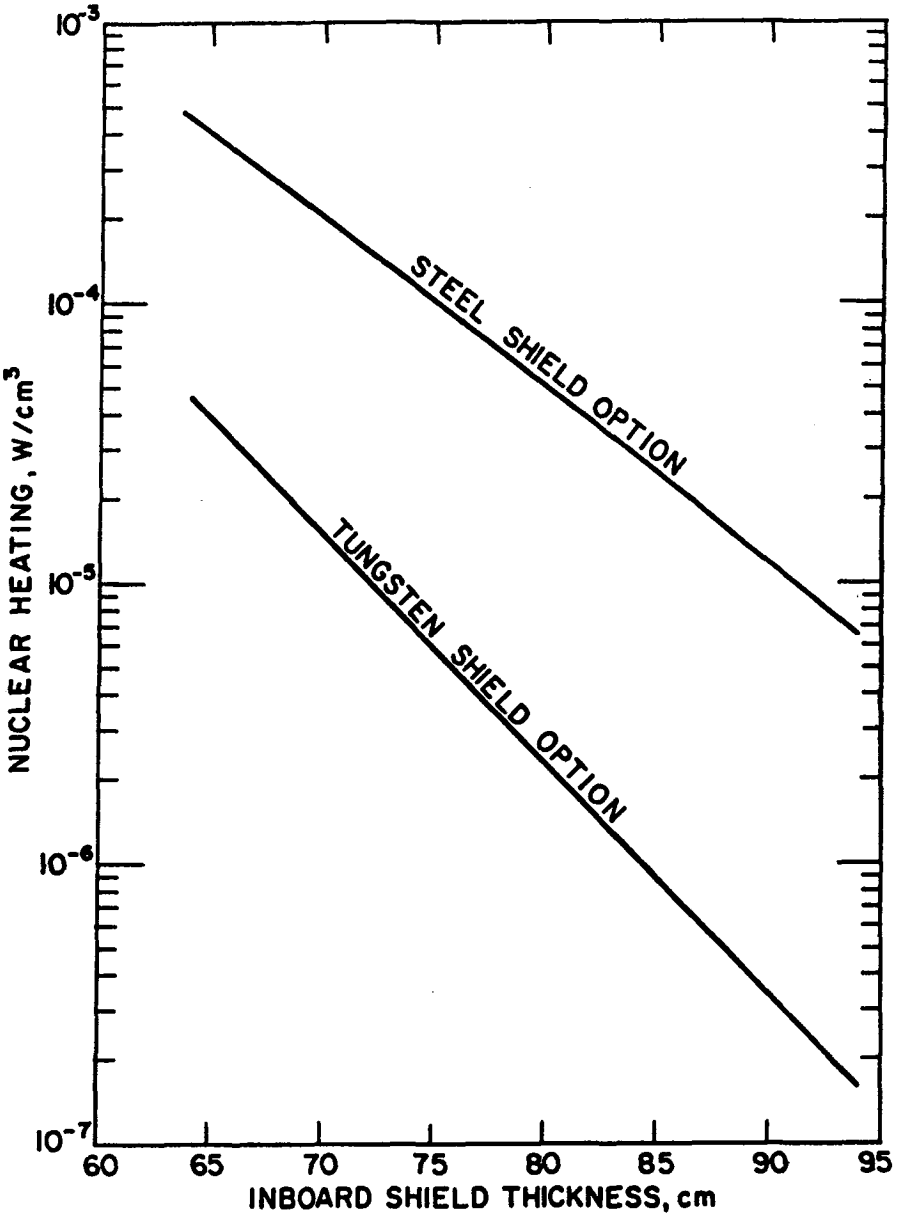

Figure 7-8. Maximum nuclear heating in the magnet case normalized to 2.12 MW/m^2 neutron wall loading at the first wall as a function of the inboard shield thickness for steel and tungsten shield.

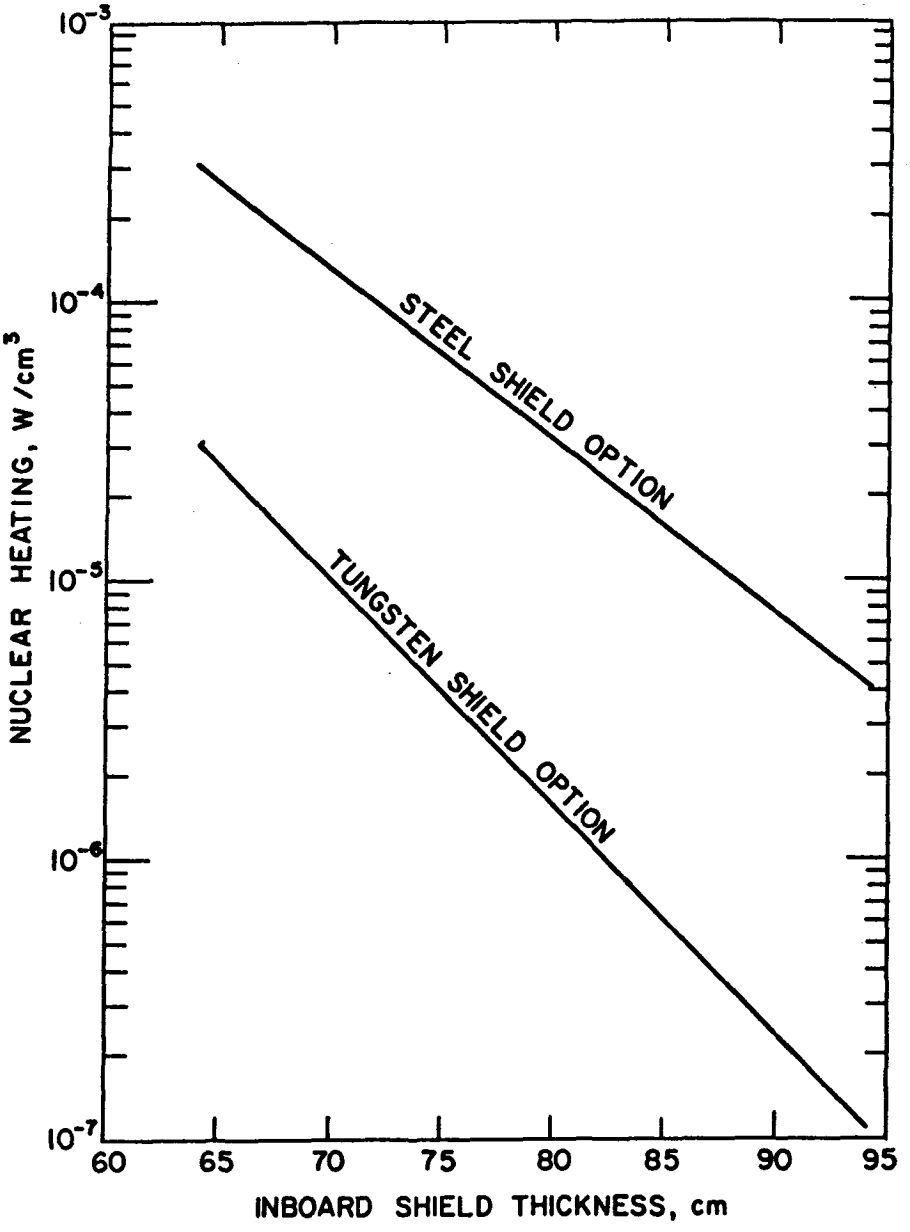

Figure 7-9. Maximum nuclear heating in the magnet normalized to 2.12 MW/m^2 neutron wall loading at the first wall as a function of the inboard shield thickness for tungsten and steel shield.

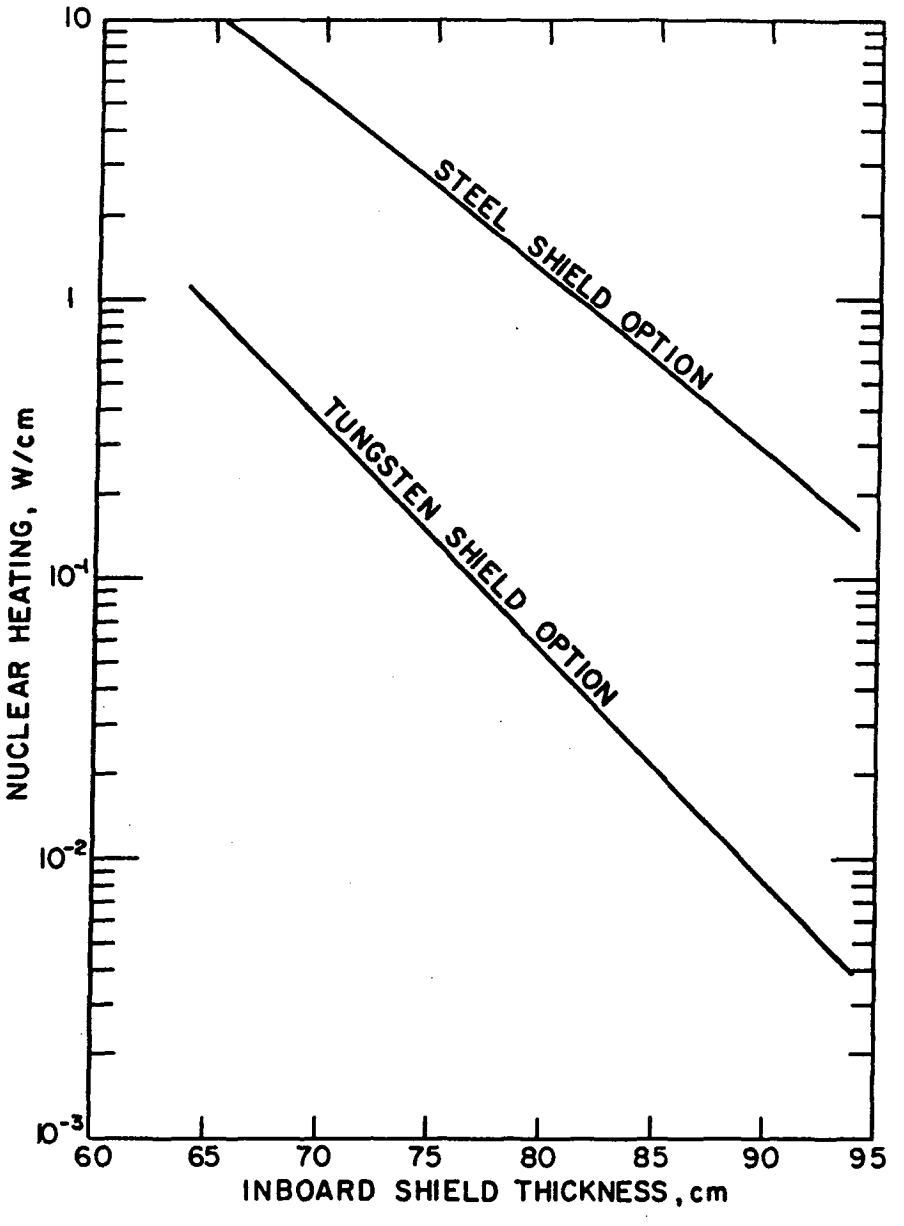

Figure 7-10. Nuclear heating in the magnet (including magnet case) per cm of the magnet length at midplane normalized to 2.12 MW/m^2 neutron wall loading at the first wall as a function of the inboard shield thickness for tungsten and steel shield.

maximum heating in the magnet case is less than 1 mW/cm^3 for the steel option. The tungsten shield option reduces the nuclear heating in the TF coils by a factor of ~ 20 relative to the steel option for the DEMO design.

In the above analysis for the inboard shield, a homogeneous composition and theoretical density were assumed for each material. However, practical considerations (cost, fabrication, and engineering) dictate a heterogeneous composition and density factor less than one for boron carbide. The heterogeneous arrangement considered for the inboard shield is given in Table 7-3. This arrangement is based on the study of Ref. 2 for similar shield compositions. The boron carbide density factor was varied from 0.7 to 1.0 in the heterogeneous arrangement, and the impact of this density variation on the shield performance was examined. Figures 7-11 through -17 display the key radiation response in the TF coils for a heterogeneous shield as a function of the boron carbide density factor. The heterogeneous arrangement for the shield reduces the dose in the insulators, neutron fluence in the TF coils, atomic displacement, and copper-induced resistivity by 26 to 52% relative to the equivalent homogeneous shield assuming a theoretical density for each material. However, the nuclear heating in the TF coils increases by a factor of two. Gamma heating causes the nuclear heating increase due to an increase in the (n,γ) reaction rate in the steel before the B_4C zone. A reduction in the boron carbide density factor increases the radiation response in the TF coils. At 0.7 density factor, all the design criteria are satisfied. The damage in the TF coils in terms of insulator dose, copper-induced resistivity, neutron fluence, or atomic displacement is almost doubled when the density factor of boron carbide is changed from 1.0 to 0.7. The corresponding increase in the nuclear heating is only 40%.

7.4.2 Outboard Shield

In addition to radiation protection of reactor components, the outboard shield was designed with the objective of meeting the dose equivalent requirement to allow for personnel access to the reactor building and reducing the cost of the shield system. Several shield options are considered with different combinations of shielding materials. Table 7-10 lists the shield dimensions and compositions for six options. The first three options consist of one basic shielding material, boron compound as a neutron absorber, and lead at the outermost surface of the shield to attenuate the decay gamma

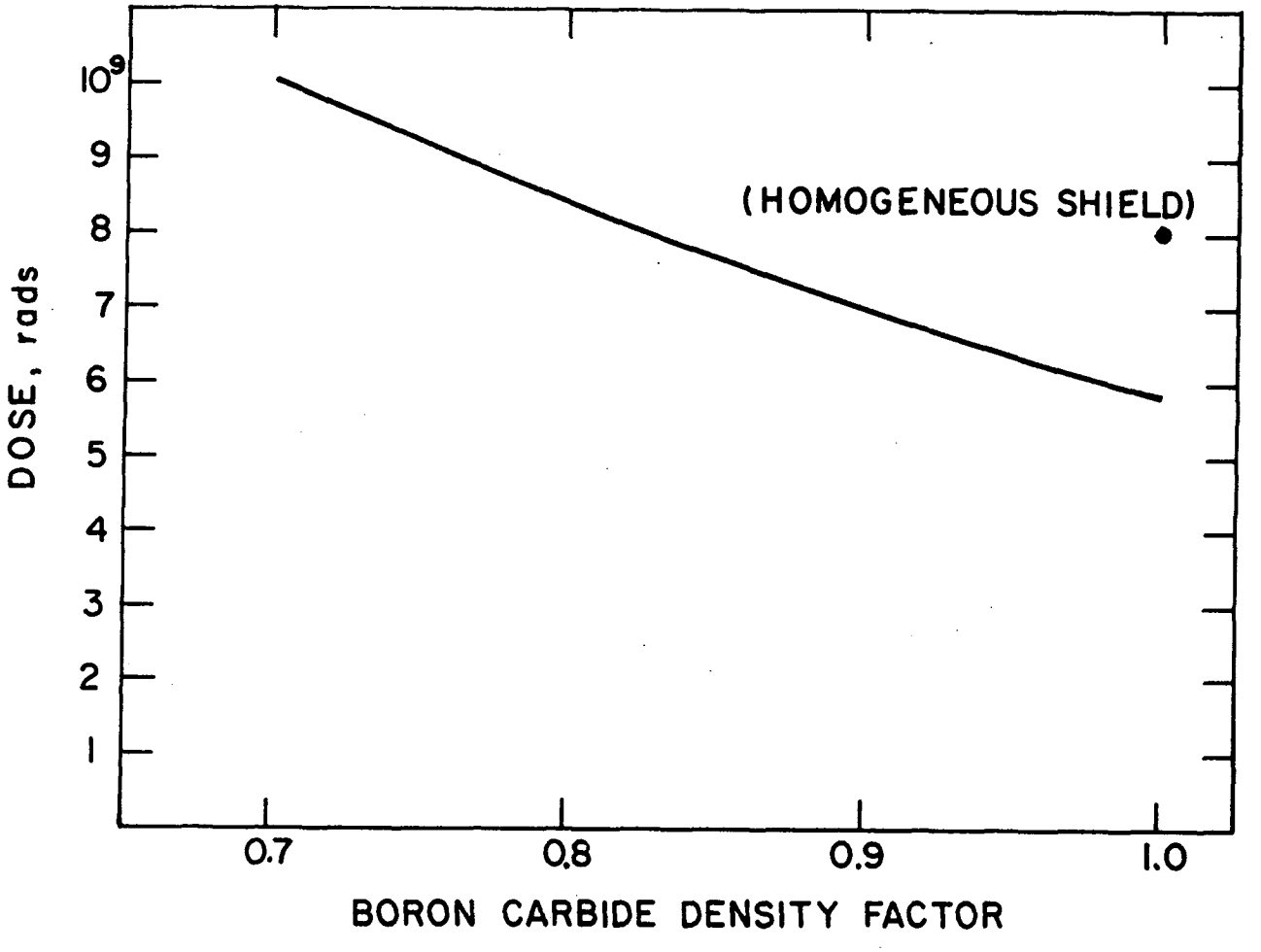

Figure 7-11. Maximum dose in the electrical insulator normalized to 21.2 $MW \cdot y/m^2$ integrated neutron wall loading at first wall as a function of the density factor of the B_4C zone in a heterogeneous analysis.

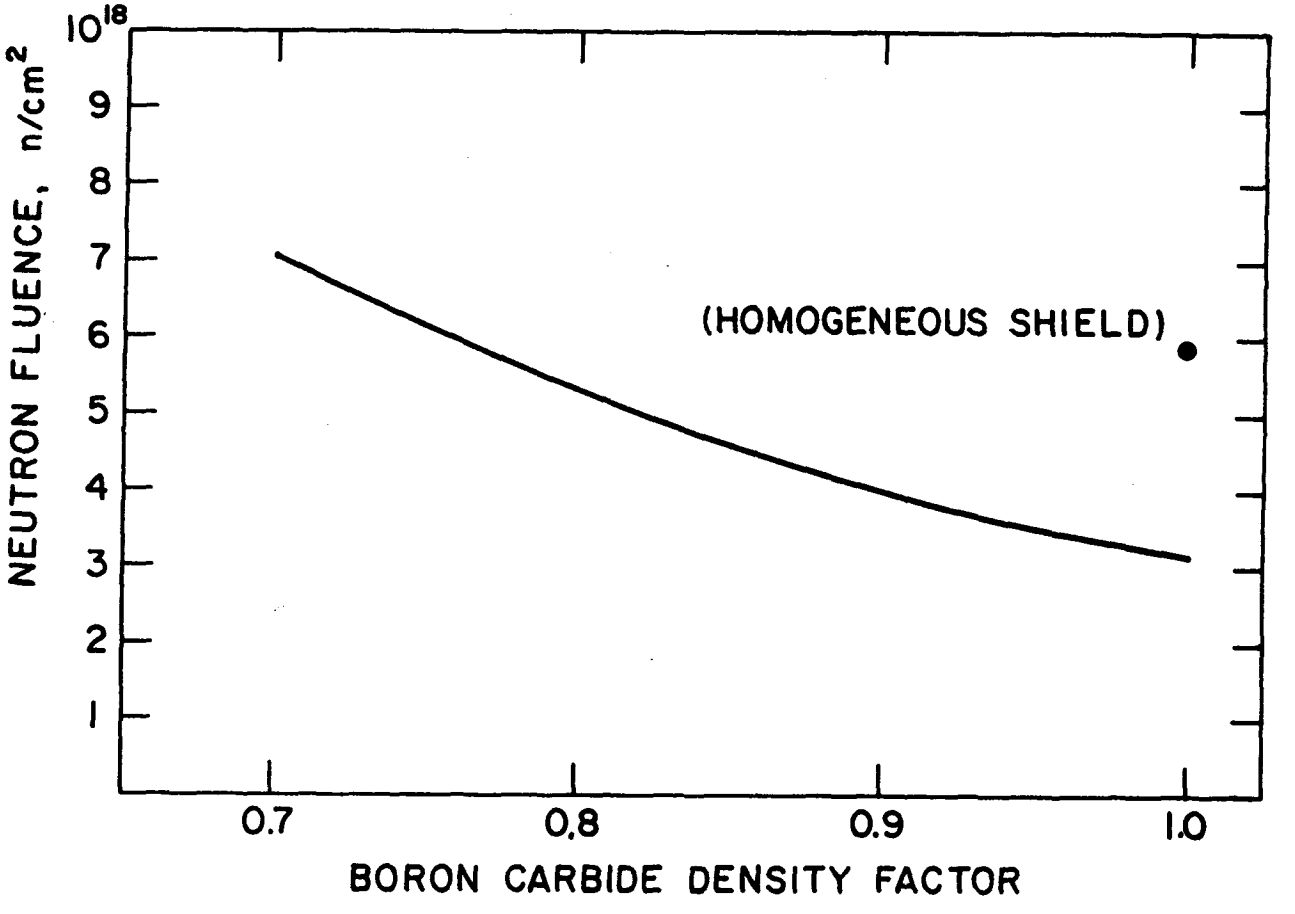

Figure 7-12. Maximum neutron fluence (E > 0.1 MeV) in the superconductor material normalized to 21.2 MW·y/m^2 integrated neutron wall loading at the first wall as a function of the density factor of the B_4C zone in a heterogeneous analysis.

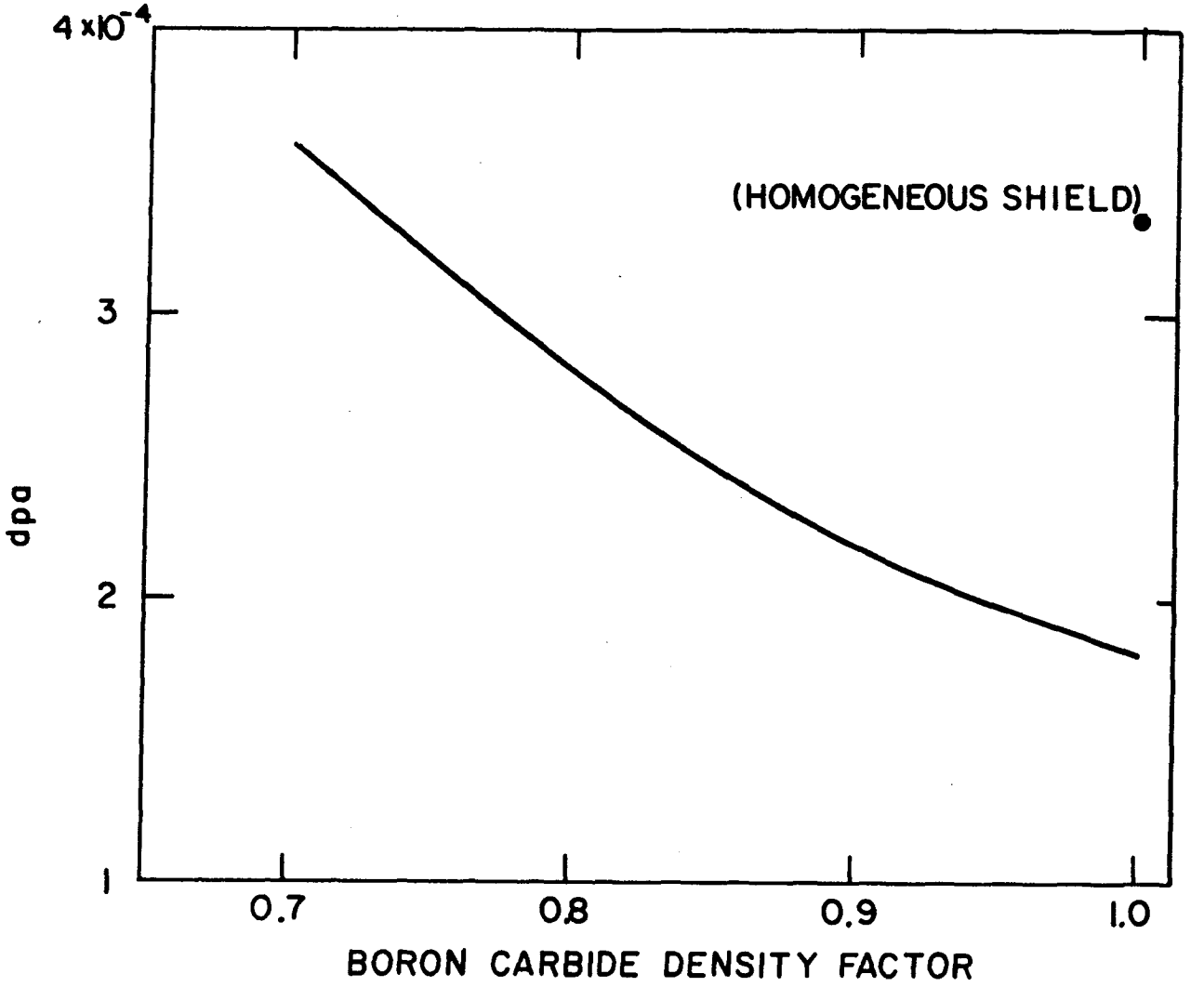

Figure 7-13. Maximum atomic displacement per atom in the copper stabilizer normalized to 21.2 MW·y/m^2 integrated neutron wall loading at the first wall as a function of the density factor of B_4C zone in a heterogeneous analysis.

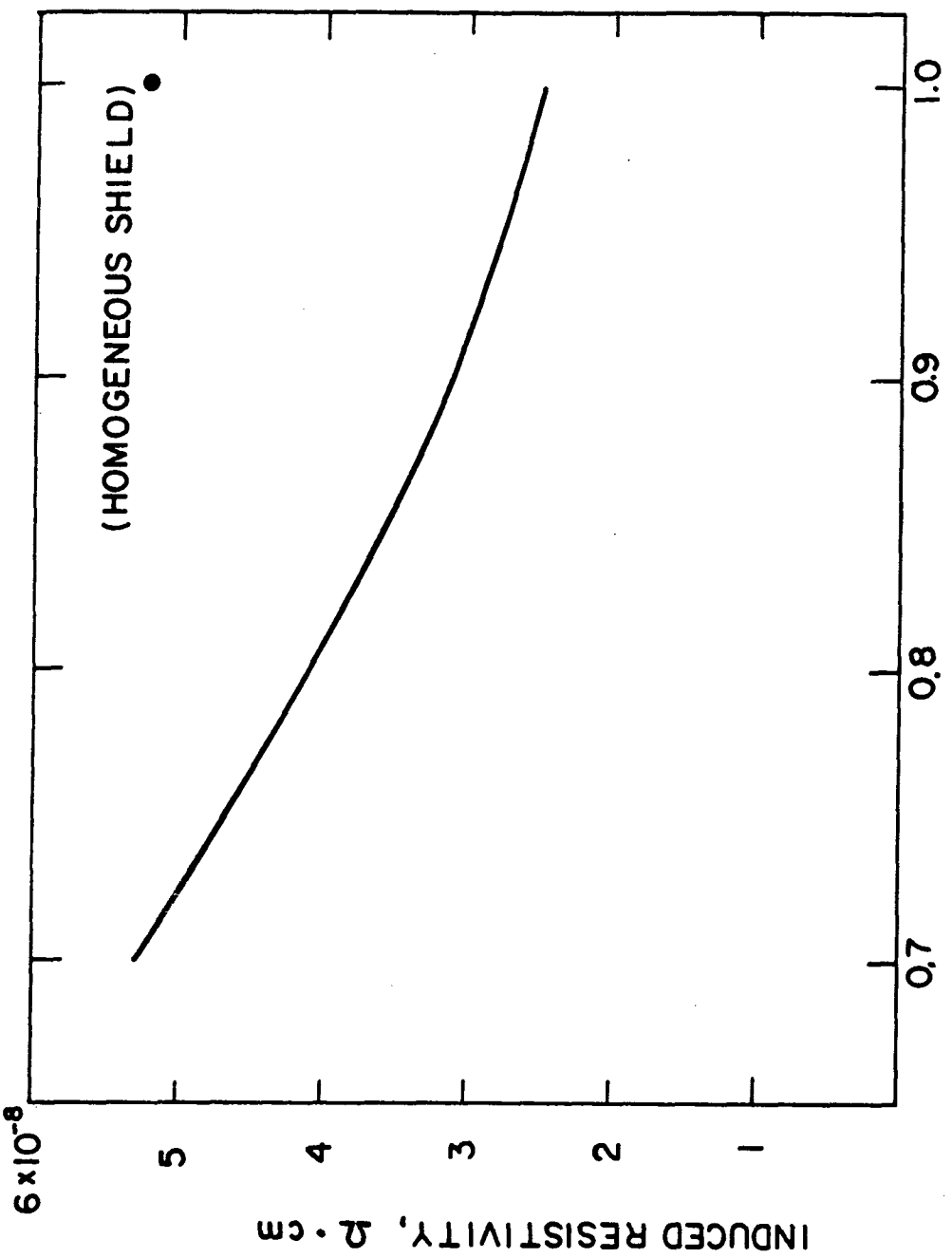

Figure 7-14. Maximum copper induced resistivity normalized to 21.2 $MW \cdot y/m^2$ integrated neutron wall loading at the first wall as a function of the density factor of the B_4C zone in a heterogeneous analysis.

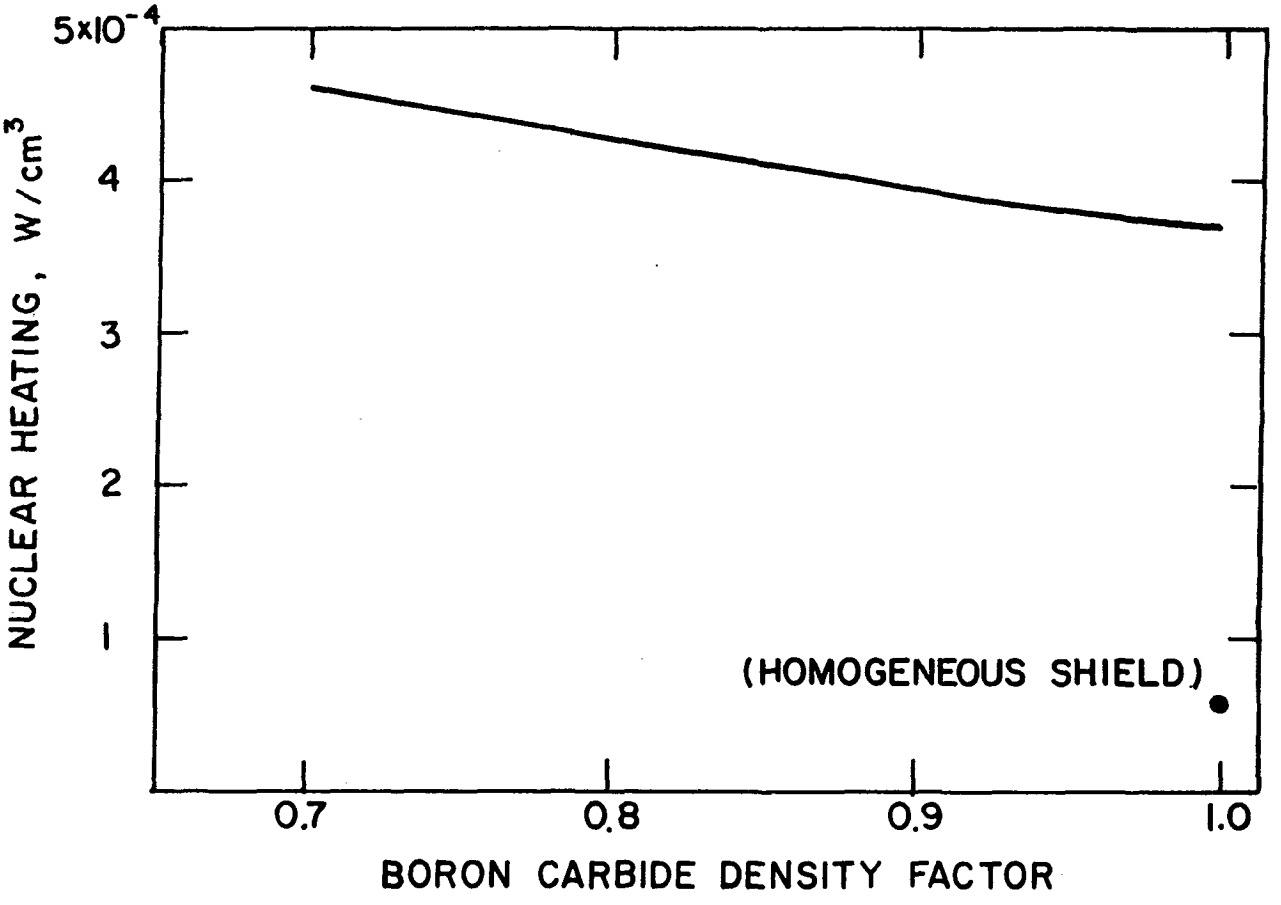

Figure 7-15. Maximum nuclear heating in the magnet case normalized to 2.12 MW/m^2 neutron wall loading at the first wall as a function of the density factor of the B_4C zone in a heterogeneous analysis.

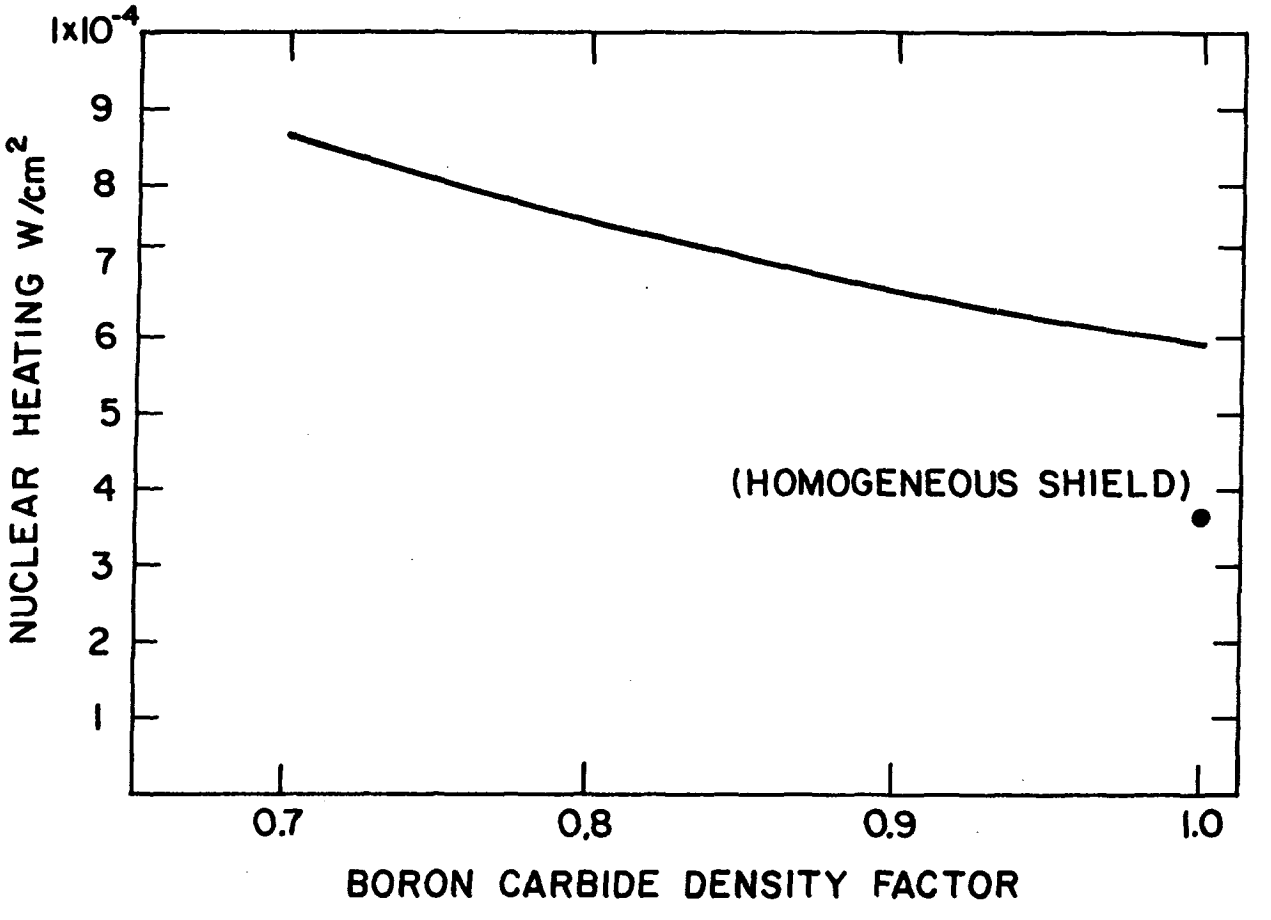

Figure 7-16. Maximum nuclear heating in the TF coils normalized to 2.12 MW/m^2 neutron wall loading at the first wall as a function of the density factor of the B_4C zone in a heterogeneous analysis.

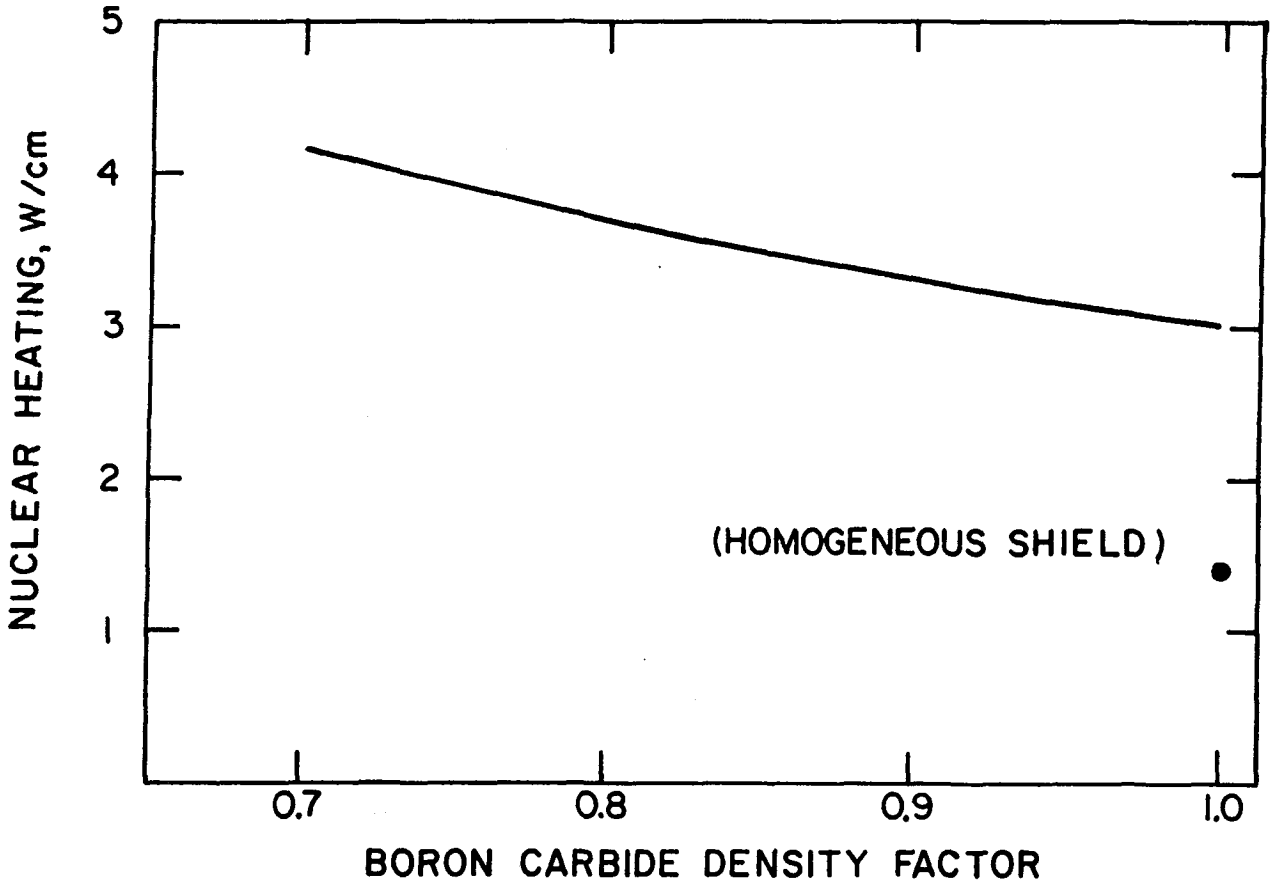

Figure 7-17. Maximum nuclear heating in the TF coils (including magnet case) per cm of the magnet length normalized to 2.12 MW/m^2 neutron wall loading at the first wall as a function of the density factor of the B_4C zone in a heterogeneous analysis.

Table 7-10. Outboard Shield Dimension and Composition for the Different Options

Option Number	Zone Thickness (cm)	Composition Percentage by Volume
1	2	100% Fe14Mn2Ni2Cr
	*	100% borated water
	2	100% Fe14Mn2Ni2Cr
	5	100% Pb
2	2	100% Fe14Mn2Ni2Cr
	*	100% ordinary concrete
	10	50% Fe14Mn2Ni2Cr + 50% B_4C
	5	100% Pb
3	2	100% Fe14Mn2Ni2Cr
	*	100% heavy concrete
	10	50% Fe14Mn2Ni2Cr + 50% B_4C
	5	100% Pb
4	2	100% Fe14Mn2Ni2Cr
	*	100% Fe14Mn2Ni2Cr
	10	50% Fe14Mn2Ni2Cr + 50% B_4C
	10	100% Pb
	*	100% ordinary concrete
	10	50% Fe14Mn2Ni2Cr + 50% B_4C
	5	100% Pb
5	2	100% Fe14Mn2Ni2Cr
	*	100% H_2O
	10	50% Fe14Mn2Ni2Cr + 50% B_4C
	10	100% Pb
	*	100% ordinary concrete
	10	50% Fe14Mn2Ni2Cr + 50% B_4C
	5	100% Pb
6	2	100% Fe14Mn2Ni2Cr
	*	100% H_2O
	5	50% Fe14Mn2Ni2Cr + 50% B_4C
	5	100% Pb

* Variable thickness in the analysis.

rays. Figure 7-18 gives the neutron flux as a function of the shield thickness for these three options. The thickness required for option 3 is about two thirds of that for option 2 to achieve the same flux level. The heavy concrete installed cost per cubic yard is about three times the ordinary concrete[23] which makes option 2 more attractive. If the total shield thickness is constrained, option 3 offers an attractive shield option from the cost point of view compared to the conventional steel-boron carbide shield. For 200 cm shield thickness, the borated water reduces the total neutron flux ($E > 0.1$ or 0.0 MeV) an order of magnitude less than the ordinary concrete. However, the attenuation performance is reversed with neutron energy above 7 MeV. For example, the 14 MeV neutron flux from the borated water shield is about a factor of two higher than the corresponding value from ordinary concrete. This difference in the attenuation of the high energy neutrons is a key factor for determining the required shield thickness based on the dose equivalent requirements and the radioactivity level in the reactor components outside the shield. The dose analysis will show later that option 1 will require more shield thickness than option 2 to satisfy the dose design criteria.

Nuclear heating at the surface of the ordinary concrete is 0.23 W/cm^3 which exceeds the 0.001 W/cm^3 design limit. As a result of this high heat load at the concrete surface, another shielding section before the concrete was considered. Options 4 and 5 shown in Table 7-10 have the first section of the shield designed to protect the concrete from excessive heating. Table 7-11 gives the maximum nuclear heating in the concrete as a function of the material and thickness in front of the concrete. The results show that a front shield thickness of 45 cm reduces the maximum nuclear heating in the ordinary concrete to $\sim$ 0.001 W/cm^3. The maximum nuclear heating is nearly the same whether Fe1422 or H_2O is used in the front section of the shield, but water is preferred from the cost and radioactivity point of view.

Based on the above analysis, options 1, 5, and 6 shown in Table 7-10 are the potential shields for the DEMO design. The analysis of these shield options was extended to determine the total shield thickness based on the dose equivalent analysis. Figure 7-19 shows the maximum dose in the reactor building one day after shutdown as a function of the total shield thickness. Option 5 requires a total material shield thickness of 197 cm (200 cm total physical thickness to account for 0.7 density factor of boron carbide) to

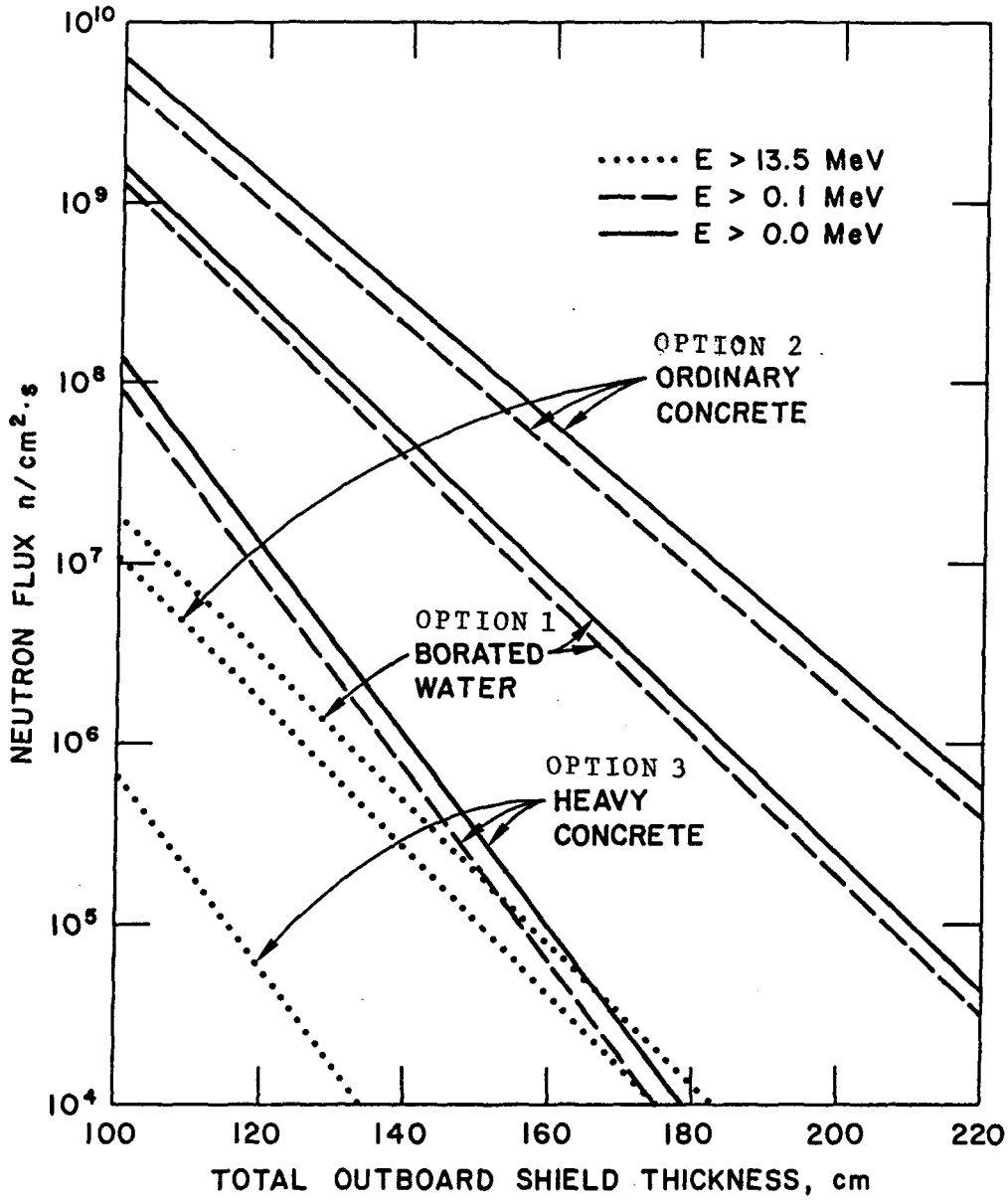

Figure 7-18. Neutron flux as a function of the outboard shield thickness for different shielding materials normalized to 2.12 MW/m^2 neutron wall loading at the first wall.

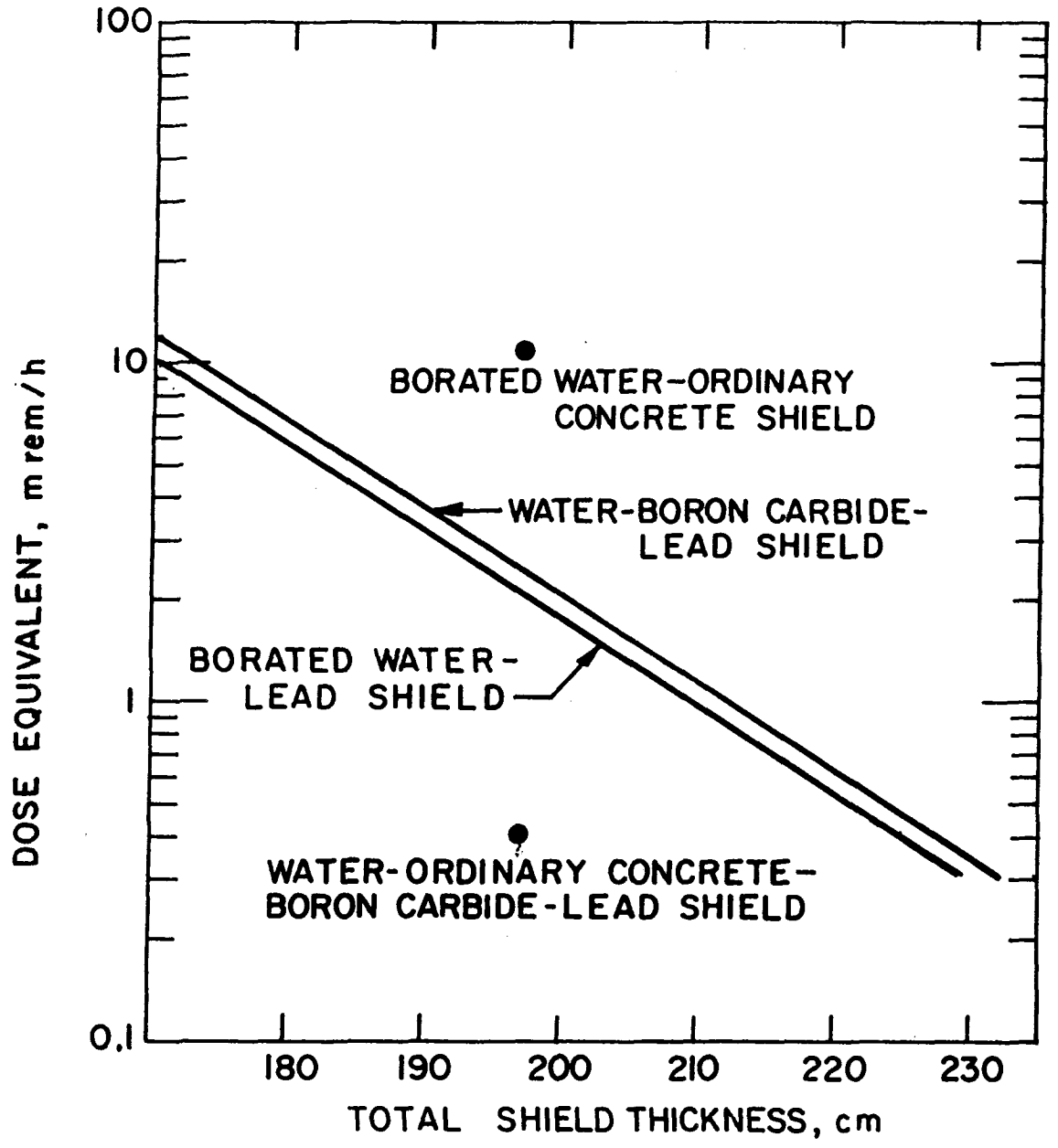

Figure 7-19. Maximum dose equivalent one day after shutdown in the reactor building as function of shield thickness.

Table 7-11. Maximum Nuclear Heating in the Concrete as a Function of the Front Shield Composition and Thickness

Front Shield Thickness (cm)				Nuclear Heating (W/cm^3)		
100% Fe1422	100% H_2O	50% Fe1422 50% B_4C	100% Pb	Total	Neutron	Gamma
0	0	0	0	2.302×10^{-1}	7.445×10^{-2}	1.558×10^{-1}
10	0	10	10	4.439×10^{-3}	2.607×10^{-3}	1.832×10^{-3}
15	0	10	10	2.591×10^{-3}	1.437×10^{-3}	1.154×10^{-3}
0	0	0	0	2.302×10^{-1}	7.445×10^{-2}	1.558×10^{-1}
0	10	10	10	4.317×10^{-3}	2.924×10^{-3}	1.393×10^{-3}
0	15	10	10	2.746×10^{-3}	1.851×10^{-3}	8.945×10^{-4}
0	25	10	10	1.156×10^{-3}	7.638×10^{-4}	3.922×10^{-4}

achieve 0.4 mrem/h one day after shutdown. For the same shield thickness, 45 cm of borated water followed by 150 cm of ordinary concrete increases the dose equivalent from 0.4 to 12.5 mrem/h one day after shutdown. This increase in the dose equivalent is due to the drastic change in the neutron spectrum at the outer surface of the shield as shown in Fig. 7-20. The neutron flux is roughly doubled for neutron energy above 2 MeV, while that below 0.1 MeV increases significantly. The increase in the low energy flux generates ^{51}Cr, ^{60}Co, and ^{56}Mn, through the (n,γ) reactions. Option 1 and 6 require 28 to 30 cm additional shield thickness to get the same dose level as option 6 (see Fig. 7-19). Figure 7-21 shows the neutron fluxes at the outer surface of the shield for option 1, 5, and 6. In comparison with option 1 and 5, the lower flux from option 5 for neutron with energy above 7 MeV reduces $^{58}Ni(n,p)^{58}Co$, $^{60}Ni(n,p)^{60}Co$, $^{54}Fe(n,p)^{54}Mn$, $^{56}Fe(n,p)^{56}Mn$, $^{55}Mn(n,2n)^{54}Mn$, $^{52}Cr(n,2n)^{51}Cr$, and $^{58}Ni(n,2n)^{57}Ni$ reactions rates; hence, option 6 has a lower activation and dose equivalent. In addition, the water has a large mean free path for the gamma rays; for example, the required thicknesses of water and ordinary concrete to reduce the 1.25 MeV gamma-ray flux by an order of magnitude are 34 and 16 cm, respectively. Table 7-12 gives the dose equivalent one day and one week from shutdown for the three shielding options at the back of the shield and the front surface of the outer leg of the TF coils.

7.4.3 Relativistic Electron Beam (REB) Duct Shield

A three-dimensional analysis was carried out to determine the radiation damage in the ceramic material of the REB duct. A three-dimensional model for a whole reactor was developed for the analysis. The model describes the plasma, first wall, tritium breeding blanket, blanket jacket and REB duct as shown in Figs. 7-22 through -24. The general-purpose Monte Carlo code MCNP[11] was used for the calculations with a continuous energy representation for the nuclear cross sections. The energy spectrum of the DT-neutrons was sampled in the calculations. Coupled neutron and neutron-induced photon transport during the operation was performed with the nuclear cross sections from ENDF/B-IV data files. The energy ranges were 2.2×10^{-8} to 15 MeV and 0.01 to 15 MeV for neutrons and 0.01 to 15 MeV for photons. The dimensions and compositions of the duct shield are given in Table 7-8. The outboard shield option was employed for the REB duct.

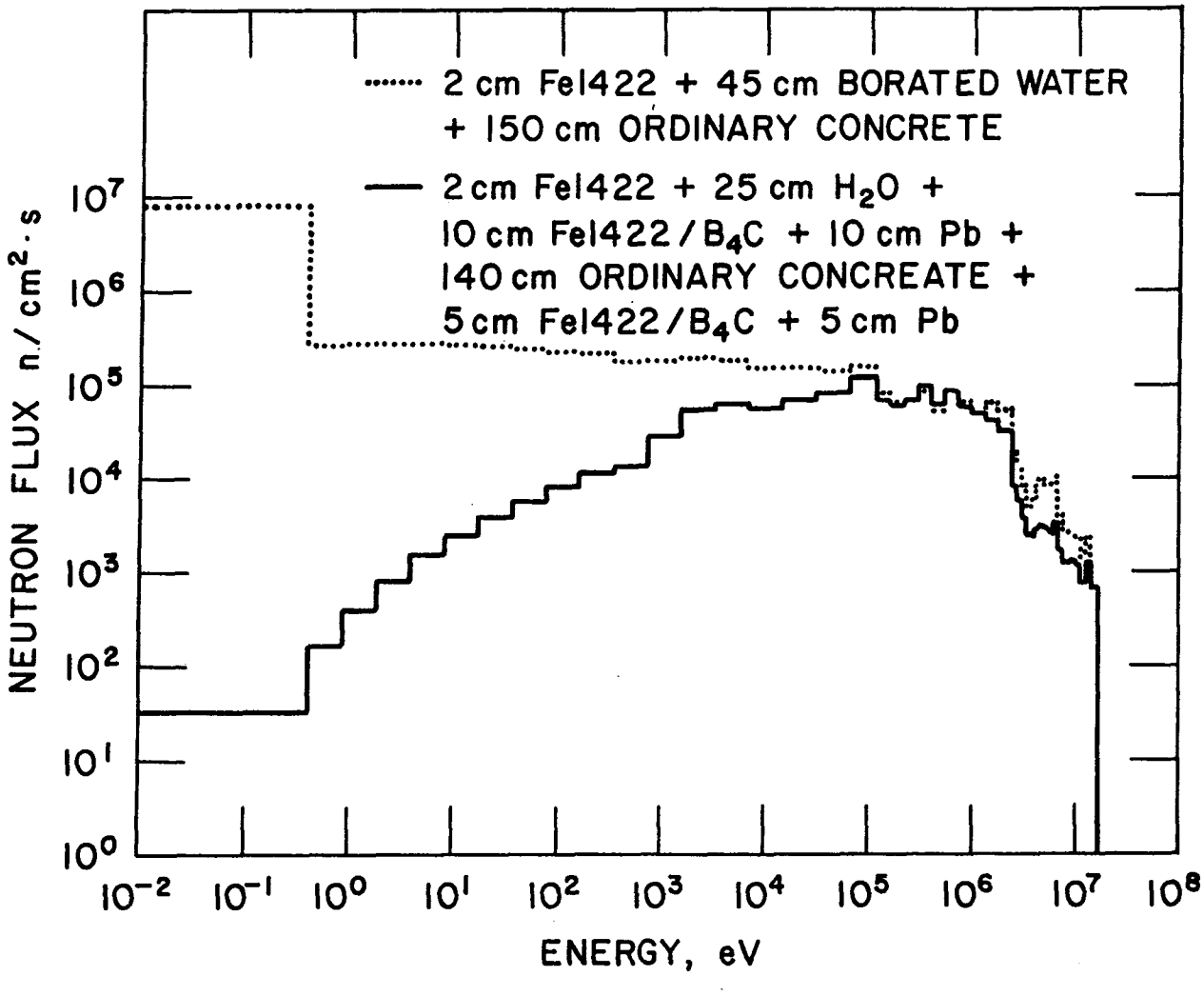

Figure 7-20. Neutron flux at the outer surface of the outboard shield.

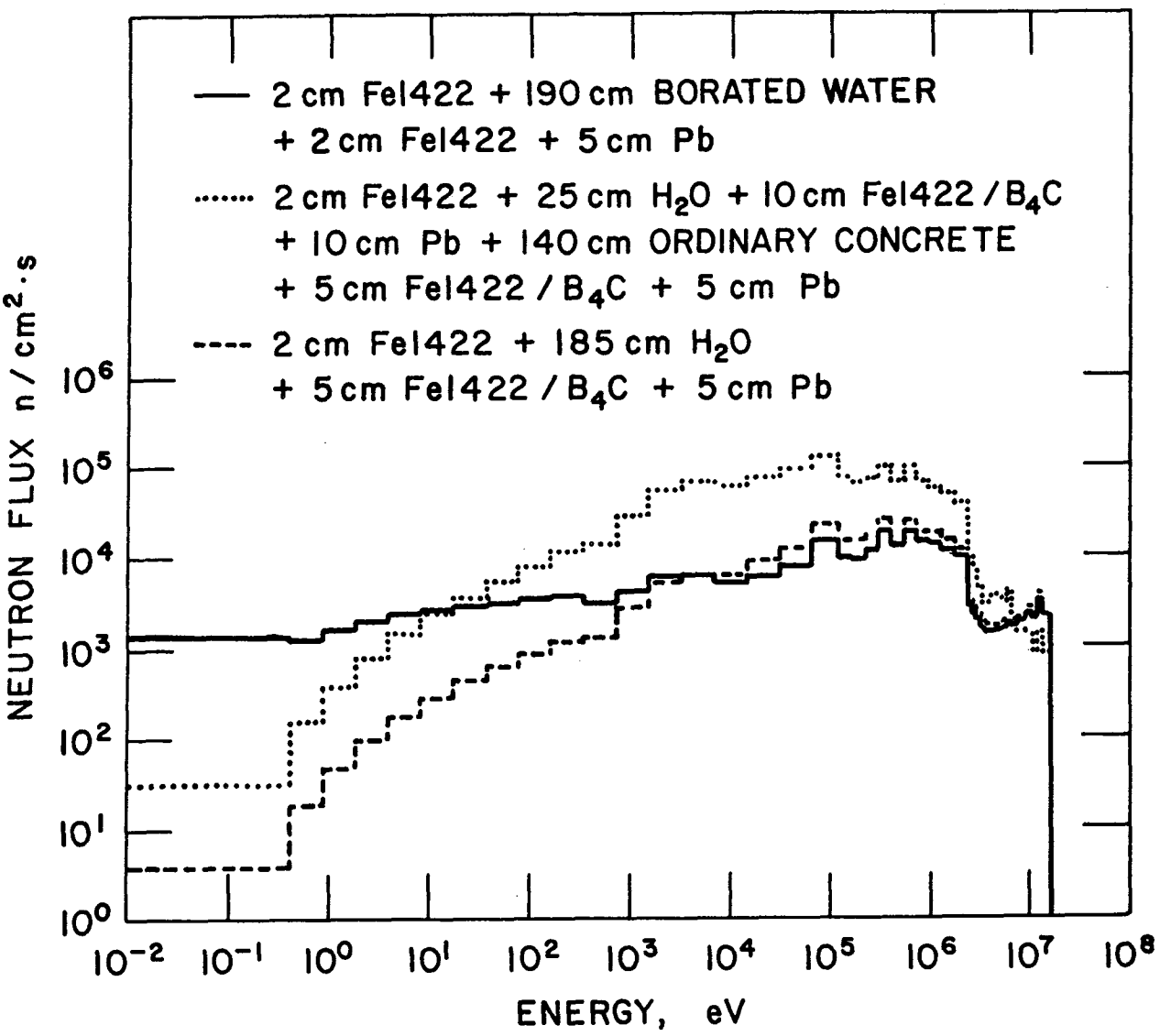

Figure 7-21. Neutron flux at the outer surface of the outboard shield.

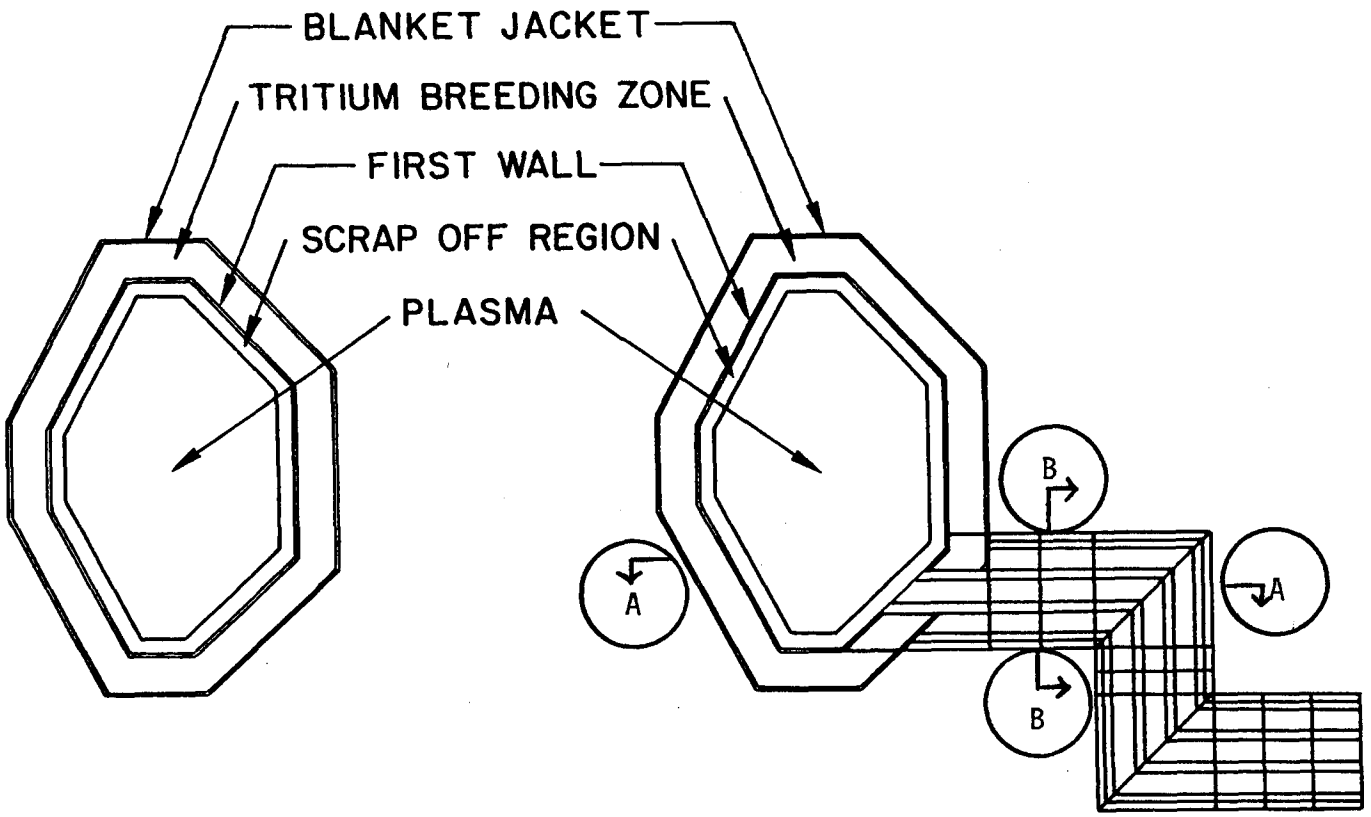

Figure 7-22. The three-dimensional geometrical model used for the REB duct analysis.

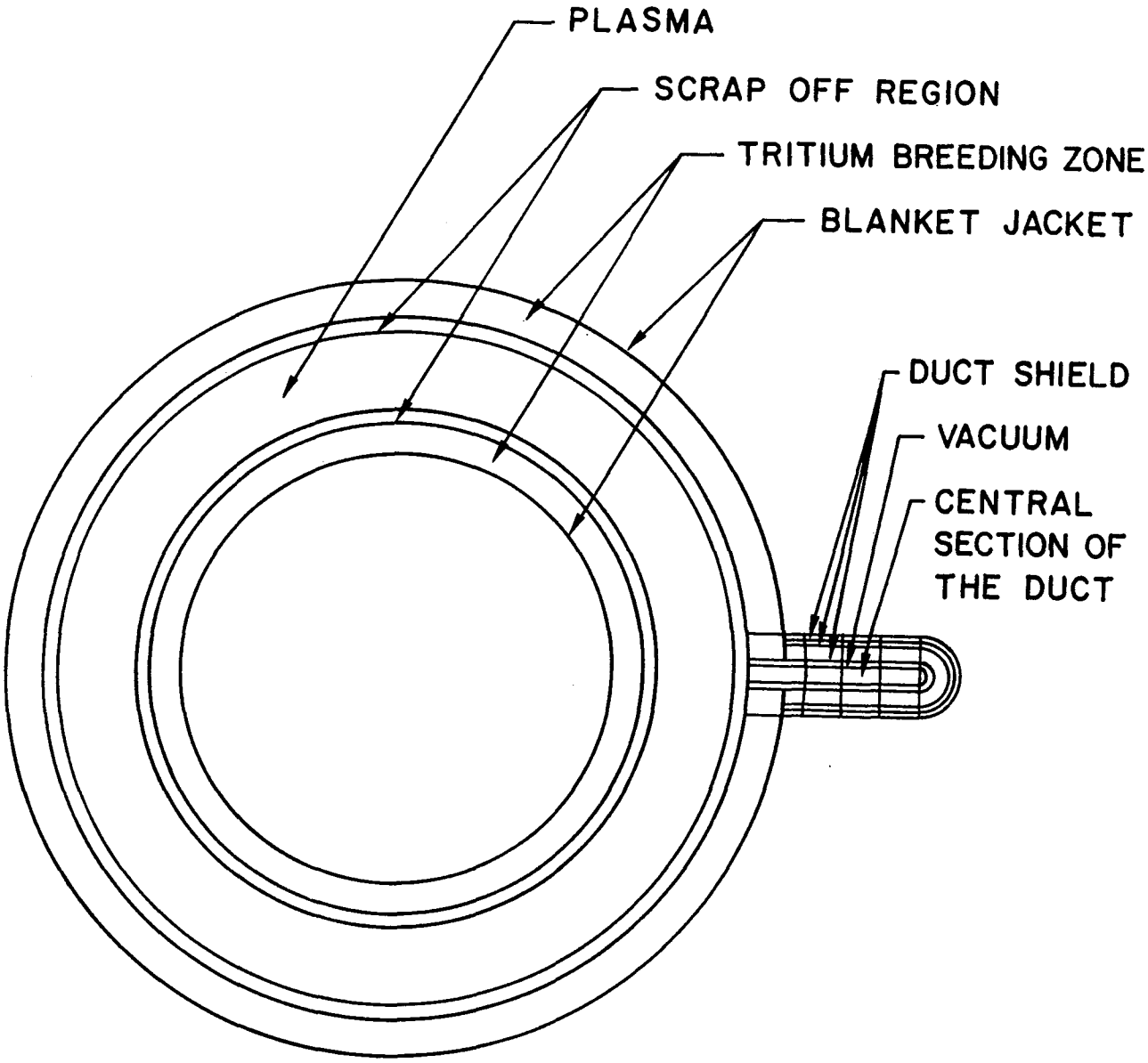

Figure 7-23. Section A-A of the geometrical model for the REB duct analysis.

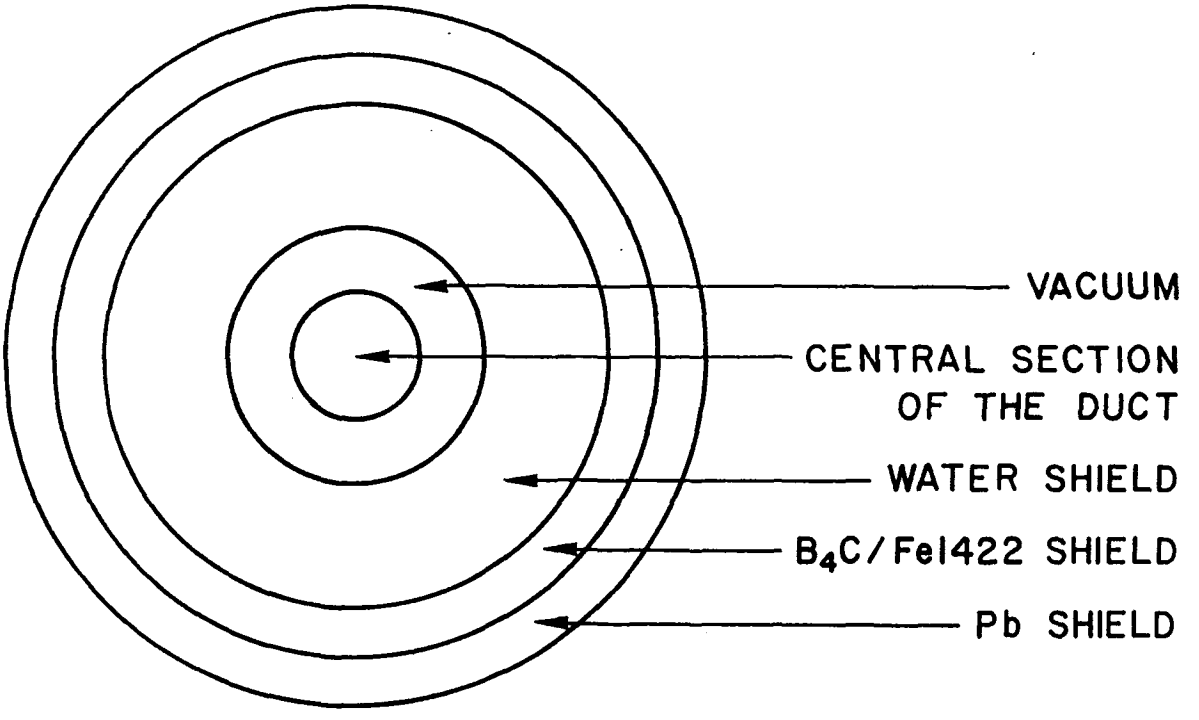

Figure 7-24. Section B-B of the geometrical model for the REB duct analysis.

Table 7-12. Maximum Dose Equivalent for Different Shielding Options After One Day and One Week from Shutdown at the Shield and TF Coils Surface in the Reactor Building

Shield Option Number	Total Shield Thickness (cm)	Dose After Shutdown (mrem/hr)			
		1 day		1 week	
		Shield Surface	TF Coils Surface	Shield Surface	TF Coils Surface
1	179	6.16	5.64	3.75	3.93
1	189	3.36	2.92	1.89	1.87
1	199	1.87	1.57	0.97	0.91
5	197	0.27	0.41	0.23	0.36
6	177	6.99	6.37	3.83	4.18
6	187	3.85	3.33	1.91	1.96
6	197	2.17	1.80	0.98	0.95

The transport calculation was performed in two steps, using the same geometrical model with a special updated version of MCNP.[22] First, a calculation was performed using a neutron source from the DT plasma and the whole geometry to generate a surface source for the REB duct. During the calculation, each time a particle crosses one of the designated surfaces for which the surface source is required, the spatial coordinates, direction cosines, energy, time, weight, particle type, history number, surface number, and cell number are written in a file. The surface source was located at the first wall surrounding the entrance of the REB duct as shown in Fig. 7-25. Next, the surface source was used to calculate the radiation damage parameters in the REB duct. With this method, the duct problem can be rerun for slightly different materials, geometry or other variance reduction techniques without having to rerun the whole problem.

The REB annular duct has a 13 cm inner radius and 26 cm outer radius. The first run started 320000 DT source neutrons, producing 9464 neutrons and photons on the surface source. The second run used a splitting factor of 43, which started 320264 particle histories. The radiation damage results were calculated for three ceramic materials (Al_2O_3, MgO, and SiO_2) in each zone of

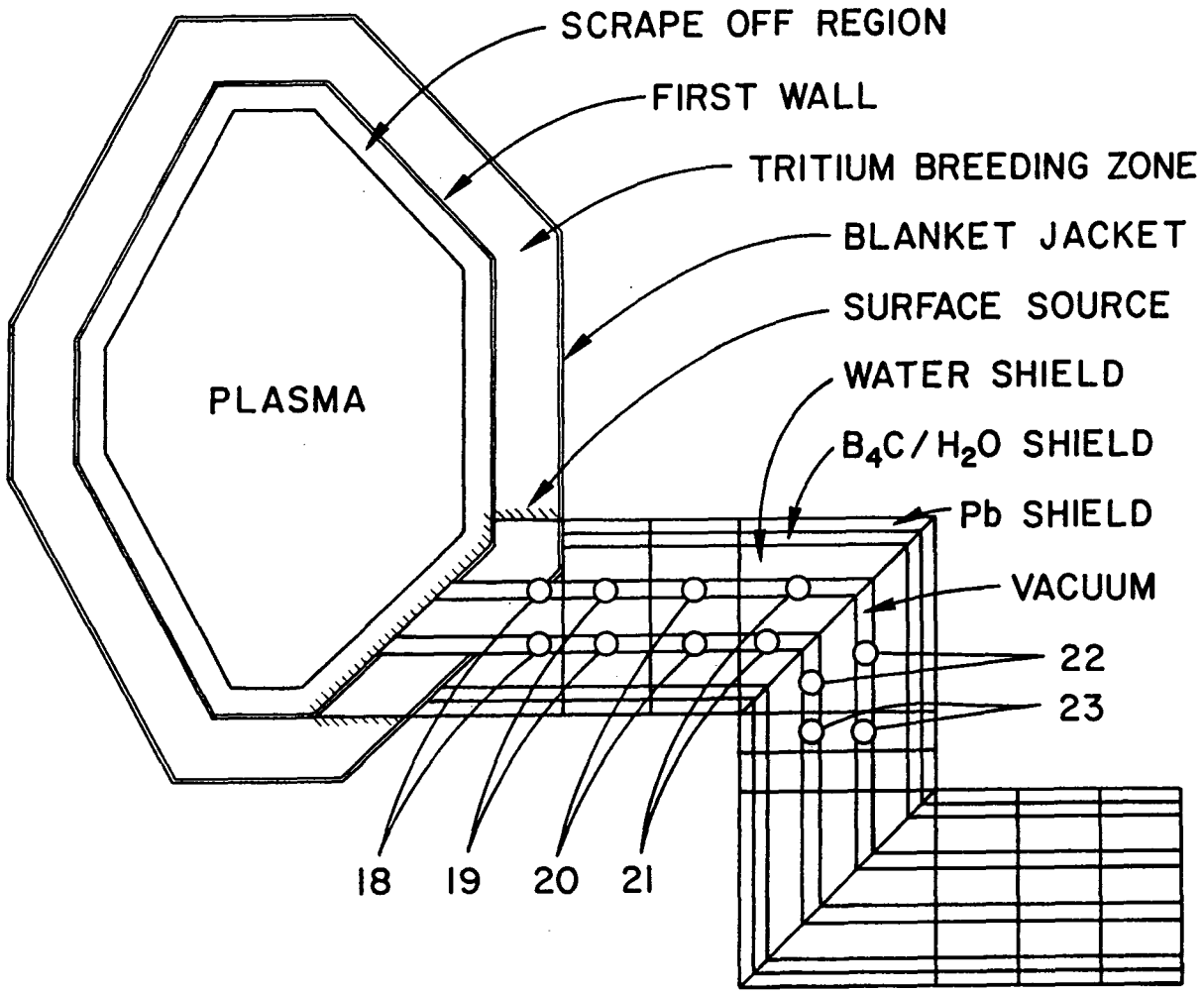

Figure 7-25. REB duct segments for the radiation response calculation in the ceramic materials.

Table 7-13. Nuclear Heating in the REB Duct Ceramic Materials in the Different Zones

Zone Number[a]	Neutron Heating (W/cm^3)	Fractional Standard Deviation	Gamma Heating (W/cm^3)	Fractional Standard Deviation	Total Nuclear Heating (W/cm^3)
A. Al_2O_3					
18	3.61	0.06	2.15	0.05	6.02
19	7.66×10^{-2}	0.09	2.57×10^{-1}	0.07	2.28×10^{-1}
20	1.61×10^{-2}	0.13	5.46×10^{-2}	0.13	6.12×10^{-2}
21	1.27×10^{-2}	0.18	2.82×10^{-2}	0.21	3.68×10^{-2}
22	2.61×10^{-3}	0.23	6.35×10^{-3}	0.26	7.86×10^{-3}
23	5.45×10^{-6}	0.59	3.34×10^{-4}	0.86	2.70×10^{-4}
B. MgO					
18	4.55	0.06	1.47	0.05	6.02
19	1.10×10^{-1}	0.08	1.76×10^{-1}	0.07	2.28×10^{-1}
20	2.39×10^{-2}	0.12	3.73×10^{-2}	0.13	6.12×10^{-2}
21	1.76×10^{-2}	0.17	1.92×10^{-2}	0.21	3.68×10^{-2}
22	3.52×10^{-3}	0.23	4.34×10^{-3}	0.26	7.86×10^{-3}
23	4.22×10^{-5}	0.50	2.28×10^{-4}	0.86	2.70×10^{-4}
C. SiO_2					
18	2.25	0.06	0.96	0.05	3.21
19	5.48×10^{-2}	0.08	1.15×10^{-1}	0.07	1.70×10^{-1}
20	1.18×10^{-2}	0.13	2.45×10^{-2}	0.13	3.62×10^{-2}
21	8.68×10^{-3}	0.17	1.26×10^{-2}	0.22	2.13×10^{-2}
22	1.76×10^{-3}	0.23	2.85×10^{-3}	0.26	4.60×10^{-3}
23	1.81×10^{-5}	0.59	1.50×10^{-4}	0.86	1.68×10^{-4}

[a] See Figure 7-25.

the duct shown in Fig. 7-25. Table 7-13 gives the nuclear heating and the fractional standard deviation in each zone. The total dose and neutron fluence at 21.2 MW•y/m^2 integrated neutron wall loading at the first wall are given in Table 7-14. The results show a neutron fluence of ~ 3 x 10^{17} n/cm^2 (E > 0.1 MeV) or total dose of ~ 10^{10} rads after the first bend of the REB duct. Such dose level is not expected to cause any significant damage to the insulator.[7,12]

Table 7-14. Total Dose in the REB Duct Ceramic Material and the Neutron Fluence (E_n > 0.1 MeV) in Each Zone From 21.2 MW•y/m^2 Integrated Neutron Wall at the First Wall

Zone Number	Total Dose (rads)			Neutron Fluence (n/cm^2)
	Al_2O_3	MgO	SiO_2	
18	1.82 x 10^{14}	1.90 x 10^{14}	1.01 x 10^{14}	2.85 x 10^{22}
19	1.06 x 10^{13}	7.20 x 10^{12}	5.38 x 10^{12}	1.76 x 10^{21}
20	2.24 x 10^{12}	1.94 x 10^{12}	1.15 x 10^{12}	3.23 x 10^{20}
21	1.29 x 10^{12}	1.17 x 10^{12}	6.74 x 10^{11}	1.99 x 10^{20}
22	2.83 x 10^{11}	2.49 x 10^{11}	1.46 x 10^{11}	3.47 x 10^{19}
23	1.07 x 10^{10}	8.53 x 10^{9}	5.31 x 10^{9}	2.96 x 10^{17}

7.5 Activation and Decay Afterheat

Activation analysis for shielding options 1, 5, and 6 with the breeding blanket described in Table 7-2 was performed to compare radioactivity concentration, afterheat, and biological hazard potential for the main reactor components. The material compositions including the impurities listed in Table 7-3 are considered. The dimensions for the reference shield design (option 5) are given in Table 7-5. The dimensions of the other two shielding options are taken from Table 7-10, with a 190- and 185-cm water zone thickness for option 1 and 6, respectively. The total shielding thickness is about the same for these options.

The results in Fig. 7-26 show that the radioactivity generated in the first wall, blanket and shield reach as a saturation value of 1.9 Ci/W_{th} after

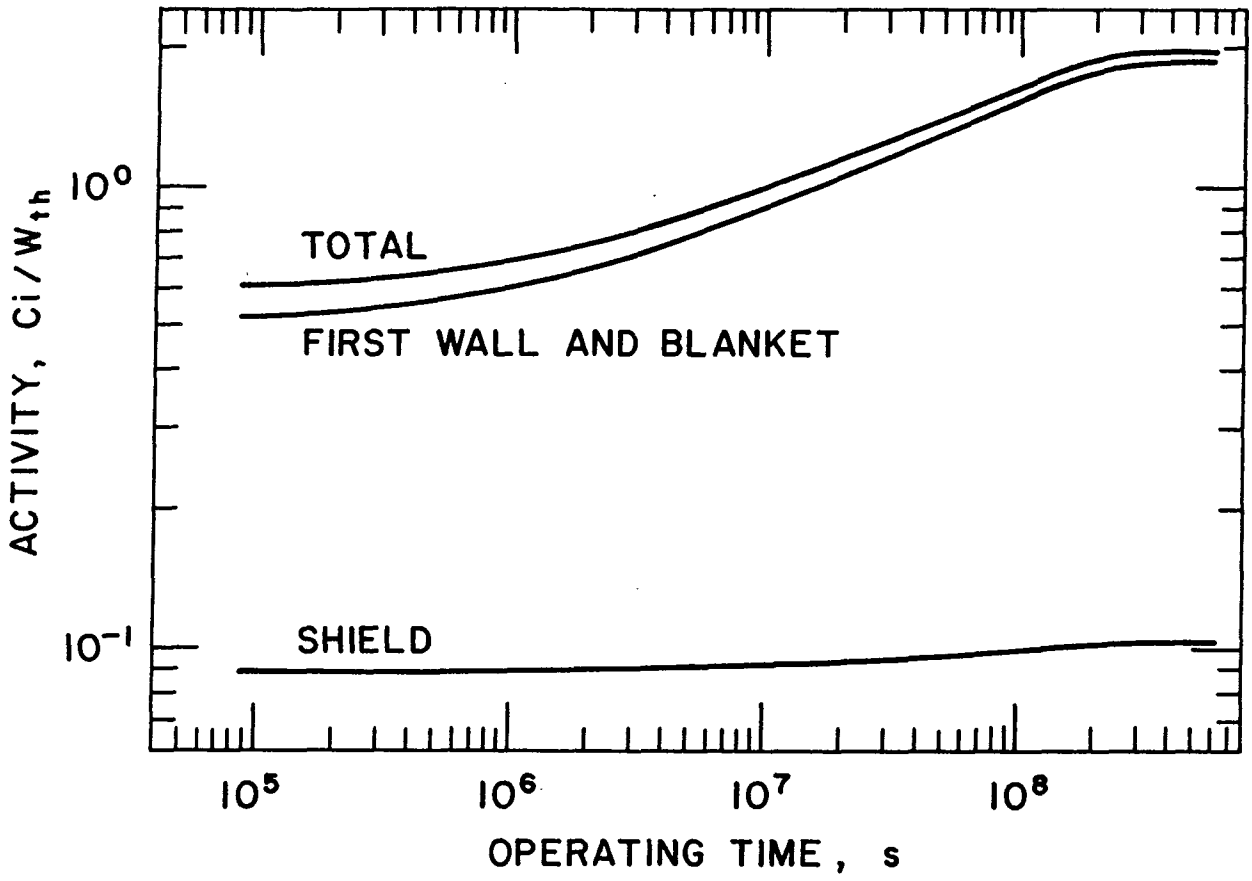

Figure 7-26. Radioactivity as a function of operating time.

10 years of operation with 2.12-MW/m^2 neutron wall loading. However, 50% of the saturation value is reached after 4 months of operation with 0.67-MW•y/m^2 integrated neutron wall loading. The production rate of ^{55}Fe is causing the slow saturation. Figures 7-27 and 7-28 show the afterheat and biological hazard potential during operation, respectively. The first wall and blanket are responsible for more than 96% of the afterheat, biological hazard potential, and radioactivity inventory as shown in Figs. 7-26 through 7-28. At shutdown, the radioactivity concentration in the first wall is 218 Ci/cm^3, compared to 9 Ci/cm^3 in the shield jacket. However, the radioactivity in the shield defines the dose equivalent in the reactor building after shutdown. The individual contribution of the different radioactive isotopes to the total inventory vary significantly with the time after shutdown. In the first wall and blanket, ^{55}Fe, ^{58}Co, ^{51}Cr, ^{54}Mn, ^{57}Co, and ^{60}Co generated from the PCA steel are responsible for more than 98% of the total radioactivity one day after shutdown. Ten years after shutdown, the first wall and blanket radioactivity are dominated by ^{55}Fe (2-7 years half-life, electron capture decay) and ^{60}Co (5.27 years half-life, β and α decay) generated from nickel isotopes. From 10 to 100 years after shutdown, the long half-life isotopes start to dominate the radioactivity concentration. At 100 years after shutdown ^{63}Ni (100 years half-life, β decay) and ^{93}Nb (13.6 years half-life, electron capture decay) generated from nickel and molybdenum isotopes are causing more than 99.6% of the total activity. Nickel and molybdenum are essential for the PCA steel alloy. Eliminating such long-term radioactivity by replacing or isotopic tailoring of the nickel and molybdenum elements[1,4] reduces the radioactivity concentration by three orders of magnitude.

Tables 7-15 through 7-17 give the activation parameters as a function of the time after shutdown in the different zones for each shielding option. The neutron fluxes at the outermost surface of the shield for these options are shown in Fig. 7-21. The use of borated water reduces the activation parameter in the shield jacket by a factor of two relative to the water. Option 5 generates less ^{58}Co, ^{58}Mn, and ^{57}Cu isotopes, which are responsible for the decay gamma rays after shutdown. The neutrons with energy above 7 MeV cause most of the (n,2n), (n,p), (n,d), (n,t), and (n,α) reactions in the shield materials producing such isotopes. Option 5 has low neutron flux with energy above 7 MeV relative to the other options, as shown in Fig. 7-21. This has impact on the dose equivalent after shutdown; option 5 reduces the dose

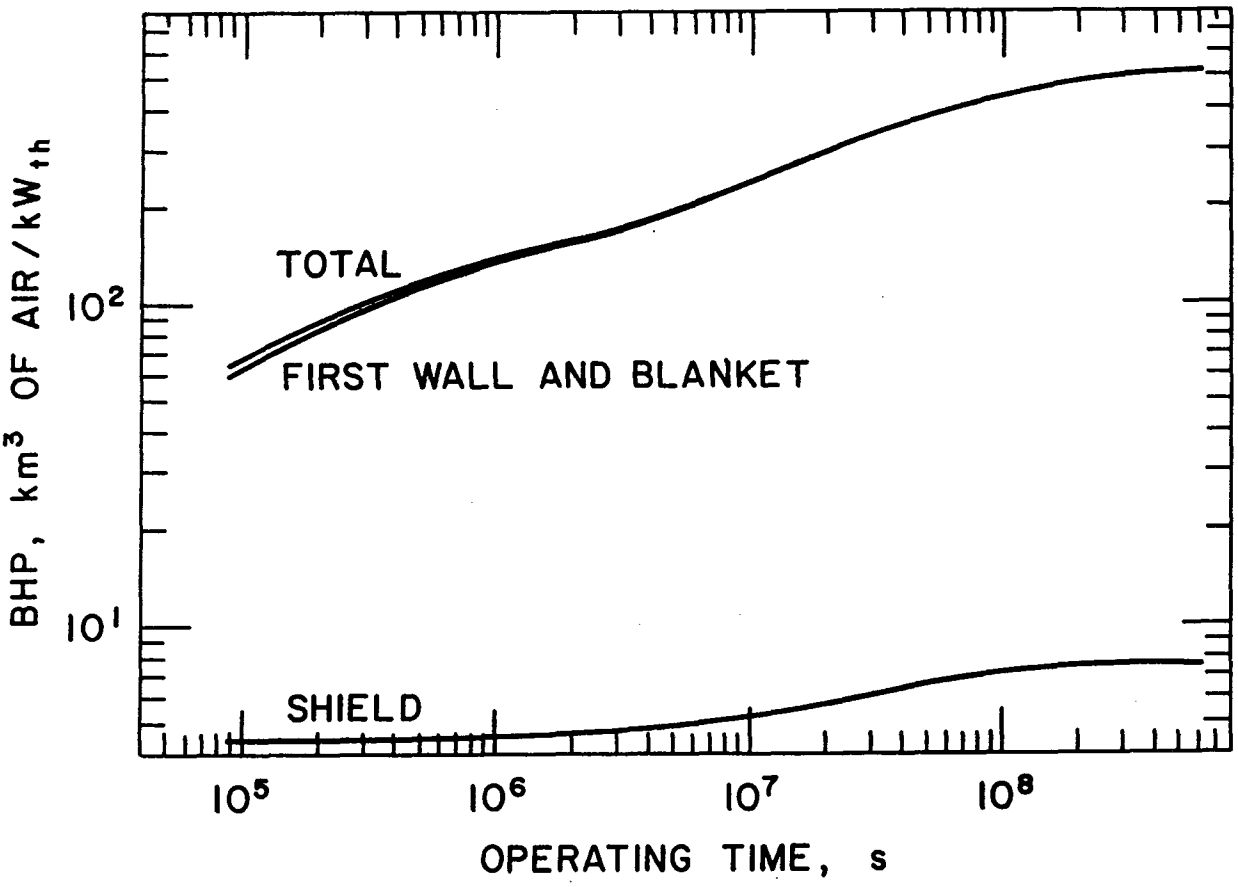

Figure 7-27. Biological hazard potential as a function of operating time.

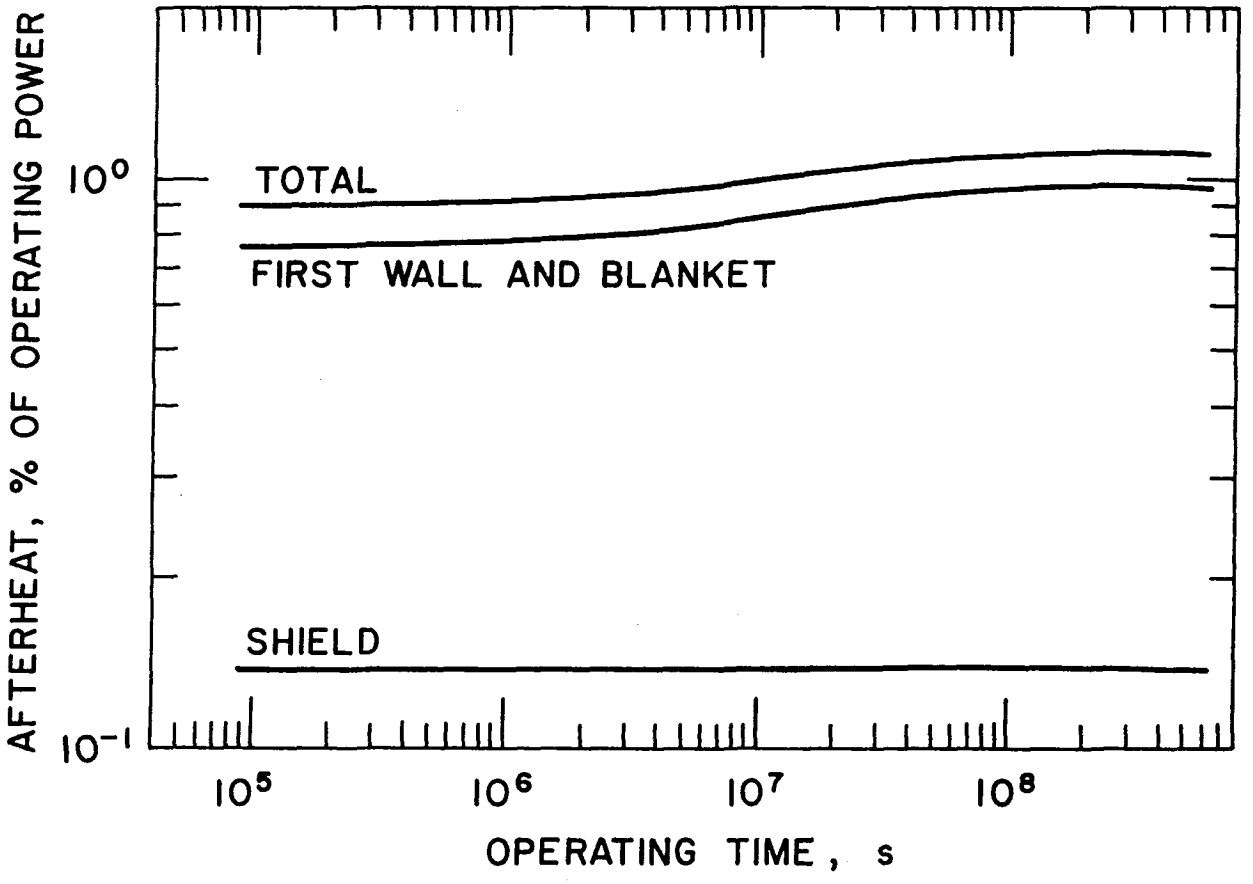

Figure 7-28. Afterheat as a function of operating time.

Table 7-15. Activation Parameters Per Zone for the Reference Outboard Shield

Zone Composition Percentage By Volume	Zone Thickness (cm)	Time After Shutdown at the End of Operating Life				
		0	1y	10y	100y	1000y
		A. Radioactivity Ci/cm^3				
First Wall/Blanket	50	7.16	3.14	2.98×10^{-1}	3.24×10^{-3}	5.03×10^{-4}
100% Fe1422	2	8.98	8.62×10^{-1}	7.80×10^{-2}	3.79×10^{-3}	3.92×10^{-5}
100% H_2O	25	6.79×10^{-3}				
42% Fe1422, 58% B_4C[a]	12	2.03×10^{-2}	7.41×10^{-3}	5.15×10^{-4}	5.26×10^{-7}	2.61×10^{-8}
100% Pb	10	3.03×10^{-4}	2.27×10^{-7}	4.92×10^{-8}	2.34×10^{-9}	2.34×10^{-9}
100% Ordinary Concrete	140	5.24×10^{-5}	2.71×10^{-6}	2.42×10^{-6}	1.22×10^{-6}	3.34×10^{-9}
42% Fe1422, 58% B_4C[a]	6	1.45×10^{-7}	8.12×10^{-9}	7.37×10^{-10}	4.37×10^{-11}	5.09×10^{-13}
100% Pb	5	2.14×10^{-10}	7.22×10^{-13}	1.53×10^{-13}	1.67×10^{-15}	1.67×10^{-15}
100% PCA Steel, Magnet Case	15	1.02×10^{-8}	5.87×10^{-10}	9.15×10^{-11}	3.67×10^{-11}	1.35×10^{-11}
		B. Radioactivity Ci/W_{th}				
First Wall/Blanket	50	1.84	7.65×10^{-1}	7.26×10^{-2}	7.89×10^{-4}	1.22×10^{-4}
100% Fe1422	2	1.01×10^{-1}	9.73×10^{-3}	8.80×10^{-4}	4.27×10^{-5}	4.42×10^{-7}
100% H_2O	25	1.02×10^{-3}				
42% Fe1422, 58% B_4C[a]	12	1.32×10^{-3}	4.82×10^{-4}	3.35×10^{-5}	3.42×10^{-8}	1.70×10^{-9}
100% Pb	10	2.05×10^{-5}	1.54×10^{-8}	3.33×10^{-9}	1.59×10^{-10}	1.59×10^{-10}
100% Ordinary Concrete	140	6.50×10^{-5}	3.37×10^{-6}	3.01×10^{-6}	1.52×10^{-6}	4.15×10^{-10}
42% Fe1422, 58% B_4C[a]	6	7.87×10^{-9}	4.42×10^{-10}	4.01×10^{-11}	2.38×10^{-12}	2.77×10^{-14}
100% Pb	5	1.18×10^{-11}	3.98×10^{-14}	8.45×10^{-15}	9.20×10^{-17}	9.20×10^{-17}
100% PCA Steel, Magnet Case	15	2.57×10^{-9}	1.49×10^{-10}	2.32×10^{-11}	9.29×10^{-12}	3.41×10^{-12}

Table 7-15. (Continued)

Zone Composition Percentage By Volume	Zone Thickness (cm)	Time After Shutdown at the End of Operating Life				
		0	1y	10y	100y	1000y
		C. Afterheat (% of Operating Power)				
First Wall/Blanket	50	9.79×10^{-1}	1.11×10^{-1}	2.01×10^{-2}	9.64×10^{-6}	1.76×10^{-6}
100% Fe1422	2	1.31×10^{-1}	8.44×10^{-4}	4.39×10^{-5}	5.26×10^{-7}	2.29×10^{-8}
100% H_2O	25	5.57×10^{-3}				
42% Fe1422, 58% B_4C[a]	12	1.11×10^{-3}	7.74×10^{-5}	2.65×10^{-6}	4.86×10^{-10}	9.02×10^{-11}
100% Pb	10	1.49×10^{-9}	3.26×10^{-13}	6.77×10^{-14}	1.75×10^{-20}	
100% Ordinary Concrete	140	1.06×10^{-8}	1.24×10^{-11}	5.75×10^{-12}	1.84×10^{-12}	4.87×10^{-14}
42% Fe1422, 58% B_4C[a]	6	1.08×10^{-9}	4.18×10^{-11}	1.98×10^{-12}	2.93×10^{-14}	1.39×10^{-15}
100% Pb	5	8.40×10^{-12}	8.49×10^{-15}	1.79×10^{-15}	4.60×10^{-22}	
100% PCA Steel, Magnet Case	15	2.78×10^{9}	2.77×10^{-11}	3.84×10^{-12}	1.06×10^{-13}	4.01×10^{-14}
		D. Biological Hazard Potential (km^3 air/kW_{th})				
First Wall/Blanket	50	5.14×10^{2}	2.11×10^{2}	4.06×10^{1}	3.10×10^{-1}	1.57×10^{-2}
100% Fe1422	2	7.17	1.32	8.98×10^{-2}	2.12×10^{-2}	3.58×10^{-5}
100% H_2O	25	3.40×10^{-2}				
42% Fe1422, 58% B_4C[a]	12	3.41×10^{-1}	1.39×10^{-1}	3.93×10^{-3}	2.06×10^{-5}	4.33×10^{-5}
100% Pb	10	4.50×10^{-4}	1.80×10^{-5}	5.11×10^{-6}	1.59×10^{-6}	1.59×10^{-6}
100% Ordinary Concrete	140	4.33×10^{-3}	1.78×10^{-3}	1.54×10^{-3}	7.57×10^{-4}	9.79×10^{-7}
42% Fe1422, 58% B_4C[a]	6	5.10×10^{-7}	6.74×10^{-8}	4.51×10^{-9}	1.18×10^{-9}	6.84×10^{-12}
100% Pb	5	4.25×10^{-10}	4.41×10^{-11}	1.02×10^{-11}	9.19×10^{-13}	9.19×10^{-13}
100% PCA Steel, Magnet Case	15	2.72×10^{-7}	5.47×10^{-8}	1.09×10^{-8}	2.23×10^{-9}	4.06×10^{-10}

[a] B_4C is used with an 0.7 density factor.

Table 7-16. Activation Parameters Per Zone for the Borated Water Outboard Shield

Zone Composition Percentage By Volume	Zone Thickness (cm)	Time After Shutdown at the End of Operating Life				
		0	1y	10y	100y	1000y
		A. Radioactivity Ci/cm^3				
First Wall/Blanket	50	7.16	3.14	2.98×10^{-1}	3.24×10^{-3}	5.03×10^{-4}
100% Fe1422	2	4.51	4.59×10^{-1}	3.58×10^{-2}	7.68×10^{-4}	8.23×10^{-6}
100% Borated Water	190	7.23×10^{-4}				
100% Fe1422	2	5.66×10^{-8}	8.62×10^{-9}	6.37×10^{-10}	1.20×10^{-11}	1.35×10^{-13}
100% Pb	5	4.14×10^{-10}	2.03×10^{-13}	4.47×10^{-14}	3.28×10^{-15}	3.28×10^{-15}
100% PCA Steel, Magnet Case	15	4.03×10^{-9}	8.92×10^{-10}	9.43×10^{-11}	1.15×10^{-11}	2.74×10^{-12}
		B. Radioactivity Ci/W_{th}				
First Wall/Blanket	50	1.84	7.65×10^{-1}	7.26×10^{-2}	7.89×10^{-11}	1.22×10^{-4}
100% Fe1422	2	5.09×10^{-2}	5.17×10^{-3}	4.10×10^{-4}	8.67×10^{-6}	9.29×10^{-8}
100% Borated Water	190	1.14×10^{-3}				
100% Fe1422	2	1.24×10^{-9}	1.89×10^{-10}	1.40×10^{-11}	2.63×10^{-13}	2.97×10^{-15}
100% Pb	5	2.29×10^{-11}	1.12×10^{-14}	2.47×10^{-15}	1.82×10^{-16}	1.82×10^{-16}
100% PCA Steel, Magnet Case	15	1.02×10^{-9}	2.26×10^{-10}	2.39×10^{-11}	2.92×10^{-12}	6.94×10^{-13}

Table 7-16. (Continued)

Zone Composition Percentage By Volume	Zone Thickness (cm)	Time After Shutdown at the End of Operating Life				
		0	1y	10y	100y	1000y
		C. Afterheat (% of Operating Power)				
First Wall/Blanket	50	9.79×10^{-1}	1.11×10^{-1}	2.01×10^{-2}	9.64×10^{-6}	1.76×10^{-6}
100% Fe1422	2	6.50×10^{-2}	6.63×10^{-4}	2.61×10^{-5}	1.07×10^{-7}	4.73×10^{-9}
100% Borated Water	190	6.24×10^{-3}				
100% Fe1422	2	1.45×10^{-9}	2.88×10^{-11}	1.03×10^{-12}	3.23×10^{-15}	1.49×10^{-16}
100% Pb	5	1.68×10^{-11}	2.38×10^{-15}	4.87×10^{-16}	1.27×10^{-22}	
100% PCA Steel, Magnet Case	15					
		D. Biological Hazard Potential ($km^3 air/kW_{th}$)				
First Wall/Blanket	50	5.14×10^{2}	2.11×10^{2}	4.06×10^{1}	3.10×10^{-1}	1.57×10^{-2}
100% Fe1422	2	4.68	1.14	4.30×10^{-2}	4.30×10^{-3}	1.15×10^{-5}
100% Borated Water	190	3.81×10^{-2}				
100% Fe1422	2	1.64×10^{-7}	5.15×10^{-8}	1.72×10^{-9}	1.30×10^{-10}	4.03×10^{-13}
100% Pb	5	4.70×10^{-10}	1.37×10^{-11}	4.36×10^{-12}	1.82×10^{-12}	1.82×10^{-12}
100% PCA Steel, Magnet Case	15	2.38×10^{-7}	8.01×10^{-8}	1.44×10^{-8}	9.67×10^{-10}	8.28×10^{-11}

Table 7-17. Activation Parameters Per Zone for the Water - B_4C Outboard Shield

Zone Composition Percentage By Volume	Zone Thickness (cm)	Time After Shutdown at the End of Operating Life				
		0	1y	10y	100y	1000y
		A. Radioactivity Ci/cm^3				
First Wall/Blanket	50	7.16	3.14	2.98×10^{-1}	3.24×10^{3}	5.03×10^{-4}
100% Fe1422	2	9.02	8.66×10^{-1}	7.84×10^{-2}	3.82×10^{-3}	3.96×10^{-5}
100% H_2O	185	7.52×10^{-4}				
42% Fe1422, 58% B_4C[a]	6	1.63×10^{-8}	5.06×10^{-9}	3.38×10^{-10}	3.56×10^{-13}	2.38×10^{-14}
100% Pb	5	4.81×10^{-10}	2.35×10^{-13}	5.17×10^{-14}	3.81×10^{-15}	3.81×10^{-15}
100% PCA Steel, Magnet Case	15	3.98×10^{-9}	9.26×10^{-10}	9.01×10^{-11}	8.56×10^{-12}	3.60×10^{-12}
		B. Radioactivity Ci/W_{th}				
First Wall/Blanket	50	1.84	7.65×10^{-1}	7.26×10^{-2}	7.89×10^{-4}	1.22×10^{-4}
100% Fe1422	2	1.02×10^{-1}	9.77×10^{-3}	8.85×10^{-4}	4.31×10^{-5}	4.47×10^{-7}
100% H_2O	185	1.15×10^{-3}				
42% Fe1422, 58% B_4C[a]	6	8.85×10^{-10}	2.76×10^{-10}	1.84×10^{-11}	1.94×10^{-14}	1.30×10^{-15}
100% Pb	5	2.65×10^{-11}	1.30×10^{-14}	2.85×10^{-15}	2.10×10^{-16}	2.10×10^{-16}
100% PCA Steel, Magnet Case	15	1.01×10^{-9}	2.34×10^{-10}	2.28×10^{-11}	2.17×10^{-12}	9.11×10^{-13}

Table 7-17. (Continued)

Zone Composition Percentage By Volume	Zone Thickness (cm)	Time After Shutdown at the End of Operating Life				
		0	1y	10y	100y	1000y
		C. Afterheat (% of Operating Power)				
First Wall/Blanket	50	9.79×10^{-1}	1.11×10^{-1}	2.01×10^{-2}	9.64×10^{-6}	1.76×10^{-6}
100% Fe14Mn2Ni2Cr	2	1.31×10^{-1}	8.49×10^{-4}	4.41×10^{-5}	5.31×10^{-7}	2.31×10^{-8}
100% H_2O	185	6.24×10^{-3}				
42% Fe1422, 58% B_4C[a]	6	8.23×10^{-10}	4.91×10^{-11}	1.60×10^{-12}	2.89×10^{-16}	6.77×10^{-17}
100% Pb	5	1.93×10^{-11}	2.73×10^{-15}	5.62×10^{-16}	1.45×10^{-22}	
100% PCA Steel, Magnet Case	15					
		D. Biological Hazard Potential (km^3 air/kW_{th})				
First Wall/Blanket	50	5.14×10^{2}	2.11×10^{2}	4.06×10^{1}	3.10×10^{-1}	1.57×10^{-2}
100% Fe1422	2	7.19	1.32	9.03×10^{-2}	2.13×10^{-2}	3.61×10^{-5}
100% H_2O	185	3.81×10^{-2}				
42% Fe1422, 58% B_4C	6	2.26×10^{-7}	8.99×10^{-8}	2.46×10^{-9}	1.24×10^{-11}	3.44×10^{-12}
100% Pb	5	5.42×10^{-10}	1.58×10^{-11}	5.03×10^{-12}	2.10×10^{-12}	2.10×10^{-12}
100% PCA Steel, Magnet Case	15	2.63×10^{-7}	8.89×10^{-8}	1.49×10^{-8}	4.36×10^{-10}	1.08×10^{-10}

[a] B_4C is used with an 0.7 density factor.

equivalent by a factor of five relative to the other options as shown in Table 7-16. Figures 7-29 through 7-31 show the decay of the activation parameters for the whole system with option 5. The shield has a small fraction of the radioactive isotopes generated during the operation. However, due to the large volume of the shield, it is important that the radioactivity and the volume containing such radioactivity are minimized from the radioactive waste disposal point of view. Both water shield options have the potential to generate less radioactive waste relative to the concrete shield option. The long-term activation in the shield components, 40 years after shutdown, is caused by the nickel content in the Fe1422 steel alloy and the nickel impurity (0.3% by weight) in the ordinary concrete. Replacing or isotopic tailoring of the 2% nickel element in the steel alloy to ^{61}Ni reduces the radioactivity concentration by two orders of magnitude. For example, the maximum radioactivity concentration in the Fe1422 steel alloy drops from 3.79×10^{-3} to 3.23×10^{-5} Ci/cm^3. The remaining radioactivity is due to ^{14}C generated from the 0.019% by weight nitrogen impurity. Also, eliminating Ni impurity from ordinary concrete reduces the average radioactivity concentration from 1.22×10^{-6} to 1.9×10^{-9} Ci/cm^3. A low nickel content in the concrete can be achieved through the selection process of cement and aggregate materials.

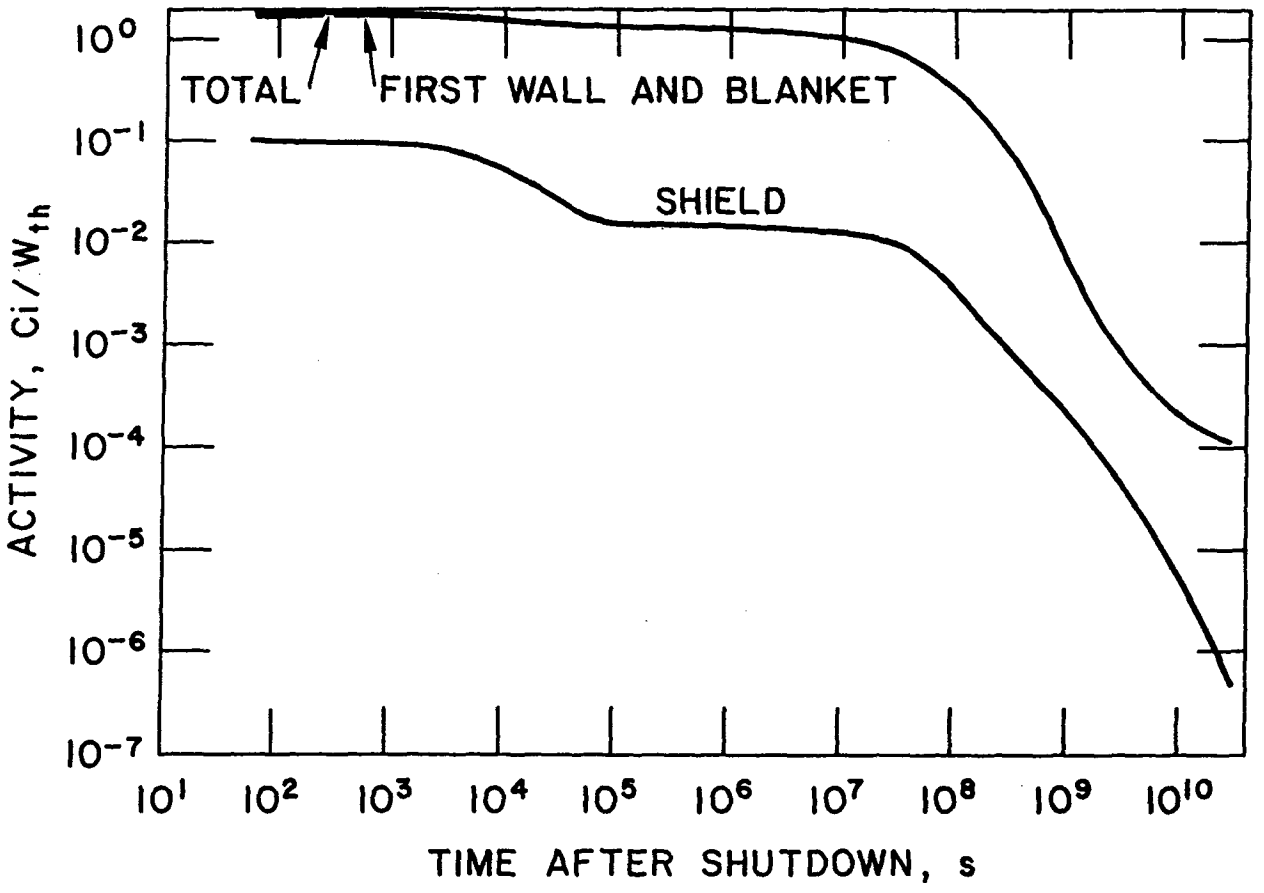

Figure 7-29. Radioactivity as a function of time after shutdown.

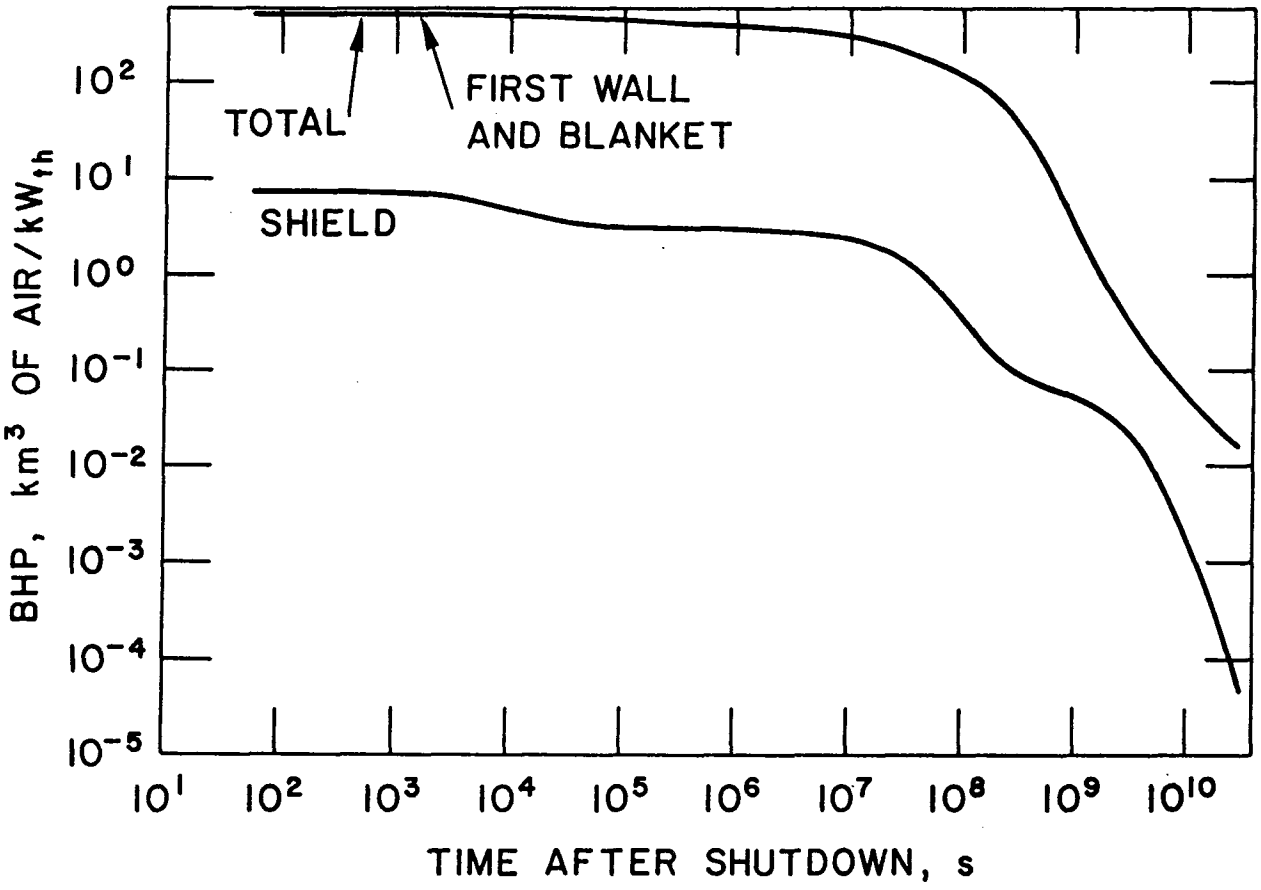

Figure 7-30. Biological hazard potential as a function of time after shutdown.

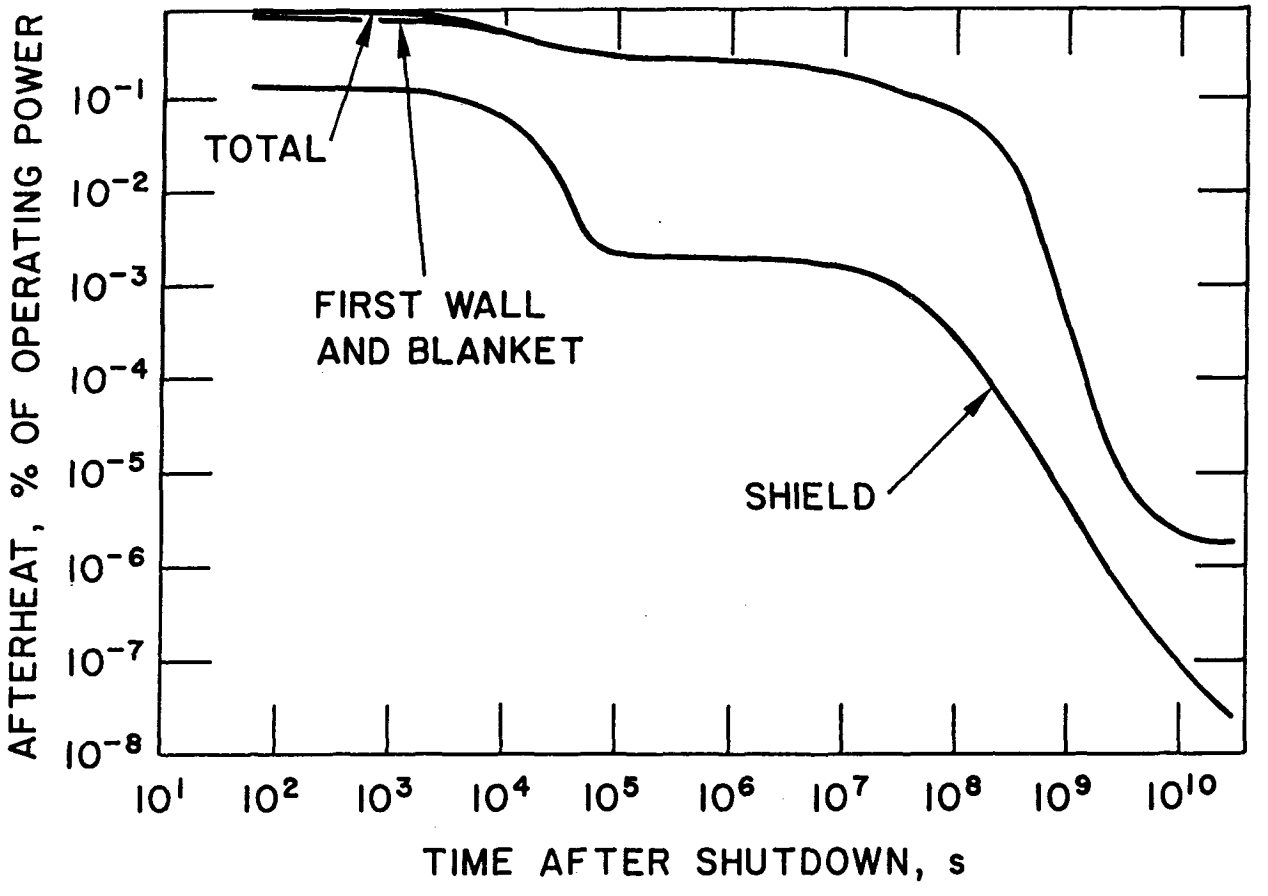

Figure 7-31. Afterheat as a function of time after shutdown.

REFERENCES FOR CHAPTER 7

(1) C. C. Baker, et al., "STARFIRE - A Commercial Tokamak Fusion Power Plant Study," Argonne National Laboratory, ANL/FPP-80-1 (1980).

(2) W. M. Stacey, et al., "INTOR, The U.S. Contribution to the International Tokamak Reactor Phase-1 Workshop, Conceptual Design," USA INTOR/81-1.

(3) W. M. Stacey, et al., "U.S. INTOR, The U.S. Contribution to the International Tokamak Reactor Workshop," November, 1979.

(4) R. W. Conn, et al., "Minimizing Radioactivity and Other Features of Elemental and Isotopic Tailoring of Materials for Fusion Reactors, Nucl. Technol. 41 (31), 389 (1978).

(5) B. S. Brown, "Radiation Effects in Superconductor Fusion-Magnet Materials," J. Nucl. Mater. 97 (1&2), 1 (1981).

(6) Panel Proceedings Series, "International Tokamak Reactor Zero Phase," International Atomic Energy Agency," Vienna, 1980.

(7) Y. Gohar, "Insulator Materials in Magnetic Fusion Reactors," Proceedings of the Meeting on Electrical Insulator for Fusion Magnets, CONF-80-1237, Germantown, Maryland, December 2-3, 1980.

(8) R. R. Coltman, et al., "Effect of Radiation at 5°K on Organic Insulators for Superconducting Magnets," Proc. 8th Symp. on Engineering Problems of Fusion Research, Vol. III, p. 1694 (1979).

(9) A. E. Profio, "Radiation Shielding and Dosimetry," A. Wiley - Interscience Publication, John Wiley & Sons, New York, 1979.

(10) W. Häfele, et al., "Fusion and Fast Breeder Reactors," International Institute for Applied Systems Analysis, A-2361 Luxemburg, Austria (1977).

(11) LASL Group X-6, "MCNP - A General Monte Carlo Code for Neutron and Photon Transport, Version 2B," Los Alamos National Laboratory, LA-7396-M, Revised (April 1981).

(12) F. W. Clinard and G. F. Hurley, "Ceramic and Organic Insulators for Fusion Applications," Second Topical Meeting on Fusion Reactor Materials, Seattle, Washington, August 9-12, 1981.

(13) Y. Gohar and M. A. Abdou, "INTOR Radiation Shielding for Personnel Access," Ninth Symposium on Engineering Problems of Fusion Research, Chicago, Illinois, October 26-29, 1981.

(14) Y. Gohar and M. A. Abdou, "INTOR Radiation Shielding System," Trans. Amer. Nucl. Soc., Volume 39, (Nov.-Dec., 1981).

(15) M. A. Abdou, "Radiation Considerations for Superconducting Fusion Magnets, "J. Nucl. Mater. 72 (1&2) 147 (1978).

(16) B. A. Engholm, "Status of FED Shielding Analysis and Design," Ninth Symposium on Engineering Problems of Fusion Research, Chicago, Illinois, October 26-29, 1981.

(17) U.S. Nuclear Regulatory Commission, "Standard for Protection Against Radiation," USNRC Rules and Regulations, Title 10, Chapter 1, Part 20 (1977).

(18) W. W. Engle, Jr., "A User's Manual for ANISN, A One Dimensional Discrete Ordinates Code with Anisotropic Scattering," Oak Ridge Gaseous Diffusion Plant, ORGDP-K-1963 (1967).

(19) R. W. Roussin, et al., "The CTR Processed Multigroup Cross Section Library for Neutronics Studies," Oak Ridge National Laboratory ORNL/RCSIC-37.

(20) Y. Gohar and M. A. Abdou, "MACKLIB-IV: A Library of Nuclear Response Functions Generated with MACK-IV Computer Program From ENDF/B-IV," Argonne National Laboratory, ANL/FPP/TM-106 (1978).

(21) J. Jung, "Theory and Use of Radioactivity Code RACC," Argonne National Laboratory, ANL/FPP/TM-122 (1979); T. Y. Sung and W. F. Vogelsang, "DKR: A Radioactivity Calculation Code for Fusion Reactors," University of Wisconsin, UWFDM-170 (1976).

(22) J. West and E. Snow, Los Alamos National Laboratory, personal communication, September, 1982.

(23) Y. Gohar, "One-Dimensional Gamma Ray Shielding Analysis for EBT-P," Argonne National Laboratory, ANL/FPP/TM-151.

CHAPTER 8

CONFIGURATION AND MAINTENANCE

Chapter 8

Table of Contents

Chapter 8

List of Figures

Chapter 8

List of Tables

8.0 CONFIGURATION AND MAINTENANCE

8.1 Introduction

The DEMO reactor configuration and maintenance approach has been selected to demonstrate it provides the most attractive features perceived for a commercial reactor. Construction and operation of DEMO will provide experience with prototypical components and will identify many improvements for a commercial reactor. Further improvements can be made in DEMO for the commercial reactor if a prototyical reactor configuration is used on the next large reactor (ETR).

The eventual measure of a commercial reactor's value will be through the cost of electricity (COE) so emphasis in DEMO was placed on reducing the elements that contribute to COE, namely:

- Outage rate (reliability and lifetime) } availability
- Replacement approach (time) }
- Capital cost

Outage rate of a reactor will be determined by the frequency of failure of critical components and by the need for preventative maintenance change-outs. Failure rate data can only be determined with high confidence by experience from extensive testing (typically to three to five times the desired time-between-failures) in similar environments[21]. The failure rate is dependent on component complexity hence DEMO has strived for design simplicity in configuration choices.

The DEMO study has emphasized configuration design for ease of replacement (maintenance). Minimum capital cost has been emphasized until it significantly impacts maintenance. The experience gained through design, construction and operation of a commercially relevant reactor configuration is expected to outweigh any cost differences. For example, the numbers and size of TF coils has been reduced as much as possible compatible with replacing one blanket sector per TF coil. Reducing the number of TF coils led to use of fewer first wall blanket sectors, fewer seals, joints and pipes which might fail and to fewer components which resulted in less total time for component replacement and a more reliable system. On the other hand, because the TF

coils had to be made somewhat larger (in terms of the radius of the outboard return leg) this was a small cost penalty.

A total remote maintenance approach was selected for DEMO based on the desire to minimize radiation exposure to workers. It is believed that remote maintenance is desired in a commercial reactor and at DEMO should show its viability for all maintenance operations. A difference between DEMO and the first commercial reactor is that DEMO needs only to show that the method is viable for a first commercial reactor. For example, the desire to minimize DEMO costs may dictate that less sophisticated maintenance tools be used that require more time to perform tasks. This is acceptable if no feasibility question exists. Workers can also be utilized in the radiation environment as a backup to the maintenance system given the developmental nature of DEMO.

The key issues addressed in the DEMO effort have been selection of the number of TF coils, minimizing their size, simplifying TF coil replacement, identifying of the location of the vacuum boundary, selecting the number and configuration of blanket shield sectors and selecting the maintenance approach. These issues were addressed because the major influence these exhibited on the STARFIRE design (5). The selected DEMO configuration reflects perceived improvements that should be incorporated into STARFIRE. This chapter first summarizes the DEMO design approach and then is followed by discussions of the key issues noted above.

8.2 Reference Reactor Configuration

The reactor configuration is made up of 8 TF coils, 8 shield sectors, 8 blanket sectors, 8 limiter modules, 8 EF coils, 4 CF coils and 2 REB launchers. A layout of the reactor is shown in Fig. 8-1 and an isometric of the reactor is shown in Fig. 8-2. Specific components are shown in Fig. 8-3, 8-4 and 8-5. The reactor is designed for complete reassembly by remote maintenance.

The TF coils are designed for a 10T peak field and utilize NbTi in a bath cooled tank. The coil vertical support is provided by a support pedestal of G-10 fiberglass. The half height of the coil is 5.46 m and the outer leg radius is 11.6m. The overturning forces are reacted through a 4°K beam structure which leaves a 6.2m wide x 7.5m high opening between TF coils for blanket

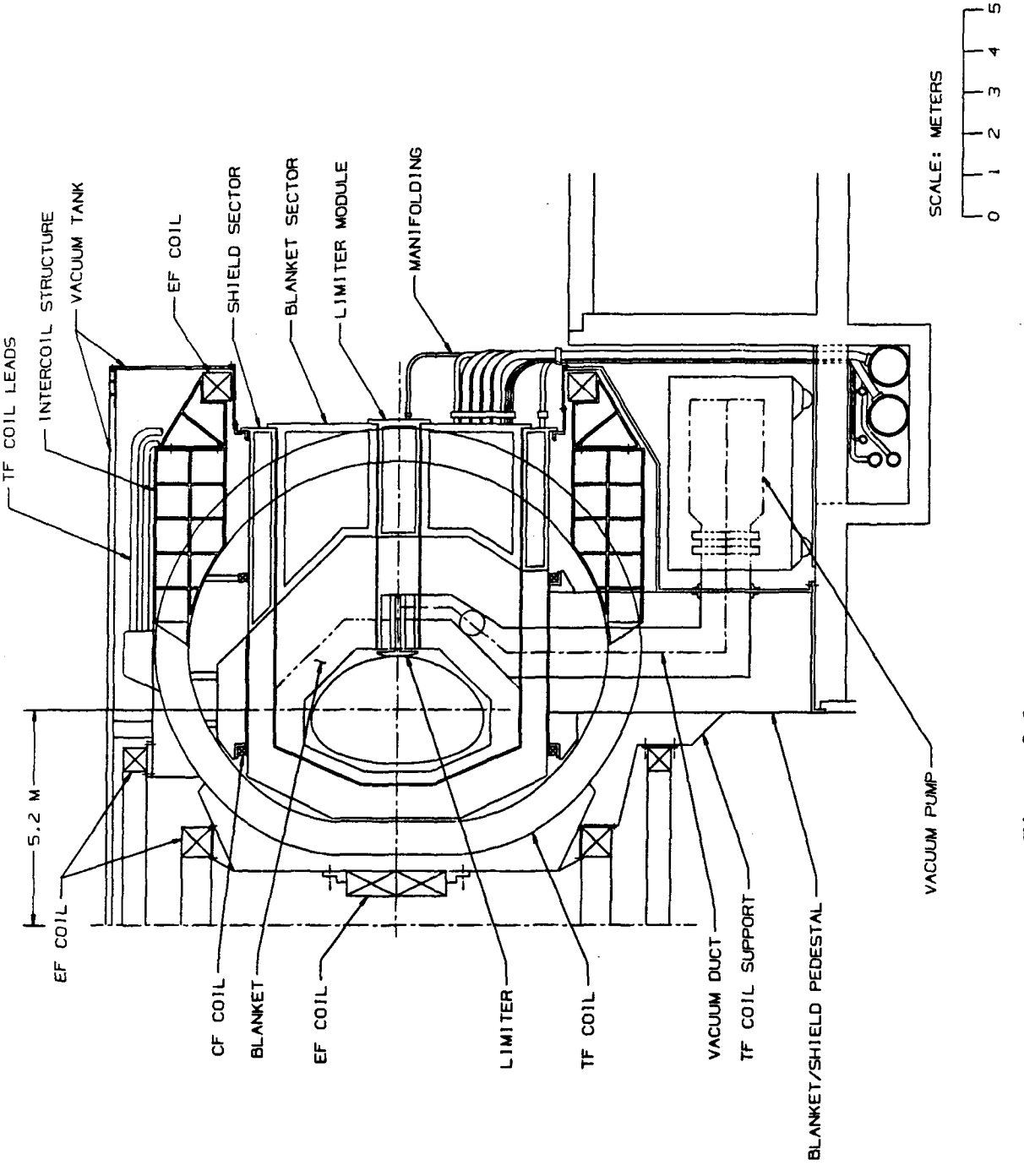

Figure 8-1. Reactor layout (Pg 1 of 2).

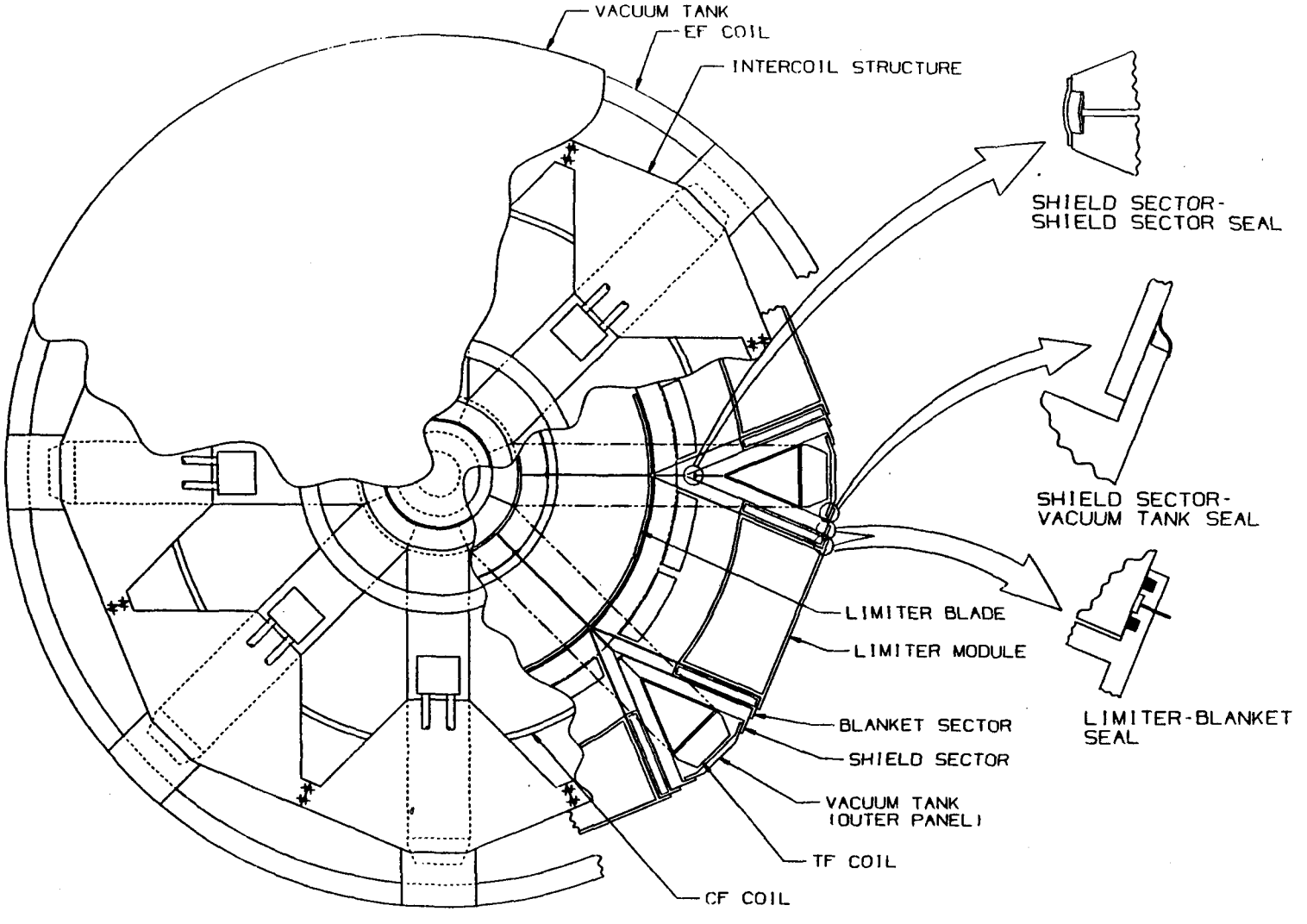

Figure 8-1. Reactor layout (Pg 2 of 2).

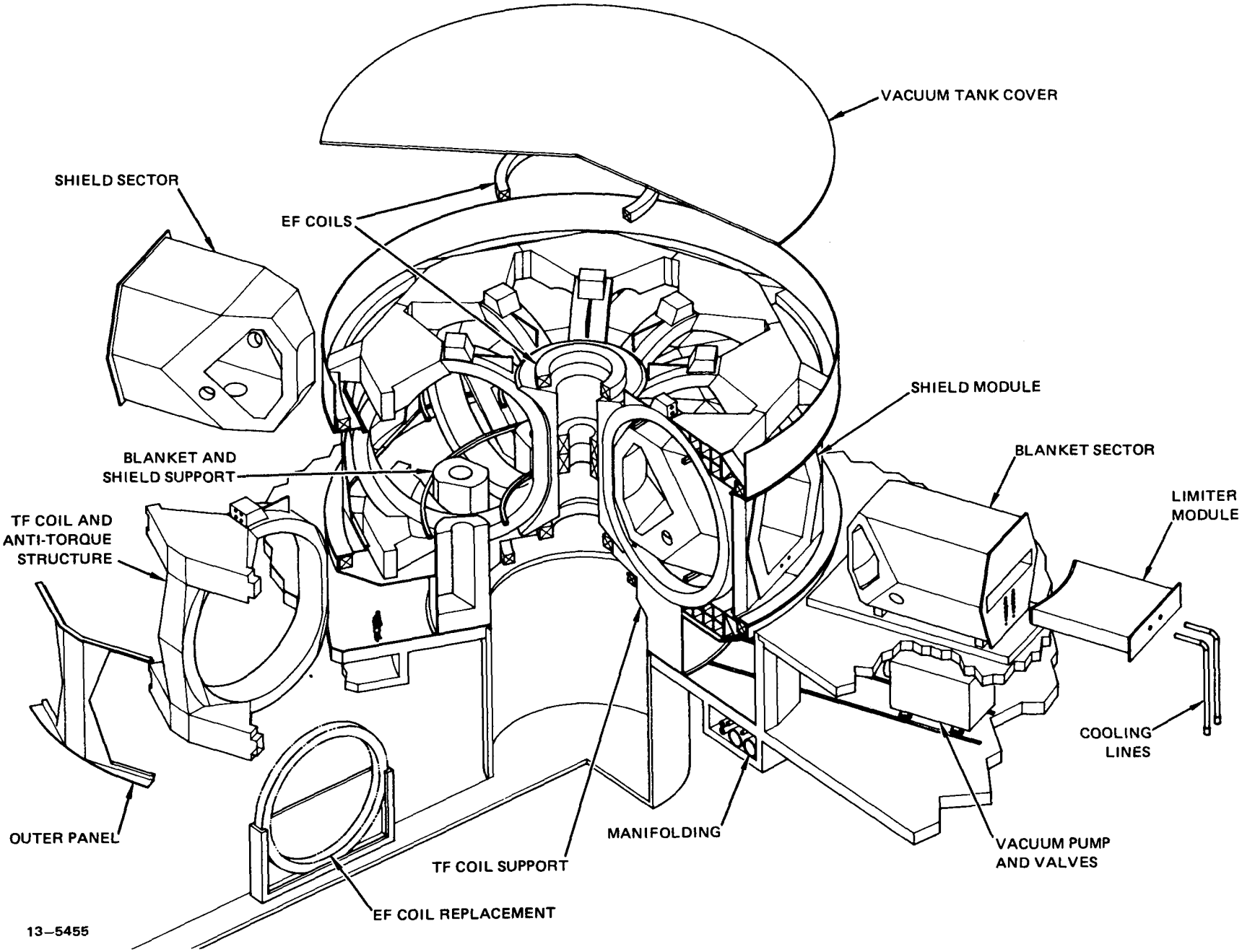

Figure 8-2. DEMO reference design.

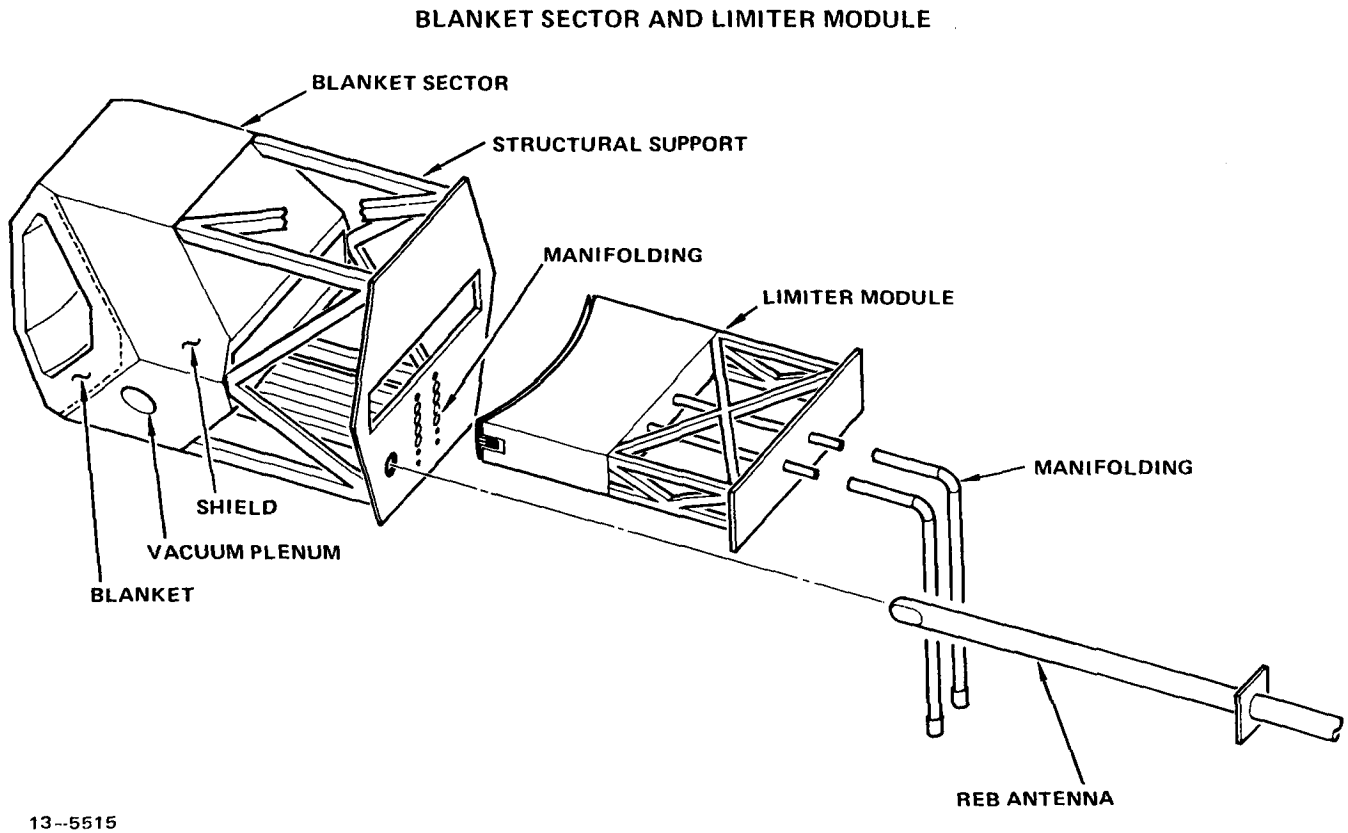

Figure 8-3. Blanket sector and limiter module.

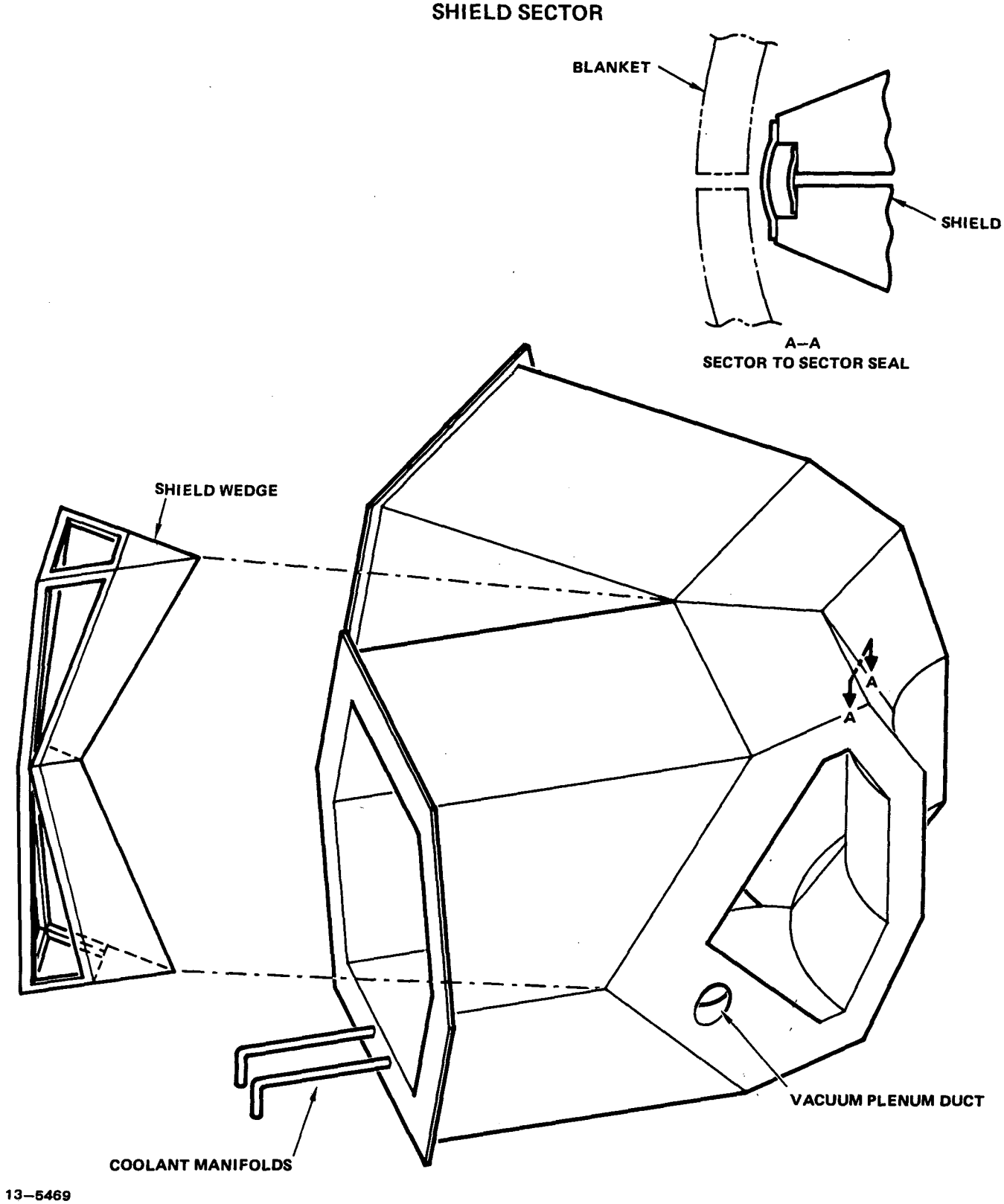

Figure 8-4. Shield sector.

TF COIL CONFIGURATION

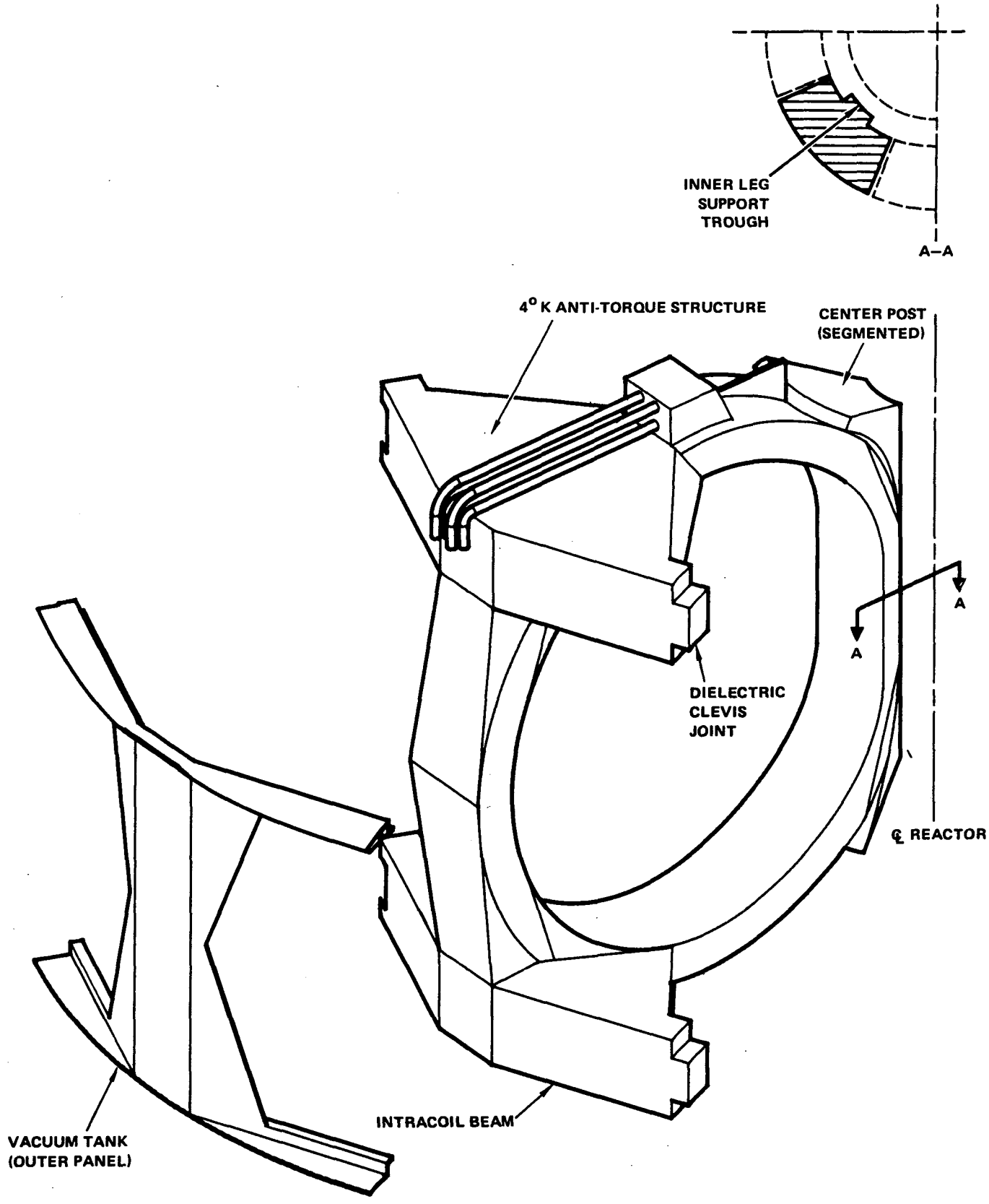

Figure 8-5. TF coil configuration.

installation. The in-plane loads on the upper and lower portions of the TF coil are supported by the center post which extends outward ~ 1.5 m. This permits use of a shortened TF coil which follows a pure tension shape in areas away from the center post. The EF coils are supported from the TF coils inside the vacuum tank. All EF coils can be replaced. The upper, inner and outer coils are replaced by removing the upper dome of the vacuum tank. The lower EF coils can be replaced through a pit below the reactor. Control field (CF) coils can be replaced by removal of the blanket and shield.

The TF coil and plasma chamber vacuum boundaries have been combined to decrease the radial build in the inner shield area and to simplify TF coil replacement. The TF coil vacuum boundary is essentially formed by a cylinder with flat ends. The plasma boundary is then formed by inserting 8 shield sectors through openings in the outer cylinder wall. These sectors are seal welded together to form an inner vacuum boundary around the plasma.

Blanket sectors with combined shielding are inserted into the shield sectors to complete the plasma vacuum. Dual elastomer seals at the outer TF coil vacuum boundary provide the final closure for the plasma boundary. All seals and welds utilize dual seals for redundancy and to simplify leak checking. Two factory installed dielectric breaks are provided in shield sectors 180° apart.

The shield consists of 8 sector modules, 8 shield wedge modules that fit behind each TF coil (Fig. 8-4) and slabs of shielding above and below the shield modules as shown in Fig. 8-1. The heating rate in the first 47 cm of the shield (nearest the blanket) requires that zone to be actively cooled. Beyond the first 47 cm the heating rate is less than 0.1 mW/cm^3 and the shielding does not require active cooling. The total heat generated in the outer 1.57 m of shielding is 137 KW of which ~ 50% is contained within the shielding in the blanket module. The remaining heat (~ 70 KW) will be conducted and radiated to either the cooled shield zone or to the liquid nitrogen system. The shield wedge modules and the slabs of shielding above and below the shield modules are not actively cooled and are made of concrete. These modules are attached to the TF coil 4°K structure through G-10 supports and liquid nitrogen shields for thermal isolation. Multi-layer insulation is fitted between the concrete modules and the TF coils LN_2 shields. Shielding

around the vacuum ducts and pumps is also predominantly concrete. Shielding components are not expected to require scheduled replacement during the life of the reactor.

The blankets, limiters, vacuum pumps and REB current drive launchers are remotely replaceable. These components are designed so they may be replaced independent of each other except for the blanket which will require removal of limiter and REB antennas with the blanket sector.

The vacuum pumps are located in the reactor building basement and can be maintained independent of other reactor components. Each of the 8 pumps are manifolded into a common plenum inside the blanket sector shield door cavity so that four of the eight can be regenerated while the other four are operating. A regeneration time of two hours is anticipated which implies two hours between pump regeneration. Dual gate valves are included on each pump for redundancy and to permit pump removal without breech of vacuum.

The anti-torque structure consists of a 4°K bending beam structure that forms a ring at the top and bottom of the coils in addition to the outer legs of the TF coil. This structural approach is based on the design development work done for FED/INTOR. The shield rests on pedestals which are made up primarily of the shielding that surrounds the vacuum ducts. The TF coil and center post vertical supports are via a support pad under each TF coil. These support pads include G-10 fiberglass pads for thermal insulation. A common vacuum tank encloses all TF, EF and CF coils and the center post. The weights of the major components are summarized in Table 8-1.

8.3 Design Approach Selection

The DEMO configuration has been selected to enhance the maintainablility of the reactor without critically detracting from the reactor performance or increasing cost. Many of the STARFIRE considerations have been carried directly into DEMO. Areas where major differences occur are in the number of TF coils, TF coil shape, TF coil support and selection of one blanket sector per TF coil. Eight TF coils are utilized instead of twelve. The decision to use one blanket sector per TF coil results in the need to use a larger coil relative to the plasma for access which, in turn, permits use of fewer coils for the same ripple. The TF coil shape is more circular than Dee but is still

pure tension in areas not supported by the center post. This shape was chosen to minimize the stored energy of the TF and EF coil systems. The 4°K overturning structure design of FED/INTOR has been adopted for DEMO. Steady state operation minimizes fatigue concerns with this structure. Another major difference is the choice of a common vacuum tank for the plasma chamber and TF coil. This choice greatly simplifies TF coil replacement. The single blanket sector per TF coil simplifies sector removal, significantly reduces the number of cooling lines and simplifies limiter replacement.

Table 8-1. Major Components Weights

	Per Sector/Item (Metric Tons)	Total (Metric Tons)	
TF COIL (8)	400	3200	
EF COIL (R = 1m)	42	84	1006
EF COIL (R = 2m)	55	110	
EF COIL (R = 4m)	56	112	
EF COIL (R = 13m)	350	700	
CF COIL (R = 4.2m)	12	24	66
CF COIL (R = 8.3m)	21	42	
LIMITER MODULE	50	400	
BLANKET SECTOR	240	1920	
SHIELD SECTOR	170	1360	
TOTAL WEIGHT		7952	

8.3.1 TF Coil Configuration

The TF coil system probably has the largest single effect on the overall reactor configuration. The number of coils will determine how many components are required and the basic size of each component. In general a lower number of TF coils means fewer components, joints, valves and connections and, in all likelihood, results in a higher reliability of the system. Fewer parts result

in fewer maintenance operations and therefore less time for maintenance. The above considerations led to higher availabilities for lower numbers of TF coils, hence our incentive to reduce the number of coils as much as possible.

Number of TF Coils - Consideration of the access requirements of the blanket and shield and the ripple limits imposed on the TF coil system has resulted in selection of 8 TF coils with an outer leg radius of 11.6m. The resulting ripple is 3.4 percent peak-to-peak at the outer edge of the plasma and 1.72 percent at $R_o + a/2$.

Ripple requirements for tokamaks have not been well established; however, the currently suggested limits are:

- 0.6 percent peak-to-peak at $R_o + a/2$
- Three percent peak-to-peak at the outer plasma edge ($R_o + a$)

The 0.6 percent peak-to-peak ripple limit has been mutually arrived at by members of a ripple limit workshop (1). This limit is compatible with current transport codes. A second ripple limit of three percent peak-to-peak at the plasma edge has been discussed more recently as a possible alternative. The DEMO study utilized this limit for the selection of the initial TF coil outer leg radius. Subsequent detailed analyses, provided by FEDC, that takes into account the actual shape of the TF coils, yields a value of 3.4% peak-to-peak ripple at the plasma edge. This value is very close to the approximate 3% limit and has been accepted for the study. Peak-to-average ripples of other designs are given in Table 8-2.

Table 8-2. Field Ripple for Design Studies

PEAK-TO-AVERAGE RIPPLE (%)

LOCATION	R_o	$R_o + a/2$	$R_o + a$
STARFIRE	0.09%	0.40	1.47
INTOR	0.10	-	0.50
FED	0.10	0.30	0.80
INTOR MODIFIED	-	0.50	1.50
DEMO	0.39	0.86	1.70

A simplified equation (Reference 2) was used to estimate the TF coil ripple prior to the more exact analyses that yielded a 1.7% peak-to-average ripple; this relationship is:

$$R_2 = 1.1\ R\ \delta^{-1/N} \qquad (1)$$

where R_2 = outer leg radius (m)

R = radius where ripple is measured (m)

δ = peak-to-average ripple

N = number of TF coils

A comparison of the results of this equation with results obtained in a more exact calculation by FEDC indicates the ripple predicted by equation 1 is ~ 0.6% high. The simplified equation indicated a ripple of 4.0% at 8 coils and an 11.6m radius. A plot using the simplified equation is shown in Fig. 8-6 to show the sensitivity of ripple to changes in the numbers of coils. Results indicate that a 1% change in ripple requires approximately a 0.4m change in the coil radius. Based on this evaluation the DEMO outer leg radius should likely be ~ 11.8m to limit the ripple to 3% at the outer plasma edge. An increase to 9 coils could also decrease the ripple to ~ 2% but access limits would still require an 11.8m outer leg radius.

The access required for installation of one first wall/blanket sector per TF coil can be estimated using simple geometry calculations. Constraints used in these calculations included the geometry shown in Fig. 8-7 and the use of a full blanket depth under each TF coil at the reactor midplane. Additionally, constraints for the shield sectors are that a 30 cm thick outer frame and a 10 cm shielding step are required. The shield sector clears the TF coil vacuum tank by 10 cm. The vacuum tank thickness, superinsulation and liquid nitrogen shroud make up a 20 cm layer enclosing the 4°K cold case. These calculations result in the mechanical access constraint that is superimposed on Fig. 8-6. Further refinement of the ripple calculations and ripple limits and better definition of the structural support, vacuum tank and shielding step sizes are required. The total access to the blanket sectors (cumulative space between TF coils) varies less than 1 m in total perimeter for changes from 8 to 12 TF coils. As more coils are used, each sector becomes proportionally narrower.

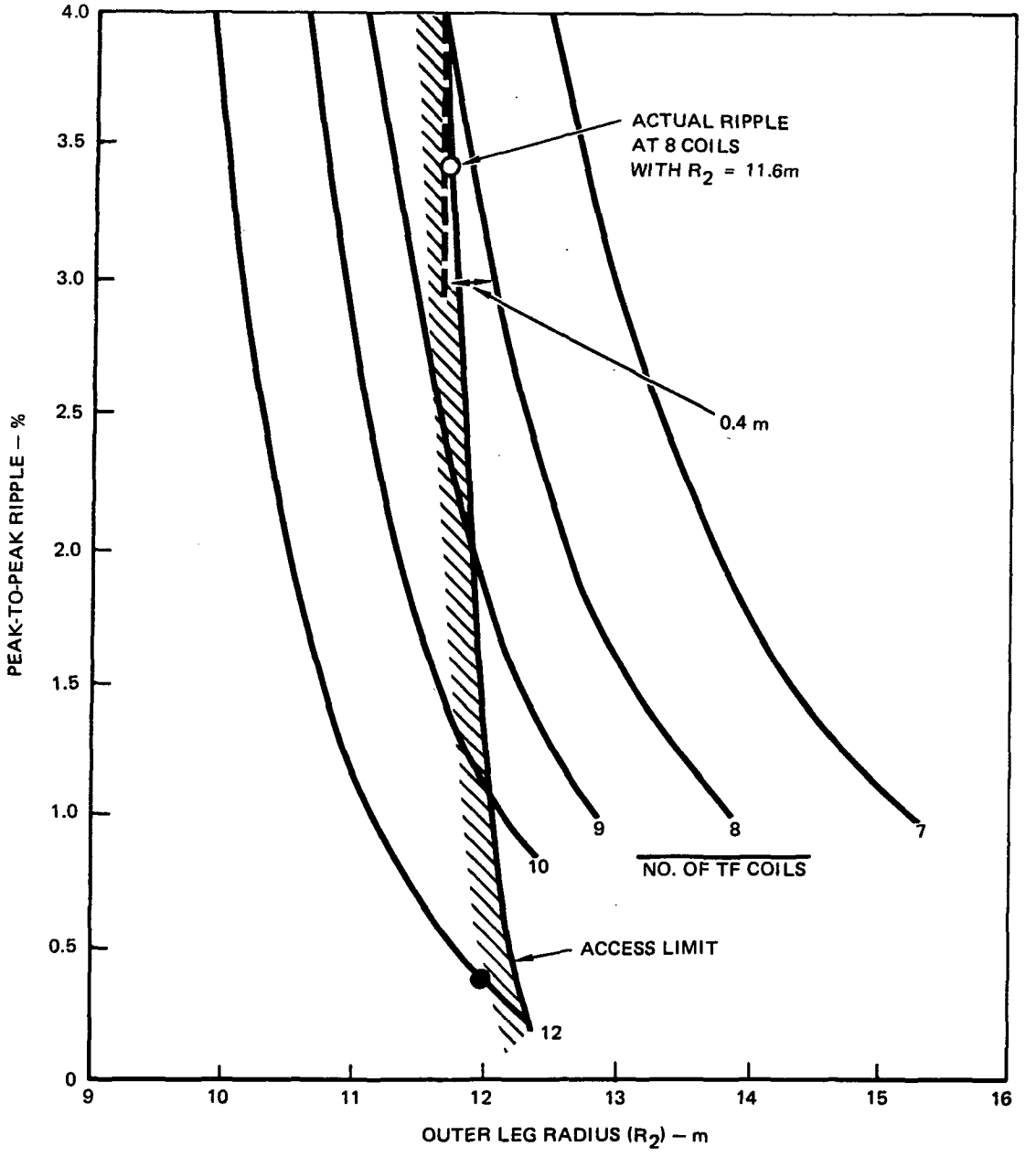

Figure 8-6. TF coil ripple at R_o + a (6.5 m) with mechanical access constraints for sector installation superimposed.

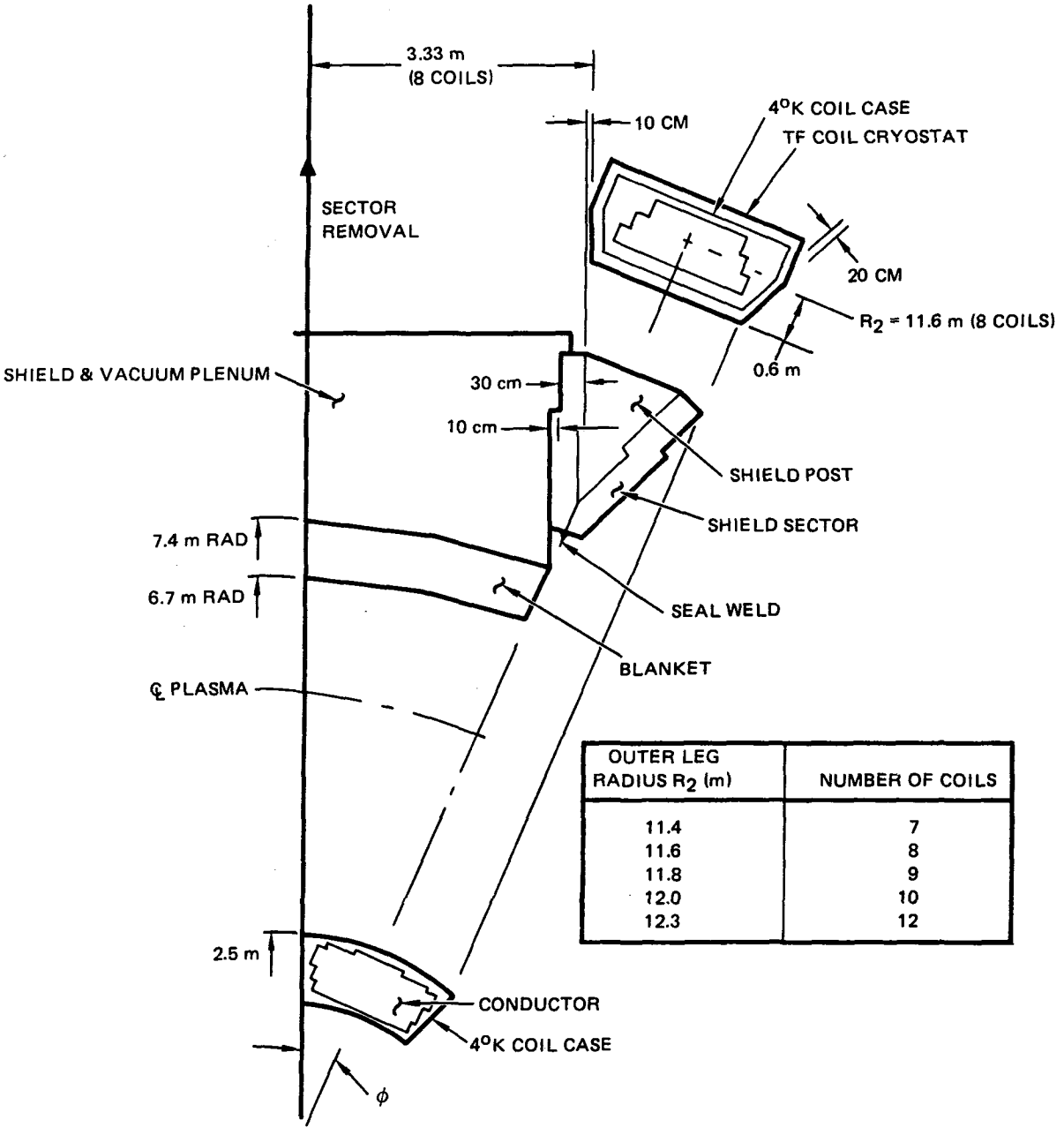

OUTER LEG RADIUS R_2 (m)	NUMBER OF COILS
11.4	7
11.6	8
11.8	9
12.0	10
12.3	12

Figure 8-7. Access geometry of reactor.

TF Coil Cross Section - The center post portion of the TF coil is frequently designed with flat sides to make the coil simpler to fabricate. However, if the coil is pancake wound, as is anticipated for the DEMO coil, the only added expense of a more closely fitting cross section is that of machining that portion of the coil case along the inner leg and in a transition area at the top and bottom inner leg. The two options are shown in Fig. 8-8. A comparison of the fabricated cost of each case indicates that a $20/kg cost is incurred for a welded plate dewar and that an additional $10/kg can pay for machining grooves. On this basis it costs ~ $0.6M more for the machined coil case. This is more than offset by locating the coil peak field turns as much as 19 cm closer to the plasma which minimizes the field requirements and major radius of the reactor. A preliminary cost evaluation based on STARFIRE indicates this can decrease the cost by as much as $50M (3).

Coil Shape - Conventional TF coil designs utilize a pure tension shape per Moses and Young's criteria (12) using a straight center post. As a result the total stored energy in the EF coil system is very dependent on the outer TF coil radius because every 1m change in radius increases the coil height by ~ 2m. This provides a great incentive for minimizing the outer leg radius. In STARFIRE this design approach resulted in the use of two blanket sectors per TF coil and complicated the maintenance operations.

The DEMO design utilizes a pure tension modified coil shape to shorten the magnet. A smaller conventional shaped pure tension magnet is used to establish the outer leg of the coil. The shape is modified where support is provided by the center post. A similar effect was provided for in the UWMAK II design (4) where the coil was made more "Dee" shaped by an attachment to the center post. The conventional coil shape and DEMO modified shape are shown in Fig. 8-9. A resulting 2.8m decrease in total height occurs. The shape was selected by plotting a series of pure tension shapes with a given R_2 needed for blanket access. After layout of the options it was found that the 5.46m half height design could be used and still permit sector installation and removal. The inner leg shape was then modified by deviating from the pure conventional tension shape on the inner leg. To reduce in-plane bending stresses as as result of this modification, the center post was brought out to the point where the deviation was started. This allows the center post to

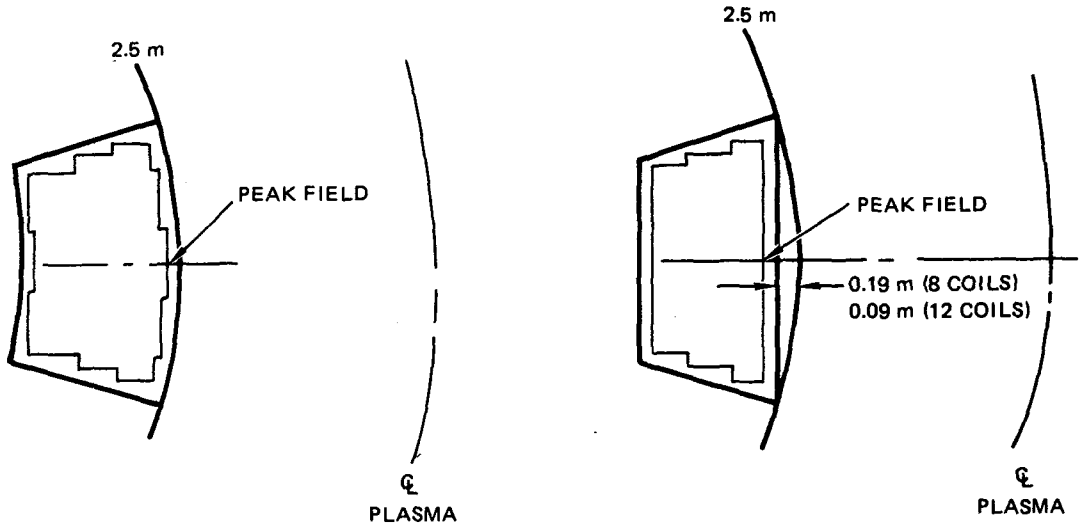

COST/LB	$30/KG	$20/KG
MANUFACTURED COST OF INNER LEG STRUCTURE	$1.9 m	$1.3 m

13–5328 A

Figure 8-8. TF coil inner leg shape comparison.

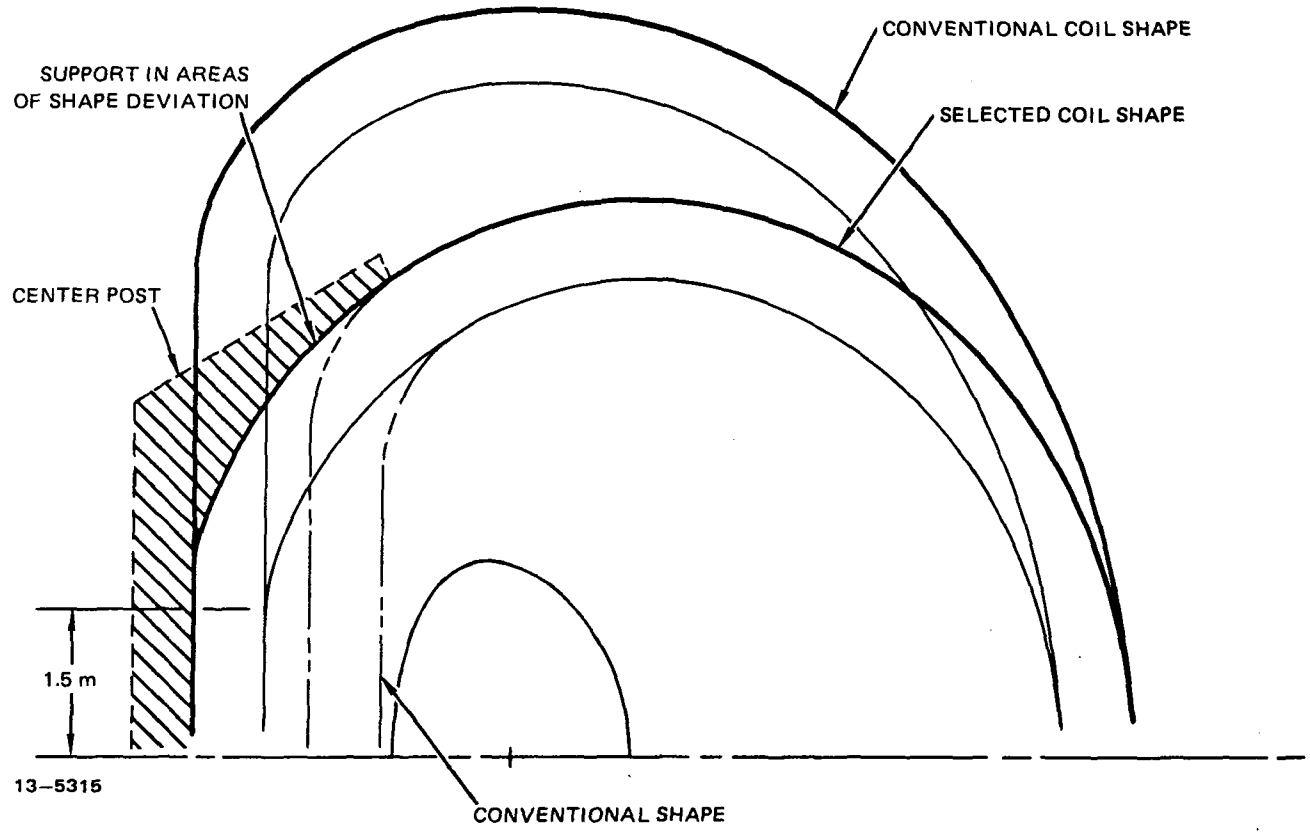

Figure 8-9. TF coil shape options.

pick up any loads that would be imposed in the coil case by deviation from the pure tension shape. It might be argued that if the shape of a portion of a TF coil system is changed from the conventional constant tension shape, then the altered field from that changed portion would result in a force pattern other than constant tension over the remainder of the coil system. Computations show that, except at the point where the outer portion and modified portion meet, the tension in the outer portion is uniform, within 1.5%, and has value of 147 MN.

The benefits of shortening the TF coil height include a reduction in reactor building height and reduction in EF coil stored energy. Reduction of each 1m in building height saves approximately 600 m^3 in reactor building volume (based on STARFIRE); this represents ~ $3M in cost savings alone. Additionally savings in EF coil stored energy costs are approximately $3 M/GJ (5).

A survey of EF stored energy was performed for several standard pure tension TF coil designs, Fig. 8-10, and plotted as a function of the product of H_{max} and R_2 of the TF coil. This is shown in Fig. 8-11. As indicated a significant incentive exists for minimizing TF coil size. The outer leg size is fixed by access for maintenance but the height is not until it starts to interfere with the blanket/shield installation. The resultant stored energy of ~ 5 GJ is substantially less that the ~ 14 GJ that would have been required for a pure tension shape. This represents ~ $27M in cost savings.

The modified shape of the TF coil system also lowers the stored energy of the TF coil system itself. The energy found by numerically integrating $B^2/2\ \mu_0$ over the toroidal volume bounded by the coils (B, the toroidal field), is 20.3 GJ. DEMO and FED have nearly the same stored energy in the TF coil system.

TF Coil Intracoil Support - The DEMO intracoil support structure has been defined utilizing the 4°K cold support system of FED/INTOR. The design is shown in Fig. 8-5. The out-of-plane loads were 805 Mn-m as compared to 620 Mn-m for FED. The design criteria used was the smaller of 1/3 F_{TU} (ultimate strength) or 2/3 F_{TY} (yield strength) at 4°K. For welded 316 LN steel this results in a design allowable stress of 372 mpa (54 ksi) for DEMO whereas, FED

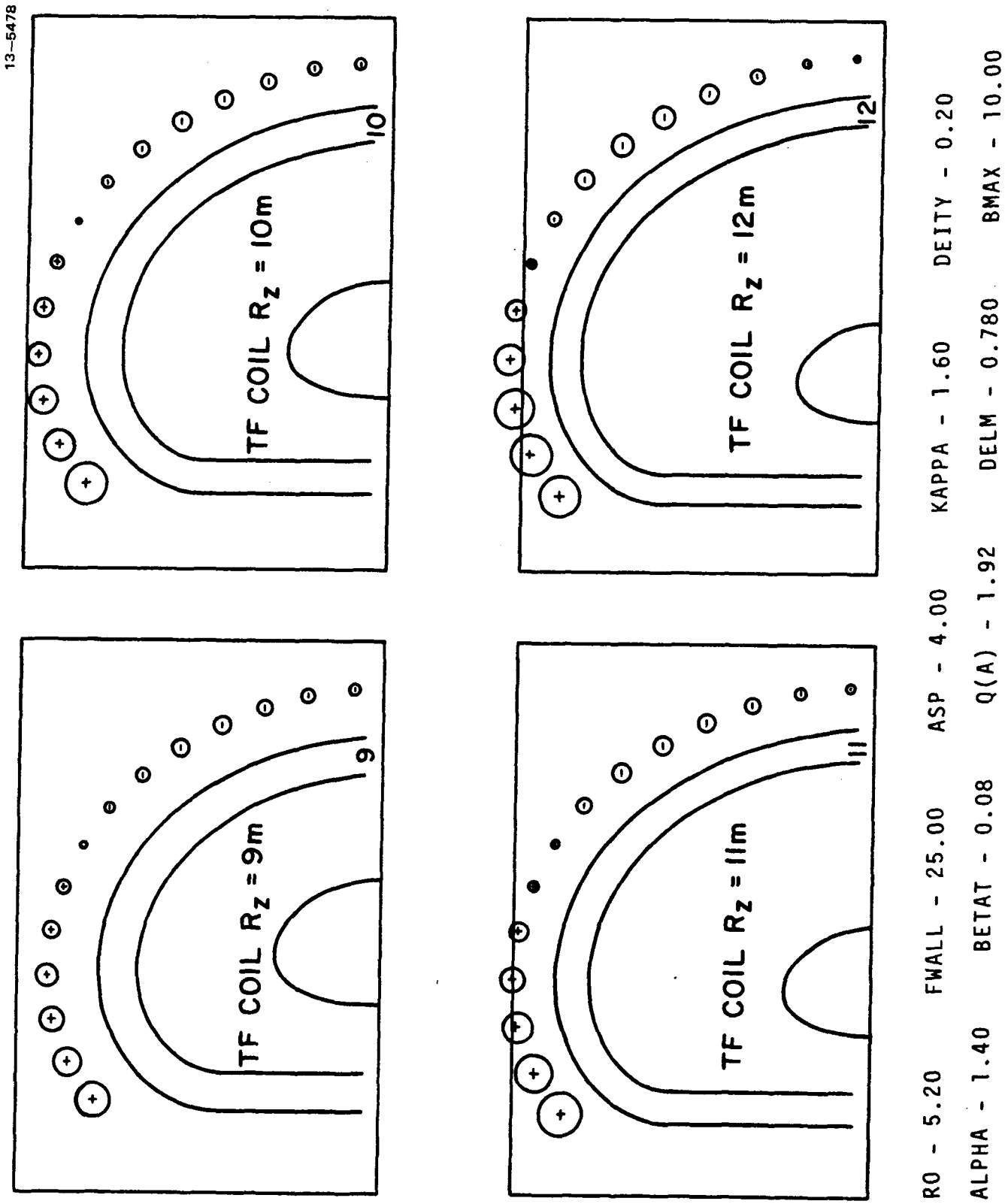

Figure 8-10. EF coil location as a function of TF coil outer radius.

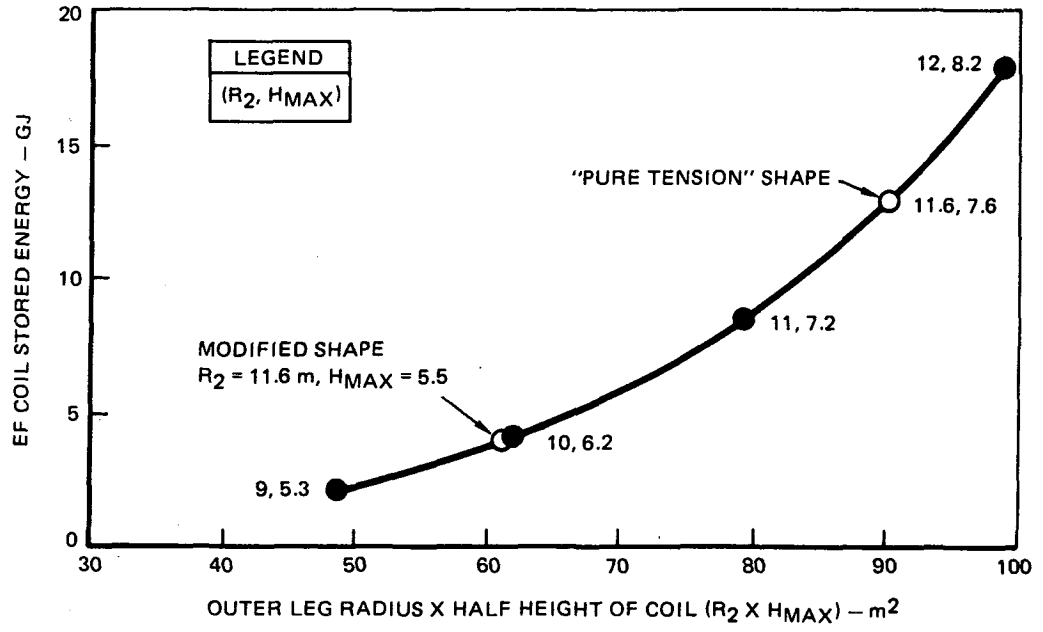

Figure 8-11. EF coil stored energy.

had to utilize a fatigue limited stress of 114 mpa (16.6 ksi). It was assumed that 82 percent of the overturning moment (10) was taken in the outer leg of the TF coil and that the inner leg would be keyed to the center post.

The intracoil beam (see Fig. 8-5) was sized to give approximately the same moment of inertia as the outer TF coil leg and found to require a 1.2 m X 1.8 m solid area. This size was then replaced with a more practical built up grid of structural elements. The grid elements extend from either side of the TF coil case and are pinned to adjacent coil structures through a dielectric clevis joint between coils (see Fig. 8-5). This joint permits removal and replacement of any TF coil without cutting and welding the basic structure.

The preliminary sizing work is felt to establish feasibility of this concept based on the substantial background provided by the FED and INTOR work.

Vacuum Tank - The TF, EF and CF coils are enclosed in a common vacuum tank which consists of a top panel, a lower enclosure and eight segmented outer panels. An isometric was shown in Fig. 8-2. Local compression support struts are provided to isolate the flat room temperature vacuum tank cover from the 4°K coil case. The common vacuum tank approach was selected to minimize the heat leak and simplify TF coil replacement.

The top of the TF coil dewar is designed as a flat panel grid structure to save in overall building height. Each 1 meter in height is equivalent to ~ $3M in savings on the building cost. The atmospheric loads are supported with local G-10 fiberglass support rods. The total atmospheric load on the dome is ~ 300,000 kg of force which can be reacted through ~ 750 cm^2 of G-10 fiberglass with a total heat leak of ~ 3 watts through ~ 1m long struts. This loss of 4°K cooling can be readily offset for less than the savings in building costs. Selection of the plasma vacuum boundary location is discussed in Section 8.3.4.

8.3.2 Poloidal Coil Systems

The poloidal coil systems consist of the Equilibrium Field (EF) coils, and Control Field (CF) coils. The EF coils provide the field which maintains the plasma at equilibrium with the desired shape, position and current profile. The EF coils are superconducting and are located outside the TF coils to avoid the need for in-situ winding. The EF coils are supported directly to the 4°K TF coil structure to simplify the thermal isolation support for the EF coils. The CF coils are located inside the TF coils. They are normal conducting coils that include segments to permit removal and replacement. These coils are closer to the plasma so they can respond to plasma motion more quickly and without the excessive power demands that would be required of the EF coil system. The CF coil design has been taken from STARFIRE (5).

EF Coils - The analyses utilized the least squares method for fitting to the external field that is required for MHD equilibrium and for minimizing the EF coil stored energy. The EF coils were designed to be located ~ 1m away from the TF coils and outside of the shaded areas in Fig. 8-12 which represent the access requirement of blanket sector installation, the vacuum duct and the center-post. The ~ 1m gap between TF and EF coils has been shown (11) to reduce the overturning moments significantly. Independent of the locations of the other coils, the outboard coil leads to lower stored energy if it is closer to the midplane than access permits. The difference between the points labeled s and u corresponds to ~ 1 GJ. The major radius of the outer coil was also varied to determine the effect on stored energy. Radii of 11.5, 12.4 and 13.0m resulted in stored energies of 4.78, 5.16 and 5.66 GJ's, respectively.

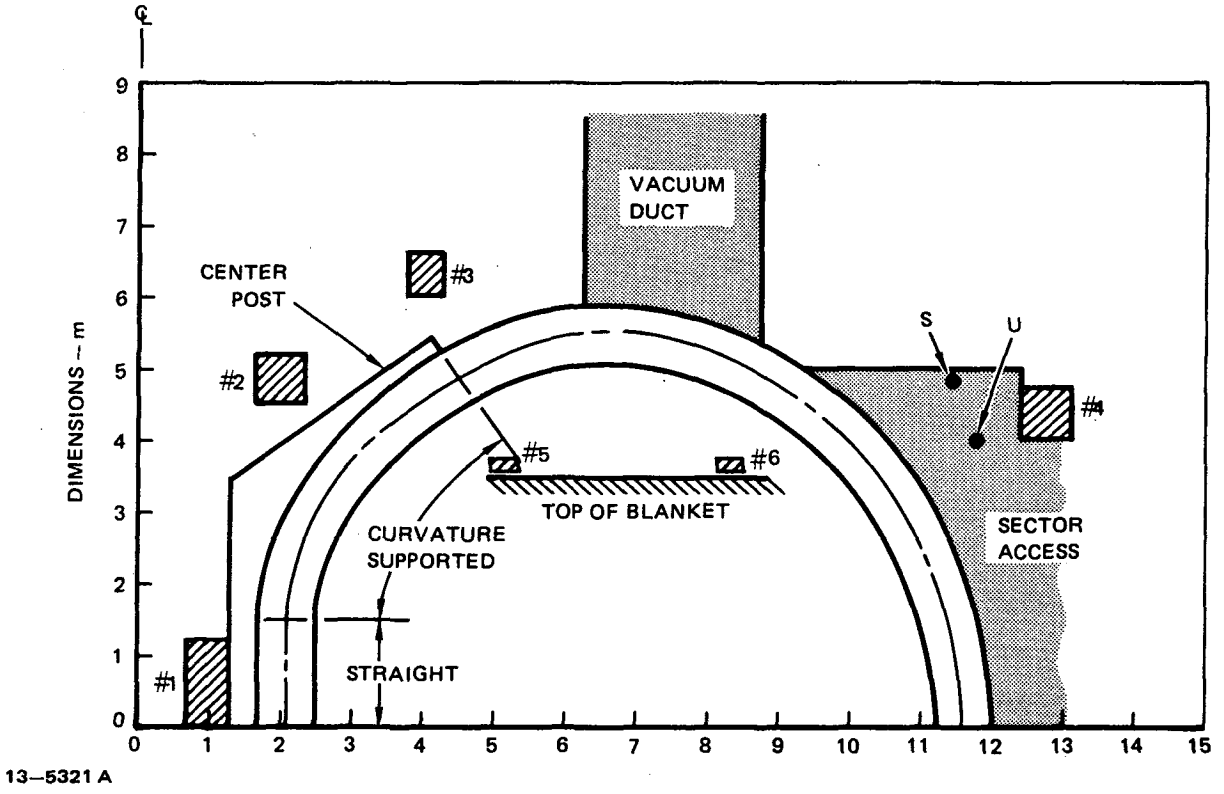

Figure 8-12. EF coil locations and constraints.

The use of the large inboard coil (#1) helps offset the energy requirements of locating the outboard coils above and below the access envelope. If necessary a design could be obtained, however, with no inboard EF coils. The coils in the upper corner (#2 and #3) are not sensitive as to their placement, but only to the rough net current near this location. Replacing them by a single coil costs ~ .2 GJ, however.

The coil locations and sizes are shown in Table 8-3. These locations are shown in Fig. 8-12. A summary of the system parameters is given in Table 8-4. Plots of the resulting field are shown in Fig. 8-13. These fields were used for determining the overturning forces on the TF coil.

The EF coils, especially the coil indicated #4 in Table 8-3, experience non-axisymmetric forces from the fringe field of the TF coils. As there are only TF coils, the fringe field and the force it produces might be expected to be large. In fact, these periodic forces are found to be an order of magnitude lower than those acting on the largest EF coil the FED design. Part of

Table 8-3. DEMO EF Coil Locations

Coil No.	Coil Location		Coil Cross Section		Current
	R (m)	Z (m)	ΔR (m)	ΔZ (m)	I (MA)
1	1.00	0.60	0.60	1.20	-12.67
2	2.00	4.82	0.73	0.73	9.55
3	4.00	6.32	0.57	0.57	3.65
4	13.00	4.40	0.70	0.70	-8.20

Table 8-4. System Parameters

System	Stored Energy (GJ)	Current (MAT)	Volume* (m^3)	Volt-Sec To Plasma (V-S)
EF	5.66	68.1	109.0	-41.5
Plasma	0.43	9.0	-	-

*Current Density ~17.6 MA/m^2

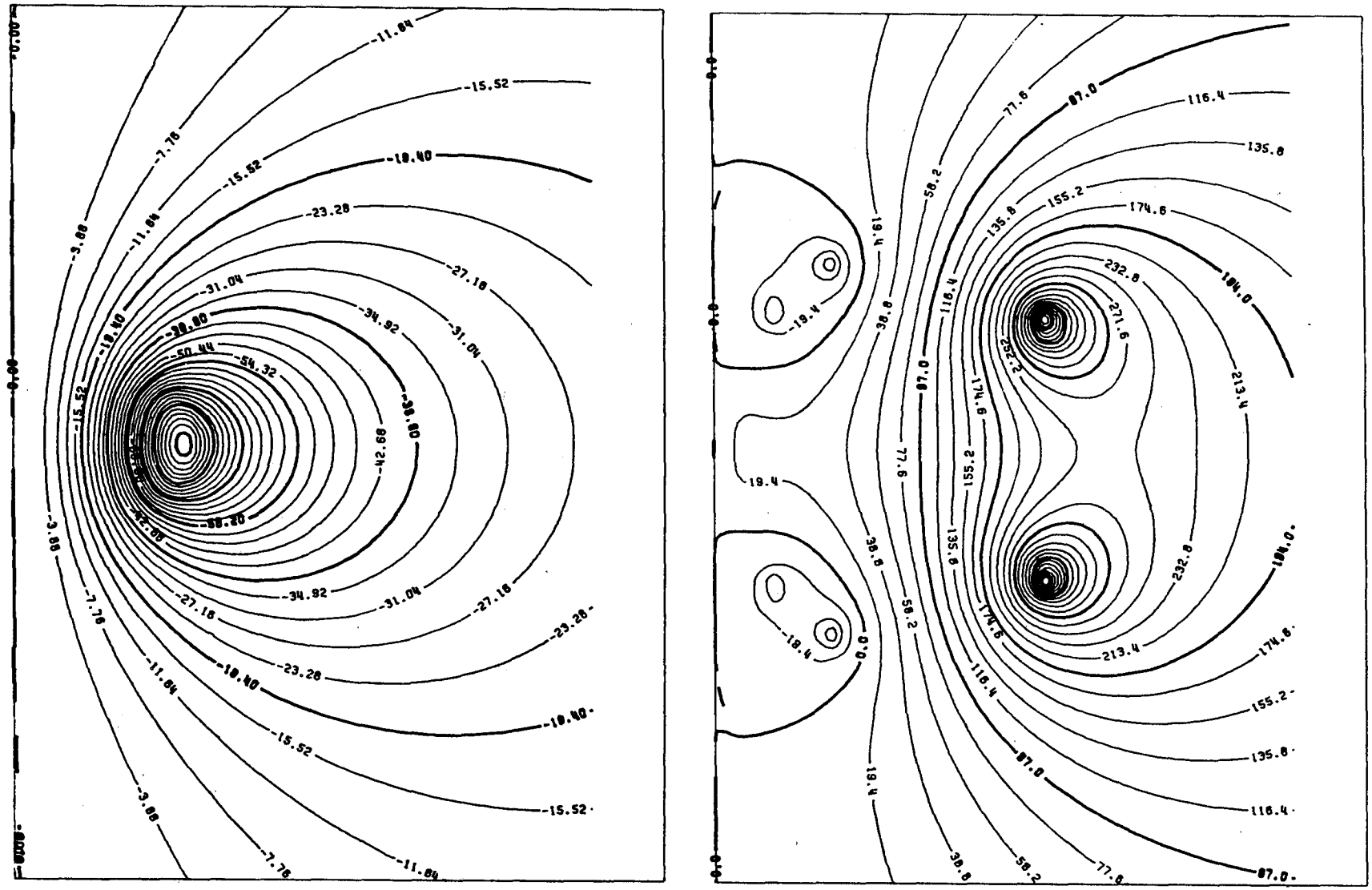

a) Plasma Field

b) EF Field

Figure 8-13. Magnetic field plots.

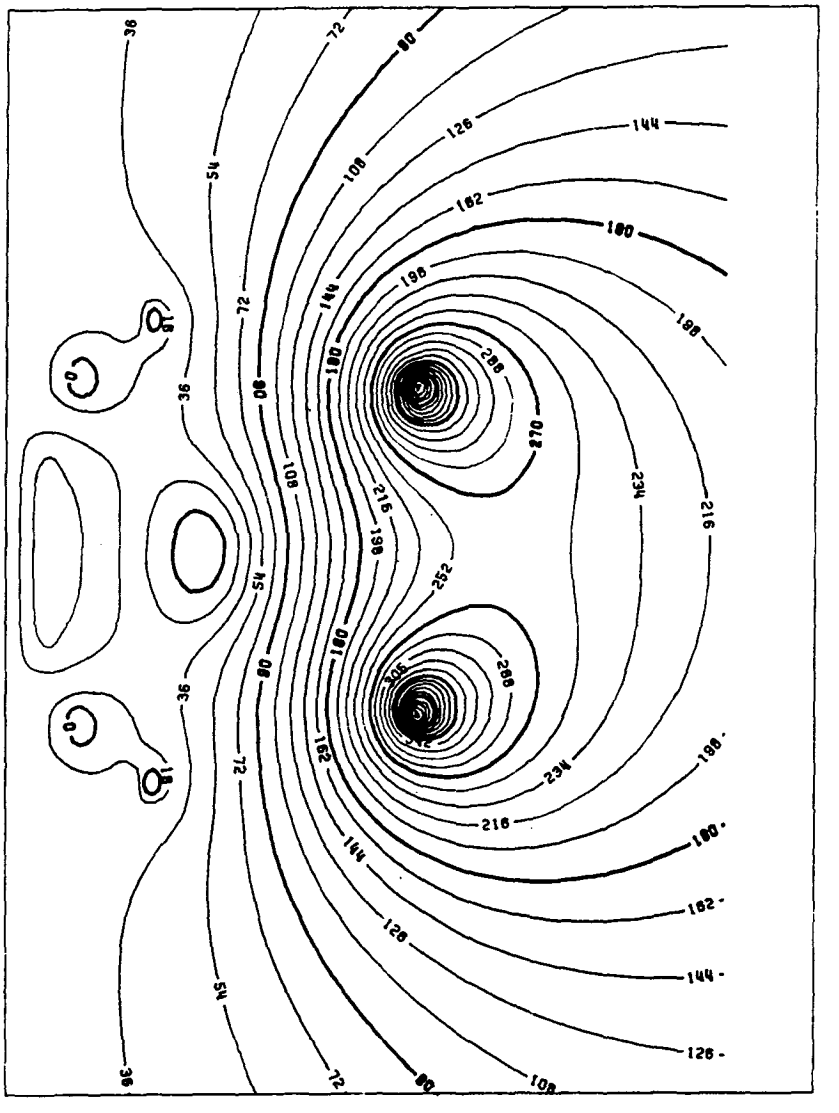

c) Total Field

Figure 8-13. Magnetic field plots (continued).

the difference is that the currents in the FED design are larger by a factor of two or three. The rest of the difference arises because the greater separation between TF and EF coils in DEMO more than compensates for the reduced number of coils (eight for DEMO, ten for FED).

The forces of the TF coils on EF coil #4 are periodic, with a 45 degree period. As shown in Fig. 8-14, the axial and radial forces peak at 0.36 and 0.31 MN/m, respectively, and vary almost sinusoidally with angle. These forces produce bending moments; the axisymmetric forces that the EF coils exert on each other do not.

Correction Field Coils

The correction field coils for DEMO were scaled from STARFIRE (5) based on a ratio of the EF coil currents of 85.5 MAT for STARFIRE and 68.1 MAT for DEMO. A current density of 4 MA/m^2 was used to size the coils. The coil locations were shown in Fig. 8-12. A tabulation of the parameters and calculated values for the system are shown in Table 8-5.

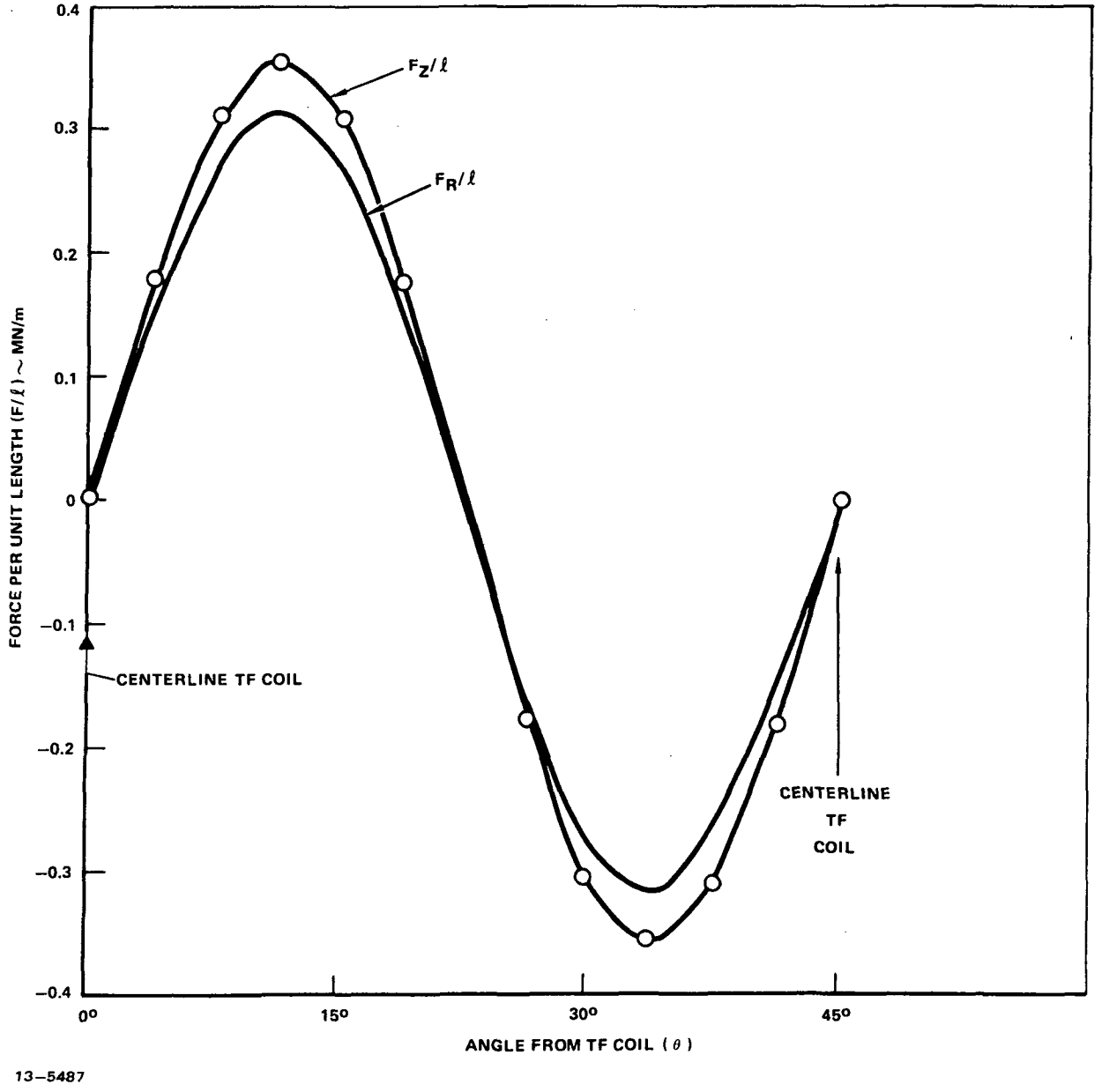

Figure 8-14. Periodic forces on DEMO outer EF coil due to fringe field from TF coils.

Table 8-5. Correction Coil (CF) Parameters

	Coil #5	Coil #6
Coil current (MA)	-0.16	-0.2
Coil current (MA/m^2)	4	4
Coil Area (m^2)	0.04	0.072
Coil cross section height (m)	0.2	0.2
Coil cross section width (m)	0.2	0.36
Equivalent coil minor radius (m)	0.113	0.151
Coil distance from midplane (m)	3.75	3.75
Coil major radius (m)	4.2	8.37
Inductance (μH)	43.2	101
Total CF coil system stored energy (MJ)	2.97	
Total CF coil system volume (m^3)	9.65	
Total CF coil current (MAT)	0.72	

The power supply for the CF coils was sized by determining the time constant of the first wall. The first wall was taken as a 10 mm Be coating over 8.2 mm effective thickness stainless steel wall. This coating is not a part of the reference design. The total wall resistance was calcualted as 9.97 μΩ and the wall inductance was determined to be 1.84 μH. These parameters result in a time constant of 184 ms for the wall.

A stored energy of 2.97 MJ and time constant of 0.184 sec results in a 16.14 MW power supply. The selected power supply is:

ENERGY STORAGE CAPACITY: 3 MJ

CONVERTOR-INVERTOR CAPACITY: 17 MW

These calculations assume a continuous conducting first wall is provided by the use of intersector connectors. If they are not provided the time constant would be substantially reduced and result in an increase int he power supply requirements.

8.3.3 Out-of-Plane Forces and Overturning Moments

The support of a TF coil system against out-of-plane forces from the poloidal field (PF) coils is one of the most serious problems encountered in a tokamak reactor design. It has caused great problems in the INTOR and FED design studies, particularly because of fatigue problems in those two reactors, which are designed for a lifetime of the order of one million pulses. Similar considerations arise in the DEMO design although steady state operation minimizes the concern. The overturning moment on each DEMO TF coil, from the PF coils, is calculated to be 805 MN-m. Table 8-6 compares the overturning moments of several recent reactor designs. Note that the DEMO numbers are small only in comparison with the other studies.

Table 8-6. Comparison of Overturning Moments

Reactor Design	Moment per Coil (MN-m)	Moment per Coil Normalized to 8 coils (MN-m)
DEMO	805	805
FED	620	775
STARFIRE	1500	2250
Wildcat (DD)	3900	5850

Figure 8-15 shows the distribution of bending moment along the TF coil circumference. It can be seen that most of the moment is contributed by the upper (and lower) portion of the coil, and that the smaller moments acting on the inner and outer legs cancel only a small fraction (18%) of the moment.

8.3.4 First Wall/Blanket/Shield (FW/B/S) Configuration

The design philosophy that has been adopted for the first wall/blanket/shield is as listed below:

- Complete sector removal
- Remove and replace coolant joints outside the vacuum boundary
- Flat seals (planar)
- Mechanical seals for scheduled replacement items
- Weld seals for life-of-plant components.

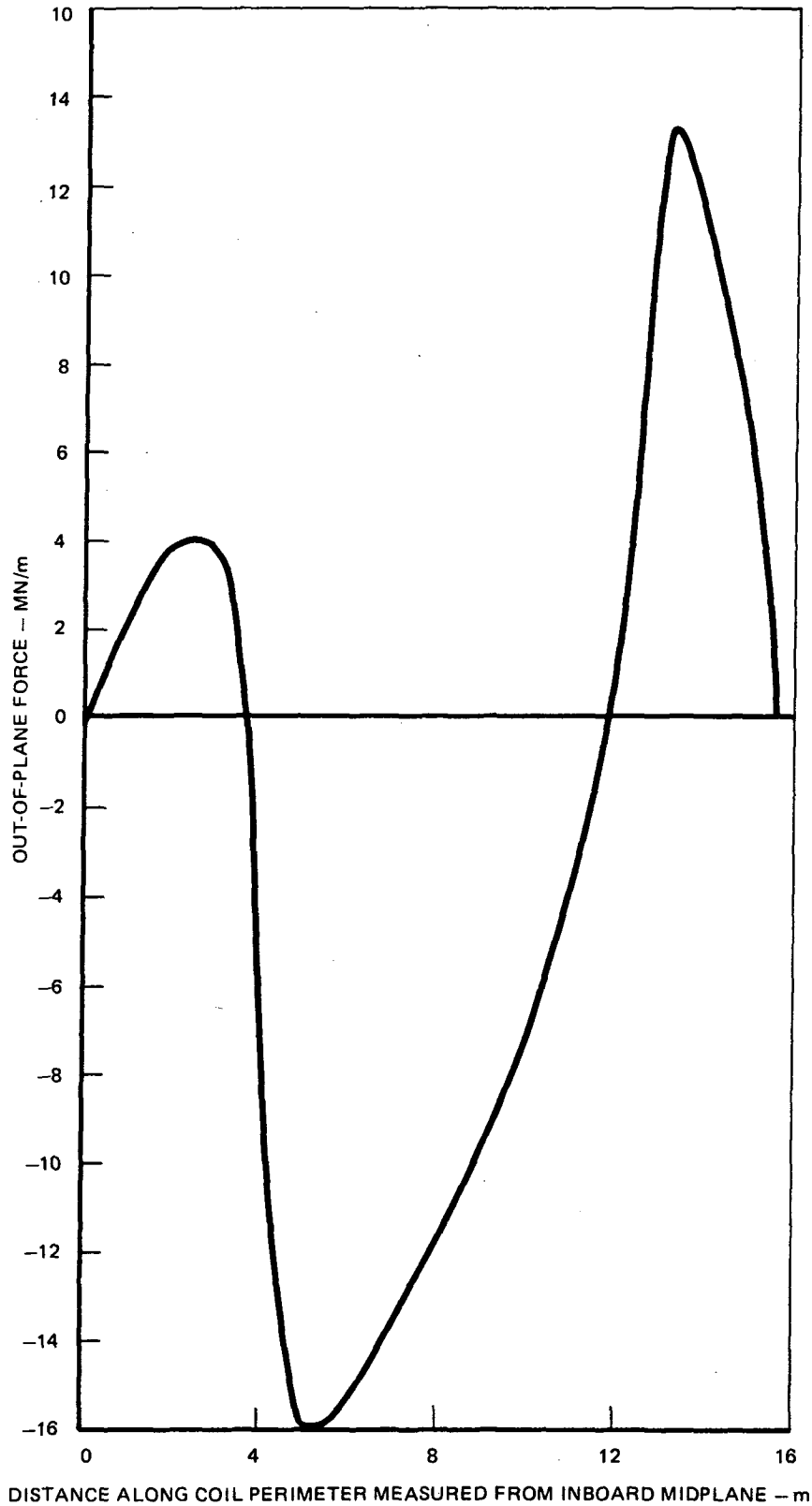

Figure 8-15. Out-of-plane distribution on TF coil.

It is generally accepted that sector removal of the FW/B/S is superior to in-situ repair (6). The logic is that removal and replacement of large sectors can be done more rapidly and with simplier maintenance equipment than with in-situ maintenance. With in-situ maintenance, many more maintenance operations must be performed before the plant can be restarted. With sector-removal, repair can be made in the hot cell while the plant is operating. Secondly, the hot cell repair will provide greater access and more elaborate maintenance equipment. The limiter and current drive antenna can be removed without removing the blanket sector.

The blanket and shield are made in sectors; however, most of the shield remains in place during blanket removal to minimize the weight of the removed sector and to minimize the shield gap size that would be required for rapid replacement. The blanket sector consists of the blanket, some outboard shielding and a vacuum door that is removed as an integral part. Blanket modules are replaced in the blanket sector shield door structure in the hot cell. The shield sector (Fig. 8-3) incorporates a seal frame at the blanket access opening to provide a continuous seal flange surface.

Vertical structural support of the blanket and shield is provided by the vacuum duct shielding. Lateral support for seismic events is provided by a bridge panel from the floor to the shield.

All coolant line disconnects have been located outside the plasma vacuum boundary to avoid the need for leak-free pressurized coolant ducts. Welded leak-free joints inside the vacuum chamber have the disadvantages of (1) contamination during weld preparation and welding and of requiring rewelding of irradiated material to virgin material during replacement; (2) welded joints require more time for replacement than mechanized joints. Leak-free mechanical joints for a pressurized coolant inside a vacuum are even more difficult to achieve than atmosphere to vacuum. The only vacuum tight disconnects that are normally opened for maintenance are atmosphere-to-vacuum at the vacuum pumps and valves, current drive antenna, limiter, sector door and fueling mechanism.

Mechanical seals have been selected for all scheduled replacement items. An ethylene-propylene elastomer seal has been chosen for all mechanical seals based on STARFIRE (5). Table 8-7 shows a comparison of the options

including welded seals. All mechanical seals have been kept in a single plane to minimize the difficulties of providing a uniform clampup force on the seal and minimizing tolerance requirements between mating parts.

An advantage of the elastomer seal is the ease of obtaining an initial seal; however, it has two limitations; bakeout temperature, and radiation damage resistance. Bakeout temperature requirements of ~ 150°C are considered the most serious limitation in DEMO. Because of its developmental nature, DEMO is expected to have many outages and require frequent breech of the vacuum. As a result, a system which can be baked to modest temperatures is desirable to minimize start-up time. Currently, it is planned to provide bakeout to the system while actively cooling the elastomer seal flange. Potentially glow discharge cleaning offers an alternative to heating and should be considered further. Elastomers are susceptible to radiation damage but STARFIRE neutronics calculations (7) have shown that doses can be maintained at acceptable levels when seals are located outside of the shield. The low partial pressures of tritium are not expected to seriously degrade the seals (8). Seals in DEMO are located at the shield exterior and also have acceptable radiation levels. High frequency 35 GHz microwaves have also been shown to cause excessive heating in elastomer seals in EBT-S (9). The REB launchers or the 82 MHZ fast wave current antennas do not pose this problem.

Metal seals are acceptable from all standpoints except they are generally very susceptible to physical damage (e.g. scratches), require extreme care to effect a seal repeatability, and have limited reuse capability.

Welded seals have been selected for all life-of-plant components. These components are those where replacement capability is provided but where replacement is not planned unless they fail. Welded seals offer the advantage of radiation resistance and reliability once they have been made and verified. In event replacement is required, more time can be allocated for remaking these seals. All shield sector seal welds have been made in a single plane. Triple point seal welds have been avoided in replacement of shield sectors. These occur when a weld must cross or butt to another weld. These welds create close fit up requirements, permit little motion, and require welding around square corners.

Table 8-7. Sealing Methods

	Repeatability	Rad. Damage Limit	Ease of Sealing	Bakeout	Durability
Elastomer	Many times	Least ($\sim 10^8$ rad.)	Most repeatable	$\sim$ 150°C	Least
Metal	1-2 times	$> 10^{10}$ rad.	Requires careful surface finish and clampup	> 300°C	Least
Welded	5-10 times	Greatest ($> 10^{10}$ rad.)	Requires closely controlled weld prep.	$\sim$ 400°C	Greatest

Selection of Number of Sectors

Three primary options considered in selecting the number of sectors and method of removing the large sectors are shown schematically in Fig. 8-16. Option A requires use of one sector per TF coil and has been used in FED and INTOR and has been selected for use in DEMO. Option B was used in the STARFIRE design. With option C composite sectors consisting of the blanket sector and outboard shielding are used. This design requires one sector be located under the TF coil and one sector between TF coils which increases the difficulty of sealing between sectors.

Our comparison will develop the rationale for selecting Option A over the other two concepts. The three key considerations in the rationale are as follows. First it is believed that sector weight and size (within a factor of two) will have little impact on the time required for component removal/replacement. Second it is believed that the number of connections made to reactor components will directly affect the time required for replacement. Third, the failure rates of the first wall and limiters are expected to be the same regardless of the number of components but the failure rate of connections and maintenance equipment is sensitive to the number of components.

The STARFIRE concept (Column B) was derived because of the perceived impact of stored energy on the overall system. STARFIRE utilized a "pure-tension" magnet per the Moses and Young criteria (12) and resulted in relatively tall magnets for an outer leg radius large enough to replace a single sector/TF coil. DEMO has decreased the TF coil height by modifying the TF coil shape (see paragraph 8.3.1.3) and minimized the amount of stored energy.

The third option shown in Column C is deemed feasible only if a triple point seal can be used. A radial view looking in at adjacent sectors is shown in Fig. 8-17. Two things are evident. The limiter cannot be removed from the sector under the TF coil without removing the other limiter and numerous triple point seals are required. Triple point seals require very close fit up during installation and can likely be accomplished only by welding. The problems of developing a triple point seal weld are expected to be difficult. As a result, this option was not pursued.

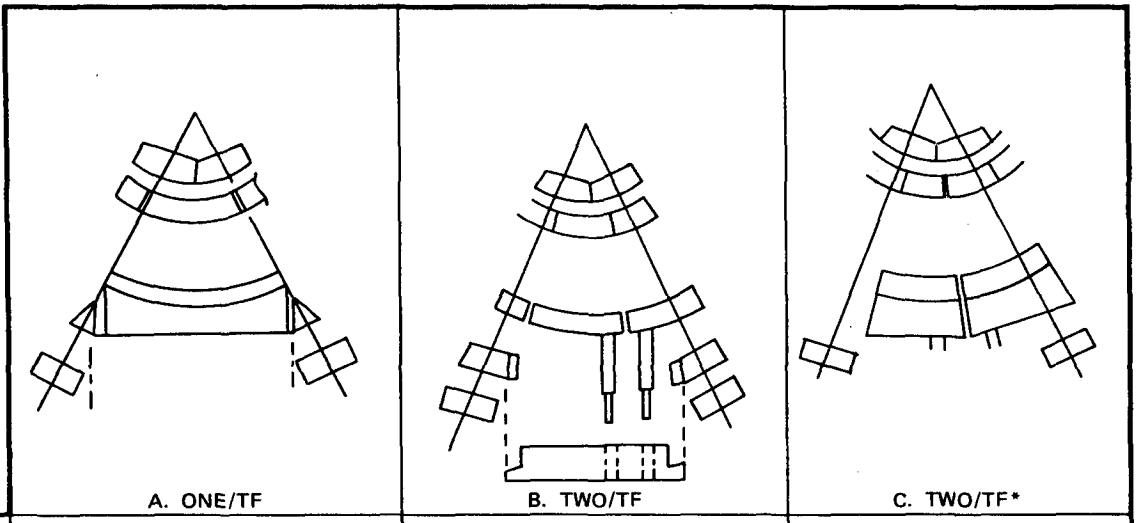

	A. ONE/TF	B. TWO/TF	C. TWO/TF*
NUMBER OF LARGE REMOVABLE PARTS	1	3	2
NUMBER OF CONNECTIONS/TF COIL	14	~ 30	~ 28
LIMITER	6 (BKT MODULE)	4	12
SHIELD	2	2	4
BLANKET (COOLANT & TRITIUM PURGE)	4	8	8
VACUUM BOUNDARY SEALS	2	16 (INCLUDES 14 CONNEC. PENE.)	4
REMOVAL DIRECTION	RADIAL	RADIAL + TRANSLATION	RADIAL + TRANSLATION
TF COIL OUTER LEG RADIUS	~11.6 m	~ 9.5 m	~ 9.5 m
LIMITER REPLACEMENT	INDEPENDENT	AFTER SECTOR REMOVAL	SEQUENCED LIMITER REMOVAL
STORED ENERGY	5 GJ MODIFIED PURE TENSION TF	2-3 GJ	2-3 GJ
			*REQUIRES TRIPLE POINT SEALS WHICH MAY BE UNRELIABLE AND TAKE A DISPROPORTIONATE AMOUNT OF TIME TO REPLACE

13–5324

Figure 8-16. One blanket sector per TF coil is preferred.

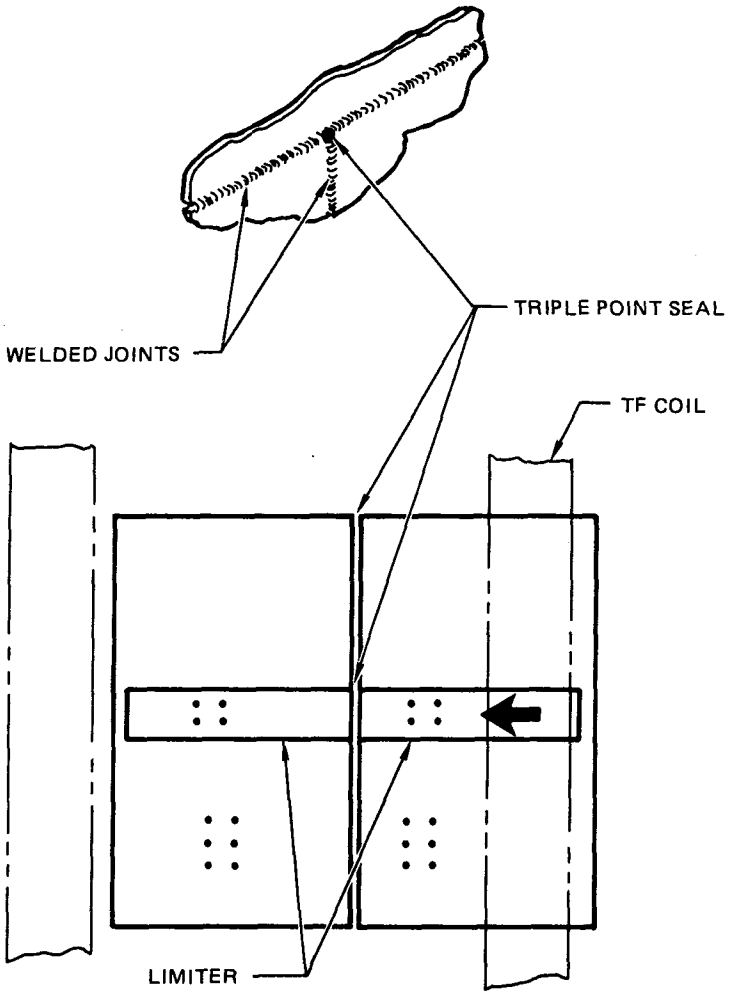

Figure 8-17. Two sector per TF coil option with triple point seals.

A comparison of the changeout times and failure rates for the three options are given in Table 8-8. The number of steps required in sector change out is a minimum for the one sector per TF coil, and it requires ~ 1/2 as long for replacement as the other two options. A comparison of the relative failure rates is made by assigning failure rates of Y and Z to components used in concept A. The total failure rate of concept A is taken as X. If the failure rate is dominated by the first wall or components such as the limiter, then the overall failure rate of the alternative approaches will be equal. If, however, the failures are dominated by connections or replacement equipment then concept B and C can have a failure rate two times as large as concept A. The true failure rate is likely to be somewhere in between.

Table 8-8. Blanket Removal Changeout Steps

A. One Sector/TF		B. Two Sectors/TF		C. Two Sectors/TF	
0. Shutdown	24 hrs	Shutdown	24 hrs	Shutdown	24 hrs
1. Disconnect 28 Connections	28 hrs	Disconnect 60 Connections	60 hrs	Disconnect 56 Connections	56 hrs
2. Unlatch Door Air to Vac Seal	2 hrs	Disconnect 16 Air to Vac Connections	16 hrs	Cut Door Seal Weld	4 hrs
3. Remove Sector	4 hrs	Remove Shield Door	4 hrs	Remove Sector A	4 hrs
4. Reverse of Above (+50% Time)	48 hrs	Remove Blanket Sector #1	4 hrs	Remove Sector B	6 hrs
5. Startup	24 hrs	Remove Blanket Sector #2	4 hrs	Reverse of Above (+50% Time)	98 hrs
		Reverse of Above (+50% Time)	123 hrs	Startup	24 hrs
		Startup	24 hrs		
Total Time to Replace	∿ 5 days		∿ 10 days		∿ 9 days
Failure Rate					
Wall	Same		Same		Same
Components	Same		Same		Same
Seal Components	Y		2Y		2Y
Removal Process Equip.	Z		3Z		3Z
Total Failure Rate	X		X to ∿ 2X		X to ∿ 2X

Based on the above, it is clear that one sector per TF coil offers clear advantages over two sectors per TF coil. The penalties in stored energy of the larger TF coil leg radius do not appear to overwhelm the choice so it is recommended that the DEMO utilize one sector per TF coil. Addition of a divertor would require an increase in the stored energy and needs further assessment.

Dielectric Break Design

The dielectric break in the shield is formed at the outer surface of the shield where the radiation dose level is anticipated to be $<10^9$ RADs based on the STARFIRE (7) analysis. It is expected that the dielectric break will be fabricated as a permanent part of the shield sector, last the life-of-the-plant and be subjected to bakeout heat loads only. The dielectric break design is shown in Fig. 8-18. It consists of dual metal spring seals that are coated with polyimide (*). The concentric seals provide the dielectric break and vacuum wall. The seal is bakeable to ~ 300°C and seals more readily than a bare metal seal. It also permits the polyimide to flow somewhat without loss of sealing. The design also incorporates intermediate vacuum pumping so it is tolerant of some leakage.

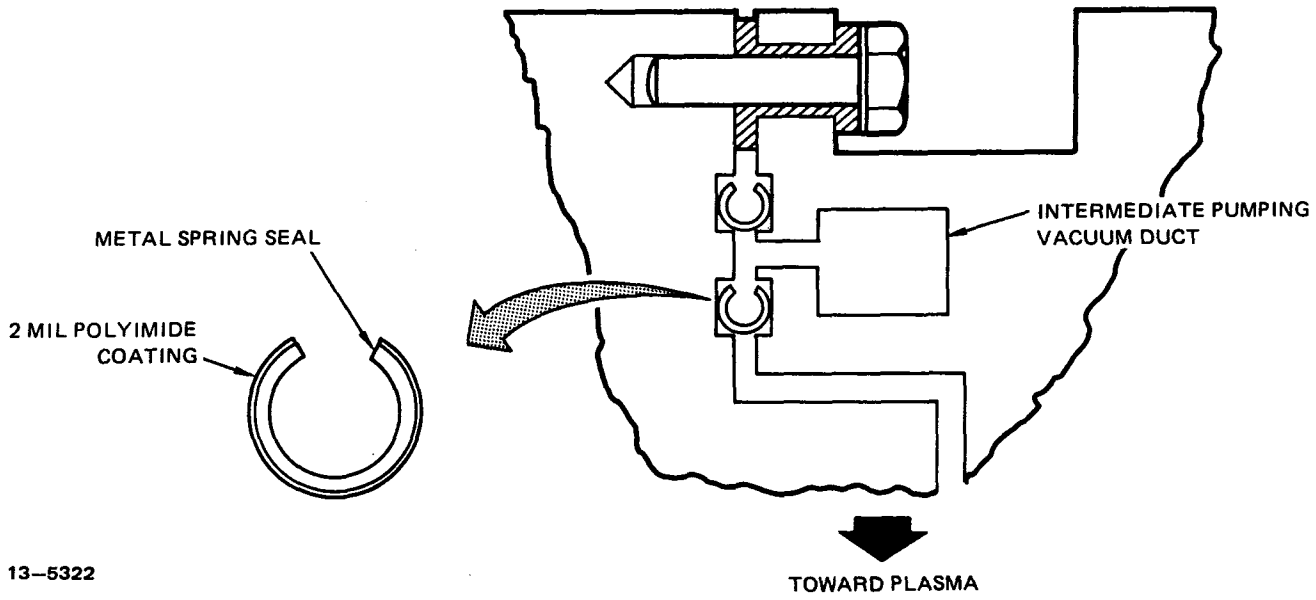

Figure 8-18. Dielectric break design.

Vacuum Boundary Location

Primary options considered for the plasma chamber vacuum boundary were locations at the shield, at the interior surface of the TF coil vacuum tank, and a combined but separate plasma and TF coil vacuum chamber. The concepts are shown in Fig. 8-19. Key considerations in the comparison are given in Table 8-9.

An advantage of combining the TF coil common vacuum tank with the plasma chamber vacuum boundary is that it can potentially simplify the reactor design by eliminating the need for seals and dielectric breaks between shield sectors and can permit limited operation with a leak between the TF coil and plasma chamber volumes. The wall between the TF coil and plasma chamber volumes is required to avoid the need for TF coil warm up when the plasma volume is opened.

Disadvantages of the common TF coil vacuum tank and plasma chamber wall (Fig. 8-19 a & b) are a severe complication in the TF coil replacement process, increased volume and surface areas, and complications in the bakeout process. An added complication is the potential for arcing of the control coils that would be located in the vacuum.

(*) MDAC proprietary.

Table 8-9. Vacuum Boundary Location Options

	At TF Coil	At Shield Interior	Combined
Pumped Volume	$\sim$ 1100 m^3	$\sim$ 300 m^3	$\sim$ 300 m^3
Exposed Surface Area	$\sim$ 4400 m^2	$\sim$ 1500 m^2	$\sim$ 1500 m^2
Bakeout		Reduced Thermal Stresses	Thermal stresses can be decoupled with a flexible flange
Leakage-In Door	Forced Outage	Forced Outage	
Leakage-In Other Areas	Continued Operation	Forced Outage	Continued Operation
Trim Coil Operation	Operation in Vacuum	Operation in Air	Operation in Vacuum
TF Coil Replacement	Complex Vacuum Tank cutting/welding	Complex vacuum Tank cutting/welding	Simplified vacuum Tank cutting/welding

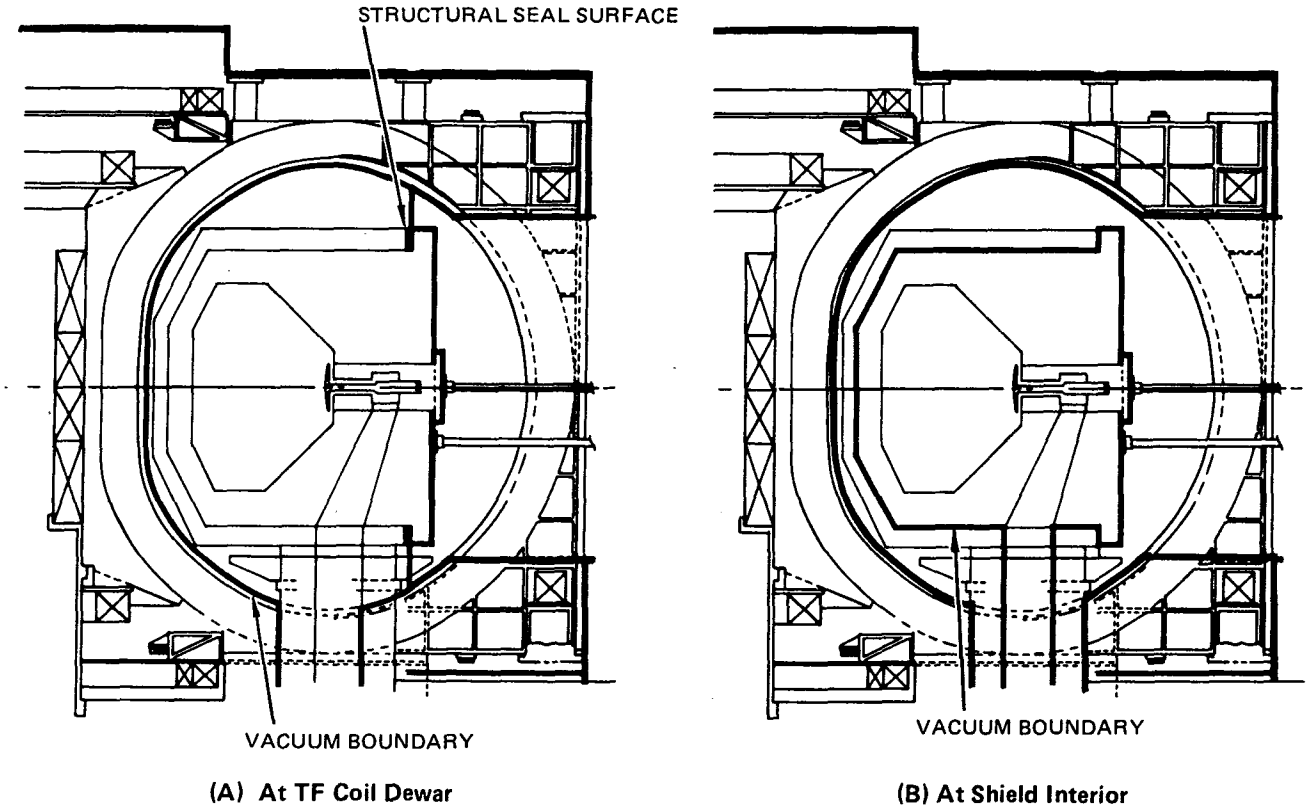

Figure 8-19. Vacuum boundary location options.

Removal of a TF coil in either of the above designs will require a structural joint at the common vacuum tank near the inner TF coil leg, that must be cut and rewelded remotely to replace a TF coil. Although this may be feasible, no concepts for readily accomplishing it are apparent.

The combined but separate plasma and TF coil vacuum tank option (Fig. 8-19c) provides several advantages over either of the above options which include:

- Reduced inner blanket shield thickness
- Simplified TF coil vacuum tank cuttings.

The inner blanket shield thickness is reduced by ~ 8 cm by the elimination of the TF coil common dewar. This results in a savings of ~ $40m in reactor capitol cost due to a decrease in reactor size. The TF coil replacement is simplified because the TF coil vacuum tank cutting and rewelding is limited to a near planar surface that is accessable. A further comparison of vacuum tank options performed for INTOR (20) also confirmed the finding that a combined but separate vacuum tank is advantageous.

DEMO has chosen the combined but separate vacuum boundary of Fig. 8-19c. Additionally the reference design has extended the TF coil vacuum tank to enclose the outer EF coils to eliminate the need for the cold to warm supports.

Intrasector Connector

The use of individually replaceable blanket sectors requires a conducting shell near the first wall. This shell provides stabilization to the plasma by permitting image currents to be created by any plasma motion and reduces the demands on the control (CF) coil system. The intrasector connector must be located near the plasma to reduce the electromagnetic forces that are generated on the blanket walls as the currents flow radially to the connectors and to prevent arcing. Additionally these connectors must be capable of carrying the full plasma current during a disruption until it decays in the blanket.

Investigation for FED (13) disclosed several connector options. Of these three are selected for consideration here. The concepts are shown in Fig. 8-20. Each must permit ~1cm of change in the gaps between blanket sectors due to thermal growth.

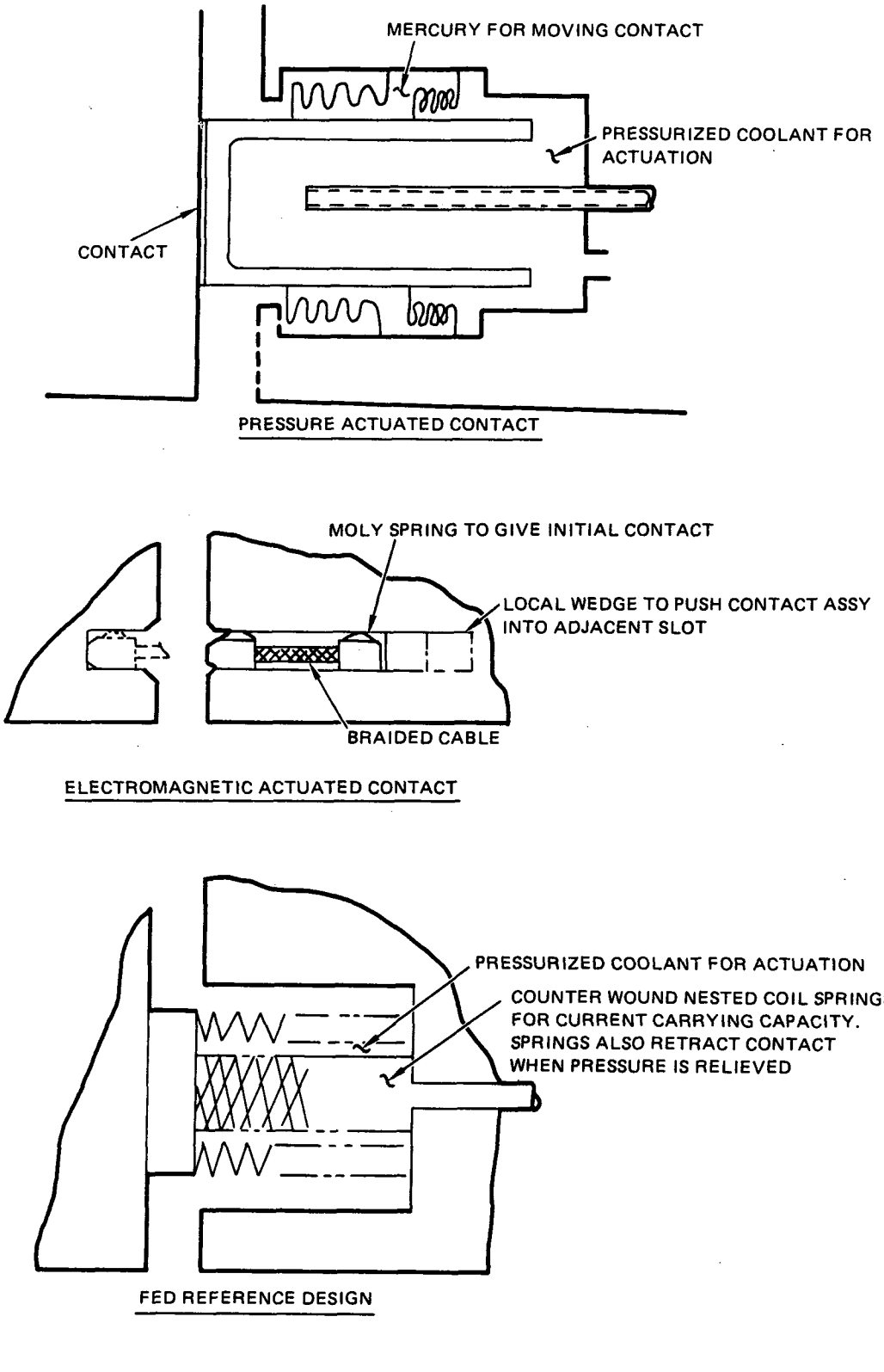

Figure 8-20. Intersector connector.

Any of the three options are acceptable to DEMO. Uncertainities in the design include the current-carrying capacity of the contacts in vacuum and the contact pressures required to avoid contact welding. Options such as sacrificial carbon arc pads were not considered in DEMO because of the volumes of material that would be vaporized and the uncertainty of where the arc would strike.

8.4 Vacuum Pumping System

The vacuum pumping system consists of eight cryosorption pumps located in the reactor building basement. Four of these pumps operate continuously while the other four are regenerated. Each pump can be isolated from the plasma chamber by use of a gate valve. Redundant gate valves are provided so operation can continue after a single valve failure.

Liquid pool cryopumps are seen as the best choice for the DEMO reactor. Two advantages of such pumps are their very high pumping speeds and their cleanliness. Capture probabilities for helium as high as 0.2 have already been achieved, and there remains potential for improvement. Possible pathways by which hydrocarbons or other contaminants could reach the plasma are eliminated, since such cryopumps have no working fluids or moveable parts. They are reliable and low cost. The thermal shielding they require does not present a major obstacle and they are compatible with the magnetic fusion environment. Although they require regeneration, this process can be combined with fuel gas recovery operations.

The required pumping speed of the system is 3.2×10^{20} atoms/sec of helium and 4×10^{21} molecules/sec of deuterium and tritium (see Chapter 5). This gas load is compatible with the use of cryosorption pumps.

The gases are pumped through a limiter slot, through the blanket, into a plenum and then into circular ducts to the pump as shown in Fig. 8-21. The total conductance of the limiter slots is 8.2×10^5 ℓ/sec. The slot extends from the leading edge of the limiter to the limiter stem where incoming particles impact the surface. The rest of the vacuum pumping system from the limiter stem through the vacuum pump has a conductance of 2.0×10^5 ℓ/sec if eight pumps are operating and a conductance of 1.1×10^5 ℓ/sec if four pumps

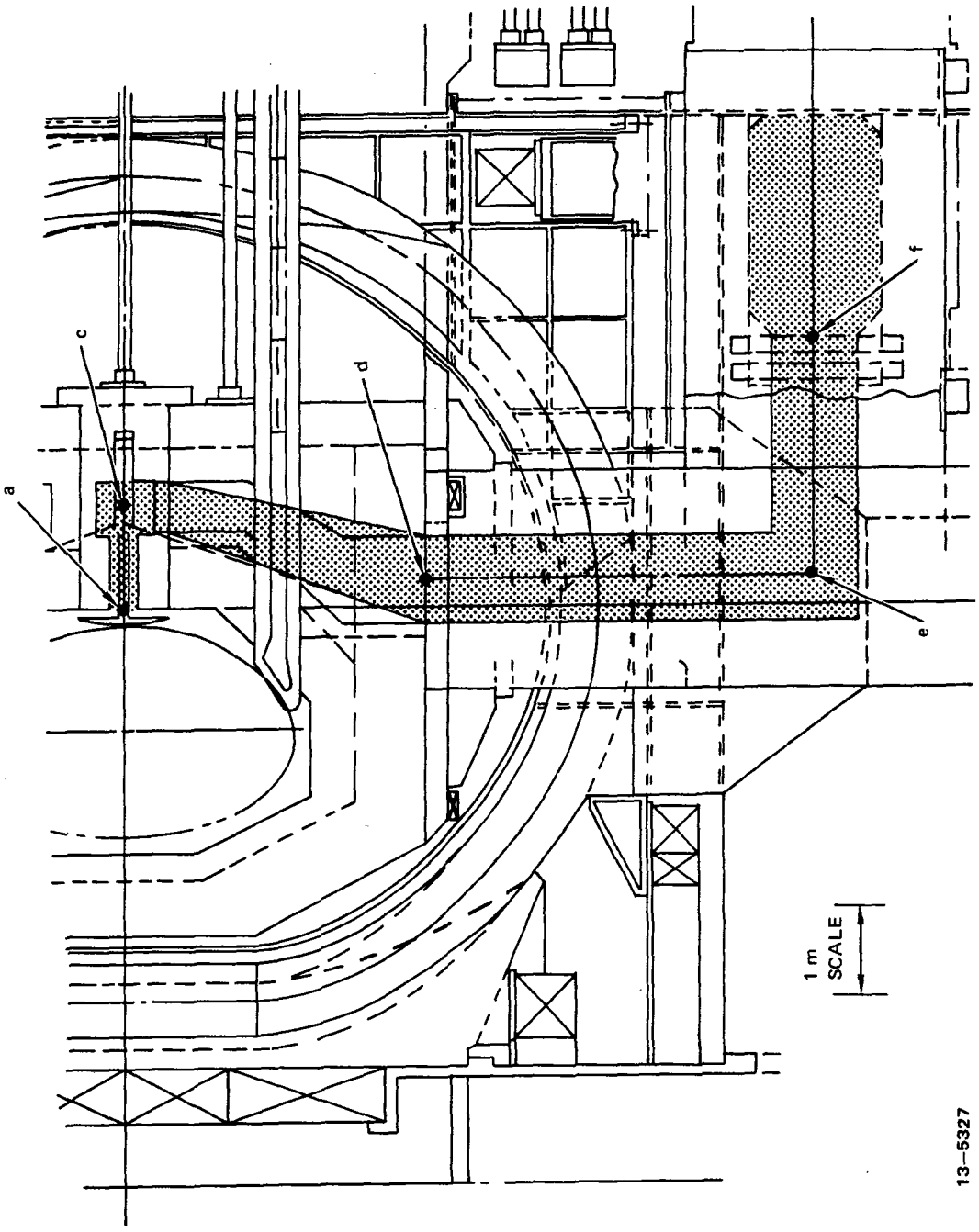

Figure 8-21. Vacuum pumping system.

are in operation. As a result the ratio of system conductance to slot conductance (γ) is:

8 pumps operating: $\gamma = 4.1$

4 pumps operating: $\gamma = 7.4$

A decrease in the duct diameter from 1.2m to 1.0m in the area from points d to f of Fig. 8-21 would increase γ to 5.8 for eight pumps operating. A 1.4m diameter duct would provide a γ of 3.1.

8.4.1 Vacuum Pump Location

The vacuum pumps were located in the reactor building basement where they could be maintained independent of the basic reactor. For conductance improvement it was desired to locate the pumps as close to the plasma as possible. Mechanical constraints imposed by the TF coils limit the pumps to ~ 3.5m below the blanket as shown in Fig. 8-21.

The allowable nuclear heating rates in the cryosorption pump was determined utilizing the work of Fisher and Watson (14). They show a critical surface heat load of 2.3×10^{-2} watts on a 320 cm^2 cryo panel. For an equivalent panel of 0.3 cm thickness this corresponds to 2.2×10^{-4} w/cm^3. A margin of safety of 2 should be included on this design and therefore a heating rate of ~ 4×10^{-4} w/cm^3 is deemed acceptable.

Scaling of the STARFIRE nuclear heating rates (7) indicates that this heating rate will occur when the pump is approximately 5.5m from the inside of this shield without bends in the duct. A single bend was put in the duct to prevent the pump from requiring a deeper reactor building basement. The bend also reduces the nuclear heating by approximately a factor of ten (7). The anticipated heating rate in the pump is expected to be $< 10^{-5}$ w/cm^3.

Pump locations at the top and side of the reactor were considered prior to selection of the basement location. Pumps on the side of the reactor provide direct access by maintenance equipment but must be removed for blanket replacement and may interfere with movement of other maintenance equipment. Pumps at the top of the reactor provide a maximum access for maintenance but interfere with simultaneous maintenance of other components.

8.4.2 Conductance Analysis

Slot Conductance - Each limiter slot has the form of a cylindrical annulus. To calculate its conductance, molecular flow was assumed. The slot was treated as equivalent to a tube of the same length but of rectangular cross section. The wide dimension a of this cross section is equal to the first wall circumference while the narrow dimension b is equal to the distance of the limiter from the first wall.

The conductance of such a rectangular tube, under the restriction that a>>b and that a>> the length ℓ, is given by

$$C = 3.638 \sqrt{\frac{T}{M}}\, ab\, \alpha$$

where C is the conductance in liters/sec, a and b are in cm, T is the absolute temperature of the gas at the inlet, and M is its molecular weight. In this expression the factor α is the probability that a given molecule which enters the inlet of the conductance will exit via its outlet, and all the other factors describe the rate at which molecules enter the inlet. It is important to note that this formula is based on the assumption that the molecular velocities at the inlet are randomly directed and have magnitudes in accordance with the temperature T.

Values for the transmission probability α for the tube of rectangular cross section were obtained by linear interpolation from a table in Reference 15, which lists α as a function of the ratio ℓ/b of length to narrowest cross-sectional dimension. Data from this table are shown graphically in Fig. 8-22.

The validity of this procedure was checked by comparing its results with those of Monte Carlo calculations of the transmission probability for the conductance of the annular space between two concentric cylinders. These results are reported in Reference 16. The good agreement between the two sets of results is shown in Table 8-10. Each of the Monte Carlo results in this table was obtained by treating 5000 individual molecules; the maximum standard deviation listed for these figures was 2.2% of the probability shown.

The last row of figures in Table 8-10 corresponds to the dimensions pertinent to the DEMO reactor; first wall radius 680 cm; limiter height 8 cm and length of limiter slot 35 cm. The corresponding transmission probability

REF: NASA sp-105 TABLE 5.6 (PAGE 98)

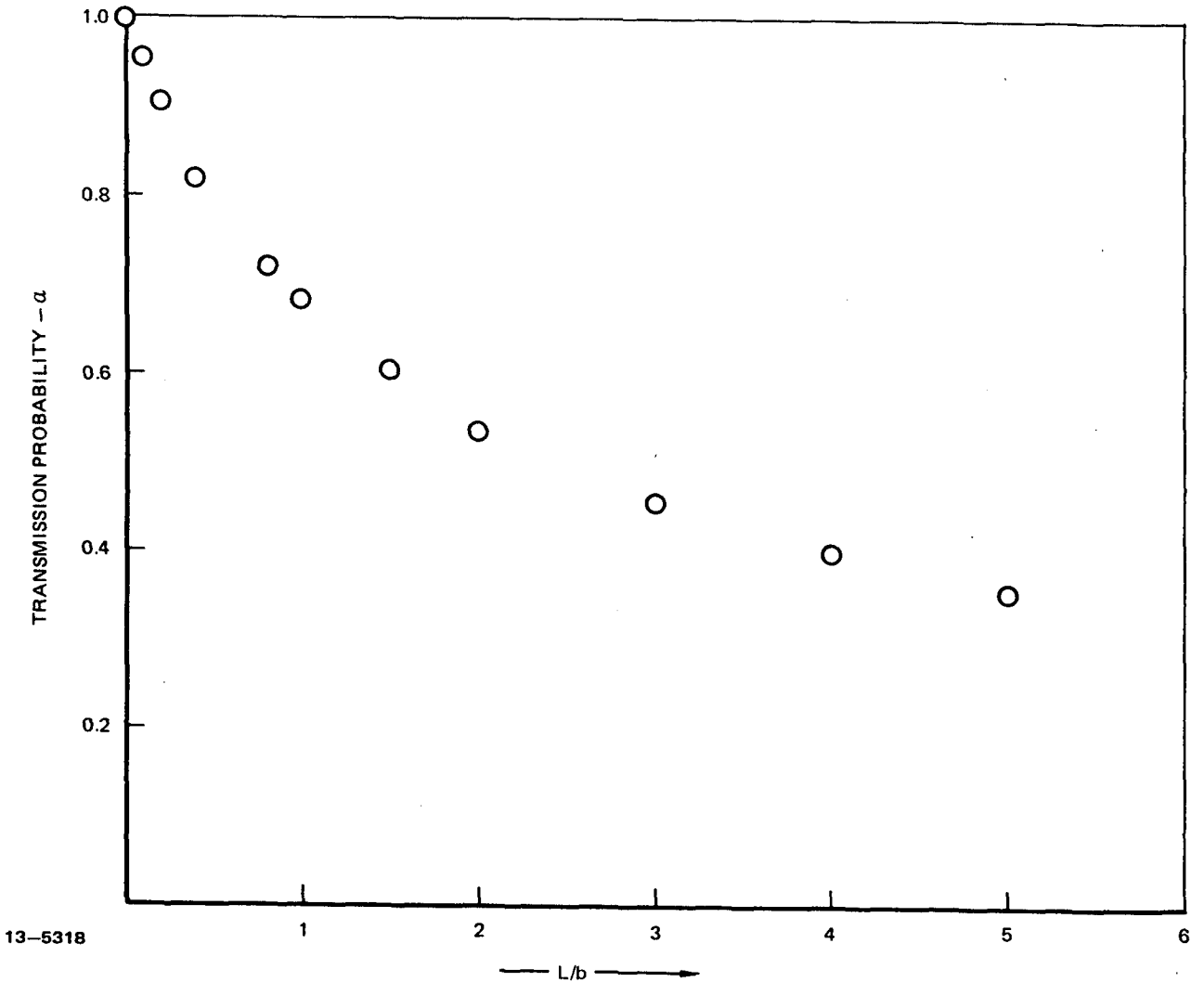

Figure 8-22. Transmission probability of a rectangular duct.

obtained by interpolation from the data of Reference 15 is $\alpha = .3843$. The corresponding conductance predicted by the previous equation is 4.1×10^5 liters/sec. if it is assumed that the gas temperature of the neutral atoms from the back surface of the limiter is 300°K. Since the limiter slots are equivalent to two such conductances, the total slot conductance is 8.2×10^5 liters/sec for helium.

Table 8-10. Comparison of transmission probabilities predicted for a cylindrical annulus by Monte Carlo analysis to probabilities predicted for the rectangular tube corresponding to the "unwrapped" annulus by interpolation from data of Fig. 8-22. R_o = inner radius, R = outer radius, ℓ = length, $b = R-R_o$.

R_o/R	ℓ/R	α, Monte Carlo Results Reference (16)	α from Reference (15)	ℓ/b
.9	.25	.488	.499	2.5
.9	.5	.351	.358	5
.9	.75	.279	.302	7.5
.75	.5	.541	.541	2
.988	.052	-	.384	4.4

Vacuum System Conductance

The vacuum system conductance is equal to the effective pumping speed at the back of the limiter slot which is calculated from the previously mentioned equation, $C = 3.638 \sqrt{T/m}\, A\alpha$, where A is the cross sectional area of the limiter duct. The vacuum system transmission probability α is obtained by combining the pump capture probability in an appropriate way with the transmission probabilities of each ductwork element between the pump and the back of the limiter slot.

This procedure will be described with reference to Fig. 8-21, which shows a cross-sectional view of the vacuum system. The first conductance encountered is the limiter duct. This conductance is approximated by a short duct of rectangular cross section. The wide cross-section dimension, equal to the circumference of the first wall, was taken as $a = 2\pi \times 6.8 = 42.73$ meters. The narrow cross-section dimension b was 15 centimeters. The length ℓ, from point a to point c in Fig. 8-21, equaled 1 meter. Since a was considerably

larger than both ℓ and b, the transmission probability can be obtained from the table in Reference 15 as described in the previous section. The transmission probability was found to be .32 for the limiter duct. Combined with the total inlet area of the two ducts, and again under the assumption that the gas at the inlet is room temperature helium, this implies a total limiter duct conductance of 1×10^6 liters/second.

The plenum region, from c to d in Fig. 8-21, was also approximated as a tube of rectangular cross section. Again the wide cross section dimension a, corresponding to the inner circumference of the plenum and taken as approximately 49 meters, was considerably larger than either the length ℓ = 3 meters or the narrow cross section dimension b = 45 to 120 cm. The value for α was taken as 0.42, leading to a conductance of 5.4×10^6 liters/second under the assumptions described above.

From d to e in Fig. 8-21 is a duct of round cross-section. Transmission probabilities for round tubes are given as a function of length to diameter ratio by equation 3.109 of Reference 17. Taking the length as 480 cm and the diameter as 1.2 meters leads to α = .23. The corresponding conductance, again under the assumption of room temperature helium at the inlet, is 8.2×10^4 liters/second for each duct. There are eight such ducts, one leading to each of the eight pumps. In a similar way, the conductance of the horizontal round tube attached to the pump inlet was found to be approximately 1.3×10^5 liters/sec.

Each pump itself is characterized by a "capture probability" which is the probability that a molecule entering the pump inlet will be pumped rather than eventually move back out the inlet. The pumping speed of the pump is related to its capture probability by equation 1, $C = 3.638 \sqrt{T/M}\, A\alpha$. For purposes of combining the effects of the pump with upstream ductwork, the pump is equivalent to a conductance element having the same inlet area, having its downstream end immersed in a perfect vacuum, and having conductance equal to the pumping speed. The pump capture probability was taken as 0.2 for helium, based on experience with cryopumps. Combined with a 1.2 meter inlet diameter, this led under the usual assumptions to an equivalent conductance of 7.1×10^4 liters/second for each pump.

After conductances are obtained for each element in the system of Fig. 8-21, it is necessary to combine them in order to get an effective net conductance or pumping speed for the system. The conductance of each pump was combined with that of the round tube connected to its inlet to produce an equivalent conductance using the approximation:

$$\frac{1}{C_{eq}} = \frac{1}{C_T} + \frac{1}{C_p} - \frac{1}{(3.638\ \sqrt{T/M}\ A)}$$

where C_T is the conductance of the tube and C_p is that of the pump. The final term in this expression is a correction term applicable when the two conductances are on the same axis. T is the absolute temperature of the gas, M is its molecular weight and A is the duct area.

This equivalent conductance was then combined with that of the vertical round tube from the plenum. The total conductance resulting was multiplied by four to account for the four concurrently operating pumps. The product was combined with the conductances of the plenum and the limiter duct. For all these cases the correction term is not used in combining the conductances; instead the equation

$$\frac{1}{C_{Total}} = \frac{1}{C_1} + \frac{1}{C_2}$$

is used.

The total conductance C_S of the entire vacuum system consisting of limiter ducts through pump was found to be 1.1×10^5 liters/second for the system shown in Fig. 8-21. A summary of the system conductances is shown in Table 8-11.

Table 8-11. He Conductance Values for the Vacuum System

ITEM	CONDUCTANCE (ℓ/sec)	FIGURE 20 REFERENCE POINTS
Limiter Ducts	1.3×10^6 (total)	a to c
Plenum	2.9×10^6	c to d
Vertical Duct	8.2×10^4 (each)	d to e
Horizontal Duct	1.3×10^5 (each)	e to f
Pump	7.1×10^4 (each)*	f to pump surfaces
Total	1.1×10^5	
Limiter Slot	8.2×10^5	Plasma to a

* This value would be 10.1×10^4 for hydrogen based on the assumption that $S_{He_5} \sim 0.7\ SD_2$ (Ref. 14) to a total conductance for hydrogen of 1.3×10^5 ℓ/sec.

Resulting Conductance ratio γ; discussion

The conductance C_S of the limiter slots, 823 m^3/sec, together with the conductance C_R of the vacuum system which was found to be 140 m^3/sec, establishes the value of the conductance ratio $\gamma = C_S/C_R$. For this case we obtain $\gamma = 4.1$ with 8 pumps operating and 7.4 with only 4 operating.

The significant of γ, as discussed in volume I of the STARFIRE report (5), is that together with the inversion probability, it determines the transmission probability for helium through the limiter slots and vacuum system. For a given value of the inversion probability, as γ decreases the transmission probability increases so that it is desirable to minimize γ.

The inversion probability describes the extent to which the limiter slots are "one-way" conductances. This effect arises because molecules which have been neutralized at the back surface of the limiter and are on trajectories which would taken them back through the limiter slots to the plasma stand a

good chance of being ionized by incoming hot electrons. Once ionized, they are accelerated toward the back of the limiter slot. The inversion probability expresses the statistical chance that this process will occur.

The calculation of the inversion probability requires the solution of a neutral transport equation, together with models of the incoming plasma; see for example FED[19]. This has not been done yet for DEMO; however, other designs such as FED have high, predicted inversion probabilities. Because of the inversion process, the removal efficiency of the system is not calculated in the manner usually employed for vacuum conductance problems. For example, if the inversion probability is one, the removal efficiency is independent of the vacuum system design, since all molecules at the inlet of the vacuum system (the back of the limiter slot) will be removed from the plasma. The transmission probability of the entire system is then independent of the conductance ratio γ, since it is already at its maximum value because of its dependence on the inversion probability. However, a complication with this type of system is that the inversion process will probably only function for a gamma below some maximum value; otherwise there is too much neutral gas in the limiter slots which may overwhelm the ability of the incoming plasma to ionize and return the neutral helium. The maximum value of gamma is design dependent and needs to be determined by detail plasma and vacuum system analyses of the limiter slot region. A ball park value of gamma equal to five has been assumed for the present.

Several approaches could lower the value for γ if necessary. Lowering the slot conductance C_S in the numerator of the expression for γ is probably the easiest possibility. This conductance scales with slot width (w) approximately as $C_S \alpha w^2$, i.e. a strong scaling, while particle flow to the slot scales weakly with w (see for example, FED report[19]).

The other way to a lower γ is to increase the conductance of the vacuum system, C_R. This includes shortening the ductwork between the back of the limiter slots and the pump, or increasing the size of the ductwork. More pumping can be applied by the use of improved pumps, or a greater number of pumps of the same type. In general, decreasing γ by increasing its denominator C_R tends to be a simple approach in that one is less likely to encounter

complicated tradeoffs with helium removal rate requirements or inversion probability mechanisms. On the other hand, increasing C_R would seem to be a more expensive way to decrease γ than decreasing C_S.

Vacuum Wall Cleaning

It will be necessary to clean all vacuum surfaces in DEMO prior to initiation of plasma operation. Low level impurities residing on vacuum surfaces are desorbed during operation and degrade the plasma. Desorption may be thermally induced or may be the result of ion impingement. The level of desorbed gases can be reduced by careful cleaning of all surfaces during fabrication and installation and by careful operation after start-up. In-situ cleaning methods must however be employed. Those most commonly used are vacuum bakeout and glow discharge cleaning. Both processes will be used on DEMO.

Two cleaning scenarios are anticipated for DEMO. The first involves the cleaning processes during construction in preparation for start-up. The second scenario addresses the cleaning associated with up-to-atmosphere maintenance periods.

Cleaning during construction is essential in ultra high vacuum (UHV) facilities. Material selection and chemical cleaning processes will be carefully controlled. Assembly will include commonly used UHV techniques including gloves, clean tools, clean room environment, etc. When construction is complete and vacuum vessel is verified to be leak tight, the vacuum system will be pumped to below 1×10^{-6} torr and in-situ cleaning will be initiated. The coolant for the first wall/blanket will be heated externally and circulated to raise the temperature of the first wall and blanket to $\sim 300^0$C, providing a vacuum bakeout. It is anticipated that the temperature of the shield will reach $\sim 100^0$C during this bakeout. To accelerate the removal of adsorbed gases, a concurrent glow discharge cleaning will be performed. A low power Taylor Discharge Cleaning (TDC) method has been successfully employed (18) to reduce impurity levels to $Z_{eff} \approx 2.0$. The discharge parameters will be the same as those proposed for STARFIRE (5), and should limit cleaning times to 3 to 5 days.

Another cleaning scenario is that required after a major vacuum system opening for maintenance. The amount of time required for cleaning becomes

quite critical, as it affects the reactor availability. After the completion of maintenance and the vessel is verified to be leak tight, it will be pumped to below 1 x 10^{-6} torr and the vacuum bakeout and glow discharge cleaning will be performed. The approach will be exactly as described above, except that the number of pulses can probably be reduced by a decade, since precautions will be taken to maintain a known gaseous environment throughout the maintenance period. Based on STARFIRE, carbon dioxide would be the backfill gas during maintenance; however its effect on cleaning time has not been fully investigated. Discharge cleaning with 10^4 to 10^5 TDC pulses, and a choice of the proper backfill gas, is expected to result in a total cleaning time of approximately 1.5 days.

Some aspects of the cleaning operation merit further investigation. The shield temperature will reach 100°C, which may not be sufficient for UHV cleaning. Normal bakeout temperatures are in the range of 250°C. The shield however will not be exposed to ion bombardment during operation and thus may not require cleanliness levels such as those on the first wall. Several surfaces, including parts of the blanket, the limiter slots, and the shield, will not be exposed to glow discharge cleaning. These same surfaces however will not experience ion induced desorption and thus may not require stringent cleanliness.

8.5 Maintenance

The DEMO reactor is being developed for total remote maintenance. The remote maintenance approach was chosen because it will result in the minimum radiation dose to plant workers. The reactor building will be exposed to tritium by permeation and releases during maintenance. Some activation outside the shield may also result from neutron streaming and spread of particulate matter. Use of remote equipment will permit maintenance with a minimal cool-down or clean-up period. In any event when the shield is opened personnel access will not be possible.

The design philosophy being followed is to maintain the radiation levels within the reactor building to < 2.5 mrem/hr within 24 hours after reactor shutdown if all the shielding is inplace; to design all components for complete remote maintenance, and to identify contact maintenance operations where personnel can safely be used with significant economic savings. When the

blanket sectors are pulled from the reactor no personnel can be in the reactor building; however, there may be periods when personnel entry is possible.

The 2.5 mrem/hr radiation criteria will limit the activated volumes of material in the reactor building and may permit human access if tritium and activation products can be controlled. The criteria should not be taken as assurance that contact maintenance can be performed over the life of the plant and designs should be developed accordingly. When the reactor is in place and operating, it may be possible to utilize personnel for some contact maintenance operations.

All components within the reactor building are replaceable. Some are replaced on a scheduled maintenance basis while others are designed for life-of-plant and are replaced only in the event of failure. Items designed for life-of-plant include the overhead crane, TF, EF and CF coils, coolant piping, reactor support structure and radiation shielding. These items represent more than 90% of the reactor total weight. The blanket assembly, impurity control components, current driver, pumps, valves, fueling mechanism, power supplies, maintenance equipment etc. are maintained on a scheduled basis. Spares are provided for all scheduled maintenance components, so that as one part is removed a pretested replacement is available and reactor operation can commence while repairs to the damaged components are being made.

The number of different maintenance operations planned in the reactor building are minimized by using a component "remove and replace" approach. This permits each maintenance action to be preplanned and designed for use with simple push-pull types of operation. This approach increases the speed of maintenance operations and simplifies maintenance equipment design requirements. Once the damaged or end-of-life components are removed from the reactor they are transported to a hot cell where more time is available for checkout, repair or disposal. The hot cell will have extensive maintenance capability for testing, component replacement, cutting, welding, machining, pinpoint leak location, and other repair.

Redundancy is planned for reactor auxiliary subsystems to permit continued operation of the plant until a scheduled maintenance period or until the component can be replaced in-service. The particular components where

redundancy is planned will be defined as the design progresses; however, candidate systems include redundant power supplies, vacuum pumps, current drivers, some valves, pumps and fueling mechanisms.

Availability goals have been established as 50 percent for extended periods of operation. The DEMO design must be developed around features which enhance maintence if this goal is to be met.

8.5.1 Maintenance Features

The reactor design is shown in exploded view in Fig. 8-2. As indicated provisions are made for replacement of all components. The design was developed to keep the top and sides of the reactor clear for access by maintenance equipment. Components were combined where practical to minimize the number of assemblies and improve access. For example, the shield duct around the vacuum duct provides support for the blanket and shield system and the shield door is combined with the blanket sector.

The blanket is replaceable as a 1/8 sector of the torus. Each blanket sector incorporates an integral first wall and limiter. Two of the sectors also contain current drive antenna. The limiter and current drive antennas can be removed independently of the blanket. The life goals for limiter and antenna are 2 years and the blanket life goal is 6.6 years. All lines to the blanket, limiter and current drive antenna utilize mechanical disconnects. The coolant is manifolded and valved so that individual replaceable components can be valved off for leak isolation. Coolant leaks will be detected by sequentially reducing the pressure in individual components and monitoring the change of the partial pressure of coolant in the plasma chamber with a gas analyzer. Detection of vacuum seal leaks to the vacuum chamber will be accomplished by injecting helium into a cavity between dual seals.

The shield is designed to last the life-of-plant and will be replaced only in event of unscheduled failures. Shielding is provided as a part of each blanket sector. The vacuum door on the blanket sector is sealed with redundant seals that are shielded locally to reduce the radiation damage. The seals are replaced each time the door is opened. The basic shield consists of sectors welded together to form the vacuum boundary. Cutting and rewelding the poloidal seals is required if shield sector replacement is required.

The magnet coils are also designed for life-of-plant although provisions have been made for their replacement. The normal conducting CF coils located inside the TF coil are segmented so they can be disassembled after adjacent shield sectors are removed. This permits replacement of a TF coil without removing all shield sectors. Although the specific CF coil design has not been developed it is thought that only one or two turns will be used in each coil and that a large design margin will be included in the design to reduce the possibility of failure.

Most EF coils can be replaced by overhead removal with partial disassembly of the vacuum tank. The lower EF coils can be replaced by lowering the coils onto a cart in a pit below the reactor. The coil and cart can then be removed through a slotted door in the vacuum tank wall of the pit.

The TF coil replacement is the most complex operation in the design and requires a major maintenance outage. Replacement requires removal of the vacuum tank cover, the outer EF coils and vacuum ring structure and cutting of welds in an outer vacuum tank panel. These welds are readily accessible to maintenance devices and will require use of tooling and remachining tools to prepare for welds and to prepare the shield seal surface. Further evaluation may show an advantage to utilizing a continuous frame that is not cut in the seal surface for maintenance.

The vacuum system utilizes redundancy to improve and minimize the effects of failures. Eight compound cryo pumps with isolation valves are provided. Four are required for operation. External valves and pumps leading to the tritium processing system utilize redundancy.

The power supplies are assumed redundant and include a replacement capability during operation. The power supply systems are located outside the primary confinement building and can be repaired during plant operation.

Failed redundant heat transport system conponents, with exception of a few in-line valves, can be replaced during reactor operation using remote/hands-on maintenance equipment.

8.5.2 Component Replacement Time Estimates

Limiter Replacement - The limiter modules can be relaced without removing other reactor components although the vacuum system must be opened and the TF coil must be discharged. A track mounted general purpose maintenance cart is utilized for coolant line removal and a track mounted limiter handling dolly is used for replacement of the limiter (see Fig. 8-23). Elastomer seals and an external structural latch system simplify the resealing and attachment task. A summary of the tasks that make up the 6.2 day estimate for limiter replacement are given in Table 8-12. The major item is 3 days for shutdown and startup of the reactor.

Table 8-12. Blanket Module Replacement Time Estimate

TASK	DURATION (HRS)
Reactor Shutdown and Access	24
Disconnect Coolant Lines (2)	8
Disconnect Limiter Module Seal	4
Retract Module and Move to Hot Cell	12
Install New Module	16
Connect Module Seal and Leak Check	12
Install Coolant Lines and Leak Check	16
Clear Reactor Room	8
Reactor Startup	48
TOTAL	148 HRS (6.2 DAYS)

Blanket Module Replacement - Blanket module replacement will also utilize a rail mounted approach so that an accurate reference point is available for maintenance operations. A cross section showing the maintenance equipment for removal of these sectors is shown in Fig. 8-24. Wheels under the blanket sector permit the module to be pulled out onto the rail mounted transport system. The limiter can be left in the blanket module during this operation. The estimated time for blanket replacement is 10.25 days based on the operations shown in Table 8-13.

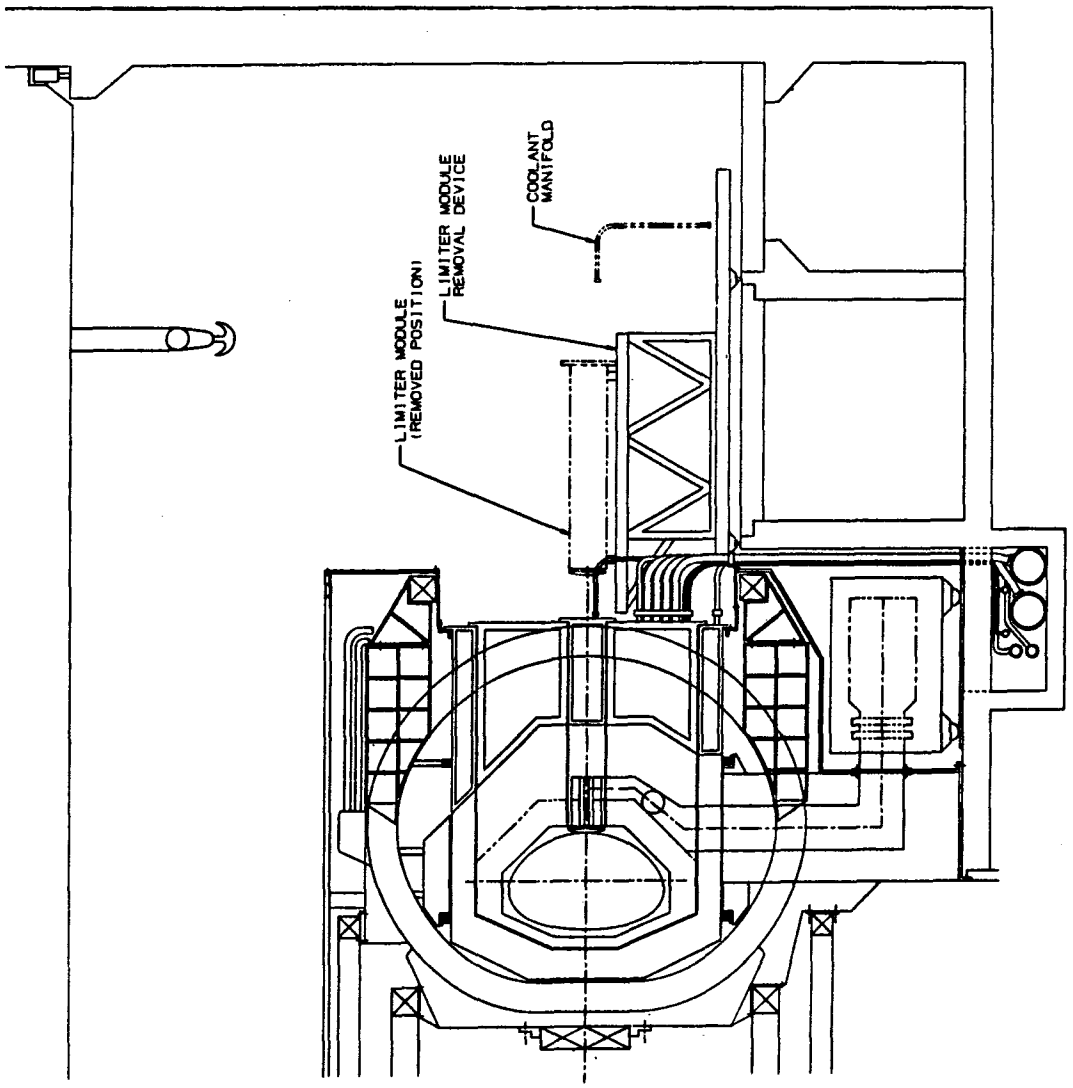

Figure 8-23. Limiter replacement.

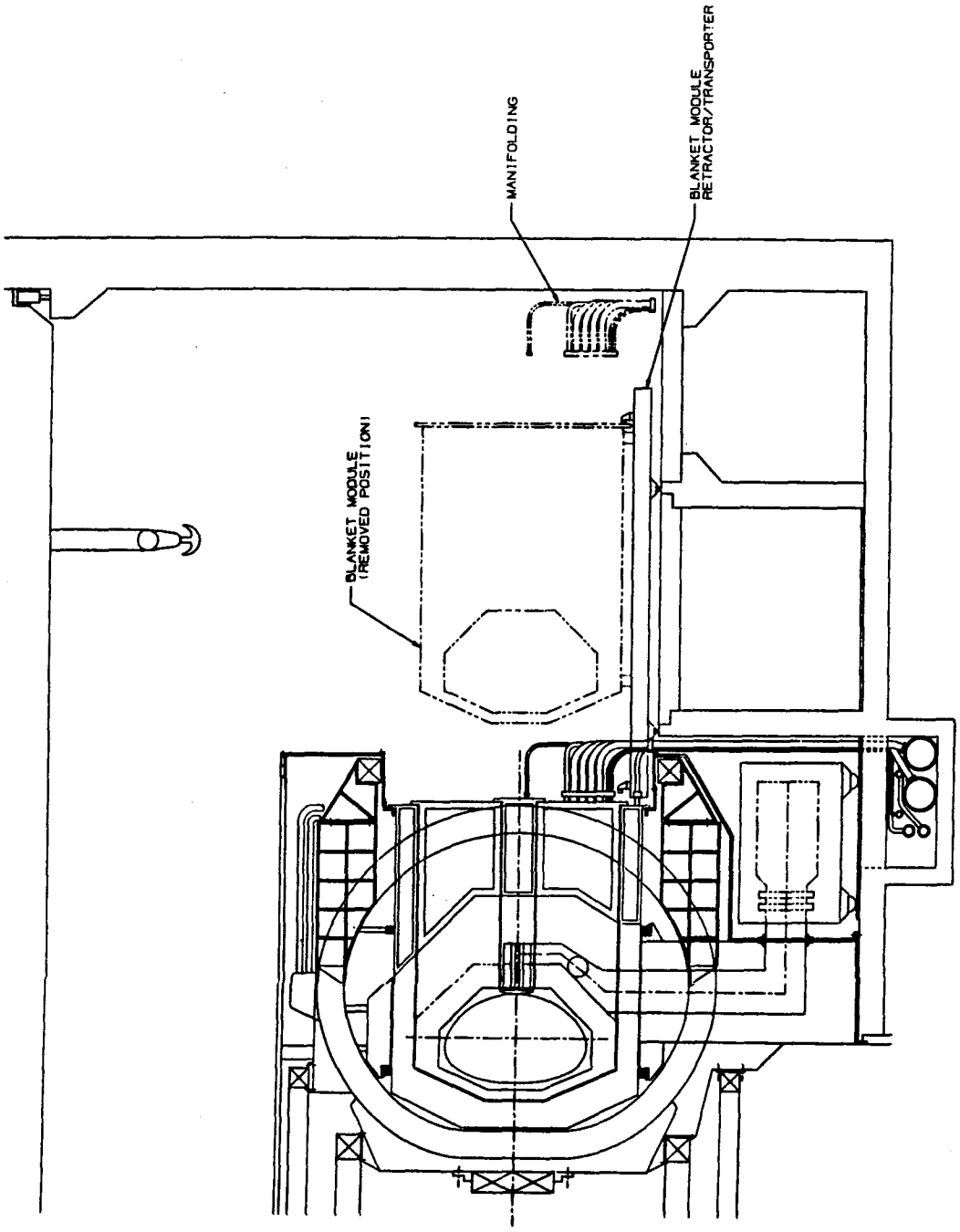

Figure 8-24. Blanket replacement.

Table 8-13. Blanket Module Replacement Time Estimate

TASK	DURATION (HRS)
Reactor Shutdown and Access	24
Disconnect Manifolding (12)	28
Disconnect Blanket Module Seal	12
Retrack Module and Move to Hot Cell	24
Install New Module	28
Connect Module Seal and Leak Check	18
Install Manifolding and Leak Check	56
Clear Reactor Room	8
Reactor Startup	48
Total	246 hrs (10.25 days)

The most time-consuming aspect of this operation is expected to be removal and replacement of fluid lines and seals. It is assumed that mechanically operated joints will be available for this operation where either a built in actuator or a single drive point is utilized. Self aligning guide pins will be essential for line reinstallation. A multipurpose manipulator which incorporates a storage rack for removing cooling lines is used for this task.

Shield Module Replacement - Failure of the sield module is seen as an infrequent event because of the relatively benign environment. However it will also have to be removed for TF and CF coil replacement. Removal requires cutting the seal between sectors and the seal between the shield and outer panel. The shield sector is replaced by hoisting the sector using the overhead crame. This requires removal of the vacuum tank lid. At this point a piece of the passive shield is removed between TF coils to permit a sling to be attached to the shield sectors. It is then sequentially moved radially with new sling positions used to straddle the CF coils and anti-torque structure. The bridge mounted manipulator is used to attach the sling. The sling

arrangement is shown in Fig. 8-25. An estimate of the replacement time is shown in Table 8-14.

Table 8-14. Shield Module Replacement Time Estimate

TASK	DURATION (HRS)
Reactor Shutdown and Access	24
Remove Blanket Modules (3)	128
Disconnect Shield Coolant Lines (3)	8
Cut Double Seal Weld Between Adjacent Shield Sectors	60
Cut Vacuum Duct & Vacuum Plenum Seals	16
Cut Outer Periphery Seal	30
Remove Vacuum Tank Tap Panel	48
Remove Upper Shield Block	8
Move Shield Module Outboard with Crane (Alternately straddling CF coil, Antitorque Structure, and EF Coil)	16
Move Module from Reactor Room	8
Move New Module to Reactor Room	8
Move Module Inboard with Crane	16
Install Upper Shield Block	8
Install Vacuum Tank Top Panel	48
Weld Outer Periphery Seal	48
Weld Vacuum Duct & Vacuum Plenum Seal	24
Weld Seal Between Adjacent Sectors	90
Install Shield Coolant Lines (2)	16
Install Blanket Modules (3)	256
Clear Reactor Room	8
Reactor Startup	48
TOTAL	916 HRS (38.2 DAYS) (5.5 WKS)

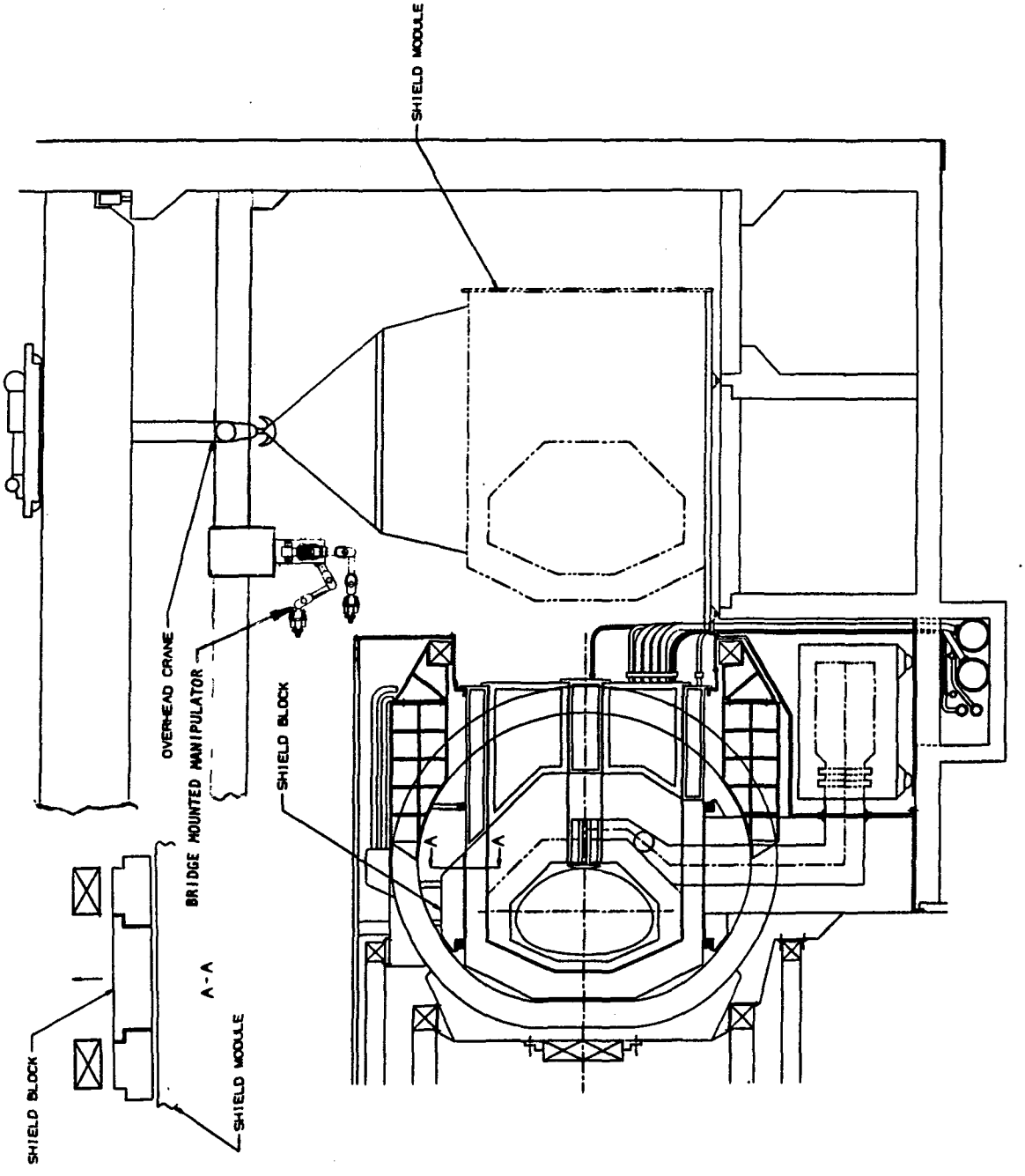

Figure 8-25. Shield replacement.

TF Coil Replacement - TF coil replacement requires removal of the vacuum tank cover, the blanket and shield modules, the upper, outer EF coil and vacuum tank rings and segmenting of the CF coils. In addition the vacuum tank outer panel must be removed by cutting structural welds. The outer vacuum panel is removed to minimize the reactor building height requirement. The panel welds are cut equidistant between TF coils and only one panel must be removed. The location of the structural weld joint at the reactor exterior permits use of tooling to reposition the parts for welding and remachining to form the shield segment seal surface. An estimate of the replacement time is shown in Table 8-15. The removal process is shown in Fig. 8-26.

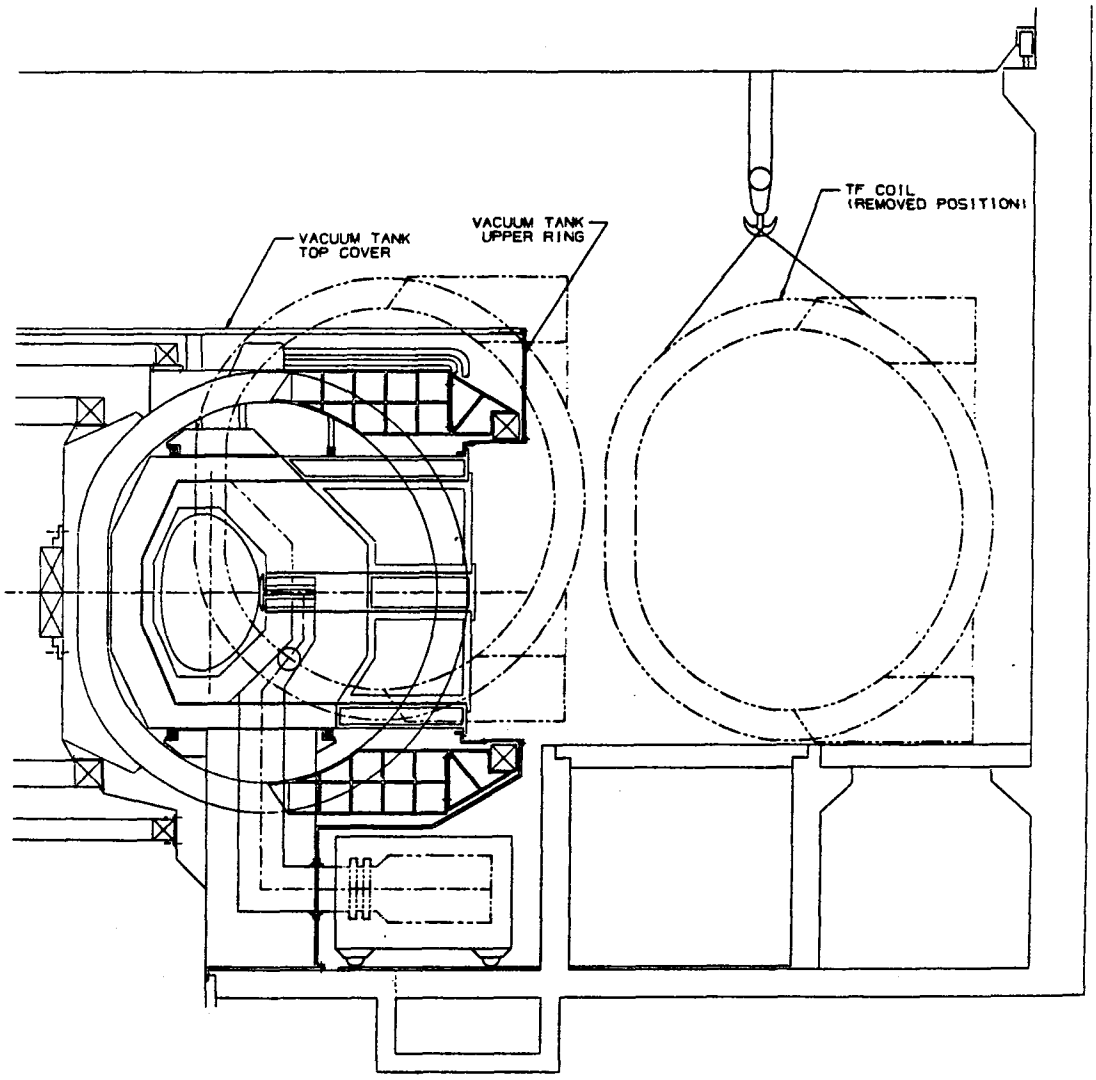

Figure 8-26. TF coil replacement.

Table 8-15. TF Coil Replacement Time Estimate

TASK	DURATION (HRS)
Reactor Shutdown and Access	24
Remove Blanket Modules (2)	96
Remove Shield Modules (2)	290
Remove Vacuum Tank Tap Cover and Upper Ring	96
Remove Vacuum Tank Outer Panel	120
Remove Upper Outboard EF Coil	336
Remove Lower EF Coil Suport Fitting	8
Remove Local Sectors of CF Coils (4)	336
Disconnect TF Coil Leads	24
Disconnect Intercoil Structure (Top & Bottom)	48
Disconnect TF Coil from Center Core Support	48
Remove TF Coil with Crane	24
Position new TF Coil	24
Connect TF Coil to Center Support	72
Install Intercoil Structure (Top & Bottom)	72
Connect TF Coil Leads	24
Install CF Coil Sectors (4)	504
Install Lower EF Coil Support Fitting	16
Install Upper Outboard EF Coil	504
Install Vacuum Tank Outer Panel	240
Install Vacuum Tank Top Cover and Upper Ring	192
Install Shield Modules (2)	430
Install Blanket Modules (2)	192
Clear Reactor Room	8
Reactor Startup	48
TOTAL	3716 HRS (155 DAYS) (22.1 WKS) (5.2 MONTHS)

EF Coil Removal - Removal of EF coils is possible without major reactor disassembly. The most difficult task is replacing the outer lower EF coil which requires approximately 96 days. Other coils require approximately 50 days. The average replacement time for an EF coil is 60 days. The time estimates are given in Table 8-16.

Table 8-16. EF Coil Replacement

a) Outer Upper EF Coil Replacement

TASK	DURATION (HRS)
Reactor Shutdown and Access	24
Remove Vacuum Tank Top Cover & Upper Ring	96
Remove Upper Outboard EF Coil	336
Install Upper Outboard EF Coil	504
Install Vacuum Tank Top Cover and Upper ring	192
Clear Reactor Room	8
Reactor Startup	48
TOTAL	1208 HRS (50 DAYS)

b) Outer Lower EF Coil Replacement

Reactor Shutdown and Access	24
Remove Vacuum Tank Top Cover & Upper Ring	96
Remove Upper Outboard EF Coil	336
Remove Blanket Limiter and Shielded Coolant Lines (128 lines with 3 machines in parallel)	86
Remove Lower Outboard EF Coil	36
Replace Lower Outboard EF Coil	504
Replace Upper Outboard EF Coil	504
Replace Limiter, Blanket and Shield Coolant Lines	172
Install Upper Vacuum Tank Cover	1922
Clear Reactor Room	8
Reactor Startup	48
TOTAL	2306 HRS (96 DAYS)

CF Coil Replacement - The CF coil is segmented to permit repair of failed portions. It is assumed that a failure would require removal of two of the eight segments which require removal of three adjacent shield segments. Time for this repair is 84 days. A time estimate is given in Table 8-17.

Table 8-17. CF Coil Replacement Time Estimate (2 Segments)

TASK	DURATION (HRS)
Reactor Shutdown and Access	24
Remove Blanket Modules (5)	240
Remove Shield Modules (3)	435
Remove CF Coil Segments (2)	100
Replace CF Coil Segments (2)	150
Replace Shield Modules (3)	650
Install Blanket Modules (5)	360
Clear Reactor Room	8
Reactor Startup	48
TOTAL	2015 HRS (84 DAYS) (12 WKS)

Vacuum Pump Replacement - The vacuum pumps and valves are located in the reactor basement and can be replaced independently of the blanket components. A separate maintenance cart is provided for pump replacement and a catacomb is located in the basement to permit access to all 8 pumps. These pumps can be replaced during reactor operation by valving off the chamber and increasing the pump recycle frequency of the remaining pumps during this operation.

Reliability Goal Setting

At this point it is too early to estimate DEMO component reliability, however, it is possible to work backwards from the requirements and set some target goals for each component to guide engineering development.

This is accomplished by starting with the availability goal of 50% which allows 182 days outage per year. It if is assumed that one third of the outages are the result of planned shutdowns then approximately 120 days are available to recover from outages caused by failures. This can be further divided into outages caused by the balance of plant (30 days/year) (7) and the reactor (90 days). The 90 days outage for the reactor is divided into minor

repairs (50 days) and major component replacement (40 days). These allocations are summarized below.

Outage Allocation

Scheduled Outage		Unscheduled Outage	
		Reactor	
Reactor & Balance of Plant	Balance of Plant	Major Replacement	Minor Replacement
62 da/yr	30 da/yr	40 da/yr	50 da/yr

These reliability allocations can then be assigned to individual systems to determine what reliabilities would be required. Table 8-18 shows an allocation that was made to distribute the requirements so as not to overly burden any single system. Results of the above analysis impose the required mean-time-between-failures (MTBF), shown in Table 8-19, that would result in a need for major component replacement.

Table 8-18. Outage Allocation Per Year

Mean-Time For Major Replacement (Days)	Number of Major Parts	Annual Allocation		Reactor System
		Major Replacement (Days)	Minor Replacement (Fix-In-Place) (Days)	
155	8	15	6	TF Coil System
60	6	4	6	EF Coil System
10	8	2	6	FW/Blanket System
6	8	6	6	Limiter System
84	4	2	6	CF Coil System
38	8	4	6	Shield System
4	8	1	1	Vacuum (System) (Redundancy-on-line replace)
6	2	1	2	REB System (Redundancy)
ND	ND	1	1	Tritium (Redundancy on-line Replace)
ND	ND	1	1	CYRO System (Redundancy on-line replace)
ND	ND	1	3	Electrical System (Redundancy)
ND	ND	1	1	Maintenance Sys (Redundancy)
			5	Other
	Total	40 days	50 days	

ND = Not Defined

Table 8-19. Required Frequency of Major Replacements

Component	Component MTBF	Number of Mature Components	Frequency of Major Replacement
TF Coil	84 yrs	8	1 coil in 10.5 yrs
EF Coil	90 yrs	6	1 coil in 15 yrs
First Wall/Blanket	40 yrs	8	1 sector in 5 yrs
Limiter	8	8	1 blade in 1 yr
CF Coil	168 yrs	4	2 segments in 42 yrs
Shield	76 yrs	8	1 sector in 9.5 yrs

The more stringent requirement on the CF coil is thought to be reasonable since it is not space limited and can be designed with substantial margin.

The above values are provided to give guidance to possible DEMO requirements. More in-depth work must be performed one each component to assure that these numbers are reasonable goals.

REFERENCES FOR CHAPTER 8

1. D. K. Bhadra, T. W. Petrie, V. A. Puron, J. M. Rawls, Ripple Burn Control, p. 11, GA15924 (May 1980).

2. Joel Schultz, Junior Woodchuck Manual, MIT (May 1980).

3. Verbal Communication, Les Waganer, McDonnell Douglas Astronautics Company (November 1981).

4. B. Badger et al., UWMAK II, "A Conceptual Tokamak Power Reactor Design," UWFDM 112, University of Wisconsin (October 1975).

5. C. Baker et al., "STARFIRE - A Commercial Tokamak Fusion Power Plant Study," Argonne National Laboratory, ANL/FPP/80-1 (September 1980).

6. G. M. Fuller, H. S. Zahn et al., "Developing Maintainability for Tokamak Fusion Power Systems," DOE COO-4184-6, p. 7-10 (November 1978).

7. C. Baker et al., "STARFIRE - A Commercial Tokamak Fusion Power Plant Study," Chapter 11, Argonne National Laboratory, ANL/FPP/80-1 (September 1980).

8. Verbal Communication, D. Coffin, LASL (October 1981).

9. D. A. Gueritt, "Intrinsic Engineering Problems for Elmo Bumpy Torus-Scale," 9th Symposium on Engineering Problems of Fusion Research, Chicago, IL (October 1981).

10. C. A. Flanagan, et al., "Initial Trade and Design Studies for the Fusion Engineering Device," Oak Ridge National Laboratory, ORNL/TM-7777 (June 1981).

11. W. M. Stacey, et al., "Tokamak Experimental Power Reactor Studies," ANL/CTR-75-2.

12. R. W. Moses, Jr. and W. C. Young, "Analytical Expressions for Magnetic Force on Sectored Toroidal Coils," Proc. of the Sixth Symposium on Engineering Problems of Fusion Research, p. 917 (1975).

13. Ken Black, FED Shield Inner Wall Electrical Contact, Informal Memo, McDonnell Douglas Astronautics Company (September 1981).

14. P. W. Fisher and J. S. Watson, "Cryosorption Vacuum Pumping of Deuterium Helium and Hydrogen at 4.2 K for CTR Applications, Oak Ridge National Laboratory, Presented at ANS Winter Meeting, Washington, D.C. (November 1976).

15. Santeler, Holkeboer, Jones and Pagano, "Vacuum Technology and Space Simulation," NASA SP-105 (1966).

16. D. H. Davis, "Monte Carlo Calculation of Molecular Flow," J. Appl. Phys. VR31, No. 7, pp. 1169-1176 (1960).

17. A. Roth, "Vacuum Technology," North-Holland (1976).

18. H. F. Dylla, et al., "Observation of Cleanliness in Residual Gas and Surface Composition with Discharge Cleaning in PLT," PPPL-1485.

19. FED Device Design Description, ORNL/TM/79-48, to be published.

20. T. G. Brown, et al., INTOR Reactor Design Studies, Fusion Engineering Design Center/Oak Ridge National Laboratory (July 1982).

21. M. A. Abdou, et al., INTOR Critical Issues, Benefits of Long-Term Testing (July 1982).

CHAPTER 9

BALANCE OF PLANT

Chapter 9

Table of Contents

Chapter 9

List of Figures

Chapter 9

List of Tables

9.0 BALANCE OF PLANT (BOP)

9.1 Introduction and Basis of Design

The BOP design of this demonstration fusion plant project is based upon the design concept developed in the STARFIRE project. It was decided that the BOP effort should concentrate on those elements which may improve the fusion reactor assembly and maintainability rather than on the conventional steam and power generation systems. This approach is based on considerations of (1) effective utilization of limited funding resources, (2) concentration on significant BOP problem areas of the fusion technology, and (3) identification of BOP design features that improve reactor maintenance. Following this approach, the main emphasis of the BOP design has been directed toward the Reactor Building. Other areas of work include (1) revising the STARFIRE BOP systems to reflect the demonstration reactor supporting requirements, and (2) developing a cost estimate for the BOP.

From the maintenance viewpoint, the demonstration plant has several new design features. All the major reactor components including the TF coils, blanket modules, limiter modules, vacuum pumps and the EF coils are to be replaceable. The replacement of the inboard EF coils is accomplished through the EF coil removal room underneath the reactor.

A key design basis for the Reactor Building is to provide building support functions necessary to facilitate reactor maintenance. Included in this provision are (1) adequate laydown space, (2) capability to transport equipment in and out of the reactor hall, (3) cranes, manipulators, and other equipment to service the reactor, (4) remote maintenance capability, (5) confinement of radioactive contamination, and (6) scenarios for moving large replacement parts such as TF coils and EF coils in and out of the Reactor Building. The conceptual design of the Reactor Building meets the requirements for totally remote maintenance, for a minimum wall thickness of 1.5 m for radiation shielding, for overpressure protection against postulated accidents and for constructibility and logical space utilization.

Although the demonstration reactor is smaller than the STARFIRE reactor, the Reactor Building has been increased both in width and in length by 4 meters. This provides additional necessary withdrawal space for the shield modules. The height of the Reactor Building is set by the EF coil replacement

requirement. Overall, the Reactor building for this project is equipped to support the maintenance and replacement of all major reactor components including the TF and EF coils.

The thermal rating of the demonstration plant reactor is 1280 MW. This is approximately one-third of the STARFIRE reactor rating. The BOP mechanical and electrical systems have accordingly been revised in size. The reduction is generally in the sizing/capacity of equipment and in the number of components in a system. For example, the number of hyperbolic natural draft cooling towers is reduced from three in the STARFIRE project to two, and the size of each cooling tower is reduced from approximately 150 m in diameter at the basin, 100 m in diameter at the top and 165 m in height to 120 m in diameter at the basin, 80 m in diameter at the top and 145 m in height respectively.

The R&D building included in the demonstration project will have offices, laboratories, computer center, conference room, library and lavatory facilities to accommodate 200 scientists and engineers. This building is required to support the test objectives of the project.

9.2 Site and Building Design

9.2.1 Site Plan

Although the fusion power plant is designed to be suitable for a wide range of potential power plant sites throughout the continental United States, the following assumptions are made for the purpose of this study:

a. Location: Kansas City, Missouri (to facilitate cost estimate)
b. Seismic: UBC Zone 2
c. Site size: 400 hectares
d. Ambient temperature for:
   (1) Cooling: 39°C
   (2) Heating: 23°C
e. Altitude (maximum): 600 m
f. Principal heat rejection system: Natural draft cooling tower
g. Water supply: Assumed adequate to satisfy all normal requirements
h. Electrical utility transmission: HV (242 kV)

Principal site elements include buildings, roads, walks, fencing, and surface and subsurface mechanical and electrical equipment and utilities, most notably the large natural draft hyperbolic cooling towers. Since the cooling towers are of such overwhelming scale relative to other site elements, they are grouped at the rear of the site to provide a visual "backdrop" as viewed from the approach to the main entrance. The remaining site elements are located and arranged to optimize functional interrelationships; that is, to minimize piping, electrical, and utility runs and at the same time provide adequate separation and circulation around and between buildings and other elements. An orderly and logical asymmetrical composition of site elements adds interest and yet maintains simplicity.

The principal buildings and their spatial relationships are summarized below:

a. The Reactor Building contains the demonstration Tokamak fusion reactor and supporting systems.

b. To the south of the Reactor Building is the Turbine and Support Building that contains the energy conversion equipment, a reactor service area in which blanket sections and other new reactor subsystems are prepared, a plant auxiliary area that houses the closed loop cooling water system, and the Hot Cell.

c. The Electrical and REB Power Supply Building is placed to the east of the Reactor Building and the Tritium Reprocessing and Cryogenics Building is located to the north of the Reactor Building.

d. The Administration Building, the R&D Building, and the facility control and site service complex are sited to the south of the Turbine and Support Building.

The layout of the balance of the plant facilities is shown on the site plan, drawing E-5959-AR-11 (Figure 9-6), included in Section 9.6.

9.2.1.1 Secondary Road Access

External access to the site from a major highway is by a secondary road of 8 km maximum length. The road terminates at the main entrance gate to the site, adjacent to the Security Building and offsite parking lot.

9.1.2.2 Parking Lot

Plant personnel and visitor parking for 250 cars is accommodated in a paved and landscaped parking lot, located outside the perimeter fence and adjacent to the Security Building.

9.1.2.3 Security Building

All traffic to and from the site is controlled at the Security Building, located at the main entrance gate at the perimeter fence. Transport and delivery trucks and railroad cars undergo inspection by security personnel. Plant personnel and visitors must pass through inspection portals and identification devices in the Security Building prior to entering the plant. Those who do not proceed on foot to their work stations in the Administration/Control/Site Service Building may ride a shuttle car to more distant work stations within the plant boundary. The use of personal vehicles within the perimeter fence is generally not permitted. Parking spaces for shuttle cars and other plant vehicles are provided adjacent to the Security Building inside the perimeter fence. Visual surveillance and control of the railroad spur entrance is also possible from the Security Building.

9.1.2.4 Perimeter Fence and Perimeter Road

The principal elements of the plant are enclosed by a chain link perimeter fence. The fence is lighted and equipped with microwave intrusion detection devices and closed circuit television, with monitors in the Security Building.

The perimeter road encompasses all site elements within the perimeter fence except the cooling towers and water reservoirs. It is assumed that a perimeter road adjacent to the perimeter fence is not necessary because of the surveillance equipment on the fence. Access to all site facilities and secondary roads is provided.

9.2.1.5 R&D Building

The R&D Building is a one-story structure containing offices, laboratories, a computer center, conference rooms, lunch and lavatory facilities to accommodate up to two hundred test and experimental personnel. This building

is located near the main entrance and the parking lot to facilitate personnel flow and communication with the adjacent Administration, Control and Site Service Building.

9.2.1.6 Administration, Control, and Site Service Building

Located next to the R&D Building near the main entrance, the Administration, Control, and Site Service Building provides facilities for plant operating personnel. A receiving area for both truck and rail transport is located on the north side of this building adjacent to the Warehouse and Maintenance Shop entrances. A widened road and driveways are provided for increased maneuverability, and give access to the Turbine and Support Building.

9.2.1.7 Turbine and Support Building

The Turbine and Support Building has the largest floor area of buildings in the plant. Adjacent to the turbine side is the main transformer yard and switchgear room, enclosed by a chain link fence. The support portion of the building includes the Reactor Service Building, the Plant Auxiliary Building, and the Hot Cell. Two connections to the Reactor Building include the air lock and the steam line passage.

9.2.1.8 Reactor Building

The Reactor Building houses the demonstration Tokamak fusion reactor device and supporting systems. The only entrance to this building is through the Hot Cell air lock, although there are two emergency exits (normally locked) in the exterior wall. The building is centrally located between the Turbine Building, auxiliary systems, Hot Cell, tritium and cryogenics facilities, Electrical and REB Power Supply Building, and other related facilities. Underground tunnels for piping, conduit, and equipment access connect lower floors to some of these other buildings, as shown on the site plan.

9.2.1.9 Tritium Reprocessing and Cryogenics Equipment Building

Equipment and storage facilities for the treatment and reprocessing of tritium are located in the Tritium Reprocessing Building. Together with the Cryogenics Equipment Building and fenced yard, where gaseous and liquid helium

and nitrogen are processed for use in the Reactor Building, these functions have minor relationships to most of the other site facilities. A parking area for onsite vehicles is provided, and a bank of helium storage tanks is located across the perimeter road.

9.2.1.10 Electrical Equipment and REB Power Supply Building

Directly east of the Reactor Building is the Electrical Equipment and REB Power Supply Building, with proximity to the main switchyard, the main transformer yard, the Onsite AC Power Supply Building, and the Reactor Building. A tunnel connects this building with the subgrade level of the Reactor Building.

9.2.1.11 Onsite AC Power Supply Building and Switchyard Control Room

In the event of loss of normal power, two gas turbine generators located in the Onsite AC Power Supply Building furnish ac power sufficient to complete an orderly shutdown of the demonstration reactor.

The adjacent switchyard control room contains all equipment necessary for the normal operation and monitoring of incoming and outgoing power in the main switchyard.

9.2.1.12 Main Switchyard

The main switchyard is a fenced area that contains all the electrical equipment necessary to accommodate incoming and outgoing HV power. It is located close to the Electrical and REB Power Supply Building and main transformer yard. Most of the components are modular SF6 gas insulated, permitting the installation of lines both above and below ground within the site.

9.2.1.13 Raw Water Reservoir and Evaporation Pond

Located outside the perimeter road, the raw water reservoir and evaporation pond are formed by compacted earth berms and lined with soil cement. The adjacent pump house contains pumps for fire and domestic use, and chlorination facilities for potable water.

9.2.1.14 Fire Water Storage Tank

Adjacent to the raw water reservoir and evaporation pond is a fire water storage tank, located below grade. This tank supplies sufficient water to extinguish the maximum credible fire.

9.2.2 Reactor Building

The Reactor Building is a steel-lined, ribbed box structure that contains the reactor, primary cooling systems, and other support systems. Details of its architectural and structural features are described below.

9.2.2.1 Architectural

Although the most significant visual aspects of the Reactor Building are essentially dictated by maintenance, structural, and shielding requirements, its most prominent architectural feature is the use of its interior space, particularly the equipment layout.

The Reactor Building houses the demonstration fusion reactor and closely related systems. These systems, broadly referred to as "process modules," include the primary loop components and steam generators, heat exchangers and pumps, the vacuum pumping and blanket purge system, the limiter feedwater loop module, and the REB cooling system module. Additional modules not directly related to the reactor include the HVAC systems and the atmospheric tritium cleanup (ATC) systems. Additional equipment laydown space is also provided. A 1.5 m-thick, partial height, shielding wall and sliding doors separate the module area from the reactor to minimize activation of materials in the process module area. The pressure boundary of the building is lined with steel. Other interior surfaces are coated with decontaminable paint.

The design of the Reactor Building is also largely based on a commitment to totally remote maintenance. Although it is envisioned that personnel need never set foot in this building (except in the crane maintenance balcony and the sub-grade level), it would not be impossible to do so under extreme and unusual circumstances. Ordinarily, however, a highly sophisticated system of remote maintenance and transport equipment is expected to perform all maintenance and repair operations, and have enough flexibility to perform unplanned

or unforeseen tasks as well. Some operations are routine and are programmable; others may be under direct operator control. Operator involvement will depend on the specific functions performed and the degree of decision-making required.

The Reactor Building is 124 m long and 54 m wide (inside clear dimensions), and consists of three levels in addition to the crane maintenance balcony, which is only a fraction of a complete floor level. The reactor and process modules are located on the ground level, The height to the under surface of the roof slab is 42.5 m. A 500-ton-capacity* bridge crane spans the level below ground is a pipe chase 3 m in height. All pipelines, conduits, and other connections between the reactor and the modules penetrate the ground level floor, run through the pipe chase to a point below the respective module, and up through the floor again. In the same manner, HVAC major duct runs extend to the corners of the building. Piping runs, therefore, are isolated from and kept clear of the remote maintenance equipment traveling on the ground floor.

The pipe chase, reactor hall, and process module areas are subject to overpressure under accident conditions. Access to the pipe chase is by two removable hatches, one at each end of the building on the ground floor.

The second level below ground is the routinely occupied sub-grade floor, which is not subject to overpressure, significant radiation, or a tritium atmosphere. Provision is made at the sub-grade level for emergency exit from the southwestern corner of the building. Located on this level are HVAC mechanical and electrical equipment. The space is divided into a rectilinear grid of 1.5-m-thick concrete walls for supporting the heavily loaded floors above. The reactor is supported by a 6-m thick, 20-m-diameter annular pedestal. A 10-m diameter EF coil removal room is located beneath the reactor to facilitate the inboard EF coil replacment. A transfer car rail runs from the EF coil removal room to a location beneath the process module room where a floor hatch may be removed to allow the lifting of the inner EF coil to the ground level for final transport to the Hot Cell. The demonstration reactor uses REB for the plasma heating rather than RF heating. The rf component area

*In this chapter, "ton" refers to a metric tonne, i.e. 1000 kg.

at the basement level of the Reactor Building in the STARFIRE design was therefore deleted. This reduces the size of the basement of the Reactor Hall and simplifies the transfer of the reactor loading to the support soil strata.

The HVAC equipment rooms open into large areaways to grade for fresh air intake. These areaways are located inside an enclosed courtyard between the Reactor Building and the Turbine and Support Buildings. They are open to the sky and accessible only from the plant auxiliary area. One end of the central corridor on this level opens to an exhaust air tunnel that leads to the stack. The top of the tunnel opens to a vertical shaft to grade with a heavy concrete hatch cover that may be removed prior to lowering large equipment into the sub-grade level spaces with a portable crane.

A sloping tunnel connects the Reactor Building sub-grade level with the Electrical and REB Power Supply Building sub-grade level, where all REB power supply equipment is located. The tunnel accommodates the electrical and REB lines and provides additional equipment and maintenance access to the Reactor Building sub-grade level.

A large crane maintenance balcony is located at the end of the building, remote from the reactor, where routine maintenance and repair are conducted on the 500-ton bridge crane, the 60-ton process module area bridge crane, and the electro-mechanical manipulators. The 60-ton crane and manipulators must be lifted and carried into the maintenance area by the 500-ton crane above. Maintenance in this area is "hands-on" by personnel wearing protective suits. Access to the balcony is from the reactor service area in the Turbine and Support Buildings by stairs or a freight elevator to the plant auxiliary area equipment mezzanine, across to a large corridor above the Hot Cell air lock, and up another set of stairs or freight elevator to a vestibule at the same level and adjacent to the balcony. The freight elevators are provided for the transport of any large or heavy tools or equipment such as fork lifts, jacks, or compressors, as well as personnel (as needed) for crane maintenance.

9.2.2.2 Structural

The Reactor Building is a steel-lined, hardened structure constructed of reinforced concrete designed for the nonconcurrent conditions of DBE seismic loading and 55 kPa internal overpressure. The 1.5 m thick building outside walls and roof prevent penetration by tornado missiles, withstand tornado

winds and a tornado-induced differential pressure, and provide adequate shielding. The building is designed as a ribbed box structure and analyzed as a series of "T-beams" with the walls and roof forming a rigid frame fixed at the ground floor. The walls acting with the floors transfer all forces to the base slab foundation. The reactor is supported on a large annular concrete pedestal that transfers the reactor loading directly to the supporting soil strata. The pressure boundary is located at the inside of the building exterior walls, at the roof, and at the top of the floor below the ground floor. Special pressure-tight penetrations are installed where piping or utility lines cross the containment boundary. The reactor hall floor transfers heavy loadings from equipment and the blanket transfer system to a grid of walls that further carries the loads to the base slab foundation.

A coated carbon-steel liner provides a leak-tight boundary and minimizes tritium release in the event of a loss of primary coolant within the building.

The demonstration plant Reactor Building is designed to withstand an internal overpressure of 55 kPa. This value is about one-third the STARFIRE design basis because of the lower energy release in a demonstration plant loss of coolant accident and because the free volume of the demonstration plant Reactor Building is larger than that of STARFIRE. The potential for modifying the roof thickness and for eliminating ribs was investigated. The minimum wall thickness of 1.5 m is required for shielding.

Due to the reduction in internal pressure by a factor of three, it was hoped that the concrete thicknesses could be reduced substantially. However, due to the increased roof span and the guidelines given in Table 9.5(d) of the ACI 318-71 Building Code Requirements for Reinforced Concrete which controls deflections, no significant reduction in concrete thickness could be predicted. Table 9.5(d) provides guidelines for slab and beam thicknesses when detailed deflection analyses are not conducted. This table indicates that the original "T-beams" 2.75 m deep, 2.0 m wide, and 10 m on centers are marginal for controlling static deflections. This result is due to the increase in clear roof span from 50 m to 54 m. Since the "T-beams" are 10 m on centers which is closer than required, it is expected that a detailed analysis would show the 2.75 m deep "T-beams" are adequate to control deflections. However, based on this preliminary review and evaluation it is evident that no significant reduction in roof or wall concrete thickness can be expected since the

static design requirements rather than the internal over-pressure requirements would limit the structural member size.

9.2.2.3 Maintenance Functions

The Reactor Building has been designed to provide necessary functional support to the maintenance of the demonstration reactor. Concerns of radiation exposure and potential tritium contamination lead to the requirement of total remote service capabilities in the Reactor Building ground floor area. This includes servicing the equipment in both the reactor hall and in the process module room. The maintenance function aspects of the Reactor Building design are described below.

a. A pair of concentric rails is located around the perimeter of the reactor. The function of these rails is to enable flatbed cars to circulate around the reactor for accessing any reactor component that requires servicing. Mounted on the flatbed is a section of monorail track which will accommodate a variety of the maintenance machine carts. Figure 9-1 shows these design features. By moving a flatbed to a preset location, the section of track on the flatbed may be aligned with the fixed monorail system. The selected maintenance machine cart may then be transferred between the reactor hall and the process module room. Figure 9-2 shows the layout of the tracks in the reactor hall. The maintenance machine carts may be transferred between the fixed monorail system and the concentric rails at two locations. Four spur monorail tracks are added to provide flexibility and temporary parking areas.

b. The fixed monorail track is 3 m wide and 1 m high off the ground floor. The track layout in the process module area is shown in Figure 9-3. The track is arranged to allow movement of system components into position to perform remote maintenance and repair functions on the process module equipment, ATC systems, and the HVAC equipment. There is a track switching junction to allow the transfer of equipment/components to and from the Hot Cell. A turntable is used to move the machine carts to and from the machine cart storage area.

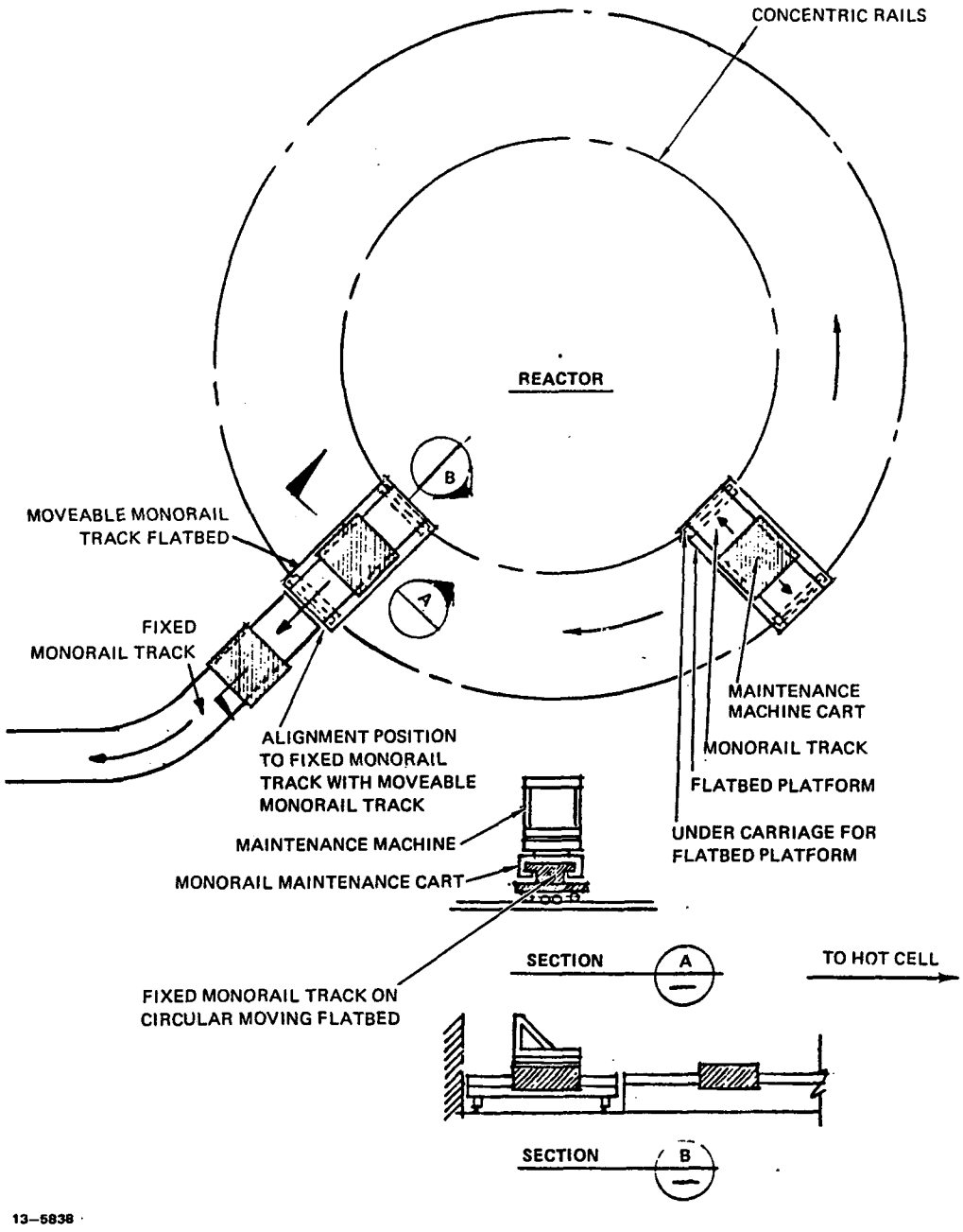

Figure 9-1. Concentric circular rails, flatbeds, and maintenance machine cart.

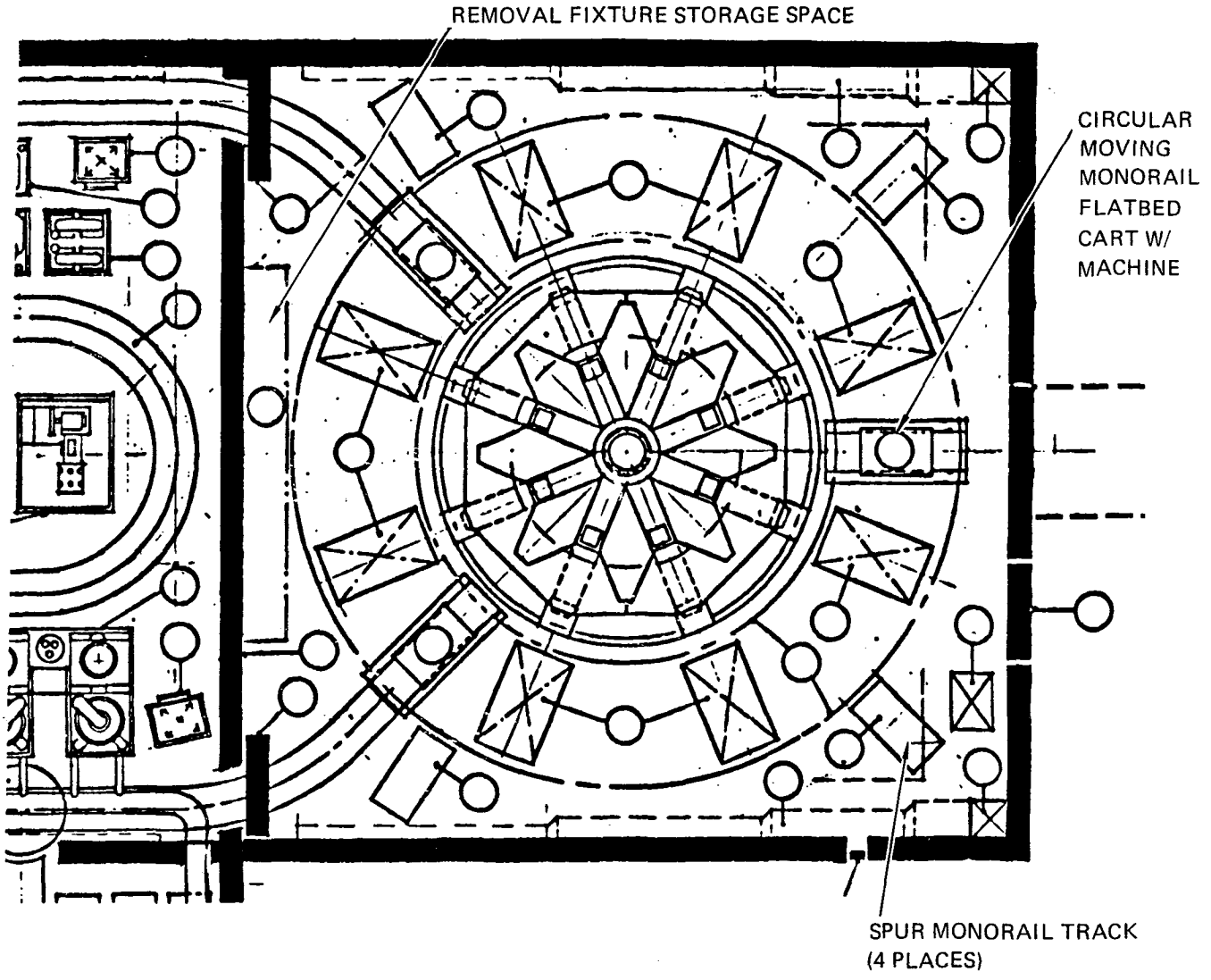

Figure 9-2. The monorail and concentric rails.

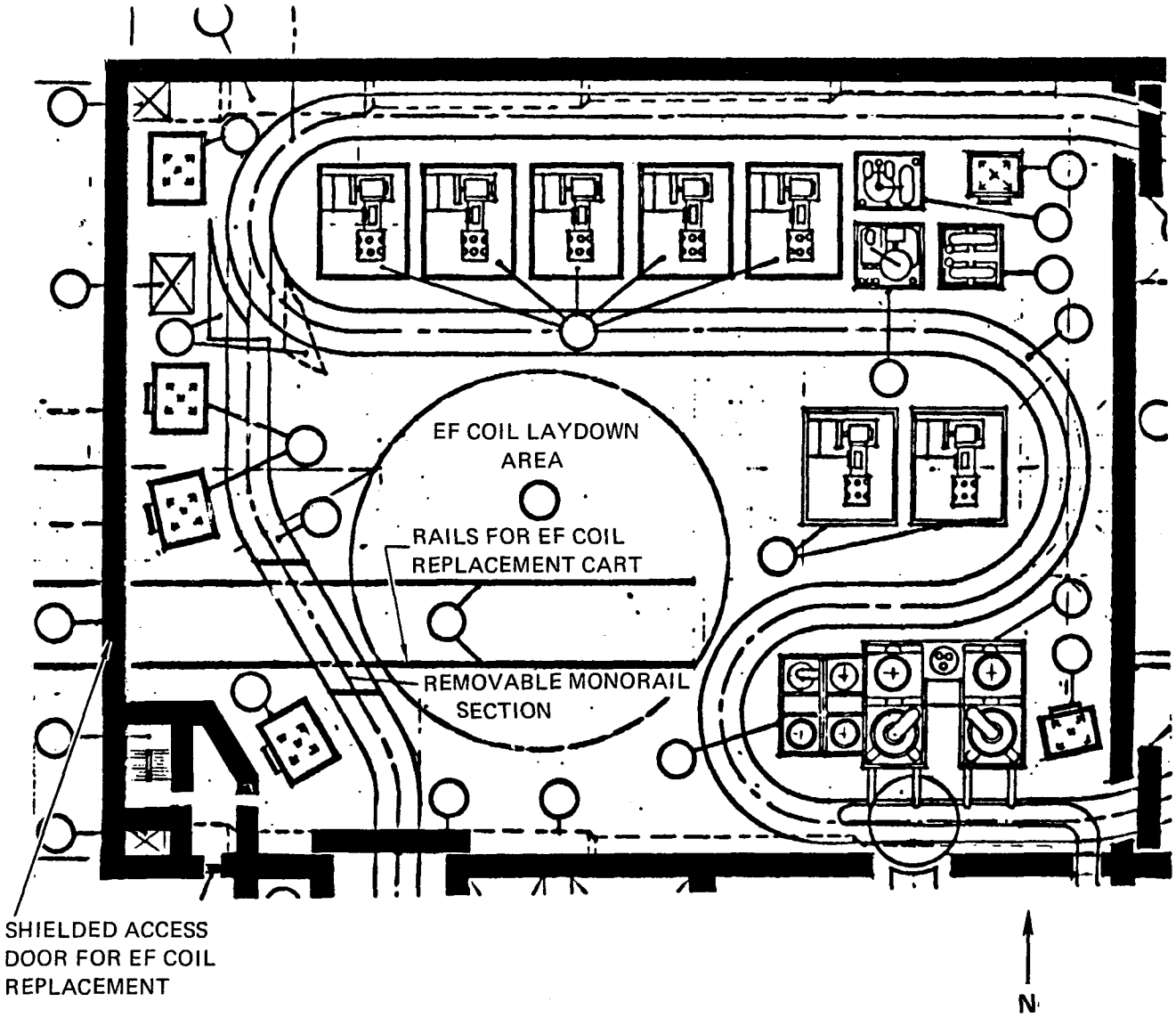

Figure 9-3. The monorail and laydown space.

c. The reactor hall and the process module room are separated by a concrete wall and two sliding doors. The 1.5 m thick wall minimizes the radiation shine to the process module room. The height of the wall is set by the clearance required for the passage of the 500-ton crane. The upper portion of the wall is constructed from removable concrete block sections to facilitate the transfer of the outboard EF coils in and out of the reactor hall to the laydown area in the process module room.

d. Figure 9-3 shows the laydown space area. This laydown space is sized to accept the outboard EF coils placed in a horizontal position. Also shown are rails to a shielded access door at the west wall of the process module room. This access door when opened will allow the transfer of large reactor component replacements, including the outboard EF coil and the TF coil, into the process module room from a staging area outside the Reactor building.

e. The Reactor Building is equipped with a 500-ton bridge crane, a 60-ton process area bridge crane, and the electro-mechanical manipulators. In addition to the floor-mounted equipment, the overhead bridge cranes and electro-mechanical bridge manipulators assist in maintenance functions by providing access to the top and upper equipment areas of the reactor and various modules not accessible to other systems. The 60-ton bridge crane at the process module end of the building is capable of lifting and removing process equipment for repair and replacement.

f. There are two basic devices for use on the monorail track.

   (1) Servo-manipulator transporter: Although there may be several variations of this device as detailed maintenance functions become defined, the basic equipment consists of a truck with wheels that firmly grip the monorail above and below for high stability during a maintenance operation and when in motion. Mounted on the truck is a rotating, telescoping tower that can extend up to 24 m in height and retract down to 12 m for passage through the airlock openings. A vertical traveling and locking trolley is mounted on the tower and moves up or down to a height as required by a specific operation. Mounted on the trolley is

a rotating, telescoping tube with a pair of parallel jaw hands, hooks, TV cameras, and other accessories.

(2) Transporter Cart: Sized to accommodate various major components of the reactor, the cart is large enough to transport a blanket module, a vacuum pump, a limiter module, or smaller items to the Hot Cell along the monorail track. The cart can be supported on a scissors-jack base that provides overall height adjustment.

g. Other miscellaneous fixtures.

(1) EF Coil Yoke Fixture: The EF coil yoke fixture is used with the 500-ton crane to transfer the 27 m diameter EF coil from its vertical position in the transfer cart to a horizontal position. The EF coil will be rotated about the X axis by two pivot points on the yoke. Once the EF coil is in the horizontal position, it is lowered to the floor in the laydown area in the process module room.

(2) EF Coil Lifting Fixture: The EF coil is lifted from its laydown area by the EF coil strongback lifting fixture. The fixture consists of a steel beam cross configuration with lifting points that attach to the EF coil. The EF coil is then lifted by the 500-ton crane over the separating wall between the process module room and the reactor hall and placed around the reactor.

(3) Lower Inner EF Coil Fixture: The inner EF coil removal trunnion fixture is located in the EF coil removal room beneath the reactor. Its purpose is to provide a means of rotating failed inner EF coils from a horizontal to a vertical attitude. The EF coil can then be removed on a mechanized cart through the basement level corridor provided.

9.2.2.4 Reactor Component Maintenance/Replacement Scenarios Significant scenarios are discussed below.

a. Limiter Module Replacement: Due to erosion the limiter blade must periodically be refurbished. This is expected to be required every 2 years. Refurbishment is accomplished by removing the limiter module and moving it to the Hot Cell. In the Hot Cell the blade is repaired or replaced. The steps required for removal and replacement are:

(1) Move general purpose manipulator to position at limiter.

(2) Disconnect and remove two (supply and return) coolant lines.
(3) Disconnect seal flange (bolted or welded) around limiter module.
(4) Move limiter module removal device into position.
(5) Retract limiter module.
(6) Move limiter module to Hot Cell.
(7) Install new module in reverse order of above steps.

The above steps may be accomplished within the current Reactor Building design. The flatbed on the concentric rail tracks will accommodate the limiter module removal device which in turn will retract the limiter module. The size of the reactor hall is large enough to allow adequate pulling space for the removal of the limiter module from the reactor. The concentric rail tracks can accommodate several flatbeds at one time. Thus, a new module may be brought in prior to the removal of the old limiter module to minimize replacement time.

b. Blanket Module Replacement: To refurbish the first wall/blanket, a blanket module is removed from the reactor to the Hot Cell. The eight blanket modules can each be radially withdrawn from the shield. An air bearing on wheeled extractor pallet is used for radial motion. Once clear of the reactor, the module is moved to the Hot Cell on a tracked platform or by crane. The weight of a module is approximately 300 tons. The steps required for module replacement are:
(1) Remove limiter module
(2) Disconnect manifolding to blanket module
    (a) Shield coolant lines (2)
    (b) Blanket coolant lines (8)
    (c) Tritium removal lines (2)
(3) Disconnect seal flange around blanket module.
(4) Remove shield plug at module base and insert extractor pallet.
(5) Position blanket module retractor/transporter at module base.
(6) Retract blanket module.
(7) Move blanket module to Hot Cell using module retractor or crane.
(8) Install new module in reverse order of above steps.

c. Shield Module Removal The shield is considered to be a permanent piece of hardware, not intended for periodic removal; however, provisions are made for removal if required. The shield is divided into 8 modules. Each module is removed radially through the TF coils. The shield can be moved radially outward using the overhead crane. Sequential steps of attaching the crane are required because of the overhead CF and EF coils and TF coil intercoil structure. The most difficult problem is the cutting and rewelding of adjacent sectors. All welds lie in a plane; however, it may be necessary to have a built-in welder track on the internal adjacent sector welds. The steps required for shield removal are:

(1) Remove limiter and blanket module from sector in question and from adjacent sectors.
(2) Disconnect and remove shield sector coolant lines (2).
(3) Position welder/cutter in shield sector.
(4) Cut double seal weld between adjacent sectors.
(5) Cut vacuum duct seal.
(6) Cut outer periphery seal.
(7) Remove access panel from top of vacuum dewar.
(8) Remove upper shield blocks.
(9) Attach crane to shield module (straddle outer CF coil).
(10) Move shield module outboard with crane (alternately straddling CF coil, anti-torque structure, and EF coil).
11. Move module from reactor room with crane (or cart).
12. Install new module in reverse order of above steps.
13. Leak check shield module.

The reactor hall has been designed to provide the necessary space for blanket/shield module removal. The pulling space requirements for retracting the shield module set the size of the reactor hall. Since the weight of a shield module is approximately 440 tons per sector, the capacity of the crane in the Reactor Building is set at 500 tons to handle the required liftings.

d. Vacuum Pump Replacement: The vacuum pumps and valves are located beneath the reactor. The pumps can be replaced without interference or removal of other reactor components. The pump and shielding are

mounted on tracks. To replace a pump the vacuum duct flange is disconnected and the pump/shielding is rolled outward. The pump is removed/replaced from the shielding and removed from the area through an overhead access cover. The pump is then placed on a transporter to be moved to the Hot Cell via the concentric rails and the monorail system.

e. TF Coil Replacement: Replacement of a TF coil is not a routine maintenance task; however, if required, replacement is possible. The TF coil weighs approximately 400 tons and is removed using the 500-ton overhead crane. The major problems that dominate the replacement are the cutting and sealing of the adjacent shield sectors and the vacuum tank. Removal/replacement of a TF coil requires the removal/replacement of the following items:
   (1) Coolant lines from the two bounding sectors.
   (2) Limiter and blanket modules from the two bounding sectors.
   (3) Shield module from the two bounding sectors.
   (4) Vacuum tank top cover and upper ring.
   (5) Vacuum tank outer panel.
   (6) Upper outboard EF coil.
   (7) Shielding blocks (top and bottom).
   (8) Local sectors of CF coils (4).
   (9) TF coil leads.

The operation is completed by performing the following steps:

- Disconnect intercoil structure from adjoining coils (top and bottom).
- Disconnect TF coil from center core support.
- Remove TF coil with 500-ton crane.

The new TF coil may be brought into the Reactor Building through a 32 m slot opening at the west wall of the process module room. This is accomplished by a railed transport cart (see Figure 9-3). Once inside the Reactor Building the new TF coil may be lifted or moved by the 500-ton crane. The removable concrete sections at the top of the sliding doorway at the east wall of the process module room are removed to allow the transfer of the TF coil into the reactor hall.

f. EF Coil Replacement: The requirement that EF coils be replaceable has significant impact on the design of the Reactor Building. All coils located above the reactor beltline and the lower outboard coil are removed by being raised upward using the overhead crane. The three lower inboard coils are removed by lowering to the EF coil removal room at the Reactor Building basement level. It should be noted that TF coil replacement (see paragraph 9.2.2.4 (e)) also involves removal of the upper outboard EF coil. The scenarios of EF coil removal are described below:

To replace the upper outboard EF coil:

1. Use the overhead crane to remove the segmented blocks at the upper section of the wall which separates the reactor hall from the process module room. This is to provide the clearance space required for transporting the defective EF coil to the laydown area in the process module room. The removed segmented blocks may be placed on the reactor hall floor.
2. Remove the outer portion of the vacuum tank top panel.
3. Disconnect the coil mounting.
4. Attach the EF coil lifting fixture to the EF coil.
5. Raise the EF coil by the 500-ton crane over the wall separating the reactor hall and the process module room and move to the laydown area (see Figure 9-4).
6. Bring in the new EF coil through the slot opening at the west wall of the process module room using a railed EF coil transporter cart. The EF coil is then in a vertical position as shown in Figure 9-5.
7. Attach the EF coil yoke fixture to the EF coil and release the EF coil from the EF transporter after the EF coil is secured by the 500-ton crane.
8. Lift the EF coil.
9. Use the 60-ton crane at the process module room to rotate the 27 m diameter coil from its vertical position to a horizontal position.
10. Lower the EF coil to the laydown area.
11. Remove the yoke fixture and return it to storage.

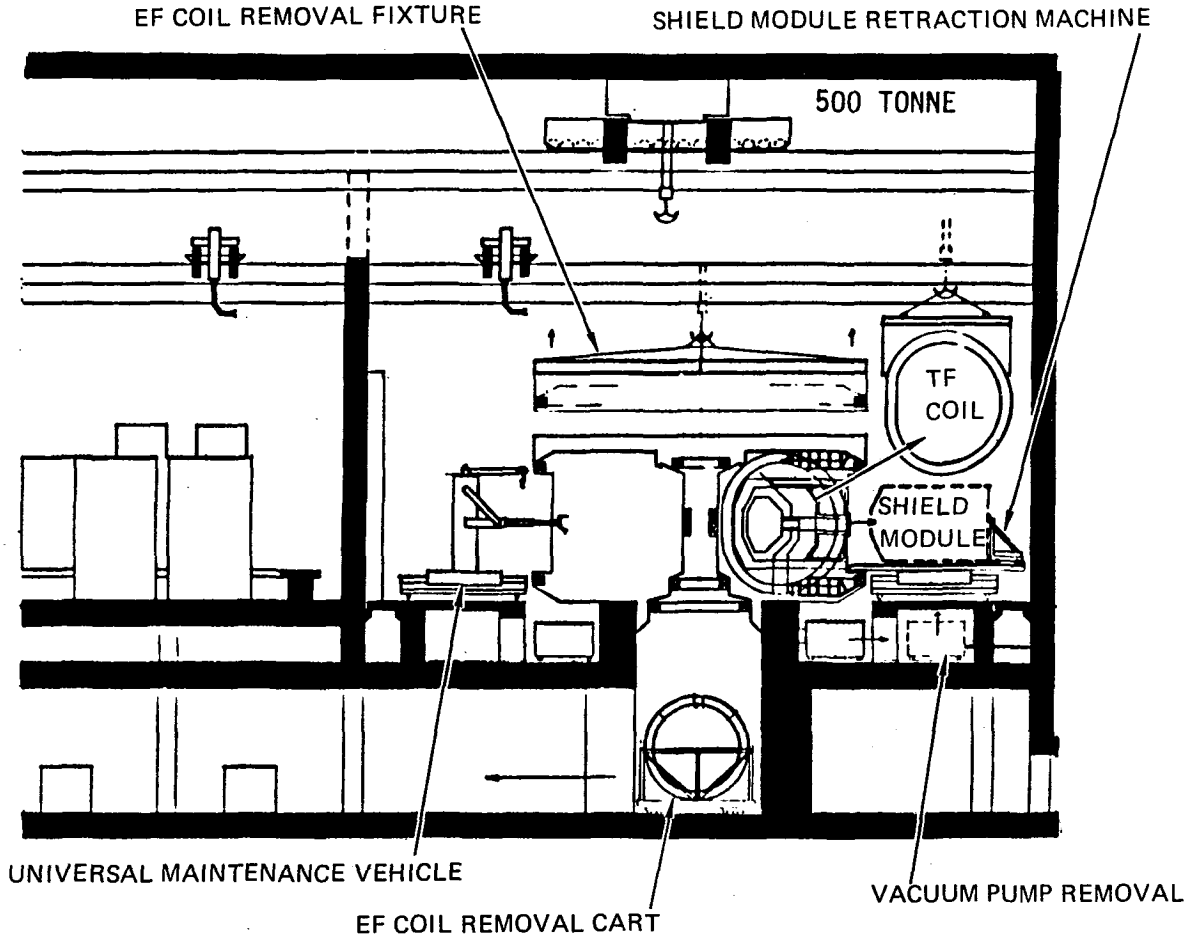

Figure 9-4. Major reactor components replacement.

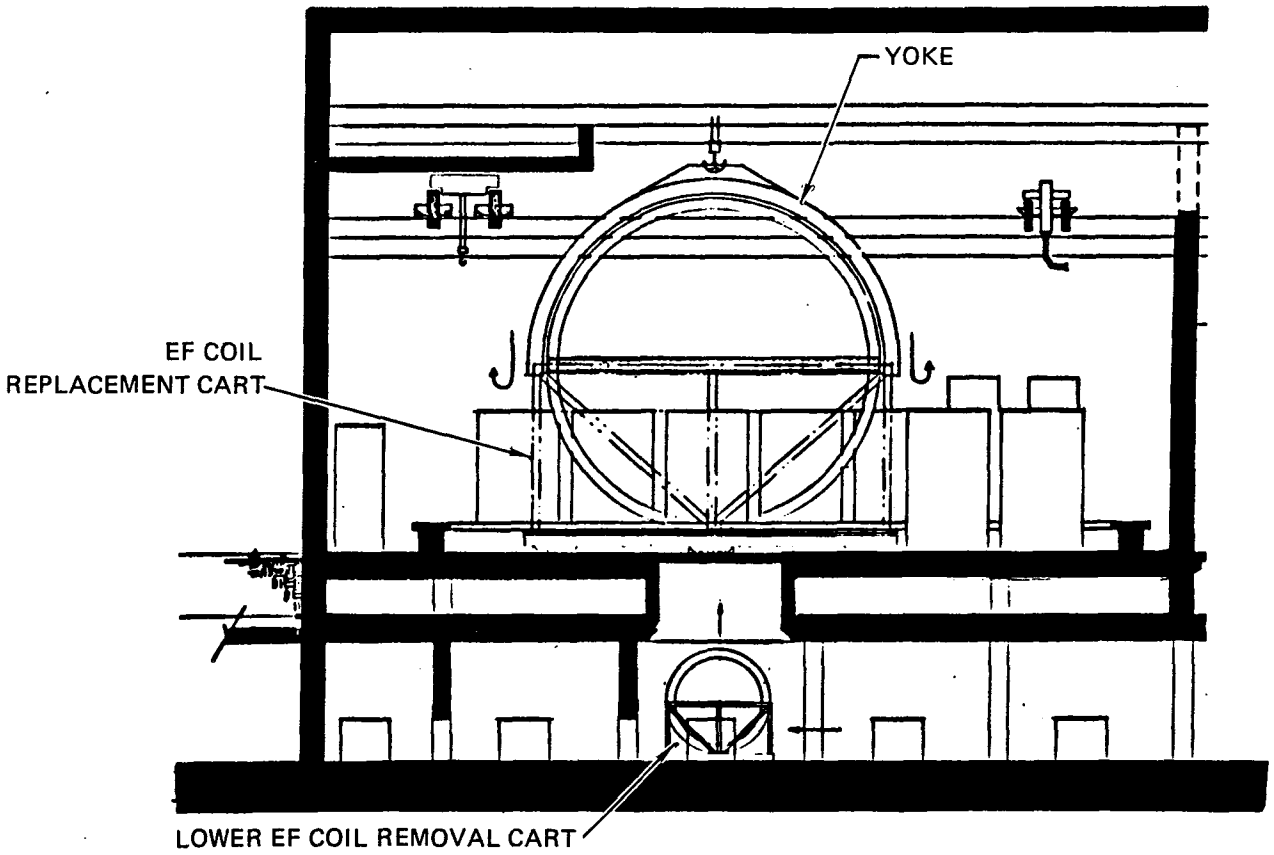

Figure 9-5. Transport of EF coils.

12. Use the EF coil lifting fixture and the 500-ton crane to raise the EF coil from the laydown area to the reactor hall and lower it to its outboard position.
13. Connect the coil mounting and reverse steps 1 and 2.

To remove the lower outboard EF coil, the upper coil and its mounting structure must first be removed. In addition, portions of the vacuum tank beneath and around the upper coil are removed. All coolant lines to the limiter, blanket, and shield modules are removed. The vacuum tank panel immediately above the lower EF coil is removed and then the lower coil itself can be raised beyond the TF coils and clear of the reactor by the overhead crane.

To remove any of the six inboard EF coils, the center section of the vacuum tank top panel is removed using the overhead crane. The coil mounting bolts are then removed by access from above or below, depending on the coil being removed. For the upper coils, the 500-ton crane is attached to the coil and the coil is lifted clear of the reactor. For the lower coils, an inner EF coil removal trunnion fixture and cart will be stationed within the EF coil removal room. Through the reactor center core the 500-ton crane hook will be lowered and connected to the trunnion fixture. The fixture is lifted from the cart and connected to the EF coil. The EF coil and fixture is lowered on to the cart in a horizontal position and secured to the cart. The trunnion rotates the EF coil from its horizontal position to a vertical position.

The EF coil removal trunnion fixture and cart is transferred from the EF coil removal room via the basement level corridor to a lift station (see Figure 9-5). Here a hatch at ground floor level is removed and the EF coil is lifted vertically by the 500-ton crane to the process module room floor for transport to the Hot Cell via the monorail system.

9.2.3 Turbine Building

Architectural and structural features of the tri-level Turbine Building are presented below.

9.2.3.1 Architectural

A major portion of the largest plant structure (in terms of floor area) is devoted to the Turbine Building, which contains a single 400-MWe turbine generator and its auxiliaries. Taking up three basic floor levels, equipment is arranged with a surface condenser in the sub-grade level, feedwater heaters at the ground floor level, and the pedestal-mounted, turbine generator at the upper level.

The building is 110 m long and 50 m wide on all three levels. The sub-grade level is occupied mainly by the condenser and concrete turbine pedestal. Additional equipment and systems located at this level include heat exchangers, condensate pumps, caustic and acid tanks, lube oil reservoirs and conditioner, a chemical equipment room, a battery room, a demineralizer equipment area, and various tanks, motors, and piping.

The ground floor level contains primarily feedwater heaters, with adequate tube-pulling and maintenance space, as well as a continuation of the turbine pedestal. An auxiliary boiler room, clean and dirty lube oil tank room, and various other tanks, pumps, and piping complete the equipment for this level. A railroad spur emerges from the adjacent Reactor Service Building and ends under an equipment hatch in the floor above. An electrical switchgear room and main and reserve transformer yards flank the Turbine Building at this level, and are enclosed within chain link fencing.

The upper level or "operating floor" contains the turbine and its casings, moisture separator/reheaters, and the generator, along with additional feedwater heaters supplementing those on the ground level. Again, adequate space for both tube and rotor pull is provided. A 250-ton bridge crane travels overhead the length of the building and is used for equipment installation, removal, and maintenance.

An additional partial upper level gallery is located on each side of the building for large HVAC ducts that provide cooling air for the Turbine Building. Equipment supplying these ducts is located in the Plant Auxiliary Building mezzanine.

9.2.3.2 Structural

The turbine pedestal portion of the Turbine Building is steel framed, with the crane columns considered fixed at the base laterally and braced longitudinally. Trusses support the roof in the turbine bay with top and bottom chord bracing transmitting horizontal loads to the columns. Crane lateral forces are considered supported at the bottom chord by means of bracing to the adjacent columns. The supported floors, which act as diaphragms, are mainly concrete and have steel decking welded to the structural support frame. Wind, seismic, and crane loading in the longitudinal direction is transferred by vertical bracing to the base mat. The base mat is used as a foundation mat, transfering all the building forces to the supporting soil strata.

The turbine generator support pedestal is designed to meet the requirements of the turbine manufacturer. The pedestal is of a low-tuned design and is separate from the Turbine Building.

9.2.4 Plant Auxiliary Building

Architectural and structural features of the Plant Auxiliary Building are discussed below.

9.2.4.1 Architectural

Equipment, including heat exchangers and pumps for the closed loop cooling water system, is housed in the two-level Plant Auxiliary Building, located between the Turbine Building and the Hot Cell and adjacent to the Reactor Service Building.

Located on the ground level are chillers, pumps, instrument air equipment, and adequate tube pulling and laydown space for maintenance. A machine shop and tool crib are used in common with the reactor service area. Stairs and a freight elevator give access to an upper level that contains air handling units, pumps, plenums, and other HVAC equipment for the balance of the building. This area also affords access to the crane maintenance areas of both the Hot Cell and the Reactor Building.

9.2.4.2 Structural

The Plant Auxiliary Building and the Reactor Service Building are attached to each other and act as one building. The combined building is a steel-framed structure using both rigid frame action and bracing to transfer horizontal forces to the foundation. The roof has both steel beams and trusses to support roof loadings with bracing to transfer horizontal loads to the columns. Concrete floors are supported on steel framing and have steel decking welded to the frame, the floor acting as a diaphragm. The columns are supported on individual spread-footing foundations.

9.2.5 Reactor Service Building

Architectural and structural features of the Reactor Service Building are described below.

9.2.5.1 Architectural

Preparation of blanket segments and other new reactor subsystems, equipment, and parts is carried out in the reactor service area, a ground level high bay area between the Hot Cell and Turbine Building, and adjacent to the Plant Auxiliary Building. The railroad spur passes through the receiving end of this building, where there is also access for large vehicles and other equipment. Storage spaces for new blanket segments and other reactor and process module components flank a large space, 20-m wide by 40-m long by 20-m high, where service operations are carried out including reactor subsystem and process module assembly. A 60-ton bridge crane travels overhead and covers both the railroad spur area during flatcar unloading operations and the service area during maintenance and assembly activities.

An electrical equipment room is located in the common space between the Reactor Service Building and the Plant Auxiliary Building areas. A mezzanine about this space and below the upper level contains personnel toilets and showers, a first aid room, a lunch room, and an office and storage area.

9.2.5.2 Structural

For the description of the structural design of the Reactor Service Building, see subsection 9.2.4.2.

9.2.6 Hot Cell

The architectural and structural features of the Hot Cell are discussed below.

9.2.6.1 Architectural

A variety of fully remote functions are performed in the Hot Cell, notably repair and maintenance of components from the Reactor Building. The Hot Cell is characterized by its massive concrete walls, up to 1.5 m thick around the perimeter, and 1 m thick within. The perimeter walls, roof, and floor of the Hot Cell are lined with steel. All surfaces are coated with decontaminable paint.

The railroad spur passes the external entrance to the Hot Cell, and road access is provided to enable trucks and other large vehicles to approach the Hot Cell entrance. A 60-ton bridge crane travels overhead and can introduce heavy loads to the Hot Cell air lock through a combination door and hatch entrance, and onto a transporter car traveling on a continuation of the monorail track to the Reactor Building monorail system. A room containing decontamination equipment and storage pool cooling equipment is located on one side of the air lock, and the Hot Cell control room is located on the other side. To the north and adjacent to the air lock is a decontamination chamber with a turntable in the track. Decontamination is required for casks containing either activated blanket segments for reprocessing offsite or solid waste for offsite recycle or disposal.

Beyond the decontamination area and located beside the control corridor are three process cells. The liquid waste processing equipment separates activated particulate matter from tritiated water that is then returned to the Tritium Reprocessing Building. The blanket module and solid waste processing cell contains the equipment required to bake out tritium from spent blanket segments and to reduce the segments into pieces conveniently sized for storage in canisters. The remote maintenance and repair shop contains equipment for shield door seal and latch mechanism replacement and for repair of failed process module components. Entrance into each cell is made by rotating the transporter cart or servo-manipulator on a monorail turntable to align it with a perpendicular track that leads through a pair of horizontal sliding doors notched around the track at the bottom. Once inside a cell, further component

handling is by a 60-ton bridge crane and an electro-mechanical bridge manipulator. Each cell is equipped with an atmospheric tritium cleanup system.

Both wet and dry solid waste storage facilities are provided in the blanket module and solid waste processing cell. Wet storage for 600 m of spent blanket segments and dry storage for 400 m of discarded shield doors, pumps, valves, and piping is available. Waste is stored in canisters lowered into storage racks by the overhead bridge crane. The rack grid provides stability for the canisters, simplifying identification and retrievability should this ever become necessary. Efficient and cost-effective use of space above the wet storage tanks is obtained by locating the bottom of the tanks at the same floor level as the cell.

Above the central corridor is a gallery in which HVAC and electrical equipment is contained. Piping and duct runs to the various cells are also made through this gallery. Access to the gallery is made at the north end of the Hot Cell, at the corridor to the crane maintenance area. Additional access is at the south end near the Hot Cell entrance.

9.2.6.2 Structural

The Hot Cell is a carbon steel lined, concrete, hardened structure designed for DBE seismic loading. The building outside walls and roof are thick enough to prevent penetration by tornado missiles, to withstand tornado winds and a tornado-induced differential pressure, and to provide adequate shielding. The inside walls and floor act with the outside walls and roof to transfer all loadings by rigid frame action to the foundation. The inside walls and floor are sized to meet shielding requirements. The base slab acts as the foundation mat, transfering all forces to the supporting soil strata. The concrete waste storage tanks are designed to withstand a DBE seismic event along with the normal loading conditions.

9.2.7 Electrical Equipment and REB Power Supply Building

The architectural and structural features of the Electrical Equipment and REB Power Supply Building are outlined below.

9.2.7.1 Architectural

Power for a number of reactor components is furnished by equipment located in the Electrical Equipment and REB Power Supply Building. This structure consists of three levels, and is 60 m long by 52 m wide. The ground level is essentially one large room that contains the power supplies for EF, CF, and TF coils, in addition to 13.8 kV switchgear. An HVAC equipment room, three sets of stairs, and a freight elevator to lower levels complete the ground level. Directly beneath the ground level is a large cable-spreading room, (shown only in section on the drawings), which occupies essentially the same space as the equipment room above.

REB power supplies are located in the normally occupied sub-grade level, together with 13.8 kV switchgear and 480 V load centers. Also located at this sub-grade level are maintenance, repair, and storage areas. A small office and control room at this level enables personnel to monitor the performance of the system and to locate any faulty components. Conduits from the REB power supplies are run overhead and routed into the overhead space of the tunnel to the Reactor Building sub-grade level.

9.2.7.2 Structural

The Electrical Equipment and REB Power Supply Building is a steel-framed structure supported on concrete basement walls and columns. The horizontal forces are taken by rigid frame action to the foundation, with roof bracing distributing these forces to other columns. The supported floors are concrete slabs resting on steel decking, which is welded to the steel frame, the floors acting as diaphragms. The basement walls are supported on continuous footings with inside columns supported on individual spread footings.

9.2.8 Tritium Reprocessing Building

The architectural and structural features of the Tritium Reprocessing Building are outlined below.

9.2.8.1 Architectural

The tritium and cryogenics facilities are combined into one building, with the tritium components located in two separate areas:

a. Areas not subject to tritium contamination, and
b. Areas subject to potential tritium contamination, in which special clothing and equipment must be used.

The portion of the Tritium Reprocessing Building that contains potentially contaminated areas is hardened in accordance with applicable seismic and tornadic design criteria, and is lined with coated carbon steel to minimize the potential escape to atmosphere of tritium released from process equipment. Tritium-free areas of the building are occupied on an everyday basis and include the offices, toilets, and showers on the ground level and the tritium equipment control room, office, and HVAC equipment room on the upper level. The control room is lined with steel to shield the operators from reactor coil magnetic fields. An air lock separates the tritium-free areas from the potentially contaminated areas. Beyond the air lock is a corridor that contains a protective suit storage alcove and an emergency shower room. The corridor also provides access to the balance of the facility.

In addition to the tritium reprocessing equipment room, there is an analytical laboratory, a maintenance and repair shop, and a storage room for new tritium and deuterium adjacent to the exterior loading dock. Uranium bed storage for reprocessed tritium and deuterium is located in a separate room. A stairway leads to the upper level, which contains a room for HVAC equipment suitable for a tritium atmosphere and another room containing atmospheric tritium cleanup modules. Equipment on the upper level in the tritium reprocessing equipment room is surrounded by a metal catwalk grating and railings. The remaining space is open to the ground level below. A 5-ton overhead traveling bridge crane is used for maintenance as well as transporting equipment to and from the equipment air lock that leads to the exterior loading dock.

Piping to and from the Reactor Building and Hot Cell is double walled, with quick-acting isolation valves located close to the building walls. The piping is routed to the Reactor Building pipe chase in an underground tunnel.

9.2.8.2 Structural

The Tritium Reprocessing Building and the Cryogenics Building are connected to each other and act as one building. The portion of the building subject to potential tritium contamination is a steel-lined, concrete, hardened structure designed for DBE seismic loading. The building outside walls and roof are thick enough to prevent penetration by tornado missiles, to withstand tornado winds and a tornado-induced differential pressure, and to provide adequate shielding. The inside walls, columns, and floors act with the outside walls and roof to transfer all loadings by rigid frame action to the foundation. The base slab acts as the foundation mat, transfering all forces to the supporting soil strata.

9.2.9 Cryogenics Building

The architectural and structural features of the Cryogenics Building are outlined below.

9.2.9.1 Architectural

The Cryogenics Building is relatively simple, consisting of one large room for helium and nitrogen compressors, with an electrical equipment room in an enclosed mezzanine covering one-third of the space below. The remaining cryogenics equipment is located in a fenced-in yard adjacent to the building. This equipment, along with gaseous helium storage tanks located across the perimeter road, is adequately described on the drawings. An underground tunnel carries liquid helium and nitrogen lines to the Reactor Building pipe chase, where the lines are routed to the reactor hall.

9.2.9.2 Structural

The Cryogenics Building adjoins the Tritium Reprocessing Building and is a steel-framed structure with pre-cast concrete panels on the exterior. The rigid frame design and bracing ensure that horizontal forces are transfered to the foundation. Vertical loadings are supported in the roof by steel beams on columns.

9.2.10 Administration Building

Architectural and structural features of the Administration Building are discussed below.

9.2.10.1 Architectural

Prsonnel operations for the entire plant are controlled and supervised in the Administration Building. Combined with the Administration Building are the Control Building and the Site Service Building, which are discussed in subsections 9.2.11 and 9.2.12, respectively.

The ground level of the Administration Building consists of a main entrance and reception area, a conference/display room, and various offices arranged on a double corridor system. A lunch room and staff toilets are provided. The facilities provided in the Administration Building are designed to support 60 individuals, the maximum number of operating and maintenance personnel anticipated onsite at any time. The upper level contains electrical and HVAC equipment for both the Administration and Site Service Buildings.

9.2.10.2 Structural

The Administration Building is a combined, steel-framed structure using both rigid frame design and bracing to transfer horizontal forces to the foundation. The building is also attached to the Control Building, where vertical and horizontal loads are supported. Vertical loadings are supported in the roof by steel beams in the administration area and by trusses in the service area. The supported floor in the administration area is a concrete slab resting on steel decking that is welded to the steel framing, the floor acting as a diaphragm. The columns take the loadings to the foundations that are individual spread footings.

9.2.11 Control Building

The architectural and structural features of the Control Building are discussed below.

9.2.11.1 Architectural

Although visually combined with the Administration Building and Site Service Building, the Control Building is a separate, two-level, hardened structure that is entered only from the rear corridor of the Administration Buiding. There is an emergency exit on the north side of the building.

The ground level contains the main control room, auxiliary equipment areas, computer equipment room, maintenance and repair shop, tools and parts storage, offices and conference rooms, toilets, and electrical equipment. The upper level contains electrical and HVAC equipment, and an observation gallery above the main control room. The main control room layout depicts anticipated technological advances of the future time for which this plant is intended. An expansion of the operator's console to include several CRTs is envisioned. Instruments and control components are expected to continue their present trends toward miniaturization and the use of micro-processor based distributed controls. The customary cable-spreading area beneath the control room is replaced by an access flooring system. Previously hard-wired controls of the reactor and various systems are replaced by multiplexed signals in a communication tunnel underground to the Reactor Building. Consequently, the relatively large distance from the Reactor Building to the control room is of minimal concern.

9.2.11.2 Structural

The Control Building is a hardened structure designed for DBE seismic loading. The building outside walls and roof are thick enough to prevent penetration by tornado missiles and to withstand tornado winds and a tornado induced differential pressure. The inside columns and floors act with the outside walls and roof to transfer all loadings, by rigid frame action, to the foundation. The base slab acts as the foundation mat transfering all forces to the supporting soil strata.

9.2.12 Site Service Building

Architectural and structural features of the Site Service Building are discussed below.

9.2.12.1 Architectural

Combined with the Administration and Control Buildings is the Site Service Building, consisting of a maintenance shop and a warehouse. Repairs and storage of items not directly related to the reactor and its systems are carried out in this building, Each space has a large door opening at the loading entrance, a receiving office, toilet room, and a small storage room. At the opposite end of the maintenance shop are separate rooms for flammable storage and welding. A 10-ton bridge crane travels overhead. In the warehouse forklifts and pallet lifts are used for moving heavy items.

9.2.12.2 Structural

The structural design of the Site Service Building is similar to that of the Administration Building, described in subsection 9.2.10.2.

9.2.13 R&D Building

Architectural and structural features of the R&D Building are discussed below.

9.2.13.1 Architectural

The one-story R&D Building consists of offices, laboratories, a computer center, conference rooms, a library and toilet rooms. The building is the same size as the Administration Building and is designed to house up to 200 scientists and engineers performing the R&D work in the plant. The R&D building is located next to the Administration Building and is adjacent to the main entrance and parking facilities.

9.2.13.2 Structural

The structural design of the R&D Building is similar to that of the Administration Building, described in subsection 9.2.10.2.

9.2.14 Onsite AC Power Supply Building

The architectural and structural features of the Onsite AC Power Supply Building are discussed below.

9.2.14.1 Architectural

The building is situated to minimize cable runs to standby power users. Two identical though opposite hand gas turbine generators are located in the hardened one-story building, which is 40 m long by 30 m wide by 10 m high. A fire wall separates the two units, and each unit has a control room, a battery room, and a 10-ton overhead bridge crane. Additional hardening is provided on the south and west walls, which are exposed to a potential lowtrajectory turbine blade missile strike zone. Interlocks on the large sliding doors of this building prevent operation of the turbine unless the doors are closed and locked.

An adjacent two-story structure to the south contains control equipment for the switchyard on the upper level and a cable-spreading room on the ground level.

9.2.14.2 Structural

The gas turbine building is a concrete, hardened structure designed for DBE seismic loading. The building outside walls and roof are thick enough to prevent penetration by tornado missiles and to withstand tornado winds and a tornado-induced differential pressure. The inside walls combine structurally with the outside walls and roof to transfer all loadings by rigid frame action to the foundation. The walls are supported on continuous spread footing foundations, with the gas turbine mat foundations separated from the building foundation. The gas turbine foundations are designed to meet the requirements of the gas turbine manufacturer including an appropriate vibration analysis and DBE seismic analysis.

9.2.15 Security Building

The architectural and structural features of the Security Building are dicussed below.

9.2.15.1 Architectural

All traffic to and from the plant is controlled from the Security Building. Transport and delivery trucks and railroad traffic undergo inspection and identification by security personnel. Plant personnel and visitors

must pass through inspection portals and identification devices in the Security Building prior to entering the plant. Radiation monitors ensure that personnel leaving the plant are free from contamination. Identification badges are stored in badge racks in the unsecured area. Closed circuit television monitors of plant-wide operations allow complete visual surveillance. Communication equipment and plant-wide alarm panels are also located in the building.

9.2.15.2 Structural

The Security Building structural design is similar to that of the Administration Building, described in subsection 9.2.10.2.

9.2.16 Pump Houses

Architectural and structural features of the Pump Houses are described below.

9.2.16.1 Architectural

The fire water storage tank pump house is located adjacent to the raw water reservoir, evaporation pond, and fire water storage tank. This structure contains pumps and chlorination facilities for the potable water system and the diesel and motor-driven fire pumps that supply the fire loop.

The circulating water pump house is located near the main cooling towers, and contains pumps and chlorination facilities for the circulating water system. A 20-ton bridge crane travels overhead to assist in the installation and removal of pumps and other equipment.

9.2.16.2 Structural

The circulating water pump house is a steel-framed structure with the crane columns considered fixed at the base laterally and braced longitudinally. Trusses support the roof with top and bottom chord bracing transmitting horizontal loads to the columns. Crane lateral forces are considered supported at the bottom chord by means of bracing to adjacent columns. Wind or seismic loads are taken by rigid frame action laterally and by bracing longitudinally to the pump pit.

The fire water storage tank pump house is a hardened, concrete structure designed for DBE seismic loading. The building outside walls and roof are thick enough to prevent prenetration by tornado missiles and to withstand tornado winds and a tornado-induced differential pressure. The walls and roof act as a rigid frame to transfer structural loadings to the foundation.

9.2.17 Site Facilities Design

This subsection discusses site development, site utilities, the pump pit, and the facility stack.

9.2.17.1 Site Development

Site development activities are outlined below.

9.2.17.1.1 Clearing and Grubbing

The site is first cleared and grubbed, with all extraneous material and obstructions removed.

9.2.17.1.2 Earthwork

Excavation and disposition of excavated material is required to establish the permanent contours of the site. There is an overall soil erosion program to stabilize the site during construction. The excavation program includes subgrades for railroads and access roads, drainage structures and channels, excavation and drainage for all structures, buildings and foundations, circulating water lines, and other underground lines. Excavated areas are backfilled to required levels with compacted fill. Where suitable, existing onsite soils are used for constructing compacted fills.

9.2.17.1.3 Roads and Parking

Sufficient roads and parking are provided within the site boundary. Parking is provided outside the boundary close to the Security Building for visitor parking. Roads are two-lane, asphalt-concrete surfaced, with 4 m-wide lanes and 1-m-wide shoulders except where continuous two-way traffic is not required. Service driveways to the different buildings are at least 6 m wide.

9.2.17.1.4 Yard Fencing

The completed site switchyard and transformer areas are protected by a chain link fence. Visitor and employee parking is located outside the fenced area, with access normally made on foot through a Security Building controlled by guards on a 24-hour basis. The area within the fence is defined as a restricted area. A check-point system is used for each phase of facility completion, both on the perimeter of and within the facility. The plant layout provides only one normal point of entrance and exit for all but railroad traffic. Emergency exits and service doors are monitored on alarm panels located in the control room and Security Building.

9.2.17.1.5 Yard Piping

Yard piping includes circulating water, plant service water, standby service water, circulating water makeup and blowdown, standby service water makeup, domestic water, fire protection, sanitary sewage, storm sewage and underground drainage, and miscellaneous piping.

9.2.17.1.6 Sanitary Sewage Disposal

Sanitary sewage from the entire facility is piped to an existing sewage treatment plant. Building service sewer connections are provided to carry peak flow based on the number of plumbing fixture units in the buildings or the maximum estimated flow based on building occupancy.

9.2.17.1.7 Subsurface and Surface Drainage

The immediate plant area surrounding the major structures is drained by installing a storm sewer system to convey the runoff into the main drainage ditch. In other areas runoff resulting from rainfall is conveyed to drainage ditches by sloping the tributary surface areas. A system consisting of ditches, culverts, chutes, and chute spillways discharges the storm runoff into the main ditch.

9.2.17.1.8 Railroad

The railroad spur line is brought into the plant area from the nearest main railroad, assumed to be 8 km from the site boundary.

9.2.17.2 Site Utilities

Site utilities are those mechanical systems required for the support of normal overall facility operations. The site utility systems include:

a. Raw water system
b. Service water system
c. Auxiliary steam system
d. Domestic water system
e. Potable water system
f. Compressed air system

9.1.17.2.1 Raw Water System

For this project a large body of fresh water (river, lake, or canal) has been assumed to be located 1.6 km from the site. It has been further assumed that all makeup water requirements are adequately met by the raw water system. The system consists of two full-capacity pumps, located at the intake structure, that deliver raw water through either of two underground pipelines supplying the raw water reservoir, located within the power plant boundary. System redundancy is such that plant shutdowns due to a single failure of water supply components are precluded. In addition, the raw water reservoir is sized to provide 30 minutes of surge capacity to support facility water requirements in the event of total loss of supply from the source.

9.2.17.2.2 Service Water System

The service water system supplies all plant water requirements (with the exception of the fire protection system) from the raw water reservoir. The principal water user is the circulating water system, to which the service water is supplied at the circulating water pump house pit. The system consists of two full-capacity pumps, a chlorination package, and the necessary piping, valves, and instrumentation and controls to support all plant water supply requirements. The pumps and chlorination package are located in a pump house adjacent to the raw water reservoir.

9.2.17.2.3 Auxiliary Steam System

An auxiliary steam system is designed to meet all of the plant's heating and hot water requirements. In addition, auxiliary steam is used for startup of the power conversion cycle. An auxiliary boiler and related components located in the Turbine Building supply the auxiliary steam requirements. Fuel oil is supplied to the auxiliary boilers by an underground oil storage tank and two full-capacity transfer pumps.

9.2.17.2.4 Domestic Water System

All domestic water requirements are supplied by the service water system.

9.2.17.2.5 Potable Water System

A potable water system is provided to meet the plant potable water demand. Water supplied by the service water system is processed in the potable water treatment package.

9.2.17.2.6 Compressed Air System

The compressed air system, that includes the plant air and instrument air subsystems, is designed to provide a reliable supply of dry, clean, oil-free air to hose stations, tools, and pneumatic instruments and controls. The major components of the system are two full-capacity compressors, filters, and holdup tanks. The system provides sufficient air for normal plant operation and maintenance, based on satisfying plant and instrument air needs in accordance with the estimated concurrent demand of each component, all at the required pressure. The plant air subsystem provides a source of backup air supply for the instrument air subsystem to prevent a plant shutdown due to loss of instrument air. Accumulators that are provided in areas where high-volume, short-term usage of instrument air is required can supply air within 1 second at the minimum operating pressure of the equipment.

9.2.17.3 Pump Pit

The concrete pump pit for the circulating water system is sized for six pumps, separated from each other by concrete walls. Screens prevent trash from entering the pumps, and stop logs allow the pump well to be emptied for

cleanup and maintenance. The pit is designed to support the circulating water pump house and transfer building loads to the supporting soil strata.

9.2.17.4 Stack

The stack that discharges gaseous effluents from the Reactor Building, Hot Cell, and the Tritium Reprocessing Building is a steel-lined, reinforced concrete outer shell of slip-form construction, supported on an octagonal foundation. The steel liner is supported vertically by a structural steel frame attached to the concrete shell. To allow for the expansion of the liner, the horizontal support of the liner is by means of guides attached to the concrete shell.

9.3 Mechanical Systems Design

This subsection presents the design of the balance of plant mechanical systems required to convert the heat generated by the fusion reactor into electrical energy. It also presents the design of cooling water systems required to maintain reactor plant auxiliary component temperatures within specified limits for all operating modes.

9.3.1 Power Conversion System

The power conversion system consists of components of conventional design for use in large central generating stations. The thermodynamic cycle itself and its components resemble the thermal cycle of a pressurized water reactor plant.

The power conversion system, is used to convert the reactor thermal energy to electrical power. 1147-MW of the 1200-MW thermal energy generated by the reactor is transferred to the power conversion system by the heat transport system.

9.3.1.1 Design Basis

The principal functions of the power conversion system are to:

a. Convert the available thermal energy to useful electrical energy at the highest thermodynamic efficiency economically possible.
b. Reject to the atmosphere the non-recoverable thermal energy.

c. Maintain the reactor first wall/blanket and limiter within the specified temperature limits.

The system must satisfy these functions subject to technical, economic, safety, and environmental constraints. The approaches discussed in this section are conceptual, without benefit of optimization and consideration of a broad spectrum of alternatives. In addition, they have been subject only to first-order analysis. However, the design selected is feasible and reasonably economic. Further, the design is comparable to recent designs of similarsized PWR steam conversion cycles. Codes and standards for a fusion reactor power plant have not yet been developed. However, it is anticipated that the secondary system will have to meet the applicable and relevant criteria of a PWR plant. The secondary system for the plant has been designed with this assumption.

The overall thermal cycle efficiency is 33.6% resulting in a gross electrical output of about 390 MWe.

9.3.1.2 Design Description

The major components of the power conversion system include:

a. Steam generators
b. Turbine generator
c. Main condenser
d. Condensate pumps
e. Steam jet air ejectors
f. Feedwater heaters
g. Feedwater pumps

The power conversion cycle, nominally rated at 1290 MWt, is designed to supply steam to a turbine generator rated at 400 MWe for the production of electric power. Steam is produced by thermal energy removed from the reactor coolant system. Main turbine exhaust steam is converted from vapor to condensate in the main condenser. Condensate is returned to each steam generator via the regenerative feedwater heating system after removal of dissolved gases and impurities.

Two steam generators are designed to provide a total of 2.16 x 10 kg/hr of slightly superheated steam at 5.2 MPa and 282°C. The system receives 1147 MWt of the total heat input from the reactor coolant system at the steam generators. The remaining 135 MWt of the heat is rejected to the closed loop cooling system. Two main steam lines are provided between the steam generators and the turbine throttle valves. Each steam line is connected to a steam generator, corresponding to one of the two reactor coolant loops. The main steam lines are provided with an isolation valve and a check valve in each line just outside the Reactor Building. The isolation valves automatically close on high steam flow and either low temperature or low pressure simultaneously, and also on high Reactor Building ambient pressure. The valves can be operated remotely from either the main control room or local panels. The swing-type check valves protect against backflow of steam into the steam generator and the Reactor Building in the event a loop is not operating for either maintenance or emergency reasons.

A turbine bypass is provided to control excess steam during startup, shutdown, and during power operation when steam generation temporarily exceeds turbine requirements. The automatic steam dump valves are capable of bypassing up to 45% of design flow to the turbine bypass system and directing it to the main condenser. In connection with the steam dump valves and turbine bypass system, auxiliary feedwater pumps are provided to safely shut down the reactor in the event of a concurrent loss of offsite power and turbine trip. One of the auxiliary feedwater pumps is driven with a steam turbine, while the other two are motor driven, using the standby power source. Turbine plant equipment is selected for high operating efficiency to provide maximum generating capability and reliability. All equipment is designed for continuous operation at 105% of the rated steam flow. The subsystems and/or components that comprise the power conversion system are:

a. Main steam supply system
b. Turbine generator unit
c. Moisture separators/reheaters
d. Main condenser
e. Condensate system
f. Feedwater system

The main steam supply system transports the superheated steam from the two steam generators to the high-pressure stage of the main steam turbine's throttle/stop valves. The pipelines from the two steam generators supply the steam with the minimum economical pressure losses, ensuring uniform heat removal from each steam generator, thus maintaining system balance. In addition, the piping arrangement provides for mixing to ensure uniform steam conditions at the inlet to the high-pressure turbine. Branches from the main steam system headers are used to provide heat to the reheaters. The high-pressure turbine exhaust is dried and reheated before entering the low-pressure turbines.

The turbine consists of one double-flow, high-pressure stage in tandem with two double-flow, low-pressure stages. The turbine is a three-casing, 1800-rpm unit with tandem-compound, four-flow exhaust. The unit is provided with two steam chest assemblies, one located on each side of the highpressure turbines. Each assembly consists of two throttle-stop valves and two governing valves. Each valve is controlled by an electro-hydraulic governing system through an individually operated valve actuator. The generator includes a hydrogen-inner-cooled, synchronous generator, with a water-cooled stator and a shaft-driven, air-cooled, brushless or static exciter. The unit has a power factor of 0.85, with a rated output of 18,000 V, three-phase, 60 hz.

Two 50%-capacity moisture separators/reheaters are provided to remove the moisture of the wet steam exhausted by the high-pressure turbine and to reheat the steam, providing approximately 40°C of superheat. The wet steam, at about 8% moisture content, enters the moisture removal section, where 100% of the moisture is removed mechanically and drained to the feedwater system to be used for heating. The dried steam then passes through the two-element reheater section, where it is first heated with extraction steam from the high-pressure turbine and then heated by the main steam. The condensed steam and the moisture removed are used in the feedwater system for heating. The superheated steam from the reheater enters the two low-pressure turbines and the two feedwater pump turbines.

A series multi-pressure condenser, with an approximately 6.0°C temperature rise for each section, is provided for a total rise of about 12°C. The steam exhausted from each low-pressure turbine is dedicated to one of the condenser stages, allowing parallel operation between turbine and condenser. Each condenser section is located directly below one of the lowpressure turbine stages, taking the exhausted steam from that particular turbine stage. The circulating water is connected in series to each condenser stage, i.e., the water passes from one stage to the next. The average back-pressure on the condensing steam is 8.5 kPa, corresponding to a saturation temperature of 42.6°C.

Two pairs of condensate pumps, with each pump sized for 50% of rated flow, are provided; two pumps are normally operating with the two redundant pumps on standby. Each pair of pumps takes suction from one of the two condenser sections, transfering the condensate to the feedwater system. This pump arrangement provides operational and control flexibility. The main function of the system is to condition the condensate by deaeration, polishing, chemical addition, and condensate makeup to provide feedwater at the purity required for the steam generators and to ensure turbine optimum performance and reliability. Gases and air are removed by steam air ejectors. A demineralizer system, provided for condensate polishing, is capable of removing suspended material such as corrosion products and ionized solids. Chemical addition is provided for pH control and for oxygen scavenging. Condensate makeup is supplied to the condenser hot well from the condensate storage tank. Makeup requirements are controlled by the hot well level.

The feedwater system supplies feedwater to the steam generators at the required flow rate, temperature, and pressure for optimum turbine output and thus cycle efficiency. The system consists of two trains of low-pressure heaters and two trains of high-pressure heaters. Three feedwater pumps are provided, each designed for 50% of the 105% rated capacity. The two pumps normally operating are steam turbine driven, taking steam from the reheaters outlet and exhausting it to the main condenser. The standby feedwater pump is motor driven. The motor-driven pump is used for startup until an adequate steam supply has been established to the turbine driven pump.

Feedwater heating is accomplished by extracting steam from the highand low-pressure turbines. In total, there are seven sets of heaters, four low-pressure heater sets (two per set), and three high-pressure heater sets (two per set). In addition, two flash tanks are provided to collect the high-pressure heater and moisture separator drain liquid for return to the system. The flashed steam is used for heating. The feedwater pumps deliver pressurized feedwater at 7 MPa to provide the required 5.3 MPa steam at the turbine throttle valves.

9.3.2 Heat Rejection System

This subsection describes the heat rejection system including the main cooling towers and the circulating water system.

9.3.2.1 Design Basis

The main function of the heat rejection system is to maintain the most economical condenser back pressure, which is a function of cooling water temperature and flow rate. This very critical economic impact on the power plant must take into account the ecological considerations of rejecting large quantities of heat to the atmosphere.

The cooling method selected is based on economic factors, with the additional assumption that once-through cooling, i.e., river, lake, or sea water, is not available at the majority of potential sites, whereas cooling towers are adaptable to any site. Furthermore, natural draft cooling towers are assumed most acceptable to environmental and regulating agencies and result in lower operating cost than the mechanical draft type.

The heat rejection system is also responsible for maintaining cooled components within specified temperature limits during normal plant operation. Cooling water is provided directly to some components, such as plant chillers, and indirectly by the use of an intermediate heat exchanger to other components such as those served by the closed loop cooling water system.

9.3.2.2 Design Description

Economic and technical analyses result in the selection of a 400 MWe turbine generator rating at 8.5 kPa average condenser back pressure. The multipressure condenser is cooled with 27.4°C inlet water with a 12°C range. The natural draft hyperbolic cooling towers selected use a 4.6°C approach at 22.8C wet-bulb temperature. The wet-bulb temperature is determined at the 95% duration design point, i.e., 95% of the time the wet bulb is at 22.8°C or below. At higher wet-bulb temperatures, the cycle efficiency and thus turbine output decrease.

The overall system consists of two hyperbolic natural draft cooling towers; four wet pit, vertical-type centrifugal pumps; a chlorination package; an evaporation pond; and a raw water reservoir for makeup. The cooling towers are aesthetic, massive structures of reinforced concrete, approximately 120 m in diameter at the basin, 80 m in diameter at the top, and 145 m in height. The pump house provided for the pumps and chlorination package contains a well with individual compartments for each pump and filter.

Makeup water is supplied to the pump well at a rate controlled by the well level. Makeup is on a continuous basis to replenish the water loss by evaporation and drift and by tower blowdown. Blowdown liquid is routed to the onsite evaporation pond to maintain the proper concentration of minerals in the circulating water. The makeup and blowdown systems have not been optimized but a continuous makeup rate of 3% to 5% of the total flow rate has been assumed, which is typical of power plant design. Makeup water is supplied from the raw water reservoir by the service water pumps. The four circulating water pumps are each designed to handle 25% of the load. The pumps take suction from the circulating water pump house well, which is connected to the two tower basins by underground piping. The pump discharge is connected to a common header, which is then routed to an underground concrete pipe to the condenser and back to the cooling towers. If a single pump fails, capability exists to increase the flow rate through the operating pumps to minimize the reduction in overall system flow rate.

9.3.3 Closed Loop Cooling Water System

This subsection describes the closed loop cooling water system.

9.3.3.1 Design Basis

The purpose of the closed loop cooling water system is to provide high quality, demineralized and deionized cooling water to reactor auxiliary components and Reactor Building cooling systems during normal plant operation. The components served by the system include the REB System, ATC Systems, Shield, TF Coils, EF Coils, Limiter, Cryogenic System, HVAC, and miscellaneous Hot Cell and Tritium Reprocessing Building equipment.

9.3.3.2 Design Description

The closed loop cooling water system consists of two full-capacity pumps, two one-half-capacity heat exchangers, a surge tank, and the necessary piping, controls, and instrumentation. The surge tank is sized to accommodate any volumetric changes due to temperature and load changes. A nitrogen blanket is supplied to the surge tank to maintain system pressure. Nitrogen rather than air is used to minimize oxidation and therefore potential corrosion products that are incompatible with maintenance of the water quality required. Heat is removed from the system at the two heat exchangers by the circulating water system and ultimately rejected to the main cooling towers. One of the closed loop water cooling system pumps is normally operating while the second pump is on standby.

Water is continuously bled from the system to maintain the desired water quality and is continuously made up from the demineralized water system. Water quality is monitored to control the bleed rate, while the surge tank level controls the makeup rate. The system is connected to the standby cooling water system to provide cooling water to the atmospheric tritium cleanup systems and the solid waste pools during normal operation. The connections include isolation valves that close automatically when the standby cooling water system goes into operation, or when the closed loop cooling water system is shut down for any reason.

9.3.4 Standby Cooling Water System

This subsection describes the standby cooling water system.

9.3.4.1 Design Basis

The purpose of the standby cooling water system is to provide high-quality, demineralized and deionized cooling water to the residual heat removal system, atmospheric tritium cleanup systems, solid waste pools, and Control Building chillers during abnormal operating conditions. Operation of the system occurs, for example, during an incident when the reactor has been shut down, offsite power is unavailable, and the plant is using the onsite standby power source. The standby cooling water indirectly maintains the blanket temperature within specified limits by providing the cooling medium to the residual heat removal system that in turn cools the blanket.

The standby cooling water system also provides cooling water to the three atmospheric tritium cleanup (ATC) systems located in the Reactor Building, the Tritium Reprocessing Building, and the Hot Cell. It is assumed, in sizing the standby cooling water system, that no more than one of the ATC systems will be operating at full load at any time. The largest ATC cooling water load occurs when the Reactor Building ATC system is in the emergency operating mode and the other two ATC systems are operating normally. The components that this system serves include the residual heat removal system, ATC, waste storage, and Control Building HVAC systems.

9.3.4.2 Design Description

The standby cooling water system consists of a dry cooling tower, two full-capacity pumps, a surge tank, and the necessary piping and instrumentation and controls. When the system is operating from a normal power source, control of the liquid in the surge tank is similar to that for the surge tank in the closed loop cooling water system. When the system is operating on standby power from the onsite gas turbines, no makeup water is introduced into the system. The surge tank is designed with sufficient capacity to supply the water requirements for 30 days of emergency operation.

The dry cooling tower is provided to maintain a closed system. A closed system is desirable to maintain water quality and to prevent the release of small quantities of tritium or activated corrosion products that may migrate to the system. The standby cooling tower is designed to supply cooling water at a temperature of 43.3°C under all weather conditions. The maximum wet-bulb temperature for the Kansas City site is 32.2°C, resulting in a design basis

approach to the tower of 11.1°C. A 33.4°C range has been selected for economic reasons, while still maintaining the specified temperature limits for the components cooled.

9.3.5 Support Systems

This subsection describes the support systems required to sustain reactor and turbine plant operations.

9.3.5.1 Carbon Dioxide Supply System

The carbon dioxide supply system provides the carbon dioxide makeup gas required for the Reactor Building atmosphere. The system consists of high-pressure gas bottles, pressure regulators, piping, valves, and instrumentation and controls. It has been assumed that the user will periodically purchase carbon dioxide gas from a supplier, who will also provide the gas bottles.

9.3.5.2 Sulfur Fluoride Gas Supply System

Sulfur fluoride (SF6) is used in the REB heating systems and HV switchgear. The system consists of high-pressure gas bottles, pressure regulators, piping, valves, and instrumentation and controls. The gas and high-pressure bottles are provided in the same manner as the carbon dioxide supply system.

9.3.5.3 Demineralized Water System

The demineralized water system includes packaged demineralized trains, a demineralized water storage tank, and demineralized water pumps. Service water, drawn from the raw water reservoir, is delivered to the demineralizer trains for processing. Two demineralized trains are provided, with one train in the standby, shutdown, or regeneration mode. Each train is sized for 100% design requirements and includes a pressure filter, two-bed cation, and stong base anion primary demineralizer followed by a secondary demineralizer. The demineralized water produced is stored in the demineralized water storage tank, and is used in the heat transport system, the closed loop cooling water system, and the standby cooling water system. Two full-capacity demineralized water pumps are provided for the initial system fill and normal makeup to the following subsystems:

a. Heat transport system

b. Closed loop cooling water system

c. Standby cooling water system

d. Turbine plant cooling water system

e. Steam and condensate system

9.3.5.4 Turbine Plant Cooling Water System

The turbine plant cooling water system is designed to provide relatively constant temperature water for cooling the turbine cycle equipment. The cooling water serves the following equipment:

a. Generator hydrogen coolers

b. Air compressors

c. Turbine electro-hydraulic controls and lube oil coolers

d. Seal water coolers

e. Plant HVAC

d. Miscellaneous coolers

The system circulates demineralized water that is cooled by the circulating water system. The system consists of two full-capacity pumps, two half-capacity heat exchangers, one surge tank and necessary piping, valves, and instrumentation and controls.

9.3.5.5 Turbine Generator Oil Conditioner and Storage System

The turbine generator oil conditioner and storage system is provided for the storage and processing of turbine lube oil consisting of clean and dirty oil storage tanks and lube oil transfer pumps. A self-contained lube oil conditioning system is capable of continuous conditioning and recirculation of turbine reservoir lube oil, and batch conditioning and transfer of dirty lube oil. A waste oil sump pump and 950-liter storage tank is provided for the accumulation and disposal of sediment from the dirty oil storage tank.

9.3.5.6 Turbine Generator Lube Oil System

The turbine generator lube oil system consists of an independent lube oil reservoir equipped with lube oil pumps to provide bearing lubrication and lube oil cooling for the turbine generator together with backup supply for the hydrogen seal oil system. Lube oil cooling is accomplished by a heat

exchanger supplied with cooling water from the turbine plant cooling water system.

9.3.5.7 Electro-Hydraulic Control System

The electro-hydraulic control system is an independent system consisting of an oil storage reservoir, motor-operated control oil pumps, and integral oil coolers. The system is designed to provide the motive power required by the servo-mechanisms to maintain desired speed/load characteristics through the turbine steam throttle valves.

9.3.5.8 Hydrogen Seal Oil System

The hydrogen seal oil system provides an independent source of seal oil to the generator shafting to maintain a hydrogen pressure within the casing, with minimal leakage loss. The system has a backup source from the bearing oil supply system and a dc motor-operated seal oil pump for emergency service.

9.3.5.9 Turbine Steam-Sealing System

To prevent the escape of steam and/or loss of condenser vacuum along the turbine shaft, steam-sealed glands are provided. The turbine steamsealing system consists of steam-sealing regulators, steam-packing ejectors, and gland seal condensers. During startup or shutdown, sealing steam is provided from the main steam line, and during operation, it is provided from the excess steam available from the high-pressure packing. Excess steam is vented to the main condenser, while sealing steam is condensed in the gland seal condenser.

9.3.5.10 Turbine Bypass System

The plant steam cycle is equipped with a 45% reactor-rated turbine steam bypass system that forwards excess main steam directly to the main condenser after a pressure-reducing and desuperheating station. This system is used during startup and shutdown and for those periods during transients when steam generator output exceeds turbine steam flow requirements. Sequentially operating pressure-reducing desuperheating bypass valves are mounted directly between main steam lines and the main condenser.

9.3.5.11 Condensate Storage and Transfer System

The condensate storage tank provides sufficient water to the suction of the auxiliary feedwater pumps to remove first wall/blanket decay heat and to cool down the components under normal maintenance and service operations. During normal plant operation, the condensate storage tank provides makeup to the system as required.

9.4 Building Services Design

This subsection discusses the HVAC, fire protection, and plumbing systems.

9.4.1 Design Basis

The following subsection provides the design basis for the HVAC systems.

9.4.1.1 Heating, Ventilating and Air Conditioning

The design of this facility incorporates HVAC systems to provide heating, cooling, ventilation, and temperature control for comfort and control of airborne contamination, and to ensure negligible release of tritium to the atmosphere under all operating conditions.

(1) Codes and Standards: Current editions of the documents, guides, standards, and publications of the following organizations are used, where applicable, in the design of the environmental system:

- (a) American Society of Heating, Refrigeration and Air Conditioning (ASHRAE)
- (b) American Society for Testing and Materials (ASTM)
- (c) American National Standards Institute (ANSI)
- (d) American Society of Mechanical Engineers (ASME)
- (e) Air Conditioning and Refrigeration Institute (ARI)
- (f) Air Moving and Conditioning Association (AMCA)
- (g) American Conference of Governmental Industrial Hygienists
- (h) Underwriters Laboratory (UL)
- (i) Sheet Metal and Air Conditioning Contractors National Association (SMACNA)

(2) Environmental Design Conditions

(a) Outdoor Design Conditions:

- o Summer: 39°C dry bulb; 20°C wet bulb.
- o Winter: (-)23.7°C dry bulb.
- o Elevation: 600 m above sea level.

The outdoor design conditions stipulated above are not for any specific location but rather represent design conditions that cover approximately 85% to 90% of the continental United States.

(b) Indoor Design Conditions: Indoor design conditions are specified in Table 9-1.

(c) Design Leak Rates of Buildings:

- o Reactor hall:

The design leak rate from the reactor hall to the atmosphere during LOCA is 0.1% of the reactor hall volume per day at 55 kPa pressure differential.

- o Hot Cell:

The design leak rate from the atmosphere to the Hot Cell is 100% of the Hot Cell net free air volume per day at (-)1.91 cm water gage static pressure differential.

(3) Seismic Classification: The HVAC seismic classifications I, II, and III are defined as follows:

I. Systems, equipment, and components that provide confinement functions to prevent and limit the release and dispersal of radioactive contamination to values comparable with applicable offsite exposure guidelines, or Systems, equipment, and components that function to provide a safe shutdown of the facility in the event of a design basis earthquake (DBE), or Systems, equipment, and components whose continuous operation is not required but whose failure jeopardizes the safety function of an essential safety item.

II. Systems, equipment, and components that could interrupt operation of the facility and are designed to withstand the effects of an operating basis earthquake (OBE).

Table 9-1. Indoor Design Conditions

Location	Temperature (°C) Design Cooling	Temperature (°C) Design Heating	Relative Humidity(%) Design	Static (1) Pressure Design
Reactor Building				
Reactor hall	32.22	26.67	50 to 60	(-)2.54 (4)
Sub-grade level	32.22	18.33	50 to 60	(-)1.27
Hot Cell				
Liquid waste processing	32.22	18.33	50 to 60	(-)1.91
Remote maintenance and repair shop	32.22	18.33	50 to 60	(-)1.91
Spent blanket module and other solid waste process	32.22	18.33	50 to 60	(-)1.91
Center corridor	32.22	18.33	50 to 60	(1)1.27
Decontamination room	32.22	18.33	50 to 60	(1)1.91
Decon equipment room	32.22	18.33	50 to 60	(-)0.64
Hot Cell control room	22.78	22.78	15 ±5	(+)0.64
Tritium Reprocessing and Cryogenics Building				
Tritium reprocessing equipment room	26.67	21.11	40 to 50	(-)1.27
New tritium and deuterium cylinder storage room	32.22	21.11	(3)	(-)1.27
Tritium and deuterium storage	32.22	18.33	(3)	(-)0.64
Monitoring equipment and maintenance room	26.67	21.11	40 to 50	(-)0.64
Analytical laboratory	26.27	21.11	40 to 50	(-)0.64
ATPS equipment room	32.22	18.33	(3)	(-)1.27
HVAC equipment room	32.22	18.33	(3)	(-)0.38
Glove boxes	(2)	(2)	(3)	(-)2.54
Control room	22.78	22.78	45 ±5	(-)0.64
Offices	22.55	21.11	45 ±5	(±)0.64
Cryogenics equipment room	32.22	18.33	(3)	(5)
Electrical equipment room	32.22	18.33	(3)	(5)

Table 9-1. (Continued)

Location	Temperature (°C) Design Cooling	Temperature (°C) Design Heating	Relative Humidity(%) Design	Static (1) Pressure Design
Control Building				
Main control room	22.78	22.78	45 +5	(+)0.64
Computer room	22.78	22.78	45 +5	(+)0.64
Offices	22.78	22.78	45 +5	(+)0.64
HVAC equipment room	32.22	18.33	(3)	(+)0.25
Administration Building				
Offices	22.55	21.11	45 ±5	(5)
HVAC equipment row	25.55	21.11	(3)	(5)
R&D Building	22.55	21.11	45 ±5	(5)
Maintenance Shop	26.67	18.33	(3)	(5)
Warehouse	32.22	18.33	(3)	(5)
Electrical and RF Power Supply Building				
Electrical equipment room	32.22	18.33	40 to 50	(+)0.64
Cable spreading room	26.67	18.33	40 to 50	(+)0.64
RF power supply	26.67	18.33	40 to 50	(+)0.64
On-Site AC Power Building	(6)	18.33	(3)	(+)0.25
Turbine Building				
Turbine room	32.22	26.67	(3)	(-)0.64
Subgrade equipment room	32.22	26.67	(3)	(-)0.64

Table 9-1. (Continued)

Location	Temperature (°C) Design Cooling	Temperature (°C) Design Heating	Relative Humidity(%) Design	Static (1) Pressure Design
Plant Auxiliary Building	32.22	18.33	(3)	(+)0.25
Reactor Service Building	26.67	18.33	(3)	(+)0.25
Switchgear Building	32.22	18.33	(3)	(5)
Pump Houses	(6)	12.78	(3)	(5)

Notes:

(1) Static pressures shown are in centimeters water gage referenced with respect to the atmosphere.

(2) Temperature control is not required.

(3) Humidity control is not needed in this area.

(4) Differential pressure will not be maintained when the atmospheric air cleanup system is operating at full capacity and the reactor hall is isolated.

(5) Differential pressure need not be maintained; building or room pressure is at atmospheric pressure.

(6) Ventilation only provided. Ventilation rate is calculated at a temperature rise of 5.6°C.

III. Systems, equipment, and components that are required to perform a safety function, but are designed according to the seismic requirements of the Uniform Building Code.

IV. Design Basis Earthquake (DBE)

The DBE is an earthquake that produces the maximum vibratory motion for which seismic I systems, equipment, and components are designed to perform their safety function. This earthquake is expected to be the largest earthquake that could occur at the site during the life of the plant.

V. Operating Base Earthquake (OBE)

The OBE is an earthquake that produces a vibratory motion in which defined facility systems are designed to survive and continue to operate without undue risk to the health and safety of the operators and the public.

VI. Design Basis Tornado

Defined HVAC systems are tornado without loss of confinement capability due to mechanical damage to the system or changes in ambient pressure at the intake and exhaust openings of the affected building. Protection against tornado missiles is provided at the intake and exhaust structures of the affected building.

VII. Filters and Plenums

The HVAC system provides filtration for the outside air intake, recirculation system, and exhaust air system.

VIII. Filter Elements

The filter elements to be used have the following characteristics:

Filter Element	Maximum Design Flow Rate (cmm)	Initial Air Pressure Drop (cm w.g.)
Prefilter	51.0	0.89
High efficiency filter	51.0	1.52
High efficiency particulate absolute filter	28.3	2.54

(a) Prefilters (PF):

Filters are 61-cm x 61-cm x 5-cm deep, fiberglass, continuously laminated by steel wire grid for support. Filters have a rated average dust spot efficiency of not less than 36% when tested on an NBS-type test for atmospheric dust.

(b) High Efficiency Filters (HEF): Filters are 61-cm x 61-cm x 5-cm deep. Filters are required to demonstrate a minimum efficiency of 80% when tested on the NBS-type test for atmospheric dust.

(c) High Efficiency Particulate Absolute Filters (HEPA): Filters are 61-cm x 61-cm x 31-cm deep, nuclear grade, in conformance with the requirements of MIL-F-51068 and UL-586. Minimum efficiency is specified to be 99.97% for 0.3-micron particles.

(d) Plenum Housing: The design of filter plenums is in accordance with the requirements of recognized standards. Provisions for individual HEPA stage in place DOP testing are required.

IX. Fans

Fans are industrial type, conforming to the AMCA qualification and testing methods, and bear the AMCA Certified Rating seal.

X. Duct Work

Air distribution duct work is divided into two types. Air ducts that are important to safety are carbon steel all-welded construction. Non-safety related duct work is galvanized steel, constructed according to the SMACNA standards for a mediumpressure system.

9.4.1.2 Fire Protection

The fire protection system for this project incorporates design provisions to achieve the required degree of safety. The defense-in-depth principle is used to achieve an adequate balance in fire prevention, rapid fire detection, fire suppression in the shortest possible time to limit property damage, and design of the plant safety systems to perform their essential safety functions during a fire by providing physical separation and redundancy of components.

a. Codes and Standards

Standards of the following organizations are used as applicable:

(1) National Fire Protection Association (NFPA)
(2) Factory Mutual Engineering Association (FM)
(3) Underwriters Laboratory (UL)
(4) American Water Works Association (AWWA)
(5) American National Standards Institute (ANSI)

b. Water Supply and Distribution

A seismically qualified underground water storage tank, sized on the basis of the largest expected fire water flow rate for a period of 2 hours is required. The flow rate is based on the following:

(1) 227 m/hour for manual hose streams, and
(2) 340 m/hour for all sprinkler heads open or operating and flowing in the largest fire area.

The underground yard fire main loop is designed to accommodate he maximum flow rate requirement.

c. Fire Water Pumps

Redundant 100% capacity pumps are required to provide for pressure and/or flow to the system. One pump is driven by a diesel engine, and the other is motor driven. A fire wall with a minimum rating of 3 hours separates the pumps.

d. Fire Hydrants

Fire hydrants are required every 76 m on the yard main system. The lateral to each hydrant from the yard main is controlled by a visually indicating or key-operated (curb) valve. Threads compatible with those used by the local fire department are provided on all hydrants. A hose house, equipped with hose and combination nozzle and other auxiliary equipment, is required every 305 m.

e. Water Sprinkler and Hose Standpipe System

Each automatic sprinkler system and manual hose station standpipe has an independent connection to the plant underground water main. Each header leading to the automatic sprinkler system and the hose standpipe system is located in a separate valve room with a 3-hour fire wall. Each header is equipped with an OS&Y gate valve and water flow alarm switch.

f. Fire Hose Stations

Fire hose stations are equipped with a maximum of 22.9 m of 3.81 cm woven, jacket-lined fire hose and suitable nozzles, and are provided in all buildings. Fire hose stations are located at intervals of no more than 30.5 m.

g. Fire Extinguishers

Fire extinguishers of appropriate types according to size and nature of the fire are provided in numbers sufficient to ensure efficient and rapid manual fire fighting. Extinguishers are located along escape routes in the vicinity of doors and staircases or at easily accessible locations within the occupied areas.

h. Interior Protection

Table 9-2 shows the fire zoning requirements, type of protection, and detection system for the facility.

i. Fire Detection and Alarm Systems

To achieve a comprehensive fire system for the project, an automated central fire detection and alarm system is required. From each fire area or fire zone equipped with fire fighting installations, status information is supplied to the control room panel. The panel contains space for the following equipment:

(1) Indicator lights showing the automatic and/or manual actuation of fire fighting systems.

(2) Audible alarms with sounds distinct from other audible alarms.

(3) Control instruments for the fire protection portions of the water supply system.

(4) Guaranteed power supply.

(5) Means of verifying the readiness of the fire fighting system and components (supervisory devices).

9.4.1.3 Plumbing

The design of the plumbing systems for this facility is based on the requirements of the Uniform Plumbing Code (UPC) and/or the National Plumbing Code (NPC), whichever is more stringent. The materials of construction meet the requirements of ASTM Standards and/or Federal specifications as applicable.

a. Plumbing System The design of the plumbing system covers the following:

(1) A complete sanitary waste and vent piping system for the amenities provided in the facility. Sanitary waste is discharged through a network of yard piping to a sanitary sewage system available at the site boundary.

Table 9-2. Fire Zoning Requirements, Type of Protection and Detection System

Zone	Area Covered	Type of Protection	Detection System
1	Reactor hall	(1)	(a) (b)
2	Reactor sub-grade level	(2)	(b)
3	Hot Cell	(1)	(b)
4	Tritium processing area	(1)	(b)
5	Tritium control room	(2) (3)	(c)
6	Balance of Tritium Building floor	(2)	(b)
7	Control/computer rooms	(2) (3)	(c)
8	Balance of Control Building floor	(2)	(b)
9	Administration Building	(2)	(b)
10	Maintenance shop	(2)	(b)
11	Warehouse	(2)	(b)
12	Electrical and REB Power Supply Building, groundfloor	(2)	(b)
13	Electrical and REB Power Supply Building, subgrade level	(2)	(b)
14	Onsite AC Power Supply Building	(4)	(c)
15	Turbine room	(4)	(c)
16	Turbine Building, subgrade level	(2)	(b)
17	Plant Auxiliary and Reactor Service Buildings	(2)	(b)
18	Switchgear Building	(2)	(b)
19	Cooling tower 1	(5)	(a) (b)
20	Cooling tower 2	(5)	(a) (b)
21	R&D Building	(2)	(b)
22	Standby cooling tower	(5)	(a) (b)
23	Yard transformers	(5)	(a) (b)

Table 9-2. (Continued)

Notes::

(1) Preaction-type sprinkler system.

(2) Wet sprinkler system.

(3) Halon 1301 total flooding system.

(4) CO_2 total flooding system.

(5) Deluge system.

(a) Rate of rise with control room alarm.

(b) Flow switch with local and control room alarm.

(c) Ionization with control room alarm.

(2) A complete domestic water system to supply the necessary hot and cold water for the facility. A water heating medium will be selected that provides an economical approach. Systems to be investigated include types using waste heat, conventional heating by electricity and steam, solar energy, or a combination thereof.

(3) Required plumbing fixtures.

9.4.2 Design Description

This subsection describes HVAC, fire protection and plumbing systems.

9.4.2.1 Heating, Ventilating and Air Conditioning (HVAC)

a. Reactor Building

The reactor hall is provided with six recirculation systems by which the containment atmosphere gas (CO2) is filtered and conditioned. The tempered gas is supplied throughout the area by distribution duct work. To prevent potential interference with remote handling equipment in the reactor hall, the HVAC system uses an underfloor concrete supply tunnel and vertical risers connected to the horizontal distribution outlets along the Reactor Building walls. The recirculation systems are divided into two groups of three units each, supplied from two different power sources. A total of four units operate normally, and two units are on standby, thereby allowing flexibility of operation during normal, off-normal, and accident conditions. In the event of a loss-of-coolant accident, the fan coil units are capable of maintaining the temperature of the Reactor Building atmosphere at or below 54.4°C. To ensure even distribution of conditioned air within the confinement space, auxiliary blowers placed at strategic locations are used.

The building inlet isolation valve is normally closed and the building exhaust isolation valve is normally open. Clean CO_2 gas is continuously added to the building atmosphere to dilute the small inleakage of air. At the same time, gas is exhausted from the

building through two 100% capacity pressure control fans that maintain the reactor hall pressure negative with respect to the environment. When the concentration of tritium within the reactor hall is detected to be above normal, the pressure control fans are de-energized, and automatic isolation of the building takes effect. This calls for automatic shift of the atmospheric air cleanup system from the normal 10% to full capacity operation. The atmospheric cleanup system provides for removal of tritium and/or particulates within the reactor hall. Provision for outdoor air purge of the reactor hall, by opening the building inlet isolation valve, is available if required.

b. Hot Cell

The Hot Cell employs 100% recirculation of filtered and tempered air to the different zones. Two 100% capacity pressure control fans are provided to maintain differing pressure requirements among confinement zones. The assignment of pressure zones ensures confinement of the potentially contaminated atmosphere and prevents its migration to other parts of the facility. Pressure assignments are such that the flow of air is from areas of lesser to areas of higher potential for radioactive contamination. During normal operation, the atmospheric tritium cleanup system operates at 10% capacity for continuous cleanup of tritium and/or potentially contaminated particulates within the Hot Cell.

The design incorporates isolation of the Hot Cell when it is determined that the concentration of tritium in the Hot Cell atmosphere is beyond the normally acceptable concentration. Upon isolation, the atmospheric tritium cleanup system located inside the Hot Cell runs at full capacity. Provision for outdoor air purge of the Hot Cell is incorporated in the design, thereby providing for the necessary ventilation should man-entry to the cell ever be necessary.

d. Control Building

The design of the HVAC system for the Control Building consists of two 100% supply air systems and two 100% recirculation/exhaust fan systems. However, redundancy in the air distribution system is not employed. Outdoor air is mixed with return air, which is filtered and tempered for distribution to the different areas of the Control Building. Variable air volume cooling and/or heating is used. The HVAC system is interlocked with the control/computer room Halon 1301 fire protection system by actuation of an outdoor switch. The HVAC system also functions to remove smoke-laden air prior to the entry of fire fighting personnel. The air intake and exhaust structures and equipment are protected from missiles and tornado-induced negative pressurization.

d. Tritium Reprocessing Building

The tritium reprocessing area, with the highest potential for radioactive contamination within the Tritium Reprocessing Building, is provided with a dedicated recirculating HVAC system. Minimum outdoor purge air for ventilation is filtered and conditioned for supply to the area. As in the Hot Cell and the reactor hall, it is expected that the atmospheric tritium cleanup system will operate at 10% capacity during normal operating modes. Full capacity operation will be in effect upon the detection of an unacceptably high concentration of tritium in the area.

The balance of the building space, consisting of the tritium and deuterium storage area, monitoring equipment and maintenance room, analytical laboratory, and the tritium HVAC equipment room, has a normal outdoor air/recirculation system capable of exhausting air from individual rooms.

e. Miscellaneous Buildings

The remaining buildings and/or areas of the project have conventional HVAC systems that meet the defined design basis. A maximum of recirculation of conditioned air is used in these buildings.

f. Chilled Water System

The main Control Building is designed to have two 100% capacity chiller and pump systems, thereby increasing reliability and maintainability, and ensuring continuous operation of the Control Building cooling system. This design is essential for proper functioning of the facility controls and computer. Three chillers provide the necessary cooling for the rest of the facility. Chilled water is delivered through distribution piping equipped with required controls. Three 100% capacity chilled water pumps are provided, two operating and one standby.

g. Hot Water System

Space heating uses hot water as the heating medium. Hot water is generated through a shell and tube heat exchanger, and is delivered by two pumping systems, one operating and one on standby, through distribution piping to users. Necessary valving and controls are provided.

9.4.2.2 Fire Protection

A dedicated seismically qualified water storage tank for fire protection is provided for the facility. Redundant pumps sized for maximum flow rate based on the design basis fire deliver water through a network of piping to the different areas including yard fire hydrants. Each pipe branch takeoff from the yard main has a post indicator valve with integral supervisory switch for proper monitoring. Fire areas or zones are provided with fire valves and the necessary supervisory devices to monitor readiness of the fire-fighting equipment and systems. Each building in the facility is equipped with fire hose stations at strategic locations to combat local fires. Each fire hose station is provided with a maximum hose length of 22.8 m, nozzles, and a portable fire extinguisher.

9.4.2.3 Plumbing

Hot and cold water supply is distributed to users as required. The facility design includes floor drains and/or floor sinks in the vicinity of pumps, and other equipment for system drainage and/or for maintenance use.

Waste from the facility plumbing fixtures, consisting of water closets, lavatories, urinals, sinks, drains, etc., is collected and routed to the site boundary connection with a sewage disposal facility.

9.5 Electrical Systems Design

This subsection presents the electrical systems design. The electrical one-line diagram, E-5959-EE-11 (Figure 9-14), is included in subsection 9.6.

9.5.1 Overall System

The design basis for the overall system is presented below.

9.5.1.1 Design Basis

The functions of the electrical power system are to provide reliable power for the plant equipment, to generate electrical power, and to transmit the net electrical power to the offsite transmission network. The plant is designed with adequate auxiliary electrical equipment, standby power and protection to provide maximum continuity of service and thus ensure operation of the essential station auxiliary equipment during normal operation and all emergency conditions. The design discussed in this section is conceptual, without benefit of optimization and consideration of a broad spectrum of alternatives. Although it has been subject only to first-order analysis, the design selected is feasible and reasonably economic.

The electrical systems design is based on the following considerations:

a. A commitment to personnel safety, and the preservation of property.
b. Reliability and continuity of service.
c. Simplicity of operation.
d. Voltage regulation and short circuit rating of equipment.
e. Maintenance.
f. Flexibility.
g. Environmental constraints.
h. First cost.

Codes and standards for a fusion reactor power plant have not yet been developed. However, it is anticipated that the electrical system design will have to meet the applicable and relevant criteria of a PWR plant. The electrical system has been designed with this assumption. In addition, all electrical equipment such as the main generator, motors, transformers, switchgear, and control equipment is selected, rated, and specified in accordance with the National Electrical Code (NEC) and with the latest applicable standards of the following institutions:

a. American National Standards Institute (ANSI)
b. Institute of Electrical and Electronics Engineers (IEEE)
c. Insulated Cable Engineers Association (ICEA)
d. National Electrical Manufacturer's Association (NEMA)
e. Occupational Safety and Health Administration (OSHA)
f. Underwriters Laboratories, Inc. (UL)

When it is available offsite power is used for startup and shutdown, i.e., the plant is not designed with "black starting" capability. During continuous operation of the generator an intermediate mechanical energy storage system is not required. Major electrical equipment associated with power generation, auxiliary electrical power supply and distribution, onsite standby power generation, and high voltage (HV) switchyard systems has been identified. The specifications indicate that these systems and equipment are within state of the art technology or technology currently being developed.

A double bus system is used as a minimum to supply power to equipment required for continuous operation and/or safe shutdown. The distribution of power to two or more identical items of equipment is such that a failure of a power supply bus does not result in a complete loss of a particular mechanical or electrical function. All vital control and protection systems and equipment are powered from the dc or uninterruptible power supply (UPS) systems to ensure maximum service continuity. Electrical equipment and systems required for an orderly and safe shutdown are redundant and are designed to withstand and function during and after a design basis earthquake (DBE).

9.5.1.2 System Description

Descriptions of electrical subsystems are presented in subsequent subsections.

9.5.2 Main Generator and Connections

The design basis for the main generator and its connections is presented below.

9.5.2.1 Design Basis

The function of the main generator and its connections is to produce 400-MWe power (gross) for delivery to the plant unit auxiliary transformers, and to deliver the net electrical power through the main step-up transformer and switchyard to the HV transmission system network. The generator connections are made with a forced cooled indoor/outdoor isolated phase bus system. The isolated phase bus system is fully rated at 16,000 A between the main generator and the main step-up transformers with reduced capacity taps to the unit auxiliary transformers. The generator surge protection equipment and potential transformers are part of the isolated phase bus system.

The main electrical generator is provided with a generator breaker to allow isolation of the generator during startup, shutdown, and maintenance, while the main step-up transformers and the unit auxiliary transformers supply offsite power for the auxiliary system. The generator is provided with primary and backup protective relaying functions. Disconnecting links are provided in the isolated phase buses to allow isolation of the generator breaker and/or the main generator during maintenance. The generator neutral is grounded through a distribution-type transformer and a loading resistor. The generator breaker is controlled remotely from the plant control room, and it is also used for synchronization of the unit with the power grid.

9.5.2.2 Design Description

As shown on the electrical one-line diagram, electrical power is generated at 18 kV and transmitted via an isolated phase bus system to the main step-up and unit auxiliary transformers. The main electrical generator is provided with a generator breaker rated at 16,000 A continuous and 20 kV. The momentary ratings of 320 kA peak and the interrupting rating of 200 kA, RMS symmetrical are adequate for the maximum available short circuit currents. During normal operation, the generator breaker is closed. During startup and shutdown, the generator breaker is open and offsite power is fed through the

main step-up and unit auxiliary transformers. The neutral point of the generator is connected to a single-phase, grounding transformer by a bus connection.

The main step-up transformer consists of a three-phase unit, rated at 400 MVA, FOA class at a 65C temperature rise. The unit is connected in a delta (low-voltage side)/grounded wye (high-voltage side) configuration having a standard impedance. The low-voltage terminals are connected to the isolated phase buses; the high-voltage terminals are connected via gas-insulated HV buses through a motor-operated disconnect switch to the switchyard. The main transformer is energized continuously, and it normally delivers power through the unit auxiliary transformers for startup and shutdown. However, during normal operation the main transformer is used to transmit the generator net power output to the HV switchyard. The main transformer is provided with redundant 480-V, 3-phase supplies for the cooling equipment to ensure continuity of service.

9.5.3 High Voltage (HV) Switchyard

The design basis for the HV switchyard is presented below.

9.5.3.1 Design Basis

It is anticipated that a minimum of two full-capacity HV transmission lines will be connected to the switchyard of the plant. The primary function of the switchyard is to provide an onsite HV switching facility that can provide a reliable power outlet for the unit and that can receive and provide the offsite power required for startup and shutdown when the main generator is off the line. The arrangement of the switchyard is based on a double-bus, breaker-and-a-half scheme that provides the utmost flexibility and reliability required for a base load plant of this size and complexity. Outdoor-type gas-insulated equipment is used. This type of equipment offers better protection from the environment and economical use of space. Operation of the switchyard power circuit breakers and motor-operated disconnect switches is accomplished from the supervisory console in the control room or from the control panels in the switchyard control house.

9.5.3.2 Design Description

All three transmission lines, the main step-up transformer, and the two reserve station transformer circuits are connected to the two main buses through two HV breakers, with the middle breaker shared between two circuits. Each circuit breaker and the three transmission lines have sectionalizing switches installed. All circuit breakers are normally closed and thus the two HV buses operate in parallel. Any circuit may be isolated (by operating the two adjacent breakers) without loss or interruption of power to any other circuit. In case of a bus fault, the entire bus may be isolated, again without interruption of any other circuit. The transmission line and transformer protective relays, as well as power circuit breaker and motor-operated disconnect switch control equipment, are located in the switchyard control house.

9.5.4 Auxiliary Electrical Power Supply and AC Distribution

The design basis for the auxiliary electrical power supply and ac distribution system is presented below.

9.5.4.1 Design Basis

a. Functional Requirements

The function of the auxiliary electrical power supply and ac distribution system is to provide continuous and reliable power to the plant auxiliary equipment for startup, normal operation, and shutdown. During startup, normal operation, and shutdown, power is supplied to the 13.8-kV and 4.16-kV auxiliary system buses from the unit auxiliary transformers connected to the generator lead isolated phase buses. There are four 13.8-kV buses, numbered Bus 1 through Bus 4, from which large motors, coil and REB system power supplies, and primary feeders to 480-V load centers are fed. Medium size motors (250 hp to 4000 hp) and drives are fed from the two 4.16-kV buses.

Each auxiliary electrical power supply bus has two sources of power supply, one from the unit auxiliary transformers and the other from the reserve station service transformers. An automatic power transfer to the reserve station service transformer is implemented when the unit auxiliary power supply fails. Loads and motors between

125 hp and 250 hp are fed from the 480-V load center switchgear. Small loads and motors of up to 100 hp are connected to 480-V motor control centers.

b. Design Criteria

Electrical loads that are vital for an orderly shutdown of the plant are grouped separately (see subsection 9.5.6 for complete details), and not mixed with normal plant auxiliary loads. The selection of transformer impedances and the grouping of loads on a particular switchgear bus are consistent with commercially available switchgear ratings and ANSI voltage regulation limits. The short circuit current at the primary of each unit auxiliary transformer is limited to a maximum of 40,000 A to allow the use of breakers with standard ratings.

It is assumed that harmonic suppression, filters, and power factor correction for the coil and REB power supplies are included in these power supplies, as required. Feeders to coil and REB power supplies are duplicated or divided so that a single switchgear bus or feeder failure does not result in loss of a function. Double-ended load center transformers rated at 480 V are designed so that a failure of any one of them does not cause loss of the associated 480-V bus. The bus tie-breaker automatically connects the "dead bus" to the other operating bus. A minimum of local controls is provided for. In general, circuit protection equipment is located on the switchgear cubicles, and control devices and functions are located in the plant control room.

9.5.4.2 Design Description

The auxiliary electrical power supply and distribution system is shown on the electrical single-line diagram. This system consists of four 13.8-kV, six 4.16-kV, and ten double-ended 480-V load center buses, and a number of 480-V motor control center buses, as required.

a. Unit Auxiliary, Reserve Station Transformers, and Switchgear

Normal power to the switchgear buses during operation is supplied from the unit auxiliary transformers. There are two 60-MVA transformers with double 13.8-kV secondary windings. These each feed a 13.8-kV switchgear bus servicing general motor, coil power supplies and unit substation loads. The two 4160-V main switchgear buses are fed from a 30-MVA, double secondary winding transformer. The switchgear bus assemblies rated at 4160-V serving different process building loads are subfed from the main 4160-V switchgear. Each unit auxiliary transformer is protected by a 20-kV primary circuit breaker preceded by a disconnecting link, reactor, and motor-operated disconnect switch for short circuit current limitation and isolation. Backup power to the switchgear buses is provided from the two reserve station service transformers. One of these transformers is rated at 60 MVA with double 13.8-kV secondary windings, and one is rated at 30 MVA with double 4160-V secondary windings.

b. 480-V Power Supplies Pwer at 480 V is provided by double-ended load center type substations located throughout the plant approximately in the center of their respective loads. Each transformer of a doubleended unit is fed from a different 13.8-kV bus for better flexibility and service continuity. Loads above 100 hp but below 250 hp are connected to these load center switchgear buses as well as 480-V motor control center feeders. Loads of up to and including 100 hp are fed from 480-V motor control centers located throughout the plant near to the center of their respective loads, as required.

9.5.5 Direct Current (DC) Systems and AC Uninterruptible Power Supply (UPS) Systems

The design basis for these systems is presented below.

9.5.5.1 Design Basis

a. General

Reliable and continuous dc battery power is required for a variety of uses, such as "trip" and "close" of electrically operated circuit breakers, solenoid-operated valves, control systems, vital lighting,

the station annunciators, communication equipment, and devices used during turbine coast-down. Through dc/ac inverters, the batteries are also used to provide power to the turbinegenerator and reactor protective system, and to instrumentation required for an orderly shutdown. The following separate subsystems are provided:

(1) Turbine-generator dc system.

(2) Instrumentation and control dc and UPS systems.

(3) Computer/data logger dc and UPS systems.

(4) Switchyard dc system.

UPS systems are provided with fast transfer switches to transfer the load from the output of the inverter to a regulated ac backup supply in case of inverter failure, feeder short circuit or maintenance.

b. Turbine-Generator DC System

The function of the turbine-generator dc system is to provide dc supply for the turbine-generator and its accessories as required, and for emergency lighting. This battery is rated at 250 V, and is adequately sized to supply the total connected load for 2 hours without the support of a charger. Two chargers are provided for this battery.

c. Instrumentation and Control DC and UPS System

The function of the instrumentation and control dc and UPS system is to provide dc supply for the plant instrumentation, control and protection systems, including switchgear dc control supplies and dcac inverter supplies. The system consists of four separate battery subsystems, each rated at 125 V dc, and adequately sized to supply the total connected load for 4 hours without the support of a charger. One charger is provided for each battery and one dc/ac inverter is fed from each battery. This system is designed to withstand DBE seismic forces.

d. Computer/Data Logger DC and UPS System

The function of the computer/data logger dc and UPS system is to provide dc/ac supply for the plant computer/data logger. This system consists of two dc batteries, three chargers, and two dc/ac inverters. These batteries are sized for 2-hours' capacity without the support of a charger.

e. Switchyard DC System

The function of the switchyard dc system is to provide dc supply for the control and protection of the switchyard circuit breakers and for the switchyard emergency lighting. This system consists of two separate battery systems, each complete with a charger, plus a spare charger. Each of these batteries is sized for 2-hours' capacity without the support of a charger.

9.5.5.2 Design Description

These battery and UPS systems consist of a storage battery, charger(s), inverter, fast transfer switch, manual bypass switch, dc switchgear or distribution panelboard, ac panelboard, and regulated backup ac supply. The charger ac input power is normally supplied at 480 V and is connected to a bus that could also be energized from the onsite standby electrical power system when all offsite ac power is lost. During normal operation the charger supplies dc power to the connected loads with the battery fully charged and floating on the dc system bus. When the charger is lost because of its own failure or because of a loss of ac input to the charger, the battery powers the dc system for the design period, as required.

9.5.6 Onsite Standby AC Power System

The design basis for the onsite standby ac power system is presented below.

9.5.6.1 Design Basis

a. General

The function of the onsite standby ac power system is to generate and distribute a reliable onsite ac source of auxiliary power if the preferred offsite source is lost. This system consists of two 100% redundant, independent, and separate onsite gas-turbine generators. Each generator is connected to a pair of redundant 4.16-kV switchgear bus systems as shown on the electrical single-line diagram. The connected loads on these buses consist of equipment and systems required for an orderly shutdown of the plant. The system is designed to meet the following requirements:

(1) Capability to function during and after a design basis earthquake.

(2) Loss of one redundant group does not prevent an orderly shutdown.

(3) Each 4.16-kV bus system can be connected to the preferred (offsite) power source or to the onsite standby gas-turbine generator.

(4) No paralleling of the two redundant generators or 4.16-kV bus system is possible.

(5) Loads cannot be transfered from one bus system to the others.

b. Gas-Turbine Generators

The gas-turbine generators are designed for starting and loading within about 60 seconds. They are required to start automatically upon loss of the ac bus voltage and to maintain rated voltage and frequency during loading and operation. Provisions are made for testing the gas-turbine generators at required time intervals.

9.5.6.2 Design Description

The onsite standby ac power system consists of two redundant gasturbine generators, each connected to a separate 4160-V switchgear bus, numbered HSBE-1 and -2, respectively. These two 4160-V buses are also connected to the plant main 4160-V buses 1 and 2, respectively. Sub-bus assemblies rated at 4160 V that are fed from buses HSBE-1 and -2 are located in the Reactor

Building, Hot Cell, and reactor supporting buildings for the supply of onsite standby power to equipment in these buildings.

During normal conditions these systems are powered from the preferred source, which is the offsite source, or from the unit auxiliary transformer. However, upon loss of the plant main ac generator and upon loss of the offsite ac power source, the gas-turbine generators feed the onsite standby ac power system to permit an orderly shutdown to be conducted. Onsite standby ac power rated at 480 V is provided by 480-V load centers connected to the 4160-V standby ac power system buses. Onsite standby ac power is further distributed to small motor loads by 480-V motor control centers connected to th 480-V load centers.

9.5.7 Facilities Electrical Services

The design basis for the facilities electrical services is presented below.

9.5.7.1 Design Basis

The functions of the facilities electrical services are as follows:

a. To provide adequate lighting including emergency lighting in accordance with the recommendations of the Illuminating Engineering Society (IES).

b. To provide the necessary grounding for systems and equipment, including a separate grounding system for "low" signal level instrumentation and controls, in accordance with the requirements of IEEE standards and the National Electrical Code.

c. To provide necessary systems for communication, including telephone, public address (PA and PAX), and sound-powered telephone systems for testing and maintenance where required.

d. To provide adequate lightning protection.

e. To provide necessary cathodic protection.

f. To provide necessary electrical heat tracing and freeze protection.

9.5.7.2 Design Description

a. Lighting

Lighting and low-energy auxiliary loads are supplied from the 120/208-V or 277/480-V solidly grounded lighting system. Lighting for each plant operating area is supplied from at least two circuits, possibly fed from separate power sources to prevent complete loss of lighting on failure of equipment or wiring. For exits and critical areas, emergency lighting circuits are transfered automatically to the 125-V dc system upon loss of the normal source. Outdoor lighting is provided for operating areas, with parking lot lighting and road lighting included. Aircraft obstruction lighting for the cooling towers and stack is furnished in accordance with Federal Aviation Agency (FAA) regulations. Lighting systems provide maintained lux levels at least equal to the minimum recommendations of the IES. Lighting fixtures using fluorescent, sodium or mercury vapor lamps are installed where feasible.

Emergency lighting is incandescent so that it may be supplied by alternating current during normal operation and from direct current during emergencies. Emergency lighting is provided in the plant at stairways, exits, the turbine room operating floor, the main control room, and at motor control and switchgear areas. Electric convenience outlets, including welding outlets, are provided throughout the plant, and where feasible are located so that a 7.6-m extension cord can reach any area. Lighting-fixture mounting height and spacing do not exceed the manufacturer recommendations except where physical constraints require some deviation.

b. Grounding System

The ground grid consists of buried bare copper cable meshes and copperclad steel ground rods driven below the water table low level. Switchgear, load centers, motor control centers, power transformers, power supplies, exciter, generator, neutral cubicle, generator potential transformer cubicles, and alternate building and corner columns are connected by cable to the ground grid. All power utilization equipment is connected either to the ground grid directly or to the

nearest building steel. Piping systems are grounded through connections to tanks and vessels. Each cable tray or stack of trays is provided with a ground cable running full length. Metallic conduits are grounded at equipment enclosures and, where entering cable trays, are connected to the tray ground cable. All embedded or buried ground connections are thermit brazed. Equipment connections are exposed and bolted. Fences are connected to a buried ground cable running the full length of the fences. Switchyard grounding systems are also provided.

c. Communication Systems

Telephone sets, public address systems, and all wiring and raceways are provided for intraplant communications. All locations, including the switchyard and outlying areas as dictated by the overall plant operation requirements, are covered. A sound-powered telephone system is provided for testing and maintenance purposes. It is installed in the main control room, cable spreading room, switchyard, switchgear area, reactor area, and at local panels.

d. Lightning Protection

Lightning protection for the power plant is provided by lightning rods located on tall buildings and/or structures with cable connections to ground rods.

e. Cathodic Protection Systems

Provisions are made for cathodic protection of all buried steel piping. Cathodic protection of building steel or reinforcing steel is provided, if necessary. All buried steel lines are connected by cable to each other and to the ground grid. Buried sections of lines are insulated from above-grade sections with insulating flanges at the entrance to buildings or structures. Lines less than 152 m in length are provided with one test connection accessible above grade. For lines 152 m in length or over, accessible test connections are installed at each end and, where required, at intermediate points. Connecting cables are insulated copper suitable for direct burial.

Connections are thermit brazed directly to the lines where line pressure permits; otherwise, a welded lug is furnished on the line for the brazed cable connection. A cathodic protection system is provided for the traveling-water screens in the intake structure and for the condenser water boxes, as required.

f. Electrical Heating

Electrical trace heating is provided for equipment and in areas where temperature maintenance is required. Electrical space heaters are provided in equipment enclosures to protect against condensation.

9.5.8 Electrical Equipment Arrangements, Raceway and Cable Systems

The design basis for the electrical equipment arrangements, raceways, and cable systems follows.

9.5.8.1 Design Basis

Electrical equipment is arranged and located logically to minimize length of runs for interconnections and to facilitate maintenance and testing. Major electrical equipment is located in separate electrical rooms with adequate space provided for possible future extensions and cable and raceway connections and with adequate mechanical and environmental protection. Raceways are grouped where practical for ease of installation and common mechanical protection. During the allocation of space for major raceway systems, adequate consideration was given to the problem of electrical interference between the different types of cables and high voltage and/or heavy current equipment. Raceways are dedicated to the particular type of cable system, and those containing different types of cable are separated. Raceways and cables serving the onsite standby ac power systems and associated with redundant equipment required for an orderly shutdown are physically separated and isolated from their redundant counterparts, and are designed to withstand DBE seismic forces.

In addition to transmitting electric power from the proper source to the designated load device, these facilities must be of a type and be properly installed and segregated to function during all modes of operation and shutdown. The electrical loadings of conductors do not exceed, and are generally

less than, the ampacities recommended by AIEE-IPCEA "Power Cable Ampacities." The percentage cross-section fill of wireways is governed by the allowable cable ampacities. The physical support of wireways meets the recommendations of the National Electrical Code. All cables have a sufficient degree of flame resistance to obviate the need for flame-retardant coating or special fire extinguishing systems.

9.5.8.2 Design Description

a. Electrical Equipment Arrangements

The main electrical system 13.8-kV and 4160-V switchgear equipment is located in a switchgear room next to the turbine-generator building at the northeast end. The unit auxiliary and reserve station transformers are located in close proximity to the main electrical switchgear room to minimize the lengths of the main incoming feeders. In addition, load centers and 480-V motor control centers are placed in this room to serve the turbinegenerator building load. The onsite standby electrical gas-turbine generators are located east of the main electrical equipment room, also within close proximity. Other electrical equipment rooms that contain electrical switchgear, load centers, and motor control centers are located in the Reactor Building, Hot Cell, and reactor support buildings to serve loads within these respective buildings. Electrical switchgear required to supply power to the REB power supplies is located in the Electrical Equipment and REB Power Supply Building. The unit auxiliary transformers and the main step-up transformers are located eastward from the main generator and as close as possible to it, to minimize the length of the isolated phase bus ducts.

b. Raceway Systems

To the extent possible and practical, continuous rigid galvanized steel or aluminum cable supports (cable trays) are used. The use of underground or trenched raceways is minimized except where practicality and economy are in favor of these two types of raceway systems. The raceway system is made up of cable trays, conduits, and underground ducts, with the electrical cables contained therein. Cable trays are of galvanized steel, ladder type or solid bottom, with

solid covers where required. Hangers for trays carrying vital circuits are designed to withstand DBE seismic disturbances. Conduits are galvanized rigid steel where embedded in reinforced concrete in building slabs. The duct banks are heavily reinforced and will withstand a DBE seismic disturbance. In the switchyard, cable trays and/or trenches are used for raceways for control, instrumentation, monitoring, and protection cables. In general, cables for power, control, and instrumentation are run in cable trays with connections from the tray to equipment and devices made with exposed rigid-steel conduits.

c. Cable Systems

Power cables for 13.8-kV and 4160-V service are single or three conductors, rated at 15 kV and 5 kV, respectively, and suitable for ungrounded neutral service. The conductors are stranded copper, EPR or XLP insulated, rated 90C temperature, shielded, and provided with a hypalon or neoprene outer jacket. The minimum sizes are determined on the basis of thermal and/or short circuit rating required for a particular service. Power cables for 480-V service are single or three conductors, rated 600 V, The conductors are stranded copper, EPR or XLP insulated, rated 90C copper temperature, with a hypalon or neoprene outer jacket. The conductor size is No. 12 AWG minimum.

Control cables are single or multiconductor, rated 600 V, EPR or XLP insulated, rated for 90C copper temperature with an overall hypalon or neoprene jacket. The control cable conductor size is No. 14 AWG, except for potential and current transformer circuits used for metering and protection, for which the conductor size is No. 10 AWG. Cables for service voltages over 50 V are type "TC" approved for installation in ladder-type cable trays.

Thermocouple extension wires are single and multipair with insulation 300 V class, and shielded overall with a neoprene or hypalon jacket. Lighting wires are single conductor, 600 V, type THW. Other types of insulated cables, such as for abnormally hot locations and intercommunications, are supplied to serve the particular applications. Instrumentation cables are EPR or crosslinked 300 V class

polyethylene-insulated, single-shielded, twisted-pair, multiple-twisted pairs with shielding overall, shielded-twisted triple, or multiconductor with shielding overall. Cables have nonflammable (hypalon or neoprene) jacket overall. All multiconductor control wiring is color-coded, and the color of each control wire will be shown on the connection diagrams.

9.6 DRAWINGS

This subsection contains the conceptual design drawings for this report. The subject drawings are listed below:

Drawing	Title
E-5959-AR-11	ARCHITECTURAL
(Figure 9-6)	Fusion Power Plant
	Site Plan
E-5959-AR-12	ARCHITECTURAL
(Figure 9-7)	Reactor, Turbine & Support, Electrical & REB Power Supply
	& Onsite A/C Power Buildings
	Sub-Grade Level Plans
E-5959-AR-13	ARCHITECTURAL
(Figure 9-8)	Reactor, Turbine & Support, Electrical & REB Power Supply
	& Onsite A/C Power Buildings
	Ground Level Plans
E-5959-AR-14	ARCHITECTURAL
(Figure 9-9)	Reactor, Turbine & Support, Electrical & REB Power Supply
	& Onsite A/C Power Buildings
	Upper Level Plans
E-5959-AR-15	ARCHITECTURAL
(Figure 9-10)	Reactor, Turbine & Support, Electrical & REB Power Supply
	& Onsite A/C Power Buildings
	Building Sections
E-5959-AR-16	ARCHITECTURAL
(Figure 9-11)	Tritium Reprocessing & Cryogenics Building,
	Administration, Control & Site Service Building
	Ground & Upper Level Plans, Sections
E-5959-AR-17	R&D BUILDING
(Figure 9-12)	Floor Plans & Building Sections
E-5959-AR-18	ARCHITECTURAL
(Figure 9-13)	Fusion Power Plant
	Site Perspective
E-5959-EE-11	ELECTRICAL
(Figure 9-14)	Unit Generator and Auxiliary Power System One Line
	Diagram

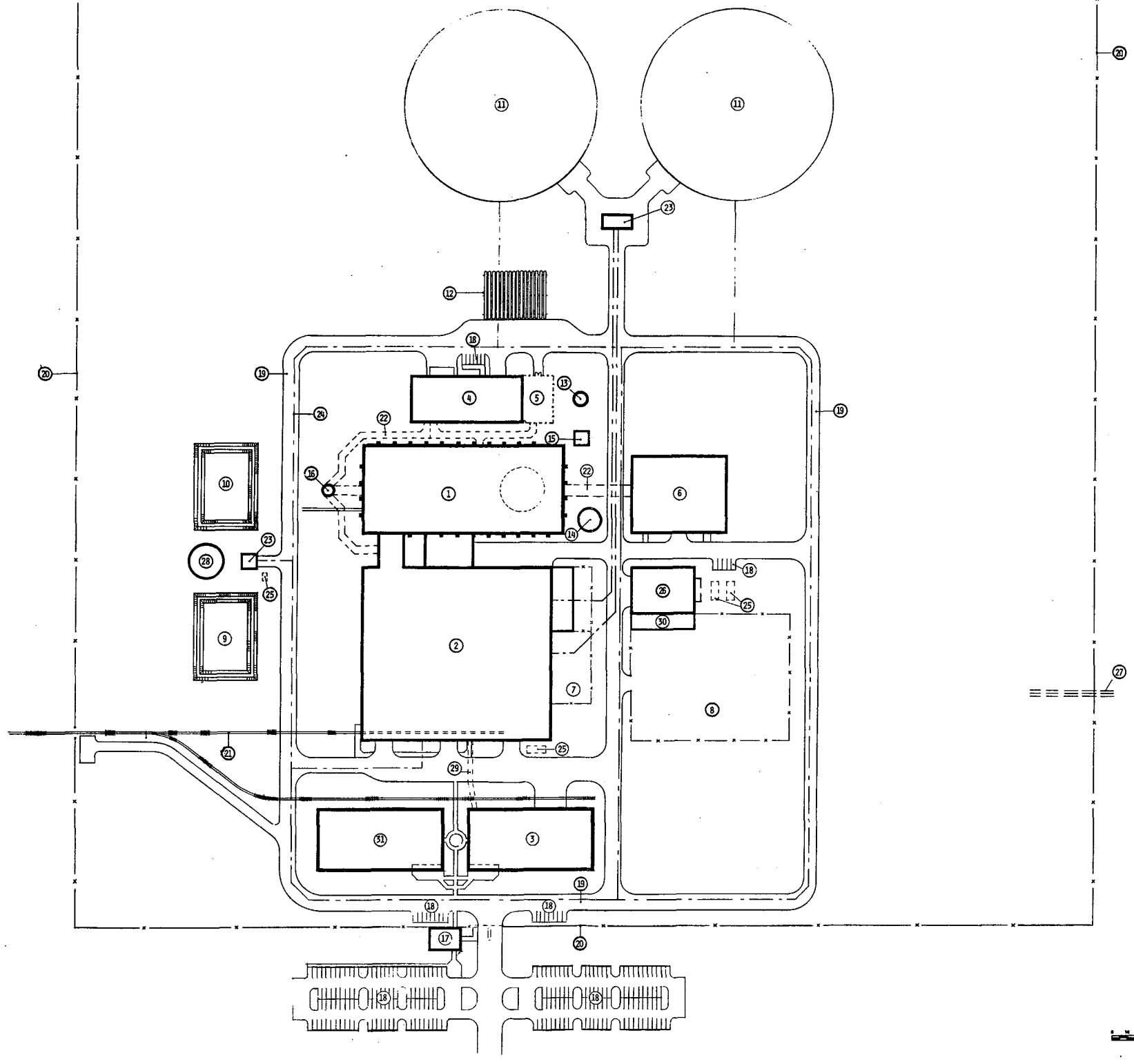

LEGEND

1. REACTOR BUILDING
2. TURBINE & SUPPORT BUILDING
3. ADMINISTRATION, CONTROL & SITE SERVICE BUILDING
4. TRITIUM REPROCESSING & CRYOGENICS BUILDING
5. CRYOGENICS EQUIPMENT YARD
6. ELECTRICAL & REB POWER SUPPLY BUILDING
7. TRANSFORMER YARD
8. MAIN SWITCHYARD
9. RAW WATER RESERVOIR
10. EVAPORATION POND
11. MAIN COOLING TOWERS
12. HELIUM GAS STORAGE TANKS
13. PRIMARY WATER STORAGE TANK
14. CONDENSATE STORAGE TANK
15. COOLING TOWER (FOR RESIDUAL HEAT REMOVAL)
16. STACK
17. SECURITY BUILDING
18. PARKING
19. PERIMETER ROAD
20. PERIMETER FENCE
21. RAILROAD SPUR
22. TUNNEL
23. PUMP HOUSE
24. FIRE LOOP
25. FUEL OIL STORAGE TANK
26. ON SITE AC POWER SUPPLY
27. OFF SITE POWER SUPPLY
28. FIRE WATER STORAGE TANK
29. CONTROL TUNNEL
30. SWITCHYARD CONTROL
31. R & D BUILDING

Figure 9-6.

REVISIONS NO.	DATE	BY	CHKD	SEC	PROJ	CLIENT	DESCRIPTION
1	11/19/81	GAL	SYH	CSK	HTHE	C.T.	APPROVED FOR FINAL REPORT
0	10/1/81	GAL	SYH	CSK	HTHE		ISSUED FOR CLIENT APPROVAL

DESIGN	Schmidt 9/19/81
CHECKED	Leung 9/19/81
APVD SECT HD	Schmidt 9/24/81
APVD PROJ MGR	Thiele 11/19/81
APVD CLIENT	Franklin 11/19/81

THE RALPH M. PARSONS COMPANY
PASADENA, CALIFORNIA

ARGONNE NATIONAL LABORATORY
ARGONNE, ILLINOIS
DEMONSTRATION TOKAMAK POWER PLANT

TITLE: ARCHITECTURAL
FUSION POWER PLANT
SITE PLAN

SCALE: 1 :1000
ACCOUNT NUMBER: —
JOB NUMBER: 5959-1
DOCUMENT NUMBER: E-5959-AR-11
REVISION: 1

ENG-GE-24 (12/79)

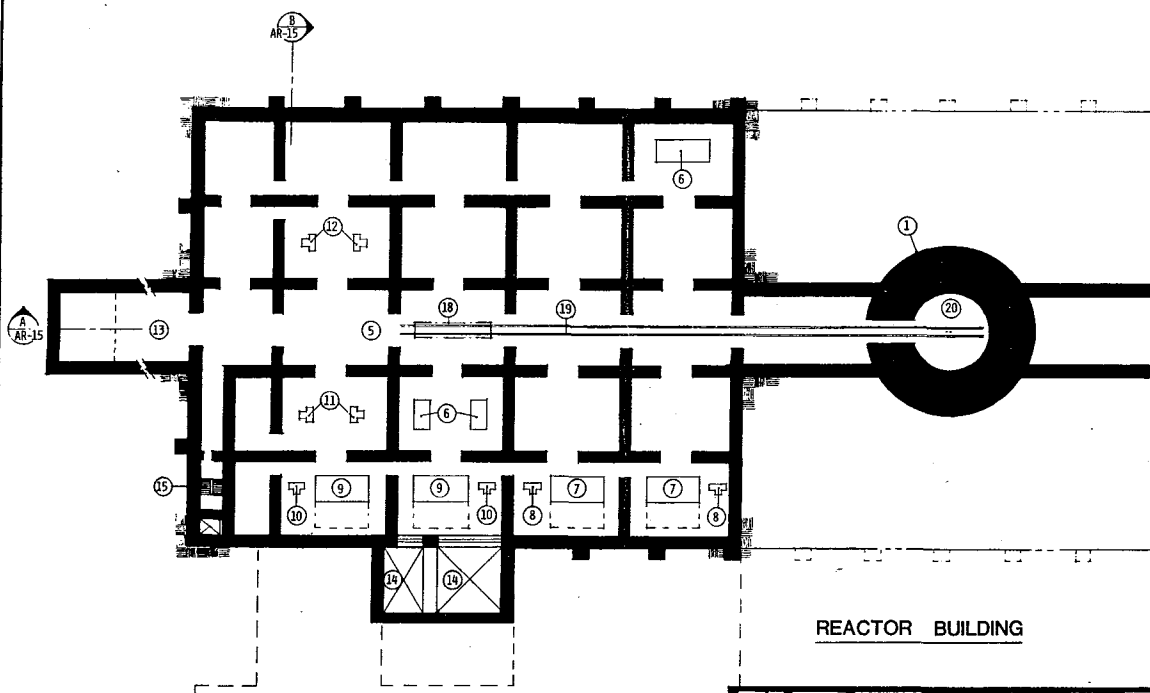

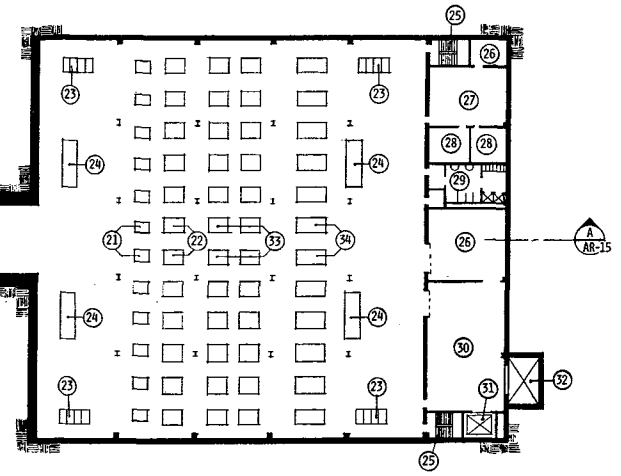

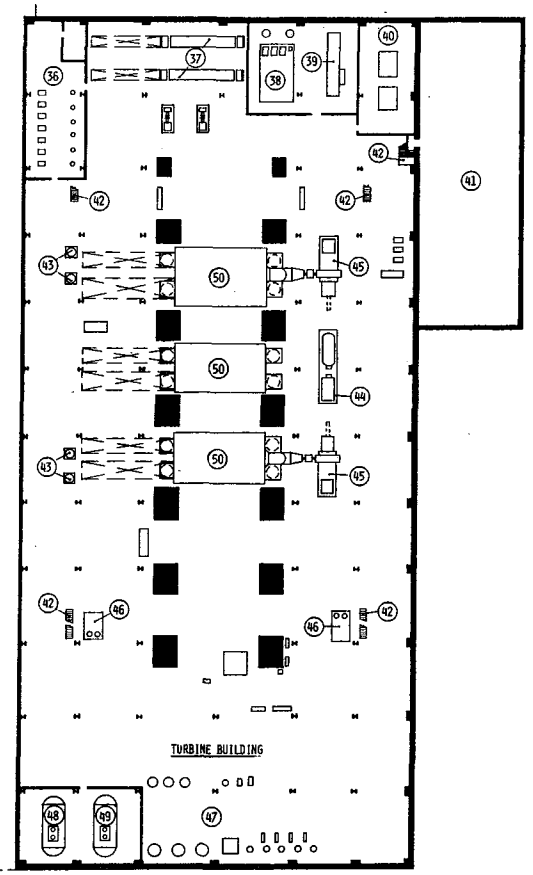

LEGEND

REACTOR BUILDING

1. CONCRETE SUPPORT PEDESTAL
2. NOT USED
3. NOT USED
4. NOT USED
5. CORRIDOR
6. ELECTRICAL EQUIPMENT
7. SUB-GRADE LEVEL AIR COOLING SYSTEM
8. RECIRCULATING/EXHAUST FAN
9. OUTDOOR AIR PURGE SYSTEM
10. SUPPLY FAN
11. PRESSURE CONTROL FANS
12. OUTDOOR AIR PURGE EXHAUST
13. TUNNEL TO STACK
14. AREAWAY
15. STAIR
16. TUNNEL TO REB POWER SUPPLY ROOM
17. NOT USED
18. EF COIL REMOVAL HATCH
19. EF COIL TRANSFER CART RAILS
20. EF COIL REMOVAL ROOM

ELECTRICAL & REB POWER SUPPLY BUILDING

21. TRANSFORMER (TYPICAL)
22. HFC COMPRESSOR (TYPICAL)
23. 13.8 kV SWITCHGEAR
24. 480 V. LOAD CENTER
25. STAIR
26. STORAGE
27. CONTROL/MONITOR ROOM
28. OFFICE
29. TOILET/SHOWER/LOCKERS
30. MAINTENANCE & REPAIR SHOP
31. FREIGHT ELEVATOR
32. AREAWAY
33. MOTOR (TYPICAL)
34. CAPACITOR (TYPICAL)
35. NOT USED

TURBINE & SUPPORT BUILDING

36. CHEMICAL EQUIPMENT ROOM
37. TURBINE PLANT HEAT EXCHANGER
38. LUBE OIL RESERVOIR
39. LUBE OIL CONDITIONER
40. BATTERY ROOM
41. CABLE SPREADING ROOM
42. STAIR
43. CONDENSATE PUMPS
44. MOTOR DRIVEN FEEDWATER PUMPS
45. TURBINE DRIVEN FEEDWATER PUMPS
46. SUMP
47. DEMINERALIZER AREA
48. ACID TANK
49. CAUSTIC TANK
50. CONDENSER

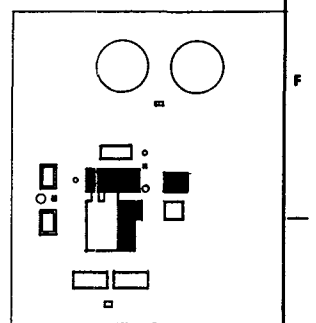

Figure 9-7.

REFERENCES	DRAWING NO.	DESCRIPTION

REVISIONS	NO.	DATE	BY	CHKD	SEC	PROJ	CLIENT	DESCRIPTION
	A	11-8-82	SDH	EJK	73715	C.T.		APPROVED FOR FINAL REPORT
	B	10-18-82	SDH	EJK	73715			ISSUED FOR CLIENT APPROVAL

PDH DRAWN	S. Hamada	9-1982
CHECKED	S. Hamada	9-19-82
APVD SECT MR	S. Hamada	9-30-82
APVD PROJ MGR	W. Tindall	11/19/82
APVD CLIENT	C. Tindall	11/19/82

THE RALPH M. PARSONS COMPANY
PASADENA, CALIFORNIA

ARGONNE NATIONAL LABORATORY
ARGONNE, ILLINOIS
DEMONSTRATION TOKAMAK POWER PLANT

TITLE	SCALE	ACCOUNT NUMBER	JOB NUMBER	REVISION
ARCHITECTURAL REACTOR, TURBINE & SUPPORT, ELECTRICAL & REB POWER SUPPLY & ON SITE A/C POWER BLDG SUB-GRADE LEVEL PLANS	1:300	—	5959-1	A
	DOCUMENT NUMBER	E-5959-AR-12		

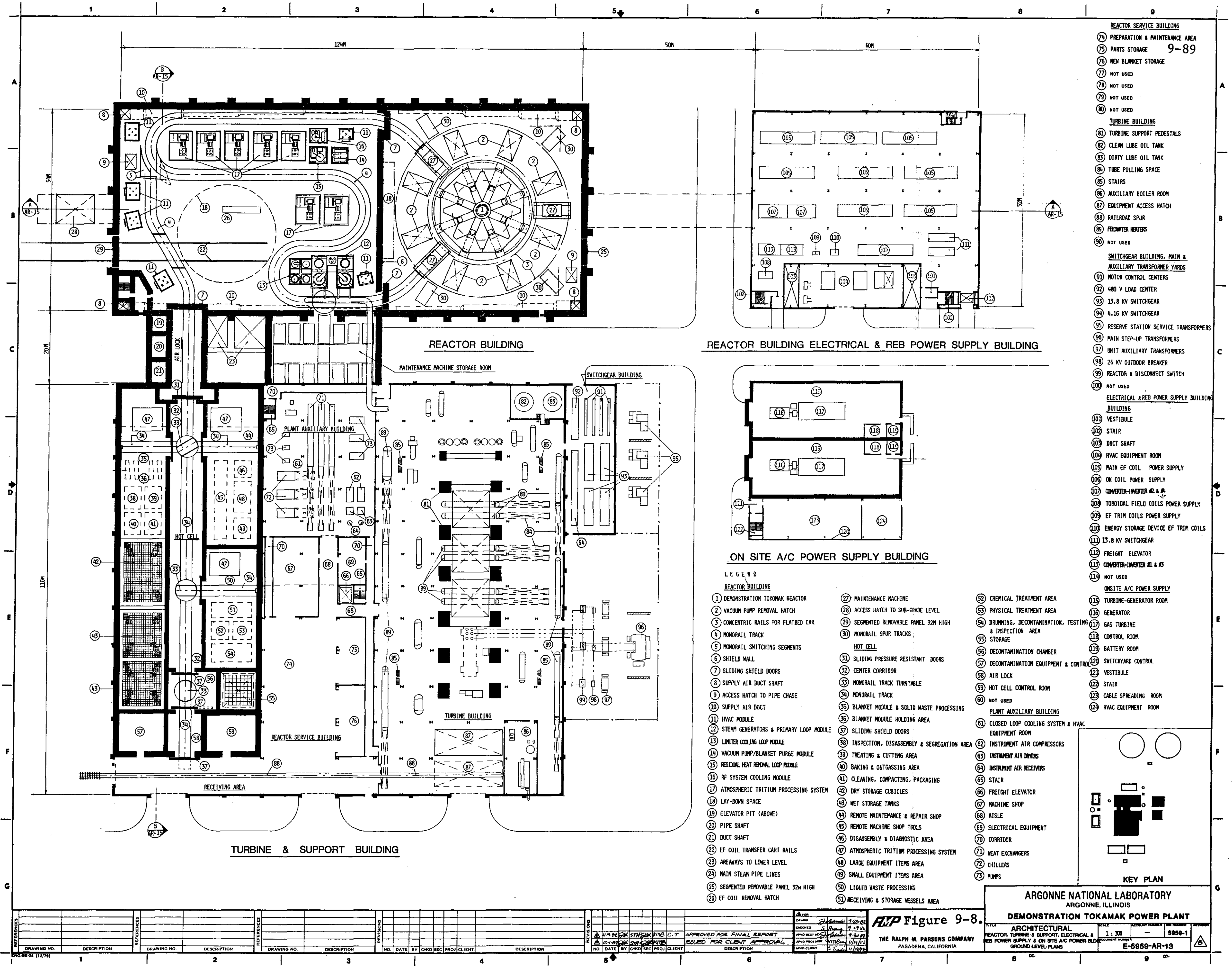

LEGEND

REACTOR BUILDING
- ① DEMONSTRATION TOKOMAK REACTOR
- ② VACUUM PUMP REMOVAL HATCH
- ③ CONCENTRIC RAILS FOR FLATBED CAR
- ④ MONORAIL TRACK
- ⑤ MONORAIL SWITCHING SEGMENTS
- ⑥ SHIELD WALL
- ⑦ SLIDING SHIELD DOORS
- ⑧ SUPPLY AIR DUCT SHAFT
- ⑨ ACCESS HATCH TO PIPE CHASE
- ⑩ SUPPLY AIR DUCT
- ⑪ HVAC MODULE
- ⑫ STEAM GENERATORS & PRIMARY LOOP MODULE
- ⑬ LIMITER COOLING LOOP MODULE
- ⑭ VACUUM PUMP/BLANKET PURGE MODULE
- ⑮ RESIDUAL HEAT REMOVAL LOOP MODULE
- ⑯ RF SYSTEM COOLING MODULE
- ⑰ ATMOSPHERIC TRITIUM PROCESSING SYSTEM
- ⑱ LAY-DOWN SPACE
- ⑲ ELEVATOR PIT (ABOVE)
- ⑳ PIPE SHAFT
- ㉑ DUCT SHAFT
- ㉒ EF COIL TRANSFER CART RAILS
- ㉓ AREAWAYS TO LOWER LEVEL
- ㉔ MAIN STEAM PIPE LINES
- ㉕ SEGMENTED REMOVABLE PANEL 32M HIGH
- ㉖ EF COIL REMOVAL HATCH
- ㉗ MAINTENANCE MACHINE
- ㉘ ACCESS HATCH TO SUB-GRADE LEVEL
- ㉙ SEGMENTED REMOVABLE PANEL 32M HIGH
- ㉚ MONORAIL SPUR TRACKS

HOT CELL
- ㉛ SLIDING PRESSURE RESISTANT DOORS
- ㉜ CENTER CORRIDOR
- ㉝ MONORAIL TRACK TURNTABLE
- ㉞ MONORAIL TRACK
- ㉟ BLANKET MODULE & SOLID WASTE PROCESSING
- ㊱ BLANKET MODULE HOLDING AREA
- ㊲ SLIDING SHIELD DOORS
- ㊳ INSPECTION, DISASSEMBLY & SEGREGATION AREA
- ㊴ TREATING & CUTTING AREA
- ㊵ BAKING & OUTGASSING AREA
- ㊶ CLEANING, COMPACTING, PACKAGING
- ㊷ DRY STORAGE CUBICLES
- ㊸ WET STORAGE TANKS
- ㊹ REMOTE MAINTENANCE & REPAIR SHOP
- ㊺ REMOTE MACHINE SHOP TOOLS
- ㊻ DISASSEMBLY & DIAGNOSTIC AREA
- ㊼ ATMOSPHERIC TRITIUM PROCESSING SYSTEM
- ㊽ LARGE EQUIPMENT ITEMS AREA
- ㊾ SMALL EQUIPMENT ITEMS AREA
- ㊿ LIQUID WASTE PROCESSING
- (51) RECEIVING & STORAGE VESSELS AREA
- (52) CHEMICAL TREATMENT AREA
- (53) PHYSICAL TREATMENT AREA
- (54) DRUMMING, DECONTAMINATION, TESTING & INSPECTION AREA
- (55) STORAGE
- (56) DECONTAMINATION CHAMBER
- (57) DECONTAMINATION EQUIPMENT & CONTROL
- (58) AIR LOCK
- (59) HOT CELL CONTROL ROOM
- (60) NOT USED

PLANT AUXILIARY BUILDING
- (61) CLOSED LOOP COOLING SYSTEM & HVAC EQUIPMENT ROOM
- (62) INSTRUMENT AIR COMPRESSORS
- (63) INSTRUMENT AIR DRYERS
- (64) INSTRUMENT AIR RECEIVERS
- (65) STAIR
- (66) FREIGHT ELEVATOR
- (67) MACHINE SHOP
- (68) AISLE
- (69) ELECTRICAL EQUIPMENT
- (70) CORRIDOR
- (71) HEAT EXCHANGERS
- (72) CHILLERS
- (73) PUMPS

REACTOR SERVICE BUILDING
- (74) PREPARATION & MAINTENANCE AREA
- (75) PARTS STORAGE
- (76) NEW BLANKET STORAGE
- (77) NOT USED
- (78) NOT USED
- (79) NOT USED
- (80) NOT USED

TURBINE BUILDING
- (81) TURBINE SUPPORT PEDESTALS
- (82) CLEAN LUBE OIL TANK
- (83) DIRTY LUBE OIL TANK
- (84) TUBE PULLING SPACE
- (85) STAIRS
- (86) AUXILIARY BOILER ROOM
- (87) EQUIPMENT ACCESS HATCH
- (88) RAILROAD SPUR
- (89) FEEDWATER HEATERS
- (90) NOT USED

SWITCHGEAR BUILDING, MAIN & AUXILIARY TRANSFORMER YARDS
- (91) MOTOR CONTROL CENTERS
- (92) 480 V LOAD CENTER
- (93) 13.8 KV SWITCHGEAR
- (94) 4.16 KV SWITCHGEAR
- (95) RESERVE STATION SERVICE TRANSFORMERS
- (96) MAIN STEP-UP TRANSFORMERS
- (97) UNIT AUXILIARY TRANSFORMERS
- (98) 26 KV OUTDOOR BREAKER
- (99) REACTOR & DISCONNECT SWITCH
- (100) NOT USED

ELECTRICAL & REB POWER SUPPLY BUILDING BUILDING
- (101) VESTIBULE
- (102) STAIR
- (103) DUCT SHAFT
- (104) HVAC EQUIPMENT ROOM
- (105) MAIN EF COIL POWER SUPPLY
- (106) OH COIL POWER SUPPLY
- (107) CONVERTER-INVERTER #2 & #4
- (108) TOROIDAL FIELD COILS POWER SUPPLY
- (109) EF TRIM COILS POWER SUPPLY
- (110) ENERGY STORAGE DEVICE EF TRIM COILS
- (111) 13.8 KV SWITCHGEAR
- (112) FREIGHT ELEVATOR
- (113) CONVERTER-INVERTER #1 & #3
- (114) NOT USED

ONSITE A/C POWER SUPPLY
- (115) TURBINE-GENERATOR ROOM
- (116) GENERATOR
- (117) GAS TURBINE
- (118) CONTROL ROOM
- (119) BATTERY ROOM
- (120) SWITCHYARD CONTROL
- (121) VESTIBULE
- (122) STAIR
- (123) CABLE SPREADING ROOM
- (124) HVAC EQUIPMENT ROOM

KEY PLAN

NO.	DATE	BY	CHKD	SEC	PROJ	CLIENT	DESCRIPTION
△	11-19-82	[illegible]	STH	[illegible]	KMB	C.T	APPROVED FOR FINAL REPORT
△	10-1-82	[illegible]	STH	[illegible]	KMB		ISSUED FOR CLIENT APPROVAL

DRAWN	J. Labuski	9-28-82
CHECKED	S. Huang	9-29-82
APVD SECT HD	J. Labuski	9-30-82
APVD PROJ MGR	KMBorg	11/19/82
APVD CLIENT	C. Trachsel	11/19/82

RMP Figure 9-8.

THE RALPH M. PARSONS COMPANY
PASADENA, CALIFORNIA

ARGONNE NATIONAL LABORATORY
ARGONNE, ILLINOIS
DEMONSTRATION TOKAMAK POWER PLANT

TITLE ARCHITECTURAL
REACTOR, TURBINE & SUPPORT, ELECTRICAL & REB POWER SUPPLY & ON SITE A/C POWER BLDG
GROUND LEVEL PLANS

SCALE 1 : 300
ACCOUNT NUMBER —
JOB NUMBER 5959-1
DOCUMENT NUMBER E-5959-AR-13
REVISION △

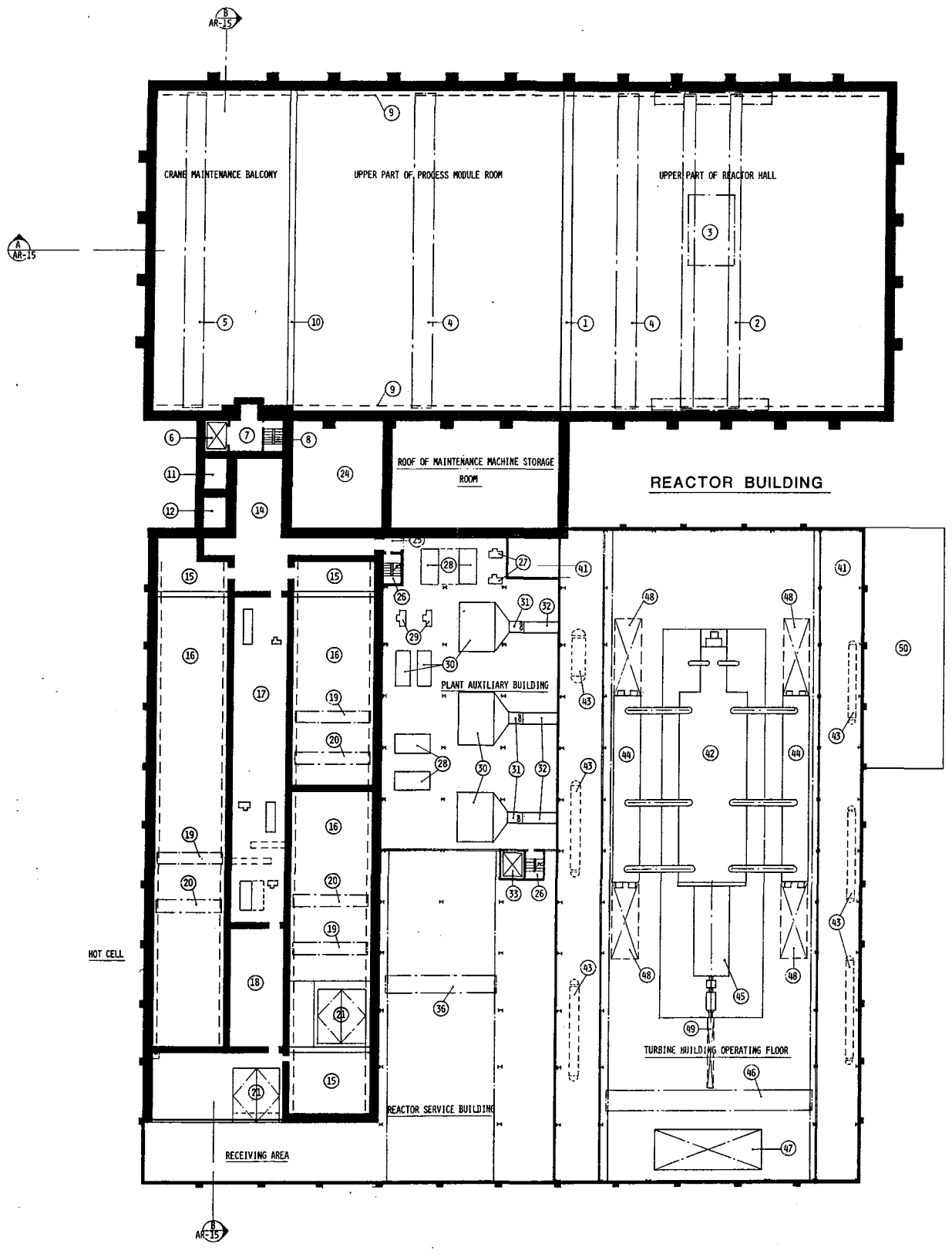

REACTOR BUILDING

TURBINE & SUPPORT BUILDING

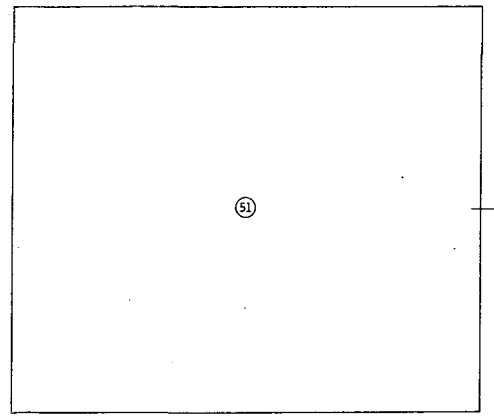

ELECTRICAL & REB POWER SUPPLY BUILDING

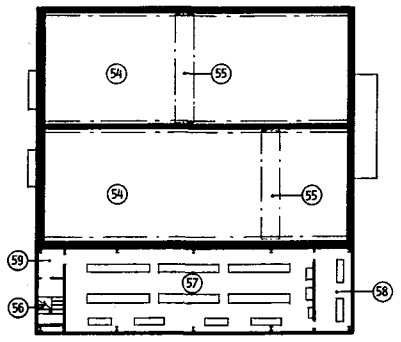

ON SITE A/C POWER SUPPLY BUILDING

LEGEND

REACTOR BUILDING
1. SHIELD WALL
2. 500 TON BRIDGE CRANE
3. 500 TON TROLLEY
4. ELECTRO-MECHANICAL BRIDGE MANIPULATOR
5. 60 TON BRIDGE CRANE (SHOWN UNDER CRANE MAINTENANCE BALCONY)
6. FREIGHT ELEVATOR
7. ELEVATOR LOBBY
8. STAIR
9. CRANE RUNWAY CORBEL
10. BALCONY RAIL
11. PIPE SHAFT
12. DUCT SHAFT
13. NOT USED

HOT CELL
14. CORRIDOR
15. CRANE MAINTENANCE
16. UPPER PART OF CELL
17. HVAC EQUIPMENT ROOM
18. ELECTRICAL EQUIPMENT ROOM
19. 60 TON BRIDGE CRANE
20. ELECTRO-MECHANICAL BRIDGE MANIPULATOR
21. REMOVABLE HATCH
22. NOT USED
23. NOT USED

PLANT AUXILIARY BUILDING
24. AREAWAY AIR WELL
25. VESTIBULE
26. STAIR
27. EXHAUST FAN
28. AIR HANDLING UNIT
29. PRESSURE CONTROL FANS
30. PLENUM
31. SUPPLY AIR FAN
32. HVAC DUCT TO TURBINE BUILDING
33. FREIGHT ELEVATOR
34. NOT USED
35. NOT USED

REACTOR SERVICE
36. 60 TON BRIDGE CRANE
37. NOT USED
38. NOT USED
39. NOT USED
40. NOT USED

TURBINE BUILDING
41. HVAC GALLERY
42. TURBINE CASING
43. FEEDWATER HEATERS
44. MOISTURE SEPARATOR/REHEATERS
45. GENERATOR
46. 250 TON BRIDGE CRANE
47. EQUIPMENT ACCESS HATCH
48. TUBE PULLING SPACE
49. ROTOR PULLING SPACE
50. SWITCHGEAR BUILDING ROOF

REB POWER SUPPLY BUILDING
51. ROOF
52. NOT USED
53. NOT USED

ON SITE A/C POWER SUPPLY BUILDING
54. UPPER PART OF TURBINE GENERATOR ROOM
55. 10 TON BRIDGE CRANE
56. STAIR
57. SWITCHYARD CONTROL EQUIPMENT ROOM
58. BATTERY ROOM
59. VESTIBULE

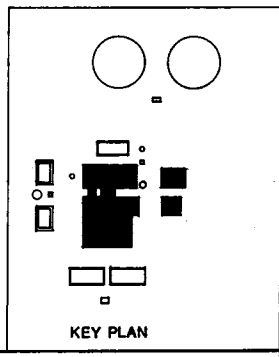

KEY PLAN

REFERENCES	DRAWING NO.	DESCRIPTION

REVISIONS	NO.	DATE	BY	CHKD	SEC	PROJ	CLIENT	DESCRIPTION
	1	11-1-82	SAK	SEH	GKC	WHC	C. T.	APPROVED FOR FINAL REPORT
	0	10-1-82	SAK	SEH	GKC	WHC		ISSUED FOR CLIENT APPROVAL

FOR DRAWN	Dickinson	9/28/82
CHECKED	S. Hwang	7/27/82
APVD SECT HD	Schwenk	9/30/82
APVD PROJ MGR	Schwenk	11/1/82
APVD CLIENT	C. Travis	11/19/82

AVP Figure 9-9.

THE RALPH M. PARSONS COMPANY
PASADENA, CALIFORNIA

ARGONNE NATIONAL LABORATORY
ARGONNE, ILLINOIS
DEMONSTRATION TOKAMAK POWER PLANT

TITLE: ARCHITECTURAL
REACTOR, TURBINE & SUPPORT, ELECTRICAL & REB POWER SUPPLY & ON SITE A/C POWER BLDG. UPPER LEVEL PLANS

SCALE: 1 : 300
ACCOUNT NUMBER: —
JOB NUMBER: 5959-1
DOCUMENT NUMBER: E-5959-AR-14
REVISION: 1

ENG-GE-24 (12/79)

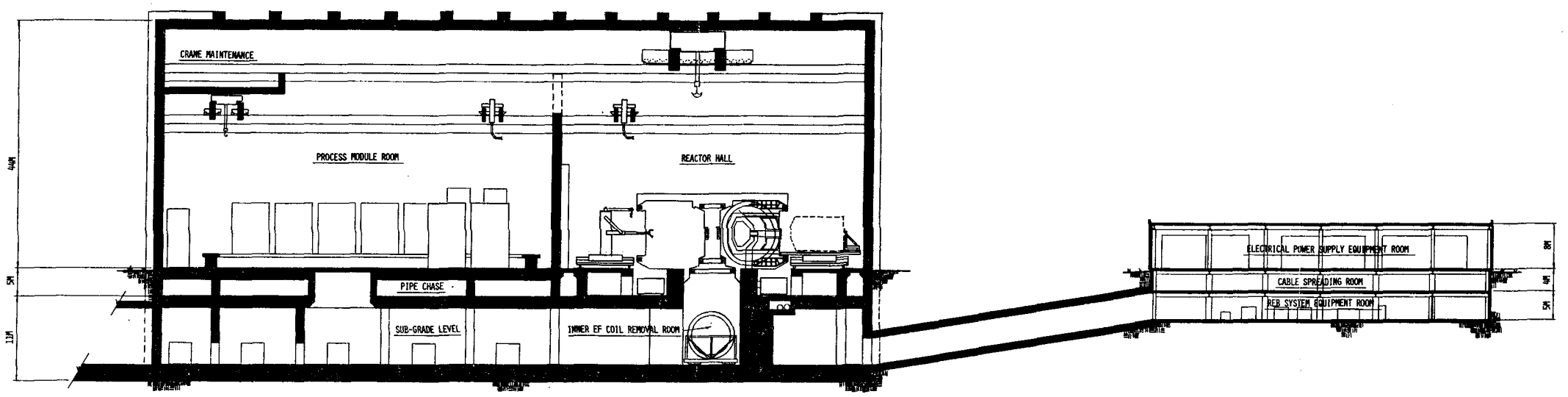

SECTION- REACTOR BUILDING, ELECTRICAL & REB POWER SUPPLY BUILDING (A / AR-15)

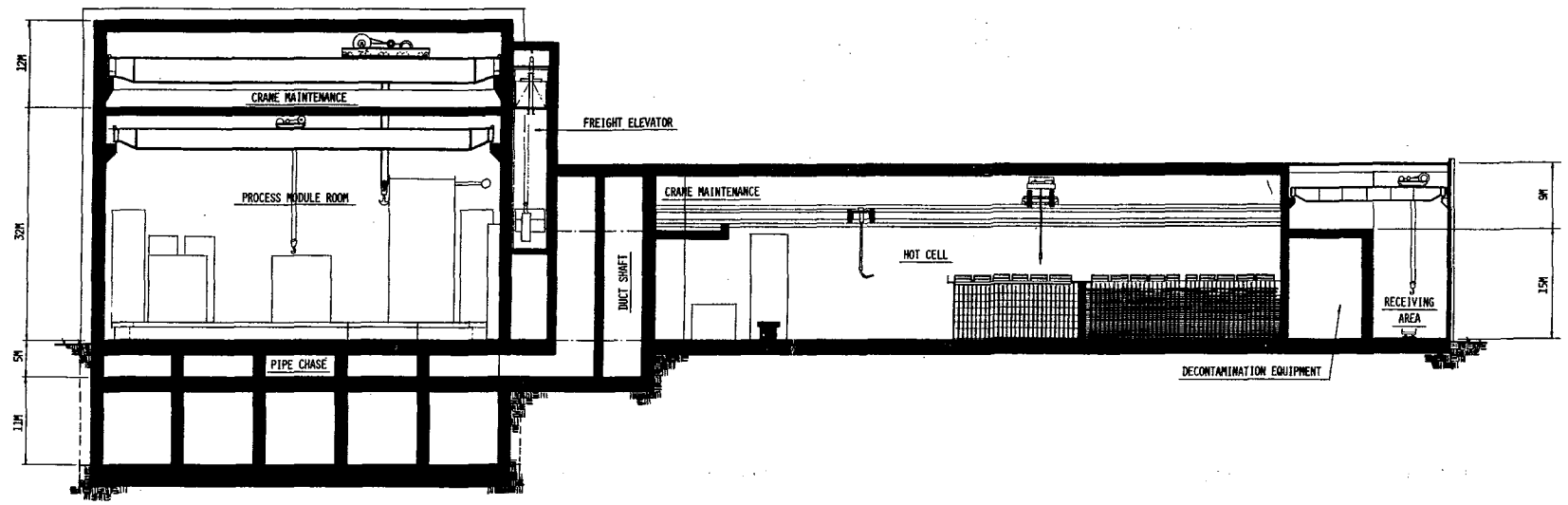

SECTION - REACTOR BUILDING, HOT CELL (B / AR-15)

Figure 9-10.

REFERENCES	DRAWING NO.	DESCRIPTION

REVISIONS	NO.	DATE	BY	CHKD	SEC	PROJ	CLIENT	DESCRIPTION
	A	11-88	GRIMM					APPROVED FOR FINAL REPORT
	B	10-89	GRIMM					ISSUED FOR CLIENT APPROVAL

FOR		
DRAWN	S. Hwang	9-29-89
CHECKED	S. Hwang	9-29-89
APVD SECT HD	[illegible]	9-30-89
APVD PROJ MGR	[illegible]	11/1/89
APVD CLIENT	[illegible]	

THE RALPH M. PARSONS COMPANY
PASADENA, CALIFORNIA

ARGONNE NATIONAL LABORATORY
ARGONNE, ILLINOIS
DEMONSTRATION TOKAMAK POWER PLANT

TITLE	SCALE	DOCUMENT NUMBER	JOB NUMBER	REVISION
ARCHITECTURAL REACTOR, TURBINE & SUPPORT, ELECTRICAL & REB POWER SUPPLY & ON SITE A/C POWER BLDG BUILDING SECTIONS	1 : 300	—	5959-1	B
	DOCUMENT NUMBER	E-5959-AR-15		

ENG-GE-24 (12/79)

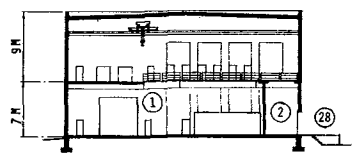

SECTION A AR-16

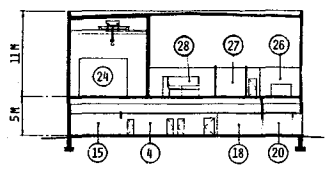

SECTION B AR-16

LEGEND

1. TRITIUM REPROCESSING EQUIP
2. EQUIPMENT AIRLOCK
3. NEW TRITIUM & DEUTERIUM CYLINDER STOR
4. CORRIDOR
5. AIRLOCK
6. TRITIUM & DEUTERIUM STOR
7. MONITOR, EQUIPMENT, MAINTENANCE & REPAIR
8. SUIT STORAGE
9. EMERGENCY SHOWER
10. ANALYTICAL LABORATORY
11. WOMEN'S TOILET
12. MEN'S TOILET
13. LOCKERS
14. SHOWERS
15. CRYOGENICS CONTROL ROOM
16. OFFICE
17. RADIATION SAFETY OFFICE
18. OPEN OFFICE
19. STAIRS
20. VESTIBULE
21. OFFICE
22. CRYOGENICS EQUIP ROOM
23. CRYOGENICS EQUIP YARD
24. ATPS EQUIP ROOM
25. HVAC EQUIP ROOM (T_2 POTENTIAL)
26. HVAC EQUIP ROOM (NON-T_2 POTENTIAL)
27. CONTROL ROOM OFFICE
28. TRITIUM CONTROL ROOM & MONITORS
29. ELECTRICAL EQUIPMENT

EQUIPMENT LEGEND

ISS	ISOTOPE SEPARATION UNIT
SWD	SOLID WASTE DISPOSAL
TWRU	TRITIATED WASTE RECOVERY UNIT
FCU	FUEL CLEANUP UNIT
TWT	TRITIUM WASTE TREATMENT
TPU	TRANSFER PUMP UNIT
He	HELIUM
N_2	NITROGEN
LHe	LIQUID HELIUM
LN_2	LIQUID NITROGEN
ATPS	ATMOSPHERIC TRITIUM PROCESSING SYSTEM
ORM	OIL REMOVAL MODULE
COMP	COMPRESSORS
LIQ CB	LIQUIFIER COLD BOX
EXP. ENG	EXPANSION ENGINE
PUR. MOD	PURIFICATION MODULE
T_2	TRITIUM
D_2	DEUTERIUM

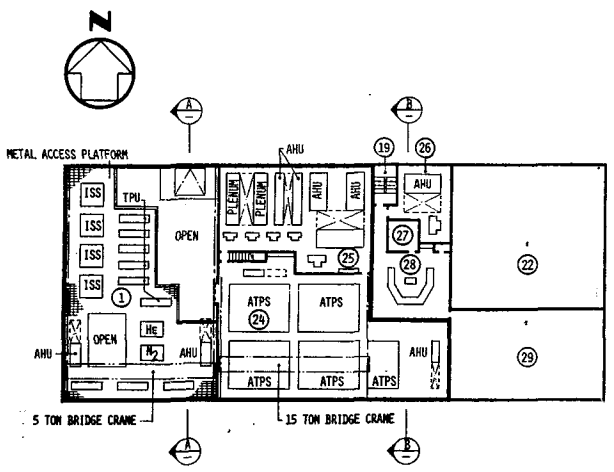

UPPER LEVEL PLAN

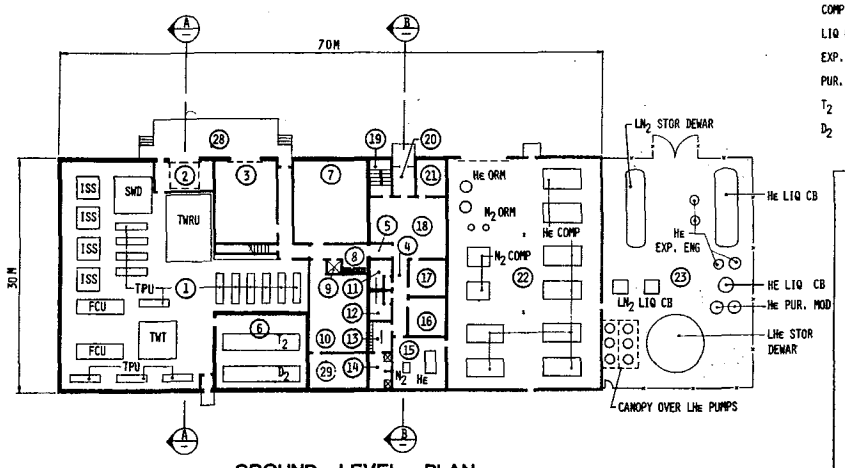

GROUND LEVEL PLAN

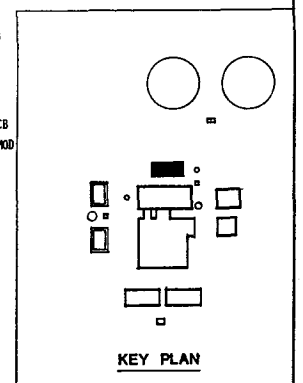

KEY PLAN

TRITIUM REPROCESSING & CRYOGENICS BUILDING

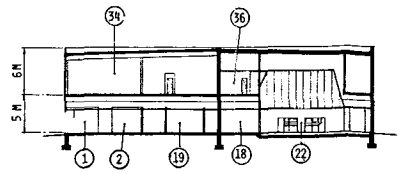

SECTION C AR-16

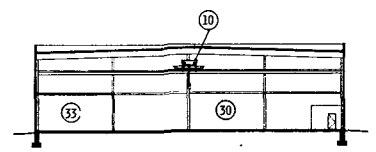

SECTION D AR-16

LEGEND

1. VESTIBULE
2. LOBBY
3. CONFERENCE
4. STORAGE
5. WOMEN'S TOILET
6. MEN'S TOILET
7. LUNCH ROOM
8. CORRIDOR
9. PLANT SUPERINTENDENT
10. PLANT ENGINEER
11. TECHNICAL SUPERVISOR
12. INSTRUMENTATION ENGINEER
13. NUCLEAR ENGINEER
14. SECRETARY
15. ASSISTANT PLANT SUPT
16. OPERATIONS SUPERVISOR
17. MAINTENANCE SUPERVISOR
18. SHIFT SUPERVISOR
19. HEALTH PHYSICIST
20. FILES
21. CONTROL OFFICE
22. MAIN CONTROL ROOM
23. ELECTRICAL EQUIP
24. COMPUTER STORAGE
25. COMPUTER
26. INSTRUMENT MAINT. & REPAIR
27. TOOLS, PARTS
28. MAINTENANCE RECEIVING OFFICE
29. WAREHOUSE RECEIVING OFFICE
30. MAINTENANCE SHOP
31. WAREHOUSE
32. TOOLS
33. WELDING
34. HVAC EQUIP
35. UPPER PART OF CONTROL ROOM
36. OBSERVATION GALLERY
37. UPPER PART OF MAINT. SHOP
38. UPPER PART OF WAREHOUSE
39. 10 TON BRIDGE CRANE

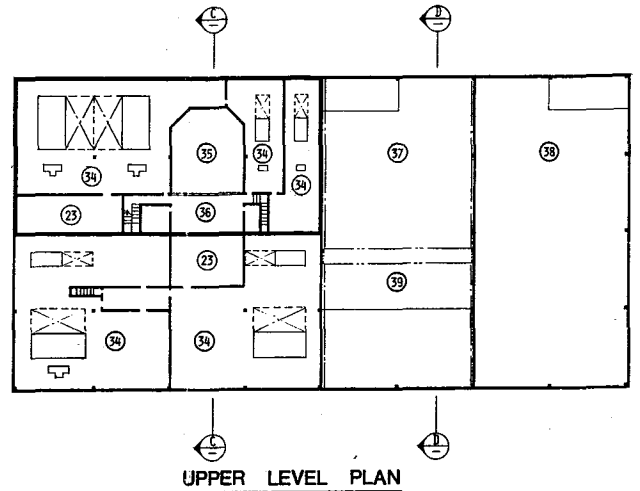

UPPER LEVEL PLAN

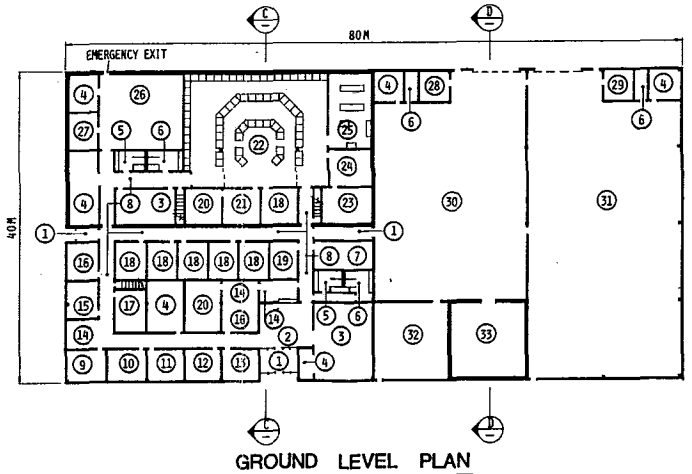

GROUND LEVEL PLAN

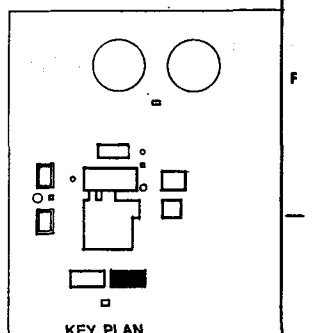

KEY PLAN

ADMINISTRATION, CONTROL & SITE SERVICE BUILDING

Figure 9-11.

REVISIONS NO.	DATE	BY	CHKD	SEC	PROJ	CLIENT	DESCRIPTION
1	11/14/82	SHP	PWK	SWT	B.C.T.		APPROVED FOR FINAL REPORT
0	10/1/82	SHP	PWK	SWT			ISSUED FOR CLIENT APPROVAL

THE RALPH M. PARSONS COMPANY
PASADENA, CALIFORNIA

ARGONNE NATIONAL LABORATORY
ARGONNE, ILLINOIS
DEMONSTRATION TOKAMAK POWER PLANT
TITLE: ARCHITECTURAL
TRITIUM REPROCESSING & CRYOGENICS, ADMINISTRATION, CONTROL & SITE SERVICES
GROUND & UPPER LEVEL PLANS, SECTIONS
SCALE: 1 : 300
ACCOUNT NUMBER: —
JOB NUMBER: 5959-1
DOCUMENT NUMBER: E-5959-AR-16
REV/ISSUE: A

1	VESTIBULE
2	LOBBY
3	SECRETARY
4	OFFICE
5	CONFERENCE
6	MEN'S TOILET
7	WOMEN'S TOILET
8	STORAGE
9	LUNCH ROOM
10	KITCHEN
11	DISHWASH AREA
12	COMPUTER CENTER
13	ELECTRICAL EQUIPMENT
14	LIBRARY
15	COMPUTER STORAGE
16	COMPUTER TAPE FILE ROOM
17	UTILITY CHASE
18	LABORATORY
19	MECHANICAL EQUIPMENT ROOM
20	CORRIDOR

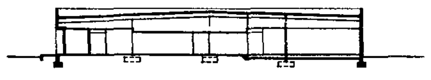

SECTION Ⓑ

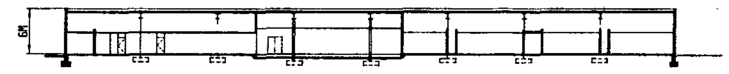

SECTION Ⓐ

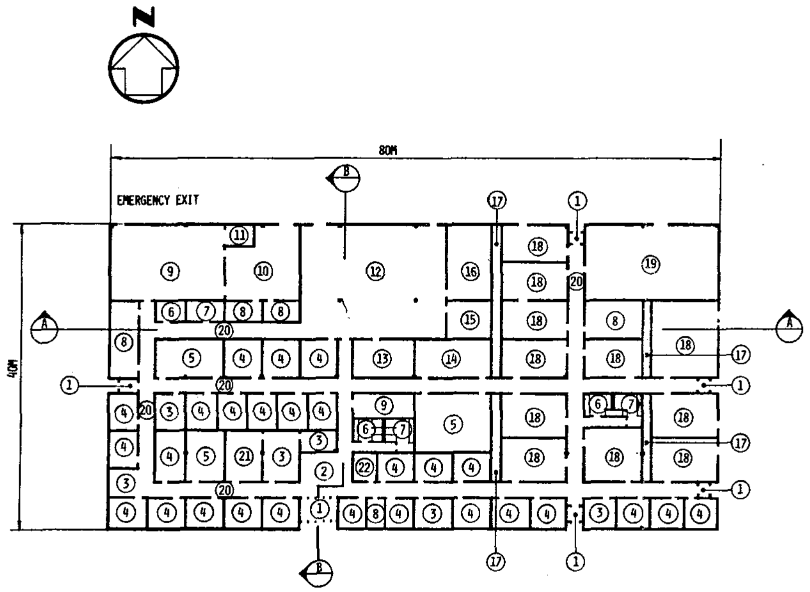

FLOOR PLAN

RESEARCH & DEVELOPMENT BUILDING

Figure 9-12.

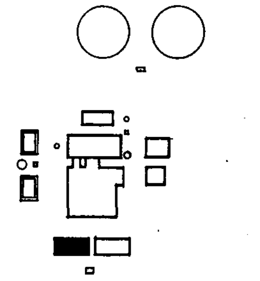

KEY PLAN

REVISIONS NO.	DATE	BY	CHKD	SEC	PROJ	CLIENT	DESCRIPTION
△	11-19-82	DK	STH	DK	KMB	C.T	APPROVED FOR FINAL REPORT
△	10-1-82	DK	STH	DK	KMB		ISSUED FOR CLIENT APPROVAL

△ FOR		
DRAWN	J. Schwartz	9-28-82
CHECKED	S. Huang	9-29-82
APVD SECT HD	J. Schwartz	9-30-82
APVD PROJ MGR	KMBa	11/19/82
APVD CLIENT	C. Trach	11/19/82

RMP
THE RALPH M. PARSONS COMPANY
PASADENA, CALIFORNIA

ARGONNE NATIONAL LABORATORY
ARGONNE, ILLINOIS
DEMONSTRATION TOKAMAK POWER PLANT

TITLE ARCHITECTURAL
RESEARCH & DEVELOPMENT BUILDING
FLOOR PLAN & SECTIONS

SCALE	ACCOUNT NUMBER	JOB NUMBER	REVISION
1 : 300	—	5959-1	△

DOCUMENT NUMBER E-5959-AR-17

REFERENCES DRAWING NO.	DESCRIPTION	REFERENCES DRAWING NO.	DESCRIPTION	REFERENCES DRAWING NO.	DESCRIPTION	REVISIONS NO.	DATE	BY	CHKD	SEC	PROJ	CLIENT	DESCRIPTION

ENG-GE-24 (12/79)

1. REACTOR BUILDING
2. TURBINE & SUPPORT BUILDING
3. ADMINISTRATION, CONTROL, & SITE SERVICE BUILDING
4. TRITIUM REPROCESSING & CYROGENICS BUILDING
5. ELECTRICAL & REB POWER SUPPLY BUILDING
6. R & D BUILDING
7. MAIN SWITCHYARD
8. RAW WATER RESERVOIR
9. EVAPORATION POND
10. COOLING TOWERS
11. STACK
12. SECURITY BUILDING
13. PARKING
14. PERIMETER ROAD
15. PERIMETER FENCE
16. RAILROAD SPUR
17. PUMP HOUSE
18. ON SITE AC POWER SUPPLY BUILDING

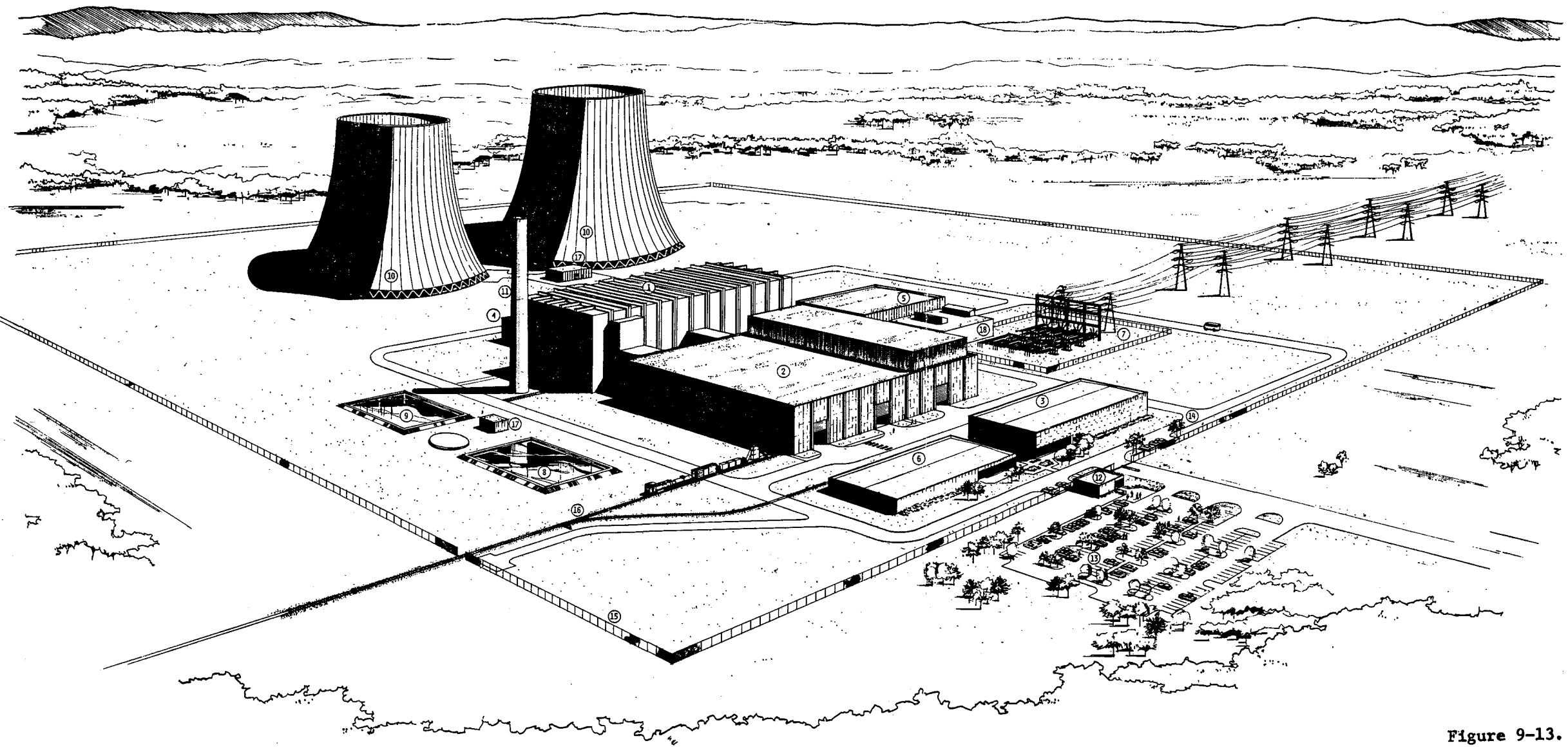

Figure 9-13.

REFERENCES — DRAWING NO. — DESCRIPTION

REVISIONS

NO.	DATE	BY	CHKD	SEC	PROJ	CLIENT	DESCRIPTION
1	11/78	DK	SATHYAPRAKASH	C.T.			APPROVED FOR FINAL REPORT
2	10-18-78	DK	SATHYAPRAKASH				ISSUED FOR CLIENT APPROVAL

DRAWN	Fa Tsai	11/78
CHECKED	S. Huang	11-19
APVD SPEC'N	C. Lewis	11-20
APVD PROJ MGR	SATHYAPRAKASH	11/24
APVD NDAC	C. Foster	11/28

AMP — THE RALPH M. PARSONS COMPANY — PASADENA, CALIFORNIA

ARGONNE NATIONAL LABORATORY
ARGONNE, ILLINOIS
DEMONSTRATION TOKAMAK POWER PLANT

TITLE	SCALE	ACCOUNT NUMBER	JOB NUMBER	REVISION
ARCHITECTURAL — FUSION POWER PLANT — SITE PERSPECTIVE	—	—	5959-1	2
	DOCUMENT NUMBER	E-5959-AR-18		

ENG-GE-64 (11/78)

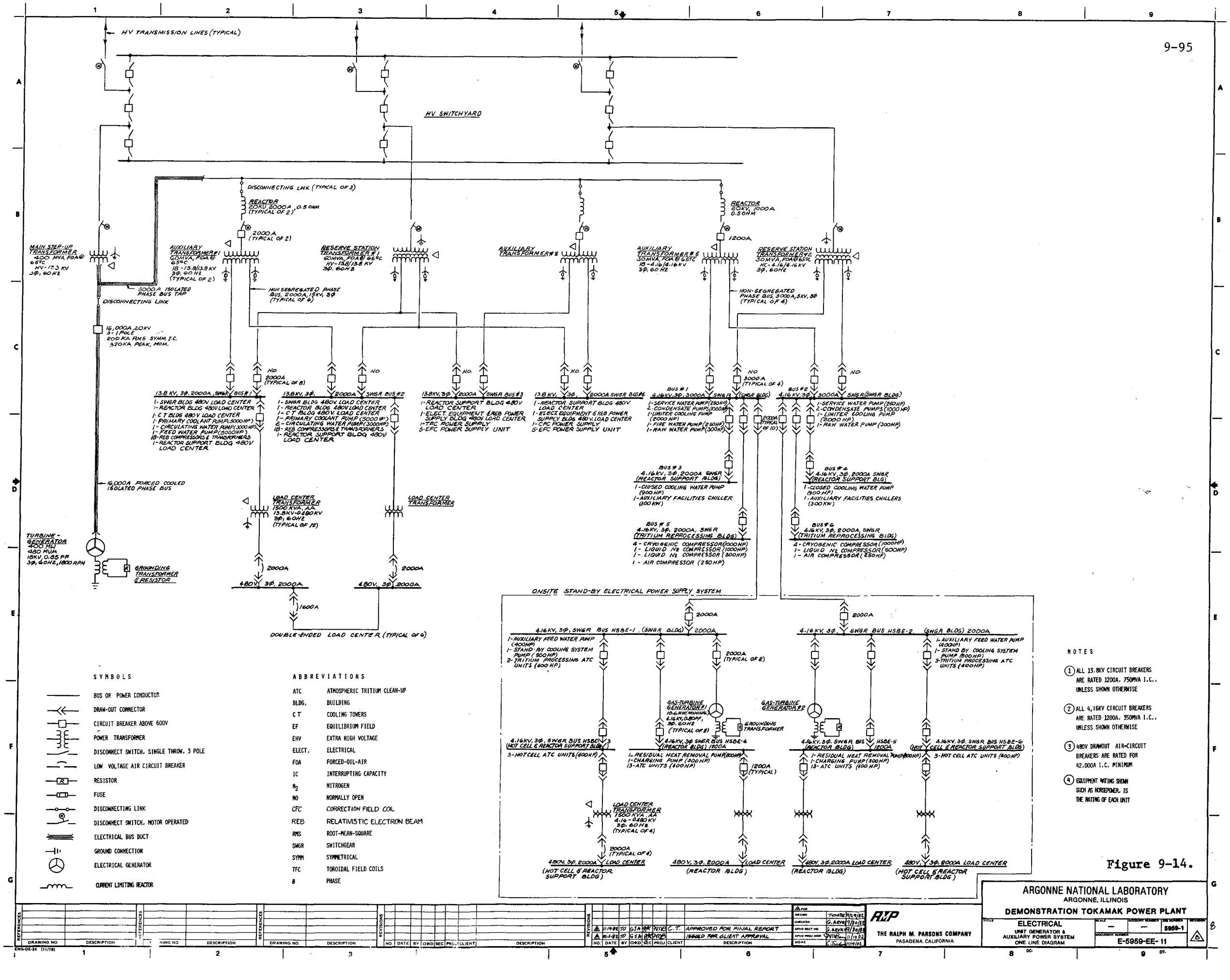

SYMBOLS

- BUS OR POWER CONDUCTOR
- DRAW-OUT CONNECTOR
- CIRCUIT BREAKER ABOVE 600V
- POWER TRANSFORMER
- DISCONNECT SWITCH, SINGLE THROW, 3 POLE
- LOW VOLTAGE AIR CIRCUIT BREAKER
- RESISTOR
- FUSE
- DISCONNECTING LINK
- DISCONNECT SWITCH, MOTOR OPERATED
- ELECTRICAL BUS DUCT
- GROUND CONNECTION
- ELECTRICAL GENERATOR
- CURRENT LIMITING REACTOR

ABBREVIATIONS

ATC	ATMOSPHERIC TRITIUM CLEAN-UP
BLDG.	BUILDING
C T	COOLING TOWERS
EF	EQUILIBRIUM FIELD
EHV	EXTRA HIGH VOLTAGE
ELECT.	ELECTRICAL
FOA	FORCED-OIL-AIR
IC	INTERRUPTING CAPACITY
N_2	NITROGEN
NO	NORMALLY OPEN
CFC	CORRECTION FIELD COIL
REB	RELATIVISTIC ELECTRON BEAM
RMS	ROOT-MEAN-SQUARE
SWGR	SWITCHGEAR
SYMM	SYMMETRICAL
TFC	TOROIDAL FIELD COILS
Φ	PHASE

NOTES

1. ALL 13.8KV CIRCUIT BREAKERS ARE RATED 1200A, 750MVA I.C., UNLESS SHOWN OTHERWISE
2. ALL 4,16KV CIRCUIT BREAKERS ARE RATED 1200A, 350MVA I.C., UNLESS SHOWN OTHERWISE
3. 480V DRAWOUT AIR-CIRCUIT BREAKERS ARE RATED FOR 42,000A I.C. MINIMUM
4. EQUIPMENT RATING SHOWN SUCH AS HORSEPOWER, IS THE RATING OF EACH UNIT

Figure 9-14.

REVISIONS NO.	DATE	BY	CHKD	SEC	PROJ	CLIENT	DESCRIPTION
1	11-9-81	TO	GSA	FOR	FINAL	C.T.	APPROVED FOR FINAL REPORT
2	11-9-81	TO	GSA	FOR	FINAL		ISSUED FOR CLIENT APPROVAL

DRAWN	Tom Dee	11/9/81
CHECKED	G. ADAMS	11/10/81
APVD ELECT MGR	D. ADAMS	11/10/81
APVD PROJ MGR	CNTC	11/10/81
MDAC	C. Tso	11/10/81

THE RALPH M. PARSONS COMPANY
PASADENA, CALIFORNIA

ARGONNE NATIONAL LABORATORY
ARGONNE, ILLINOIS
DEMONSTRATION TOKAMAK POWER PLANT

TITLE: ELECTRICAL
UNIT GENERATOR & AUXILIARY POWER SYSTEM ONE LINE DIAGRAM

SCALE: —
ACCOUNT NUMBER: —
JOB NUMBER: 5959-1
DOCUMENT NUMBER: E-5959-EE-11
REVISION: 2

ENG-GE-24 (11/78)

CHAPTER 10

COST ANALYSIS

Chapter 10

Table of Contents

Chapter 10

List of Tables

10. COST ANALYSIS

This chapter presents the cost analysis of the DEMO reactor. The reactor and the attendant facilities are assumed to be procured as a government-financed project. Accordingly, the costs are developed consistent with this assumption. The Plant and Capital Equipment (PACE) costs for DEMO are presented in Table 10-1.

The total direct cost of the individual accounts is approximately 1.5 billion dollars including a twenty percent contingency and design allowances of twenty to fifty percent. With a ten percent allowance for construction facilities and equipment and a twenty percent allowance for engineering and construction management services, the total capital cost approaches two billion dollars. Adding in an average inflation rate of five percent over a six year construction time period increases the PACE costs to 2.354 billion dollars. The direct cost total of 1.5 billion dollars compares to estimates of FED direct costs of approximately 1 billion dollars and STARFIRE direct costs of 2 billion dollars. Table 10-2 compares the estimated costs for STARFIRE (escalated to 1982 dollars) and the estimated costs for DEMO. The table illustrates only the more important cost elements. The indirect cost and estimates for interest and escalation allowances are not shown on this comparison due to differing economic ground rules. Care must be exercised when comparing these cost estimates because of differing assumptions, which are explained in this report, relating to the objectives of the device - DEMO versus STARFIRE.

Table 10-1. Summary of DEMO PACE Costs

ACCOUNT NUMBER	ACCOUNT TITLE	COST (M$)
20	Land and Land Rights	0.20
21	Structures and Site Facilities	396.90
22	Reactor Plant Equipment	763.32
23	Turbine Plant Equipment	198.08
24	Electrical Plant Equipment	117.38
25	Miscellaneous Plant Equipment	45.88
26	Special Materials	0.30
	Subtotal	1522.06
91	Construction Facilities, Equipment and Services (10%)	152.21
92	Engineering and Construction Management Services (20%)	304.41
	Subtotal	1978.68
95	Escalation During Construction	375.16
	Total PACE Cost	2353.84

Table 10-2. Comparison of Cost Estimates for Major Plant Elements

ACCOUNT NO.	ACCOUNT TITLE	COST (M$) STARFIRE	DEMO
20	Land and Land Rights	3.83	0.20
21	Structures and Site Facilities	422.82	396.90
21.02	Reactor Building	192.07	159.26
22	Reactor Plant Equipment	1123.60	763.32
22.01	Reactor Equipment	683.54	408.50
22.01.01	Blanket and First Wall	95.54	45.81
22.01.02	Shield	215.84	46.71
22.01.03	Magnets	199.02	160.73
22.01.04	Heating and Current Drive	38.85	11.13
22.01.05	Primary Structure and Support	61.18	95.29
22.02	Main Heat Transfer and Transport	81.01	52.01
23	Turbine Plant Equipment	304.61	198.08
24	Electric Plant Equipment	143.08	117.38
25	Miscellaneous Plant Equipment	49.74	45.88
26	Special Materials	0.30	0.30
	Subtotal of Direct Costs	2047.98	1522.06

10.1 Economic Guidelines and Assumptions

The costs for DEMO in this report are developed and defined according to the current definition of PACE (Plant And Capital Equipment) costs, based upon a survey of PACE costs for TFTR, TFET, MFTF-B, EBT-P and FED. Table 10-3 reflects the assumed breakdown of the DEMO cost elements into either the PACE costs or the operations-technology support costs. Costs associated with the operation of the facility after an initial operational date will not be addressed because current knowledge of the operations-technology support tasks are not well enough defined to develop costs in this area. In this cost analysis PACE costs will be developed for all DEMO cost accounts.

The cost estimate for the PACE cost elements for DEMO structures and site facilities and the BOP equipment will be costed by either supplier quote, estimate of required men and materials or by analogy with a similar system, building or equipment. Portions of the reactor equipment can be

TABLE 10-3. Allocation of DEMO Cost Elements

GENERAL COST CATEGORY	PACE	OPERATIONS-TECHNOLOGY SUPPORT
Land and Land Rights	- Land and land rights purchased exclusively for DEMO	- Leased parcels for the use of DEMO
Structures and Site Facilities	- All DEMO unique buildings and necessary site improvements	- Leased buildings plus any building expense associated with a support function not directly related to DEMO
Reactor and BOP Equipment	- All engineering, fabrication, installation, inspection and management costs associated with procurement of the baseline device hardware - Acceptance testing of the device - Indirect costs for the purchased construction facilities and equipment - Contingency and escalation allowances (interest costs do not apply for a government funded project)	- Inventories and spare parts - Research and development costs associated with basic technology, component, subsystems or systems - Prototype/verfication testing - Pre-operational testing and other startup costs - Support activities (physics, technologies, diagnostics and data acquisition) - Leased services (power supplies, cryogenics, electrical substations, etc.) - Technical support management including liaison with other devices - Experiment planning, preparation and procurement - Project definition studies - Any costs associated with project or system upgrades or flexibility packages - Capital equipment not related to construction but related to R&D in the facility - Indirect costs for leased construction facilities and equipment - Indirect costs for construction services (utilities, security, educational and testing programs, materials receiving and storage of miscellaneous materials, inspection and testing of construction materials, site cleanup and O&M of construction facilities and equipment)

costed in a similar manner, e.g., cryogenics or radioactive waste handling. However, a majority of the reactor equipment represents new technology of which only a few prototypes will have been built. These prototypes will be demonstrated in earlier devices and be of a smaller size and/or power (or capacity) rating. This class of equipment will be costed using cost estimating relationships (CER's) which attempt to predict the cost based upon required performance and quantity to be purchased as correlated to historical cost data. This procedure was utilized in the STARFIRE estimate where it had the advantage of projecting costs to a fully developed and mature data base. Comparison to other mature systems helped rationalize the cost estimate. On the other hand, the DEMO PACE cost estimate will represent a cost snapshot of a multitude of diverse components and subsystems, each in differing degrees of evolution. Moreover, some of the systems envisioned have not yet been demonstrated in a practical scale in any fusion device and those that have been demonstrated are at least two generations away from commerical practice.

All hardware costs will be presented in accordance with the Uniform Capital Cost Accounts recommended in Ref. 1. This is also the format used in STARFIRE[2], which will allow a direct comparison of hardware costs.

The DEMO PACE cost estimate will explicitly exclude any R&D effort necessary to develop the technology or the prototype equipment. Only the engineering, quality assurance and acceptance testing associated specifically with DEMO hardware will be accounted in the PACE costs.

The cost ground rules for the economic studies for conceptual designs for commercial fusion reactors have assumed a mature industry[1] (i.e., estimated costs reflect learning curve characteristics of the tenth plant built of a specific design technology). This philosophy eliminates the high costs associated with the first-of-a-kind hardware. However, cost estimates for all current and proposed near-term devices reflect the first-of-a-kind cost figures, and this will also apply to the DEMO estimate. For example, for equipment with an assumed learning curve of 85%, this represents a first unit fabrication cost 70 percent higher than the tenth unit. This will not be true for all equipment because much of the DEMO facility equipment may be commercial equipment or at least will have been purchased in limited numbers

for other prior projects. Inherent to the cost estimates for DEMO will be design allowances for the direct capital cost items. The allowance will be included within the estimate for each individual piece of equipment and will be in the range of 20 to 50% for first-of-a-kind reactor equipment and 10 to 20% for new BOP equipment. The design allowance provides an allotment of money to compensate for lack of complete technical design definition. This allowance may apply to engineering, management, construction labor or materials. Table 10-4 lists the assumed design allowances for the DEMO Reactor Plant Subsystems.

Table 10-4. Design Allowances for Reactor Plant Subsystems

Allowance	Applicable Subsystems
50%	REB Heating and Current Drive
40%	Impurity Control, Fuel Handling, I&C
35%	Maintenance Equipment, Blanket and First Wall
30%	Rad Waste, Power Supplies, Magnets
25%	Cyrogenics, Vacuum, Shielding
20%	Primary Structure and Support, Main Heat Transfer and Transport

Indirect costs will be included to account for any purchased construction (temporary) facilities and equipment necessary for the project. An allowance of 10 percent of the direct cost elements should be adequate for this purpose. Construction services, such as utilities, security forces, educational and testing programs, etc., will be included in the operations-technology support budget. Any leased facilities or equipment will be assumed to be an operations-technology support cost. Prior projects have not identified major expenditures in this area, but a project of this size may require consideration of those costs.

Engineering and construction management services directly applicable to the baseline device hardware are also considered to be indirect cost items. An allowance of 20 percent is provided for this purpose, which would yield

approximately 300 million dollars. This amount should be adequate, assuming that a device to demonstrate engineering feasibility would immediately precede the DEMO device.

The final indirect cost account for power plants usually include other costs, such as taxes, insurance, staff training, plant startup and owners G&A. Since the project is costed as though it will be a government-financed project, taxes, insurance and owners G&A do not apply. Staff training and plant startup are considered to be included in the operations-technology support area. Thus no PACE costs will be considered in this indirect cost area.

Contingency for DEMO will be estimated at 20% of the total project costs. This is consistent with assumed allowances prior to start of construction of other DOE projects:

- TFTR (1976) 16%
- MFTF-B (1/81) 15%
- EBT-P (9/80) 25%
  (2/82) 22%
- FED (10/81) 30%

The overall contingency allowance of 20% equates to approximately 30% allowance applied to hardware costs only. A 15% hardware contingency allowance was assumed in STARFIRE.

No interest allowances will be used as this is assumed to be a government-funded project. The project will be costed in constant 1982 dollars and in real year dollars appropriate with the time frame when construction is assumed to commence and end. A six-year construction time period is assumed for DEMO. This time period is only for construction and preoperational testing activities. Over this time period an escalation rate of five percent is used to estimate the real year expenditures required. The five percent escalation rate was recommended by Ref. 1 for fusion reactor design studies. Although this value is less than the recent experience since 1973, inflation from 1950 to 1973 averaged three percent as measured with the GNP Price Level Deflator. Thus five percent may be a reasonable

long term estimate of inflation. This escalation, applied over the expected expenditure pattern as shown in Ref 1, yields an escalation factor of .1896.

A complete cost estimate is not recommended for all the DEMO operations-technology support areas at this time. The following list summarizes the key factors of this decision.

- Leased land and buildings cannot be accurately identified at this early date.
- Inventories and spare parts can only be estimated on larger items with an allowance for the lesser items.
- Research and development of certain associated technology or hardware items are not well defined at this time.
- Prototype/verification testing, pre-operational testing, other startup costs and support activities need a much more detailed definition of hardware design to estimate these elements.
- Experiment planning has not commenced because the project definition is still in the formulative stages along with any system upgrades.
- Indirect costs for leased construction facilities and equipment and construction services could be estimated using allowances but detailed estimates are not possible at this stage.

The aforementioned costing guidelines for DEMO are consistent with the anticipated funding of such a project. The operations costs will be developed as the project becomes better defined. In summary, the DEMO cost guidelines are:

- PACE costs only
- Design allowance for individual systems
  - 10 to 20% for the new BOP equipment
  - 20 to 50% for first-of-a-kind reactor equipment
- 10% indirect allowance for purchased construction facilities and equipment
- 20% indirect allowance for engineering and management services
- 20% overall contingency allowance covering hardware, installation engineering and management
- No interest charges

- Project costed in 1982 dollars and escalated to real year dollars using 5%/year escalation over a 6 year construction period.

10.2 Key Design, Performance and Operational Features

There exists many factors which influence the cost of a demonstration power facility. The previous section discussed the pertinent economic factors and applicable cost accounting guidelines. This section will highlight the key design, performance and operational features of DEMO.

The size and cost of the facility (land and buildings) required for a DEMO factor facility is very nearly identical to that required by a full-sized power plant. Although the thermal and electrical power generated by the DEMO are reduced almost by a factor of four, the physical size of the reactor has decreased only slightly. In some cases, the sizes required have actually increased. This DEMO design stressed a reduced number of TF magnets which, in turn, reduced the number of all associated hardware elements. The design approach also stressed simplified maintenance methods and approaches which tended to increase the cost of the primary structural elements and increase the maintenance area requirements.

Reactor shielding proved to be a costly subsystem in STARFIRE, thus particular emphasis was placed on choosing effective but lower cost materials. The use of large amounts of concrete reduce the need for steel as structure and shielding. The area of the first wall is roughly one-half that of STARFIRE with two-thirds of the neutron wall loading. The DEMO First Wall and Blanket subsystem developed a somewhat simpler design approach compared to STARFIRE which resulted in one-half of the cost of STARFIRE, even considering increased design allowances and learning-curve effects.

In summary, the costing of DEMO reflects a facility which is very similar to STARFIRE. All the key elements are represented in DEMO and, although they are smaller, their costs for the first-of-a-kind demonstration plant are close to the costs associated with a mature, full-sized fusion power plant.

10.3 PACE Costs

This section presents the logic and the supportive data for the DEMO PACE cost estimate. The cost estimate is expressed in 1982 dollars. Any Reactor Plant Equipment costs using the STARFIRE cost basis are escalated by the factor of 1.16 which is the ratio of the estimated 1982 and actual 1980 GNP price level deflators. Balance of plant equipment and labor costs have risen at a slight higher rate (1.20 to 1.25) and these costs are adjusted accordingly. The hardware costs include material, fabrication, installation, inspection and acceptance-testing. Design allowances for new equipment are included in the estimate with rational for such allowances given in the supportive logic. System engineering and project management along with contingency are costed using indirect allowances. The total capital PACE costs are shown in Table 10-5. The total direct capital cost is $1.522B with the Reactor Plant costing $763M, or about 35% of the total cost. The following sections discuss in more detail the plant elements, their costs and their cost bases.

10.3.1 Land and Land Rights (Account 20)

The land requirements for the DEMO facility includes sufficient land for the major buildings, cooling towers, switchyard, water reservoir and evaporation pond. The major requirement will be an exclusion boundary to insure adequate tritium dispersion. STARFIRE[2] used a 1000 acre site for a privately owned facility. Since this is assumed to be a government-owned facility, probably on federal lands, 250 acres would likely be adequate. For purposes of this analysis, the land acquisition will assumed to be a no cost item due to siting on federal lands. The cost of clearing land, demolition of existing structures and relocation of buildings, highways and railroad is estimated at $200,000. Thus the cost for the land and land rights for DEMO is:

$$C_{20} = \$0.2M$$

Table 10-5. DEMO Pace Costs

Account No.	Account Title	Costs (1982 M$)
20	Land and Land Rights	0.20
20.01	Land and Privilege Acquisition	0.00
20.02	Relocation of Buildings, Utilities, Highways, and Other Services	0.20
21	Structures and Site Facilities	396.90
21.01	Site Improvements and Facilities	14.05
21.02	Reactor Building	159.26
21.03	Turbine Building	44.19
21.04	Circulating Water System Structures	6.70
21.05	Electrical Equipment and Power Supply Building	8.24
21.06	Plant Auxiliary Systems Building	3.98
21.07	Hot Cell Building	65.81
21.08	Reactor Service Building	2.31
21.09	Service Water Building	0.81
21.10	Fuel Handling and Storage Building	10.58
21.11	Control Room Building	3.77
21.12	On-Site AC Power-Supply Building	2.47
21.13	Administration Building	1.07
21.14	Site Service Building	1.07
21.15	Cryogenics and Inert Gas Storage Building	1.11
21.16	Security Building	0.38
21.17	Stack	2.23
21.18	Research and Development Building	2.72
21.98	Spare Parts Allowance	(2.17)[a]
21.99	Contingency Allowance (20%)	66.15
22	Reactor Plant Equipment	763.32
22.01	Reactor Equipment	408.50
22.01.01	Blanket and First Wall	45.81
22.01.02	Shield	46.71
22.01.03	Magnets	160.73
22.01.04	REB Heating and Current Drive	11.13
22.01.05	Primary Structure and Support	95.29
22.01.06	Reactor Vacuum	2.84
22.01.07	Power Supply, Switching and Energy Storage	28.90
22.01.08	Impurity Control	17.09
22.02	Main Heat Transfer and Transport Systems	52.56
22.02.01	Primary Coolant System	44.13
22.02.02	Intermediate Coolant System	-
22.02.03	Limiter Cooling System	7.74
22.02.04	Residual Heat Removal System	0.69

Table 10-5. DEMO PACE Costs (Continued)

22.03	Cryogenic Cooling System	17.38	
22.03.01	Helium Liquefier Refrigerator		8.98
22.03.02	LHe Transfer and Storage		4.20
22.03.03	He Gas Storage		3.26
22.03.04	LN_2 System		0.94
22.04	Radioactive Waste Treatment and Disposal	4.80	
22.04.01	Liquid Waste Processing and Equipment		1.70
22.04.02	Gaseous Wastes and Off-Gas Processing System		1.80
22.04.03	Solid Wastes Processing Equipment		1.30
22.05	Fuel Handling and Storage Systems	46.75	
22.05.01	Fuel Purification Systems		22.54
22.05.02	Liquefaction		-
22.05.03	Fuel Preparation Systems		0.64
22.05.04	Fuel Injection		3.03
22.05.05	Fuel Storage		1.15
22.05.06	Tritium Extraction and Recovery		2.67
22.05.07	Atmospheric Tritium Recovery System		16.72
22.06	Other Reactor Plant Equipment	66.91	
22.06.01	Maintenance Equipment		58.85
22.06.02	Special Heating Systems		0.00
22.06.03	Coolant Receiving, Storage and Make-Up Systems		0.34
22.06.04	Gas Systems		0.12
22.06.05	Inert Atmosphere System		0.00
22.06.06	Fluid Leak Detection		3.10
22.06.07	Closed Loop Coolant System		2.80
22.06.08	Standby Cooling System		1.70
22.07	Instrumentation and Control	39.20	
22.07.01	Reactor I&C Equipment		14.00
22.07.02	Monitoring Systems		5.60
22.07.03	Instrumentation and Transducers		19.60
22.98	Spare Parts Allowance	(76.43)[a]	
22.99	Contingency Allowance (20%)	127.22	
23	Turbine Plant Equipment	198.08	
23.01	Turbine Generators	73.10	
23.02	Main Steam System	2.41	
23.03	Heat Rejection Systems	22.05	
23.04	Condensing Systems	12.59	
23.05	Feed Water Heating Systems	6.35	
23.06	Other Turbine Plant Equipment	37.56	
23.07	Instrumentation and Control Equipment for BOP	11.01	
23.98	Spare Parts Allowance	(2.54)[a]	
23.99	Contingency Allowance (20%)	33.01	

Table 10-5. DEMO PACE Costs (Continued)

24	Electric Plant Equipment		117.38	
24.01	Switchgear			9.08
24.02	Station Service Equipment			16.23
24.03	Switchboards			9.08
24.04	Protective Equipment			2.56
24.05	Electrical Structures and Wiring Containers			18.42
24.06	Power and Control Wiring			32.49
24.07	Electrical Lighting			9.96
24.98	Spare Parts Allowance			(1.08)[a]
24.99	Contingency Allowance (20%)			19.56
25	Miscellaneous Plant Equipment		45.88	
25.01	Transportation and Lifting Equipment			17.91
25.02	Air and Water Service Systems			11.72
25.03	Communications Equipment			7.66
25.04	Furnishing and Fixtures			0.94
25.98	Spare Parts Allowance			(0.55)[a]
25.99	Contingency Allowance (20%)			7.65
26	Special Materials		0.30	
		Total Direct Cost	1522.06	
91	Construction Facilities, Equipment and Services	(10%)	152.21	
92	Engineering and Construction Management Services	(20%)	304.41	
93	Other Costs	(0%)	0.00	
		Subtotal	1978.68	
			1982 CONSTANT	1988 THEN-CURRENT
94	Interest During Construction		0.00	0.00
95	Escalation During Construction		0.00	375.16
		Total PACE Cost	1978.68	2353.84

a) Spare Parts Costs are not included in PACE Costs.

10.3.2 Structures and Site Facilities (Account 21)

This account encompasses all the direct costs associated with the permanent buildings, cooling system structures, site improvements and facilities and miscellaneous structures and building work. The cost estimates for this account have been prepared by The Ralph M. Parsons Company largely based a comparison with the previous STARFIRE cost estimate. The buildings are similar in function to the STARFIRE buildings although slightly smaller in size. The labor and materials have been escalated to the prevailing rates in 1982. The escalation values will vary slightly depending upon the mix of materials and labor. The total cost of the Structures and Site Facilities is:

$$C_{21} = \$396.90M$$

10.3.2.1 Site Improvements and Facilities (Account 21.01)

This account includes all site improvements and facilities necessary for the DEMO facility. Land clearing and relocation of existing buildings are included in Account 20. Table 10-6 summarizes the direct costs for this account which total:

$$C_{21.01} = \$14.05M$$

Table 10-6. Site Improvements and Facilities Costs

CATEGORY	COSTS (M$)
General Site Improvements	
Site Work, Fencing and Storm Sewer	5.07
Earth Moving Equipment	4.19
Tank and Pump Foundations	0.84
Fire Protection	1.09
Sanitary Sewer	0.37
Transportation Access	
Highway (5 miles)	1.02
Railway (5 miles)	1.47
Total Site Improvements and Facilities, $C_{21.01}$ =	14.05

10.3.2.2 Reactor Building (Account 21.02)

Although the physical size of the DEMO reactor is slightly smaller than the STARFIRE reactor, the increased size of laydown space has increased the actual size of the Reactor Building. The basic size of the building is 54m X 124m X 44m high above the ground level. The steel liner has been reduced from 1/2" thick steel in STARFIRE to 1/4" thick to reduce costs. The volume of the basement also has been minimized which helps to reduce the required concrete. A special tunnel under the main floor allows replacement of the lower EF coils. A monorail track allows maintenance in the reactor room and the auxiliaries room. The cost for the Reactor Building is:

$$C_{21.01} = \$159.26 \text{ M}$$

10.3.2.3 Turbine Building (Account 21.03)

The thermal power to the turbine is reduced to 1147 MW but there is no appreciable reduction in size in the DEMO turbine or the laydown space required for servicing the turbine. Thus the cost of the Turbine Building including inflation is:

$$C_{21.03} = \$44.19\text{M}$$

10.3.2.4 Circulating Water System Structures (Account 21.04)

The costs associated with the Circulating Water System Structures are adjusted to reflect the reduced coolant flow and the inflation effects of this system. The water storage tank, evaporation pond and reservoir are unchanged, except for inflation. The costs are estimated to be:

$$C_{21.04} = \$6.70\text{M}$$

10.3.2.5 Electrical Equipment and Power Supply Building (Account 21.05)

This building size is also reduced because of the smaller electrical power demand from the REB heating system and the coil power supplies. This building is estimated at:

$$C_{21.05} = \$8.24M$$

10.3.2.6 Plant Auxiliary Systems Building (Account 21.06)

This building is unchanged from STARFIRE. The cost is adjusted for inflation effects and the total cost is:

$$C_{21.06} = \$3.98M$$

10.3.2.7 Hot Cell Building (Account 21.07)

The functions required in the DEMO Hot Cell Building are basically the same as those envisioned for STARFIRE, although some of the equipment and components handled would be slightly smaller. However, for this estimate, no changes were assumed. Thus the cost of the Hot Cell Building is:

$$C_{21.07} = \$65.81M$$

10.3.2.8 Reactor Service Building (Account 21.08)

No changes are anticipated in this building. Thus the inflated cost will be:

$$C_{21.08} = \$2.31M$$

10.3.2.9 Service Water Building (Account 21.09)

The make-up water and the firewater pump house remain the same as for the STARFIRE design. The cost is estimated at:

$$C_{21.09} = \$0.81M$$

10.3.2.10 Fuel Handling and Storage Building (Account 21.10)

The Fuel Handling System requirements increased in functions associated with the fuel flow handled. However, these requirements can be accommodated without any increase in building volume. The fuel storage and extraction systems were reduced in size, which again didn't alter the volume requirement of the buildings. The final building cost is estimated at:

$$C_{21.10} = \$10.58M$$

10.3.2.11 Control Room Building (Account 21.11)

The requirements for the DEMO will be very similar for the control facilities. The cost of the building will be:

$$C_{21.11} = \$3.77M$$

10.3.2.12 On-Site AC Power Supply Building (Account 21.12)

The building for the On-Site AC Power Supply will be identical to the STARFIRE building. The cost is estimated at:

$$C_{21.12} = \$2.47M$$

10.3.2.13 Administration Building (Account 21.13)

This building is identical in size and function to STARFIRE and is costed at:

$$C_{21.13} = \$1.07M$$

10.3.2.14 Site Service Building (Account 21.14)

This building is also similar in size and function to the STARFIRE building and is costed at:

$$C_{21.14} = \$1.07M$$

10.3.2.15 Cryogenics and Inert Gas Storage Building (Account 21.15)

The reactor components that require cryogens differ significantly from their counterparts in STARFIRE, but the overall cryogenic requirements are very nearly the same. Thus the Cryogenics Building and the outdoor storage areas are estimated at:

$$C_{21.15} = \$1.11M$$

10.3.2.16 Security Building (Account 21.16)

The security requirements for a DEMO device and a utility power reactor may vary widely, but the present estimate uses the identical Security Building as defined in STARFIRE:

$$C_{21.16} = \$0.38M$$

10.3.2.17 Stack (Account 21.17)

The DEMO facility requires a stack to vent the low-level radioactive gases above ground level. The requirements are identical to STARFIRE and the cost of the stack is:

$$C_{21.17} = \$2.23M$$

10.3.2.18 Research and Development Building (Account 21.18)

This building is an addition to the basic contingent of buildings required for STARFIRE. It is basically an office and laboratory building and is costed at:

$$C_{21.18} = \$2.72M$$

10.3.3 Reactor Plant Equipment (Account 22)

This cost account includes the cost for all reactor plant equipment. This equipment has the largest technical uncertainty of the plant. Consequently more design allowance is incorporated. Several design features of

DEMO are significantly different from the STARFIRE design and have influenced the estimated costs. Although the external size of the reactor is only slightly smaller, the surface area of the plasma chamber is roughly one-half that of STARFIRE, thus reducing the First Wall area and Blanket/Shielding volumes by that same ratio. Not only has this effect reduced the costs, but the lower power requirements and lower availability have allowed the use of less expensive materials and techniques. Great attention was given to designing the reactor with low cost materials. For example, the estimated cost of reactor shielding has been substantially reduced. Only a few Reactor Plant cost accounts actually increased their cost when compared to STARFIRE; Primary Structure (different approach to modular construction), Impurity Control (different material and design approach), Cryogenic Cooling (learning curve effects and design allowance offset capacity decrease), Fuel Handling and Storage (some capacities actually increased due to lower tritium burn-up fraction), Other Reactor Plant Equipment (nearly the same equipment increased due to inflation effects) and I&C (increased data and instrumentation requirements). Table 10-7 compares the STARFIRE and the DEMO Reactor Plant Equipment cost estimates on a 1982 normalized cost basis.

The costs outlined in Table 10-7 show a reasonable cost for the DEMO Reactor Plant Equipment. It now represents less than half the overall cost of the entire plant. In fact, the fusion core (first wall, blanket, shield and magnets) constitute less than one-third of the Reactor Plant costs. The rest of this section defines in more detail the cost estimate for the Reactor Plant Equipment cost which totals:

$$C_{22} = \$763.32M$$

10.3.3.1 Blanket and First Wall (Account 22.01.01)

This cost account includes the costs associated with the entire first wall, all the blanket, and all manifolds for both the Blanket Sector and the Limiter Module. Not included in this account are the limiter blades which are costed in the Impurity Control (Account 22.01.08) and the structural support elements outboard of Blanket Sector and the Limiter Module, which is costed in the Primary Structure and Support (Account 22.01.05).

Table 10-7. Comparison of STARFIRE and DEMO Reactor Plant Equipment Costs

ACCOUNT	ACCOUNT TITLE	STARFIRE COST (M$)[a]	DEMO COST (M$)[a]
22.01	Reactor Equipment	683.54	408.50
22.01.01	Blanket and First Wall	95.54	45.81
22.01.02	Shield	215.84	46.71
22.01.03	Magnets	199.02	160.73
22.01.04	Heating and Current Drive	38.85	11.13
22.01.05	Primary Structure and Support	61.18	95.29
22.01.06	Reactor Vacuum	5.64	2.84
22.01.07	Power Supply Switching and Energy Storage	61.36	28.90
22.01.08	Impurity Control	2.84	17.09
22.01.09	ECRH Plasma Breakdown	3.27	-
22.02	Main Heat Transfer and Transport	81.01	52.56
22.03	Cryogenic Cooling System	17.28	17.38
22.04	Radioactive Waste Treatment and Disposal	5.57	4.80
22.05	Fuel Handling and Storage	44.78	46.75
22.06	Other Reactor Plant Equipment	50.75	66.91
22.07	Instrumentation and Control	27.16	39.20
22.98	Spare Parts	77.00	-
22.99	Contingency	136.50(15%)	127.22(20%)
Total Reactor Plant Equipment Cost, C_{22}		1123.60	763.32

[a]STARFIRE cost is normalized to 1982$ by inflating the 1980 dollar estimate with a 1.16 multiplier.

The costs for the Blanket and the First Wall are listed by function and material in Table 10-8, and are subdivided into the costs by Blanket Sector and Limiter Module. The unit installed costs for various materials used in this estimate were developed based upon a mature manufacturing capability[1,2,3], (i.e., tenth-of-a-kind). The cost for the DEMO must be for a first-of-a-kind. Since the blanket and first wall of the DEMO will likely have no identical systems preceding the DEMO, and the learning curve for this type of system can reasonably be represented by an 85% learning curve, the ratio of a first-of-a-kind to a

Table 10-8. Blanket and First Wall Costs

FUNCTION	INSTALLED COST ($/kg)	WEIGHT (Tonnes)	COST[a] (M$)
BLANKET SECTOR			
First Wall and Breeding Blanket			
- PCA SS	40	107.8	7.40
- Li_2O, Natural	38	244.5	15.94
- Be	300	0.9	0.46
First Wall and Non-Breeding Blanket			
- PCS SS	40	101.8	6.99
Manifolds			
- PCA SS	30	12.2	0.63
Support Structure (Cost is included in Account 22.01.05)			
Subtotal of Blanket Sector		467.2	31.42
LIMITER MODULE			
Limiter Blades (Cost is included in Account 22.01.08)			
First Wall and Breeding Blanket			
- PCA SS	40	11.0	0.76
- Li_2O, Natural	38	25.0	1.63
- Be	300	0.1	0.05
Manifolds			
- PCA SS	30	1.3	0.07
Support Structure (Cost is included in Account 22.01.05)			
Subtotal of Limiter Module		37.4	2.51
Subtotal Weight and Cost		504.6	33.93
Design Allowance (35%)			11.88
Total Blanket and First Wall Cost, $C_{22.01.01}$ =			45.81

[a]Learning curve multiplier is 1.716.

tenth-of-a-kind is 1/(10 raised to the ln (.85) ' ln (2)) which is 1.716. This will be used to develop the costs for the Blanket and First Wall subsystem costs as well as any other DEMO systems with no prior identical subsystems. Due to the existing state-of-development for the blanket and first wall, it was thought prudent to include a design allowance of 35% on this system.

To provide a comparison, Table 10-9 displays the subsystem costs for both the STARFIRE reactor[2] and the DEMO reactor in 1982 dollars. Major differences from the STARFIRE costs are the absence of a multiplier (Zr_5Pb_3) or a reflector (C). Additionally the weight of the breeding material and coolant tubes and internal structure are down by a factor of two due to a corresponding decrease in surface area. Although the wall area is reduced by a factor of 2 the beryllium coating is twice as thick (2 mm), and the cost is nearly the same. The final result is that the DEMO total blanket and first wall weights are one-third of the STARFIRE and the costs are roughly one-half. This change in cost ratio is due to learning curve effects for the quantity production assumed in STARFIRE and a significant design allowance (35%) assumed for DEMO. The use of natural Li_2O in place of the 60% enriched $LiAlO_2$ also has reduced the blanket costs. The cost of natural Li_2O is assumed to be \$38/kg based upon data in Reference [3] inflated to 1982 dollars. Thus the overall costs for the Blanket and First Wall subsystem are estimated at:

$$C_{22.01.01} = \$45.81M$$

Table 10-9. Comparison of STARFIRE and DEMO Blanket and First Wall Costs

MATERIAL	STARFIRE WEIGHT (Tonnes)	STARFIRE COST[a] (M$)	DEMO WEIGHT (Tonnes)	DEMO COST[b] (M$)
PCA SS	421.1	15.32	234.1	21.40
$LiAlO_2/Li_2O$	626.5	58.14	269.5	23.72
Zr_5Pb_3	336.8	19.53	-	-
C	161.7	2.25	-	-
Be	1.0	0.30	1.0	0.51
	1547.1	95.54	504.6	45.81

[a]The 1980 STARFIRE[2] costs have been inflated by 1.16 to obtain 1982 dollars.

[b]The DEMO costs have the learning curve multiplier and the design allowance included.

10.3.3.2 Shielding (Account 22.01.02)

The bulk and penetration shielding are included in this account. Shielding is physically located in several different sectors, modules and discrete elements as listed in Table 10-10. The shielding is comprised of concrete, lead, boron carbide and a structural steel, FE1422. These materials were selected, both for their shielding effectiveness and because of their low capital cost. Although the total weight is 3716 metric tonnes, the cost, including a learning curve multiplier of 1.716 and a design allowance of 25%, is only $46.71 million dollars. This subsystem is considerably cheaper than the STARFIRE cost estimate, as illustrated in Table 10-11. The weight of the DEMO shielding is only 28% of the weight of STARFIRE and the cost is only 22%, reflecting the use of the cheaper materials. The significant use of concrete has reduced the use of more costly shielding and structural materials. A portion of the Primary Structure associated with the shielding function (Account 22.01.05) should be added in for a complete cost comparison. The shielding system costs represent a cost-effective technique to provide shielding for the DEMO reactor. The shielding costs are:

$$C_{22.01.02} = \$46.41M$$

10.3.3.3 Magnets (Account 22.01.03)

This cost account covers the cost for the entire reactor magnet system including eight toroidal field (TF) coils, eight equilibrium field coils (EF) and four correction field (CF) coils. No ohmic heating (OH) coils are required in the DEMO design. The TF and the EF coils are superconducting and the CF coils are removable copper coils.

The DEMO TF coils deviate from the classical constant tension shape. The design uses a modified coil shape with reduced vertical height resulting in a cost savings for the TF and the EF coils, the reactor structure and the reactor building. Offsetting this savings is a more complex and stronger centerpost which must provide more support to the TF coils. The TF and EF coils use a NbTi superconductor with a copper stabilizer wound in a pancake (spiral) technique with stainless steel interturn conductor support and epoxy fiberglass laminate insulator, similar to the STARFIRE design. The helium vessel is also a 316LN

Table 10-10. Shielding Costs

FUNCTION	INSTALLED COST ($/kg)	WEIGHT (Tonnes)	COST[a] (M$)
BLANKET SECTOR			
- Concrete	0.80	392	0.54
- Lead	3.50	196	1.18
- B_4C (70% dense)	41.00	29	2.04
- FE1422	12.00[b]	323	6.65
		940	10.41
LIMITER MODULE			
- Concrete	0.80	117	0.16
- Lead	3.50	59	0.35
- B_4C (70% dense)	41.00	9	0.63
- FE1422	12.00[b]	97	2.00
		282	3.14
SHIELD SECTOR			
- Concrete	0.80	373	0.51
- Lead	3.50	187	1.12
- B_4C (70% dense)	41.00	28	1.97
- FE1422	12.00[b]	308	6.34
		896	9.94
SHIELD WEDGE			
- Concrete	0.80	12	0.02
- Lead	3.50	10	0.06
		22	0.08
SHIELD SLAB (Top & Bottom)			
- Concrete	0.80	71	0.10
- Lead	3.50	35	0.21
- B_4C (70% dense)	41.00	5	0.35
- FE1422	12.00[b]	58	1.19
		169	1.85
PENETRATION SHIELDING[c]			
- Concrete	0.80	664	0.91
- Lead	3.50	442	2.65
- B_4C (70% dense)	41.00	44	3.10
- FE1422	12.00[b]	257	5.29
		1407	11.95
Subtotal		3716	37.37
Design Allowance (25%)			9.34
Total Shielding Cost, $C_{22.01.02}$			46.71

[a] Learning Curve Multiplier is 1.716.

[b] Unit Cost is based principally on the bulk shielding application.

[c] Includes vacuum ducting, vacuum pump cover pods and REB transmission lines and diodes.

Table 10-11. Comparison of STARFIRE and DEMO Shielding Costs

MATERIAL	STARFIRE WEIGHT (Tonnes)	STARFIRE COST[a] (M$)	DEMO WEIGHT (Tonnes)	DEMO COST[b] (M$)
FE1422	9,900	116.20	1,043	26.84
B_4C	887	36.02	115	10.11
W	840	48.72	-	
Ti-^{6}Al-^{4}V	147	11.08	-	
TiH_2	1,646	3.82	-	
Concrete	-	-	1,629	2.80
Lead	-	-	929	6.96
Total	13,420	215.84	3,716	46.71

[a]The STARFIRE[2] costs have been inflated by 1.16 to obtain 1982 dollars.

[b]The DEMO costs have the learning curve multiplier and the design allowance included.

stainless steel design similar to STARFIRE. There is no separate TF vacuum vessel necessary in this design. The complete reactor is included in a vacuum enclosure formed by the blanket/shield sector and the support structure. There is a nitrogen cryopanel and superinsulation covering on the outer surfaces of the inner TF coil legs and completely surrounding the outer TF coil legs. This nitrogen shield is also utilized on the largest EF coil. All other coils are enclosed in a common liquid nitrogen shield enclosure with the TF coil inner legs.

The magnet coils are costed on a material basis assuming a mature manufacturing capability. Modifying this cost is the learning curve effect of producing near-first-of-a-kind hardware. A mature TF coil industry would have produced approximately 12 prototype coils, four preproduction coils, 120 production coils, and four spare coils, yielding a quantity of 140 units. Contrasted to this is the DEMO with two prototype TF coils and 8 production coils. A learning curve of 88% is assumed which is indicative of a labor intensive production with some process materials included. The above assumptions yield a cost ratio, or a learning curve multiplier, of DEMO TF coils to mature TF coils of 1.775. In

a similar manner, a mature industry would have produced 20 production EF coil units and five additional prototypes, preproduction units and spares for each of the four sizes of EF coils, whereas DEMO would require only two production units plus one prototype of each EF coil size. This yields a learning curve multiplier of 1.530 using the same 88% learning curve. Similar logic for the CF coil produces a multiplier of 1.495.

The cost of the NbTi superconductor is taken to be of $64/kg reflecting a significant production base for NbTi superconductor. The cost of the structure at $16/kg reflects a very simple shape and fabrication process of manufacturing the cable and support structure for the conductor support module. The helium tank for the TF coil is much more complex requiring load carrying ability and leak-tight construction, thus it is costed at $30/kg. The nitrogen shield on the coils is an aluminum cryopanel system evaluated at $18/kg. Most other magnet materials are costed at STARFIRE values adjusted for inflation effects. The weights of the coil components were scaled from the STARFIRE analyses.

The total cost of the DEMO magnet system is shown in Table 10-12. The materials and their unit costs per kilogram are listed along with the weight of the material and cost applicable for each magnet subsystem. The costs shown include the learning curve multiplier unique for each coil subsystem. After a subtotal, a 30% design allowance is added, reflecting the anticipated technical uncertainty implicit in the current design and costing effort. Although the TF coils weigh and have a stored energy approximately 40% of the STARFIRE set, the cost of the DEMO TF coils cost nearly as much as STARFIRE ($110M vs $145M). The weights and stored energy of the EF coils are not scaled down as much as the TF coils which results in a cost exceeding the STARFIRE EF coil set. The CF coils are nearly equal to the STARFIRE costs. Thus the resulting magnet system cost is:

$$C_{22.01.03} = \$160.73M$$

10.3.3.4 REB Heating and Current Drive (Account 22.01.04)

The REB Heating and Current Drive Subsystem is a relatively low cost subsystem with a substantial portion of the equipment off-the-shelf, with only the transformer and the Active Rotary Flux Compressor (ARFC) being in a developmental phase. No learning curve multiplier is applied as these costs represent current

Table 10-12. Cost of the Magnets

Material	Unit Cost $/kg	TF (8 Coils) Learning Curve Multiplier = 1.775 Weight (Tonnes)	TF (8 Coils) Learning Curve Multiplier = 1.775 Cost (M $)	EF (8 Coils) Learning Curve Multiplier = 1.530 Weight (Tonnes)	EF (8 Coils) Learning Curve Multiplier = 1.530 Cost (M $)	CF (4 Coils) Learning Curve Multiplier = 1.495 Weight (Tonnes)	CF (4 Coils) Learning Curve Multiplier = 1.495 Cost (M $)
NbTi Superconductor	64	50	5.68	16	1.57	-	-
Copper Stabilizer	19	670	22.60	218	6.38	-	-
Copper Conductor	29	-	-	-	-	68	2.95
SS Structure	16	910	25.84	227	5.56	6	0.15
SS Helium Tank	30	445	23.70	285	13.08	-	-
SS Vacuum Dewars	30	-	-	138	6.33	-	-
SS Nitrogen Shield	18	26	0.83	8	0.26	-	-
Aluminum	29	-	-	-	-	8	0.35
G-10 CR Insulator	23	24	0.98	42	1.48	-	-
Fiberglass Insulation	16	-	-	44	1.08	-	-
Superinsulation	116/m^2	1450m^2	0.30	622m^2	0.07	-	-
Circuit Protection	-	-	4.45	-	-	-	-
Subtotal		2125	84.38	978	35.81	82	3.45
Design Allowance, 30%			25.31		10.74		1.04
Total			109.69		46.55		4.49

Total Magnet System Cost, $C_{22.01.03}$ = $160.73M

Note: Cost = (Unit Cost) x (Weight) x (Learning Curve Multiplier)

estimates as shown in Table 10-13. However, the costs associated with this specific application is highly uncertain, so a design allowance of 50% is applied. The steady-state motors sets and the startup motor sets associated with this system are assumed to be power supplies or energy storage and so they are costed in Power Supply, Switching and Energy Storage, Account 22.01.07. This yields a system cost of:

$$C_{22.01.04} = \$11.13M$$

Table 10-13. REB Heating and Current Drive Systems Costs

COMPONENT	QUANTITY	UNIT COST (M$)	TOTAL COST (M$)
Transmission Line/Diode	2	1.14	2.28
Multiple Primary Transformer	2	0.30	0.60
Diodes, Ignitron, Trigger and Misc Hardware	12 sets	0.05	0.60
ARFC, Capacitor, Controls, etc.	12 sets	0.12	1.44
Support Structure, Installation Hardware		-	1.00
Installation and Checkout			1.50
Subtotal			7.42
Design Allowance (50%)			3.71
Total REB Heating and current Drive Systems Cost, $C_{22.01.05}$			= 11.13

10.3.3.5 Primary Structure and Support (Account 22.01.05)

This primary structure and support account includes all the cost elements associated with reacting all the gravity, seismic and magnetic loads on the major reactor components. Most of the support elements are cyrogenic, either at liquid nitrogen or liquid helium temperatures. The major components are G-10CR fiberglass centerpost, the G-10CR fiberglass TF support pedestals and the FE1422 antitorque structure between the TF coils. The weight of the antitorque structure was estimated using the FED intercoil support structure[4] as a design basis, scaling up for the slightly larger DEMO size and reducing the weight in proportion to the design allowables (58 ksi vs 16 ksi). The design allowable difference resulted from the requirement to meet 350,000 cycles for FED as opposed to

steady-state conditions for the DEMO. The most outboard EF coil set is supported by structure cantilerered from the antitorque structure.

The vertical loads of the TF coils are reacted by large G-10CR support pedestals directly beneath the TF coils. Those support structure costs are shown in Table 10-14. The blanket and shield are supported by pedestals which also function as shielding and vacuum ducts. The cost for these items are accounted in the shielding account (22.01.02).

Surrounding this cold structure on all sides is a nitrogen cryopanel system. This system is assumed to be an aluminum panel coil design costed at $18/kg which reflects high fabrication and quality control cost factors. Enclosing all of this structural system is a vacuum dewar of FE1422 designed to withstand the atmospheric pressure loads. The vacuum dewar is an integral part of the primary structure of the shield and blanket sectors and will not be costed separately. The weights and costs of all of the primary structure and support system elements are shown in Table 10-14. The learning curve multiplier for this system assumed a learning curve of 85% with no similar systems preceding the DEMO. The mature system would, therefore, be represented by the tenth unit with the ratio of DEMO to a mature system being 1.716. With this factor being considered in all component costs, the subtotal cost is $79.41M and with a 20% design allowance added, the system cost is:

$$C_{22.01.05} = \$95.29M$$

10.3.3.6 Reactor Vacuum System (Account 20.01.06)

The reactor vacuum system is very similar to the STARFIRE design except it is scaled down in capacity. The same cryosorption pumps are used in fewer numbers. DEMO has a total of eight cryovacuum pumps with four operating at a time. The components to be costed in this account include the roughing and the high vacuum pumps, the valves, and the system piping. The vacuum ducts and pods are considered to be shielding elements and, as such, are costed in the shielding account.

Table 10-15 lists the vacuum system components and their estimated costs. As stated in the STARFIRE cost estimate, the cryovacuum pumps were estimated to cost, in small lot quantities, $100,000 each in 1980 dollars or approximately

Table 10-14. Primary Structure and Support Systems Cost

COMPONENT MATERIAL	UNIT COST ($/kg)	WEIGHT (MT)	COST[a] (M$)
Centerpost			
- G-10CR Fiberglass	23	138	5.45
TF Support Pedestal			
- G-10CR Fiberglass	23	76	3.00
Blanket Sector Support Structure			
- FE 1422	23	514	20.29
Blanket/Shield Support Pedestal	(See Shielding Component)		
Shield Sector Support Structure			
- FE 1422	23	428	16.89
Limiter Module Support Structure			
- FE 1422	23	13	0.51
Wedge Shield Support Structure			
- FE 1422	23	16	0.63
Antitorque Structure			
- FE 1422	23	650	25.65
EF Coil Supports			
- FE 1422	23	130	5.13
Nitrogen Shield			
- Aluminum	18	44	1.36
- Superinsulation	120/m^2	2450m^2	0.50
Subtotal		1980	79.41
Design Allowance (20%)			15.88
Total Primary Structure and Support Cost, $C_{22.01.05}$ =			95.29

[a]Learning Curve Multiplier is 1.716

$120,000 in 1982 dollars. Mounting hardware would add approximately 15% to the system costs. The system uses dual 1.2 meter diameter gate valves in each vacuum duct. In small lot quantities these would cost approximately $55,000 each. With a design allowance of 25%, the vacuum system cost will be:

$$C_{22.01.06} = \$2.84M$$

Table 10-15. Reactor Vacuum System Costs

COMPONENT	COST (M$) EQUIPMENT	MOUNTING HARDWARE	TOTAL
Cryosorption Pumps (8)	0.96	0.14	1.10
Gate Valve (16)	0.88	0.09	0.97
Regeneration System	0.10	0.10	0.20
Subtotal			2.27
Design Allowance (25%)			.57
Total Cost Reactor Vacuum System Cost, $C_{20.01.06}$ =			2.84

10.3.3.7 Power Supply Switching and Energy Storage Costs (Account 22.01.07)

The Power Supply, Switching and Energy Storage system provides all the conditioned electrical power to the magnet coil systems and the plasma heating and current drive system. The system is similar, but smaller than that proposed for STARFIRE. However, there is no ohmic heating coils required in this reactor design. Most of the applications listed in this system shown in Table 10-16 use a low-voltage, high-current power supply which are estimated to cost $100/kW. The correction coils require an energy storage device in order to be able to respond with high power demand over a short time period without increasing the input power supply. The REB heating and current drive system uses a moderate-sized power supply. All of the power supply system components are commercially available or represent a reasonable scale-up from existing components. Thus no learning curve multiplier will be applied. But a design allowance of 30% will be applied to cover possible design change during detailed design and development. Thus the system cost is:

$$C_{22.01.07} = \$28.90M$$

Table 10-16. Power Supply, Switching and Energy Storage Costs

SUBSYSTEM	COST (M$)
Toroidal Field Coils	
- Power Supply (1.0 MVA)	0.1
- Protective Circuit (Costed in Account 22.01.03)	-
	0.1
Equilibrium Field Coils	
- Power Supply (156 MVA)	15.6
- Dump Circuit	1.6
	17.2
Correction Field Coils	
- Power Supply (3 MW)	0.3
- Capacitive Energy Storage (3 MJ, Total)	0.7
- Converter-Inverter (17 MW)	2.0
	3.0
REB Heating and current drive	
- Power Supply (18.7 MW)	1.9
	1.9
Subtotal	22.2
Design Allowance (30%)	6.7
Total Power Supply, Switching and Energy Storage Cost, $C_{22.01.07}$ =	28.9

10.3.3.8 Impurity Control (Account 22.01.08)

The subsystem components of the Impurity Control System included in this account are only the limiter and its related support structure and cooling tubes. Like STARFIRE, the DEMO limiter is a water-cooled structure in intimate contact with the plasma. The coolant is at a lower temperature (approximately 100°C) and is not used for feedwater heating. Two possible materials are being considered for the base limiter material, support structure and the interfacing coolant tubes; Cu-2 Be and V-15 Cr-5 Ti. For costing purposes, the vanadium material was chosen to represent the cost of the limiter. Although the price of vanadium sheet is currently in the $175/kg to $260/kg range, the price is dropping and further usage will likely result in plate prices in the vicinity of

$130/kg.[5] For purposes of this study, a somewhat higher price of $150/kg cost is assumed for the V-15 Cr-5 Ti material plus a $50/kg adder for fabrication, handling, assembly and installation, yielding an installed cost of $200/kg. Table 10-17 list the material requirements and the associated costs.

Tantalum also is currently somewhat overpriced, with the plate price between $130/kg and $165/kg. A more reasonable long term price would likely fall in the $80/kg to $100/kg range.[5] Again, a somewhat higher basic material cost will be adapted of $120/kg plus a $50/kg adder for fabrication, etc. Only a small amount of tantalum is used for the leading edge coating application. Beryllium has been used as a coating material in several fusion reactor design studies. The installed cost for a similar first-wall application[2] was $250/kg in 1980 dollars. Escalating this to 1982 dollars would yield an estimated cost of approximately $300/kg.

This system has a high degree of manual labor and fabrication required, which could be represented with a learning curve of 85%. Although other reactors or experiments may precede DEMO with somewhat similar limiters, no learning effects are assumed to apply to DEMO. The mature commercial system is represented by the tenth unit, yielding a learning curve multiplier of 1.716. Adding in a 40% design allowance, the Impurity System cost is

$$C_{22.01.08} = \$17.09M$$

Table 10-17. Impurity Control System Costs

Function	Material	Weight (Tonnes)	Unit Cost ($/kg)	Total Cost[a] (M$)
Heat Sink	V-15 Cr-5 Ti	24.7	200	8.48
Support Structure and Tubing	V-15 Cr-5 Ti	7.4	200	2.54
Surface Coating	Be	2.2	300	1.13
Leading Edge Coating	Ta	0.2	170	0.06
Subtotal		34.5		12.21
Design Allowance (40%)				4.88
Total Impurity Control System Cost, $C_{22.01.08}$ =				17.09

[a]Learning Curve Multiplier assumed is 1.716.

10.3.3.9 Main Heat Transfer and Transport (Account 22.02)

This account includes all the costs associated with the principal heat transport systems; primary coolant system, limiter coolant system and the residual heat removal system. On STARFIRE there were four steam generators handling a total of 3800 MW delivered from the primary coolant. In DEMO there is a total of 1147 MW delivered to two steam generators. However, the size, the pressure rating and the length of the piping remain essentially the same. The primary coolant subsystem has been estimated to cost $44.13M in current dollars. The limiter coolant subsystem will handle 151 MW of thermal energy as opposed to the 200 MW in STARFIRE; however, the coolant is at a lower temperature and is not used for energy production. The limiter system is costed at $7.74M. The residual heat removal system is unchanged and is costed at $0.69M. Thus the Main Heat Transfer and Transport System is costed at:

$$C_{22.02} = \$52.56M$$

10.3.3.10 Cryogenic Cooling System (Account 22.03)

The cryogenic cooling system supplies all liquid helium and nitrogen needs for the fusion reactor and BOP equipment. The main user of the cryogens is the superconducting magnets. The cost for this system is estimated by scaling from STARFIRE cost estimate. The sum of the volumes of the superconducting coils for DEMO is roughly one-half that of the STARFIRE design. The DEMO TF coil volumes are approximately 40% of that of STARFIRE while the EF coils are about 60%. There are no comparable OH coils on DEMO. Although the capacity is reduced to one-half, the cost will likely scale down a lessor amount, such as 60%. To estimate the learning curve effects on the cryogenic system, all earlier cryogenic magnet devices will serve as prototypes for the DEMO and commercial machines, such as MFTF-B, EBT-P, and FED/ETR. With that assumption, the learning curve multiplier, assuming a learning curve of 85%, would be 1.34. These scaling relationships produce the estimated cost as shown in Table 10-18. With a design allowance of 25%, the cryogenic system cost is:

$$C_{22.03} = \$17.38M$$

Table 10-18. Cyrogenic System Costs

ACCOUNT	SUBSYSTEM	COST (M$)
22.03.01	He Liquefier/Refrigerator	7.18
22.03.02	LHe Transfer and Storage	3.36
22.03.03	GHe Storage	2.61
22.03.04	LN_2 System	0.75
	Subtotal	13.90
	Design Allowance (25%)	3.48
	Total Cyrogenic System Cost, $C_{22.03}$=	17.38

10.3.3.11 Radioactive Waste Treatment and Disposal (Account 22.04)

This system processes all the radioactive waste from the reactor plant. This waste, excluding elemental tritium or tritium compounds, can be gaseous, liquid or solid. The requirements and the processing are similar to that defined in the STARFIRE reactor[2]. The quantities of the generated radioactive waste will be substantially reduced from that of a commercial reactor, but the equipment requirements would not be substantially reduced. In fact, the thirty percent design allowance will likely offset the savings obtained from the reduction in equipment requirements. Thus the cost is assumed to be similar to the STARFIRE costs of:

- Liquid Waste Processing and Equipment = $1.7M
- Gaseous Waste and Off Gas Processing System = $1.8M
- Solid Wastes Processing Equipment = $1.3M

The total cost for the Radioactive Waste Treatment and Disposal System is:

$$C_{22.04} = \$4.80M$$

10.3.3.12 Fuel Handling and Storage System (Account 22.05)

The Fuel Handling and Storage System performs all the cleanup, purification, storage, preparation and injection functions for the deuterium and tritium fuel for the DEMO reactor. The functions and equipment are identical to STARFIRE, only scaled up or down in capacity or volume. The associated costs are shown in Table 10-19. The costs are largely based upon TSTA/LANL and the Mound facility

Table 10-19. Fuel Handling and Storage System Costs

ACCOUNT	FUNCTION	STARFIRE COST (M$)	SCALING BASIS	SCALING FACTOR	DEMO COST (M$)
22.05.01	Fuel Purification				
	- Isotope Separation Unit (4)	4.8	Capacity	1.67	8.02
	- Fuel Cleanup Unit (4)	2.0	Capacity	2.15	4.30
	- Pumps, Piping, Valves & Install.	2.0	Capacity	1.89	3.78
		8.8			16.10
22.05.02	Liquefaction (Included in 22.05.01)				
22.05.03	Fuel Preparation				
	- Fuel Blending Unit (2)	0.2	Capacity	1.54	0.31
	- Pumps, Piping, Valves & Install.	0.1	Capacity	1.54	0.15
		0.3			0.46
22.05.04	Fuel Injection				
	- Fuel Gass Puffer (4)	0.2	Capacity	1.54	0.31
	- Pumps, Piping, Valves & Install.	1.2	Capacity	1.54	1.85
		1.4			2.16
22.05.05	Fuel Storage				
	- Tritium Storage Unit (40)	1.6	Volume	0.41	0.66
	- Deuterium Storage	0.1	Volume	0.41	0.04
	- Pumps, Piping, Valves & Install.	0.3	Volume	0.41	0.12
		2.0			0.82
22.05.06	Tritium Extraction and Recovery				
	- Tritiated Water Recovery Unit (1)	0.8	Capacity	0.41	0.33
	- Tritium Waste Treatment Unit (1)	0.5	Capacity	0.41	0.21
	- Blanket Recovery Unit (4)	2.0	Capacity	0.26	0.52
	- Ion Exchange/Filter Units	0.1	Capacity	0.26	0.03
	- Pumps, Piping, Valves & Install.	2.0	Capacity	0.41	0.82
		5.4			1.91
22.05.07	Atmospheric Tritium Recovery				
	- Tritium Facility System Building	2.2	Capacity	1.67	3.67
	- Reactor Building	12.0	Capacity	0.41	4.92
	- Hot Cell Building	2.5	Capacity	0.41	1.03
	- Pumps, Piping, Valves & Install.	4.0	Capacity	0.58	2.32
		20.7			11.94
Subtotal		38.6			33.39
Design Allowance (40%)					13.36
Total Fuel Handling and Storage System Costs, $C_{22.05}$ =					46.75

data. Most of the system elements are available commercially, thus no learning curve multipliers are applied. However, the specific design configuration and overall performance capability for DEMO are yet to be completely defined and, therefore, a design allowance of 40% is applied. This yields a system cost of:

$$C_{22.05} = \$46.75M$$

10.3.3.13 Other Reactor Plant Equipment (Account 22.06)

This account collects the remainder of the Reactor Plant Equipment, but the highest cost element is the Maintenance Equipment. Other important plant systems include the Coolant Receiving, Storage and Make-up System, the Gas System, the Fluid Leak Detection System, the Closed Loop Coolant System and the Standby Cooling System. These systems are near identical to those proposed in the STARFIRE reactor design and the costs shown in Table 10-20 reflect the escalation in cost from 1980 dollars to 1982 dollars. The maintenance equipment total cost, $43.60M plus a design allowance of $15.25M, is broken down in more detail in Table 10-21. An Antitorque Panel Handling Machine and a Shield Door Handling Machine are not required in the DEMO, but a Limiter Module Machine has been added. The cost of the remaining equipment has risen with inflation.

Table 10-20. Other Reactor Plant Equipment

ACCOUNT	TITLE	COSTS[a] (M$)
22.06.01	Maintenance Equipment	58.85
22.06.02	Special Heating System	0.00
22.06.03	Coolant Receiving, Storage and Make-Up System	0.34
22.06.04	Gas System	0.12
22.06.05	Inert Atmosphere System	0.00
22.06.06	Fluid Leak Detection	3.10
22.06.07	Closed Loop Coolant System	2.80
22.06.08	Standby Cooling System	1.70
Total Other Reactor Plant Equipment		66.91

[a]All total costs listed include a design allowance of 35%.

Table 10-21. Maintenance Equipment Costs

MAINTENANCE EQUIPMENT	QUANTITY		TOTAL COST (M$)
Reactor Building			
Reactor Overhead EM Manipulator	1		0.90
Process Module Overhead Manipulator	1		0.90
Coolant Line Handling Machine	1		1.15
RF Duct Handling Machine	1		1.15
Limiter Module Handling Machine	1		1.75
Blanket Sector Handling Machine	2		4.65
Isolation Valve Handling Unit	1		0.70
Universal Remote Maintenance Vehicle	3		7.00
Mobile Servo-Manipulator Vehicle	1		1.75
Steam Generator Tube Inspection Equipment	1		(0.80)
Steam Generator Tube Leak Detector	1	Contracted	(0.60)
Steam Generator Tube-Plugging Equipment	1	Services	(1.70)
Steam Cenerator Replacement Equipment	1		(6.40)
Airlock Door Seal Replacement Equipment	-		0.35
Remote Viewing Equipment	-		0.80
Crane Bay Maintenance Equipment	-		3.50
Special Remote Tools	-		2.30
Holding Stands, Lift Fixtures and Slings	-		3.50
Auxiliary Lighting	-		0.25
	Reactor Subtotal		30.65
Hot Cell Building			
EM Manipulator	3		1.75
Remote Viewing Equipment	-		0.30
Auxiliary Lighting	-		0.25
Disassembly/Reassembly Stands, Fixtures	-		5.80
and Slings	-		.60
Crane Bay Maintenance Equipment	-		2.50
Test Fixtures	-		1.75
	Hot Cell Subtotal		12.95
Maintenance Equipment Subtotal			43.60
Design Allowance (35%)			15.25
			58.85

As in STARFIRE, no Special Heating is required. The Coolant Receiving, Storage and Make-up System remains the same size and serves the same requirements. The Gas System is comprised of the systems to accomplish the inert CO_2 atmosphere in the Reactor Building. The Inert Atmosphere has no specific hardware requirement so no costs are included in this account. Fluid Leak Detection is similar to STARFIRE, as is the Closed Loop Coolant System and the Standby Cooling System. The final cost for the Other Reactor Plant Equipment cost is:

$$C_{22.06} = \$66.91M$$

10.3.3.14 Instrumentation and Control (Account 22.07)

Since the DEMO represents an experimental or developmental device, the instrumentation and control (I&C) needs will exceed the requirements of a commercial machine especially in the areas of monoritoring, data acquisition and diagnostics. The PACE reactor I&C costs will include all reactor I&C equipment necessary to monitor and control the reactor and the reactor equipment. All the costs associated with diagnostic and data acquisition functions for the reactor and/or experiments are considered to be Operation-Technology Support costs and will not be included in this cost. Table 10-22 lists the general PACE I&C areas considered along with an estimate of the cost required. The reactor I&C equipment is increased substantially over the STARFIRE estimate, reflecting more local analysis and instrumentation requirements. Also the monitoring system estimate is doubled to account for an increased data base, displays and sequencing systems. The instrumentation costs are held approximately equal because some of the instrumentation needs can be satisfied by the data acquisition system. Since the I&C system requirements have not been thoroughly analyzed and appropriate hardware selected and/or designed, a significant design allowance of 40% was levied on this system. This results in a total PACE cost of $39.20M with a likely data acquisition and diagnostic system cost of the same magnitude. These costs are significantly higher than published EBT-P or TFTR costs, which may be indicative of lesser I&C system requirements for those experiments. On the other hand, the FED I&C estimate is roughly double the DEMO cost which may include the data acquisition and diagnostic function. Considering these bounds, the DEMO cost estimate seems to be a reasonable value.

$$C_{22.07} = \$39.20M$$

Table 10-22. Reactor Instrumentation and Control System Costs

ACCOUNT	TITLE	COST (M$)
22.07.01	Reactor I&C Equipment	10.00
	- Local Controllers	
	- Communication Concentrators	
	- Local Analysis/Control	
	- Communication Control	
	- Plasma Instrumentation	
22.07.02	Monitoring Systems	4.00
	- Data Base and Network Communication	
	- Displays and Controls	
	- Sequencing System	
	- Alarm/Monitoring	
	- Remote Access w/Communication Link	
22.07.03	Instrumentation and Transducers	14.00
	- Reactor Instrumentation	
	- Remote Handling Equipment	
	Subtotal	28.00
	Design Allowance (40%)	11.20
	Total Instrumentation & Control Costs, $C_{22.07}$ =	39.20

10.3.3.15 Reactor Spare Parts Allowance (Account 22.98)

The need for spare parts to maintain the reactor in a ready condition is a necessary function, but the cost allowance for this function is not included in the PACE costs but is considered to be in the costs associated with the Operations - Technology Support Costs. However, to gain some insight into the relative costs involved, a cost estimate for spare parts was calculated but not included in the PACE costs.

Table 10-23 lists the major cost elements for spare parts and for all other spare parts, an allowance of two percent is assumed. The estimated lifetime of the major elements are largely unknown at this time but the values shown give an

indication of the magnitude of the times involved. The total cost estimated for this account is:

$$C_{22.98} = (\$76.43M)$$

Table 10-23. Cost of Reactor Plant Equipment Spare Parts

MAJOR COMPONENTS	ESTIMATED LIFETIME (YRS)	QUANTITY IN SERVICE	SPARE PARTS QUANTITY	COST OF SPARES (M$)	QUANTITY ANNUALLY REPLACED
Blanket Sector	6-7	8	4	39.60	1 or 2
Limiter Module	2	8	5	4.90	4
REB Diode (Antenna)	1	2	2	3.42	2
Vacuum Pump	2	8	5	4.80	4
Vacuum Pump Isolation Valve	2	16	10	11.00	8
Subtotal Cost				63.72	
2% Allowance of Reactor Plant Equipment				12.71	
Total Reactor Plant Equipment Spare Parts Cost, $C_{22.98}$				= (76.43)[a]	

[a]PACE Costs do not include an allowance for spare parts or operational replacements, so these costs are shown only for comparison.

10.3.4 Turbine Plant Equipment (Account 23)

This account encompasses all the costs associated with the Turbine Plant Equipment. The DEMO thermal energy is considerably reduced from the STARFIRE power level (1147 versus 3800 MW primary coolant). The costs do not scale down directly with the thermal power level because many elements are required regardless of power level. Other costs are adjusted downward, but not in direct proportion. Most of the equipment is of conventional design and no design allowance is assumed. A contingency allowance of 20% is assumed to cover unexpected cost increases. The total PACE cost of the Turbine Plant Equipment is:

$$C_{23} = \$198.08M$$

10.3.4.1 Turbine Generators (Account 23.01)

The thermal power to the turbine generator set is 1145 MW, operating at a 33.6% efficiency and delivering 385 MW electric at the generator output terminals. An estimate was obtained on this specific equipment from a supplier and represents a current cost estimate. The cost includes the turbine generator set, the lube oil conditioning system and the labor costs to install it. The total cost is:

$$C_{23.01} = \$73.10M$$

10.3.4.2 Main Steam System (Account 23.02)

The lower steam system requirements and capacities are driven by the lower thermal powers handled. The steam conditions are identical to STARFIRE (299°C at 6.3 MPa). The cost for this system was adjusted to reflect the DEMO requirements and is:

$$C_{23.02} = \$2.41M$$

10.3.4.3 Heat Rejection Systems (Account 23.03)

This system also is similar to the design of STARFIRE but is smaller in capacity. The adjusted cost is:

$$C_{23.03} = \$22.05M$$

10.3.4.4 Condensing Systems (Account 23.04)

This system handles the 762 MW of steam exhausted from the turbine. Principal elements are the main condenser and tubes, the condensate pump, steam primary pump and steam air injector. The cost of this system is estimated to be:

$$C_{23.04} = \$12.59M$$

10.3.4.5 Feed Water Heating System (Account 23.05)

This system is similar in function to that of STARFIRE but the source of heat is not the limiter as was the case in STARFIRE. The DEMO limiter coolant water was judged to be too low a temperature to be useful in providing feedwater heating and thus the feedwater heat is obtained from the primary coolant system. The adjusted cost for this system is:

$$C_{23.05} = \$6.35M$$

10.3.4.6 Other Turbine Plant Equipment (Account 23.06)

Principal cost elements in this account include gas storage, turbine plant cooling water systems, chemical treatment, condensate and steam blowdown systems and the associated process piping. Some of the elements scale with the power level while others are invariant. The adjusted cost for this system is:

$$C_{23.06} = \$37.56M$$

10.3.4.7 Balance of Plant Instrumentation and Control Equipment (Account 23.07)

This account includes all the instrumentation and control for the BOP equipment. It was assumed that there would be no change in requirements and the DEMO BOP I&C needs would be identical to that of STARFIRE. Thus the escalated costs are:

$$C_{23.07} = \$11.01M$$

10.3.5 Electric Plant Equipment (Account 24)

The Electric Plant Equipment includes the costs associated with the switchgear for the generator circuits and station service, the station service equipment, the switch boards, the protective equipment, the electrical structures and wiring containers, the power and control wiring and the lighting for the complete plant. Table 10-24 lists the individual accounts and their adjusted costs. The Switchgear, Station Service Equipment and the Power and Control Wiring accounts were adjusted to reflect a reduced capacity requirement while

the remaining accounts are only adjusted for inflation effects. The total cost for the Electrical Plant Equipment is:

$$C_{24} = \$117.38M$$

10.3.6 Miscellaneous Plant Equipment (Account 25)

This account includes systems which support the entire power plant, transportation and lifting equipment, air and water services, communications, furnishings and fixtures. Table 10-25 lists the cost accounts for this category. The transportation and lifting equipment is reduced somewhat because the crane in the Reactor Building was decreased from 600 tonnes to 500 tonnes. The Air and Water Service System is also decreased in cost to reflect reduced requirements. The total cost for this account is:

$$C_{25} = \$45.88M$$

Table 10-24. Costs of the Electric Plant Equipment

ACCOUNT	TITLE	COST (M$)
24.01	Switchgear	9.08
24.02	Station Service Equipment	16.23
24.03	Switchboards	9.08
24.04	Protective Equipment	2.56
24.05	Electrical Structures and Wiring Containers	18.42
24.06	Power and Control Wiring	32.49
24.07	Electrical Lighting	9.96
24.98	Spare Parts Allowance	(1.08)
24.99	Contingency Allowance (20%)	19.56
	Total	117.38

[a]Spare Parts Costs are not included in PACE costs.

Table 10-25. Costs of the Miscellaneous Plant Equipment

ACCOUNT	TITLE	COST (M$)
25.01	Transportation and Lifting Equipment	17.91
25.02	Air and Water Service Systems	11.72
25.03	Communications	7.66
25.04	Furnishings and Fixtures	0.94
25.98	Spare Parts Allowance	(0.55)[a]
25.99	Contingency Allowance (20%)	7.65
	Total	45.88

[a]Spare Parts Allowance costs are not included in PACE costs.

10.3.7 Special Materials (Account 26)

This account includes the cost of special (non-fuel and non-structural) materials and special (other than light water) heat transfer fluids or gases. These materials will be purchased and introduced to the reactor just prior to plant startup. These costs are estimated to be:

$$C_{26} = \$0.30M$$

REFERENCES FOR CHAPTER 10

1. S. C. Schulte, T. L. Wilke, and J. R. Young, "Fusion Reactor Design Studies - Standard Accounts for Cost Estimates," Battelle Pacific Laboratory, PNL-2648 (May 1978).

2. C. C. Baker, et al., "STARFIRE - A Commercial Tokamak Fusion Power Plant Study," Argonne National Laboratory, ANL/FPP-80-1 (September 1980).

3. S. C. Schulte, W. E. Bickford, C. E. Willingham, S. K. Ghose, H. G. Walker, "Fusion Reactor Design Studies - Standard Unit Costs and Cost Scaling Rules," Battelle Pacific Laboratory, PNL-2987 (September 1979).

4. C. A. Flanagan, D. Steiner, L. E. Smith, FED Center Staff, "Fusion Engineering Device Design Description," ORNL/TM-7948/V1 (December 1981).

5. J. W. Davis, Private Communications, MDAC, 30 August 1982.

Distribution for ANL/FPP-82-1

Internal:

M. Abdou
C. Baker
E. Beckjord
C. Boley
J. Brooks
F. Cafasso
Y. Cha
R. Clemmer
D. Ehst
K. Evans
P. Finn
Y. Gohar
L. Greenwood
D. Gruen
A. Hassanein
C. Johnson
J. Jung
M. Kaminsky
S. Kim
Y-K. Kim
R. Kustom
R. Lari
R. Leonard
Y. Liu
B. Loomis
S. Majumdar
V. Maroni
R. Mattas
B. Misra
W. Praeg
J. Roberts
D. Smith
R. Smith
M. Steindler
H. Stevens
L. Turner
FPP Files (50)
ANL Contract File
ANL Libraries (2)
ANL Patent Dept.
TIS Files (6)

External:

DOE-TIC, for distribution per UC-20 and -20d (128)
Manager, Chicago Operations Office, DOE
University of Chicago Special Committee for the Fusion Program:
- S. Baron, Burns & Roe, Inc.
- H. Forsen, Bechtel National, Inc.
- M. Lubin, Standard Oil Company of Ohio
- G. Miley, University of Illinois
- P. Reardon, Princeton Plasma Physics Laboratory
- D. Steiner, Rensselaer Polytechnic Institute
- K. Symon, University of Wisconsin
- K. Thomassen, Lawrence Livermore National Laboratory

S. Abdel-Khalik, University of Wisconsin
N. Amherd, Electric Power Research Institute
J. Anderson, Los Alamos National Laboratory
D. Anthony, General Electric Company
G. Arvey, The Ralph M. Parsons Company
V. Bailey, Pulse Sciences, Inc.
K. Barry, The Ralph M. Parsons Company
W. Bauer, Sandia National Laboratory-Livermore
S. Berk, DOE/Office of Fusion Energy
M. Billone, Northwestern University
W. Bird, University of Texas-Austin
K. Black, McDonnell Douglas Astronautics Company
R. Blanken, DOE/Office of Fusion Energy
P. Bonanos, Princeton Plasma Physics Laboratory
R. Boom, University of Wisconsin
R. Botwin, Grumman Aerospace Corporation
W. Briggs, McDonnell Douglas Astronautics Company
T. Brown, Fusion Engineering Design Center
R. Burk, McDonnell Douglas Astronautics Company
M. Buttram, Sandia National Laboratory-Albuquerque
G. Carlson, Lawrence Livermore National Laboratory

J. Cecchi, Princeton Plasma Physics Laboratory
R. Cherdack, Burns & Roe, Inc.
J. Chi, Westinghouse Electric Corporation
J. Citrolo, Princeton Plasma Physics Laboratory
M. Clarke, Combustion Engineering
M. Cohen, DOE/Office of Fusion Energy
D. Cohn, Massachusetts Institute of Technology
R.Conn, University of California-Los Angeles
B. Coppi, Massachusetts Institute of Technology
B. Cramer, Fusion Engineering Design Center
J. Crocker, EG&G Idaho, Inc.
J. Davis, McDonnell Douglas Astronautics Company
M. Davis, Sandia National Laboratory-Albuquerque
S. Dean, Fusion Power Associates
D. DeFreece, McDonnell Douglas Astronautics Company
J. de la Mora, The Ralph M. Parsons Company
C. Dillow, McDonnell Douglas Astronautics Company
D. Dingee, Battell-Pacific Northwest Laboratory
D. Driemeyer, McDonnell Douglas Astronautics Company
G. Emmert, University of Wisconsin
J. Fillo, Brookhaven National Laboratory
C. Flanagan, Fusion Engineering Design Center
G. Fuller, Fusion Engineering Design Center
J. Gilleland, General Atomic Company
R. Gold, Westinghouse Electric Corporation
J. Gordon, TRW, Inc.
G. Haas, DOE/Office of Fusion Energy
S. Harkness, Bettis Atomic Power Laboratory
C. Head, DOE/Office of Fusion Energy
H. Helava, Physics International Company
N. Hoffman, Energy Technology Engineering Center
G. Hollenberg, Hanford Engineering Development Laboratory
J. Holmes, Hanford Engineering Development Laboratory
P. Hsu, EG&G Idaho, Inc.
S. Huang, The Ralph M. Parsons Company
D. Jassby, Princeton Plasma Physics Laboratory
C. Karney, Princeton Plasma Physics Laboratory
M. Kazimi, Massachusetts Institute of Technology
H. Klumpe, The Ralph M. Parsons Company
R. Krakowski, Los Alamos National Laboratory
D. Kummer, McDonnell Douglas Astronautics Company
B. Kusse, Cornell University
J. Leloudis, The Ralph M. Parsons Company
L. Lidsky, Massachusetts Institute of Technology
P. Lykoudis, Purdue University
J. Maniscalco, TRW, Inc.
H. Mantz, McDonnell Douglas Astronautics Company
L. Masson, EG&G Idaho, Inc.
D. Mattox, Sandia National Laboratory-Albuquerque
C. Maynard, University of Wisconsin
D. McAlees, Exxon Nuclear Corporation
R. McGrath, Pennsylvania State University
A. Mense, McDonnell Douglas Astronautics Company
B. Merrill, EG&G Idaho, Inc.

D. Metzler, Fusion Engineering Design Center
D. Mikkelsen, Princeton Plasma Physics Laboratory
D. B. Montgomery, Massachusetts Institute of Technology
G. D. Morgan, McDonnell Douglas Astronautics Company
G. Nardella, DOE/Office of Fusion Energy
A. Opdenaker, DOE/Office of Fusion Energy
R. Parker, Massachusetts Institute of Technology
M. Peng, Fusion Engineering Design Center
C. Petty, University of Missouri-Columbia
S. Piet, EG&G Idaho, Inc.
D. Post, Princeton Plasma Physics Laboratory
G. Proulx, Physics International Company
T. Reuther, DOE/Office of Fusion Energy
F. Ribe, University of Washington
G. Rohwein, Sandia National Laboratory-Albuquerque
R. Rose, Westinghouse Electric Corporation
S. Rosenwasser, INESCO, Inc.
P. Rutherford, Princeton Plasma Physics Laboratory
M. Sabado, Ebasco Services, Inc./Princeton Plasma Physics Laboratory
P. Sager, Fusion Engineering Design Center
J. Schmidt, Princeton Plasma Physics Laboratory
K. Schultz, General Atomic Company
F. R. Scott, Electric Power Research Institute
J. L. Scott, Oak Ridge National Laboratory
D. L. Sevier, General Atomic Company
T. Shannon, Fusion Engineering Design Center
C. Singer, Princeton Plasma Physics Laboratory
P. Spampinato, Fusion Engineering Design Center
W. Stacey, Georgia Institute of Technology
L. Stewart, Exxon Nuclear Corporation/Princeton Plasma Physics Laboratory
P. Stone, DOE/Office of Fusion Energy
V. Stubblefield, McDonnell Douglas Astronautics Company
I. Sviatoslavsky, University of Wisconsin
D. K. Sze, University of Wisconsin
W. Terry, Purdue University
A. Tobin, Grumman Aerospace Corporation
C. Trachsel, McDonnell Douglas Astronautics Company
L. Waganer, McDonnell Douglas Astronautics Company
K. Wakefield, Princeton Plasma Physics Laboratory
H. Willenberg, Mathematical Sciences Northwest, Inc.
G. Woodruff, University of Washington
H. Woodson, University of Texas-Austin
N. Young, Ebasco Services, Inc.
Library, Max Planck Institute fur Plasmaphysik, Fed. Rep. of Germany
Library, Culham Laboratory, United Kingdom
Library, Centre for Nuclear Studies, Grenoble, France
Library, Centre for Nuclear Studies, Fontenay-aux-Roses, France
Library, Centre for Nuclear Studies, Saclay, France
Library, Centre de Recherches en Physique des Plasma, Lausanne, Switzerland
Library, FOM-Institutu voor Plasma-Fysika, The Netherlands
Library, Comitato Naxionale per L'Energia Nucleare, Frascatti, Italy
Library, Joint Research Centre, Ispra Establishment, Ispra, Italy
Library, Japan Atomic Energy Research Institute
T. Drolet, Ontaria Hydro, Toronto, Ontario, Canada